

HABITAT CENTER
920 W. DIMOND L.I.S.
ANCHORAGE, ALASKA 99502
Est. 1997

Environmental Assessment of the Alaskan Continental Shelf

Annual Reports of Principal Investigators
for the year ending March 1978

Volume IX. Transport



U.S. DEPARTMENT OF COMMERCE
National Oceanic and Atmospheric Administration



U.S. DEPARTMENT OF INTERIOR
Bureau of Land Management

VOLUME I	RECEPTORS -- MAMMALS BIRDS
VOLUME II	RECEPTORS -- BIRDS
VOLUME III	RECEPTORS -- BIRDS
VOLUME IV	RECEPTORS -- FISH, LITTORAL, BENTHOS
VOLUME V	RECEPTORS -- FISH, LITTORAL, BENTHOS
VOLUME VI	RECEPTORS -- MICROBIOLOGY
VOLUME VII	EFFECTS
VOLUME VIII	CONTAMINANT BASELINES
VOLUME IX	TRANSPORT
VOLUME X	TRANSPORT
VOLUME XI	HAZARDS
VOLUME XII	HAZARDS
VOLUME XIII	DATA MANAGEMENT Resources

ARLIS

Library & Information Services
Anchorage, Alaska

Environmental Assessment of the Alaskan Continental Shelf

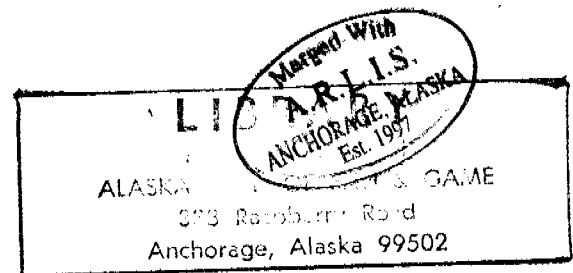
GC
85.2
.A4
E57
1978
V.9

Annual Reports of Principal Investigators
for the year ending March 1978

Volume IX. Transport

Outer Continental Shelf Environmental Assessment Program
Boulder, Colorado

October 1978



U.S. DEPARTMENT OF COMMERCE
National Oceanic and Atmospheric Administration

U.S. DEPARTMENT OF INTERIOR
Bureau of Land Management

ARLIS
Alaska Resources
Library & Information Services
Anchorage, Alaska

DISCLAIMER

The National Oceanic and Atmospheric Administration (NOAA) does not approve, recommend, or endorse any proprietary product or proprietary material mentioned in this publication. No reference shall be made to NOAA or to this publication furnished by NOAA in any advertising or sales promotion which would indicate or imply that NOAA approves, recommends, or endorses any proprietary product or proprietary material mentioned herein, or which has as its purpose an intent to cause directly or indirectly the advertised product to be used or purchased because of this publication.

ACKNOWLEDGMENT

These annual reports were submitted as part of contracts with the Outer Continental Shelf Environmental Assessment Program under major funding from the Bureau of Land Management.

TRANSPORT

Contents

<u>RU #</u>	<u>PI - Agency</u>	<u>Title</u>	<u>Page</u>
048	Barrick, D. - Wave Propagation Lab/ERL/NOAA Boulder, CO	HF Surface-Current Mapping Radar 1977 Alaskan Operations --- Lower Cook Inlet	1
091	Aagaard, K. - Univ. of Washington Seattle, WA	Current Measurements in Possible Dispersal Regions of the Beaufort Sea	40
138	Schumacher, J. - Pacific Marine et al. Environmental Lab/NOAA Seattle, WA	Gulf of Alaska Shelf Circulation	61
140	Galt, J. - PMEL/NOAA et al. Seattle, WA	Alaska Numerical Modeling	214
141/549	Coachman, L. - Univ. of WA Kinder, T. Seattle, WA Schumacher, J.-PMEL/NOAA Charnell, R. Seattle, WA	Bristol Bay Oceanographic Processes (B-BOP)	327
151	Aagaard, K. - Univ. of WA Seattle, WA	STD Measurements in Possible Dispersal Regions of the Beaufort Sea	575
217	Hansen, D. - Atlantic Oceanographic & Meteorological Labs, NOAA Miami, FL	Lagrangian Surface Current Measurements on the Outer Continental Shelf	590
244	Barry, R. - Inst. of Arctic & Alpine Research Univ. of Colorado Boulder, CO	Study of Climatic Effects on Fast Ice Extent and Its Seasonal Decay along the Beaufort-Chukchi Coasts	604
250	Shapiro, L. - Geophysical Inst. et al. Univ. of Alaska Fairbanks, AK	Mechanics of Origin of Pressure Ridges, Shear Ridges and Hummock Fields in Landfast Ice	720

ANNUAL REPORT

Research Unit #48

HF SURFACE-CURRENT MAPPING RADAR
1977 ALASKAN OPERATIONS --- LOWER COOK INLET

Donald E. Barrick

NOAA/ERL/Wave Propagation Laboratory
Boulder, Colorado 80302

April 1, 1977 - March 31, 1978

HF SURFACE-CURRENT MAPPING RADAR
1977 ALASKAN OPERATIONS --- LOWER COOK INLET

ANNUAL REPORT

Research Unit #48

Donald E. Barrick

NOAA/ERL/Wave Propagation Laboratory

Boulder, Colorado 80302

SUMMARY

The objectives of our initial Alaskan experiments in the summer of 1977 were twofold: (1) to demonstrate the feasibility and utility of a transportable HF radar system for operational near-real-time mapping of surface currents in remote coastal areas, and (2) to gather environmental baseline data on surface circulation around Kachemak Bay in the Lower Cook Inlet.

This brief report answers primarily the first objective. By presenting sample radar-produced current maps at two opposing periods in the tidal cycle and comparing these data with drifter buoy velocity measurements, we herein establish the credibility of the claim that such systems can play a major role in future coastal current-data gathering studies of this nature. In particular, our results show that: (1) a single current-vector map covering thousands of square kilometers can be produced after 15 minutes operation; (2) at least three orders of magnitude more data can be gathered in a given twelve-hour period than by any alternative technique; (3) the system rms error is at worst one-half knot (current velocity), and most likely considerably better. In addition, we have made current vector maps over a 24 hour period and have decomposed the tidal currents into the 12 and 24 hour period components, the scatter in this fit was very small, less than 8 cm/sec std deviation for max tidal amplitudes of ± 80 cm/sec.

I. SITE LOGISTICS AND LOCATIONS

The radar equipment for both sites was transported to Alaska in our Aspen trailer, pulled by our Dodge van; this gear left Boulder for Seattle on May 23. From Seattle these two vehicles were transported by ferry, arriving Anchorage on June 2. In Anchorage a four-wheel-drive vehicle was rented, along with an additional house trailer. The radar system was given a preliminary inspection before leaving Anchorage to verify that no obvious damage had been incurred in shipping. Arrangements were made to have a Sears utility shed (approximately \$300 retail cost) shipped to Anchor Point to provide additional operating space in the field.

The vehicles and equipment then left Anchorage June 6 for Anchor Point on the Kenai Peninsula (about 20 miles north of Homer). The Sears shed was erected at this site. All of the radar and computer gear were exercised at Anchor Point for several days, verifying proper performance. Then the Aspen trailer — pulled by the rented vehicle — left for Homer; from there this equipment was transported by ferry to Seldovia on June 14. Hardware and software engineers went through a series of tests; these are necessary to ensure that subsequent radar operations and data gathering will produce valid results. The location of the Anchor Point site was Lat. $59^{\circ}46'12''N$, Long. $151^{\circ}51'53.4''W$; that of Seldovia was Lat. $59^{\circ}27'27.5''N$, Long. $151^{\circ}42'30''W$. Figure 1 is a general map of the area, showing the two sites (as dots) at Anchor Point and Seldovia.

A Mini-Ranger system was rented and installed at three sites in this area; this was necessary for later comparisons of radar-deduced surface currents with simultaneous drifter measurements. These sites were surveyed in by LCDR. John Murphy of the NOAA Corps. They were located near Anchor Point (Lat. $59^{\circ}46'11.148''N$, Long. $151^{\circ}51'53.411''W$); at Bluff Point (Lat. $59^{\circ}39'37.645''N$, Long. $151^{\circ}39'44.972''W$); and near Seldovia (Lat. $59^{\circ}27'09.854''N$, $151^{\circ}43'08.282''W$). The Mini-Ranger system was used in conjunction with ships tracking drifters during the week of June 26; the system was dismantled and returned to the owner on July 3.

Operations at the two HF radar sites continued through July 15. Beginning on July 16 the gear was repacked for transportation back to Boulder. All of the gear had arrived safely in Boulder by July 28.

II. DATA COLLECTION AND PROCESSING

The first collection of "simultaneous" two-site sea-echo data* commenced on June 18, and continued intermittently through July 15. Several "runs" were made over a complete 12-hour tidal cycle (i.e., high

* Sea-echo data collected nearly simultaneously is required to construct maps with total current vectors.

tide to high tide), with at least two runs over 24 hours. On June 27, 28, 29, 30, and July 1 drifters were tracked within the coverage area of the radar; the radar systems were operated concurrently with these drifter-tracking operations for comparisons.

"Simultaneous" radar site operation in a few cases refers to concurrent operation of each radar, on different frequencies. Because of concerns about possible mutual interference, however, most of our "simultaneous" operations were actually sequential in nature, with one site operating for 8 1/2 minutes (512 seconds) during which the other site was silent. Thus the data that were later combined from both sites were at most recorded ten minutes apart; we consider this sufficiently close to be "simultaneous" in light of the 12-hour tidal cycle.

A typical 512-second recording session at each site actually consists of four 128-second coherent runs. This means that the digitally filtered time series of HF sea echo from each of the four receiving antennas and for each of sixteen range (time-delay) gates are sampled every quarter second (for both in-phase and quadrature receiver channels). Thus one 128-second period for each site actually results in $4 \times 16 \times 4 \times 2 \times 128$ words, each 10-bits in length; this is a total of 65,536 words per 128-second run (or 655,360 bits of data). Five blocks of four such 128-second runs are stored on a single data tape (13 million words or 130 million bits of data), spanning a measurement period of approximately one hour and forty minutes. Over a 12-hour tidal cycle, more than seven tapes per site are recorded for a total of 187 million words. Without question, one such twelve-hour run provides a greater volume of raw data on currents than has been gathered by all nations, over all oceans, in the history of mankind. The point is — having returned from Alaska with a total of ~ 150 such data tapes — we cannot possibly present all of this information sensibly. Thus considerable thought is being given as to how to effectively utilize and interpret this massive amount of data.

The raw time-series data stored on tape are archived in Boulder for later use; these same data were also processed further in the field on our PDP 11/34 minicomputers during hours when the radar is not operating. This post-processing consists of (i) Fourier transforming each of the sixteen 128-second runs for each of the four antennas; (ii) extracting the angle of arrival of the signal from the Fourier transform output (at each frequency) using the four antenna signals; (iii) averaging the current radial velocity component (directly proportional to the Doppler frequency at the Fourier transform output) vs angle of arrival for the four 128-second runs constituting the 8 1/2 minute data block. In this process, angles associated with weak signals are excluded, and angles associated with stronger signals are weighted more heavily in the averaging process. Thus the tape-recorded output of this next processing phase for each 8 1/2-minute block at each radar site is an array of radial current velocities vs range and azimuth angle.

The final phase of processing is the construction of a current vector map. This is done by taking the radial current data from both sites vs polar coordinates (range and azimuth) and combining them trigonometrically at a preset rectangular grid of points spaced 3 x 3 km geographically. Gaps will occasionally occur in the maps where no vectors appear; this happens because the signals from one or both of the two sites fell below a threshold deemed acceptable for quality averaging. Hence these basic current-vector maps often look somewhat sporadic in coverage and random in terms of the current field. Smoothing, interpolation, and spatial averaging techniques can then be used to refine the maps further.

The ultimate combination of averaging, thresholding, weighting (by signal-to-noise ratio), interpolating, and integrating the equation of continuity has by no means yet been optimized. We are still in a learning mode, experimenting with the various processing parameters. The criteria we are using at present to decide when a given processing scheme is superior to previous ones are (i) use of simulated random sea echo in which we know exactly the input current field, and (ii) comparisons with drifter-deduced surface currents. Thus the maps to be shown subsequently should be considered an interim product, by no means representative of our final, more optimal results.

III. SAMPLE PRELIMINARY CURRENT MAPS

Two current maps are selected for display here as Figs. 3 and 4. They were made from data taken July 1. This particular day was chosen because of simultaneous drifter-deduced currents; of all of our ship tracking of drifters, July 1 represented the one day during which the greatest amount of drifter data was obtained over the widest possible area. We recorded, processed, and mapped currents out to only 42 km on July 1 because ship operations were confined to this coverage area.

The first — at the bottom of Fig. 3 — represents the surface currents (as obtained from the computer pen-plotter) at 1120 hours. At this point in the tidal cycle (some 2 1/2 hours before high tide), the current influx into Cook Inlet was near — but had not yet reached — maximum Northward flow. Maximum flow occurred close to 1230 hours, as seen in a subsequent table of drifter velocities. The familiar flow into the Kachemak Bay toward the south is evident, as is the curving Northward flow around the Anchor Point head.

The second — at the top of Fig. 3 — was obtained at 1920 hours, coinciding within minutes of low tide. The outflow from the inlet is clearly in evidence, with maximum surface current velocities near 5 knots. The southward outflow is nearly maximum at this time. There is some indication of a "null zone" in the southernmost portion of the radar coverage area. We have seen this phenomenon in other radar-current maps also, and it has been suggested as real by the Alaska Fish and Game Service based upon some of their investigations. We intend to examine

this region more extensively using sets of our radar data covering this area out to a greater range.

Each of these computer-generated current maps required seventeen minutes of radar-observations to produce (8 1/2 minutes per site). The maps were generated entirely within the computer software, with no human editing done to remove bad points. Four consecutive 128-second runs for each site were averaged, with the resulting radial current vector thresholded and weighted by the signal-to-noise ratio; this eliminates data points associated with weak signals. Both the positive and negative Doppler sidebands were employed, and total semi-averaged current vectors were calculated for each grid point. Finally, data at the grid points were recalculated, averaging the four Doppler sideband combinations together with signal-to-noise ratio weighting and a weighted spatial interpolation. The maps are the result. Again, this processing is by no means yet optimized. Vectors near the baseline joining the sites are especially "noisy" in these maps. Software is nearly completed which improves the accuracy in these regions — as well as extending accurate coverage further out to the north and south. In addition, the removal of an unsymmetrical bias shift in the Doppler sidebands — presently under investigation — appears to improve the accuracy further. As these improvements are made, the resulting current maps available in the near future will be even more meaningful and complete representations of the near-surface circulation than the preliminary but useful maps shown here.

IV. COMPARISON WITH DRIFTERS

The only presently meaningful way to make comparisons with radar-deduced currents during operations is to simultaneously track drifter buoys within the radar coverage area. This was done during the week of June 26. However, the boat that was available through June 29 was so slow (i.e., the "Puffin" from Alaska Fish and Game Service) that it precluded obtaining more than four or five points per day, and these were too close to the baseline between the radar sites to give meaningful comparisons over most of the radar coverage area. Consequently, we rented a faster charter fishing boat on June 30 and July 1. The data from July 1 are presented here for comparison because (i) the time over which drifter data were obtained was longer, from 1130 to 2100 hours on station; (ii) the spatial coverage was much greater than on June 30; (iii) one of the radar sites was inoperable for three hours on June 30 in the middle of the drifter measurements because of gasoline generator problems.

The comparison between radar-deduced currents and drifter-deduced currents is given in Table I. The current vectors for each case are broken into North and West components. Typically; the drifter — drogued with baffle plates 0.5 m deep — was tracked over a 15 minute period, noting its position at the beginning and end of that period.

The mean position of each drifter measurement is shown as an x-y position. The coordinate origin of this system is the center of the line joining the two sites (36 km long), with x pointing along the line toward the North site and y pointing perpendicularly outward from the line in a (generally) Westward direction. With this coordinate system and scale, the position of the various drifter measurements can be estimated quickly if desired.

Table I — spanning nearly 3/4 of a tidal cycle in time — shows the north/south reversal in the current, detected and tracked both by the drifter and by the radar. The radar signal processing used to estimate the surface currents is described at the end of the preceding section. These current-extraction algorithms are presently in a state of optimization, and we expect closer agreement soon based upon improvements. There are a number of physical reasons why radar-deduced surface currents (essentially Eulerian spatial averages over 3 x 3 km areas) can be expected to differ from drifter-deduced surface currents (which are Lagrangian in nature). However, our measurements from Florida show that — due to surface current turbulence — individual drifter estimates of currents within the same 3 x 3 km patch seen by the radar can vary as much as 10-15 cm/s.

A scatter plot of the data represented by Table I is shown in Fig. 4, along with the regression fit to the data. The values of the coefficients "a" and "b" indicate that the regression fit is very close to the desired 45° line. Also, the regression quality coefficient, $r^2 = 0.92$, is quite close to the unity value for a perfect fit.

Table II gives a summary of the means and standard deviations between the radar and drifter currents shown in Table I. The standard deviations of ~ 30 cm/s compare with our Florida drifter analyses, which yielded ~ 27 cm/s. This is nearly one-half knot in both cases. Because of standard deviations between individual drifter measurements within a given radar cell of ~ 10 -15 cm/s, we hesitate to say we compared our radar data with "ground truth." At worst, we can say that — even with our preliminary radar signal processing — the rms radar error does not exceed one-half knot. At best, the radar accuracy may be as good as — or better than — 15-20 cm/s rms when drifter variability is taken into account.

V. CURRENT MAPS OVER A 15 HOUR TIME PERIOD

The first set of figures represent the spatial distribution of surface currents. The contours show regions of equal energy (i.e., $1/2 (u^2 + v^2)$ where u is the N-S component and v is the E-W component). These contours are normalized to an arbitrary value. The time that the data were taken is given in bold numbers in the lower center; the date is shown in the lower right hand side.

Figure 4. 02:30; The flow is almost zero with a small surface-current into Kachemak Bay at the North Entrance. There the velocity resolution appears to be much better than 25 cm/sec., but the contribution due to any vertical and horizontal shear may be important. B. Weber in our group is working on corrections that may give lower limits to the measurement resolution than 25 cm/sec.

Figure 5. 03:30; The flow out of the inlet has increased considerably, with the maximum flow in a line almost West from Anchor Point.

Figure 6. 04:00; The strength of the flow has increased considerably, with the maximum currents on the order of 0.5 m/sec.

Figure 7. 06:00; There is a doubling of the flow rate compared to the 04:00 and the max, again just south of Anchor Point on a westerly line is about 1.0 m/sec. There is a small flow into the North end of Kachemak Bay.

Figure 8. 08:00; The southward flow is decreasing and there does not appear to be any flow into Kachemak Bay.

Figure 9. 08:30; We see a further decrease in the current with a null zone to the south of the center of radar coverage. There is a development of the northerly flow closer to Anchor Point with the main flow still to the south.

Figure 10. 09:30; The southerly flow has decreased even more, the null zone still exists in about the same location, and the northerly flow near Anchor Point has increased in strength.

Figure 11. 11:00; All the flow is toward the North, with a maximum to the S.W. of Anchor Point. The maximum velocity is about 0.5 m/sec.

Figure 12. 12:30; The flow velocity has increased more, with the maximum now several km further to the S.W.W. of Anchor Point.

Figure 13. 14:00; The flow is almost zero, with some flow into Kachemak Bay from the North and West.

Figure 14. 14:30; The flow from the North is increasing, and at 15:00 has increased with the maximum about 20 km from Anchor Point to the S.W.

VI. PROBLEMS ENCOUNTERED/RECOMMENDED CHANGES

One of the major problems encountered is an interference signal. We are presently writing software to handle this and the data will be reprocessed when the programs are completed. The source of this interference is unknown at this time. It may be sky-wave or man-made. Whatever it is, it does not pose an insurmountable problem in the analysis of the data. What should be remembered is that some of the figures presented here may be altered in removing the interference. This interference did not appear in all of the data.

VII. PUBLICATIONS

An article entitled 'Ocean Surface Currents Mapped by Radar' by D. E. Barrick, M. W. Evans, and B. L. Weber has been published in 14 October 1977 issue of Science, Vol. 198.

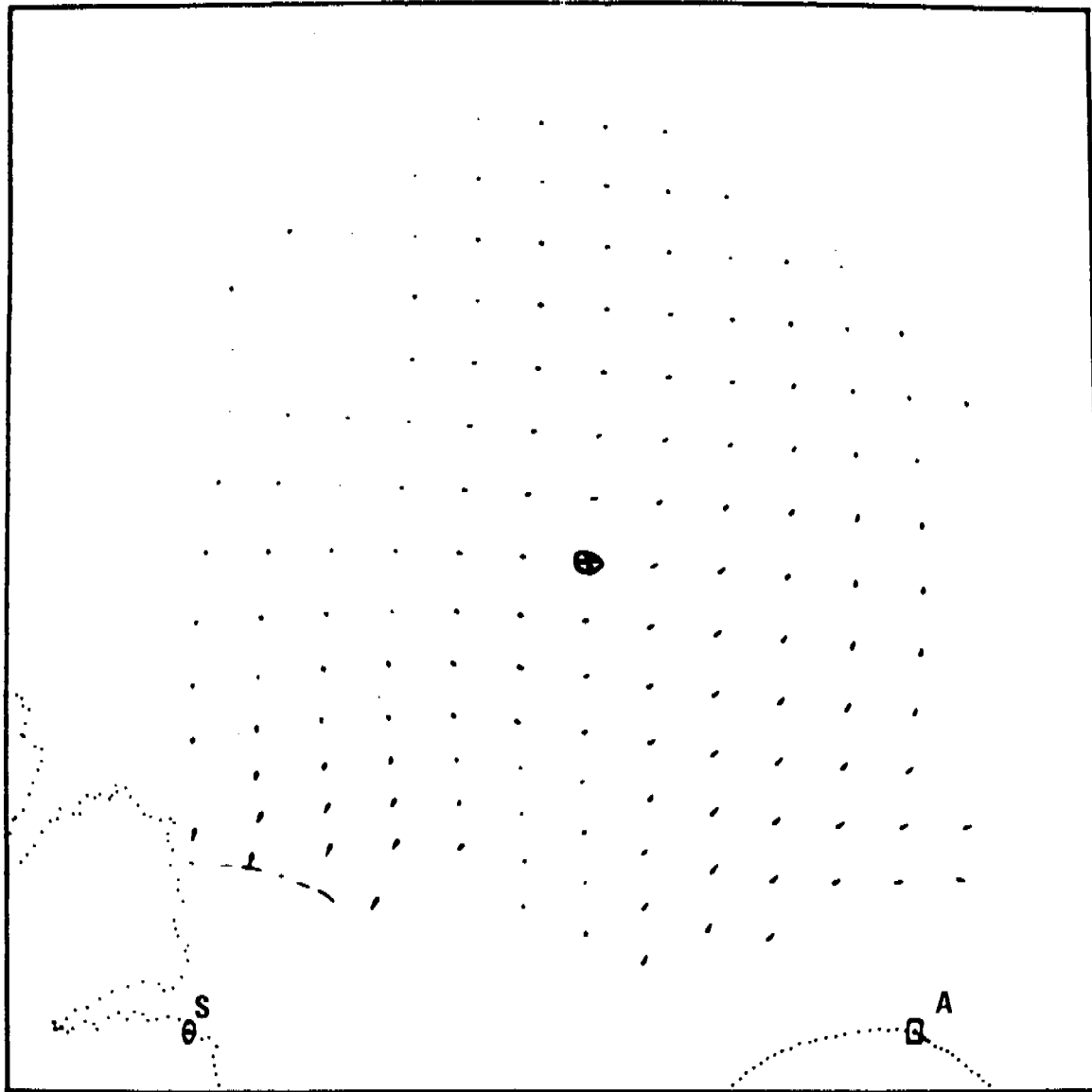
In addition, a paper by Frisch and Weber entitled 'Observations of Surface Tidal Components in Lower Cook Inlet Using a Two-Site HF Doppler Radar System' is in WPL review at the present time. A copy of the draft is included at the end of this report.

VIII. FUTURE WORK

Field Trips. At the time of writing the two radars are being operated at another location in Cook Inlet, namely at Cape Douglas and the south side of Augustine Island. They have taken 4 days of continuous data, for the first 3 days the data were taken every 40 minutes, the 4th day every 3 hours. On the second and third day, a storm came through the area with estimated 40 kt winds at Cape Douglas. The data taking is scheduled for several more days sampled at 3 hour intervals.

Data Analysis. Depending upon the level of funding next fiscal year we plan to 1) increase the coverage area in some locations by using the equation of continuity and 2) analyze the July 78 data for tides, effect of the storm on the surface currents, and 3) collaborate with PMEL for tidal analysis using both the current meter and radar data taken in the same location in Lower Cook Inlet.

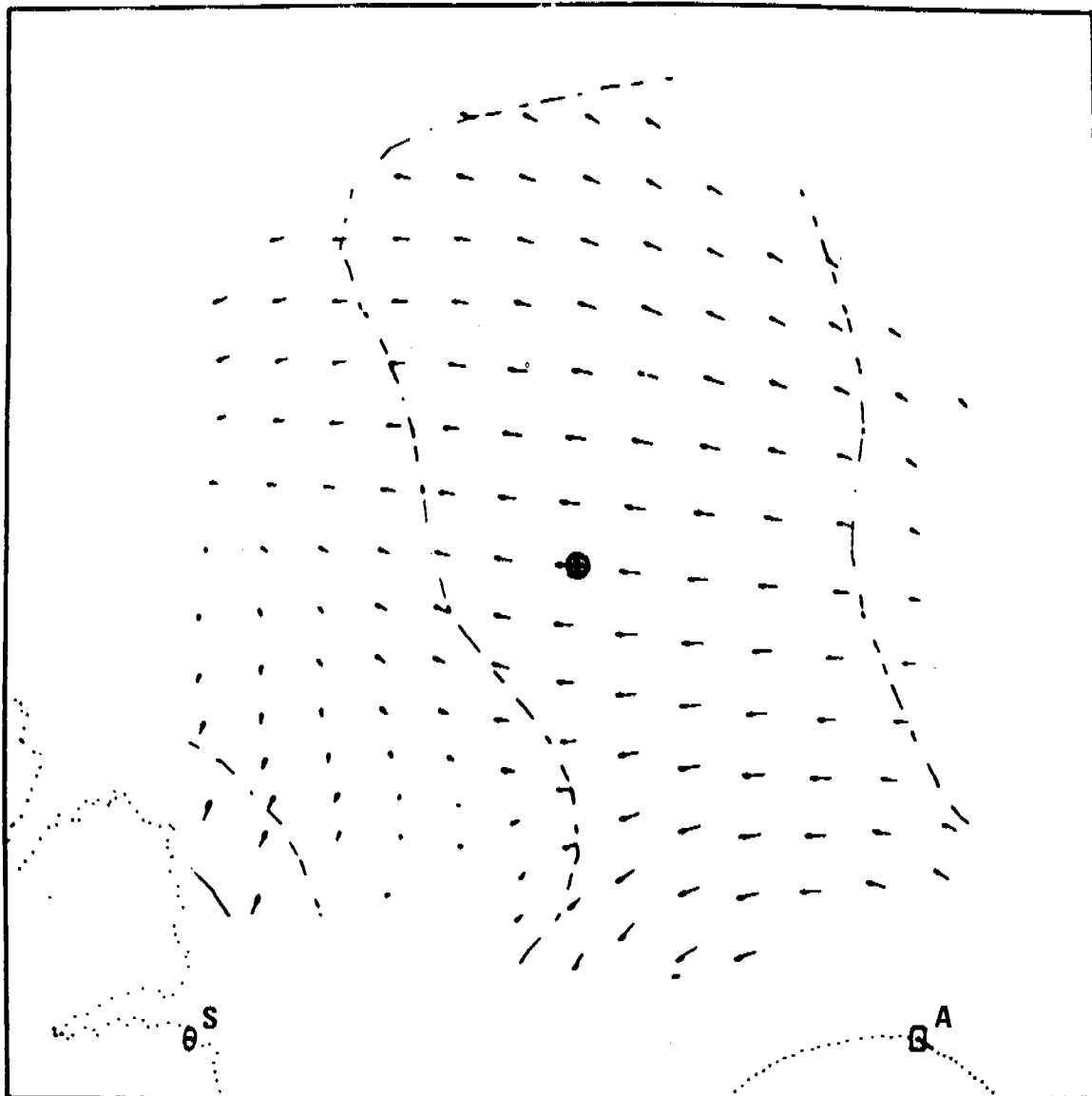
Figure 4. 02:30;



02 : 30

DATE 07/13/77

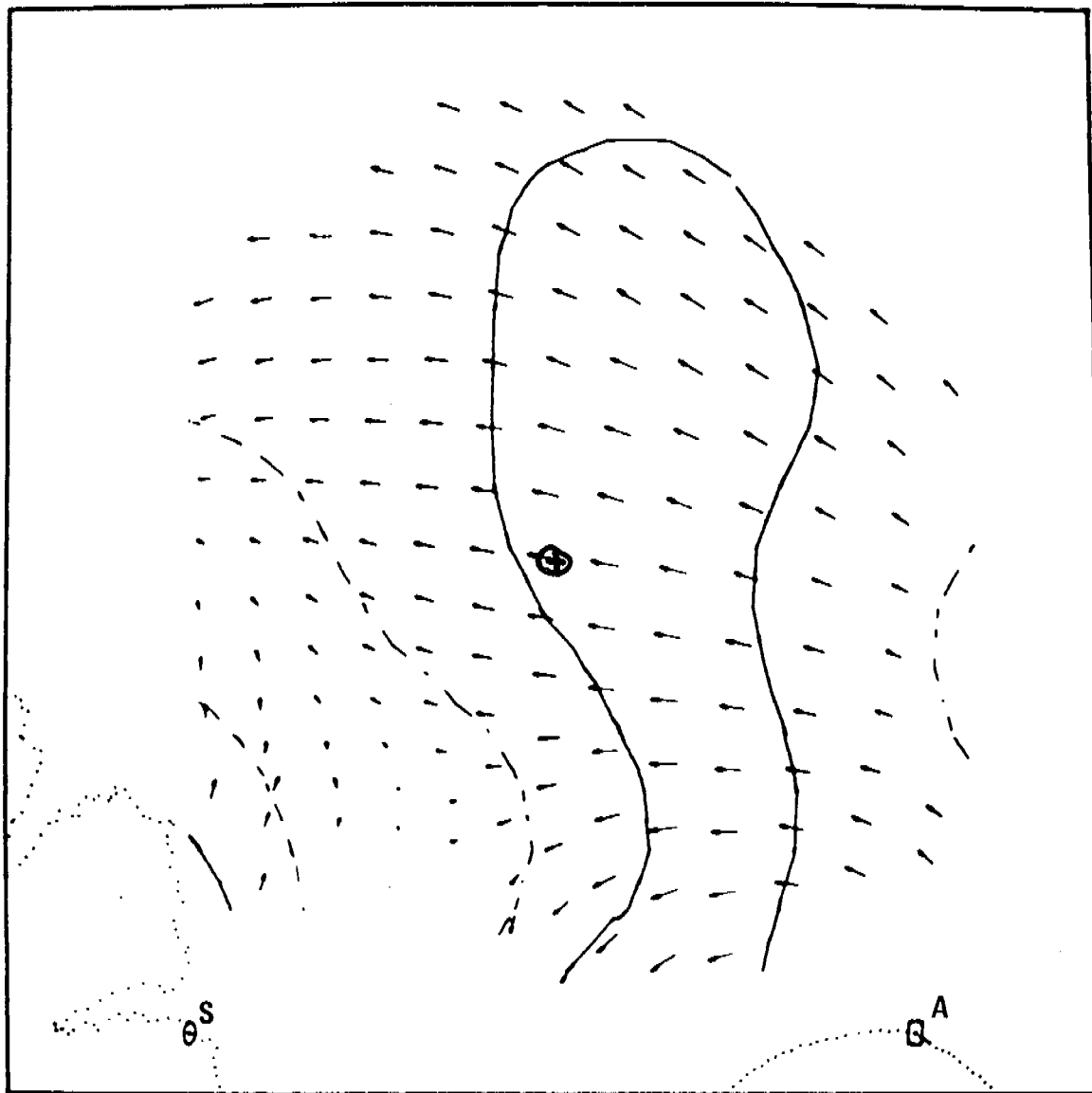
Figure 5. 03:30;



03 : 30

DATE 07/13/77

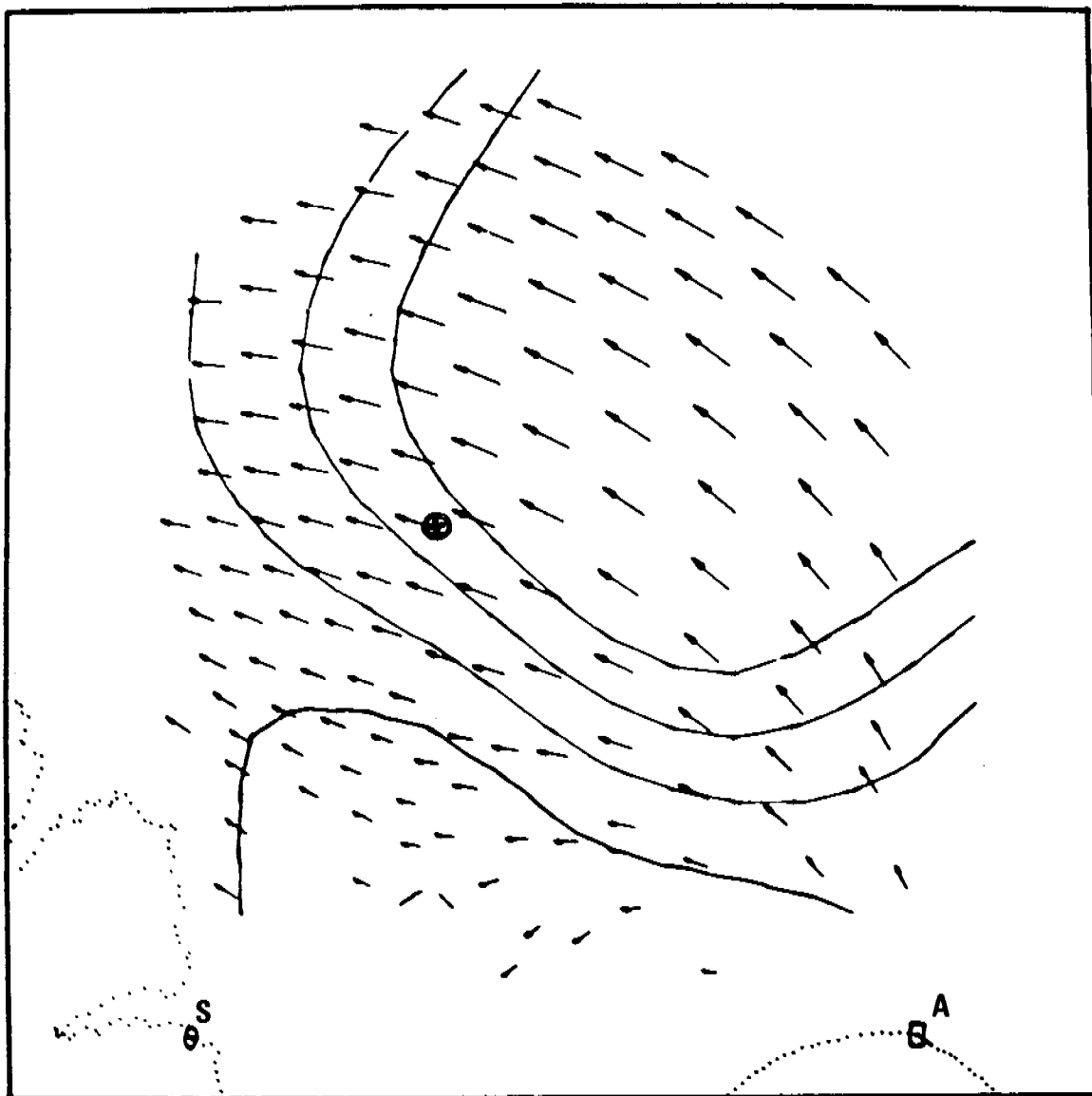
Figure 6. 04:00;



04 : 00

DATE 07/13/77

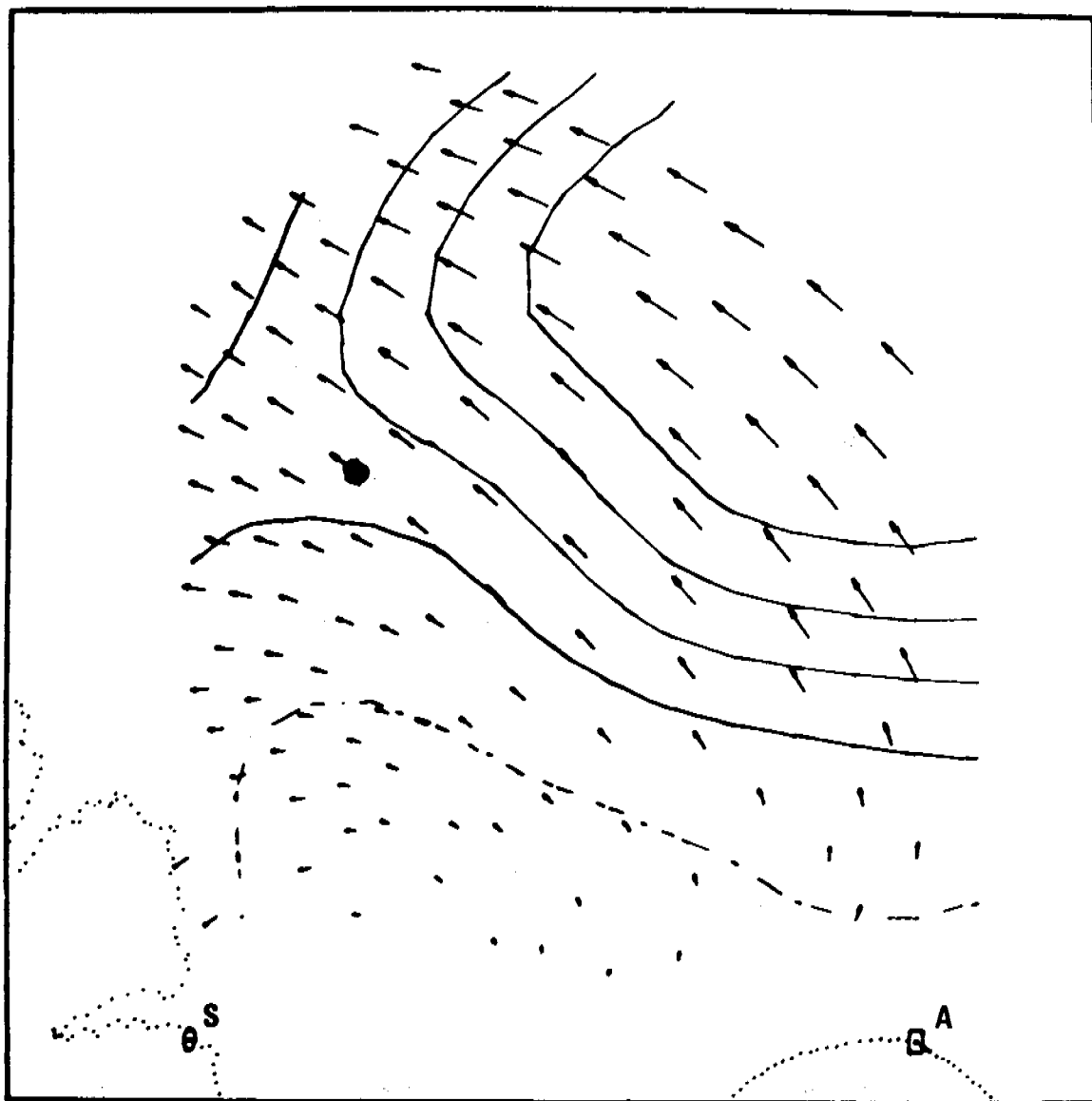
Figure 7. 06:00;



06 : 00

DATE 07/13/77

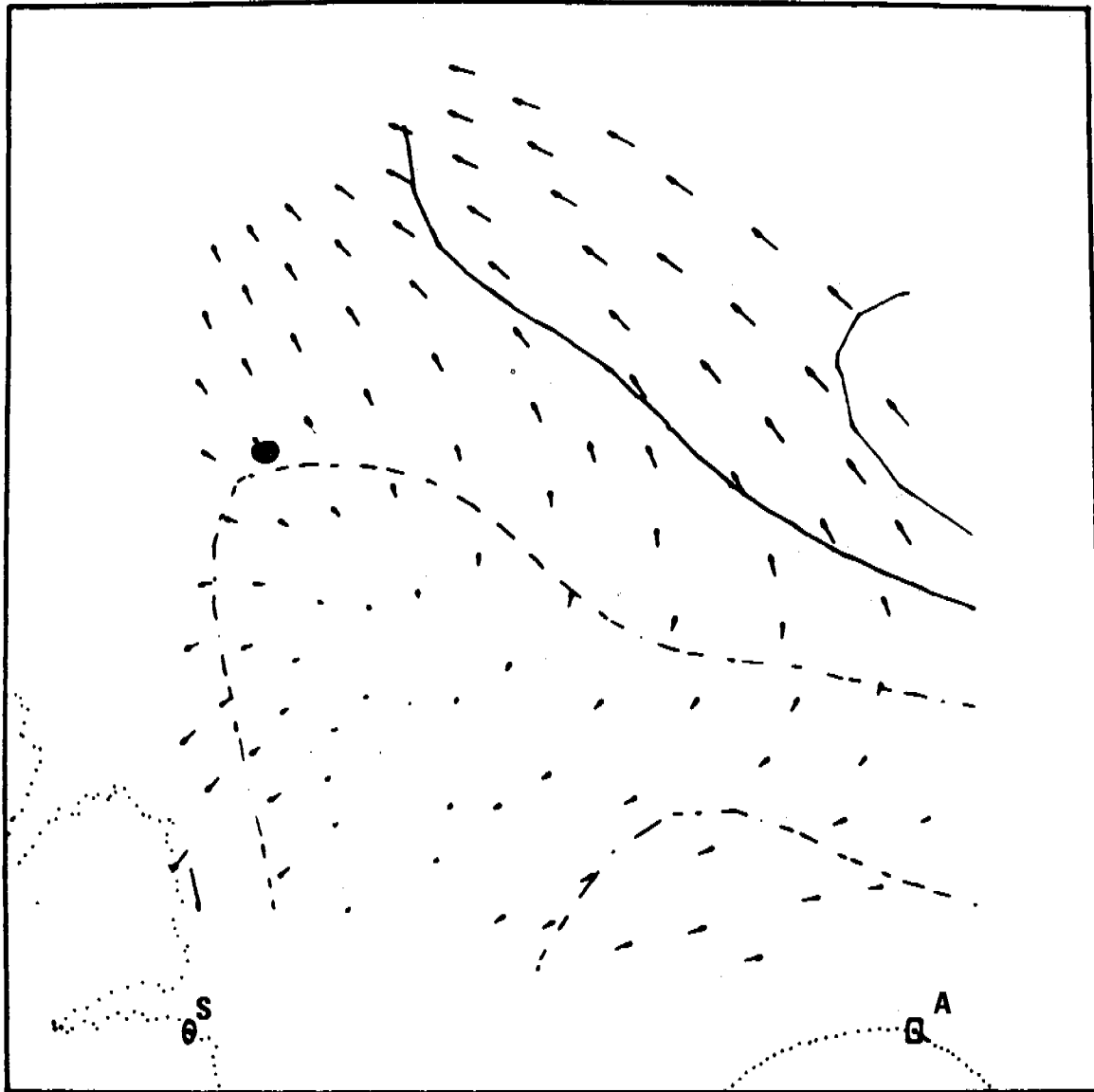
Figure 8. 08:00;



08 : 00

DATE 07/13/77

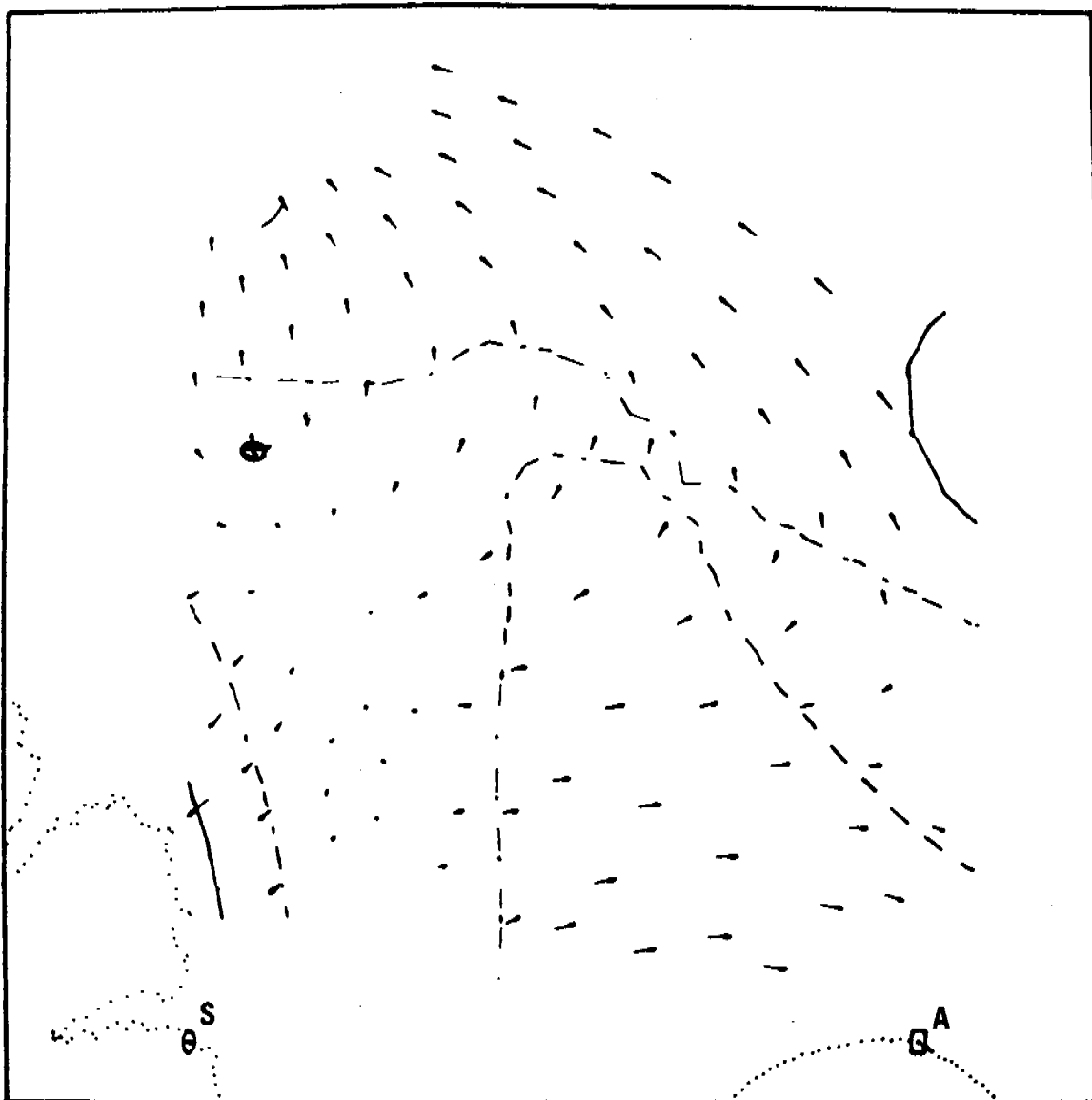
Figure 9. 08:30;



09 : 00

DATE 07/13/77

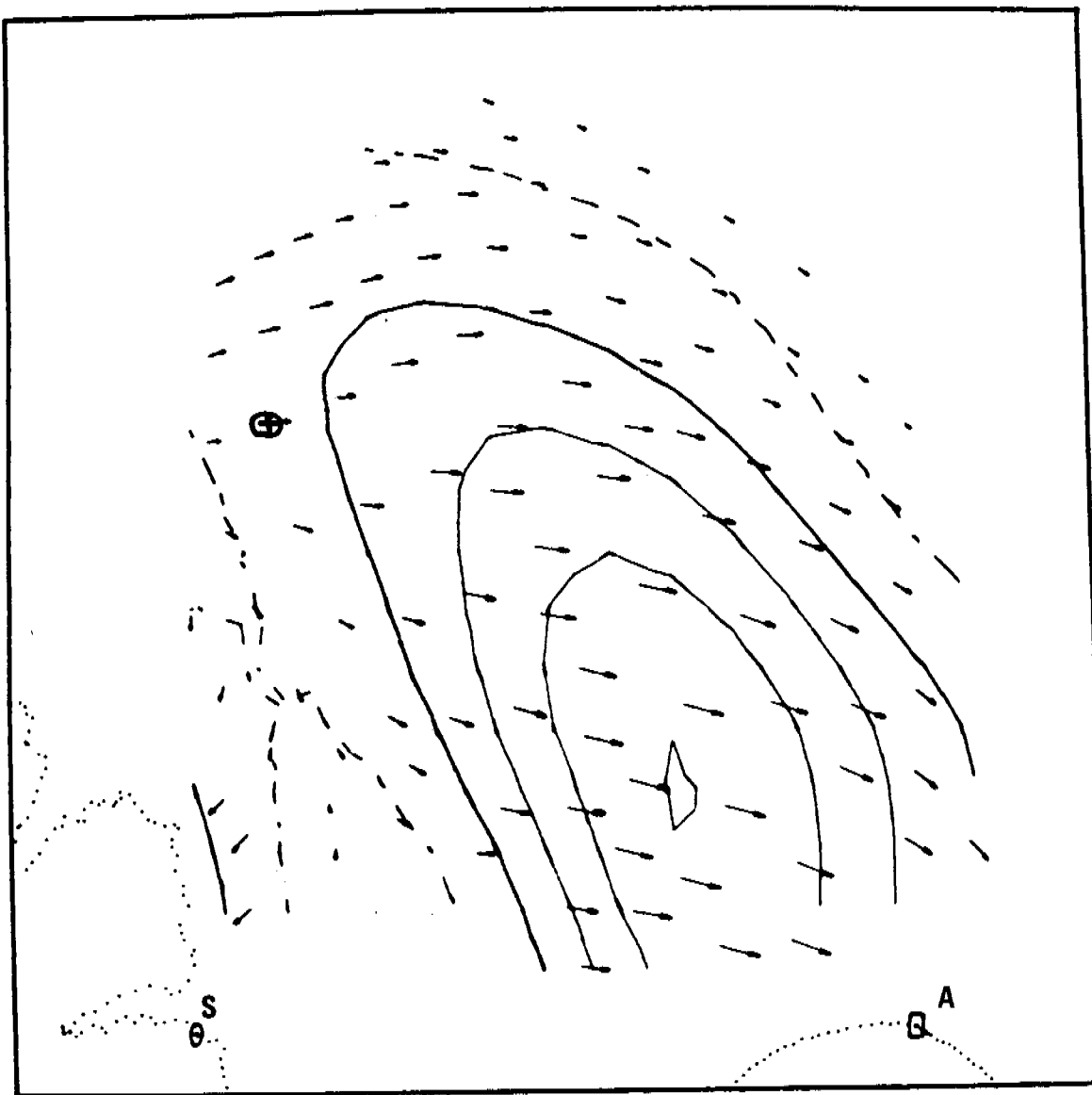
Figure 10. 09:30



09 : 30

DATE 07/13/77

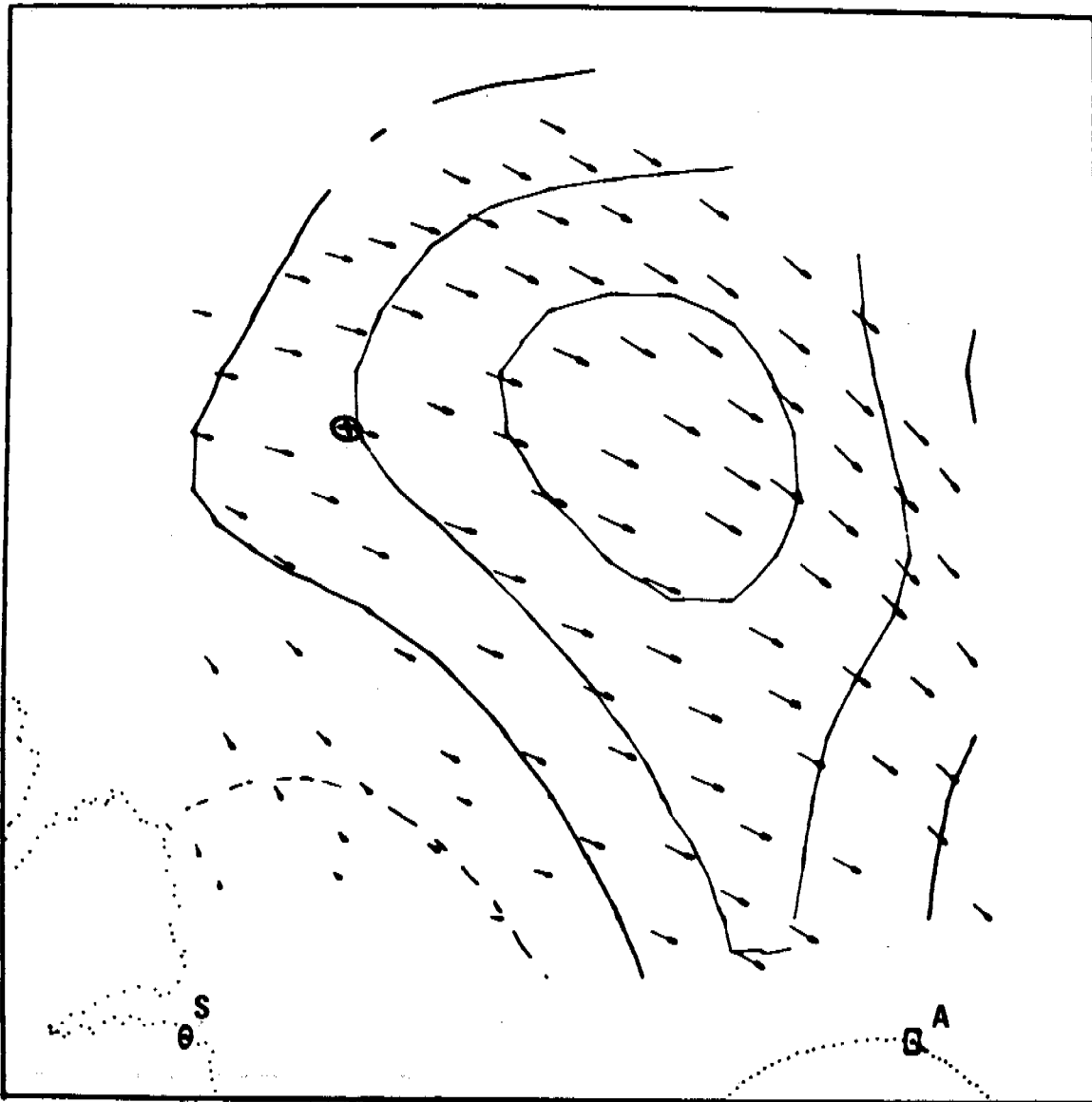
Figure 11. 11:00;



11 : 00

DATE 07/13/77

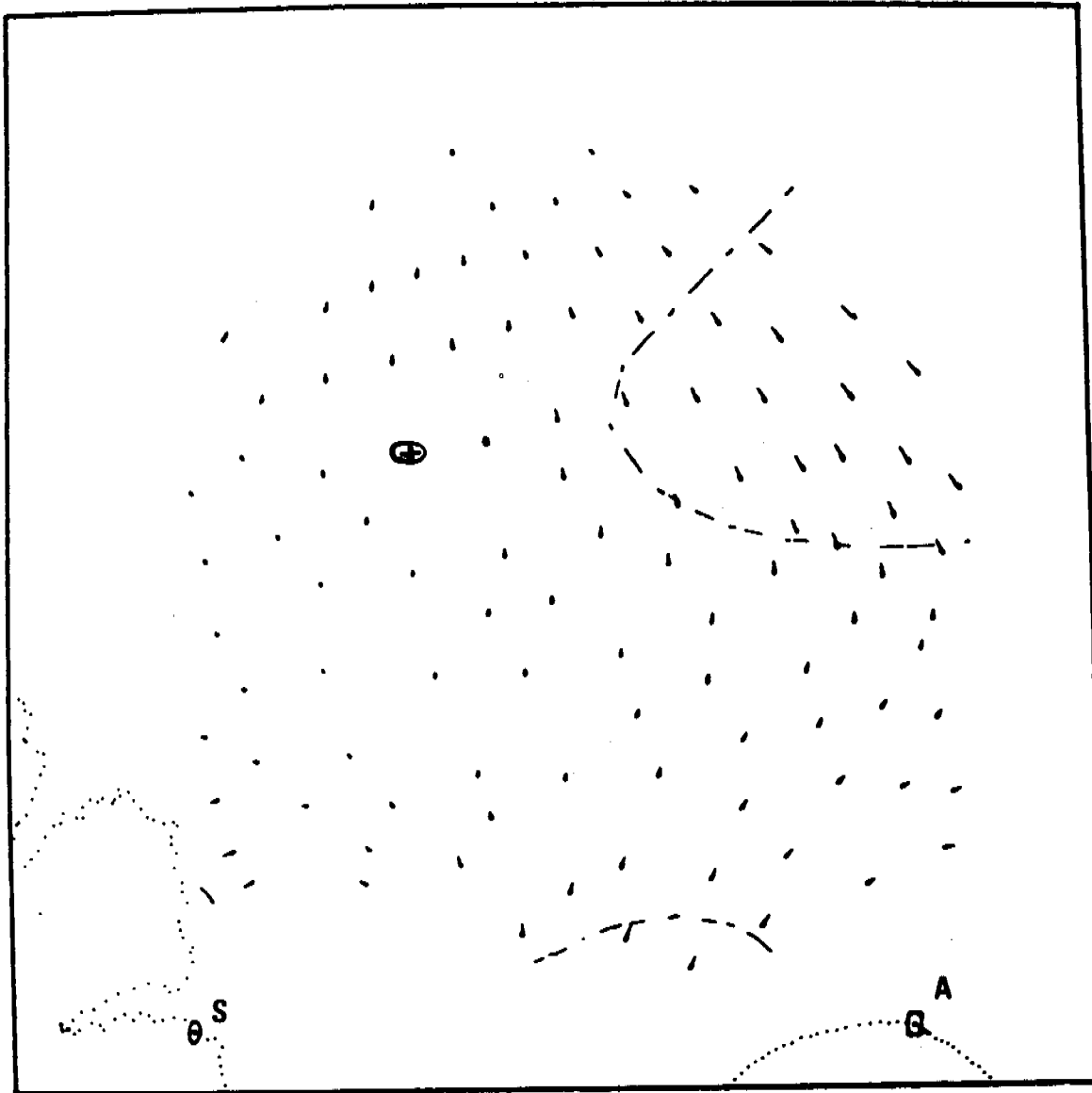
Figure 12. 12:30;



12 : 30

DATE 07/13/77

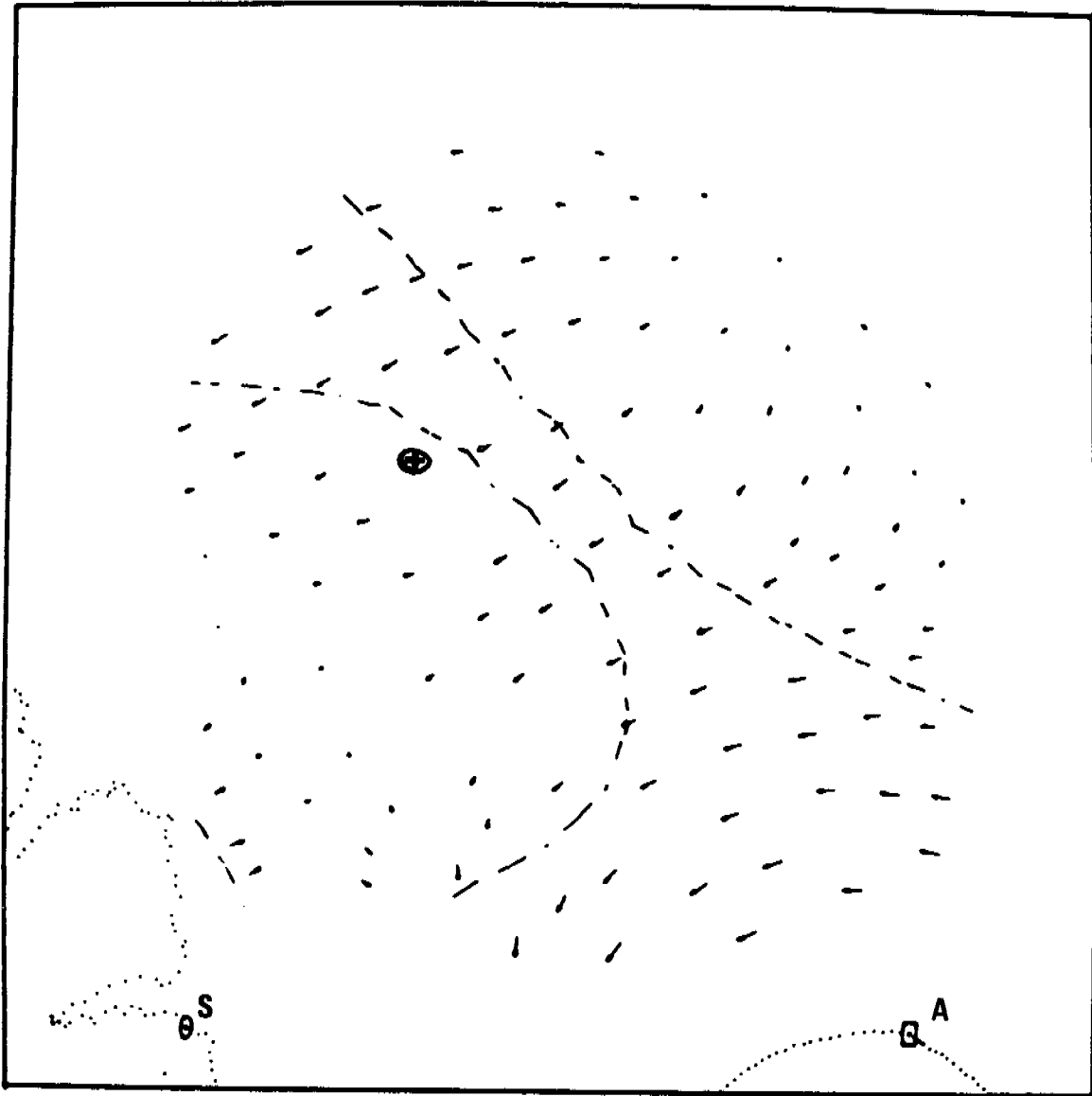
Figure 13. 14:00;



14 : 00

DATE 07/13/77

Figure 14. 14:30;



14 : 30

DATE 07/13/77

OBSERVATIONS OF SURFACE TIDAL COMPONENTS IN LOWER
COOK INLET USING A TWO-SITE HF DOPPLER RADAR SYSTEM

A. S. Frisch and B. L. Weber
NOAA/ERL/Wave Propagation Laboratory
Boulder, Colorado 80302

Introduction

Surface current observations until now, have been made using either current meters or some kind of a drifter. If one wanted to obtain the tidal components from these observations, they were limited in their sampling, both in time and space. The use of Doppler high-frequency (HF) radar techniques (Barrick and Evans, 1976; Barrick et al., 1977) now allows one to determine the tidal components sampled over an area on the order of 2500 km².

The purpose of this paper is to show some of the results of this technique applied to an area in lower Cook Inlet, Alaska. We have selected various locations in the radar coverage area for presentation.

The initial discovery of surface current effects on backscattered high-frequency (HF) radar was made by Crombie (Crombie, 1972). Since then, theoretical and experimental studies of surface-current effects have been conducted Barrick, et al. (1974), Stewart and Joy (1974),

Barrick et al. (1977). Stewart and Joy (1974) have shown that the radial component of surface current measured by the HF radar compares well with radial velocities determined by tracking a float by conventional techniques. Barrick and Evans (1976) describe a two-site technique which provides both components of surface currents rather than just the radial component. This technique was tested in Florida using HF radars at Fort Lauderdale and Miami Beach (Barrick et al. 1977).

For the experiment described here two radars were operated simultaneously at Seldovia and Anchor Point, Alaska which are located on the edge of lower Cook Inlet (Figure 1). Operating each radar in turn for 15 minutes every half hour for a 24 hour period, we obtained approximate estimates of the 12 and 24 hour tidal components for the surface currents as a function of position. The vector components of velocities at selected locations (denoted on Figure 1) were decomposed into semi-diurnal and diurnal components. The results show considerable amplitude and phase variations in these components over the radar coverage area.

Method

The system for measuring surface currents uses two HF shore-based transportable Doppler radars (Barrick and Evans, 1977 and Barrick et al., 1978). These currents are determined for 3 km x 3 km areas of ocean out to 70 km from shore, and are displayed at the centers of each such area within a rectangular grid.

The mechanism behind these observations that — permit the measurement of near-surface currents — involves scattering of H-F waves from ocean waves. Ocean waves are the "target" for the radar system. Since this target is moving, it produces a "Doppler shift" on the received echo. This means that the signal returns at a different frequency than that transmitted, because of the radial rate of closure of the target. The radar receiver/processor measures this Doppler shift, and this permits the determination of the radial component of the current velocity. Once these radial components of the currents are determined, at two locations, the components are combined to yield 2-dimensional current vectors in a more conventional Cartesian coordinate system.

In the experiment in lower Cook Inlet, the observations were made every half hour for 24 hours. The velocity vector is resolved into an (approximately) N-S and an E-W component*. To obtain the tidal parts of our surface currents, we used some of the results of Doodson (1921) who examined all the frequencies of importance in the moon-sun-earth system. Neumann and Pierson () point out that no matter how complex the boundary conditions, or how strong or weak the effects of friction, the solution for the tidal amplitudes and tidal currents must contain these same periodic terms. However, the amplitudes of these components will be

* The current components and x-y coordinate system are actually defined in the radar site geometry orientation shown in Figure 1; thus u and v are approximately in the N and W directions respectively.

dependent upon the geometry of the location, such as the length and depth of a particular embayment. Some of the important frequencies are listed in Defant (1961) and Neumann and Pierson (1966). Since we have limited data timewise (24 hours), we cannot separate out any amplitude coefficients within the semi-diurnal or diurnal components. What we have done is to take the principle solar and lunar frequencies and average them with weights proportional to the coefficients given in Defant's (1961) table. This turned out to be approximately 12.3 hours. Similarly, we have taken the Luni-solar diurnal and the principle lunar diurnal and averaged them to approximately 24.8 hr. We then fit the N-S and E-W components of the data to the sine and cosine terms of these two periods, i.e.,

$$u = a_1^u \sin \left(2\pi \frac{t}{\tau_1} \right) + b_1^u \cos \left(2\pi \frac{t}{\tau_1} \right) + a_2^u \sin \left(2\pi \frac{t}{\tau_2} \right) + b_2^u \cos \left(2\pi \frac{t}{\tau_2} \right)$$

and

$$v = a_1^v \sin \left(2\pi \frac{t}{\tau_1} \right) + b_1^v \cos \left(2\pi \frac{t}{\tau_1} \right) + a_2^v \sin \left(2\pi \frac{t}{\tau_2} \right) + b_2^v \cos \left(2\pi \frac{t}{\tau_2} \right)$$

where u is the N-S component,

v is the E-W component,

τ_1 is the 12 hour period,

τ_2 is the 24 hour period,

and the a 's and b 's are the coefficients that are computed using a least squares fit of the data.

Results

The results are plotted for the locations represented in Figure 1. The data were taken on July, , starting at midnight local daylight savings time. The coordinates of Anchor Point are approximately $59^{\circ} 45'$ lat. $151^{\circ} 50'$ long. Data from the first set (shown in Figures 2 through 7) are along a line roughly parallel to the baseline between the two radars. The main flow is in the x direction with the velocity component denoted by u. The data are shown for locations A and G, 39 km from a line drawn between the radars.

Figure 2 shows the data for the x component and the least squares fit for the sum of the sine and cosine terms for the two locations. Notice that data from location G, farther up Cook Inlet, lag data from location A by a little more than one hour. The decomposition curves are shown in Figure 3. The largest amplitude is the 12-hour component with G data lagging A data by almost two hours. Since the distance between A and G is 21 km, the corresponding phase velocity of this component would be about 3 mm/sec.

Figure 4 shows the data for the y component for the same locations. The lines show the least squares fit of the two frequencies and the points represent the actual radar data. The separate frequency components are shown in Figure 5. The 24-hour components have amplitudes about 1/4 the values for the 12-hour components for both locations. The time difference

between the maxima of the 24-hour components is about one hour with G data lagging A data. The 12-hour component maximum occurs two hours later for G relative to A. This difference in phase of the 12 and 24 hour component is comparable to the difference between the corresponding x components of velocity at the same locations.

Figure 6 shows the x component of velocity with least squares fit of the two tidal periods for points B, D, E and F. These are located on a line perpendicular to the baseline between the two radars and about 9 km north of Seldovia.

Figure 7 shows the decomposition of u into 12- and 24-hour periods for B, C, D, and F locations. The 12-hour component shows no phase difference between locations B and C, which are in the deeper water, whereas E and F show some displacement in phase. The amplitudes of these components are also much smaller in the shallower water close to Kachemak Bay. The 24-hour component shows a much larger amplitude in the deeper water B and C locations where the main flow is located.

Figure 8 shows data for the y component of velocity, which is roughly along the axis of Kachemak Bay. The data for E and F locations, which are closer to the Bay, show almost no semi-diurnal components. This is even more evident in Figure 9. At E location, the 12-hour component has an amplitude of only 5 cm/sec compared with 30 cm/sec at locations B and C in the main part of lower Cook Inlet.

Errors

The relative accuracy of the radar is very good as indicated by comparison of the actual data points relative to the least squares fit of the data to the 12 and 24 hour periods. This is particularly noticeable with the data taken furthest from shore where boundary effects are expected to be less pronounced. Figure 2 is a good example of this. Here the total velocity variation is about 180 cm/sec., yet the standard deviation from the fit is less than 8 cm/sec.

Barrick et al. (1977) compared radar and surface drifter measurements off Miami, Florida in the Gulf Stream. They reported a 27 cm/sec standard deviation when the mean velocity was about 200 cm/sec. Later analysis of the data showed considerable time variation in the Gulf Stream during the time the drifter observations were made. When the drifter observations and radar observations were made within an hour of each other, the differences were less than 10 cm/sec^{-1} .

Summary

The use of two HF radars for tidal surface current studies appears especially useful for looking at the spatial variability in complex coastal and estuarine areas. With limited data we have been able to see spatial effects in the 12 and 24 hour phase and amplitude of the tides. More analysis will be required to interpret the small residual

velocities after tidal effects are removed, i.e., to determine whether they are due to runoff, wind, or effects which may be associated with scatter from the sea surface.

References

Crombie, D. C., in Proceedings of IEEE Ocean '72 Conference (IEEE Publ. 72 CHO 660-10CC Institute of Electrical and Electronics Engineers, New York 1972), pp 173-179.

Barrick, D. E., Headrick, J. M., Bogle, R. W. and Crombie, D. D., 1974, Sea Backscatter at HF: interpretation and utilization of the echo, Proc: IEEE, Vol 62 pp 673-680.

Stewart and Joy 1974, HF radio measurements of surface currents, Deep Sea Research, 21, 1039-1049.

Barrick, Evans and Weber, 1977, Ocean surface currents mapped by radar, vol 198, No. 4313 Science. 14, Oct. 1977.

Barrick and Evans, 1976, Implementation of coastal current-mapping HF radar system, Progress Report No. 1, NOAA Tech. Report ERL 373-WPL 47.

Figure Captions

Figure 1. Map of measurement area. Alphabetical characters denote locations where the data were sampled.

Figure 2. This is a time plot of the amplitude of the N-S component, u at location A and G. The solid and dashed lines are the least squares fit of the sine and cosine terms of a 12 and 24 period to the data. The dots and squares represent the actual data points.

Figure 3. This figure shows the 12 and 24 hour terms of u at locations A and G.

Figure 4. Shows the same type of information as Figure 2 for the East-West component of velocity for locations A, B and G.

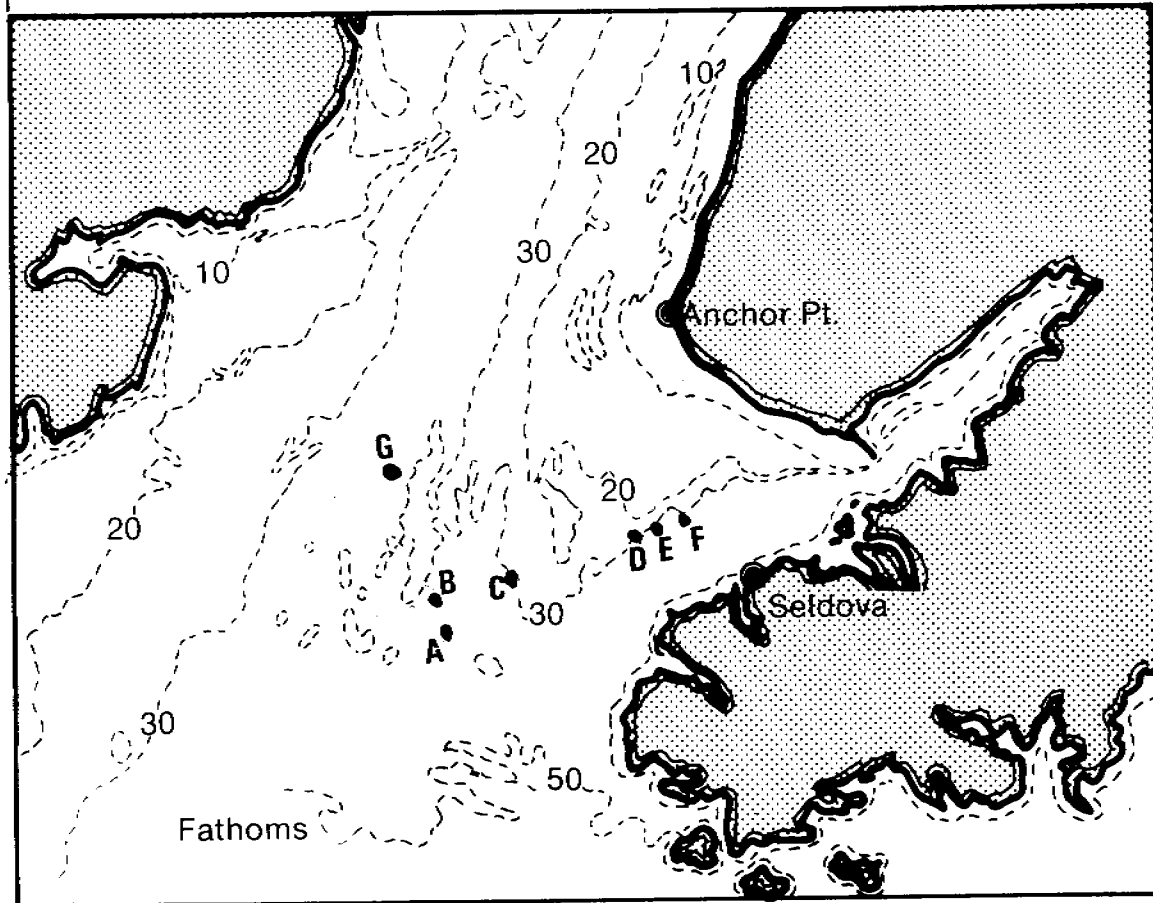
Figure 5. Shows the least squares fit of the 12 and 24 hour components for v at locations A and G.

Figure 6. Shows the same kind of display as Figure 2 for the N-S component of velocity, u for locations B, D, E and F.

Figure 7. Shows the 12 and 24 harmonic decomposition of u for B, C, E, and F.

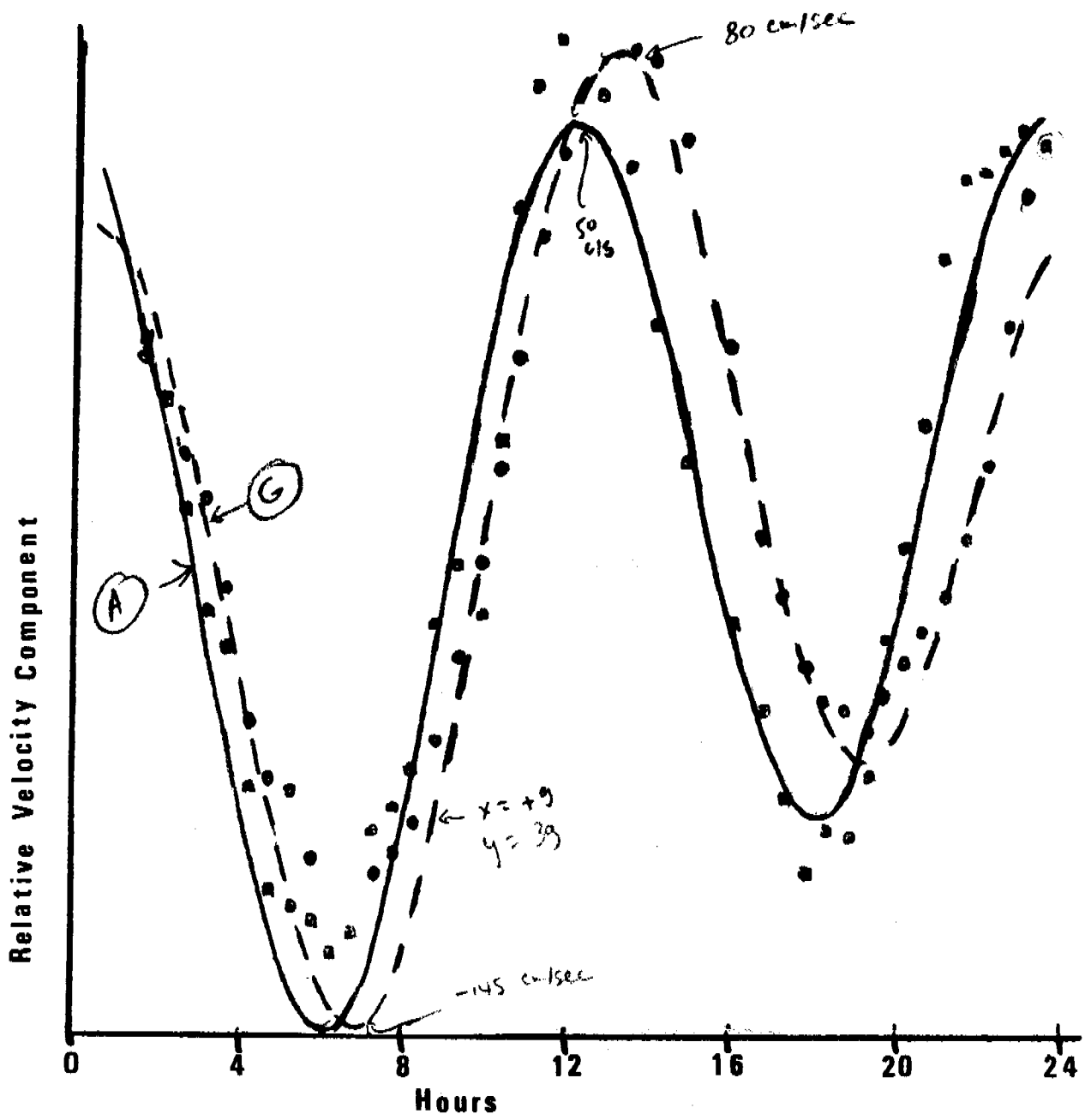
Figure 8. Shows the same display of the data as Figure 2 for v at locations B, C, E, and F.

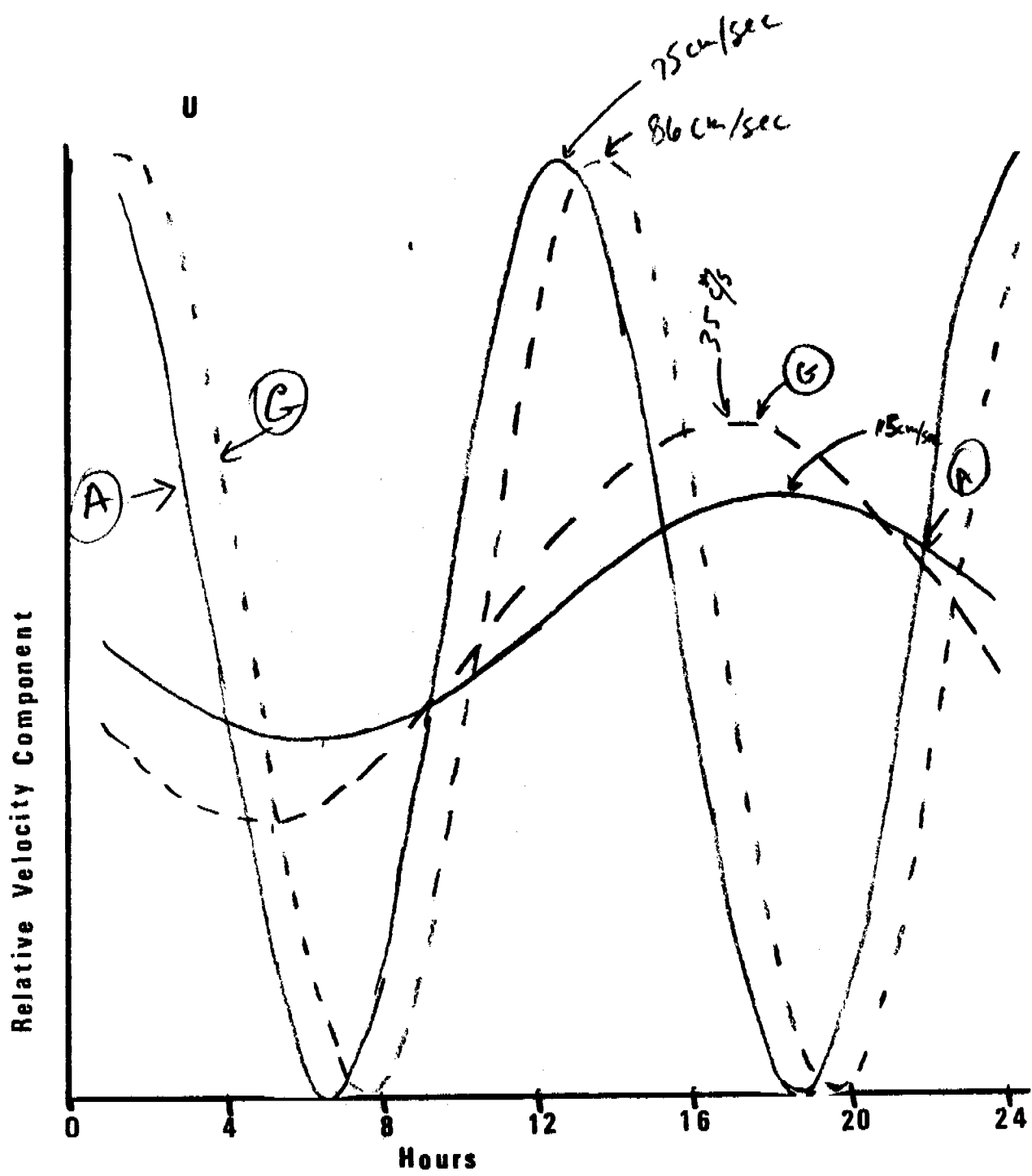
Figure 9. Shows the 12 and 24 harmonic decomposition of v at locations B, C, E, and F.



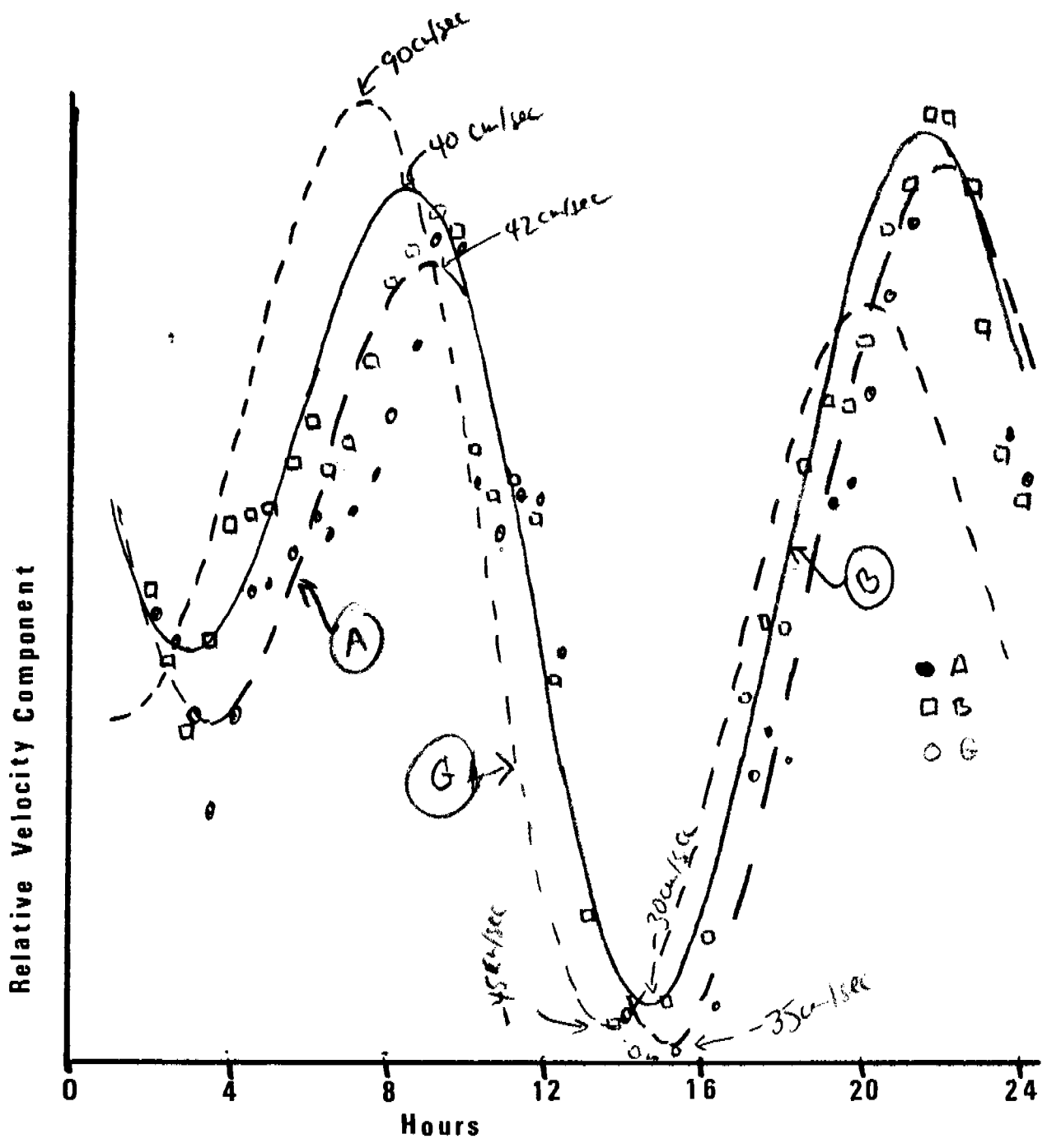
Q0854
20472B
4:

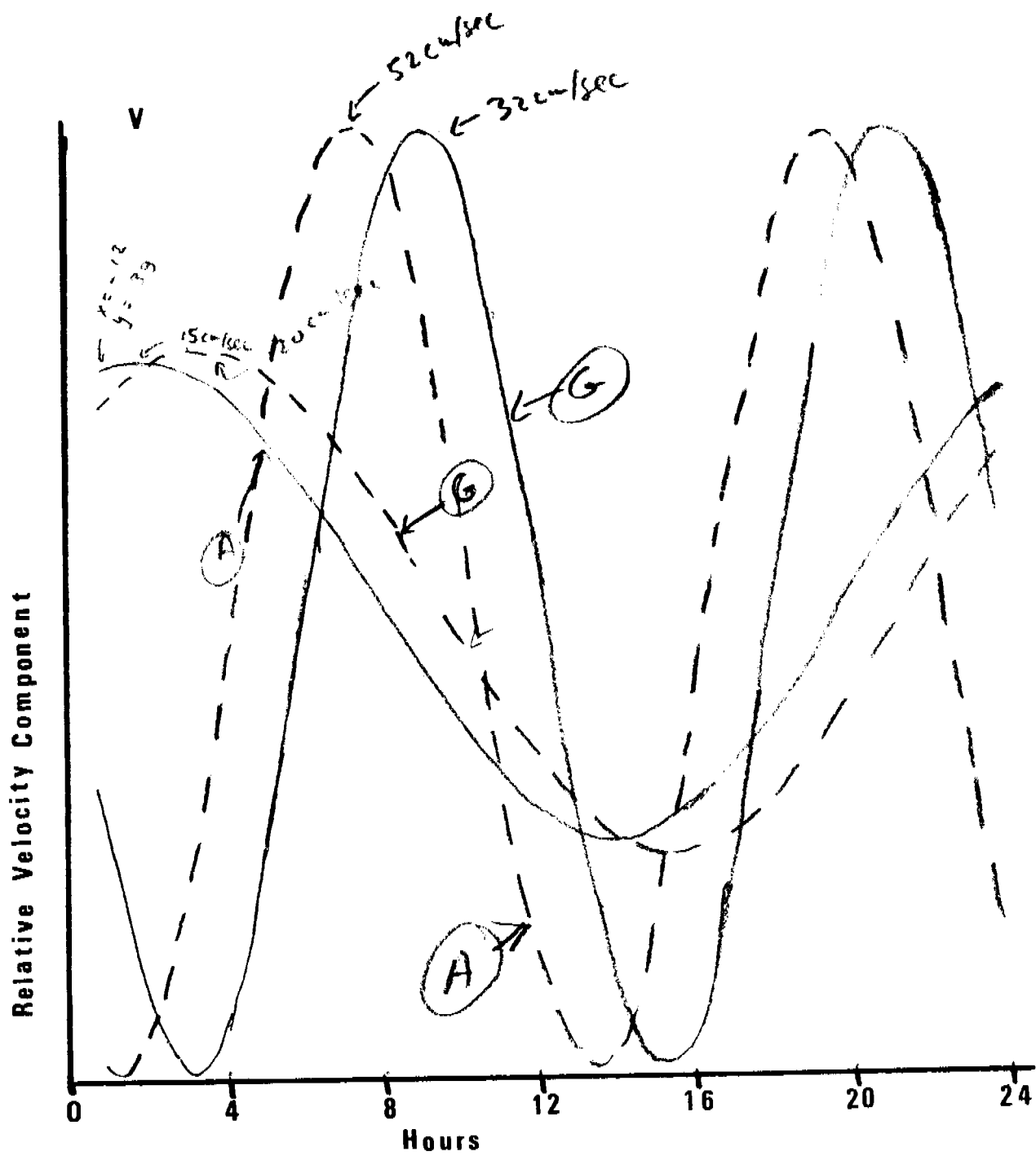
U

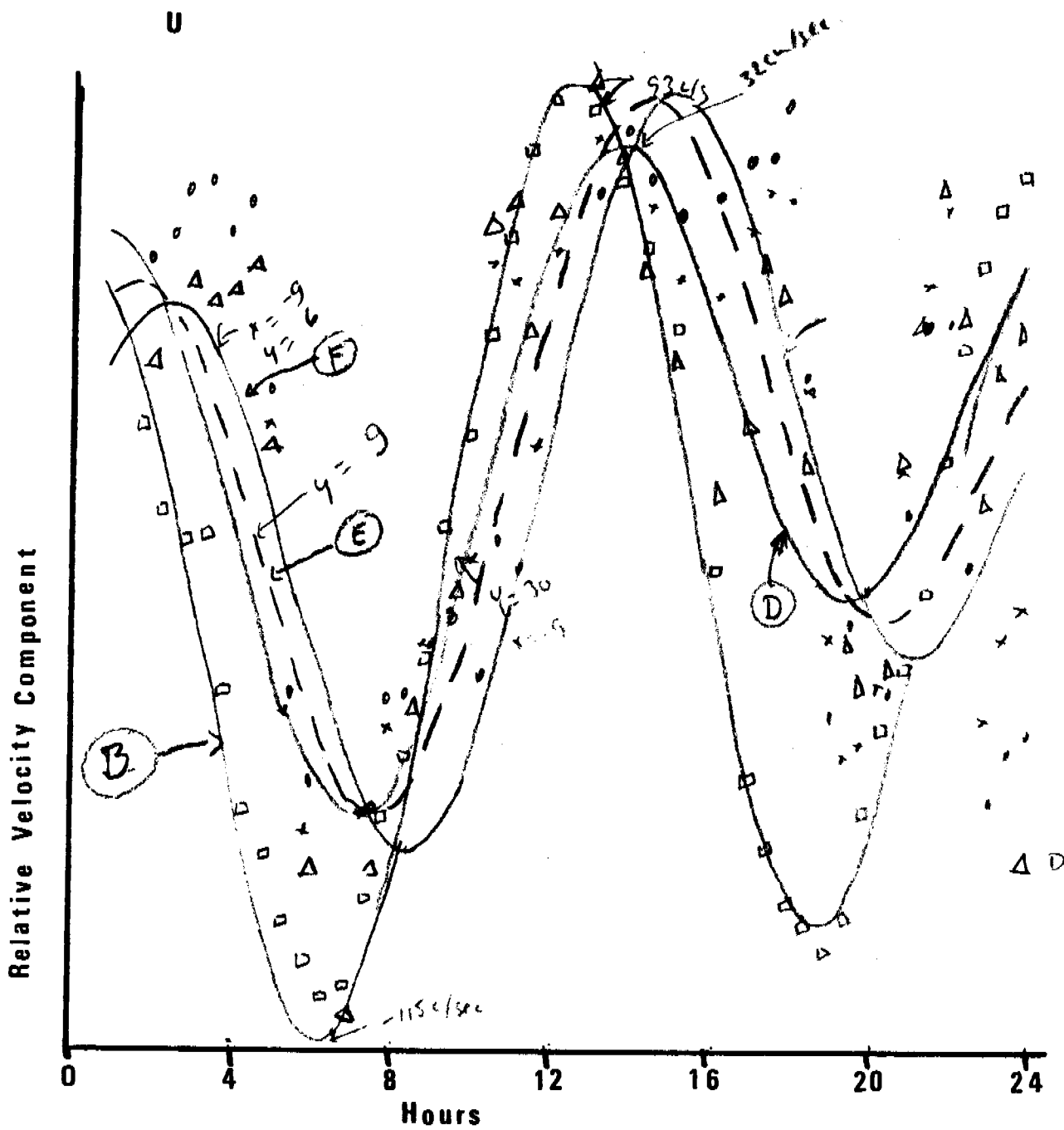


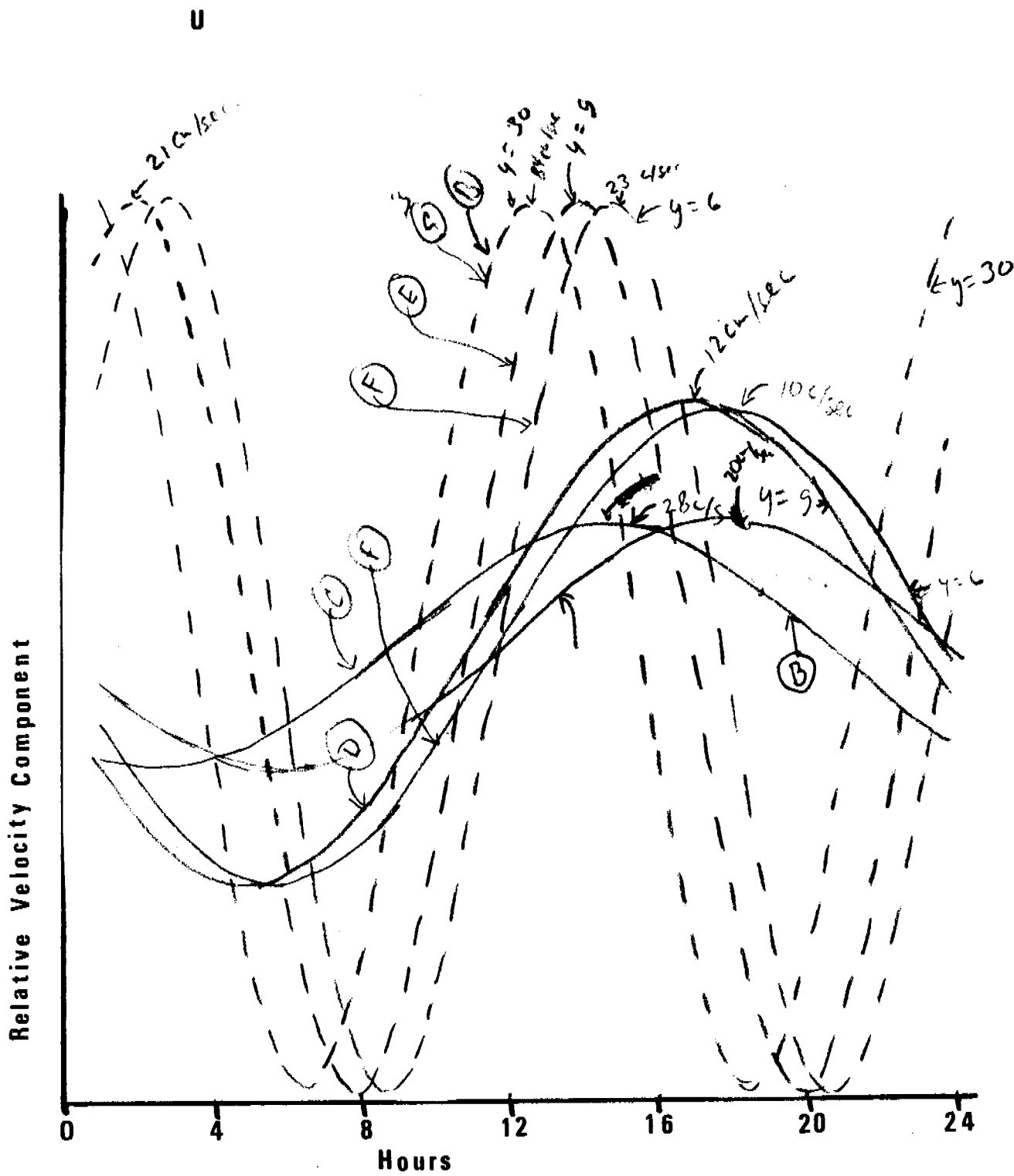


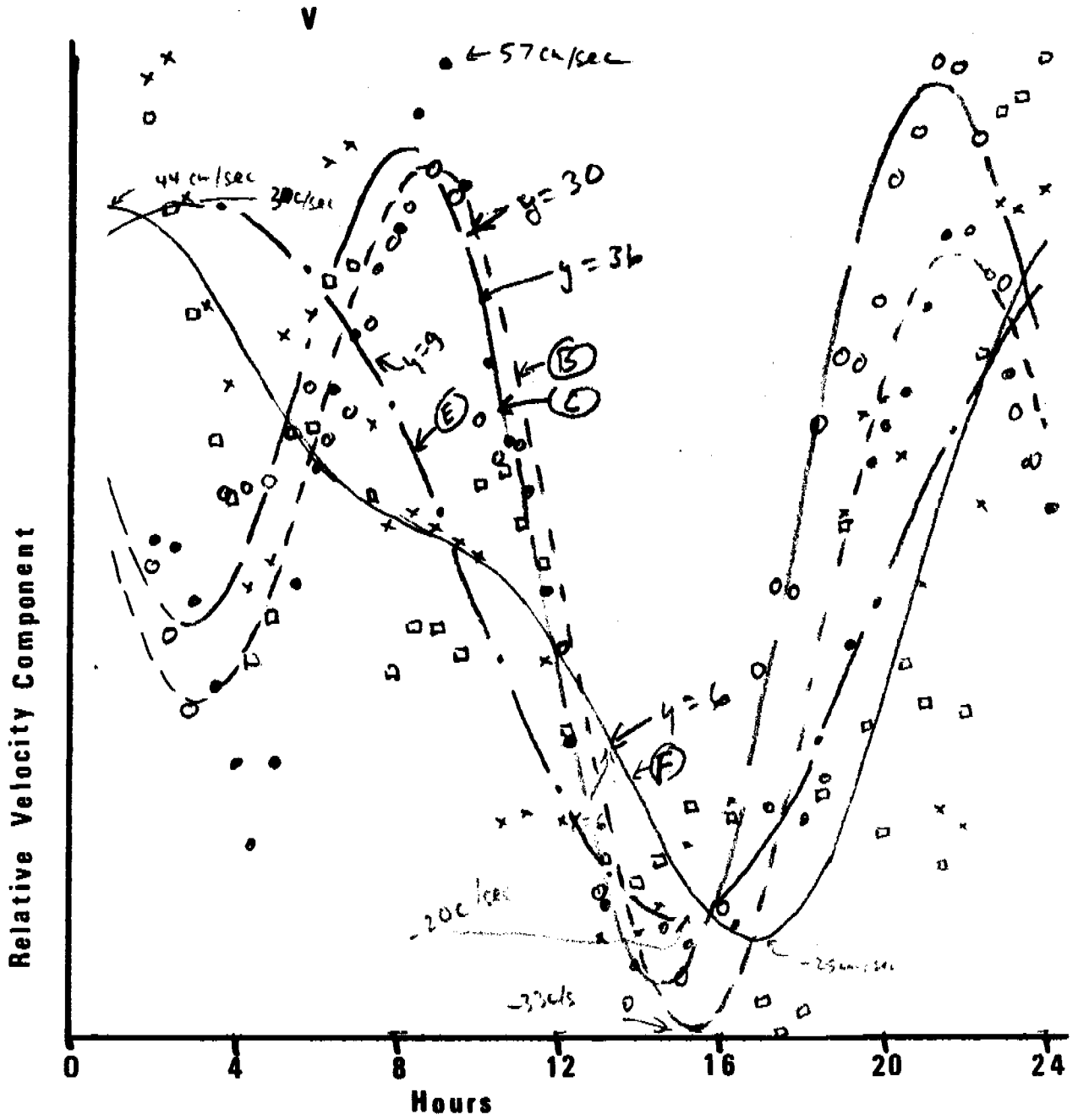
V

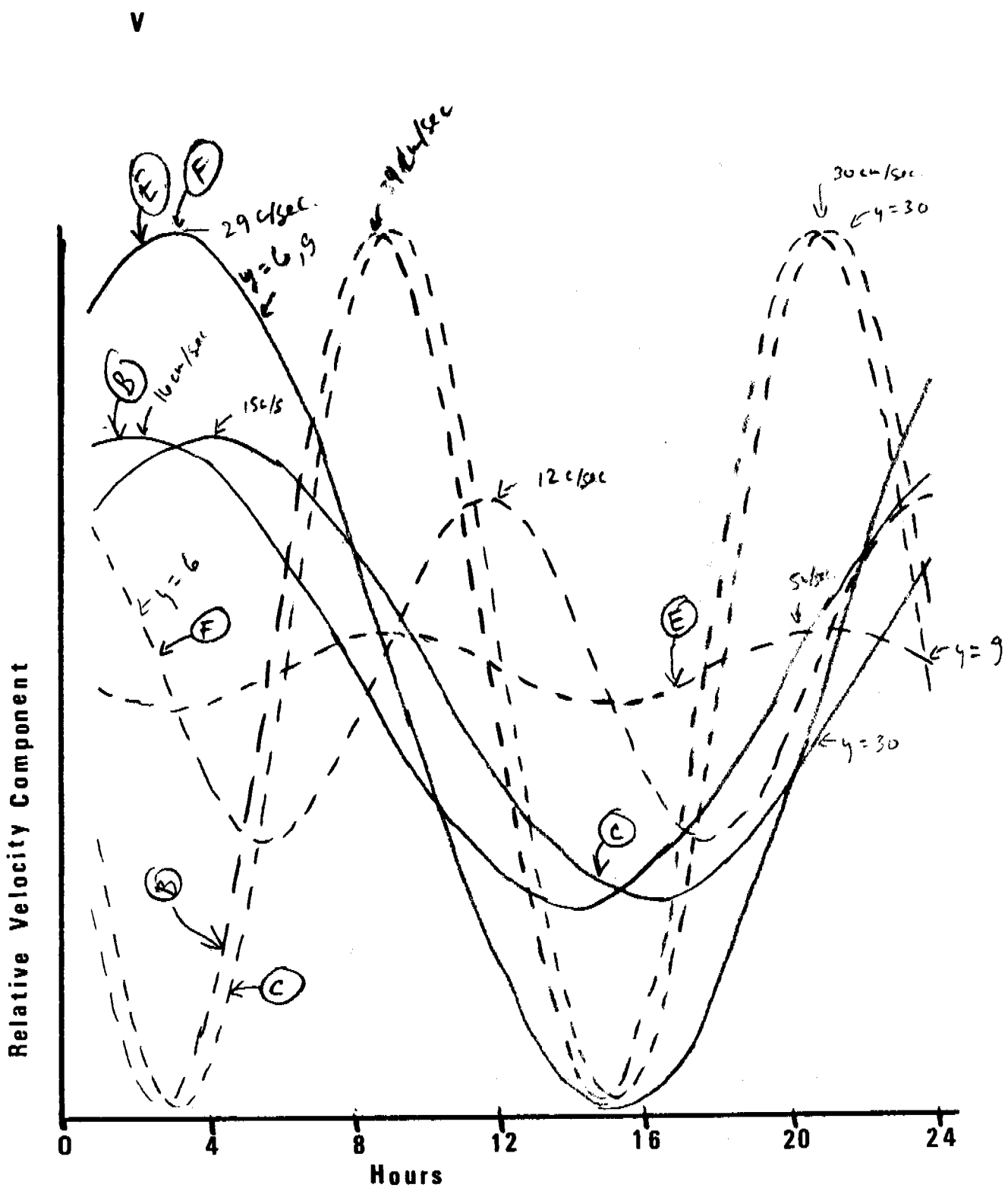












Annual Report

Contract No.: 03-5-022-67, T.O.3
Research Unit No.: 91
Reporting Period: 1 April 1977-31 March 1978
Number of Pages: 21

Current Measurements in Possible Dispersal Regions
of the Beaufort Sea

Knut Aagaard

Department of Oceanography
University of Washington
Seattle, Washington 98195

19 April 1978

I. Summary

The picture which emerges from the work done on the outer shelf to date is of a regime that is quite energetic over a broad band of sub-tidal frequencies. The mean flow calculated for a sufficiently long period (possibly up to several months) is unquestionably eastward. The flow appears to be steered by the local bathymetry. Although the energetic time scales of the flow are those of synoptic meteorological events, no clear relationship between atmospheric and oceanic events has been shown to date, even in a phenomenological fashion.

The implication with respect to the sub-surface transport of pollutants and other substances on the outer shelf is that 1) in the mean they will move significant distances eastward along the shelf, and 2) trajectory prognosis would be meaningless at our present level of understanding.

II. Introduction

The objective of this work has been to obtain long-term Eulerian time series of currents at selected locations on the outer shelf of the Beaufort Sea. Such measurements are necessary to describe and understand the circulation on the shelf and the exchange between the shelf and the deep Arctic Ocean. It is this circulation and exchange which transports and disperses the plankton, substances of biological and geological consequence, and pollutants. The water motion also influences the ice distribution and drift. The current time series must be long enough to define the important temporal scales of motion.

III. Current state of knowledge

Much of what is known about the circulation on the outer shelf is in fact based on hydrography. Such inferences have been discussed in this year's annual report for RU 151.

There have also been several direct measurements of currents on the outer shelf. Hufford (unpublished data) measured the flow at 25 m in water 54 m deep some 60 km east of Barrow for two weeks in August 1972. He found a strong eastward flow, averaging 60 cm sec^{-1} the first week. The current then decreased to less than 10 cm sec^{-1} , and on occasion reversed its direction, before resuming its eastward flow at more than 40 cm sec^{-1} a week later. The decrease during the second week occurred during a period of strong easterly winds.

In last year's annual report for RU 91 we discussed a current series from 100 m, in water 225 m deep, north of Oliktok. The measurements extended from late May to the beginning of September 1976, during which time the velocity varied between 56 cm sec^{-1} easterly and 26 cm sec^{-1} westerly. The entire 95-day record was dominated by large low-frequency oscillations which had a typical peak-to-peak amplitude exceeding 50 cm sec^{-1} and a time scale of order 10 days. In effect, the oscillations represented long bursts of

high easterly velocity separated by shorter periods of lesser flow toward the west. Between the easterly bursts there were frequently smaller oscillations with amplitude and time scale of order 10 cm sec^{-1} and two days, respectively. August showed particularly large and long eastward bursts. The flow did not alternate strictly between east and west, for there were also appreciable north-south motions. Rather there was a tendency for the water to have a southerly component of motion when moving east, and northerly when moving west. The relative magnitude of these components was such as to direct the oscillations along the line 100° - 280° T. This is identical to the local isobath trend, so that the oscillations nearly represent alternating motion along the shelf edge. The mean motion also appears to be steered by the bathymetry. During 27 May-14 July the mean set was 7.0 cm sec^{-1} toward 100° T and during 16 July-1 September 18.5 cm sec^{-1} toward 98° T.

These same records show rather clear tidal signals, considerably larger than those recorded on the inner shelf and reported in last year's annual report for RU 91. The tidal amplitude was in the neighborhood of 5 cm sec^{-1} , and there appeared to be a diurnal inequality near the time of maximum lunar declination. Examination of the spectral estimates in the tidal band showed typical amplitudes of 2 - 4 cm sec^{-1} for the M_2 , S_2 , K_1 and O_1 constituents.

Neither the wind nor the surface pressure records from shore stations during the period of current measurements have shown any convincing correlation with the flow measured in 1976.

IV. Study area

The area of interest extends eastward from Pt. Barrow along the entire northern Alaska coast, *i.e.*, from about $156^\circ 30' \text{W}$ to 141°W , a lateral distance of 600 km. The shelf is narrow, with the shelf break typically 80-90 km offshore. The total runoff is small and highly seasonal. Tidal amplitudes are also small; they are mixed, predominantly semi-diurnal. Meteorological tides can exceed the astronomic tide by a factor of ten. The prevailing winds are from the ENE and are generally light. The entire area is covered by sea ice, both first- and multi-year, through all but two to three months. Even during the height of summer, ice is usually found well onto the shelf.

V. Data collection

The rationale of data collection has been discussed in the previous annual reports.

VI. Results

Field work accomplished during this reporting period includes cruises W-28 and W-30. Cruise W-28 was described in the quarterly report of 10 January 1978 for RU 91, while cruise W-30 is described in the preliminary report (ref. M78-18) appended to this report.

VII. Discussion

Of the two instruments recovered on W-28, one recorded from 29 March to 21 October 1977. This meter was located at a nominal depth of 152 m NNE of Lonely in water 192 m deep. The second instrument was at 78 m and recorded from 29 March to 6 April.

As was the case on the shelf north of Oliktok, the flow is quite energetic over a broad range of subtidal frequencies. As an example, in the very low-frequency band, consider Table 1. This shows the mean current vector for consecutive time segments of three weeks each. The mean can

Table 1

3-week time segment no.	Vector mean current magnitude cm sec ⁻¹	Vector mean current direction °T
1	11.2	305
2	1.5	257
3	1.8	180
4	9.4	139
5	2.0	219
6	12.4	136
7	3.2	127
8	9.3	131
9	6.3	127

vary by an order of magnitude and be in opposite directions. Thus, even on this time scale the mean is clearly not a stationary statistic. Likewise, the variance of the flow is not stationary. Figures 1-9 show the spectral estimates for the north-component of velocity, again over consecutive three-week segments (note that energy is presented, rather than energy density). The differences in the spectra at subtidal frequencies are striking. We are thus dealing with a highly variable and irregular flow.

There is, however, evidence for a certain amount of vertical coherence in the flow. The upper current meter recorded the events about 75 m higher in the water column during the first eight days of the long record discussed above. Both it and the lower meter show northwesterly flow the first two to three days, followed by a reversal for a similar time, and then a return to northwesterly flow. The current vector at both meters appears to have rotated cyclonically. However, the records at the two levels are sufficiently different to indicate that the variability has a significant baroclinic component. For example, the initial northwesterly flow was as much as 25 cm sec⁻¹ at the lower meter, but less than 15 cm sec⁻¹ at the upper. On the other hand, during the reversal the upper meter showed speeds of 10 cm sec⁻¹, while the lower meter indicated threshold speeds (less than 2 cm sec⁻¹).

There is also evidence for topographic control of the flow. As can be seen from Table 1, the predominant direction was about 130°T; during the first three weeks the motion was strongly in the reciprocal direction. This is probably quite close to the local isobath trend, although the proximity

1315/3 DEPTH 152M

3/29/77 0545

2048 POINT SEGMENT 1

Y-COMP

DELTA-T =15 MIN

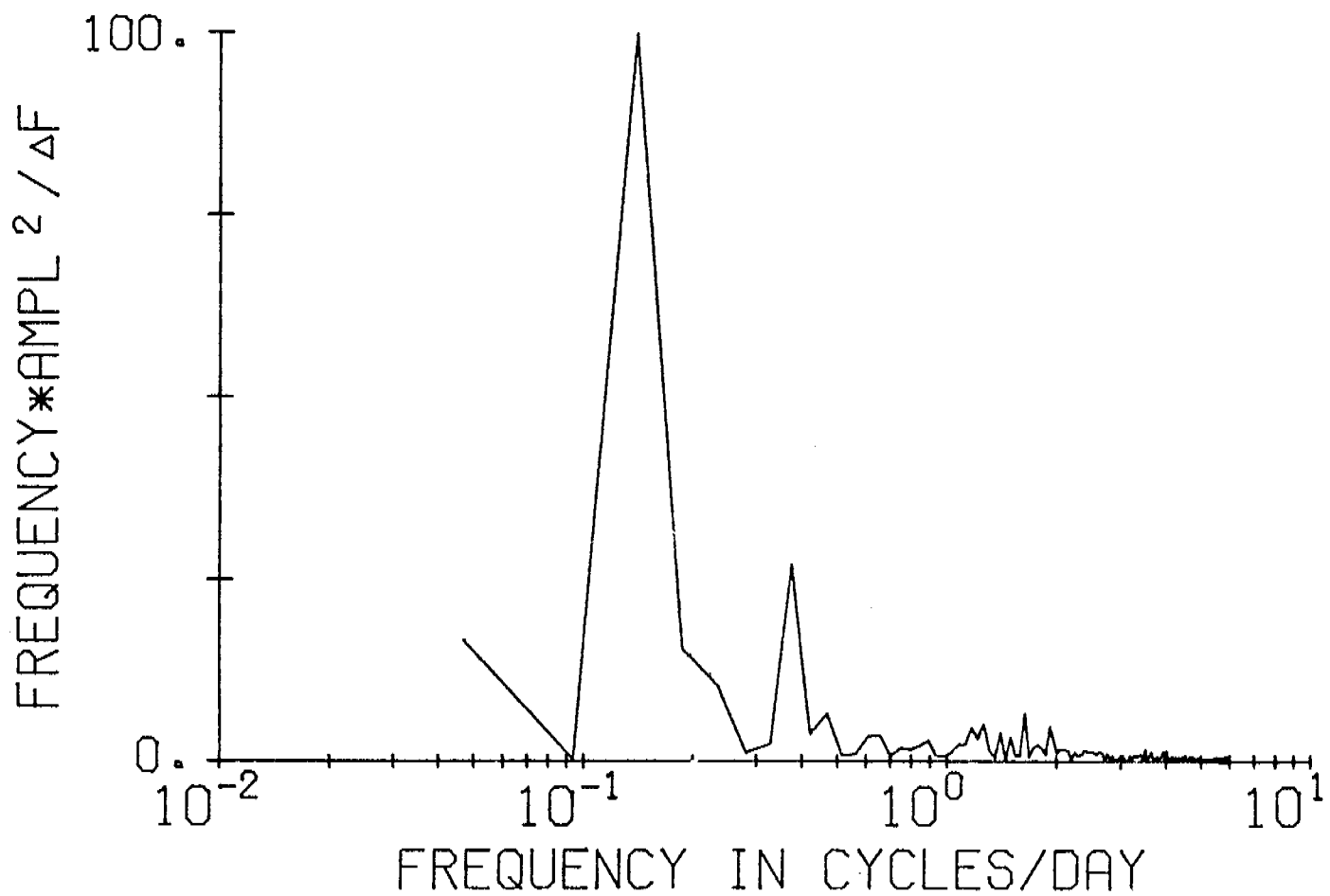


Figure 1

1315/3 DEPTH 152M
3/29/77 0545

V-COMP

2048 POINT SEGMENT 2
DELTA-T =15 MIN

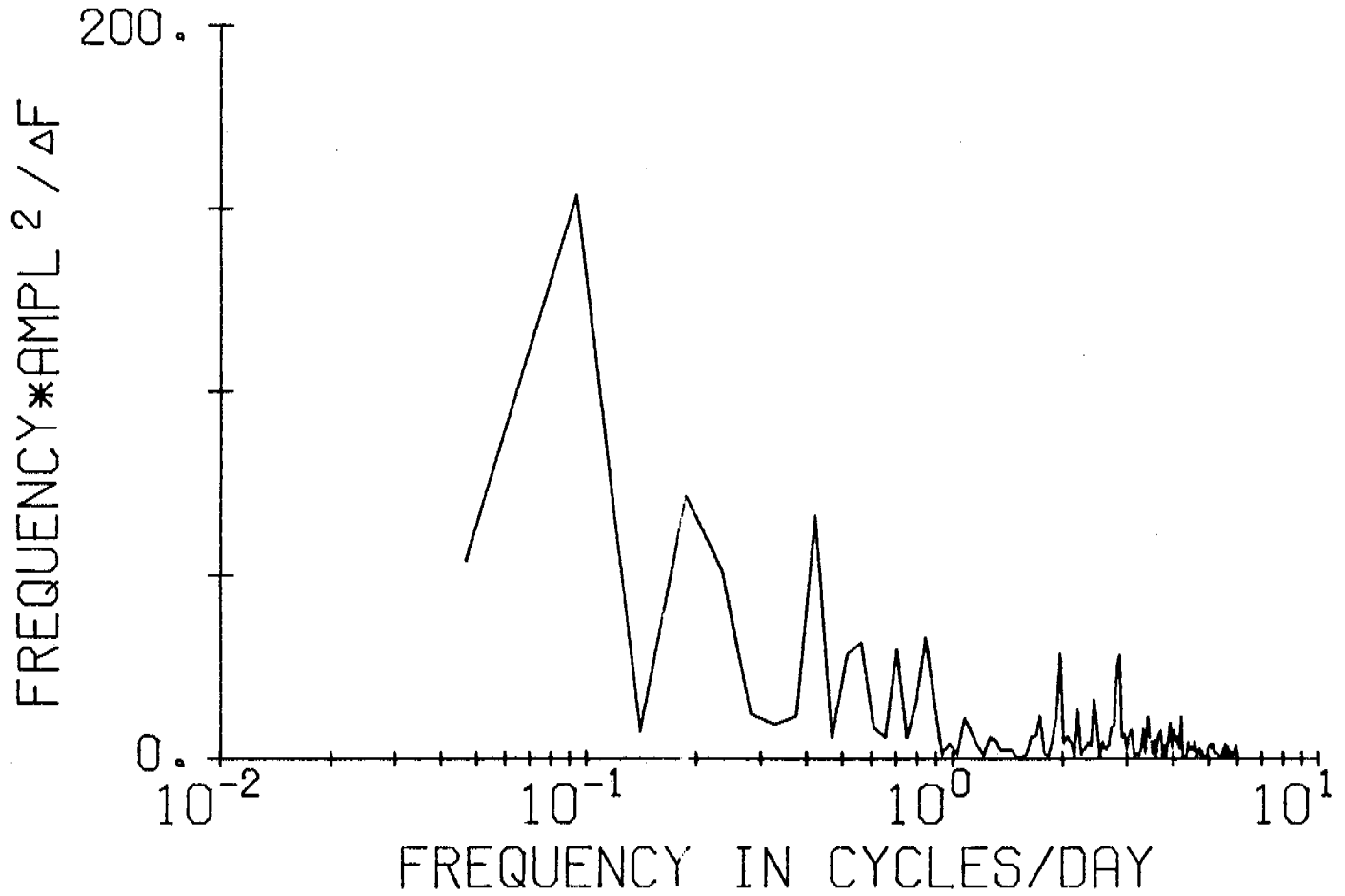


Figure 2

1315/3 DEPTH 152M
3/29/77 0545

2048 POINT SEGMENT 3
V-COMP DELTA-T =15 MIN

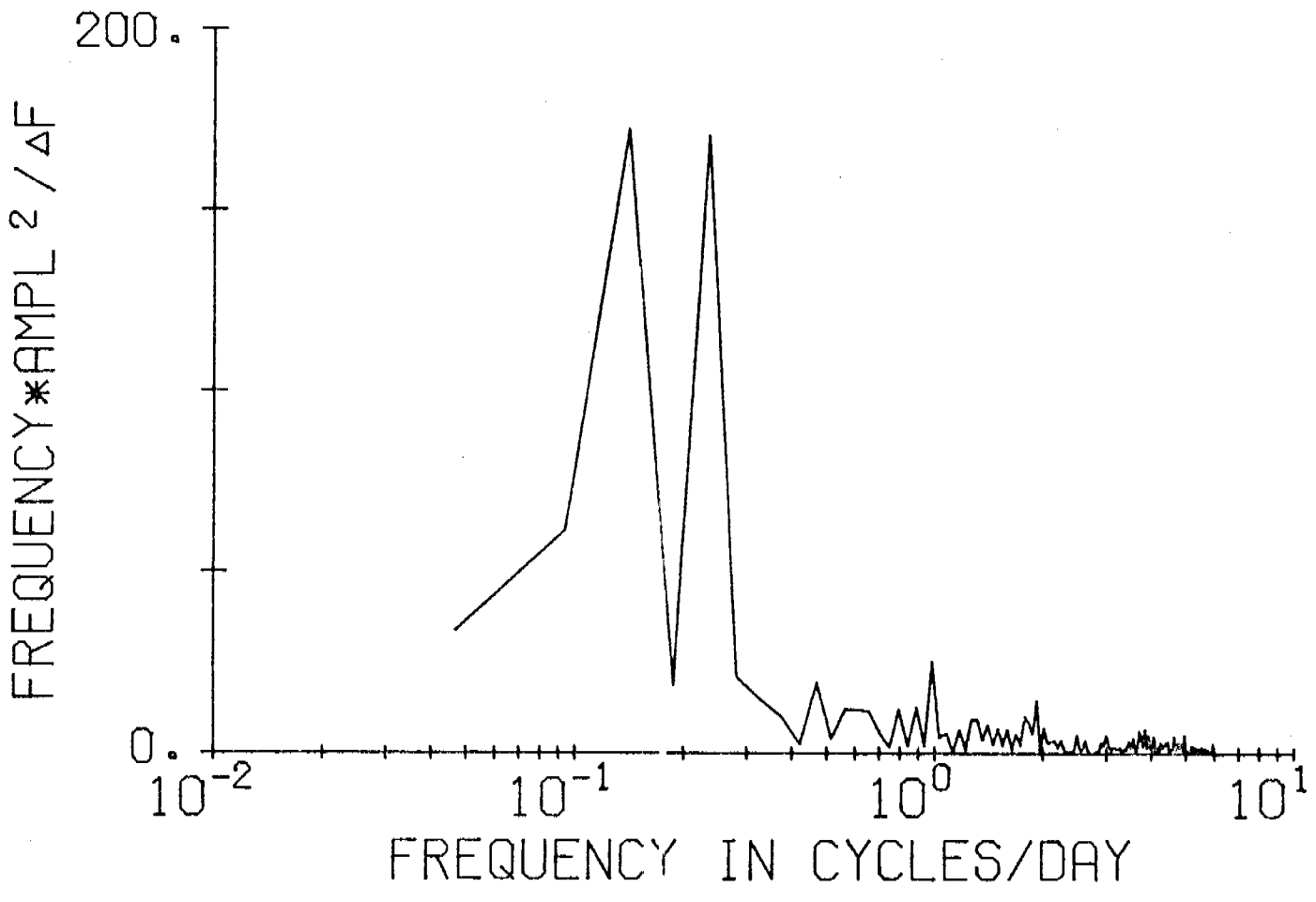


Figure 3

1315/3 DEPTH 152M
3/29/77 0545

V-COMP

2048 POINT SEGMENT 4
DELTA-T =15 MIN

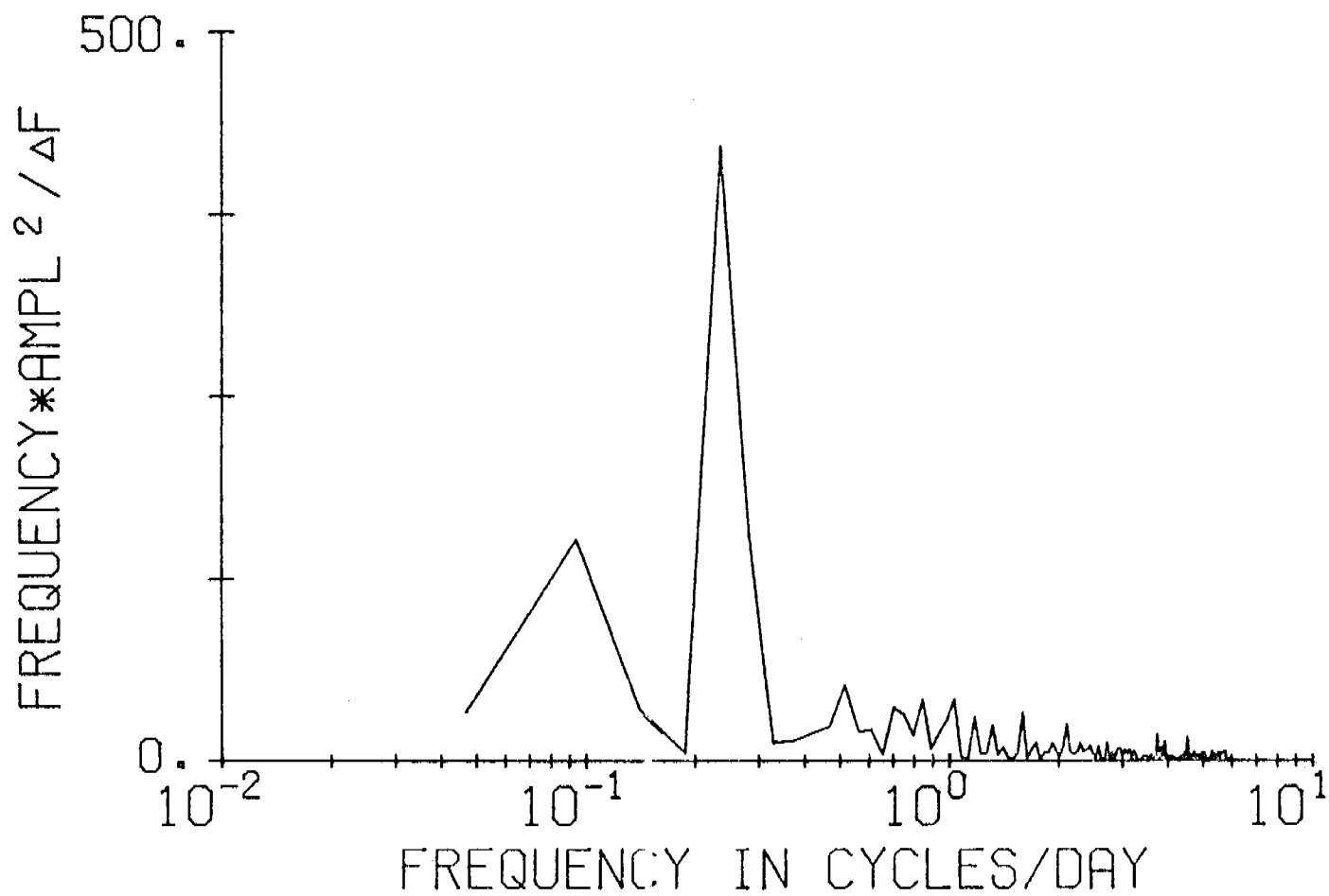


Figure 4

1315/3 DEPTH 152M

3/29/77 0545

V-COMP

2048 POINT SEGMENT 5

DELTA-T =15 MIN

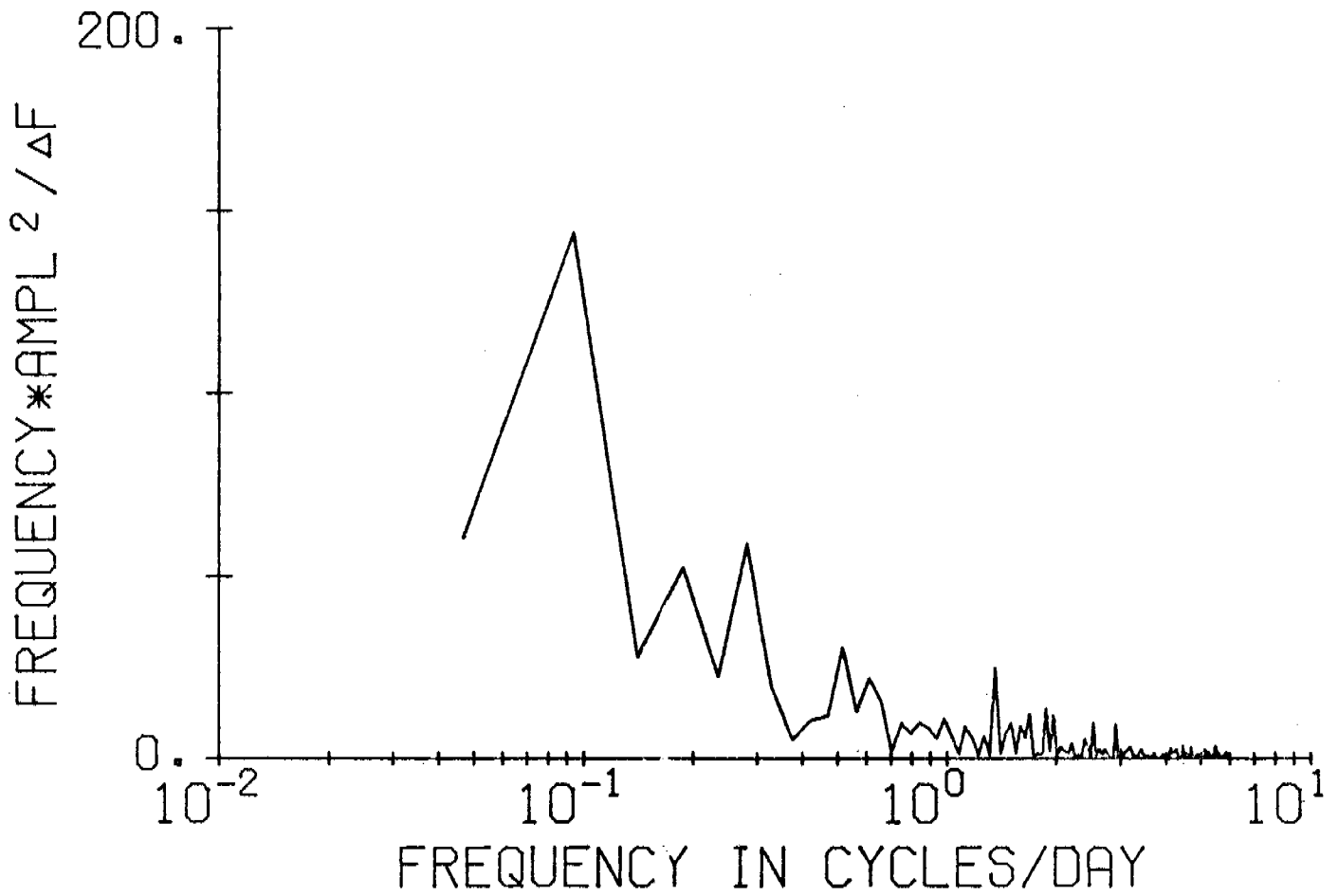


Figure 5

1315/3 DEPTH 152M
3/29/77 0545

V-COMP

2048 POINT SEGMENT 6
DELTA-T =15 MIN

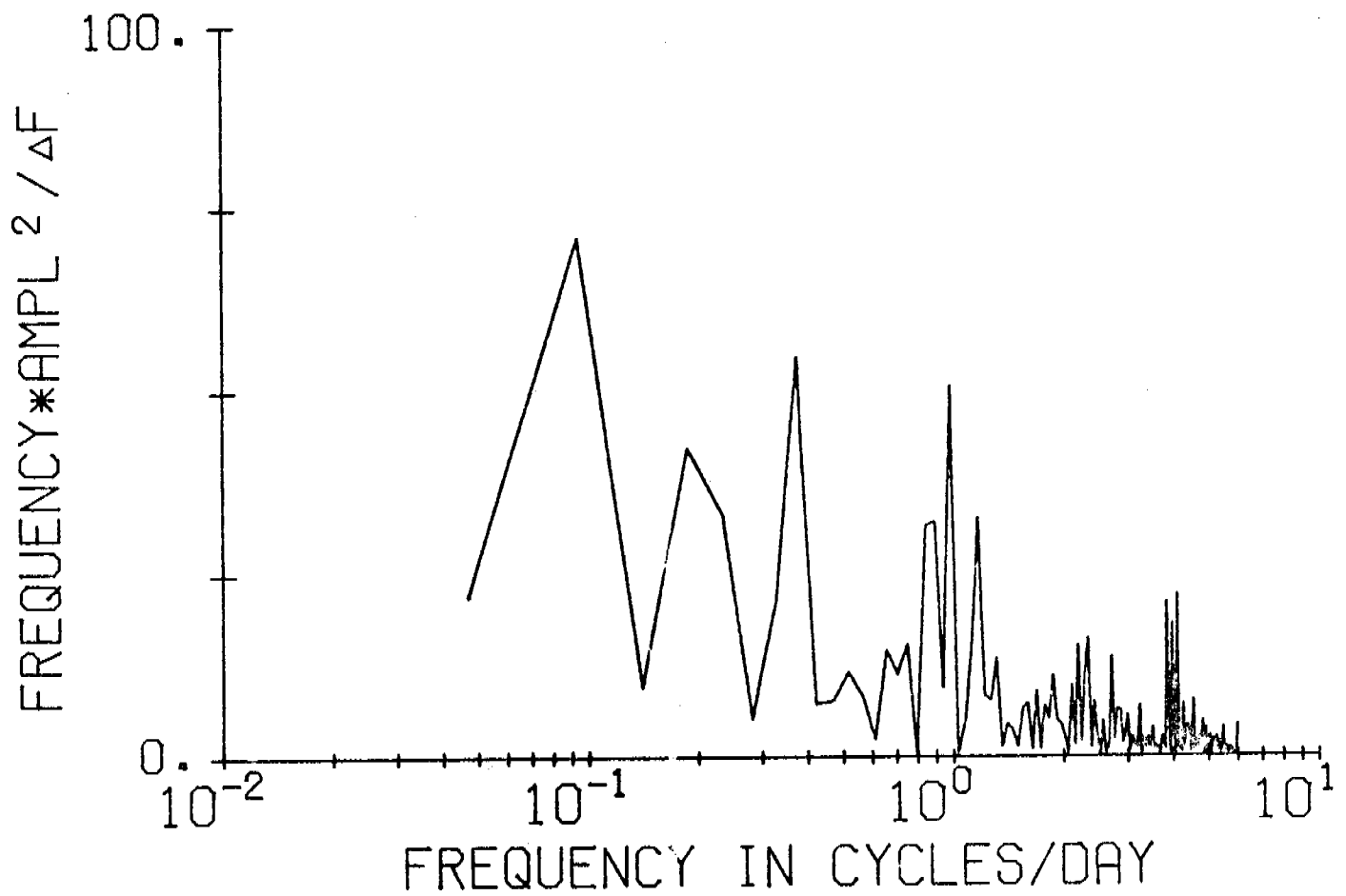


Figure 6

1315/3 DEPTH 152M
3/29/77 0545

V-COMP

2048 POINT SEGMENT 7
DELTA-T =15 MIN

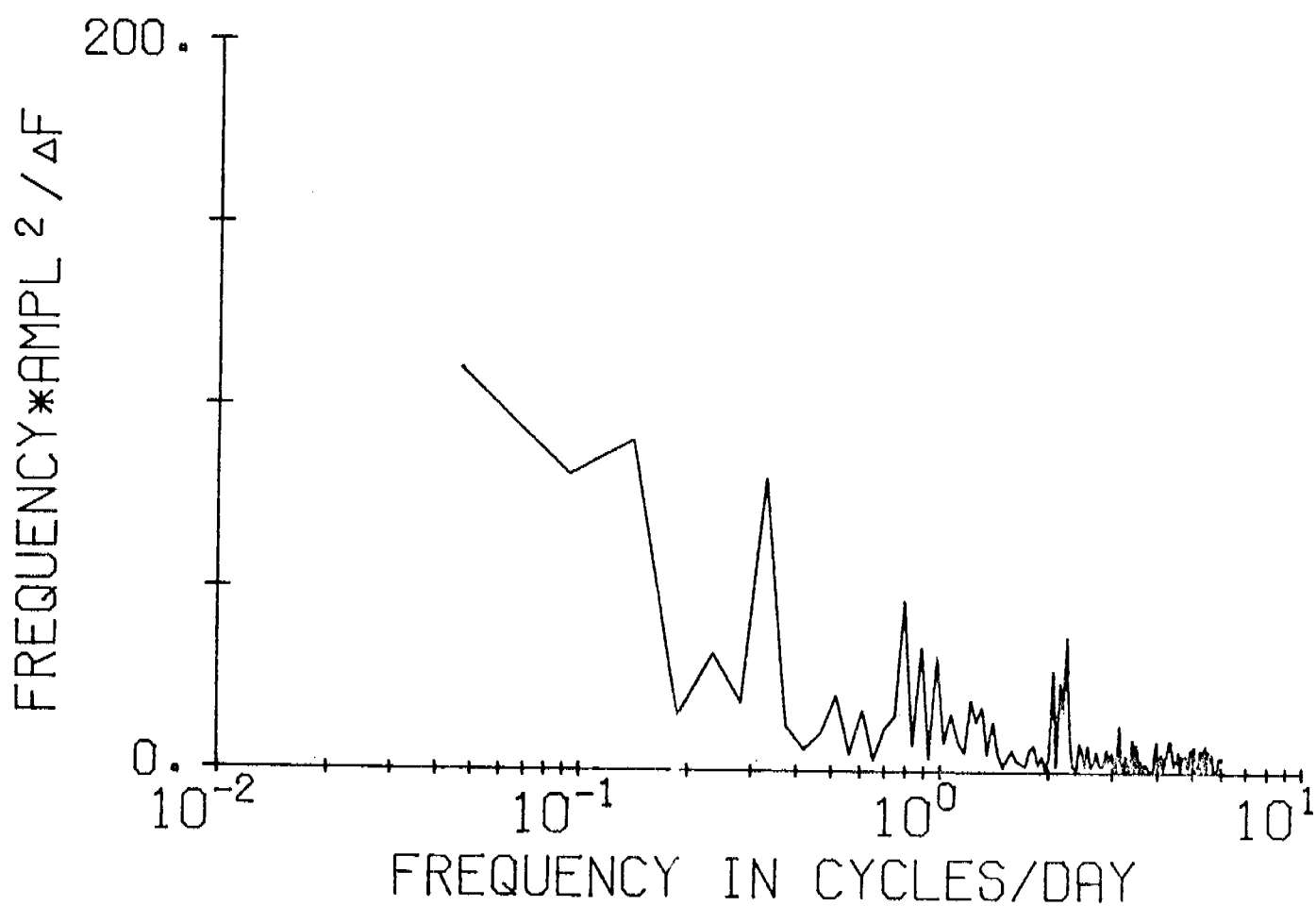


Figure 7

1315/3 DEPTH 152M
3/29/77 0545

V-COMP

2048 POINT SEGMENT 8
DELTA-T =15 MIN

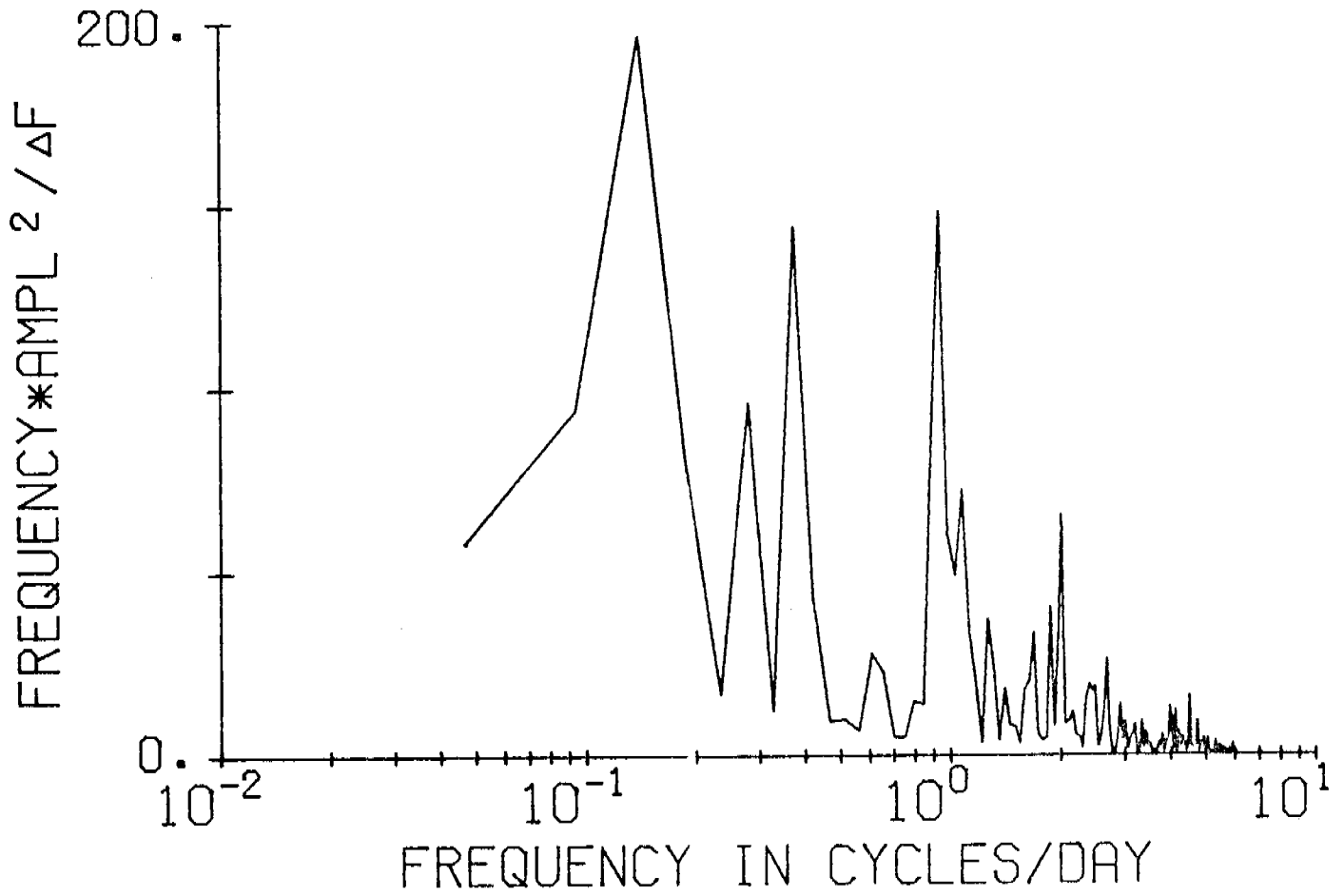


Figure 8

1315/3 DEPTH 152M
3/29/77 0545

V-COMP

2048 POINT SEGMENT 9
DELTA-T =15 MIN

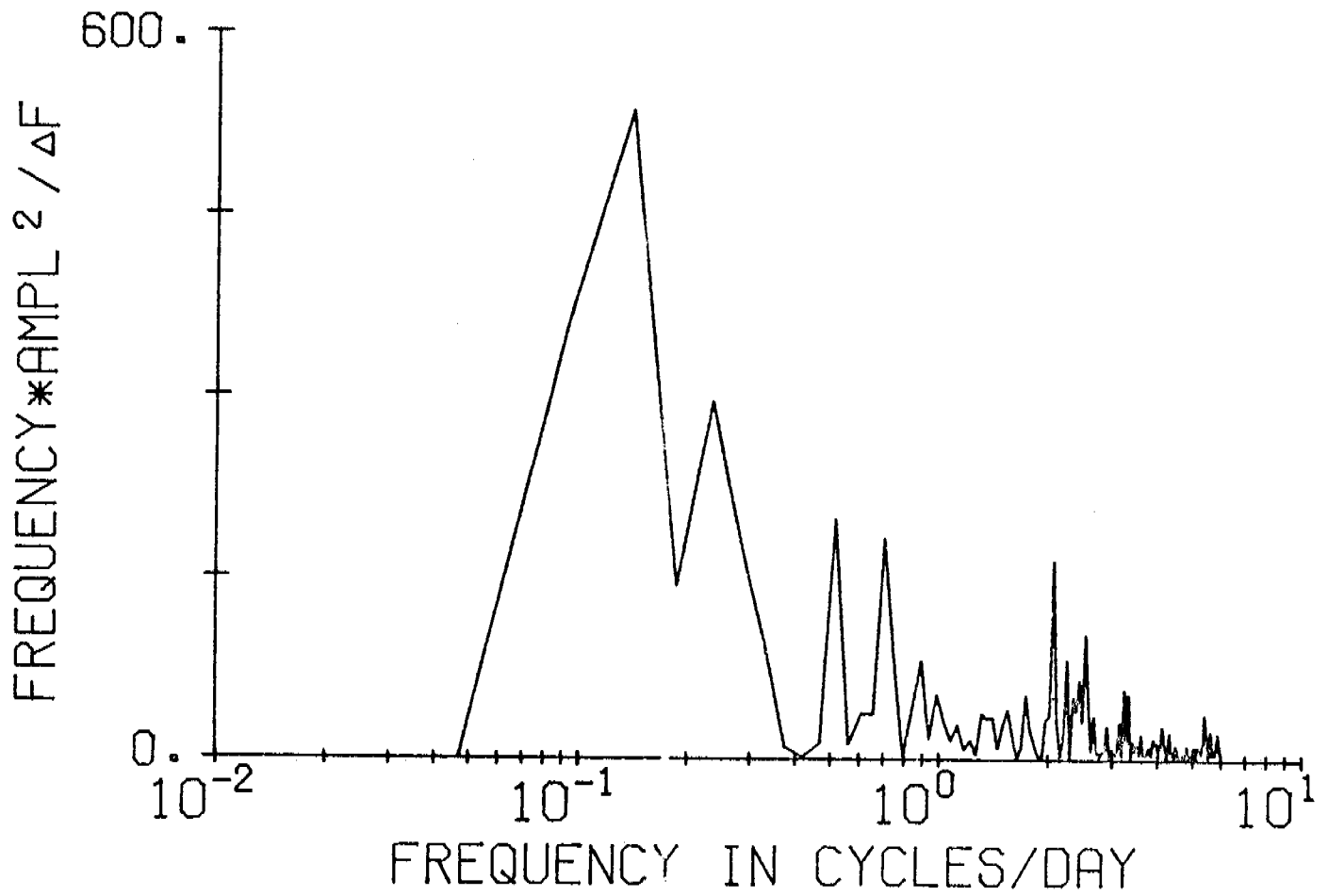


Figure 9

of what is probably a sea valley complicates the picture somewhat. The vector mean flow over the entire record was also in about the same direction, *viz*, toward 145°T at 3.4 cm sec⁻¹.

On the whole there is in the record a sense of reciprocating motion along the shelf, much as was found north of Oliktok (cf. Section III above), with the north- and east-components of velocity being about 180° apart in phase over the coherent frequency bands. On the other hand, there were a few times during which the current was more nearly rotatory.

There were also considerable temperature fluctuations. However, the coherence between the velocity and temperature records is generally quite poor. The few cases that do show significant coherence differ among themselves in phase.

VIII. Conclusions

The picture which emerges from the work done on the outer shelf to date is of a regime that is quite energetic over a broad band of sub-tidal frequencies. The mean flow calculated for a sufficiently long period (possibly up to several months) is unquestionably eastward. The flow appears to be steered by the local bathymetry. Although the energetic time scales of the flow are those of synoptic meteorological events, no clear relationship between atmospheric and oceanic events has been shown to date, even in a phenomenological fashion.

IX. Needs for further study

We anticipate detailed analyses of the records presently in hand, as well as of those to be recovered in the fall.

Future current studies on the Beaufort shelf should be concentrated on 1) determining the dynamics of the along-shore low-frequency flow, 2) determining the cross-shelf spectral distribution, *i.e.*, how the statistics of the flow vary across the shelf, and 3) examining the possibility of significant cross-shelf movement.

X. Summary of 4th quarter operations

A. Field operations

See appended report.

B. Problems

We have been delayed in our analysis by the changeover to a new computer system in the department. We experienced a release failure in the field work as per the appended report.

University of Washington
Department of Oceanography
Seattle, Washington 98195

Preliminary Report

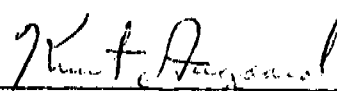
University of Washington Participation in
NOAA Recovery/Deployment Phase of Cruise W-30
Current Measurements in Possible Dispersal Regions
of the Beaufort Sea
1 March - 13 March 1978

by

Clark Darnall

NOAA Contract 03-5-022-67, TA 3

Approved by:



Knut Aagaard, Research Associate Professor
Principal Investigator



George Anderson, Professor
Associate Chairman for Research

Ref: M78-18

1. Objectives

To look at the time-dependent circulation and dynamics of the outer continental shelf of the Beaufort Sea, by means of long-term Eulerian time-series current studies at selected locations, where the ice cover is not seasonally removed. Cruise W-30 was a recovery/deployment phase of the current meter studies.

2. Narrative

Mooring recovery phase

One mooring (designated Lonely 2, deployed on Cruise W-27, in April 1977) was to be recovered. This would be accomplished (as in previous recoveries) by:

(1) General area relocation (within 7 km) by use of the helicopter's GNS 500A, VLF navigation equipment.

(2) Precise mooring relocation by ranging and bearing on the mooring's acoustic transponding release. Upon satisfactory relocation, the mooring would be released, allowing the flotation to lie against the underside of the ice cover.

(3) After further pinpointing of the mooring (within 100 m) a diving hole would be cut through the ice, and scuba divers would secure a retrieval line to the mooring. The mooring would then be recovered through the same hole.

Mooring deployment phase

Two moorings were deployed 50-60 mi NE of Lonely, Alaska. The inshore mooring was deployed in 99 m (water depth) with current meters at 64 m and 84 m, and an acoustic transponder/release at 89 m. The offshore mooring was in 203 m with current meters at 68 m and 188 m, and an acoustic transponder/release at 193 m.

A physical description and location of the moorings is in the Appendix.

The report of events is as follows:

1 March 1978 D. Hanzlick arrived in Barrow, and began unpacking and checking out equipment, anchors and flotation.

5 March 1978 NOAA helicopter N57RF with Lt. Harrigan and Bob Nield arrived Barrow.

6 March 1978 S. Harding and C. Darnall arrived in Barrow. Hanzlick departed Barrow in a chartered fixed-wing aircraft to transport anchors and flotation to Lonely. Flight time one hour.

7 March 1978 Weather clear, wind 060°T 13 kt, temperature -28°C.

0817 AST - Hanzlick, Harding and Darnall depart Barrow in N57RF (Harrigan, Nield). We refueled at Lonely and headed for the Lonely 2 (1000 m) mooring site.

1116 AST - Arrived GNS position 71°40.0'N, 152°10.1'W. We received transponder replies indicating the mooring to be 2.1 km range at 304°M. The timed pinger of the release would not reply. Subsequent transponder replies indicated that the ice was moving relative to the mooring (approximately 1/2 kt). The wind was 020°M at 25 kt. There were many open leads and ice fog. After 5 relocation/transponding moves, we decided to wait for stabler ice condition before releasing the mooring. The timed pinger mode would not reply at any of the 5 locations. We returned to Barrow. There were many new open leads along this flight path. Day's flight time 4 hours 23 minutes.

8 March 1978 Weather - snow, low visibility, wind 070°T 20 kt. Temperature -20°C. No flying. We prepared for deployment of Lonely 6 (200 m) mooring.

1720 AST - We started the first record cycle on RCM-4 s.n. 433 and s.n. 1315.

9 March 1978 Weather - low stratus and snowing, wind 070°T 17 kt, temperature -23°C.

0825 AST - Harding, Hanzlick and Darnall departed Barrow in N57RF (Harrigan and Nield). We refueled at Lonely, and decided that Hanzlick would remain at Lonely to arrange for pickup of anchors and flotation.

1057 AST - We arrived first sounding site, 280 fathoms. We would move inshore approximately 5 n. mi.

1224 AST - After 4 landing/soundings we had 114 fathoms water depth. We unloaded our deployment equipment and set up the ADF beacon. Due to poor weather conditions and winds (18 kt), we didn't leave anyone on the ice, but returned with N57RF to pick up the anchors and flotation at Lonely.

1404 AST - Harding and Darnall departed Lonely in N57RF (Harrigan and Nield). With the weight of the anchors, flotation and fuel for round trip, we were unable to take Hanzlick out. The ADF signal was very weak, and we were never able to use it for navigation.

1457 AST - We arrived GNS position 71°17.5'N, 150°37.3'W. We started the deployment hole and set up for the deployment. After we started the mooring in, Darnall dropped the clevis hook to the release. As there was no way to replace or jury-rig this part on the ice, we

cut the anchor loose, packed up and returned to Lonely for fuel and Hanzlick. We returned to Barrow, and began replacing the anchors, chain and line lost. A long, hard day had been for naught. Day's flight time 5 hours 10 minutes.

10 March 1978 Weather - low stratus, wind 070°T 8 kt, temperature -17°C, visibility 5 miles. We called Seattle to arrange for replacement of release clevis hook.

0910 AST - Harding and Darnall departed Barrow in N57RF (Harrigan, Nield). With the weight of the anchors we were carrying, we had to leave Hanzlick at Barrow. He would check on the ESP shipment, and its transfer in Faribanks.

We refueled in Lonely and returned to mooring area.

1118 AST - After 2 landing/soundings, we had 111 fathoms water depth. We unloaded and N57RF returned to Lonely for fuel, anchors, and flotation. The weather was OK (no wind), and Harding and Darnall started digging the deployment hole. The ice proved to be 4-1/2 ft. thick.

1340 AST - N57RF returned GNS position 71°17.7'N, 150°37.9'W. We started the mooring in.

1447 AST - AMF 322 release (s.n. 702971 rec. No. 8, xpdr. freq. 9.0 kHz) in the water. We heard it occasionally pinging.

1458 AST - RCM-4 in the water.

1520 AST - RCM-4 in the water.

1540 AST - The mooring was cut loose and at depth. We loaded up and returned to Barrow.

As the weather had been calm for several days, we decided to attempt to recover the Lonely 2 (1000 m) mooring. We set up our diving/recovering equipment. Day's flight time 4 hours 30 minutes.

11 March 1978 Weather - thin cirrostratus, wind - calm, temperature -22°C.

0821 AST - Hanzlick, Harding and Darnall departed Barrow in N57RF (Harrigan and Nield). We refueled in Lonely and headed for the mooring site.

1045 AST - In the area of the mooring site, there were many new refrozen leads (6-12 inches thick). The transponder replies indicated a 1.66 km range at bearing 336°M. There was no reply to the timed pinger command. After 2 landing/transpondings we had a range of 210 m. As the release was 190 m below the surface, the mooring had to be within a 100 m radius beneath us. We sent the release command and received no release verification. The transponder range did not change. For 45 minutes, we tried various transducer depths, receiver channels, and commands to no avail.

1220 AST - We gave up on releasing this mooring and returned to Lonely. En route we stopped at moorings Lonely 3 and 4 (deployed in November 1977) and tried the transponders and timed pinger commands. Both transponder/releases replied satisfactorily (timed pinger replied 1 pulse/2 sec for 60 sec). We arrived Barrow in the early afternoon. N57RF (Harrigan, Nield, Brooks) ferried 8 anchors to Lonely, and we set up for deploying the Lonely #5 mooring.

1740 AST - We started the first record cycle on RCM-4 s.n. 3169, and s.n. 3170. Day's flight time 2 hours 50 minutes.

12 March 1978 Weather - low stratus, wind 080°T 7 kt, temperature -18°C, visibility approximately 2 miles.

0824 AST - Hanzlick, Harding and Darnall departed Barrow in N57RF (Harrigan, Nield). We refueled at Lonely and headed for the mooring site.

1031 AST - Our first sounding was 76 fathoms. One move, and we had 54 fathoms water depth. The weather was clear and calm here. We unloaded and started the mooring hole. N57RF returned to Lonely to pick up anchor, flotation and fuel.

1310 AST - N57RF returned, GNS position 71°16.9'N, 150°44.1'W. We started the mooring in.

1321 AST - AMF 322 release s.n. 602390 rec. no. 10, xpr. freq. 11.0 kHz was in the water. The release occasionally pinged.

1330 AST - RCM-4 was in the water.

1340 AST - RCM-4 was in the water

1347 AST - Mooring was cut loose and at depth. We loaded up, and returned to Barrow.

We packed our equipment for return shipment to Seattle. Day's flight time 4 hours 35 minutes.

13 March 1978 Hanzlick, Harding and Darnall returned to Seattle.

3. *Methods*

Deployment phase

The current meter moorings were designed and constructed at the Department of Oceanography, University of Washington. The flotation was 28-inch O.R.E. steel spheres distributed along the mooring. The current meters were Aanderaa Model RCM-4. The acoustic transponder/releases were AMF Model 322. The mooring line was 1/2-inch diameter Nolaro using parallel polyester fibers; it was pre-measured, cut and loaded on aluminum reels with connecting links at all instrument and flotation points. The anchor consisted of lengths of railroad rails (each approximately 70 lbs.), with galvanized chain laced through holes cut in one end.

The deployment equipment consisted of a ten-foot high A-frame, which holds the mooring line reel, and is used for an anchor-first, vertical deployment mode. Hydraulic disc brakes and a stopper controlled the descent speed, and allowed for insertions of instruments and flotation. All components of the

deployment system are of lightweight material and can be broken down for helicopter-borne operations.

Recovery phase

An AMF Model 301 ranging and bearing command system was used for precise relocation of the AMF Model 322 transponder/releases. Since the release failed to work, there were no diving operations.

4. *Personnel*

Clark Darnall	Oceanographer	University of Washington
Steve Harding	Research aide	University of Washington
Dennis Hanzlick	Graduate student	University of Washington
Lt. W. Harrigan	Pilot	NOAA
Robert Nield	Mechanic	NOAA

Acknowledgments

Lt. Harrigan's and Mr. Nield's assistance in getting our operations on the ice, and their willingness to give us the maximum working time on the ice, was greatly appreciated. The personnel of the Naval Arctic Research Lab were very helpful in the accomplishment of our project.

APPENDIX

Mooring locations:

Lonely 2 (1000 m) deployed Spring 1977

71°13.1'N, 152°11.0'W.

Lonely 5 (200 m) deployed 12 March 1978

71°16.9'N, 150°44.1'W.

Lonely 6 (100 m) deployed 11 March 1978

71°17.7'N, 150°37.9'W

Flight time:

NOAA Helicopter N57RF - 21 hours 28 minutes.

Fourth Annual Report
Gulf of Alaska Shelf Circulation

J. Schumacher
R. Charnell
S. Hayes
H. Mofjeld
R. Muench

Pacific Marine Environmental Laboratory
Environmental Research Laboratory, NOAA
3711 15th Avenue N. E.
Seattle, Washington 98105

Contract No.: RP0000R7120847
Research Unit: 138
Period: 1 Apr. 1977 - 31 March 1978

TABLE OF CONTENTS

I. Summary

II. Introduction

III. Study Area

IV. Present Status

 A. Winter circulation and hydrography at
 Shelikof Strait and the northwest Gulf of
 Alaska continental shelf

 B. Variability of current and bottom pressure
 across the continental shelf in the north-
 west Gulf of Alaska

 C. Lower Cook Inlet circulation

 D. Seasonal variability of hydrography and
 circulation on the northwest Gulf of Alaska
 continental shelf

V. Cooperation

VI. Publications

VII. Need for further study

VIII. Conclusions

IX. Fourth Quarter Operations

 Appendix 1: Cruise Reports

 Appendix 2: Data Acquisition
 (April 1977 to 31 March 1978)

I. Summary

Field investigations, begun in Autumn 1974, have and continue to provide data which aids our understanding of hydrographic, current and pressure regimes in the Gulf of Alaska. Many important features have been identified, including: the relation between bottom pressure and velocity; cross-shelf coherence; gyral circulation west of Kayak Island; the pronounced effect of the Alaskan Current inflow through Shelikof Strait; the presence of shelf edge waters in the near-shore regions of troughs; and, a description of flow in Lower Cook Inlet. Further work, primarily intensive data analysis, will focus on understanding these and similar features, and estimating their importance in assessing hazards related to petroleum development. Additionally, an extensive analysis of the data, in conjunction with that collected by T. Royer (RU289), D. Hansen (RU217), M. Reynolds (RU367) and numerical studies by J. Galt (RU140) will lead to a synthesis of the regional physical oceanography.

II. Introduction

Objectives: The general objective of the program is to characterize circulation patterns with emphasis on determining likely distributions of water-borne contaminants. Specific objectives are:

A. Kodiak Island:

- 1) To examine flow in the troughs and banks off Kodiak Island and on the shelf downstream from Shelikof Strait using current meters, surface drift cards, seabed drifters and density data.
- 2) To characterize temporal and spatial variability in the flow field as function of season (summer/winter).
- 3) To relate observed and computed surface winds to observed currents.
- 4) To determine spatial variability of tidal currents.
- 5) To characterize seasonal distribution of density.

B. NEGQA:

- 1) Continue analysis of data from FY 76 and FY 77 in order to:
 - a) Interrelate bottom pressure gradients, currents, and wind measurements.
 - b) Investigate importance of topographic, tidal, local and non-local forcing upon the current regime in the Northeast Gulf.
- 2) Summarize the results of analysis into a final report (1 October 1978).

C. Lower Cook Inlet:

- 1) To relate observed and computed over-the-water winds to direct observations of currents.
- 2) To correlate surface currents obtained by Lagrangian techniques with subsurface Eulerian measurements.
- 3) To relate surface currents obtained by Doppler radar techniques to Lagrangian surface current measurements.

C. Lower Cook Inlet:

- 4) To characterize temporal and spatial variability in the flow field including flows through the Barren Islands and upper Shelikof Strait as a function of season (winter/summer).

D. Mitrofanina Island:

- 1) To examine correlations between observed currents, meteorological parameters and sea level variations.
- 2) Determine influence of bathymetry on the flow.
- 3) Examine local and non-local forcing.
- 4) Relate Icy Bay results to this new area in order to test their general applicability.

Tasks: The objectives of data acquisition are as follows:

1. Hydrographic data. These data are collected and analyzed to:
(1) determine the impact of the Alaskan Current upon waters in troughs off Kodiak Island and Shelikof Strait (2) determine the extent and seasonal variation of stratification over the shelf (3) infer flow from dynamic contours and baroclinic geostrophic calculations and (4) determine seasonal variability of transport by the Alaskan Current.
2. Current meter data. We are using current records to: (1) elucidate the relations among winds, bottom pressure, and currents in the Icy Bay, Kodiak Island, Lower Cook Inlet and Mitrofanina Island regions, (2) examine the velocity field characteristics in bank/trough areas, (3) determine if shelf edge waters cross trough sills and whether this is a mean or episodic flow, (4) to define mean flow, and (5) characterized tidal behavior in the various regions.
3. Pressure gage data. This data supports current meter data in determining the dynamical balances associated with barotropic flow components. These data are being used to generate tidal harmonics, and to determine meteorological impact upon flow.
4. Meteorological data. This data is required to examine oceanic response to atmospheric forcing and thereby understand some of the flow field components.
5. Ancillary data. Infrared satellite imagery, seabed drifters, surface drift cards and Lagrangian drifter data are being used to extend our description and understanding of the regional circulation.

III. Study Area

The study area continues to be the Gulf of Alaska, approximately bounded by Yakutat Bay on the east and Unimak Pass on the west. Field studies for the remainder of FY 78 will concentrate on the Lower Cook Inlet, Shelikof Strait and Kodiak Island regions. More detailed descriptions are presented in previous Annual Reports, in the manuscripts, (see Present Status section below), and in prior publications.

IV. Present Status

In addition to reports already published, the most comprehensive analyses of the data is that being prepared for publication. We therefore include pre-prints and/or condensations of these manuscripts along with a short report of work in progress. The contents of this section are:

- A. Winter circulation and hydrography of Shelikof Strait and the northwest Gulf of Alaska continental shelf - a condensed preprint of a Technical Report by Schumacher, Sillcox, Dreves and Muench.
- B. Variability of current and bottom pressure across the continental shelf in the northeast Gulf of Alaska - a preprint by S. Hayes.
- C. Lower Cook Inlet circulation - a condensed preprint by Muench, Mofjeld and Charnell.
- D. Autumn hydrography - ongoing work.

A. WINTER CIRCULATION AND HYDROGRAPHY OF SHELIKOF STRAIT AND THE NORTHWEST GULF OF ALASKA CONTINENTAL SHELF

ABSTRACT

Temperature and salinity observations were made in the complex bank and trough shelf region east of Kodiak Island and in Shelikof Strait during winter 1977. A warm ($>6^{\circ}\text{C}$) subsurface (~ 75 m) core was observed extending northwest along the axis of a shelf trough toward the north end of Shelikof Strait. Overlying this core in the nearshore region adjacent to the Kenai Peninsula, we observed a shallow (~ 50 m) band of low salinity (<32.0 g/kg) water. The 0/100 db dynamic topography suggests that this band was a region of relatively high westerly baroclinic flow (~ 15 cm/s) toward Shelikof Strait. Current records from a five-month winter period in Shelikof Strait were dominated by strong southwesterly mean flow (~ 40 cm/s at 20 m depth and ~ 25 cm/s at 100 m depth); with no flow reversals. Temperature and salinity profiles revealed weak stratification. The 0/200 db dynamic topography suggested a weak (~ 5 cm/s) baroclinic flow maintained by local coastal freshwater addition. The stronger measured flow indicated an appreciable barotropic component which was likely driven by inflow related to the Alaska Current. A second core of warm water over the shelf edge was the locale of a shallow minimum salinity band. The 0/100 db dynamic topography suggested a strong westerly flow (~ 25 cm/s) along the shelf break which was compatible with flow observed in winter current records. Overlying the bank region which lies between the two bands of relatively high flow, the water was characterized by lower temperatures and a lack of vertical structure. Dynamic topography suggested a weak cyclonic flow on this region. Current measurements from a mooring on the bank also indicated a weak (~ 3 cm/s) mean flow. We suggest that the temperature of the warm cores implies they are nonlocal advective features and originated from the Alaska Current which flows southwest along the shelf break. The cores may reflect a bifurcation of this flow upstream. Some of the Alaska Current's transport then flows along the trough and ultimately west through Shelikof Strait providing continuity for the observed barotropic flow.

A1. Introduction

Since August 1974 the Pacific Marine Environmental Laboratory (PMEL) has participated in field operations supporting NOAA's Outer Continental Shelf Environmental Assessment Program (OCSEAP) in the Gulf of Alaska. One facet of this program was an exploratory field experiment in the Kodiak Island-Shelikof Strait region (Figure 1) which included current meter moorings and conductivity, temperature versus depth (CTD) measurements. In this report we present CTD data collected during two cruises in March 1977. Current records for the period October 1976-March 1977 are presented and discussed. Additionally, satellite imagery is used to aid in defining surface temperature features.

A2. Data Acquisition and Reduction

Current meter station locations are shown in Figure 1. Aanderaa RCM-4 current meters were used on taut wire moorings with an anchor and acoustic release at the bottom and 1,000-lb subsurface buoyancy float above the top current meter. The taut-wire mooring tends to minimize surface wave-induced noise on the Aanderaa's Savonius rotor. A summary of duration and depth of each station's current meters and current record statistics are given in Table 1.

The current data were resolved into north and east components and low-pass filtered to remove high-frequency noise. Two new data series were then produced using a Lanczos filter (cf. Charnell and Krancus, 1976). The first series was filtered such that over 99% of the amplitude was passed at periods greater than 5 hours, 50% at 2.86 hours, and less than 0.5% at 2 hours. This series was re-sampled at one point per hour and used for tidal current analysis. The second series, filtered to remove most of the tidal energy, passed over 99% of the amplitude at periods of over 55 hours, 50% at 35 hours, and less than 0.5% at 25 hours. This was resampled at 6-hour intervals and was used for examining non-tidal circulation.

Temperature and salinity data were collected from the NOAA ship DISCOVERER using a Plessey model 9040 CTD system with a model 8400 data logger. This system sampled twice a second for simultaneous values of conductivity temperature and depth. Data were recorded during the down cast using a lowering rate of 30 m min^{-1} . Nansen bottle samples were taken at each station to provide temperature and salinity calibration data. The data were meaned to provide 1-m temperature and salinity values from which sigma-t was then computed.

A3 THE SETTING

A3.1 Previous Studies

Mean circulation in the Gulf of Alaska is dominated by the Alaskan Gyre (Dodimead, *et. al.*, 1963, Roden, 1969 and Ingraham, *et. al.*, 1976). This gyre is the Alaskan Current which flows westward generally paralleling the coastline. Royer (1975) discussed seasonal changes or hydrographic properties across the Alaskan continental shelf and relates these changes to wind forcing. In winter, the Aleutian Low controls storms with southeasterly winds (Danielson, *et. al.*, 1957). There is evidence that this atmospheric regime is accompanied by a seasonal change in the transport of the Alaskan current and the velocity of

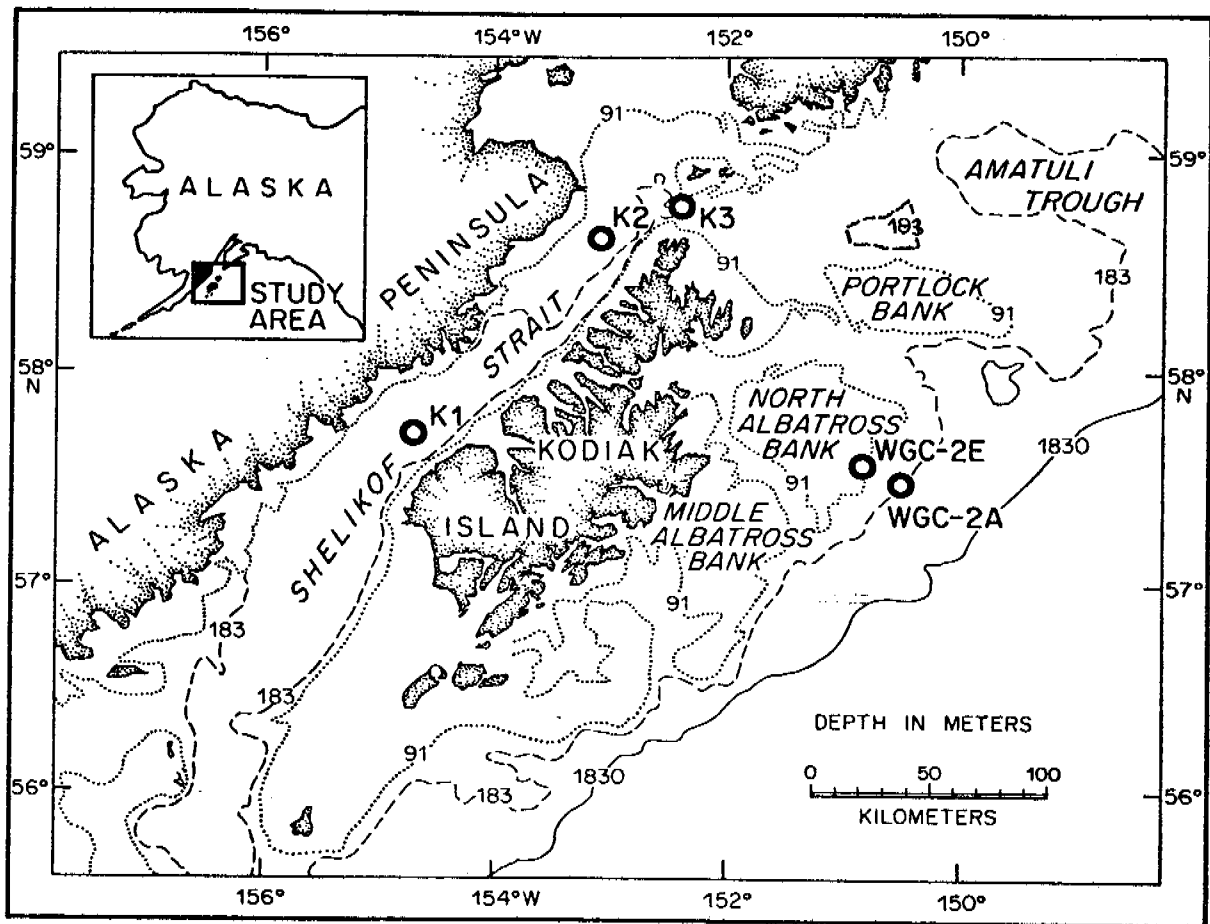


Fig. 1. Study area including locations of moored current meters (0).

TABLE 1

Current Meter Mooring Summary and Record Statistics

Current Meter Station	Position	Meter Depth(m)	Observation Period	Record Length(days)	Mean Speed(cm/s)	Variance (cm/sec ²)		Mean Flow Speed(cm/s)	Direction(^o T)
						U	V		
K1A	57 44.7N 154 43.7W	100	16 October 1976 to 26 March 1977	163	32.9	269.8	322.8	27.1	237
K2A	58 37.2N 153 05.0W	20	15 October 1976 to 27 March 1977	163	42.8	337.7	448.9	38.6	214
		100	16 October 1976 to 27 March 1977	163	30.2	247.2	288.7	26.2	223
K3A	58 45.5N 152 10.4W	20	15 October 1976 to 21 Nov. 1976	37	53.6	2088.5	750.7	30.1	298
WGC-2A	57 27.1N 150 29.5W	20	9 September 1975	68	34.2	322.1	281.5	32.9	225
		100	to 28 Nov. 1975	68	30.2	233.1	194.6	26.6	235
WGC-2E	57 33.8N 159 49.3W	20	2 October 1976 to 26 March 1977	156	41.2	897.1	1016.2	2.5	239

the accompanying flow along the continental shelf (Favorite, 1974; Hayes and Schumacher, 1976). Higher transport and velocities are observed during winter. There are indications that flow further intensifies off Kodiak Island (Favorite, 1967) and that a warm surface feature is present along the shelf break (Royer and Muench, 1977). The most comprehensive study of hydrographic structure and inferred baroclinic flow on the shelf off Kodiak Island was presented by Favorite and Ingraham (1977), and Wright (1970) presented a reconnaissance of waters in Shelikof Strait and the shelf region off Kodiak Island.

A3.2 Bathymetry

Bathymetry southeast of Kodiak Island is dominated by a series of four relatively shallow (<90 m) areas (Figure 1). These are, from north to south; Portlock, North, Middle and South Albatross banks. They are separated from one another by narrow channels which cleave the shelf in a direction roughly normal to the coastline.

Stevenson Trough, between Portlock and North Albatross banks, is approximately 110 m deep. Chiniak Trough, separating North and Middle Albatross banks, has an apparent sill depth of 145 m. Kiliuda Trough, southernmost of the three cuts, lies between Middle and South Albatross banks and has a sill depth of 150 m. Amatuli Trough, the most northerly of the features in the study area, lies north of Portlock Bank and is a large, deep (>200 m) cleft gouging the shelf from east to west. The westward extension of Amatuli Trough bifurcates at the Barren Islands to form Kennedy Entrance north of the islands and Stevenson Entrance between the Barren Islands and Afognak Island. Kennedy Entrance is the narrower entrance but is deeper with depths nearly to 200 m; the maximum depth to Stevenson Entrance is little more than 120 m.

Shelikof Strait is between Kodiak and Afognak islands and the Alaska Peninsula. Along with Kennedy and Stevenson entrances it connects Lower Cook Inlet with the Gulf of Alaska. The northern half of Shelikof Strait, between Afognak Island and the Alaska Peninsula, is generally less than 180 m deep. The southern half is deeper than 200 m. The extension of the Strait southwest of Kodiak Island is bounded on both sides by banks. On the east, the bank extends past the Trinity Islands to Chirikof Island, with depths from 30-40 m. To the west, a 100 m shoal area extends southward from the Peninsula to encompass Sutwick Island and the Semidi Islands.

Between these shoals, which extend some 160 km offshore southwest of Kodiak Island, the trough leading out of Shelikof Strait curves south and is oriented nearly due north - south where it accesses the Gulf. At the southernmost limit of the trough the adjoining banks create a 200 m sill across its mouth, limiting flow below that depth. Stevenson Trough extends from Stevenson Entrance southeasterly past the western end of Portlock Bank, separating Portlock and North Albatross banks. At its shallowest point, in the narrow passage west of Portlock Bank, the Trough is 110 m deep.

A4 OBSERVATIONS

A4.1 Hydrography: Kodiak Island Shelf

We present the CTD data (see Figure 2 for station locations) in a series of surface, bottom, and surface-bottom difference contours for temperature (Figures 3-5) salinity (Figures 6-8) and sigma-t (Figures 9-11). Cross-shelf vertical sections of temperature and salinity, are shown in Figures 12-15.

Surface temperature contours indicate that a tongue of relatively warm ($>6^{\circ}\text{C}$) water extended across Portlock Bank southwestward toward Stevenson Trough. A second band of warm ($> 6^{\circ}\text{C}$) surface water extended westward from Amatuli Trough into Kennedy Entrance, roughly paralleling and adjacent to the Kenai Peninsula coastline. Cold ($< 5.0^{\circ}\text{C}$) surface waters occurred over North and Middle Albatross banks and seaward of the 1000 fathom (1829m) depth contour. Warmer waters generally occurred over trough features, eg., Chiniak and Kiliuda troughs, and colder waters occurred over banks. Bottom temperature contours also indicate that the coldest waters tended to lie on the banks and seaward of the 1000 fathom (1829m) depth contour. The tongue of warm water over southern Portlock Bank was less extensive on the bottom than at the surface. The region of warm waters off the Kenai Peninsula was by contrast more extensive on the bottom than on the surface, and was generally warmer. Additionally, these warm bottom waters were closer to shore and extended farther west-southwest than warm surface waters (station 24). The temperature difference (surface - bottom) contours indicate that little or no thermal stratification was present over North and Middle Albatross banks (Figure 5). The strongest positive temperature differences occurred in the region west of Amatuli Trough and seaward of the shelf break. Waters over Kiliuda and Chiniak Troughs, the depression running from the port of Kodiak to Stevenson trough and the depression extending from Amatuli Trough into Kennedy Entrance showed the strongest negative temperature differences (thermal inversions).

Surface salinity contours indicate that a tongue of low salinity ($<32.0^{\circ}/\text{oo}$) water extended west-southwest roughly coincident with the shelf break. A second low salinity ($<32.0^{\circ}/\text{oo}$) region occurred in a near-coastal band along the Kenai Peninsula. Between these two regions of low salinity the salt content was greater (up to $32.3^{\circ}/\text{oo}$), and the highest salinities observed ($>32.4^{\circ}/\text{oo}$) occurred seaward of the shelf break salinity minima. Bottom salinity contours show a tongue of high salinity water ($>32.8^{\circ}/\text{oo}$) extending westward from Amatuli Trough. On either side of this tongue, salinity values decreased; the lowest salinities observed were along the Kenai Peninsula. On all three banks, observed bottom salt content was lower than in the surrounding troughs and valleys. The $32.6^{\circ}/\text{oo}$ contour represents a minimum salinity band. The $32.6^{\circ}/\text{oo}$ to $33.0^{\circ}/\text{oo}$ contours indicate "tongue-like" features protruding into Stevenson, Chiniak and Kiliuda troughs. Bottom salinity values also exceeded $32.6^{\circ}/\text{oo}$ in the depression off Kodiak. Salinity difference (bottom-surface) contours indicate near vertical homogeneity over the banks. A band of stratified water ($\Delta S=0.6^{\circ}/\text{oo}$) was present along the Kenai Peninsula; seaward of the banks this band reflects the presence of bottom high salinity tongues extending into the troughs. Over the shelf break, surface salinity minima and increased bottom salinities resulted in crowding of the contours.

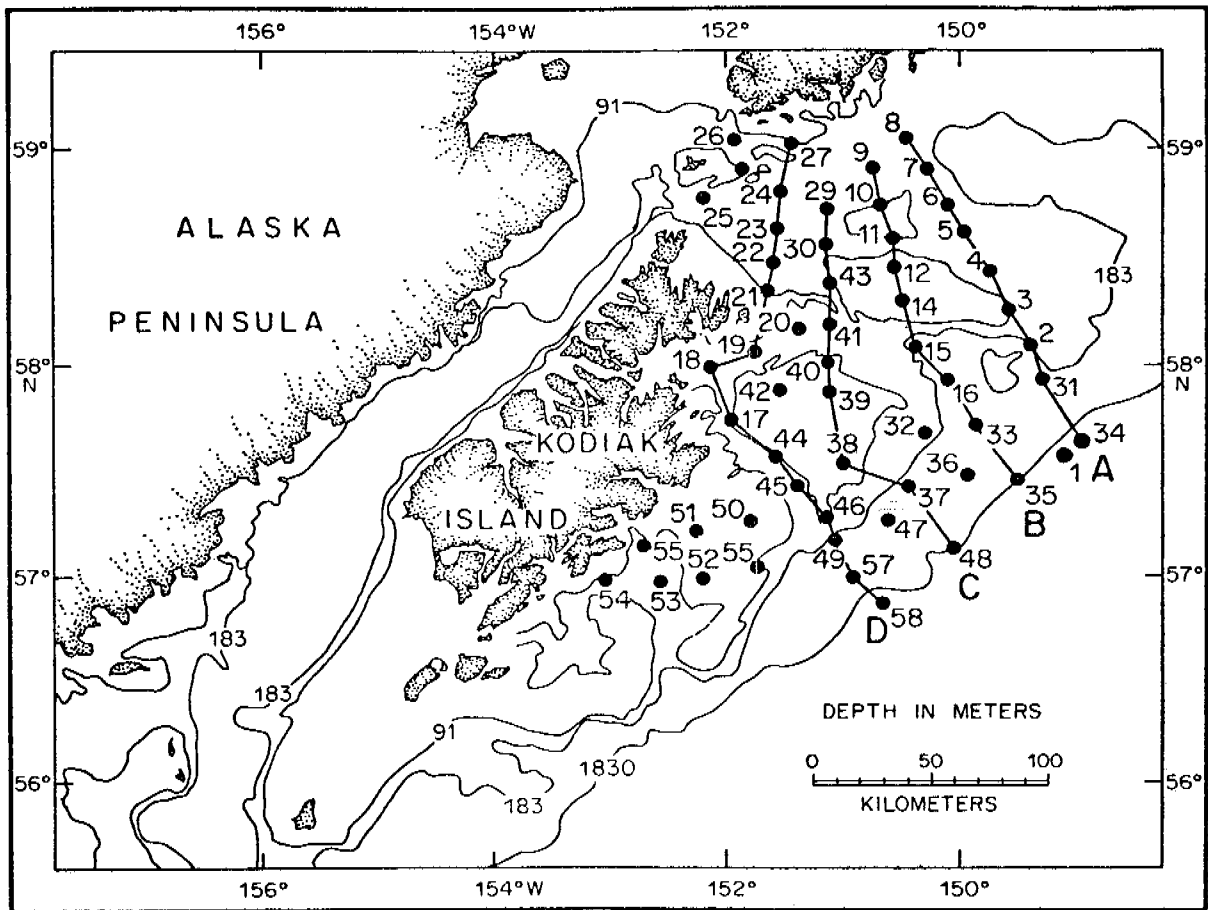


Fig. 2. CTD station locations for 2-10 March 1977, LEG II.

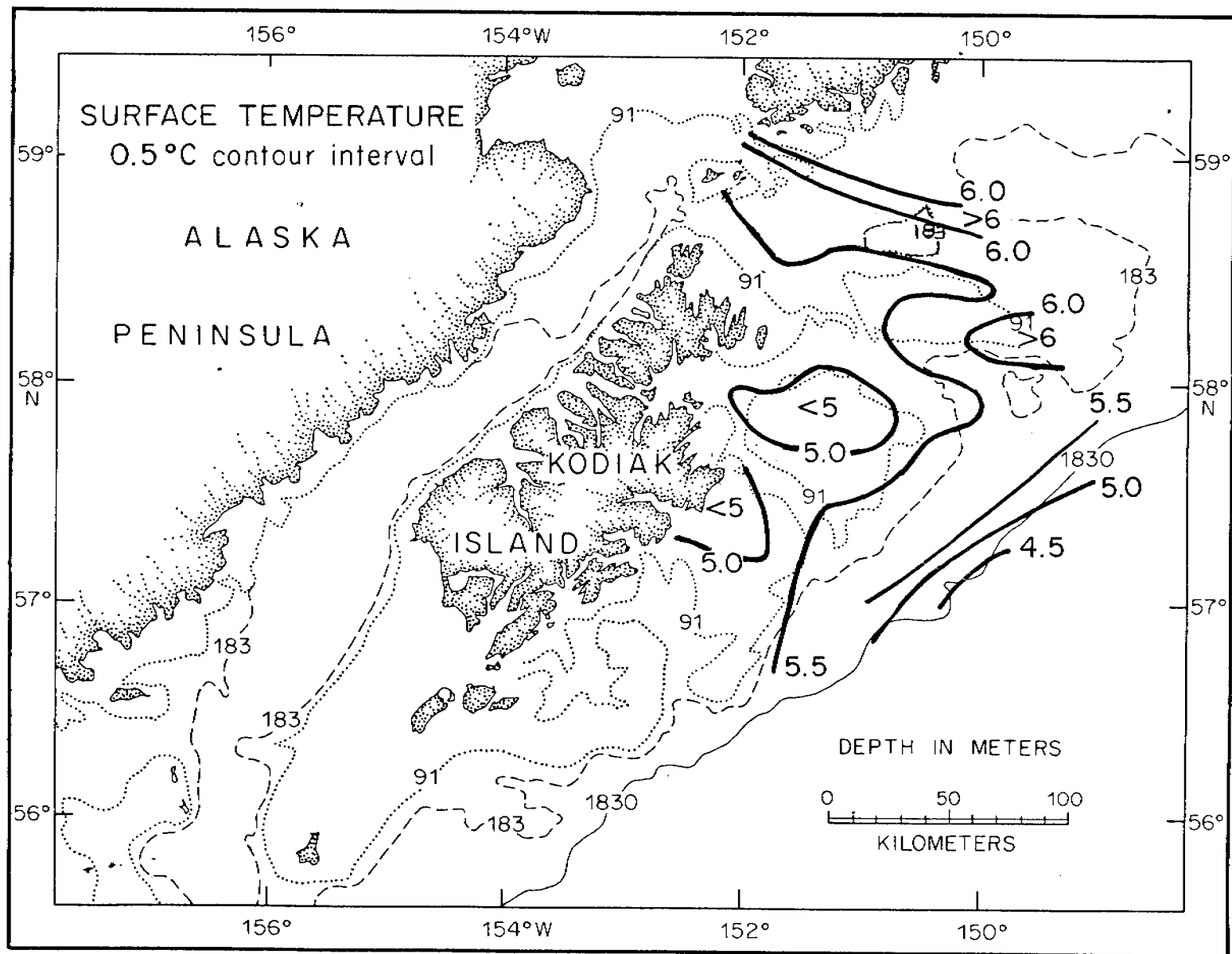


Figure 3. Surface temperature contours: 2-10 March 1977.

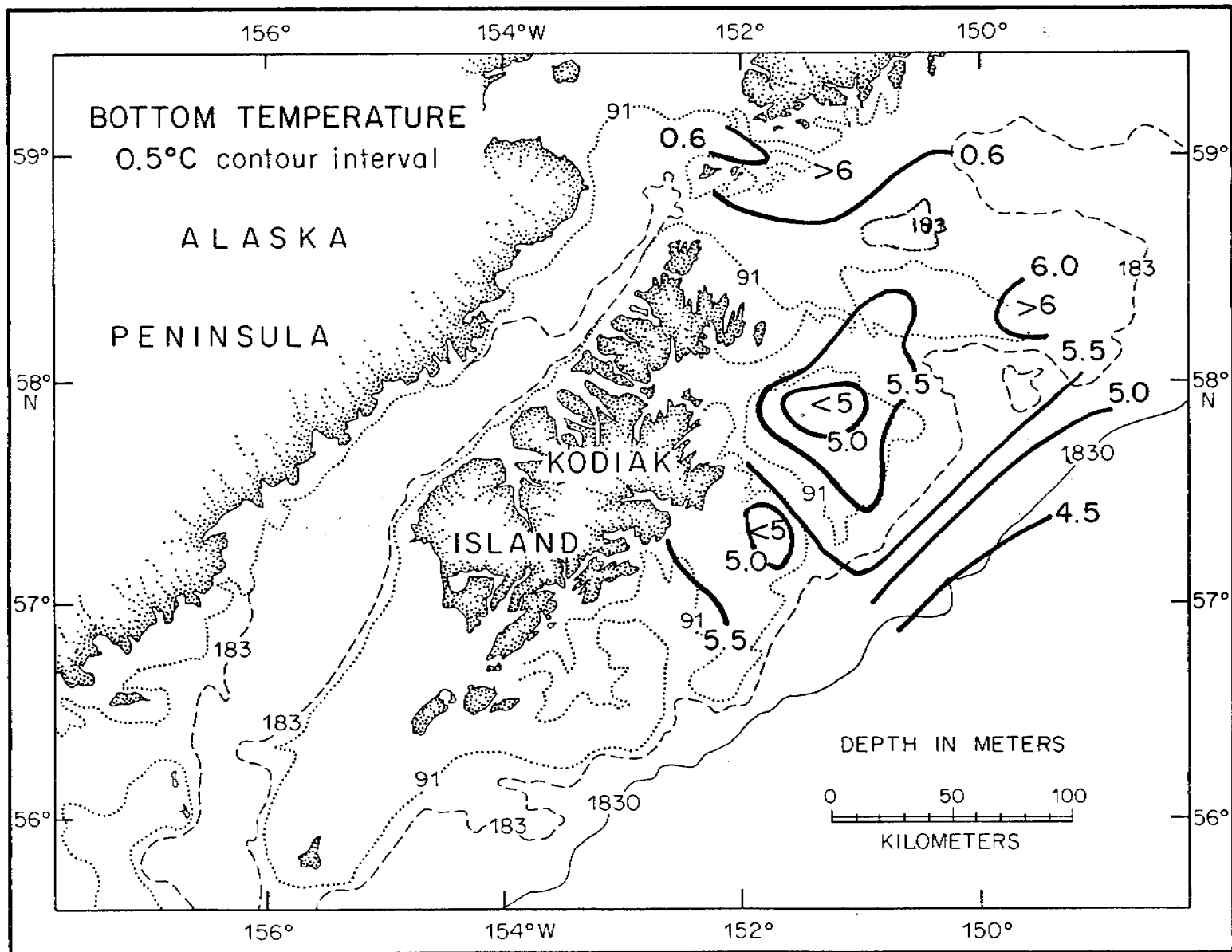


Figure 4. Bottom temperature (or 200 m) contours: 2-10 March 1977.

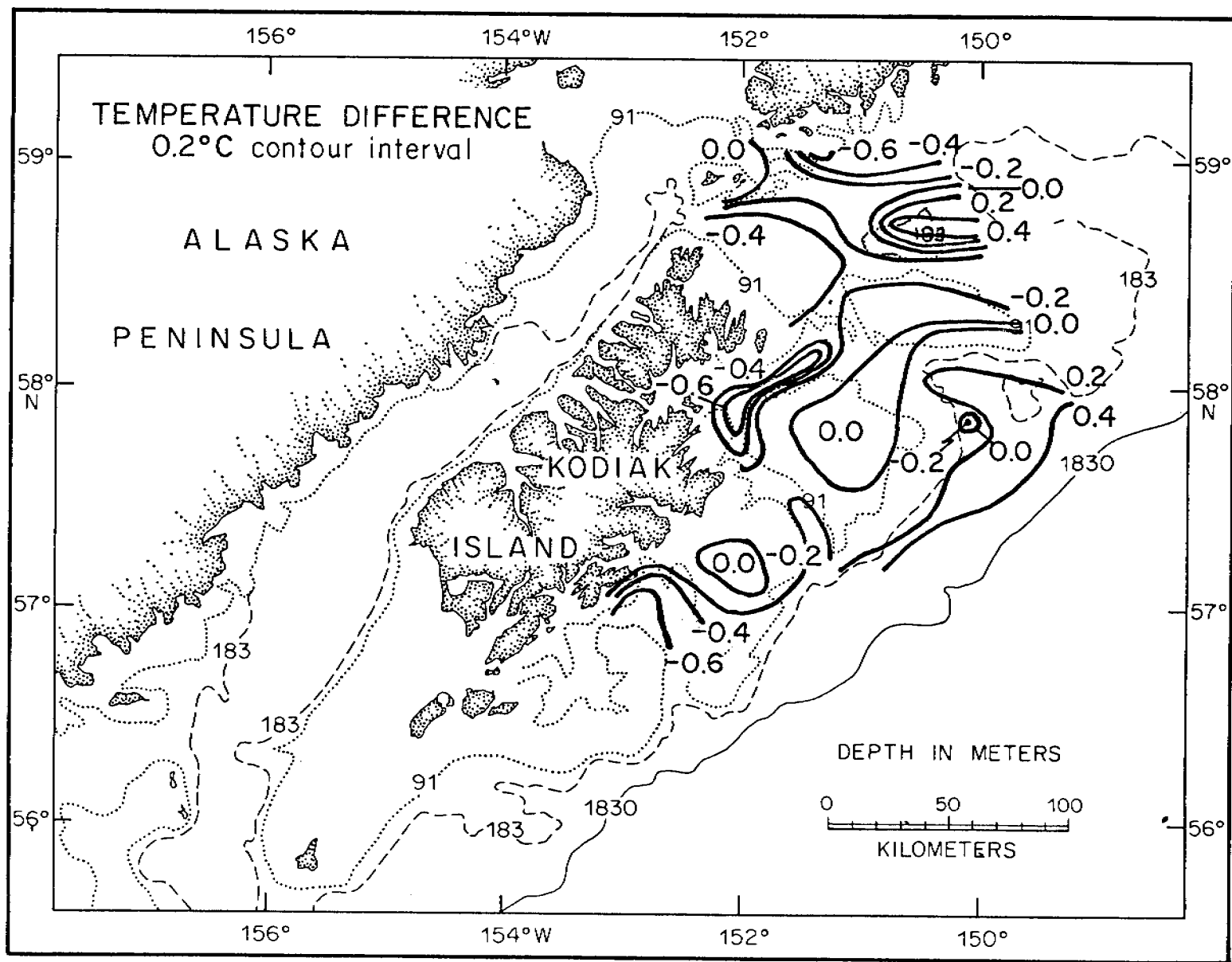


Figure 5. Surface - Bottom temperature difference contours ΔT : 2-10 March 1977.

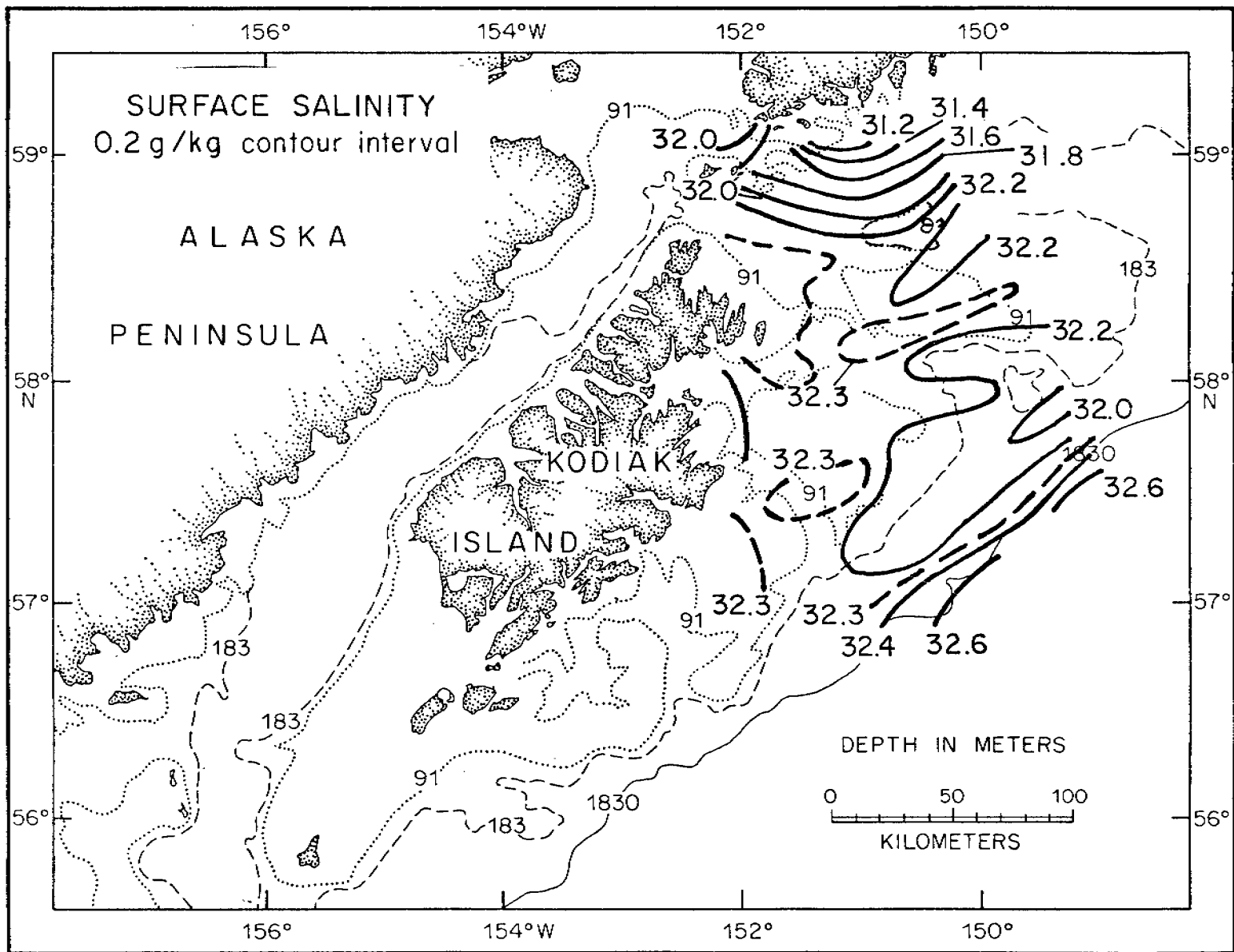


Figure 6. Surface salinity contours: 2-10 March 1977.

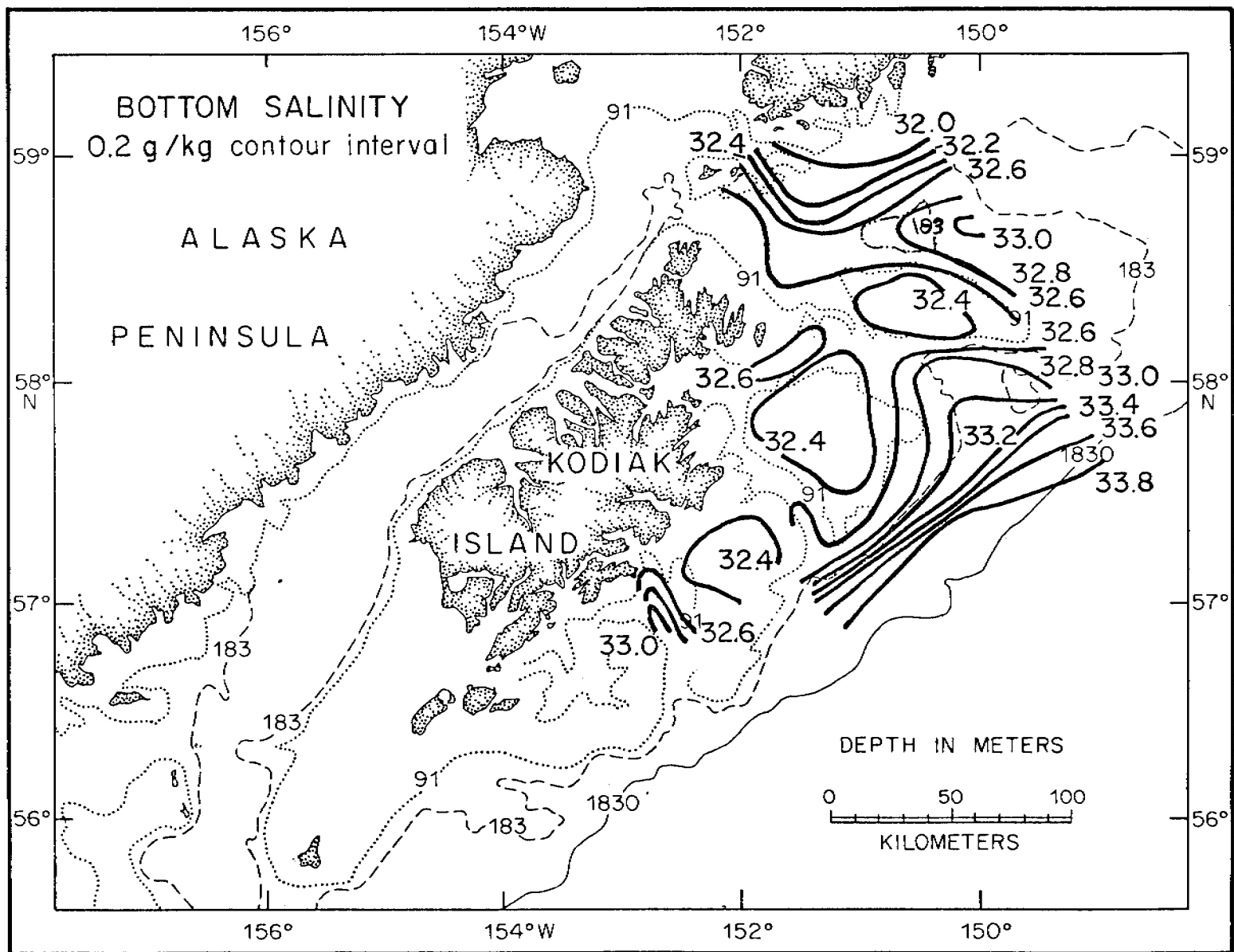


Figure 7. Bottom salinity (or 200 m) contours:: 2-10 March 1977.

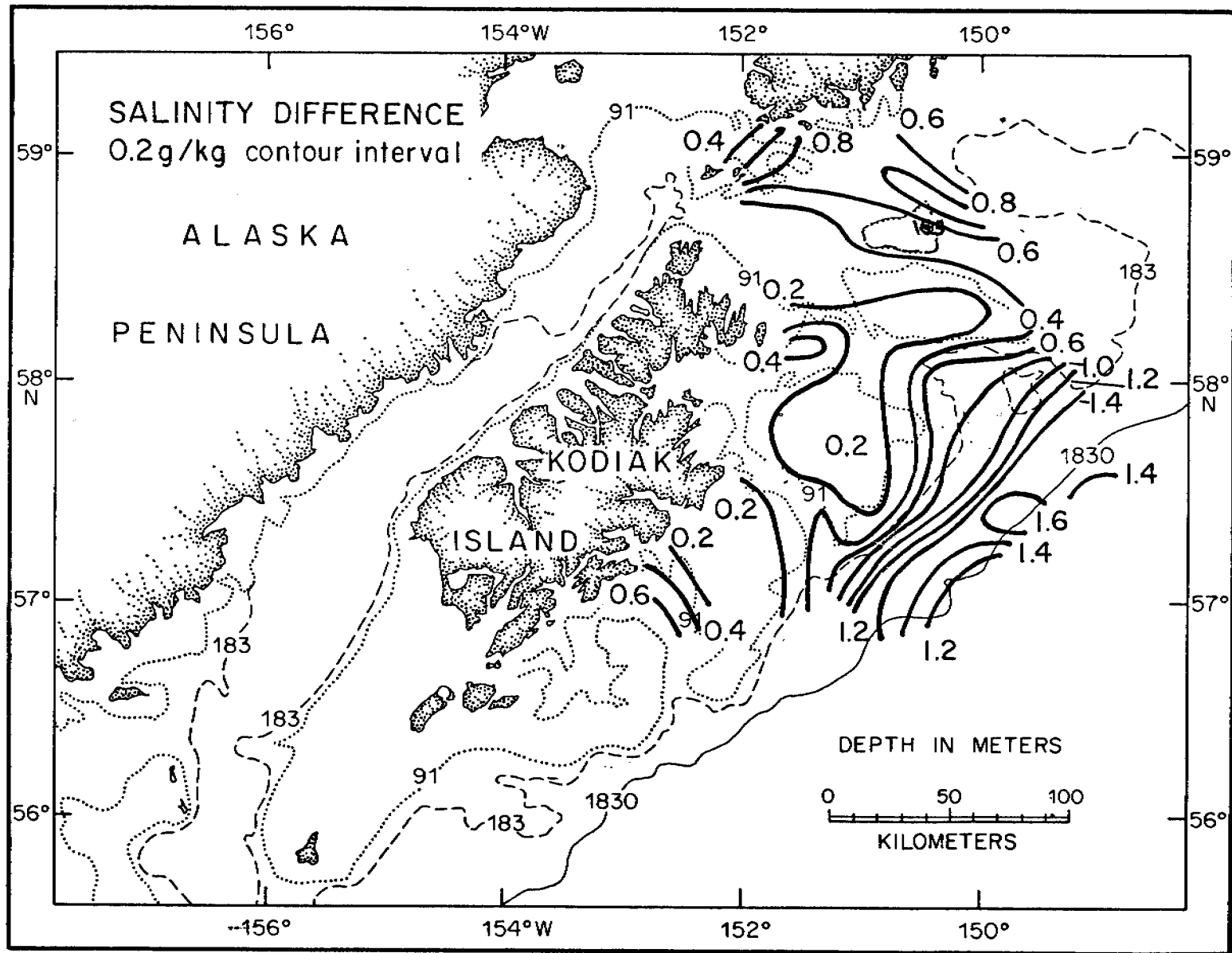


Figure 8. Bottom (or 200 m) - Surface salinity differences contours ΔS : 2-10 March 1977.

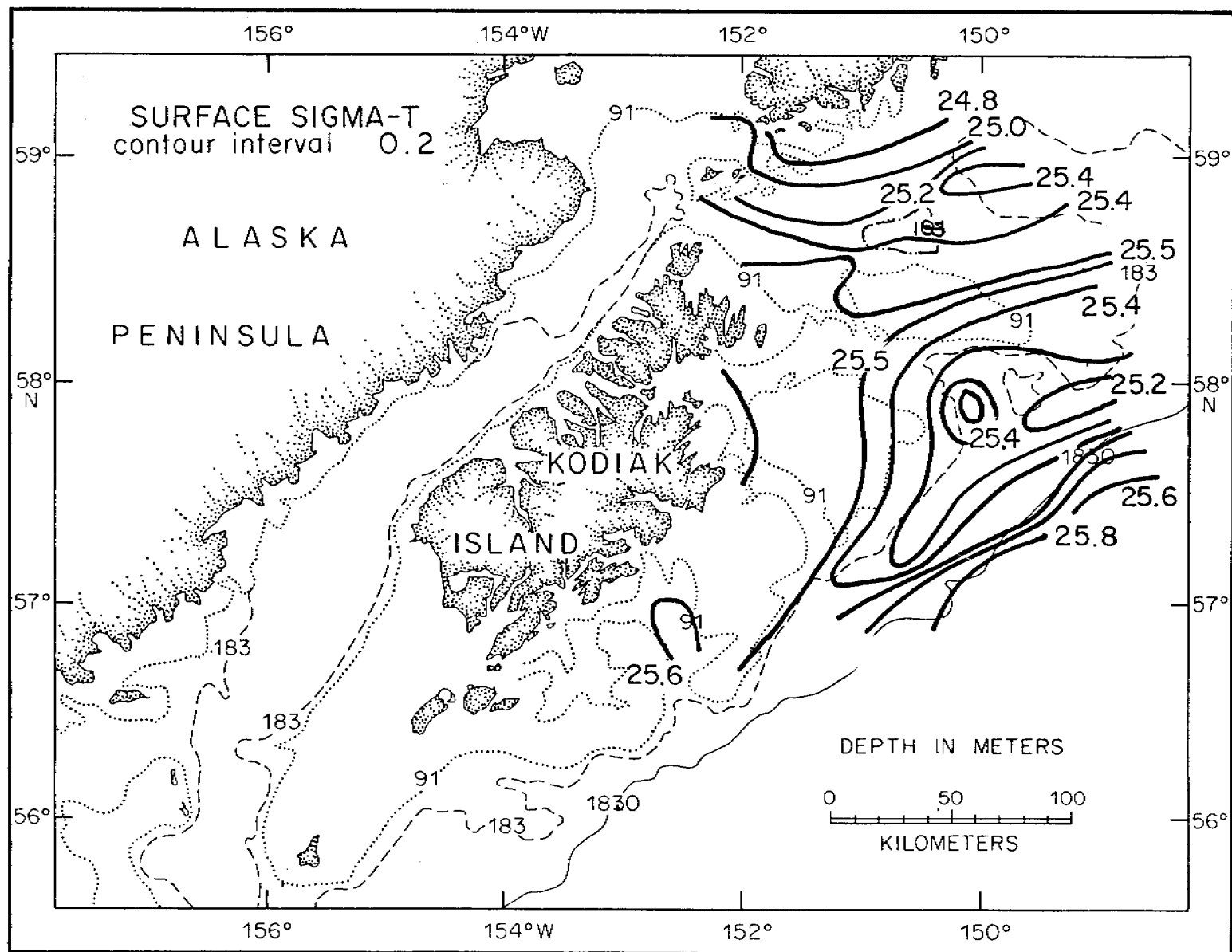


Figure 9. Surface sigma-t contours: 2-10 March 1977.

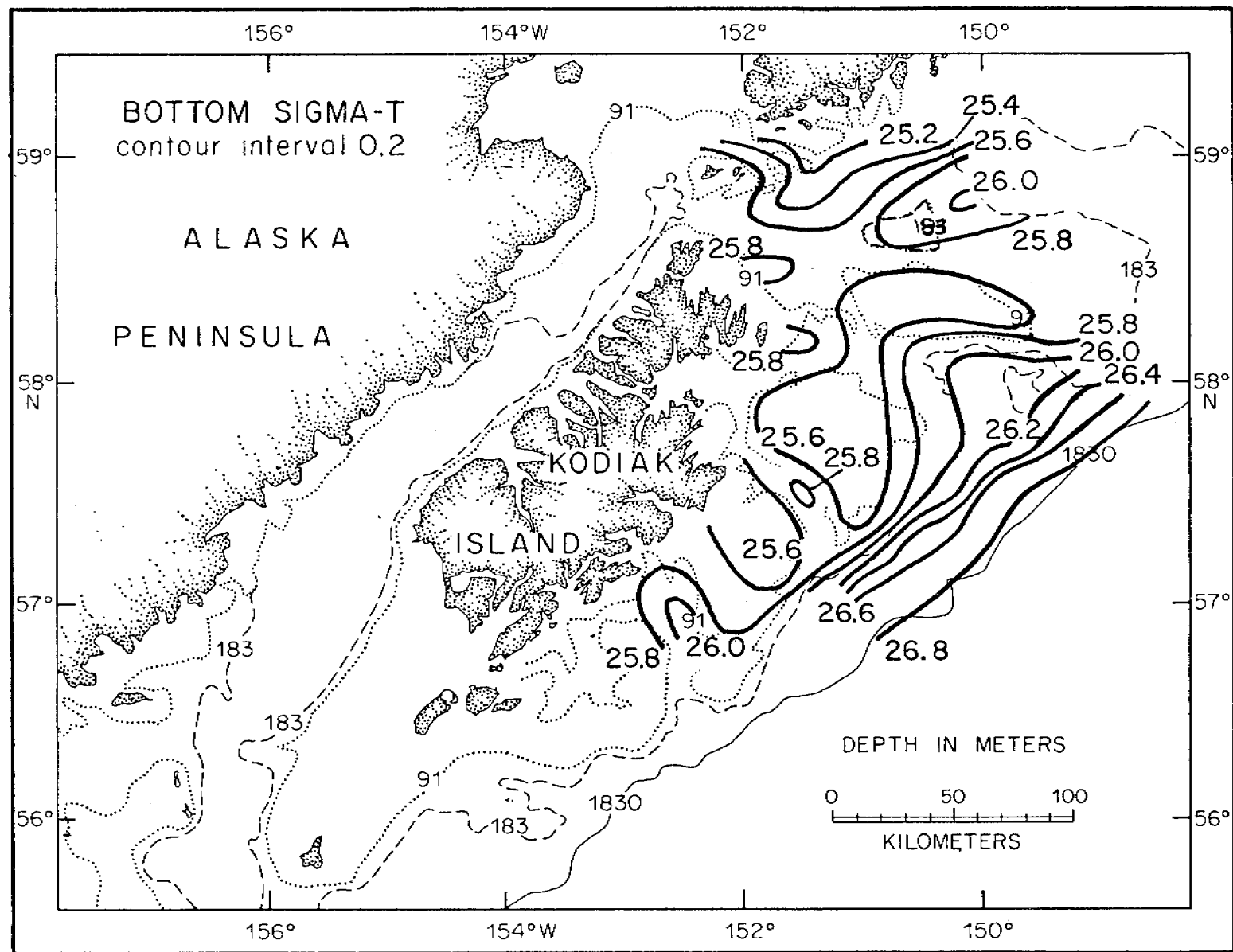


Figure 10. Bottom sigma-t contours: 2-10 March 1977.

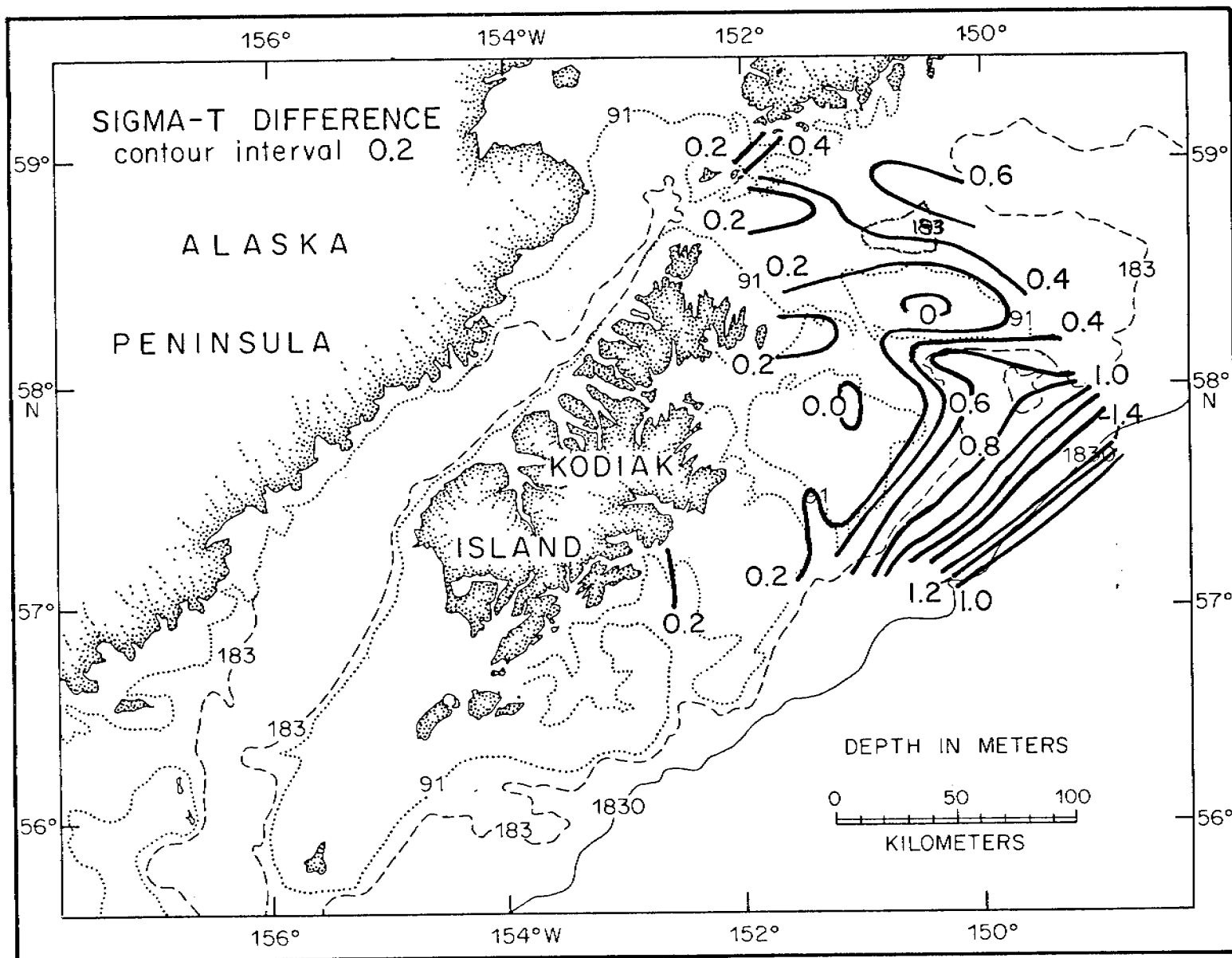


Figure 11. Bottom (or 200 M) - Surface sigma-t contours $\Delta\sigma_t$: 2-10 March 1977.

Surface sigma-t contours resembled salinity contours. The region extending westward across Portlock Banks was relatively low density as indicated by the 25.5 sigma-t contour. As expected from the salinity distribution, a surface density minima paralleled the shelf break and denser bottom waters appeared in the trough and valley features. Sigma-t difference (bottom-surface) contours further substantiate the vertically homogeneous nature of waters over the banks and the contrasting presence of vertical stratification over troughs (Figure 11). Over the slope, sigma-t contours indicate the greatest stratification (up to 1.4 sigma-t units) over the upper 200 m of the water column.

We present vertical sections (Figures 12-15) of temperature and salinity to further elucidate the extent of the warm cores and salinity minimas. At the "upstream" boundary of the region (Figure 12), warm water ($>6.0^{\circ}\text{C}$) was observed from the surface to approximately 125 m depth over the shelf edge, with maximum temperatures ($>6.3^{\circ}\text{C}$) at depths of 60 - 70 m. We noted that the apparent bimodal temperature distribution over the shelf edge, i.e. at stations 3 and 31, may be an artifact of sampling. Stations 2 through 8 were occupied consecutively between 2 and 3 March, while 31 and 34 were occupied on 7 March. Thus, the apparent configuration may represent a seaward meander of the warm core; however, the existence of this feature is clear. Coincident with the more seaward portion of the shelf edge warm core (at station 31) was a shallow (<40 m) salinity minima.

A second warm core at about 75 m extended 50 km seaward from station 8 (~ 25 km from the Kenai Peninsula). Maximum temperatures, ($>6.2^{\circ}\text{C}$) were observed on the shoreward side where the warm region ($>6.0^{\circ}\text{C}$) extended from the bottom to ~ 50 m. Seaward of this location, the warm core narrows to a 10 - 15 m thick region at a depth of 70 m. Low salinity was observed only at station 8 and values $<32.0^{\circ}/\text{oo}$ occurred to a depth of 105 m. We note that salinity values observed over Amatuli Trough were equivalent to those at a similar depth over the shelf edge.

In the three "downstream" sections (Figures 13, 14 and 15) the salient features were: a shallow (<50 m) salinity minima ($<32.25^{\circ}/\text{oo}$) located over the shelf edge region, a warm, subsurface temperature maximum ($>6.2^{\circ}\text{C}$) subsurface core along the Kenai Peninsula. The figures indicate continuity of those features over a 100 km Kenai Peninsula. Additionally, it is evident that vertical structure was attenuated on the shoal bank regions.

A4.2 Hydrography: Shelikof Strait

Three sections of CTD stations (Figure 16) were occupied on 28 - 30 March 1977 in the Shelikof Strait - lower Cook Inlet region. Since horizontal and (Figures 17 and 18) vertical gradients were small, we present composites of temperature and salinity.

Temperature observations from Kennedy and Stevenson entrances (Figure 17) indicate little thermal stratification; typical values had a magnitude less than 0.25°C with a maximum $\Delta T = -0.62^{\circ}\text{C}$ observed at station K4.3. In general, water temperatures were colder (less than 5.0°C) in Kennedy Entrance than in Stevenson Entrance; however, they contained a warmer ($>5.5^{\circ}\text{C}$) bottom layer on the Kenai Peninsula side of the entrance. Salinity observations also indicated little stratification. A maximum $\Delta S = 0.39^{\circ}/\text{oo}$ was measured at station 4.3 on the northeast side of Kennedy Entrance and typically values were $\sim 0.25^{\circ}/\text{oo}$. In general, waters in Kennedy Entrance were less saline than in Stevenson Entrance, with a maximum salinity of 31.98 g/kg observed near the bottom at two stations on

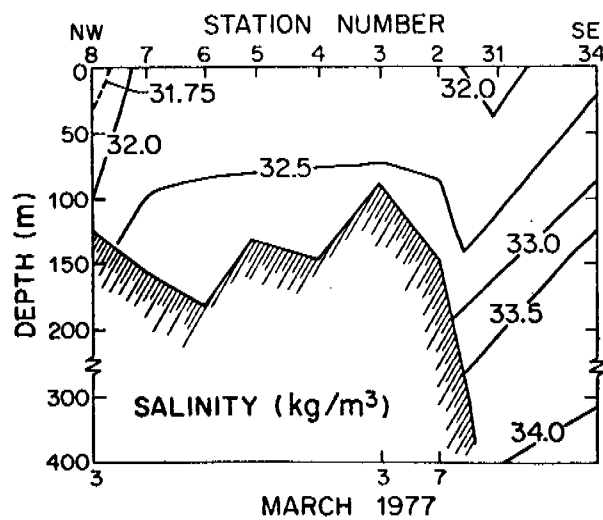
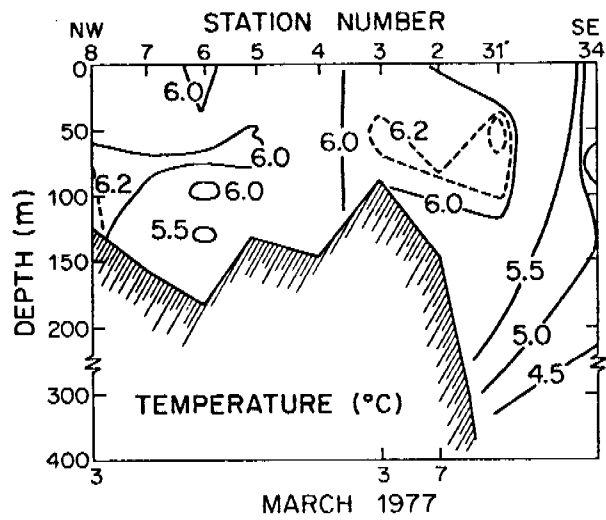
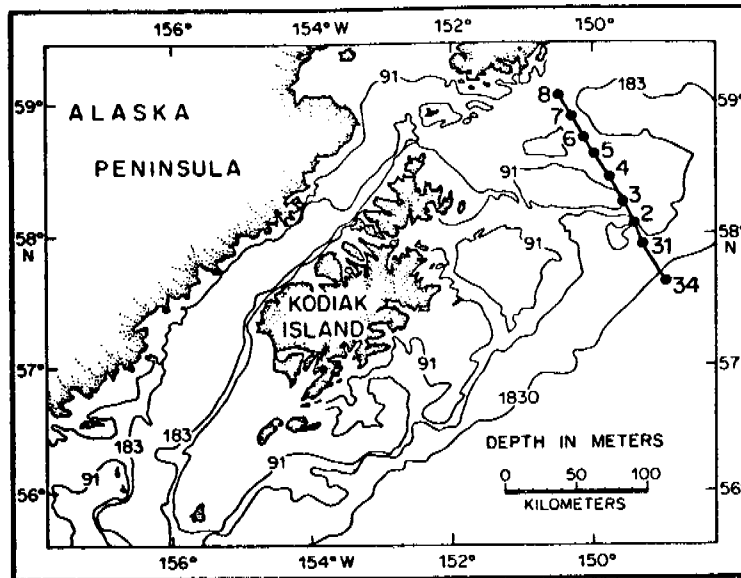


Fig. 12. Temperature and salinity section, LEG II.

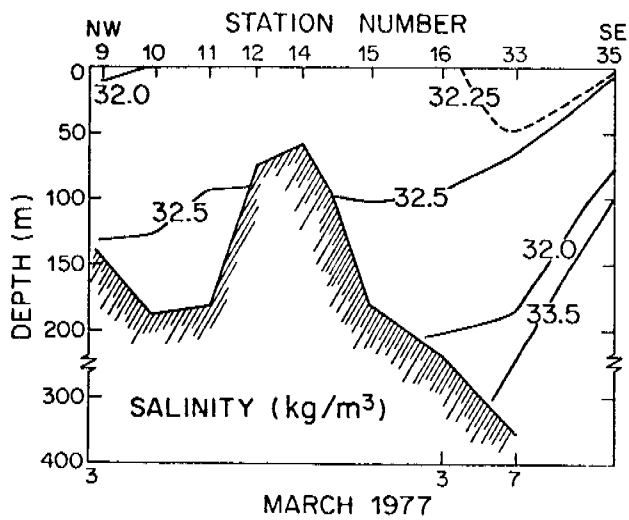
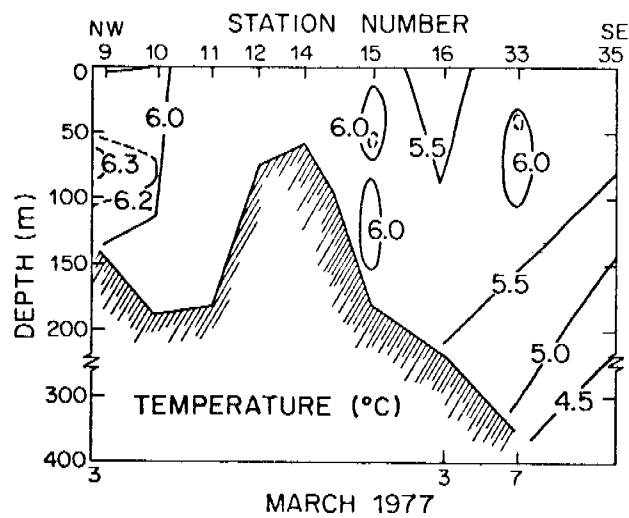
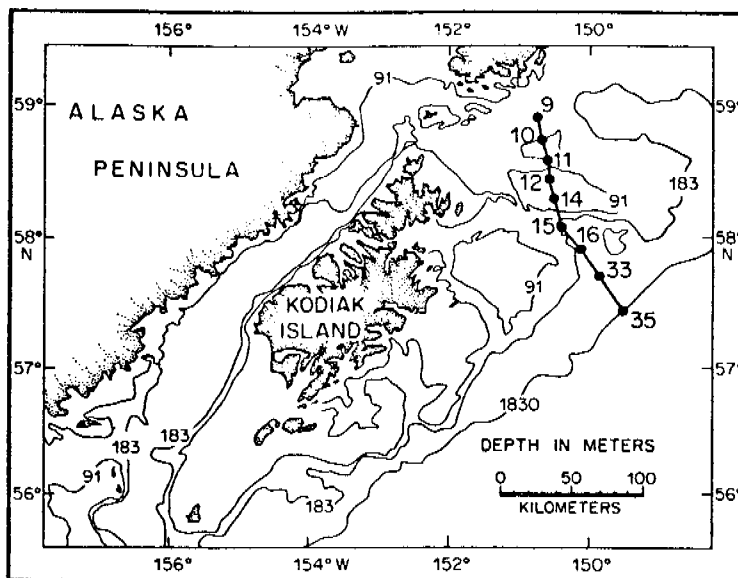


Fig. 13. Temperature and salinity section, LEG II.

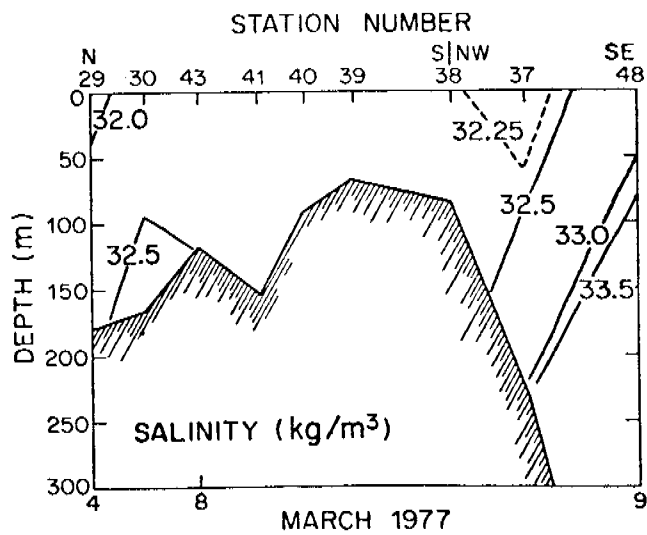
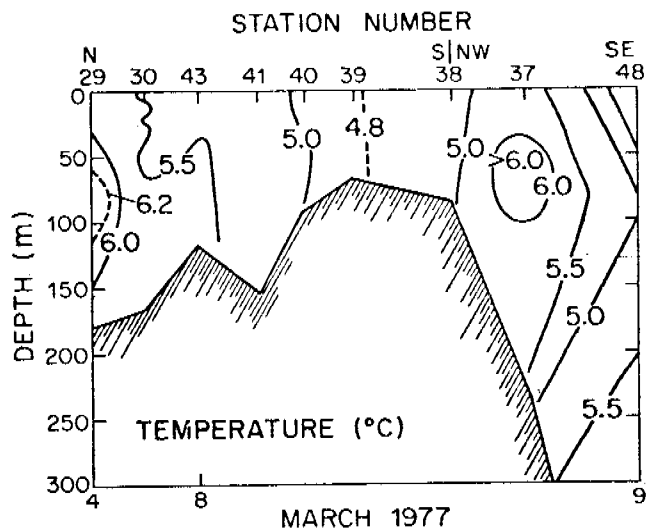
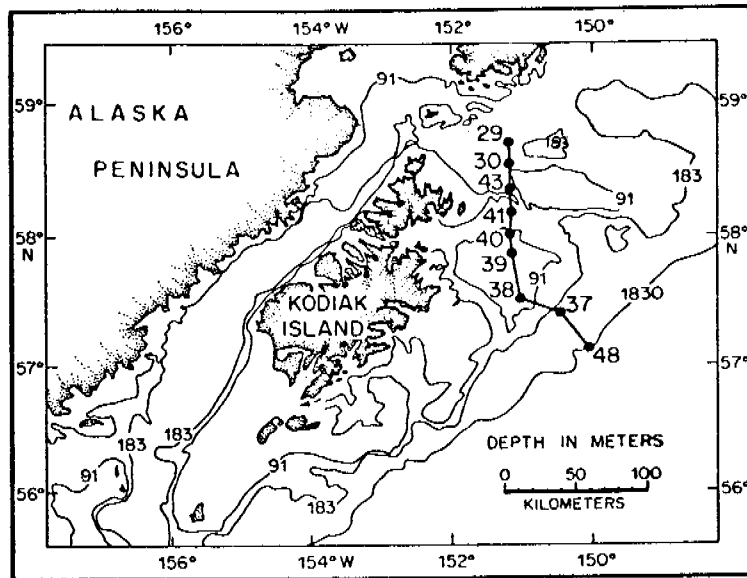


Fig. 14. Temperature and salinity section, LEG II.

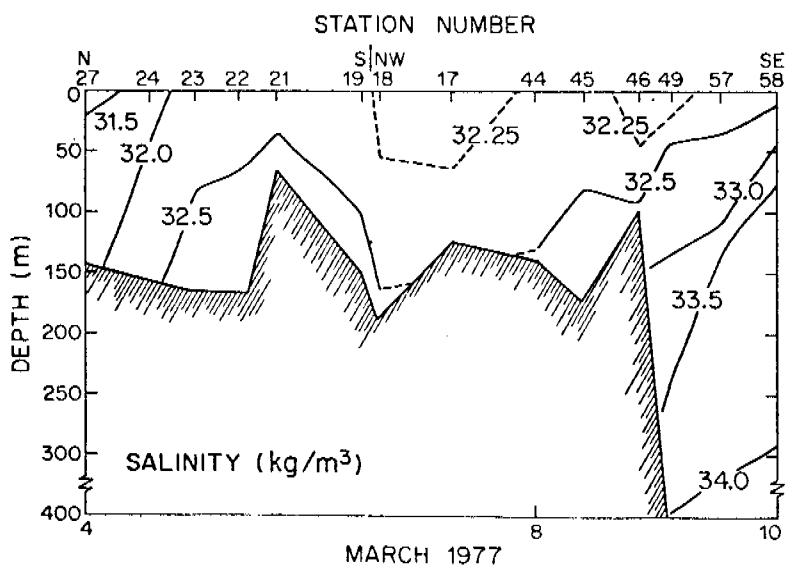
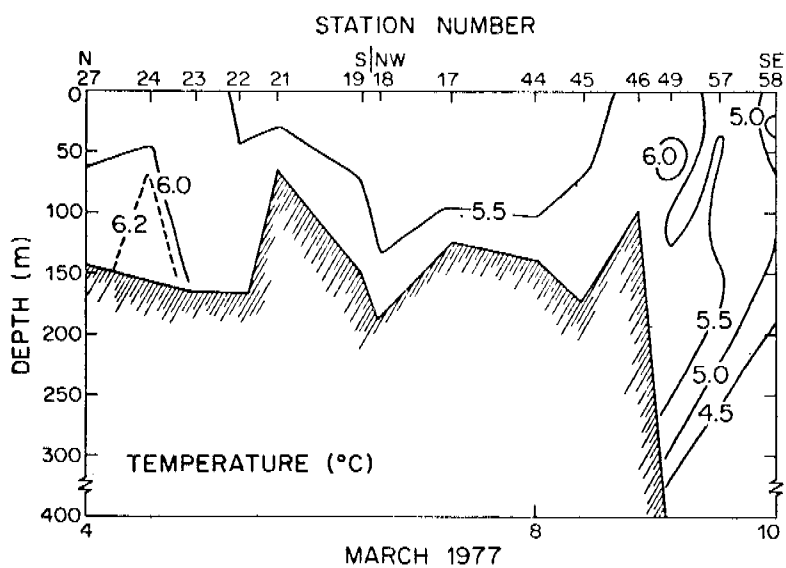
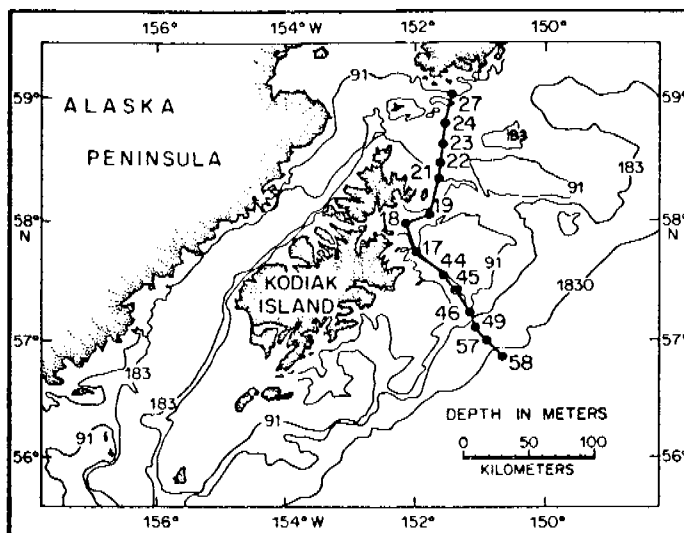


Fig. 15. Temperature and salinity section, LEG II.

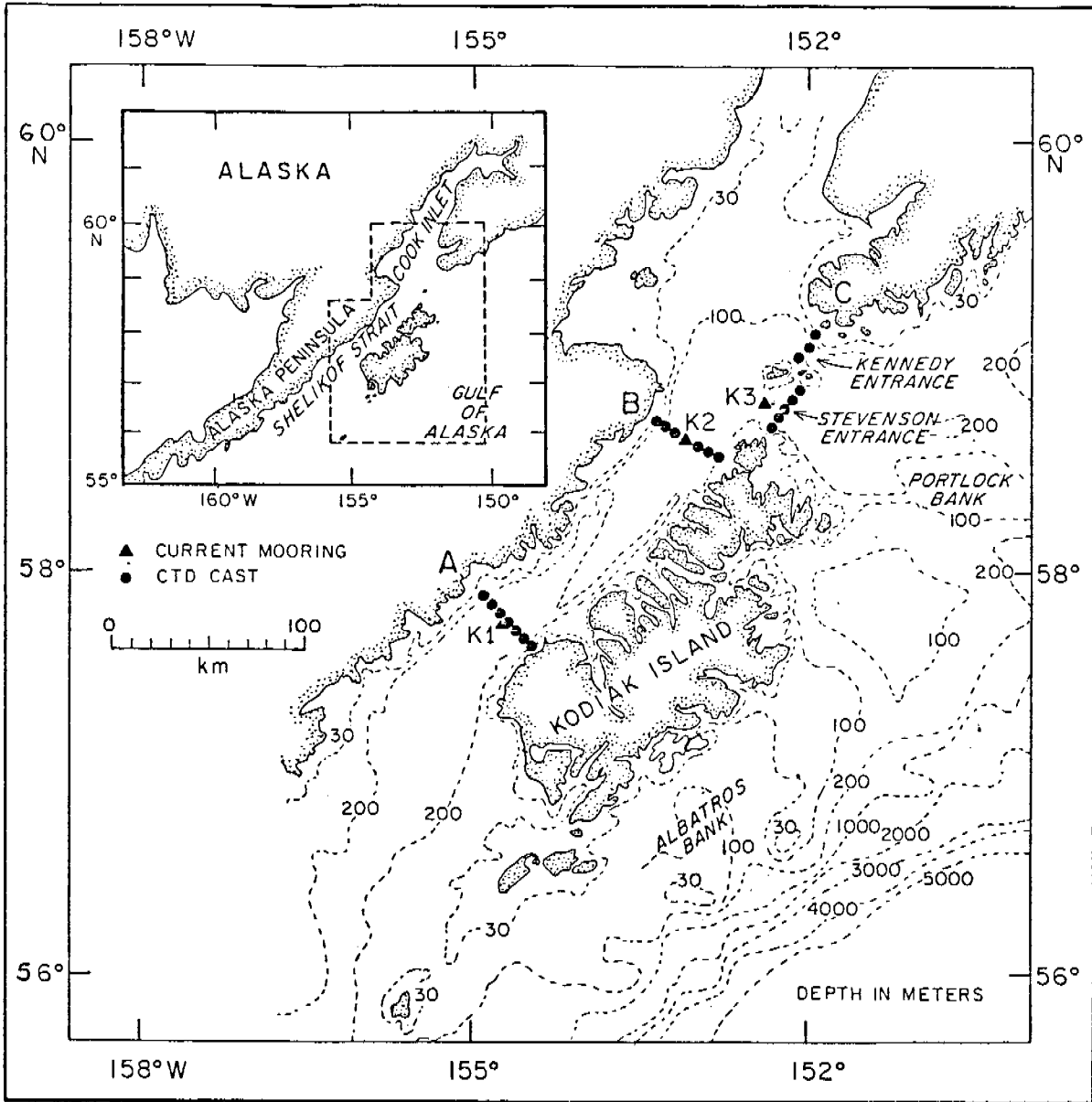


Figure 16. CTD station locations, 28-30 March 1977

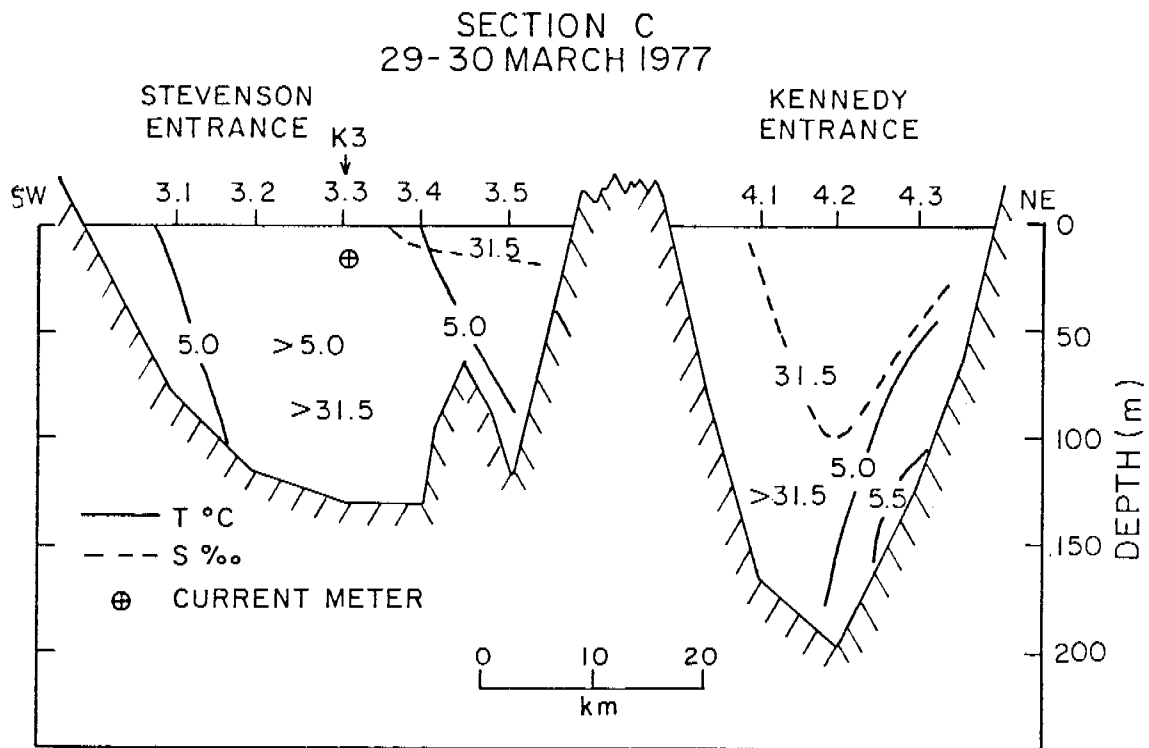


Figure 17. A composite temperature and salinity section across Kennedy and Stevenson Entrance. Also shown is the location of current meter mooring K3.

the southwest side of the latter. Density differences were generally <0.15 units, with a maximum of 0.30 units at station K3.3.

In Figure 18, we present data from both the northeast (Section B) and the southwest end of Shelikof Strait (Section A). We note that the upper 50 m of the water column on the northwestern or Alaskan Peninsula side of the Strait alone exhibited significant thermal structure. At station K2.6, surface temperatures were 2.31°C ; a bottom temperature of 5.41°C yielded $\Delta T = -3.14^{\circ}\text{C}$. In the center of the Strait (~ 18 km towards the southeast), observed values of 5.01°C at the surface and 5.40°C at the bottom yield $\Delta T = -0.39^{\circ}\text{C}$. The colder water was associated with the lowest observed salinities; surface values were $<31.00^{\circ}/\text{oo}$ centered at station 2.6. In general, salinity values for the entire section were below $\sim 32.00^{\circ}/\text{oo}$ with a maximum value of $32.19^{\circ}/\text{oo}$ observed at station K2.2. The maximum $\Delta S = 1.11^{\circ}/\text{oo}$ was observed at station K2.6, whereas $\Delta S = 0.20^{\circ}/\text{oo}$ was typical of values for the entire southeastern half of the section. The ensuing density difference values (σ_t bottom - σ_t surface) were $\Delta\sigma_t = 0.66$ units at station K2.6, with values of less than 0.20 units on the southeastern side.

Surface temperatures from the southwestern end of Shelikof Strait (section A) were warmer than those noted for the northeastern end, with a similar horizontal distribution, i.e. a minimum of $T = 3.80^{\circ}\text{C}$ was observed at station K1.6. Vertical thermal structure was observed across the entire section; however, this structure was not as strong as noted for section B (cf. the maximum $\Delta T = -1.87^{\circ}\text{C}$ with values generally $>-1.50^{\circ}\text{C}$). Salinity values exhibited small horizontal gradients, minimum surface values ($31.38^{\circ}/\text{oo}$) obtained along the Alaska Peninsula and slightly higher values ($31.50^{\circ}/\text{oo}$) off Kodiak Island. Near bottom (200 m) isohalines, e.g. $32.5^{\circ}/\text{oo}$ were not inclined and attained a maximum value of $32.84^{\circ}/\text{oo}$ at station K1.6. Thus values of $\Delta S > 1.0^{\circ}/\text{oo}$ pertain through out this section. Density difference values were ~ 0.80 units with a maximum of $\Delta\sigma_t = 1.01$ unit at station K1.6. We note the lack of inclination of the isopycnals as indicated by the isohaline structure.

A5. DIRECT OBSERVATIONS OF CURRENT

5.1 Low Frequency Flow

We present low-pass filtered current records for the Shelikof Strait region in Figures 19 and 20. As indicated in these records, net flow generally enters Shelikof Strait through Stevenson Entrance (K3A) and likely through Stevenson Entrance. From 28 October to 15 November, flow was consistent in direction and appeared to be increasing in magnitude with a maximum speeds of the order of 70 cm/s. The mean velocity for this 37 day record was 30.1 cm/s directed toward 298° (T).

The two current records from the northwestern end of Shelikof Strait (K2A) indicated that flow was predominantly along axis (where the axis of Shelikof Strait was taken to be 230°T), toward the southwest. During the period flow was exiting Stevenson Entrance, flow at K2A was noticeably weaker than usual, but for the majority of time maintains a flow component along the major axis. The two time series from K2A were visually well correlated. Mean flow at 100 m was 9° to the right of the mean flow at 20 m; mean speed at 100 m was less by 12.4

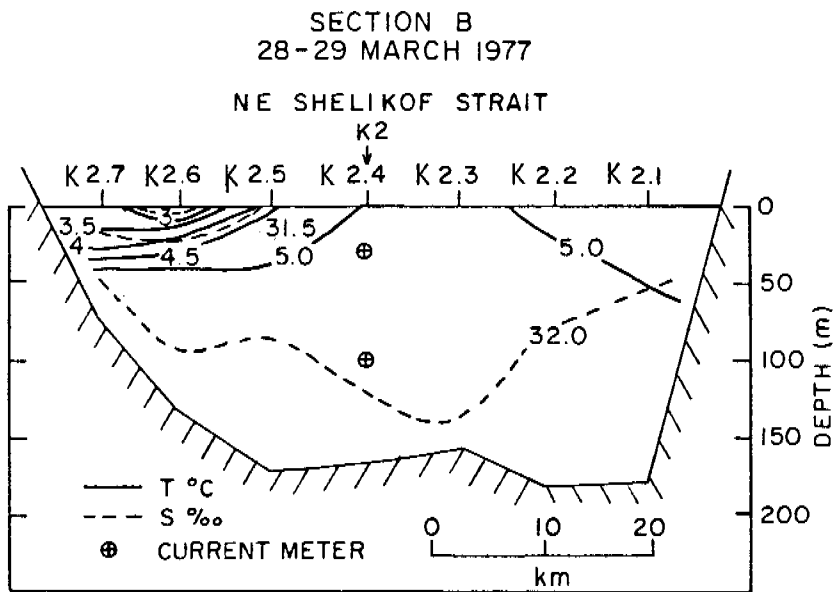
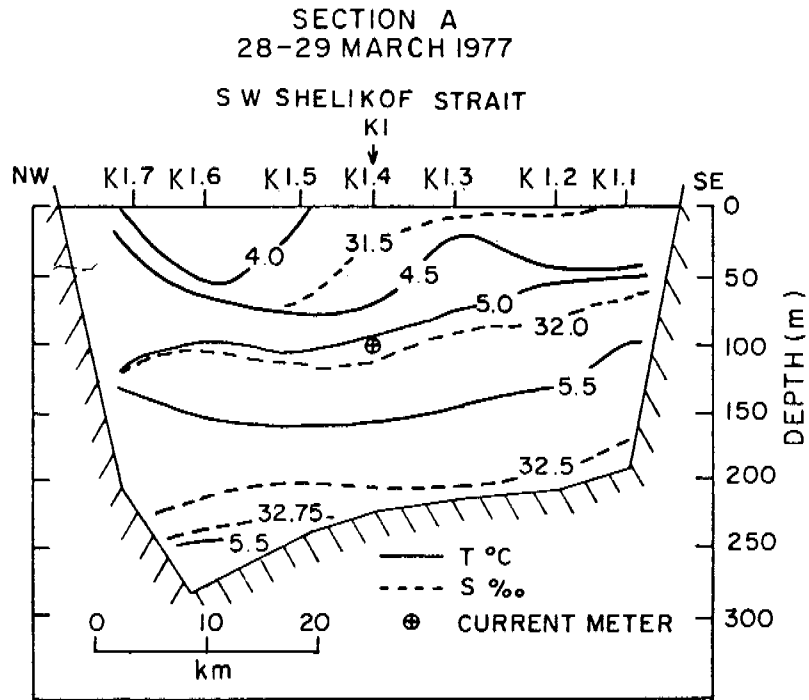


Fig. 18. Composite temperature and salinity sections for northeastern Shelikof Strait (Section B) and southwestern Shelikof Strait (Section A). Note current meter locations.

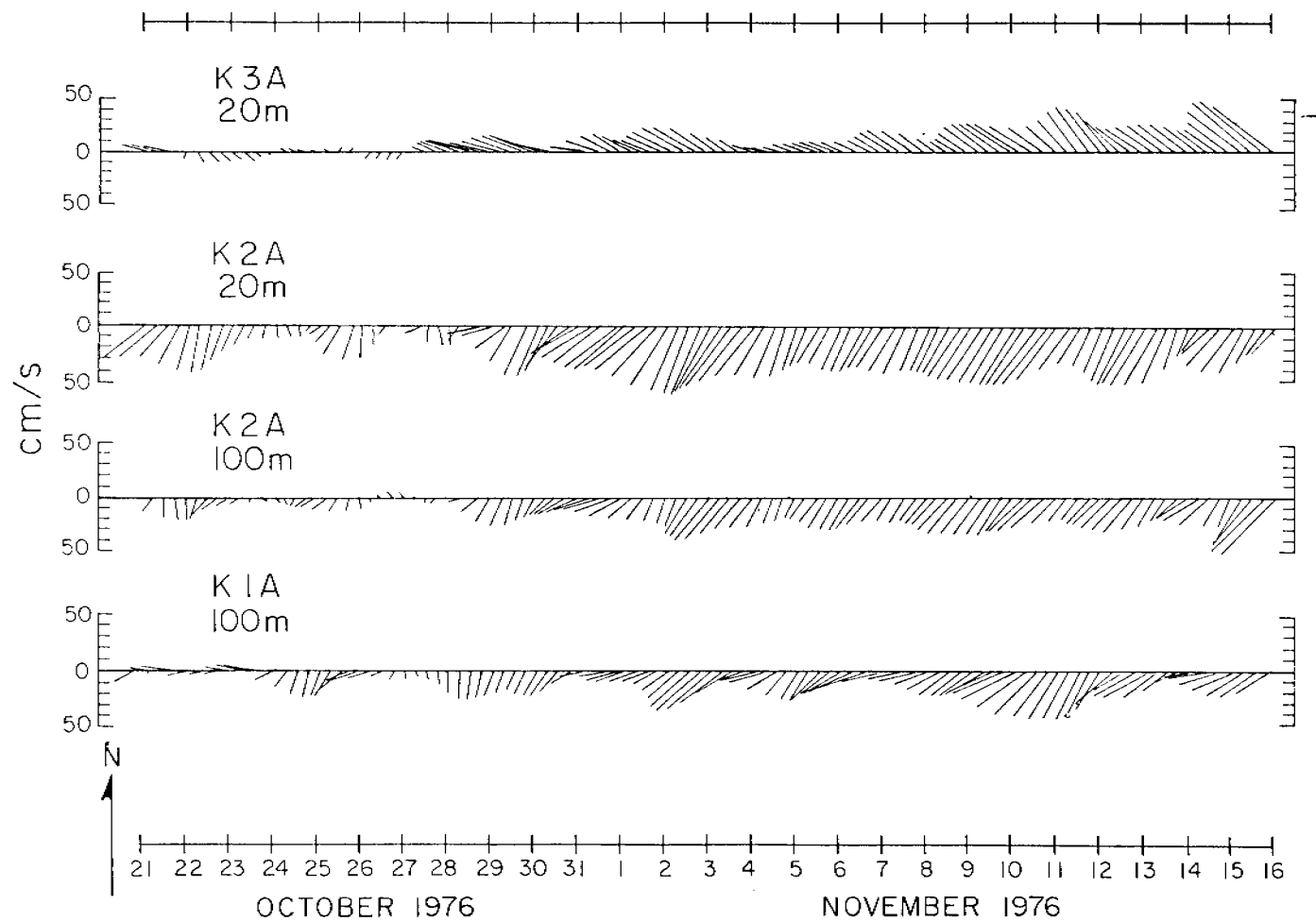


Figure 19. Low pass filtered current records from Stevenson Entrance (K3) and Shelikof Strait (K1 and K2).

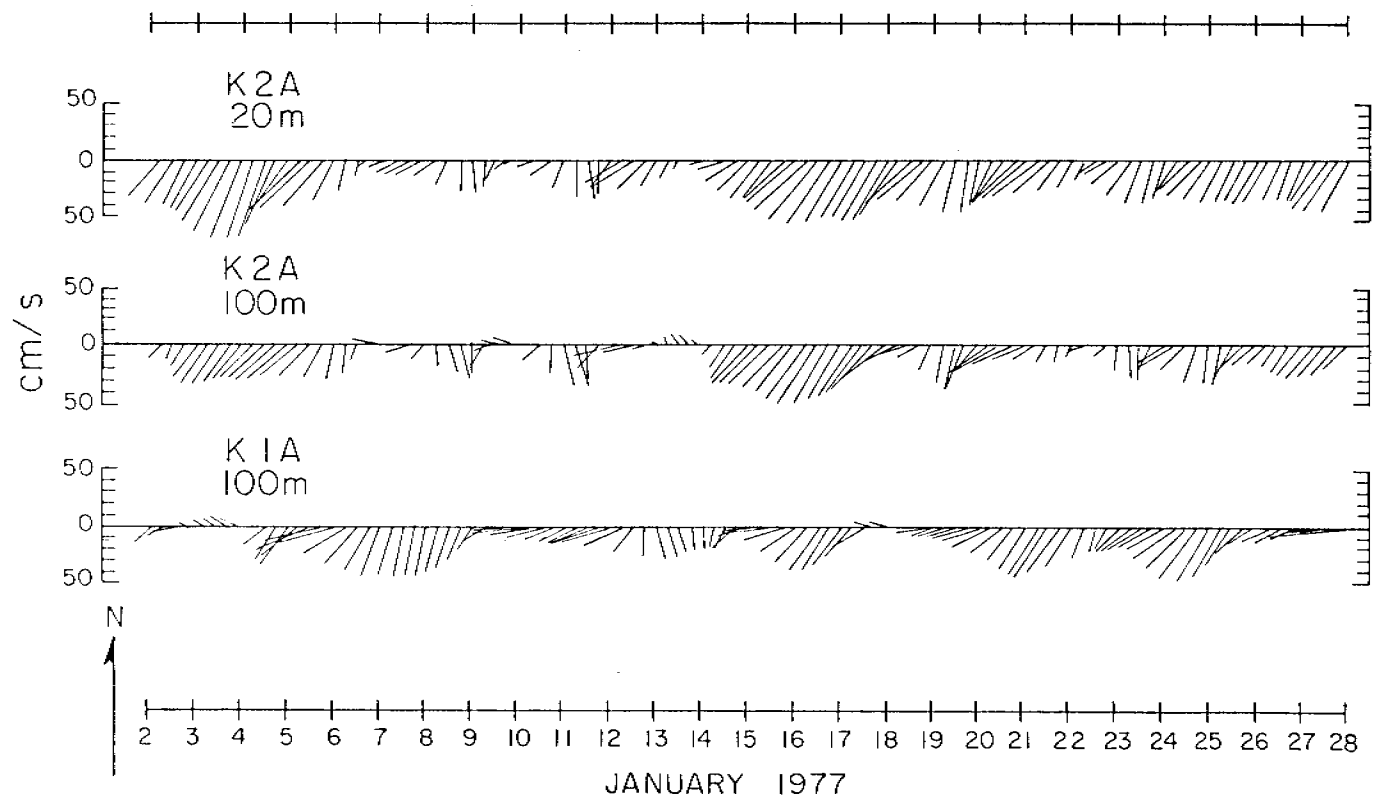


Figure 20. Low pass filtered current records from Shelikof Strait during January 1977.

cm/s (Table 1). These values indicate a mean vertical shear, along the axis of the Strait, of $-1.11 \times 10^{-3} \text{ s}^{-1}$. The 100 m record from K1A (southwestern end of the Strait) was similar to those at K2A, i.e., there was a strong tendency for low frequency flow along the major axis. There appeared however to be a greater degree of cross-channel variation.

In order to further examine variability of the sub-tidal flow, we present scatter plots of the Shelikof Strait current data (Figure 21). Each point represents the head of a single vector created on a 6 hr time base. It is evident from the plots that winter flow was predominantly into Stevenson Entrance and southwest through Shelikof Strait. Scatter about the mean was greater at K1A than at K2A, as was suggested by the stick diagrams.

In contrast to the consistent strong sub-tidal flow observed in Shelikof Strait, the current record from North Albatross Banks, mooring WGC-2E, indicated weaker flow with a substantial number of reversals (Figure 22). From 22 October - 8 November 1977, flow was consistent with speeds of the order of 15 cm/s. A more complex flow mode was evident in the 7-26 February record segment. During this period there were several periods when flow was reversed from the mean direction (239°T). We note that over this 156 day record there were 12 distinguishable clockwise rotations of the current vector. Periods of these events were 2-3 days. The scatter plot for this record (Figure 22) clearly shows the high degree of variability superimposed on a mean flow towards the southwest. We note that the maximum speed events ($\sim 30 \text{ cm/s}$) tended to parallel the local bathymetry (235°T).

A6. DISCUSSION

A6.1 Stratification

Over Middle Albatross, North Albatross, and Portlock banks we observed little or no stratification, with $\Delta\sigma_t < 0.2 \text{ kg/m}^3$ (see Figure 11). This lack of vertical structure was also noted by Favorite and Ingraham (1977) during late April and early May. Winter thermohaline convection, coupled with turbulence due to impingement of currents on the banks, contribute to this mixing. During summer, heating and freshwater addition would be expected to result in substantial stratification on all but the shallowest bank regions.

Over the troughs, along the Kenai Peninsula and seaward of the shelf edge, stratification was stronger ($\Delta\sigma_t > 0.4$). This stratification was caused primarily by salinity, which exerts dominant control over density (Royer and Muench, 1977). Occurrence of high salinity water in the troughs (e.g. $S > 33.00$ ‰ at station 53 in Kiluida Trough), was also noted by Wright (1970). The apparent source of these waters was the shelf edge portion of the Alaska Current. This current advects water whose temperature and salinity at 150 m depth (the sill depth of Kiluida Trough) are similar to those observed inside the sill. Seabed drifter data suggest a net onshore flow of near-bottom waters shoreward of midbank (Favorite and Ingraham, 1977). We suggest that deep shelf edge water flows shoreward in the troughs and that this flow is likely to be episodic.

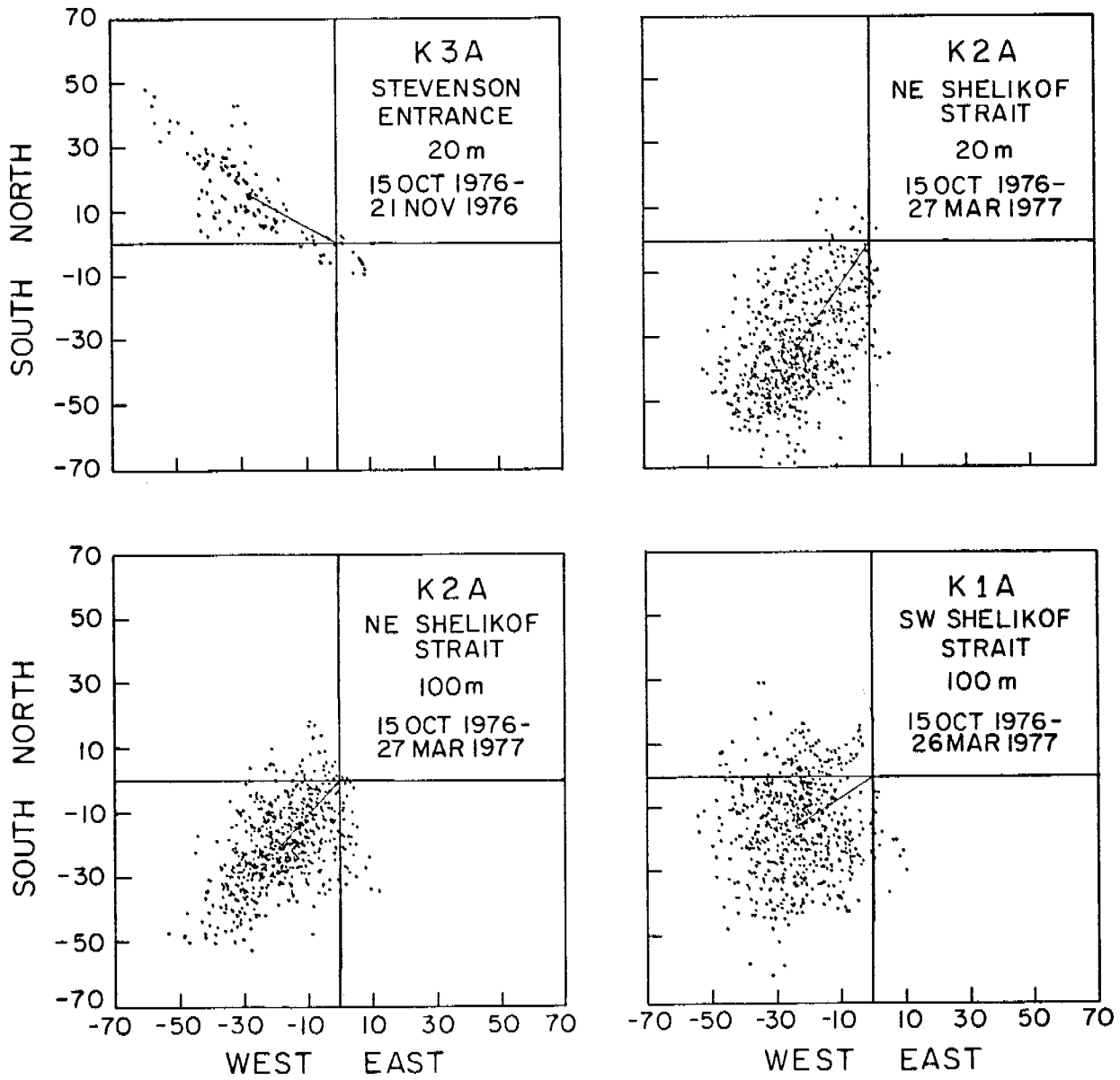


Fig. 21. Scatter diagrams for all current records from Shelikof Strait. Note: the vector on each plot represents the mean current.

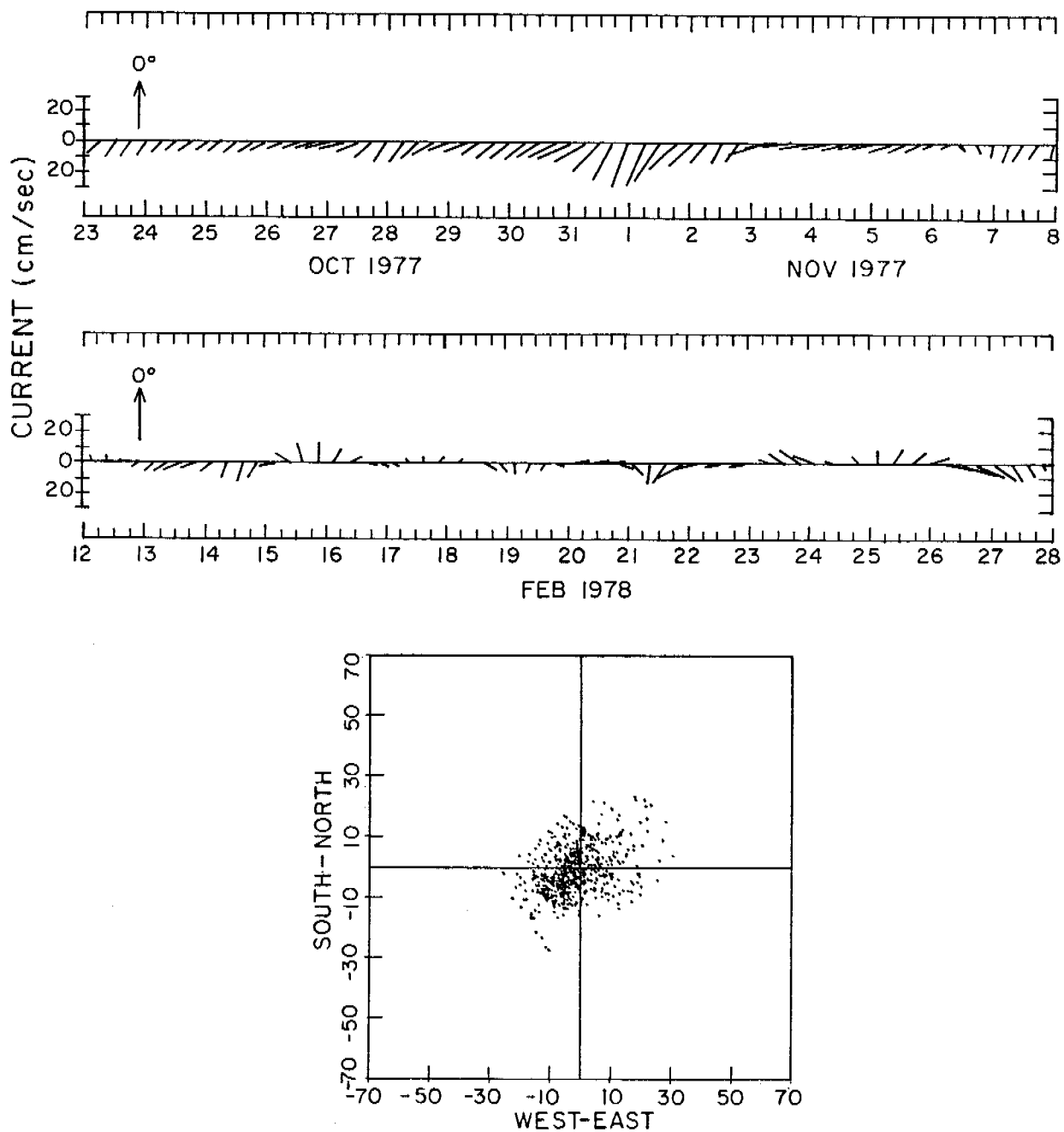


Figure 22. Current record from North Albatross Bank (WGC-2E) showing periods of constant and highly variable flow. Also shown is a scatter plot of low-pass filtered current data.

Stratification over the shelf edge results from presence there of a shallow (<50 m) salinity feature. This is probably an extension of the fresh water filament noted by Royer and Muench (1977) which lies over the shelf edge approximately 500 km to the east. The source of such water is runoff which accumulates around the perimeter of the northeast Gulf of Alaska and is diverted seaward by topography. Favorite and Ingraham (1977) observed a similar feature. We conclude that the low salinity filament is a permanent feature of the winter hydrography on the Kodiak Island shelf. During summer, we believe that increased freshwater input will reduce the salt content over the entire shelf and thereby mask the filament. The effect of the filament on circulation will be discussed later.

The stratified region along the Kenai Peninsula again demonstrates the pronounced effect of salinity upon density. Although there was a negative ΔT (see Figure 5) or thermal inversion, the observed low salinity band of coastal water resulted in relatively strong stratification. The probable sources of this low salinity water are Prince William Sound and the Copper River. Enhancing stratification along the Kenai Peninsula were the high salinity (33.06⁰/oo at station 6) bottom waters observed at the western end of Amatuli Trough. As these waters flow into upper Shelikof Strait via Stenvenson and Kennedy entrances, vigorous tidal mixing (note the record variance from K3A, Table 1) resulted in reduced stratification.

Stratification at the northwestern end of Shelikof Strait was generally of similar magnitude to that observed in the Barren Island section; however, a more highly stratified band was observed on the northern side of the Strait. The low salinity and temperature of this ~50 m deep band appear related to outflow from Lower Cook Inlet. In this region, ice formed in Upper Cook Inlet melts, thus providing the observed water characteristics. The low salinity cold band appeared to have been laterally diffused across the southwestern portion of the Strait, reducing stratification in the upper 50 m; however, more saline (>32.75⁰/oo) bottom waters compensated for the reduced stratification in the upper water column. At the southwestern end of Shelikof Strait, stratification generally increased by a factor >3 than that observed in the northeastern end.

6.2 Horizontal Distributions

As shown by Figure 18, waters in the northeastern end of Shelikof Strait were colder and less saline than those at the southwestern end. Advection of temporally changing source water may have caused the difference. Current records indicated a consistent mean flow of 25 - 40 cm/sec toward the southwest in the upper 100 m of the water column. The origin of these waters was the shelf region seaward of the Barren Islands. During March 1977, a thermister record from K2A (100 m), three CTD casts over the shelf edge, and reoccupation of three CTD stations in the Barren Island region indicated (Figure 23) an ~0.025⁰C/day temperature decrease. Assuming a net speed of ~30 cm/s, water from K2A would have reached K1A in 8 days, so that there was a time difference of 10 days (2 days due to cruise track). Using the observed time change and time difference, their longitudinal temperature difference would be ~0.25⁰C, the observed difference. A similar, but less detailed signature (there was a high degree of scatter in the record from a conductivity cell) appeared in the salinity measurements. There was an ~0.02⁰/oo salinity difference between the locations with a 10-day time lag between K2A and K1A; this gradient would have resulted in longitudinal salinity differences of ~0.2⁰/oo, as observed in the upper 100 m.

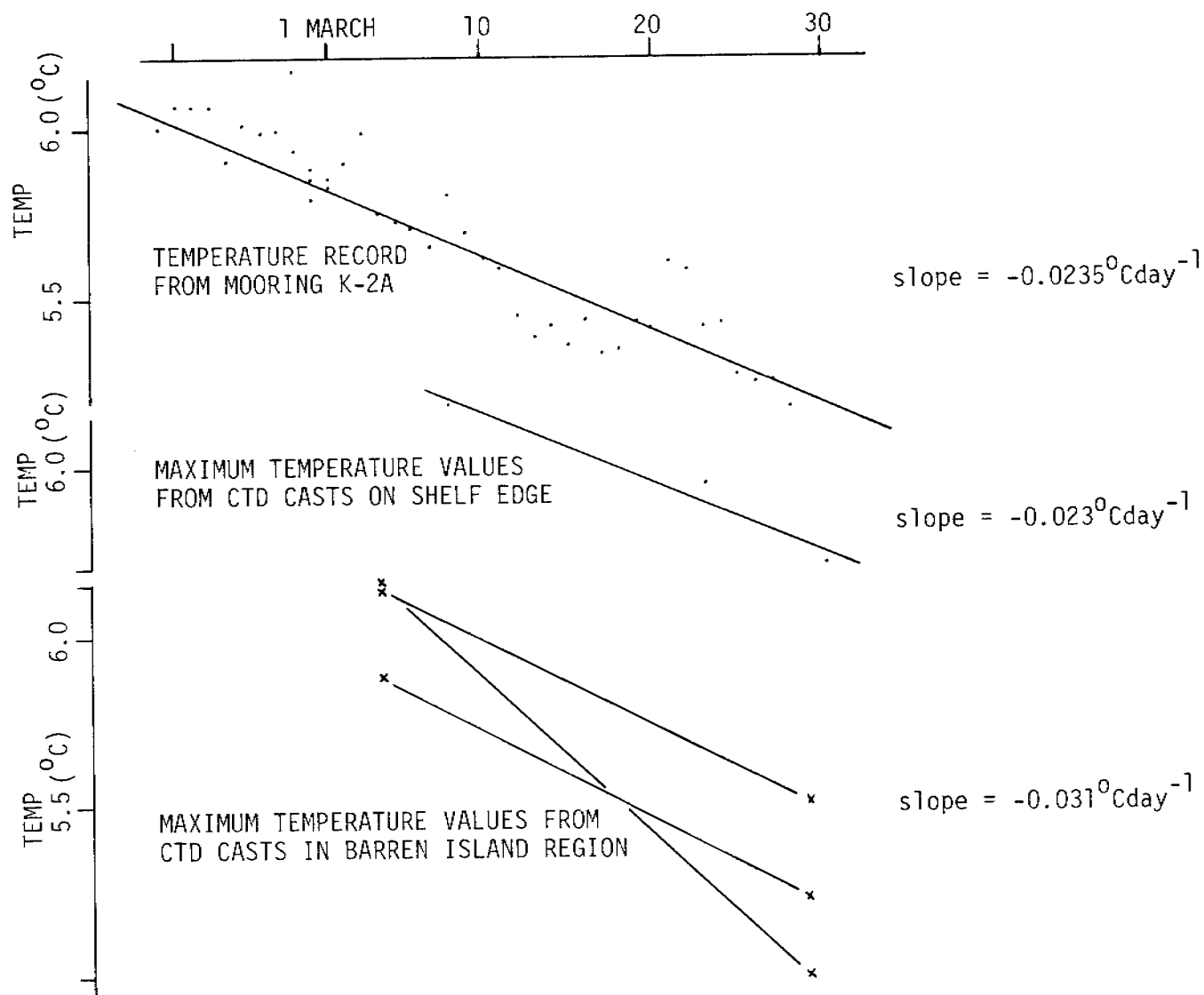


FIGURE 23. TEMPERATURE GRADIENT OBSERVED IN WATERS AROUND KODIAK ISLAND IN MARCH 1977.

Royer (1975) reported that subsurface salinities and temperatures give evidence of an annual cycle independent of local insolation and freshwater addition. Our data indicated such a signal, and we suggest that there is an annual temperature cycle associated with subsurface waters transported by the Alaska Current.

An annual signal associated with the Alaskan Current may explain the longitudinal difference in water properties observed in Shelikof Strait; however, we note (Figure 18) that below about 150 m temperature and salinity values are greater than can be accounted for by considering the seasonal signal. Indeed, values present in the near-bottom layer closely resemble those observed at the shelf edge (Figure 15). In concert with the lack of sufficiently saline waters near the Barren Islands, we suggest this observation implies that shelf edge waters enter Shelikof Strait at depth via its southern terminus (sill depth ~ 200 m). The entrainment of such waters by the strong southwesterly flow in the upper waters would require, invoking continuity, a net flow into the Strait of near-bottom waters.

A6.3 Circulation

Advection of warm cores and the shelf edge salinity minima into the study area by the westward-flowing Alaska Current was a prominent feature. Infrared satellite imagery shows the surface manifestation of the warm cores (Figure 24). Such data, in concert with hydrographic data (Figure 25) suggest that the Alaska Current was bifurcated in the vicinity of Amatuli Trough; one branch flowed axially into the trough toward the Barren Islands, and the other branch continued southwest along the shelf edge. The spatial distribution of warm, less saline water (cf. figure 25) clearly demonstrates the impact of non-local advection due to the Alaska Current.

Dynamic contours (Figure 26) indicate the baroclinic geostrophic component of flow in response to the cross-shelf bimodal distribution of mass. A reference level of 100 db was used so that the majority of CTD data could be included. Over the slope the highest geostrophic speeds, e.g. the relative flow to the southwest between station 58 and 57, was calculated to be 24 cm/s (0/100db), 34 cm/s (0/200db) and 66 cm/sec (0/1200db). The tendency for warmer, less saline waters to extend into Stevenson Trough resulted in a clockwise flow sense with relative speeds of the order of 2-3 cm/s. Along the Kenai Peninsula, 0/100db dynamic contours indicated another region of relatively strong flow between stations 8 and 7; calculated westward speed (0/118db) was of the order of 20 cm/s. Inflow speed through Stevenson Entrance was calculated to be about 8 cm/s (0/116db) and through Kennedy Entrance about 9.1 cm/s (0/181db). We note that the stations used above do not entirely span the two entrances and that calculated values seaward of these features indicated values of 15 cm/s (0/116db between stations 23 and 24) and 11 cm/s (0/116db between stations 24 and 27). The two bands of relatively strong baroclinic geostrophic flow, i.e. along the Kenai Peninsula and coincident with the slope, were separated by a region of weak flow with a clockwise tendency. Current records from North Albatroas Bank (WGC-2E), the shelf edge (WGC-2A) and Stevenson Entrance (K3A) support these computed estimates.

Baroclinic geostrophic calculations for the northeastern end of Shelikof Strait indicated weak flow, e.g. between stations K2.5 and K2.3; 0/150db speed

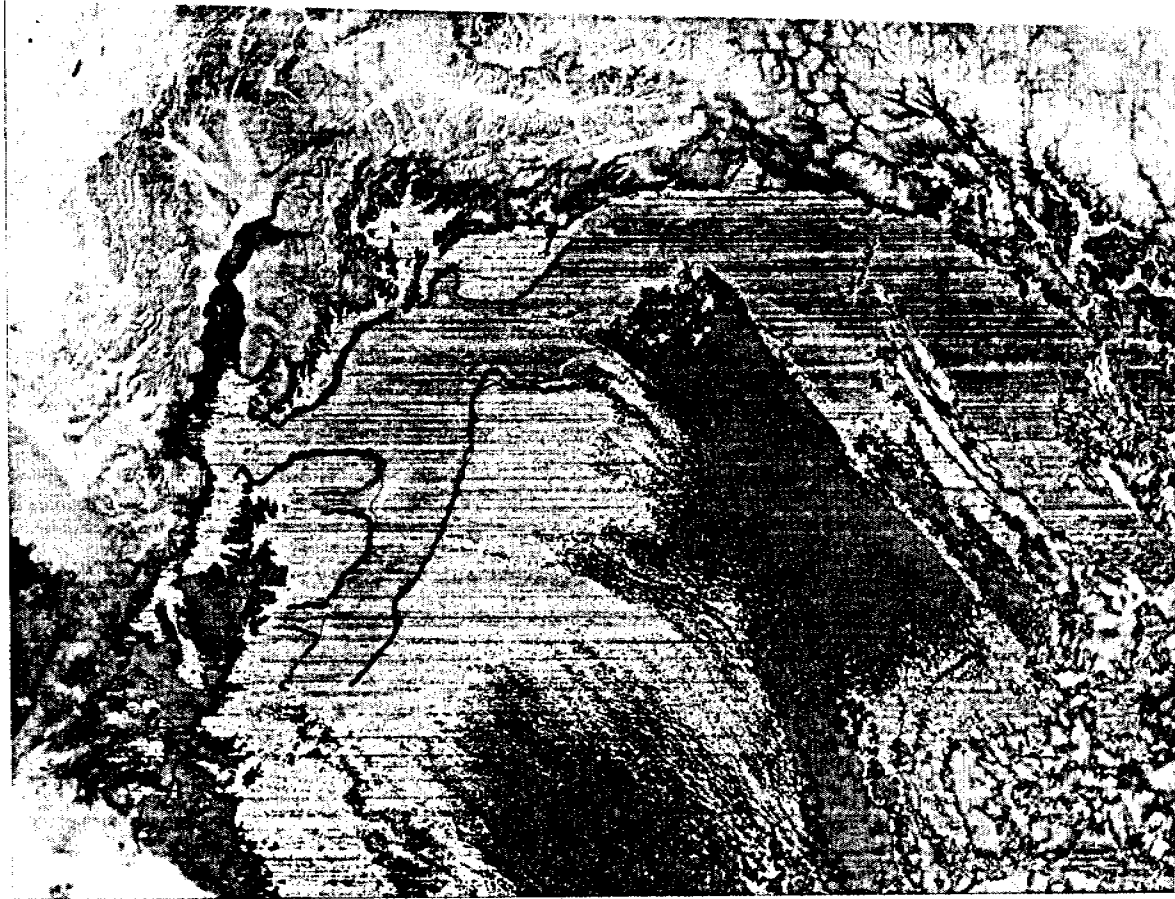


Fig. 24 Infrared satellite imagery indicating regions of warm (dark) surface waters. The region of warmer water has been outlined for clarity. Photograph was taken on 29 February 1976.

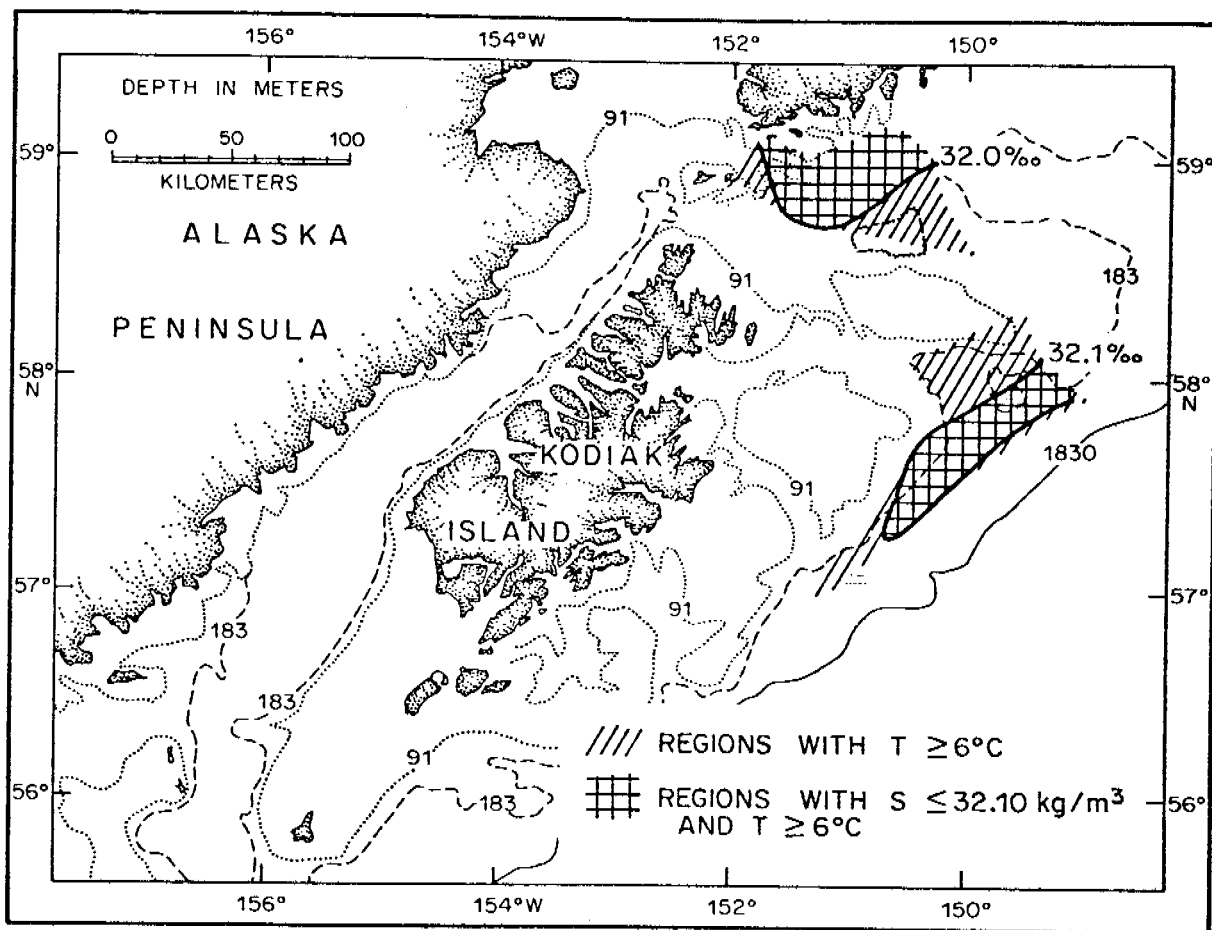


Fig. 25. The spatial distribution of warm less saline waters observed during March 1977.

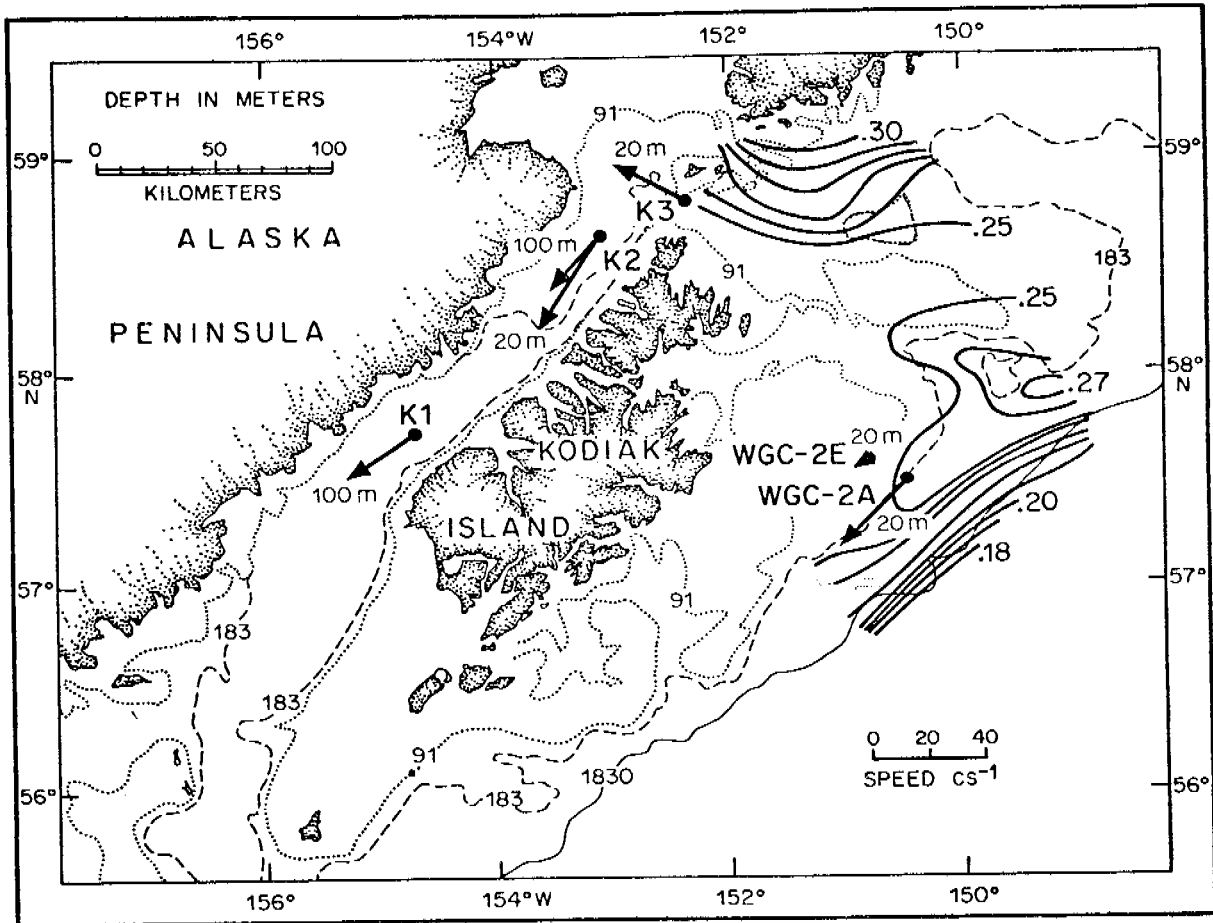


Fig. 26. The dynamic topography (0/100db) for observations during March 1977 (contour interval 0.1 dynamic meter). As shown are current record means for various winter observation periods (see Table 1).

was ~ 5 cm/s, and 30/110db speed was ~ 3.6 cm/s with both speeds representing flow toward the northeast. We note that this flow was in the opposite direction from the mean flow and represents approximately 1/3 of the observed vertical shear. At the southwestern end of the strait, calculated geostrophic flow was ~ 10 cm/s (0/215 db) toward the southwest. These geostrophic baroclinic speeds were all much less than those observed. The lack of strong baroclinicity, and little evidence for wind forcing, leads us to believe that a dominant driving mechanism was a bifurcated branch of the Alaskan Current.

A7.0 SUMMARY

Observations from moored current meters, recording conductivity/temperature/depth (CTD) units and satellite imagery have been utilized to describe temperature, salinity and flow fields for a region extending from the banks east of Kodiak Island westward through Shelikof Strait. These measurements were obtained during winter, 1976-77. The temperature-salinity field was dominated by the presence of two sub-surface cores of warm ($>6.0^{\circ}\text{C}$), saline ($\sim 32.5^{\circ}/\text{oo}$) water; one roughly coincident with the shelf break, and one extending northwest from the shelf break into Amatuli Trough. The region between these bands, generally overlying Albatross Bank, was characterized by lower temperatures and salinities. The bands themselves were of the proper temperature and salinity to have originated in the Alaska Current, which suggests that bifurcation of this current occurred near the southeastern end of Amatuli Trough with consequent flow of some Alaska Current water northwest through the trough. Infrared satellite imagery supports the concept of such a bifurcation. A shallow band of relatively low salinity ($<31.6^{\circ}/\text{oo}$) water a manifestation of fresh water input from continental drainage to the east paralleled the Kenai Peninsula coast.

Current records from northern Shelikof Strait indicated consistent southwesterly flow during the entire October 1976-March 1977 mooring period. Mean currents at 30 m depth were 38.6 cm/s toward the southwest, while mean currents at 100 m were ~ 26 cm/s toward the southwest. Few flow reversals were observed; only 1% of the low-pass filtered records indicated a northeasterly flow component. A 37-day current record from Stevenson Entrance indicated strong mean flow (~ 30 cm/s) westward into Shelikof Strait. Presence of these strong flows with no reversals, coupled with a lack of density structure in the water column, indicate a barotropic driving mechanism for the flow. We suggest that a longshore pressure gradient set up by the westward flowing Alaska Current was sufficient to drive observed flow through Shelikof Strait. The forcing due to the Alaskan Current was augmented by a westward baroclinic flow resulting from fresh water input along the coastline.

Flow over the banks northeast of Kodiak Island was less well defined than in Shelikof Strait. Low temperature, weakly stratified water was observed over the banks, while in the troughs water was stratified with warmer, more saline water near the bottom. The deep water in the troughs may indicate that a net onshore flow of bottom water was occurring, or that shelf edge water episodically was driven across the sills into the troughs. Dynamic topography suggested a weak tendency for cyclonic flow over North Albatross Bank, in sharp distinction

to the pronounced westward flows to the north (along the Kenai Peninsula) and south (the Alaska Current). A current record from northern Albatross Bank indicated also weak (2.7 cm/s) flow. Only 7% of this record's variance also was contained in subtidal frequencies, and there were frequent flow reversals with direction changing in an anticyclonic sense. We suggest that the weak mean flow was driven by the Alaska Current, while the fluctuations may have been a reflection of shelf waves, or eddies resulting from potential vorticity changes as the strong shelf edge flow passes over Stevenson Trough.

8. ACKNOWLEDGEMENTS

We wish to thank all who have assisted in field operations, data processing, drafting and typing, in particular: the compliment and Captain S. Miller of the NOAA ship DISCOVERER, Jim Haslett (Chief Scientist), and Eugenie Darchuck whose perserverance in translating handwritten scribble into a manuscript is greatly appreciated.

"This study was supported in part by the Bureau of Land Management through interagency agreement with the National Oceanic and Atmospheric Administration, under which a multi-year program responding to needs of petroleum development of the Alaskan Continental Shelf is managed by the Outer Continental Shelf Environmental Assessment Program (OCSEAP) Office."

9. References

- Charnell, R. L., and G. A. Krancus, 1976: A processing system for Aanderaa current meter data. NOAA Tech. Memo. ERL PMEL-6, Seattle, 49 pp.
- Danielson, E. F., W. V. Burt, and M. Rattray, Jr., 1957: Intensity and frequency of severe storms in the Gulf of Alaska. EOS Trans. Am. Geophys. Union, 38, 44-49.
- Dodimead, A. J., F. Favorite, and T. Hirano, 1963: Salmon of the North Pacific Ocean region. Bull. 13, Inst. N. Pac. Fish. Comm., Vancouver, B. C., 195 pp.
- Favorite, F., 1974: Flow into the Bering Sea through Aleutian passes, Oceanography of the Bering Sea. Occas. Publ. 2, Inst. of Mar. Sci., Univ. of Alaska, Fairbanks, 623 pp.
- Favorite, F., 1967: The Alaskan stream. Int. N. Pacific Fish. Comm. Bull., No. 21, 53 pp.
- Favorite, F., and W. J. Ingraham, 1977: On flow in Northwestern Gulf of Alaska, May 1972. J. Oceanographical Society of Japan, 33(2), 67-81.
- Hayes, S. P., and J. D. Schumahcer, 1976: Description of wind, current, and bottom pressure variations on the continental shelf in the Northeast Gulf of Alaska from February to May 1975. J. Geophys. Res., 81, 6411-6419.
- Ingraham, W. J., A. Bakun, and F. Favorite, 1976: Physical oceanography of the Gulf of Alaska. In: Environmental Assessment of the Alaskan Continental Shelf, 11. NOAA Environmental Research Laboratories, Boulder, Colorado.
- Roden, G. I., 1969: Winter circulation in the Gulf of Alaska. J. Geophys. Res., 74, 4523-4534.
- Royer, T. C., 1975: Seasonal variations of waters in the northern Gulf of Alaska. Deep-Sea Res., 22, 403-416.
- Royer, T. C., and R. D. Muench, 1977: On the ocean temperature distribution in the Gulf of Alaska, 1974-1975: J. Phys. Oceanogra., 7, 92-99.
- Wright, F. F., 1970: An oceanographic reconnaissance of the waters around Kodiak Island, Alaska. Univ. of Alaska Report No. R70-19, 23 pp.

B. VARIABILITY OF CURRENT AND BOTTOM PRESSURE
ACROSS THE CONTINENTAL SHELF
IN THE NORTHEAST GULF OF ALASKA

S. P. Hayes

Pacific Marine Environmental Laboratory
Environmental Research Laboratories
National Oceanic and Atmospheric Administration
Seattle, Washington 98105

VARIABILITY OF CURRENT AND BOTTOM PRESSURE
ACROSS THE CONTINENTAL SHELF IN THE NORTHEAST GULF OF ALASKA

S. P. Hayes

ABSTRACT. The low-frequency velocity ($< .025$ cph) and bottom pressure variability were studied in the Northeast Gulf of Alaska from March to August 1976. Measurements of velocity in 100, 170, and 250 m of water showed a contrast between the flow at the shelf break and that on the shelf. The former circulation had a weak mean alongshore flow (5 cm/s), but large anticyclonic low-frequency fluctuations. On the shelf the flow was almost entirely aligned along isobaths. The anticyclonic shelf break fluctuations did not propagate onto the shelf. Bottom pressure variations measured at four locations showed little variation along the shelf and a linear decrease in bottom pressure variance across the shelf. Correlations of bottom pressure gradient with velocity indicate much of the alongshore flow was consistent with barotropic quasi-geostrophic dynamics. Cross-shelf flow could not be related to the pressure gradients. Examination of the pressure field response to the wind showed that the near-shore sea level setup accompanied on-shore winds, whereas in the outer shelf the setup accompanied alongshore winds.

1. INTRODUCTION

Hayes and Schumacher (1976) discussed the results of a pilot study to determine low-frequency variability of currents in the Northeast Gulf of Alaska off Icy Bay. Their main results were (a) largely barotropic flow on the shelf (100 m isobath) in winter; (b) predominantly along-shore flow; and (c) good correlation between along-shore velocity and bottom pressure fluctuations measured at the 100-m isobath in winter, but poor correlation in spring. In order to extend the work of Hayes and Schumacher, a spring-summer experiment was conducted in this region from March-August 1976 and a winter experiment from October 1976-March 1977. The spring-summer experiment will be discussed here.

Coastal circulation in the Northeast Gulf of Alaska is influenced by the westward-flowing Alaska Current which generally parallels the coastline (Dodimead et al., 1963). The structure and variability of this boundary current have not been studied extensively. Royer (1975) discussed seasonal changes in hydrographic properties across the Alaskan continental shelf and related these changes to wind forcing. In winter the Aleutian Low controls the weather systems, leading to frequent severe storms with southeasterly winds (Danielson et al., 1957). This wind pattern produces onshore Ekman transport, a setup of sea level along the coast, and downwelling. During summer, winds are weak and the system relaxes. There is some evidence that the varying atmospheric regimes are accompanied by a seasonal change in the transport of the Alaska current and the velocity of the accompanying flow on the continental shelf (Favorite, 1974; Hayes and Schumacher, 1976). The higher transport and velocities are observed in winter.

The experiment site off Icy Bay is shown in Figure 1. As discussed by Hayes and Schumacher, the terrain near Icy Bay is extremely mountainous. These coastal mountains and the glaciated valleys have a large influence on

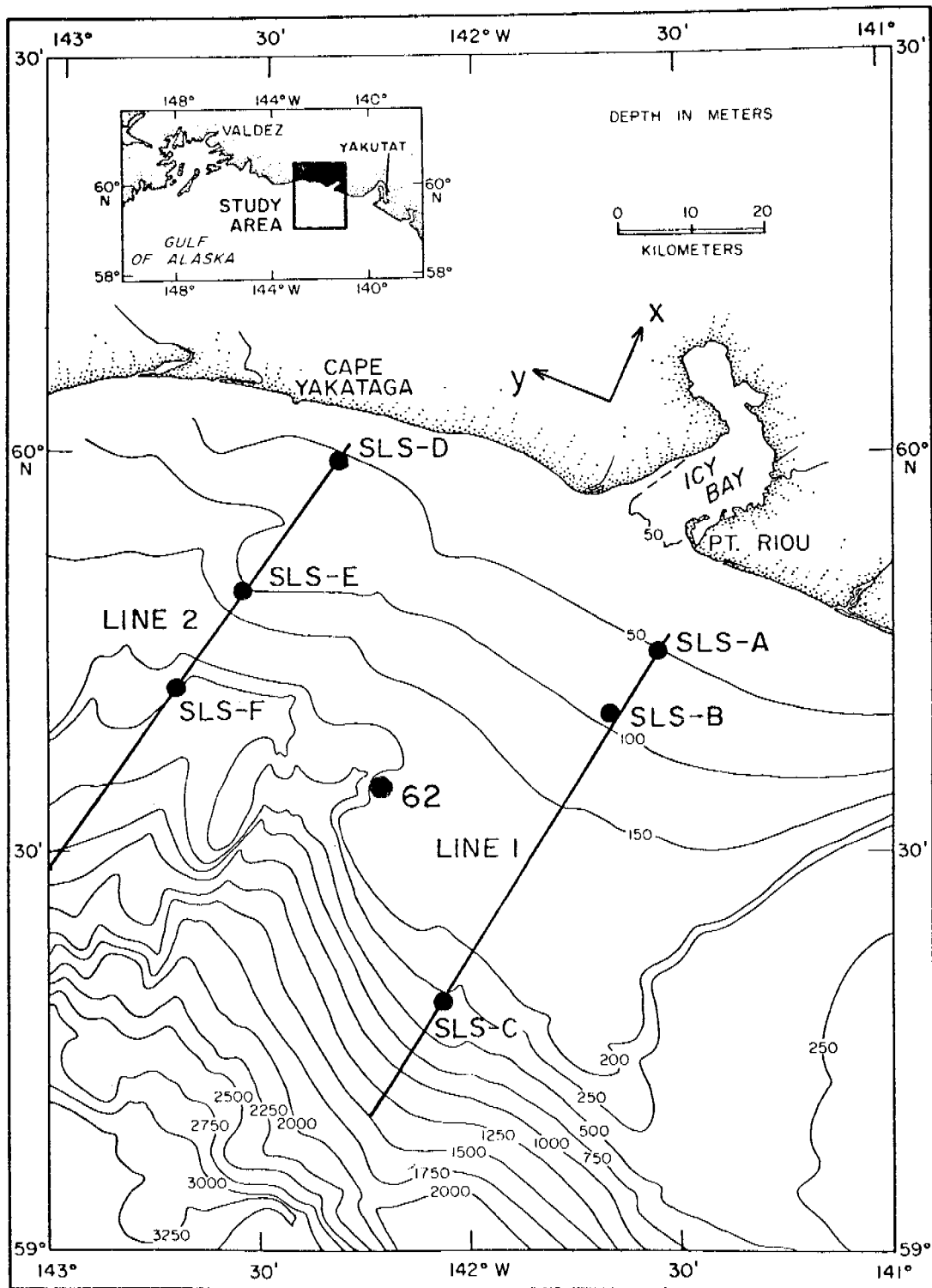


Fig. 1. Location of the experiment off Icy Bay, Alaska. The coordinate system indicates the alongshore direction, y , and cross-shelf direction, x .

the coastal wind patterns (Reynolds and Walter, 1976). While winds from winter storms often parallel the coast, there are periods of locally strong cross-shelf winds which are funneled down from the glaciers. The bathymetry adjacent to the experiment site is also complex. East of Icy Bay a trough leads into Yakutat Bay; the 100-m isobath which is 25 km offshore at Icy Bay is only 5 km offshore near Yakutat. In addition, a ridge (Pampaloma Spur) distorts the 250-m isobath just west of 62 in Figure 1.

The plan for the experiment was to measure bottom pressure at the six locations, A-F, and to measure currents at several depths at B, C, and 62. These measurements span the continental shelf from the 50-m isobath to the shelf break at 250 m. Due to mooring and equipment failures, this complete data set was not obtained. Table 1 lists the records analyzed at each location. In brief, 6-month (March-August) current records at B and 62 and pressure records at B, D, E, and F were obtained. Shorter current records (March-May) were obtained at C. In addition to the moored measurements, CTD stations were taken along the two lines A-C, D-F when instruments were deployed and recovered.

In this paper low-frequency ($f < .025$ cph) velocity fluctuations will be described and related to bottom pressure changes and to wind. In addition to characterizing velocity and pressure fields across the shelf, the usefulness of along- and across-shelf measurements of bottom pressure in the interpretation of the flow field will be considered. Several recent studies (Beardsley and Butman, 1974; Smith, 1974; Hayes and Schumacher, 1976) have noted close correlation between along-shelf current fluctuations and sea level measured at a nearby tide gage or bottom-moored pressure gage. An interpretation of this result is that much of the low-frequency variability is quasi-barotropic. If so, then direct measurement of the cross-shelf

Table 1. Duration of data records at each location.*

Location	Mar	Apr	May	June	July	Aug	
B	[Solid bar]						50 m
	[Solid bar]						90 m
			[Solid bar]				75 m
	[Hatched bar]						P
C	[Solid bar]						50 m
	[Solid bar]						100 m
	[Solid bar]						240 m
D	[Hatched bar]						P
E	[Hatched bar]						P
F	[Hatched bar]						P
62	[Solid bar]						20 m
	[Solid bar]						50 m
	[Solid bar]						100 m

*Current meters are solid bars; bottom moored pressure gages are hatched.

bottom pressure gradient fluctuations can provide a time series of the barotropic transport.

Allen and Kundu (1977) recently reviewed some of the dynamical features common to many time-dependent shelf circulation models. In the absence of forcing, the equations for the depth integrated velocity components may be written:

$$v_t + fu = -gP_y \quad (1)$$

$$fv = gP_x \quad (2)$$

The coordinate system is shown in Figure 1; u is the cross-shelf velocity component increasing on shore, and v is the alongshore velocity increasing to the northwest. Subscripts denote differentiation. In the alongshore direction the velocity is geostrophically balanced; in the cross-shelf equations the acceleration term may be important. If baroclinic effects are small, then the bottom pressure gradient across and along the shelf approximate P_x and P_y . The velocity and pressure time series will be used to test the appropriateness of equations (1) and (2).

2. HYDROGRAPHIC MEASUREMENTS

Hydrographic sections were made during deployment cruises in March, May, and August. Additional sections from Royer (1977) provided data in February, April, and September. Typical density sections for winter, spring, and summer are shown in Figure 2. The February and May sections show weak vertical stratification and downwelling. In the summer a shallow seasonal pycnocline develops. Figure 3 compares the temperature, salinity, and density stratification at the three depth contours where bottom pressure measurements were made. Through May, little vertical gradient was observed at the 50- and 100-m locations. Salinity stratification largely determines the density gradient, and temperature gradient can be of either sign. At

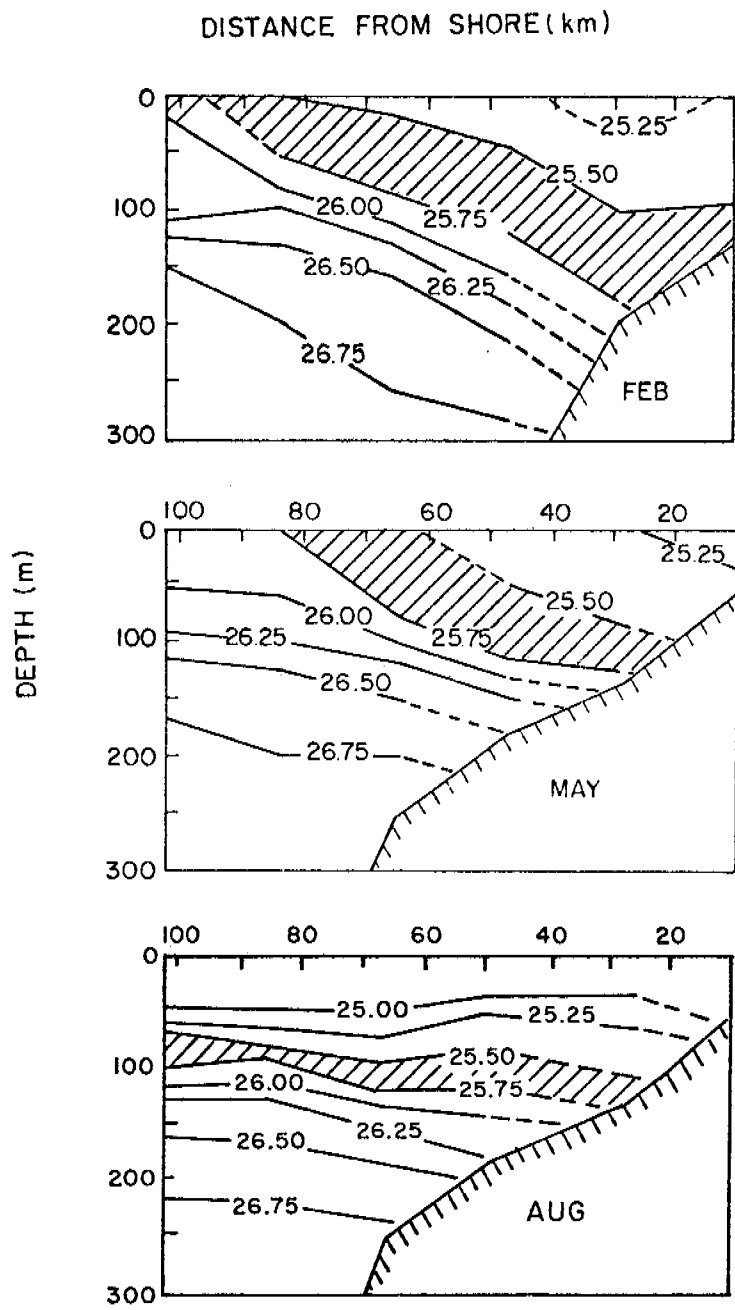


Fig. 2. Typical cross-shelf density sections for February, May, and August.

50 m the temperature increased 3.2° from March to May. This increase was probably due to advection rather than seasonal heating. In August, a seasonal thermocline was seen at all locations. However, at 50 m effects of river runoff produce a shallow, cold, low-salinity layer.

Surface water near the shelf break had a seasonal structure similar to that on the shelf. However, at about 150 m, the permanent halocline of the Alaskan Gyre occurs. This halocline can be expected to isolate the deeper from the surface flow. Temperature in the halocline is variable and has been used as a water mass tracer (Royer, 1975).

3. WIND TIME SERIES

Measurements of surface wind over the Northeast Gulf of Alaska are scarce. Two sources are measured winds at Yakutat (approximately 150 km east of Icy Bay) and winds calculated from the 6-hourly synoptic surface atmospheric pressure analyses produced by Fleet Numerical Weather Central (Bakun, 1975). As discussed in Hayes and Schumacher (1976), Yakutat winds are not representative of oceanic winds because of the mountainous local topography. The FNWC winds have received considerable attention recently (Hickey, 1977; Halpern and Holbrook, 1978). In the vicinity of Icy Bay the coastal mountains form a barrier to storms propagating to the northeast; the resultant packing of isobars may yield actual winds which are stronger than those inferred from the large-scale (3° grid) pressure gradients used by FNWC. In addition, katabatic winds which blow offshore from the coastal glaciers have been observed near Icy Bay by Reynolds and Walter (1976). Such winds are not included in the FNWC calculation. With these reservations the FNWC winds are presented in Figure 4. The wind vectors have been low-pass filtered (40-hr cutoff) and rotated into approximate onshore and alongshore

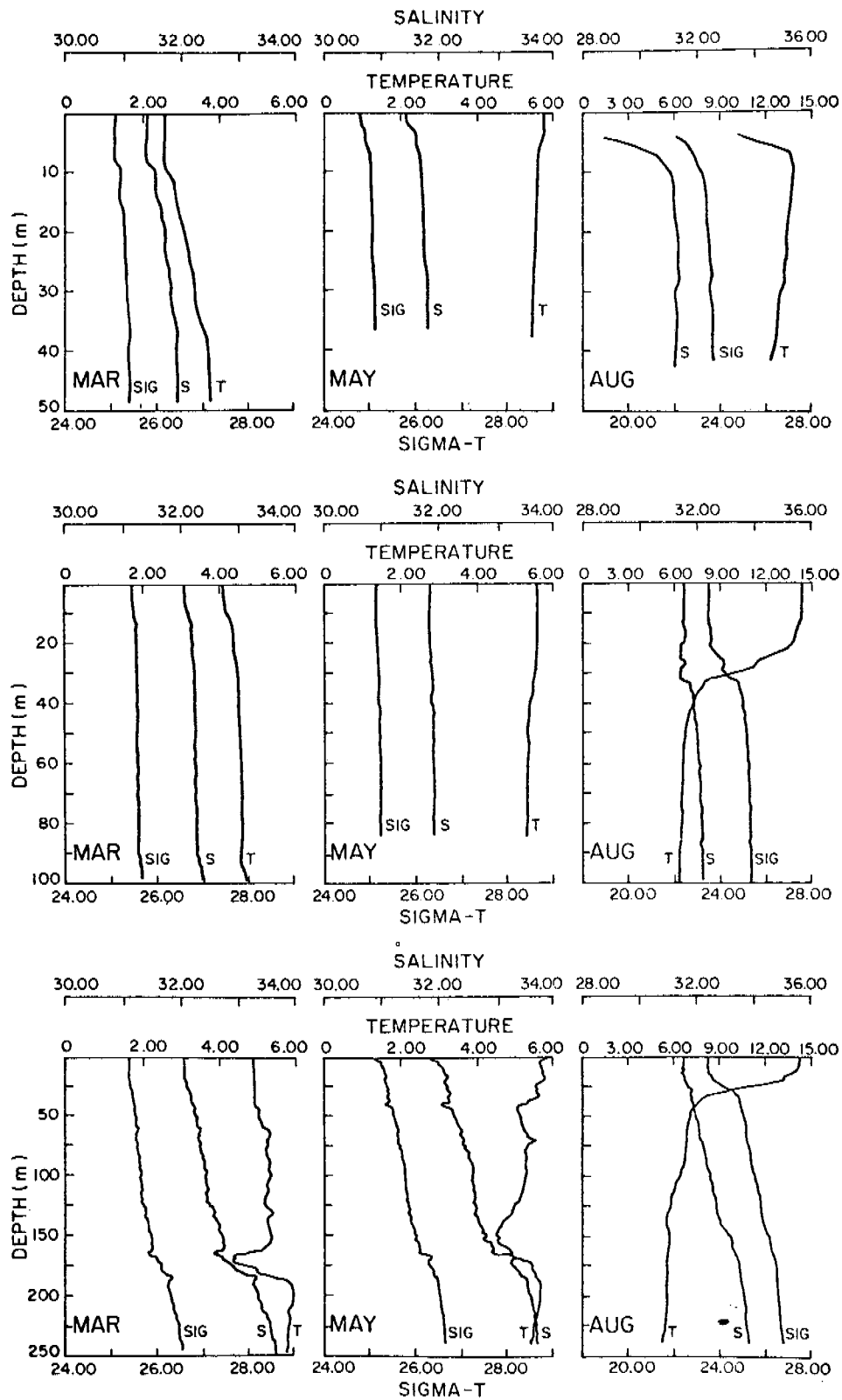


Fig. 3. Seasonal variation of the temperature, salinity, and sigma-t profiles at the three depths where bottom pressure was measured.

axes. Visually the record can be divided into a spring period (March-May) when the wind is large and variable with a significant alongshore component toward the west and a summer period (June-August) when the wind is smaller and often has an eastward alongshore component. The vector mean wind speed was 5.8 m/s in spring and 2.9 m/s in summer. This variation is typical of the seasonal wind patterns described by Ingraham *et al.* (1976).

The wind spectrum for the March-August period (Fig. 5) was calculated after detrending the time series by joining the end points (Frankignoul, 1974). At the 95% confidence limit no significant peaks were observed. The energy density had a frequency dependence of about ω^{-1} at low frequencies. This frequency dependence and the energy level are similar to the wind spectrum presented by Hayes and Schumacher (1976). However, the latter spectrum had significant structure near .02 cph.

4. VELOCITY OBSERVATIONS

Aanderaa current meters were used for the velocity measurements listed in Table 1. Instrument data tapes were reduced to standard format using the programs described by Charnell and Krancus (1976).

Moorings at B and C had the uppermost flotation at 45 m depth. This flotation was well below the surface in order to minimize contamination due to surface waves (Halpern and Pillsbury, 1976). However, mooring 62 which had a current meter at 20 m depth had flotation 17 m below the surface. There is some evidence that during high wind periods this record may be erroneous. Figure 6 shows unfiltered kinetic energy spectra of the current data at 50 m depth on B, C, and 62 for the period 15 March-15 April and on B and 62 for the period 15 July-15 August. Note the order of magnitude difference in the high-frequency energy level between B and 62 during the first

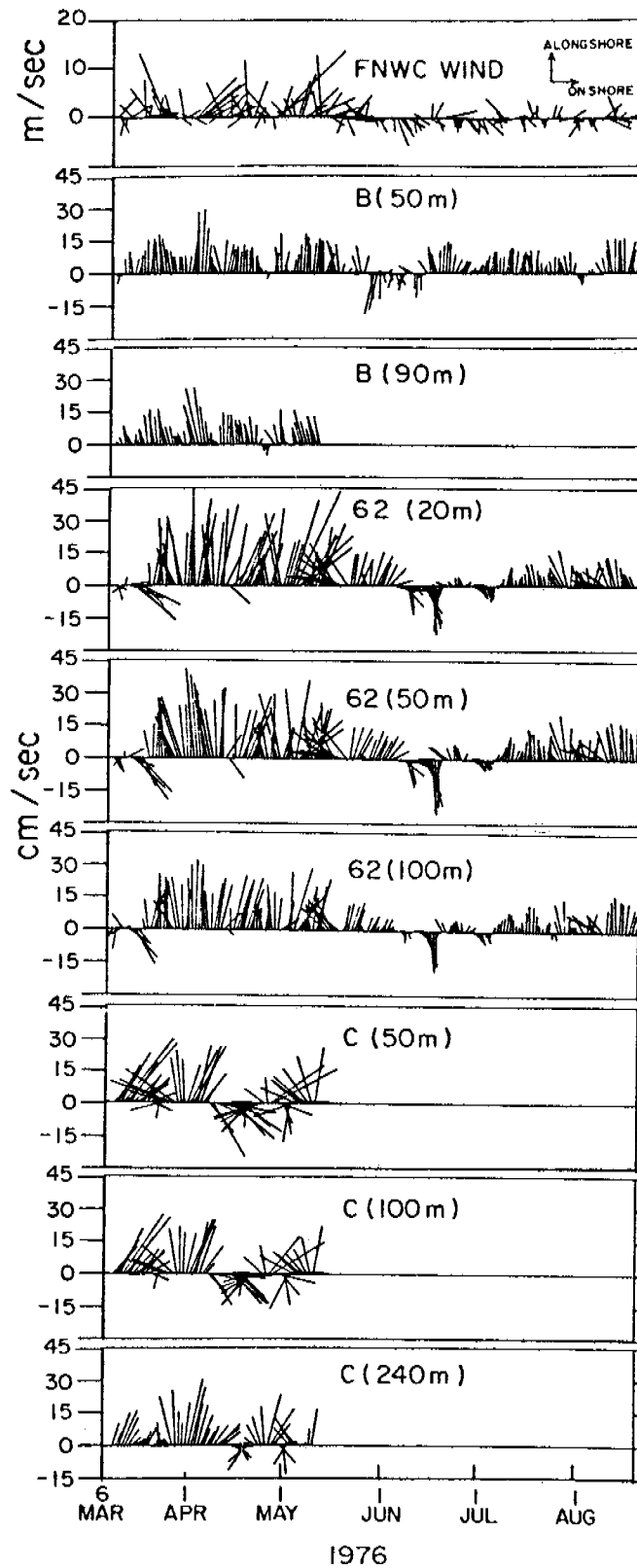


Fig. 4. FNWC vector time series for the calculated wind and measured currents. All vectors have been low-pass filtered and rotated into alongshore and onshore axes as discussed in text.

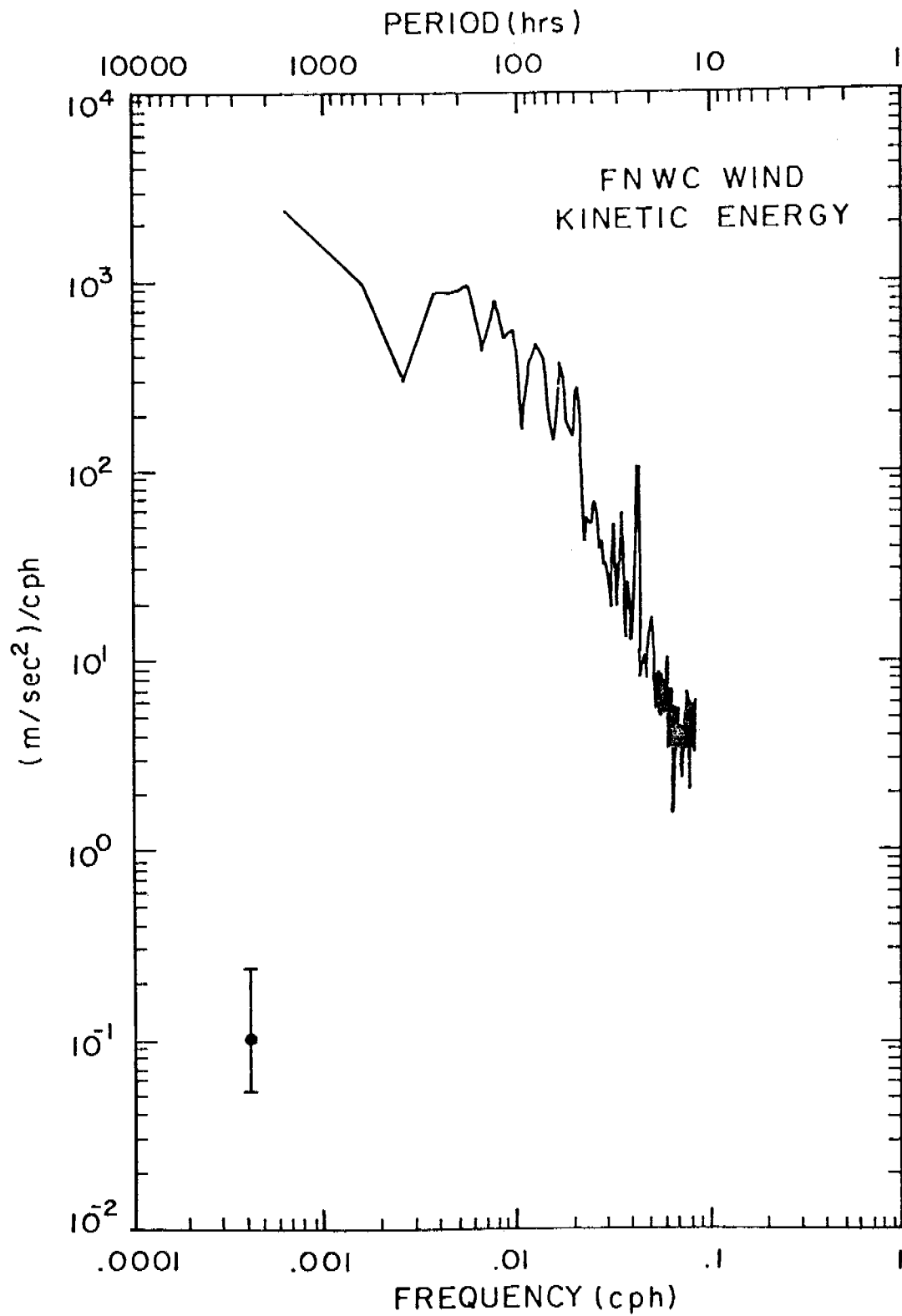


Fig. 5. Kinetic energy spectrum of the FNWC wind. The error bars indicate 95% confidence interval.

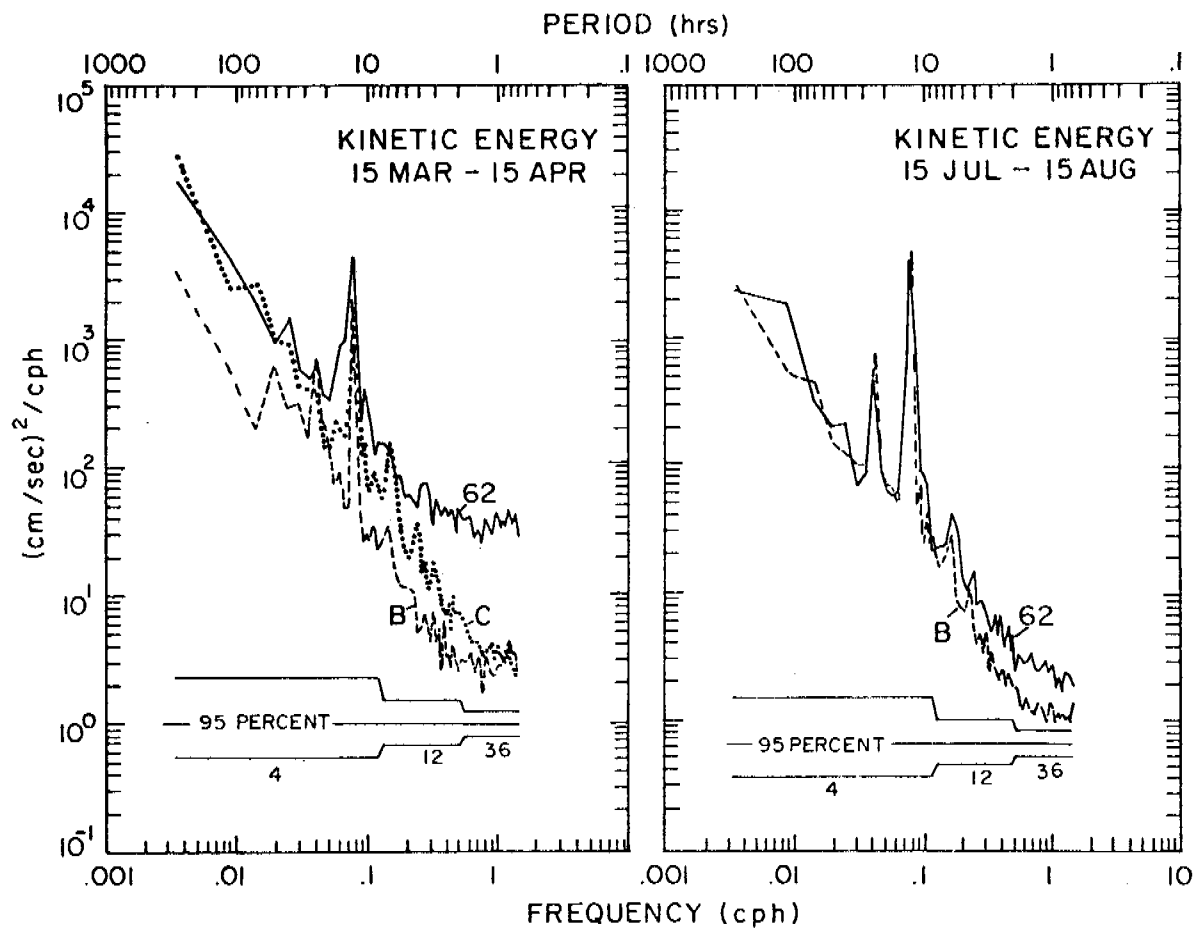


Fig. 6. Comparison of the kinetic energy spectra at locations 62, B, and C in spring and at B and 62 in summer. Moorings B and C had upper flotation at 45 m, mooring 62 had flotation at 17 m.

period. The similarity of the Brunt-Väisälä frequency at all locations makes it unlikely that this difference is real. In summer when winds were generally lighter, the high-frequency spectral levels more nearly agreed. The high spectral level observed in March is similar to that commonly seen when comparing current records obtained on moorings contaminated with high-frequency noise (Halpern and Pillsbury, 1976; Gould and Sambuco, 1975). Since we have no direct, nearby comparison, we cannot ascertain whether the low-frequency oscillations are also erroneous. However, results observed in mooring inter-comparison experiments indicate that caution is advisable when interpreting the velocity data at 62.

4.1 Velocity Time Series

Velocity vectors were rotated into an approximate cross-shelf (u) and alongshelf (v) coordinate system which was determined by consideration of the principal axes (Fofonoff, 1969) of the data, the local bathymetry, and the mean velocity vector. The principal axes were significant (based on the stability of the ellipse) (Gonella, 1972) at the 50-m and deeper current meters on B and 62. At C only the near-bottom (240 m) current record had a stable axis. At all locations the principal axis of the deepest current record was within 10° of the orientation of the local bathymetry. This direction was chosen as the alongshore coordinate, and the current vectors at all depths were rotated accordingly. For the three locations, B, C, and 62, the alongshore axes were 300°T , 300°T , and 310°T , respectively.

The rotated velocity time series were filtered using a tidal eliminator filter (Godin, 1972). This filter was chosen since it removes the strong tidal component seen in the pressure records. However, its half-power point is at a period of about 72 hr. Therefore, in calculating spectra or coherence

the unfiltered time series are used and only the low-frequency ($< .025$ cph) estimates are presented. Filtered data are used in time series plots and correlation function calculations.

Figure 4 shows the low-pass filtered vector time series of the velocity observations considered here. The data have been subsampled to give daily values. Statistical characteristics of these records are given in Table 2. In all cases, a bar indicates the mean value over the length of the series, a prime refers to the time-dependent velocity with frequencies less than .025 cph. Mean kinetic energy (per unit mass) \overline{KE} is defined as $\frac{1}{2}(\bar{u}^2 + \bar{v}^2)$ and eddy kinetic energy $KE' = \frac{1}{2}(u'^2 + v'^2)$. In referring to velocity series a subscript indicates mooring location, and depth of the current meter is given in parentheses.

4.1.1 Vertical Structure

The mean velocity at all locations is predominantly alongshore. The shear in this component is small; the largest velocity difference (5 cm/s) occurred between \bar{v}_{62} (20) and \bar{v}_{62} (100) during spring. In the cross-shelf direction vertical structure during March-May was consistent with downwelling circulation. On the shelf at B and 62, the near-surface current (\bar{u}_{62} (20 m)) was onshore and the near-bottom current (\bar{u}_B (90)) was offshore. However, at the shelf break (C) the current at all depths was onshore which may indicate that the downwelling circulation did not extend this far offshore. At all locations cross-shelf flow was small, and a slight error in assigning axis orientation could affect the interpretation.

In summer the seasonal thermocline could support larger mean shear. If such shear occurred, it must be above 20 m, since in the mean there was negligible gradient between the 20- and 100-m currents in May-August. The dominant difference between spring and summer was a reduction in magnitude

Table 2. Statistics of velocity time series. Overbars indicate mean values, u' and v' are the standard deviations of these components. Standard error estimates on the mean values, \overline{KE} , and KE' are discussed in the text.

Location	Date	Depth (m)	\bar{u} (cm/s)	\bar{v} (cm/s)	u' (cm/s)	v' (cm/s)	\overline{KE} (cm/s) ²	KE' (cm/s) ²
B	7 Mar-14 May	50	.1±.5	11.1±1.4	2.6	7.3	62	30
		90	-1.6±.3	8.8±1.1	1.4	6.0	40	19
	15 May-20 Aug	50	.1±.7	4.9±1.2	4.1	7.7	12	38
	7 Mar-20 Aug	50	.1±.2	7.2±.9	2.0	7.6	26	31
C	9 Mar-13 May	50	3.2±3.7	5.6±3.7	14.9	14.8	21	221
		100	2.9±3.0	5.6±3.3	12.2	13.1	40	160
		240	2.2±1.4	7.1±2.5	5.5	10.1	28	66
62	7 Mar-14 May	20	4.6±1.9	19.5±3.3	9.0	15.9	201	167
		50	0.5±1.7	16.9±3.1	8.0	14.8	143	142
		100	1.2±1.2	14.0±2.5	6.0	11.8	99	87
	15 May-20 Aug	20	-.1±1.1	3.8±1.6	6.5	9.1	7.2	62
		50	.2±1.2	5.2±1.8	6.6	10.0	14.1	72
		100	.4±.6	4.2±1.3	3.7	7.6	8.9	36
	7 Mar-20 Aug	20	1.6±1.0	9.9±1.8	7.1	13.6	50	117
		50	.4±.9	10.1±1.7	6.5	12.9	51	104
100		.9±.5	8.4±1.4	4.0	10.2	36	60	

of the mean flow. At B, the mean speed dropped by a factor of 2; at 62, it dropped by a factor of 4. (However, mooring motion may affect this result.)

Vertical structure of the time-dependent velocity components varied across the shelf. At B and at 62, the rms speeds had little vertical structure; however, at C these rms speeds decreased from 21 cm/s at 50 m to 11.5 cm/s at 240 m. Presumably, shear across the permanent pycnocline is responsible for this decrease. Linear cross-correlation between alongshore velocities at different depths show high correlations at B and 62. For the spring period (March-May) the correlation coefficient was 0.95 between v_B (50) and v_B (90) and 0.93 between v_{62} (20) and v_{62} (100). In summer (May-August), the correlation between v_{62} (20) and v_{62} (100) was not significantly reduced (0.88). At C, the correlation between velocity components was worse than observed on the shelf (0.71 between v_C (50) and v_C (240)); however, the rotary nature of the flow (see 4.1.2) at the shelf break makes the correlation of the rectilinear components less useful.

During the experiment there were three opportunities to compare measured shear with geostrophic calculations. This comparison is in Table 3. In each case the geostrophic shear is compared to the low-pass filtered shear averaged over 4-day intervals. Since the CTD sections were taken during deployment and recovery of moorings, the measured and calculated velocities are not always obtained over coincident periods. In general, geostrophic shear is a fair indication of measured shear. In March and May both of these quantities were small on the shelf. However, at C in March there was considerable shear across the permanent pycnocline. Both measured and calculated velocities show this, but measured shear was twice the calculated shear. Difficulties in extrapolating the density field across rapidly sloping bathymetry may account for some of this difference.

Table 3. Comparison of measured shear and geostrophic shear calculations for three periods. In each case the measured shear is based on 4-day averaged current measurements.

Date	Location	Depths (m)	Measured Shear (cm/s)	Calculated Shear (cm/s)
5 March	B	50-100	-1.5	< 3
		50-250	7.2	25
	62	20-100	-1.6	< 3
		50-100	0	< 3
		50-250	12.2	< 3
13 May	B	50-100	-1.3	4
		50-250	12.2	< 3
	62	20-100	2.0	< 3
		50-100	3.8	< 3
		50-250	12.2	< 3
19 August	62	20-100	-6.2	5
		50-100	1.8	4

4.1.2 Cross-Shelf Structure

Figure 4 shows a clear difference in the current field as we proceed across the shelf. At the 100-m isobath mean flow and low-frequency oscillations were largely parallel to the coast. At the 250-m isobath the flow was still predominantly alongshore, but there was significant cross-shelf flow. Even the near-bottom current meter (240 m depth) showed this effect. There is little visual coherence between velocity at B and C; however, B and 62 appear related to each other and to the wind.

The statistics in Table 2 characterize cross-shelf variations. In spring, at the 50-m depth \bar{v} increased from B (11 cm/s) to 62 (17 cm/s) and then decreased at C (6 cm/s). In view of possible contamination of the record at 62 by surface waves, we cannot be certain of the relatively high mean velocity at this location. Low-frequency eddy kinetic energy at 50 m increased from B (30 cm²/s²) to C (221 cm²/s²). Also, the balance between contribution of alongshore and cross-shelf fluctuations changed; at B the alongshelf fluctuations dominated whereas at C the two components contributed equally. Flow 10 m off the bottom had less cross-shelf variability; however, KE' still increased by a factor of 3.5 between B and C.

In order to compare time scales of low-frequency velocity fluctuations, the autocorrelation functions were calculated. The low-pass filtered velocity time series were used with a time step, $\Delta\tau$, of 4 hours. The results for sites B and C are shown in Figure 7. The integral time scale, T_{ij} , for each velocity series was estimated from the equation

$$T_{ij} = \sum_{n=-N}^N r_i(n\Delta\tau) r_j(n\Delta\tau) \quad (3)$$

(Allen and Kundu, 1977), where $r_i(\tau)$ and $r_j(t)$ are the autocorrelation functions for series i and j . $N\Delta\tau$ was chosen to be 8 days so that the contribution

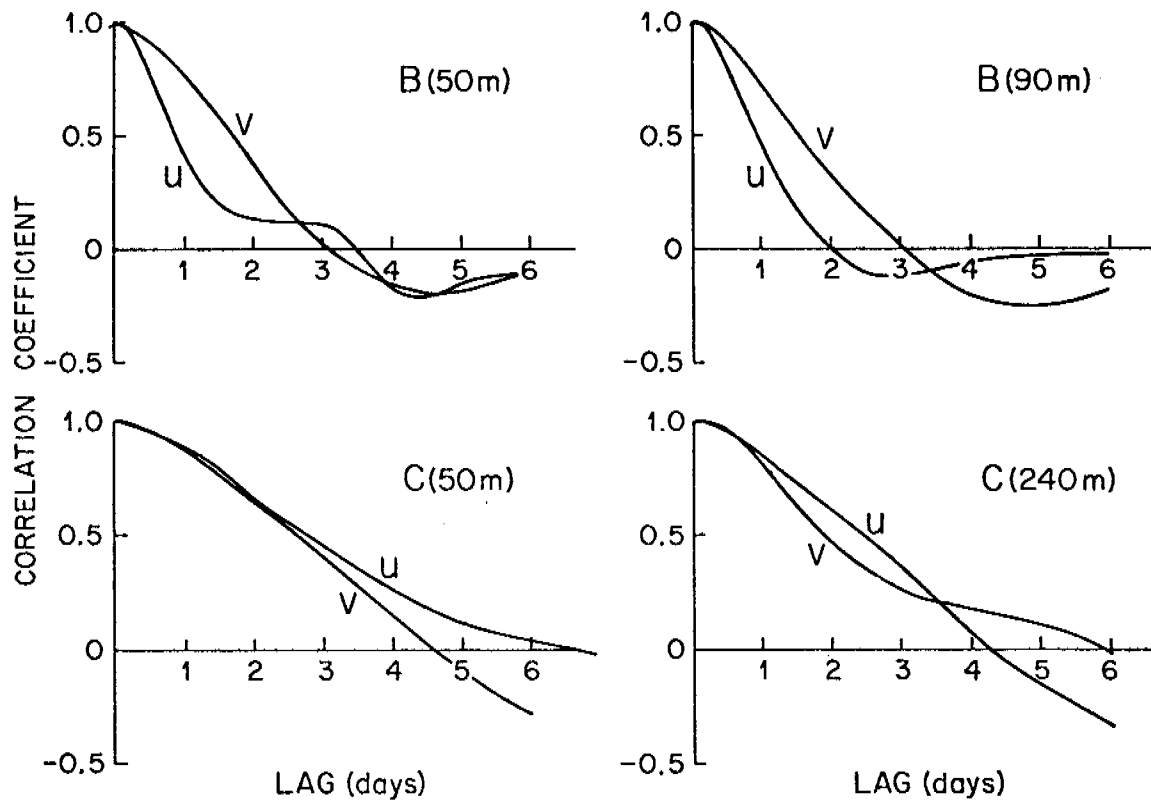


Fig. 7. Autocorrelation functions of the low-pass filtered velocity components at B and C. Results for records at 50 m depth and at 10 m above the bottom are shown in each case.

to T from $n > N$ was negligible. The integral time scale determines the time required to obtain independent measurements. At 50 m, v' had a time scale of about 2.5 days at B and 4 days at C. Similarly, the u' time scale increased at the shelf break. Figure 7 also shows the autocorrelation functions for the near-bottom currents at the two locations. Although the details change, motions at C had longer time scales than those at B.

Having established T for each velocity series, root-mean-square error in the mean velocities can be estimated from

$$\sigma_1 = \sigma / \left(\frac{T}{\tau}\right)^{1/2} \quad (4)$$

(Kundu and Allen, 1975), where σ_1 is the rms error of the mean and σ is the standard deviation of the time series of length T . Integral time scales of 2.5, 3, and 4 days at B, 62, and C were used to obtain the error limits shown in Table 2. These error limits indicate that the differences in \bar{v} at B, C, and 62 (during spring) are probably not due to random fluctuations.

Spectral decomposition of the kinetic energy is shown in Figure 8 for the 50-m velocity at B, C, and 62 in spring. As expected, at the lowest frequency the energy density at the 100-m isobath (B) was an order of magnitude smaller than that observed near the shelf break (C). At higher frequencies the spectra at C falls rapidly with no significant peaks. However, at B there is a significant energy density peak at about 0.017 cph (60-hr period).

Spectra at B and C are further compared in Figure 9 where rectilinear and rotary spectra are shown. At B the low-frequency flow paralleled the isobath so that the v spectra exceed the u spectra; at C the flow was rotary with a clockwise rotation. Near-bottom kinetic energy spectra are similar to those shown even though the 240-m velocity at C was more nearly aligned with the bathymetry. Clockwise polarization was still observed. These spectra

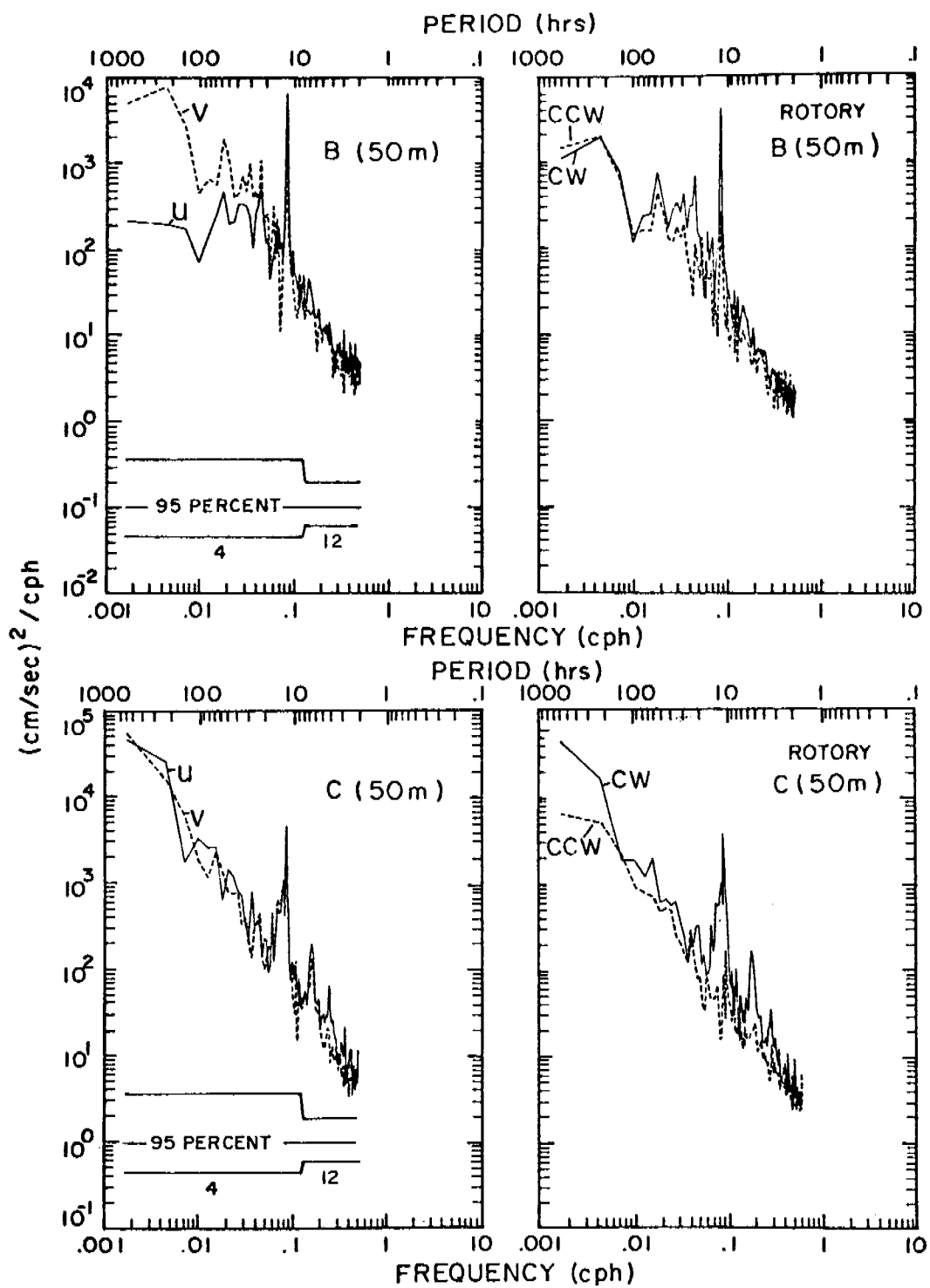


Fig. 9. Rectilinear and rotary kinetic energy spectra at the 50-m depth at locations B and C.

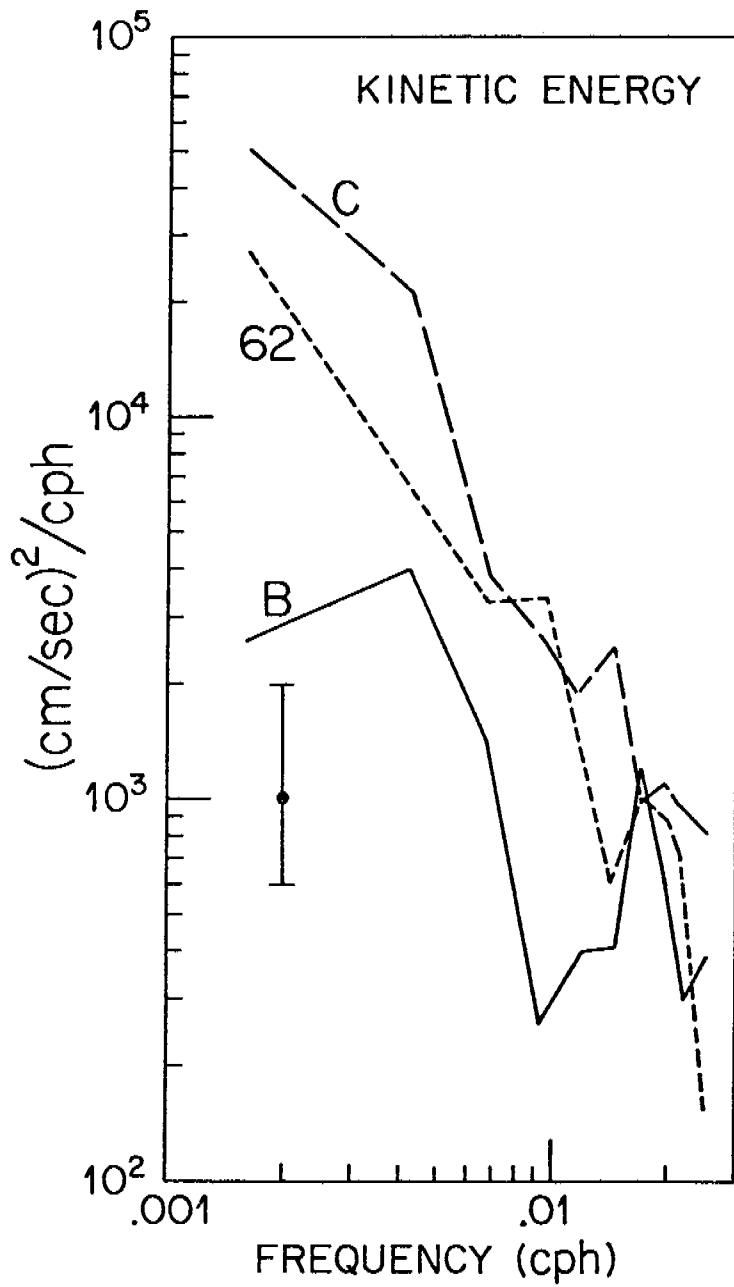


Fig. 8. Kinetic energy spectra of the low-frequency fluctuations at B, C, and 62 for the period 15 March-15 May.

indicate that the flow on the shelf was directly steered by the bathymetry, while at the shelf break where the bottom gradient is greater, the flow was rotary.

Cross-correlation functions of currents at the three sites were computed. These correlations were not large for any of the series. In spring the 50-m cross-correlation coefficients were $r_u = .2$, $r_v = .4$ between B and 62 and $r_u = .1$, $r_v = .3$ between B and C where the subscript indicates the velocity component. Similar results occurred between near-bottom currents at B and C. Based on a joint time scale of about 3 days, the 10% significance level for these correlations is about .35. Therefore, the observed correlations are at best marginally significant. The change in polarization of the flow across the shelf may result in small linear correlation of the u and v velocity components even if the rotary components are coherent. To investigate this, rotary coherence (Mooers, 1973) between the velocity series was computed. This coherence is independent of the coordinate system. To obtain a measure of the overall coherence, spectral estimates with periods greater than 3 days were ensemble-averaged. These coherence estimates have a 95% confidence level for zero coherence of 0.40 (Carter *et al.*, 1973). In spring at the 50-m level the counterclockwise (C_+) and clockwise (C_-) coherences were $C_+ = .50$, $C_- = .19$ between B and C; $C_+ = .49$, $C_- = .35$ between B and 62; and $C_+ = .23$, $C_- = .06$ between 62 and C. Thus, the dominant clockwise oscillations observed at C (Fig. 9) do not propagate onto the shelf. These oscillations are coherent and have no phase shift in the vertical direction ($C_+ = .25$, $C_- = .86$, $\phi_- = 3^\circ$ between 50 and 240 m). The motions at C appear to represent quasi-barotropic motions along the shelf break.

5. BOTTOM PRESSURE OBSERVATIONS

The measured bottom pressure is composed of several terms,

$$P_B = \bar{P} + P_a + g \int_0^H \rho'(z,t) dz + \rho_o g \eta . \quad (5)$$

\bar{P} , the mean pressure at the mean depth, H , of the gage, can be ignored since we are only concerned with time-dependent pressure. P_a , the atmospheric pressure, is often assumed to be compensated for by the inverse barometer effect (i.e., an equivalent change in sea level). However, if sea level compensation is depth-dependent, then atmospheric pressure fluctuations will produce changes in the bottom pressure gradient. Such an effect is difficult to isolate, since winds accompanying the changes in P_a are expected to dominate (Buchwald and Adams, 1968). The third term in (5) represents the density effect. Local changes in the density distribution could affect the measured bottom pressure. Finally, the last term represents pressure changes due to the sea level, η . Using equations (1) and (2), this term can be related to the barotropic current. Thus, before assigning dynamical significance to the measured bottom pressure gradient, the influence of all the various other terms must be considered.

5.1 Instrumentation

Instrumentation and processing used to measure the pressure fluctuations are described by Hayes et al. (1978). The pressure gage consisted of a 400-psia full-scale quartz pressure transducer manufactured by Paroscientific Corporation in Redmond, Washington, a temperature sensor, and a digital recording system. The gages all continuously averaged pressure and recorded at 15-min intervals. Temperature corrections were applied to account for the temperature coefficient of the pressure transducer. Final data series were low-pass filtered using the tidal eliminator filter of Godin (1972).

5.2 Time Series

The low-pass filtered time series of atmospheric pressure at Yakutat, adjusted sea level (atmospheric pressure in millibars added to sea level in centimeters) at Yakutat, and bottom pressure at sites B, D, E, and F are shown in Figure 10. All pressures are given in centimeters assuming 1 cm = 1 mbar. The atmospheric pressure data have been low-pass filtered using a Fourier filter with a 0.025 cph cutoff. Mean pressure calculated over the record length was subtracted from each time series. At site B, the total record was constructed by joining records from two consecutive deployments; at other locations the data are continuous measurements by a single gage.

In Table 4 the mean trend and variance (with this trend removed) are given for all filtered bottom pressure records. Yakutat adjusted sea level was not included in this table since the tide gage data had numerous gaps. Visually, the Yakutat series is similar to the bottom pressure record from D. The mean trend, based on a least squares linear regression, varied between sites. At the 100-m isobath (B and E) the trend was negligible; however, at 50-m (D) and 250-m (F) isobath the trend was almost 1 cm/mo. These trends were not constant throughout the record and they may be influenced by the low-frequency fluctuations in the series. In addition, instrumental effects (Hayes *et al.*, 1978) cannot be ruled out.

The small observed trends can be compared with seasonal water density changes at each site. CTD casts near each mooring showed an increase in dynamic height from spring (February, March, April) to summer (August, September). This increase amounted to 12.5 cm, 6.6 cm, and 4.8 cm at the 50-, 100-, and 250-m isobaths, respectively. If sea level were constant over this period, then the bottom pressure at each site would show a decrease comparable to the dynamic height increase. None of the bottom pressure records show such a decrease, thus shallow water density changes do not appear important.

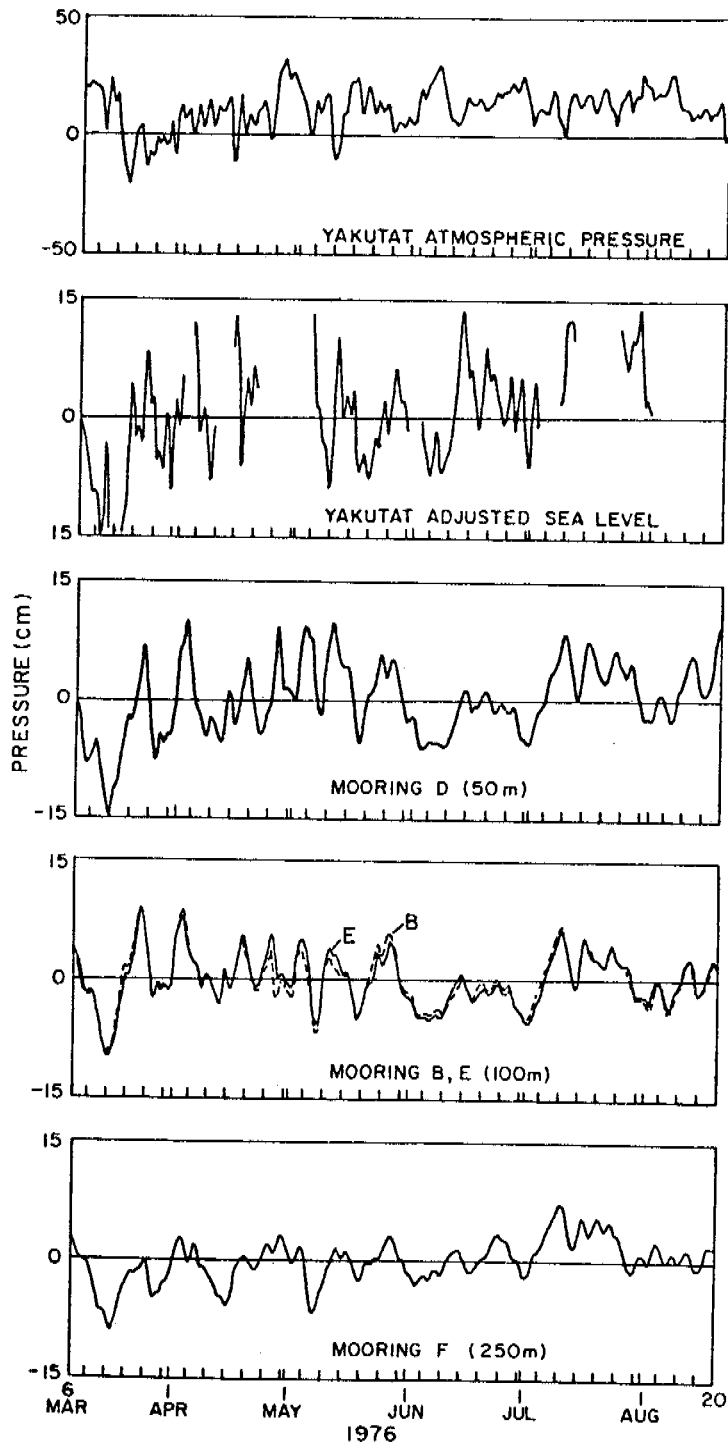


Fig. 10. Time series of atmospheric pressure and adjusted sea level at Yakutat and of bottom pressure at B, D, E, and F. All records have been low-pass filtered. The gaps in adjusted sea level are caused by missing tide gage data.

Table 4. Statistics of bottom pressure for the period 6 Mar-20 Aug, 1976. The variance was calculated after removing the linear trend.

Location	Variance (cm ²)	Trend (cm/mo)
B	11	0.04
D	19	0.99
E	11	0.05
F	5.8	0.93

Reid and Mantyla (1976) found good agreement between seasonal changes in Yakutat adjusted sea level and changes in the density field in the deep waters off the continental shelf. Based on historical data the monthly mean adjusted sea level at Yakutat increased by 5 cm between April and August. This change is similar to the pressure trend observed at 50 and 250 m. Using CTD observations in 1500 m of water, we calculated spring (three casts) to summer (two casts) change in dynamic height between 1000-dbar and 50-, 100-, and 250-dbar surfaces to be 6.2, 5.1, and 4.2 dyn cm, respectively. These changes support the conclusion of Reid and Mantyla (1976) that seasonal sea level changes observed on the shelf are related to the deep water density field. They also suggest that the trends observed in the bottom pressure may be real.

Bottom pressure variance across the shelf varies inversely with water depth H (Fig. 11). If one assumes that bottom pressure fluctuations represent sea-level oscillations associated with a nondivergent wave, then the inverse relation of pressure variance with depth implies that the depth-integrated horizontal kinetic energy is constant across the shelf, i.e., $V \approx H^{-\frac{1}{2}}$. As pointed out by Kundu and Allen (1975), theories of continental shelf waves lead to such a velocity-depth relationship.

5.3 Pressure Spectra

Low-frequency ($< .025$ cph) spectral estimates of the unfiltered pressure records are shown in Figure 12. At the lowest frequencies these spectra are all similar. They have a weak slope up to about .003 cph and then a sharp falloff (ω^{-3}) with frequency. This frequency dependence is greater than that observed for kinetic energy (Fig. 8). At high frequencies the pressure spectra at D (50 m) and E (100 m) show a significant peak at 0.017-0.020 cph (60-50 hr period). This peak is not seen in the shelf break record at C

(250 m). A similar peak was noted in the velocity spectra at B (Fig. 8). In the frequency band of this spectral peak, pressure variance across the shelf fell more rapidly than H^{-1} . The ratios of variance estimates at the 100-m and 250-m isobath to the 50-m variance were 0.55 and 0.15. This rapid falloff is consistent with an exponential depth dependence.

5.4 Pressure Correlations

The pressure field has a longer cross-shelf coherence scale than velocity. Cross-correlation between the 50-m and 250-m record was 0.59. In part, this larger scale could represent pressure fluctuations which are not related to on-shelf effects. For example, if the conclusions of Reid and Mantyla (1976) are correct, then seasonal variance is associated with changes in deep water structure of the Alaska Current. For many purposes it would be useful to isolate pressure variance due to deep water variability from the on-shelf pressure effects. Although all the data records presented here are probably highly influenced by shelf circulation, the 250-m record should most accurately reflect off-shelf pressure fluctuations. Except for the .017 cph energy peak, the pressure variance spectra (Fig. 12) are similar at all locations and offer little hope of separating shelf effects on the basis of frequency. However, the coherence between locations D and F (Fig. 13) shows that only the lower frequency variance ($\omega < .006$ cph) is significantly coherent across the shelf. This suggests that oscillations with periods longer than about 7 days are more likely associated with off-shelf (or, in any case, very broad) current structures.

The single pressure comparison obtained in the along-shelf direction indicates high coherence. Time series at B and E are nearly identical, and the cross-correlation coefficient between sites (both at 100 m depth) is 0.98.

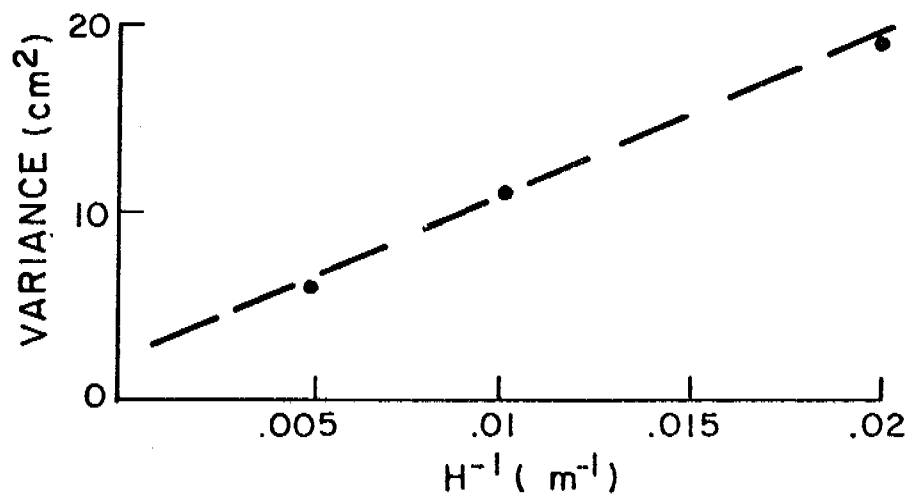


Fig. 11. Low-frequency variance of the bottom pressure plotted as an inverse function of water depth, H . A linear trend has been removed from the time series before variance was calculated.

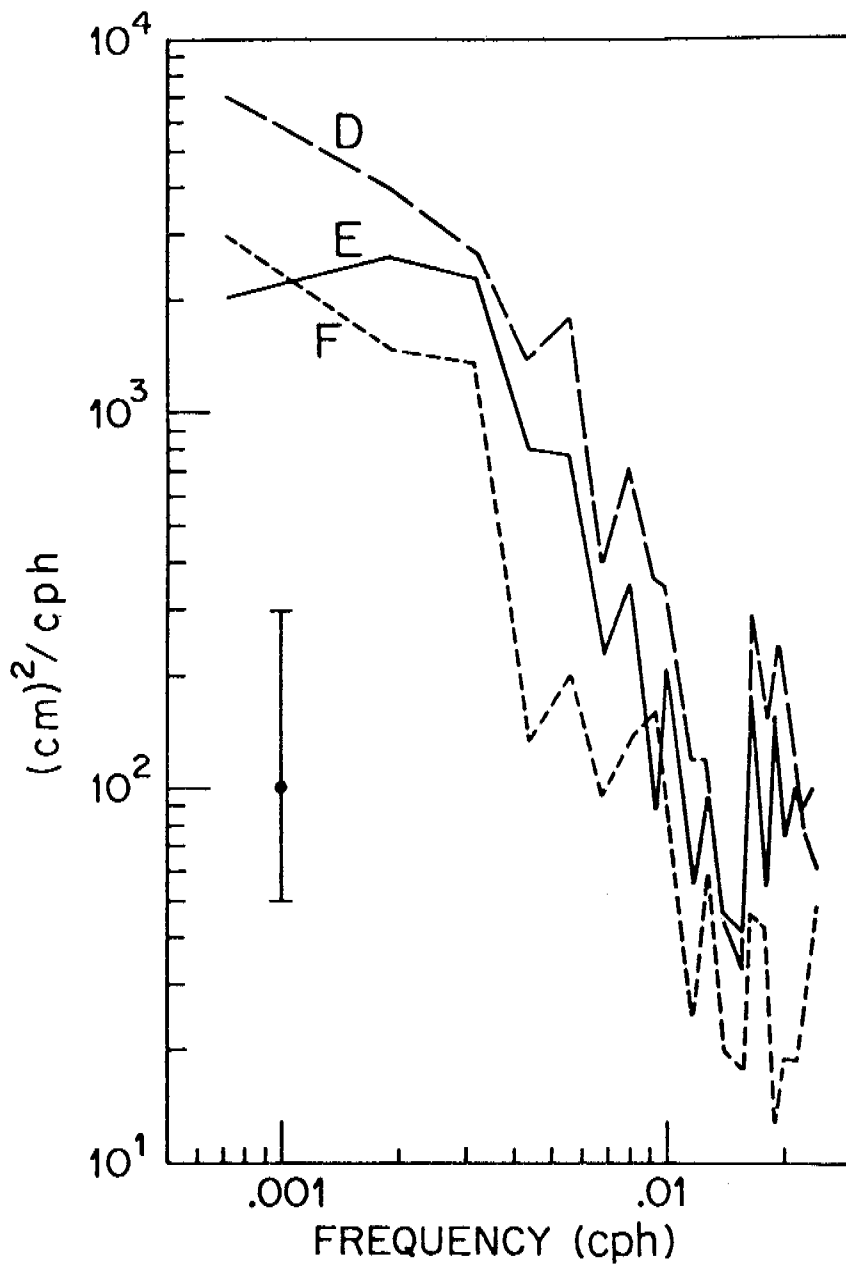


Fig. 12. Spectra of the bottom pressure records at D, E, and F. The error bars indicate 95% confidence interval.

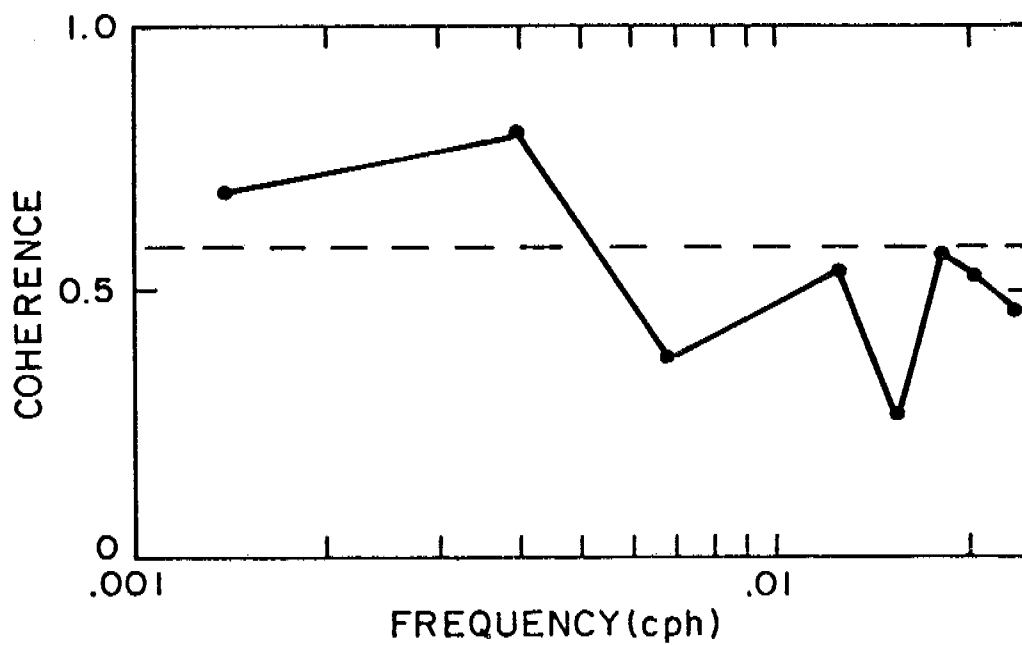


Fig. 13. Coherence between bottom pressure measured at D (50 m depth) and F (250 m depth). The dashed line indicates the 95% confidence level for zero coherence.

A small phase lag of 2 hours, if significant, indicates propagation from E to B. This lag is counter to the direction expected for free shelf waves, but may be related to the eastward propagation of most storm systems.

6. VELOCITY-PRESSURE RELATIONS

As noted in the introduction, variations in bottom pressure gradient and current provide information on dynamical balances in the equations of motion. To investigate terms in equations (1) and (2), we first consider the velocity field. The accelerations u_t and v_t were calculated from the low-pass filtered time series using a central difference approximation with a time increment of 12 hours. For both the 50-m current at B and the 100-m current at 62, the rms along-shore velocity term, f_v , exceeded the rms cross-shelf acceleration by a factor of 40. Thus neglect of u_t in equation (1) is reasonable. In equation (2) the rms value of f_u exceeded rms v_t by factors of 5 and 10 at sites B and 62, respectively. Therefore, the cross-shelf velocity dominates, but the acceleration terms may not be negligible.

Table 5 compares alongshore velocity with the pressure time series. Cross-correlation coefficients have been calculated between alongshore velocity measurements at four current meters (B (50 m), 62 (100 m), C (100 m and 240 m)) and the bottom pressure and bottom pressure gradient. Where data are available, correlations are presented for three periods: the total record, spring (15 March-15 May), and summer (15 June-15 August). In all cases low-pass filtered data were used. The 5% significance level for the correlation coefficient was estimated using integral time scales defined by autocorrelation functions of the component series (equation (3)). For the total record the 5% significance level was 0.25; for the two subintervals it was 0.45.

Table 5. Linear correlation coefficients between velocity and pressure or pressure gradient. The 5% level of significance is approximately 0.45 for the 2-month pieces and 0.25 for the total record.

Velocity	Pressure	7 Mar-14 May	15 June-15 Aug	7 Mar-15 Aug
B-50 m	P_D	0.52	0.56	0.47
	P_E	0.33	0.35	0.36
	P_F	0.02	-0.02	0.08
	P_D-P_E	0.52	0.87	0.49
	P_D-P_F	0.63	0.68	0.56
	P_E-P_F	0.54	0.45	0.47
C-100 m	P_D	0.01	-	-
	P_E	-0.08	-	-
	P_F	-0.04	-	-
	P_D-P_E	0.14	-	-
	P_D-P_F	0.05	-	-
	P_E-P_F	-0.08	-	-
C-240 m	P_D	0.21	-	-
	P_E	0.25	-	-
	P_F	0.27	-	-
	P_D-P_E	0.05	-	-
	P_D-P_F	0.09	-	-
	P_E-P_F	0.12	-	-
62-100 m	P_D	0.75	0.39	0.61
	P_E	0.77	0.41	0.58
	P_F	0.32	0.13	0.18
	P_D-P_E	0.40	0.11	0.41
	P_D-P_F	0.68	0.41	0.63
	P_E-P_F	0.77	0.74	0.67

Results in Table 5 can be summarized by considering the largest velocity-pressure correlations. At the 100-m contour (B), for the total record interval, the highest correlation (0.56) was with the pressure gradient estimated over the entire shelf ($P_D - P_F$). This correlation was slightly better than that obtained with the pressure measurement at 50 m (P_D) alone. In the spring period similar results were obtained. However, during summer a distinct improvement in the correlation was found when the 50-m velocity at B was compared to the pressure gradient between the 50- and 100-m isobaths ($P_D - P_E$). This correlation (.87) was the highest observed. At the 180-m isobath (62) the best correlation (.67) for the total record was with the pressure gradient between the 100- and 250-m isobaths. Again, this pressure gradient correlation was only slightly better than the correlation (.61) with the single pressure measurement at 50 m. During the spring period results were similar. The summer period had poor correlation with the individual pressure measurements, but correlation with the pressure gradient between 100-m and 250-m isobaths was large (.74). Finally, at the 250-m isobath (C) the correlations for all pressure and velocity combinations were below the 5% significance level.

The pattern of the pressure-velocity correlation suggests that the pressure field across the shelf is simpler in spring than in summer. During the March-May period correlations which involved a single pressure measurement on the shelf were almost as high as those which involved a pressure gradient measurement. Thus, in spring a reasonable model for the pressure-velocity relation is a linear sea level slope across the shelf with little or no response at the shelf break. The slight enhancement of the correlation at 62 (180-m depth) when the outer shelf pressure gradient ($P(100\text{ m}) - P(250\text{ m})$) is used indicates that this model is not entirely adequate and that there is some difference in shallow water sea level response. During the

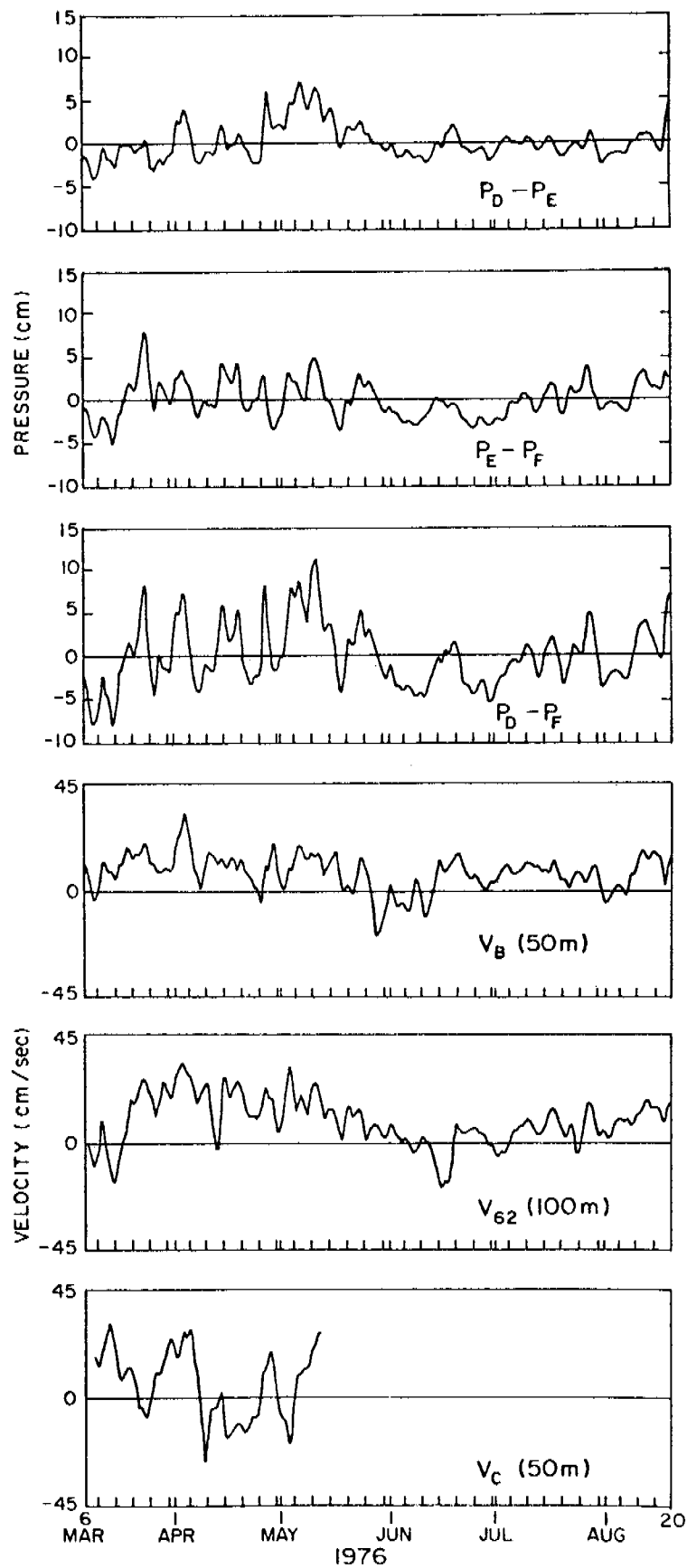


Fig. 14. Comparison of the cross-shelf difference of bottom pressure and the alongshore velocity. All series are low-pass filtered.

summer period individual pressure measurements gave significantly poorer velocity correlations than the pressure gradients. Also, the difference between pressure gradients measured over the inner (P (50 m)-P (100 m)) and outer (P (100 m)-P (250 m)) shelf region was large. The interior gradient correlated well with velocity at B ($r = 0.87$); the outer gradient correlated with velocity at 62 ($r = 0.74$).

Summer stratification could account for the complex pressure field. For example, the pressure gradient between 50 m and 100 m isobaths includes a cross-shelf density gradient term as well as the sea surface gradient. Variations in this density gradient term reflect baroclinic velocity fluctuations which would be observed by the current meter at the 50-m level at B. To measure these baroclinic effects the shear in v was correlated with the pressure gradients. No significant correlations were found. However, since we expect the barotropic term to dominate both velocity and pressure fluctuations, the small correlation coefficients do not necessarily preclude baroclinic effects.

In summary, comparison of the along-shore velocity and pressure measurements indicates that on the continental shelf 50-70% of the current variance can be accounted for by equation (1). At the shelf break, current and bottom pressure are uncorrelated. The cross-shelf velocity coherence and these pressure-velocity correlations show that the shelf break separates the circulation into two distinct regimes.

With the present data a definitive test of equation (2) is not possible. Figure 15 shows v_t , f_u , and ΔP estimated from the 50-m velocity at B and the along-shelf pressure difference between B and E. Although there are periods when v_t or f_u appear correlated with ΔP , the overall correlations are not significant. Similarly, the sum, $v_t + f_u$, is not correlated with pressure

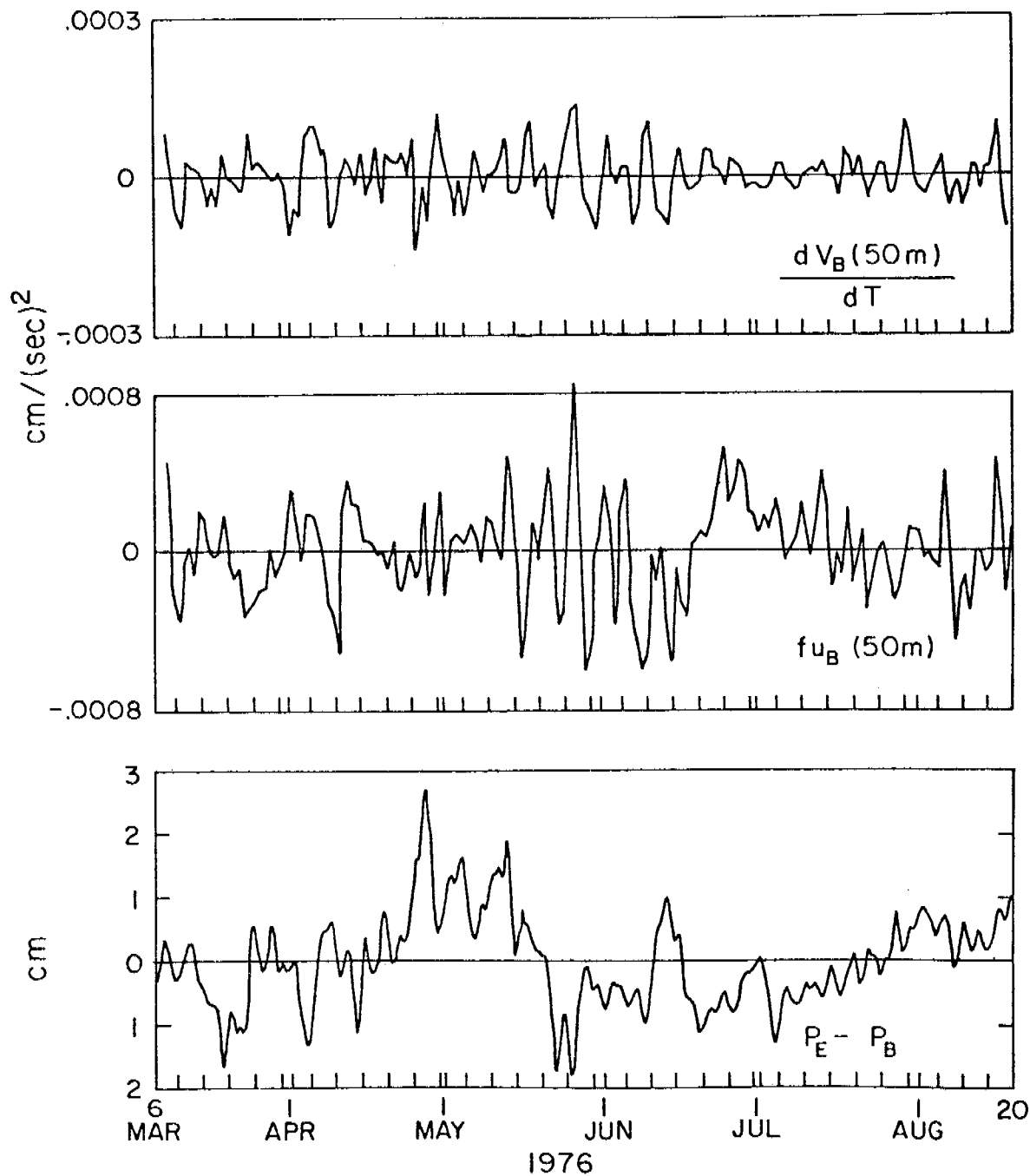


Fig. 15. Acceleration of the alongshore velocity compared with the crossshelf velocity and the alongshelf bottom pressure difference. Measurements were made at the 100-m isobath. Velocity records are from 50 m depth; f is the Coriolis parameter.

difference $P_E - P_B$. This lack of correlation is not surprising considering the small magnitude of the quantities. Errors in axis orientation could contaminate the u series; density and local topography could influence the longshelf pressure gradient.

7. WIND CORRELATIONS

In the above discussions the forcing term has been neglected. We expect, particularly in spring, that atmospheric forcing will be important in driving current and setting up sea level slope. The available atmospheric measurements are the pressure and winds at Yakutat and the FNWC calculated wind field. As discussed in section 3, the FNWC wind calculations are probably not representative of the local wind field. However, in lieu of direct oceanic wind measurements, these calculated winds are used to investigate the gross features of the response.

From Figure 10 we see that variations in atmospheric pressure, P_a , exceed variations in any of the bottom pressure series. The low-frequency variance in P_a was 81 cm^2 , a factor of 4 greater than the bottom pressure variance at D. The inverted barometer effect has been shown to reduce bottom pressure fluctuation in the deep ocean (Brown et al., 1975) and at the shelf break (Beardsley et al., 1977). Here we see that the reduction in bottom pressure variance occurs across the shelf. In addition, the linear correlation between bottom pressure fluctuations and P_a was insignificant at all sites ($r = -.13, -.14, -.18$ between P_a and P_D, P_E, P_F). We thus feel confident in neglecting the contribution of the atmospheric pressure term in equation (5).

Table 6 shows correlation coefficients between wind and current or pressure measurements over the 6-month record. At both B and 62 along-shore current components are significantly correlated with along-shore wind, but

Table 6. Linear correlation coefficients between wind components and velocity or pressure series.

Series	u_{wind}	v_{wind}
u_B (50 m)	0.10	-0.03
v_B (50 m)	0.27	0.51
u_{62} (100 m)	-0.12	0.20
v_{62} (100 m)	0.08	0.52
$P_D - P_E$	0.33	0.15
$P_E - P_F$	0.05	0.63

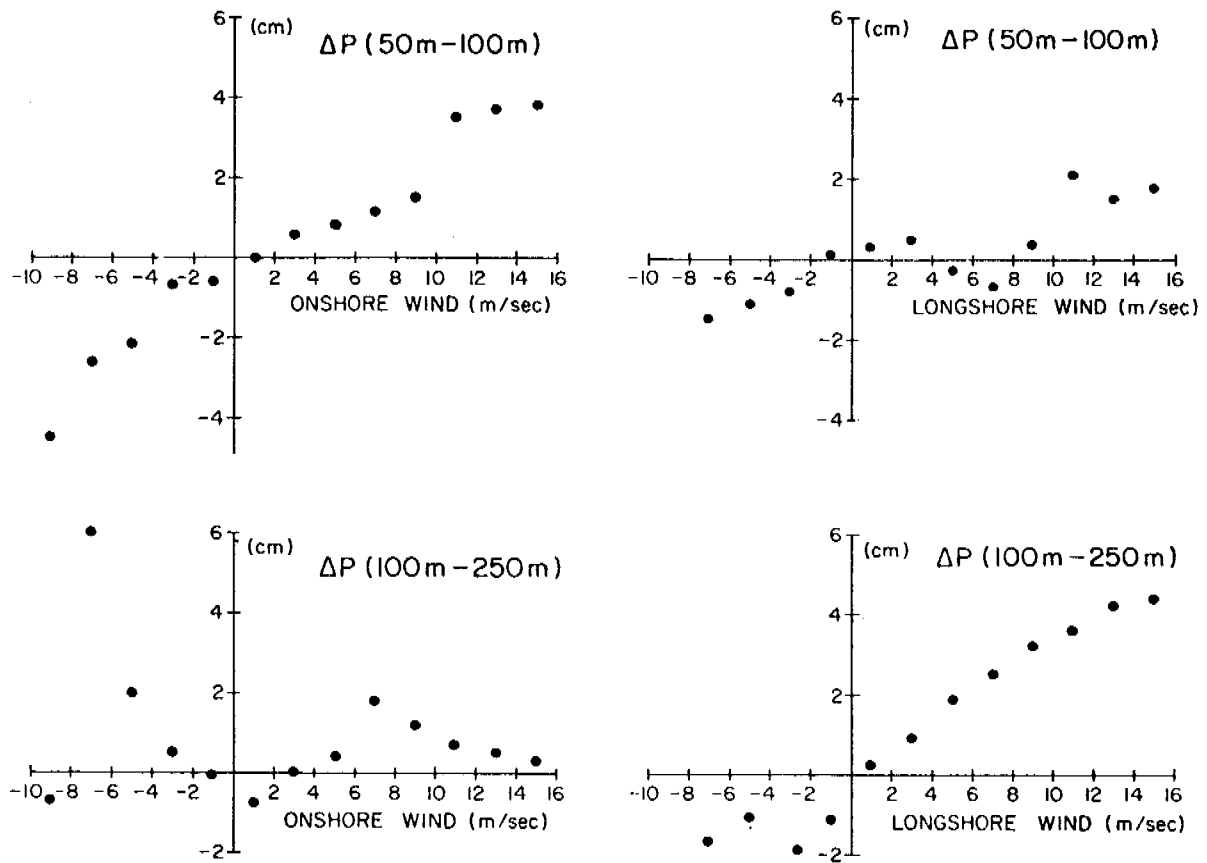


Figure 16. Cross-shelf pressure gradient between indicated depth contours versus onshore and alongshore wind.

cross-shelf wind and current components are unrelated. Correlation of wind and current at C was also calculated; no significant correlation was found. These velocity correlations substantiate what is clear from the time series plots (Fig. 4); along-shore flow on the shelf is related to along-shore winds, but the flow at the shelf break is not.

The pressure gradient correlations suggest an interesting difference in response across the shelf. On the inner shelf (between 50-m and 100-m isobaths) the pressure gradient is significantly correlated (assuming a 5% significance level of 0.25) with the onshore wind; on the outer shelf (between 100- and 250-m isobaths) the significant correlation is with the along-shore wind. This relationship is further described by binning the pressure differences according to the component wind speed using 2 m/s bins. Resultant scatter diagrams between pressure difference and wind (Fig. 16) show a clear tendency for the shallow water to respond to onshore winds while the deep water responds to along-shore winds. This relationship is consistent with simple dynamical ideas. In the deep water, Ekman-like response produces an onshore transport accompanying an along-shore wind (Ekman, 1905). If, however, the Ekman depth is equal to or less than the water depth, then direct wind setup (Welander, 1957) becomes more important. It must be kept in mind that wind estimates are crude (particularly for the onshore component). Until more accurate measured winds are available in conjunction with pressure gradient measurements, the distinction between the inner and outer shelf regimes must be treated with caution.

8. SUMMARY

Low-frequency ($f < 0.025$ cph) variations in current and bottom pressure have been studied on the continental shelf in the Northeast Gulf of Alaska.

Current was measured at three stations located in 100, 170, and 250 m of water; bottom pressure was measured at the 50-, 100-, and 250-m isobaths. The analysis has shown that:

(1) Flow on the shelf differed from flow at the shelf break. At the 100-m contour mean and fluctuating velocity components were aligned with bathymetry, and depth dependence was small. At the 250-m contour mean along-shore flow was reduced by 50%, fluctuating components were largely anti-cyclonic, and eddy kinetic energy increased by a factor of 7. These anti-cyclonic low-frequency motions were vertically coherent, but did not propagate onto the shelf. In general, cross-shelf coherence between all velocity series was small.

(2) The bottom pressure field across the shelf was more coherent than the velocity. Along the 100-m isobath the correlation coefficient was 0.98 for a separation of 50 km and the pressure differences did not exceed 3 cm. Cross-shelf bottom pressure variance was an inverse function of water depth. The correlation coefficient of 0.59 between pressure measurements at 50-m and 250-m isobaths indicates large cross-shelf scales for a significant fraction of the variance. These larger scale fluctuations were predominantly low-frequency (periods greater than 7 days) motions.

(3) On shelf, the 50-m and 100-m isobath bottom pressure variance and 100-m horizontal kinetic energy spectra had a significant peak at about 0.017 cph. Station separation was not sufficient to observe propagation (if any). The oscillations may be a local forced response.

(4) On the continental shelf, bottom pressure and velocity correlations can be interpreted in terms of a simple geostrophic barotropic model. Along-shore velocity fluctuations were balanced by cross-shelf bottom pressure gradients. However, cross-shelf velocity and along-shelf pressure gradients

were too small to permit a test of this component equation. Alongshore current-cross-shelf pressure correlations were simpler in spring than in summer. In the former case, a single near-shore pressure measurement was representative of the sea level slope across the shelf. In summer, possibly because of increased baroclinicity, pressure gradient measurements enhanced the velocity correlation.

(5) The contribution of atmospheric pressure to the bottom pressure changes can be neglected even in water depths of 50 m.

(6) Simple dynamical models describe features of the sea level response to wind forcing. In shallow depths, sea level slope responded directly to onshore winds; in deeper water only the alongshore wind component caused setup. This depth-dependent response can be expected to yield a near-shore coastal current which differs from the current over the outer shelf.

Low-frequency variance on the continental shelf has been shown to correlate with the wind. The Alaska Current is an additional, potentially important, source. Royer and Muench (1977) noted temperature structures in this current which they interpreted as anticyclonic eddies with spatial scales of tens of kilometers. These eddies could correspond to the anticyclonic flow observed at the shelf break. As discussed above, this flow does not propagate onto the shelf. A possible explanation for this result is provided by the theory for topographic Rossby wave transmission across an exponential shelf break (Kroll and Niiler, 1976). By choosing exponential shapes which fit the Northeast Gulf of Alaska shelf and shelf break, we calculated that the maximum transmission coefficient for low-frequency ($< .014$ cph) waves corresponds to an alongshore wavelength of 400 km. Ignoring friction, this transmission coefficient is a broad function of alongshore wavelength; however, the coefficient does indicate that small-scale waves (< 50 km) will tend to

be reflected at the shelf break. Thus, assuming scales similar to those noted by Royer and Muench, the observed lack of cross-shelf current coherence is expected. In order to improve our understanding of the relative importance of various low-frequency sources, better spatial resolution of the current field and direct nearby wind measurements are required.

9. ACKNOWLEDGMENTS

We wish to thank D. Halpern for many suggestions regarding this experiment. J. R. Holbrook and J. D. Schumacher contributed helpful discussions on the analysis. We appreciate the support of R. L. Charnell in providing for the current meter preparation and data reduction. N. Soreide's contribution to the data processing is greatly appreciated. This study was supported by the Outer Continental Shelf Environmental Assessment Program of the National Oceanic and Atmospheric Administration, which administers oil exploration hazard research in Alaska for the U.S. Bureau of Land Management, and by the Environmental Research Laboratories.

10. REFERENCES

- Allen, J. S., and P. K. Kundu, 1977: On the momentum, vorticity, and mass balance off the Oregon coast. J. Phys. Oceanogr. (in press).
- Bakun, A., 1975: Wind-driven convergence-divergence of surface waters in the Gulf of Alaska. (Abstract) EOS Trans. Am. Geophys. Union, 56, 1008.
- Beardsley, R. C., and B. Butman, 1974: Circulation on the New England continental shelf: Response to strong winter storms. Geophys. Res. Lett., 1, 181-184.
- Beardsley, R. C., H. Mofjeld, M. Wimbush, C. N. Flagg, and J. A. Vermersch, Jr., 1977: Ocean tides and weather-induced bottom pressure fluctuations in the middle-Atlantic bight. J. Geophys. Res., 82, 3175-3182.
- Brown, W., W. Munk, F. Snodgrass, H. Mofjeld, and B. Zetler, 1975: Mode bottom experiment. J. Phys. Oceanogr., 5, 75-85.
- Buchwald, V. T., and J. L. Adams, 1968: The propagation of continental shelf waves. Proc. R. Soc. London, A305, 235-250.
- Carter, G. C., C. H. Knapp, and A. H. Nuttal, 1973: Statistics of the estimate of the magnitude-coherence function. IEEE Trans. Audio Electroacoust., AU-21, 383-389.
- Charnell, R. L., and G. A. Krancus, 1976: A processing system for Aanderaa current meter data. NOAA Tech. Memo. ERL PMEL-6, Seattle, Washington, 49 pp.
- Danielson, E. F., W. V. Burt, and M. Rattray, Jr., 1957: Intensity and frequency of severe storms in the Gulf of Alaska. EOS Trans. Am. Geophys. Union, 38, 44-49.
- Dodimead, A. J., F. Favorite, and T. Hirano, 1963: Salmon of the North Pacific Ocean region. Bull. 13, Inst. N. Pac. Fish. Comm., Vancouver, B.C., 195 pp.
- Ekman, V. W., 1905: On the influence of the earth's rotation on ocean currents. Arkiv for Matematik, Astron. ock Fys., 2, 1-52.
- Favorite, F., 1974: Flow into the Bering Sea through Aleutian passes, Oceanography of the Bering Sea. Occas. Publ. 2, Inst. of Mar. Sci., Univ. of Alaska, Fairbanks, 623 pp.
- Fofonoff, N. P., 1969: Spectral characteristics of internal waves in the ocean. Deep-Sea Res., 16, 59-71.
- Frankignoul, C., 1974: A cautionary note on the spectral analysis of short internal wave records. J. Geophys. Res., 79, 3459-3452.
- Godin, G., 1972: The Analysis of Tides. Univ. of Toronto Press, Toronto, 264 pp.

- Gonella, J., 1972: A rotary-component method for analyzing meteorological and oceanographic vector time series. Deep-Sea Res., 19, 833-846.
- Gould, W. J., and E. Sambuco, 1975: The effects of mooring type on measured values of ocean currents. Deep-Sea Res., 22, 55-62.
- Halpern, D., and J. R. Holbrook, 1978: Moored near surface current measurements during February 1975 on the Gulf of Alaska outer continental shelf. J. Geophys. Res. (in press).
- Halpern, D., and R. D. Pillsbury, 1976: Influence of surface waves on subsurface current measurements in shallow water. Limnol. and Oceanogr., 21, 611-616.
- Hayes, S. P., J. Glenn, and N. Soreide, 1978: A shallow water pressure-temperature gage (PTG): Design, calibration, and operation. NOAA Tech. Memo. (in press).
- Hayes, S. P., and J. D. Schumacher, 1976: Description of wind, current, and bottom pressure variations on the continental shelf in the Northeast Gulf of Alaska from February to May 1975. J. Geophys. Res., 81, 6411-6419.
- Hickey, B. M., 1977: The use of a numerical model as a diagnostic tool to interpret current and density measurements from the Washington shelf. EOS Trans. Am. Geophys. Union, 58, 1158.
- Ingraham, W. J., A. Bakun, and F. Favorite, 1976: Physical oceanography of the Gulf of Alaska. In: Environmental Assessment of the Alaskan Continental Shelf, 11. NOAA Environmental Research Laboratories, Boulder, Colorado.
- Kroll, J., and P. P. Niiler, 1976: The transmission and decay of barotropic topographic Rossby waves incident on a continental shelf. J. Phys. Oceanogr., 6, 432-450.
- Kundu, P. K., and J. S. Allen, 1975: Three dimensional structure of low frequency current fluctuations near the Oregon coast. J. Phys. Oceanogr., 6, 181-199.
- Mooers, C. N. R., 1973: A technique for the cross-spectrum analysis of complex-valued time series with emphasis on properties of polarized components and rotational invariants. Deep-Sea Res., 20, 1129-1141.
- Reid, J. L., and A. W. Mantyla, 1976: The effect of the geostrophic flow upon coastal sea elevations in the northern North Pacific Ocean. J. Geophys. Res., 81, 3100-3110.
- Reynolds, R. M., and B. A. Walter, 1976: A study of convective activity in the Bering Sea and air-mass modification on the southern Alaskan Coast. Bull. Am. Meteorol. Soc., 56, 139.
- Royer, T. C., 1975: Seasonal variations of waters in the northern Gulf of Alaska. Deep-Sea Res., 22, 403-416.

- Royer, T. C., 1977: Hydrographic data report, Northeast Gulf of Alaska, July 1975-June 1976. Univ. of Alaska, Fairbanks.
- Royer, T. C., and R. D. Muench, 1977: On the ocean temperature distribution in the Gulf of Alaska, 1974-1975. J. Phys. Oceanogr., 7, 92-99.
- Smith, R. L., 1974: A description of current, wind, and sea level variations during coastal upwelling off the Oregon coast, July-August 1972. J. Geophys. Res., 79, 435-443.
- Welander, P., 1957: Wind action on a shallow sea: Some generalizations on Ekman's theory. Tellus, 9, 45-52.

C. LOWER COOK INLET CIRCULATION

C1.1 Previous Work

Previous field programs have focussed primarily on upper Cook Inlet (e.g. Kinney et al., 1970a; 1970b), but personnel from the Auke Bay Fisheries Laboratory, National Marine Fisheries Service attempted to define the circulation in Kachemak Bay using surface drifters (Knull and Williamson, 1969), and the Alaska Department of Fish and Game carried out a similar study in the lower Inlet (Burbank, 1977). The LANDSAT series of satellites indicate surface suspended sediment distribution, and have led to several qualitative expositions on Cook Inlet surface circulation (e.g. Wright et al., 1973; Gatto, 1976). At the onset of the present work the most complete information on lower Cook Inlet circulation was contained in Burbank's (1977) synthesis. Present knowledge remains, however, too incomplete for evaluation of the effects of resource development on the extant fishery.

C1.2 Geographical Setting

Cook Inlet is a broad (70-90) km), shallow (mean depth ~ 60 m (33 fm)) elongate embayment extending north-northeasterly from the Gulf of Alaska (Figure 1). Water exchange with the Gulf can occur via Kennedy and Stevenson entrances and Shelikof Strait. This study deals with the lower portion of Cook Inlet, defined as that region bounded on the north by the Forelands and on the south by Kennedy and Stevenson entrances and northern Shelikof Strait. At the northern end of the study area, Kalgin Island and its associated shoals reduces water flow in the western half of the Inlet.

In the centrally-located axial region of the northern lower Inlet, the bottom attains maximum depths of 60-70 m (~ 100 fm) in the depression west of Stevenson Entrance; the increase is gradual with the exception of a prominent ramp-like feature which traverses the Inlet in arcuate fashion along the 100 m (~ 50 fm) isobath. Several embayments extend laterally from the Inlet.

C1.3 Oceanographic Setting

As a coastal embayment, Cook Inlet reacts both to variations in marine source waters and terrestrial drainage. Marine water input originates in the northern Gulf of Alaska, where seasonal temperature and salinity variations are dominated by a strong seasonal signal (Royer, 1975) (Figure 2). Lowered salinities and elevated temperatures occur during summer due to freshwater input and insolation, respectively. During winter, thermohaline and wind mixing decrease stratification, while cooling and cessation of freshwater input lead to lower temperatures and high salinities. Seasonal trends are augmented by coastal downwelling (winter) and upwelling (summer) tendencies driven by regional winds (cf. Bakun, 1973; Royer, 1975).

During summer, freshwater input along the Gulf of Alaska coast east of lower Cook Inlet leads to development of a low salinity (hence low density) westerly coastal current (T. C. Royer, personal communication) although the details and extent of this feature are not well documented.

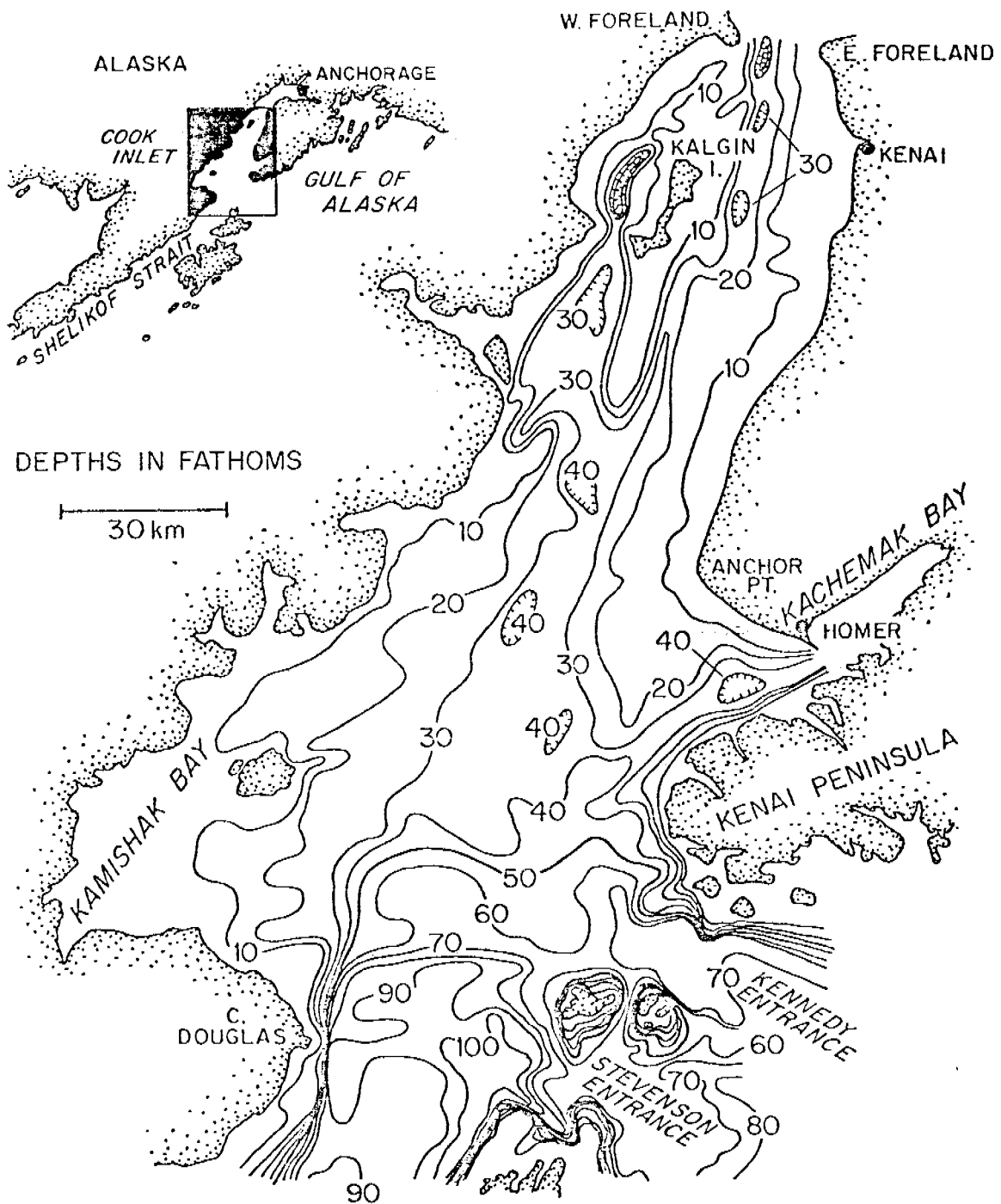


Figure 1. Location and bottom topography of lower Cook Inlet, Alaska.

Like regional oceanographic parameters, freshwater input is dominated by an annual signal. Most gauged river input enters the upper Inlet north of the Forelands, but the Kenai River enters the lower Cook Inlet in its northeastern portion. Most freshwater input occurs during the summer months (April-October) due to snow melt and storm-caused discharge, the latter occurring typically during September-October (Figure 3). Seasonal changes are abrupt; discharge increases by nearly two orders of magnitude during the relatively brief spring thaw period. In the upper Inlet, freshwater is well mixed with marine waters. This relatively low salinity mixture flows through the Forelands into the lower Inlet.

C2. OBSERVATIONS

C2.1 The 1973 Field Program

Data were acquired during May-September 1973 by NOAA's National Ocean Survey as part of an ongoing program to update tidal information in U. S. Coastal waters. The period brackets the transition from winter to summer oceanographic conditions (cf. Figure 2). The survey consisted of currents, temperatures, and salinity observations from a line connecting Cape Douglas and the Chugach Islands, north to roughly the latitude of Anchor Point (cf. Figure 1).

Taut-wire moorings using Aanderaa current meters positioned 7 m and 23 m below the surface, and 15 m above the bottom at the indicated locations (Figure 4) were deployed. These current meters measured current speed and direction, temperature and pressure at 10 min. intervals. Approximately 7 current stations were occupied simultaneously for periods of from two weeks to a month, after which the stations were moved to new locations. At 63 stations temperature and salinity were measured as functions of depth using a Plessey model 9040 STD (Figure 4). Many stations were occupied repeatedly during the course of the summer and provide time series of temperature and salinity.

These moorings are subject to some wave-induced and mooring noise, particularly at the upper meters. The directions of flow are felt to be reliable but current speeds from the 1973 moorings are not used quantitatively. Where both 7 m and 23 m records (1973) exist, visual coherence between the low-pass filtered records was good, indicating a relatively uniform flow structure in at least the upper 23 m of the water column. Records from deep meters (15 m above the bottom), indicate cross-isobath flow in all cases, and currents decoupled from upper currents. However, deep records were too scattered in both space and time to reveal a coherent pattern of deep water motion.

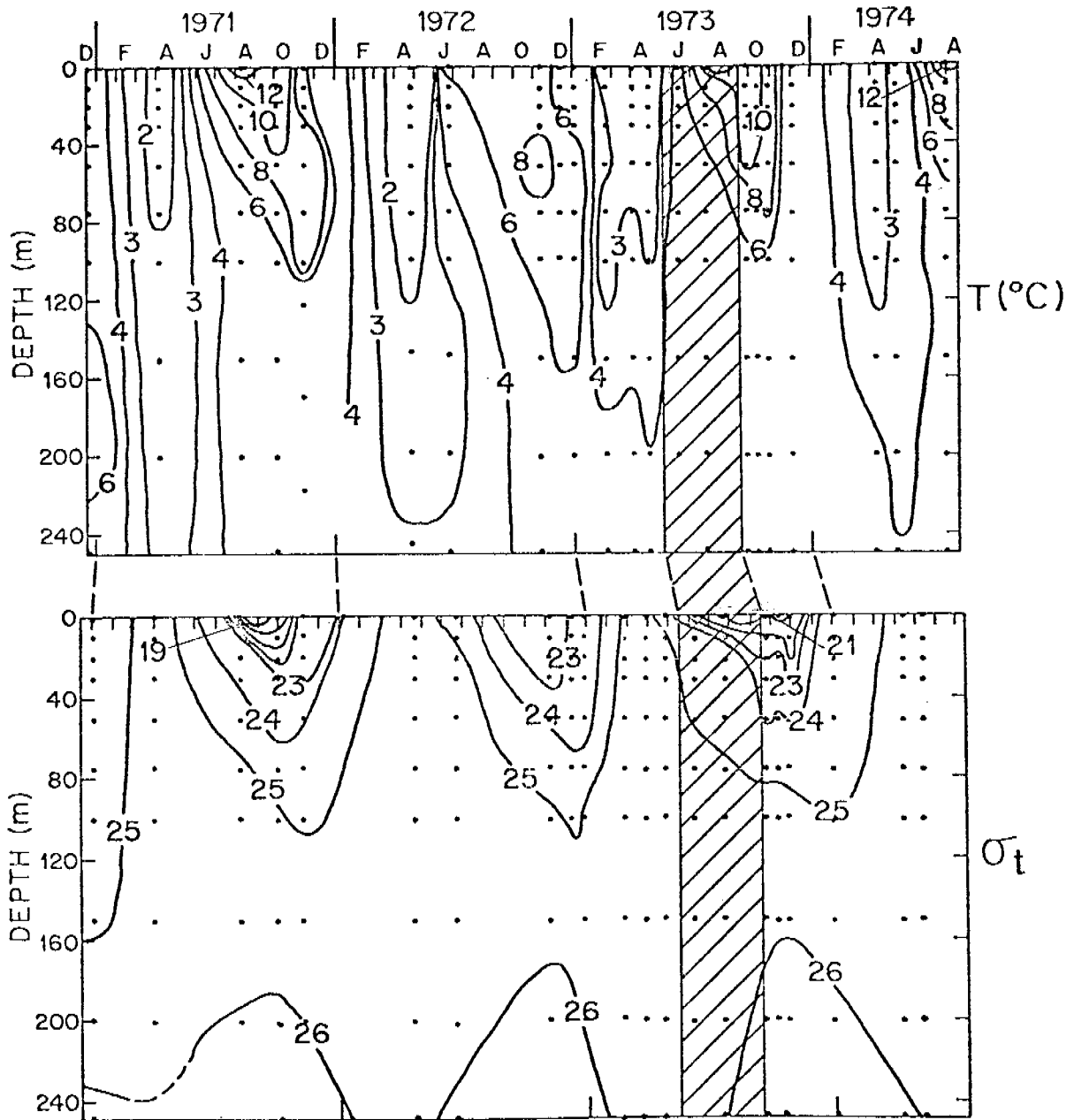


Figure 2. Variation of temperature and density (σ_t) at a near-coastal station in the northern Gulf of Alaska from 1971-1974. Shaded area indicates time interval of field work discussed in this report. (Taken from Royer, 1975)

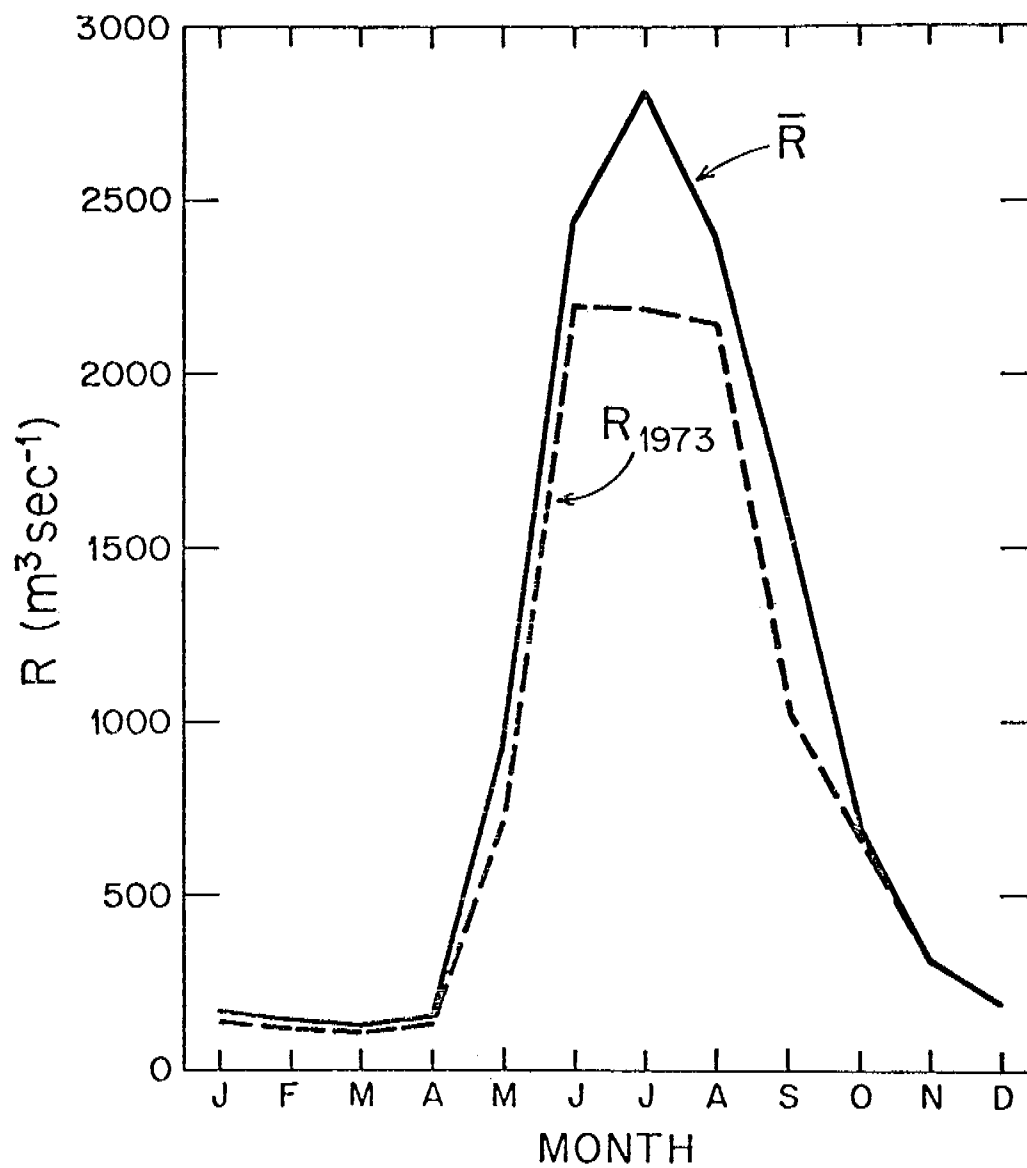


Figure 3. Gauged river input (R) into Cook Inlet, showing both annual mean input and input during 1973. These figures were compiled from USGS streamflow records from the Kenai R. at Soldotna, the Knik R. near Palmer, the Matanuska R. at Palmer, the Susitna R. at Gold Creek, the Talkeetna R. near Talkeetna and the Skwentna R. near Skwentna.

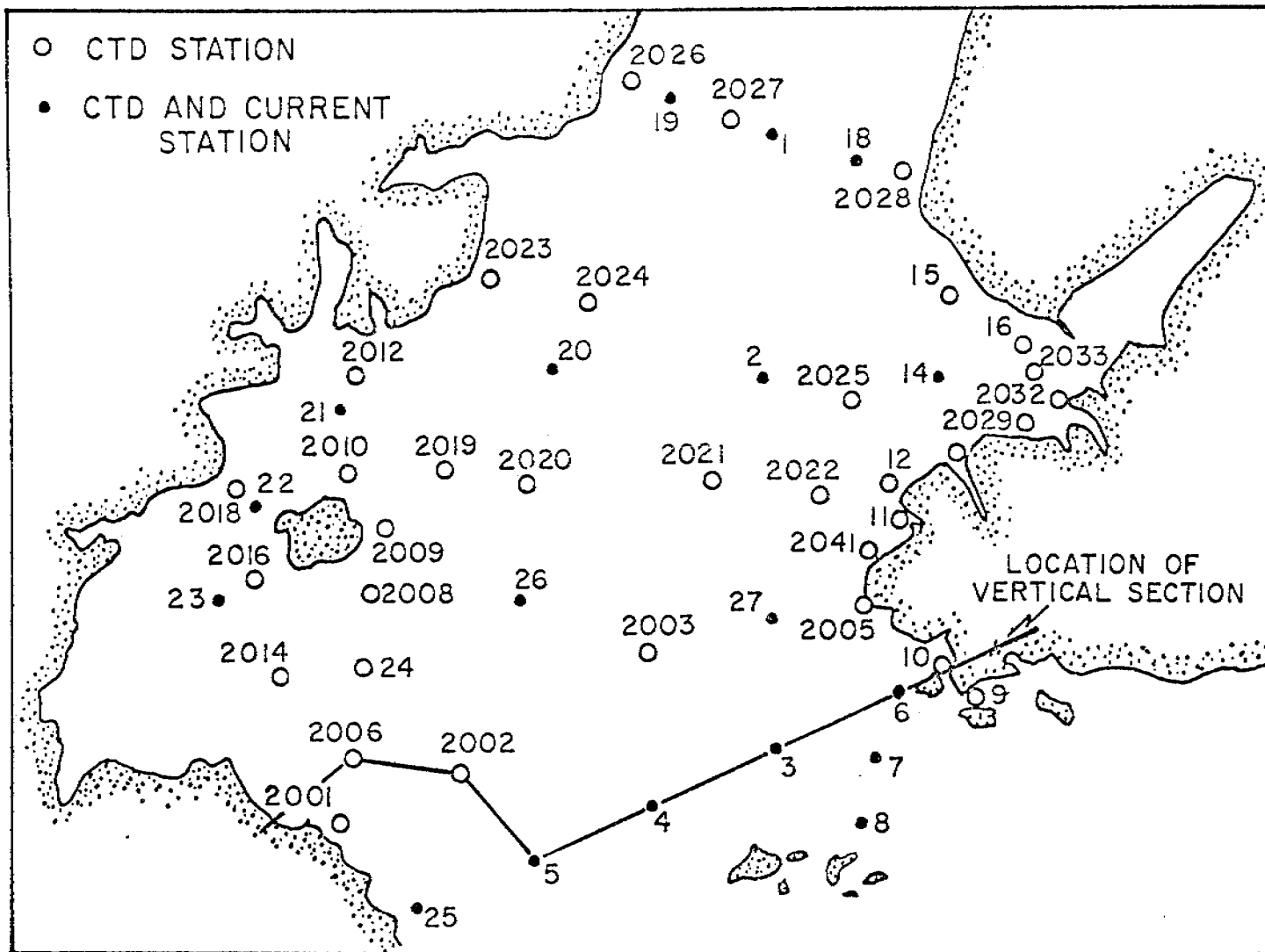


Figure 4. Locations of CTD and current stations utilized in this study. Numbers are NOS station numbers, and heavy line indicates location of vertical sections shown on Figure 6.

C2.2 Distributions of Temperature, Salinity and Density

Several horizontal salinity distribution features persisted throughout summer 1973. While evident throughout the vertical water column, they were most pronounced at the surface. Figure 5 qualitatively presents these 1973 surface distributions:

1. Surface salinities were relatively low in the western third of the Inlet; isohalines approximately paralleled the coastline. Salinities decreased from 30.4-31.4⁰/oo in late May to 26.0-30.5⁰/oo by early September, with stronger east-west gradients in the latter. In early September higher salinity water (>30.2⁰/oo) in southwestern Kamishak Bay was isolated from the rest of the Inlet by the lower salinity water.
2. The eastern two-thirds of the Inlet contained more saline water than the western third. Salinities decreased from 31.6-32.0⁰/oo in May to 30.5-31.2⁰/oo by September. A curved tongue-like feature of high salinity water extends northward then eastward from the vicinity of Shelikof Strait. It is better defined in early and late summer than mid-season.
3. A tongue of low salinity water extends westward from the Kenai Peninsula south of Kachemak Bay in early and late summer, lowering the salinity along the eastern shore of the Inlet. It exhibits lower salinities in early September (<30.0⁰/oo) than in May (<31.8⁰/oo), and is not evident in July.

Surface temperature distribution represents that throughout the water column (Figure 5). Major temperature features are:

1. Higher temperatures (>11⁰C in the extreme western Inlet. The highest occur in Kamishak Bay during late summer, these coinciding with low salinities (except in Kamishak Bay). Horizontal temperature gradients are largest during July.
 2. A low temperature tongue extended northward from Shelikof Strait in mid-late summer. In September a low temperature, high salinity region develops west of Kachemak Bay.
 3. Elevated temperatures (>8.5⁰C in July and >10.5⁰C by September) occur in the near-shore region south of the Kenai Peninsula in mid-late summer generally coinciding with the low salinities there. These patterns were not evident in May. Unlike later in the season, temperatures decrease from south to north and were considerably lower (4.5 - 6.5⁰C) than later in the summer. In May, highest temperatures (>6.5⁰C) occurred in Kamishak Bay. Vertical distribution features persist throughout the summer (Figure 6). Density (σ_t) is used rather than salinity, along with temperature, since density is the dynamically significant variable. It essentially duplicates the salinity distribution at the observed, low temperatures.
1. Isotherms and -pycnals exhibit pronounced upward doming in the central southern portion of the Inlet, particularly in July. By September the dome is less developed than in July and has shifted westward.
 2. Warm (8.5-10.0⁰C), low density (σ_t <4.6) near-surface water in Inlet coastal regions during mid-late summer is a reflection of the warm, low salinity coastal bands observed in horizontal distributions. Thermal and density fields associated with these bands extend to the bottom.

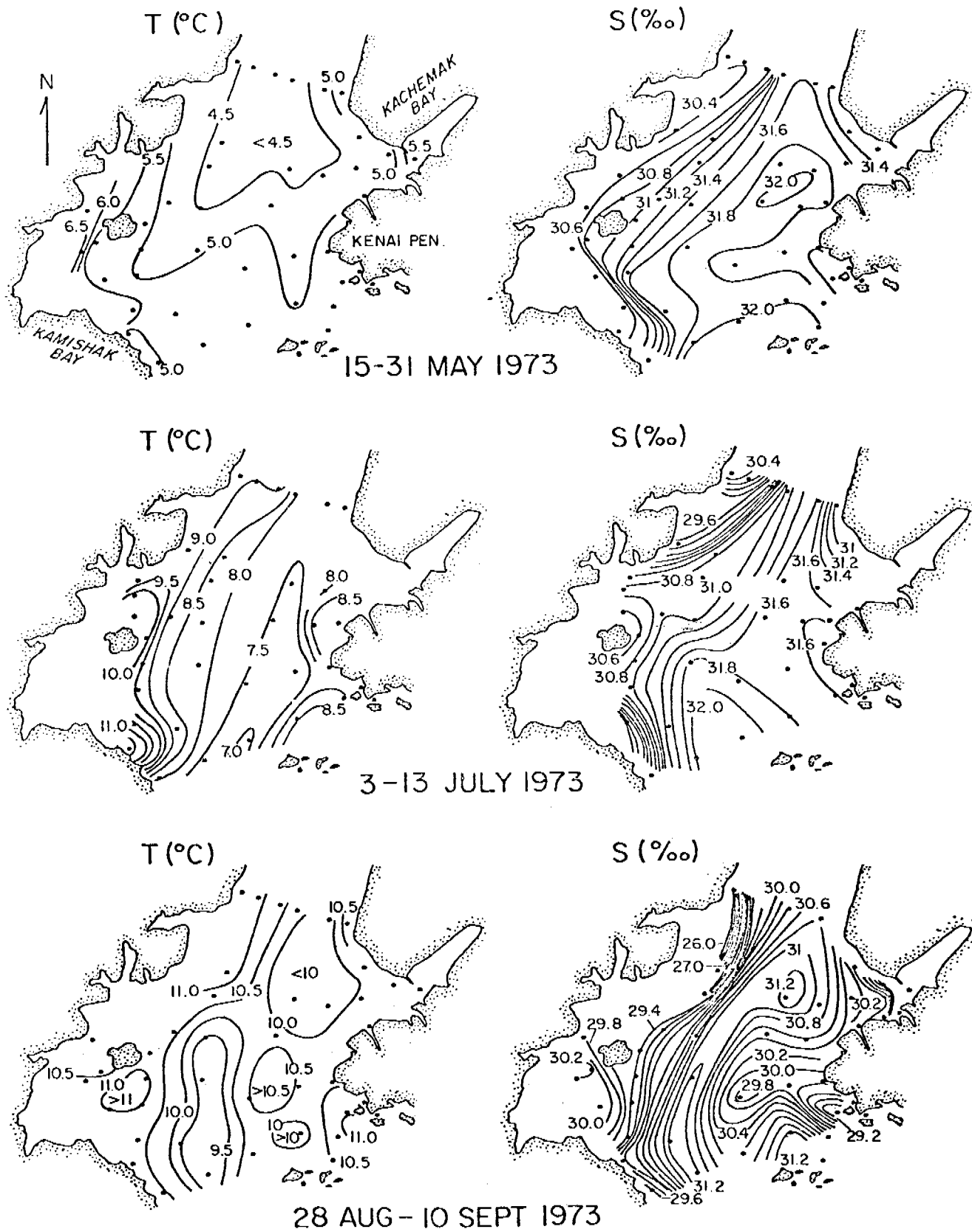


Figure 5. Surface distributions of temperature and salinity in lower Cook Inlet for three different periods during Spring-Summer.

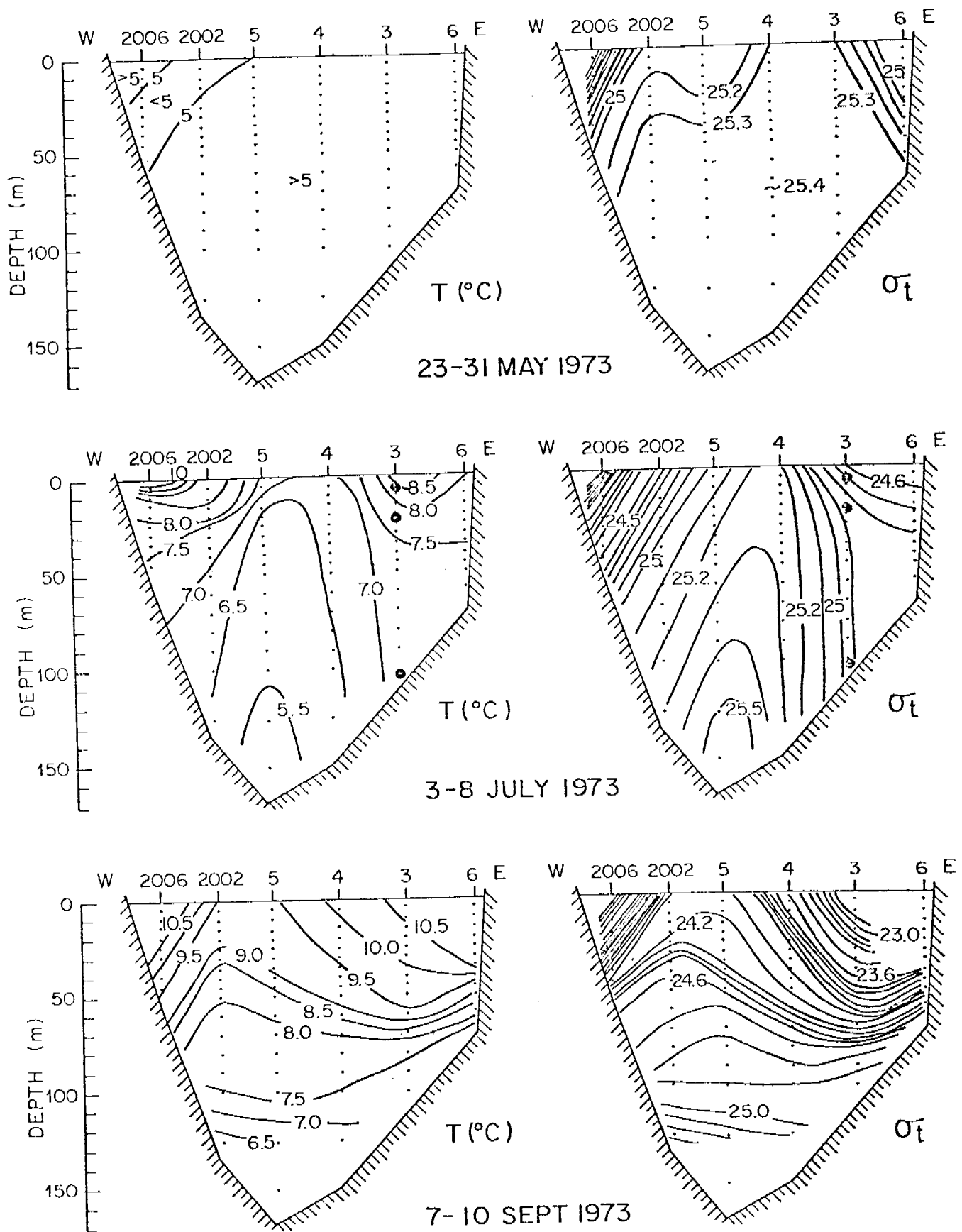


Figure 6. Vertical distributions of temperature and density (σ_t) at a section across lower Cook Inlet during summer 1973.

Generally, temperature decreases with depth while density increases, reflecting summer distributions in the Gulf of Alaska (cf. Figure 2). Upward doming of isotherms and -pycnals is associated with the northward extending tongues of cold, saline water (cf. Figure 5).

It is apparent that temperatures increase, salinities decrease and the gradients of both intensify during the course of the summer. Temperatures increase with no detectable geographical dependency, while surface salinity changes vary depending upon position in the Inlet (Figure 7):

1. In the eastern two-thirds of the Inlet salinity decreases at a constant rate from May-September. Some scatter occurs during late August-early September, but salinities generally remain within a $0.5^{\circ}/\text{oo}$ envelope.
2. The western third exhibits lower overall salinities. A decrease of about $1.0^{\circ}/\text{oo}$. Additionally, a higher concentration of surface suspended sediment occurs here than the eastern regime.

A convergence (Burbank, 1977) separates the two regimes, evidenced by the distribution of suspended sediment.

C2.3 Current Observations

1973 current meter records were processed using methods detailed in Charnell and Krancus (1976) to obtain low-pass filtered time series of current speed and direction, plotted in a vector time series format (cf. Figure 8). Records were analyzed for tides using the Munk-Cartwright method. Table 1 gives harmonic constants for Station 1 off Anchor Point; the data show that M_2 is the dominant constituent. The M_2 tidal ellipses suggest considerable complexity (Figure 9), with most tidal energy propagating along isobaths in the eastern portion of the inlet and little energy along the western part. Tidal energy was virtually zero at station 26 in the western central Inlet. The reasons for this complex tidal behaviour are uncertain.

The low-pass filtered current records indicated that flow in lower Cook Inlet was generally dominated by events having scales of order 3-4 days (cf. for example the inflow event observed during early September at Station 7, Figure 8). Due to their short lengths (<15 days), a reliable estimate of the mean current cannot be obtained from many of the records (Table 2). These cases will be discussed within the context of an event-dominated flow regime. It is felt that significant mean flow values were obtained from stations 3, 6, 8 and 25, all of which support the prior concept of southwesterly flow through Shelikof Strait.

C3. DISCUSSION

Field data bracket the transition period from late winter through fall conditions. Horizontal salinity distribution changed little with time, while temperature distribution underwent significant changes. Water in the northern inlet was colder than that to the south during spring, probably a result of atmospheric cooling due to a relatively long residence period. In line with this, most ice formation occurs in the cooler water north of the Forelands.

During summer, the temperature conditions reverse, and warmer water is found to the north. Then, the longer residence time allows the water to respond to heating by insolation. Additionally, circulation in the lower inlet may deliver colder deep water to the near surface layers.

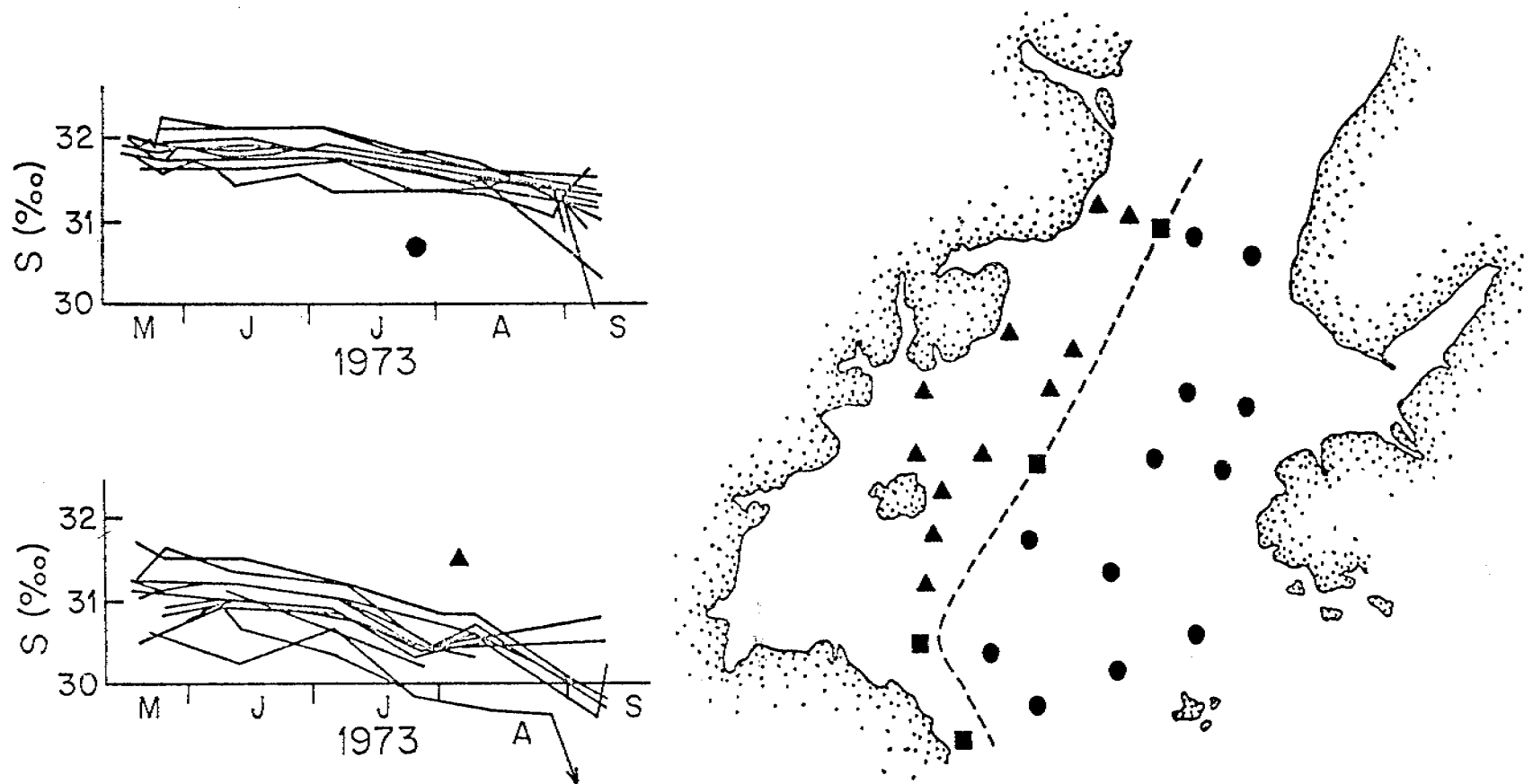


Figure 7. Time variation of salinity in eastern and western lower Cook Inlet during Spring-Summer 1973, showing horizontal distributions of the two patterns of temporal variation. Dotted line shows approximate location of boundary between eastern and western regimes.

Table 1. Harmonic constants of tidal currents at Station 1 (meter depth = 23 m: cf Figure 4) obtained from a Munk-Cartwright response analysis based on 3 complex weights (leads at -48h, 0h, + 48h) and using the tidal potential as the reference series.

<u>Component</u>	<u>Current Ellipse Axes</u>		<u>Major Axis</u>	<u>Phase</u>	<u>Sense of</u>
	<u>Minor</u>	<u>Major</u>	<u>Direction</u>	<u>Lag</u>	<u>Rotation</u>
	<u>(c/ms)</u>	<u>(cm/s)</u>	<u>(^oT)</u>	<u>(^oG)</u>	
O ₁	5.9	11.6	44	348	anti-clockwise
K ₁	1.8	19.1	5	45	anti-clockwise
N ₂	2.7	15.3	7	312	clockwise
M ₂	0.8	98.0	15	314	clockwise
S ₂	0.6	38.4	21	350	clockwise

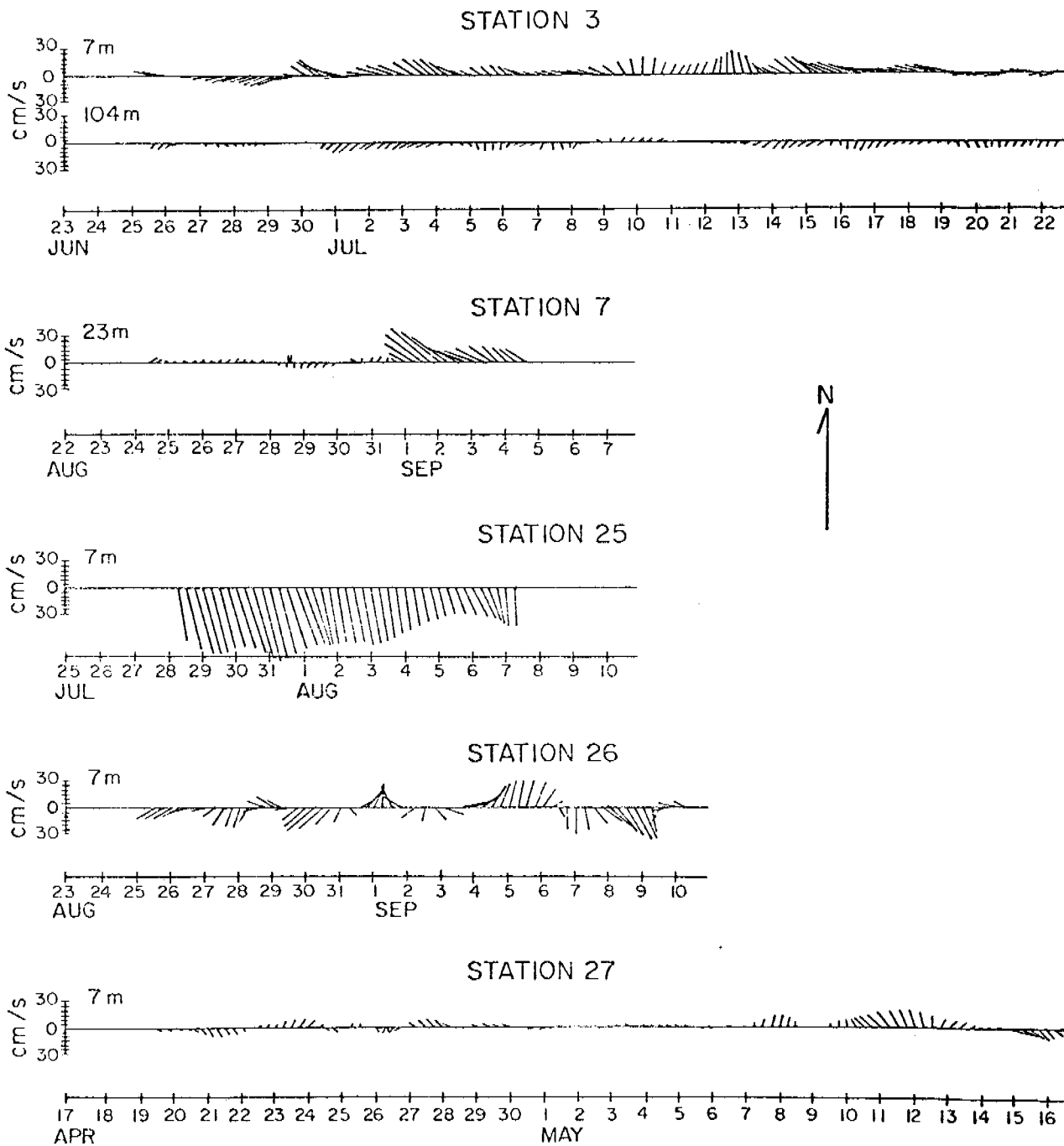


Figure 8. Non-tidal currents at selected locations in lower Cook Inlet. Locations of stations are indicated on Figure 4.

Table 2. Current station parameters used in mean circulation analysis.
Records shorter than 10 days, have been omitted.

Station	Dates	Record Length (days)	Record Depth (m)	Mean Speed (cm/s)	Mean Direction($^{\circ}$ T)
1	17 June 19 July	29	23	4.2	55
2	15 May- 3 June	19	7	1.8	56
	15 May- 15 June	31	23 55	1.4 1.4	110 122
3	23 June- 25 July	32	7 23 104	22.4 18.5 4.4	286 291 202
4	22 July- 21 August	30	7 23 133	2.9 3.2 5.3	83 72 110
5	10 July- 7 August	28	7 155	5.1 2.0	236 152
6	21 July- 22 August	31	7	12.7	286
7	22 August- 1 September	10	7	3.9	249
	22 August- 7 September	16	23	12.6	300
	10 August- 26 August	16	149	3.6	65
8	10 August- 25 August	15	7 23	13.1 10.5	144 118
14	5 June- 22 June	17	7 23	5.5 6.0	184 173
19	22 May- 22 June	31	7 21	13.4 11.9	64 45

Table 2 (Continued)

Station	Dates	Record Length (days)	Record Depth (m)	Mean Speed (cm/s)	Mean Direction ($^{\circ}$ T)
20	19 May- 29 May	10	7	5.4	28
	19 May- 4 June	16	26	3.1	242
21	8 August- 16 August	11	7	3.6	207
22	23 August- 9 September	17	7	8.8	208
25	26 July- 9 August	15	7	39.7	172
			23		
26	23 August- 10 September	21	23	2.0	146
27	17 April- 18 May	32	7	1.3	58
			23	0.7	66

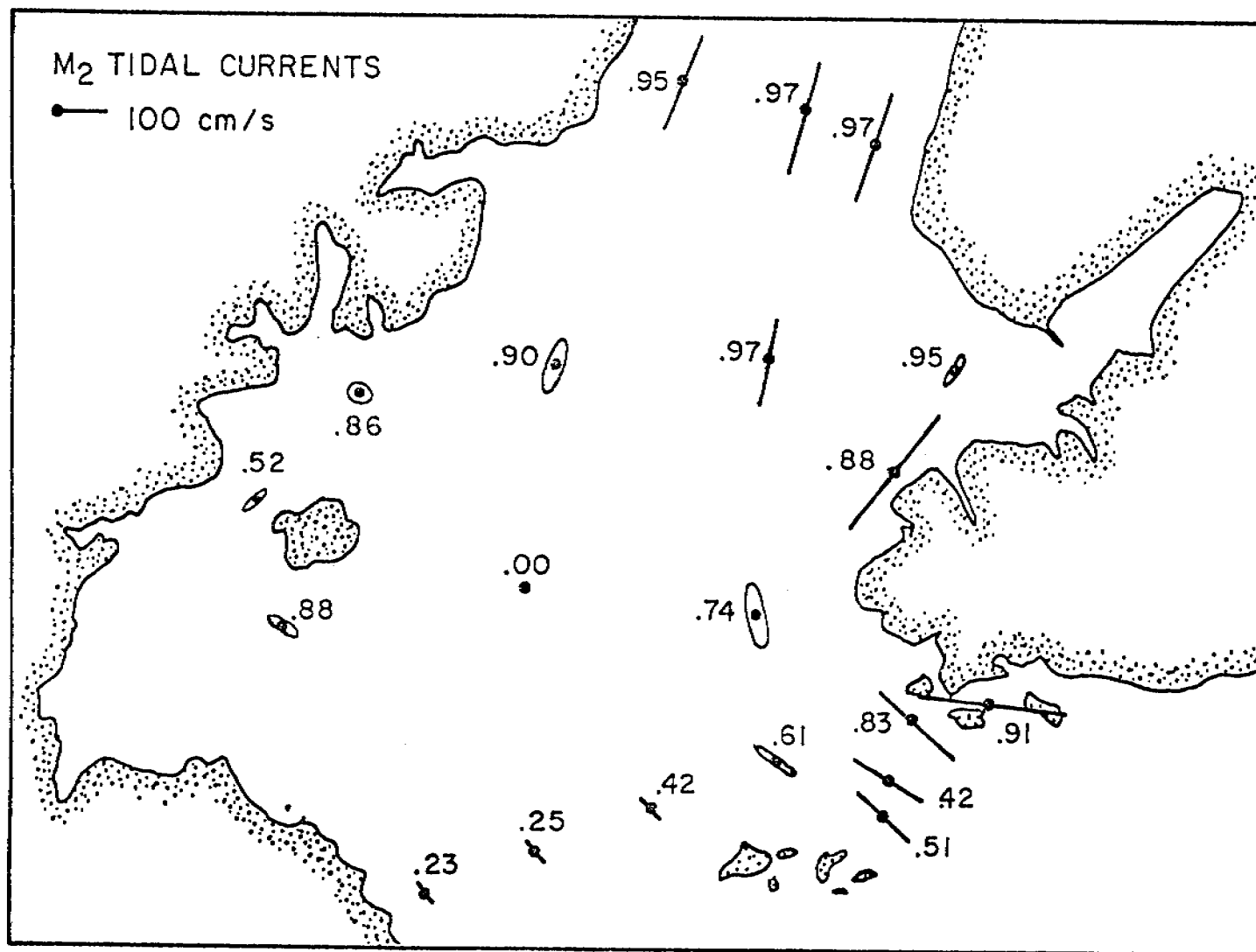


Figure 9. Distribution of the M_2 tidal component in lower Cook Inlet. Numbers are percent of coherent tidal variance energy contained in the semi-diurnal tidal band.

Continental freshwater runoff during spring and summer causes the Inlet salinity to decrease. The time change (Figure 7) indicates a uniform decrease over the May-August period, probably a result of a time lag between maximum fresh-water input in the upper Inlet and its appearance in the lower Inlet.

Certain features in the temperature-salinity distribution persist through the spring-summer transition period and last well into the summer:

- 1) the low salinity, high temperature (except during May) western band;
- 2) the northward tongue of high-salinity, cold water in the central southern Inlet; and 3) the westward tongue of low salinity, warm (except in May) water in Kennedy Entrance. Isotherms and isopycnals across the lower Inlet dome upward, especially in July, and baroclinicity is greater in the western than eastern Inlet. Continuation of these features suggests that they reflect persistent circulation and mixing processes.

The low salinity band along the western shore was a southwestward extension of water exiting from upper Cook Inlet, becoming a concentrated stream near Cape Douglas.

Low salinity water originating in Kennedy Entrance persists well into the lower Inlet. The density field suggests a westerly baroclinic flow (Figure 6). This flow is consistent with earlier work (Favorite and Ingraham, 1977), probably driven in part by a longshore sea surface slope due to the Alaska Current. This flow is bathymetrically steered as it crosses the Inlet. The feature intensifies during summer, due both to salinity lowering consequent to freshwater addition, and to seasonal intensification of baroclinic flow (by a factor of 2-3 for 0/100 db estimated currents).

The cold, saline water in the central lower Inlet is maintained by a slow northward drift of water in the eastern two-thirds of the Inlet, exiting via the south-flowing western current.

The upward doming of isotherms and -pycnals leads to a tendency for upwelling in the central lower Inlet, supplying cold water from deep to near-surface layers, and accentuating low temperatures of the northward tongue. This is biologically significant; upwelling transports nutrients to the near-surface layers, where northerly flow carries them into a biologically rich region. Therefore, biological productivity, at least in part, depends on the observed flow patterns.

Temperature and salinity fields represent general flow conditions in lower Cook Inlet but, the instantaneous flow regime is dominated by events having time scales on the order of 3-4 days. Consequently, temperature and salinity distribution represents a history of numerous short term events, whose traces have been smoothed by diffusion.

C4. SUMMARY

The lower Cook Inlet mean flow can be characterized as follows (Figure 10):

- 1) A southerly flow occupied roughly the western third of the lower Inlet and consisted primarily of water diluted by fresh water input into upper Cook Inlet. This flow paralleled isobaths and rounded Cape Douglas as a concentrated warm (at least, during summer), low salinity band, exiting the system to the southwest via Shelikof Strait.

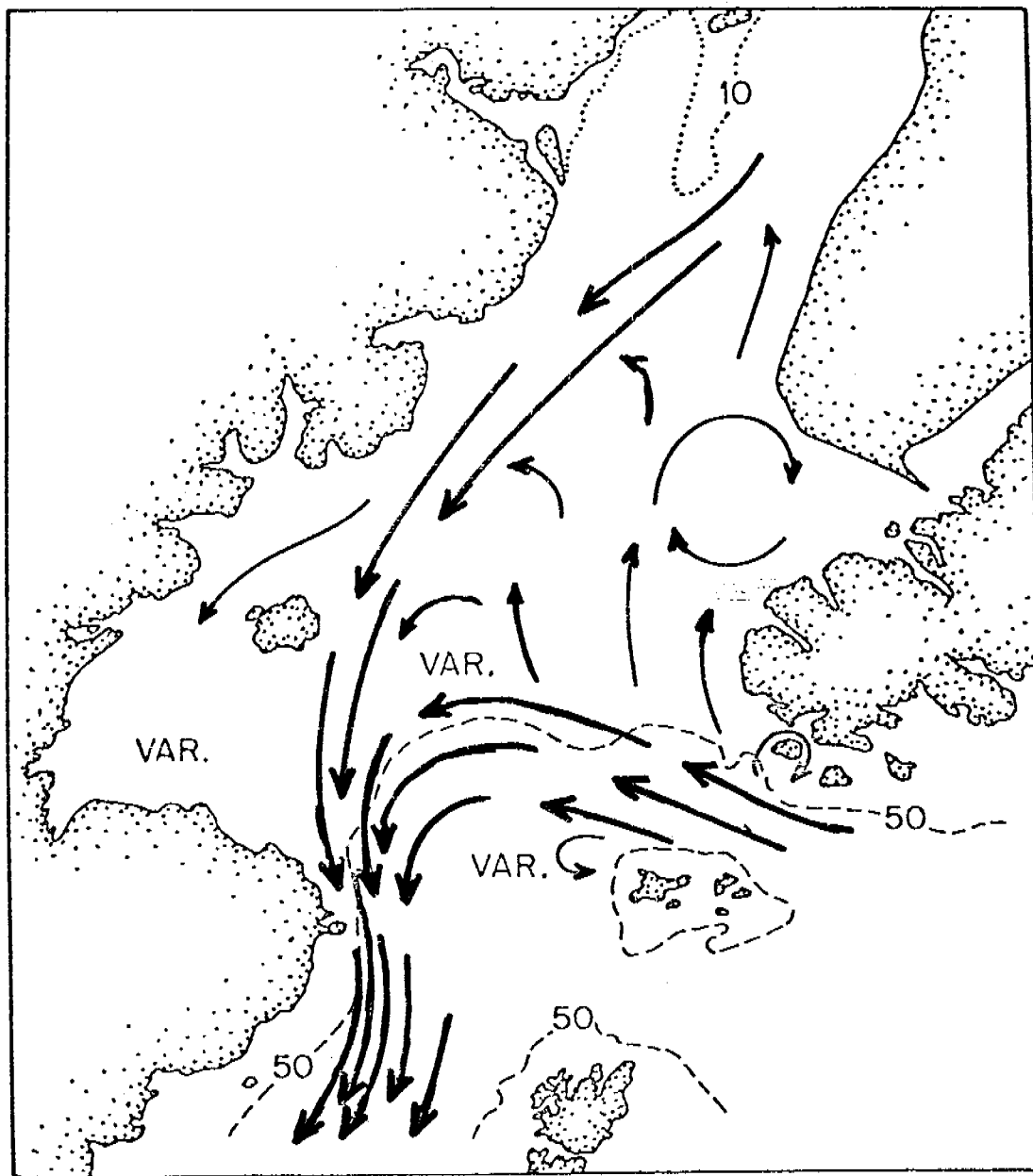


Figure 10. Proposed summer circulation in lower Cook Inlet, based upon analysis of the 1973 field data.

2) A weak northward flow in the central and eastern lower Inlet was responsible for the summer presence there of more saline, colder water. This northward flow replaced water entrained into the southward flow in the western Inlet.

3) A westerly flow extended from Kennedy Entrance across the lower Inlet toward Cape Douglas, paralleling bottom contours along the ramp-like break in bottom topography which extends in arcuate fashion across the Inlet. This westerly flow was in part driven by a sea surface slope due to the westerly flowing Alaska Current and in part by the near-coastal baroclinic field established by coastal freshwater input.

This circulation led to an upwelling tendency in the lower Inlet and a consequent supply of cold, saline, and presumably (in view of its deep origin) nutrient-rich water to the near-surface waters. The circulation can therefore have important consequences relative to biological productivity.

The instantaneous flow field was dominated by tidal currents and by events which were large relative to the mean flow. These events were of the proper time scale to be due to local or regional meteorological events. They were in turn superposed upon primarily semidiurnal tidal signals which varied from prominent in the eastern lower Inlet to negligible in the central western portion of lower Cook Inlet.

C5 REFERENCES

- Bakun, A., Coastal upwelling indices: West coast of North America, NOAA Tech. Rept. NMFS SSRF-671, Seattle, Washington, 1973.
- Burbank, D. C., Circulation studies in Kachemak Bay and Lower Cook Inlet, Alaska Dept. of Fish and Game, Anchorage, Alaska, 1977 (Unpub. Man.).
- Charnell, R. L. and G. A. Krancus, A processing system for Aanderaa current meter data, NOAA Tech. Memo. ERL PMEL-6, Seattle, Washington, 1976.
- Favorite, F., and W. J. Ingraham, On flow in Northwestern Gulf of Alaska, May 1972, J. Oceanogr. Soc. Japan, 33, 67-81, 1977.
- Gatto, L. W., Baseline data on the oceanography of Cook Inlet, Alaska, CRREL Rept. 76-25, U. S. Army Cold Regions Res. and Eng. Lab., Hanover, N. H., 1976.
- Kinney, P. J., D. K. Button, D. M. Schell, B. R. Robertson and J. Groves, Quantitative assessment of oil pollution problems in Alaska's Cook Inlet, Inst. of Mar. Sci., Univ. of Alaska Rept. R-169, Fairbanks, Alaska, 1970a.
- Kinney, P. J., J. Groves, and D. K. Button, Cook Inlet environmental data, R/V Acona Cruise 065 - May 21-28, 1968, Inst. of Mar. Sci., Univ. of Alaska Rept. R-70-2, Fairbanks, Alaska, 1970b.
- Knull, J. R., and R. Williamson, Oceanographic survey of Kachemak Bay, Alaska, Manuscript Rept. 60, Bur. Comm. Fish. Lab., Auke Bay, Alaska, 1969.
- Royer, T., Seasonal variations of waters in the northern Gulf of Alaska, Deep-Sea Res., 22, 403-416, 1975.
- Wright, F. F., G. D. Sharma, and D. C. Burbank, ERTS-1 observations of sea surface circulation and sediment transport, Cook Inlet, Alaska, Symposium on Significant Results Obtained from the Earth Resources Technology Satellite -1, NASA SP-327, 1315-1322, 1973.

D. Seasonal variability of hydrography and circulation on the northwest Gulf of Alaska continental shelf.

We are presently comparing hydrographic data from winter (March) and Autumn (September to November) observations. There is an appreciable difference in forcing due to seasonality of wind stress, freshwater addition and possible changes in the offshore Alaskan Current. One approach is to calculate and contour the 0/100db dynamic topography. How realistically such contours reflect actual flow is a critical question. We compare mean observed currents and dynamic contours for March in Figure 1. The current record flow at K3A is in good agreement with geopotential topography. The weak mean flow at WGC-2E also is consistent with the small relief indicated by the hydrographic data. Mooring WGC-2A was located where the geopotential topography suggests the flow may be changing direction; thus the comparison here is somewhat ambiguous, but a southwestward flow along the slope break is probably present. This comparison would suggest that the geopotential topography of the sea surface, referred to a level of 100 lb, can be used with some confidence. We suspect this to be true in areas over the continental shelf where the bathymetry is not highly complex; offshore in the Alaskan Stream, the 100 db reference level is sometimes too shallow to be meaningful because of the considerable baroclinic relief below this level.

The March data (Fig. 1) suggest the following circulation pattern: 1) a relatively intense southwest flow (the Alaskan Stream) along the continental slope; 2) another fairly intense flow westward into Shelikof Strait; 3) a weakly developed eastward flow just inshore of the Alaskan Stream; and 4) the absence of any organized flow off central and northern Kodiak Island. In September, both the inshore portion of the Alaskan Stream and the westward flow through Shelikof Strait were present, but the relief across them was less than in March. This implies that circulation in the Gulf is generally intensified in winter, especially if the westward flow through Shelikof Strait is indeed a branch of the Alaskan Stream that flows through Amatuli Trough. The September data also show rather continuous southeast flow over the continental shelf in the southern part of the area, and a small, rather intense eddy-like feature was present near 58°N, 151°W. This latter feature was not indicated by the March data; in addition, neither data set showed a highly continuous eastward flow along the edge of the continental slope (inshore of the westward flow) as indicated by May 1972 data reported by Favorite and Ingraham (1977). It appears that the major circulation features are a westward flow along the continental slope with a small branch of this flow entering Shelikof Strait. On the continental shelf, the flow appears to be highly variable; at times, rather well-organized opposing flows appear to exist, but sometimes there is little evidence for any organized circulation. The causes of this variability are uncertain, but interactions of local wind forcing and the bathymetry are likely possibilities.

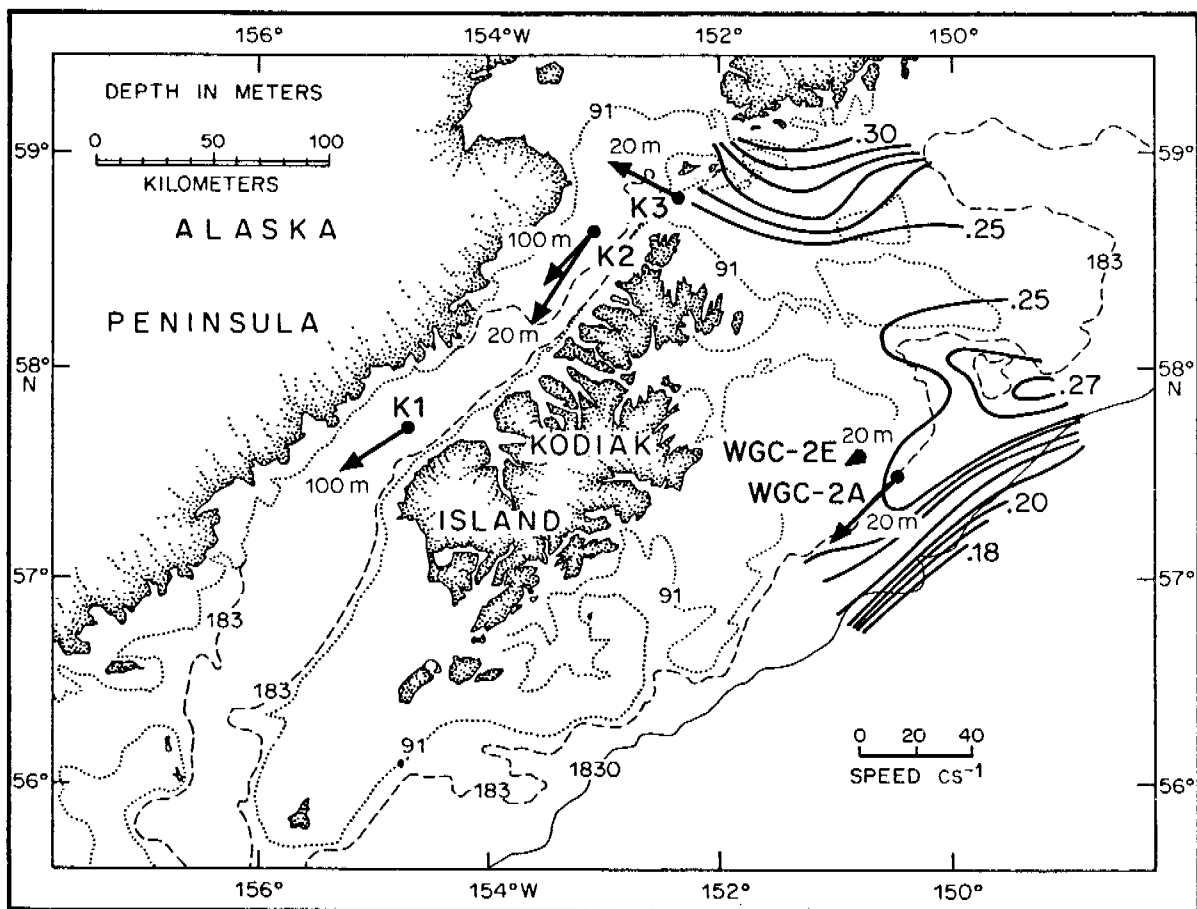


Figure 1. Dynamic contours (0/100db) for March 1977. Also shown are mean current vectors from current records (see Table 1, Section IV.A for details).

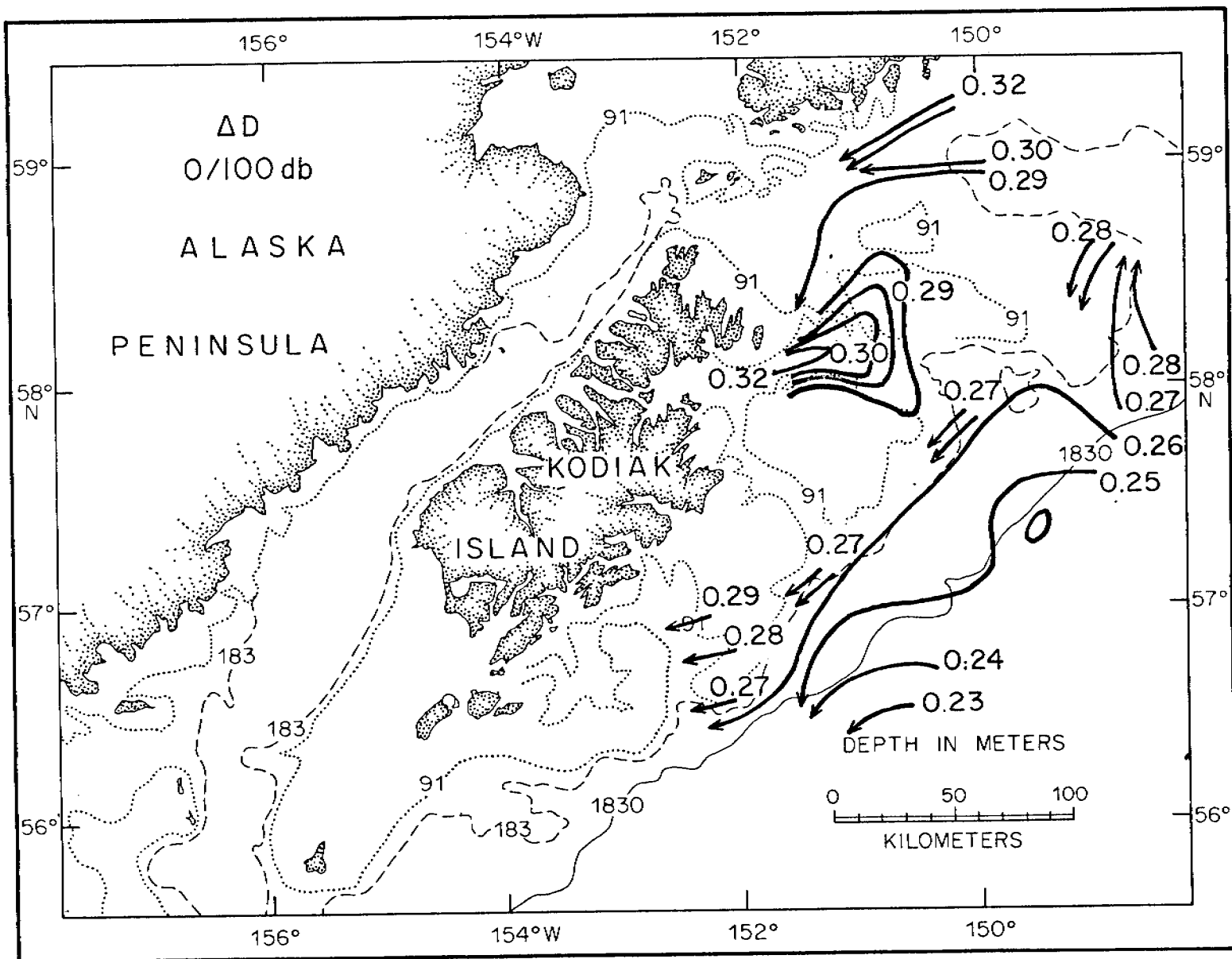


Figure 2. Dynamic contours observed during September 1977.

V. Cooperation

We are cooperating with the following research units:

289 (Royer) satellite imagery usefully delineates surface temperature features. We also are exchanging ideas and data, particularly during PI workshops.

217 (Hansen) satellite tracked drifters have aided our understanding of near-surface flow in the northeastern Gulf of Alaska. During the present field season, we will be deploying several of these drifters across the shelf region northeast of Kodiak Island to further elucidate flow over the bank/trough region.

367 (Reynolds) We are exchanging ideas and data on the effects of local meteorology on the oceanography.

140 (Galt) We provide hydrographic, current and pressure data.

153 (Cline and Feely) We are designing and deploying current meter, nephelometer and sediment trap arrays and correlating sediment transport with physical processes (see Section VI.)

327 (Hampton and Bouma) Cooperative field experiments and analysis of sediment interactions with physical factors.

348 (Barrick) We will be providing current records and perhaps surface drifter data to provide 'ground truth' for his radar mapped near-surface currents in Lower Cook Inlet.

425 (Larrance) We process data tapes and exchange ideas relating physical processes to plankton.

551, 552, 553 (Kodiak Island Food Web Study). We have coordinated the physical oceanographic studies with all aspects of the Kodiak Island program. This was accomplished during a synthesis meeting (March 1977) and a coordination meeting (January 1978). Such meetings have been beneficial in our attempt to address the OCSEAP goals.

VI Publications resulting from Gulf of Alaska work:

1. Charnell, R. L., and G. A. Krancus (1970): A processing system for Aanderaa current meter data. NOAA Tech. Memo. ERL PMEL-6.
2. Feely, R. A., E. T. Baker, J. D. Schumacher, G. J. Massoth and W. M. Landing (1978): Processes affecting the distribution and transport of suspended matter in the northeast Gulf of Alaska. Submitted to Deep-Sea Res.
3. Galt, J. A. (1976): Circulation studies on the Alaskan continental shelf off the Copper River Delta. U. S. Dept. of Comm./NOAA/ERL: 36 pp.
4. Hayes, S. P. (1978): Variability of current and bottom pressure across the continental shelf in the northeast Gulf of Alaska. Submitted to J. Phys. Oceanogr.

5. Hayes, S. P. and J. D. Schumacher (1976): Description of wind, current and bottom pressure variations on the continental shelf in the northeast Gulf of Alaska from February to May 1975. J. Geophys. Res., 81: 6411-6419.
6. Holbrook, J. R. and D. Halpern (1977): A compilation of wind, current, bottom-pressure and STD/CTD measurements in the northeast Gulf of Alaska, February - May 1975. NOAA Tech. Memo ERL-PMEL 10.
7. Muench, R. D., H. Mofjeld and R. L. Charnell (1978): Oceanographic Conditions in Lower Cook Inlet, Spring and summer 1973. In press. J. Geophys. Res.
8. Royer, T. C. and R. D. Muench (1977): On the ocean temperature distribution in the Gulf of Alaska, 1974-1975. J. Phys. Oceanogr., 7: 92-99.
9. Schumacher, J. D., R. Sillcox, D. Dreves and R. D. Muench (1978): Winter circulation and hydrography of Shelikof Strait, northwest Gulf of Alaska continental shelf. PMEL/ERL Tech. Rept. in preparation.

Additionally, several presentations are scheduled for the spring American Geophysical Union meeting, see EOS, 59(4) for abstracts.

VII. Needs for further study

We believe that the continued study of the Gulf of Alaska should emphasize analysis of data obtained through this year. Some of the questions under study are:

- A. Communication of near-shore and embayment waters with shelf edge waters via troughs: Does this occur in all or only some troughs? Is this an episodic or mean flow feature? What are the driving mechanisms?
- B. Bottom pressure and currents on the northwest Gulf of Alaska shelf: Is the relationship between currents and bottom pressure similar to that found on the Icy Bay shelf? Is non-local forcing i.e. the Alaskan Current, important to flow on this shelf as was observed for Icy Bay region?
- C. Tidal analysis: What is the amplitude and phasing of tides around Kodiak Island? Are there regions over the shallow banks where tidally generated mixing dominates buoyancy input?
- D. Seasonal impact of the Alaskan Current on shelf and Shelikof Strait flow: Does the Alaskan Current force flow through Shelikof Strait during summer or does baroclinicity become dominant? How does the reduced transport and velocities noted during summer impact flow in the Amatuli Trough, Portlock and North Albattross bank regions?
- E. A more complete analysis and synthesis of data from the northeast Gulf of Alaska, including hydrography (Royer), Lagrangian drifters (Hansen), local meteorology (Reynolds) and bottom pressure and currents records from our research unit.

These and similar questions are best addressed by a combination of studying data acquired through this year with interpretations from numerical and analytical investigations.

VIII. Conclusions

Observational studies in the Gulf of Alaska region have resulted in a more complete understanding of the physical oceanography. This is reflected in Section IV of this report, in previous reports, and in the publications listed in Section VI.

Major elements from this reporting period include:

- (1) On the northeast Gulf of Alaska continental shelf, bottom pressure and velocity correlations can be interpreted in terms of a simple geostrophic barotropic model.
- (2) Flow on the above shelf differed from shelf edge flow. The former flow had mean and fluctuating components which were aligned with bathymetry while at the shelf edge (250 m contour) mean along shore was reduced by 50%, fluctuating components were largely anticyclonic and eddy kinetic energy increased by a factor of seven.
- (3) The contribution of atmospheric pressure to bottom pressure can be neglected even in water depths of 50 m.
- (4) Simple dynamical models describe features of sea level response to wind forcing, with the response varying depending on water depth.
- (5) A portion of the Alaskan Current appears to be bifurcated in the region of Amatuli Trough. This flow provides major forcing for the observed currents in Shelikof Strait.
- (6) Dynamic contours (0/100 db) can be used to infer flow over the shelf and indicate that between two regions (shelf edge and along Amatuli Trough and the Kenai Peninsula) of relatively strong, consistent flow, flow is weak and variable.
- (7) The circulation in Lower Cook Inlet leads to an upwelling tendency in the southwestern portion.
- (8) Hydrography suggests that bottom water characteristics in Shelikof Strait and Kiliuda Trough are not locally formed and that such waters originate from the shelf edge region.

IX. Fourth quarter operations

The following field operations were conducted during the fourth quarter:

- A. SURVEYOR cruise RP-4-SU-78A, LEG II
- B. DISCOVERER cruise RP-4-01-78, LEG I

Details are provided in Appendix 1: Cruise Reports

A compilation of CTD, current, and pressure measurement programs is given in Appendix 2: Data Acquisition 1 April 1977 to 31 March 1978.

Appendix 1:
Cruise Reports

CRUISE REPORT

Surveyor Cruise RP-4-SU-78A, leg II

Chief Scientist: Robin D. Muench
Research Oceanographer
NOAA/PMEL

Other Scientific Personnel: Stewart A. Macklin
Meteorologist
NOAA/PMEL

Brad Eckert
Electronic Technician
NOAA/NOS

Introduction:

The Coastal Physics Group, Pacific Marine Environmental Laboratory (PMEL), Seattle, Washington has for the past three years been actively participating in the Outer Continental Shelf Environmental Assessment (OCSEA) program. This cruise was carried out in support of the OCSEA program, which has as its general objectives: (1) provide comprehensive environmental data and information on the Alaskan continental shelf lease areas; (2) define the probable ecological impact of oil exploration, production, storage and transshipment on the continental shelf; (3) refine our understanding of key ecological dynamic processes; and (4) provide a basis for predictive or diagnostic models of the ecosystem response to contamination by petroleum and its by-products.

In response to these general objectives, PMEL has been carrying out field programs designed to measure water temperature, salinity and density fields and their associated circulation patterns, and to survey coastal weather phenomena. Major goals have been to define critical circulation and mixing parameters in the water and to offer means of prediction of mesoscale coastal wind features too small to be delineated by the synoptic network of the National Weather Service (NWS), NOAA. Towards this end, field studies have been carried out throughout the Alaskan continental shelf from Norton Sound to the Yakutat Bay region. With the 1978 fiscal year, two new areas have been selected for intensive study: (1) the shelf region surrounding Kodiak Island, with particular emphasis on Albatross and Portlock banks; and (2) lower Cook Inlet and Shelikof Strait.

Cruise Objectives:

This cruise supported that portion of the OCSEA program addressing physical oceanographic and meteorological problems in the northwest Gulf of Alaska and lower Cook Inlet regions. Oceanographically, its purpose was to utilize a profiling conductivity/temperature/depth (CTD) system to determine mid-winter temperature, salinity and density fields. Drift cards (surface drifters) were deployed at selected locations to provide later information on surface water motions. Specific scientific problems

were: (1) circulation and mixing processes in the Portlock and Albatross banks region, particularly bifurcation of the mid-depth (200-250 m) westward-flowing warm core of the Alaska Current east of Portlock Bank; (2) structure and dynamics of the Alaska Current, a major westward-flowing boundary current which coincides roughly with the continental shelf break, from about 148°W to 158°W; (3) shelf circulation and mixing processes southwest of Kodiak Island to Mitrofanina Island; (4) circulation through Shelikof Strait; and (5) circulation and mixing processes in lower Cook Inlet south of roughly the latitude of Anchor Point.

Meteorologically, the objectives of this cruise were three-fold: (1) to test and evaluate new atmospheric profiling equipment; (2) to obtain quality surface meteorological comparison measurements between the Surveyor and environmental data buoys in lower Cook Inlet and on Albatross Bank; and (3) to identify and cross-section expected mesoscale atmospheric flows in lower Cook Inlet.

Methods:

Overall program objectives for the northwest Gulf of Alaska during this period were addressed via a two-vessel operation using the NOAA vessels Surveyor and Discoverer. Operations of the two vessels were closely coordinated via daily radio contact between the Chief Scientists, in addition to detailed pre-cruise discussion. This report is concerned with the work undertaken by the Surveyor.

Oceanographic objectives of this cruise were addressed by occupying section lines of CTD stations in a generally northwest-southeast direction across Portlock and Albatross banks east and south of Kodiak Island. An especially high station spatial density in the Portlock-eastern Albatross banks region was intended to allow resolution of the bifurcating core of warm, subsurface water and of vertical mixing on shoal areas of these banks. These closely-spaced stations addressed the first of the five oceanographic problems outlined above. These CTD data will be supplemented with data from five current meter moorings which were recovered from central Albatross Bank early during this cruise, by the Discoverer.

The second oceanographic problem, structure and dynamics of the Alaska Current, was approached by extending all CTD sections from the banks well out over the shelf break (200 m) into the current core. Two sections, one over Portlock Bank and one running south from the Trinity Islands, were extended seaward to completely traverse the current. All sections extending off the shelf break will be used to define temperature and salinity structure in the current. The two extended sections will be used, in addition, to compute baroclinic volume transport of water by the current. Ship drifts during occupation of CTD stations in the current were specifically monitored to provide estimates of surface water motion (allowing for wind effects).

The third oceanographic objective, circulation and mixing processes southwest of Kodiak Island, was addressed by the Discoverer concurrently with this cruise. They occupied CTD stations and recovered current meter moorings which had been deployed in October 1977.

The fourth objective, circulation through Shelikof Strait, was approached jointly by this cruise and the Discoverer. We occupied a closely-spaced section of CTD stations across southwestern Shelikof Strait, while Discoverer occupied stations axially up the Strait and close-spaced sections across the northeastern end. These data will be used to compute baroclinic current speeds and to examine temperature-salinity distributions for evidence of mixing and flow processes. Toward this end, a moored current meter array containing three meters in the northeastern end of the Strait was recovered by Discoverer; this array was deployed in October 1977.

The final oceanographic problem, that concerned with circulation and mixing in lower Cook Inlet, was addressed entirely by Discoverer, with CTD sections and recovery of moored current meters and pressure gauges.

Overall study of surface water circulation on Portlock and Albatross banks was supplemented, in addition to the CTD casts, by deployment of drift cards at selected locations on the banks (cf. Appendix B). These cards, marked with three languages (English, Russian and Japanese) with instructions for return of information on their recovery and promises of a \$1 US reward, are designed to float at the water's surface. Their eventual recovery, from beaches and by fishing vessels, will allow reconstruction of approximate pathways for surface water motion (trajectories).

To ensure quality control of the CTD data, temperature and salinity calibration samples were taken with a Nansen bottle every other cast. In addition, 5-sample temperature and salinity calibration casts were taken on the first ~~and final~~ stations of the cruise. Data tapes from the DDL were replaced with fresh tapes and replayed about once each day and a half (whenever the 7" reels were filled), to verify proper functioning of the CTD system. In addition, analog charts were routinely taken at each cast. Some variation in lowering rates was attempted in order to better define temperature and salinity through high gradient regions. Decrease of the lowering rate from 30 to 10-20 m/min through the upper 300 m of the water column did not markedly improve the quality of data (as determined by the salinity spiking). It was, moreover, impossible to accurately control lowering rate at these low speeds. In view of these facts, coupled with the considerable additional time required for the slower lowering rate (20 min/cast for casts deeper than 300 m), it was decided to retain the 30 m/min lowering rate. Below 300 m, the lowering rate remained at 60 m/min.

Some use was made of the Surveyor PDP8/E computer's capability to plot vertical temperature, salinity and density profiles using the DDL tapes, particularly when trouble-shooting. In view of the appreciable time required for these plots, coupled with lack of calibration and lowering rate/response time corrections for the data, it was decided not to use this plotting capability on a routine basis. The analog temperature and salinity plots from the CTD system were adequate for monitoring system performance cast by cast and for observing features in the water column.

The first two meteorological objectives were achieved in "piggyback" fashion concurrent with the CTD measurements. The initial CTD transects allowed adequate time for familiarization with and evaluation of the newly acquired Airsonde atmospheric profiling system. Weather permitting, sondes

were launched at 1115 and 2315 UT (standard NWS radiosonde ascent times). This scheme was selected because it allows comparison of Airsonde data with simultaneous NWS-derived profiles from selected south Alaska stations.

Close proximity of EB-72 to the CTD stations on Albatross Bank allowed pursuit of the second meteorological objective with minimal disruption of the oceanographic operation. In order to verify operation of the environmental data buoy and to obtain at least a crude calibration with PMEL standard instrumentation, Surveyor conducted three routine hourly deck weather observations while positioned within one mile of EB-72. The ship was stationed such that no flow interference patterns were generated over either platform. ~~Due to in cruise scheduling, it was necessary to assign verification/calibration of the lower Cook Inlet environmental buoy, EB-39, to the Discoverer.~~

The third meteorological objective, identification of lower Cook Inlet wind patterns, was also originally scheduled as a piggyback operation. This has been redesigned as a primary endeavor and is discussed in a separate section appended to this report (Appendix C).

Low level profiles through the atmospheric boundary layer were acquired using an expendable AS-1C Airsonde and associated TS-2AR ground station, all manufactured by the Atmospheric Instrumentation Research Company, Boulder, Colorado. The Airsonde is an aerodynamically-shaped styrofoam package containing wet and dry bulb thermistors for temperature measurement, a capacitance-interfaced aneroid cell for pressure sensing, switching circuitry and a 403 MHz transmitter with antenna. The shape of the sonde allows it to spin about a central vertical axis thus aspirating the thermistors as the sonde is carried aloft by a 30 gram sounding balloon inflated to 350 grams static lift. The sonde is powered by a 9V transistor battery, is precalibrated and transmits its A data frame (wet and dry bulb temperatures, pressure) every 6-8 seconds.

The TS-2AR ground station is a receiver and micro-processor which decodes the incoming signal, converts to physical units and reencodes the data for relay to any of three peripheral devices: strip-chart recorder, cassette recorder or Hewlett-Packard Model 97 printing calculator. This complete ground package is encased in an aluminum suitcase suitable for shipping.

Preliminary Results:

This cruise consisted of two phases. The first phase lasted from 3-17 March and consisted primarily of occupation of 182 consecutive CTD casts along NW-SE section lines traversing Portlock and Albatross banks (Appendix A). Occupation of these sections commenced at the NE end of the study region and worked southwestward to the Trinity Islands region. The Surveyor then proceeded north around the Trinity Islands and occupied the final CTD section of the cruise across southwestern Shelikof Strait. During this first phase, drift cards were deployed at 13 locations over the banks (Appendix B), eleven airsondes were launched (cf Table 1 and

discussion below) and a three-hour set of surface meteorological observations were obtained adjacent to data buoy EB-72 for later comparison with data from the buoy.

On 17 March Surveyor proceeded north to lower Cook Inlet and carried out the second phase of the cruise. This was a survey of surface and upper-air meteorology of lower Cook Inlet designed to study local winds. On 19 March, Surveyor returned to Kodiak and the cruise was terminated on schedule.

Rigorous analysis of temperature and salinity data from the CTD must await final processing at PMEL. This processing includes calibration and corrections for error due to lowering rate in conjunction with vertical temperature gradients. Monitoring of the analog output from the CTD, and of digital printout derived from the DDL tapes, allows however some observations of a preliminary nature.

- 1) The warm subsurface core of the Alaska Current was readily apparent along the shelf break and to seaward. This core occurred at depths of approximately 100-200 m and attained maximum temperatures of the order of 6°C.
- 2) The upper portion of the warm core was characterized by considerable vertical temperature and salinity structure having scale lengths of the order of tens of meters and sharp vertical gradients. There was negligible correlation between details of this structure at adjacent stations, and in one case the structure had changed appreciably between a down- and upcast at the same station. These small features appear to be transient, and may be related to lateral interfingering of the cold, vertically uniform water on the banks with the warmer water of the Alaska Current.
- 3) Water on the banks off Kodiak Island was vertically well-mixed, as anticipated. Horizontal gradients in both temperature and salinity were apparent in the vertically mixed regions.
- 4) There was evidence of the warm subsurface layer from the Alaska Current near-bottom east of Kennedy Entrance. This supports the prior concept of westward flow of water from the Alaska Current through Kennedy Entrance.

In addition to the CTD observations, ship drift clearly located the high-speed core of the Alaska Current. At one deep off-shelf station, for example, drift was about 10 km to the southwest during the 90-minute duration of the station. Winds were from the northwest, and the ship held into the wind and was near-motionless with respect to the surface water. This suggests a surface current of about 3.6 knots to the southwest. Previous estimates of baroclinic current speed in the Alaska Current are on the order of 2 knots at the surface, so this estimate of total speed is in rough agreement. Extreme wire angles for the CTD, despite little ship motion relative to the water, suggested that a strong vertical shear was present. This is in agreement with the concept of a baroclinic current, with speeds decreasing with depth.

Eleven Airsondes were launched over the period 2-16 March 1978. Time and position of launch, pertinent surface meteorological data and ceiling of usable information obtained are given in Table 1. A favorable launch routine was established whereby a single person can prepare and launch a sonde in 10-15 minutes. Ascent to 3000 m then requires an additional 15-20 minutes. Data acquired can be replayed through the system, generating a finished data product in an additional 60-90 minutes. Two major drawbacks (both correctible by the manufacturer) were discovered and are detailed below.

The Airsonde system is clearly superior to the radiosonde system which it replaces. The lightness of the sonde allows launch using a much smaller balloon, a critical factor in working from a vessel. Its precalibration cuts preparation time in half. Real-time printout of physical units permits the researcher to immediately discern atmospheric structure, allowing more prudent use of scientific resources. Most important, automatic processing of the data removes the element of human error and generates a finished product in a much shorter time. The data density allows definition of fine-scale atmospheric structure undiscernable with radiosondes.

As alluded to above, this shipment of prototype Airsondes was plagued with two difficulties. Poor signal-to-noise ratio at intermediate altitudes (1500-2000 m) prevented proper operation of the micro-processor with subsequent loss of usable data. It is felt that this is a unique problem of the marine environment, as land-based flights have been made routinely to altitudes of 10,000 m. Increasing transmitter power and/or preamplifying and filtering the reception would cure this problem. Secondly, the wet-bulb thermistor malfunctioned occasionally, its indicated temperature suddenly becoming higher than that of the dry-bulb thermistor, a physical impossibility. This phenomenon was often observed to occur during penetration of a cloud layer and is probably caused a mis-design of the wicking and reservoir.

In the early morning hours of March 14, Surveyor made three passes within one mile of EB-72 on Albatross Bank. The exact times and positions as well as the meteorological data recorded for later comparison with buoy tapes are listed in Table 2. ~~A similar program was carried out by the NOAA ship Discoverer at EB-39 in lower Cook Inlet.~~

All objectives of the lower Cook Inlet meteorological program, as detailed in Appendix C, were attained except the Discoverer-Tustumena surface meteorological data intercomparison. This objective could not be completed in the short time span dictated by the Tustumena's schedule; future experimental plans will include this objective.

The Surveyor began the lower Cook Inlet meteorological survey on 17 March 1978 at 1900 UT just north of Shuyak Island, then cruised northwest to Cape Douglas, Kamishak Bay and on to the other locations detailed in Appendix C. She finally arrived at data buoy EB-39 at 1500 UT, 18 March 1978. Airsondes were released at all stations, including the Barren Islands station occupied after the EB-39 time series. Surveyor maintained station at EB-39 until 0700 UT on 19 March. Routine meteorological

observations were conducted hourly, and airsondes were released at two-hourly intervals commencing at 1800 UT, 18 March. A summary of lower Cook Inlet Airsonde activity is contained in Table 3.

Between the 1900 and 2000 hourly surface observations on 18 March at EB-39, Surveyor and Discoverer made two meteorological intercomparison passes. Temperature measurements were made with a sling psychrometer on the weather side bridge wing. Surveyor reported winds from both the port and starboard anemometers. At times of observation, the ships were within $\frac{1}{4}$ mile of each other, steaming parallel courses into the wind and travelling at the same rate of speed. Results from this intercomparison are presented in Table 4.

Summary and Acknowledgments:

This cruise was an extremely successful one from a scientific viewpoint. We've obtained a more complete set of environmental data than ever before from this region at this time of year; this will be invaluable in defining the complex regional oceanographic and meteorological regimes. This success has been due to extremely efficient and trouble-free operations on the part of Surveyor and her personnel, aided by a period of abnormally mild weather. Since all personnel involved have functioned as a team, individual names will not be mentioned. Especial thanks are due, however, to the ship survey crew whose care and attentiveness during scientific operations ensured data quality under often less-than-ideal conditions. They and they alone are responsible for the consistently high quality data obtained. We acknowledge, also, the efforts made by Captain Grunwell, the officers and men of Surveyor in carrying out this operation in a trouble-free and professional manner.

This cruise was carried out under the auspices of the BLM-sponsored Outer Continental Shelf Environmental Assessment Program.

Problems Encountered and Suggestions:

Problems encountered during this cruise were minimal. The DDL of the CTD unit malfunctioned and had to be replaced with another unit, which caused the loss of digital data from one station. On another occasion, the underwater unit failed and a minor repair cured the problem with no loss of data. On deep (1500 m) casts in regions of high current shear, the CTD underwater unit tended to stream away from the ship with consequent large wire angles, erratic lowering rates and some decrease in data quality. Addition of more weight to the unit did not cure the problem completely, but eased it considerably. This would not be a common problem, as few locations in the normal operating areas have current shears as high as those encountered in the Alaska Current off Kodiak Island.

It was felt by us they the ship survey technicians are capable of carrying out more complex and responsible tasks than are presently assigned to them. While this particular cruise was limited in scope,

consisting primarily of CTD work, some cases in point come to mind.

- 1) Use of the UGR is essential in defining distance between the CTD unit and the bottom, yet the survey techs have apparently not been trained in making appropriate adjustments to this unit. Misinterpretation of the UGR trace (the machine's fault) in one instance necessitated repeating a cast; adjustment of the unit would have eliminated the problem. We feel that anyone using a piece of gear should understand its operation and be capable of adjusting it to obtain maximum information.
- 2) The PDP8/E computer has considerable capabilities. Given the appropriate software (much of which is available), the survey techs could be taught to run relatively complex routines on data. Since the calibration samples are run aboard ship, there is no reason why the CTD data could not be run through the mill and the Chief Scientist provided with a final, corrected product. Going a step further, this could then be used to generate vertical sections, profiles, etc. and allow data analysis to commence aboard ship. (The research vessel Thompson has such a capability.)
- 3) Smooth plotting should be done on the computer. This would be faster, more accurate than hand plotting. Admittedly, this can't be implemented overnight. If done, however, it would free the survey techs to pursue item 2 above. It seems to me that these personnel, several of whom have had considerable training, could be better used than for plotting.

These comments are intended as constructive. Surveyor, with its heavy weather capabilities, computer and ample complement of personnel, is capable of doing better than its already better-than adequate best.

APPENDIX A

CTD Casts taken during Surveyor cruise RP-4-SU-78A, Leg II.

PORTLOCK-ALBATROSS BANK REGION						
<u>CAST NO.</u>	<u>STA. NO.</u>	<u>JD *</u>	<u>HOURL *</u>	<u>LATITUDE</u>	<u>LONGITUDE</u>	<u>DEPTH(m)</u>
001	519	63	1652	58-09.2	147-43.5	2195
002	518	63	1948	58-14.5	147-57.3	2048
003	517	63	2135	58-18.2	148-07.4	1400
004	516	63	2326	58-21.6	148-18.7	1170
005	515	64	0113	58-23.7	148-27.1	640
006	514	64	0303	58-28.6	148-38.2	122
007	513	64	0409	58-31.4	148-48.5	114
008	512	64	0509	58-34.5	148-58.0	110
009	511	64	0610	58-38.1	149-07.3	130
010	510	64	0721	58-41.4	149-16.6	142
011	509	64	0819	58-45.2	149-27.6	185
012	508	64	0939	58-47.9	149-36.8	215
013	507	64	1046	58-51.7	149-46.4	240
014	506	64	1306	58-54.0	149-55.4	232
015	505	64	1507	59-00.1	149-56.7	205
016	504	64	1602	59-05.3	149-59.6	180
017	503	64	1653	59-11.5	150-02.0	132
018	502	64	1736	59-15.6	150-03.1	195
019	501	64	1827	59-21.6	150-06.4	170
020	520	64	1925	59-16.7	150-07.0	182
021	521	64	2012	59-13.1	150-11.8	117
022	522	64	2102	59-11.8	150-21.8	177
023	523	64	2154	59-08.1	150-29.8	111
024	524	64	2251	59-04.6	150-39.4	108
025	525	65	0024	59-01.4	150-45.3	165
026	528	65	0125	59-02.3	150-56.1	152
027	527	65	0211	59-06.0	150-57.4	177
028	526	65	0313	59-10.0	150-58.7	62
029	549	65	0359	59-07.4	151-06.0	97
030	550	65	0445	59-03.8	151-06.3	100
031	551	65	0535	58-59.7	151-05.6	157
032	529	65	0633	58-57.7	150-55.0	140
033	530	65	0750	58-51.4	150-52.9	160
034	531	65	0852	58-44.6	150-50.2	180
035	532	65	1002	58-38.6	150-47.2	200
036	533	65	1101	58-31.9	150-45.0	132
037	534	65	1204	58-27.8	150-33.5	73
038	535	65	1259	58-25.1	150-22.4	71
039	536	65	1358	58-21.1	150-11.1	50
040	537	65	1442	58-18.6	150-03.2	46
041	538	65	1546	58-16.2	149-52.0	60
042	539	65	1643	58-13.4	149-43.2	59
043	540	65	1755	58-10.3	149-19.6	100
044	541	65	1842	58-07.9	149-23.1	125
045	542	65	1954	58-03.7	149-10.2	108
046	543	65	2050	58-01.7	149-02.4	119
047	544	65	2156	57-59.0	148-52.3	575
048	545	66	0010	57-57.9	148-47.0	807

*All dates and times are UT.

APPENDIX A (cont'd)

<u>CAST NO.</u>	<u>STA. NO.</u>	<u>JD*</u>	<u>HOURL*</u>	<u>LATITUDE</u>	<u>LONGITUDE</u>	<u>DEPTH(m)</u>
101	591	69	1200	58-18.1	151-02.7	145
102	592	69	1338	58-12.0	150-59.6	105
103	600	69	1435	58-05.7	150-57.2	143
104	601	69	1533	58-02.5	150-49.9	148
105	602	69	1619	57-58.2	150-44.6	119
106	603	69	1711	57-55.3	150-37.0	121
107	604	69	1759	57-51.9	150-28.7	95
108	605	69	1846	57-49.2	150-22.4	100
109	606	69	1930	57-47.0	150-15.5	115
110	607	69	2033	57-42.9	150-06.9	177
111	608	69	2125	57-40.7	149-59.4	225
112	609	69	2242	57-35.0	149-51.0	236
113	610	69	2344	57-31.2	149-48.5	1030
114	611	70	0132	57-27.2	149-42.9	1600
115	612	70	0321	57-23.2	149-39.2	1830
116	613	70	0515	57-18.9	149-32.8	2100
117	626	70	0816	56-59.9	149-40.8	3500
118	625	70	1006	57-03.8	149-48.1	2340
119	624	70	1155	57-08.5	149-55.7	1617
120	623	70	1329	57-12.6	149-59.5	1700
121	622	70	1532	57-16.5	150-05.7	1520
122	621	70	1733	57-21.8	150-10.7	669
123	593	71	2239	57-59.9	152-05.0	180
124	628	71	2340	57-55.1	152-01.6	198
125	629	72	0038	57-50.1	152-03.7	113
126	630	72	0153	57-44.6	152-00.6	110
127	631	72	0317	57-36.9	151-53.1	146
128	644	72	0436	57-29.8	151-55.8	86
129	632	72	0549	57-33.8	151-41.0	120
130	633	72	0646	57-31.4	151-33.4	145
131	634	72	0750	57-26.5	151-26.3	165
132	635	72	0852	57-21.4	151-23.1	150
133	636	72	0955	57-16.2	151-18.3	155
134	637	72	1101	57-11.3	151-15.0	143
135	638	72	1212	57-05.7	151-06.5	430
136	639	72	1327	57-01.8	151-02.7	578
137	640	72	1454	56-55.4	150-58.7	1200
138	641	72	1627	56-51.7	150-55.1	1700
139	642	72	1823	56-45.9	150-46.9	2100
140	643	72	2018	56-39.3	150-44.9	2926
141	654	72	2322	56-21.5	150-54.5	5415
142	653	73	0208	56-29.8	151-01.2	3100
143	652	73	0440	56-39.7	151-08.6	2200
144	651	73	0624	56-43.5	151-10.0	1465
145	650	73	0807	56-48.5	151-15.7	955
146	649	73	0932	56-53.2	151-20.1	900
147	648	73	1058	56-58.3	151-24.8	677
148	647	73	1225	57-04.1	151-29.6	165
149	646	73	1309	57-06.7	151-35.3	115

*All dates and times are UT.

APPENDIX A (cont'd)

<u>CAST NO.</u>	<u>STA. NO.</u>	<u>JD*</u>	<u>HOUR*</u>	<u>LATITUDE</u>	<u>LONGITUDE</u>	<u>DEPTH</u>
150	645	73	1712	57-16.3	151-42.3	55
151	656	73	1926	57-10.3	152-20.3	80
152	657	73	2106	57-03.1	152-07.8	75
153	667	73	2320	57-03.7	152-50.4	86
154	668	74	0021	56-59.7	152-42.1	145
155	669	74	0112	56-56.0	152-36.9	145
156	670	74	0206	56-53.7	152-33.9	154
157	671	74	0312	56-48.7	152-29.5	159
158	672	74	0508	56-42.6	152-29.7	163
159	673	74	0608	56-38.2	152-28.6	160
160	674	74	0726	56-32.2	152-29.3	265
161	675	74	0859	56-25.1	152-24.3	295
162	676	74	1010	56-22.0	152-20.2	540
163	677	74	1135	56-18.0	152-16.8	2000
164	678	74	1432	56-13.3	152-09.0	3880
165	776	74	2121	55-13.0	152-47.7	3475
166	775	74	2309	55-19.5	152-56.4	4950
167	774	75	0146	55-28.0	153-09.2	5267
168	773	75	0358	55-36.6	153-20.8	4050
169	700	75	0559	55-42.7	153-24.3	3000
170	699	75	0829	55-45.8	153-29.6	1355
171	698	75	1053	55-49.8	153-36.1	990
172	697	75	1259	55-54.3	153-41.0	270
173	696	75	1400	55-58.9	153-44.8	105
174	695	75	1525	56-07.5	153-56.3	185
175	694	75	1646	56-14.5	154-06.6	145
176	693	75	1808	56-23.7	154-15.6	40

SHELIKOF STRAIT

177	330	76	0205	57-20.6	154-56.0	159
178	329	76	0306	57-24.0	154-01.3	236
179	328	76	0402	57-26.7	155-07.3	238
180	327	76	0500	57-29.8	155-14.3	247
181	326	76	0604	57-33.0	155-20.5	285
182	325	76	0702	57-36.1	155-26.6	220

*All dates and times are UT.

APPENDIX A (cont'd)

<u>CAST NO.</u>	<u>STA. NO.</u>	<u>JD*</u>	<u>HOURL*</u>	<u>LATITUDE</u>	<u>LONGITUDE</u>	<u>DEPTH(m)</u>
049	546	66	0143	57-55.7	148-39.9	450
050-51	547	66	0325	57-51.8	148-33.1	1756
052	548	66	0600	57-51.2	148-25.6	1830
053	772	66	1157	56-52.7	148-12.2	4389
054	771	66	1445	57-00.5	148-23.4	4680
055	770	66	1726	57-08.1	148-38.6	4930
056	769	66	2013	57-15.2	148-49.6	3475
057	768	66	2228	57-22.6	149-01.1	2516
058	767	67	0043	57-30.7	149-13.3	2560
059	572	67	0219	57-32.6	149-17.3	1950
060-61	571	67	0521	57-36.1	149-20.7	1463
062	570	67	0753	57-40.4	149-28.4	970
063	569	67	0921	57-44.4	149-34.1	505
064	568	67	1046	57-48.2	149-39.6	278
065	567	67	1159	57-53.0	149-46.1	240
066	566	67	1314	57-56.5	149-53.3	261
067-68	565	67	1416	57-59.9	149-57.6	280
069	564	67	1546	58-04.1	150-06.5	320
070	563	67	1652	58-06.8	150-16.8	250
071	562	67	1735	58-08.9	150-20.1	170
072	561	67	1836	58-12.3	150-27.7	993
073	560	67	1942	58-18.5	150-38.6	61
074	559	67	2037	58-24.9	150-48.9	75
075	558	67	2147	58-31.4	151-01.5	155
076	557	67	2226	58-33.7	151-07.1	174
077	556	67	2357	58-40.0	151-06.5	170
078	555	68	0050	58-44.1	151-04.9	165
079	554	68	0157	58-48.7	151-04.0	139
080	553	68	0252	58-53.9	151-03.5	168
081	552	68	1511	58-56.7	151-06.3	161
082	573	68	1655	58-57.8	151-16.0	152
083	574	68	1813	59-00.3	151-25.6	131
084	575	68	1909	59-02.3	151-37.6	142
085	576	68	2000	59-04.3	151-45.7	100
086	577	68	2038	59-03.9	151-55.2	192
087	578	68	2206	59-00.3	151-46.6	128
088	579	68	2307	58-54.6	151-47.2	110
089	580	69	0027	58-49.9	151-38.9	137
090	581	69	0126	58-46.2	151-45.4	210
091	582	69	0234	58-40.8	151-47.0	132
092	583	69	0335	58-36.0	151-44.0	159
093	584	69	0424	58-32.2	151-46.6	177
094	585	69	0518	58-27.6	151-50.0	104
095	586	69	0610	58-27.6	151-46.5	195
096	587	69	0714	58-25.5	151-36.8	174
097	588	69	0843	58-24.2	151-28.5	170
098	589	69	0956	58-23.4	151-19.0	120
099	589	69	1002	58-23.4	151-19.1	120
100	590	69	1116	58-21.3	151-07.0	117

*All dates and times are UT.

APPENDIX B

Data on drift card deployments over Portlock
and Albatross banks

3-20 March 1978

<u>CARD NO's</u>	<u>JD</u> *	<u>HOUR</u> *	<u>LATITUDE</u>	<u>LONGITUDE</u>
101-200 (exc. 165)	64	2250	59-04.6	150-39.4
201-300	65	1115	58-31.8	150-45.0
301-400	65	1546	58-16.2	149-52.0
401-500	65	2001	58-03.6	149-10.3
1401-1500	69	0036	58-50.0	151-39.0
501-600 (exc. 513)	69	0505	58-27.6	151-50.0
901-1000	69	1133	58-21.4	151-06.9
601-700	69	1617	57-58.3	150-44.6
701-800	72	0806	57-25.8	151-25.8
801-900	73	1718	57-16.3	151-42.2
1001-1100	73	2106	57-03.1	152-07.8
1101-1300 (exc. 1207)	74	0201	56-53.6	152-33.9
1301-1400	75	1522	56-07.5	153-56.2

*All dates and times are UT.



APPENDIX C

LOWER COOK INLET

METEOROLOGICAL EXPERIMENT

OBJECTIVES:

1) Survey of lower Cook Inlet (see figure) with stops at:

a) Shuyak Island	58° 41.0' N
	152° 19.0' W
b) Cape Douglas	58° 58.5' N
	153° 19.5' W
c) Kamishak Bay	59° 17.7' N
	153° 37.0' W
d) Augustine Island	59° 21.3' N
	153° 16.2' W
e) Chinitna Point	59° 34.1' N
	153° 00.0' W
f) Kachemak Bay	59° 32.3' N
	151° 41.0' W
g) EB-39	59° 10.1' N
	152° 45.2' N
h) Barren Islands	58° 56.0' N
	152° 07.0' W

2) Surface meteorological intercomparison with NOAA Ship DISCOVERER, Alaska State Ferry TUSTUMENA, EB-39.

3) 12-hour time series at EB-39.

METHODS:

- 1) Surface meteorological data are collected routinely by the Quartermaster. In addition, strip chart provides constant analog trace of surface winds. Airsonde ascent at each station plus an additional ascent on Shuyak - Douglas leg and Chinitna - Kachemak leg.

TOTAL: 8 Stations
10 Airsondes

- 2) To be arranged with DISCOVERER, TUSTUMENA, if possible at least one comparison measurement of surface meteorological parameters will be executed. Ships should attempt to steam parallel to each other into the wind as close as safety permits. DISCOVERER will intercompare with TUSTUMENA, SURVEYOR with DISCOVERER, if possible.

- 3) Time permitting, the EB-39 station is extended by 12-hours. Airsondes are released every two-hours, plus routine deck weather measurements.

TOTAL: 7 Airsondes

(Continued)



SCHEDULING:

- 1) This experiment requires 41-hours to complete (28-hours without EB-39 time series).
- 2) Approximate distance between stations:

Shuyak - Douglas	36 NM
Douglas - Kamishak	21 NM
Kamishak - Augustine	12 NM
Augustine - Chinitna	16 NM
Chinitna - Kachemak	40 NM
Kachemak - EB-39	40 NM
EB-39 - Barren Island	27 NM

- 3) Tentative Schedule * (local time):

		<u>With Time Series</u>		<u>Without Time Series</u>	
Arr:	Shuyak	3/17	1415	3/18	0215
Dep:	Shuyak		1445		0245
Arr:	Douglas		1845		0645
Dep:	Douglas		1915		0715
Arr:	Kamishak		2130		0930
Dep:	Kamishak		2200		1000
Arr:	Augustine		2330		1130
Dep:	Augustine	3/18	0000		1200
Arr:	Chinitna		0200		1400
Dep:	Chinitna		0230		1430
Arr:	Kachemak		0630		1830
Dep:	Kachemak		0700		1900
Arr:	EB-39		1100		2300
Dep:	EB-39	3/19	0015	3/19	0015
Arr:	Barren Islands		0100		0100
Dep:	Barren Islands		0130		0130

* Time schedule assumes ship averages
10 knots between stations.

Table 1: Airsonde ascents for evaluation period

Airsonde Designation	Date/Time (UT)	Position Lat (n)/Long (W)	Surface Meteorological Conditions					Height Attained (m)
			Pressure (mb)	Wind (dir/kts)	Temp (°C)	Wet bulb (°C)	Sea sfc (°C)	
LC1	03-02-78 2254	57-43.6 152-30.9	1017.3	calm	4.8	3.0	---	4217
LC2	03-04-78 2339	58-21.2 148-18.4	1002.8	240/15	2.0	-0.3	4.9	3008
LC3	03-05-78 1115	58-51.5 149-45.8	996.4	265/06	2.0	-0.3	4.6	1121
LC4	03-05-78 2320	59-05.2 150-39.0	996.8	100/05	1.5	-0.6	4.6	1730
LC5	03-06-78 1112	58-31.8 150-45.0	996.1	080/03	0.9	-1.1	4.4	1710
LC6	03-07-78 0010	57-57.9 148-47.0	985.3	345/18	2.6	0.9	4.7	710
LC7	03-09-78 2317	58-54.8 151-47.7	999.2	308/09	3.3	2.4	4.4	2077
LC8	03-10-78 1125	58-21.3 151-07.0	1010.6	290/06	1.7	-0.5	4.3	2755
LC9	03-10-78 2344	57-31.2 149-48.5	1014.8	100/12	3.1	2.0	4.9	1561
LC10	03-11-78 1100	57-04.4 149-49.2	1017.6	107/12	3.3	2.4	4.6	1390
LC11	03-16-78 2318	56-46.6 155-00.5	1012.0	300/05	-0.1	-2.1	3.3	3419

Table 2: Positions and surface data from EB-72 comparison.

Date	Time (UT)	Position Lat/Long	T(°C) T _w (°C)	Wind spd. Wind dir.	T _{sea} (°C) Vis (mi)	Swell (m) Dir(°T)	Wave(m) P(''Hg)
3-14-78	1359	57-07.0	3.3	26 kts.	3.9	2	1
		151-44.9	2.2	065°T	3	075	29.35
3-14-78	1455	57-08.2	2.2	28 kts.	3.3	7	1
		151-45.4	1.7	056°T	3	075	29.36
3-14-78	1555	57-08.1	2.2	18 kts.	3.3	7	1
		151-44.7	2.2	076°T	3	075	29.33

Table 3: Airsonde ascents for lower Cook Inlet

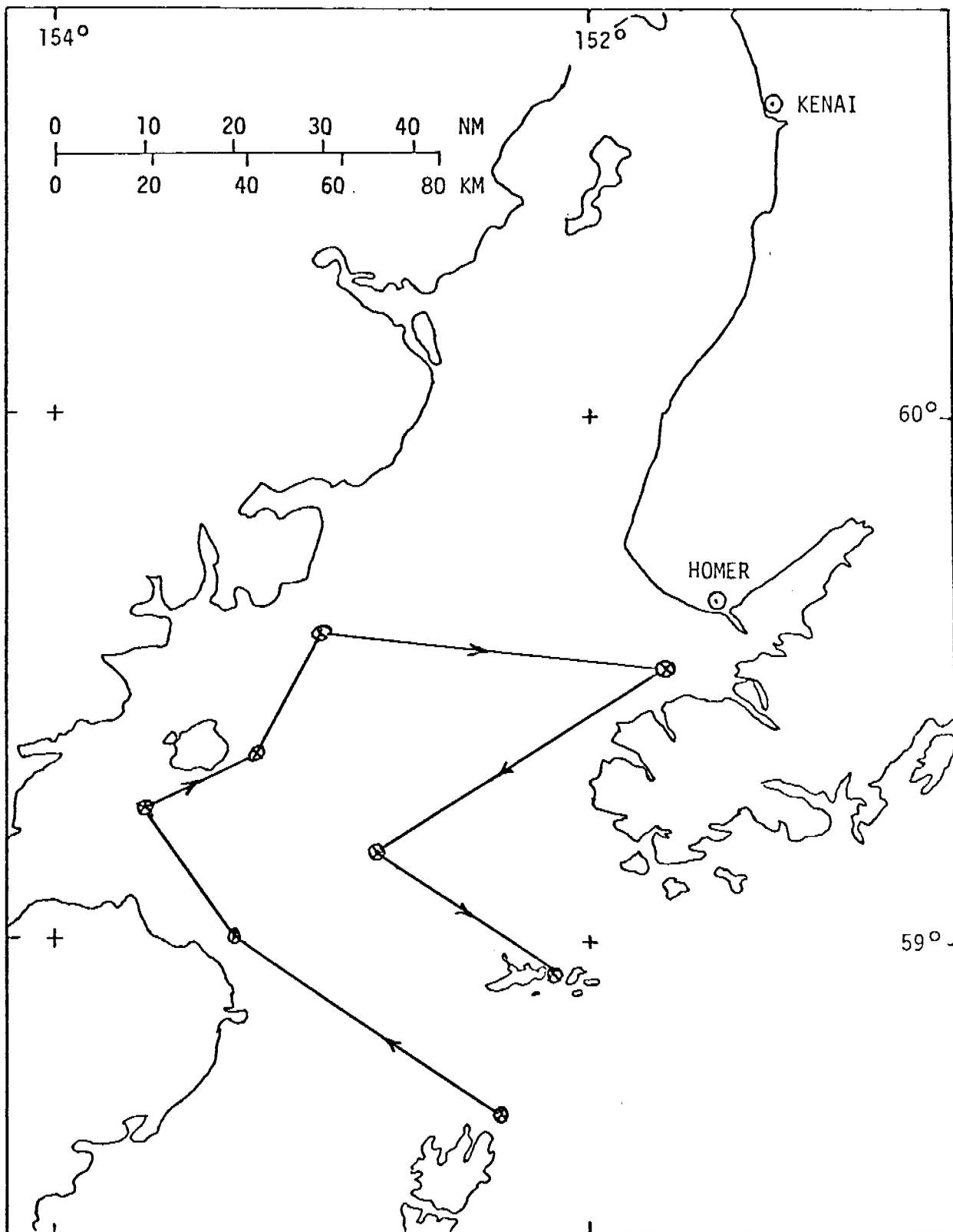
Airsonde Designation	Date/Time (UT)	Position Lat (N)/Long (W)	Surface Meteorological Conditions					Height Attained (mb)
			Pressure (mb)	Wind (dir/kts)	Temp (°C)	Wet bulb (°C)	Sea sfc (°C)	
LC12	03-17-78 1920	58-41.7 152-18.7	1006.7	352/09	0.5	-1.0	4.4	762
LC13	03-17-78 2104	58-50.2 152-47.5	1007.6	017/14	0.1	-1.6	4.4	729
LC14	03-17-78 2241	58-59.6 153-14.5	1008.2	297/11	0.9	-0.5	2.7	565
LC15	03-18-78 0130	59-17.8 153-37.3	1008.9	045/01	-0.8	-2.9	1.5	625
LC16	03-18-78 0349		1008.9	031/09	0.1	-2.5	1.8	700
LC17	03-18-78 0540		1009.5	033/08	0.1	-2.1	2.7	600
LC18	03-18-78 0817		1009.3	020/17	0.2	-1.2	4.0	469
LC19	03-18-78 1005		1009.1	063/08	0.0	-1.3	3.9	747
LC20	03-18-78 1735		1008.0	020/17	0.6	-0.7	4.3	(5m)
LC21	03-18-78 1753		1007.9	020/14	0.6	-0.7	4.3	929
LC22	03-18-78 2013		1006.9	020/22	0.5	-0.6	4.3	800
LC23								
LC24								
LC25								
LC26								
LC27								
LC28								

Table 4: Surveyor-Discoverer meteorological intercomparison.

Date/ Hour(UT)	Present Weather	Vis. (n.m.)	Wind/ Dir.	Wave/ Swell	T _{sea} (°C)	T(°C)/ T _w (°C)	P(mb)	Ship
3-18-78 0927	Cloudy	25	26(p) 24(s)/ 020	1'/ 0	3.3(int) 4.3(B)	0.8/ -0.5	1007.3	<u>Surv.</u>
			26/ 020		4.1	0.2/ -1.0	1007.5	<u>Disco.</u>
3-18-78/ 0935	Cloudy	35	22(p) 24(s)/ 020	1'/ 0	4.3	0.8/ -0.5	1007.3	<u>Surv.</u>
			22/ 020		-	0.0/ -1.2	1006.9	<u>Disco.</u>

At time of observations, Surveyor speed = 7 knots, course 020°T.

Position of <u>Surveyor</u> :	<u>1st pass</u>	<u>2nd pass</u>
	59-10.6	59-11.5
	152-46.3	152-45.7



Cruise Report RP-4-DI-78A, LEG I

March 4-24, 1978

I. Introduction

The general objective of the cruise is stated in paragraph 2.1 of the project instructions. On this Leg, the specific assignments were to recover moored current meter arrays in lower Cook Inlet and around Kodiak Island with CTD stations as given by the PMEL Grid to be occupied if time and weather allowed. The study area is broken into three subdivisions; lower Cook Inlet with moorings designated by C, Kodiak Island designated by K, and Mitrofanina designated by MI. Because of excellent weather for this season, very little time was lost. Including casts at current meter stations, a total of 180 CTD stations were occupied.

II. Personnel: Jane Hanuksela, Bill Parker and Jim Haslett (Chief Scientist) all from PMEL.

III. Operations

Because March weather is capricious and usually severe, the plan was to recover as many moorings in open waters as possible, with work in lower Cook Inlet being reserved for periods of foul weather in the Gulf of Alaska. As it turned out, there was exceptionally good weather with operations halted only once by severe weather. Heavy weather several times caused operations to be moved to a different area but really did not stop work.

Twenty-three moorings were scheduled to be recovered. Eighteen were recovered intact and parts of two (C-7 and C-8) were recovered. Chart I and Table I give locations and summarize data. Three moorings (C-9, C-11 and MI-C) were not recovered and are presumed lost. One common factor associated with all five lost or damaged is that they were located in regions where fishing activities are high. This is particularly true with respect to C-7, 8, 9 and 11. All four were located generally on the southeastern part of Cook Inlet where intensive crabbing is carried out. The upper flotation was missing on C-7 and C-8. Presumably it is also missing on C-9 and C-11 with the additional possibilities that the secondary flotation has been destroyed and/or the release is damaged and/or trapped. The release indicated they had fired and tripped for all three moorings reported lost. In the case of C-9 and C-11 the present locations are known with C-11 being one mile from the original position.

The present location of MI-C is unknown, although because of the experience with C-9, it is presumed to be near the original location. A search of nearly eleven hours was carried out before being discontinued because of heavy weather. The release (type 322) was interrogated to determine range and bearing without success. A search pattern was set up based on possible local currents. When the search proved to be useless, the ship was returned to the original position. After no response again with the 301 deck unit, the release was interrogated with the 200 unit. A positive response was received. By utilizing the two deck units it was possible to obtain a range estimate of about 350 yards or less from the ship.

Two moorings had been recovered previously and the ranges given by the 301 unit had been good. In addition the mooring was equipped with an OAR strobe light, radio beacon, and a radar target. Because of the various systems available to track the mooring and good visibility to the horizon, the decision was made to fire the release even though it was becoming dark. The release indicated a positive firing. All flotation should have been on the surface in less than two minutes with the back-up tracking systems on the surface in less than thirty seconds. No visual, radio, or radar contact was ever reliably reported. Repeated attempts to interrogate the release suggested the mooring was either drifting away from the ship or that the batteries were failing. Increasingly severe weather caused the search to be stopped.

A comparison can be made with C-9 which also was not recovered. It was fired under excellent conditions and no visual contact was reported. A search was carried out in the direction currents would have taken the mooring had it been just barely at the surface or dragging the bottom. The acoustic signal finally faded suggesting drifting or bad batteries. The effort was finally discontinued because of darkness and heavy weather. However, here an opportunity to return to the site without undue steaming existed. This was done three days later and the mooring was still located at the site of deployment.

All Mitrofanina moorings had marker floats times to be released in April. The markers were missing on the three recovered. Either the timer had worked prematurely or the markers had floated free sometime after deployment.

Sediment traps were on C-1, C-4 and C-11. On the recovered traps the timers had not worked. A quick check of the batteries on two of the timers showed them to be bad or marginal. By the time recoveries were made the ways for the coverings of the traps to slide in were so fouled they could not be closed.

After the recovery program was under temporal control, a routine CTD program was initiated in lower Cook Inlet, northern Shelikof Strait, and off Kodiak Island. Chart I shows the location of the lines run while the stations occupied from the PMEL grid are listed in Table II.

IV. Acknowledgements

I would like to thank all departments of the ship for the courtesy and consideration which were shown us while onboard. As usual, because of my close contact with them, I wish to express my appreciation of the professionalism exhibited by the deck and survey departments. These are qualities we have come to expect from the Discoverer; consequently, they are easy to overlook.

TABLE I

CM= current meter

PG= tide gauge

ST= sediment trap

N= nephelometer

<u>Mooring</u>	<u>Position</u>	<u>Depth</u>	<u>Instrumentation</u>	<u>Comments</u>
C1	59 ⁰ 10.8' 153 ⁰ 18.0'	42m	2CM, 2S7	Recovered ST did not work
C2	59 ⁰ 13.6' 153 ⁰ 07.6'	64m	2CM	Recovered
C3	59 ⁰ 24.2' 152 ⁰ 53.2'	59m	2CM	Recovered
C4	59 ⁰ 16.9' 152 ⁰ 54.0'	84m	2CM, 2S7, 1PG	Recovered ST did not work
C5	59 ⁰ 09.9' 152 ⁰ 38.3'	128m	3CM	Recovered
C6	59 ⁰ 18.0' 152 ⁰ 38.3'	71m	2CM	Recovered
C7	59 ⁰ 19.1' 152 ⁰ 11.8'	71m	2CM	Float and upper meter lost
C8	59 ⁰ 02.5 152 ⁰ 03.6	191m	3CM	Float and upper meter lost
C9	58 ⁰ 47.3' 152 ⁰ 16.3'	122m	3CM, 1PG	Still at original location
C10	58 ⁰ 30.2' 153 ⁰ 11.6'	170m	3CM, 1PG	Recovered
C11	59 ⁰ 33.8' 151 ⁰ 51.8'	40m	1CM, 2ST, IN	Position is 1 n m from original radar fix, not recovered. Chart 16645
K6A	57 ⁰ 13.4' 152 ⁰ 26.0'	75m	2CM	Recovered
K7A	57 ⁰ 03.4' 152 ⁰ 18.0'	80m	2CM	Recovered
K8A	57 ⁰ 07.0 152 ⁰ 45.0'	150m	3CM, 1PG	Recovered

TABLE I (cont'd)

<u>Mooring</u>	<u>Position</u>	<u>Depth</u>	<u>Instrumentation</u>	<u>Comments</u>
K9A	57 ⁰ 00.6' 152 ⁰ 36.9'	158m	3CM, 1PG	Recovered
K10A	56 ⁰ 51.1' 152 ⁰ 26.0'	154m	2CM, 1PG	Recovered
K11A	56 ⁰ 01.9' 155 ⁰ 07.8'	60m	1CM	Recovered
K12A	55 ⁰ 59.6' 156 ⁰ 17.8'	213m	2CM, 1PG	Recovered
K13A	56 ⁰ 20.5' 156 ⁰ 50.4'	112m	2CM	Recovered
MI-A	55 ⁰ 47.4' 158 ⁰ 39.0'	71m	1CM, 1PG	Recovered, marker deployed prematurely
MI-B	55 ⁰ 25.1' 157 ⁰ 58.8'	110m	3CM, 1PG	Recovered-marker as above
MI-C	54 ⁰ 54.4'	250m	2CM, 1PG	Not recovered, possibly at original location *
MI-D	54 ⁰ 45.6' 157 ⁰ 31.4'	118m	2CM, 1PG	Recovered, marker as in A & B

* Marker for MI-C most likely deployed prematurely.

TABLE II

CTD stations from the PMEL Grid

337 through 346

332, 326, 324, 320

144 through 150

127 through 135

114 through 119

97 through 105

81 through 89

27 through 33

2 through 7

38 through 49

23, 17, 11, 25, 19, 13

549 through 570 CTD and weather problems (terminated work for the day)

600 through 611

623 through 616

634 through 640

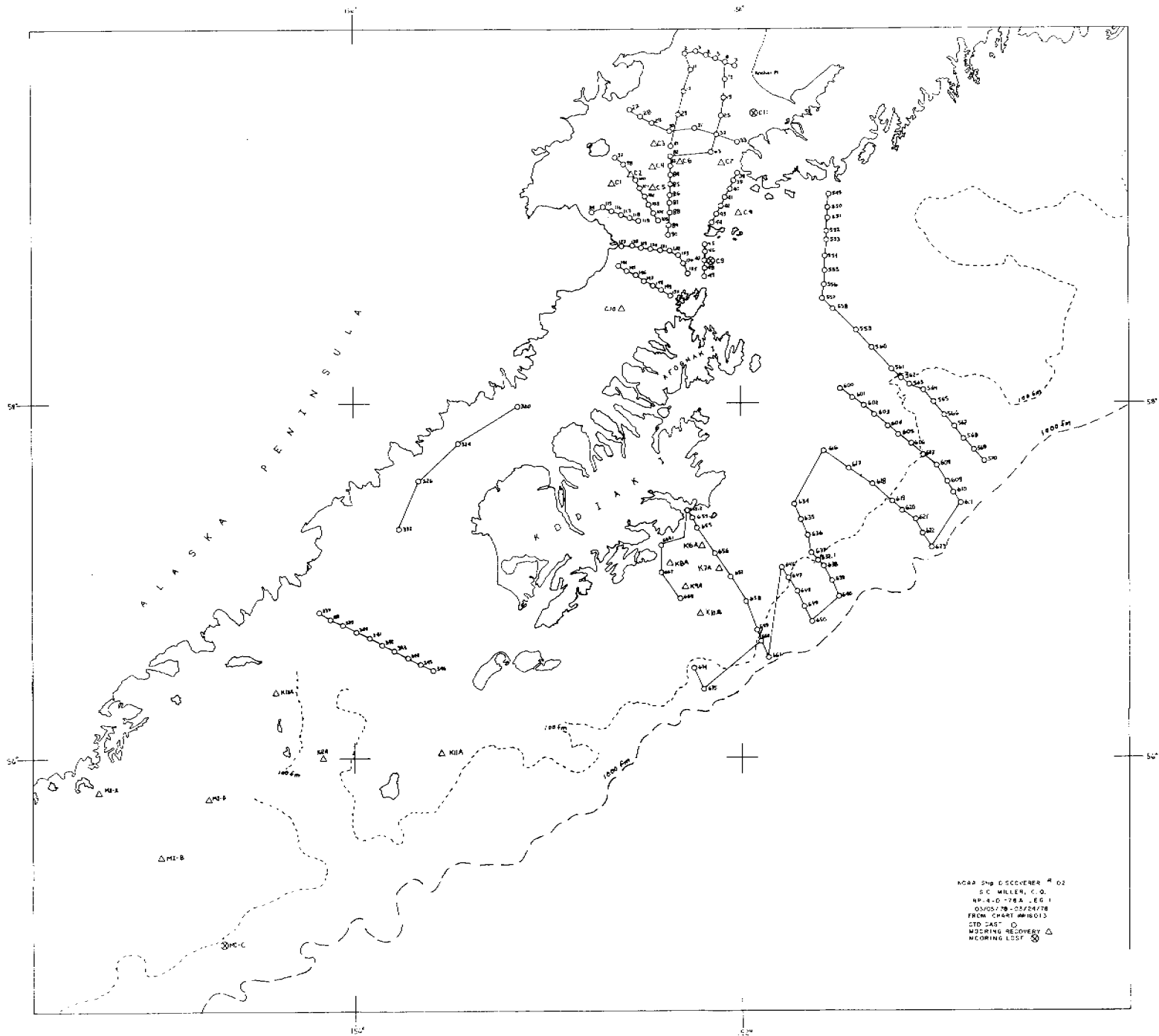
650 through 646

661 through 655

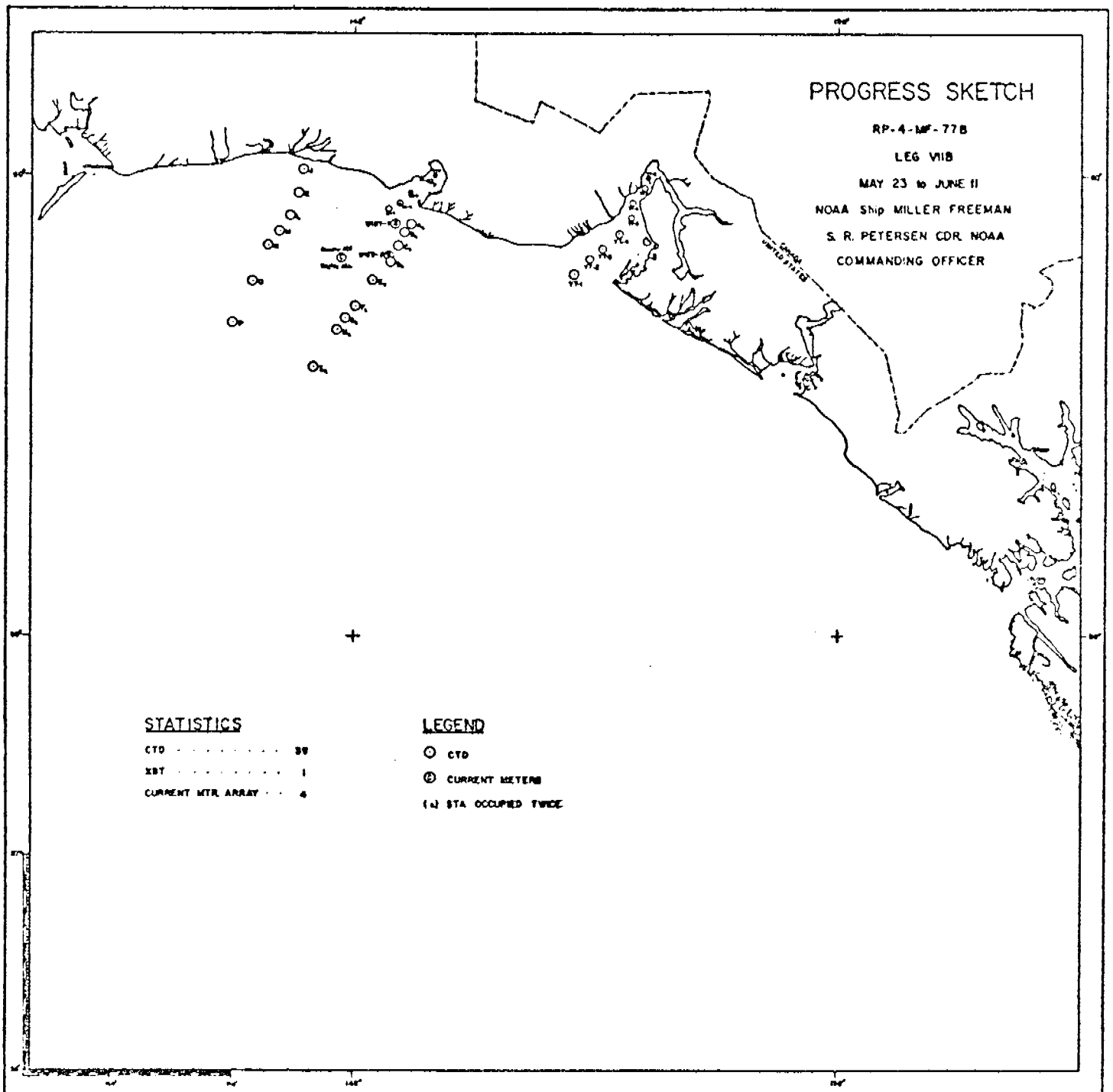
655.1 and 655.2 in Ugak Bay

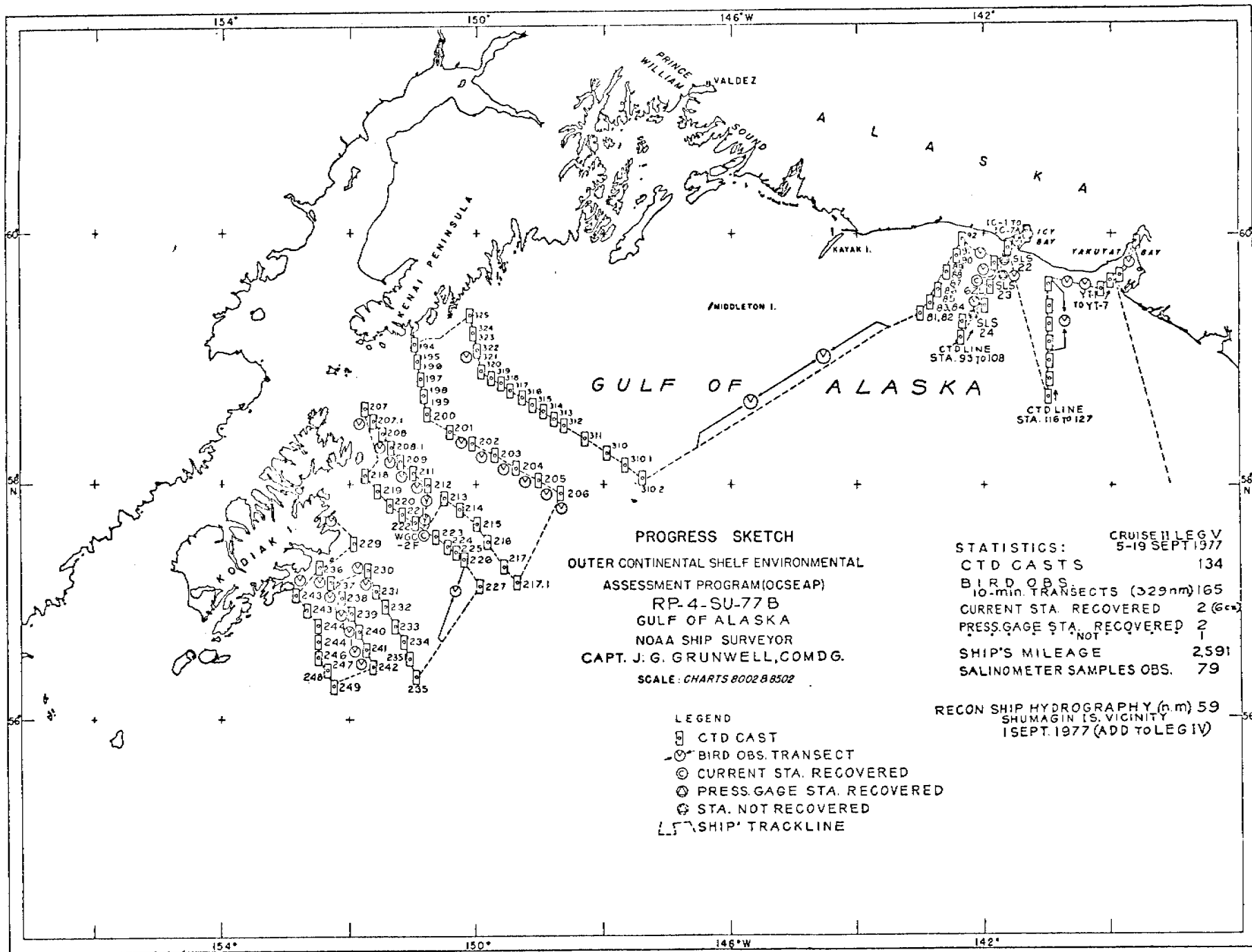
667.1 in Kiliuda Bay - mouth

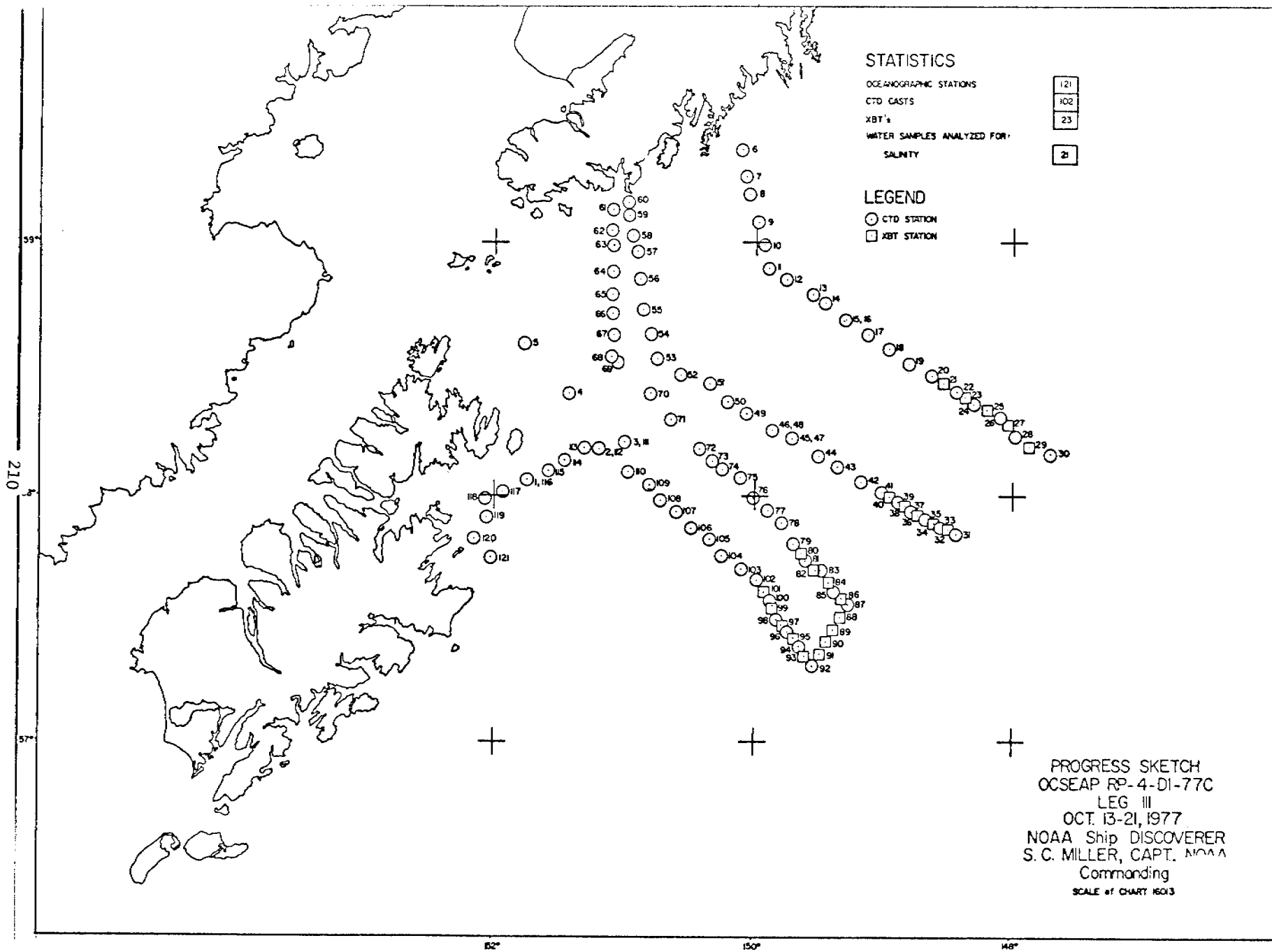
667, 669, 633, 632, 631

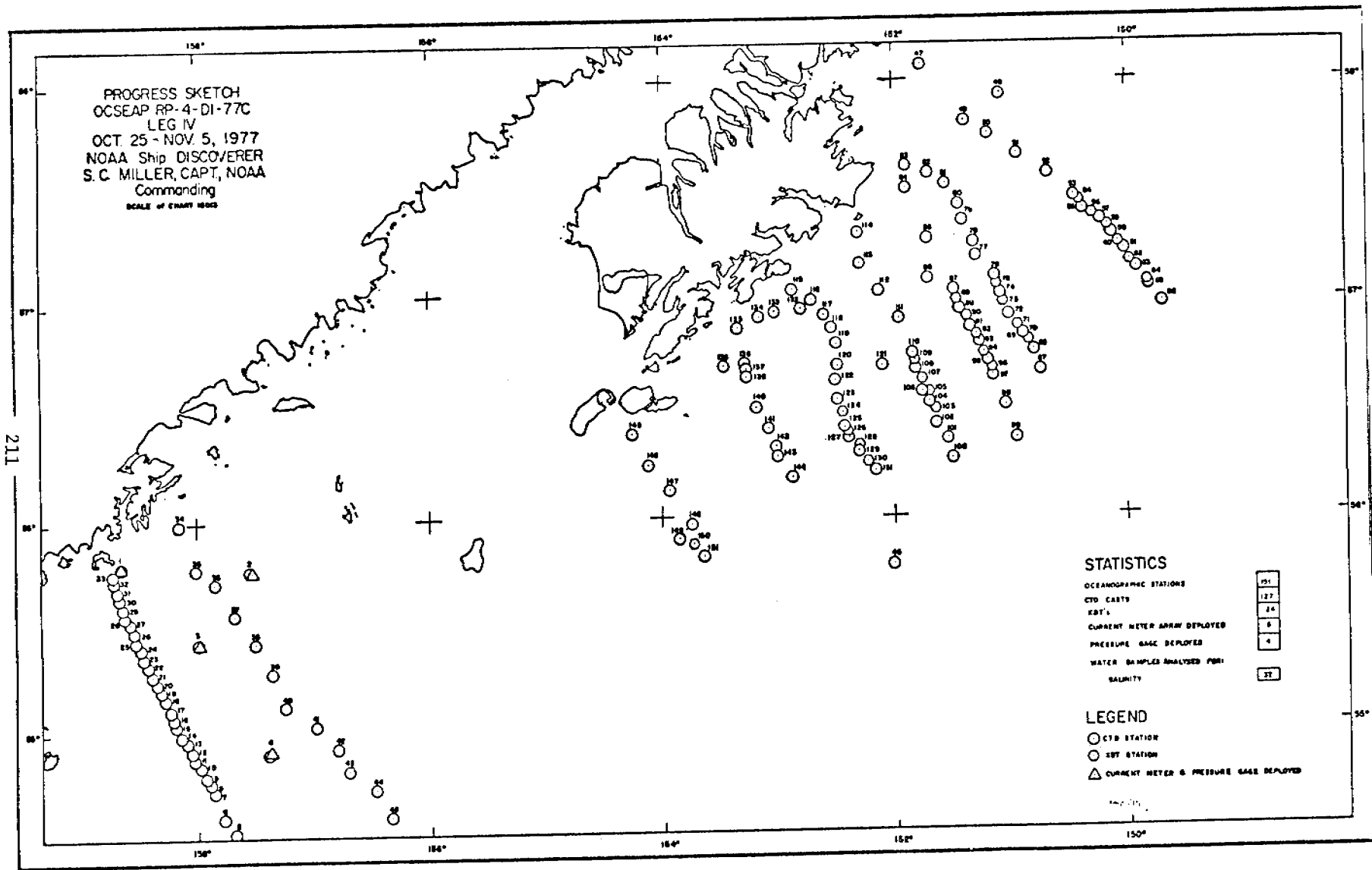


Appendix 2: Data acquisition (April 1977 to 31 March 1978)
 CTD Data Collected. Note: CTD data collected
 during March 1978 is included with cruise reports.
 (see Section IX, Appendix 1)









Current Meter and Pressure Gage Moorings during report period.

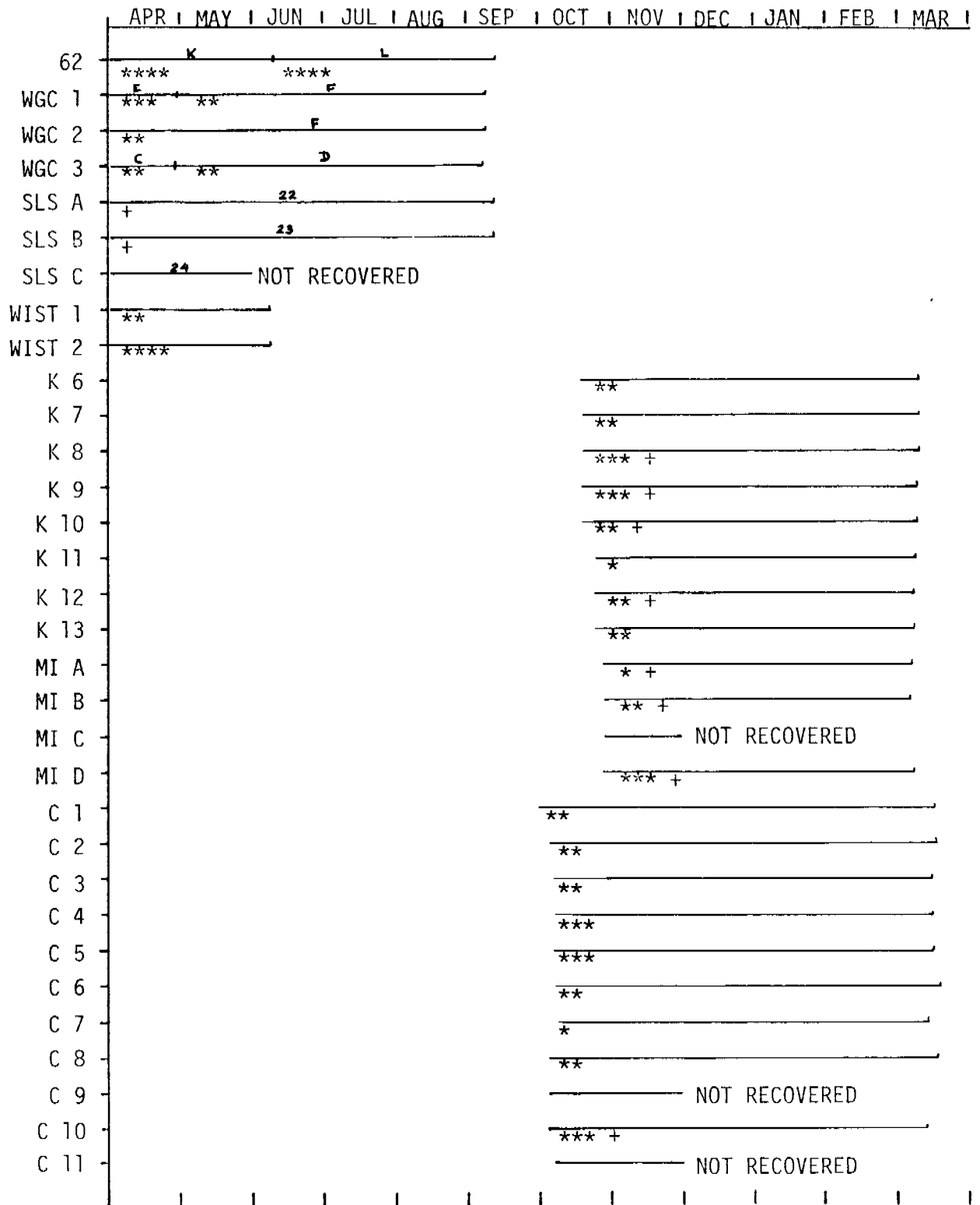
Mooring Locations
1 April 1977 - 31 March 1978

<u>Station Designation</u>	<u>Latitude (N)</u>	<u>Longitude (W)</u>
62	59 38.3	142 06.9
WGC 1	54 03.8	163 05.8
WGC 2	57 34.3	150 49.6
WGC 3	55 12.0	156 57.3
SLS A	59 47.4	141 39.5
SLS B	59 40.6	141 41.2
SLS C	59 21.9	142 09.7
WIST 1	59 47.5	141 36.7
WIST 2	59 39.9	141 40.6
K 6	57 13.4	152 26.0
K 7	57 03.4	152 18.0
K 8	57 07.0	152 45.0
K 9	57 00.6	152 36.9
K 10	56 51.1	152 26.0
K 11	56 01.9	155 07.8
K 12	55 59.6	156 17.8
K 13	56 20.5	156 50.4
MI A	55 47.4	158 39.0
MI B	55 25.1	157 58.8
MI C	54 54.4	157 21.5
MI D	55 45.6	157 31.4
C 1	59 10.8	153 18.0
C 2	59 13.6	153 07.6
C 3	59 24.2	152 53.2
C 4	59 16.9	152 54.0
C 5	59 09.9	152 56.3
C 6	59 18.0	152 38.3
C 7	59 19.1	152 11.8
C 8	59 02.5	152 03.6
C 9	58 47.2	152 16.3
C 10	58 30.2	153 11.6
C 11	59 34.9	151 52.3

GULF OF ALASKA

1 APR 1977 - 31 MAR 1978

MOORING DEPLOYMENT AND RECOVERY SUMMARY



* Represents one current meter
 + Represents one pressure gauge

Station locations are on the following page.

FOURTH ANNUAL OCSEAP REPORT

Alaska Numerical Modeling

J. Galt

J. Overland

R. Stewart

C. Pease

M. Hitchman

Pacific Marine Environmental Laboratory
National Oceanic and Atmospheric Administration
Environmental Research Laboratories

3711 15th Ave., NE
Seattle, Washington 98105

Contract Number: R7120845
Research Unit : 140
Period : 4/1/77 - 3/32/78
Number of Pages: 111

15 May 1978

TABLE OF CONTENTS

I. Summary

II. Introduction.

III. Present Status

 A. Diagnostic Model Development.

 B. Diagnostic Model Utilization.

 C. Development of the General Trajectory Model

 D. Environmental Disk Development.

 E. Meteorological Model Calibration and Synthesis
 of Meteorological Program Observations.

 F. Development of Regional Wind Climatologies for
 Application to the Spill Trajectory Model

 F1. Development of Objective Techniques for Analyzing
 Regional Wind Climatologies

 F2. Subjective Weather Patterns for Coastal Gulf of Alaska. .

 F3. Grid Point Data Subroutines for the Study of Regional
 Wind Climatologies.

IV. Cooperation

V. Conclusions and Needs for Further Study

I. Summary

Numerical modeling of oceanographic and meteorological regimes provides an aide to the understanding of currents and winds in the Gulf of Alaska. Many important components have been developed, including: a diagnostic model for the prediction of surface currents, a regional meteorological model for the prediction of surface winds, and methodologies for simulating the temporal and spatial variations in the velocity fields. Later this year we will interpretate field data and integrate these parts to give estimates of pollutant trajectories for the region with particular emphasis on NEG OA.

The report presents a careful evaluation of the diagnostic model with a formalized approach to the boundary conditions and a restructuring of the model equations. Data sets are identified for applying the diagnostic model to NEG OA. The results of a one dimensional calculation with the regional meteorological model for NEG OA and a system for extrapolating the results to develop typical coastal wind fields are discussed. Results of two methods for arriving at a set of pressure maps which provide a good coverage of the climatology for the Gulf of Alaska are presented. Trajectory model development and schemes for incorporating field data and results from other models into trajectory calculations through an environmental disk system are also discussed. Future work is outlined with the discussion of the current progress on each individual task.

II. Introduction

This report summarizes the work being carried out by the Numerical Studies group at PMEL. The particular sections cover the various activities that have been proposed for FY78 and which are described in some detail in the work statement. This work is part of a multi-year project using numerical modeling and analyses techniques to assist in the interpretation of field data and provide integrated estimates of pollutant trajectories. A number of routines have been developed to represent the dominant processes effecting the advection and spreading of surface pollutants.

This work can be thought of as being carried out in a number of stages. The initial stages all center around identifying the key physical mechanisms operative within the study area. Then the necessary algorithms

must be developed. Once this is accomplished, their numerical and computational characteristics will be carefully explored. In addition, the model sensitivity to input data and boundary conditions must be understood. Once development has carried through this stage it is possible to use the model to study observational data sets. Later work will focus on appropriate documentation and explanation of computational algorithms and model outcomes. As a final point the various model components will be linked together to give a coherent picture which integrates all of the available data and model output.

The object of task A, described in the work statement, is to develop standard computer routines for use with the diagnostic model. These routines are to present strategems for how to approach a new STD or CTD data set for a region. They should include techniques for evaluating boundary conditions and the appropriate graphics routines to present the results. In the past the diagnostic model has been used in a number of different regions for various density data sets. These have been presented thus far in an ad hoc manner with trial and error involved in obtaining appropriate boundary conditions and the subsequent vector flow fields. Our latest work on this task has centered around a formal approach to the mathematics and boundary conditions associated with the diagnostic model. This formalism has led to a decomposition of the model equations and the reconstruction of a total solution based on the absolute linear character of the model. The model physics represented in each component are carefully explored, and an unambiguous technique for establishing the boundary conditions is presented. In addition this work has led to new theories on the

appropriate patterns which can be represented by the diagnostic model. This has led to a better understanding of the number of degrees of freedom within the model. These results have led to not only a better understanding on the relationship between model, output and observational data, but have also provided a vastly more efficient technique for using the model in any particular area and for ultimately storing the model output for use in an environmental library.

The object of task B is to use the diagnostic circulation model to study various data sets from a number of OCS regions. Standard approaches are to be used in treating new data sets and in presenting the output from model runs. In order to accomplish this task, data sets which look like they can be profitably explored using the diagnostic model must be identified. Thus far work on this task has led to the compilation and identification of existing data sets. A preliminary choice of NEGOA data sets has been made. Future work will carry out circulation studies on all of these sets and create as comprehensive a picture as possible of circulation fields for the NEGOA region.

Task C, the development of a general trajectory model, has as its goal the development of a spill trajectory model that presents, in graphic form, the results of advective, diffusive and weathering data for surface oil. This program is basically an integration routine that combines the advective effects from the diagnostic model results with the wind drift effects from the regional meteorological model and algorithms representing weathering and beaching processes. The model development calls for the use of a PDP 11/34 computer and an attached graphics terminal. The routines for handling the data from the component models will be developed. In this report the status of the general trajectory model is discussed along with estimates for its completion.

Task D is to develop an environmental disk library. The goal of this task is to design and implement a standardized environmental data library system for use with the oil spill trajectory model. Contract work this year calls for the development of a prototype library for the NEGOA region. The environmental library stands as an interface between the output from various model components and the general trajectory model. A directory that outlines environmental data that is available for a particular region and a file retrieval system for extracting the model results for any particular trajectory scenario will be included. Routines must be documented and keying strategies must be developed that allow the library output to represent regional current and wind fields. A status report on the conceptual design and progress of the environmental library system is presented in this report.

Task E involves the use of the meteorological model to investigate local wind fields and predict small scale wind patterns from large scale pressure data. For each region that is to be studied, the model must be configured to represent local terrain. Test runs will be carried out to determine the model's general sensitivity to the region and to the input data. Model runs will be compared to observational results from the field meteorological experiments. Their dominant weather patterns must be investigated to provide model wind fields for the local region. Primary emphasis on this study is focused on the NEGOA region, but preliminary studies have begun on both the Kodiak and Lower Cook regions. A discussion of research and representative model domains is presented in this report.

The purpose of task F is to develop a methodology that will allow us to simulate the time and space varying wind fields in a fashion that takes advantage of both the improved empirical data base and our improved theoretical understanding of winds in the coastal region. The main idea behind our approach is that if we can limit the problem to modeling a limited number of wind conditions, then it is possible to analyze these cases fairly well. Task F deals specifically with cutting the job down to a manageable size. The first approach is a review of the existing literature on the classification of weather systems in the Alaskan region. Two studies, Putnins (1966) and Sorkina (1963) have been found that deal with this problem. These papers have been reviewed and their conclusions applied to our problem. Section F summarizes our findings on this subjective approach. The second approach is an objective analysis based on the method of factor analysis. This is a purely statistical approach based on the analysis of historical records. This method is discussed in detail in section F1. We anticipate combining the complementary results of F1 and F2 and completing task F in the near future. Some further development of the objective technique is also planned prior to submission of our final report.

Task G was to develop objective techniques for validation of the diagnostic model. The object of this task was to develop techniques of estimating errors and appropriate measures of success for use with the diagnostic model in simulating currents. Since the research output from this task has been incorporated into the work carried out under both tasks A and F, this will not be reported individually in this report.

This report summarizes the progress made towards completion of work unit 140. It should be understood that this work is continuing and results should be considered of a preliminary nature. Our purpose in writing this annual report is to provide OCSEAP planners and investigators with information on our work in sufficient detail that they can better understand our techniques and prospective products. We believe that the analysis and results to date are correct, but caution that this is not to be considered as a final report. In our view the material will not be ready for publication or citation until we've reviewed it for a final report.

From a conceptual point of view most of the model requirements proposed for regional trajectory analysis have been developed. In many instances they have been compared to observational data and thoroughly studied for sensitivity to numerical or computational problems. Our present research efforts are focused on the development of strategies for using these models. In particular we wish to understand not only the relationships between model parameterizations and input data, but also the techniques that can be used most profitably to insure that the statistical nature of the environmental data is appropriately reflected in the model output. Once this has been accomplished, we will be able to use the models to represent realistic environmental conditions. These representations include not only the effects of mean states, but also the correlations which are needed to represent dispersive or mixing processes. Final efforts will focus on integrating model components together and synthesizing unified trajectory estimates.

A. Diagnostic Model Development

In this report we will look into the formulation of the boundary conditions and certain linear aspects of the diagnostic model equations. In contrast to past reports on the diagnostic model which all concentrated on studying the circulation in a particular area, this report will have a more formal approach and look at the decomposition of the equations into modes. We will discuss the implications of various boundary condition specifications in terms of these modes.

The basic derivation of the governing equations of the diagnostic model were presented by Galt (1975) and they have been described in detail in other places. Using the diagnostic model to study a particular area raises questions that are not directed at the model formulation, but at the choice of boundary conditions. The model formulation is a simple combination of geostrophic and Ekman modes. The choice of boundary conditions for the diagnostic model are complicated by two factors. The first factor is that the model equations are second order due to a term which is small compared to the other terms in the dynamic balance. Because of this term, the boundary conditions required to solve the equation come close to overspecifying the flow. As a result, spurious solutions are possible which are related to this particular term. A second difficulty associated with the boundary conditions is a result of the model being used in open ocean regions. That is, the model usually has a large segment of boundary which is open ocean, and the solution must specify the flow all around the model edge. This flow is generally unknown so various approximations are made and the choice of these then leads to potential ambiguities in the solutions. The

purpose of this discourse is to review the various approximations used to obtain boundary conditions in the past and to discuss possible ways of specifying a less arbitrary formulation for future studies.

Typically, whenever the diagnostic model is applied to a coastal region one edge of the model lies along the coastline, another edge runs offshore through deep water, and two lateral boundaries connect these from deep water across the shelf to the shore. For a variety of reasons the two boundaries which run across the shelf introduce problems. The coastal boundary has a strong physical constraint associated with it which makes the formulation of the boundary conditions along the coast relatively easy. The physical statement of the problem is that there is no flow through the coast. Along this coastal boundary four potential modes of flow are allowed: baroclinic and barotropic geostrophic components and Ekman modes at the surface caused by wind stress and at the bottom caused by frictional drag. Setting the four of these to a net sum of zero involves a mixed Neumann type (Courant and Hilber, 1962) boundary condition. The offshore boundary is typically located in deep water, a region where the classical dynamic height approximations tend to be valid. As a standard, we have simply imposed a dynamic height condition that allows for the flow to be zero at some fixed level, typically 1200 meters. To impose this boundary condition, we simply balance the barotropic and baroclinic geostrophic modes such that there is no flow below this depth.

Now consider the two model boundaries which run normal to the coast. When we first started using the model we assumed that winds along the coast tended to set up the sea surface or push it down across the continental shelf in a mechanism that was suggested by Beardsley and

Butman (1974). By assuming that the sea surface elevation across the shelf was represented by a simple wind dependent hinge, we were able to obtain solutions for the NEGOA region. The results of these initial studies appeared in the circulation study on the continental shelf off the Copper River Delta, Galt (1976). A moderate refinement on this study was to specify the inflow boundary condition or the flow along the eastern boundary to be a simple hinge, but to adjust the left hand boundary by hand so that a smoother set of streamlines was obtained along the outflow or western boundary. This was an admittedly ad hoc approach to the problem, but the result did show some improvement and flow patterns from this study were presented by Galt and Pease (1977) where this method was used to simulate drift trajectories for a number of different wind conditions.

When the diagnostic model was applied to the area around Kodiak, a problem arose with the use of the simple hinge concept. In the Kodiak region the topography is so complex that a simple hinge approach will not reflect the complex circulation that occurs over the many banks and canyons that cut across the shelf. To handle the boundary conditions at Kodiak we made use of the fact that a reduced set of model equations defined characteristics to a first order partial differential equation. These characteristics are very closely related to f/h contours where f is the coriolis term and h is the depth. Along these contours the surface elevation is related by a simple form of the differential equation. Using this method we then generated a set of boundary conditions such that the inflow boundary was specified as a simple wind dependent slope and the outflow boundary was related to the inflow boundary using the characteristics that were defined by the simplified model equations.

This approach led to circulation patterns which could then be related to wind conditions. Using this parameterization, a series of different cases were investigated and the predicted currents from the model were then compared to the scatter that was seen in current meter records from four different locations in the Kodiak area. The results of these studies were presented at the OCSEAP Physical Oceanographers' PI meeting in November, 1977 and at a recent AGU meeting (Galt, 1977). This characteristic technique was also used in the NEGOA area and the results of these studies indicated the existence of several distinct domains within the NEGOA area that seem to be strongly related to each other. In particular the independent circulation regime off Montague Island was compared to studies which Royer reported on at the OCSEAP meeting. A final improvement in the combination hinge and characteristic technique for determining boundary conditions was the introduction of a sea surface slope inversely proportional to depth to replace the hinge. This meant that steeper sea surface slopes were obtained in shallower water along the coast by the same wind. This tended to give a more realistic appearance to the current patterns and these techniques were applied in the Kodiak and NEGOA regions.

A characteristic of these techniques is that they were applied to specific regions to obtain flow patterns for particular studies. They are also all derived in a heuristic way, which is typically labor intensive. The boundary conditions were tried, and if they did not give reasonable results alternate formulations were used. Although these empirical results give interesting current patterns, and in some cases appear to accurately reflect direct observations, there is still some

reason to be skeptical of the results. In particular we would like to derive techniques which are location independent and reflect a more solid coupling of the fundamental physics to the model. What we are trying to discover is a more formal way to approach the open boundary problem as it relates to the diagnostic model.

In the next section we will discuss the decomposition of the model equations into a purely baroclinic mode, a minimum barotropic mode needed to satisfy continuity, and a barotropic wind set up mode. These various modes will be related to the kinds of data needed to solve the respective problems and to the number of degrees of freedom that are expected in the solutions. Following the decomposition of the equations we will discuss the types of boundary conditions which will be imposed on each of the separate modes and how these can be combined to give a more general solution that reflects the given density fields as well as the geometry of the specific region that is being studied. From these discussions we will derive a consistent approach for determining the boundary conditions in a general study area. In addition we will be able to determine the flow patterns that are likely to result from these particular sets of boundary conditions and relate them to observational data that can be obtained from CTD measurements and current meter data. To the extent that observational data does not fit the modular decomposition that is predicted by the model, we will also derive an objective way of determining whether the assumed boundary conditions are correct for the region or not.

1. Decomposition of the Diagnostic Model

The diagnostic model equations are linear. This suggests that it

is possible to decompose the governing equations into a number of different parts, each of which can be evaluated individually and then added up to give the total solution. The impetus for decomposing the model equations has come from two different areas. First of all, the simple hinge type boundary conditions that were used in a number of earlier studies led to a difficulty when the wind velocity degenerated to zero. Under these conditions, the sea surface slope across the shelf also went to zero, thus, there was no barotropic transport across these particular boundaries. Nonetheless, the density field which was already specified gave a baroclinic transport that could not be balanced without invoking some rather exotic circulation patterns in the bottom Ekman mode. These results were clearly wrong indicating that there was some minimum barotropic mode that had to exist to satisfy continuity in the presence of a non-uniform density field. A second reason for suggesting a decomposition of the model equations became apparent when we started looking at the number of degrees of freedom to be expected in the general class of solutions. Since the equations are linear, the number of degrees of freedom to be expected must be related to the number of degrees of freedom that are allowed in specifying the boundary conditions. The hinge formulation introduced a single wind parameter, and therefore any similarity type distribution of sea surface elevation across the shelf would always lead to a single pattern in the flow. In order to better understand these patterns, it was thought that it would be useful to break the boundary conditions into inhomogeneous parts related to the density field and a homogeneous and/or similarity part related to the set up by the wind. To see that this is possible,

we may begin by looking at the diagnostic model equation.

$$N_2 \nabla^2 \xi - J(\xi, d) + N_1 N_2 \nabla^2 \alpha - N_1 J(\alpha, d) - k \cdot \nabla x \tau = 0$$

This can be separated into two parts such that

$$\xi = \xi_1 + \xi_2$$

where these new variables satisfy the following equations:

$$N_2 \nabla^2 \xi_1 - J(\xi_1, d) + N_1 N_2 \nabla^2 \alpha - N_1 J(\alpha, d) = 0$$

(which we will refer to as the density driven response)

$$N_2 \nabla^2 \xi_2 - J(\xi_2, d) - k \cdot \nabla x \tau = 0$$

(which we will refer to as the wind driven response).

Next we must consider the boundary conditions needed to solve these equations. To do this we will look at a typical model domain consisting of a coastline, shelf and deeper offshore section (see figure 1). The various segments of the boundary can be described in the following manner:

Segment a) This coastline boundary satisfies the physical condition that the net flux through the coast must be zero. To do this we simply sum the barotropic, baroclinic, surface Ekman and bottom Ekman modes in a non-dimensional form (Galt, 1975).

$$-d \frac{\partial \xi}{\partial s} + N_1 \left(\frac{\partial \Delta}{\partial s} + \alpha \frac{\partial d}{\partial s} \right) - \tau_s$$

$$+ N_2 \left(\frac{\partial \xi}{\partial n} - \frac{\partial \xi}{\partial s} \right) + N_1 N_2 \left(\frac{\partial \alpha}{\partial n} - \frac{\partial \alpha}{\partial s} \right) = 0$$

where \bar{n} is a unit vector normal to the coast pointing offshore and \bar{s} is a unit vector given by $\bar{k} \times \bar{n} = \bar{s}$, where \bar{k} is positive up. These represent mixed Neumann type boundary conditions involving both normal and tangential derivatives of the dependent variable.

Segment b) This offshore or deep water boundary is assumed to be deep enough so that the concepts appropriate to classical dynamic heights can be used. To implement this in the diagnostic model we simply set the sea surface elevation at any station deeper than the level of no motion to:

$$\xi = -N_1 \alpha$$

Segments c & d) These cross shelf boundary regions require special attention. By specifying the surface elevation along this boundary, we supply Dirichlet type boundary conditions and determine the barotropic flow normal to the boundary. These nonhomogeneous conditions have been approximated in a variety of ways and to understand the rationale behind each potential problem we must look into these in some detail.

Basically the sea surface's departure from a level surface is caused by both thermohaline forcing and wind forcing. From a conceptual and computational point of view it is useful to separate these into a number of independent cases or modes. However, first we can outline the problems that are likely to occur if the boundary values are incorrectly specified.

In the model equation geostrophic and Ekman flow are both allowed and must be balanced to maintain continuity of mass. Moreover, around

the boundary of the model most of the flow is determined by the independent variables (density, wind stress) or by the boundary conditions. In particular the density data determines the baroclinic/geostrophic flow through the boundary; the wind stress determines the surface Ekman transport through the boundary; and, the specification of the sea surface elevation determines the barotropic/geostrophic transport through the boundary. If these do not balance so that there is a no net flow through the boundary, the model will establish a secondary flow in the bottom Ekman layer to complete the balance. To do this a strong barotropic current must flow parallel to the boundary. To get a better understanding of how this takes place, we may look at the following simple example (see figure 2)

model domain:

$$0 \leq x \leq l$$

$$0 \leq y \leq m$$

depth: $d = -(2 - \frac{y}{m})$

α -field: $\alpha = ax + by$

wind field: $\tau = 0$

Substituting these into the governing equation gives:

$$N_2 \nabla^2 \xi + \frac{1}{l} \frac{\partial \xi}{\partial x} = -N \frac{a}{m}$$

and boundary conditions will specify that flow enters from the right and exits from the left of the domain, i.e.;

$$\begin{aligned} \xi = y & \quad x = 0 & ; & \quad 0 \leq y \leq m \\ & \quad x = l & ; & \quad 0 \leq y \leq m \end{aligned}$$

$$\xi = 0 \quad 0 \leq x \leq l; \quad y = 0$$

$$\xi = y \quad 0 \leq x \leq l; \quad y = m$$

To solve this we will use the homogeneous part of the equation to satisfy the non-homogeneous part of the boundary conditions. Thus

$$\xi = \xi' + \xi''$$

where ξ' satisfies

$$N_2 \nabla^2 \xi' + \frac{1}{l} \frac{\partial \xi'}{\partial x} = 0$$

subject to the boundary conditions given above. The solution for this part of the decomposition is easily seen to be:

$$\xi' = y$$

The remaining part of the solution will satisfy the full non-homogeneous equation subject to the homogeneous boundary conditions, i.e.;

$$N_2 \nabla^2 \xi'' + \frac{1}{l} \frac{\partial \xi''}{\partial x} = -N \frac{a}{m}$$

$$\xi''(0,y) = \xi''(l,y) = \xi''(x,0) = \xi''(x,m) = 0$$

This differential equation and boundary conditions are well known in the field of oceanography as they are identical to the one proposed by Stommel (1949) to represent general ocean circulation. For this secondary barotropic flow the surface elevation will also be streamlines (see figure 3).

This pattern shows a strong western boundary current analogous to general ocean circulation with the depth gradient taking the place of the β term and the baroclinic/bottom interaction term replacing the wind stress curl. Several general characteristics of the model can be demonstrated from this simplified case.

As previously stated the secondary flow is the result of a continuity imbalance. The basic barotropic mode $\xi' = y$ is nondivergent over the entire domain. The baroclinic forcing on the other hand is not. The density field will induce a flow with both north and west components, which carries water from deep to shallow regions. This requires a secondary flow that results in a southerly drift and/or divergence in the bottom Ekman layer. We can easily see that this clockwise flow will support a bottom Ekman layer that transports water out of the domain, primarily through the strong western boundary current region. This strong asymmetry is another general characteristic of the secondary flow generated by the model. The coefficient N_2 is small and as a result the leading and highest order term typically will not contribute significantly to the balance except in boundary regions where the derivative in the dependent variable can become large (Cole, 1968). For most of the interior and right hand boundary (to the right when facing from deep to shallow) regions the primary balance within the model is between the $J(\xi, d)$ term and the forcing terms. From this we may deduce two additional points. First as the bottom friction ($\approx N_2$) becomes smaller the western boundary current becomes more narrow and more intense. Secondly, for most of the model domain, the solution is totally dominated by the right hand boundary conditions and first order reduced equation. The intense western boundary current is clearly an artifact of imposing additional boundary conditions, required by the second order

equation, but redundant to the dominant first order dynamics. This then explains the problem of picking appropriate boundary values across the c and d regions. They are coupled and in general cannot be set independently without expecting to get large, extraneous secondary flows.

With the problem demonstrated, we may now consider several techniques that can be applied in a systematic way to determine appropriate boundary values and define the degrees of freedom, or independent patterns that can be expected from the model.

We will begin by considering the density driven response in the model, i.e.;

$$N_1 \nabla^2 \xi' - J(\xi, d) + N_1 N_2 \nabla^2 \alpha - N_1 J(\alpha, d) = 0$$

To better understand how to proceed we will look only at what we know to be the dominant physics, i.e., the first order equation that remains when the bottom friction is negligible.

$$J(\xi, d) + N_1 J(\alpha, d) = 0$$

This corresponds to simple geostrophic flow over variable bathymetry.

Consider a triangular region of the ocean in which the depth, the sea surface elevation and the vertical integral of the density can be approximated as linear functions of x and y. Thus if we define

$$\alpha = \int_d^0 \rho \, dz$$

we may write

$$\begin{aligned}\alpha &= A_1\phi_1 + A_2\phi_2 + A_3\phi_3 && \text{alpha field} \\ d &= D_1\phi_1 + D_2\phi_2 + D_3\phi_3 && \text{depth} \\ \xi &= Z_1\phi_1 + Z_2\phi_2 + Z_3\phi_3 && \text{surface elevation}\end{aligned}$$

where

$$\begin{aligned}\phi_1 &= a_1x + b_1y + c_1 \\ \phi_2 &= a_2x + b_2y + c_2 \\ \phi_3 &= a_3x + b_3y + c_3\end{aligned}$$

are the interpolating weight factors or shape functions associated with the triangle in question. (Zienkiewicz, 1971)(See figure 4).

The gradient in the α -field and thus the gradient in the bottom pressure will be:

$$\begin{aligned}\vec{\nabla}\alpha &= \left(\frac{\partial\alpha}{\partial x}\right)\vec{i} + \left(\frac{\partial\alpha}{\partial y}\right)\vec{j} \\ &= (A\cdot a)\vec{i} + (A\cdot b)\vec{j}\end{aligned}$$

Where the indicated three component vectors A , a and b are known from the geometry and the density data given at the vertices. For the moment we will refer to $g\nabla\alpha$ as the baroclinic component of the pressure gradient. Given this assumption we may define an internal velocity component, or the velocity at the bottom due to the density variations as:

$$\begin{aligned}
\vec{V}_I &= \left(-\frac{g}{f\rho} \frac{\partial \alpha}{\partial y}\right) \vec{i} + \left(\frac{g}{f\rho} \frac{\partial \alpha}{\partial x}\right) \vec{j} \\
&= \frac{g}{f} (\bar{k} \times \bar{\nabla} \alpha) \\
&= \left(-\frac{g}{f\rho} (A \cdot b)\right) \vec{i} + \left(\frac{g}{f\rho} (A \cdot a)\right) \vec{j}
\end{aligned}$$

This velocity component will be rotated 90° to the left of $\bar{\nabla} \alpha$.

We may now look at the depth gradient which can be written as:

$$\begin{aligned}
\bar{\nabla} d &= \left(\frac{\partial d}{\partial x}\right) \vec{i} + \left(\frac{\partial d}{\partial y}\right) \vec{j} \\
&= (D \cdot a) \vec{i} + (D \cdot b) \vec{j}
\end{aligned}$$

In order to satisfy the continuity requirement that there is no flow through the bottom we must require that the net horizontal bottom flow is along an isobath. Thus there is a minimum barotropic mode that must accompany the internal velocity V_I unless $\bar{\nabla} \alpha$ and $\bar{\nabla} d$ are co-linear. This minimal external or barotropic bottom velocity component will be parallel to the depth gradient and be given by (Galt, 75 - eq. 21)

$$\begin{aligned}
\bar{V}_{EM} &= -\left(V_I \cdot \frac{\bar{\nabla} d}{|\bar{\nabla} d|}\right) \frac{\bar{\nabla} d}{|\bar{\nabla} d|} \\
&= \frac{g}{f [(D \cdot a)^2 + (D \cdot b)^2]} \left[(A \cdot b)(D \cdot a)^2 - (A \cdot a)(D \cdot b)(D \cdot a) \right] \vec{i} \\
&\quad + \left[(A \cdot b)(D \cdot a)(D \cdot b) - (A \cdot a)(D \cdot b)^2 \right] \vec{j}
\end{aligned}$$

This can be related to the sea surface elevations as follows:

$$\begin{aligned}
\frac{\partial \xi}{\partial x} &= \frac{f}{g} (V_{EM})_{\vec{j}} = (z \cdot a) \\
\frac{\partial \xi}{\partial y} &= \frac{f}{g} (V_{EM})_{\vec{i}} = (z \cdot b)
\end{aligned}$$

or

$$(z \cdot a) = \frac{1}{\rho} \frac{[(A \cdot b)(D \cdot a)(D \cdot b) - (A \cdot a)(D \cdot b)^2]}{[(D \cdot a)^2 + (D \cdot b)^2]}$$

$$(z \cdot b) = \frac{-1}{\rho} \frac{[(A \cdot b)(D \cdot a)^2 - (A \cdot a)(D \cdot b)(D \cdot a)]}{[(D \cdot a)^2 + (D \cdot b)^2]}$$

and with no loss of generality we can set

$$z_1 = 0$$

These three equations can now be solved for the coefficients z_1 , z_2 , and z_3 to find the minimum barotropic mode.

It can be seen that the minimum barotropic mode is equivalent to specifying the component of the sea surface slope along an isobath, i.e., it determines the barotropic velocity normal to the depth contours. To think of the problem more graphically, the three conditions above are equivalent to placing vertex 1 of the triangle in the $x y$ plane and then rotating it around the ∇d axis until the slope is sufficient to give V_{EM} (see figure 4).

Thus far we have determined only one component of the sea surface slope. It is also possible to rotate the solution plane for the sea surface elevation around the axes formed by the isobath. This can be done independently of the rotation around ∇d , and physically it will result in a barotropic current that is parallel to the isobath and thus it has no effect on the continuity balance. It can be seen that this degree of freedom can be used to obtain a solution throughout a region composed of a number of triangular elements connected along an isobath

or characteristic (see figure 5). Specifying a slope for triangle 1 is equivalent to specifying the flow along the isobath and the single boundary condition needed to solve the first order partial differential equation. Triangle 2 can be rotated around the isobath until its two common vertices with triangle 1 match up, i.e., the solution plane for triangle 1 and for triangle 2 are continuous along the common side AB. In a similar manner triangle 3 is rotated around the isobath and matched up along the common side with triangle 2. This process can be carried on through triangles as we follow an isobath or characteristic.

In order to get a better understanding of what is meant by this minimum barotropic mode, it is necessary to look into the physical implications of such a flow. For a single triangle this mode is clearly the barotropic component needed to align the bottom flow with the isobaths. This is an absolute minimum current because any other barotropic currents that are consistent with the density field and bathymetry will have components of the current along the isobath. These other cases would subsequently result in a sea surface slope with higher potential energy. When moving from one triangle to another along an isobath, continuity of flow across the boundary will determine this along isobath component.

The question now becomes: Why should we be interested in a sea surface distribution with minimum potential energy? We may note that in a different context this problem was considered by Wunch (1977). He discussed minimum energy solutions subject to a variety of conservation constraints, but none of his constraints happened to be bottom flow following f/h contours. He did, however, recognize this possibility.

To answer our question in the context of the present problem, recall that during the decomposition of the governing equation the density driven response did not include any wind forcing. Under these conditions the wind set up would relax and the sea surface would tend to decrease to the lowest energy level consistent with the dynamics represented by this component of the equations.

The problem then is to solve the density response partition of the diagnostic model equations, subject to the constraints that the surface elevation should be at a minimum potential energy and that there are no strong currents generated parallel to the boundary. Following this we look for solutions to the wind driven response partition of the problem, assuming homogeneous water and some similarity profile for the wind set up. The linear sum of these two solutions will be the total flow for the diagnostic model problem.

2. Density Driven Response

In this section we will concentrate on the density driven response of the model. This will include the baroclinic mode and the minimum barotropic mode required for continuity. There are several different ways to approach this problem and we will outline three of them. Each represents a somewhat different approach and they correspond to various degrees of mathematical rigor. As one might guess the computational effort required is quite different for each one of these and a comparison of results is of considerable practical interest.

2.1 Minimum potential along characteristics

The coastal boundary segment previously labelled (a) (see figure 1)

must satisfy the no net flux condition. In addition the deep water segment (b) will be represented by dynamic heights assuming a level of no motion on the order of 1000 - 1200 meters. The remaining undetermined boundary values are for the segments (c) and (d) connecting the offshore and coastal regions. To evaluate these we will make use of the reduced equation which we know to represent the dominant physics, i.e.;

$$J(\xi,d) = -N_1 J(\alpha,d)$$

we then proceed as follows:

At each boundary point along these segments the surface elevation is set to an unknown constant c . From this point we will integrate along a characteristic, satisfying the relationship obtained from the above equation:

$$\delta\xi = -N_1 \delta\alpha$$

Once the depth contour, or characteristic, is traced all the way across the model the initial constant is adjusted to yield the minimum potential energy for the surface profile along that path. For a graphical interpretation for each triangle along the isobath see figure 6. The potential energy along this path can be written as:

$$PE_i = \int_0^{\delta s_i} \int_0^{\xi} \rho g z dz ds$$

And this gives

$$PE_i = \int_0^{\delta s_i} \frac{1}{2} \rho g \xi^2 ds$$

where

$$\xi = (\xi_i + c) \left(\frac{\delta s_i - x}{\delta s_i} \right) + (\xi_{i+1} + c) \frac{x}{\delta s_i}$$

which leads to

$$\begin{aligned} PE_i &= (2\xi_i^2 + \xi_i \xi_{i+1} + 2\xi_{i+1}^2) \frac{\delta s_i}{6} \\ &+ (4\xi_i + (\xi_i + \xi_{i+1}) + 4\xi_{i+1}) \frac{\delta s_i}{6} c \\ &+ \frac{5}{6} \delta s_i c^2 \end{aligned}$$

And summing these contributions for each of the triangles connected by the isobath with the understanding that $\xi_1 = 0$, gives:

$$\begin{aligned} \overline{PE} &= \frac{1}{12} \rho g \sum_{i=1}^{\Sigma} \delta s_i (2\xi_i^2 + \xi_i \xi_{i+1} + 2\xi_{i+1}^2) \\ &+ (4\xi_i + (\xi_{i+1} + \xi_i) + 4\xi_{i+1}) c + 5c^2 \end{aligned}$$

And to obtain the minimum value for the potential energy along this path we differentiate with respect to c and equate the result to zero giving:

$$c = \frac{\sum_{i=1}^{\Sigma} (\xi_{i+1} + \xi_i) \frac{\delta s_i}{2}}{\sum_{i=1}^{\Sigma} \delta s_i}$$

Once this is done for each of the points along the (c) and (d) boundaries the interior should give a minimum potential energy surface except for the contribution from the small bottom stress terms. A closer look, however, reveals several unresolved ambiguities and potential degenerate cases.

First of all this minimum potential energy approach will give elevations along segments (c) and (d) relative to other members of this set, but doesn't suggest how to connect these sections to the onshore and offshore segments whose elevations are also only defined relative to other members of their sets. To resolve this problem we have adopted the convention that along the boundary (d) the offshore and onshore segments are connected in a relative position to provide the intervening triangles with just the barotropic component normal to the isobath.

The degenerate cases that must be considered involve places along the boundary where neighboring points are the same depth (characteristic runs along the boundary) or where the boundary point is a local maximum or minimum in the depth (characteristic does not penetrate the model domain). To set boundary values at these points a quadratic interpolation is used that fits a curve through two points on one side of the unknown point and one on the other. This procedure is done from both sides and averaged as shown in figures 7 and 8.

To summarize this procedure, then, we have the following:

- 1) Coastal boundary points set relative to each other using a no net flux constraint.
- 2) Deep water boundary points set relative to each other by assuming level of no motion and using dynamic heights method.
- 3) Cross shelf boundaries set relative to each other by minimizing potential energy along characteristics subject to the reduced form of the density driven equation.
- 4) Coastal and deep water segments linked to cross shelf boundary with minimum flow constraint for the intervening triangles.

5) Degenerate cases are resolved by using interpolation techniques.

Once these steps have been done the complete density driven response is calculated giving a flow field including the effects of bottom friction. This solution can be expected to approximate the minimum potential energy (or most relaxed set up) consistent with continuity considerations, the given density field, and the bathymetry.

2.2 Green's function to minimize regional potential energy

In this section we will derive a technique for obtaining a complete solution to the minimum potential energy, density driven response. To do this we will make use of the complete linearity of the diagnostic model equation.

To demonstrate this we start with the following equation:

$$N_2 \nabla^2 \xi - J(\xi, d) + N_1 N_2 \nabla^2 \alpha - N_1 J(\alpha, d) = 0$$

and consider the following series of problems:

1) The solution to the above equation subject to the following boundary conditions:

- a) no net flux through the coastal segment.
 - b) deep water boundary segment given by dynamic height and assumed level of no motion.
 - c) all of the cross shelf boundary values set to zero.
- 2) The solution to the homogeneous equation:

$$N_2 \nabla^2 \xi - J(\xi, d) = 0$$

subject to the following boundary conditions

- a) no net flux through the coastal segment
- b) all remaining boundary points are set equal to zero except one which is given a unit magnitude.

This problem gives the numerical solution to the Green's function which represents the response of the system to a unit impulse from a particular boundary point. If there is a total of M boundary points along the cross shelf boundary segments we repeat problem two above with each point in turn acting as a source point for the Green's function.

In all we obtain M+1 solutions for each nodal point in the model domain and along the boundaries. After doing this we write the total solution as the following linear sum.

$$\xi^j = \xi_0^j + \sum_{i=1}^M c_i \xi_i^j$$

where the subscript i indicates Green's functions the solution is associated with, the superscript indicates the nodal point value and c_i is the 'as yet' undetermined amplitude associated with each of the Green's functions.

We will now determine the values of the c_i 's such that the potential energy for the total solution is a minimum. To do this we will consider a triangle with vertices l , m , and n and area Δ (see figure 9). With the shape functions ϕ_l , ϕ_m , and ϕ_n we define the surface elevation as:

$$\xi = \xi^l \phi_l + \xi^m \phi_m + \xi^n \phi_n$$

and the potential energy of the surface relative to to a flat surface at zero height (where the integration is over the triangle) is given by

$$\begin{aligned}
 PE &= \int_{dx} \int_{dy} \int_0^{\xi} \rho g z dz dy dx \\
 &= \frac{1}{2} \rho g \int_{dx} \int_{dy} \xi^2 dx dy
 \end{aligned}$$

And substituting our expression for surface elevation into this gives:

$$PE = \frac{1}{2} \rho g \int_{dx} \int_{dy} (\xi_0^2 + \xi_0^2 \phi_l^2 + \xi_0^2 \phi_m^2 + \xi_0^2 \phi_n^2 + 2\xi_0^l \xi_0^m \phi_l \phi_m + 2\xi_0^l \xi_0^n \phi_l \phi_n + 2\xi_0^m \xi_0^n \phi_m \phi_n) dx dy$$

To evaluate the integrals of these shape functions, we may use the formula given by Zienkiewics (page 120, eq. 7.34) which states

$$\int_{dx} \int_{dy} \phi_1^a \phi_2^b \phi_3^c dx dy = \frac{a!b!c!}{(a+b+c+2)!} \Delta^2$$

and the above integral becomes:

$$PE = \frac{1}{12} \rho g (\xi_0^2 + \xi_0^m + \xi_0^n + \xi_0^l \xi_0^m + \xi_0^l \xi_0^n + \xi_0^m \xi_0^n) \Delta$$

And substituting our linear sum representation for ξ into this gives:

$$\begin{aligned}
 PE &= \frac{1}{12} \rho g \left(\xi_0^2 + \sum_{i=1}^M C_i \xi_i^2 \right)^2 + \left(\xi_0^m + \sum_{i=1}^M C_i \xi_i^m \right)^2 + \left(\xi_0^n + \sum_{i=1}^M C_i \xi_i^n \right)^2 \\
 &\quad \left(\xi_0^2 + \sum_{i=1}^M C_i \xi_i^2 \right) \left(\xi_0^m + \sum_{i=1}^M C_i \xi_i^m \right) + \left(\xi_0^2 + \sum_{i=1}^M C_i \xi_i^2 \right) \left(\xi_0^n + \sum_{i=1}^M C_i \xi_i^n \right) \\
 &\quad \left(\xi_0^m + \sum_{i=1}^M C_i \xi_i^m \right) \left(\xi_0^n + \sum_{i=1}^M C_i \xi_i^n \right)
 \end{aligned}$$

And expanding this out gives:

$$\begin{aligned}
 PE &= \frac{1}{12} \rho g \left(\xi_0^2 \right)^2 + \left(2\xi_0^2 \sum_{i=1}^M C_i \xi_i^2 \right) + \left(\sum_{i=1}^M \sum_{j=1}^M C_i C_j \xi_i^2 \xi_j^2 \right) + \left(\xi_0^m \right)^2 \\
 &\quad + \left(2\xi_0^m \sum_{i=1}^M C_i \xi_i^m \right) + \left(\sum_{i=1}^M \sum_{j=1}^M C_i C_j \xi_i^m \xi_j^m \right) + \left(\xi_0^n \right)^2 + \left(2\xi_0^n \sum_{i=1}^M C_i \xi_i^n \right)
 \end{aligned}$$

$$\begin{aligned}
& + \left(\prod_{i=1}^M \prod_{j=1}^M C_i C_j \xi_i^n \xi_j^n \right) + (\xi_0^l \xi_0^m) + \left(\xi_0^l \prod_{i=1}^M C_i \xi_i^m \right) + \left(\xi_0^m \prod_{i=1}^M C_i \xi_i^l \right) \\
& + \left(\prod_{i=1}^M \prod_{j=1}^M C_i C_j \xi_i^l \xi_j^m \right) + (\xi_0^l \xi_0^n) + \left(\xi_0^l \prod_{i=1}^M C_i \xi_i^n \right) + \left(\xi_0^n \prod_{i=1}^M C_i \xi_i^l \right) \\
& + \left(\prod_{i=1}^M \prod_{j=1}^M C_i C_j \xi_i^l \xi_j^n \right) + (\xi_0^m \xi_0^n) + \left(\xi_0^m \prod_{i=1}^M C_i \xi_i^n \right) + \left(\xi_0^n \prod_{i=1}^M C_i \xi_i^m \right) \\
& + \left(\prod_{i=1}^M \prod_{j=1}^M C_i C_j \xi_i^m \xi_j^n \right)
\end{aligned}$$

This is once again the potential energy associated with a single triangle as a function of the Green's function contribution from each boundary point along the cross shelf segment. The total potential energy for the region will be the sum of this expression over each triangle. To minimize this we must differentiate with respect to each of the C's and set the resulting system of equation to zero, i.e., for $i = 1, 2, \dots, m$

$$\begin{aligned}
& 2\xi_0^l \xi_i^l + 2\xi_0^m \xi_i^m + 2\xi_0^n \xi_i^n + \xi_0^l \xi_i^m + \xi_0^m \xi_i^l + \xi_0^l \xi_i^n + \xi_0^n \xi_i^l + \xi_0^m \xi_i^n \\
& + \xi_0^n \xi_i^m + 2\xi_i^l \left(\prod_{j=1}^M \xi_j^l C_j \right) + 2\xi_i^m \left(\prod_{j=1}^M \xi_j^m C_j \right) + 2\xi_i^n \left(\prod_{j=1}^M \xi_j^n C_j \right) \\
& + \xi_i^l \left(\prod_{j=1}^M \xi_j^m C_j \right) + \xi_i^m \left(\prod_{j=1}^M \xi_j^l C_j \right) + \xi_i^l \left(\prod_{j=1}^M \xi_j^n C_j \right) + \xi_i^n \left(\prod_{j=1}^M \xi_j^l C_j \right) \\
& + \xi_i^m \left(\prod_{j=1}^M \xi_j^n C_j \right) + \xi_i^n \left(\prod_{j=1}^M \xi_j^m C_j \right) = 0
\end{aligned}$$

This gives M equations in the M unknown C's which can be written in the following matrix form.

$$A c = \Gamma$$

Where:

$$\Gamma_i = -[(\epsilon_o^l + \epsilon_o^m + \epsilon_o^n)(\epsilon_i^l + \epsilon_i^m + \epsilon_i^n) + (\epsilon_o^l \epsilon_i^l + \epsilon_o^m \epsilon_i^m + \epsilon_o^n \epsilon_i^n)]$$

And

$$A_{ij} = [(\epsilon_i^l + \epsilon_i^m + \epsilon_i^n)(\epsilon_j^l + \epsilon_j^m + \epsilon_j^n) + (\epsilon_i^l \epsilon_j^l + \epsilon_i^m \epsilon_j^m + \epsilon_i^n \epsilon_j^n)]$$

where it is understood that these terms are summed over all the triangles.

Solving this system for the C_i 's we then obtain the minimum potential energy solution for the density driven response partition of the diagnostic model.

2.3 Natural boundary conditions for the Finite Element Solution

The third method of estimating the boundary conditions for the density driven response to the model is by far the simplest and actually depends to some extent on serendipity. The basic procedure can be described as follows:

The density driven response partition of the diagnostic equation is solved using the finite element technique and first order linear shape functions subject to the following conditions:

- a) Along the coastal boundary segment a zero net flux condition is specified.
- b) Along the deep water boundary segment the elevations are set using dynamic height considerations.
- c) Along the cross shelf boundaries no boundary conditions are imposed after the finite element matrix is assembled.

Having carried out the above procedure one finds the somewhat surprising result that without giving the elliptic problem explicit boundary conditions surrounding the domain a solution is obtained. Not only that, the flow pattern that results appears to be very close to the one that was obtained using the technique of minimizing the potential energy along a characteristic outlined in section 2.1. To understand how this takes place we must first consider the finite element technique that is being used along with its basic set of functions. Following this it will be necessary to investigate the physical implications of these mathematical conditions and discuss why these should lead to a low or minimum potential energy state.

We start by making the observation that the differential operator represented by the diagnostic model equation is second order and that we therefore expect the solution to come from the general function space of twice differentiable functions. On the other hand, the interpolation functions which are used to make up the solution function space are only linear and piecewise continuous. This presents no particular problem in that the actual Galerkin formulation that is used to assemble the FEM solution matrix is in the "weak form" where higher derivatives in the operator are transformed to boundary constraints via integration by parts. When this is done certain essential and natural type boundary conditions are identified (Strang and Fix, 1973). In the absence of the specification of essential boundary conditions (Dirichlet in this case) the solution will tend to optimize its approach to the natural boundary conditions (homogeneous Neumann type). In essence

when no boundary conditions are specified over some segment of the boundary, the FE solution using first order elements and the weak Galerkin form will tend towards the normal derivative going to zero.

Next we must investigate the physical consequences of this FE solution. We may recall that the sea surface slope normal to the boundary of the model corresponds to a barotropic flow along the edge of the domain. This type of circulation pattern has been previously identified as resulting from continuity mismatches around the boundary. It is at least plausible that by approaching natural type boundary conditions across the boundary segments crossing the shelf, the secondary flows will be small in some sense. Thus we can expect the total solution constrained with essential conditions only around the deep water segment to approach a minimum energy state.

In this section we have presented three different approaches to solving the density driven response to the diagnostic model equations. Each represents a somewhat different point of view and requires different amounts of computational effort. These are each being investigated to add formalism to the understanding of the model and standardize the approach to its use. This is in strong contrast to previous explorations where trial and error and oceanographic intuition were major factors in model applications.

3. Wind Driven Response

In this section we will consider the wind driven response of the model. In doing this we will be investigating the partition of the

diagnostic equation given by:

$$N_2 \nabla^2 \xi - J(\xi, d) - k \cdot \nabla \chi_T = 0$$

As is suggested this equation represents the wind forcing of the model region. The wind driven effects can be conveniently divided into two separate components. The first of these is the surface Ekman flow, which enters into the vorticity equation as the curl of the wind stress. This is the local wind forcing caused by the winds within the model region. The second category of wind forcing can be referred to as global. This is the result of large scale wind patterns and is transmitted to the model through the set up of the boundary points. Typical patterns associated with this process are modeled by imposing a slope across the continental shelf region that is proportional to the alongshore component of the wind stress. The assumed mechanism hypothesizes that the Ekman transport pushes water up against the coast inducing a barotropic set up and subsequent alongshore currents. Such behavior has been qualitatively observed in many continental shelf areas and quantitatively documented by Beardsley and Butman (1974).

Looking more closely at the local wind forcing we find that there are two ways that the model can be forced directly by winds within the model domain. The first of these is through the wind stress curl which for typical length and time scales (100 km, days) is small. For most cases the open ocean wind driven convergence or divergence is a secondary contributor to the mass balance, or sea surface set up. The second way that the local winds drive the model is through the mass convergence or divergence at the coastline. This effect enters through the no net flux boundary conditions. This direct forcing of the model

covers all possible ways winds effect the dependent variable, i.e., sea surface elevation and subsequently the geostrophic currents at the surface. It is important to remember however that these effects don't include all of the wind driven currents. Superimposed on this surface geostrophic current is the Ekman layer which is added onto the diagnostic model solution and clearly depends on local winds.

The global wind forcing to be used in the model presents essentially two distinct problems. The first is theoretical, the second numerical. It is known that regional winds set up the sea surface. The details of how the physical processes operate in continental shelf regions with complex bathymetry and stratification are essentially unknown. Because of this various assumptions have been made and tested with the model. The measure of success of these assumptions is a comparison of model results to current meter observations or Lagrangian drifter data. To date only the simplest one parameter similarity profiles have been used specifying either a uniform slope across the shelf or a slope inversely proportional to the depth. In these cases using the complete model, the density driven and wind set up effects could not be clearly separated and it was difficult to determine the actual degrees of freedom represented by the model or specified in the boundary formulation. The natural way to specify these wind driven elevation values across the shelf would be to have sea surface or bottom pressure measurements from a series of gauges. Using this data, an observed cross shelf profile could be used to drive the model. The pressure data would need to be filtered to remove non geostrophic components. In addition it would be encouraging to find the appropriate geostrophic scale signal falling

along a simple one parameter cross shelf profile. If the signal was not forthcoming, various combinations of profiles could be considered.

When trying to key the wind driven model response to various cross shelf profiles it is important to remember that the system is linear. For example with n data points across the shelf, n different empirical orthogonal modes can be derived from the records. Then all possible profiles can be represented as linear combinations of these few model profiles. Then these studies can expect the most productive output by concentrating on empirically derived profiles.

An alternate technique for keying the wind driven response of the model would be to develop a Green's function for various slope conditions between nodal points across the shelf. The methods for doing this would be similar to those presented in the preceding chapter. These then could be put together in linear combinations to represent any given cross shelf profile.

The second general problem associated with the global wind forcing in the model is numerical and was discussed in the previous section of this report. As mentioned, the boundary layer nature of the governing equation and the dominant first order physics associated with the bathymetric interaction term make it essential to consider the coupling between the right hand and left hand cross shelf boundary segments. In essence the two opposite boundary values must be related along bathymetric contours if we expect to avoid the presence of extraneous boundary currents in the secondary flow. There are several options possible in approaching this problem which were discussed in the previous

section. The first approach would be to specify the surface elevation at only one point on each isobath and determine the second boundary value by using the reduced equation and integrating along the characteristic. The second approach would make use of the natural boundary condition behavior of the finite element solution technique. In this case the elevation would be set on each characteristic and the remaining boundary conditions would remain unspecified to be determined by the solution technique in such a way as to suppress extraneous boundary currents.

As a final point on the wind driven response in the model, we note that this partition of the model equation does not depend in any way on the density data. We may also recall that the initial finite element grid or nodal point positions were determined by the locations of CTD stations which supplied the density input. It is also common that ship time and weather constraints limit the station coverage, and spatial distribution is not as detailed as one might like to resolve complex bathymetry. With the density and wind driven responses of the model partitioned as indicated, it is not necessary to restrict both partitions to the same finite element mesh. In fact, the wind driven response can be run once for any region on as dense a grid as is needed to resolve the relevant topographic features.

4. Summary

In this report we have concentrated on a formal partitioning of the diagnostic model equations. The objective is to explore the boundary value problem and to develop strategies for its systematic resolution

based on a more rigorous approach to the mathematical nature of the equations. Consistent use has been made of the linearity of the system. During this investigation a number of model characteristics have come to light. These have profound implications on our understanding of the model output, on the strategies used to set up model runs, and on the economy of model operations. In addition the degrees of freedom in the solution or the number of independent circulation patterns predicted by the model are now clearly understood. This leads to theories on how the model solution space can be constructed and suggests objective ways to determine the measure of model success and ultimately to aid the development of keying strategies for model utilization.

By partitioning the model equations we find that all of the density effects can be represented by a wind independent portion of the system. We can identify an associated minimum potential energy barotropic mode which represents a mass conserving solution consistent with both the density and bathymetric data. This solution yields a single current pattern per density field. The problem of how to obtain the boundary conditions for this density driven circulation field are discussed in some detail in section 2. Three separate solution techniques are introduced. The complete formal solution to the problem is given in terms of a Green's function derivation and in addition two approximation techniques are presented. It remains to compare the output from these alternate techniques and recommend a strategy for the most efficient operation of the model. A second partitioning of the equations represents the wind driven response of the model. This subset of the equations is forced by both local wind effects and global wind

effects. The local winds effect the model within the domain and the global forcing effects enter the model through set up along the boundaries. If the local winds and the global set up are linearly related, then a single circulation pattern results. If these two components of the wind forcing are not linearly related, then two additional circulation modes are introduced. It is significant to note that the wind driven response of the model is independent of the density field or oceanographic station data and depends only on the geometry of the region that is being considered. This means that for any given wind set up profile hypothesized for a region a single model study will be sufficient to determine the response pattern. This study need not be run on the same finite element grid on which the density data is run. In fact, the study can be run with much higher resolution for the area in question and then linearly added to the results of the density studies from any number of oceanographic cruises in the area. This partitioning of the model equations has led to a clear identification of the linearly independent circulation patterns which are possible, subject to the model dynamics. In turn, these can be related to the forcing associated with the oceanographic density field and the sea surface elevation variations across the continental shelf region. To the extent that both of these can be determined from observations and independently compared to current meter and Lagrangian drogue data, we have an objective way of determining the success of predicting regional currents by the diagnostic model. In addition we have derived a technique for looking at the circulation response associated with various independent modes of sea surface elevation

that can be measured across a shelf region. This relatively small number of linearly independent circulation patterns can then be stored in an environmental library and all possible circulation patterns can be represented by linear combinations of these fundamental circulation patterns. Once this library is available the problem of developing circulation patterns for trajectory analysis or advective forecasts can be reduced to the development of appropriate keying strategies. These keying strategies will attempt to establish the correlation between easily observed environmental parameters and the occurrence of the fundamental independent modes. So, not only can optimal use be made of environmental library data, but we are also assured that the libraries themselves are stored in a most compact form. The obvious benefits from this type of decomposition and modal structure are twofold. First we can expect increased efficiency in computer algorithms and secondly we can obtain an understanding of the data fields to an extent not possible before. Finally, circulation patterns predicted by the model can be objectively compared to observations in such a way that estimates can be made of the model adequacy in representing environmental conditions.

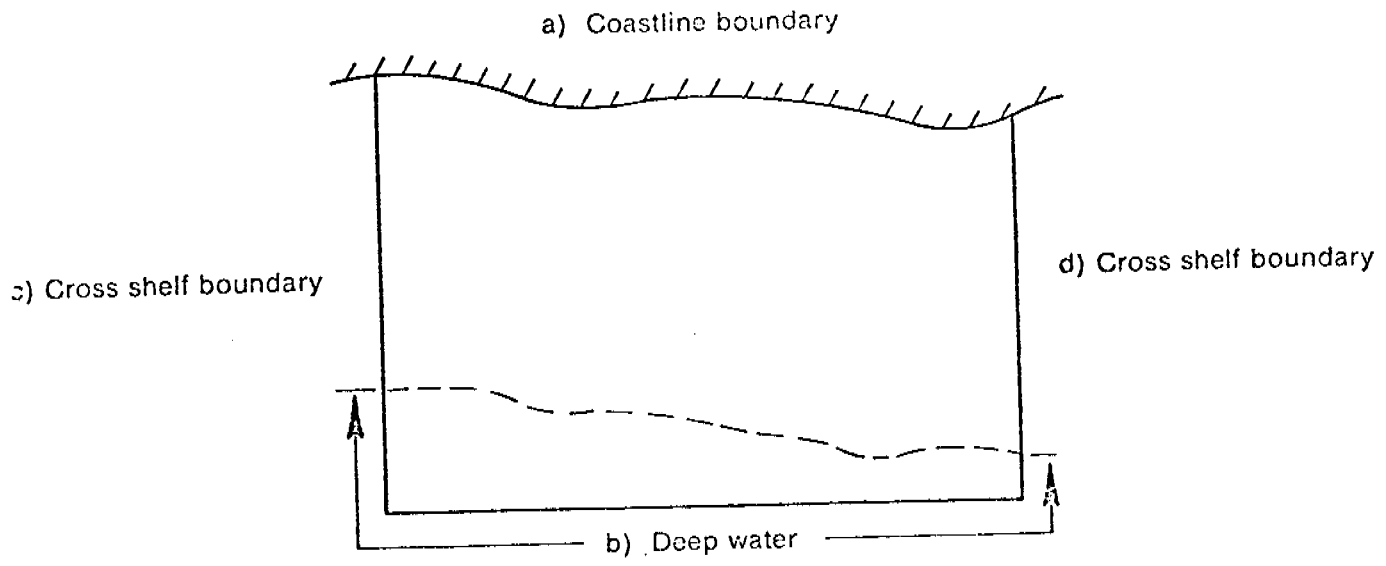


Figure A1

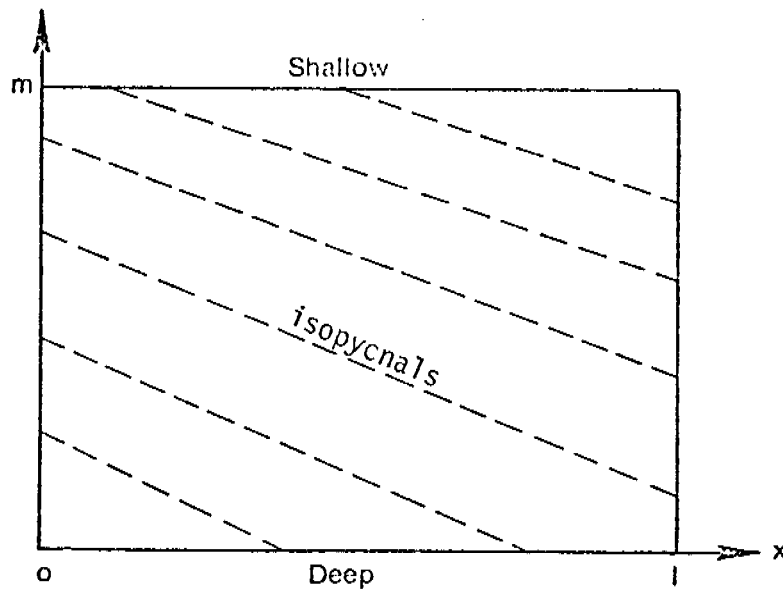
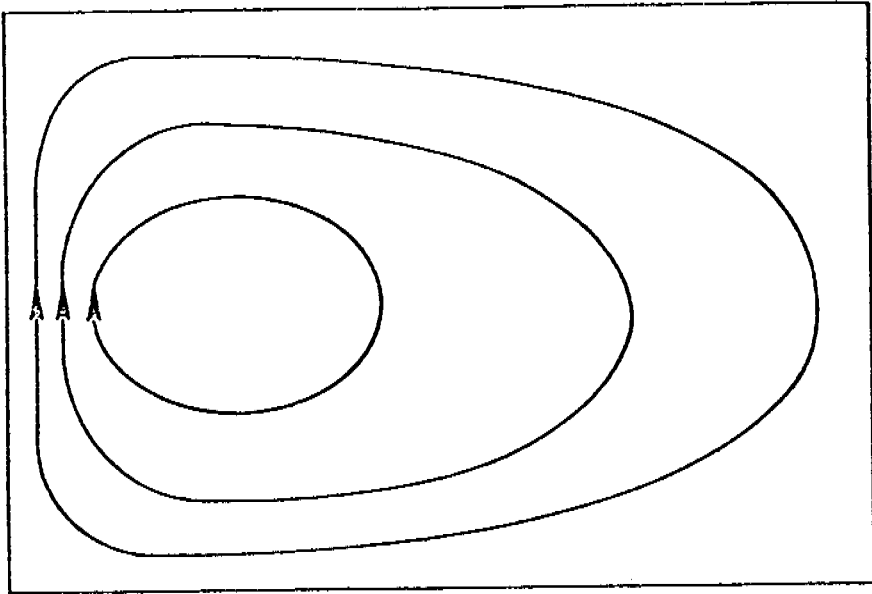


Figure A2



ξ''

Figure A3

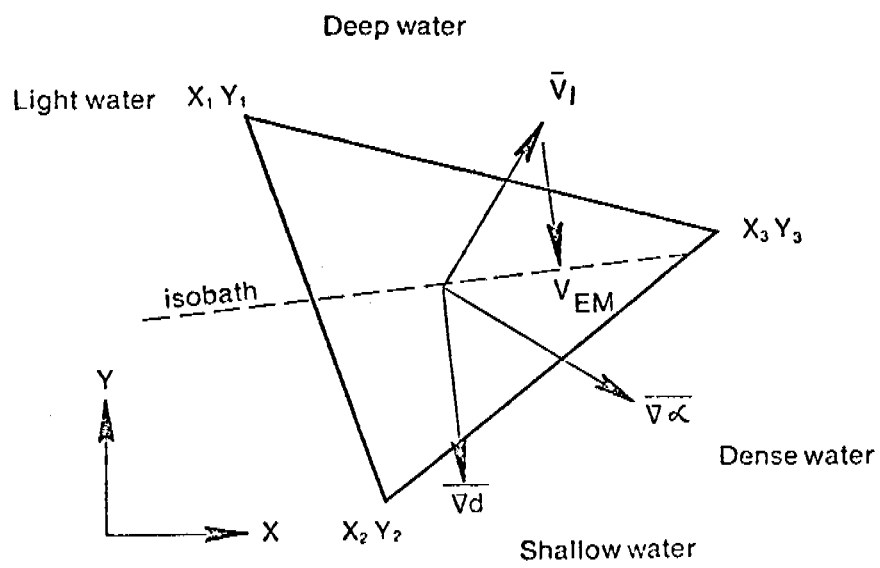


Figure A4

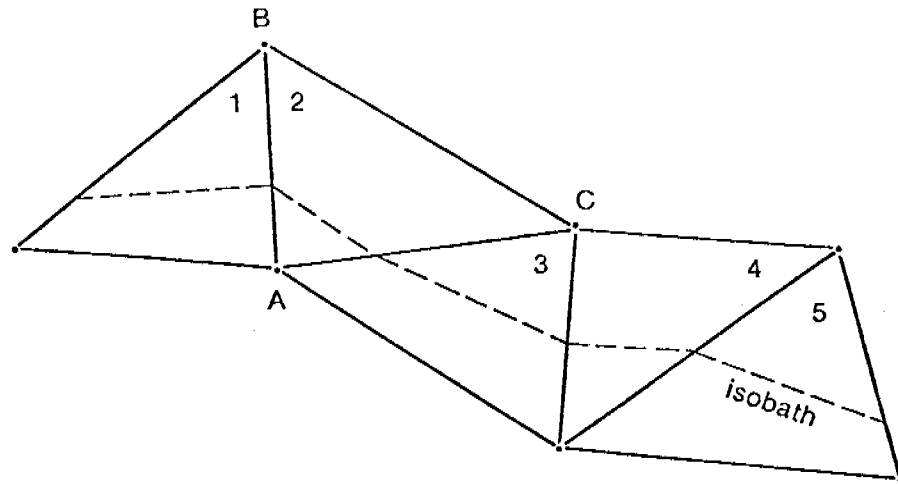


Figure A5

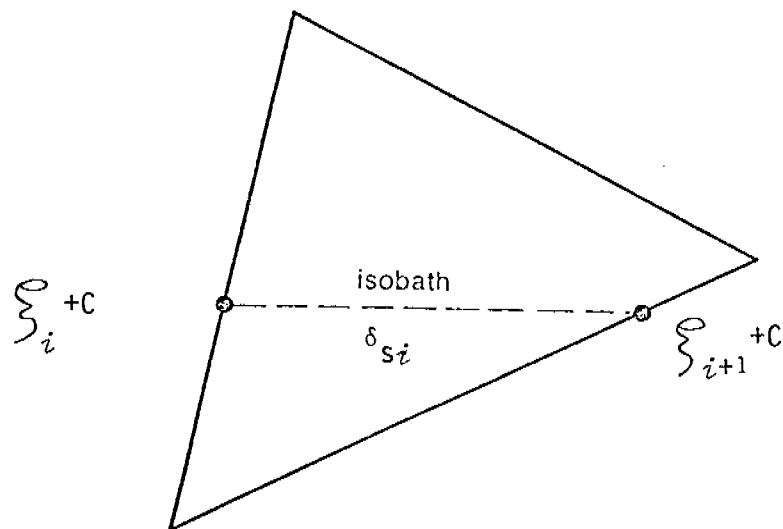


Figure A6

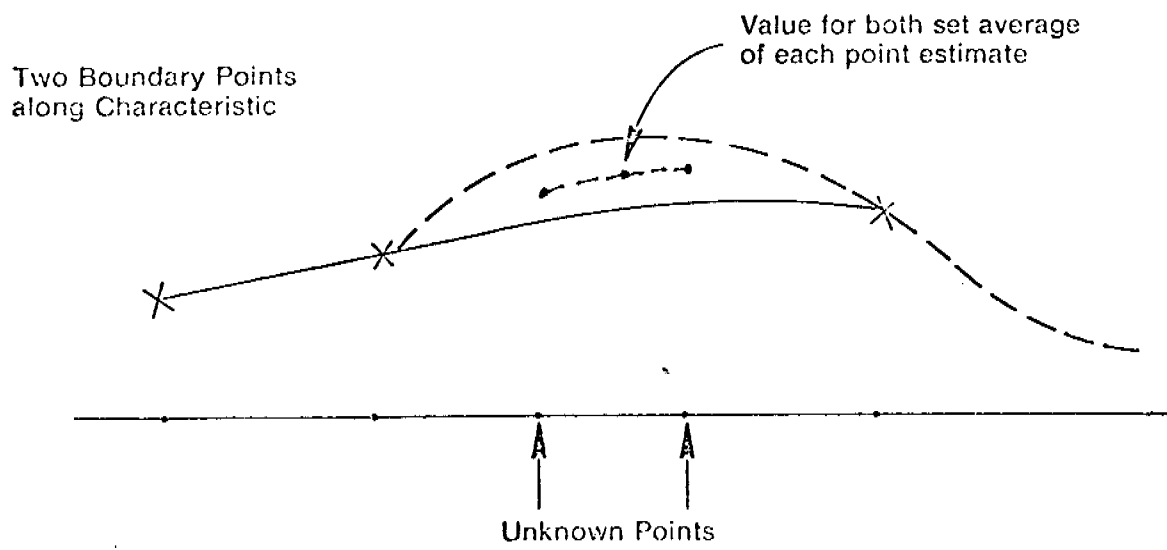
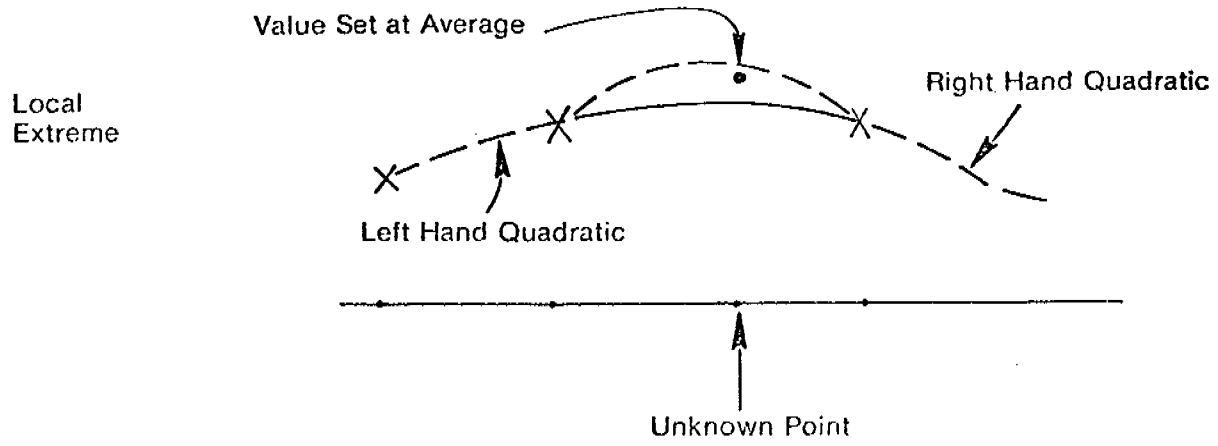


Figure A7

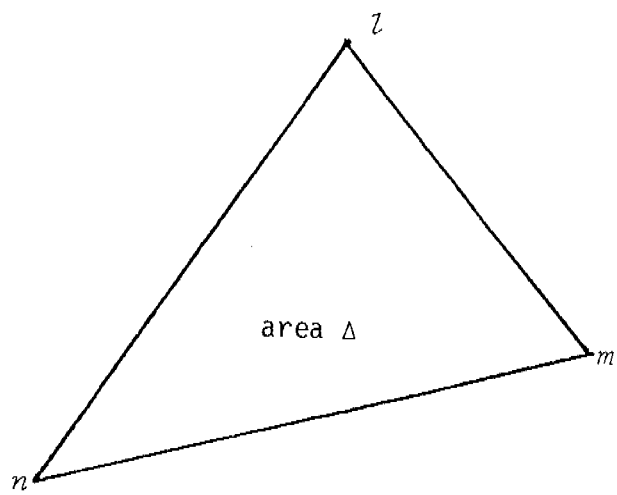


Figure A8

REFERENCES

- Beardsley, Robert C. and Bradford Butman (1974): Circulation on the New England continental shelf; response to strong winter storms, Geophy. Res. Letters 1(4); pp 181-184.
- Cole, Julian (1968): Perturbation Methods in Applied Mathematics, Blaisdell, New York, 260pp.
- Courant, R. and D. Hilbert (1962): Methods of Mathematical Physics, Vol. II, Interscience Publishers, New York, NY, 830 pp.
- Galt, J. A. (1975): Development of a simplified diagnostic model for the interpretation of oceanographic data. NOAA Technical Report ERL 339-PMEL 25, National Oceanic and Atmospheric Administration, U.S. Department of Commerce, Washington, DC, 46 pp.
- Galt, J.A. (1976): Circulation studies on the Alaskan Continental Shelf off the Copper River Delta. National Oceanic and Atmospheric Administration, U.S. Department of Commerce, Washington, DC, 36 pp.
- Galt, J.A. (1977): A diagnostic circulation of the flow in the vicinity of Kodiak, EOS, Vol. 58, No. 12, p. 1173. (Abstract only)
- Galt, J. A. and C.H. Pease (1977): The use of a diagnostic circulation model for oil trajectory analysis, Proceedings of 1977 Oil Spill Conference, March 8-10, New Orleans, Louisiana. pp 447-454.
- Stommel, H. (1948): The westward intensification of wind-driven ocean currents, American Geophysical Union, Transactions, Vol. 29, No. 2, pp 202-206.
- Strang, G. and G. J. Fix (1973): An Analysis of the Finite Element Method, Prentice-Hall Inc., Englewood Cliffs, NJ, 306 pp.
- Wunch, C. (1977): Determining the general circulation of the oceans: a preliminary discussion, Science, 196, pp 871-875.
- Zienkiewicz, O.C. (1971): The Finite Element Method in Engineering Science, McGraw-Hill Publishing Co., New York, NY, 521 pp.

B. Diagnostic Model Utilization

The aim of this portion of the study is to use the diagnostic circulation model to analyze sets of STD data for particular areas and produce the results in a standardized graphical format. We will use the computer routine developed for the diagnostic model to study oceanographic data for a number of specific cruises.

The immediate objective of this study is to identify the data sets to be used for the NEGOA region. There are several criteria for the applicability of the model to a set of data. First, the STD station average must span the area of interest in a moderately dense fashion. Second, the stations need to be spatially uniform enough to resolve the hydrographic features of the region. Third, the STD casts need to be taken over a relatively short time span, or at least not during a period of abrupt change, so that the assumption of synoptic conditions is not jeopardized. And last, the choice of sets must reflect the needs of the contractor for information content, such as seasonal cases, year to year changes, etc.

The tentative sequence of model runs to be made for the NEGOA area are given in table 1. A full analysis of the data sets using the criteria outlined above has not been made yet, so the list must be considered mutable. Once the list has stabilized we will proceed for each case by determining the appropriate boundary conditions, running the case, and documenting the run.

TABLE B1
 CASES TO BE RUN ON THE DIAGNOSTIC MODEL FOR THE NEGOA REGION

	<u>File ID</u>	<u>Cruise Date</u>
W I N T E R	1) { 202 IMS 200 IMS	November 1974 October 1974
	2) { 805 IMS 205 IMS	February 1975 February 1975
	3) 207 IMS	March 1975
<hr/>		
S U M M E R	4) 212 IMS	June 1975
	5) 811 JMS	August 1975
	6) MW5 IMS	July 1976

C. Development of the General Trajectory Model

The goal of this section of the research unit is to develop an oil spill trajectory model which will present the results of trajectory calculations based on currents, winds, and other physical processes developed by the rest of the work unit. The model development is approximately on schedule with respect to the proposal. However, the developer of the model, Joseph Karpen, has departed the laboratory and we foresee that this will disrupt the model development in the immediate future.

To minimize the impact of these problems on the OCSEAP schedule, Dr. Robert Stewart has assumed responsibility for the model. He is in the process of familiarizing himself with the general model with a view toward streamlining the model's capabilities around OCSEAP requirements. Portions of the model have been identified which are of immediate use. Examples of these routines are the coastline inside/outside routines, the bit map routine, and the various parts of the graphics package. Examples of less important routines which may not be included in the final version of the OCSEAP model are the tape storage routines and those subprograms controlling the interactive mode of program operation.

The philosophy underlying this culling process is two-tiered. First, we recognize that the principal contribution of OCSEAP towards understanding the physical behavior of oil in the Gulf of Alaska is the much improved understanding of the spatial and temporal behavior of the wind and currents. Second, by focusing on these environmental aspects of the problem and ignoring the related but unresolved problems of oil behavior on the ocean, we can reduce the complexity of the spill

trajectory model. Also by applying the batch mode concept instead of the present interactive mode, we can greatly reduce the time and effort required for the multiple production runs required by OSCEAP. We believe these simplifications will allow us to more readily meet our OCSEAP production commitments, although this change in focus will be at the expense of the model's generality.

D. Environmental Disk Development

The purpose of this portion of the project is to design and implement a standardized environmental data library system for use with the oil spill trajectory model. The prototype library will be developed for the NEGOA region from field data and output from other model pieces. The actual physical construction of this disk will be the last support unit to be completed for the general spill model because it depends on the current output of the diagnostic model and the wind fields developed by the meteorological routines. We can, however, work on the conceptual design of the library.

For the purposes of designing an environmental data library and the concomitant Fortran code for reading and using the data in an oil spill trajectory model, we would like to identify the generic data types which such a disk would include. We will restrict our discussion to information sufficient for choosing velocity components for trajectory calculations.

One very straightforward way to provide velocity data to a model is with a time dependent sequential file of observed or forecast velocities at a single geographic point. The serial file could be attached directly by the program and be interrogated at the appropriate time interval. This method is occasionally used when data for a region is either very sparse or very simply ordered in space so that the file acts as a best guess for the entire region that the model is considering. An example of appropriate useage for this is a real time anemometer record supplied for an area smaller than meteorological scales and with relatively flat relief.

A more complex method of supplying velocity information to the model can be established if the velocity field is known in some sense over the entire area for certain cases. These cases can be as simple as a velocity field for each season or as complicated as a velocity field assumed for different weather types. There are some requirements for such a system to work. A technique must exist for sequencing these cases to simulate the desired evolution of the velocity field in time. This can be either a predetermined list of page numbers or a function of other files in the library. This function must be well ordered. The cases included in the library must also approximate a complete bases set either by assumption or by objective analysis of empirical observations.

For efficient application of such schemes, we would require the data to be arranged by case on a regular grid on a direct access file. Each case would occupy one page on the file. The cases or pages of the file must be ordered in the sense of the ordering of the keying parameter scheme. An example of a use of this kind of velocity routine is the results of the diagnostic model calculations for a region for different wind stress cases interpolated to a regular grid and ordered so that the magnitude of the current velocity at some station is a monotonic sequence and keyed by a real current record at that station. An example of another sequencing scheme that might be considered is a system of tables of transition probabilities for use in a stochastic model. The table or tables would occupy a direct access file and would allow the creation of sequences of cases that simulate the time wise evolution

of wind or current fields. A stochastic velocity routine would require a random number generator as part of the mechanism for choosing an appropriate velocity case via the transition probabilities. The transition probabilities would be calculated from empirical velocity records. A stochastic sequence of velocities could be assumed to be a complete description of the velocity for a region or could be used as a keying sequence for another paging type scheme from the library.

A major class of velocity routines to be considered is the possible set of deterministic algorithms for currents or winds. A significant example of this type is a tidal current model for an estuary. The machine requirements for this type of routine would be less rigid than other types of velocity routines since the deterministic types would have routine species dependent files. For an applied regional tidal model one would need a table of amplitude and coefficient data for the appropriate tidal stations and another table which would relate grid position with the proportional tidal stations. In this example the two arrays would best be developed as direct access files.

A summary of these approaches is outlined in table 1. Standardized routines need to be written to interface the appropriate velocity components with the general trajectory model. Documentation will be completed and test cases will be run on the general model using this prototype disk.

TABLE D.1
SUMMARY OF APPROACHES TO VELOCITY PROBLEM

Time-Wise Evolution

1. Observed
2. Forecast
3. Stochastic Simulation
 - A. Keying on Function of Observations
 - B. Transition Models
4. Deterministic Simulations

Spatial Dependence

1. Homogeneous by assumption
2. Dynamic/Kinematic interpolation and extrapolation schemes
3. Stochastic simulation based on observed correlations

E. Meteorological Model Calibration and Synthesis of Meteorological Program Observations

A major intent of the regional wind element is to provide spatially varying winds to the trajectory calculations which account for the mesoscale influence of terrain and differential heating and roughness between land and water. Specifically these fields are to relate in a one-to-one correspondence with a chosen set of synoptic pressure pattern types so that the local winds can be assigned from climatology. The approach to providing these fields is a subjective combination of observational case studies and the regional meteorological model (RMM). The model is used to assist in rationally exploring the case studies and in providing a systematic method for extrapolation into sparse data regions based upon dynamic and kinematic principles.

1. NEGOA

A draft Technical Report (Reynolds, Hiester and Macklin) presents the results of the meteorological field program for the southeastern NEGOA region. These studies consisted of ship transects normal to the coast in March 76, instrumented aircraft flights February 23 - March 3, 1977 and buoy and coastal anemometer comparisons for March and May 1977. Three types of modifications are significant. The dominant feature is coastal blocking of geostrophic flow by the mountain chain. Flow is rectified to the alongshore direction for a large range of offshore geostrophic wind directions. This influence extends 75 - 200 km offshore. The second feature is the existence of very shallow katabatic layers generated by surface cooling over land and subsequent flow of the dense air offshore. This general drainage is a persistent

winter feature but its influence is limited to 20 km of the coast as a result of rapid surface heating by the sea surface. No catastrophic katabatic events were evident during the observation periods. The third area is a general category of local influences due to alongshore variations in topography. Channeling by mountain passes, enhanced katabatic flow off of the Malaspina Glacier and modification over water by Yakutat Bay fall into this class. Their influence also tends to be limited to a narrow coastal strip.

The results from the two dimensional RMM generally support the inferences derived from the field program. Figure 1 shows elevation and Figure 2 shows a local wind plot with arrow spacing of 5 km corresponding to alongshore geostrophic flow. The detailed influence of channeling and convergence patterns on the lee side of the mountains is constrained to within 25 km from shore. Katabatic winds are confined to a shallow layer imbedded in the planetary boundary layer and cannot be included in the present form of the RMM.

The extent of the diagnostic model and domain for the trajectory computations extend seaward to the shelf break, a distance of 150 - 200 km. Nominal resolution is 10 - 20 km. The alongshore distance extends west past Kyak Island. Thus in the context of trajectory calculations it is very important to resolve the change in wind direction due to coastal blocking, but input from detailed mesoscale features are confined to one or two estimates near the coastline. To facilitate the trajectory calculations, a uniform 5' latitude - 10' longitude grid will be superimposed over the entire area. When the weather map typing is completed winds will be assigned to each cell for

each weather type. The critical factor is the seaward extent of the mountain influence for each geostrophic wind direction. This will be assigned based upon case studies by M. Reynolds and the results of a one dimensional version of the RMM.

The 1-D model has augmented the study because it is an excellent tool to study coastal influence. The model domain can be extended so that the open boundaries are far removed from the coastal zone. To see the importance of coastal mountains we contrast figure 3 with figure 4. Figure 3 shows the wind direction and speed, boundary layer height and the ratio of magnitude for flat topography, changing from water to land as the wind flows from left to right in the figure. The wind speed is reduced and turned by surface friction over the land. However, inertia is strong enough so that the induced pressure gradient (caused by the slope of the boundary layer height) is not felt seaward of the coastline. This case sharply contrasts with figure 4 which is the same except for a 700 m coastal mountain. Backpressure caused by the mountains creates a coastal boundary layer of 90 km width in which the wind speed is reduced and the wind direction slowly rotates to be more parallel to the coast.

2. Lower Cook Inlet and Kodiak

Figure 5 shows the elevation grid for the 2-D RMM for Lower Cook Inlet. Kodiak Island is in the left corner with upper Cook Inlet off the upper right corner. Figure 6 shows the elevations for Kodiak Island. Both regions are ideal for the 2-D RMM because the physics of the model emphasize channeling and inertia effects caused by headlands.

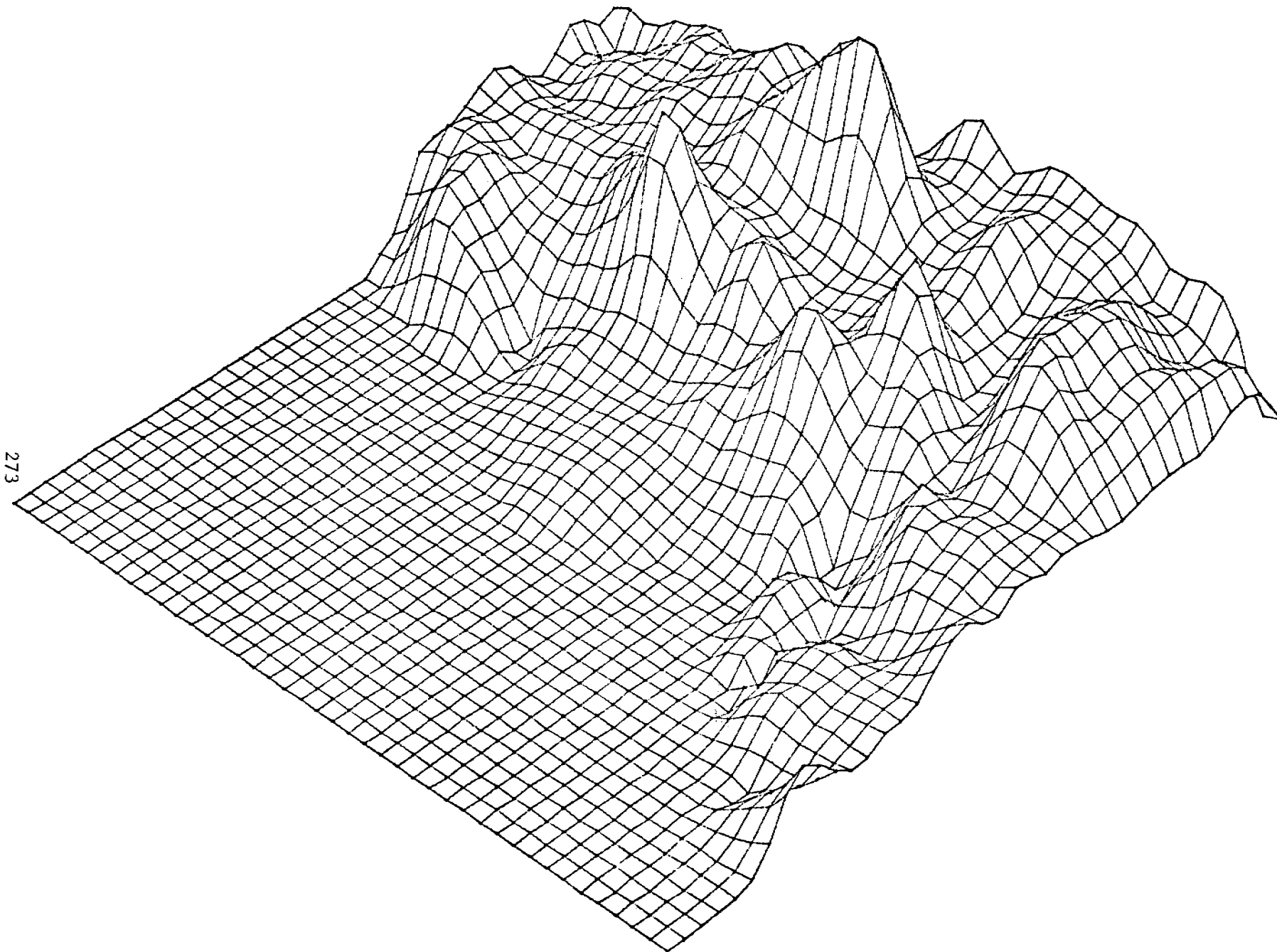
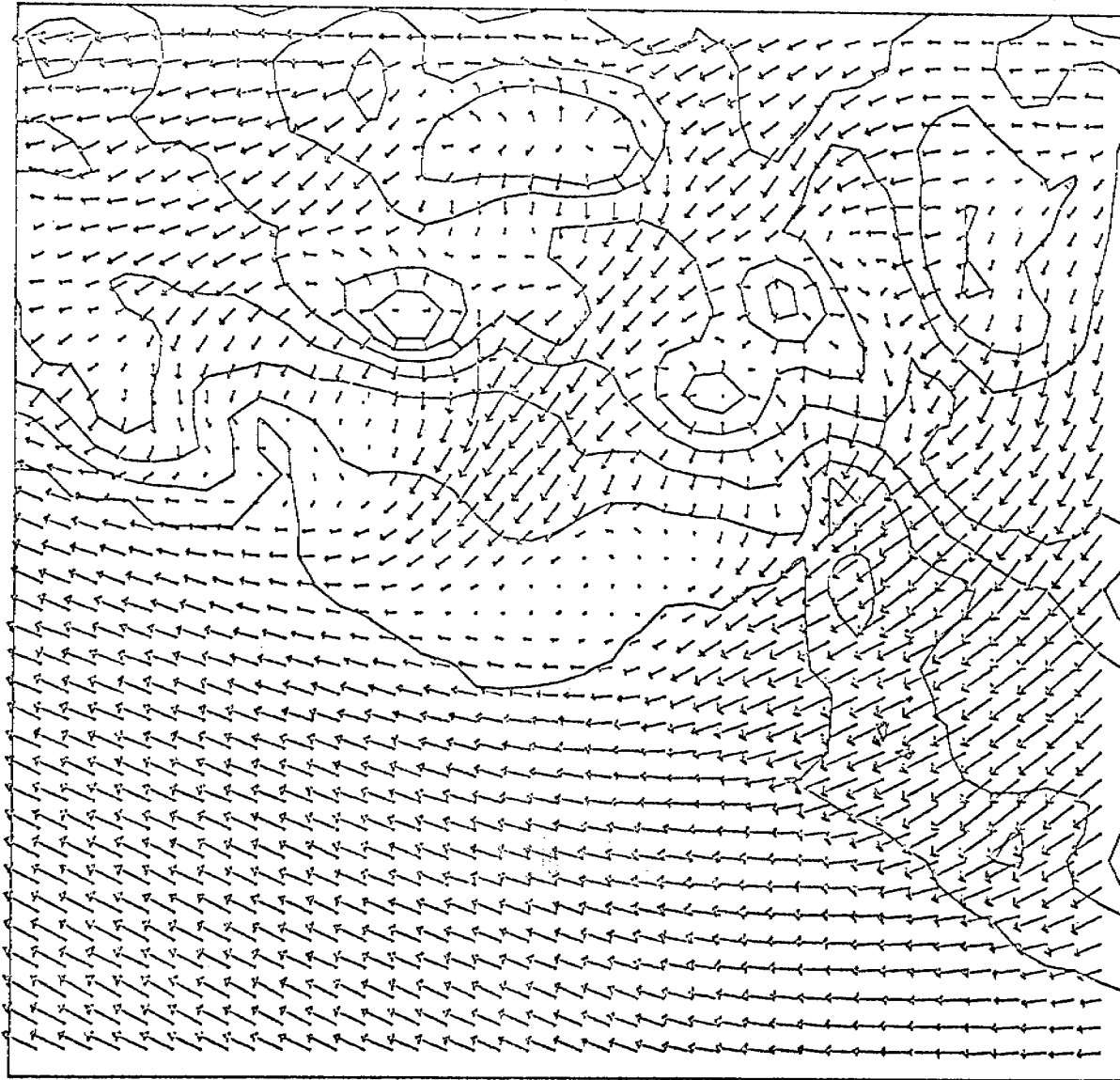


Figure E1 Elevation Grid for NEGOA

VELOCITY VECTOR PLOT



10 METERS PER SECOND

Figure E2. Geostrophic wind at 135° relative to top of figure at 13 m/s.

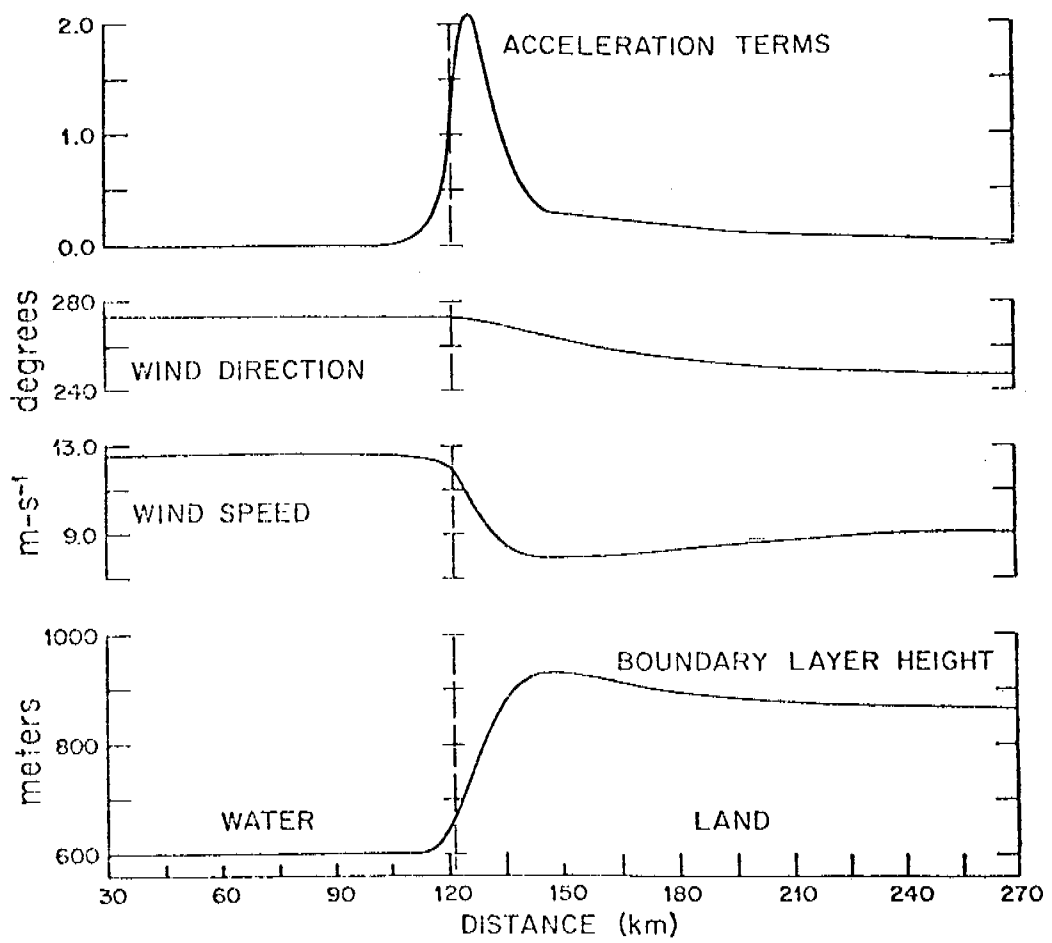


Figure E3. Wind parameters for onshore flow with flat coastline.

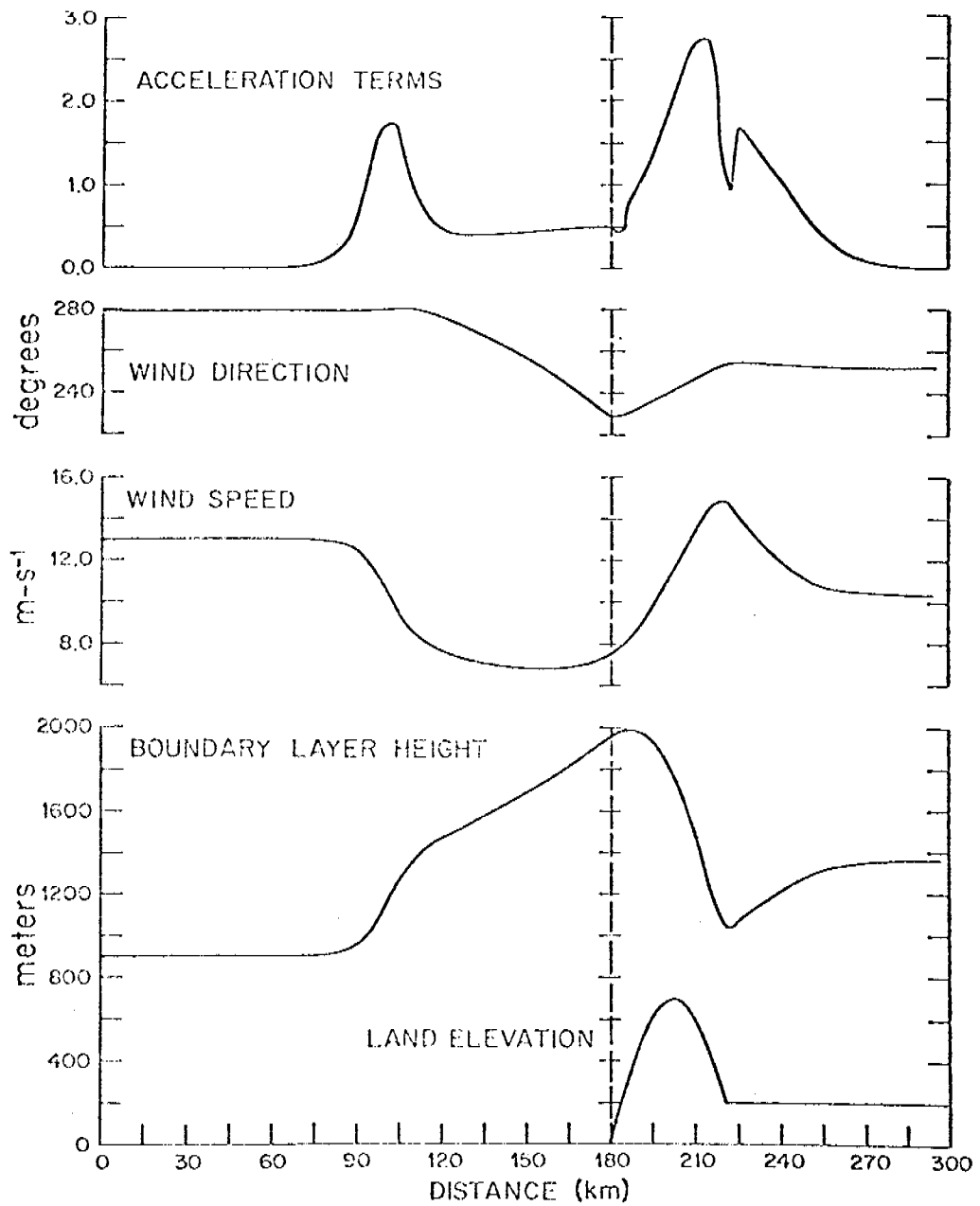


Figure E4. Wind parameters for onshore flow with coastal mountains.

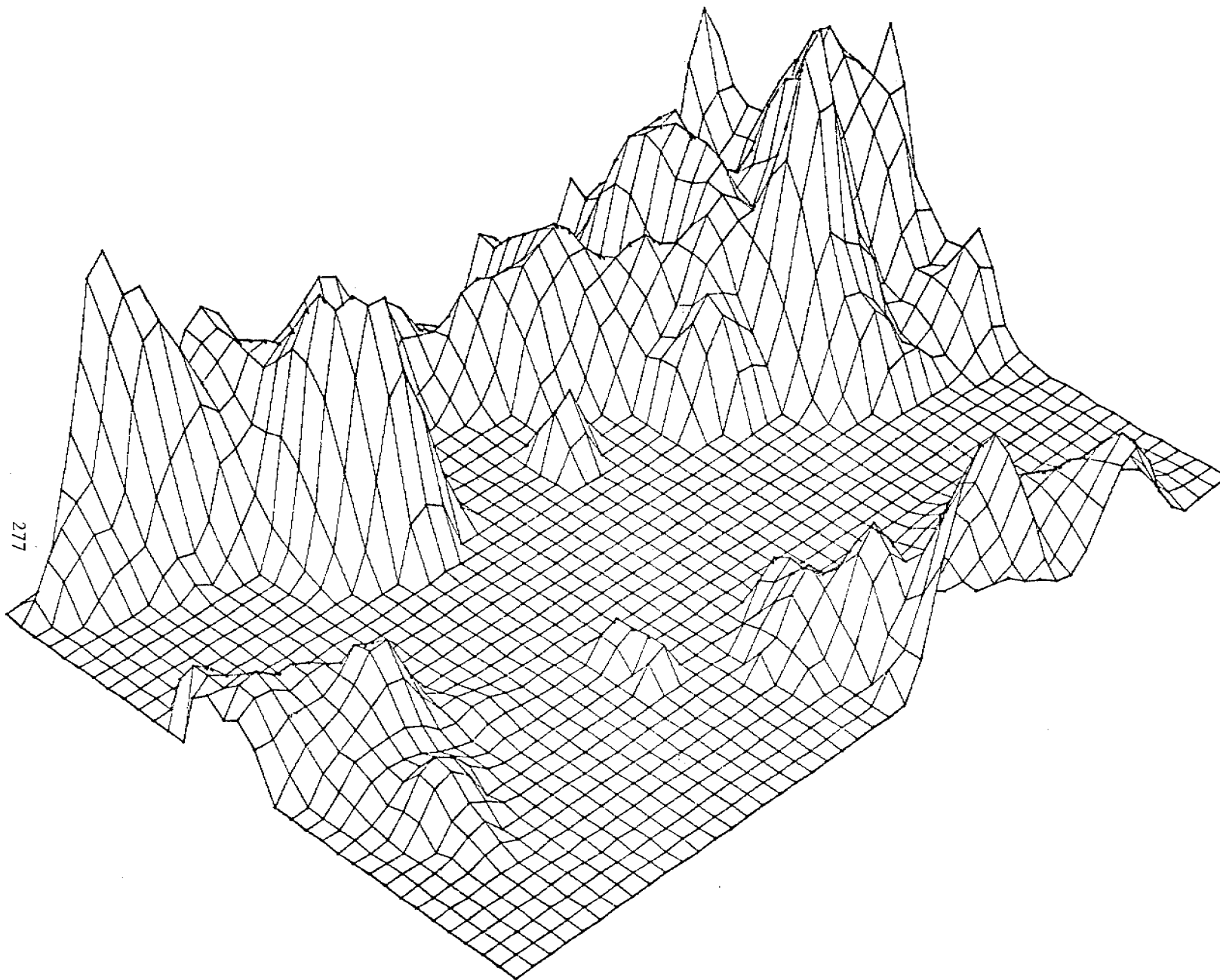


Figure E5. Lower Cook Inlet Elevation Grid

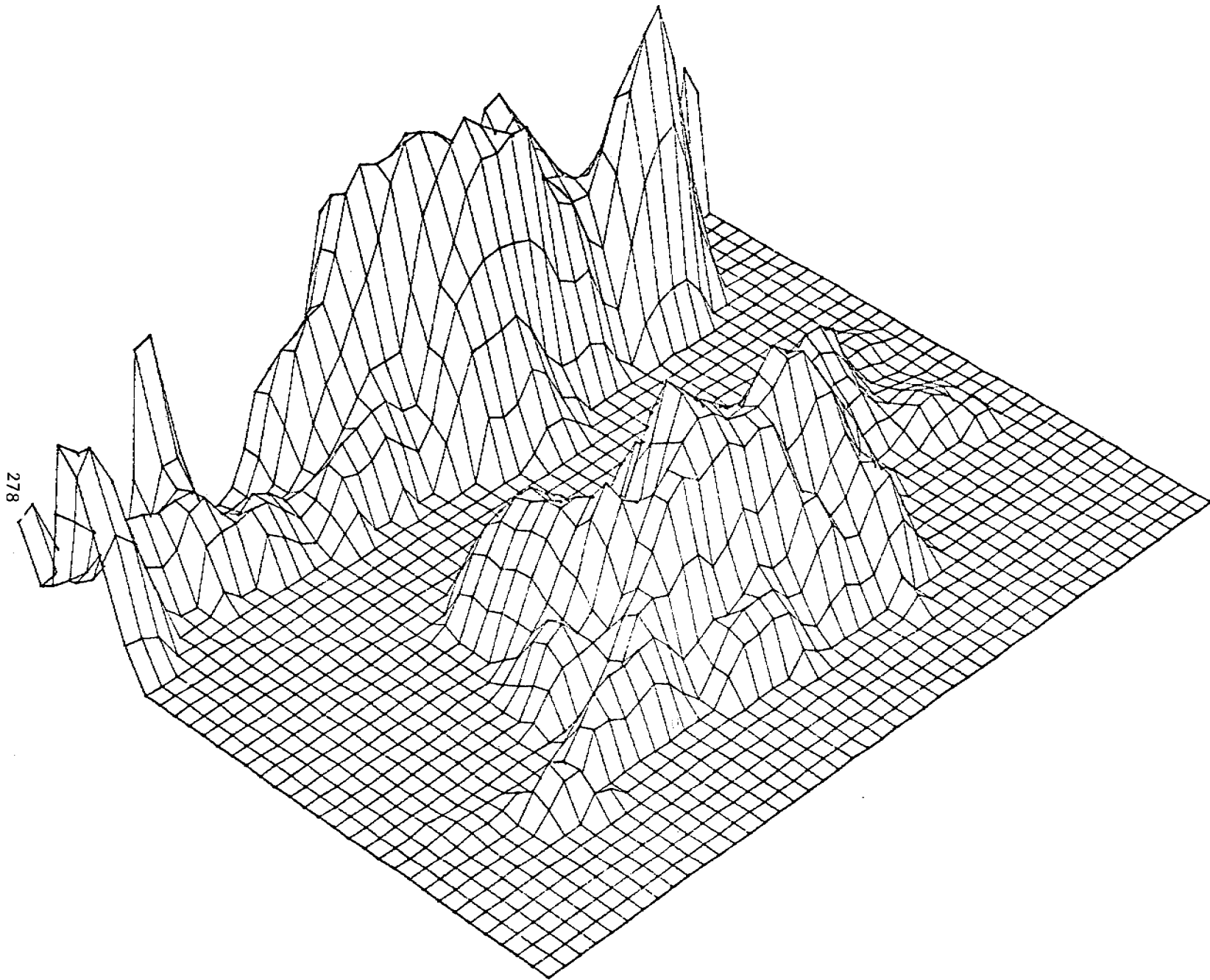


Figure E6. Kodiak Elevation Grid

F1. Development of Objective Techniques for Analyzing Regional Wind Climtologies

To better resolve the spatial behavior of the wind we have developed a regional meteorological model that allows us to specify the orographically influenced wind field in the coastal region. This model is a steady state model, and its purpose is to allow us to interpolate or extrapolate in space at a given time. Because the model is too expensive to be run for every possible large scale baric pattern, the goal of task F1 is to develop an objective technique for identifying an economically feasible subset of the baric weather patterns which can then be used as the basis for approximating all spatial dependencies in the wind field.

There are several statistical techniques that lend themselves to the problem of selecting a representative collection of baric patterns. The simplest is based on an examination of the correlations between patterns. In this technique, the analyst selects some cutoff value for significant correlations (like .7) and then groups all patterns exhibiting a correlation greater than or equal to this cutoff. The technique is sequential in that the analyst first determines which group has the greatest number of members. He then selects that group as his first pattern and creates a new correlation matrix with this group deleted, whereupon the process is repeated for the second group and so on. An example of this type of analysis is Lund (1963). The drawbacks of this technique are that it does not explicitly consider the structural properties of the patterns (and so there is no quantitative assessment of the potential resolution of the data by this method)

nor does the technique consider all the data simultaneously. For these reasons it can be ambiguous. For example, if we had four observations with the following correlation matrix, a solution based on a grouping of any three of the four would satisfy the technique.

$$R = \begin{bmatrix} 1 & .8 & .6 & .7 \\ .8 & 1 & .9 & .4 \\ .6 & .9 & 1 & .7 \\ .7 & .4 & .7 & 1 \end{bmatrix}$$

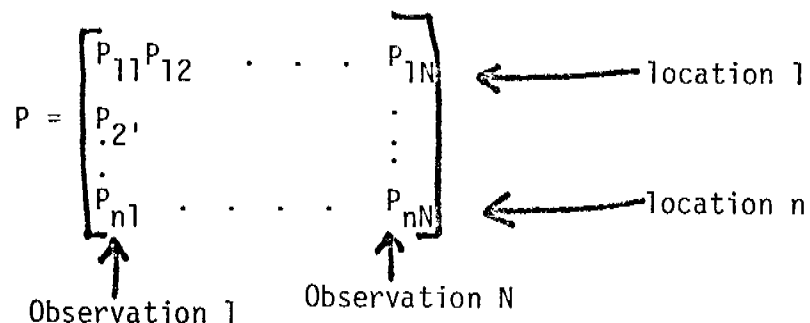
Another statistical technique for identifying similar patterns is discriminant analysis. This method is based on the perception that if we plot the results of a large number of observations in an n-dimensional space, where n is the number of parameters measured at each observation, we might expect to find the data grouped in cloud-like clusters around mean values that are linked to pattern types. If the distance between the various means is large compared to the cloud dimensions, then it is possible to fit surfaces between the clouds, and to generate decision functions based on these hyperplanes which identify pattern types. An example of this type of analysis is McCutchan and Schroeder (1973). The utility of this type of approach is strongly dependent upon the degree to which the observations are clustered.

A third approach, and the one we chose to follow, is that of factor analysis. This technique is based on the correlation matrix, but unlike Lund's method, it both considers the errors associated with a solution and it looks at all groupings simultaneously. Also, it is based on an explicit model of the process. Furthermore, through the use of various quantitative criteria it is possible to determine a unique solution to the problem. The following section discusses the method in more detail.

Our original schedule indicated that we would have completed an analysis of the NEGOA region in time for this annual report. Due to the unforeseen switch to the central ERL Boulder computer, and due to software problems in reading IBM tapes on CDC systems, we have not yet analyzed the NEGOA baric patterns. However, we have looked at 100 twelve-hourly NMC sea surface pressure analyses for August and September 1975 in the Bering Sea region. These serve to demonstrate and verify the approach and so we discuss these results in the third section of this report. The classification of weather patterns for the Gulf of Alaska region (including NEGOA, Lower Cook Inlet and Kodiak Island) should proceed quickly once the IBM tapes are read.

1. Description of Technique

The solution technique may be discussed most simply if we define the problem in terms of matrices and matrix operations. Assume we have observed the pressure simultaneously at n locations at N different times. These observations may be displayed as a matrix P composed of n rows and N columns. That is, in the K th column of P , we may write the n simultaneous pressure observations taken at the K th measurement interval. For example:



In the case we analyze here, the pressure field is a 10 X 11 grid

centered over the Bering Sea. The pressure values are from the 12-hour objective analyses of the National Meteorological Center. With two observations a day, a fifty day record may thus be presented as a 110 X 100 matrix ($n = 10 \times 11$, $N = 2 \times 50$).

The Regional Meteorological Model (RMM) is insensitive to the spatially averaged pressure. However, for any given pressure field the magnitude of the geostrophic wind will be proportional to the square root of the variance of the pressure gradients. The RMM may exhibit some nonlinear behavior with respect to these winds which serve as boundary conditions in the model. This suggests that the analyses should be performed in terms of the centered pressure variate, P'_{ij} , which is created by subtracting the column averages from the observed pressures, i.e.,

$$P'_{ij} = P_{ij} - \frac{1}{n} \sum_{k=1}^n P_{kj} \quad (1)$$

However, existing subjective pattern analyses (e.g., Putnin, 1966) do not consider a variate of this type, but rather concentrate on similarities based on the locations of the high and low pressure features. This means that for comparative purposes the analysis is best done in terms of the nondimensional standard deviate z_{ij} , formed by dividing P'_{ij} by the square root of the variance, i.e.,

$$z_{ij} = \frac{P'_{ij}}{\left(\frac{1}{n} \sum_{k=1}^n P'^2_{kj} \right)^{1/2}} \quad (2)$$

where P'_{ij} is as defined as above.

The observations in standard deviate form may be presented in terms

of the $n \times N$ Z matrix,

$$Z = \begin{bmatrix} Z_{11} & Z_{12} & \dots & Z_{1N} \\ Z_{21} & & & \\ Z_{n1} & \dots & \dots & Z_{nN} \end{bmatrix}$$

Notice that if we plot the j th column vector, \vec{Z}_{ij} , in the ' n ' dimensional location space, it will form a vector of length $n^{1/2}$ and it will furthermore be constrained to fall in the $(n-1)$ hyperspace defined by:

$$\sum_{k=1}^n Z_{kj} = 0.$$

Thus Z_{ij} is of lower dimensionality than P_{ij} . For example, in a two dimensional location space, \vec{Z}_{ij} is either $(-\sqrt{2}, +\sqrt{2})$ or $(+\sqrt{2}, -\sqrt{2})$, i.e., it is one of two points on a line bisecting the second and fourth quadrants. In a three dimensional location space, the \vec{Z}_{ij} lie on a circle of radius 3.

If two pressure fields have high and low pressure features in the same locations and if the intensities of these features are in proportion, then we may say that the two fields have the same pattern. One way of characterizing this pattern correspondence is with a correlation coefficient of the form

$$\rho_{k\ell} = \frac{1}{n} \sum_{i=1}^n Z_{ik} * Z_{i\ell} \quad (3)$$

When $Z_{ik} = Z_{i\ell}$ for all i , then $\rho_{k\ell} = 1$. In general, $-1 \leq \rho_{k\ell} \leq 1$. In terms of the column vectors \vec{Z}_{-k} and $\vec{Z}_{-\ell}$ in the $n-1$ dimensional hyperspace, $\rho_{k\ell}$ is related to the cosine of the angular separation,

$\theta_{k\ell}$, between the column vectors,

$$\rho_{k\ell} = \cos \theta_{k\ell}$$

A negative ρ_{ij} may indicate an inversion of the high and low pressure features. For our purposes, such an inversion will require interpretation as two distinct patterns since we know high and low pressure perturbations behave differently.

If we assume that the observed pressure fields exhibit (with some useful frequency) m characteristic patterns, then we might consider modeling our observations with an equation of the form:

$$Z = P F + U^{1/2} Y \quad (4)$$

Here, P is an $n \times m$ matrix composed of the m characteristic patterns. F is an $m \times N$ matrix whose K th column, for example, contains the weights of each of the m patterns for the K th observations. U is an $n \times n$ diagonal matrix whose entries are the magnitudes of the unique variance of Z variate at each of the n locations. And, Y is an $n \times N$ matrix containing the weight of the unique part of the pressure variation for all n locations at all N observations.

Both P and U are fixed, that is deterministic. F and Y , however, may be considered to be random variates. If we examine the K th observation, \vec{Z}_{-k} , we can better understand the roles of P , U , F and Y , i.e.,

$$\vec{Z}_{-k} = P \vec{f}_{-k} + U^{1/2} \vec{Y}_{-k} \quad (5)$$

where $F = [f_{ij}]$ and $Y = [Y_{ij}]$, and \vec{f}_{-k} and \vec{Y}_{-k} are vectors of length n formed from the K th columns of F and Y . The value of the standard

deviate at location ℓ is thus composed of the sum:

$$Z_{\ell k} = P_{\ell 1} f_{1k} + P_{\ell 2} f_{2k} + \dots + P_{\ell m} f_{mk} + u_{\ell \ell}^{1/2} Y_{\ell k} \quad (6)$$

Implicit in the idea behind the model is the expectation that there will be many observations where the magnitude of one of the f_{jk} is large relative to the other f 's, and furthermore that the $u_{\ell \ell}^{1/2} Y_{\ell k}$ are small, at least over most of the region (over most of the locations indexed by the parameter ℓ).

It will now be convenient to impose some constraints on the proposed solution. To begin with, we shall assume that the pattern types (i.e., each of the column vectors of P) are orthogonal to one another and each has a zero mean value. Further, we shall assume that each pattern has a scalar length of $n^{1/2}$, i.e., $\vec{P}_{-j} \cdot \vec{P}_{-j} = n$. If we now form the scalar length of \vec{Z}_{-k} in terms of our model variables we find

$$\vec{Z}_{-k} = \text{SQRT} \left[\sum_{\ell=1}^n \left[(P_{\ell 1} f_{1k} + P_{\ell 2} f_{2k} + \dots + P_{\ell m} f_{mk})^2 + 2(P_{\ell 1} f_{1k} + P_{\ell 2} f_{2k} + \dots + P_{\ell m} f_{mk}) u_{\ell \ell}^{1/2} Y_{\ell k} + u_{\ell \ell} Y_{\ell k}^2 \right] \right] \quad (7)$$

The assumption of orthogonality allows us to reduce the first squared term in (7) to simple form

$$\sum_{\ell=1}^n (P_{\ell 1} f_{1k} + P_{\ell 2} f_{2k} + \dots + P_{\ell m} f_{mk})^2 = n \sum_{i=1}^m f_{ik}^2$$

The other two terms, however, are not so easily dealt with, and they require further stipulations regarding the model's components. Since the $u_{\ell \ell}^{1/2} Y_{\ell k}$ terms are meant to simulate unique perturbations at location

ℓ , it is perfectly reasonable to assume that the $Y_{\ell k}$ are independent, normally distributed random variates with zero mean value and unit variance. With this definition of the $Y_{\ell k}$, we see that the $U^{1/2}$ terms serve the purpose of injecting spatial heterogeneity into the model. If the perturbations to the pressure patterns are of similar size over the whole region (that is if this heterogeneity is not required), then we may put $U = \sigma_p^2 I$, and the last term in (7) is seen to be a chi-squared random deviate with n degrees of freedom, i.e.,

$$\sum_{\ell=1}^n \sigma_p^2 Y_{\ell k}^2 = \sigma_p^2 \chi_n^2 \quad . \quad *$$

For large n , the chi-square distribution is approximately normal, having a mean value of n and a standard deviation of $\sqrt{2n}$. Thus the last term is given approximately by a summation of the form:

$$\sigma_p^2 [n + O(n^{1/2})]$$

The crossproduct terms in (7) may also be estimated for large n since they are the summation of n normally distributed random variables for each of zero mean. This summation will thus tend to be normally distributed about zero with a standard deviation that is, again, proportional to \sqrt{n} . Remembering that $|\vec{Z}_{-k}|$ was equal to $n^{1/2}$, we can therefore see that

$$\sum_{i=1}^m f_{ik}^2 = 1 - \sigma_p^2 \pm O\left(\frac{p}{\sqrt{n}}\right)$$

* The heterogeneous case also leads to a convenient, analytic form for this term, but we will stick with the assumption of spatially homogeneous perturbations as this leads to the simplest possible form.

This shows that for small σ_p the f_{ij} are only slightly dependent on the y_{ij} 's. It also shows that the f 's are not independent of one another. Both of these effects are the result of the normalization that is an explicit part of forming the standard deviate.

We may now form a correlation matrix, R , whose elements are products of the form given by (3). The indices in (3), k and l , will both range over $(1, N)$. Obviously, this matrix is symmetric.

In terms of matrix operations, we may write:

$$R = \frac{1}{n} Z^T Z = \frac{1}{n} [PF + U^{1/2} Y]^T [PF + U^{1/2} Y] \quad (8)$$

$$= \frac{1}{n} [F^T P^T F + Y^T U^{1/2 T} U^{1/2} Y + Y^T U^{1/2 T} P F + F^T P^T U^{1/2} Y]$$

But $P^T P = n I$ and $U^{1/2 T} U^{1/2} = \sigma_p^2 I$. Furthermore, since the y_{ij} 's are independent, the off-diagonal elements in $Y^T Y$ and all the elements due to the crossproduct terms $Y^T U^{1/2 T} P F$ and $F^T P^T U^{1/2} Y$ will have expected values of zero. The diagonal elements in $Y^T Y$ and all the elements due to $F^T F$ will thus form the core of the correlation matrix R with some random perturbations of the order $\frac{1}{\sqrt{n}}$ arising from the other stochastic products.

The problem now is to find an F matrix that approximately recreates the observed correlation matrix. The correspondence need be only approximate because we know there will be random perturbations to the ρ_{ij} . Since these perturbations may be of either sign, a least squares fitting criteria obviously suggests itself. But the problem is not trivial. We have $N \times m$ unknown coefficients in the F matrix; $N(N+1)/2$

equation based on the off-diagonal correlations. The functional we seek to minimize may be written either as:

$$\min_F \left\| [R-I] - [F^T F - \text{DIAG}(F^T F)] \right\| \quad (9a)$$

or

$$\min_{f_{ij}} \left[\sum_{k=j+1}^N \sum_{j=1}^{N-1} \left(p_{jk} - \sum_{p=1}^m f_{jp} f_{kp} \right)^2 \right] \quad (9b)$$

The problem is thorny because of its large dimensionality (i.e., $N(N-1)/2 = 4950$) and because of the quadric f_{ij} behavior.

Fortunately, a solution technique based on a Gauss-Siedel iteration exists due to Harman and Jones (1966). This technique has been widely applied in the social sciences, and it is available as a "MINRES" (minimum residuals) factor analysis subroutine in most scientific subroutine packages. The procedure is to specify an m and turn the program loose. If the proper number of factors have been specified, then a statistic may be formed based on the R and $F^T F$ matrices, which is approximately chi-squared. This may then be tested for significance. Another indication that the proper number of factors has been specified is the behavior of the variance that is not accounted for by the diagonal of $F^T F$. This should be tightly clustered about some value which we may take to be σ_p^2 .

Once we have obtained an F that satisfies the minimization criteria of (9), we may then subject this solution to a rigid body rotation. Such a rotation will not effect the correlation properties of the rotated matrix, as can be seen from the following argument. Let

$$G = T F$$

where, for example,

$$T = \begin{bmatrix} \sin & \cos & 0 & \dots & 0 \\ \cos & -\sin & 0 & \dots & 0 \\ 0 & 0 & 1 & \dots & 0 \\ 0 & \dots & \dots & \dots & \dots \end{bmatrix} \quad (m \times m)$$

Now $T^T T = I$, and $T T^T = I$, since T is defined to be a solid body rotation. (also called an orthogonal transformation) Thus

$$F = T^T G \quad \text{and}$$

$$R = \frac{1}{N} F^T F = \frac{1}{N} (T^T G)^T (T^T G) = \frac{1}{N} G^T T T^T G$$

and so we find

$$R = \frac{1}{N} G^T G$$

Clearly, there are an infinite number of such transformations, each of which satisfies (9). We may now try to find that transformation, T_Q , which maximizes the difference in magnitudes of the coefficients in any one column of G . Such a transformation leads us to that solution which requires the fewest patterns to explain an average observation. As we recall, the existence of such a weighting matrix was an explicit consideration in framing our model, (4), of the process. Again, existing methods of factor analysis may be invoked, this time, the "quartimax" rotation. This completes the solution technique.

2. Pattern Classification Results

Using NMC analysis data for the period 1 August 1975 to 19 September 1975 we performed a test of the technique. We first determined the correlations between the 100 patterns, and then using the IMSL sub-routines OFCOMM and OFROTA, we determined the quartimax rotated F matrices for models based on four, six, and eight patterns (factors). As we may recall from the proceeding section, the magnitude of the f_{ij} coefficient denotes the amplitude of the i th pattern in day j . We arbitrarily selected a magnitude of f_{ij} of .8 or greater as denoting a day in which the overall pattern might be modeled reasonably with pattern i . (If f_{ij} equals .8, then pattern i accounts for 64% of the total variance on day j .) Table 1 presents the pattern sequences for the period based on this criteria. The unique variance is also shown on a day by day basis as this indicates the amount of variance that could not be explained with a linear combination of the "m" factors. Notice that the 6 and 8 factor models yielded very similar results, although the 4 pattern model did not. Notice that the eight factor model modifies the A pattern slightly with respect to the six pattern model and creates a G pattern which is used to cover the large variance of August 19.

The long period in the middle of August in which no one pattern predominates is not necessarily a sign that more patterns are needed. In particular, we can see that in the 8 pattern model, there are only four days in which the unexplained variance was greater than .2. Thus, these days were days in which the observed patterns could be fairly well approximated with linear combinations of patterns A through H.

The identification of the pattern types could now proceed using a least squares criteria and an inversion of the matrix equations (4). However, we feel that the orthogonality criteria that underlies the analysis is not necessarily optimum with respect to recreating observable patterns. Consequently, we judge it just as appropriate to typify the patterns based on actual realizations in which the unique variance was small and the pattern coefficient large. Figures 1 through 7 show patterns A through G based on this approach. It can be seen that the selections are approximately orthogonal. However, if we look at the correlation between these days we find some strong correlations between patterns as shown in table 2.

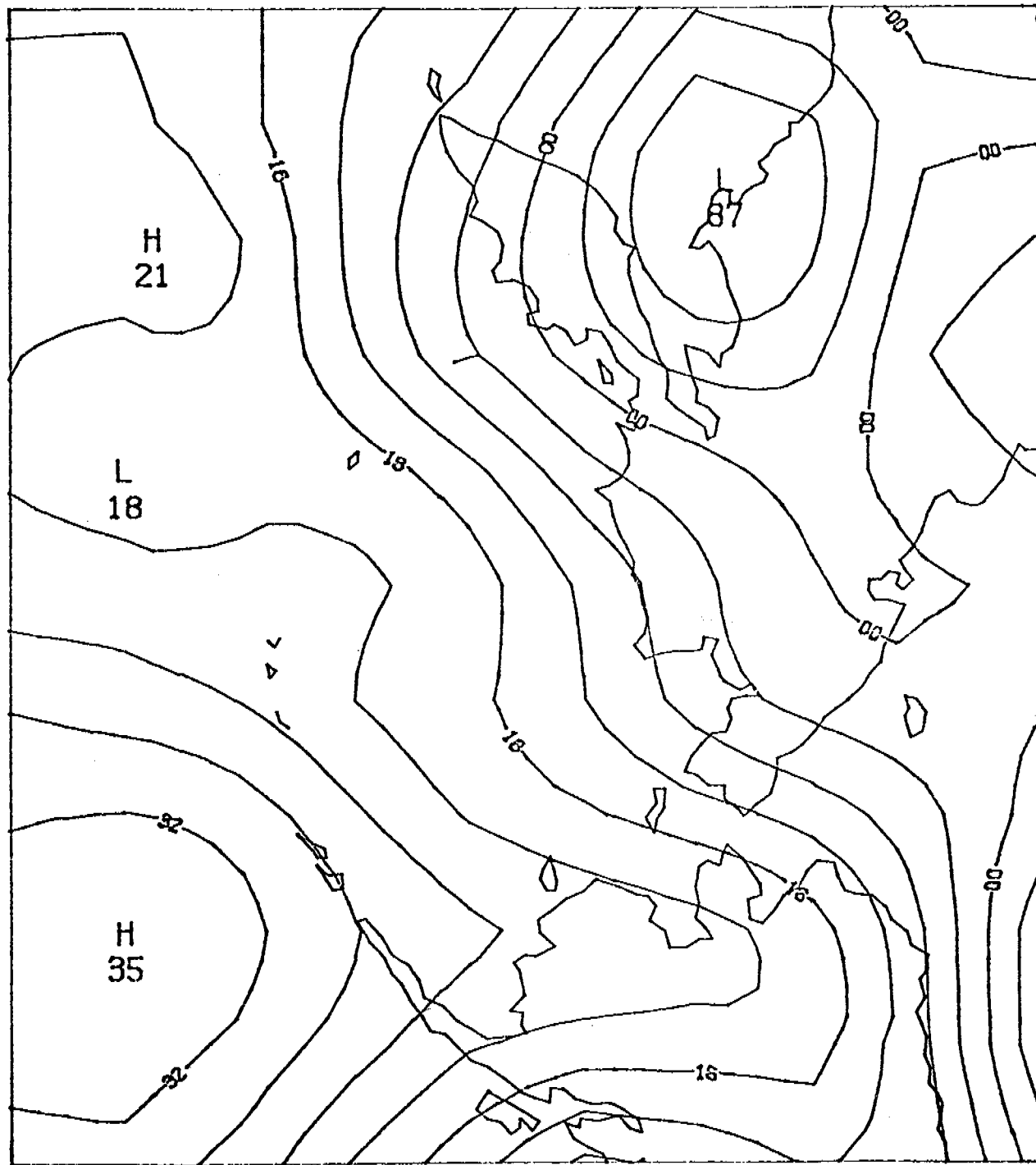
We attempted to relate the pattern types shown in figures 1 through 7 to those shown in Putnins and those selected in the subjective analysis portion of this task. This is not an ideal comparison because the subjective analyses focuses on the behavior of the patterns in the region lying to the east of our grid and for all twelve months. We could not match these conditions due to the data limitations we spoke of earlier. Table 3, nevertheless, shows the correspondence between the subjective classifications and objective results. Some indication of the difficulties posed by the subjective technique is the ambiguity in relating our pattern A with subjective patterns I or V.

In the period we analyzed, patterns A, B and G accounted for 28% of the days. If our correspondence is correct, Putnins would expect patterns A''', A., and F to account for only 8% of the days. Subjective pattern I, on the other hand, accounts for 28.2% of the days in August and 40.7% in September. This is in rough agreement with our observation provided the correspondence between patterns is correct.

Table F(1) 1:Pattern Sequences: 64% of Variance Cutoff

	Four Pattern Model		Six Pattern Model		Eight Pattern Model	
	Pattern Type	Unique Variance	Pattern Type	Unique Variance	Pattern Type	Unique Variance
AUGUST	1	B .34	B .13	B .13	B .13	B .13
	2	.47	B .20	B .17	B .17	
	3	B .11	B .06	B .06		
	4	B .05	B .05	B .05		
	5	B .20	B .14	B .07		
	6	.51	.20	.15		
	7	.43	.16	.11		
	8	.50	.28	.27		
	9	.42	.34	.21		
	10	.39	.37	.14		
	11	.33	.28	.11		
	12	.16	.15	.11		
	13	.31	.20	.16		
	14	.45	.30	.29		
	15	.48	.36	.29		
	16	.22	.20	.15		
	17	.24	.13	.09		
	18	.45	.33	.20		
	19	.76	.62	G .16		
	20	.67	B .25	B .12		
	21	.49	.22	.12		
	22	D .24	D .18	D .13		
	23	.26	D .13	D .12		
	24	.18	.15	.12		
	25	.36	.20	.12		
	26	.40	.29	A .14		
	27	A .24	A .18	A .05		
	28	A .13	A .09	A .06		
	29	A .21	A .11	A .09		
	30	A .33	A .25	A .13		
	31	.21	.20	.17		
SEPTEMBER	1	.13	.09	.07		
	2	A .31	.22	.16		
	3	A .28	.21	.15		
	4	.40	A .16	A .11		
	5	.20	A .14	A .11		
	6	.22	.15	.12		
	7	.30	C .15	C .13		
	8	.57	C .28	C .20		
	9	.53	.45	.15		
	10	.67	.20	.10		
	11	.53	F .19	F .16		
	12	.24	.18	.16		
	13	.41	.16	.10		
	14	.56	E .20	E .15		
	15	C .24	E .10	E .10		
	16	C .24	.20	.13		
	17	.40	.36	.32		
	18	.32	C .19	C .15		
	19	B .27	C .24	C .16		
	15/50	21/50	23/50			

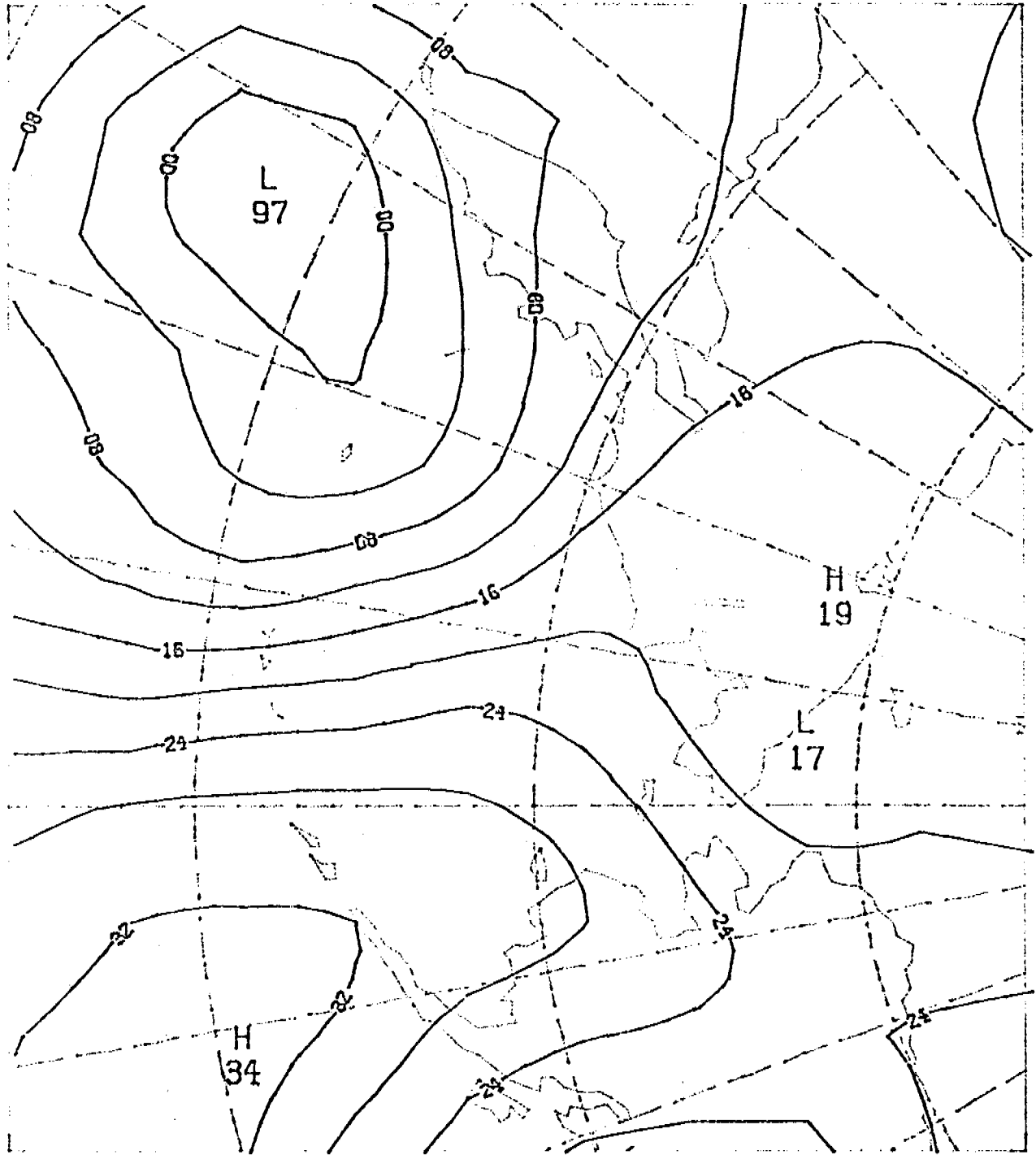
OBSERVED PRESSURES



00Z 28 AUG 1975

Figure F(1) 1 Pattern A

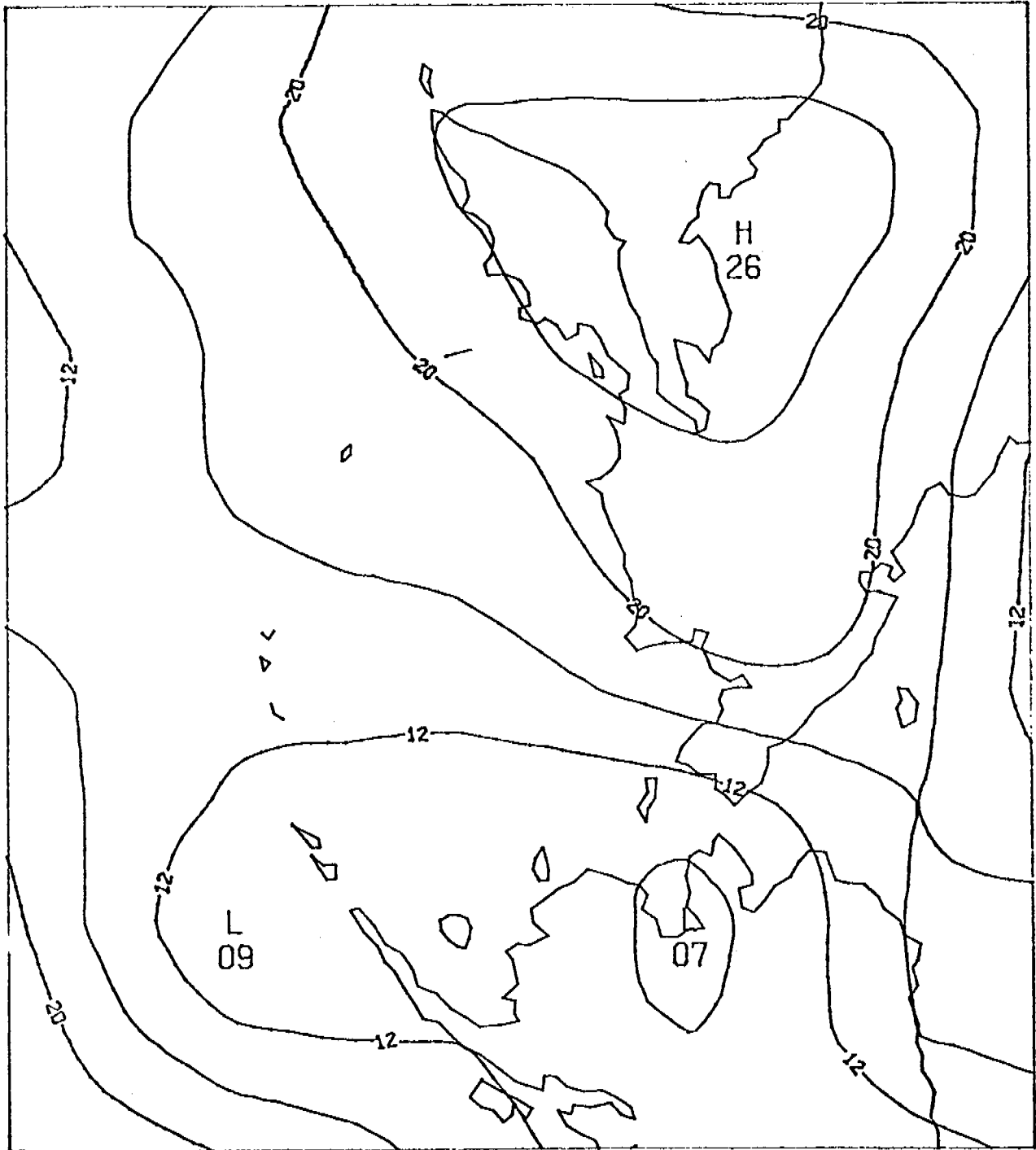
OBSERVED PRESSURES



00Z 4 AUG 1975

Figure F(1) 2 Pattern B

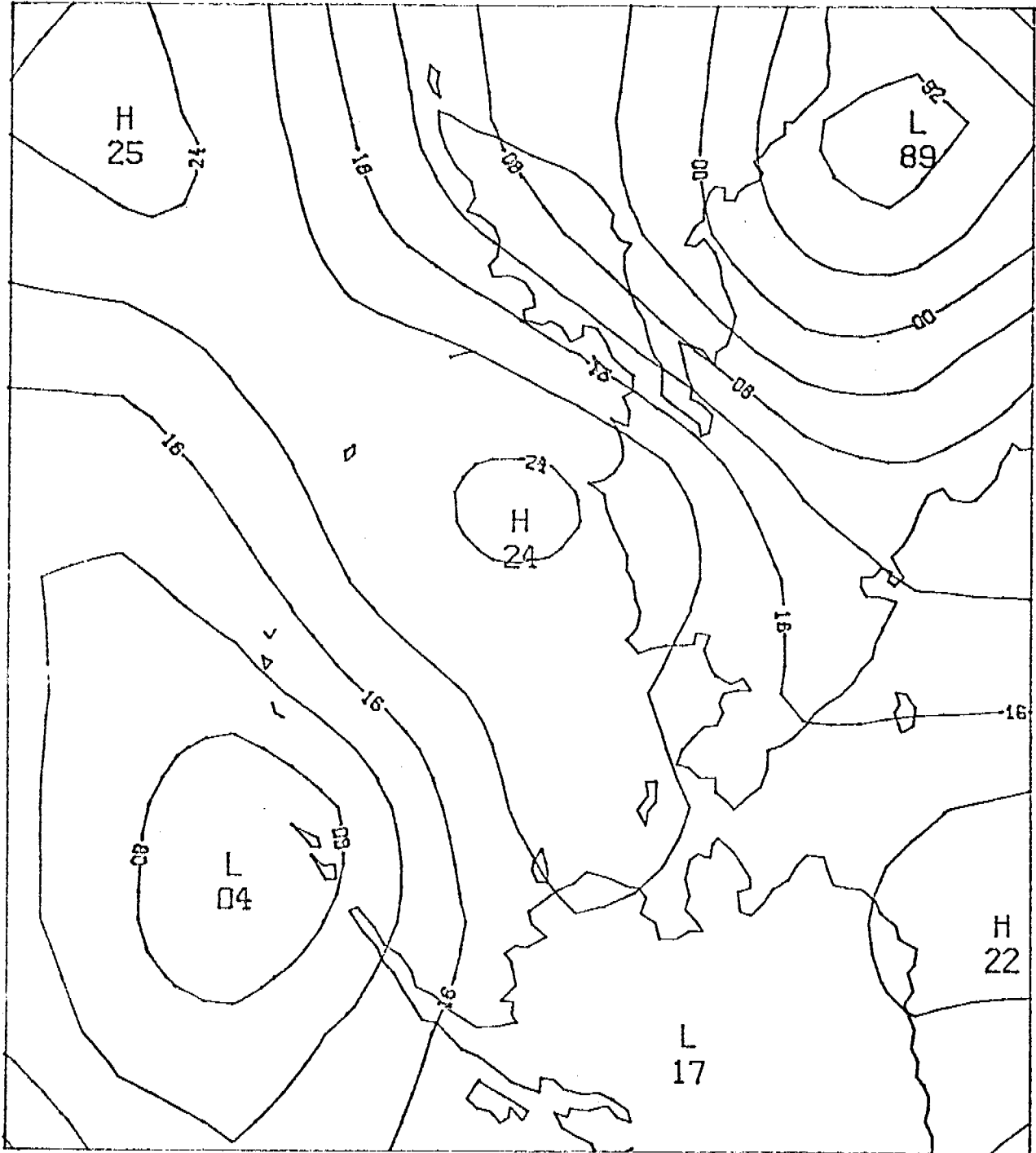
OBSERVED PRESSURES



00Z 8 SEP 1975

Figure F(1) 3 Pattern C

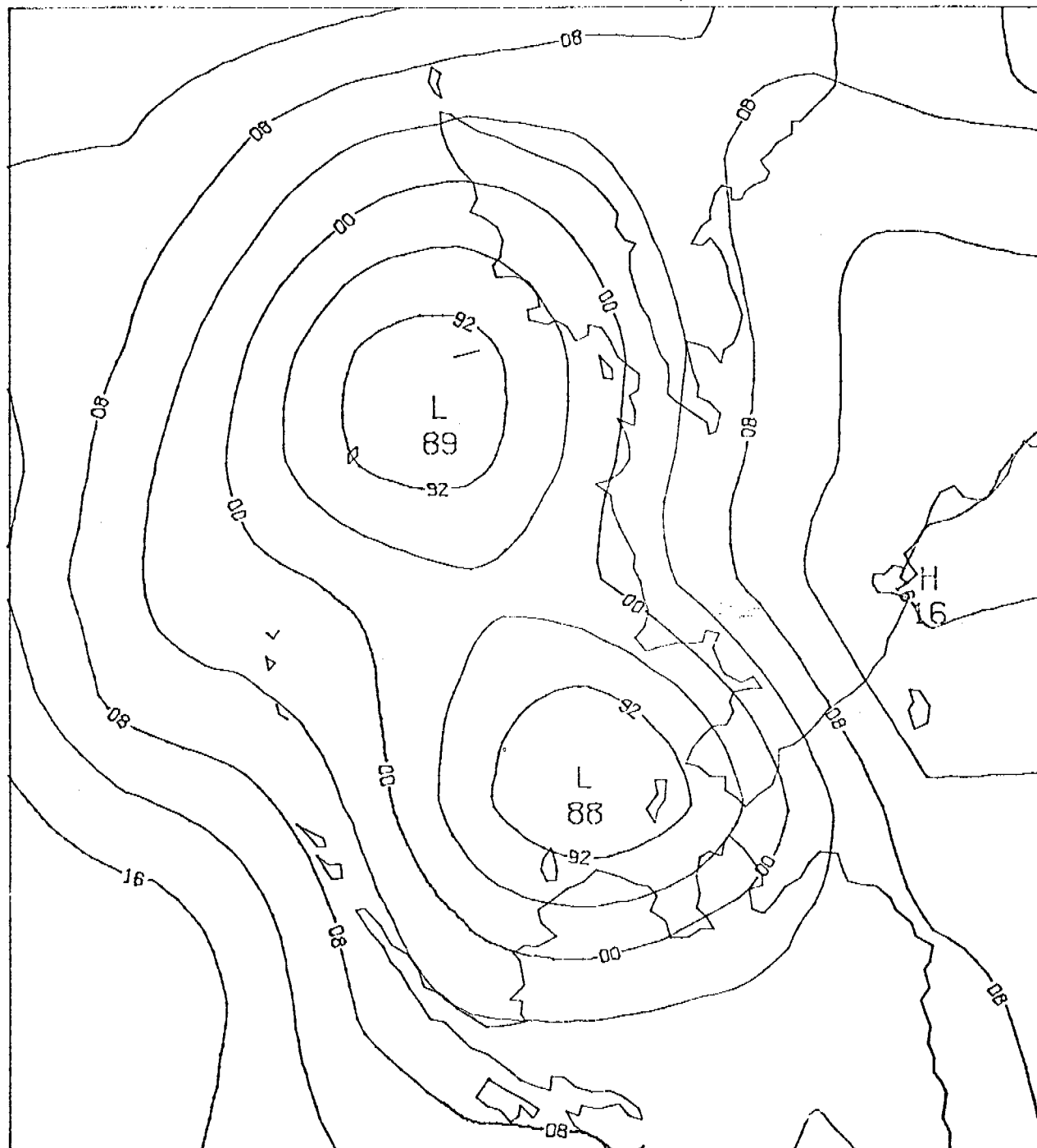
OBSERVED PRESSURES



12Z 23 AUG 1975

Figure F(1) 4 Pattern D

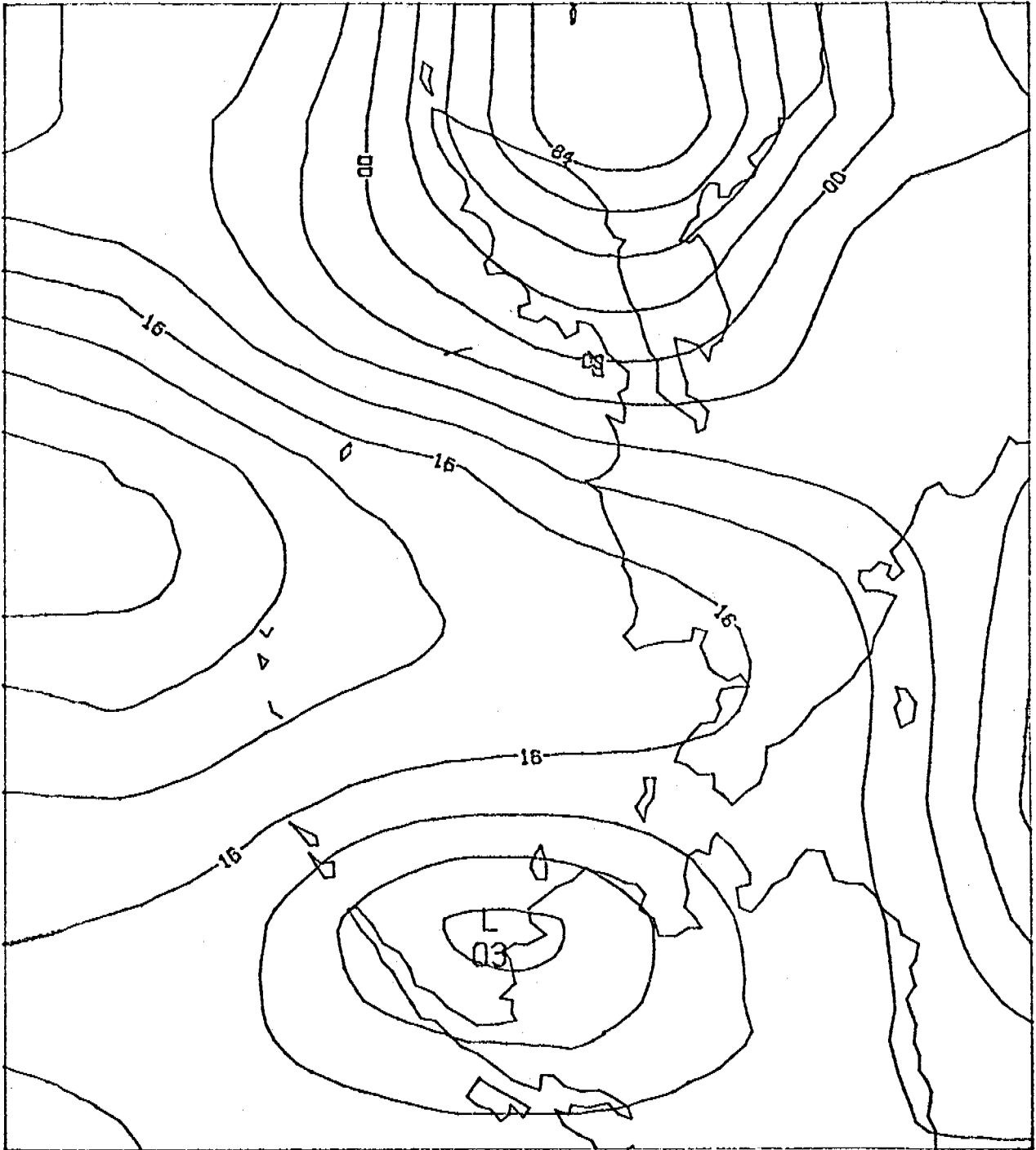
OBSERVED PRESSURES



00Z 15 SEP 1975

Figure F(1) 5 Pattern E

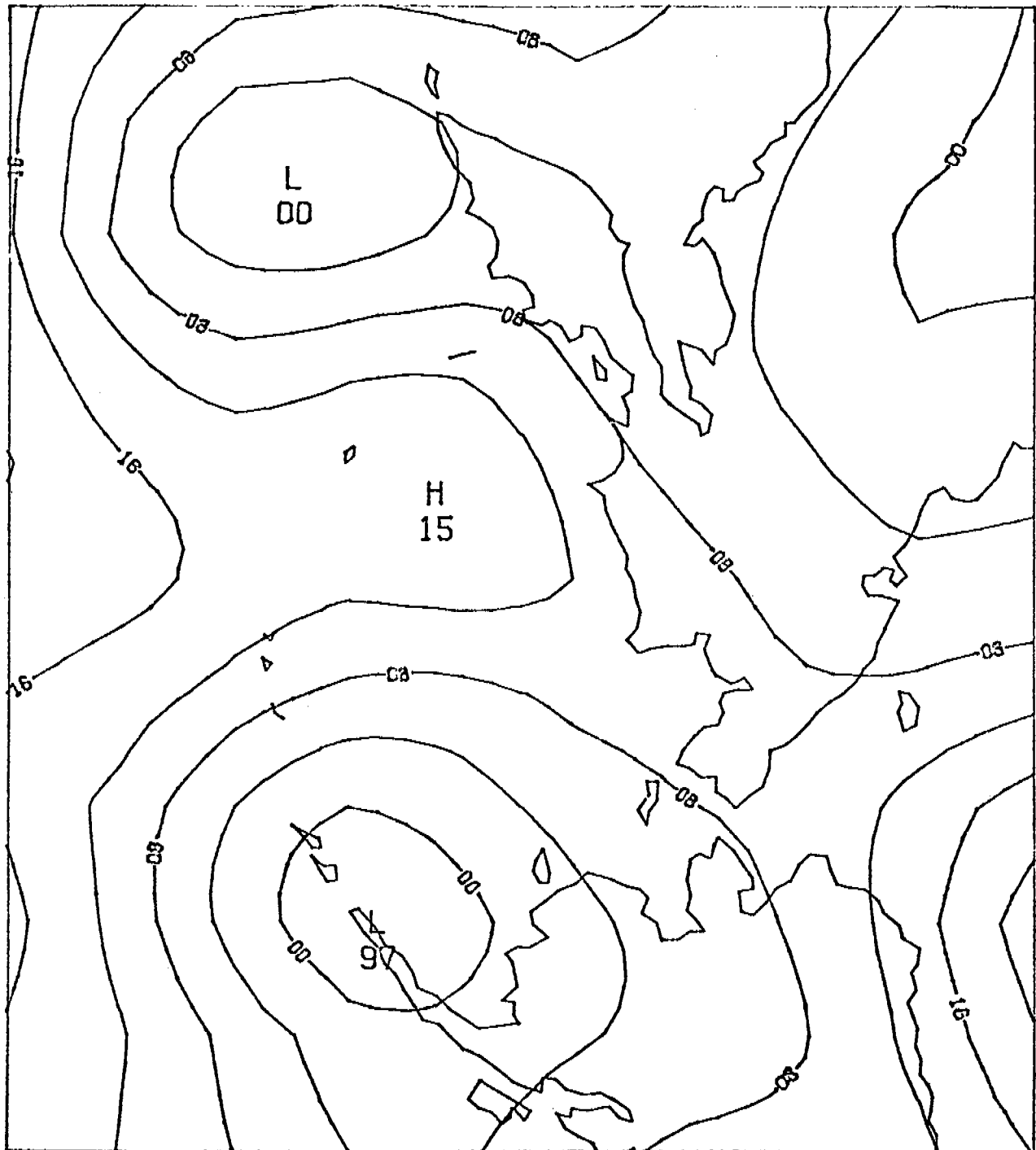
OBSERVED PRESSURES



12Z 11 SEP 1975

Figure F(1) 6 Pattern F

OBSERVED PRESSURES



00Z 19 AUG 1975

Figure F(1) 7 Pattern G

TABLE 2
PATTERN CORRELATION MATRIX

	A	B	C	D	E	F	G
A	1	-.36	-.34	.35	.40	-.04	.21
B		1	-.20	.12	.36	-.36	.16
C			1	-.40	-.17	-.06	-.03
D				1	-.08	.18	.47
E					1	.13	.14
F						1	.42
G							1

TABLE 3
CORRESPONDENCE BETWEEN OUR PATTERNS AND PUTNINS'

Task F Objective Pattern Type	Task F Subjective Pattern Type	Putnins' Corresponding Pattern
A	I or V	A'''
B	I	A ₁
C	?	?
D	II	C
E	V	E or E ₁
F	?	?
G	I (Sorkina 4c)	F

3. Extensions and Future Work

The technique as it exists now is of sufficient utility to warrant its application to the pattern classification problem without further modification. However, the limitation of the present technique to orthogonal, or nearly orthogonal, patterns is undesirable, and some additional effort will be expended to extend the technique to oblique patterns. This will probably be straightforward, and it would enhance the coverage. We will also investigate the use of discriminant analysis based on the principle component amplitudes. This may prove to be a valuable technique for "typing" weather maps, and this could simplify the construction of time series pattern sequences.

REFERENCES

- McCutchan, M.H. and M.J. Schroeder (1973): "Classification of Meteorological Patterns in Southern California by Discriminant Analysis" J. App. Met., Vol. 12, pp 571-577.
- Land, Iver A. (1963): "Map-Pattern Classification by Statistical Methods", J. App. Met., Vol. 2, pp 56-65.

F2. Subjective Weather Patterns for Coastal Gulf of Alaska

As discussed in the section on meteorological typing, the determination of pressure map types is the basis for extending the implication of weather service archives to the trajectory calculations. The sequence of types key the local wind fields as well as the barotropic current in the diagnostic model. In order for these type patterns to be successful the underlying physical processes leading to these patterns should be recognizable. That is, they should be meteorologically significant. In addition to objective typing, a review of subjective typing by previous authors was undertaken. One type pattern ought to represent an energy minimum, a quasi steady-state of the atmosphere, which is frequently observed. A type pattern which is an average of several rather different sequential daily maps (i.e., monthly average) is not proper as it would ignore the daily variability of the wind field and there would be little chance of recognizing it as the closest pattern to any of the daily maps. The synoptic climatology approach assumes that it is possible to choose a set of patterns which can be weighted and grouped in certain ways so that they yield any observed pattern. Two previous subjective studies to find type patterns, duration, and transition probabilities which cover the region of interest are available (Sorkina, 1963 and Putnins, 1966). These will be discussed in terms of their utility for the Gulf of Alaska. Six patterns for the region of interest will be described which are a result of modifying Putnins' patterns in the following ways:

- a) combining like patterns
- b) modifying them according to Sorkina's patterns

c) using fall, winter and spring of 77-78 LFM and PE sea level pressure analyses from the National Meteorological Center to test the patterns for verification and to modify them accordingly.

1. Two Investigations of Type Patterns

Sorkina's book is a careful description of the surface circulation patterns over the entire North Pacific Ocean. The fifteen patterns she obtains are based on 16,000 daily synoptic maps spanning 47 years (1899-1939, 1954-1959) and are well founded in the underlying governing physical processes, which Sorkina elucidates. Seasonal duration and transitional probability statistics are established. Sorkina found that each of her daily maps fit one of her patterns satisfactorily. Sorkina's patterns were applied to a new data set, the daily Pacific surface analyses at 1800Z from September 1977 to December 1977 prepared by the Ocean Services Unit of the Weather Service Forecast Office in Seattle. Three underlying regional physical processes were evident in her patterns which were combined and rearranged to make each pattern, zones of cyclogenesis, high pressure regions and regions for stagnation of lows. Depending on the season, the arrangement of continents and oceans determines the general horizontal temperature variation in certain regions. For example, a seasonal arctic front is oriented SW-NE near Japan in the mean, where cyclogenesis occurs. The newly formed cyclones travel rapidly toward the northeast. Another atmospheric forcing is the curved coastline of Alaska where these lows stagnate. Highs and zones of cyclogenesis alternate at mid-latitudes, while regions of stagnation and zonal bands of rapid movement for lows alternate at

higher latitudes. Each pattern is seasonally persistent and tends to lead to specific other patterns. An analysis of map sequences for September 1977 to December 1977 for the middle and eastern North Pacific showed that the maps would closely resemble one of Sorkina's patterns in general character for a day or two, followed by three or four days of less identifiable character as the cyclones moved rapidly from cyclogenesis regions to stagnation regions, when the maps would again closely resemble a type pattern for another few days.

Sorkina's book is thus very useful in a study of this nature, where cataloging daily map types is desired. Unfortunately her type patterns cover the whole northern Pacific and are not adequately resolved for the comparatively small and peripheral coastal Gulf of Alaska area. Putnins' patterns, to be discussed shortly, are on a more applicable scale. However, Sorkina excels Putnins in establishing physical bases for her patterns and were used as a general guideline for deciding which type patterns to implement.

Putnins' twenty-two patterns were also obtained from a large data set. Weather maps, both surface and 500 mb, for the period 1 January 1945 to 31 March 1963 were used to determine them "in such a way that for every day of this period a specific baric weather pattern could be assigned". Duration and transition frequencies were also found. The 500 mb patterns were used to assign either a 'cyclonic', 'anti-cyclonic' or 'mixed' designation to the flow pattern aloft. Most of Putnins' patterns can be related to one or another of Sorkina's patterns. While it is desirable that Putnins' patterns are actual surface weather maps, he considered to be representative, several of the infrequently occurring ones are somewhat arbitrary. Furthermore, his patterns apply

to all of Alaska so that the difference between any two pattern is sometimes due to a difference occurring far from the coastal Gulf of Alaska. Thus many of his patterns have been grouped and redrawn to be more useful for Gulf of Alaska studies. The occurrence frequencies have also been regrouped, taking care to insure commonality of season and process.

2. The Six Surface Weather Type Patterns

Six type patterns are shown in figures 1-6. All 22 of Putnins' patterns can be incorporated into these slightly more general patterns. Each of the six is associated with one of Sorkina's patterns, and almost all of the 77-78 surface maps closely resembles one or another of the six. More importantly, these six patterns are meteorologically significant in the sense described above.

An example of how these patterns were obtained is given for the very common case of a stagnating low tucked into the center of the coastal Gulf of Alaska. The underlying broad pattern, Sorkina's 4c, is shown in figure 7. Putnins' type patterns A₁ and A' shown in figures 8 and 9 reveal more of the necessary details and the effect of the land and ocean on the isobar patterns here: packing together meridionally. Type pattern 1, figure 1, was thus determined concentrating on the orientation of the geostrophic wind along the coastal Gulf of Alaska.

Type pattern I is a manifestation of the natural stagnation region for cyclones provided in fall, winter, and spring by the high, relatively cooled land to the west and north. This condition creates a very stable anticyclone over the Yukon, which often becomes so strong as to dominate the coast, as typified by pattern III. In both cases the coastal mountains tend to contain the cold air while the relatively warmer

water constitutes a good substrate for cyclonic conditions, making for closely packed isobars parallel to the coast.

Type pattern II represents the average position of cyclones as they are transported in the westerlies to eventually die out in the northeastern Gulf. However, cyclones often linger over the beginning of the Aleutians. This frequented position is likely associated with the well known mean Aleutian low at 500 mb as the disturbances align vertically in old age. The 500 mb low can be shown to be positioned correctly in terms of global wave numbers and continental - ocean forcing.

In the summer the comparatively cool northeast Pacific Ocean surface provides for a well developed anticyclone. This often encroaches on the region of interest and therefore is the basis of type pattern V. In this milder part of the year, the equator to pole temperature gradient lessens and cyclonic systems become weaker and are found farther to the north. Lows tend to move through Alaska itself to influence the coastal Gulf area, most frequently being observed as shown in pattern IV.

Somewhat less commonly observed than the first five patterns, type pattern VI shows a cyclone positioned near the Queen Charlotte Islands, with a high over northeast Alaska and the Bering Sea. This occurs when cyclogenesis occurs farther to the east and south than for the lows observed in the other cases. The cyclone often migrates up towards the central Gulf coast or may travel somewhat into the continent, usually dying out.

Each of the six patterns are listed in table 1 with the season with which it most commonly is associated, the Putnins patterns from which

it is derived and the underlying Sorkina pattern. Table 2 gives the monthly frequency of occurrence in percent of the six patterns, obtained by combining the corresponding Putnins statistics. This illustrates the seasonality of each pattern and confirms the physical basis for each.

Work to be completed soon includes establishing transition and duration probabilities using a similar method and testing these for a new data set, digitizing the six patterns on a grid and comparing the grid fields with the patterns obtained by objective techniques.

TABLE F(2) 1

	Sorkina	Putnins	Season
I	4c	A', A ₁ , G, H	Winter
II	5b	A, C, E, A _C	Winter
III	6a	D, B, D	Winter
IV	1a	A'', A ₃ , F	Summer
V	1b, 5a	A''', A ₂ , E', E' ₁	Summer
VI	7a	D', E'', E ₁ , F ₁	Transition

TABLE F(2) 2
MONTHLY FREQUENCY OF OCCURRENCE IN %

	I	II	III	IV	V	VI
JAN	32.1	20.2	23.2	1.8	17.9	4.6
FEB	36.4	19.2	17.0	2.1	21.9	3.4
MAR	49.0	17.9	14.0	2.5	13.4	3.2
APR	48.4	18.1	10.7	5.3	15.1	3.3
MAY	34.7	18.5	11.7	6.0	27.7	1.5
JUN	26.1	14.5	6.0	15.5	32.7	4.7
JUL	23.0	12.0	7.5	15.6	27.7	4.1
AUG	28.2	18.1	4.7	17.2	28.5	3.4
SEP	40.7	23.0	5.9	8.2	19.4	2.6
OCT	51.3	22.3	7.2	6.4	9.3	3.4
NOV	41.4	24.5	8.7	3.0	16.8	5.5
DEC	46.2	18.5	13.3	5.2	12.0	4.8

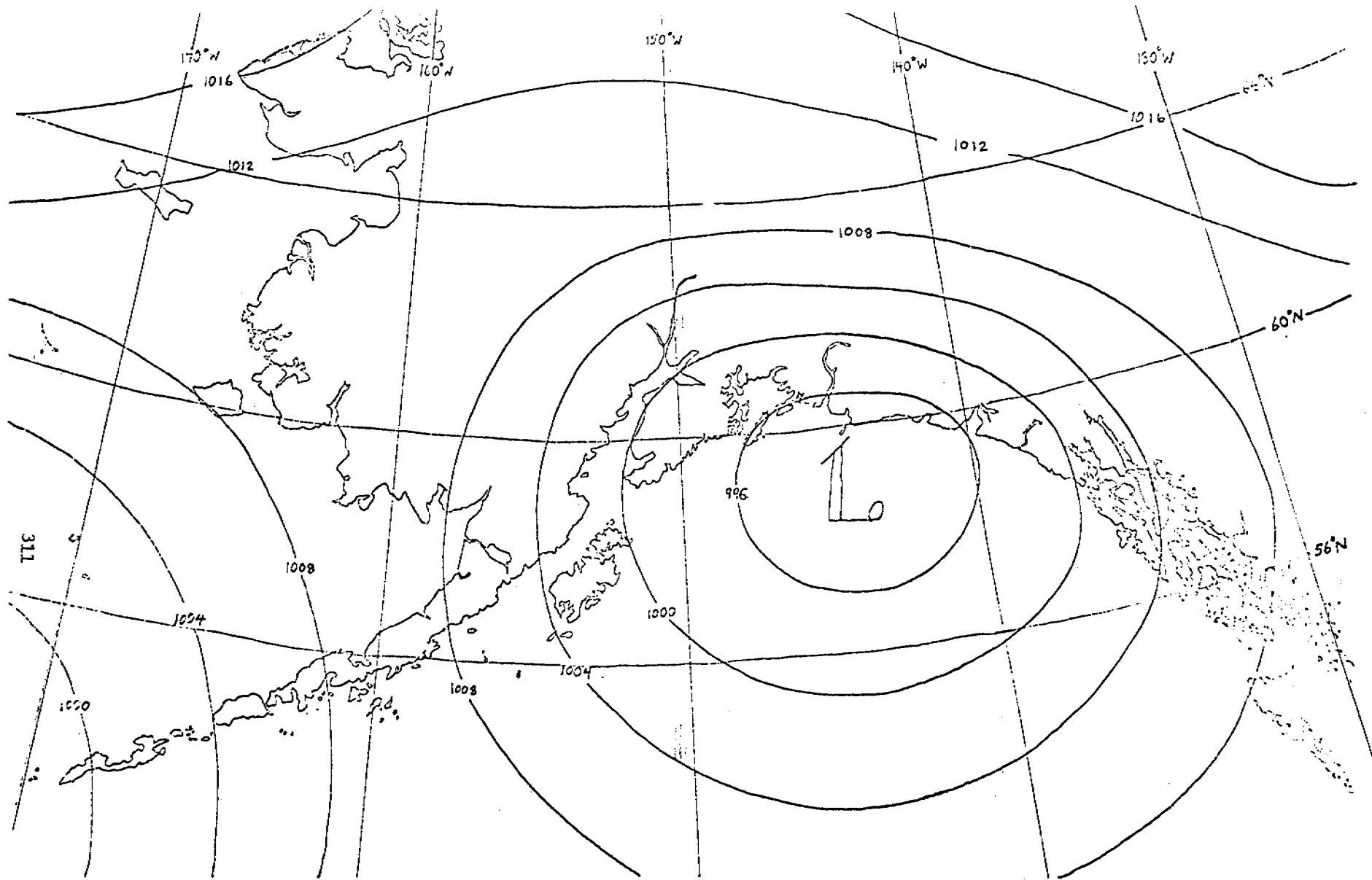


Figure F(2) 1, Type Pattern I

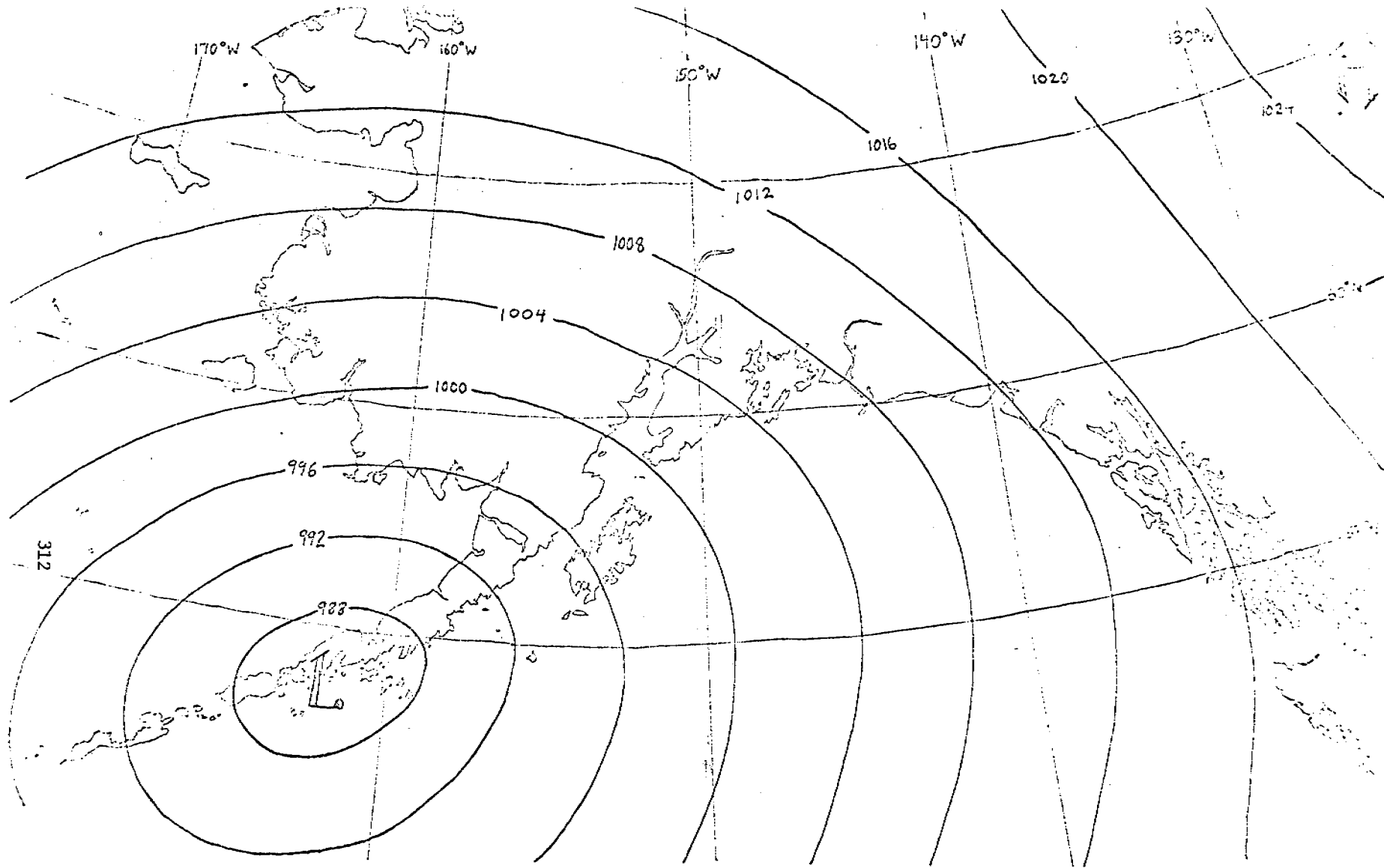


Figure F(2) 2 Type Pattern II

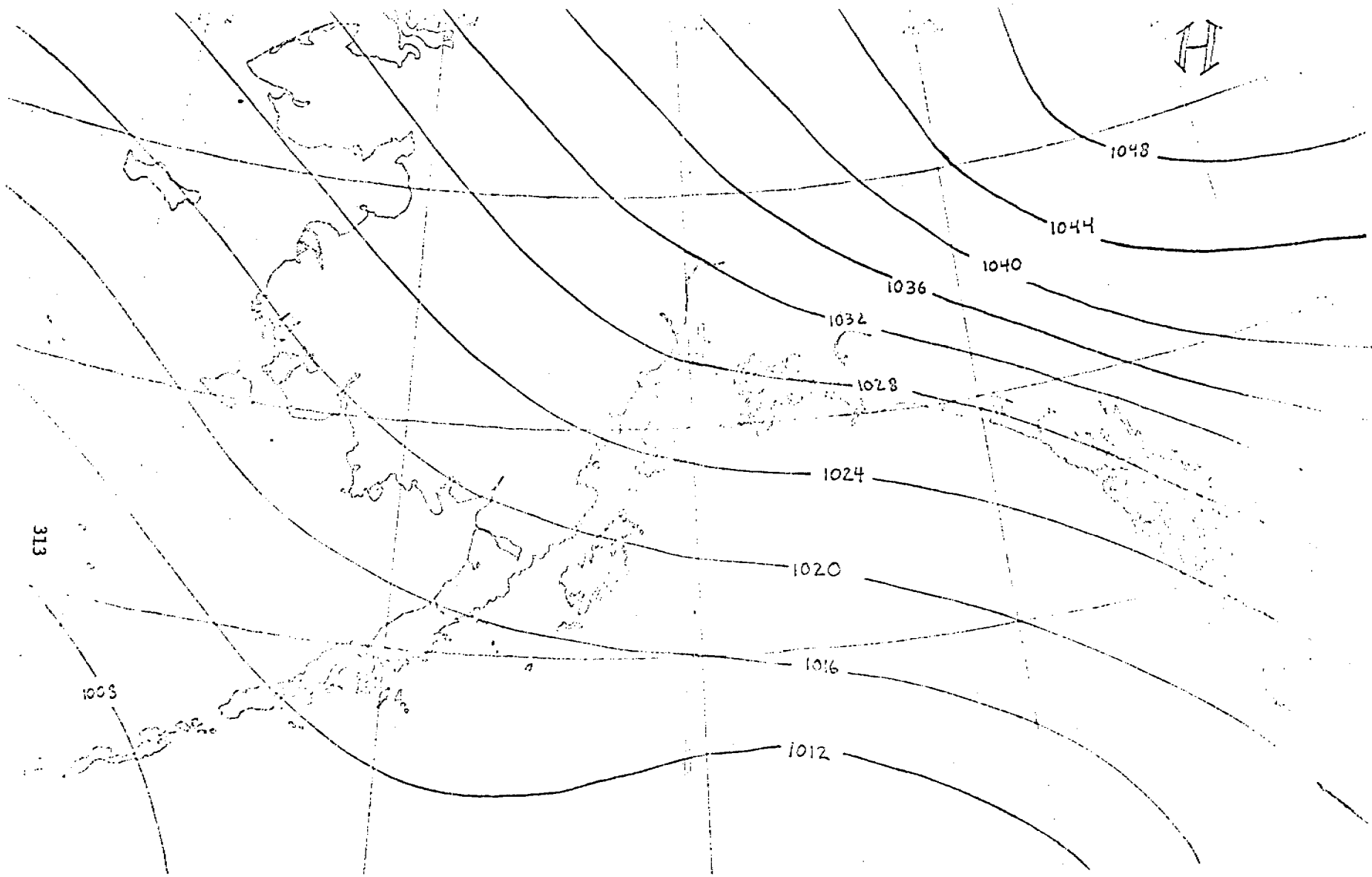


Figure F(2) 3 Type Pattern III

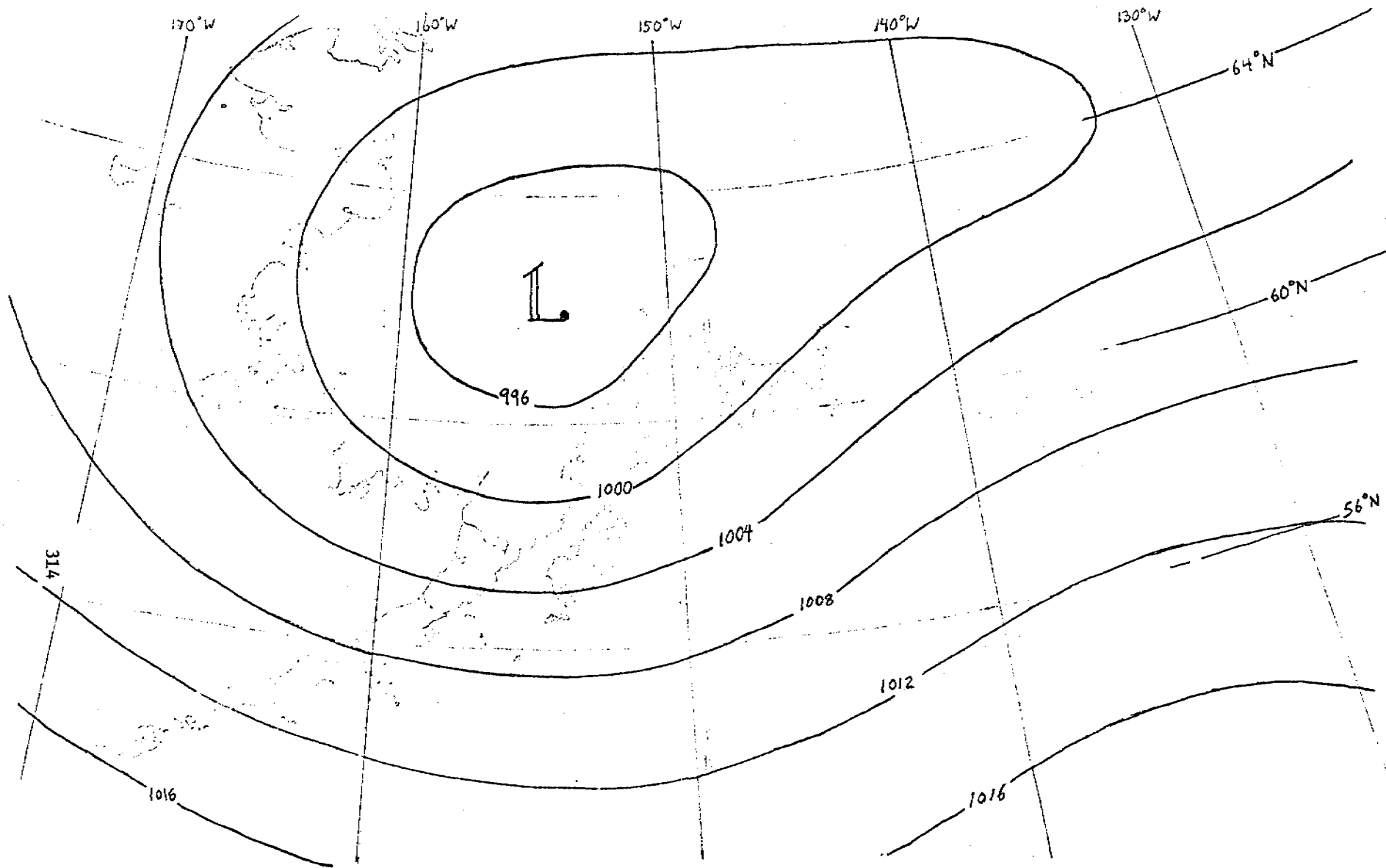


Figure F(2) 4, Type Pattern IV

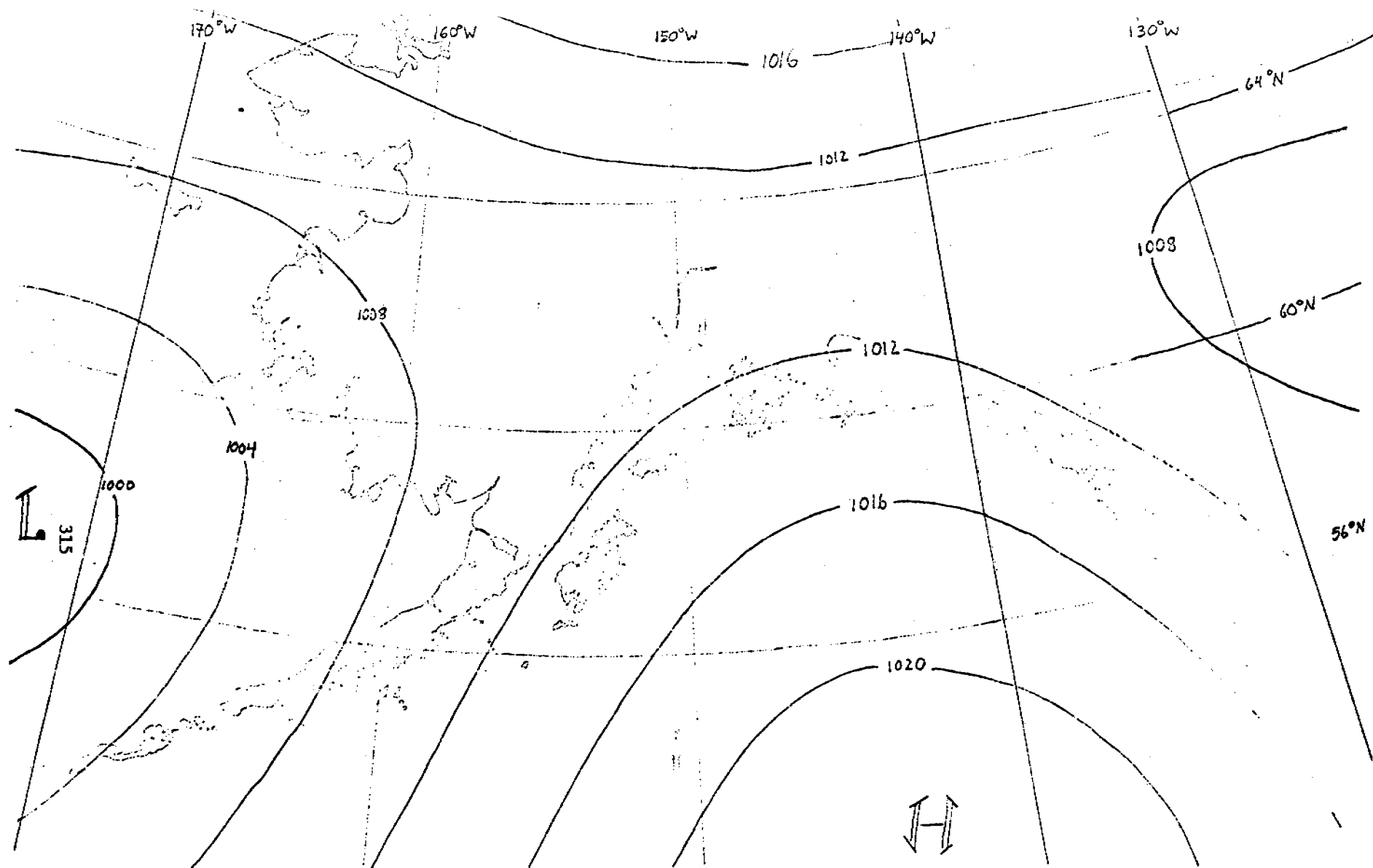


Figure F(2) 5 Type Pattern V

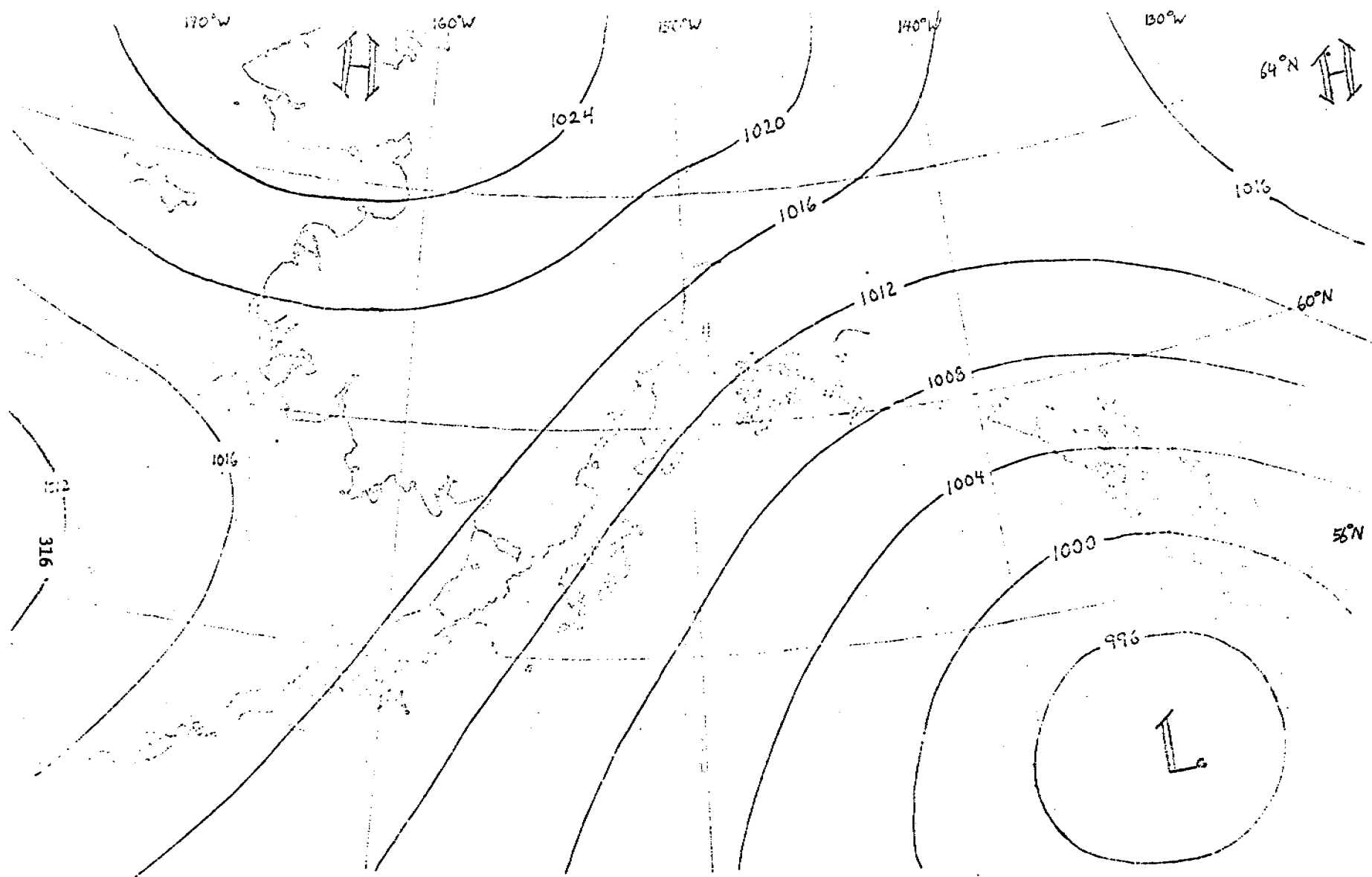


Figure F(2) 6 Type Pattern VI

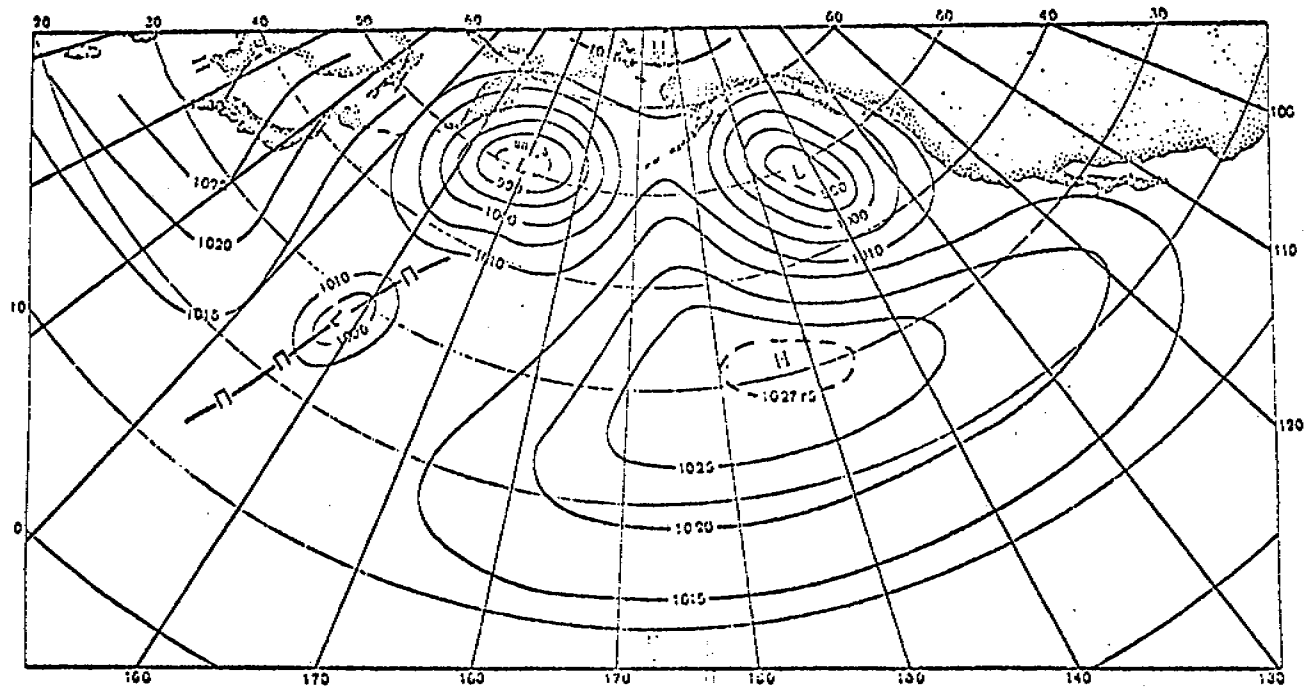


Figure F(2) 7 Sorkina's Pattern 4c

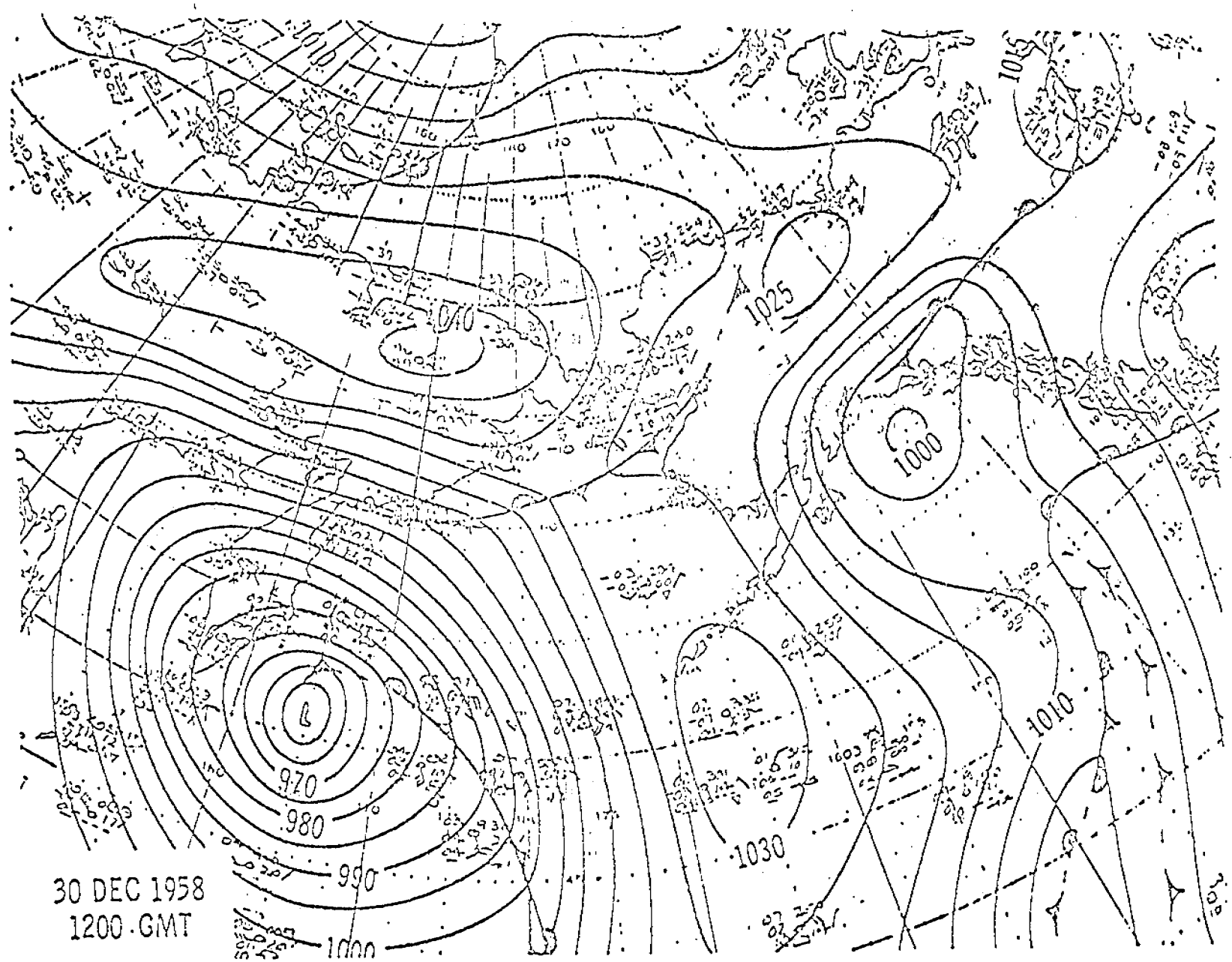


Figure F(2) 8 Putnins' Pattern Type A₇

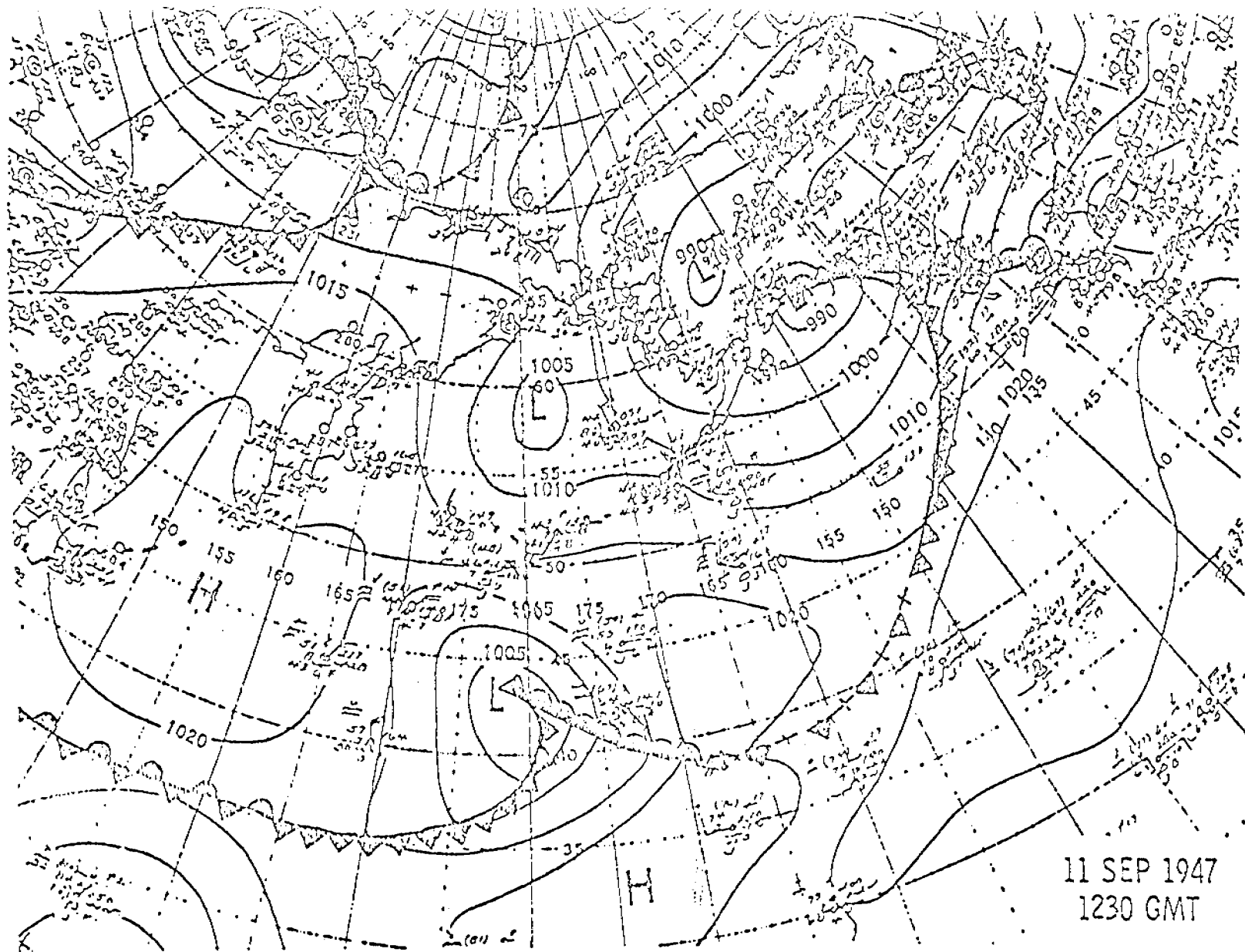


Figure F(2) 9 Putnins' Pattern Type A'

F3. Grid Point Data Subroutines for the Study of Regional Wind Climatologies

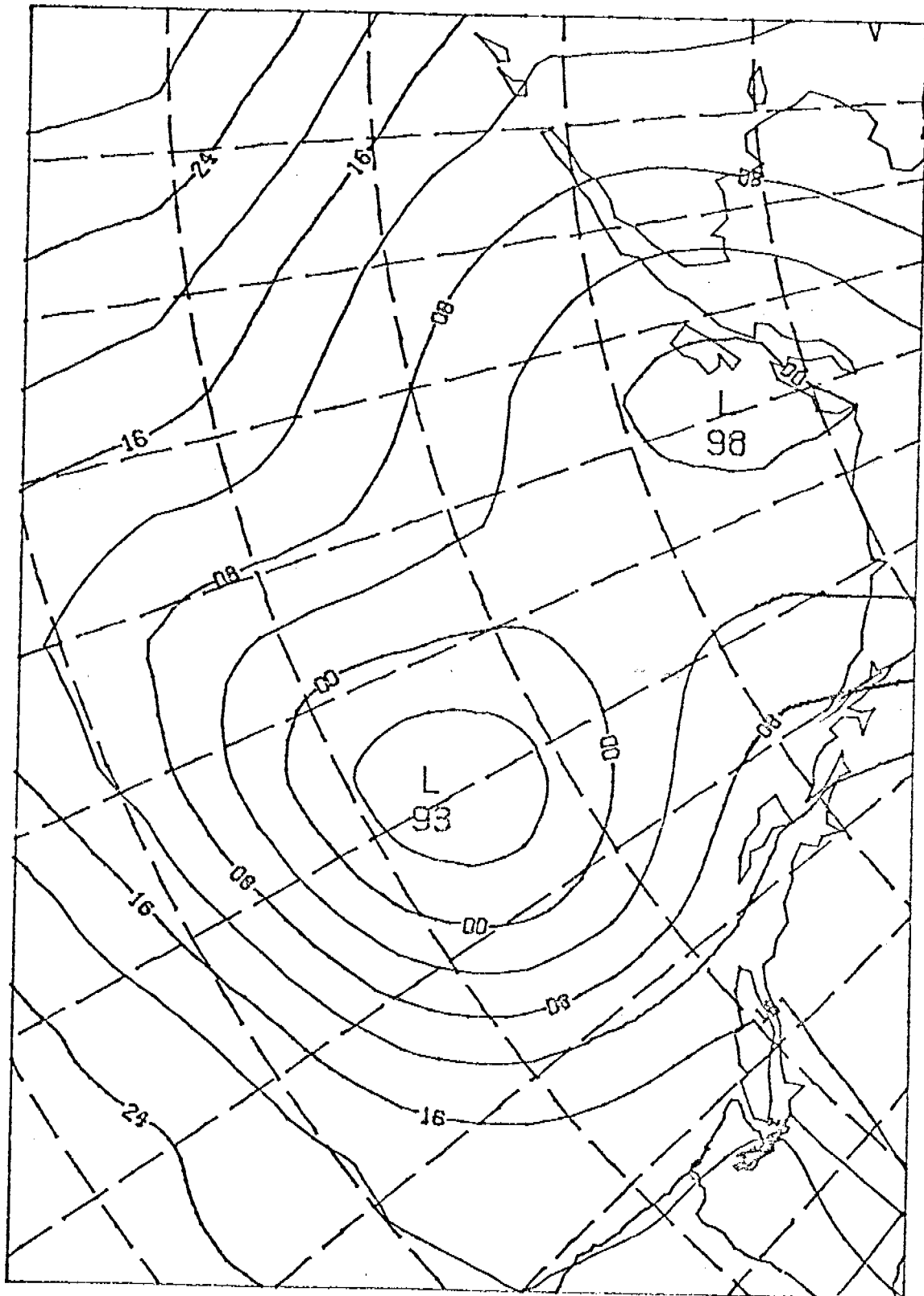
A set of programs has been written to catalogue and process atmospheric pressure and related fields on polar stereographic grids such as those generated at the National Meteorological Center and Fleet Numerical Weather Central. These fields form the data sets for objective weather map typing and the long term synoptic climatology base for providing event frequency information to the trajectory calculations. Grid point pressure analyses are also part of meteorological case studies, serving as boundary conditions for the regional meteorological model and large scale information for the meteorological field program. A specific example of the latter is the winter 1977-78 study in Lower Cook Inlet.

The subroutine library is quite general for manipulating grid point fields and includes biquadratic interpolation, plotting package, conversion of latitude-longitude locations to and from grid point I-J, and grid point wind components to and from earth oriented meteorological convention. A second set of routines calculates geostrophic, gradient, thermal and surface winds from pressure and temperature grid point fields. Three master programs calculate winds at all grid points, create time series of winds at particular locations for comparison with anemometer records and plot sequences of maps. Plotting routines are based upon the NCAR package which plots coastlines and contours fields. An example for the Northeast Pacific is figure 1. A list of routines is provided as Table 1.

The National Meteorological Center (NMC) produces sea level pressure (SLP) and surface temperature (SAT) analyses at 0000 and 1200 GMT on one

of two polar stereographic meshes: the PE grid with spacing of 381 km at 60°N covering the northern hemisphere and the LFM grid, a fine mesh grid with spacing of 190.5 km at 60°N, covering North America and adjacent waters. PE and LFM are historical names standing for "Primitive Equation" and "Limited Area Fine-mesh Model". Coarse mesh pressure fields produced by Fleet Numerical are on the same grid as the Weather Service PE grid. Master tapes are archived by the National Center for Atmospheric Research (NCAR) and by the Environmental Data Service (EDS) for the PE grids. At present the LFM data are not routinely archived for general distribution. Data tapes obtained from archives must be reduced to the area of interest (i.e., Gulf of Alaska) and fields of interest (i.e., SLP) as all upper air fields are normally sorted by data along with the SLP. Table 2 lists our processed data sets. Recent sets were obtained directly from the Weather Service so they include LFM data. Missing dates will be obtained from EDS master tapes to coincide with OCSEAP field experiment periods.

ANALYSIS



00Z 1 NOV 1977

Figure F(3) 1 Sample pressure contour plot for grid point pressure field

TABLE F(3) 1
PROGRAM/SUBROUTINE LIBRARY FOR GRIDED FIELDS

1. Edit Primary data sets (EDIT)
2. Create Windfields (ALLPTS)
3. Create time series (PTWND)
4. Plot pressure maps (PLOTTP)
5. Subroutines
 - A. Interpolation (INTERP, EDGE)
 - B. Geostrophic Wind (GEOWIN)
 - C. Gradient Wind (GRDWD)
 - D. Thermal Wind (TMWND)
 - E. Location on Grid (W3FB00, W3FB01)
 - F. Speed and Direction Conversion (W3FC00, W3FC02)
 - G. Surface Wind by Empirical Constants (MODEL1)
 - H. Surface Wind by Cardone PBL Model (MODEL6, CARON, PSI, SHR)

TABLE F(3) 2
 PROCESSED SEA LEVEL PRESSURE FIELDS

Area	Dates	Grid	Source
Bering Sea	May 75 - Apr 76	PE	NMC
Gulf of Alaska	Nov 77 - Mar 78	PE	NMC
Gulf of Alaska	Nov 77 - Mar 78	LFM	NMC
Northern Hemisphere	Jan 68 - Dec 75	PE	NCAR

IV. Cooperation

We are cooperating with the following research units:

- 138 (Hayes and Schumacher) We exchange ideas on the circulation around Kodiak Island and NEGOA. They provide STD station data, current meter data and pressure gauge data. We offer suggestions about interesting oceanographic features and about station locations.
- 289 (Royer) They provide STD station data, particularly for the NEGOA area. We exchange ideas about the general circulation features in the Gulf.
- 367 (Reynolds) We exchange ideas about the near-shore meteorology in southern Alaska. They provide wind data for keying and comparing with the regional wind model.
- 217 (Hansen) They provide results of satellite tracked drifters which we can use to enhance our understanding of diagnostic model results and trajectory calculations.

V. Conclusions and Needs for Further Study

Numerical Studies in the Gulf of Alaska region have resulted in a more complete understanding of the current and wind regimes. This is reflected in the discussions in Section III of this report. The continued study of the Gulf from this unit should emphasize the application of the models developed up to now to problems of interpretation of oceanographic and meteorological data. We should also then combine the knowledge gained in these studies into trajectory calculations for the region.

Major elements from this reporting period include:

- The components of the diagnostic model have been rigorously evaluated and an unambiguous technique for establishing boundary conditions has been developed.
- STD data sets have been identified for applying the diagnostic model to NEGQA.
- The sensitivity of the meteorological model has been tested in one dimension for NEGQA and the results extrapolated to a coastal wind field.
- Both subjective and objective methods of typing pressure maps in the Gulf of Alaska were studied to understand the regional climatology.
- The objectives of the trajectory model calculations were outlined.
- Schemes for handling field data and model results for use with the full trajectory model were developed.

Third Annual Report

Bristol Bay Oceanographic Processes (B-BOP)

L. K. Coachman
T. H. Kinder

Department of Oceanography
University of Washington
Seattle, Washington 98195

J. D. Schumacher
R. L. Charnell

Pacific Marine Environmental Laboratory
Environmental Research Laboratories, NOAA
3711 15th Avenue NE
Seattle, Washington 98105

Contract No: R 7120840

Research Unit: 141/549

Period: 1 April 1977-31 March 1978

Number of Pages: 247

30 March 1978

Table of Contents

	<u>Page</u>
I. Summary	1
II. Introduction	1
A. Objectives	
B. Tasks	
III. Study Area	2
IV. Present Status	2
A. On Lateral Water Mass Interaction - A Case Study, Bristol Bay, Alaska	3
B. A Structural Front Over the Continental Shelf of the Eastern Bering Sea	67
C. Structural Fronts in the Bering Sea	102
D. The Evolution of the Hydrographic Structure over the Continental Shelf near Bristol Bay, Alaska, during Summer 1976	105
E. The Deep Eddy South of the Continental Shelf	181
F. Tidal Analysis	181
G. Sub-tidal Flow During Summer in Bristol Bay (current meters, drifters, meteorology)	184
H. Winter Hydrography	186
I. The Front Overlaying the Continental Slope in the Eastern Bering Sea	203
V. Cooperation	237
VI. Publications Resulting from Bristol Bay Work	237
VII. Needs for Further Study	238
VIII. Conclusions	239
Appendix A. Hydrographic Summary	240
Appendix B. Mooring Summary	245
Appendix C. UW Budget	247

I. Summary

Field investigations, begun in Autumn 1975, are now beginning to bear fruit and our understanding of the hydrographic and current regimes in Bristol Bay is growing. Many interesting and important features have been identified, including fine structure, fronts, anomalously diminished tidal currents, and an eddy. Further work, primarily requiring intensive data analysis, will focus on understanding these and similar features, and estimating their importance in assessing hazards of petroleum development. This future understanding should lead to a reasonable synthesis of the regional physical oceanography.

II. Introduction

A. Objectives

This work unit attempts to relate oceanic advective and diffusive processes to problems that petroleum development may cause.

Specific goals are:

1. To describe and understand general water circulation and hydrographic structure in the study area throughout the year; and,
2. To determine the spatial and temporal variabilities of the velocity and hydrographic fields, and to understand their causes.

B. Tasks

1. Hydrographic data. The present thrust of hydrographic data acquisition and analysis is to: (1) refine the spatial resolution near the structural front; (2) determine the hydrographic structure during winter; (3) further investigate fine structure near the shelf break; (4) examine the effect of the hydrographic structure on the tides; and, (5) examine the deep eddy observed south of the continental slope.

2. Current meter data. We are using current meters to: (1) elucidate the tides; (2) examine the velocity field near the structural front; (3) investigate the low frequency flow; and, (4) to continue defining the mean flow.

3. Pressure gage data. This data is being used to support current meter data in understanding the dynamical balances associated with different flow components. Specifically, we are examining tidal frequencies and low frequencies (i.e. "meteorological" frequencies).

4. Meteorological data. This data is required to correct pressure gage data to water level data, and to examine the oceanic response to atmospheric forcing.

III. Study Area

The study area continues to be the southeastern Bering Sea, approximately bounded by the Alaskan coast from Unimak Pass to Nunivak Island, thence by a line running southwest to the Pribilof Islands and then by the shelf break to Unimak Pass. We have also worked over the shelf to the north of this area, and over the continental slope and rise to the south of the area. More detailed descriptions may be found in earlier annual reports, in the publications listed below, and in the Present Status section which follows immediately.

IV. Present Status

In addition to reports already published, the most complete and well thought-out writing about this work is that being prepared for publication. We therefore include preprints of this work along with short reports of work that are in progress. The contents of this section:

- A. Lateral water mass interaction in Bristol Bay - a preprint by Coachman and Charnell.
- B. Structural Front - a preprint by Schumacher, Kinder, Pashinski, and Charnell.
- C. Structural Fronts - ongoing work.
- D. Seasonal evolution of hydrographic structure - preprint of Technical Report by Kinder, Schumacher, Tripp, and Haslett.
- E. Deep Eddy - ongoing work.
- F. Tidal Analysis - ongoing work.
- G. Current meters, drifters, meteorology - ongoing work.
- H. Winter Hydrography - ongoing work.
- I. Slope Front - preprint by Kinder and Coachman

A. On Lateral Water Mass Interaction -
 A Case Study, Bristol Bay, Alaska

L. K. Coachman

Department of Oceanography, University of Washington, Seattle 98195

R. L. Charnell

NOAA/Pacific Marine Environmental Laboratory, Seattle 98105

ABSTRACT

Salinity-temperature-depth data obtained on several spring and summer cruises during 1976 and 1977 from outer Bristol Bay in the southeast Bering Sea indicate the existence of a zone, between two well-defined water masses, where details of the interaction process are observable. This interaction zone is approximately 100-150 km wide and is characterized by a plethora of mid-water-column finestructure, in both temperature and salinity, that exhibit an hierarchy of vertical scale sizes. Vertical mixing energy within the zone appears low, which results in persistence of interleaving signatures induced by horizontal interaction of the two adjacent water masses. Such interaction probably occurs between all laterally juxtaposed water masses of nearly the same density; outer Bristol Bay allows enhanced examination of the process because of the broad lateral extent of the transition zone.

Introduction

For the past two years we have been studying the oceanic regime of Bristol Bay, Alaska, to determine potential material redistribution hazards accompanying oil and gas exploitation of the Bering Sea shelf. In the course of this investigation it has become evident that we have been presented a unique opportunity to study processes extant in water mass interaction.

The continental shelf of the eastern Bering Sea, whereon Bristol Bay occupies the southeastern portion, exhibits the characteristics of a typical shelf sea in higher latitudes. A comprehensive synthesis and overview of the physical property and dynamic regimes of shallow seas was recently reported by Csanady (1976). Flow over the shelf is dominated by "first-order" events, driven primarily by winds and tides, while the residual (longer-term) mean flows are insignificant in the transport of mass properties. Thus, as a consequence, salt transport on the shelf is decoupled from the mean circulation, and the excess of freshwater introduced along the coast is primarily fluxed across the shelf by a "lateral diffusion" broadly defined to include tidal scales. In such regimes isohalines tend to follow the isobaths with a general increase in salinity seaward across the shelf. The eastern Bering Sea shelf is unusual in that it is extraordinarily wide (>500 km). As the shelf is exposed to relatively severe environmental conditions each winter (about 90% of the shelf is ice-covered each February/March, see *e.g.*, Muench and Alhnäs, 1976), enormous quantities of a shelf water mass are formed each year which are recognizably homogeneous in time and space. Though it exhibits the cross-shelf increase in salinity (~ 1 gm/kg) demanded by the freshwater balance and small (~ 0.5 gm/kg) annual variations, it is always 1-2 gm/kg less saline than the oceanic water off-shelf, and, while a seasonally active surface layer shows large annual temperature variations the bulk of the water remains very cold.

Waters over the continental shelf are separated from those over the adjacent ocean basins by semi-permanent fronts. The signature of the frontal zone is a seaward rise of isopycnals; the horizontal gradient of average upper-layer density is steeper than it is over the shelf proper. In higher latitudes where salinity exerts strong influence on density, the front is evident as a relatively strong horizontal gradient in average upper-layer salinity. In the oceanic regimes, seaward of the front, the horizontal gradients of these properties are markedly less.

Location of the front appears to be tied to the continental shelf break. Csanady (*op. cit.*) cited ~ 100 m as the depth over which the front was typically located, but the region he used for formulating his conceptual model was the mid-Atlantic bight where the shelf break occurs at ~ 100 m depth. In the eastern Bering Sea, the front is centered over ~ 150 m depth, approximately the shelf break in this area. The typical width of the front would appear to be ~ 50 km.

Oceanic water abutting the front on the seaward side is relatively invariant in temperature and salinity compared with shelf waters, and therefore also forms a specific water mass. The upper layers of this water mass are typically warmer and more saline than those on the adjacent shelf. Along the outer edges of continental shelves in general is located a transition zone where major water masses with diverse properties are in lateral juxtaposition. The transition zone demarks the region of interaction between the water masses, of which the fronts are a manifestation.

The shelf-oceanic front of the eastern Bering Sea, from the Pribilof Islands northwest to Cape Navarin, was recently described by Kinder and Coachman (1978). Based on 13 summer cross-sections spread over eight years, the transition between

~0 horizontal salinity gradient over the basin to the mean shelf gradient of $3.7 \times 10^{-3} \text{ gm kg}^{-1} \text{ km}^{-1}$ occurs 20-100 km seaward of the shelf break. In the ~100 km segment landward from this transition, that is, over the slope, the horizontal gradient of salinity is considerably greater than the average, $\sim 4.7 \times 10^{-3} \text{ gm kg}^{-1} \text{ km}^{-1}$, constituting the front.

The front develops because of a decrease in the lateral diffusion coefficient. In cross-section, the upper layer isohalines rise to the surface and are more closely spaced. Kinder and Coachman (*op. cit.*) argued that as the mixing regime over the shelf is basically tidally generated, for a given tidal wave the amount of mixing achieved must be proportional to tidal excursion, and therefore inversely proportional to water depth. Lateral mixing decreases significantly where the water deepens significantly, *i.e.*, over the slope, which gives rise to a front with steeper horizontal salinity gradients. They further noted that an important consequence of the front was that it served as a barrier to the lateral flux of properties, including nutrients, plankton, and pollutants. They reported that across the front near Pribilof Canyon proceeding shoreward PO_4 decreased by a factor of 5 and NO_3 by a factor of 10.

It should be noted that the more tightly packed isohalines of the front do not *ipso facto* connote a reduced cross-front flux of salt. Even though the horizontal eddy coefficient is reduced, the horizontal gradient is increased and the flux might be the same as over the shelf inshore. However, the marked change in nutrient concentrations suggests there is, in fact, a reduced lateral flux across the fronts.

Finestructure in either T or S, or both, has recently been recognized as common in vertical soundings made along lateral water mass boundaries. The fine-

structure signals are from water layers 1 to 10's of meters vertical extent alternately expressing a greater influence of first one and then the other of the basic water masses involved. A recent perspective paper by Joyce (1977) shows how the "interleavings" of the finestructure are intermediate in scale between the large, or bulk, interaction of one water mass laterally with the other, and that in turn the finestructure layers are sources for small-scale mixing phenomena which may include salt fingers, double diffusive fluxes, etc. The latter are represented by microstructure signals in the vertical soundings (<1 m vertical extent).

In the transition zones associated with the edges of continental shelves, the sources of the interleavings, or lateral intrusions, are large lateral gradients in T and S provided by the two basic water masses, shelf and oceanic. These T and S gradients are invariably compensating (Joyce, *op. cit.*) so that the associated density gradients are much less dramatic. Normally, finestructure layers are arranged vertically such that each successive layer is of the same or greater density than those above, *i.e.*, the water columns are statically stable. However, rare instances of unstable layers of finestructure size have been reported (see Coachman and Charnell, 1977). The few cases have all been associated with major lateral water mass boundaries; that of Spilhaus, Ehrlich and Miller (1950) was in the shelf-water/slope-water front south of New England and the two cases reported by Gregg and Cox (1972) were from the boundary between California Current and Equatorial Water off southern California, while the largest reported statically unstable layer (Coachman and Charnell, 1977) was found in the transition zone of outer Bristol Bay.

Joyce (*op. cit.*) pointed out that finestructure interleaving or intrusions of a front represents a mechanism for cross-frontal exchanges for heat and salt.

The correlation between reported incidences of finestructure and transition zones between laterally juxtaposed major water masses suggests that interleaving is an extremely important form of their interaction; in fact, this layering might be the primary mechanism effecting cross-frontal exchanges of not only heat and salt, but such other properties as nutrients. However, interleaving studies have as yet not answered questions as to 1) space and time scales, 2) the special dynamics causing the variability, and 3) the rates of cross-frontal exchange (Joyce, *op cit.*). Further detailed description of transition zones would seem to be required both to construct reasonable conceptual models and design appropriate field experiments. This paper presents a description of the transition zone in outer Bristol Bay based on extensive data collected over the past two years.

Oceanographic Setting and Data Base

Bristol Bay is the southeasternmost portion of the very large continental shelf of the eastern Bering Sea (Figure 1). It is bounded on the south by Unimak Island and the Alaska Peninsula and on the east and north by the coast of Alaska. The western (seaward) boundary is the shelf break and slope, which runs northwest from Unimak Pass, the easternmost pass in the Aleutian chain, to the Pribilofs. The area under consideration is outer Bristol Bay, extending from Unimak Pass to the Pribilofs and onto the shelf approximately 200 km.

The outer Bristol Bay shelf is very flat, uniform and featureless. It gradually deepens seaward from about 70 m depths in the central bay to 150 m, the shelf break. The abrupt continental slope seaward of 150 m shows two indentations: the northern one, immediately south of St. George Island (southernmost of the Pribilofs), is Pribilof Submarine Canyon, and the southern one, just north of Unimak Pass, is Bering Canyon. These are two of the world's largest known slope valleys (Scholl, *et al.*, 1970) but their presence is evidenced only in the deeper bathymetry; no

trace of Bering Canyon can be seen landward of the 150 m isobath.

Seven recent hydrographic surveys have provided extensive STD coverage in outer Bristol Bay (Table 1). Because a large, unstable finestructure layer was discovered by the March 1976 survey (Coachman and Charnell, 1977) our data processing techniques for correcting T and S and calculating S from conductivity have been reviewed and revised. These revised processing procedures compensate for both the longer response time of the temperature sensor and the apparent lag in logging time between the temperature and conductivity sensors. For all data reported herein a thermal response correction of 0.4 sec and a logging lag correction of 0.4 sec were used. Additionally, values of temperature and salinity (conductivity) were rejected when the local thermal rate-of-change exceeded 0.1°C between observations; this thermal change is equivalent to a thermal gradient of $1.0^{\circ}\text{C}/\text{m}$ for the standard (for these cruises) lowering rate of 30 m/min. Rationale and details for this procedure are reported elsewhere (Charnell, Pearson and Coachman, 1978).

In this paper we work with 1-m average corrected value data sets, which has the effect of reducing variations in property values on scales less than 1 m and hence virtually eliminating microstructure signals. This procedure was adopted because of uncorrectable uncertainties in the accuracy of data at microstructure scales obtained by the standard instruments employed (Plessey model 9040 CTD and model 9006 STD) while the larger scale finestructure features are still well described by the smoothed data.

Circulation

The previous concept of circulation in Bristol Bay was of a general cyclonic flow around the Bay. An influx of water from Unimak Pass and the southeastern corner of the Bering Sea basin flowed in-shelf parallel to the Alaska Peninsula,

Table 1

Cruises Providing Extensive STD Data
from outer Bristol Bay

	<u>DATES</u>	<u>VESSELS</u>	<u>NO. STAS.</u>	<u>SPONSOR</u>
<u>1976</u>	9 Mar.- 1 Apr.	Moana Wave, Surveyor	36	OCSEAP ¹
	26 Apr.-28 May	Acona	80	PROBES ²
	26 May -18 June	Miller Freeman	54	OCSEAP
	2 Aug.-13 Aug.	Acona, Moana Wave	98	OCSEAP
	17 Sept.-3 Oct.	Moana Wave, Acona	44	OCSEAP
<u>1977</u>	26 Apr.-16 May	Discoverer	53	OCSEAP
	11 May -31 May	Acona	70	PROBES

¹OCSEAP = Outer Continental Shelf Environmental Assessment Program (NOAA)

²PROBES = Processes and Resources of the Bering Sea Shelf (NSF). PROBES stations also include complete O₂ and nutrient data.

then turned north and west in general conformity with bathymetric contours. This circulation scheme was deduced by Takenouti and Ohtani (1974) based on water mass analysis, but in the absence of definitive data. This concept was the generally accepted scheme until as recently as 1977 (cf. Coachman and Charnell, 1977).

Now that numerous data from outer Bristol Bay are available, we must revise our concept of the circulation. There is not a general inflow into Bristol Bay parallel to the Alaska Peninsula. Rather, there is an extremely slow drift from the vicinity of Unimak Pass and Unimak Island in the southeast toward the Pribilof Islands to the northwest. The drift tends to follow the bottom contours.

Evidence for the new concept comes from detailed dynamic topographies from the recent data. The first detailed map obtained in March 1976 (see Coachman and Charnell, *op. cit.*, Figure 11, p. 881), showed inflow with a bifurcation. Bering Sea source water, in part from the Alaska Stream which enters the region through Unimak Pass and in part from the basin to the west, was entering onto the shelf at this time west and northwest of Unimak Island. The eastern portion of this inflow appeared to continue into Bristol Bay parallel to the Alaska Peninsula, while the majority of the flow turned northwest and flowed approximately parallel to the bottom contours toward the Pribilofs. Data from all subsequent cruises showed no evidence of inflow along the Alaska Peninsula, not even a suggestion of a partial inflow with a bifurcation (a representative example of these dynamic topographies is shown in Figure 2). Thus, the dynamic topographies recently obtained belie a general in-bay current, but rather the data suggest a northwest drift along the outer shelf. The speed of this drift is indicated to be very slow - locally, in the extreme southeastern corner of the basin northwest of Unimak Island, speeds of 5-10 cm/s are suggested by some topographies, but the

general speeds are indicated to be much less than 5 cm/s.

Care must be taken in utilizing dynamic topographies to represent the flow field in shallow water. In this situation we believe the topographies to be a reliable index to the general, or longer-term mean (~ 1 month), flow field. There are two lines of supporting evidence. First, conservative property distributions do not show signs of a strong in-bay advection. For example, Figure 3 shows the mean 0-100 m salinity distribution for 3-10 August 1976. Bering Sea source water provides a strong high-salinity (~ 33 gm/kg) signal in contrast with the water columns on the shelf shallower than 100 m ($\bar{S} \sim 31.5$ gm/kg) and if there were significant in-bay advection near Unimak Island the isohalines would be much more strongly warped toward the east in this area than observed (cf. also the 50- and bottom salinity distributions for 7-18 June 1976; Kinder, 1977, Figure 9 and 10). Rather, the isohalines, like the dynamic contours, are oriented, in general, parallel to bathymetric contours, with some inbowing northwest of Unimak Island and southeast of St. George Island, where the 150 and 200 m isobaths indicate the presence of Bering and Pribilof submarine canyons, respectively.

Second, a few direct current measurements are now available from the area. In a companion study, three locations in outer Bristol Bay are sites where current meters have been moored for varying periods of time. Mean values for periods of three weeks overlapping the hydrographic surveys were calculated and compared with the appropriate dynamic topography (during June 1976, records were obtained from BC-3 and BC-13, and the mean flow vectors are shown in Figure 2). The correlation between the averaged measurements and the dynamic topographies is excellent; all indicate very low net speeds, of the same order as the dynamic topographies (1-5 cm/sec). There is a definite tendency for the flows at the various locations to parallel the local bathymetry.

During summer 1977, six surface drogues tracked by satellite were launched in the area. Their reported positions are shown in Figure 4. We see that the drogues deployed northwest of Unimak Pass did not move in-bay, but rather west-northwest along the slope and offshore. Those deployed over the central part of the slope headed north and then turned west over Pribilof Canyon. These two tracks are strikingly similar to the dynamic contours there (cf. Figure 2) and mean drogue speed of ~ 5 cm/sec compares with that estimated from the contour spacing, approximately 4-5 cm/s.

Thus, the normal circulation in outer Bristol Bay apparently does not include a current component into Bristol Bay along the Alaska Peninsula. Some Bering Sea/Alaska Stream source water enters onto the shelf (over the 150 m isobath) in the south, northwest of Unimak Island as well as near Pribilof Submarine Canyon, but once on the shelf the motion is a slow (order 1 cm/sec) net drift to the northwest parallel to the bathymetry. Kinder (1977) reported that in June 1976, the influence of source water (relatively warm and saline conditions) was evident close in to the Alaska Peninsula, in water <50 m deep, farther in-bay. Most hydrographic sampling conducted in the area has remained outside of the 50 m isobath, and therefore there remains the possibility of a small in-bay advection in the shallow water near shore. But, as pointed out by Schumacher, Charnell and Coachman (1977), such flow, if present, can only constitute a very minor part of the source water flux onto and along the shelf. We believe that Kinder's observation of source water penetration in-bay close to the Alaska Peninsula can alternatively be explained as a differential effect of lateral diffusion in achieving a horizontal flux of properties.

The only possible suggestion of flow which might be termed a current in the area occurs south and southeast of St. George Island, over the shelf and part of

the Pribilof Canyon. Where data are available, dynamic topographies show a packing of the contours (speeds ~ 10 cm/s; cf. Figure 2). Dr. T. Fujii (personal communication) claims there is a westward setting current off-shelf south of the Pribilofs, and when we spent three days in the vicinity of $55^{\circ}25'N$, $168^{\circ}W$ during May 1977, we experienced a westward set. The track of one of the drogues (Figure 4) offers supporting evidence for such a flow.

Water Masses

The classification of Bristol Bay waters into three water masses by Takenouti and Ohtani (1974), modified by newly acquired data, still appears to be appropriate. We can, however, add considerable refinement to their T and S characteristic values and time and space distributions.

Coastal water has been found to lie landward of a front demarked by a sharp change in vertical water column structure (Kinder, 1977). As this front appears to be always located close to the 50 m isobath, and 50 m depths occur very close to shore in outer Bristol Bay (cf. Figure 1), coastal water does not participate in transition zone formation.

Shelf water fills the large central shelf area between approximately the 50 and 100 m isobaths (cf. Figure 1). In summer, the water columns are strongly two-layered; a warm upper layer, and, deeper than 20-30 m, masses of quite homogeneous and cold water. There is little salinity stratification. The few data available from winter show the heat and slight salinity stratification to be removed at that time, the water being reduced to a practically homogeneous cold mass. The deeper layer remains cold over the summer due to insulation by the upper layer.

There are year-to-year variations in the T and S of shelf water. Figure 5, based on the *Oshoro Maru* data from June 1963-1973 and the June 1976 data, shows the approximate range of values observed and the mean value (determined by plani-

metry). There is little correlation between T and S, nor does the salinity appear to be correlated with the previous seasonal or annual runoff from Alaska (based on gage data from the Kvikchak, Nuyakuk and Kuskokwim rivers). There is a large year-to-year variation in bottom layer temperature, which is highly correlated with the degree-days of frost of the previous winter (Figure 6).

Shelf water salinity shows an increase seaward of between 0.2 and 0.7 gm/kg over the approximately 200 km distance between the 50 and 100 m isobaths, which translate into horizontal salinity gradients between 1×10^{-3} and 3.5×10^{-3} gm kg⁻¹ km⁻¹ with a mean of 2.5×10^{-3} gm kg⁻¹ km⁻¹.

Thus, shelf water is relatively invariant in salinity, 31.9 ± 0.4 gm/kg, probably because runoff volumes are small compared with water volumes on the broad shelf and other environmental factors conditioning salinity (e.g. ice, precipitation) may not be significant. The major variation in salinity structure is a cross-shelf gradient. On the other hand, temperatures vary widely, 3-4°C, bespeaking the dominant role in the shelf water heat budget of surface exchange processes (Reed, 1978).

Bering Sea/Alaska Stream water is that which overlies the southeast corner of the basin. It penetrates onto the shelf (<150 m) in an area northwest of Unimak Island. Figure 7 shows T and S envelopes for both outer shelf water and Bering Sea/Alaska Stream water for the most comprehensive data set, August 1976 (station locations shown in Figure 8).

On the shelf, the deep layers of Bering Sea/Alaska Stream source water always have $33.0 < S < 33.2$ gm/kg and $3 < T < 4$ °C. Salinities decrease upward more or less uniformly to $32.0 < S < 32.5$ gm/kg. The temperature likewise exhibits more or less uniform gradients with depth, but the upper layers go through an annual cycle - colder than the bottom layers in winter and warmer in summer. These changes are

illustrated in Figure 9, which shows Bering Sea/Alaska Stream source water envelopes for the recent cruises (stations used were from the same area northwest of Unimak Island in each case).

Figure 9 also shows there are small year-to-year differences in characteristics. For example, warming in spring 1977 occurred earlier than in spring 1976, probably because winter 1975-1976 was abnormally cold and the spring transition abnormally late. The upper layers in March 1976 were somewhat fresher than usual, probably connected with the unusual southward extent of the ice cover then (cf. Coachman and Charnell, 1977). This was likewise true in May 1977, but the cause is not known.

That the source water bathes the slope from Unimak Pass to Pribilof Canyon is shown in Figure 10. The envelope encloses all T and S values for the slope stations from the August 1976 cruise (see Figure 8). Comparison with Figure 7 shows the source water on the shelf to be the shallow water portion (<150 m) of this same water mass. Stations 8 and 9, near Pribilof Canyon, exhibit beneath ~55 m a colder and fresher influence, but this layer is undoubtedly due to water moving westward (off-shelf, see above) and is not source water to the shelf regime.

Transition Zone

We have established that the transition zone of outer Bristol Bay is the deeper shelf region, between 100-150 km wide, extending from Unimak Island to Pribilof Canyon. The zone is bordered by the shelf water on the landward side (water depths <100 m), persistently colder and less saline, and the warmer and more saline Bering Sea/Alaska Stream water mass along the continental slope on the seaward side. We have also established that there are no persistent currents of any significance in outer Bristol Bay, neither inflow into the bay nor a major current along the continental slope, with the possible exception of an off-shelf

flow south of the Pribilofs. These are the characteristics of a shelf-oceanic frontal zone outlined by Csanady (1976) and a lateral water mass boundary zone as discussed by Joyce (1977). We now describe the zone based on the extensive observations recently made. Of specific interest are the May 1976 cruise of RV *Acona*, the August 1976 cruises of RV *Acona* and RV *Moana Wave*, and the May 1977 cruise of RV *Acona*.

Characteristics of the transition zone in outer Bristol Bay were investigated by generating average cross-shelf sections, using data from cruises which provided the most detailed coverage from the slope to the 100 m isobath, a broad band ~ 130 km in width (Figure 1). For the data of May 1976, August 1976, and May 1977, lines of 4-6 stations approximately parallel to the bathymetric contours (and isohalines, cf. Figure 3) were selected, and the data averaged to create a representative station for the cross-shelf location (see Figure 8 for the August station selection). These averaged stations were used to construct cross-shelf sections.

Figure 11 shows the average 0-100 m salinities for the three sections. The striking result is that the outer Bristol Bay transition zone contains two fronts, separated by a 50-100 km wide band in which the horizontal salinity gradient is ~ 0 . The outer front is centered over the shelf break and the inner one over the 100 m depth contour. The slopes of the horizontal salinity gradients in both fronts are similar, $9.3 \times 10^{-3} \text{ gm kg}^{-1} \text{ km}^{-1}$. Though this value appears to be twice as great as the mean value of $4.7 \times 10^{-3} \text{ gm kg}^{-1} \text{ km}^{-1}$ reported by Kinder and Coachman (1978) for the Bering Slope front, the spatial resolution of the averaged section is finer than that of their sections - in the vicinity of Zhemchug and Pribilof canyons, where stations were more closely spaced, Kinder and Coachman reported values of 5×10^{-3} and $13 \times 10^{-3} \text{ gm kg}^{-1} \text{ km}^{-1}$, respectively.

We can safely interpret the outer front to be analogous with the Bering Slope front of Kinder and Coachman, demarking the boundary between the oceanic regime of the basin and the shelf regime. It would appear that the sharp change in horizontal salinity gradient occurs at about the position of the farthest offshore stations, or 25-30 km seaward of the shelf break.

The fronts can be seen in cross-shelf average salinity and temperature sections (*e.g.* Figure 12 and 13). The inner front is pronounced between lines #2-5 from the surface to the bottom. The outer front, between lines #6-9, becomes less pronounced beneath 60-80 m. An interpretation of the bulk exchange across the section is: throughout mid-depths shelf water is moving seaward, its influence reaching deeper toward the outer front and also upward between the fronts; and the offshore (oceanic) water is intruding landward as a bottom layer as far as the inner front.

Water Structure in the Transition Zone

A unique and surprising feature of vertical T and S profiles taken in and between the fronts is the presence of an extremely rich finestructure in both T and S. Figure 14 shows three examples from different locations cross-shelf (see Figure 8). In the Bristol Bay columns the temperature and salinity pass through maxima or minima in vertical distances of from one to as great as 20-30 m. Even though the changes in T and S are always correlated and hence the layers tend to be density-compensated, the greater influence of salinity on density in colder water leads to many of these layers being statically unstable (by calculation).

Coachman and Charnell (1977) reported one such layer found in the March 1976 data. The layer showed a nominal static instability of nearly $0.2 \sigma_t$ over 10 m. The layer occurred in the mixing zone between Bering Sea source water and shelf

water, was traced over a horizontal distance of 100 km, and was found to be transient but with a lifetime of nearly one week.

The numerous data acquired since March 1976 show that stable finestructure is not an unusual occurrence but ubiquitous in the central outer shelf region. The comprehensive data of August 1976 have been closely examined in regard to the finestructure, and Figure 15, 16, and 17 present three examples. Certain generalizations about finestructure characteristics (which can be seen in Figure 15 - 17) are:

A. Temperature and salinity always act in consort, that is, when the temperature rises so does the salinity, and *vice versa*. Each extremum in salinity, either a maximum or minimum, is always accompanied by a corresponding maximum or minimum in temperature, though the signal is hard to detect in regions of large temperature change. The reason for this is the characteristics of the two basic water masses engaged in lateral mixing, the dominant process occurring throughout the broad transition zone. The shelf water is cold and less saline and the intruding Bering Sea/Alaska Stream source water is warm and more saline. All structure in the water columns represents alternating layers reflecting to a greater or lesser extent the influence of first one basic water mass and then the other.

B. There is an hierarchy of finestructure scale features. For example, at Station 61 (Figure 17) the large temperature maximum between 30-60 m contains three noticeable maxima of approximately 10, 8 and 4 m vertical thickness. Statistics were generated on this phenomenon by examining all stations from August 1976 for finestructure layers which were less dense by $0.10 \sigma_t$ than above or below. The size frequency distribution of such layers is shown in Figure 18.

The suggested curve of increasing numbers of layers with smaller vertical dimensions supports the hierarchical concept. The hierarchy probably extends into the smaller (microstructure) scales, but this cannot be determined from these data which are limited by instrument resolution.

C. The temperature and salinity maxima and minima are vertically offset, with the salinity extrema 1 to 5 m higher than the corresponding temperature extrema. These are marked in Figure 16 and 17. There appears to be no correlation between the amount of offset and the vertical dimension of the layer.

The cause for this phenomenon may be ascribed to different vertical diffusion rates for heat and salt. As the water columns in summer are always warmer at the surface than at depth there is a bulk heat flux downward, while there is little bulk vertical salinity gradient (cf. Figure 14). With differential vertical diffusion, T and S extrema that are initially coincident will become separated vertically, with the T extremum displaced downward relative to the corresponding S extremum.

Lateral Water Mass Interaction

The rich finestructure, where the two major water masses are interacting, is found in the transition zone, in and between the fronts. Figure 19 shows the areal distribution of stations with a high incidence of layers in the water column less dense by $0.1 \sigma_t$ than the layer above or below, that is, a significant lower density intrusion. The presence of this phenomenon is seen to be confined to the central outer shelf, as the surrounding stations have two or less such intrusions and those around the periphery of the study area show none.

Also indicated in Figure 19 are the frontal zones as defined by the average cross-shelf section. We do not believe it coincidental that the area dominated by finestructure is so closely associated with the area in and between the

frontal zones. The transition zone is the area in which the lateral meeting and mixing of two major water masses is the primary physical phenomenon, and we conclude that the primary way these water masses interact is through layering, which is expressed in the water columns by the finestructure.

In the vertical, finestructure is never observed in the surface layer nor in the layer immediately above the bottom. The thickness of these boundary layers was estimated using the criterion of homogeneity in density to within $0.02 \sigma_t$. In March 1976, for 27 stations, the surface layer was between 10 m and 70 m with a mean depth (\bar{Z}) of 37 m. In May 1976 the depth was markedly shallower, the average for 80 stations was $\bar{Z} = 14.6$ m, and in summer (August 1976) this depth was between 5-15 m with an average of less than 10 m. The thickness of the bottom boundary layer for 69 stations in water <150 m deep for August 1976 was $\bar{Z} = 37$ m above bottom, and only four stations had distances less than 10 m.

Thus, the picture we have developed of the transition (lateral interaction) zone coincides with the description of a thermohaline front presented by Joyce (1977; his Figure 1 reproduced here as Figure 20). The large-scale interaction (upper panel) is represented here by colder, less saline shelf water intruding into the warmer and more saline Bering Sea water at mid-depths in the water column, between ~ 20 m and 60-80 m depths. Joyce's medium-scale motions (middle panel) are represented by the plethora of finestructure, and the small-scale vertical mixing (lower panel) is probably microstructure, hinted at in the CTD data but not properly sampled.

Joyce's study implies that in lateral water mass interactions with well-developed medium-scale motions (intrusions and interleavings), it is this scale

which provides the major mechanism for cross-frontal exchanges of heat and salt. To investigate more closely the modifications in mass and heat energy of the medium-scale (finestructure), lines of stations from August 1976 were selected which showed T and S signals which could reasonably be assumed to be associated with the same layer sequence station-to-station. One section is presented in Figure 21 - 23, and the location indicated in Figure 8. The stations progress from 18 in the shelf water through 58, 60, 61, to 65 which shows little vestige of shelf water. Vertical profiles of T and S of these stations between 30-90 m are shown in Figure 21 and 22 and their T-S diagrams in Fig. 23.

We key on the remarkably similar sequence of layers at stations 60 and 61, numbered 1 through 9 in Figure 21 and 22, which we do not believe coincidental. These layers were extrapolated seaward to station 65 and in-bay through station 59 to station 18, due regard being given to matching depths for both T and S (inflection points not exactly coincident, and small depth variations between stations).

The general modifications in mass and heat energy are suggested in the T and S changes (Figure 23). The pure shelf water (station 18) is on the large-scale blending into the source water (station 65) approximately along $\overline{\sigma_t} = 25.5$. The water column structure at intermediate stages (stations 59 - 61) is very complex. The noticeable cusped forms in the T and S curves signal transitions between alternating layers of colder, less saline and warmer, more saline layers of the finestructure. These layers appear to develop preferentially near the top and bottom of the bulk of the colder, less saline intermediate-depth layer of shelf water. However, frequently the transitions aren't simply cusped in the T-S plane, but cyclonic whorls, a consequence of the vertically offset T and S

inflections noted earlier. Such a transition downward from a warmer, more saline layer to a colder, less saline layer constitutes a static instability in the water column.

To ascertain the possible effects of a differential vertical flux of heat and salt on the finestructure layer properties, a simple model was constructed. An arbitrary layered water column was created such that the T and S profiles, both the values and depth variations, were similar to those observed at station 61 (Fig. 17). The layers were arranged initially such that (a) the T and S maxima and minima coincided in depth and (b) the column was statically stable (Fig. 24). On the assumption that the time change of the profiles was due solely to vertical diffusion, and therefore $\frac{\Delta\phi}{\Delta t} = K_{\phi} \frac{\Delta^2\phi}{\Delta Z^2}$ where $\phi = T, S$, the profiles were integrated for 10^6 s in steps of 10^5 s with $K_T = 10^{-1}$ cm²/s and $K_S = 10^{-2}$ cm²/s. The results indicate two significant observed features of the finestructure can be generated by differential diffusion, *viz.*, that static instability can arise from an initially stable configuration, and that T and S extrema initially coincident in depth can be vertically offset. Thus, it appears that differential vertical diffusion is one component of the mixing process active within the transition zone. This exercise also suggests that, in the absence of moderate vertical mixing energy, finestructure may be a common occurrence between adjacent water masses.

Because of the complexity of water column structure, individual layers cannot be positively traced in the T-S diagram. The mixing history in the section was simplified by assigning approximate values of T and S for each numbered layer at each station (Fig. 21 - 22), and the simplified T and S curves generated thereby are shown in Fig. 25. Certain conclusions can be reached:

- 1) The shelf water does not interleave simply along a density surface, rather,

its bulk density is increased significantly;

(2) The bulk shelf layer is heated both from above and from below, the heat reaching into the cold core (layer 6) last;

(3) The deepest layer (9) is recipient of sufficient mixing energy to achieve a regular mass-and energy conserving mixture at intermediate stages (straight line in the T-S plane):

(4) The vertical flux of heat into the cold core is faster than that of salt. The transition of layers 1-4 show a distinct upward bowing in the T-S plane, indicative of a more rapid heat flux, which is also evident to a lesser extent in layers 7 and 8 beneath the core. One consequence of this is to add just enough buoyancy to the upper layers to counteract the increase in density due to increased admixtures of salt, such that they end up interleaving at approximately their original density. The deeper layers show a progressively greater increase from their original density, and end up interleaving through a broader band of density in the offshore water.

Quantitative estimates of the medium-scale interaction were achieved by applying Joyce's (1977) model to the August 1976 data. He separated the variables into the three scales of motion (Fig. 20); large (overbar), medium (tilde) and small (prime), thus $\phi = \bar{\phi} + \tilde{\phi} + \phi'$, $\bar{\phi}' = \tilde{\phi}' = 0$, where $\phi = T, S$. After parameterizing diffusive fluxes in terms of eddy coefficients, and hypothesizing that in both the vertical and horizontal the scale ratios (small/medium) and (medium/large) are small, he showed that in a steady-state balance

$$\bar{A}^H = \frac{\tilde{A}_\phi^V \left(\frac{\partial \tilde{\phi}}{\partial z} \right)^2}{\left(\frac{\partial \bar{\phi}}{\partial y} \right)^2}$$

where y is the cross-frontal direction.

The August 1976 data are well suited for estimation of the gradients. The large-scale horizontal gradients were based on the stations averaged by lines

(Fig. 8) and meaned over the middle portion of the water column (20-80 m). The medium-scale vertical gradients were estimated from T and S profiles for stations in three groupings; inner front, between fronts, and outer front. The data and results were compiled in Table 2.

In the absence of appropriate velocity measurements, values of the lateral eddy coefficients can be calculated by choosing \tilde{A}^V , the vertical eddy coefficient associated with the finestructure. However, neither \tilde{A}_S^V nor \tilde{A}_T^V are known. Joyce (1977) selected a value of $5 \text{ cm}^2/\text{s}$ from among appropriate estimates in the literature. In contrast, we achieved realistic results for decay of a finestructure layer using an \tilde{A}^V of order $10^{-1} \text{ cm}^2/\text{s}$ (Coachman and Charnell, 1977). In light of our conviction that the environment within which finestructure is well-developed (that is, clearly observable) must be a low energy environment, we believe appropriate values of \tilde{A}^V must be at least as small as order $10^{-1} \text{ cm}^2/\text{s}$. The most reasonable and internally consistent results are obtained by choosing $\tilde{A}_S^V = 10^{-2} \text{ cm}^2/\text{s}$.

Because \tilde{A}^V and \overline{A}^H are directly coupled in Joyce's model, the order of \tilde{A}^V sets the order of \overline{A}^H . Work on horizontal diffusion has shown a correlation between horizontal scale size of the system and \overline{A}^H (e.g. Okubo, 1971). If the horizontal scale of the outer Bristol Bay regime is between 10^7 and 10^8 cm , \overline{A}^H should lie between 10^6 and $10^7 \text{ cm}^2/\text{s}$, but certainly not be greater than $10^7 \text{ cm}^2/\text{s}$. The results are listed in Table 2.

The results lead to the following conclusions:

(1) The medium-scale (finestructure) vertical gradients become progressively less steep going seaward. This is consistent with the concept that the finestructure is basically associated with the interleaving of shelf water into the offshore water, which then progressively decays;

Table 2

Gradients and Eddy Coefficients

	<u>INNER FRONT</u>	<u>BETWEEN FRONTS</u>	<u>OUTER FRONT</u>
STATIONS	41-45, 51-53, 58-60	39-40, 46-50 61-62	4-11
$\frac{\Delta \bar{S}}{\Delta y}$ gm kg ⁻¹ cm ⁻¹	0.84 x 10 ⁻⁷	0.22 x 10 ⁻⁷	0.80 x 10 ⁻⁷
$\frac{\Delta \bar{S}^{\vee}}{\Delta Z}$ gm kg ⁻¹ cm ⁻¹	0.14 x 10 ⁻²	0.10 x 10 ⁻²	0.08 x 10 ⁻²
$\frac{\Delta \bar{T}}{\Delta y}$ °C/cm	7.2 x 10 ⁻⁷	1.0 x 10 ⁻⁷	
$\frac{\Delta \bar{T}^{\vee}}{\Delta Z}$ °C/cm	0.17 x 10 ⁻²	0.13 x 10 ⁻²	
with $\bar{A}_s^{\vee} = 10^{-2}$ cm ² /s:			
\bar{A}^H cm ² /s	2.8 x 10 ⁶	20 x 10 ⁶	1 x 10 ⁶
\bar{A}_T^{\vee} cm ² /s	4.7 x 10 ⁻¹	1.2 x 10 ⁻¹	

(2) The lateral eddy coefficient is the same order within each front, but an order greater between fronts. An implication derived from this is that the lateral flux $\left[A_H \frac{\partial \phi}{\partial y} \right]$ of a mass property (represented by salinity) is 3 to 4 times greater between fronts than in the fronts, or, *vice versa*, the fronts inhibit lateral fluxes of mass (salt). This is not true of heat energy, however; the results in Table 2 suggest the same magnitude of lateral heat energy flux across the inner front as between fronts;

(3) On the assumption that the large-scale lateral eddy coefficient is the same for both T and S, medium-scale vertical eddy conductivity is calculated to be an order greater than the eddy diffusivity, lending support to the qualitative conclusions of differential diffusion arrived at earlier.

Discussion

We have established that a salient feature of the water mass distributions in Bristol Bay is a large mass of shelf water (colder, less saline) in lateral juxtaposition with an oceanic water (warmer, more saline) over the continental slope, and that these waters are interacting across a transition zone where water column structure is very complex, in particular with much interleaving. The bulk interaction is that of oceanic water encroaching landward along the bottom and the shelf water pushing seaward at intermediate depths. The driving force for the bulk interaction must lie primarily in the baroclinic pressure field. Figure 26 contrasts the density distributions at stations 18 and 65, at the ends of the finestructure section depicted in Fig. 21 - 23. Relatively, we can interpret a tendency for on-shelf forcing in the upper (0-30 m) layer and also deeper than 60 m, while over mid-depths the tendency is less, perhaps even reversed.

Such interaction must be typical of most higher latitude shelf-basin boundary regimes. But there are certain features of outer Bristol Bay which are either

unique or a combination of circumstances which provides an exceptionally clear exposure of the details of the transition zone and water mass interaction.

These are:

A. The absence of significant currents, either on or off the shelf, which has two effects:

(1) water is not being rapidly advected into or out of the region but has a relatively long residence time; and

(2) there is no significant source of shear (mixing) energy available from the mean advective field to destroy the finestructure layers.

B. The extremely wide shelf, with only a slight bottom slope to a relatively deep shelf break (~ 150 m), means that various depth ranges subtend very broad portions of the shelf. For example, the region within the depth band 50-100 m is 180 to 200 km wide, and that within 100-150 m is ~ 130 km wide (Fig. 1).

C. There are only two sources of energy for mixing the water columns, wind and tidal motion, and by far the dominant source is the tides. Table 3 summarized the 1975-76 data from moored current meters on the southeastern shelf (Schumacher, *et al.*, 1977). Of these, BC-3, BC-12 and BC-13 were located in outer Bristol Bay. The only location on the whole shelf where the longer-term flow was sufficient to produce energy comparable to that in the tidal bands was BC-3 and, in this case, there is the probability the speeds in the record are inflated due to rotor pumping at the shallow depth (Halpern, 1976).

Turbulent energy for mixing from wind and tidal currents is produced by shear at the boundaries and extends only a finite distance into the water column before being dissipated. The evidence cited earlier suggests that in Bristol Bay wind mixing energy is effective down from the surface to ~ 10 -20 m in spring and

Table 3

Moored Current Meters 1975-76
 Long Term Mean and Tidal Component Energies (cm/s)²
 Compiled from Schumacher, *et al.*, 1977

Station	Depth (m)	Long Term (>35 hr)		24 hr		12.5 hr		Record Length (days)
		U ²	V ²	U ²	V ²	U ²	V ²	
BC-2C	20	0.2	0.4	73.0	0.5	147.2	46.1	118
BC-3C*	15	10.8	285.1	46.4	30.0	181.0	268.6	122
BC-3C	100	0.1	44.8	34.4	30.0	148.9	161.8	122
BC-4C	25	1.2	0.5	46.2	57.0	312.8	302.6	56
BC-5A	20	T	0.2	51.1	3.0	101.6	30.1	119
BC-5A	50	T	T	322.7	22.1	659.8	122.3	119
BC-6A	20	T	0.3	50.0	4.6	101.3	18.0	120
BC-6A	50	0.4	0.6	106.6	15.5	213.3	24.8	120
BC-8A	26	0.8	0	37.4	35.7	205.0	201.4	59
BC-8A	54	T	0.3	52.4	37.4	211.6	188.9	59
BC-9A	17	T	T	69.5	92.4	306.6	296.3	59
BC-9A	27	0.1	T	74.8	81.4	233.9	208.0	59
BC-12A	39	0.4	T	27.3	5.4	52.1	16.5	84
BC-13B	100	0.4	2.1	39.1	10.7	132.3	92.1	35
BC-14A	37	0.4	0.2	72.2	18.3	152.0	19.6	124
BC-15A	20	5.7	T	148.4	3.8	449.7	213.2	118

T - trace

* At the shallow depth of this meter there is probability of some rotor pumping due to wind-induced mooring motion (Halpern, 1976).

summer, while in winter when there is both less density stratification and more frequent and stronger storms this depth is $\sim 50-60$ m. The effective penetration distance upward of turbulent energy generated by tidal shear at the bottom depends on the speed of the tidal currents, and in Bristol Bay, which has vigorous tidal currents, this distance appears to be 30-50 m.

We now present an hypothesis to explain the presence of the two fronts in outer Bristol Bay bracketing a broad interfrontal zone replete with fine structure. Kinder, *et al.* (1978) have described what they term a "structure front" bordering inner Bristol Bay. Detailed salinity and temperature sections have disclosed that around the perimeter of the bay there occurs a zone where water column structure changes from relatively homogeneous surface-to-bottom property distributions on the landward side to a marked two-layer structure on the seaward side. The zone is narrow (5-10 km) and always located in water depths of about 40-50 m. Their explanation for the cause of this front is a change in overall energy balance at about these depths. Seaward of the front, water is sufficiently deep that the two sources of turbulent energy needed to mix the water columns (wind down from the surface and tidal up from the bottom), are not sufficient to mix the entire column; rather, they independently create relatively homogeneous layers, with a sharp interface and little exchange between them. In water shallower than 40-50 m the two energy modes overlap, giving rise to well-mixed water columns. The transition in distribution of energy modes, which changes the character of the vertical property distributions, produces a front in horizontal property distributions.

Our hypothesis extends this concept of energy mode distributions to the deeper parts of Bristol Bay (Fig. 27). The markedly two-layer structure of the central shelf waters occurs seaward only to depths of 80-100 m, which is still ~ 150 km from the shelf break. We believe that over the shelf seaward of these depths the wind

and tidal energy generated at their respective boundaries is dissipated without meeting, leaving a central portion of the water column with relatively little turbulent energy for mixing. It is within this central portion of the column that the bottom shelf water is moving seaward and, in the absence of significant turbulent energy, the primary mechanism appears to be in the form of the sheets and layers of the finestructure.

The finestructure phenomenon exhibiting a large density inversion that we reported previously (Coachman and Charnell, 1977) is now seen to be a particular case among the finestructure. On the shelfwater (landward) edge of the transition zone, where water columns show evidence of a two-layered structure, but also a finestructure layer, this finestructure layer is always associated with the pycnocline separating the layers. Multiple finestructure layers are only found seaward, in deeper water, where the water columns are no longer distinctly two-layered.

Normally in Bristol Bay this transition occurs in water depths of 80-100 m (the inner front), at least in summer. During March 1976, the two-layered shelf water mass had been moved south of its usual position into deeper water, and the layer we traced over ~100 km was that associated with the pycnocline interface. A perusal of our Fig. 7 (Coachman and Charnell, 1977, p. 877) shows that at three stations in deeper water, without well-defined two-layer structure, there were multiple finestructure layers spread over the depth range 50-150 m.

The degree to which finestructure is observable in the transition zone also depends on the degree of temperature and salinity contrast between the shelf and source water masses. Figure 28 shows temperature and salinity profiles from three stations taken during May 1977 at cross-shelf locations approximating those of the three stations of Fig. 14. The amount of finestructure throughout the water columns is not as dramatic as it is in the summer 1976 data, though the mid-outer-

shelf station (station 224) shows many layers between 20 and 100 m. The differences between data sets are two: (1) the differences to be expected in finestructure signals due to different spring and summer T and S values. The greatest contrasts in both T and S (and hence the greatest finestructure signals) will be achieved in summer; and (2) the temperature of bottom shelf water in 1977 was $\sim 3^{\circ}\text{C}$ warmer than in 1976 (+ 2 vice -1°C).

The question regarding static stability of finestructure layers, how unstable layers can develop and persist for significant periods of time, is complex and cannot be addressed rigorously without data from properly designed experiments. In particular, we believe measurements of velocity shear across the layers and employment of microstructure CTD profiling instruments will prove essential to an adequate theoretical formulation of the structure.

Summary and Conclusions

1. Bristol Bay, the southeasternmost portion of the Bering Sea continental shelf, is extraordinarily broad (~ 500 km). The bottom slopes gently offshore to a relatively deep (~ 150 m) shelf break. Thus, various shelf depth zones subtend broad lateral expanses: depths between 50-100 m occupy a zone 180-200 km wide, and between 100-150 m, 100-150 km.
2. Data for this study were from seven cruises during 1976-77, each providing extensive CTD station coverage in the outer bay. Supplemental current data were provided by a few moored current meters and satellite-tracked drogues. Salinities were calculated from the CTD data by a method which minimized the possibility of erroneous values.
3. There is no significant mean circulation in the area, no current neither onto nor off the shelf nor strong current along the continental slope. Thus, water masses and associated materials tend to have long residence times, the net motion being a slow (~ 1 cm/s) drift to the northwest parallel to the bathymetry.

The dominant water motion on the shelf is due to tidal currents. Turbulent energy for mixing water columns comes only from two sources, the tidal currents and the wind. The effective depths of downward penetration of wind energy is about 10-20 m in spring and summer and ~50 m in winter. The effective distance of mixing upward from the bottom from tidal current shear is ~40-50 m.

4. Outer Bristol Bay is dominated by two water masses, which are laterally juxtaposed but separated by the 100-150 km band of the deep outer shelf zone.

Shelf water normally occupies the central shelf out to depths ~100 m. Water columns are typically two-layered; a seasonally variable upper layer ~10-30 m thick, which warms to ~10°C in summer, overlies a large homogeneous mass of cold water. The temperature of the deep layer is quite constant seasonally, and is conditioned by the severity of the previous winter. Year-to-year variations in bottom-layer temperature have been as large as 3°C (-1 to +2°C). There is only little difference between upper- and lower-layer salinities (<0.5 gm/kg), and the water mass shows a cross-shelf gradient of mean salinity of $\sim 2.5 \times 10^{-3} \text{ gm kg}^{-1} \text{ km}^{-1}$ increasing seaward.

Alaska Stream/Bering Sea water bathes the continental slope from Unimak Island to south of the Pribilofs. The chief characteristic is a regular variation of properties with increasing depth to near constant values at 150 m of $33 < S < 33.2 \text{ gm/kg}$ and $3 < T < 4^\circ\text{C}$. Salinities always show a small increase with depth, while upper-layer temperatures cycle seasonally; warmer than the deeper water in summer and colder in winter.

5. In high-latitude shelf regimes with little advection and a net addition of freshwater along the landward boundary, the freshwater is fluxed laterally across the shelf by diffusion. In Bristol Bay, lateral diffusion is clearly dominated by tidal scales. The transition zone, where the shelf water mass interacts with

adjacent oceanic water, is typically located over the shelf break. Isopleths in this zone are more closely spaced and angled toward the surface or bottom, constituting a front. Another signature of this zone is a sharp increase in horizontal salinity gradient going seaward.

The outer Bristol Bay transition zone exhibits two fronts; the outer one is located over the shelf break, while the inner one lies ~ 100 km inshore near the 100 m isobath. The outer front is an extension of the eastern Bering Sea shelf-basin front described previously (Kinder and Coachman, 1977). Horizontal salinity gradients in both these fronts are $\sim 10 \times 10^{-3} \text{ gm kg}^{-1} \text{ km}^{-1}$, but between them are ~ 0 . The large-scale lateral exchange taking place in and between the fronts is (i) intrusion of Alaska Stream/Bering Sea water across the shelf in a bottom layer to the inner front and (ii) a bulk movement and intrusion of shelf water seaward at mid-depths.

6. Water columns in the transition zone, between the fronts, show high incidence of finestructure. The finestructure is alternating layers of warmer, more saline and colder, less saline water with vertical dimensions of 1 to 10's of meters, reflecting a dominant influence of first one and then the other of the basic water masses. Observations and conclusions regarding the finestructure are:

(a) the finestructure exhibits an hierarchy of scales, with increasing numbers of layers having smaller vertical dimensions. The hierarchy probably extends into microstructure scales (< 1 m) which are not properly sampled by the standard CTD instruments employed;

(b) the layers exhibit correlated T and S extrema, but with the T extremum displaced vertically 1-5 m below its corresponding S extremum. This vertical displacement, together with the generally smoother vertical profiles of T than S, can be ascribed to a differentially greater vertical flux of heat than salt;

(c) the general T and S correlation in the finestructure layers tends to

density-compensate the water column, but in some layers the vertical offset of T and S extrema leads to statically unstable layers. However, differential diffusion can create statically unstable layers from an initially stable configuration;

(d) finestructure layering is common in water columns in and between the fronts, but uncommon or absent in water columns outside the transition zone. Finestructure is confined to the middle portions of the water column, and is never observed in the upper, wind-mixed layer (in Bristol Bay in summer, the top 10-20 m, and in winter approximately the top 50 m) nor in a tidally-mixed bottom layer (in Bristol Bay the bottom 30-50 m).;

(e) some finestructure layers can be traced horizontally over a few 10's of km. As some of the layers are statically unstable, there can be no significant mixing energy available in the water column else the finestructure would certainly be destroyed;

(f) an adequate theoretical formulation of the finestructure probably awaits data from appropriately designed experiments.

7. The primary physical process occurring in the transition zone is interaction between two laterally juxtaposed water masses, and the picture developed from the numerous data coincides precisely with the model of a thermohaline front presented by Joyce (1977). The interaction is considered in three scales: the large-scale is represented here by the colder, less saline bottom shelf water intruding into the warmer, more saline Bering Sea water throughout mid-depths (20-80 m); the medium-scale by sheets and layers a few meters thick (the finestructure); and the small-scale is turbulence and microstructure (not sampled). In lateral interactions where the medium-scale is well-developed, it provides the major mechanism for cross-frontal exchanges of properties. Application of Joyce's model to our data suggests

that (1) lateral eddy coefficients in the inter-frontal region are an order larger than they are within each front; (2) the lateral flux of heat across the inner front is about the same as it is in the inter-frontal region, but the lateral salt flux is about one-half order less across the fronts; and (3) vertical eddy conductivity associated with the medium-scale (finestructure) is an order greater than the vertical eddy diffusivity.

8. An hypothesis is presented to account for the general disposition of fronts and inter-frontal zone of outer Bristol Bay. The hypothesis is based on the distribution of energy modes and the water depths. Mixing energy is available to the water columns from only two sources, wind down from the surface and tidal up from the bottom. With the conditions extant in Bristol Bay, the distances from the respective boundaries over which these energy inputs are effective in mixing the water columns are the top 10-20 m (in summer, deeper in winter) and the bottom 30-50 m. Over the central shelf, in depths <100 m where the water columns are two-layered, the two independent energy regimes nearly meet, aiding in maintenance of a two-layer structure. On the outer shelf, in depths 100-150 m, a zone in Bristol Bay >100 km wide, the two energy regimes are separated significantly. In the middle portion of the water column there is thus no significant mixing energy, and the lateral water mass interaction is dominated by an interleaving and layering of the waters with vertical scales of a few meters.

9. All boundaries between laterally juxtaposed water masses of nearly the same density probably manifest to a greater or lesser degree the various characteristics in their interaction that we have been able to describe for the outer Bristol Bay transition zone. In particular, most shelf/basin frontal zones should contain these features. A unique aspect of outer Bristol Bay is that in effect the transition zone is stretched enormously in lateral extent, exposing many of the details attendant to the lateral interaction, notably the medium-scale phenomena (finestruc-

ture), to our primitive sampling techniques.

Acknowledgments. A number of persons were instrumental in completing this study. In particular, we thank the officers and crews of the research vessels *Moana Wave*, *Discoverer* and *Acona*. We acknowledge the support of the staff at our institutions, including specifically Carl Pearson, Tom Kinder and Dick Tripp. This project was supported in part by the Outer Continental Shelf Environmental Assessment Program of the National Oceanic and Atmospheric Administration, which administers oil exploration hazard research in Alaska for the U. S. Bureau of Land Management, and in part by NSF through the PROBES (Processes and Resources of the Bering Sea Shelf) of the Division of Polar Programs.

References

- Charnell, R. L., C. A. Pearson and L. K. Coachman, 1978: A processing method for CTD data. Manuscript, to be published.
- Coachman, L. K. and R. L. Charnell, 1977: Finestructure in outer Bristol Bay, Alaska. *Deep-Sea Res.*, 24, 869-889.
- Csanady, G. T., 1976: Mean circulation in shallow seas. *J. Geophys. Res.*, 81, 5389-99.
- Gregg, M. C. and C. S. Cox, 1972: The vertical microstructure of temperature and salinity. *Deep-Sea Res.*, 19, 355-76.
- Halpern, D., 1976: Accuracy of moored current measurements in shallow-water. *Oceans '76 Conference Record*, Marine Technology Soc., Washington, D. C., pp. 20B-1 to 20B-5.
- Joyce, T. M., 1977: A note on the lateral mixing of water masses. *J. Phys. Oceanog.*, 7, 626-9.
- Kinder, T. H., 1977: The hydrographic structure over the continental shelf near Bristol Bay, Alaska, June 1976. University of Washington, Department of Oceanography Tech. Rpt. Ref: M77-3, 61 pp.
- Kinder, T. H. and L. K. Coachman, 1978: The front overlaying the continental slope in the eastern Bering Sea. *J. Geophys. Res.* (Chapman Conference Issue). In press.
- Kinder, T. H., J. D. Schumacher, D. Pashinski and R. L. Charnell, 1978: Structural fronts over the continental shelf of the eastern Bering Sea. Amer. Geophys. Un. 1978 Spring Meeting, Miami, Fla.
- Muench, R. D. and K. Ahlnäs, 1976: Ice movement and distribution in the Bering Sea from March to June 1974. *J. Geophys. Res.*, 81, 4467-4476.
- Okubo, A., 1971: Oceanic diffusion diagrams. *Deep-Sea Res.*, 18, 739-802.
- Reed, R. K., 1978: The heat budget of a region in the eastern Bering Sea, summer 1976. *J. Geophys. Res.* (In press).

- Scholl, D. W., E. C. Buffington, D. M. Hopkins and T. R. Alpha, 1970: The structure and origin of the large submarine canyons of the Bering Sea. *Marine Geology*, 8, 187-210.
- Schumacher, J. D., R. L. Charnell and L. K. Coachman, 1977: Bristol Bay Oceanographic Processes (B-BOP), Second Annual Report, submitted to ERL/NOAA, Boulder, CO. 64 pp. (mimeographed).
- Spilhaus, A. F., A. Ehrlich and A. R. Miller, 1950: Hydrostatic instability in the ocean. *Trans. A.G.U.*, 31, 213-15.
- Takenouti, A. Y. and K. Ohtani, 1974: Currents and water masses in the Bering Sea: a review of Japanese work. In: *Oceanography of the Bering Sea*, D. W. Hood and E. J. Kelley, editors, Inst. Marine Sci., Univ. of Alaska Occas. Publ. No. 2, pp. 39-57.

Figure Legends

1. Bristol Bay. Bering Canyon lies deeper than 200 m just west of Unimak Island and Pribilof Canyon is the Y-shaped feature southeast of the Pribilofs. Inset: Bering Sea.
2. Dynamic topography (0/100 dbar) for June 1976 in dyn. m., and 3-week averaged currents from moored meters at two locations.
3. The 0-100 m mean salinity distribution in August 1976.
4. The positions of satellite-tracked surface drogues May-July 1977, connected to give a sense of their flow path. Two average speeds are indicated.
5. Mean temperatures and salinities and approximate ranges for shelf water in June of various years. Based on data from *Oshoro Maru* from 1963-73 and *Miller Freeman* 1976.
6. Correlation between mean bottom layer temperature of shelf water in June (1963-73, 1976) and the number of degree-days with air temperatures $<0^{\circ}\text{C}$ (average of daily mean values reported from St. Paul and Cold Bay) over the previous winter.
7. T-S envelopes of the two basic water masses of outer Bristol Bay for August 1976.
8. Station locations for August 1976. The dashed lines connect stations meant to produce stations for the averaged cross-sections. The dot-dash line connects stations of the finestructure section (Figs. 21-23).
9. T-S envelopes of Bering Sea source water at various times.
10. T-S envelope of Bering Sea source water along the continental slope, August 1976.
11. 0-100 m mean salinities for the three averaged cross-shelf sections constructed from data of May 1976, August 1976, and May 1977. Positions of the 100 m and 150 m depth contours are indicated.

12. Averaged cross-shelf salinity section (August 1976).
13. Averaged cross-shelf temperature section (August 1976).
14. Temperature and salinity profiles for three stations from various cross-shelf locations (August 1976).
15. Vertical temperature and salinity for a portion of *Moana Wave* 9, 4 August 1976. The paired arrows indicate corresponding maxima and minima in the T and S curves.
16. Same as Fig. 15 for *Moana Wave* 10, 4 August 1976.
17. Vertical temperature and salinity for a portion of *Acona* 61, 8 August 1976.
18. Size frequency distributions of intrusions less dense than the water above or below by $>0.1 \sigma_t$, based on 104 stations from *Acona* and *Moana Wave*, August 1976.
19. The area encompassing stations with 3 or more major density inversions ($>0.1 \sigma_t$), and locations of the fronts (August 1976).
20. Schematic of frontal zone scales, from Joyce, 1977, Fig. 1, p. 627.
21. Temperature profiles from stations of a cross-shelf section (see Fig. 8 for location), with nine selected layers indicated. Data of August 1976.
22. Same as Fig. 21, salinity profiles.
23. T-S diagrams of the stations of the cross-shelf section.
24. Effect of differential vertical diffusion of heat and salt on temperature, salinity and sigma-t profiles of an arbitrary layered water column.
25. T-S diagram of the layer changes along the cross-shelf section.
26. Sigma-t profiles and dynamic height differences, *Acona* 18 minus *Acona* 65, August 1976 (see Fig. 8 for locations).

27. Schematic of energy mode distributions by depth ranges and accompanying water column structure.
28. Temperature and salinity profiles taken during May 1977 from approximately the same locations as the three stations of Fig. 14.

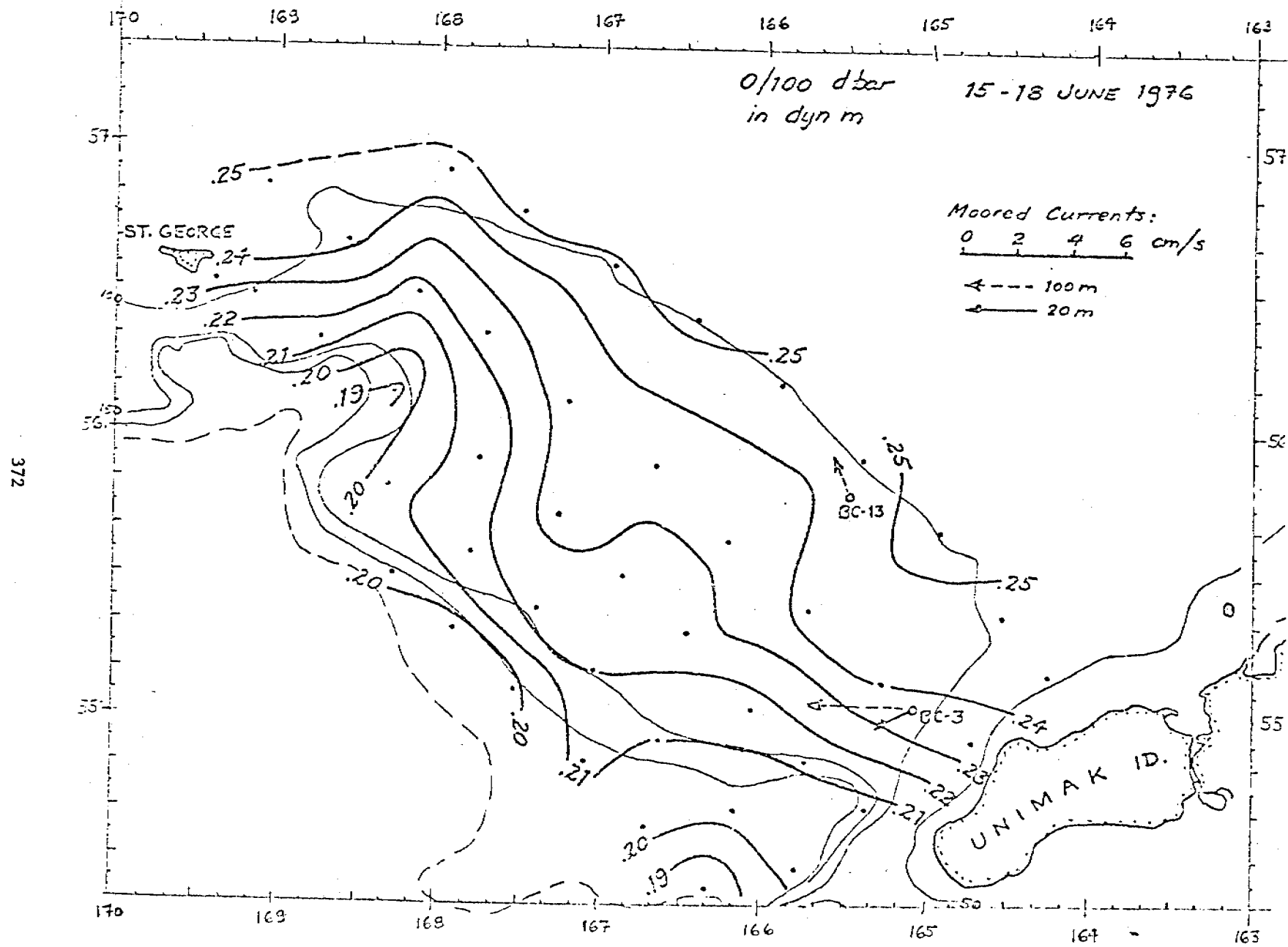


Figure 2

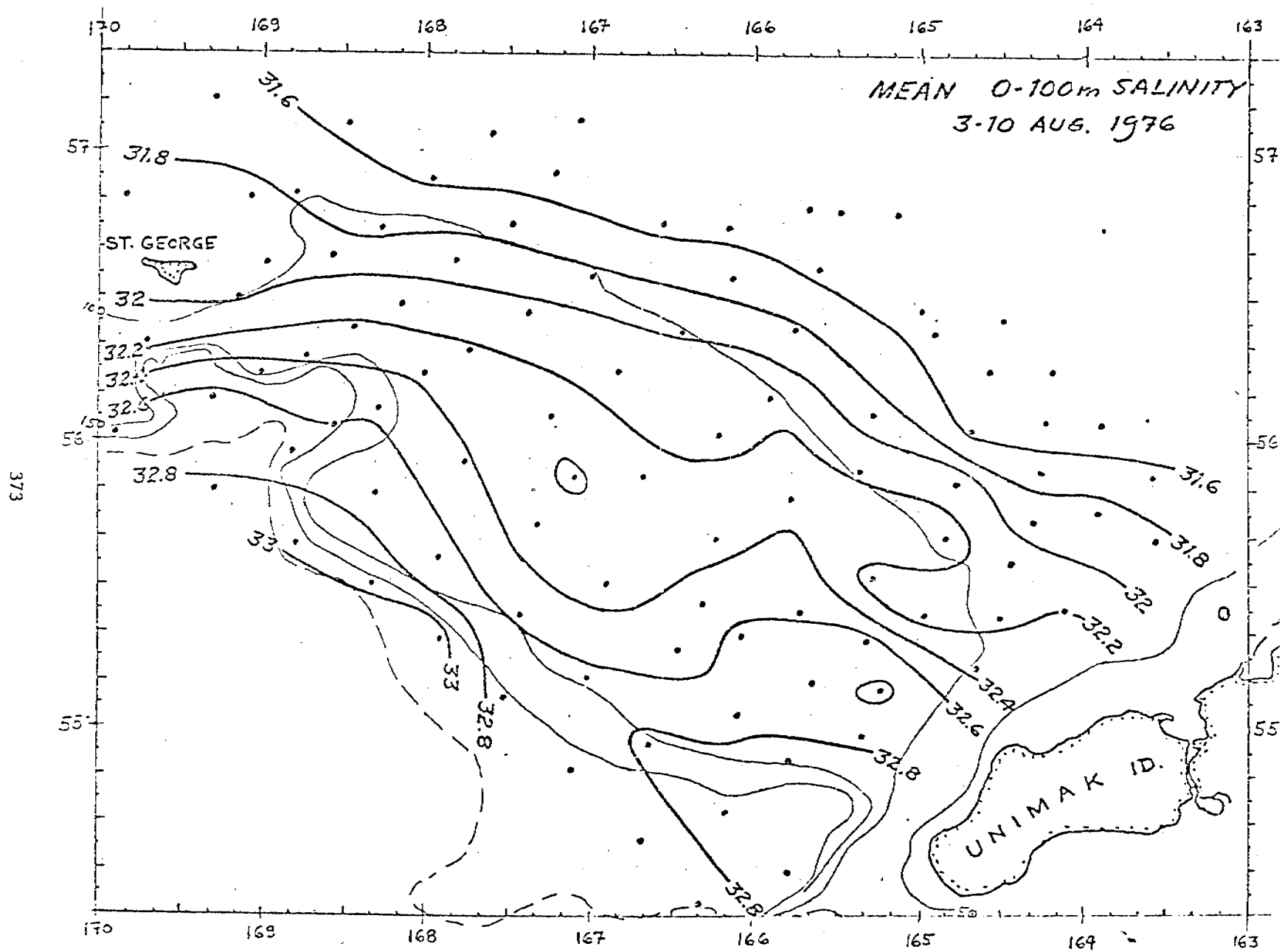


Figure 3.

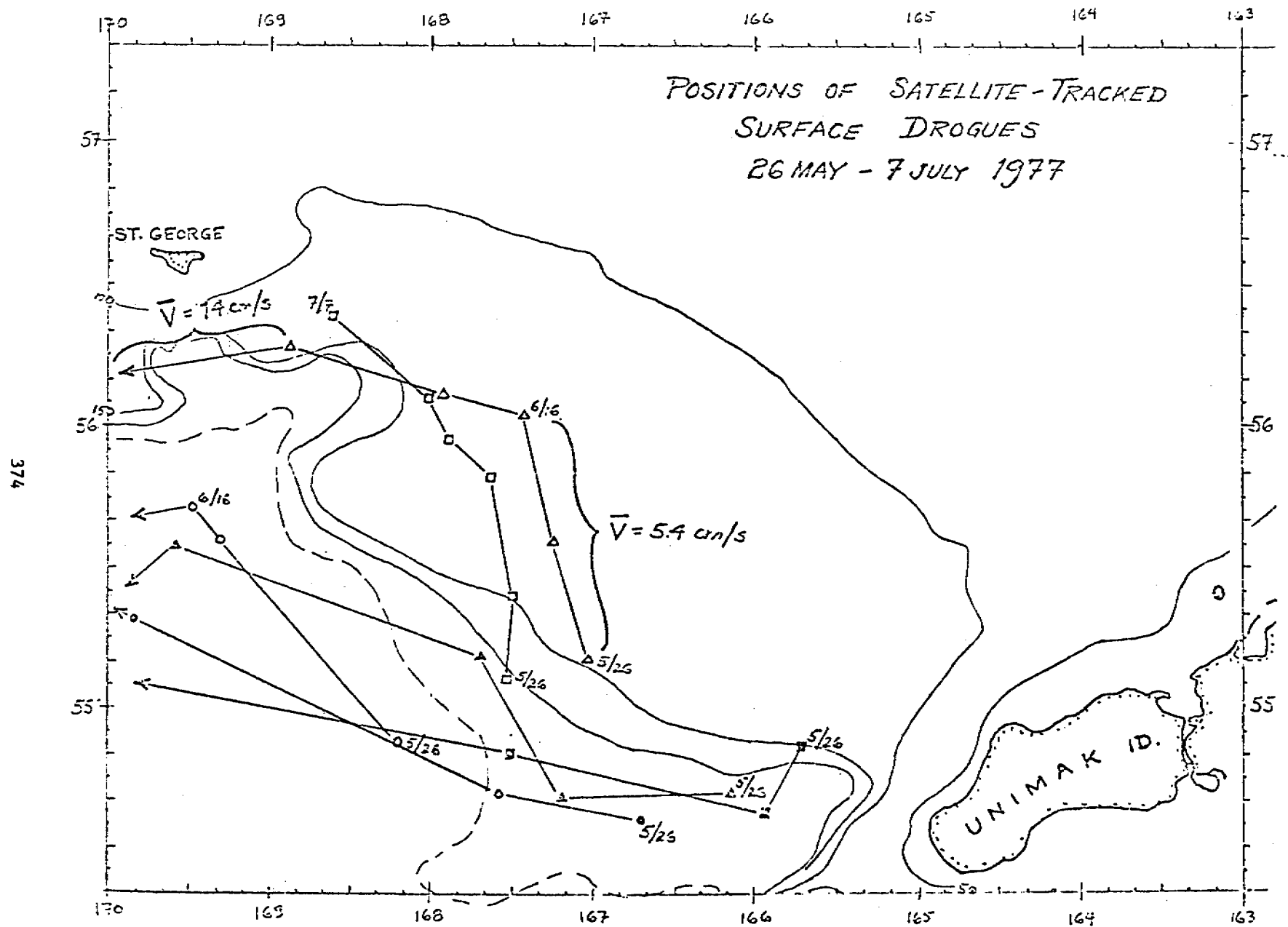
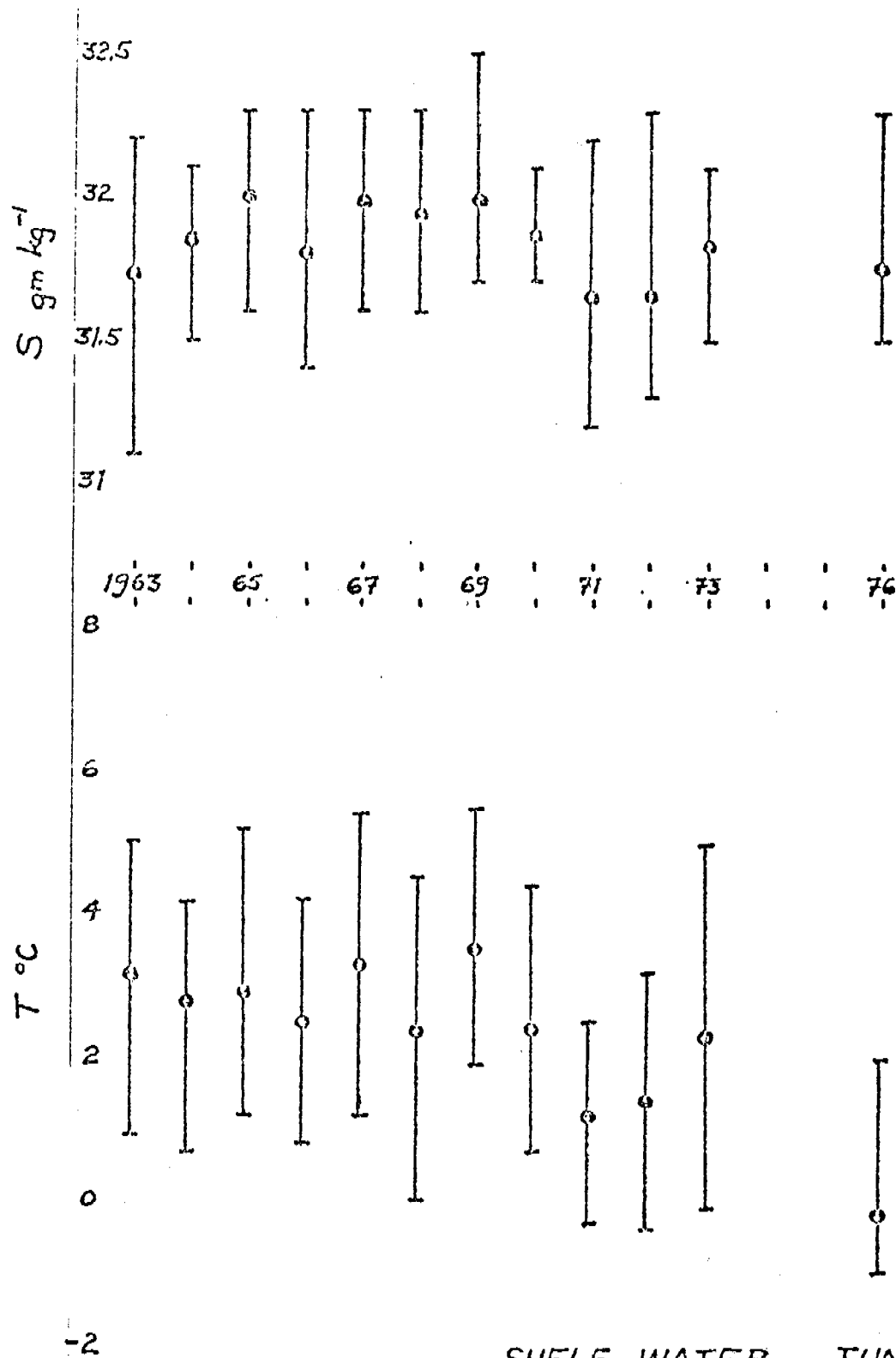


Figure 4



SHELF WATER, JUNE
T, S means and ranges, bottom layer

Figure 5

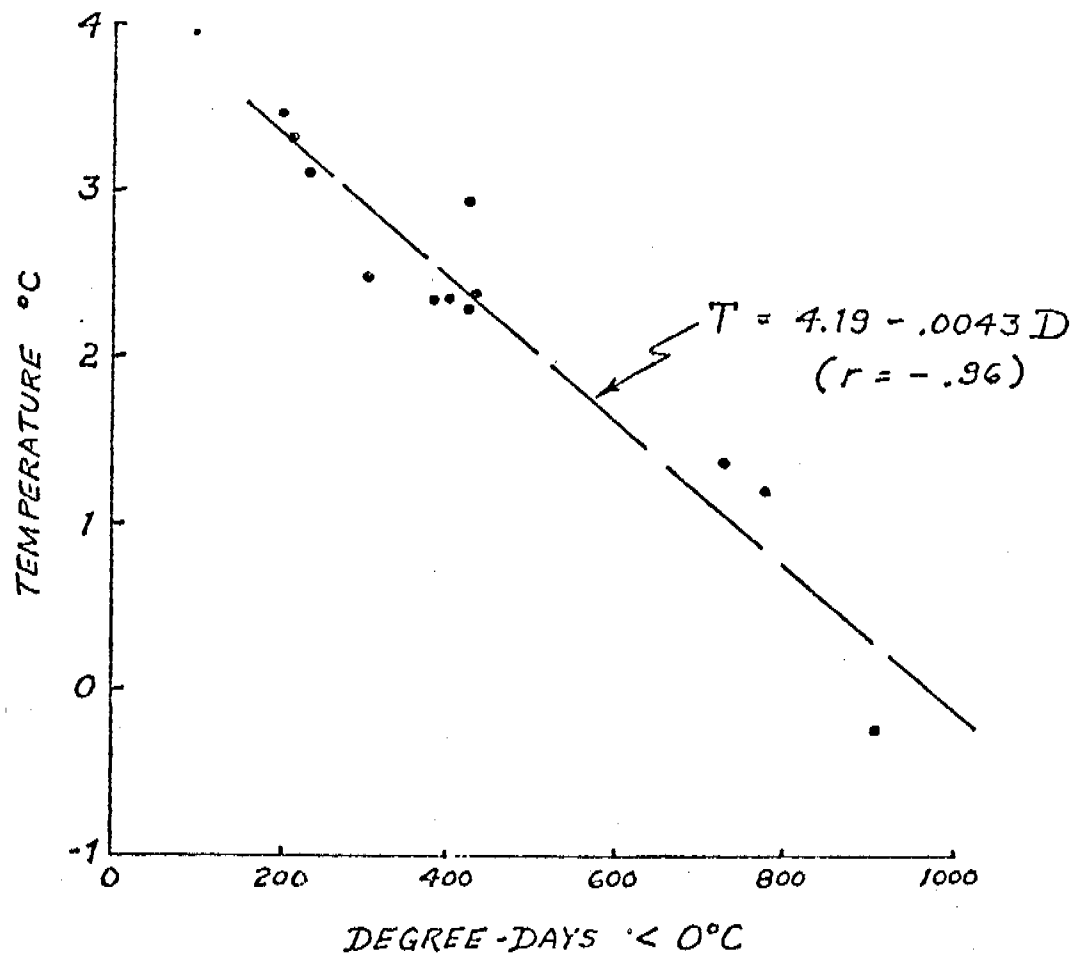


Figure 6

SOURCE WATER MASSES
AUGUST 1976

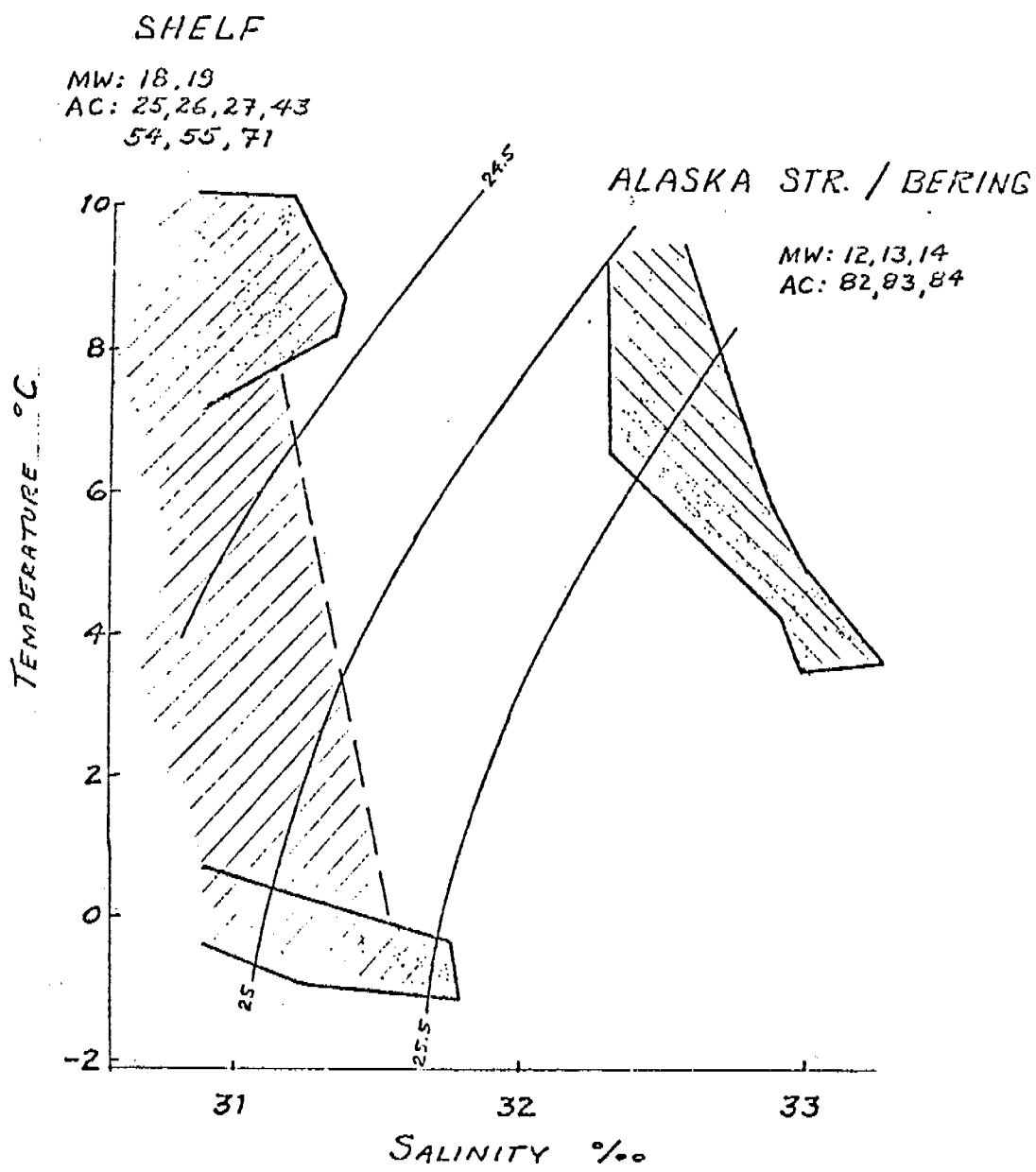


Figure 7

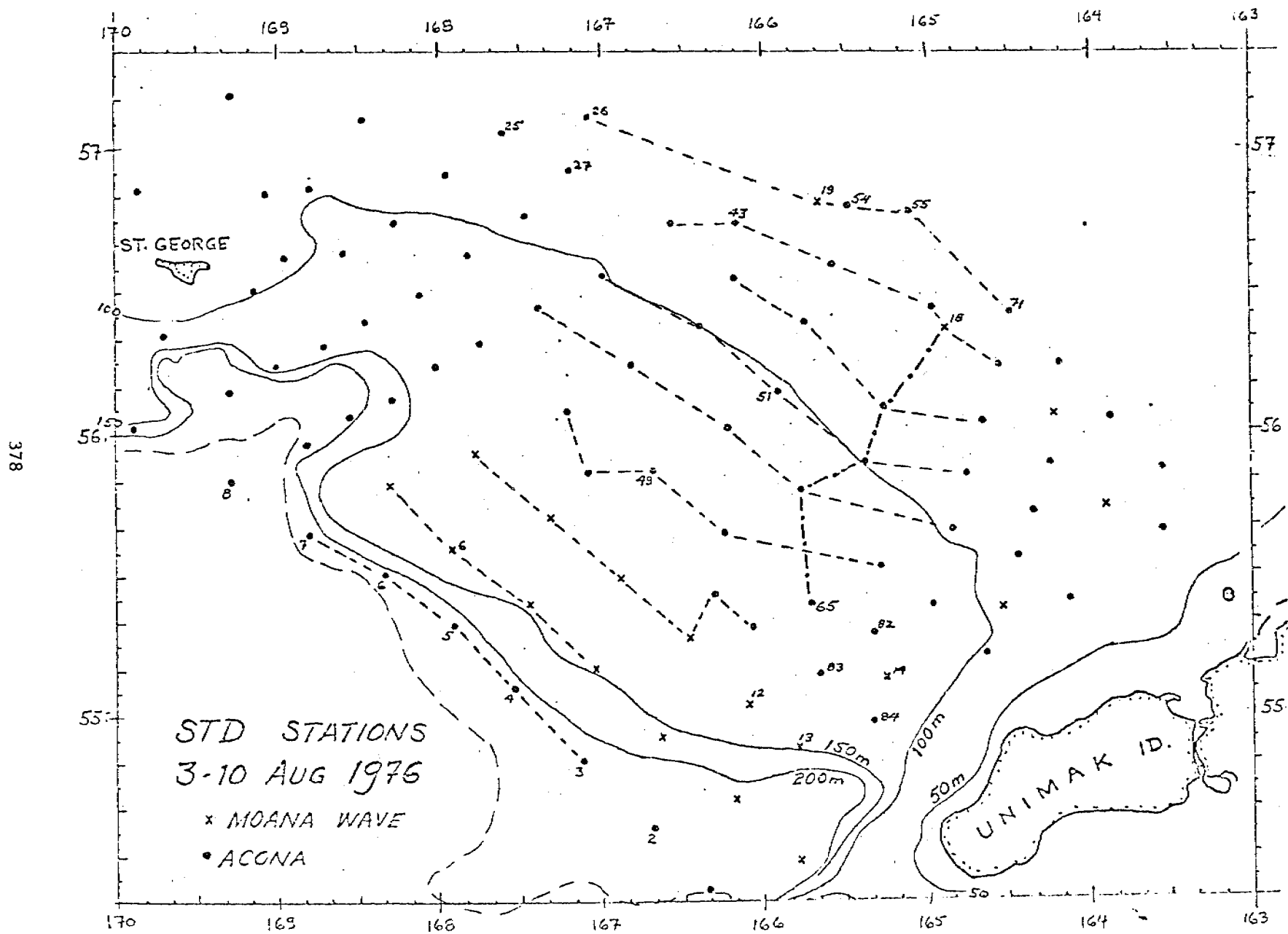


Figure 8.

BERING SEA / ALASKA STREAM
SOURCE WATER

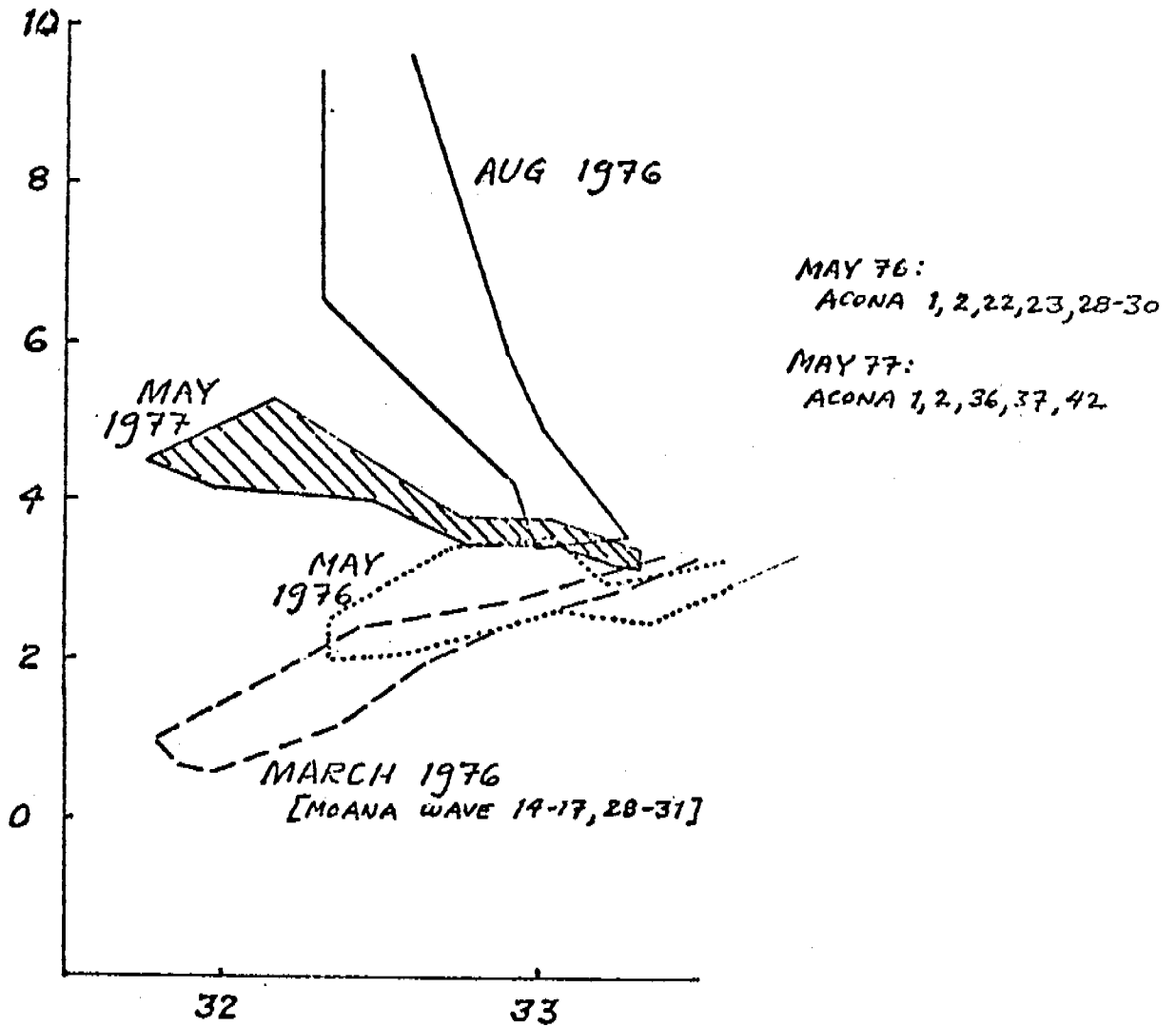


Figure 9

BERING SEA WATER ALONG
CONTINENTAL SLOPE
AUG. 1976

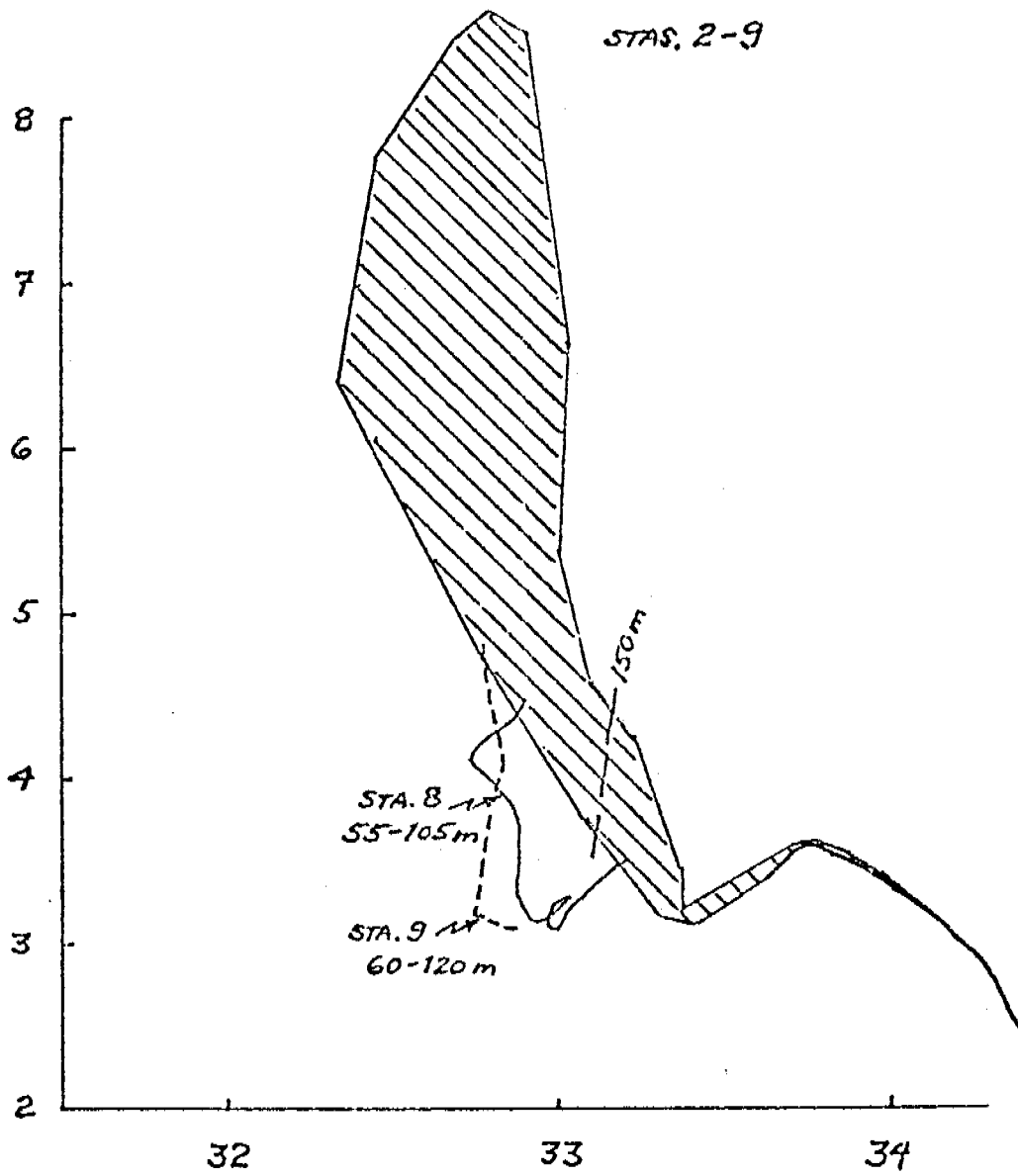


Figure 10

0-100 m MEAN SALINITIES CROSS-SHELF

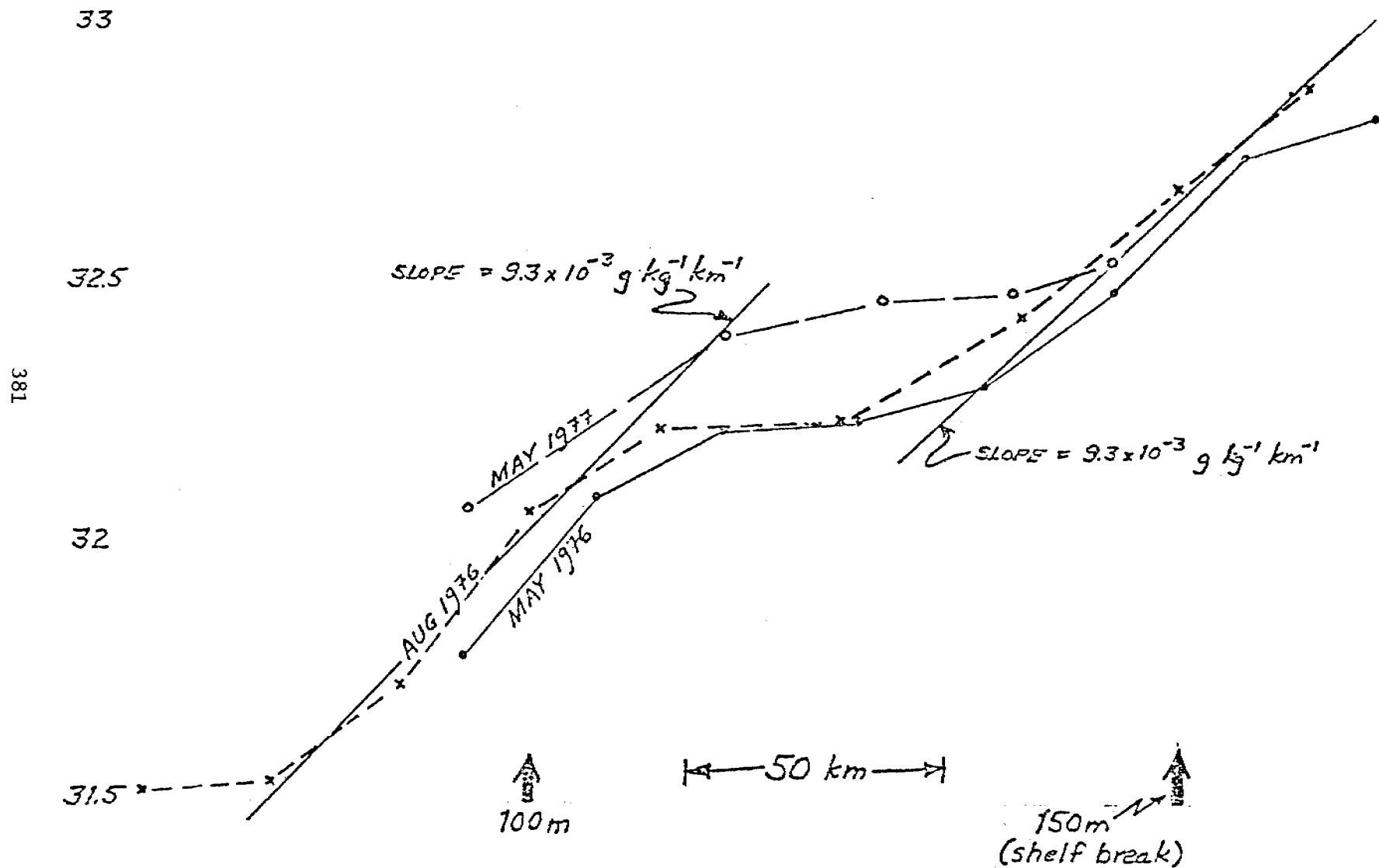


Figure 11

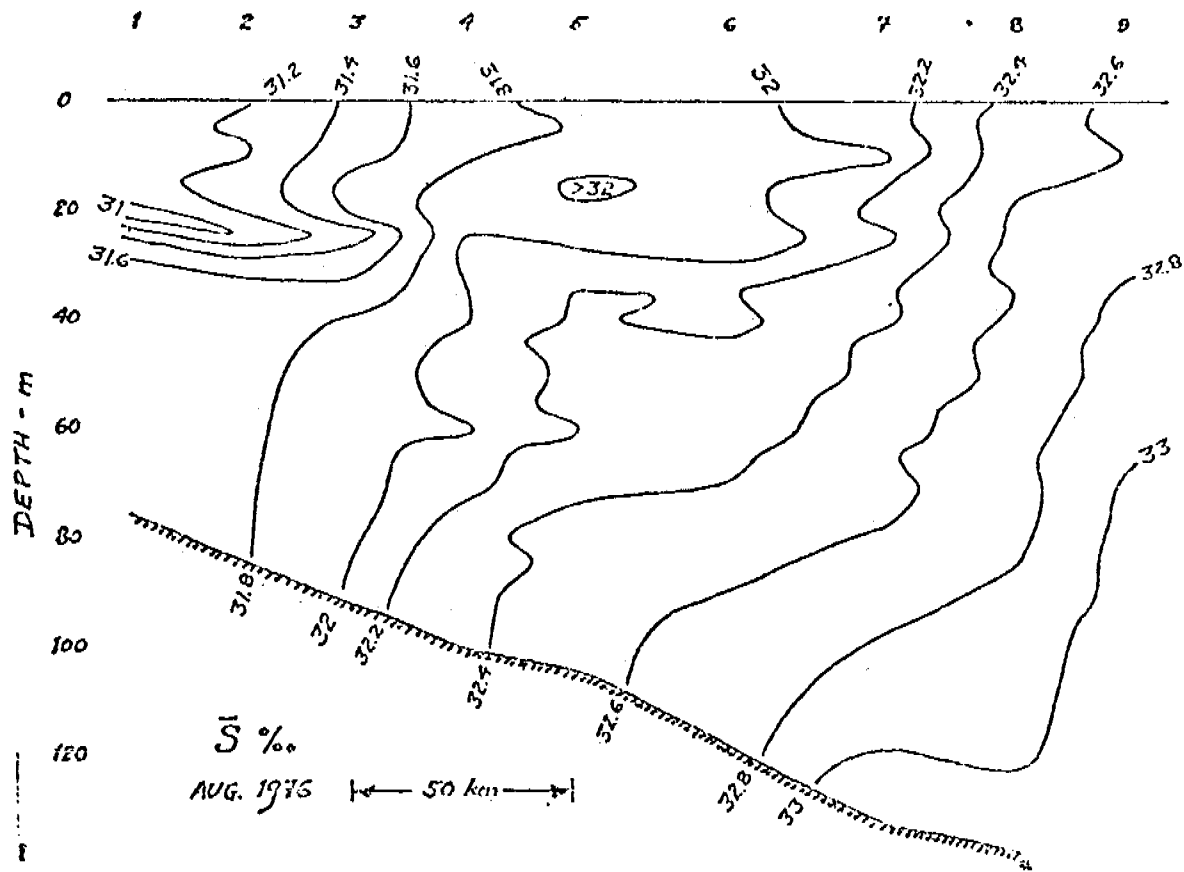


Figure 12

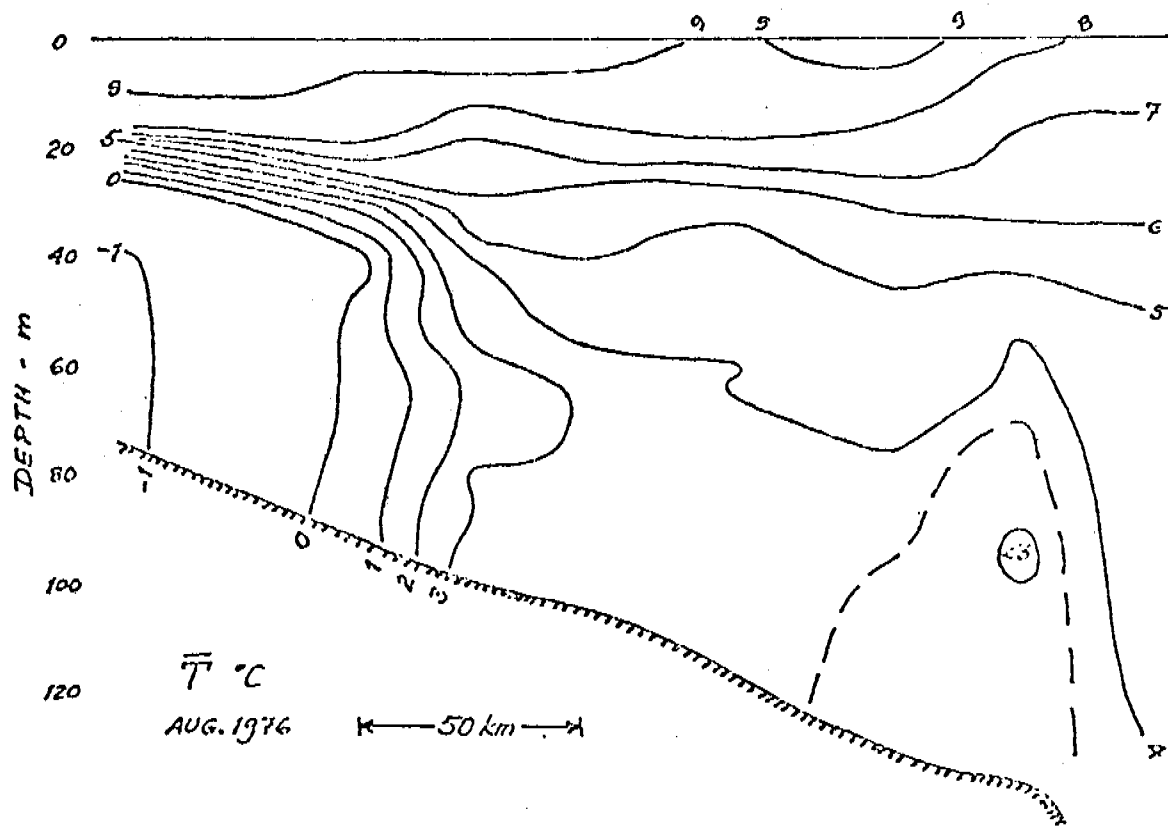


Figure 13

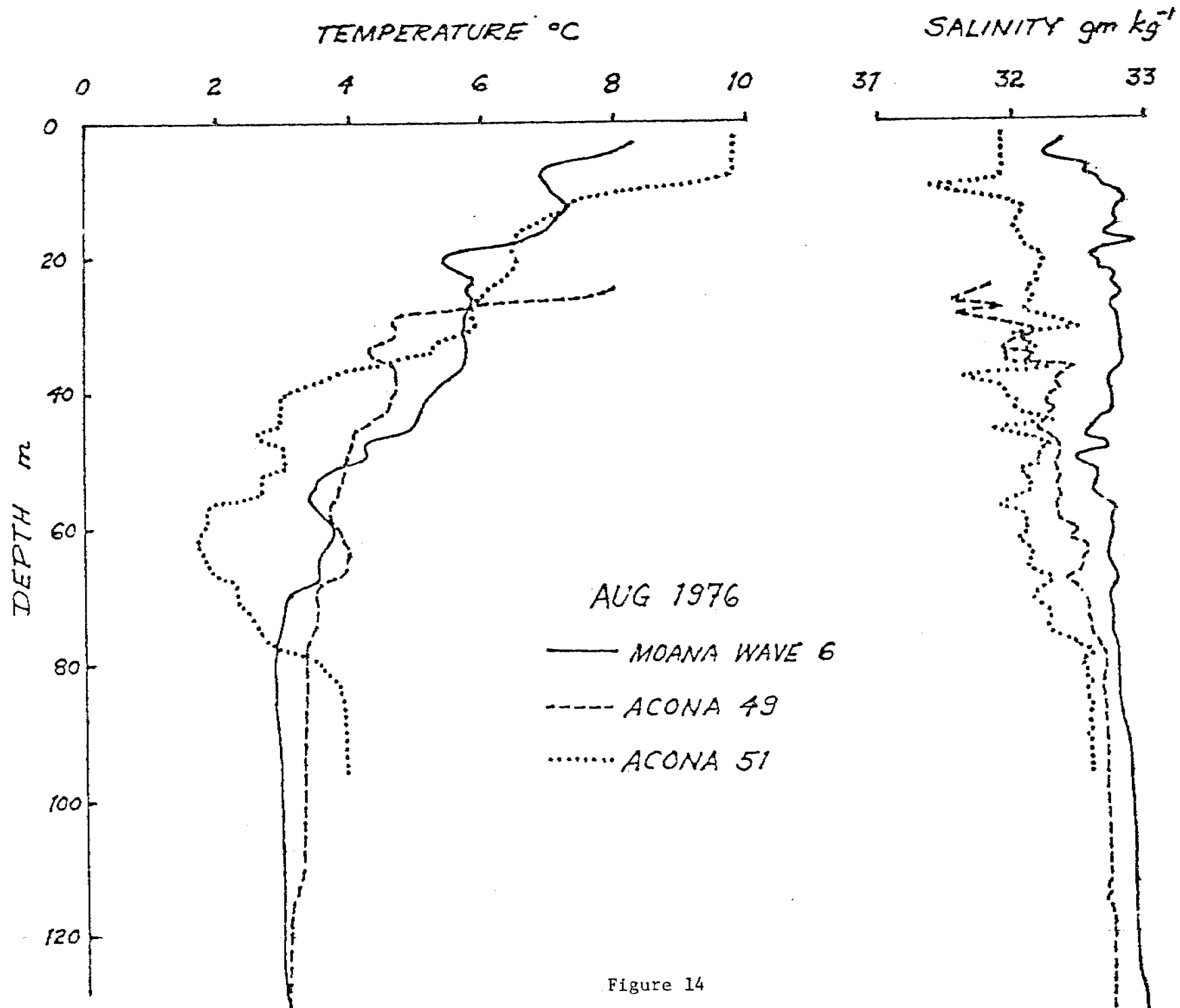


Figure 14

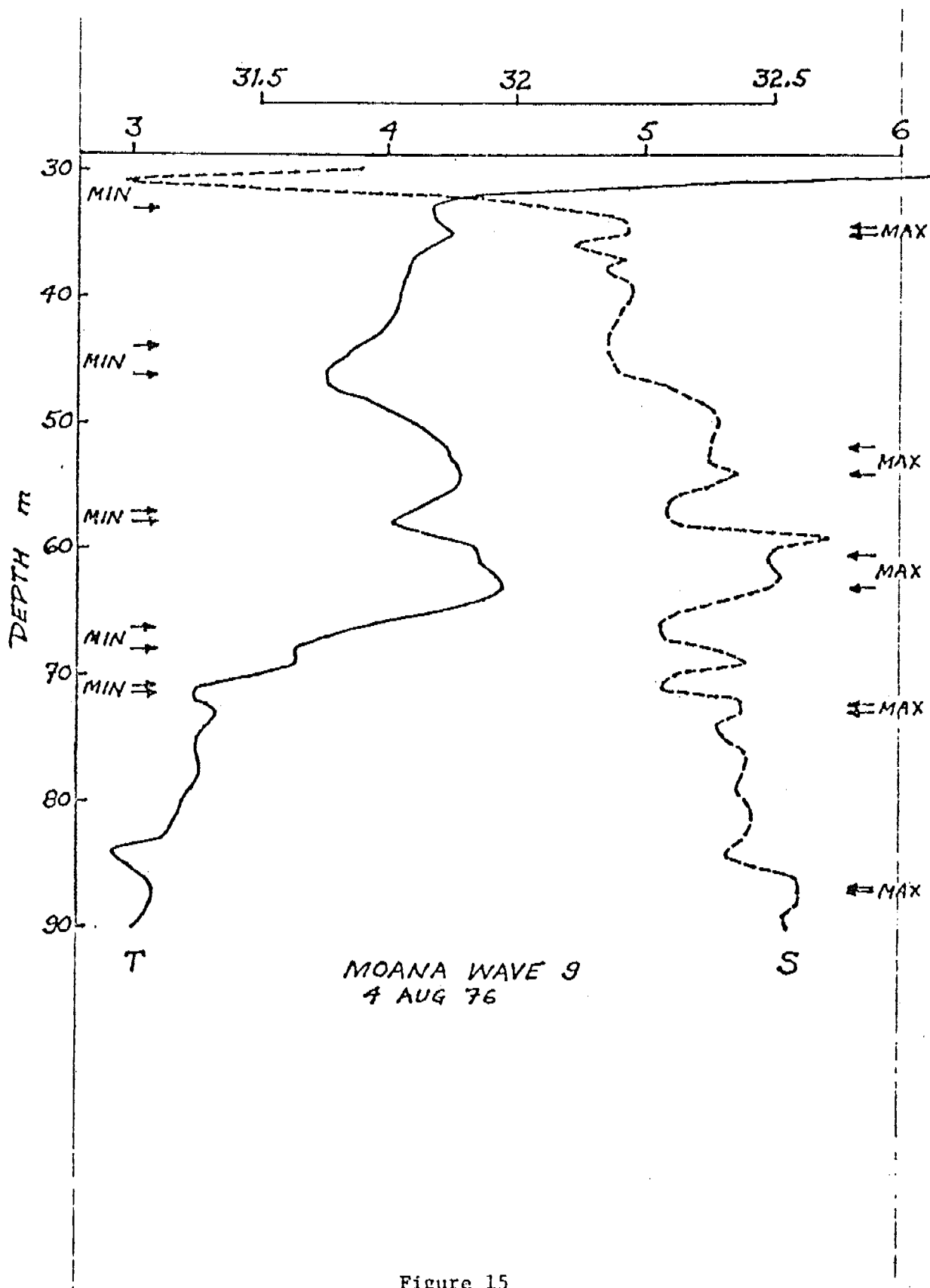


Figure 15

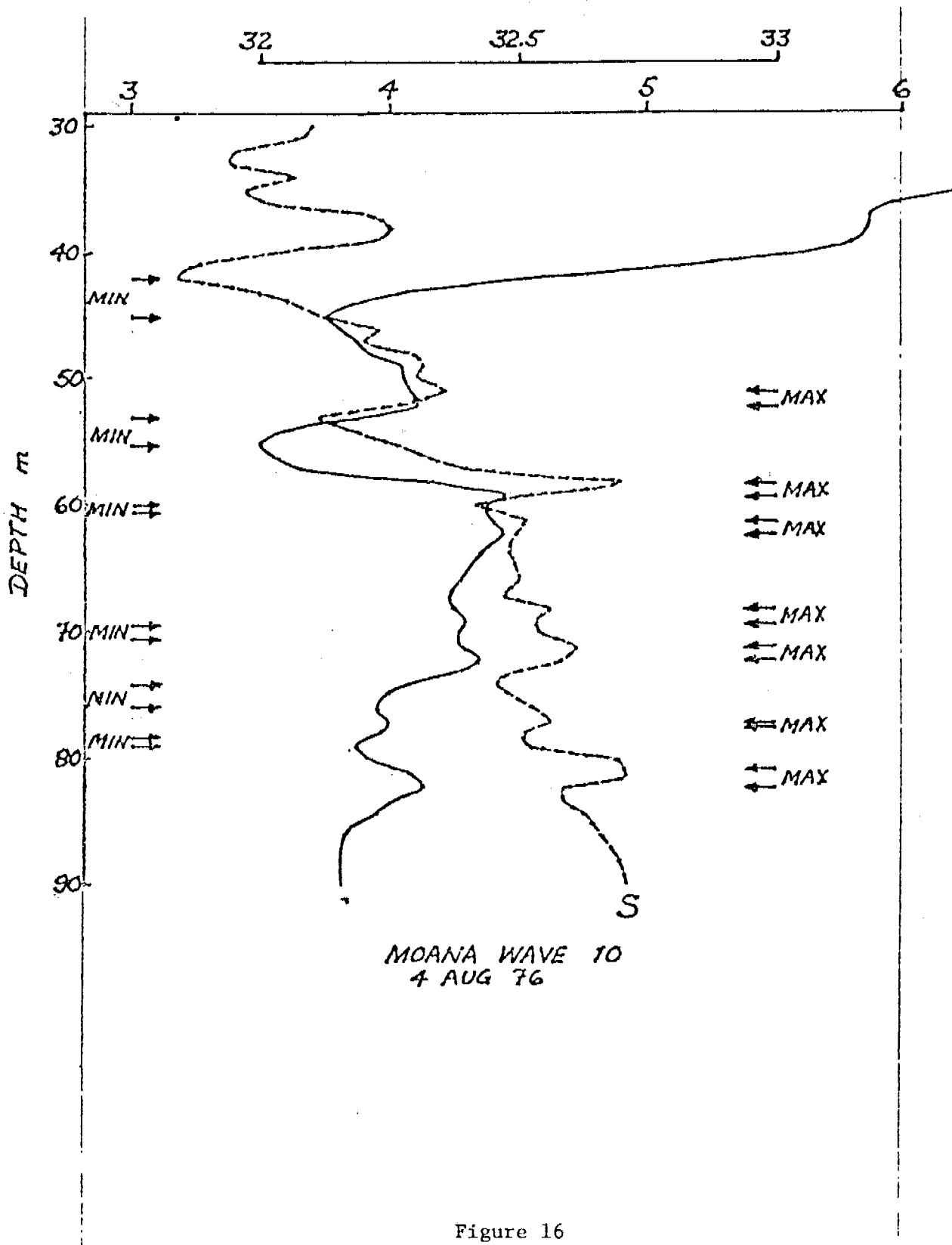
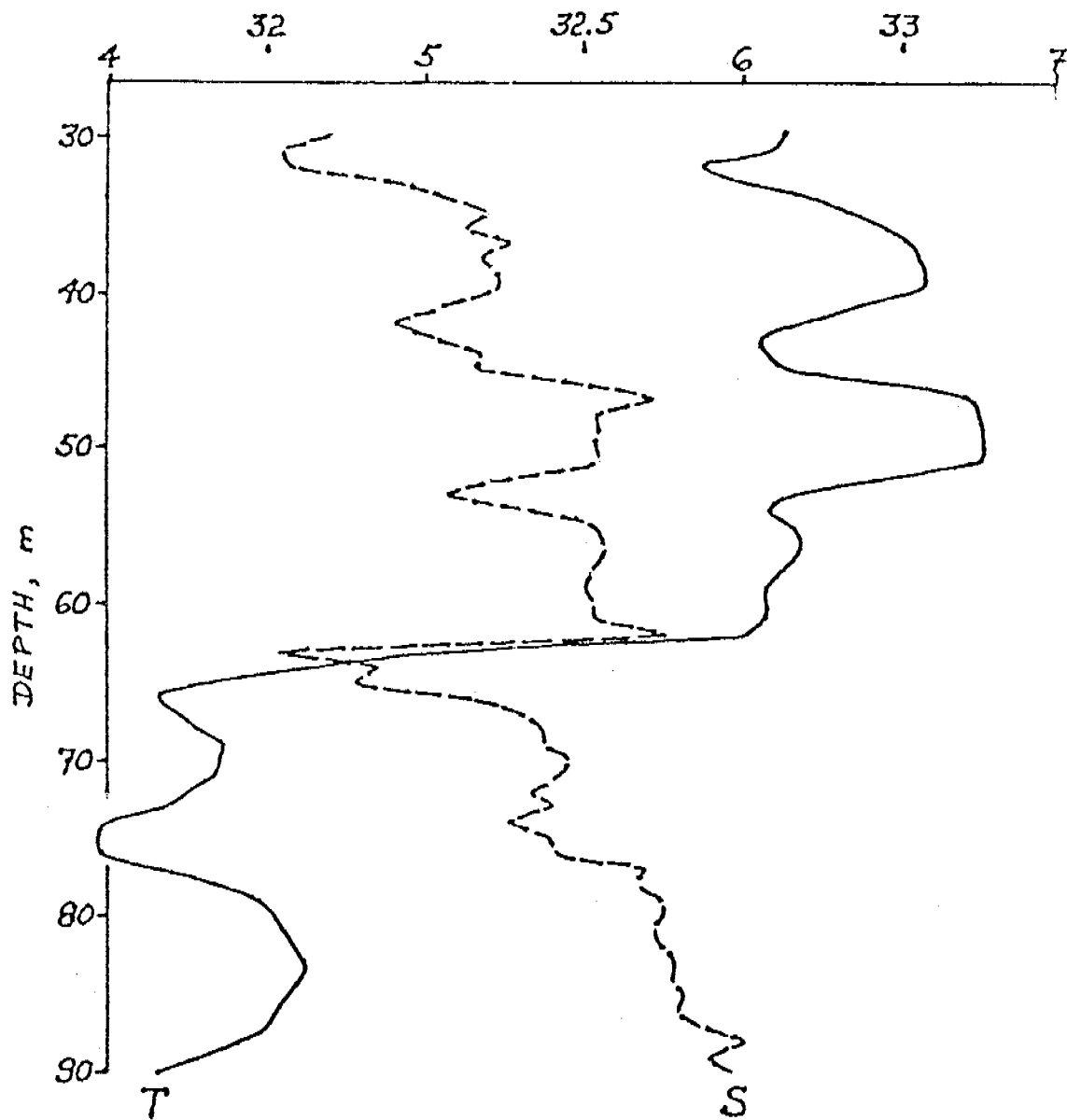


Figure 16



ACONA 61
8 AUG 76

Figure 17

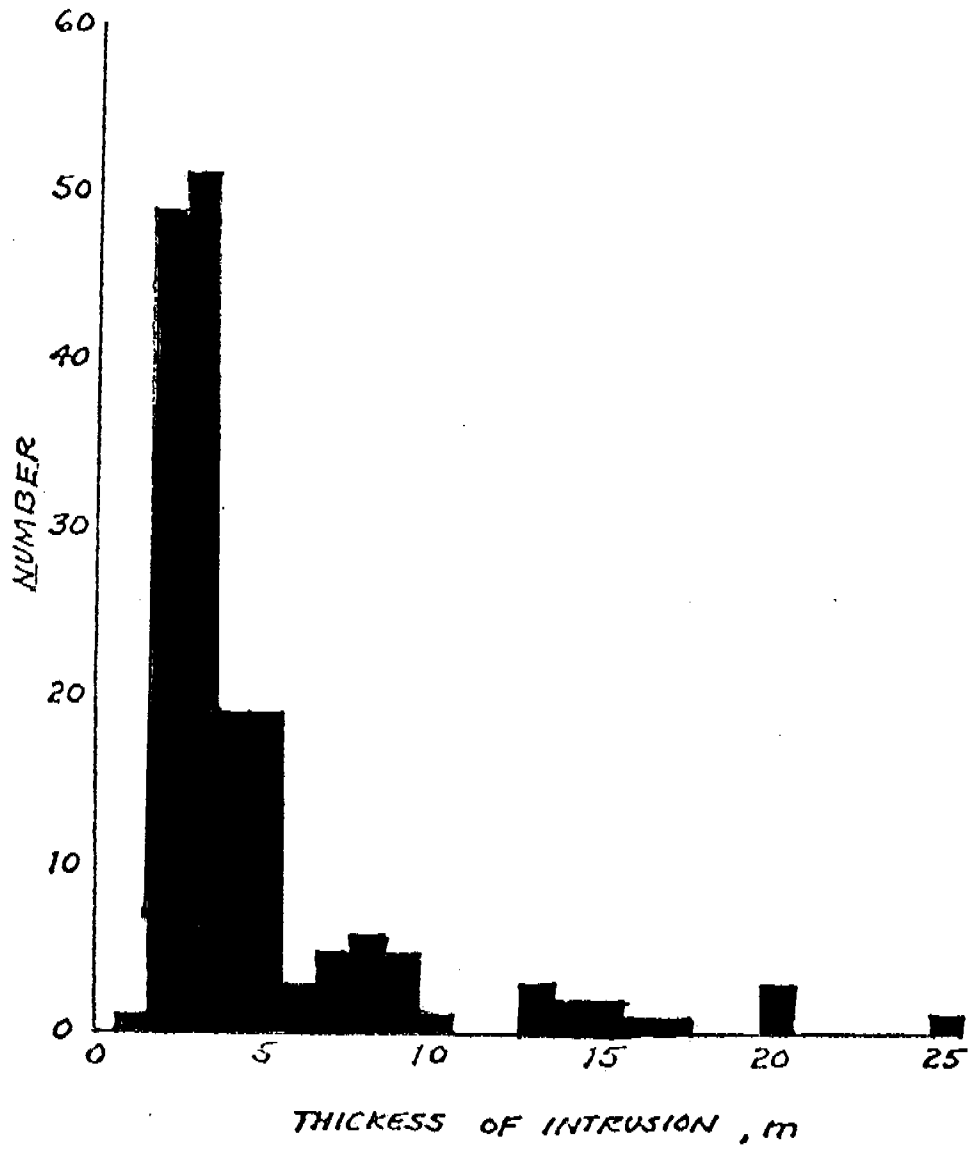


Figure 18

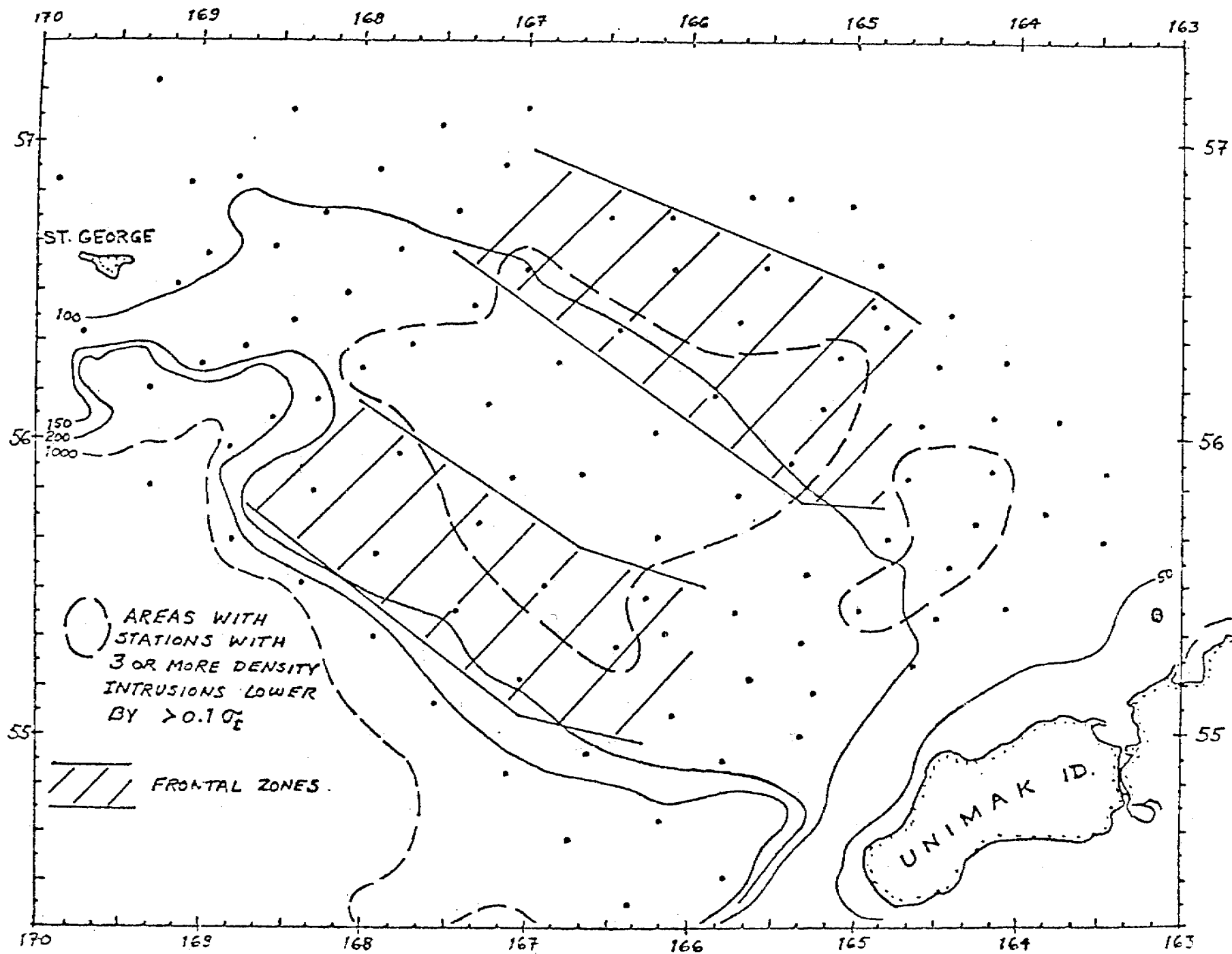


Figure 19

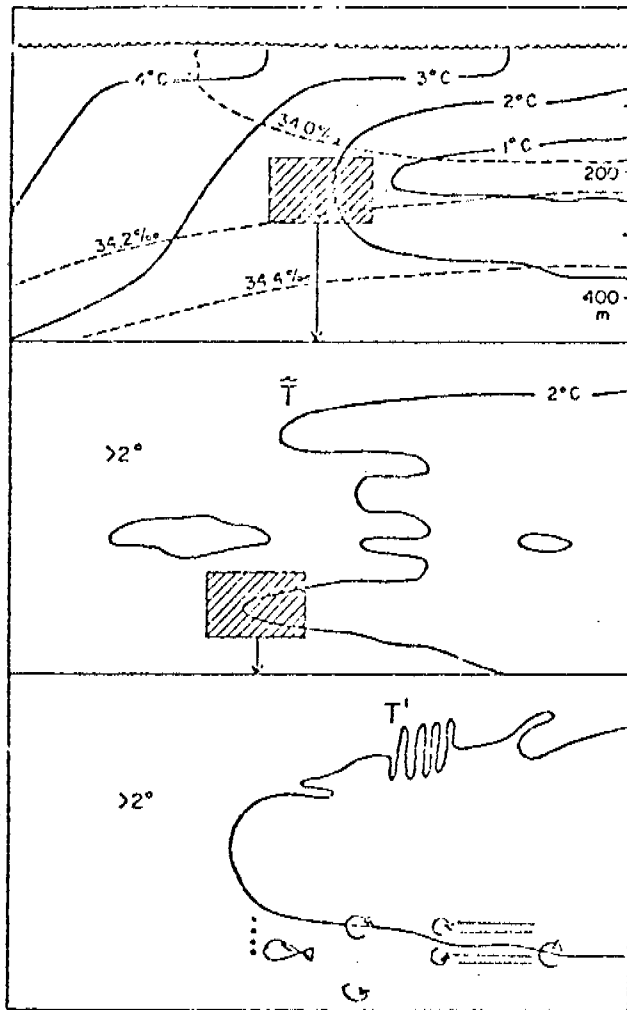


FIG. 1. Schematic representation of different scales of motion near a thermohaline front. Large-scale field forced by air-sea interaction (this example representative of Antarctic Polar Front) shown on upper figure; medium-scale motions, interleaving and intrusions, center; small-scale vertical mixing, mechanical and double diffusive, lower.
 From Joyce (1977).

Figure 20

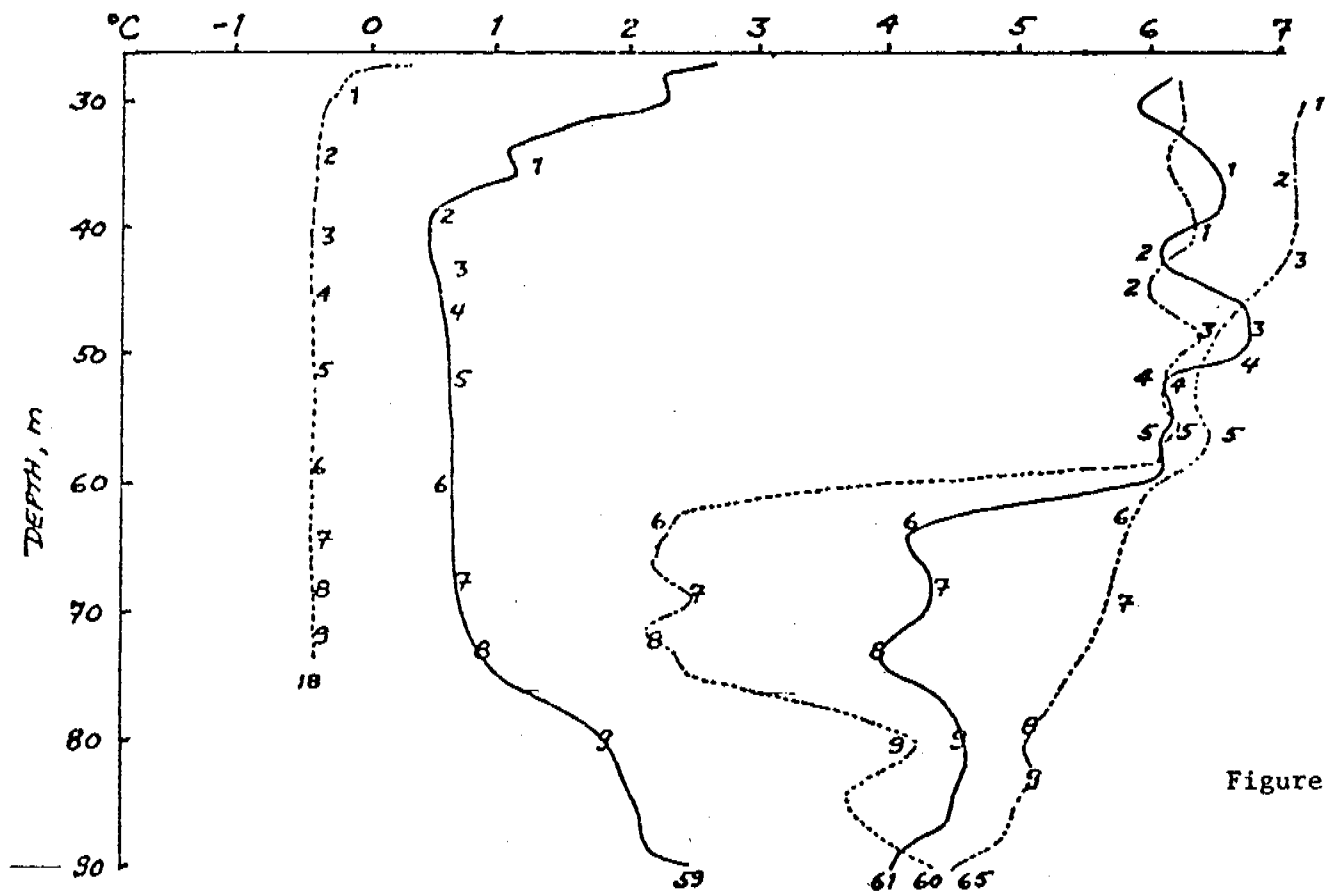


Figure 21

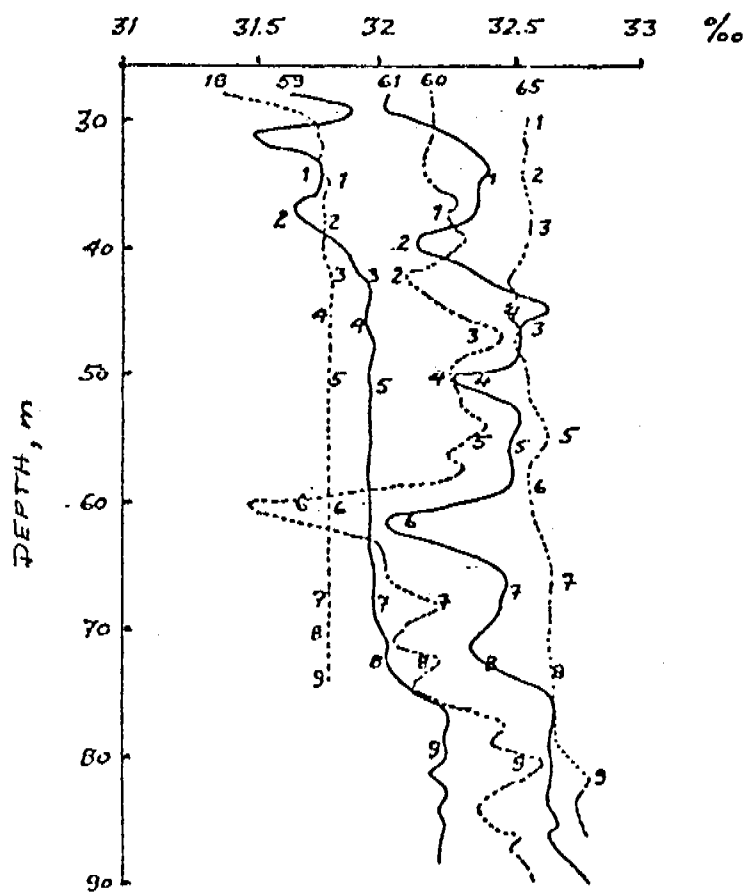


Figure 22

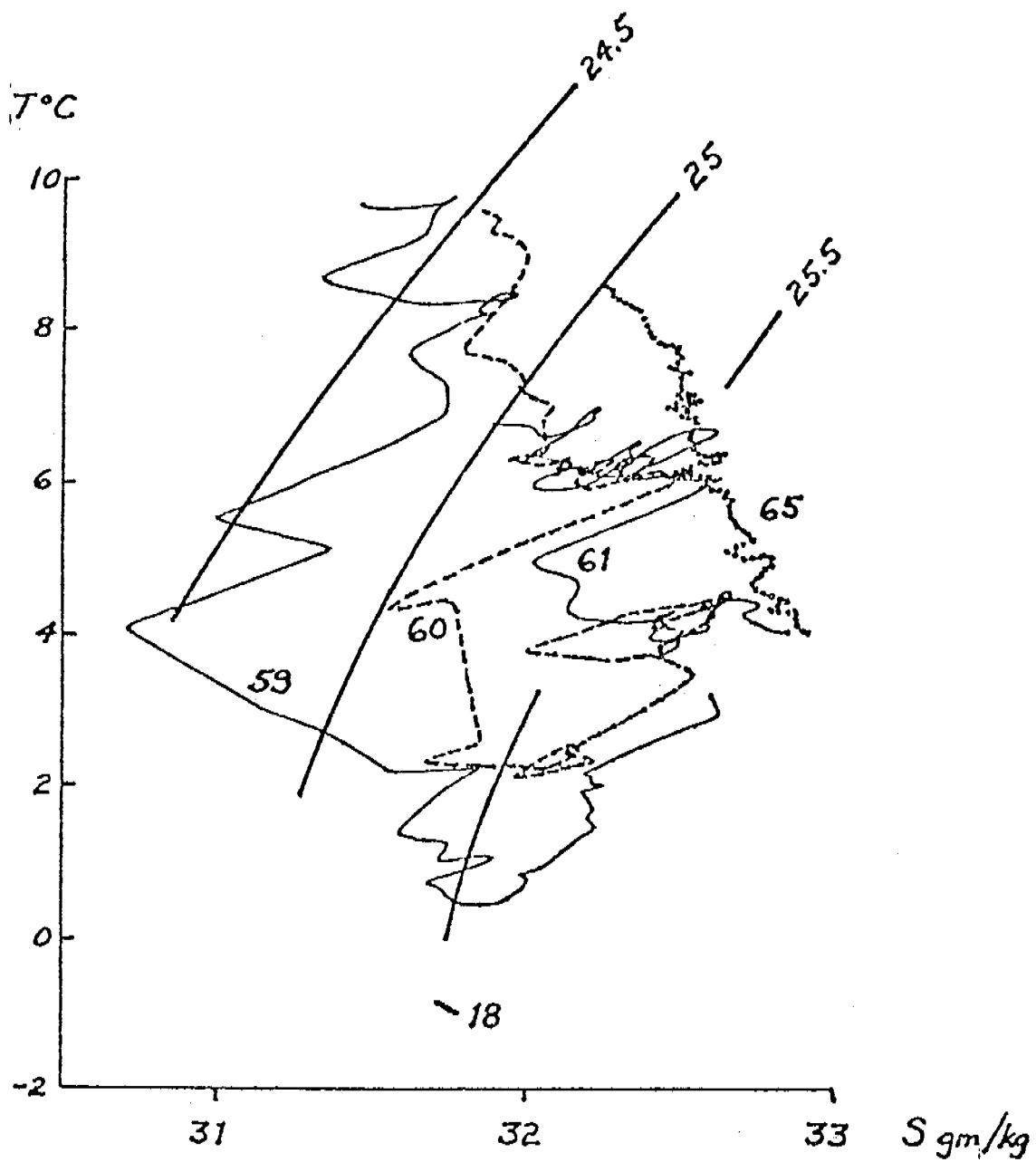
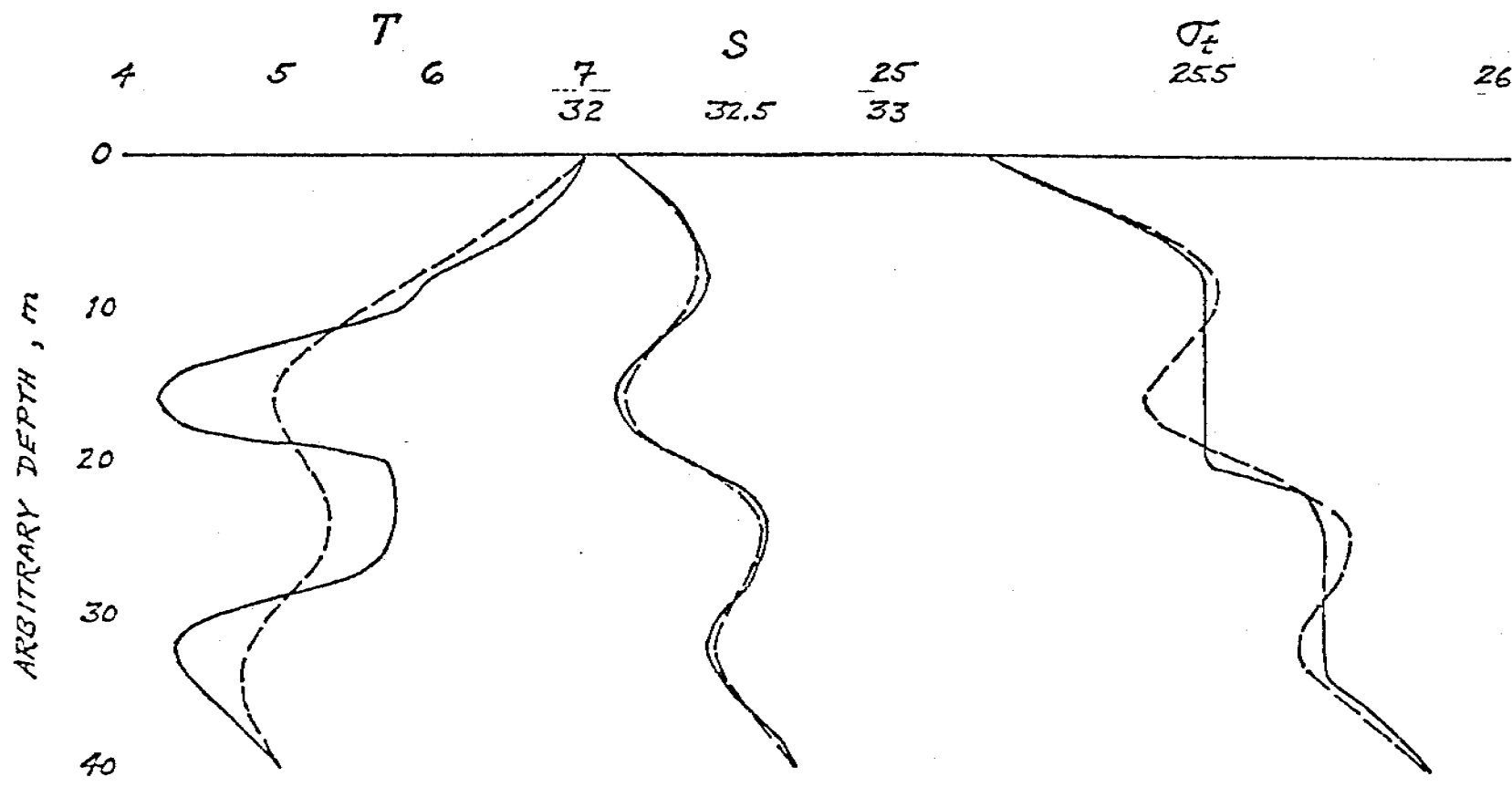


Figure 23



— BEFORE INTEGRATION
 - - - AFTER INTEGRATION: OVER: $\Delta t = 10^6 \text{ s}^{-1}$
 $K_T = 10^{-1} \text{ cm}^2/\text{s}$; $K_S = 10^{-2} \text{ cm}^2/\text{s}^{-1}$

INTEGRATED T/S PROFILES.

Figure 24

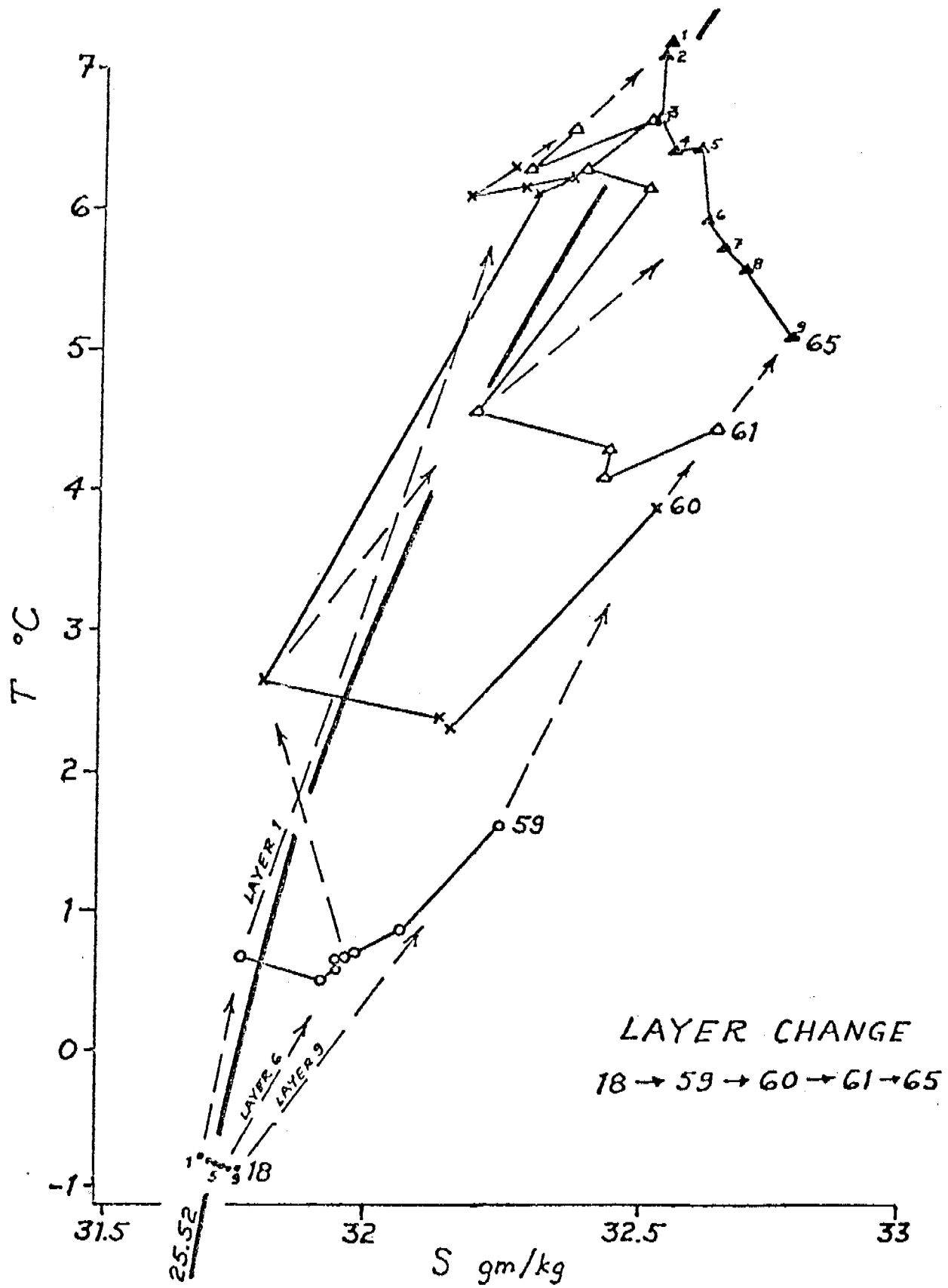


Figure 25

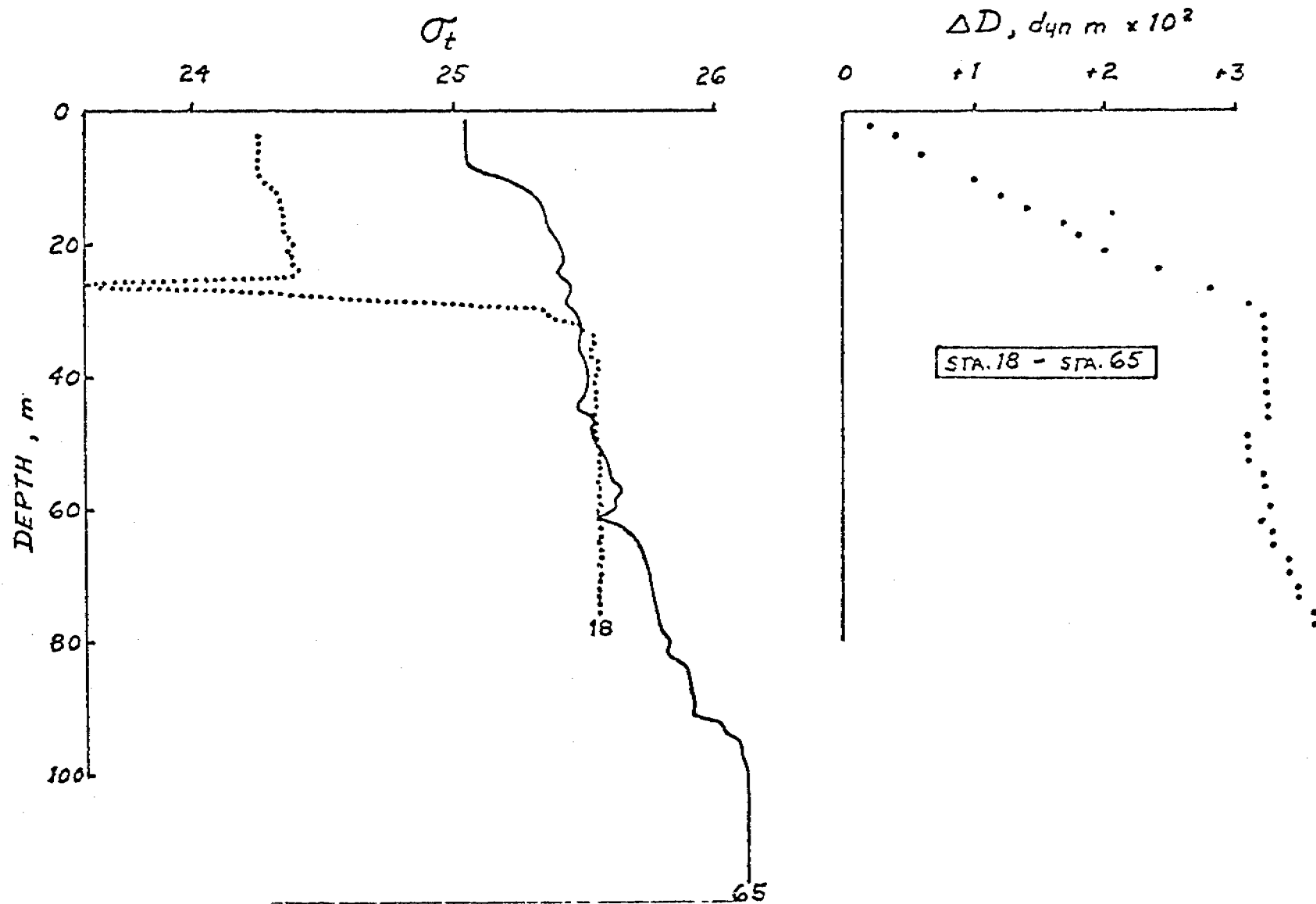


Figure 26

BRISTOL BAY ENERGY REGIMES

WATER DEPTHS	ENERGY MODE DISTRIBUTIONS	PROPERTY DISTRIBUTIONS	REMARKS
$D < 50\text{m}$			<ul style="list-style-type: none"> ◦ STIRRING OVER WHOLE COLUMN ◦ PROPERTIES ~ HOMOGENEOUS
$50 < D < 100$			<ul style="list-style-type: none"> ◦ SHARP FRONT (5-10 km) ◦ 2-LAYERED ~ SHARP INTERFACE ~ LOW VERTICAL TRANSFER ACROSS INTERFACE ◦ FRONT
$100 < D < 150$			<ul style="list-style-type: none"> ◦ MID-LAYER WITH LOW MIXING ENERGY ◦ FINESTRUCTURE ◦ SHELF-BREAK FRONT

ENERGY MODES:

1. SURFACE (WIND) ENERGY, DOWN TO ~ 20 m (DEEPER IN WINTER)
2. BOTTOM (TIDAL) ENERGY, UP TO 40-50 m

Figure 27

B.

A Structural Front Over the Continental

Shelf of the Eastern Bering Sea*

J. D. Schumacher¹

T. H. Kinder²

D. J. Pashinski¹

R. L. Charnell¹

* Contribution No. 0352 from the NOAA/ERL Pacific Marine Environmental Laboratory

¹ Pacific Marine Environmental Laboratory/ERL/NOAA
3711 15th Avenue N.E., Seattle, Washington 98105

² Department of Oceanography, University of Washington, WB-10
Seattle, Washington 98195

ABSTRACT

Conductivity and temperature versus depth (CTD) and expendable bathythermograph (XBT) data taken during the ice-free seasons of 1975-1977 define a structural front paralleling the 50m isobath. This front forms a narrow transition separating a well-mixed coastal domain from a two-layered central shelf domain. In the spring, during frontogenesis, vertical mean temperatures and salinities are continuous across the front: it is not a water mass boundary. The changing balance between buoyant energy input and tidally-generated mixing determines frontal location and the frontal width correlates with bottom slope. The front is similar to those reported around the British Isles, but we find that in the Bering Sea the salinity distribution is important, that the ice cover influences the seasonal evolution of the hydrographic structure and that the geostrophic (baroclinic) speed differences across the front are small (<2 cm/s). We hypothesize that frontogenesis depends critically on positive feedback between stratification and mixing.

1. Introduction

It has long been known that fronts separate shallow well-mixed waters nearshore from more stratified waters offshore (e.g. Uda, 1959). The formation of such shallow water fronts may be attributed to a change in the energy balance between tidally generated mixing and buoyancy input. Recently, fronts of this type found around the British Isles have been discussed by Simpson (1971, 1976), Simpson and Hunter (1974), Pingree et al.(1974), Fearrhead (1975), and James (1977). Muench (1976) first suggested the presence of a similar front over the shelf near Bristol Bay, Alaska, and our measurements confirm the existence of such a front.

We have collected numerous conductivity and temperature versus depth (CTD), expendable bathythermograph (XBT), and current meter data between August 1975 and July 1977 over the continental shelf of the eastern Bering Sea. Data collected near Bristol Bay show a front during ice-free conditions. We call this front "structural," to emphasize that it is a transition separating two distinct vertical hydrographic structures: homogeneous and two-layered. Intermediate temperatures and salinities characterize the well mixed domain while the stratified domain has two layers, the upper warmer and fresher, and the lower colder and saltier than in the well mixed domain. After formation of the stratified central shelf domain, vertical mean temperatures and salinities for the whole water column on either side of the front are still nearly the same.

a. Setting

The Bristol Bay study area is the southern portion of the large continental shelf of the eastern Bering Sea, including Bristol Bay proper (Figure 1). It is bounded on the south by the Alaska Peninsula and on the east by the Alaskan

coast north to Nunivak Island. A line connecting Nunivak Island with the Pribilof Islands is the approximate northern boundary, and the western boundary is the shelf break, running southeast from the Pribilofs to Unimak Pass.

Freshwater runoff, primarily from the Kuskokwim and Kvichak watersheds, annually accounts for 1% of the total volume of Bristol Bay. This flow of freshwater maintains a salinity difference of about 2 g/kg between the waters overlaying the shelfbreak and those near the coast. For five months (December to April) about 60% of Bristol Bay is covered with first year ice which is generally less than 1 m thick. Ice formation begins in sheltered areas early in November and builds to the most extensive coverage in March. Ice retreat is generally northward, beginning in April, providing a local source of freshwater as it melts.

The general hydrography of Bristol Bay has been detailed by Dodimead et al. (1963), Kinder (1977), Kinder, et al. (1978), and Coachman and Charnell (1977). During ice-free conditions, the two water domains germane to this paper are the coastal and central shelf. Waters of the coastal domain characteristically have little or no stratification while the central shelf is a domain of strong stratification (Figure 2). Generally, the coastal domain is restricted to shoreward of the 50 m isobath, with the central shelf domain between the 50 m and 100 m isobaths. Twenty-eight CTD station pairs across the 50 m isobath indicate the boundary between these two domains (Figure 1).

We observed velocities using both moored current meters and satellite-tracked drifters (Schumacher, et al., 1977; Hansen 1977). Energies at tidal frequencies dominate, accounting for over 90% of the total variance. The weak mean flow shows a cyclonic tendency around the perimeter of Bristol Bay, with maximum speeds (~ 3.5 cm/s) found near the 50 m isobath and in the coastal

waters. Speeds observed over a three month period in the central waters are extremely low (mean values <1.0 cm/s) and there is no sense of an organized circulation. Over the ice-free season, direct current and hydrographic measurements indicate that advection by the mean flow is so small that it does not affect the hydrographic structure significantly.

b. Measurements

We use hydrographic data obtained from various ships using Plessey Model 9040 CTDs, or in a few cases a Bisset-Berman model 9040 salinity-temperature-depth profiling system (STD). In either case, Nansen bottle samples were taken on most casts for calibrating temperature and salinity. These CTD and STD data are accurate to $\pm 0.02^\circ\text{C}$ and ± 0.02 g/kg.

To supplement these observations, we used Sippican XBT's with shallow water probes (0 - 200 m), that have an estimated accuracy of $\pm 0.2^\circ\text{C}$. We calibrated each XBT section against CTD casts. During one cruise, a recorder malfunction degraded the accuracy of temperatures shallower than 15 m; since there is usually a surface isothermal layer exceeding 15 m thickness, this loss of data is not critical.

2. The Front

a. Frontal Structure

Hydrographic data taken in June 1976, shortly after ice breakup, illustrate the nature of the front in spring (Figure 2). The vertical temperature difference, surface minus bottom (ΔT), ranges from $\Delta T=3^\circ\text{C}$ over the central shelf to $\Delta T=0^\circ\text{C}$ in the coastal water. Similarly, the salinity difference, bottom minus surface (ΔS) changes from $\Delta S=0.5$ g/kg to $\Delta S=0$ g/kg. Where the water depth approximately equals the thickness of the bottom mixed layer (~ 50 m), the entire water column is well-mixed. Where the water depth equals the sum of the surface mixed layer (~ 20 m) and the bottom mixed layer, the stratification is maximum.

This suggests that the mixing energies from the bottom and the surface are not simply additive, and only where the bottom layer encompasses the entire water column do we find the water homogeneous.

No such abrupt change occurs in the horizontal gradients of vertical mean temperatures and salinities. At station 138 the vertical means are 0.20°C and 31.44 g/kg , while at station 139, 50 km from 138 but on the other side of the front, they are 0.37°C and 31.57 g/kg . The resulting gradients are $3.3 \times 10^{-3}^{\circ}\text{C/km}$ and $2.5 \times 10^{-3}\text{ g kg}^{-1}\text{ km}^{-1}$ which are smaller than the mean gradients across the shelf (Kinder, 1977; and Kinder and Coachman, 1978). Thus the primary difference between water in the coastal and central shelf domains across the front is in their vertical distributions of temperature and salinity: coastal water can be made from shelf water by mixing.

Widely spaced CTD stations along the same line in the fall (Figure 3) reveal vertical structure similar to that in late spring. Thermal and haline stratification change abruptly between stations 138 and 139; the mean salinity gradient changes sign and the mean temperature gradient is an order of magnitude larger: $-0.8 \times 10^{-3}\text{ g kg}^{-1}\text{ km}^{-1}$ and $30 \times 10^{-3}^{\circ}\text{C/km}$. In order to see if these changes in gradient are typical, we grouped 20 CTD station pairs which spanned the central shelf and coastal water boundary into three subsets: spring (May-June, 11 pairs), summer (July-August, 3 pairs), and fall (September-October, 6 pairs). The mean temperature gradient increases about one order of magnitude during the ice-free season (Figure 4), from about $2 \times 10^{-3}^{\circ}\text{C/km}$ in the spring to $25 \times 10^{-3}^{\circ}\text{C/km}$ in the fall. Although the trend is statistically insignificant, the mean salinity gradient reverses during the summer, but its magnitude is always low ($\sim 1 \times 10^{-3}\text{ g kg}^{-1}\text{ km}^{-1}$).

Seasonal changes are evident at individual stations also. In the spring, station 138 is strongly stratified with $\Delta\sigma_t = 0.63\text{ kg/m}^3$ (Table 1). Nearly 80% of this density stratification is due to the salinity difference because of

the small temperature difference and the low temperatures. In the fall, the density stratification has increased to 0.95 kg/m^3 , but less than 40% of this is caused by salinity. We find this is generally true over the central shelf; in the early spring salinity controls the density structure, but as insolation heats the shelf water temperature becomes increasingly important so that by late summer temperature controls density (Kinder *et al.*, 1978).

The density gradients inferred from the closely spaced CTD stations may affect the mean flow. Dynamic calculations of the geostrophic velocity difference across the front are typically 1 to 2 cm/s. While this is small compared to the greater than 20 cm/s tidal currents, the long term (about two years) mean flow measured by a mooring southwest of Nunivak Island is ~ 1.5 cm/s. Thus, even a modest velocity difference may influence the mean flow in Bristol Bay.

To examine smaller spatial scales, we obtained data from several crossings of the front in 1977, using both CTDs and closely-spaced XBTs (Figures 5-7). Because the winters of 1975-1976 (severe) and 1976-1977 (mild) in the Bering Sea were markedly different, we anticipated changes in the frontal character. As delineated by our data, however, the gross features of the front were the same in 1976 and 1977. Line 1 (Figure 5), taken shortly after ice breakup in 1977 is similar to the 1976 cross section (cf. Figure 2). At station 79 $\Delta T = 1.34^\circ\text{C}$ and $\Delta S = 0.30 \text{ g/kg}$, comparable to values found in 1976 (Table 1). Four additional XBT sections across the front (Figure 6) show similar features. Moving towards shore, the isotherms splay from the well-defined thermocline. Isotherms seaward of the front parallel the bottom (*i.e.* the thickness of the bottom mixed layer is nearly constant). Sections 6 and 7 (Figure 7) from July 1977 shows a transition similar to other sections, but the coastal water is not mixed completely. For section 6, station 90.2 has $\Delta T = 6.87^\circ\text{C}$ and

Table 1

Station 138

	13 June 1976	24 September 1976
Upper layer	T = 1.52°C S = 31.19 g/kg $\sigma_t = 24.98 \text{ kg/m}^3$	T = 6.77°C S = 31.31 g/kg $\sigma_t = 24.57 \text{ kg/m}^3$
Lower layer	T = -1.57°C S = 31.82 g/kg $\sigma_t = 25.61 \text{ kg/m}^3$	T = -0.50°C S = 31.75 g/kg $\sigma_t = 25.52 \text{ kg/m}^3$
Stratification	$\Delta T = 3.09^\circ\text{C}$ $\Delta S = 0.63 \text{ g/kg}$ $\Delta\sigma_t = 0.63 \text{ kg/m}^3$	$\Delta T = 7.27^\circ\text{C}$ $\Delta S = 0.44 \text{ g/kg}$ $\Delta\sigma_t = 0.95 \text{ kg/m}^3$

The stratification is defined as the difference between upper and lower layer values.

$\Delta S = 0.08$ g/kg while station 90.1 has $\Delta T = 1.16^\circ\text{C}$ and $\Delta S = 0.21$ g/kg. Similarly for section 7, station 94 has $\Delta T = 7.74^\circ\text{C}$ and $\Delta S = 0.08$ g/kg, while station 119 has $\Delta T = 2.10^\circ\text{C}$ and $\Delta S = 0.16$ g/kg. As expected, these summer data show decreasing thermal stratification as the coast is approached. Haline stratification, however, increases toward the coast.

Some of the XBT sections illustrated in Figures 6 and 7 do not define the front clearly. To show the front in these sections, and to examine the impression that frontal width depends on bottom slope, we define a horizontal gradient of thermal stratification by:

$$T'_n = \frac{(\Delta T_n - \Delta T_{n+1})}{L}$$

where: L = station spacing

$\Delta T_n = T_{15} - T_{40}$ at station n , and

T_{15}, T_{40} = temperature at 15 m and 40 m depth.

Values at depths of 15 m and 40 m represent the temperatures of the upper and lower layers. We expect ΔT_n to be high in the strongly stratified central shelf domain, and nearly zero in the well mixed coastal domain. The horizontal gradient of thermal stratification, T'_n , has low values within both water domains, but high values across the front. We find that plotting T'_n versus distance across the front (Figure 8a) defines an unambiguous frontal width for lines 1 to 6 (Line 7 did not yield an unambiguous result), the closely spaced cross sections. Widths ranged from 10.8 km for line 1, to 5.2 km for line 6, and the linear correlation of width on bottom slope (Figure 8b) is significant at the 95% level. The front is clear when the data are manipulated this way (Figure 8a), in spite

of the ambiguity in Figures 6 and 7. Some of the variability demonstrated by Figures 2-8 is seasonal, and can be understood.

b. Seasonal Evolution

There is sufficient data to outline the seasonal evolution of the front. At the end of winter, water near the 50 m isobath is vertically homogeneous having been mixed by wind and tidally generated turbulence, and by convection driven by surface cooling and brine rejection during freezing. Ice covers most of the shelf, preventing insolation from warming the waters beneath. In the spring, with ice breakup and melting dramatic changes occur.

Within a few weeks positive buoyancy input increases from nearly zero to high values as melting ice adds freshwater and insolation adds warmth. The changing balance between tidal mixing energy and buoyant energy then determines the transition between strongly stratified and well mixed domains (see Section 2C, Energy Balance, below).

As the summer progresses, a gradient of surface temperature develops. In the central shelf water, most of the heat from insolation is stored in the shallow (~25 m thick) upper layer, while in the adjacent coastal water heat is stored throughout the water column (~50 m deep). The heat balance is primarily with the atmosphere (Reed, 1978), and the resulting thermal structure has two salient features. First, throughout summer the surface temperatures in the two-layered water are higher than those in the coastal domain. Second, because the two-layered water has higher surface temperatures, radiative and evaporative losses to the atmosphere are higher than losses from the coastal water and so more heat can be stored in the coastal water. July and August data show the gradient of surface temperatures (cf. Figure 7) and the horizontal gradient of vertically averaged temperature (Figure 4) shows the increase in heat storage. In the fall when surface cooling begins, the surface temperature

gradient reverses, as convection abets rapid cooling over the central shelf (Figure 3). During late fall and winter convection and turbulent mixing establish vertical homogeneity over the central shelf again, completing the annual cycle.

Because of the active fisheries over the shelf, inferring the structure of the water column by remote sensing is potentially useful. During summer, the front's thermal structure has a surface signature which satellite-borne infrared sensors can detect (Figure 9). In spite of frequent fog and clouds, bottom temperature and stratification can be monitored usefully. Additionally, we suspect that the front affects late summer nutrient distribution, as Simpson and Hunter (1974) found in the Irish Sea.

It is not temperature, but salinity which strongly affects the density field, especially in the spring. As noted above, it is the contribution of melt water which initially stratifies the central shelf domain, accounting for more than 3/4 of the density stratification. We also think the seasonal change in salinity gradient suggested by Figure 4 is accurate. In early spring, the salinity of the coastal waters is higher than in waters of the central shelf (Kinder, 1977; Kinder *et al.*, 1978). Ice freezing near Nunivak Island and in Kuskowim Bay is blown southward (Muench and Ahlnäs, 1976), leaving most of its salt behind. Because the ice melts elsewhere, this coastal divergence of ice locally reverses the cross-shelf salinity gradient, bypassing any impediment that the front offers to the cross-shelf salt flux. Freshwater from the rivers, which reach peak runoff in July, restores the salinity gradient; salinity then decreases shoreward.

Other seasonal changes occur. Sections 6 and 7, taken in July 1977 (Figure 7), show some stratification in the coastal domain. In both cases, the CTD station nearest shore reveals stronger haline stratification than the offshore station.

We believe river discharge and the increased buoyancy from insolation (generally higher temperatures, Table 3) causes this stratification. Whether the front generally migrates shoreward later in the summer or perhaps moves shoreward locally, we do not know. Along the Nunivak to Pribilof line (where our data is most extensive), we find no evidence for seasonal change in frontal position. Section 7 was also occupied by closely spaced (~ 10 km) CTD stations in spring 1976 (Kinder, 1977), and the front then is more distinct than in summer 1977 (Figure 7); it is less clear, however, than the spring 1976 front farther west (Figure 2). These observations suggest some spatial and temporal variability of the front, and satellite imagery (Figure 9) implies that the front has a more sinuous path than does the 50 m isobath. We cannot resolve these features and we implicitly assume no variability in some discussions for simplification. Complete understanding of the front, however, will require accounting for such variability.

c. Energy Balance

We have already noted that the current regime over this shelf is tidally dominated, and that the front occurs where the height of the bottom mixed layer approximately equals water depth. Our current records show that 90% to 95% of the velocity variance is tidal, and that mean speeds are an order of magnitude smaller than tidal currents. While wind stress is required to maintain the well-mixed upper layer over the central shelf, neither direct wind mixing at the surface nor wind-induced currents generating mixing at the bottom appear as important as do the tides. We therefore think that this transition between structural domains results from a changing balance between buoyant (available potential) energy and mixing energy which is tidally generated at the bottom. Seaward of the front, in the central shelf domain, tidal mixing is insufficient

to overcome the buoyancy added by insolation, melting, and freshwater runoff. Because buoyancy inhibits mixing, a thin pycnocline separates the wind-mixed surface layer and the tidally mixed bottom layer. Shoreward of the front in the coastal domain, however, tidal mixing reaches completely to the surface. Estimating the buoyant and mixing energies confirms the plausibility of this idea.

The potential energy for a two-layer water column, relative to its well-mixed state is:

$$E = 1/2 \rho' g h (H-h)$$

where ρ' is the density difference between layers,

g is the acceleration of gravity,

h is the thickness of the upper layer generated by wind mixing,

and

H is the water depth.

The generation of mixing energy is:

$$E = \rho C_D V^3$$

where ρ is the density

C_D is the drag coefficient, and

V^3 is the mean cubed speed

Using hydrographic and current meter data, we estimate these parameters.

For these calculations three water columns of 50 m depth were selected, representing the water column on either side of the front and the water column in winter. (Table 2). Warming the winter water from a mean temperature of -1.5°C to 0°C requires about $3.1 \times 10^8 \text{ J m}^{-2}$; over five weeks (the estimated duration of ice breakup in 1976), this is equal to $100 \text{ W m}^{-2} \approx 0.15 \text{ ly/min}$. These figures are reasonable, although somewhat lower than the 0.23 ly/min from Reed's (1978) calculation for the southeastern Bering Sea during summer. Over the

Table 2 Water Columns

	<u>Temperature</u> <u>(C°)</u>	<u>Salinity</u> <u>(g/kg)</u>	<u>Density</u> <u>(kg/m³)</u>
Winter	-1.5	31.8	25.60
Homogeneous	0	31.5	25.31
Stratified: Upper	1.5	31.3	24.99
25 m			
Lower	-1.5	31.8	25.60
25 m			
Mean	0	31.5	---

same period, we assume 0.5 m of fresh ice melted locally, thus lowering the mean salinity from 31.8 g/kg to 31.5 g/kg. The ice thickness used is less than often given (~ 1 m), but is also reasonable. These temperature and salinity changes agree with the hydrographic data, and are used to estimate the buoyant energy.

The mean rate of buoyancy addition is $\frac{\Delta p}{\Delta t}$, where $\Delta t =$ five weeks. The buoyant energy addition is thus $\frac{1900 \text{ J m}^{-2}}{5 \text{ weeks}} \sim 6.3 \times 10^{-4} \text{ W/M}^{-2}$. From current measurements we estimate $V \sim 20$ to 25 cm/s and we take $C_D \sim 3.1 \times 10^{-3}$ (Sternberg, 1968). Tidal dissipation is about $340 \times 10^{-4} \text{ W/m}^{-2}$ (using $V \sim 22$ cm/s), but is, of course, highly sensitive to the choice of speed. We thus find that $\frac{6.3 \times 10^{-4} \text{ W/m}^2}{340 \times 10^{-4} \text{ W/m}^2} \sim 2\%$ of the tidal dissipation mixes the water column. Fearnhead (1975) similarly estimated about 1% around the British Isles, essentially an identical result. We conclude that the balance between buoyant and mixing energy is fundamental to understanding this front. While this calculation demonstrates the plausibility of the tidal mixing versus buoyancy balance, it does not address the nature of the transition between the two domains of vertical structure.

3. Frontogenesis

Looking for all the causes of frontogenesis, we note that the frontal position follows the 50 m isobath (Figures 1 and 9), that the frontal width is about 10 km and correlates with the bottom slope, that the shelf current regime is tidally dominated, and that a balance of buoyant energy input with tidal mixing power explains the two distinct domains. The narrowness of the transition between domains (i.e., frontal character) suggests a strong gradient in the forcing.

There is no reason, however, (including direct current measurements) to suspect a strong gradient in tidal mixing power, nor a strong gradient in buoyancy input (not along the 50 m isobath, up to 100 km from shore). Gradients of wind stress have helped explain the broad transition zones of the Pacific Ocean (Roden, 1977), but they can only be of secondary importance here. First, away from the mountainous coast, gradients of wind stress are unlikely to vary sharply, nor are convergences likely to fortuitously align with the 50 m isobath. During winter, strong gradients of wind stress appear plausible. Satellite imagery, however, reveals that the ice "edge" often is a transition zone up to 100 km wide, much broader than the frontal width; nor does the ice edge follow the 50 m isobath. The meteorologically forced component of flow (i.e., low frequency: 35 hour low-pass filtered current records) is typically weak (1 to 2 cm/s) and oscillatory (4 to 5 day period), so that it is not important. Finally, a convergence of quasi-geostrophic flow in the bottom frictional layer (Fearnhead, 1975) might sharpen the transition between domains, but in the spring, when frontogenesis occurs, the baroclinic gradient necessary to drive the cross-frontal convergence is virtually zero. Indeed, because of the reversal of the cross-shelf salinity gradient (i.e., higher salinities in the coastal domain) and the cold temperatures, the baroclinic gradient across the front changes sign in spring as the coastal domain warms and becomes fresher. Thus, the obvious forcing functions are unlikely to show strong gradients over a 10 km transition, and do not explain frontogenesis.

Instead, we hypothesize that frontogenesis depends on the positive feedback inherent in establishing stratification. James (1977) used current meter and hydrographic data to model the evolution of thermal stratification in the Celtic Sea. Importantly, James' model incorporates a vertical mixing

coefficient that depends on stratification (contained within a Richardson number), so that stratification retards mixing. Applying this model to widely spaced stations (coincident with current data), he successfully predicted both two-layered and well-mixed domains, but course resolution prevented elucidation of the transition between them. Similarly, Garwood (1977) modeled the establishment of the seasonal thermocline in the open ocean, and predicted that formation occurs in a single diurnal cycle. It is likely that if James' model had finer horizontal and temporal resolution (he reported about 50 km and 28 days) a stratified domain would form suddenly as in Garwood's model, and that the separation between domains would be small. Because stratification and mixing are linked (in the models, through variable vertical mixing coefficients) stratification begets stratification and well mixed waters persist. This positive feedback permits large changes in vertical structures over a few kilometers without correspondingly large changes in forcing functions.

While James stopped just short of expounding on the importance of this feedback in frontogenesis and demonstrating it, one dimensional models are inherently unable to describe frontogenesis completely. As the two separate stratification domains form close together, large gradients of salinity, temperature, and density form, so that horizontal balances must become significant. Our data clearly show that most of the variation is in the vertical and cross-frontal direction, so that a two dimensional model probably could incorporate all the obvious features of the front.

While positive feedback between mixing and stratification may be the primary cause of frontogenesis, many features require elaboration. Frictional convergence may contribute importantly to maintaining the front, and there

may be subtle differences between fronts because of this. Although gradients of forcing functions do not explain frontogenesis, we find a strong correlation between frontal width and bottom slope (i.e., gradient of V^3/H); apparently bottom slope is an important secondary factor in frontal structure.

4. Comparison to Fronts Around the British Isles

Fronts similar to that described above have been reported around the British Isles. These fronts have similar energy balances between buoyant and mixing energies (Simpson and Hunter, 1974, Fearnhead, 1975). In addition to the marked similarities between the Bering Sea and British Isles fronts, there are interesting differences.

Recognizing the basic energy balance that determines frontal location, it is possible to empirically predict the front's position. If the buoyant energy input is constant over a region, then variation of mixing energy alone will indicate the front's position. A simple estimate of this variation is the tidal power density $(\frac{V^3}{H})$. Using typical (MKS) values for the Bering Sea, and defining $k = -\log_{10}(\frac{V^3}{H})$, then $k = \log_{10}(\frac{0.25^3}{50}) \sim 3.5$. Using a similar parameter, typical values of 2 to 3 were calculated around Britain: 1.7 to 2.0 (Simpson and Hunter, 1974), 1.5 to 2.0 (Simpson, 1976), 2.5 to 3.0 (James, 1977), and 2.0 to 2.5 (Fearnhead, 1974).

The difference has two causes, one a matter of definition, and one a matter of importance. We use measured values of V^3 , but most of the British values are based on tidal atlases, and they use current amplitude to define k for basically rectilinear flow (e.g. Fearnhead, 1975; Simpson and Hunter, 1974). This causes a discrepancy of $4/3\pi$ in V^3 , or 0.4 in k . More fundamentally, using k assumes a constant buoyancy input. The Bering Sea and Britain are at

similar latitudes and receive similar insolation, but the buoyancy inputs from this source vary. Input of buoyant energy varies as ρ' , which is a function of the thermal expansion coefficient,

$$\beta = \frac{1}{\rho} \frac{\partial \rho}{\partial T}$$

This coefficient depends strongly on temperature and also on salinity (Table 3), so we see that in the spring β varies by a factor of 4.6 ($\log_{10} 4.6 = 0.7$) between the two regions. Melting, a buoyancy source not available around the British Isles, only partly compensates for the smaller thermal buoyancy source in the Bering Sea. Thus, in terms of k , the discrepancy disappears: similar values of k obtain in the Bering Sea, when adjusted for definitions of V^3 and for different values of β .

Throughout most of the Bering Sea, k is redundant: H (=50 m) predicts the front as well as k does, but this does not hold where V varies much from 0.25 m/s (e.g. near the Pribilof Islands). More importantly, there is no fundamental difference between the Bering Sea front and those around Britain. In detail, however, there are important differences: melting ice and river runoff affect the Bering Sea fronts, while heating is of secondary importance. The dynamical mechanisms may be the same in both regions, but in the generally colder waters of the Bering Sea the salinity distribution dictates the hydrographic structure.

Bering Sea hydrographic data indicate a baroclinic velocity difference across the front of less than 2 cm/s, agreeing with the low mean speeds registered by current meters spanning the front (Figure 1). A speed of 11.4 cm/s parallel to a front in the British Isles and a baroclinic calculation of 30 cm/s across that front were reported by Simpson (1976). Fearnhead (1975) speculated that a frictional convergence of this (quasi-) geostrophic velocity is critical for frontogenesis. The Bering Sea Front has widths and thermal gradients similar

Table 3. Thermal expansion coefficients

(Sverdrup et. al., 1942) ($^{\circ}\text{T}^{-1} \times 10^{-6}$)

Temperature ($^{\circ}\text{C}$)	-2	0	5	10	15	20
Salinity (g/kg)						
30	7	36	101	157	206	250
35	23	51	114	167	214	257

Bering Sea in spring: $T = 0^{\circ}\text{C}$, $S = 30 \text{ g/kg}$, $\beta = 36$

British Isles in spring: $T = 10^{\circ}$ $S = 35 \text{ g/kg}$, $\beta = 167$

to the fronts around the British Isles, but our calculated velocity difference is lower in part because of smaller density differences (β is smaller, Table 3) and in part because of the depth of water is less (~ 50 m vice ~ 100 m). Frictional convergence may not be critical to frontogenesis, but it may be significant to frontal maintenance, and 2 cm/s is the same magnitude as measured mean currents over the shelf.

Finally, the distribution of buoyant energy input in the Bering Sea is more complex than for the British Isles. Ice cover retards this input until late in spring, and then suddenly adds fresh water simultaneously with allowing the sun to warm the water. The initial stratification, which is necessary for frontogenesis, comes from melting, rather than insolation. Later in summer, large quantities of freshwater empty into the coastal domain. This critical role of ice, and the late addition river runoff probably modify the Bering Sea front, but the general picture remains similar to that found near the British Isles.

5. Summary and Conclusions

Hydrographic data collected during the ice-free seasons from 1975-1977 describe a structural front separating a well-mixed coastal domain from a two-layered central shelf domain over the southeastern Bering Sea shelf. The front separates different vertical hydrographic structures, and not water masses; it is located where the input of buoyant energy balances the tidally generated mixing energy. Satellite imagery and hydrographic data show that in general the front coincides with the 50 m isobath, and XBT data indicate that a typical frontal width is about 10 km.

We hypothesize that this narrowness in the transition between structural domains results from the feedback between mixing and stratification as suggested by James' (1977) one-dimensional model. Substantial understanding of frontogenesis

awaits modeling in two dimensions which may incorporate secondary affects such as the observed correlation between frontal width and bottom slope.

Comparisons with fronts around the British Isles demonstrates their similarity to the Bering Sea front, but in the Bering Sea salinity distribution, freezing and melting influence the frontal processes significantly.

REFERENCES

- Coachman, L.K. and R.L. Charnell, 1977: Finestructure in outer Bristol Bay, Alaska. Deep-Sea Res. 24 (10): 869-889.
- Dodimead, A.J., F. Favorite and T. Hirano, 1963: Salmon of the North Pacific Ocean, Part II: Review of oceanography of the subarctic Pacific Region, 1960-71, Bulletin 33, International North Pacific Fisheries Commission, Vancouver. 187 pp.
- Fearnhead, P.G., 1975: On the formation of fronts by tidal mixing around the British Isles. Deep-Sea Res. 22 (5): 311-322.
- Garwood, R.W., 1977. The spring retreat of the ocean surface boundary layer. EOS, 58 (12): 1156.
- Hansen, D.V., 1977: Outer continental environmental assessment program annual report, Lagrangian Surface Current Observations. 19 pp. Unpublished report, available from the authors.
- James, I.D., 1977: A model of the annual cycle of temperature in a frontal region of the Celtic Sea. Estuarine and Coastal Marine Science 5: 339-353.
- Kinder, T.H., 1977: The hydrographic structure over the continental shelf near Bristol Bay, Alaska, June 1976. University of Washington, Department of Oceanography Technical Report, Ref: M77-3, 61 pp.
- Kinder, T.H. and L.K. Coachman, 1978: The front overlaying the continental slope of the Eastern Bering Sea, submitted to J. Geophys. Res.
- Kinder, T.H., J.D. Schumacher, R. Tripp and J. Haslett, 1978: The evolution of the hydrographic structure over the continental shelf near Bristol Bay, Alaska. University of Washington, Department of Oceanography Technical Report.

- Muench, R.D., 1976: A note on the Eastern Bering Sea hydrographic structure. Deep-Sea Res. 23: 245-247.
- Muench, R.D. and K. Alnäs, 1976: Ice movement and distribution in the Bering Sea from March to July, 1974. J. Geophys. Res. 81(24): 4467-4476.
- Pingree, R.D., G.R. Foster and G.K. Morrison, 1974: Turbulent convergent tidal fronts. J. of the Mar. Biological Association of the UK. 54:469-479.
- Reed, R.K., 1978: Heat budget in the Eastern Bering Sea. Submitted to J. Geophys. Res.
- Roden, G.I., 1977: Oceanic subarctic fronts of the Central Pacific: structure of and response to atmospheric forcing. J. Phys. Oceanogr. 7(6): 761-778.
- Schumacher, J.D., R.C. Charnell and L.K. Coachman, 1977: Outer Continental Shelf Environmental Assessment Program Second Annual Report, Bristol Bay Oceanographic Process. 64 pp. Unpublished report, available from the author.
- Simpson, J.H., 1971: Density stratification and microstructure in the western Irish Sea. Deep-Sea Res. 18 309-319.
- Simpson, J.H., 1976: A boundary front in the summer regime of the Celtic Sea, Estuarine and Coastal Marine Science 4: 71-81.
- Simpson, J.H. and J.R. Hunter, 1974: Fronts in the Irish Sea. Nature, London 250: 404-406.
- Sverdrup, H.U., M.W. Johnson and R.H. Fleming, 1942: The oceans. Prentice-Hall, Inc., 1087 pp.
- Uda, M., 1954: Water mass boundaries - "Siome." Frontal theory in oceanography. Fish. Res. Bd. Canada manuscript report series, No. 51, Seminar 2, pp. 10-20.

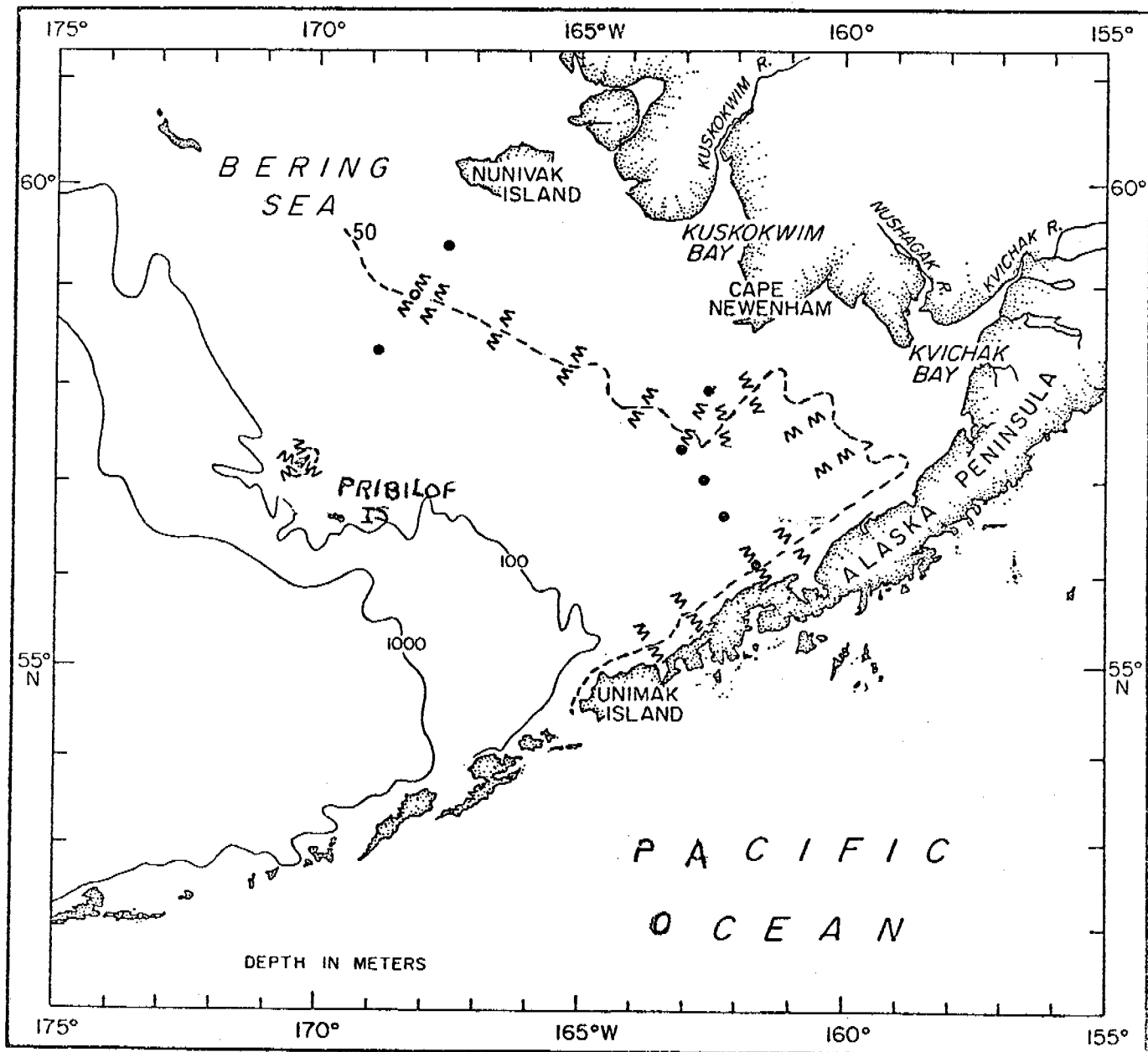
List of Illustrations

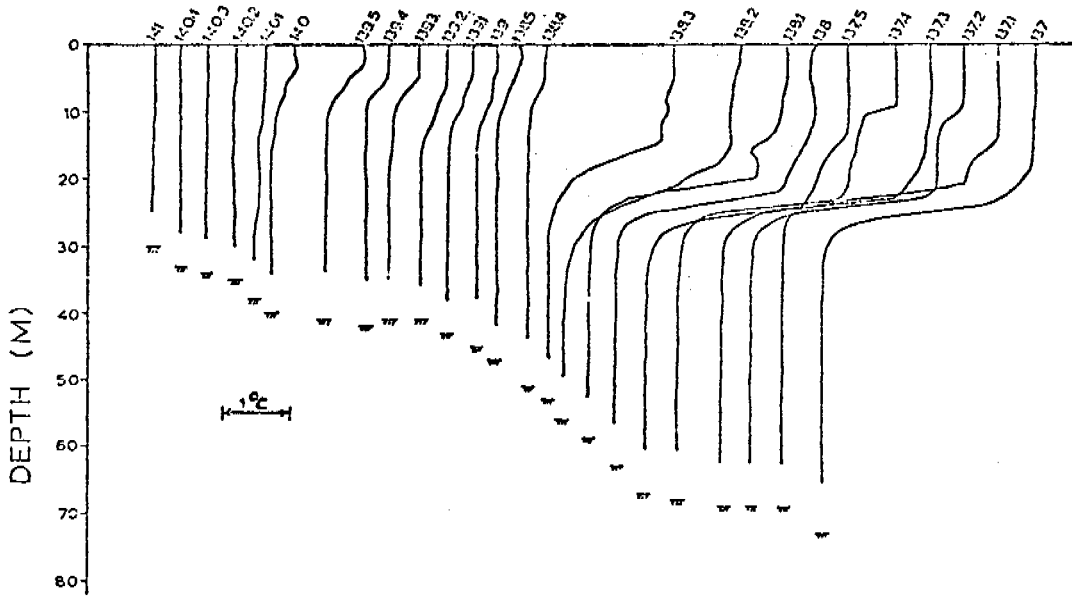
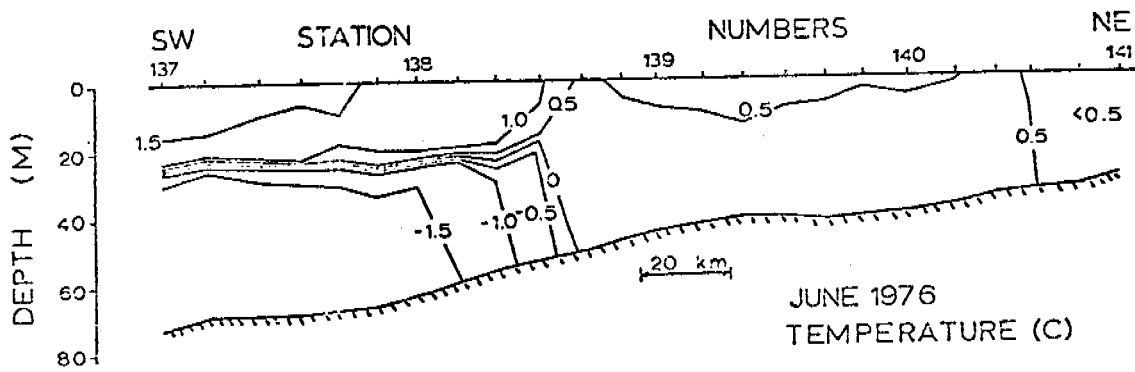
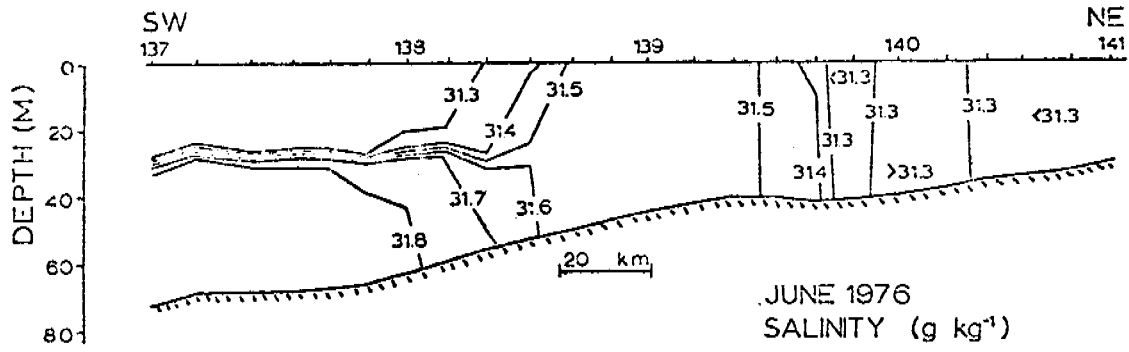
- Figure 1. General study area in the southeast Bering Sea. Shown are the 18 locations where the front (\mathcal{M}) was observed 28 times. Also shown are the sites (\odot) of moored current meters.
- Figure 2. Typical central shelf and coast domain hydrographic features during spring. The rapid transition from homogeneous to stratified water structure is shown by temperature profiles (See Figure 5 for station locations).
- Figure 3. Typical central shelf and coastal domain hydrographic features during fall (see Figure 5 for station locations).
- Figure 4. Variation across the front of the mean horizontal average temperature and mean horizontal average salinity gradients with season. Error bars indicate one standard deviation.
- Figure 5. (a) Locations of XBT and CTD lines for 1977, (b) temperature (solid line) and salinity (dashed line) section for Line 1 and (c) XBT section for Line 1 on the same scale as (b).
- Figure 6. XBT sections (0.5°C contour interval) from data collected along Lines 2 to 5, Spring 1977. Temperature values in parenthesis are from CTD data. Tick marks are given every 0.5°C unless otherwise noted.
- Figure 7. XBT sections (1.0°C contour interval) from data collected along Lines 6 and 7, summer 1977. Temperature values in parenthesis are from CTD data. Tick marks are given every 1.0°C unless otherwise noted.
- Figure 8. (a) An example of the use of variations in the horizontal gradient of thermal stratification (T') to determine a frontal width. (b) The correlation between frontal width and bottom slope.

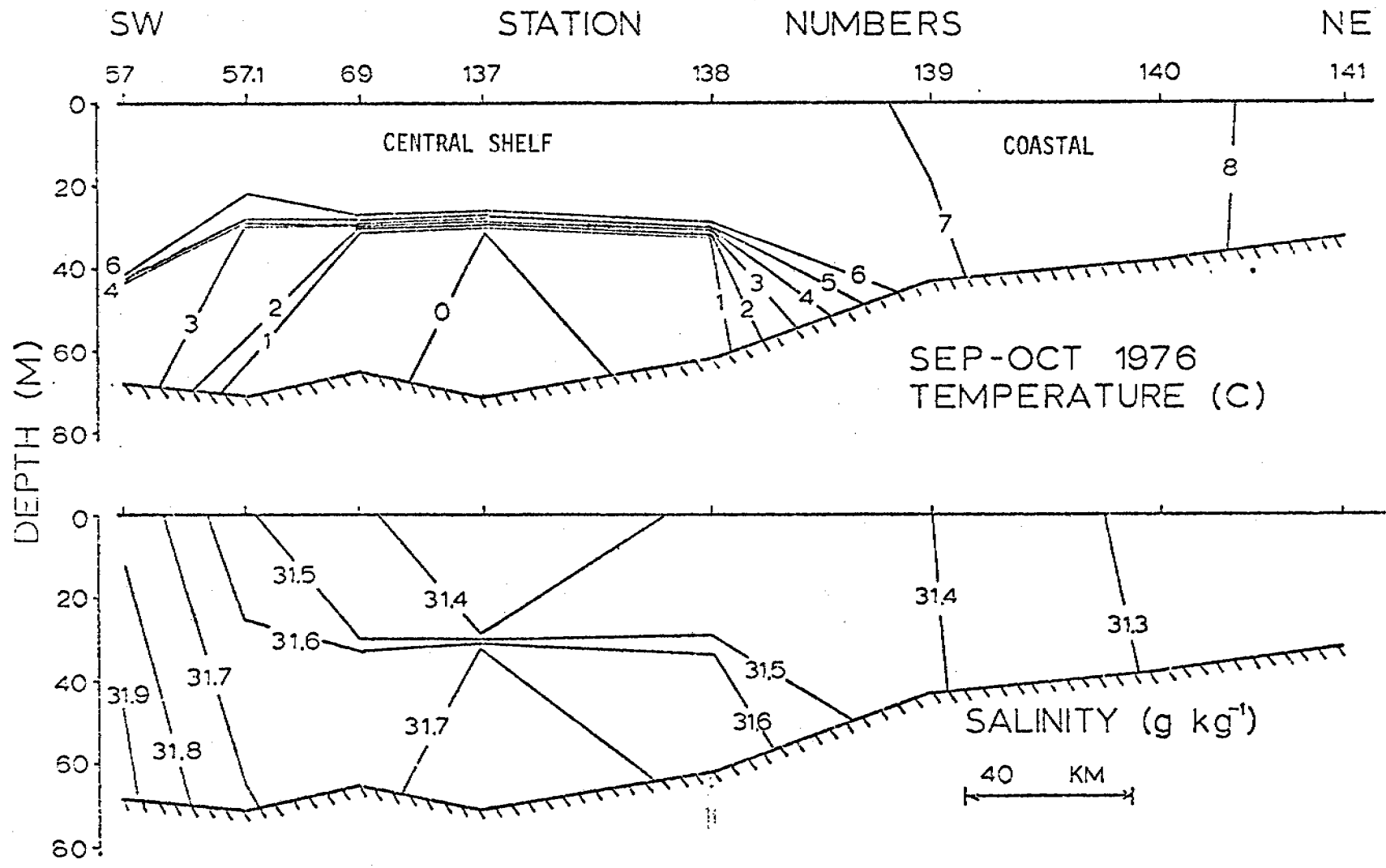
Figure 9. Satellite infrared image of the southeastern Bering Sea: 1 August 1977. We note the rapid transition from warmer (darker) surface waters of the central shelf domain to cooler (lighter) coastal domain waters. This surface manifestation of the front is in the Kuskokwim Bay and St. Paul Island regions. The spur between St. Paul and the Alaska Peninsula is caused by cloud cover which also obscures waters along the Peninsula.

Acknowledgments

We wish to acknowledge the large number of contributors who supported this program. In particular, we thank the officers and crews of the research vessels Moana Wave, Miller Freeman, Discoverer, Acona, and Surveyor. We greatly appreciate the support rendered by the staff at both institutions, specifically, but not limited to R.B. Tripp, J.C. Haslett. K. Ahlén¹¹ provided satellite photographs. We also wish to thank L.K. Coachman and G.I. Roden for critically reading our manuscript and providing useful suggestions. This project was supported in part by Outer Continental Shelf Environmental Assessment Program of the National Oceanic and Atmospheric Administration, which administers oil exploration hazard research in Alaska for the U.S. Bureau of Land Management.

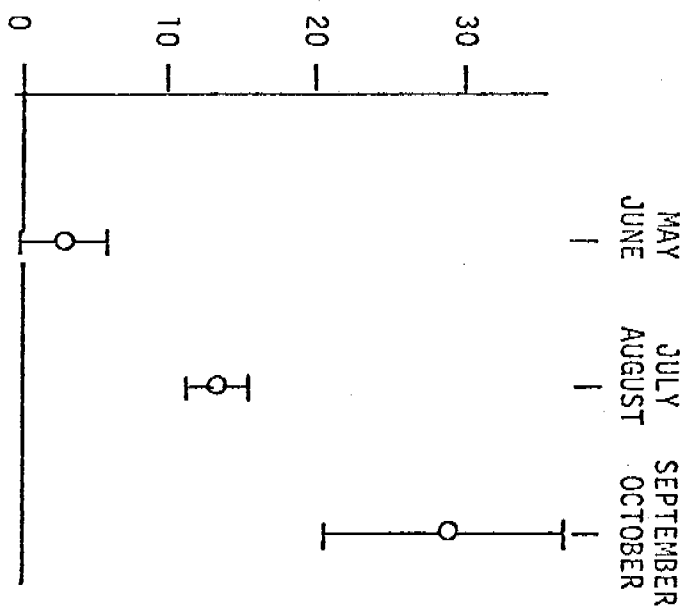




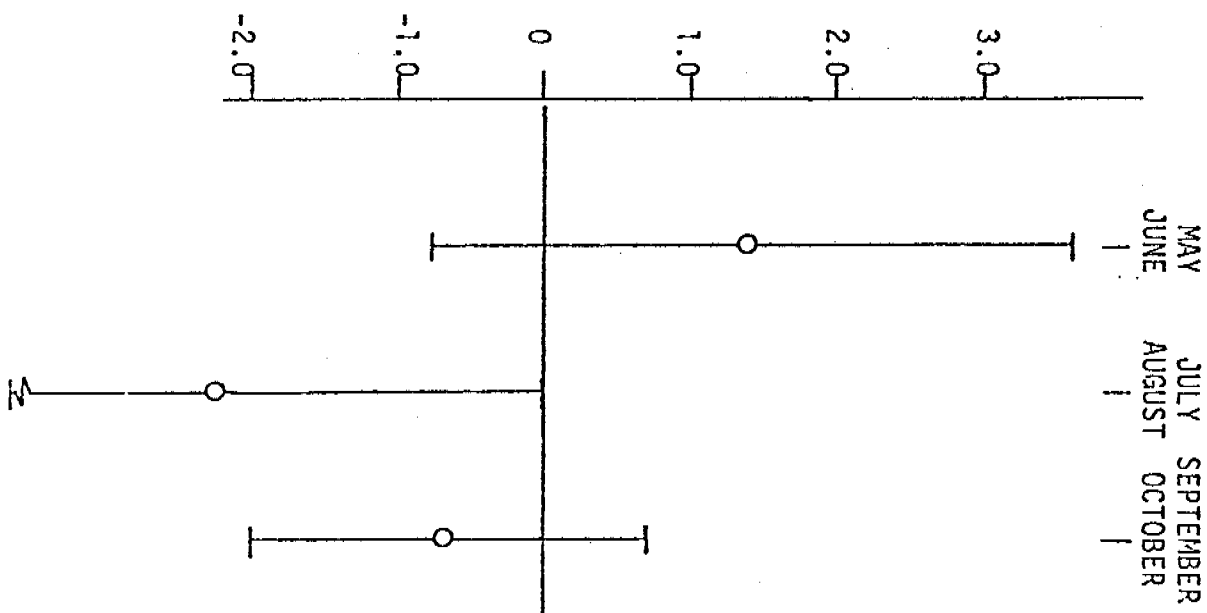


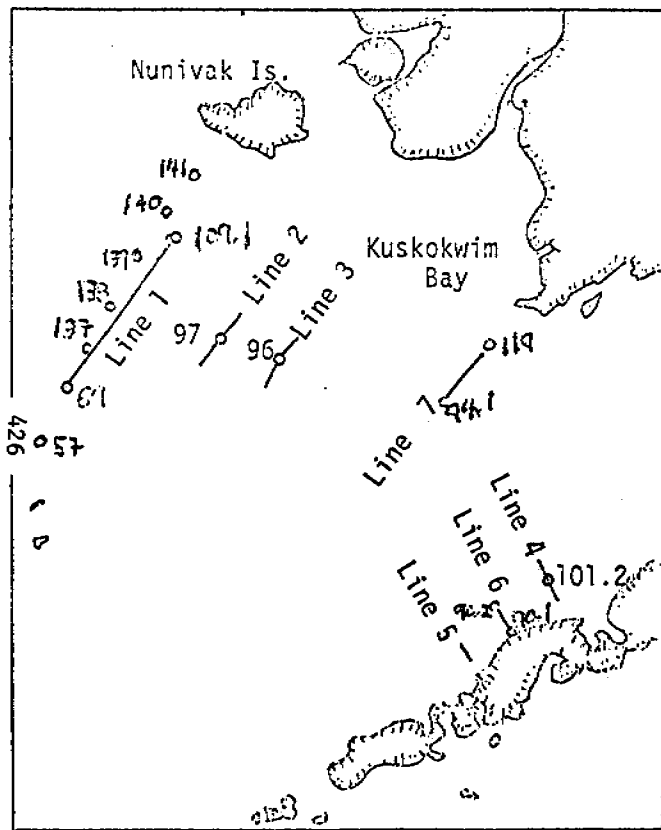
424

MEAN HORIZONTAL AVERAGE TEMPERATURE

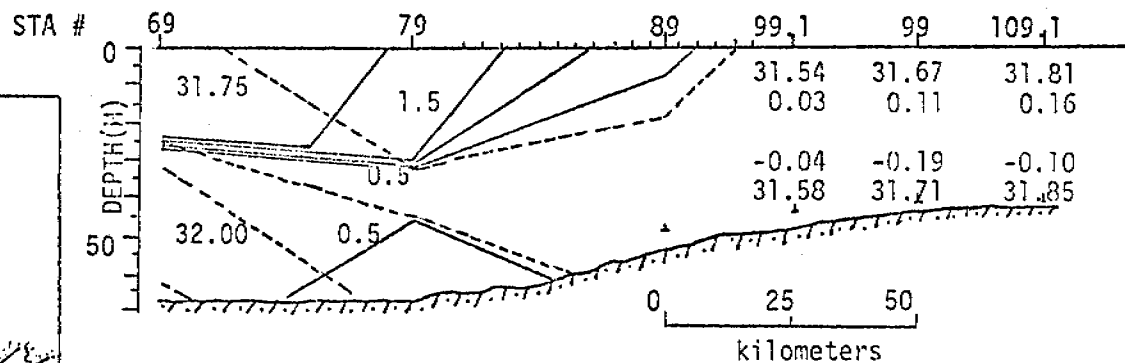
GRADIENT: $10^{-3} \text{ }^{\circ}\text{C km}^{-1}$ 

MEAN HORIZONTAL AVERAGE SALINITY

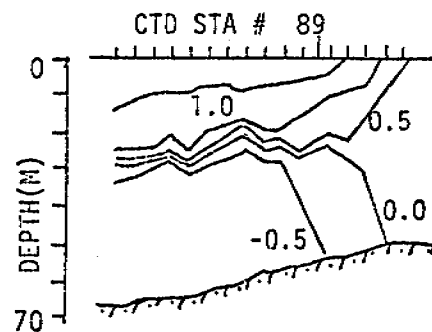
GRADIENT: $10^{-3} \text{ g kg}^{-1} \text{ km}^{-1}$ 



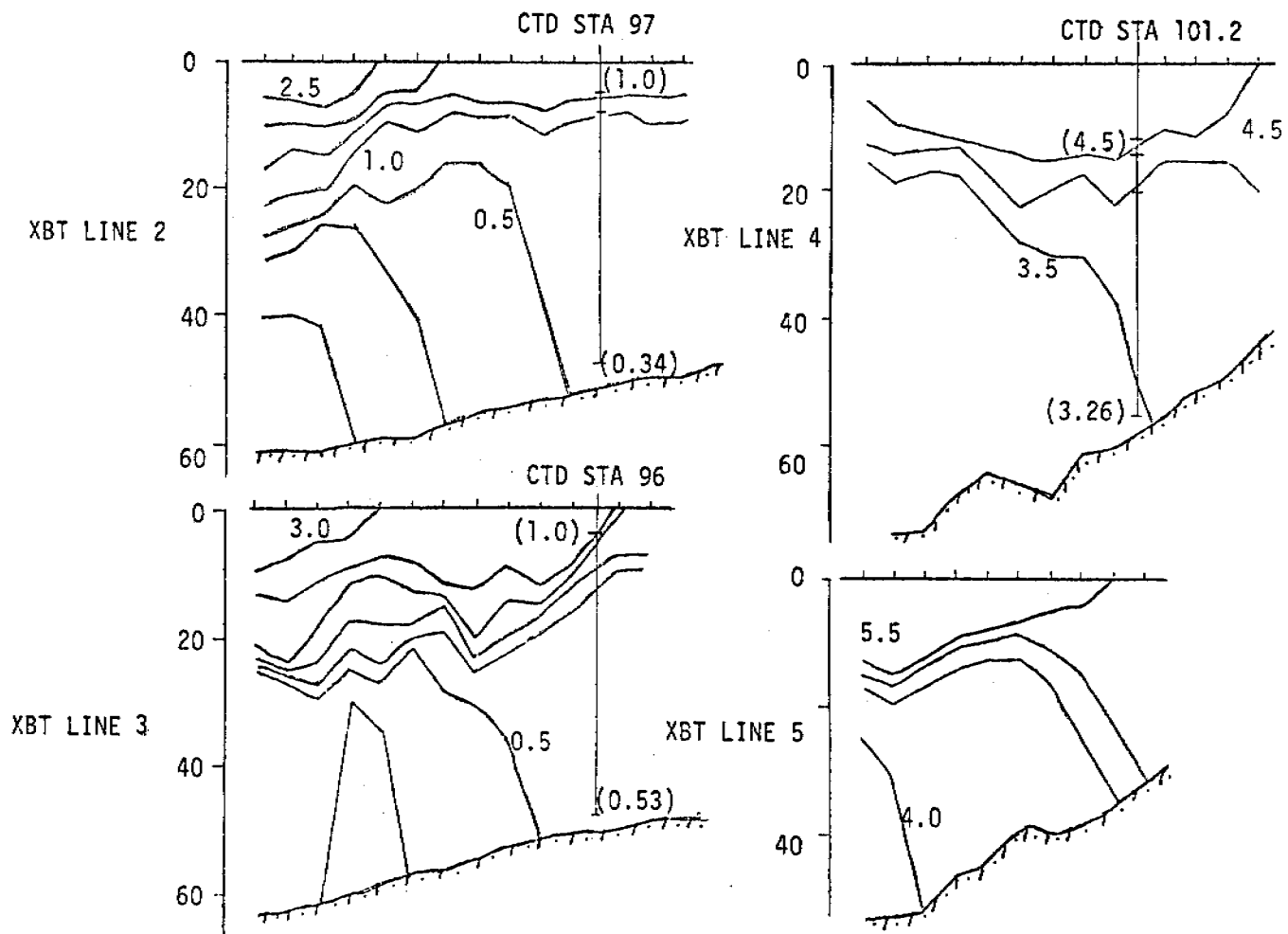
(a) Station locations

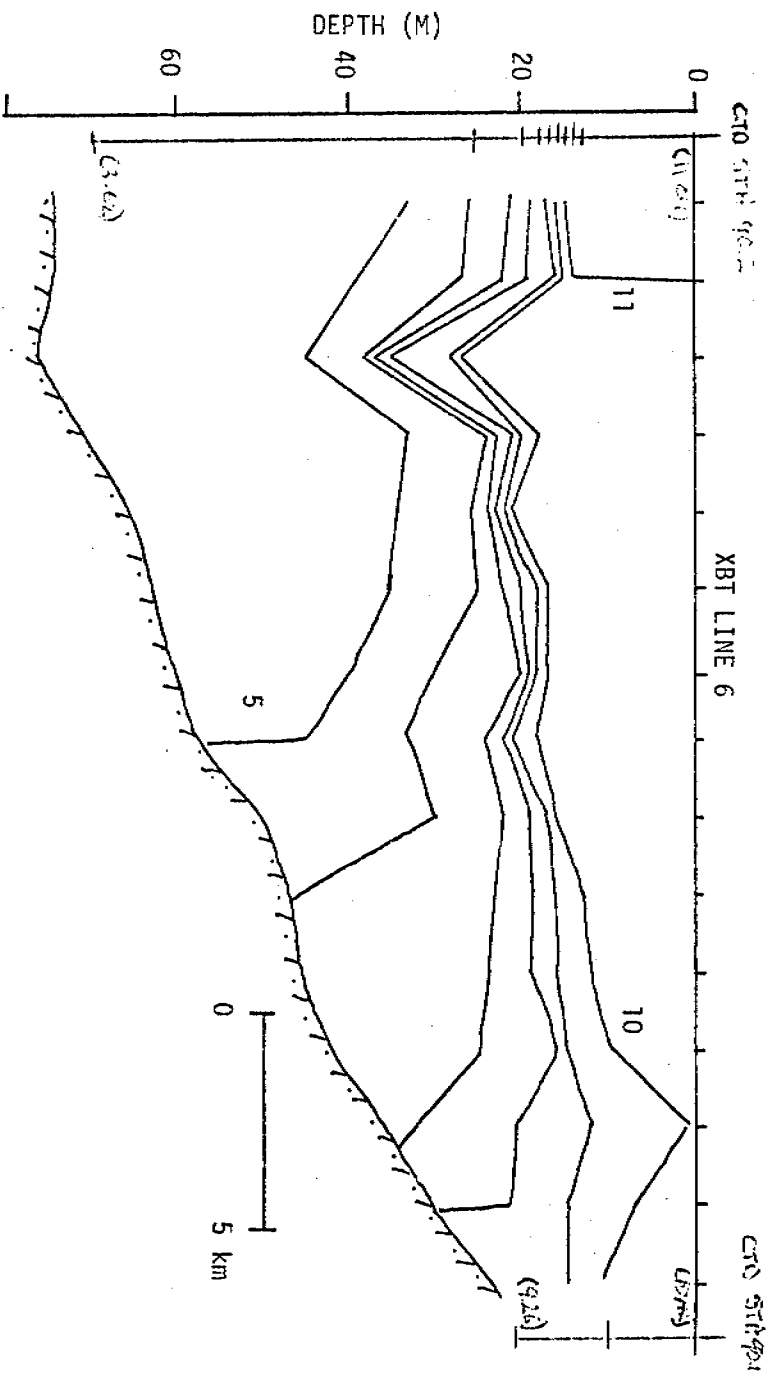
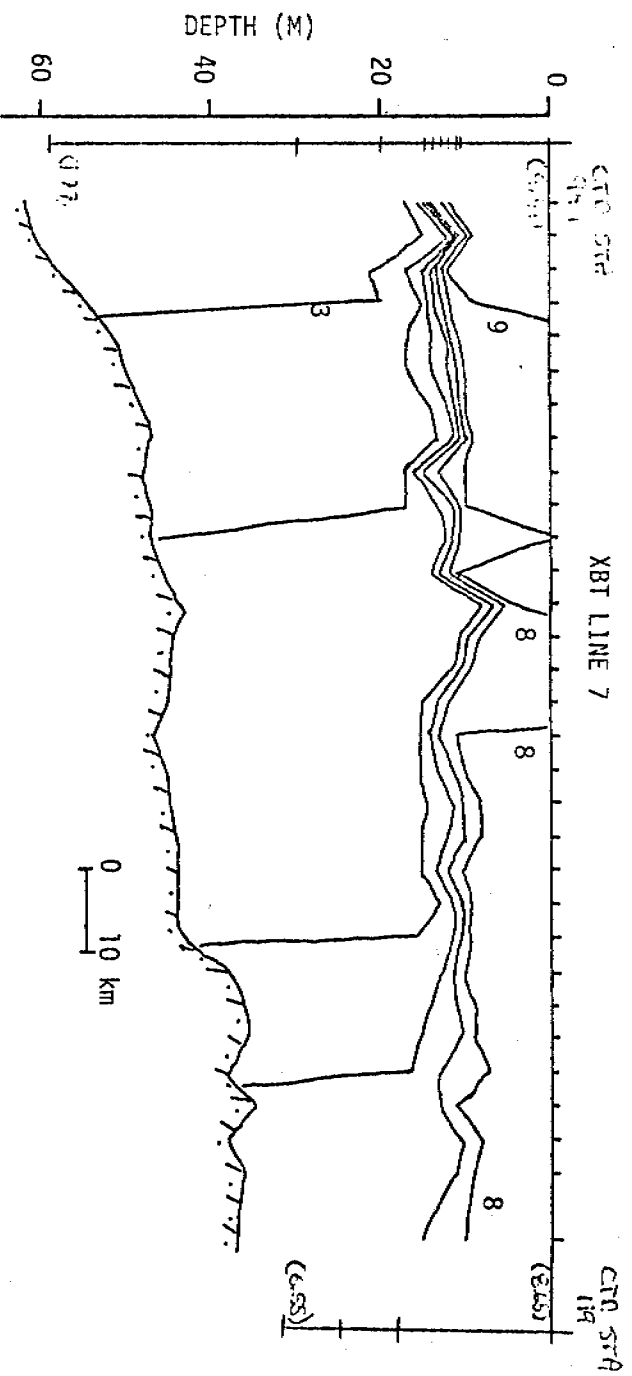


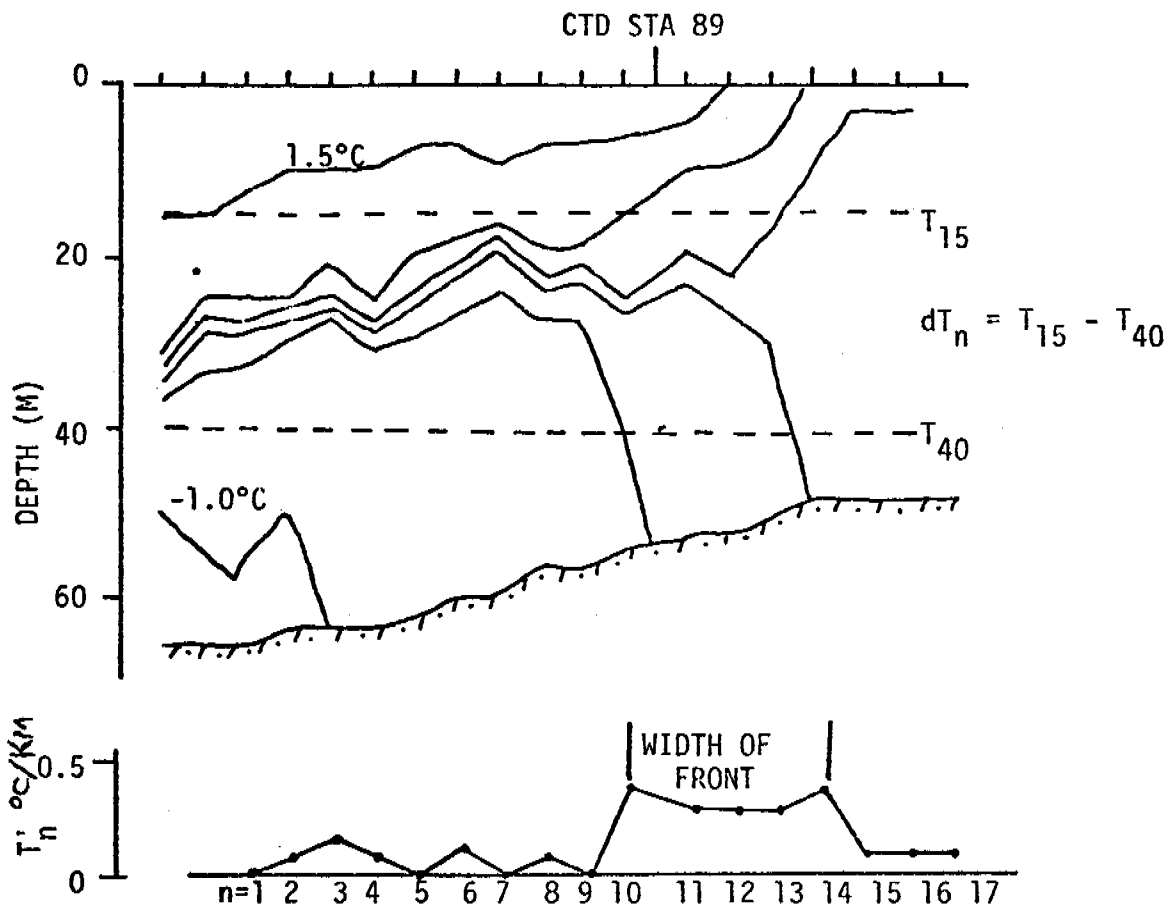
(b) Temperature (0.5°C interval) and salinity (0.25 g/kg) section for Line #1 from CTD data. Surface and bottom values are given for STA #99.1 to STA #109.1.



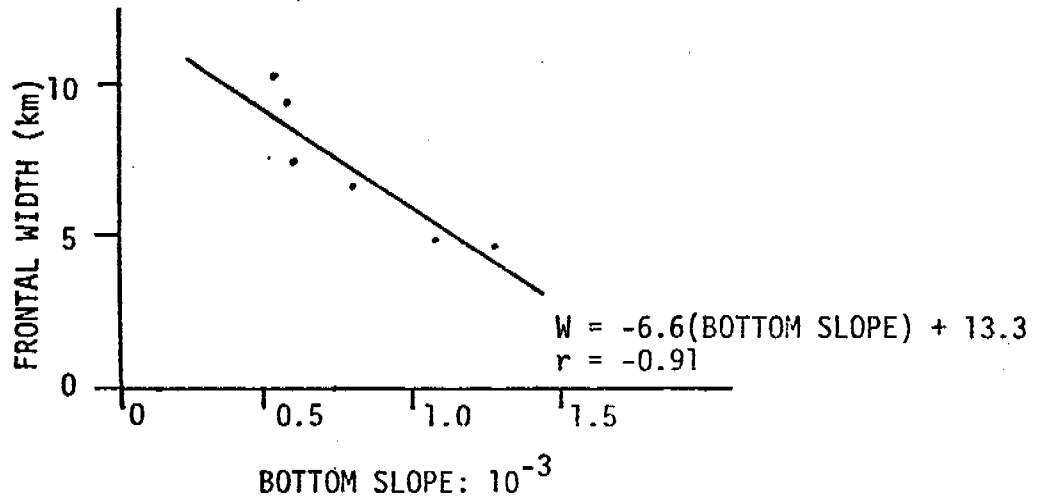
(c) Temperature section (0.5°C contour interval) for Line 1 from XBT data. This section is on the same scale as above. The XBT stations were 1.8 km apart.







(a) XBT station (tick marks) separation: $dx = 1.8$ km. Contour interval is 0.5°C .



C. Structural Fronts in the Bering Sea

In addition to the structural front that parallels the 50 m isobath in the Bristol Bay area, we've seen two additional locations with similar structure. Satellite imagery and hydrographic data from summer 1977 show that an extension of the front observed in Bristol Bay continues north of Nunivak Island, apparently to near Saint Lawrence Island. Additionally, a similar front exists near the Pribilof Islands, most clearly near Saint Paul Island.

Preliminary analysis of data obtained during August 1977 indicates that the front near Saint Paul has the same character as the others, i.e., a narrow transition separates well-mixed coastal water from strongly-stratified shelf water (Figure 1). One difference between the Pribilof front, and the 50 m front (discussed in B, above) is that the topography limits the extent of the well-mixed coastal water near Saint Paul Island, so that it is similar to that of the front itself.

Because of the extensive data compiled on birds around the Pribilofs (with some concurrently gathered physical data), we are attempting to correlate our understanding of the physical regime to the distribution of birds. One step in this process, relating the vertical hydrographic structure to the surface temperature (which is available during bird observation), appears fruitful. Figure 2 shows the correlation of density stratification (i.e., bottom minus surface density) on surface temperature. Our initial impression is that the distribution of birds can be related to the physical oceanography, and we intend to pursue this possibility.

Also, we want to understand the frontogenesis and dynamical balance of structural fronts. To this end, we are exploring possibilities of modeling with Jim Overland, PMEL.

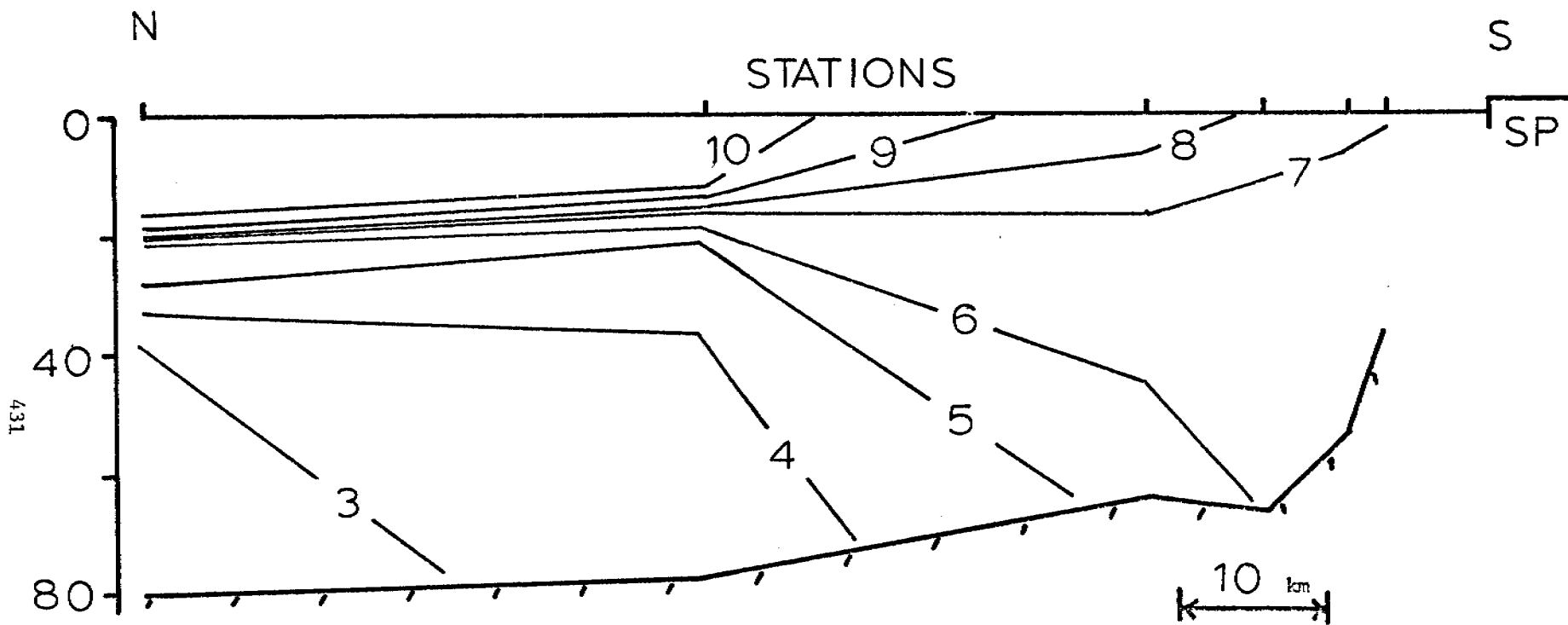


Figure 1. North to south temperature cross section near Saint Paul Island, August 1977. Temperature is in degrees C, depth in m, and distance in km.

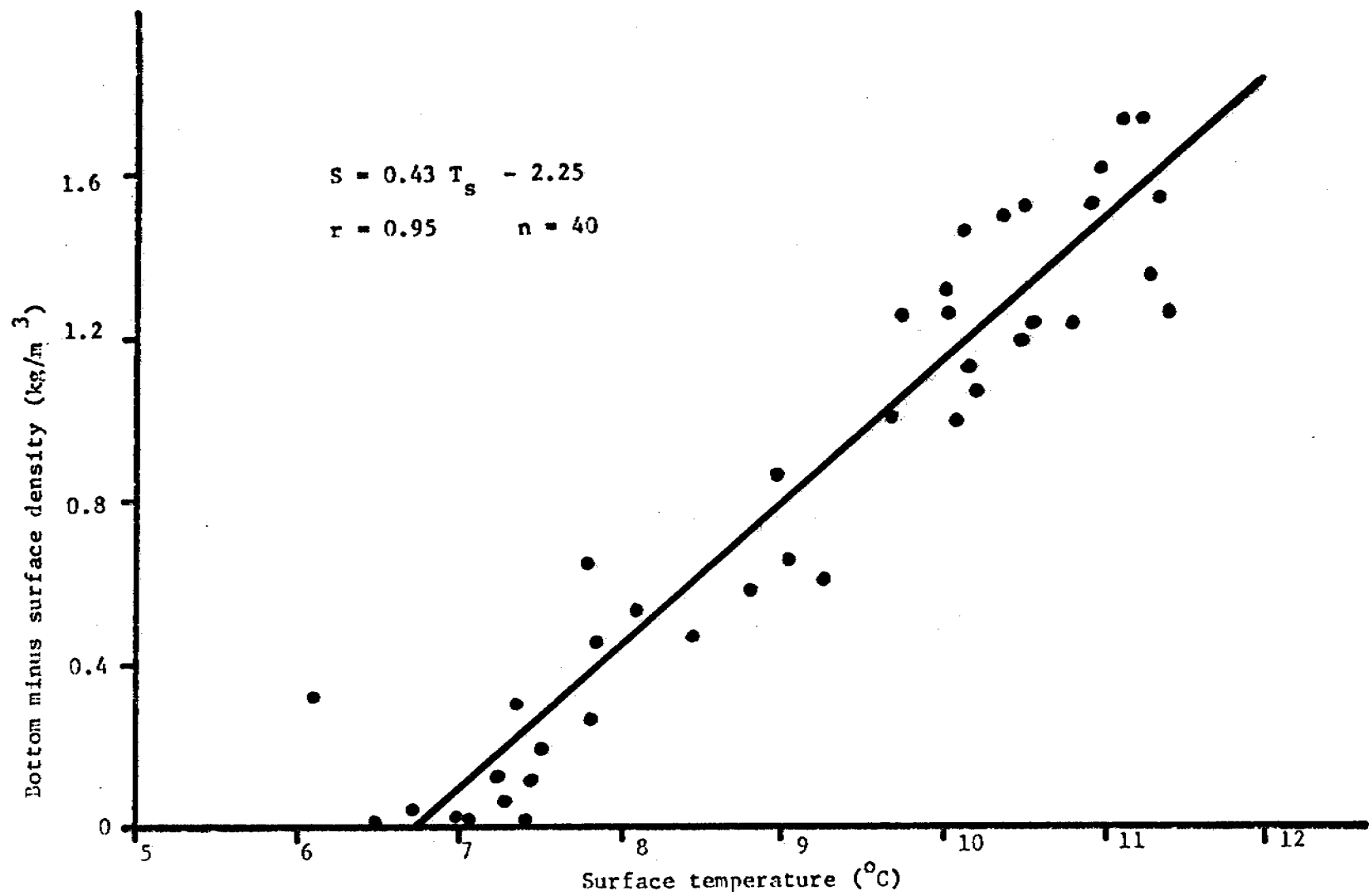


Figure 2. Correlation of density stratification on surface temperature.

- D. The Evolution of the Hydrographic Structure over the Continental Shelf near Bristol Bay, Alaska, during Summer 1976, by Thomas H. Kinder, James D. Schumacher, Richard B. Tripp, and James C. Haslett

Table of Contents

	<u>Page</u>
Acknowledgement	i
List of Figures	ii
I. Introduction	1
Objectives	1
Cruises and Data	1
Setting	2
II. Distributions - September and October 1976	3
Horizontal Distributions	3
Vertically Averaged Properties	5
Vertical Profiles	6
Temperature-Salinity Correlations	7
Cross Sections	9
Stratification	9
Frontal Section	11
Geopotential	11
III. Seasonal Changes - Summer 1976	11
Temperature	12
Salinity	12
Heat	13
Stratification	13
IV. Discussion	14
Mixing	14
Water Categories	18
Seasonal Evolution	18
Questions	22
References	23

Acknowledgement

We would like to thank the officers and crew of R/V Acona, J. Johnson commanding, and R/V Moana Wave, W. Willis commanding, for their fine work during the cruises. L. K. Coachman, J. Severn, L. Veneroso, R. Sillcox, K. Uhlinger, and W. Parker participated in the field work, and Scott Rauum supervised the data processing. Ron Reed reviewed this draft and made helpful suggestions. Diane Thors prepared the manuscript. This report is a contribution of the Bristol Bay Oceanographic Processes (B-BOP), a cooperative study between the University of Washington and the Pacific Marine Environmental Laboratory (PMEL), Environmental Research Laboratories (ERL), National Oceanic and Atmospheric Administration (NOAA). B-BOP is one component of the Outer Continental Shelf Environmental Assessment Program (OCSEAP), funded by the Bureau of Land Management and managed by NOAA.

List of Figures

1. The Bering Sea
2. The Bristol Bay Study Area
3. Track of R/V Acona
4. Track of R/V Moana Wave
5. Temperature at the surface
6. Temperature at 50 m
7. Temperature at the bottom
8. Salinity at the surface
9. Salinity at the bottom
10. Density at the surface
11. Density at the bottom
12. Mean temperature
13. Mean salinity
14. Mean density
15. Correlation of mean temperature and salinity
16. Vertical profiles, station 111
17. Temperature profiles
18. Salinity profiles
19. Finestructure profiles
20. Temperature minimum profiles
21. Distribution of finestructure
22. Profiles without bottom mixed layers
23. Temperature-salinity correlation
24. Temperature cross section into Bristol Bay
25. Salinity cross section into Bristol Bay

26. Density cross section into Bristol Bay
27. Cross sections along 100 m isobath
28. Cross sections along 85 m isobath
29. Cross sections along 75 m isobath
30. Cross section across inner Bristol Bay
31. Maximum vertical temperature difference
32. Maximum vertical salinity difference
33. Maximum vertical density difference
34. Correlation of temperature and salinity differences
35. Correlation of temperature difference and depth
36. Correlation of salinity difference and depth
37. Correlation of density difference and depth
38. Sections across the front
39. Geopotential (0/50)
40. Geopotential (0/100)
41. Change of mean temperature
42. Change of mean salinity
43. Change in heat per unit area
44. Change in heat per unit volume
45. Change in thermal stratification
46. Change in haline stratification
47. Schematic of box diffusion models
48. Approximate boundaries of water domains

I. Introduction

We present distributions of temperature, salinity, and density for the waters of Bristol Bay and the adjoining continental shelf in the southeastern Bering Sea (Figures 1 and 2) during late September and early October, 1976. This report complements a similar one for June 1976 (Kinder, 1977), and together they show the seasonal change in the hydrographic structure during summer 1976. Our purpose is to show the general features of the hydrographic structure, and to infer its seasonal evolution. Because of the combination of broad areal coverage, seasonal synopticity, close station spacing, and good vertical resolution of our data, we are able to add considerable detail to earlier reports (e.g., Dodimead et al., 1963; Ohtani, 1973; Favorite et al., 1976).

Objectives

The principal objectives of the physical oceanographic phase of the Outer Continental Shelf Environmental Assessment Program (OCSEAP) in the southeastern Bering Sea (B-BOP: Bristol Bay Oceanographic Processes) are to elucidate the circulation and the hydrographic structure, and their temporal and spatial variability with application to the impact of petroleum development. Here we display the early autumn distributions, and focus on the changes since the time of ice breakup in early summer.

Cruises and Data

R/V Acona and R/V Moana Wave occupied stations during 21 September to 2 October 1976. R/V Acona began with station 35 on 27 September and finished with station 90 on 2 October (Figure 3). R/V Moana Wave began with station 15 on 21 September and finished with station 25 on 30 September (Figure 4).

R/V Acona used a Bisset-Berman (now Plessey) Model 9040 STD (salinity-temperature-depth profiling system), and R/V Moana Wave used a Plessey Model 9040 CTD (conductivity-temperature-depth profiling system). Temperature and salinity samples, taken on about one-half of the casts, indicate that the data are accurate to $\pm 0.02^{\circ}\text{C}$ and ± 0.02 g/kg.

The Pacific Marine Environmental Laboratory (PMEL) processed the data into one-meter averaged values. Large salinity inversions, usually associated with strong temperature gradients, were smoothed to remove static instabilities. Although there is reason to believe static instabilities on the scale of fine-structure actually occur in this region (Coachman and Charnell, 1977), we do not discuss these salinity structures further; instead we concentrate on large scale features.

Distortion of the various distributions by the ~ 20 cm/s tidal currents is slight. Although values at a point change significantly over a tidal cycle, the general spatial patterns survive. Station spacing usually is greater than 20 km, while the tidal excursion is 6 to 10 km (Schumacher and Coachman, 1976). Thus the broad areal distributions presented here are only affected slightly. Realizing that some tidal aliasing occurs, we present the data as simultaneous.

Setting

The survey encompassed an area much larger than Bristol Bay (Figures 1 and 2) because the shelf regime is an integral system: processes in Bristol Bay must be studied within the context of the entire shelf. This area receives freshwater runoff from the adjacent land exceeding an annual average of $1500 \text{ m}^3/\text{s}$ (Roden, 1967), mostly from the Kuskokwim and Kvichak rivers during May to October.

We think of the annual oceanographic cycle over this shelf as composed of four seasons: ice freezing (winter), ice melting (spring), heating (summer), and cooling (autumn). From historical data these seasons are defined: winter is from December to March, spring from April to May, summer from June to August, and autumn from September to November (Favorite et. al., 1976; Ingraham, 1973). The duration, strength, and phasing of these seasons profoundly affect the shelf waters. Specifically, during autumn and winter, negative buoyancy is added at the surface through cooling and brine rejection during freezing. In spring and summer, however, positive buoyancy is added by runoff, ice melting, and insolation. Additionally, the winds vary seasonally, with higher mean speeds and a greater incidence of storms in autumn and winter. We expect these seasonal changes to modulate the hydrographic structure over the shelf.

Our June measurements were made just at the beginning of summer, within two weeks of the ice breakup (Kinder, 1977). The September-October measurements reported here were made in early autumn, after the water column had begun cooling (Reed, 1978). Thus, we span the summer, and most of the change occurring in the water between the two surveys reflects the dominant summer processes of insolation and river runoff.

II. Distributions - September and October 1976

Horizontal Distributions

Surface temperatures (Figure 5) are generally warmer than June, averaging about 7°C; this is lower than the long-term annual maximum, which is about 8°C and occurs in August (Ingraham, 1973). In part, we attribute this difference from the long-term maximum to early autumnal cooling at the surface (Reed, 1978). The patch of cooler (<6°C) water in Bristol Bay probably corresponds to a persistent feature which Myers (1976) attributed to upwelling. The highest tempera-

tures ($>9^{\circ}\text{C}$) are found in the very shallow (<40 m) water south of Nunivak Island.

Major features of the 50 m (Figure 6) and the bottom (Figure 7) temperature distributions are similar. Figure 6 is included only for comparison with the June data (Kinder, 1977). There sometimes are strong vertical gradients of temperature and salinity at 50 m, so that the interpretations of plots at this depth are more complicated than for June 1976. Prominent in the bottom temperature distribution are the cold ($<0^{\circ}\text{C}$) tongue, the thermal front along the 50 m isobath, the thermal front along the 100 m isobath, and the warm ($>7^{\circ}\text{C}$) coastal water south of Nunivak Island and along much of the Alaska Peninsula. All these features are recognizable in the June bottom temperature, but here they are more prominent because the range of temperature has doubled.

Salinity distributions (Figures 8 and 9) display higher gradients near the shelf break, an intrusion of high salinity water along the Alaska Peninsula, a low salinity (<30.4 g/kg) lens of surface water in Bristol Bay, and a generally monotonic decrease in salinity from the shelf break toward the coast. Although the near-shore coverage is poorer than in June, there is no evidence for the near-shore high salinity anomalies found then, and we think that they do not remain intact through the summer.

Surface densities (Figure 10) are much lower in fall than they were in spring because of surface heating. The density generally decreases shoreward, with the largest density gradients between the 100 m isobath and the shelf break. Both the cold surface water (Figure 5) and lens of fresher water (Figure 8) are reflected in density southeast of Cape Newenham. Bottom density (Figure 11) seaward of the 50 m isobath is similar to that in spring, but near shore much lower densities (<25.0 kg/m³) reflect both the absence of the high salinity water found in spring and the presence of higher water temperatures in fall.

Vertically Averaged Properties

Temperature, salinity, and density were averaged vertically from the surface to 100 m or the bottom, whichever was shallower. Mean temperature (Figure 12) shows a wider range than in June, from less than 2°C to greater than 9°C, and the central tongue of cold water (<3°C in September-October) remains. Unlike June, the mean temperature in autumn delineates three regions over the southeastern shelf. The shelf break domain (bottom depth >100 m) is separated from the central shelf domain (100 m ≥ D ≥ 50 m) by a high temperature gradient: the shelf break domain has mean temperatures of about 5°C < T < 7°C, while the central shelf domain has T < 3°C. Similarly, the coastal domain (T > 6°C), shoreward of the 50 m isobath, is separated from the central domain by a high temperature gradient. Along the Alaska Peninsula a narrow strip of coastal water abuts both the shelf break and central waters.

Mean salinity (Figure 13) decreases shoreward and has high gradients between the 100 m isobath and the shelf break. The 32 g/kg isohaline suggests an inward flow of saltier water along the Alaska Peninsula. Mean density (Figure 14) isopleths are not congruent with the isohalines, as they were in spring, but also reflect strong thermal effects. Strongest gradients are seaward of the 100 m isobath, and shoreward of the 50 m isobath: the former is primarily an effect of salinity, and the latter of temperature (cf. Figures 12 and 13).

Plotting the correlation diagram for mean temperature and salinity (Figure 15) suggests a similar correlation to the June data. At low salinities (S < 31.5 g/kg) and high temperatures (T > 5°C) is the coastal water. At moderate values of salinity (31.5 g/kg ≤ S < 32.0 g/kg) and low temperatures (T < 4°C) is the central shelf water. Finally, at high salinities (S ≥ 32.0 g/kg) and moderately warm temperatures (T > 4°C) is the shelf break water. Much of the scatter in the

correlation comes from stations near the Alaska Peninsula where the three domains coexist. These temperatures and salinity limits are arbitrary, and they certainly change seasonally (e.g., see the June correlation, Kinder, 1977, Fig. 17). This division into three domains, however, is preserved throughout summer.

One prominent difference between June and September-October hydrographic structures is the changing importance of temperature. Early in the summer, temperature is low and its range small, so the effect on density is small. In contrast, later in the year, temperature is higher and its range large, so that it markedly affects density. For example, station 111 (Figure 16), occupied in October, shows only a small vertical salinity difference (~ 0.1 g/kg), which in June implies a small density difference. Because of a large temperature difference ($\sim 6.0^\circ\text{C}$), however, there is a large difference in density (~ 0.7 kg/m³). Less than 0.1 kg/m³ of this difference can be attributed to salinity.

Vertical Profiles

Vertical profiles from a section into Bristol Bay (Figures 17 and 18) illustrate the three water domains, with larger temperature range and warmer temperatures than in June. Stations 15, 26, 36, 47, and 59 are moderately stratified in temperature, stations 81, 91, 101, and 111 are strongly stratified, and station 126 is isothermal. These categories of thermal stratification correspond to shelfbreak, central shelf, and coastal domains, and stations 71 and 115 are transition stations between these domains. The domain boundaries have moved inshore since June, when stations 59 and 111 delineated the domains. Salinity profiles indicate similar domains, and also show seasonal salinity changes (Figure 18). In September-October the coastal stations (126 and 115) are fresher than they were in June, while the central shelf stations (101, 91, and 81) are saltier.

As in June, many of the September-October temperature profiles have features which we define as finestructure: a temperature inversion of at least 0.1°C having a vertical extent of 3 to 20 m. Three of the more impressive profiles, showing inversions of nearly 1°C over a few meters, are displayed in Figure 19. Of 108 stations, 24 exhibited finestructure. A second feature of many temperature profiles is a temperature minimum underlying the thermocline (Figure 20). These minima occur at 14 of the stations. Such minima could form by advection of warm water in the bottom layer.

Finestructure and temperature minima usually occur seaward of the 100 m contour (Figure 21). Comparing the frequency of occurrence of these features (and considering the different station coverage), we see that they are as common in September-October as in June (Table 1). Their distributions are also similar, although in June the features were found farther into the bay along the Alaska Peninsula (Kinder, 1977, Figure 22).

We illustrate a third feature in Figure 22. Although the sensors were always stopped a few meters above the bottom, most temperature profiles show a nearly homogeneous layer near the bottom (cf. Figures 17, 19, and 20). Several stations, however, exhibit strong gradients near the bottom, as though recent near-bottom advection had occurred such that frictionally-generated bottom turbulence had not yet been able to establish a bottom mixed layer (Figure 22; also see station 59, Figures 17 and 18). Stations near the Alaska Peninsula most strongly exhibited this structure.

Temperature-Salinity Correlations

The correlation diagram of temperature and salinity for the stations along the section into Bristol Bay (Figure 23) is similar to June. Representatives of the coastal (126), central shelf (111, 101, 81, and 91), and shelf break

Table 1. Distribution of Finestructure

	<u>JUNE</u>	<u>SEPTEMBER-OCTOBER</u>
	number (% of total)	number (% of total)
Total stations	171 (100)	108 (100)
Finestructure	30 (18)	24 (22)
Temperature minimum	16 (9)	14 (13)
Both	6 (4)	8 (7)
Either	40 (23)	30 (28)

domains (59, 47, 36, 26, and 15) show clearly. All stations are warmer, the coastal stations are fresher, and the central shelf stations saltier than in June. Also, the boundaries of the domains have shifted into the bay about 40 km (one station): these boundaries are marked by stations 71 and 115 in September-October instead of 111 and 59 in June.

Cross Sections

Sections of temperature, salinity, and density constructed from the same stations into the bay (Figures 24-26) show the more stratified central shelf water (stations 81-111), flanked to the southwest by the moderately stratified shelf break domain (stations 15-59) and to the northeast by the homogeneous coastal domain (126). Again, temperature clearly influences the density structure strongly in September-October, while in June its effect was small.

Cross sections normal to the Alaska Peninsula (Figures 27 - 29) suggest an inflow of warmer and saltier water along the foot of the peninsula. Similar evidence appears in horizontal distribution (cf. Figures 8 and 9), and also in a cross section along the 100 m isobath in June (Kinder 1977, Figures 26 and 29).

A section across inner Bristol Bay (Figure 30) shows the higher salinity and lower temperature anomaly at station 117. Meyer (1976) documented that this feature is usually present during summer. It is unclear whether this is caused by upwelling as Meyer suggested, or perhaps by mixing (as occurs in the adjacent coastal water).

Stratification

Vertical differences of temperature (ΔT), salinity (ΔS), and density ($\Delta \sigma_t$) (Figures 31 - 33) illustrate the variation in stratification across the shelf. We have chosen to use the maximum differences, rather than the 0-50 m differences used in June, because the vertical structure seaward of the 100 m contour seems

more complex in September-October. Nevertheless, similar features show in the September-October figures. In temperature, the central shelf is highly stratified ($\Delta T > 6^\circ\text{C}$), the shelf break domain is moderately stratified ($5^\circ\text{C} > \Delta T > 2^\circ\text{C}$), and the coastal domain is well-mixed ($\Delta T < 1^\circ\text{C}$). In haline stratification the coastal domain generally has $\Delta S < 0.2$ g/kg, the central shelf is intermediate (0.2 g/kg $< \Delta S < 0.5$ g/kg), and because of its greater depth the shelf break domain has higher salinity differences ($\Delta S > 0.5$ g/kg). The density distribution is similar to salinity, but the central shelf's stratification is comparable to the shelf break domain shoreward of the 200 m isobath.

The correlation of temperature and salinity differences (Figure 34) has wider scatter than in June (Kinder, 1977, Figure 32), even though the salinity difference was taken to only 100 m, thus limiting depth dependence. When separated into depth zones, roughly corresponding to the three structural domains already discussed, however, correlations emerge. Both the shallow (coastal) (depth < 50 m) and the intermediate (central shelf) ($50 \text{ m} \leq \text{depth} < 100$ m) zones show strong positive correlation. In shallow water, near the source of freshwater, the ratio of (salinity difference)/(temperature difference) is greater than over the central shelf. In the deep (shelf break) zone (depth ≥ 100 m) the salinity difference is independent of temperature difference.

We have also plotted vertical differences versus depth. Temperature differences (Figure 35) closely follow the June distribution: low values ($\Delta T < 2^\circ\text{C}$) in water less than 50 m deep increasing to high values ($\Delta T > 6^\circ\text{C}$) at 60 - 80 m depth in the central shelf domain and then decreasing to moderate values ($\Delta T \sim 4^\circ\text{C}$) which vary little from the 100 m isobath to the continental slope. Salinity differences have a similar distribution (Figure 36), but here we examine the differences in the upper 100 m. This eliminates from the diagram the increase in salinity with depth that occurs below 100 m at many of the deeper stations (cf. Figure 18).

Again, the coastal stations have low values ($\Delta S < 0.3$ g/kg), there is a peak ($\Delta S > 1.0$ g/kg) near 90 m depth over the central shelf which falls to a lower constant value ($\Delta S \sim 0.6$ g/kg) in the shelf break domain. Density differences over the upper 50 m (Figure 36) show the same pattern, although all the temperature and salinity "anomalies" are reflected in this diagram. Inshore of 50 m depth $\Delta \sigma_T < 0.25$ kg/m³, over the central shelf domain, it peaks at $\Delta \sigma_T > 1.0$ kg/m³, and then falls to a constant ~ 0.3 kg/m³ over the shelf.

Frontal Section

Temperature and salinity sections (Figure 38) between the Pribilofs and Nunivak island reveal the front near the 50 m isobath. Although poorly resolved because of station spacing, the front apparently is located between stations 138 and 139, as in June (Kinder, 1977, Figures 35 and 36).

Geopotential

The dynamic topography of 0/50 db (Figure 39) is similar to that in June, showing about three dynamic centimeters difference across the shelf seaward of the 100 m contour, and suggesting ^{north} westward flow. Another feature of the topography, a clockwise circulation around the central shelf which terminates inside Bristol Bay, may be persistent, but the geopotential probably does not describe the flow accurately in this shallow water. Similar to the June data, the dynamic topography of 0/100 db (Figure 40) shows a contorted westward flow over the shelf break domain. This westward flow over the deep shelf, and its meanders, are typical of geopotential distributions based on historical data (L. K. Coachman, personal communication).

III. Seasonal Changes - Summer 1976

By comparing the June and September-October data, we can estimate the changes that occurred over this shelf during summer 1976. Because the winter of 1975-76

was an unusual one (i.e., colder temperatures and more persistent ice cover than normal) some of the changes that we see may be abnormal. For instance, the high salinity water found in the coastal domain during June is apparently formed because ice freezing there is blown away and melts elsewhere. Thus, the strength and extent of this salinity anomaly are probably related to the weather during the preceding winter. While there may be differences from year to year, it is reasonable to assume that similar changes occur over the summer every year, and historical hydrographic compilations support this (e.g., Dodimead et al., 1963; Favorite et al., 1976; Ohtani, 1973). Thus, we use the changes over the summer of 1976, described in this section, to infer the seasonal evolution of the hydrographic structure, discussed in the following section.

Temperature

The change of mean temperature (Figure 41) reflects the structure of the water column. Over the central shelf, where the heat gained from insolation is confined to a shallow layer above the pycnocline, the mean temperature increase is small ($<3^{\circ}\text{C}$). In the coastal domain (<50 m depth), heat mixes throughout the water column so that the change in temperature is large ($>6^{\circ}\text{C}$). In the shelf break domain the temperature change is generally small, but has a wide range ($<2^{\circ}\text{C}$ to $>4^{\circ}\text{C}$).

Salinity

Salinity changes (Figure 42) reveal broader trends which show through several small salinity features. The northern coastal domain is fresher because of the summer peak of river runoff, perhaps including the flushing of the near-shore high salinity water. Over the central shelf the water is somewhat saltier (~ 0.2 g/kg). In June this region was surrounded by water of higher salinity, and thus isolated from sources of freshwater. Along the Alaska Peninsula and in the shelf break domain, the distribution is complex, but generally shows an increase in mean salinity. This increase is caused by higher salinities in the lower layer; the shallow salinities are lower in the shelf break domain than in June.

In the shelf break domain and along the Alaska Peninsula, advection probably is the prime factor in the distribution of properties, so Figure 42 may reflect an advective change. Since the velocity field displays episodic pulses with "periods" of several days (Schumacher *et al.*, 1977), this change in salinity may not be seasonal.

Heat

We also look at the heat gain of the water column over the summer. Reed (1978) has done a careful heat budget for a small section (166°-164°W by 56°-57°N) of the shelf using these data; our attempt to examine a broader area in less detail is complementary. During June through August, Reed obtained a balance between net surface exchange and local change of heat; he estimated that horizontal diffusion was less than 10% of the local change.

To calculate the local change of heat, we used all stations which were occupied during both periods (*i.e.*, June and September-October), calculated the heat storage to 100 m or the bottom (whichever was shallower), and divided by the time between occupations of the station. These calculations are somewhat low, as surface cooling had begun by late September (see Horizontal Distribution, p. 3).

Over the summer the heat gained per unit area (Figure 43) is low ($<100 \text{ w/m}^2$) over the central shelf. It is higher ($>100 \text{ w/m}^2$) in the coastal domain, where the heat is more efficiently mixed throughout a smaller water column. When the heat addition is normalized by the depth (to 100 m), so that heat added per unit volume is examined (Figure 44), the coastal domain is a region of high heat gain ($>2.5 \text{ w/m}^3$), while the central shelf has low heat gain ($<1.5 \text{ w/m}^3$): this is identical to mean temperature patterns (Figure 40). Because of the rapid transition between these domains, it is clear that the water structure and not just the depth produce these differences. In the shelf break domain no obvious pattern is established.

Stratification

Changes in thermal stratification (Figure 45) are as expected over the central

shelf and coastal domains. The coastal domain remains well-mixed, so that no important change occurs there ($\Delta T \sim 0^\circ\text{C}$). Because the initial stratification in June inhibits vertical mixing, the central shelf domain grows more stratified ($\Delta T > 4^\circ\text{C}$) over the summer, while the shelf break shows no clear pattern.

With the exception of two small features, the coastal and shelf domains show little change ($|\Delta S| < 0.5 \text{ g/kg}$) in haline stratification over the summer (Figure 46). The shelf break domain generally increases in haline stratification ($> 0.5 \text{ g/kg}$). This reflects the changes in salinity discussed for Figure 42, and cannot be readily interpreted as local seasonal change.

IV. Discussion

Mixing

Using our hydrographic data, we estimate diffusivities for the shelf. Although the assertion that flux = diffusivity x mean gradient greatly simplifies the actual mechanism of "turbulent" diffusion over the shelf, we think that it can be applied effectively here. Csanady (1976) discusses the validity of applying this simplification to shelf regimes.

Selecting the central shelf domain, where the mean advection is very low, we estimate the vertical and horizontal diffusivities. If the entire heat gain in the layer below the thermocline is caused by vertical diffusion, the vertical diffusivity is:

$$K_v = -\frac{\Delta H}{\Delta t} \left[\rho C_p \frac{\overline{\Delta T}}{\Delta Z} \right]^{-1}$$

Where:

ΔH is the gain of heat in the lower layer between the two surveys,

Δt is the time between occupations of the station,

ρ is the density, taken as 1.02 g/cm^3 ,

C_p is the specific heat, taken as $4.0 \text{ J g}^{-1} \text{ }^\circ\text{C}^{-1}$,

$\frac{\overline{\Delta T}}{\Delta Z}$ is the maximum vertical temperature gradient over 3 m depth intervals; 3 m was chosen arbitrarily to further smooth the 1 m averaged values, and still retain the strong gradients.

These calculations for various central shelf stations (Table 2) yield a mean of $5 \times 10^{-2} \text{ cm}^2/\text{s}$, ranging from $7 \times 10^{-3} \text{ cm}^2/\text{s}$ at station 82 to values approaching $1 \text{ cm}^2/\text{s}$ (e.g., station 110: $K_v \sim 0.6 \text{ cm}^2/\text{s}$) near the shelf break domain. These contrast to high values in the coastal domain (e.g., station 141: $K_v \sim 260 \text{ cm}^2/\text{s}$) where there is no thermocline and vigorous tidally-generated mixing maintains nearly isothermal conditions. These diffusivities are probably maximum limits because we assume that all heat gain is by vertical diffusion. They quantify the slow vertical mixing rates over the strongly-stratified central shelf.

We can make a similar calculation for the horizontal diffusivities for heat and salt:

$$K_H = -\frac{\Delta H}{A \Delta t} \left(\rho C_p \frac{\overline{\Delta T}}{\Delta X} \right)^{-1} \quad \text{and}$$

$$K_H = -\frac{\Delta M}{A \Delta t} \left(\rho \frac{\overline{\Delta S}}{\Delta X} \right)^{-1}, \quad \text{where}$$

ΔH = heat gain in the lower layer of the central shelf,

ΔM = salt gain over the central shelf,

Δt = $9.5 \times 10 \text{ s}$ interval between surveys,

A = area around perimeter of the central shelf through which the heat or salt fluxes,

$\frac{\overline{\Delta T}}{\Delta X}$ = the mean horizontal temperature gradient normal to the boundary of the central shelf, and

$\frac{\overline{\Delta S}}{\Delta X}$ = the mean horizontal salinity gradient, normal to the boundary of the central shelf.

For heat we assume a box 130 km wide by 440 km long (Figure 47) with equal

Table 2. Vertical mixing coefficients

<u>Station No.</u>	<u>$\overline{\Delta T/\Delta Z}$ ($^{\circ}\text{C}/\text{m}$)</u>	<u>K_v (cm^2/s)</u>
68	1.0	0.08
69	0.9	0.1
72	0.3	0.5
73	1.0	0.1
74	1.4	0.06
75	1.3	0.05
81	0.4	0.3
82	0.9	0.007
84	1.8	0.03
85	1.4	0.03
86	1.0	0.05
91	0.6	0.2
92	1.1	0.07
103	0.6	0.08
110	0.4	0.6
111	0.6	0.2
112	0.6	0.1
137	1.2	0.04
138	1.2	0.06
139	0.03	6.0
140	0.007	40
141	0.001	260
BC-5	1.3	0.04

temperature gradients all around ($\sim 6 \times 10^{-7} \text{ }^\circ\text{C/cm}$), and a bottom layer averaging 45 m thickness. Neglecting diffusion through the ends of this box, 4.2 w/cm^2 must diffuse through the boundary to add $1.6 \times 10^{19} \text{ J}$ to the central shelf over the summer. Under these assumptions we calculate $K_H \sim 1.7 \times 10^6 \text{ cm}^2/\text{s}$.

For salt we consider horizontal diffusion from seaward of the 100 m isobath only into a similarly shaped box: in spring the coastal waters are more saline than those over the central shelf, and in autumn this is reversed. Because the sign of the salinity gradient changes during summer on the shoreward boundary of the box, it is difficult to select an appropriate mean salinity gradient. We simplify by assuming that the net flux across the boundary is zero. With a mean gradient of $6.2 \times 10^{-8} \text{ g kg}^{-1} \text{ cm}^{-1}$, $7 \times 10^{-5} \text{ gm cm}^{-2} \text{ s}^{-1}$ of salt must flux into the central shelf to add $2.6 \times 10^{14} \text{ gm}$ of salt. The required diffusivity is $1.1 \times 10^6 \text{ cm}^2/\text{s}$.

Again, these coefficients probably are upper limits, because we assume that all the change is due to horizontal diffusion. Many of our assumptions are arguable, but any similar calculation will yield similar results. We note that Kinder and Coachman (1978) calculated $3 \times 10^6 \text{ cm}^2/\text{s}$ for a diffusive salt balance over the entire shelf, and Csanady (1976) estimated $2 \times 10^6 \text{ cm}^2/\text{s}$ for the mid-Atlantic bight.

The heat budget for the central shelf is dominated by surface exchange (Reed, 1978), and the salt budget for the entire shelf by advection (Kinder and Coachman, 1978). Nevertheless, the strong stratification and isolation of the waters of the central shelf domain permit these estimates of the mixing efficiencies. Over the central shelf domain the salt balance is diffusive, *i.e.*, driven by flow at tidal and meteorological frequencies. The transfer of heat from the upper layer to greater depth also may be accounted for by diffusion. So "turbulent diffusion" is important in the salt and heat budgets of restricted regions, and is important also in the dispersion of passive material such as plankton and petroleum.

Water Categories

Throughout our presentation of distributions we have divided the shelf waters into three domains: coastal, central shelf, or shelf break. Although our categories are imperfect, we think that the water above the shelf can be fruitfully categorized by vertical structure primarily, and secondarily by temperature-salinity properties. For instance, defining a coastal domain by low salinity is nonsensical in June of 1976, since the coastal domain was then more saline than the central shelf domain; the coastal domain remained clearly recognizable, however, by its vertical structure.

Table 3 lists the important characteristics of these three domains. Happily, these domains (Figure 48) are generally congruent to those regions defined by schemes based primarily on temperature and salinity properties (e.g., Dodimead et al., 1963; Favorite et al., 1976; Takenouti and Ohtani, 1974).

Seasonal Evolution

With these data we can follow the vertical structure as it evolves over the summer, and extrapolate to the entire year. By March, at the end of winter, we think the water is vertically homogeneous over the coastal and central shelf domains, which are covered by ice. Over the outer shelf break domain and along the Alaska Peninsula, which remain free of ice during winter (Muench and Ahlnäs, 1976), the water remains vertically non-uniform in salinity and temperature. Over the northern section of the coastal domain, the salinity has been raised above that of the adjacent central shelf water by freezing of ice which is then driven south by the prevailing winds.

In May, the ice breakup occurs. Insolation has already warmed the waters over the ice-free portions of the shelf, but over most of the shelf surface warming begins only after the ice leaves. In the coastal domain, tidal mixing keeps the heat and salt uniformly spread over the water column. Melting ice in

Table 3. Water Domains in Summer

	<u>COASTAL</u>	<u>CENTRAL SHELF</u>	<u>SHELF BREAK</u>
vertical structure	homogeneous	two-layer	surface mixed layer stratified interior bottom mixed layer finestructure
stratification	very low	very high	moderate
depth	<50 m ~thickness of bottom (tidal) mixed layer	50 m ≤ depth < 100 m ~thickness of surface + bottom mixed layer	≥100 m >surface + bottom mixed layers, thus an interior region exists
temperature	very warm in late summer (efficient heat transfer through- out water column)	very cold bottom temperature throughout summer (vertical heat transfer impeded by stratification)	moderate
salinity	generally low (<31.5 g/kg), but may be relative- ly high following winter (>32 g/kg: brine rejection during ice freezing)	moderately low (~31.5 g/kg)	high (>32 g/kg)
influences	river runoff ice freezing	ice melting	adjacent water overlying deep basin; Bering Slope Current

the coastal domain is inadequate to compensate for the salt gained during the winter, as much of the ice formed there melts elsewhere. Over the central shelf, the tidal mixing cannot overcome large additions of positive buoyancy, so that a surface wind-mixed layer develops above the bottom tidally-mixed layer. Thus, freshwater from melting ice and heat from insolation are largely retained in the surface layer. Because of the low temperatures, the initial density stratification is formed primarily from meltwater.

Through the summer the coastal domain remains well-mixed, although positive buoyancy from insolation and river runoff is added continually, probably causing the boundary to shift inshore. Because of its shallowness and efficient mixing, the coastal domain stores a large amount of heat at relatively high temperatures, and with the summer peak of river runoff this domain becomes fresher than the adjacent central shelf. Over the central shelf, heat added by insolation is trapped in the upper layer, so that heat is not stored efficiently: higher surface temperatures cause higher losses to the atmosphere. Initially the central shelf is surrounded by more saline water, so that its salinity increases by diffusion over the summer. Over the coastal and central shelf domains the waters are directly affected by boundary phenomena: tidal mixing, insolation, river runoff, freezing, and melting. The shelf break domain is somewhat insulated from these phenomena by its greater depth, and influenced by the mean advection near the shelf break.

In autumn, river runoff decreases, surface cooling begins, and more frequent and more energetic storms promote mixing. We believe that most of the shelf becomes vertically homogeneous during the winter, and many locations are well-mixed before ice formation. For example, many stations over the deep basin to the south and west were well-mixed to >50 m in October-November 1973 (T. G. Thompson cruise 85, unpublished), and winter data shows mixing to 200 m depth

in the western Bering Sea (Natarov, 1963). With the formation of ice, increasing the salinity of the northern coastal waters, the cycle is complete, and awaits spring breakup to begin again.

We note the important role that ice plays in the evolution of the hydrographic structure. In the spring, it is the ice breakup that determines the initiation of warming the surface waters. While the ice cover remains, heat transfer with the atmosphere is reduced greatly. Over the central shelf, the formation and subsequent melting of ice alters the water column, from one initially homogeneous in autumn to one which is haline-stratified in early spring. This initial stratification is then reinforced by insolation during summer.

Ice also causes non-local changes. The northern coastal regime is often free of ice during the winter, according to Muench and Alhnäs (1976) and to satellite photographs that we have examined for 1976 and 1977. Ice forms there, leaving behind much of its salt in the water, and then the prevailing northerly winds blow this ice southward. This divergence of ice is an effective method for transporting salt from the southern shelf (where the ice presumably melts), to the coastal domain. Salinity distributions support this hypothesis. To form the 32.25 g/kg water seen in June from the 31.5 g/kg autumnal water in 30 m depth, only 70 cm of ice (with 100% brine rejection) is required, a reasonable thickness.

Compare this to Kinder and Coachman's (1978) estimate of a mean annual salt flux of 50 t/s ($1 \text{ t} = 10^6 \text{ g}$) needed to raise the salinity of the coastal waters to 31 g/kg. Estimating that freezing and ice divergence raise the salinity of water averaging 25 m depth over a 100 km x 300 km area from 31.5 g/kg to 31.8 g/kg, then the effective salt flux is about 6 t/s. Neither the total volume of the higher salinity water nor its magnitude are well-known. The order of magnitude of the flux, however, probably is correct. Thus, this divergence mechanism accounts for ~10% of the shoreward salt flux.

Over the central shelf, even the local cycle of freezing and melting is important. For example, if 40 cm of ice freeze above a 70 m deep column originally at 31.75 g/kg, a new salinity of 31.9 g/kg results. When the ice melts and the freshwater mixes over the upper 30 m, a two-layer system with salinities of 31.5 g/kg and 31.9 g/kg forms, similar to that observed in spring. Thus, the ice not only strongly affects the timing of the seasons over the shelf, but it directly transports salt and changes stratification as well.

Questions

Although we consider this report a preliminary one, we can pose some questions for future study.

1. What is the vertical structure in winter?
2. How does the vertical structure adjust to the onset of the ice? E.g., does the tidally-generated front slowly retreat into deeper water?
3. The timing of the ice-breakup determines the arrival of spring over most of the shelf. What effect does this have on the biology of the region? Phasing of plankton blooms is known to be critical for the mortality in year classes of some fish, so that the ice-breakup may profoundly influence trophic dynamics over the shelf.
4. Examination of the diffusive components of the heat and salt fluxes suggested that these processes are associated with a $K_H = 1 \text{ to } 2 \times 10^6 \text{ cm}^2/\text{s}$. Because of the distinctly different hydrographic structures, however, the detailed physics of these fluxes probably differ. What are the details of the horizontal diffusion within each domain?

References

- Coachman, L. K. and R. L. Charnell, 1977. Finestructure in outer Bristol Bay, Alaska, Deep-Sea Res. 24(10):869-889.
- Csanady, G. T., 1976. Mean circulation in shallow seas, J. Geophys. Res. 81: 5389-5399.
- Dodimead, A. J., F. Favorite and T. Hirano, 1963. Salmon of the North Pacific Ocean, Part II: Review of oceanography of the Subarctic Pacific Region, Int. North Pacific Fish. Comm. Bull. 13:195 pp.
- Favorite, F., A. J. Dodimead, and K. Nasu, 1976. Oceanography of the Subarctic Pacific Region, 1960-71, Bulletin 33, International North Pacific Fisheries Commission, Vancouver. 187 pp.
- Ingraham, W. J., Jr., 1973. Maps of mean values of water temperature (°C) and salinity (‰) in the Eastern Bering Sea by 1° x 1° quadrangles. Unpublished report of Northwest Fisheries Center, National Marine Fisheries Service, Seattle, 24 pp.
- Kinder, T. H., 1976. The continental slope regime of the Eastern Bering Sea, Ph.D. dissertation, University of Washington. 272 pp.
- Kinder, T. H., 1977. The hydrographic structure over the continental shelf near Bristol Bay, Alaska, June 1976, University of Washington, Department of Oceanography, Technical Report, Ref: M77-3, 61 pp.
- Kinder, T. H. and L. K. Coachman, 1978. The front overlaying the continental slope of the Eastern Bering Sea, submitted to J. Geophys. Res.
- Kinder, T. H., L. K. Coachman and J. A. Galt, 1975. The Bering Slope current system, J. Phys. Oceanogr. 5(2):231-244.
- Muench, R. D., 1976. A note on the Eastern Bering Sea hydrographic structure, Deep-Sea Res. 23:245-247.
- Muench, R. D. and K. Alhnäs, 1976. Ice movement and distribution in the Bering Sea from March to July, 1974, J. Geophys. Res. 81(24)4467-4476.
- Myers, R. L., 1976. On the summertime physical oceanography of Bristol Bay, 1969-1970, University of Alaska M.S. thesis.
- Natarov, V. V., 1963. On the water masses and currents of the Bering Sea, Tr. VINRO, 48; Tzv. TINRO, 40. (Translation, 1968: Soviet Fisheries Investigations in the Northeast Pacific, NTIS, Springfield, Va., 110-130)
- Ohtani, K., 1973. Oceanographic structure in the Bering Sea, Memoirs of the Faculty of Fisheries, Hokkaido, Univ. 21(1):65-106.
- Reed, R. K., 1978. The heat budget of a region in the Eastern Bering Sea, summer, 1976, J. Geophys. Res., in press.
- Roden, G. I., 1967. On river discharge into the Northeastern Pacific and the Bering Sea, J. Geophys. Res. 72: 5613-5629.

Schumacher, J. D., R. L. Charnell and L. K. Coachman, 1977. Bristol Bay Oceanographic processes, second annual report. Unpublished, 64 pp.

Schumacher, J. D. and L. K. Coachman, 1976. Bristol Bay oceanographic processes, annual report. Unpublished, 34 pp.

Takenouti, A. Y. and K. Ohtani, 1974. Currents and water masses in the Bering Sea: A review of Japanese work, In: Oceanography of the Bering Sea. D. W. Hood and E. J. Kelley, eds., Institute of Marine Science, University of Alaska, Fairbanks, pp. 39-58.

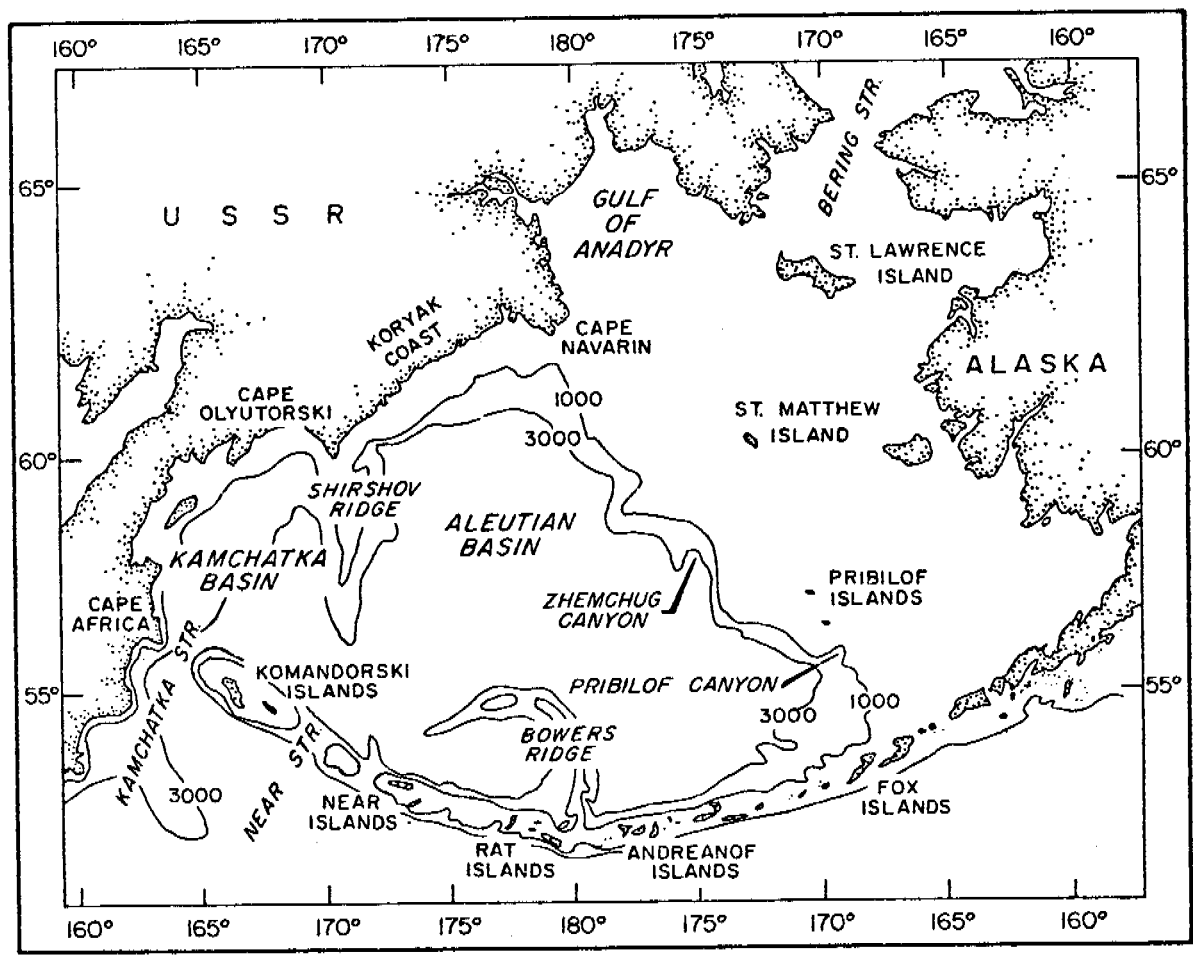


Figure 1. The Bering Sea. The isobaths are for 1000 m and 2000 m.

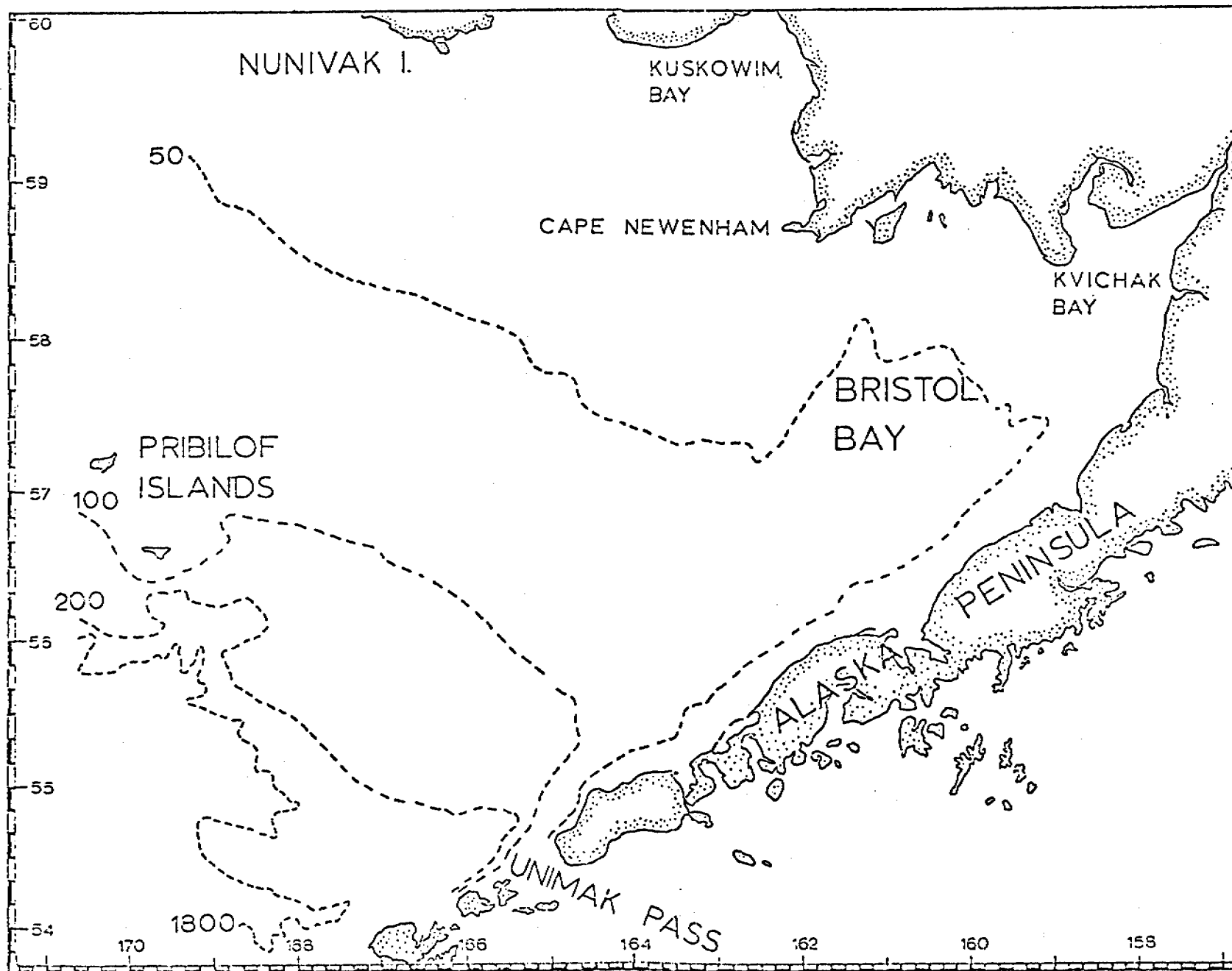


Figure 2. The Bristol Bay Study Region, The 50 m, 100 m, 200 m, and 1800 m isobaths are shown.

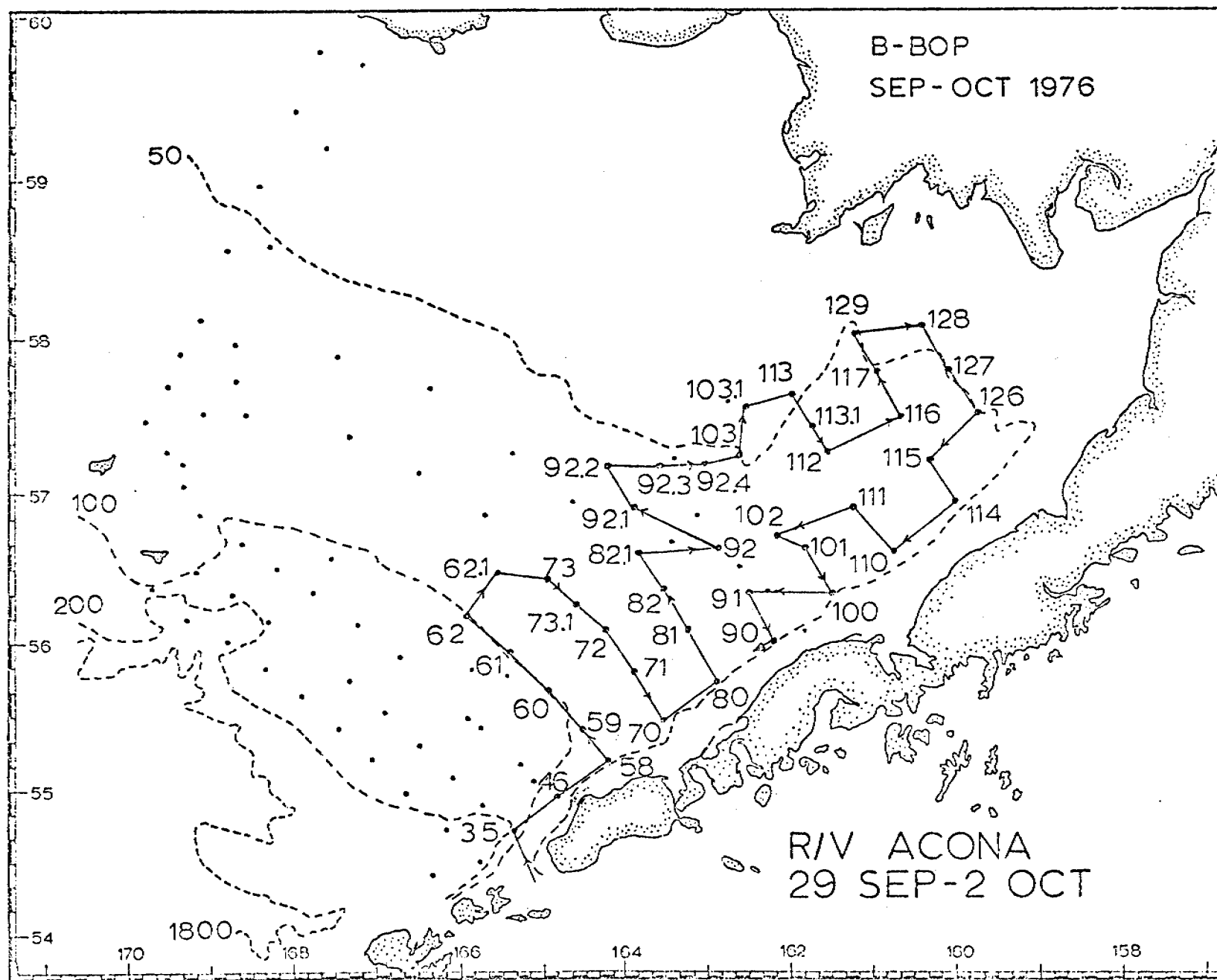


Figure 3. Track of R/V Acona. The unconnected dots are stations occupied by R/V Moana Wave.

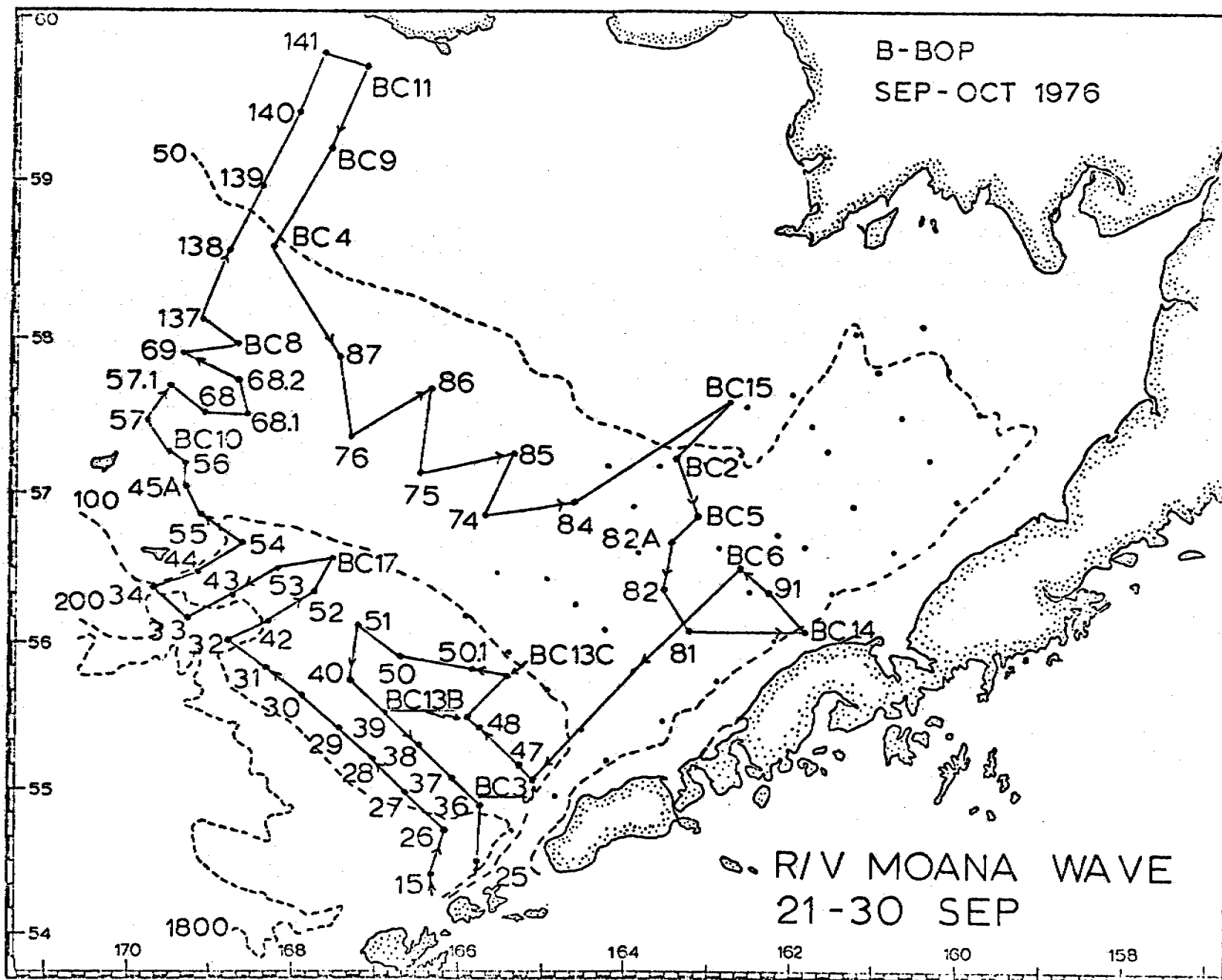


Figure 4. Track of R/V Moana Wave. The unconnected dots are stations occupied by R/V Moana Wave.

465

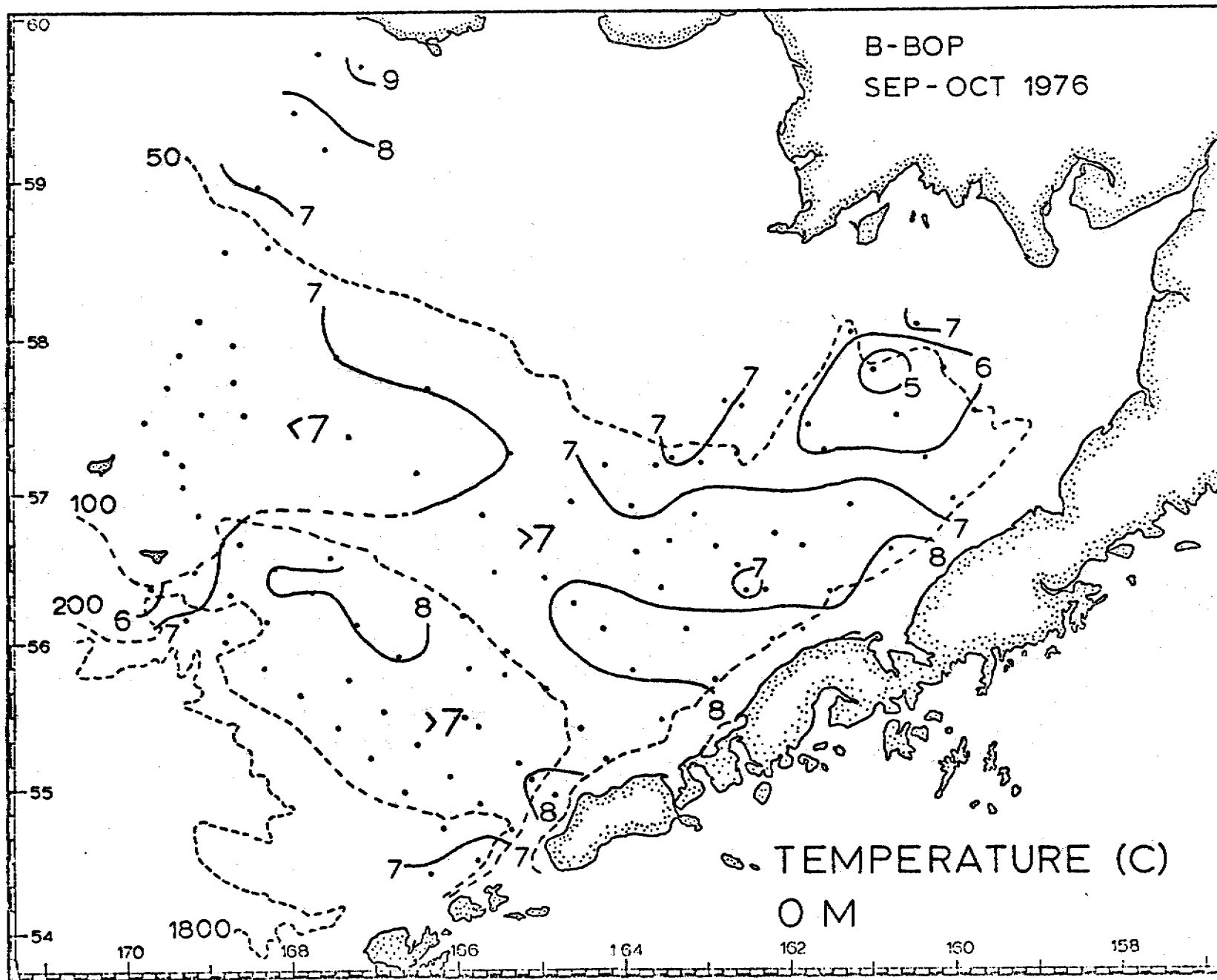


Figure 5. Surface temperature.

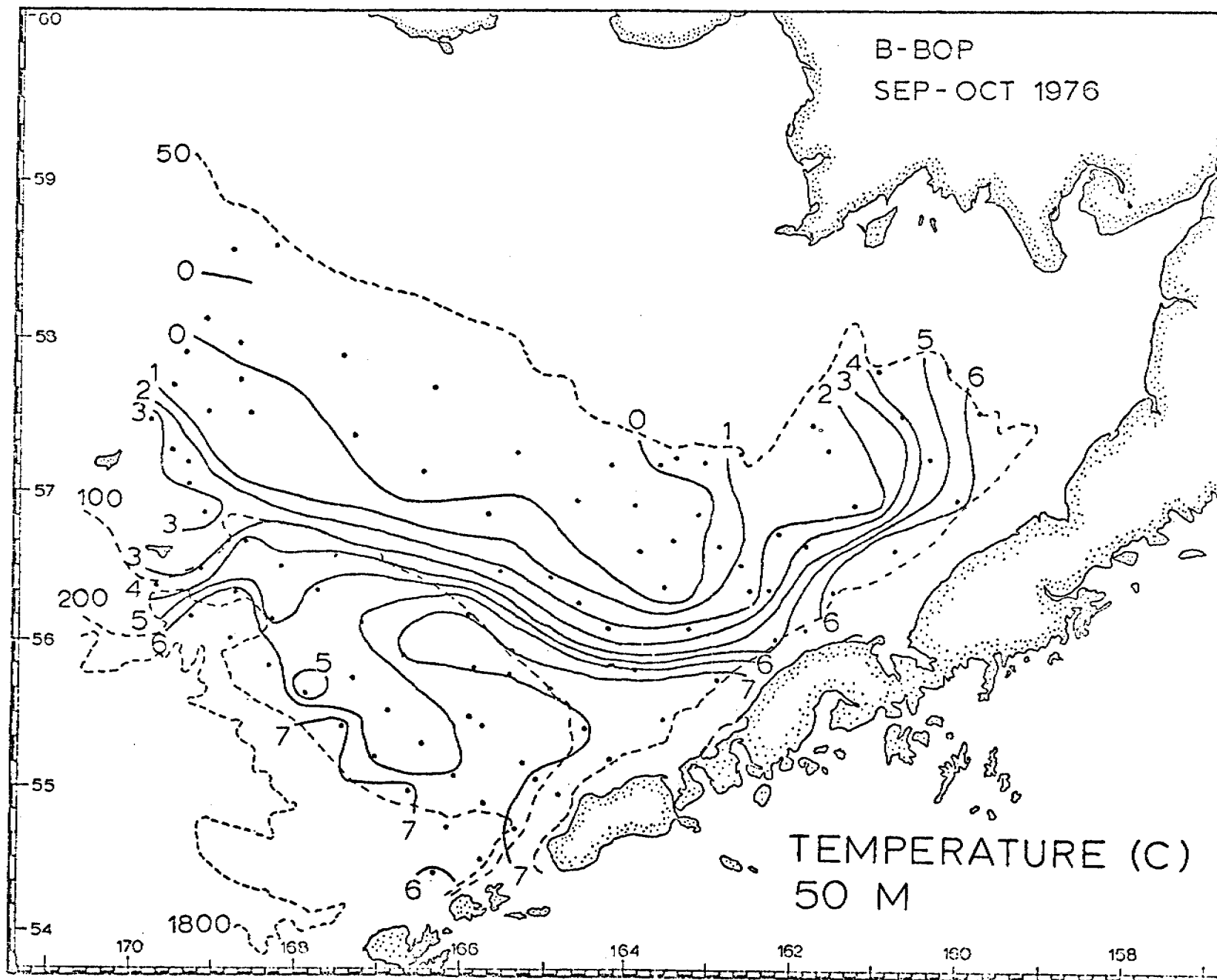


Figure 6. Temperature at 50 m.

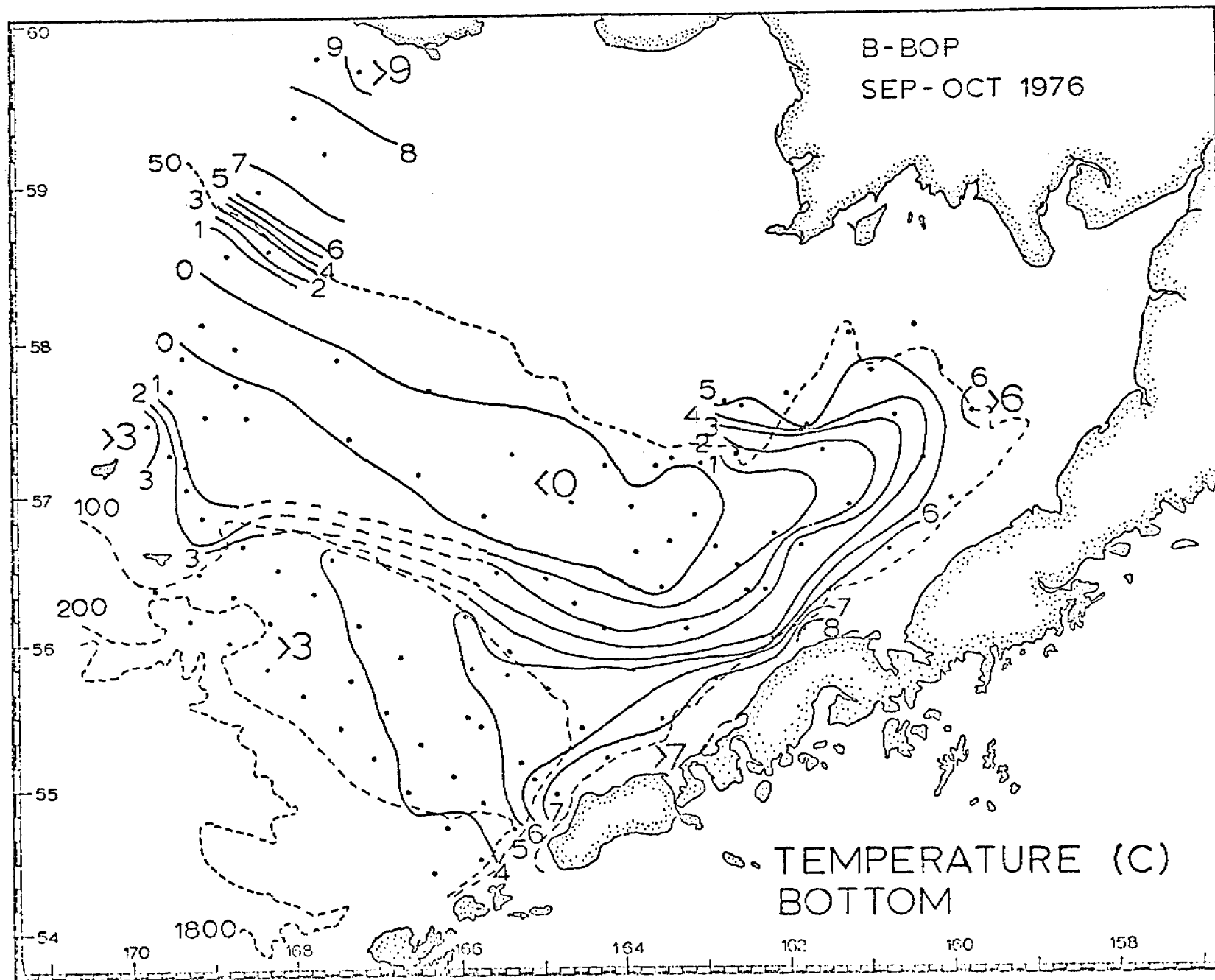


Figure 7. Temperature at the bottom.

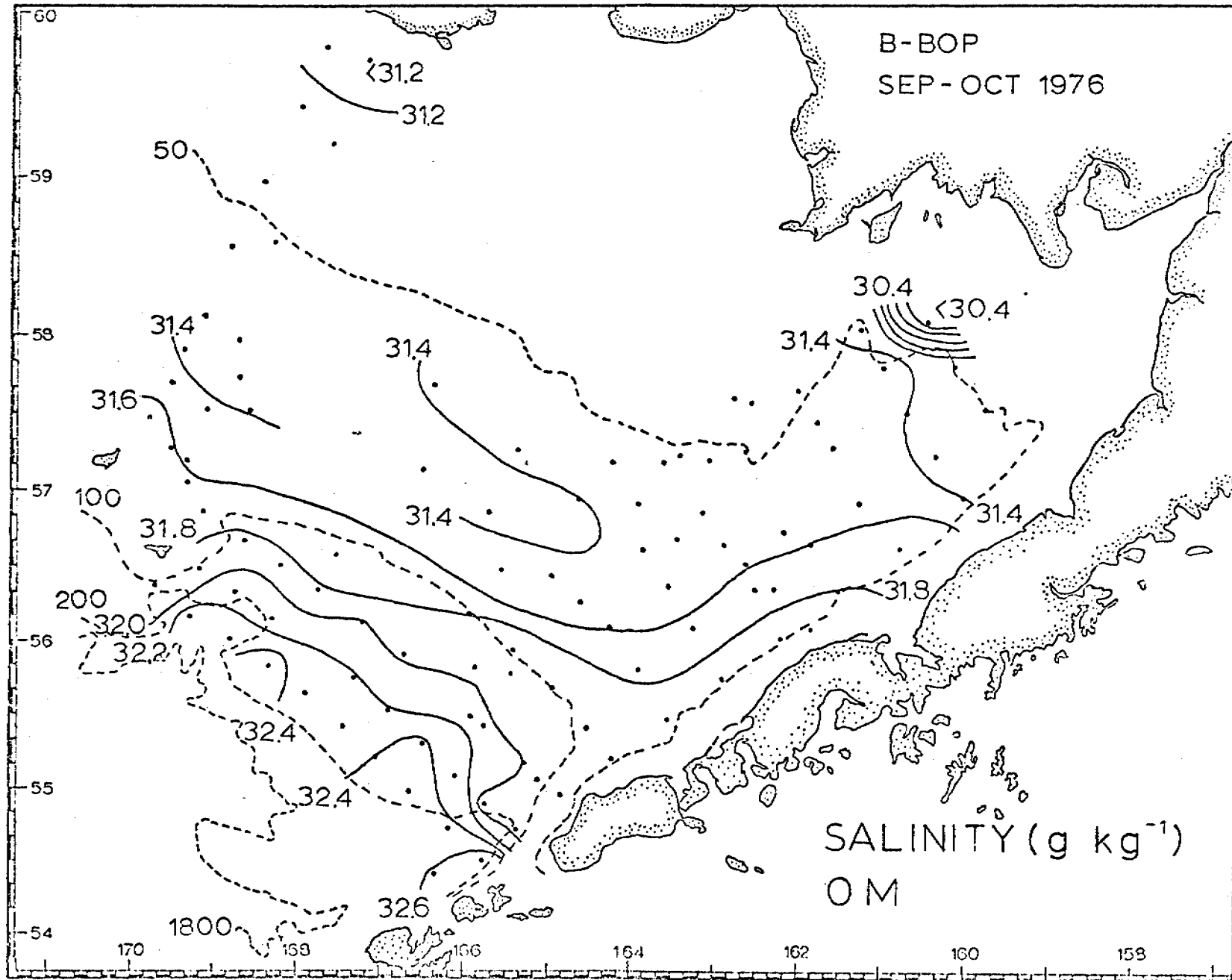


Figure 8. Surface salinity.

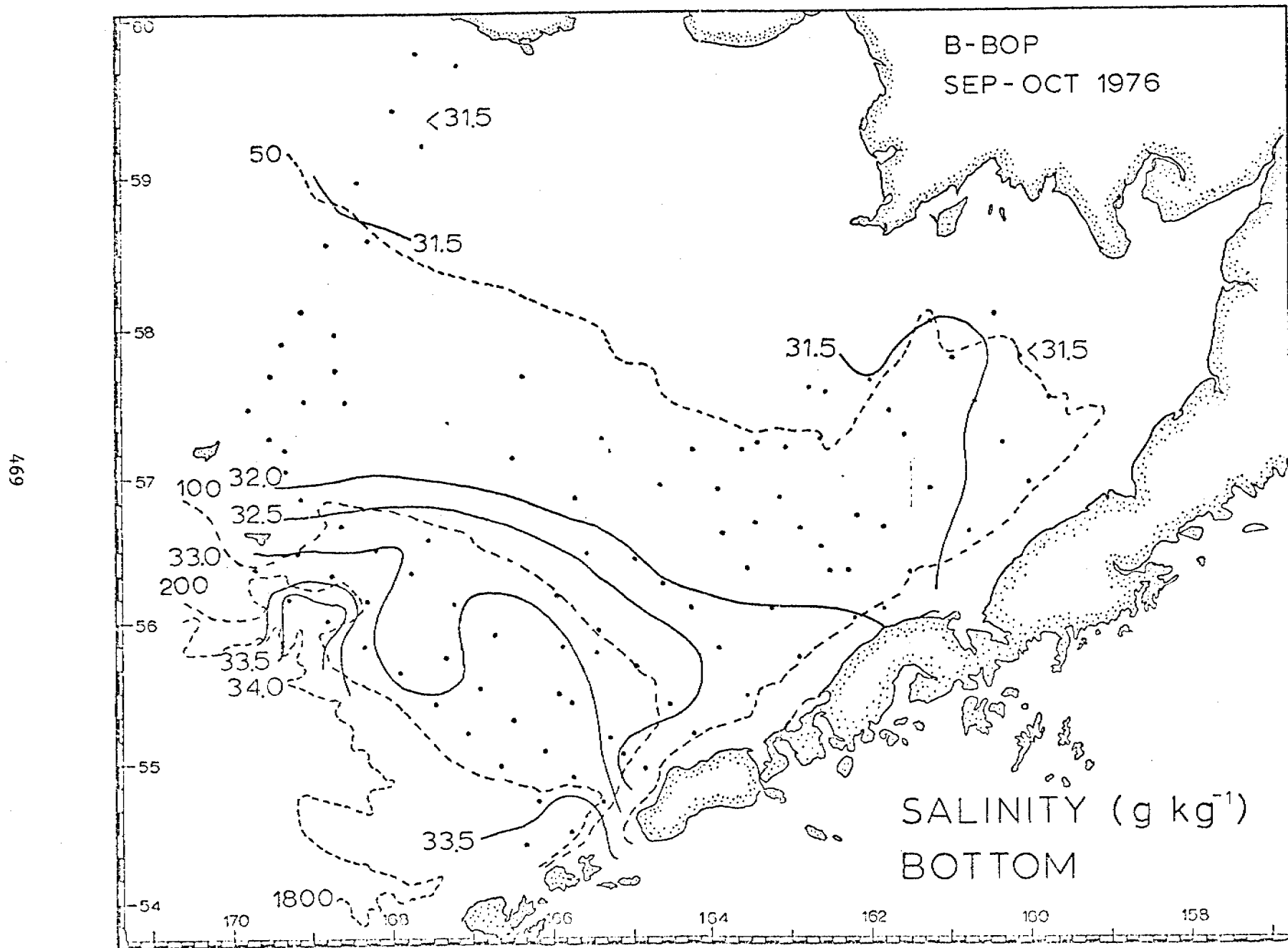


Figure 9. Salinity at the bottom.

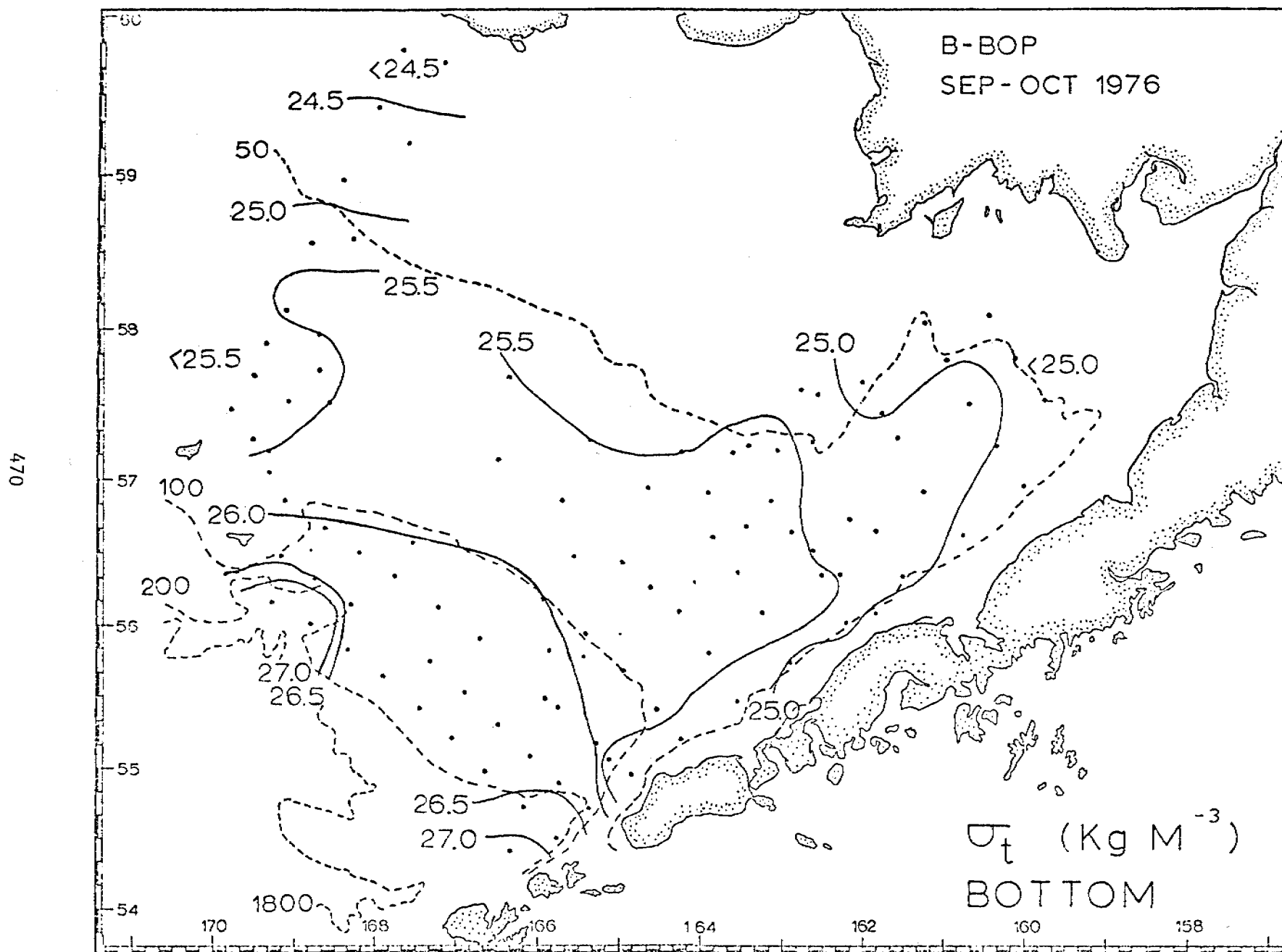


Figure 10. Surface density.

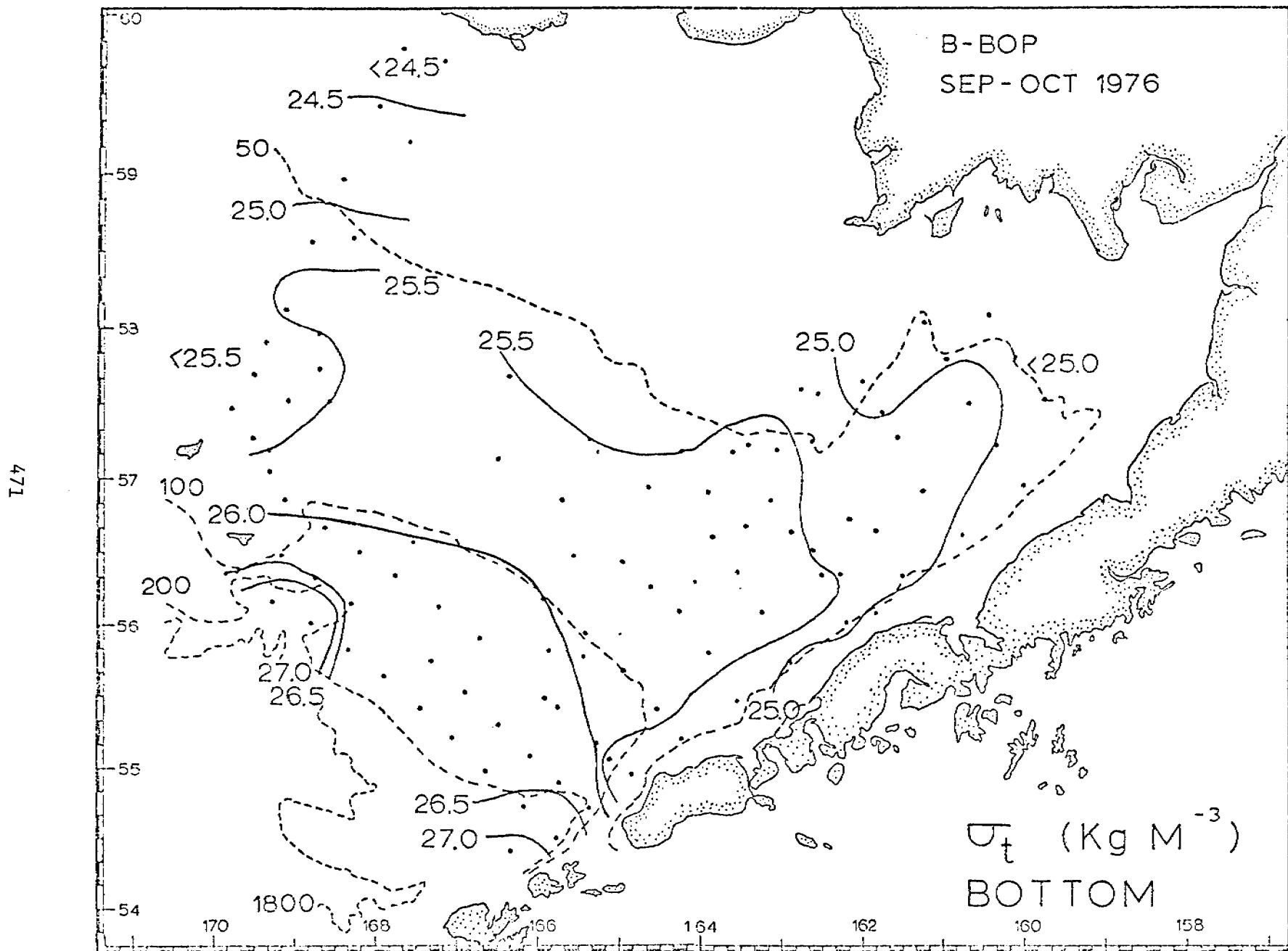


Figure 11. Bottom density.

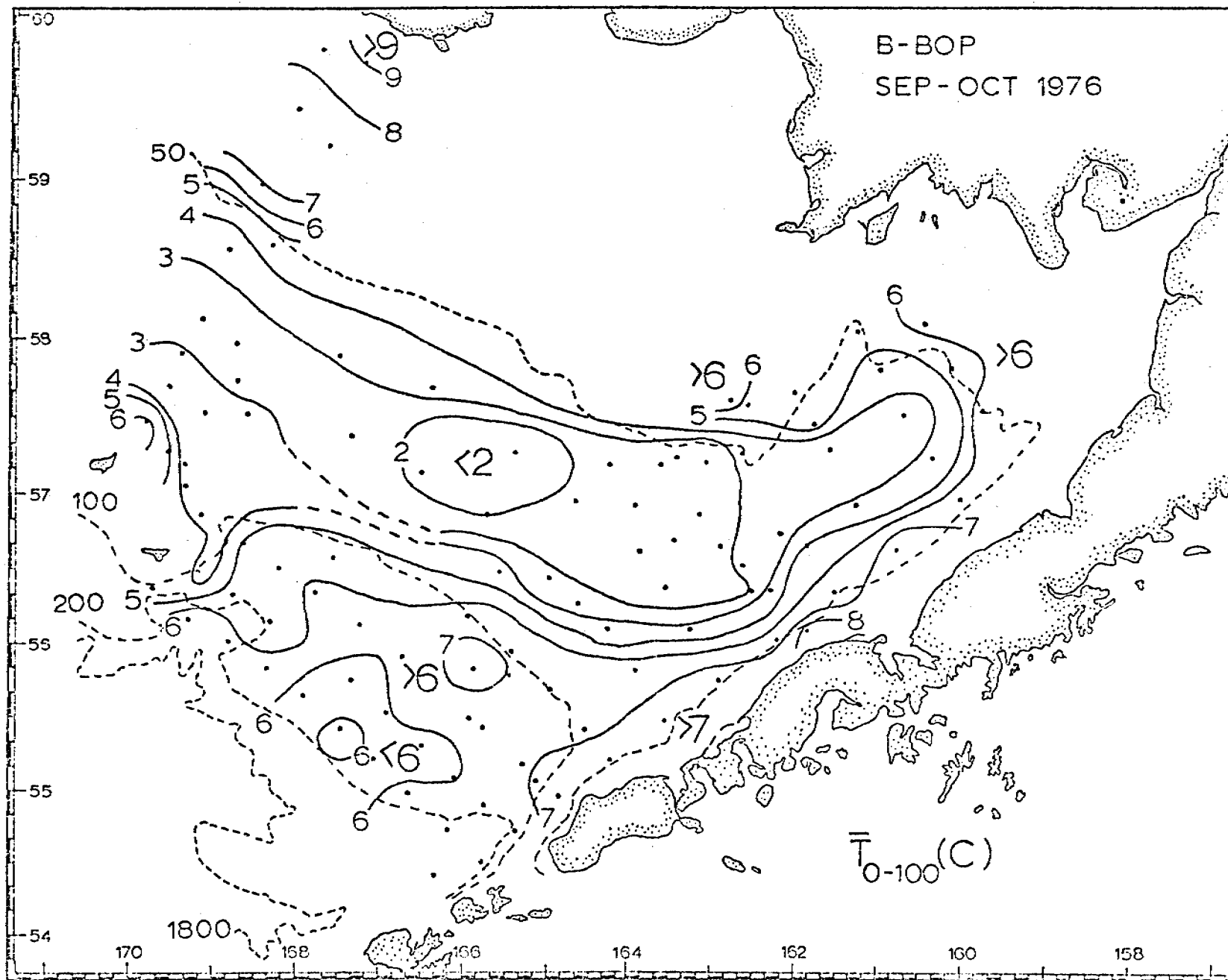


Figure 12. Vertical mean temperature, surface to 100 m or the bottom (whichever is shallower).

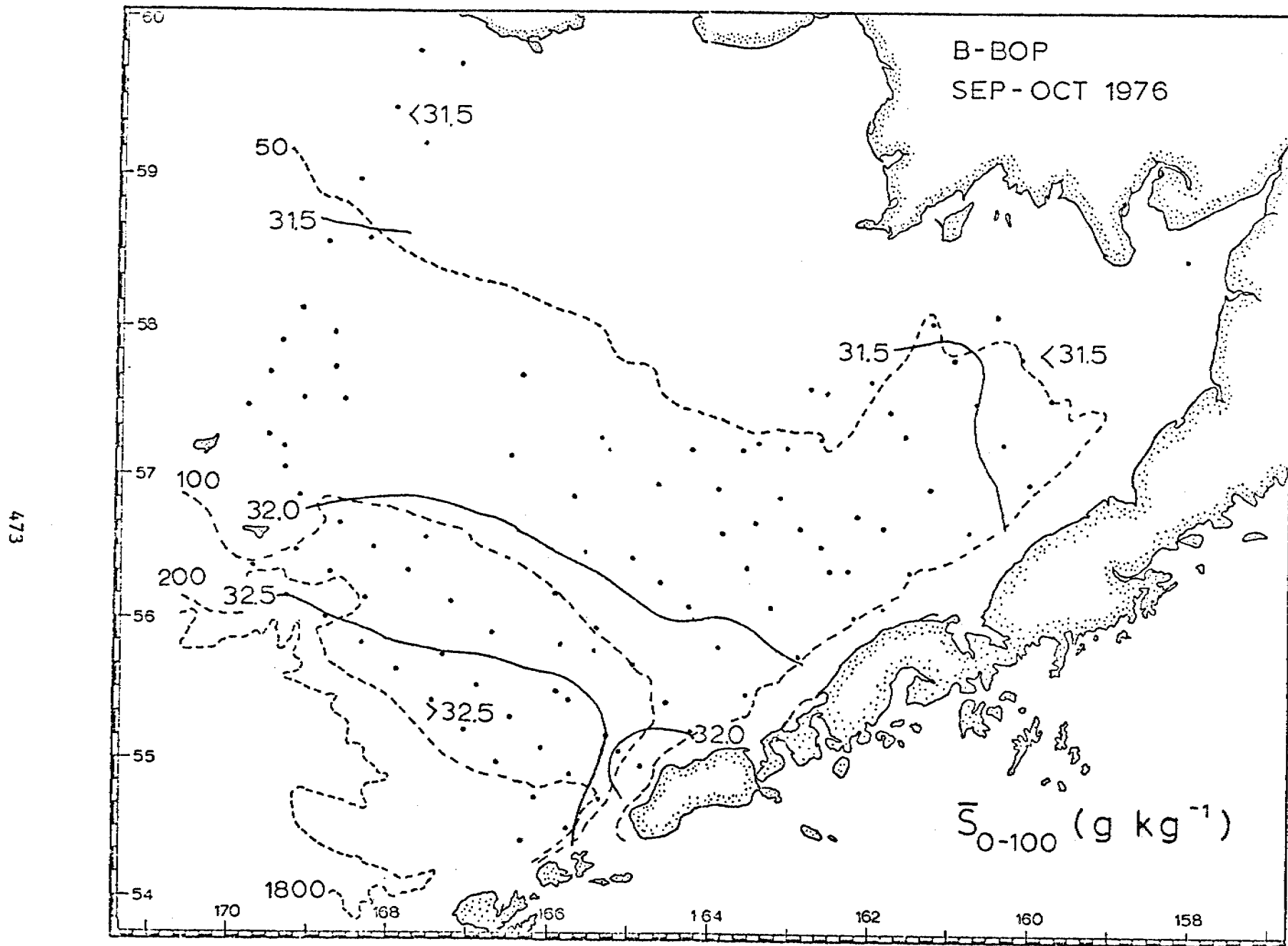


Figure 13. Vertical mean salinity, surface to 100 m or the bottom (whichever is shallower).

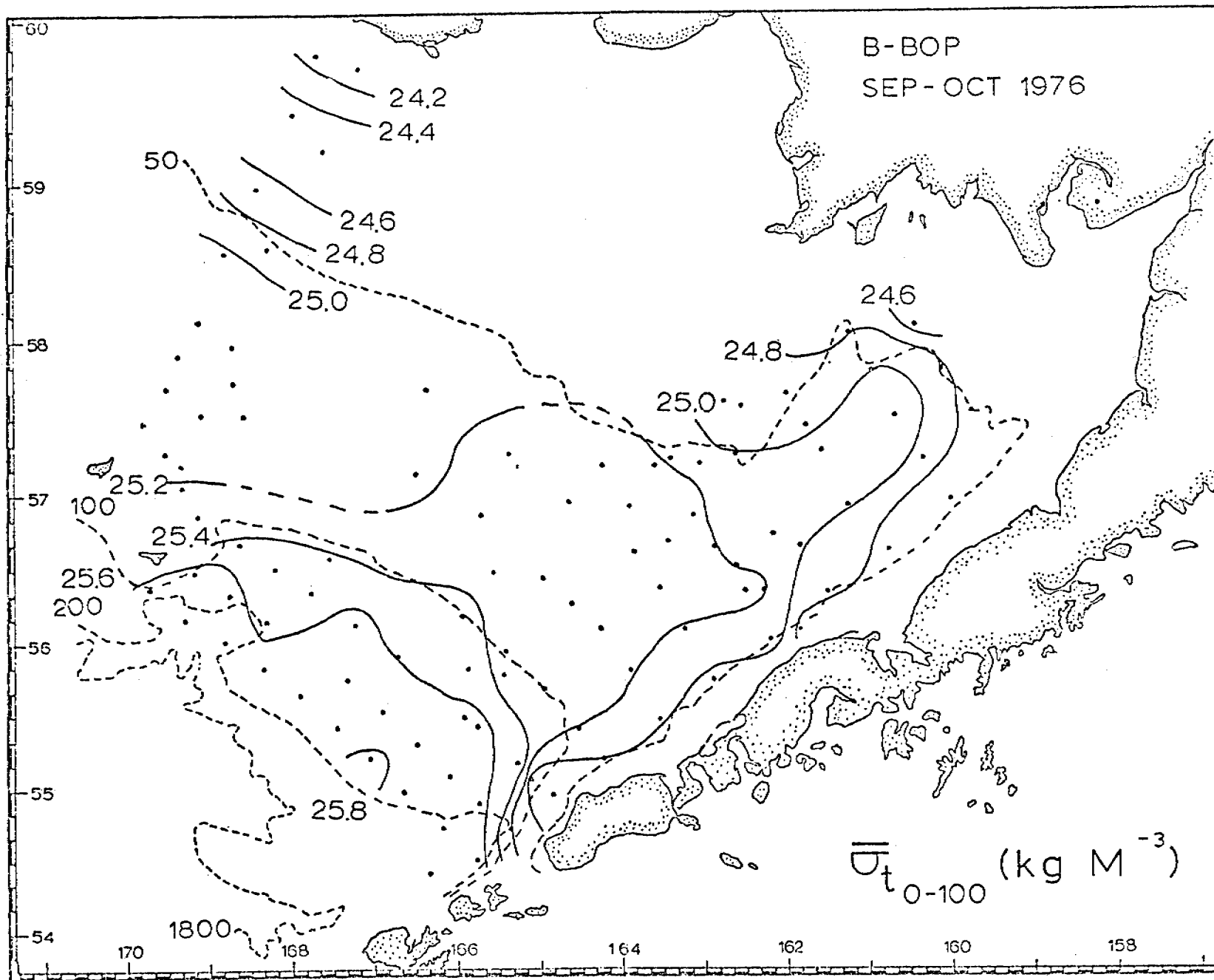


Figure 14. Vertical mean density, surface to 100 m or the bottom (whichever is shallower).

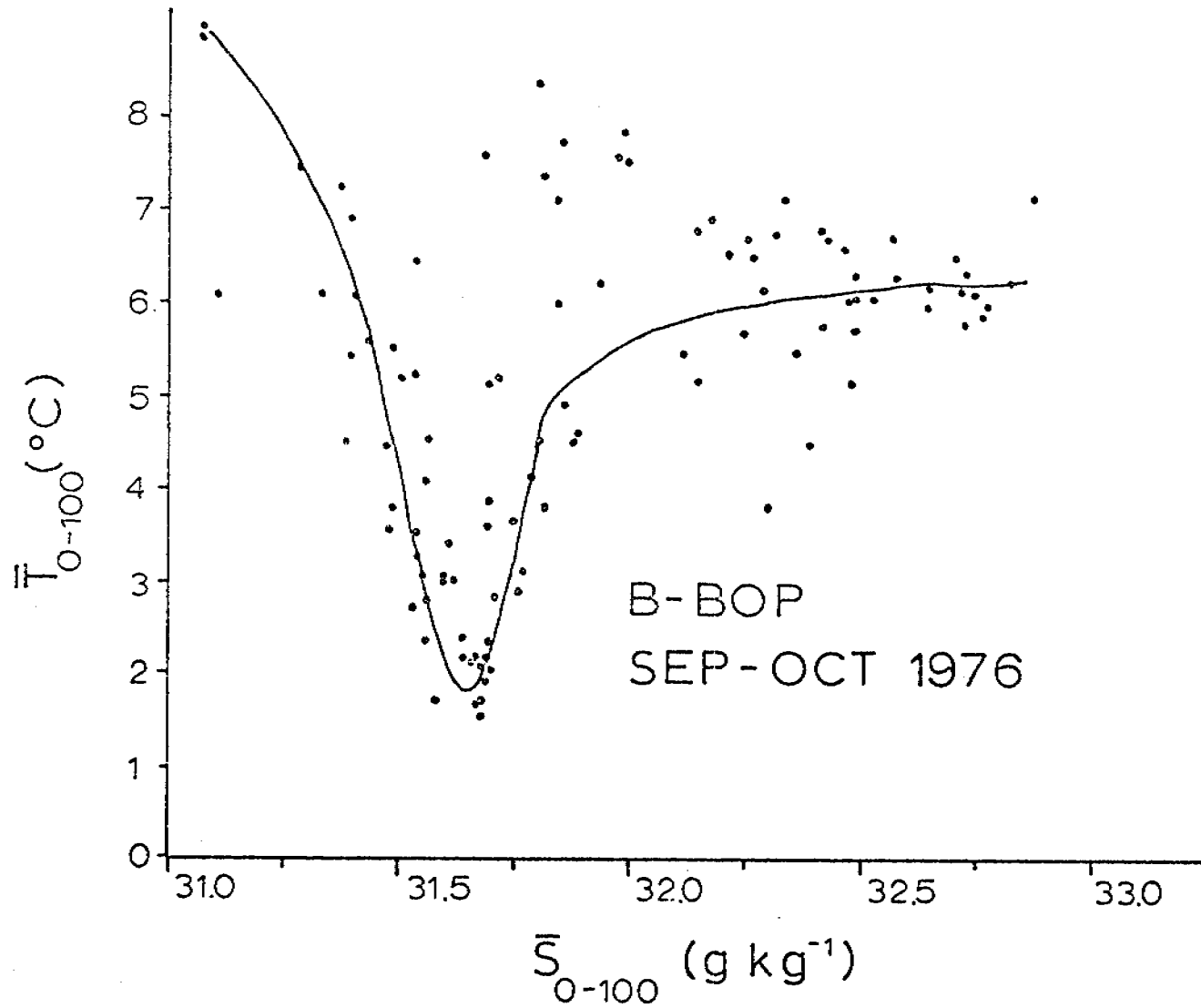


Figure 15. Correlation of mean temperature and salinity.
The line is drawn by eye.

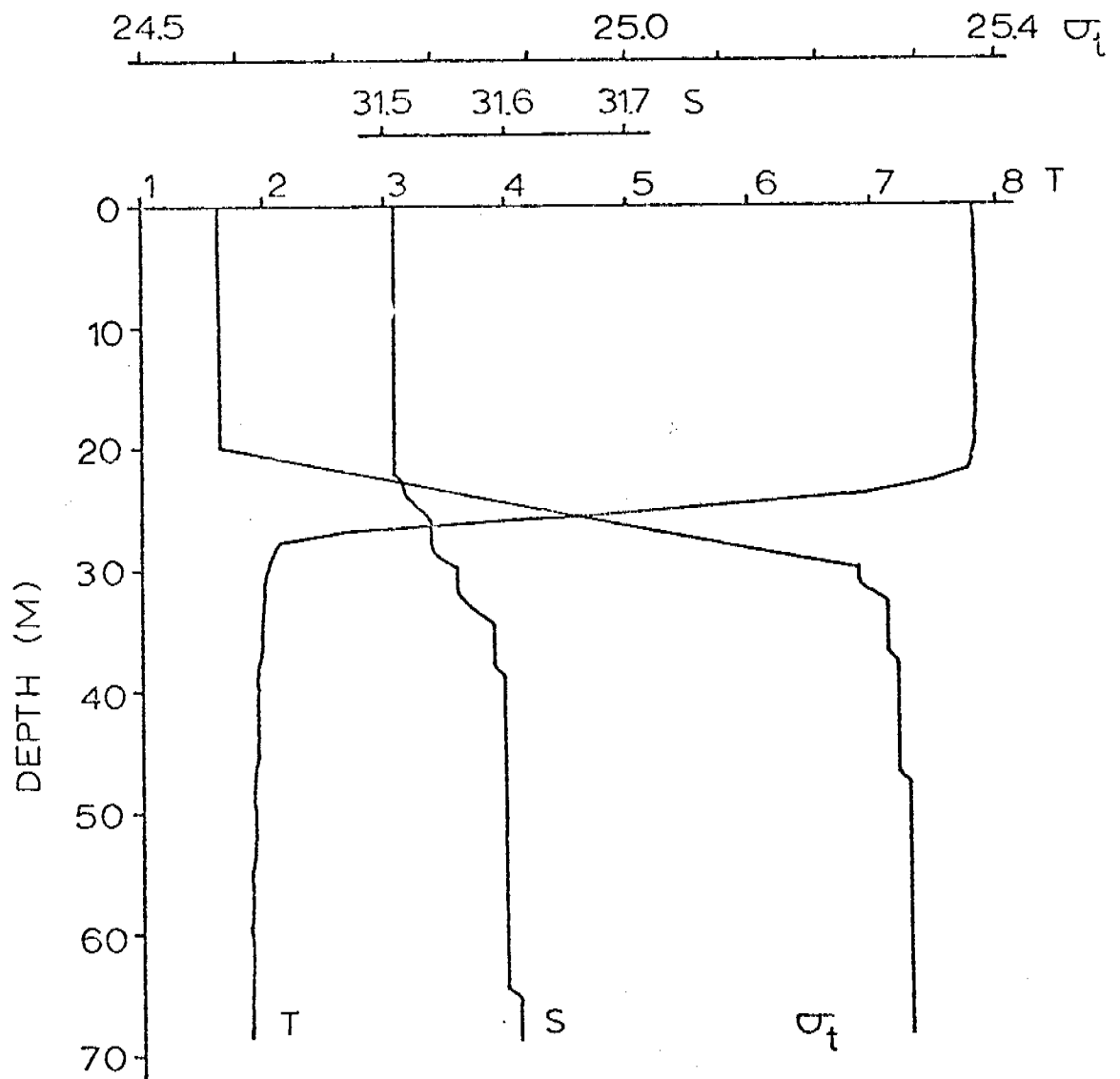


Figure 16. Vertical profiles at station 111, October 1976. (kg/m^3 , g/kg , and $^{\circ}\text{C}$).

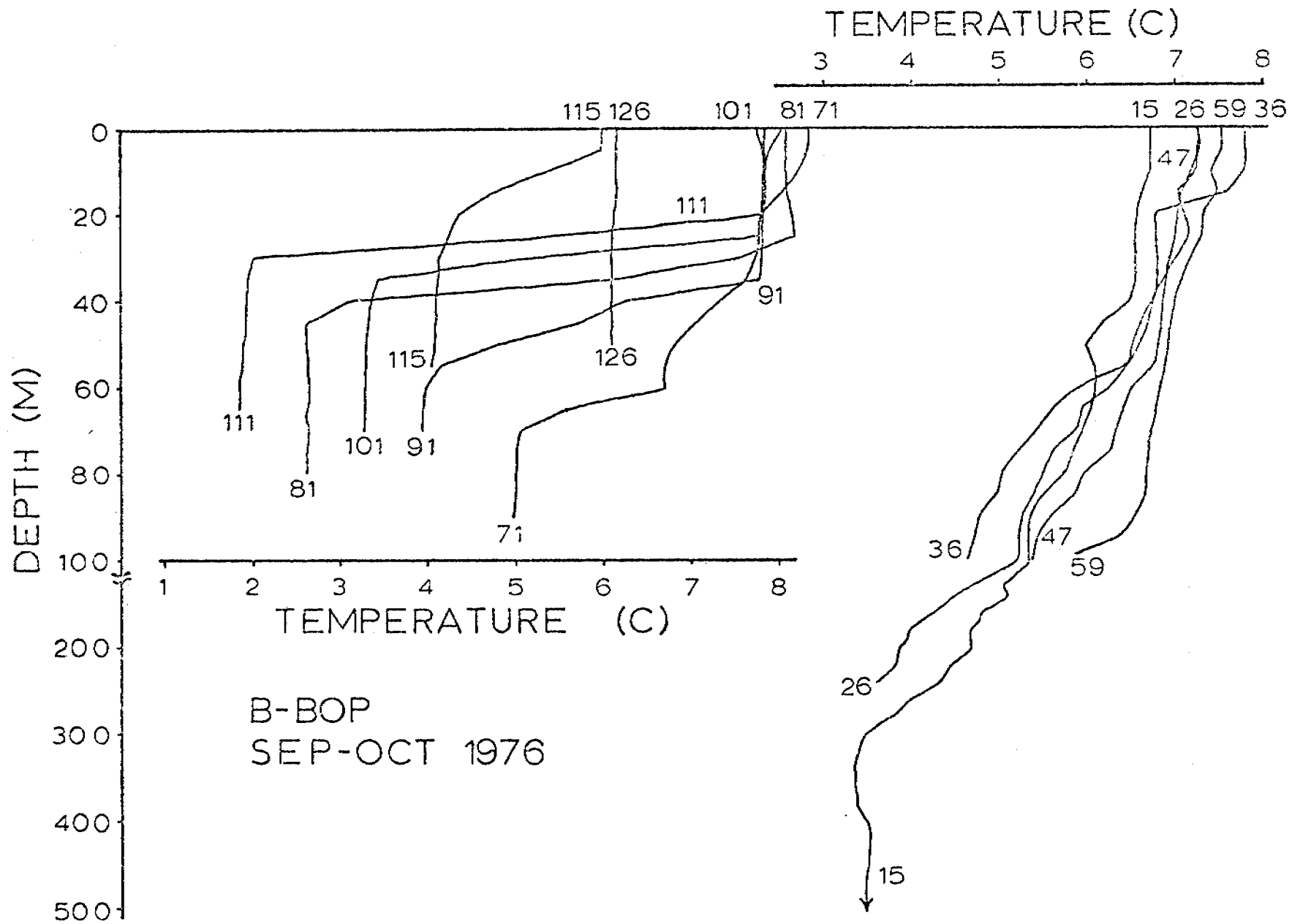


Figure 17. Temperature profiles (cf. Figures 18, 23, and 24).

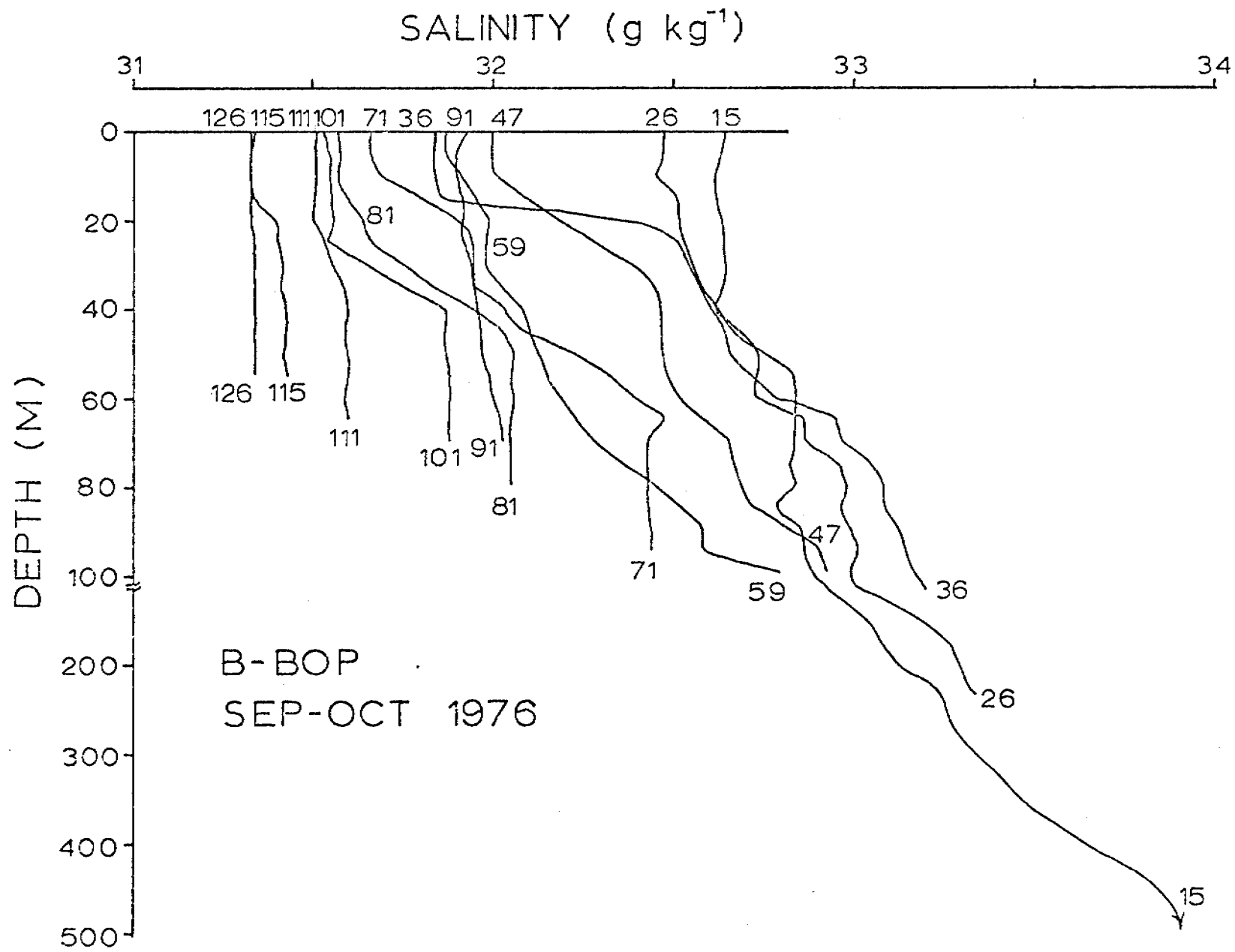


Figure 18. Salinity profiles (cf. Figures 17, 23, and 25).

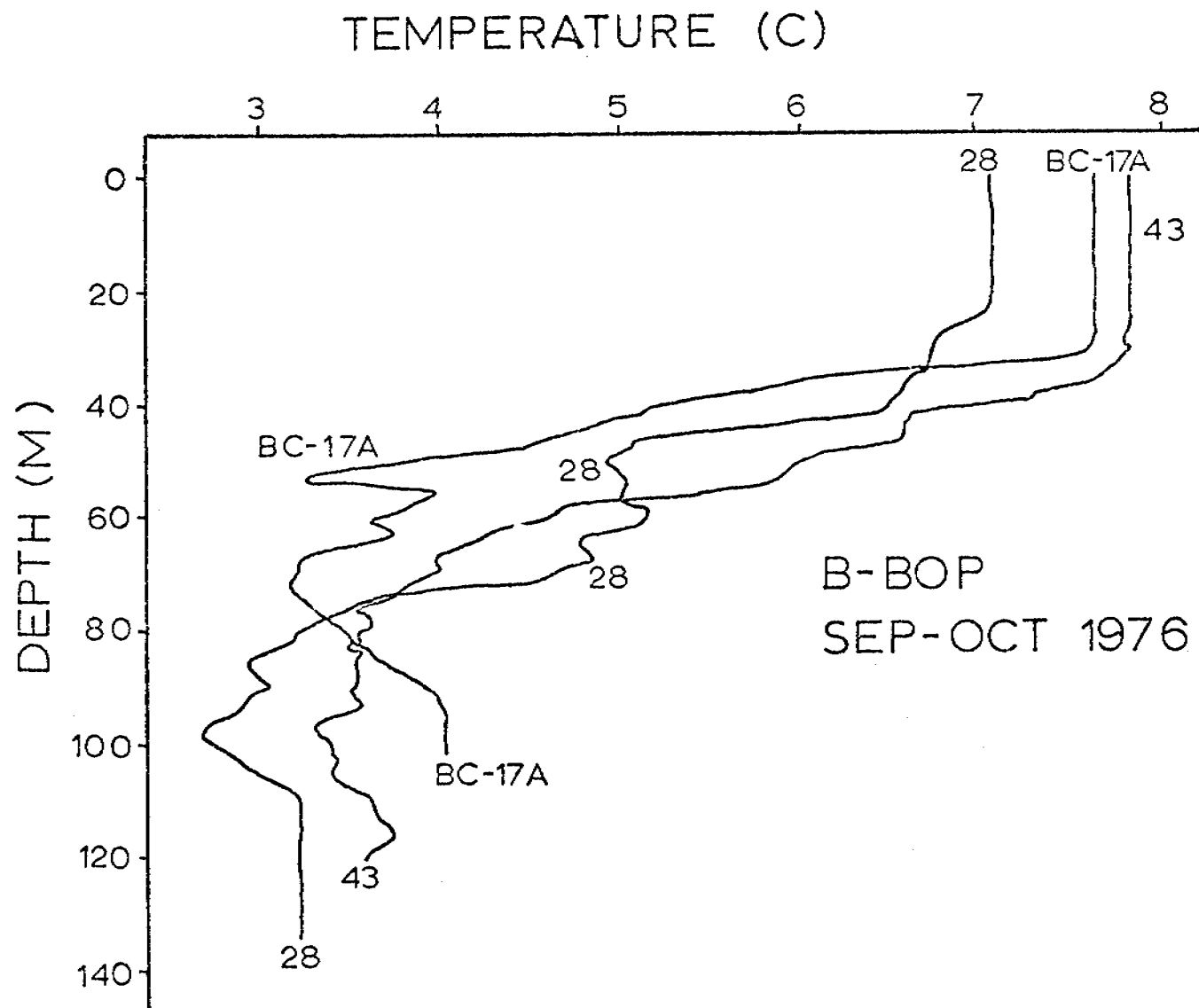


Figure 19. Finestructure profiles of temperature.

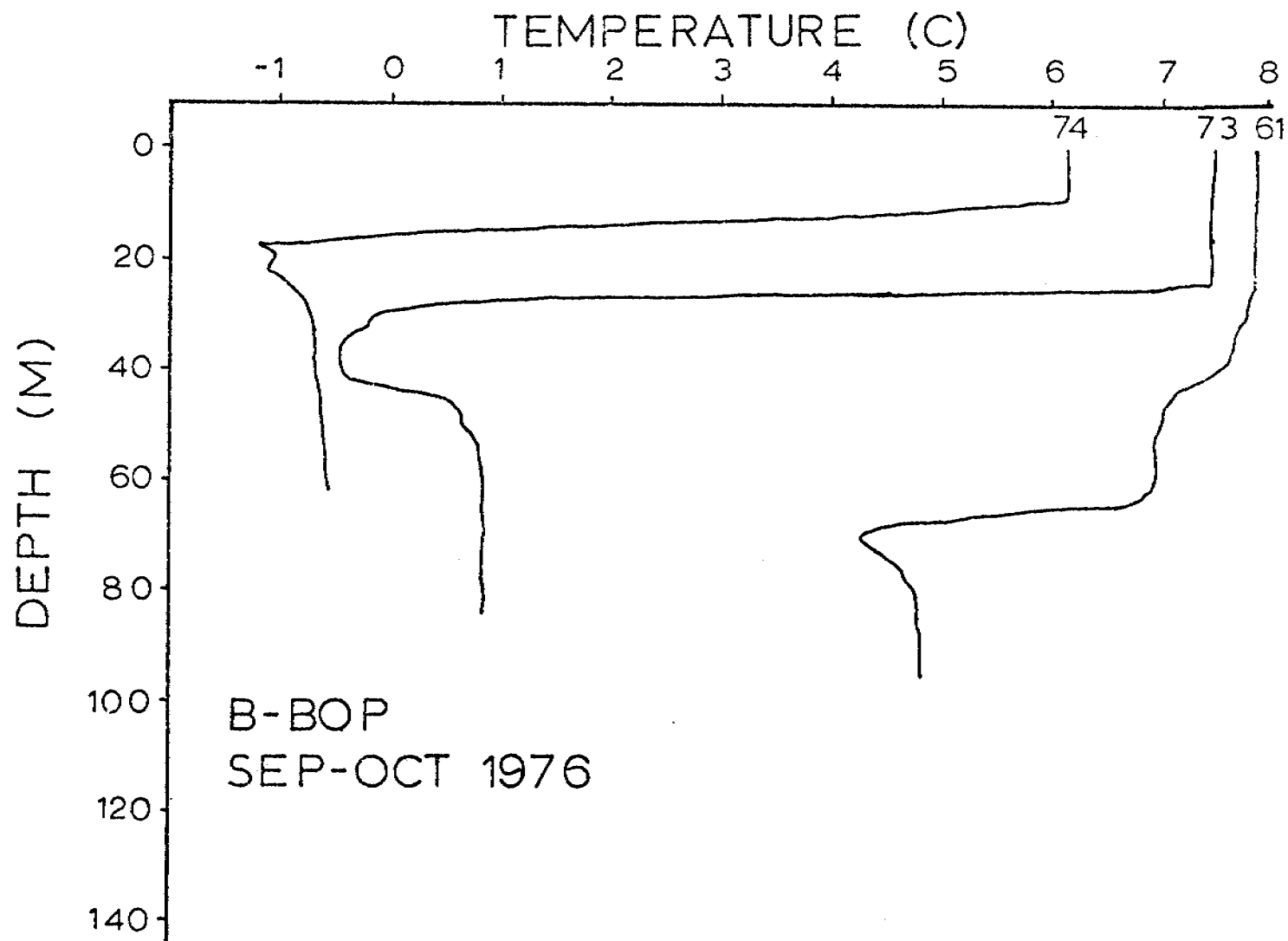


Figure 20. Temperature minimum profiles.

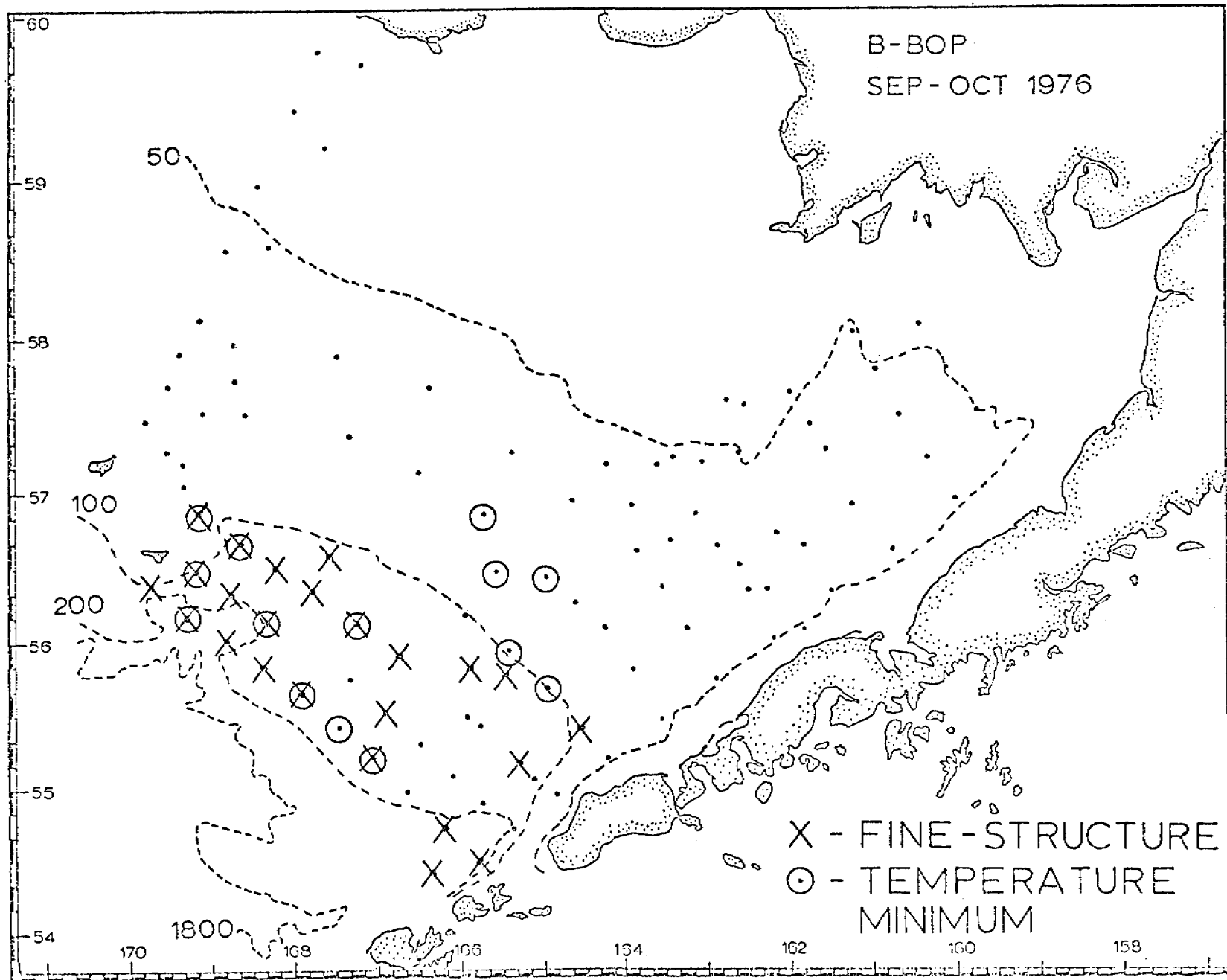


Figure 21. Distribution of finestructure (see Figures 19 and 20).

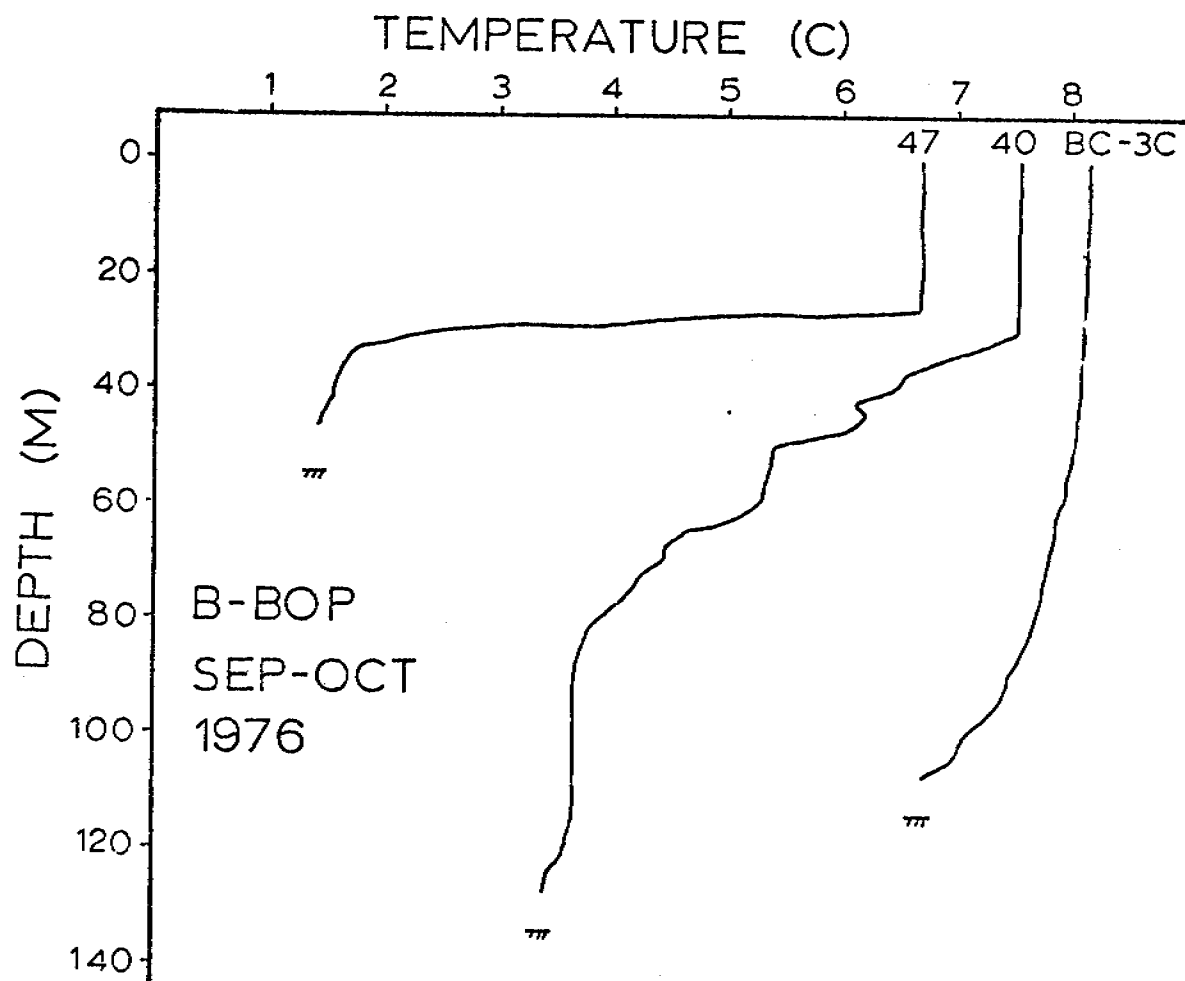


Figure 22. Temperature profiles without bottom mixed layers.

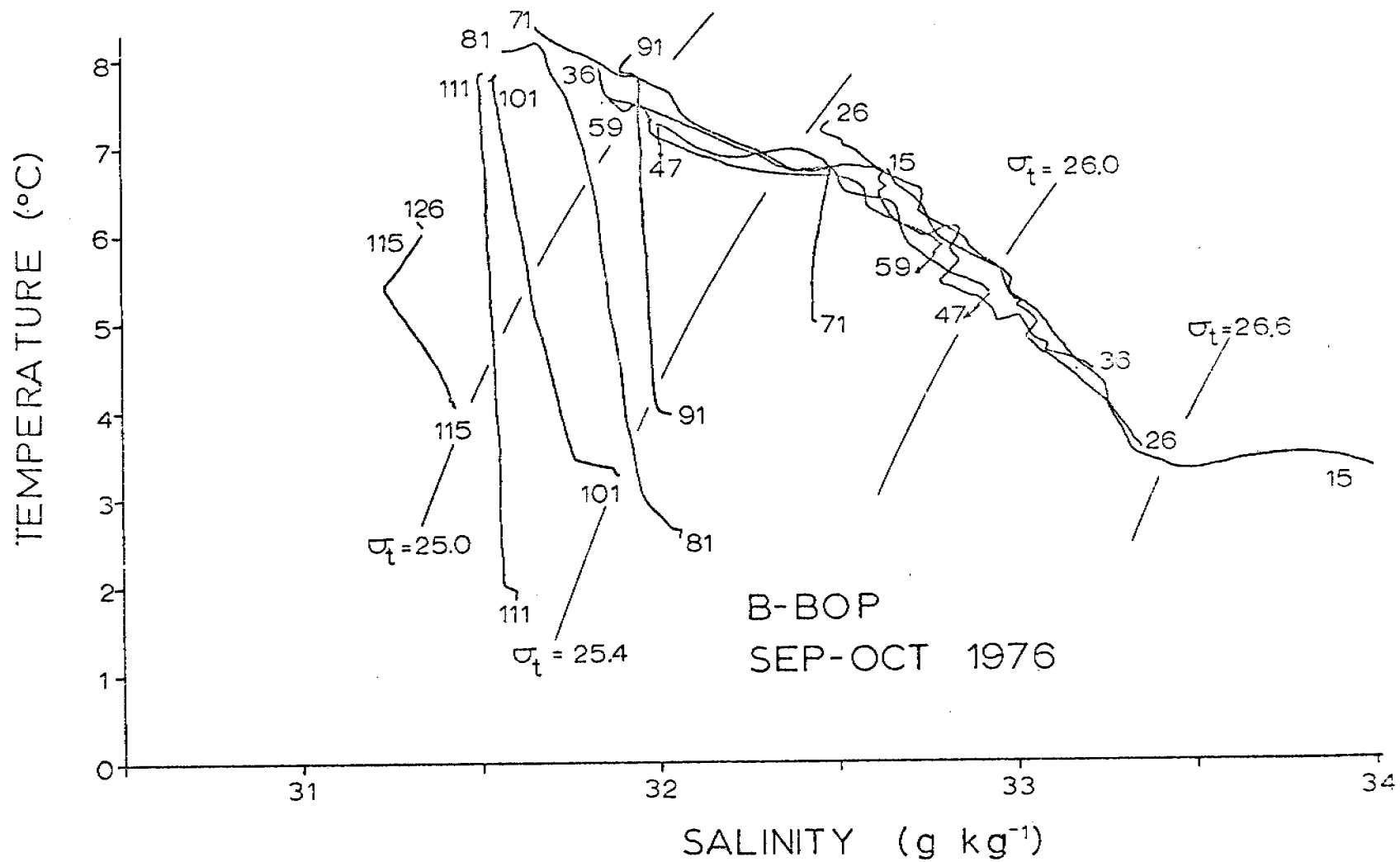


Figure 23. Temperature-salinity correlation (cf. Figures 17 and 18).

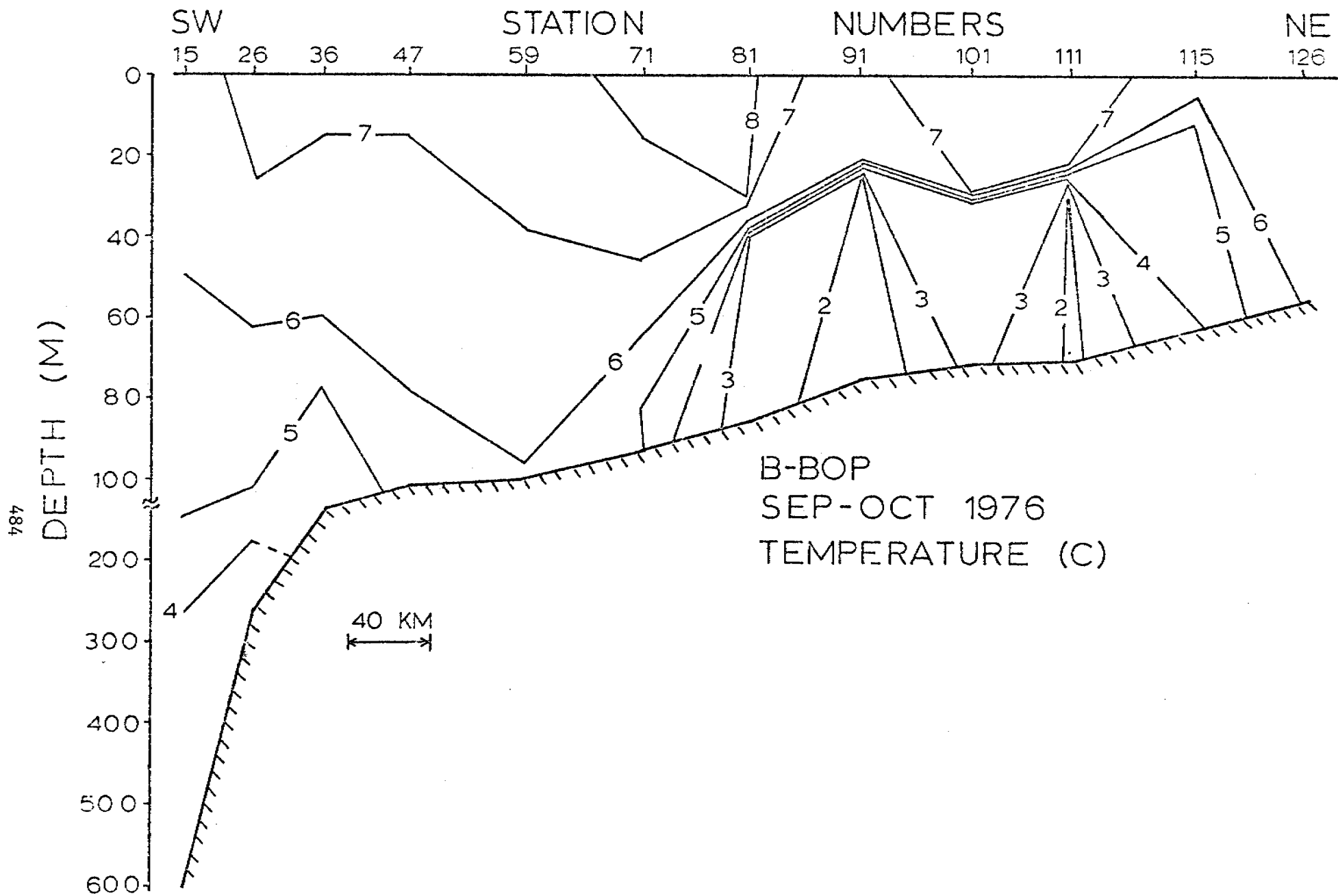


Figure 24. Temperature cross section into Bristol Bay (cf. Figures 25 and 26).

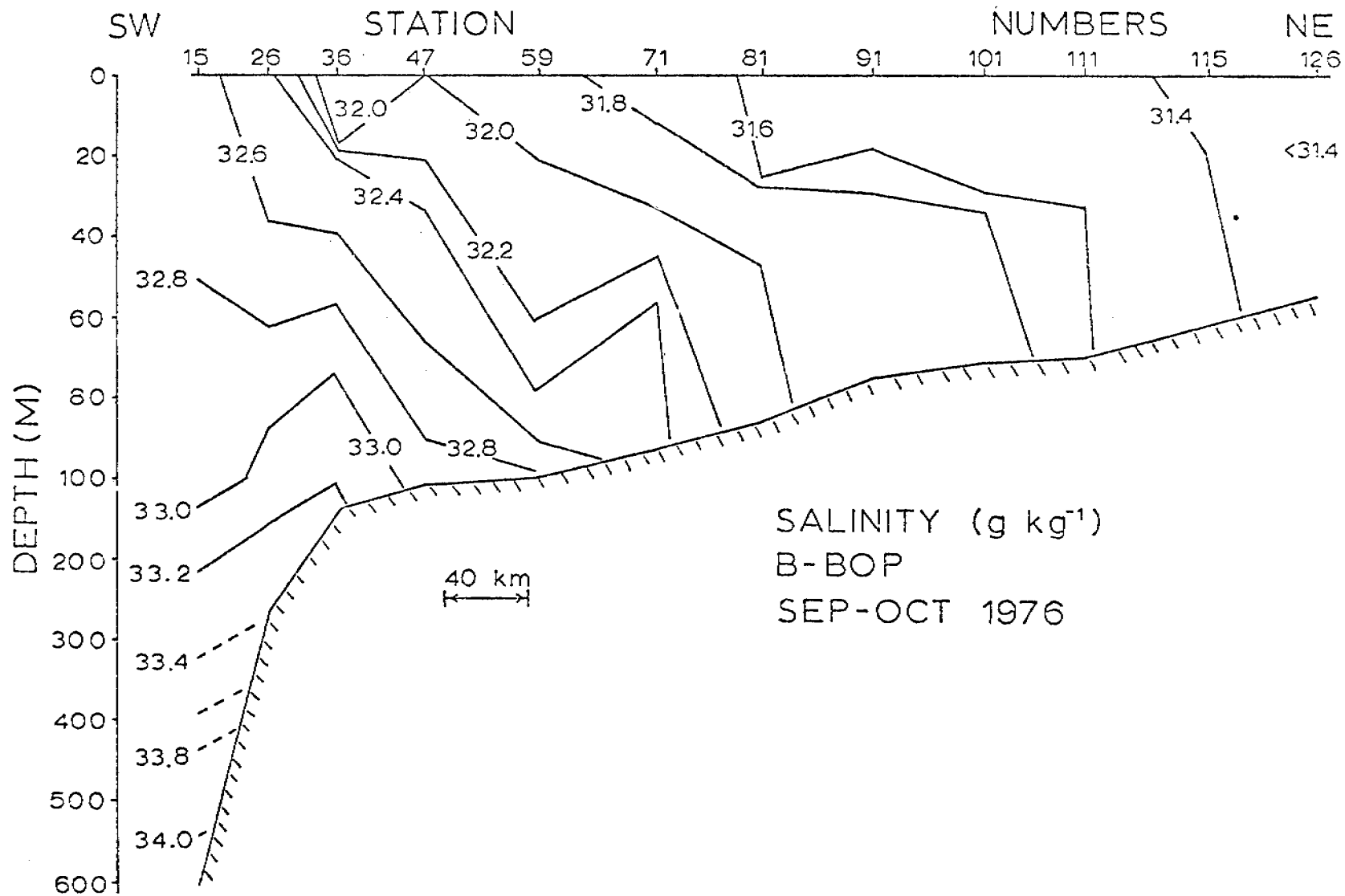


Figure 25. Salinity cross section into Bristol Bay (cf. Figures 24 and 26).

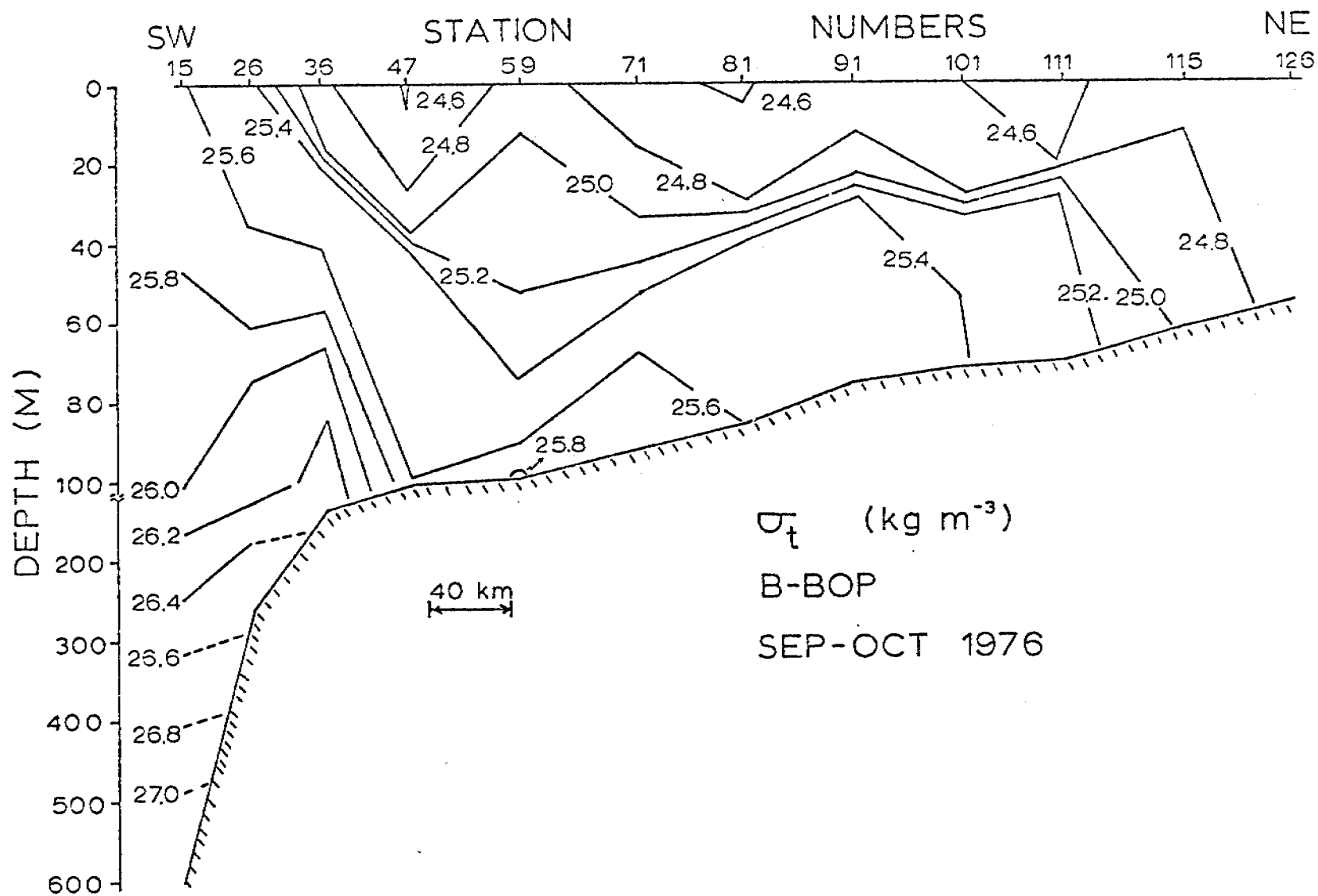


Figure 26. Density cross section into Bristol Bay (cf. Figures 24 and 25).

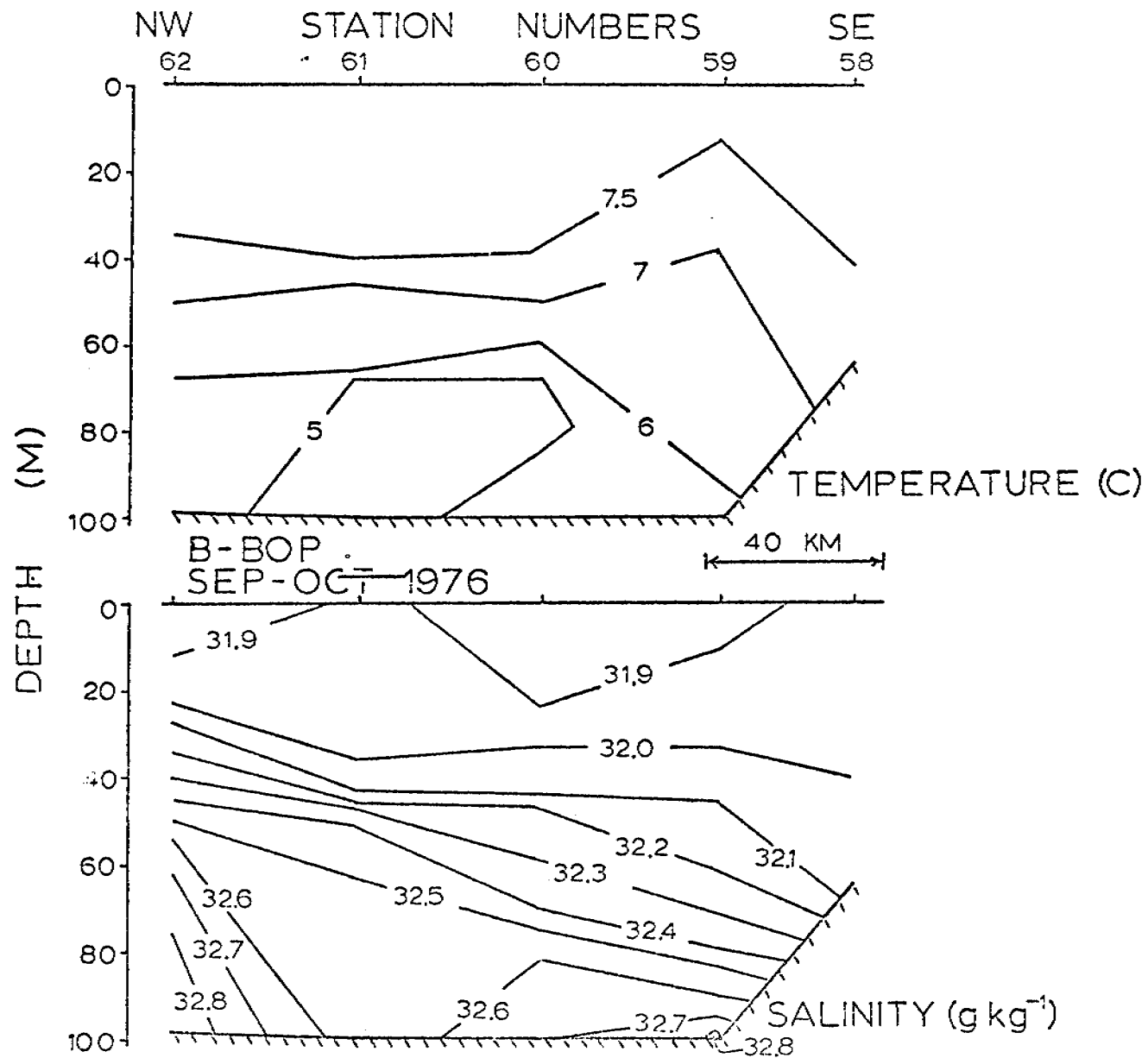


Figure 27. Cross sections along 100 m isobath.

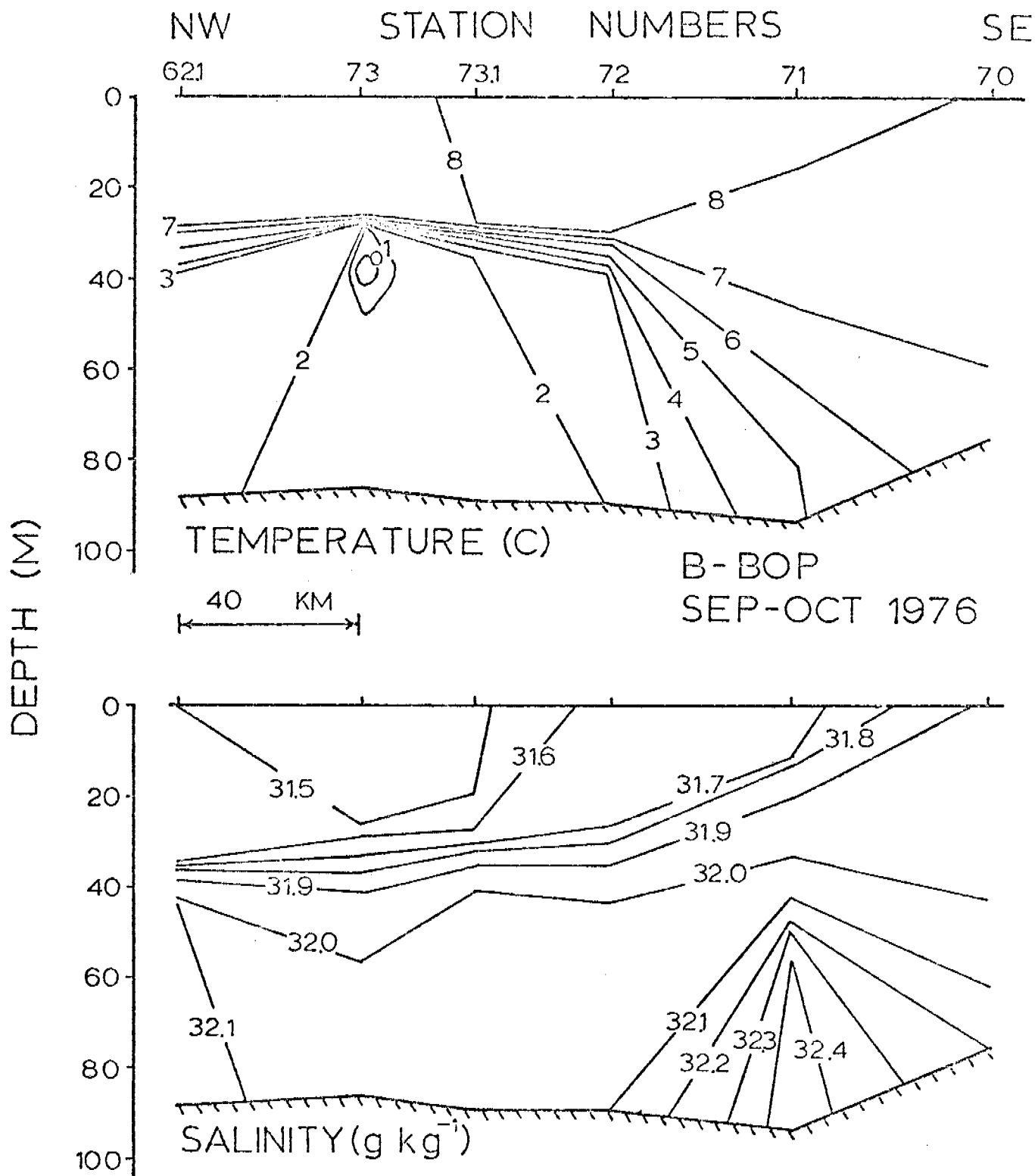


Figure 28. Cross sections along 85 m isobath.

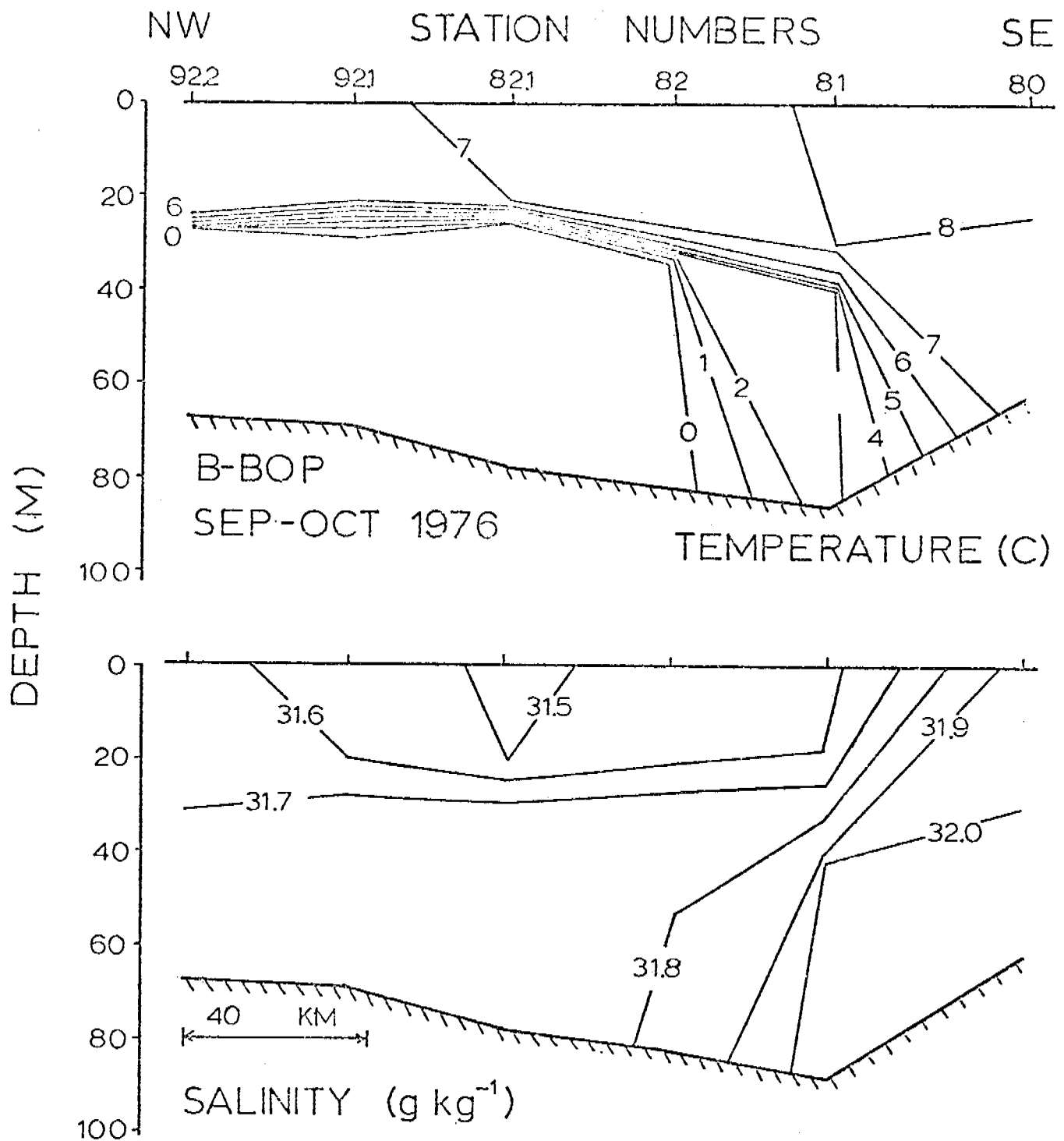


Figure 29. Cross sections along 75 m isobath.

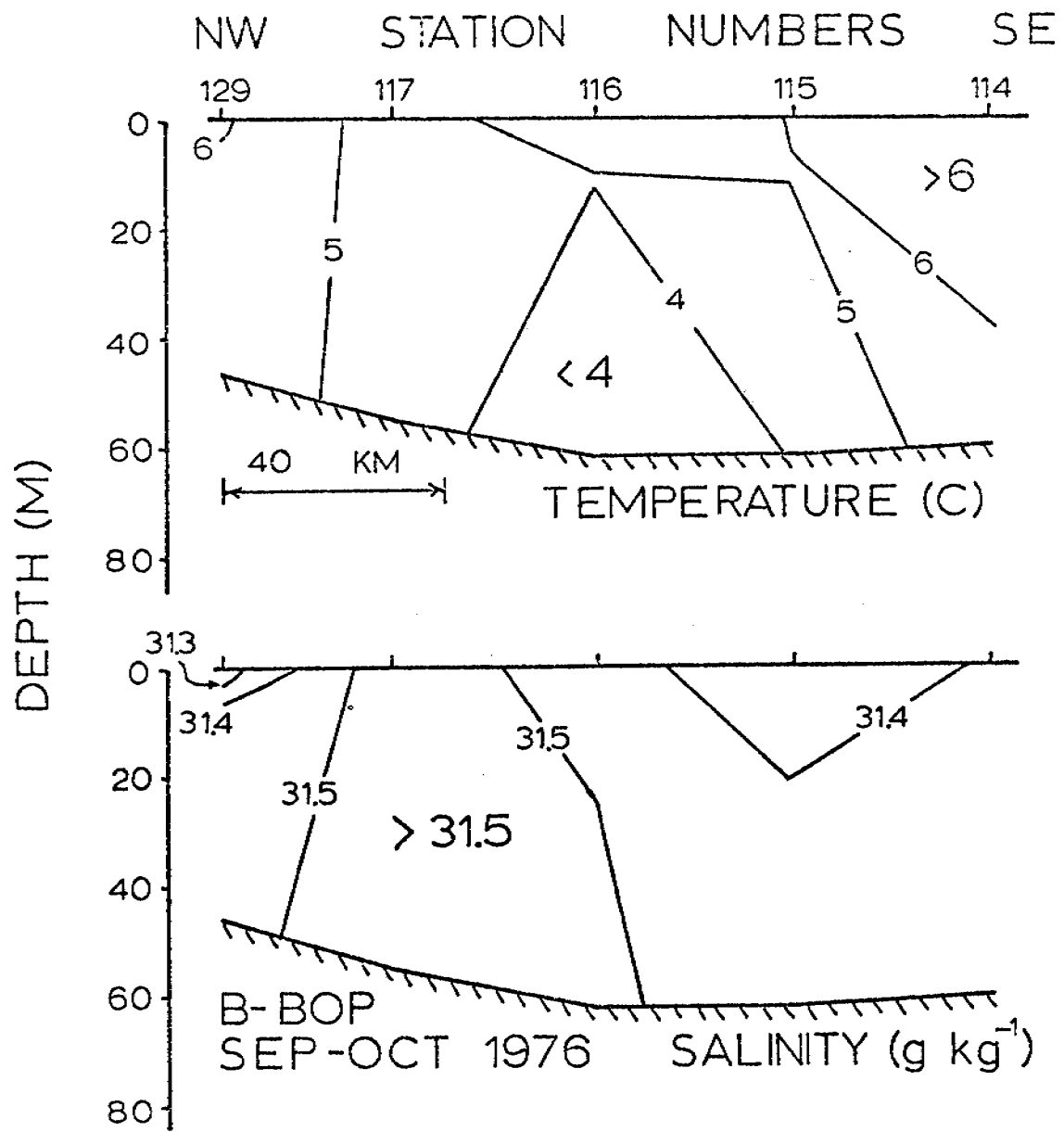


Figure 30. Cross sections across inner Bristol Bay.

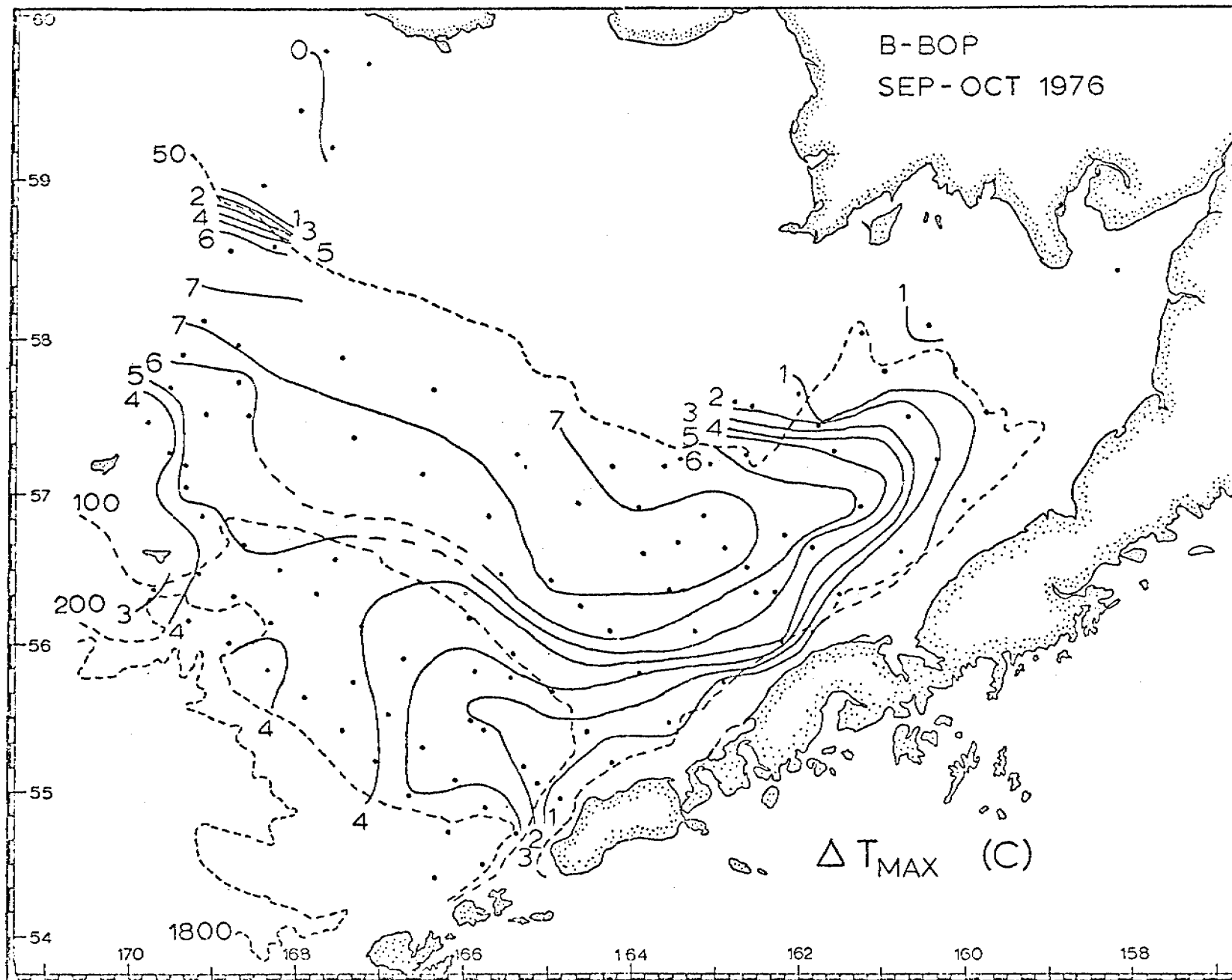


Figure 31. Maximum vertical temperature difference.

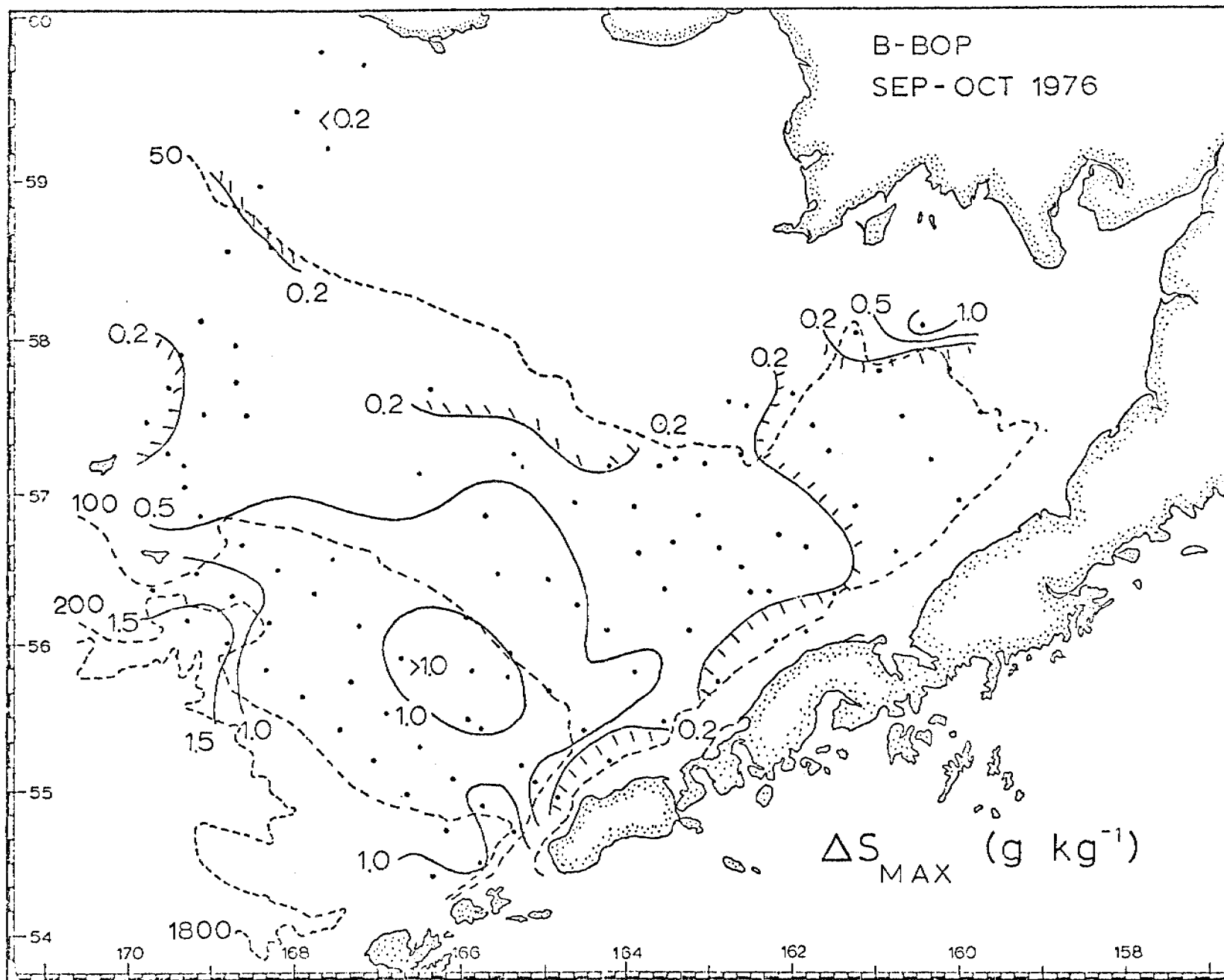


Figure 32. Maximum vertical salinity difference.

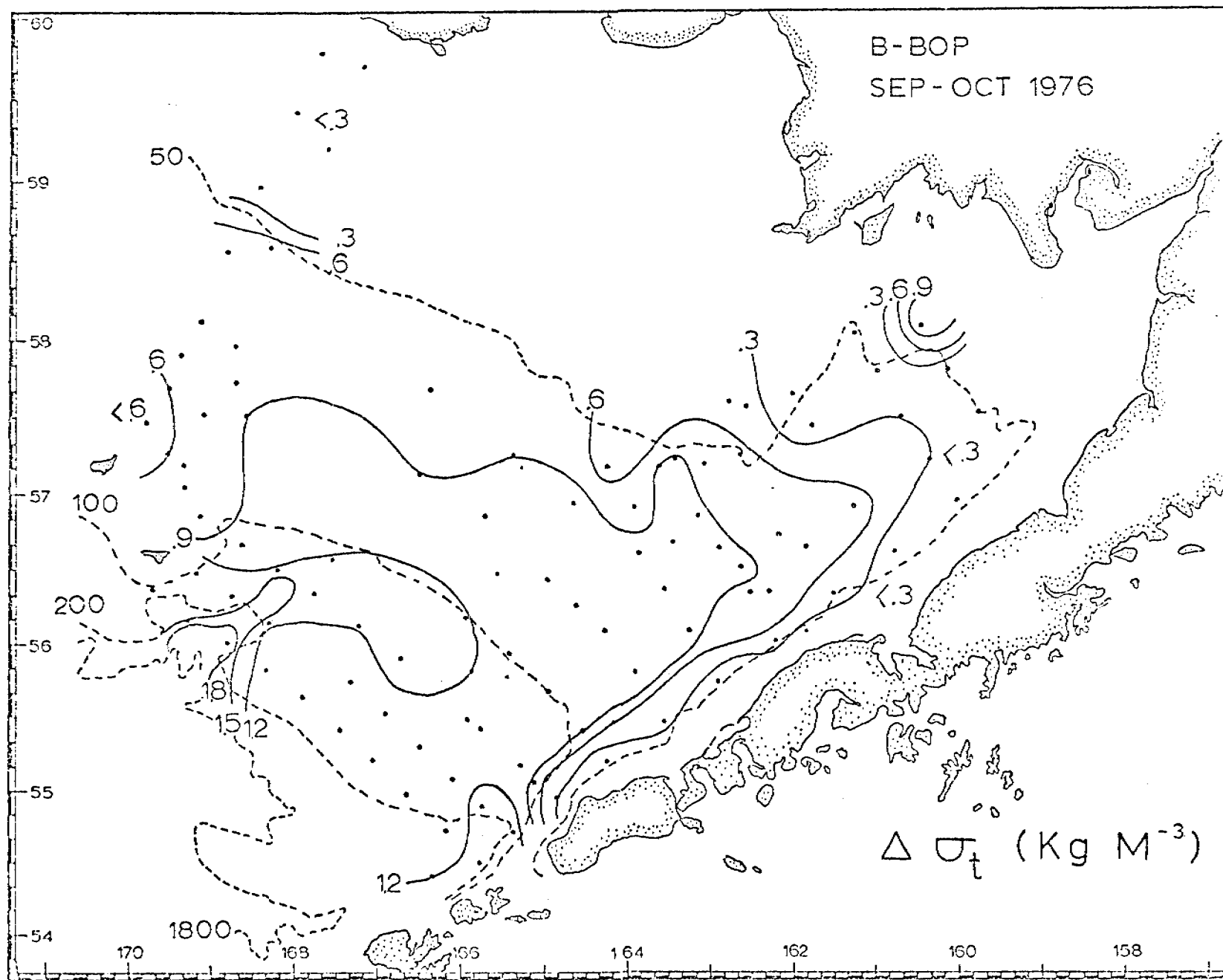


Figure 33. Maximum vertical density difference.

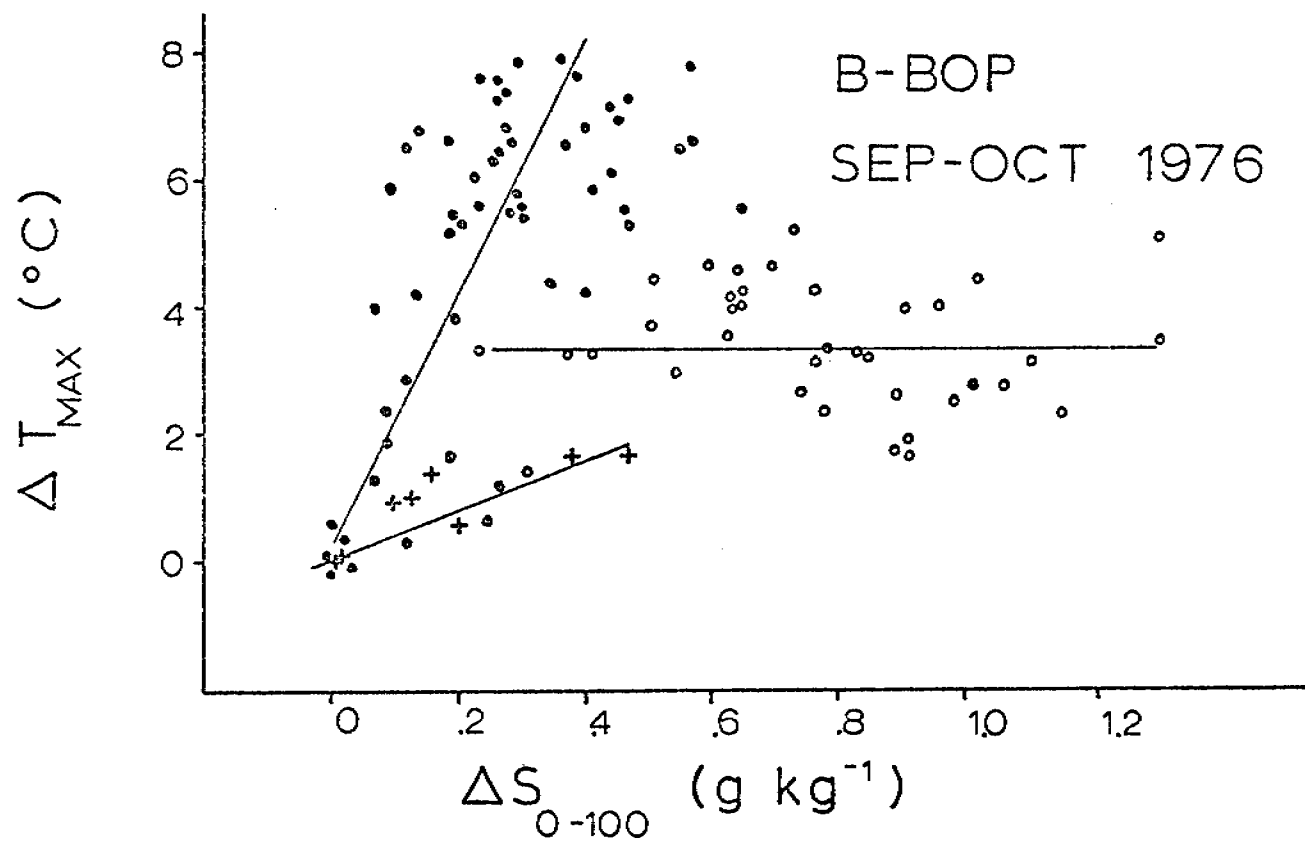


Figure 34. Correlation of maximum vertical temperature difference and vertical salinity difference (100 m or bottom minus surface). The crosses are stations <50 m depth (coastal), the solid circles for stations 50 m ≤ depth < 100 m (central shelf), and the open circles for stations ≥ 100 m (shelf break).

B-BOP
SEP - OCT 1976

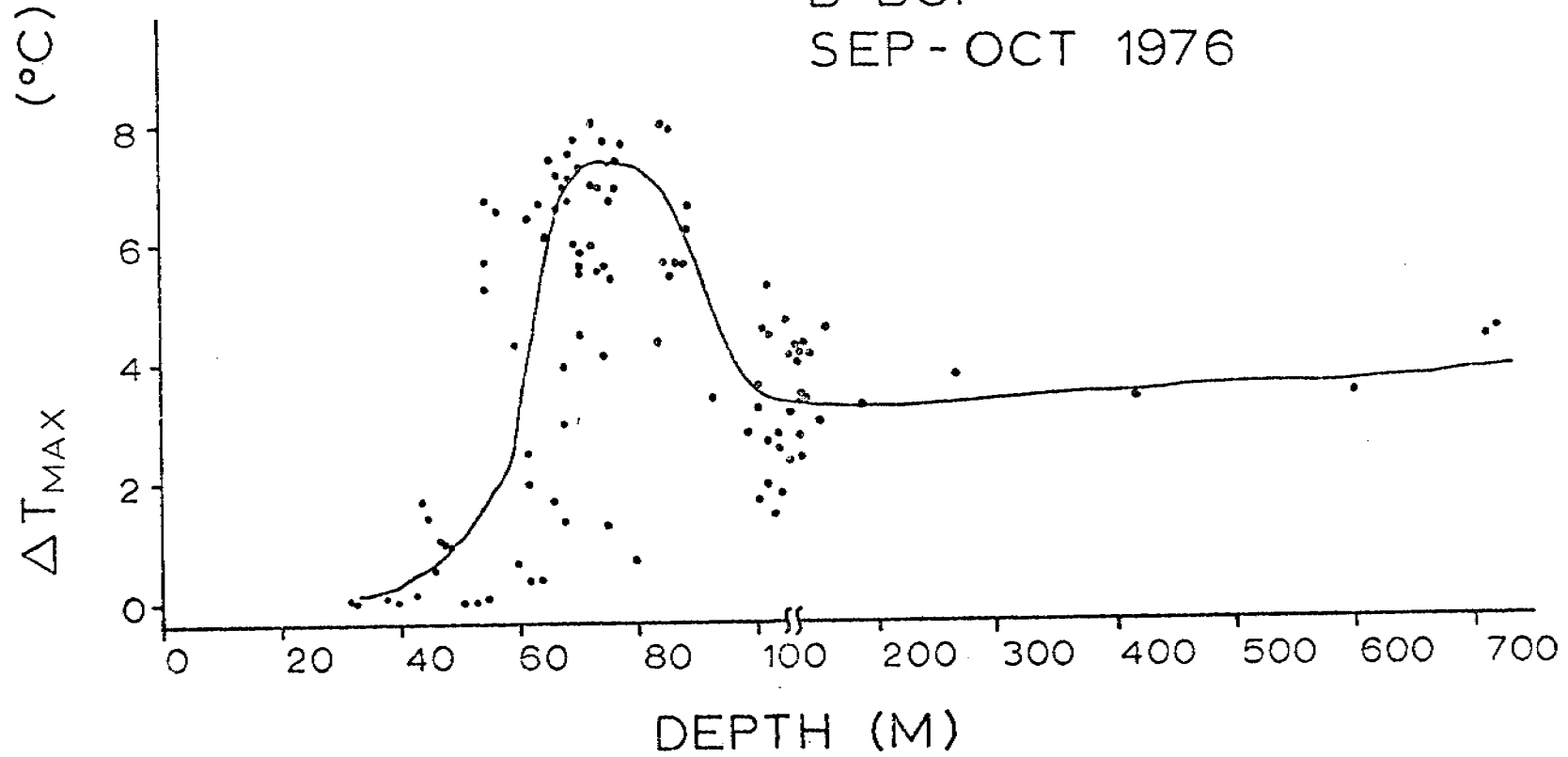


Figure 35. Correlation of maximum vertical temperature difference and depth. The line is drawn by eye. Note scale change at 100 m depth.

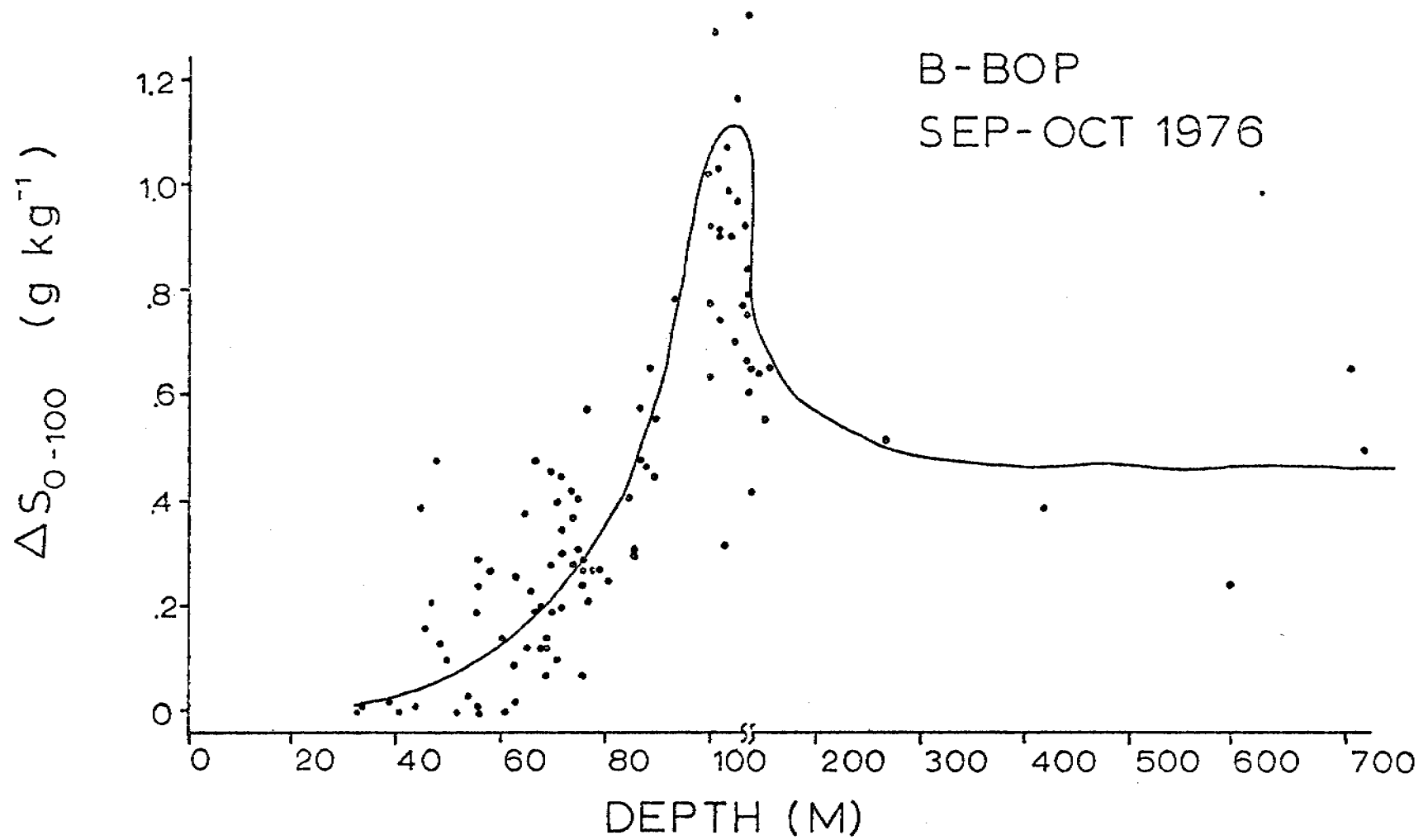


Figure 36. Correlation of vertical salinity difference (100 m or bottom minus surface) versus depth. The line is drawn by eye. Note scale change at 100 m depth.

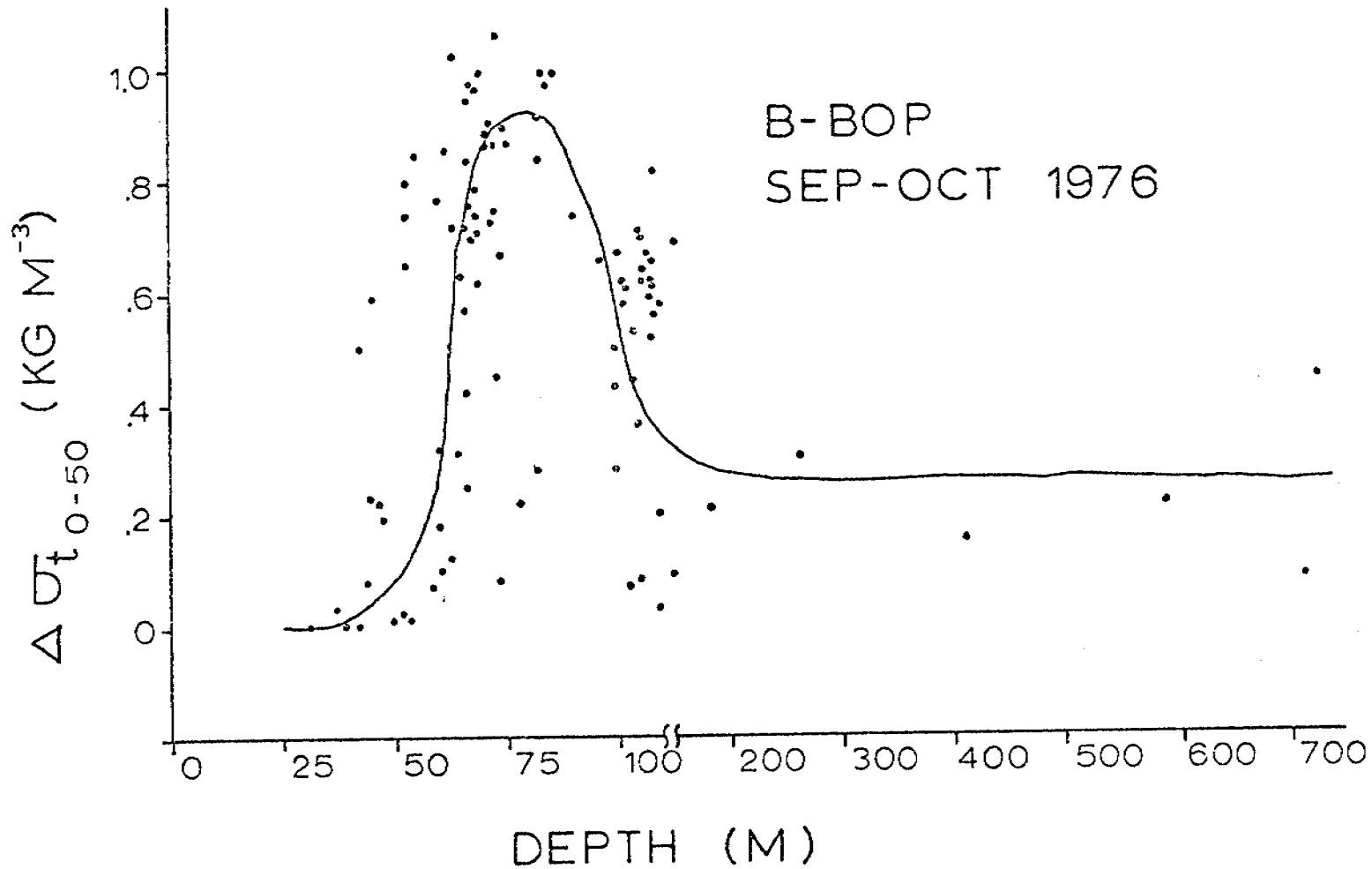


Figure 37. Correlation of vertical density difference (50 m or bottom minus surface) versus depth. The line is drawn by eye. Note scale change at 100 m.

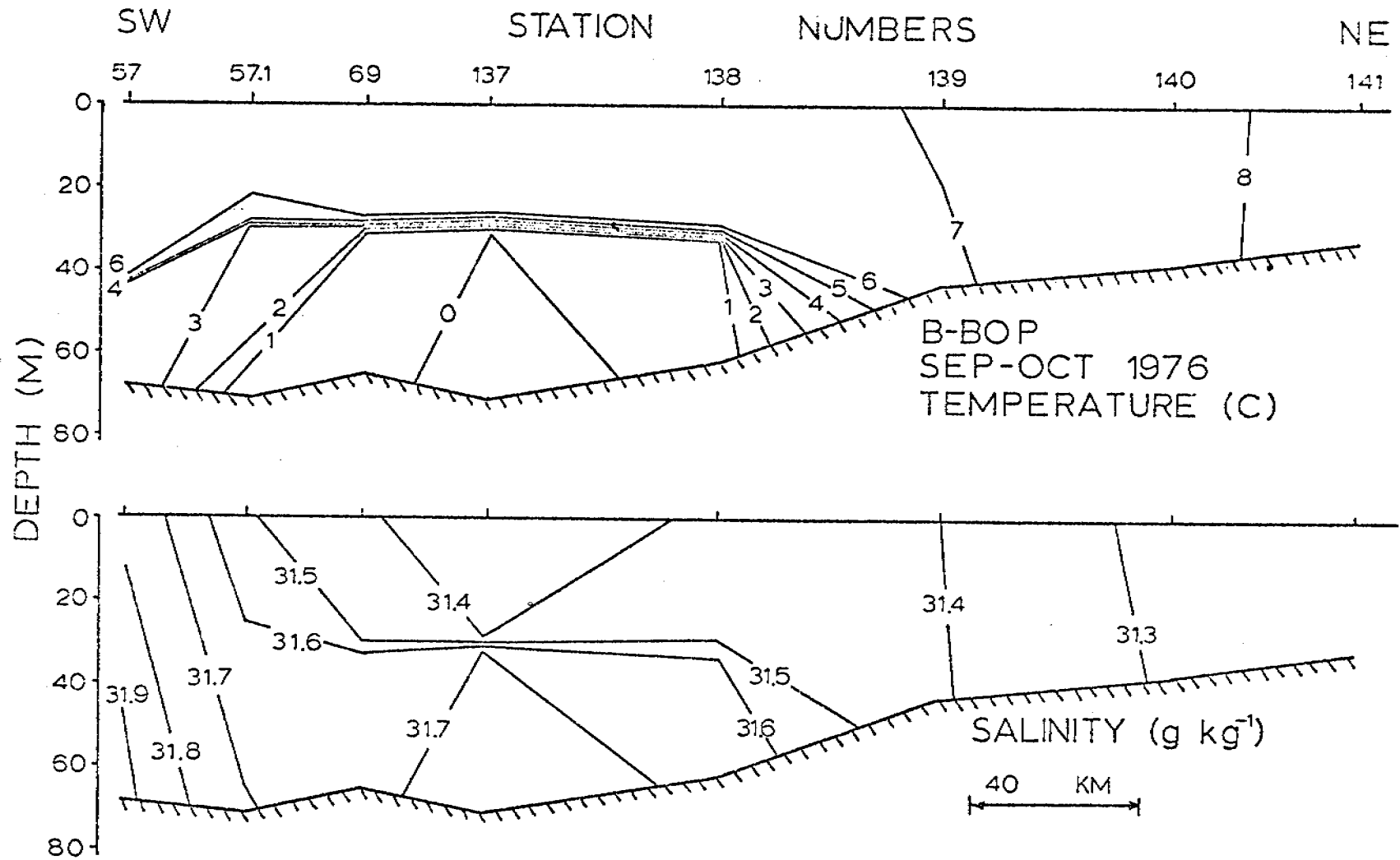


Figure 38. Sections across the front.

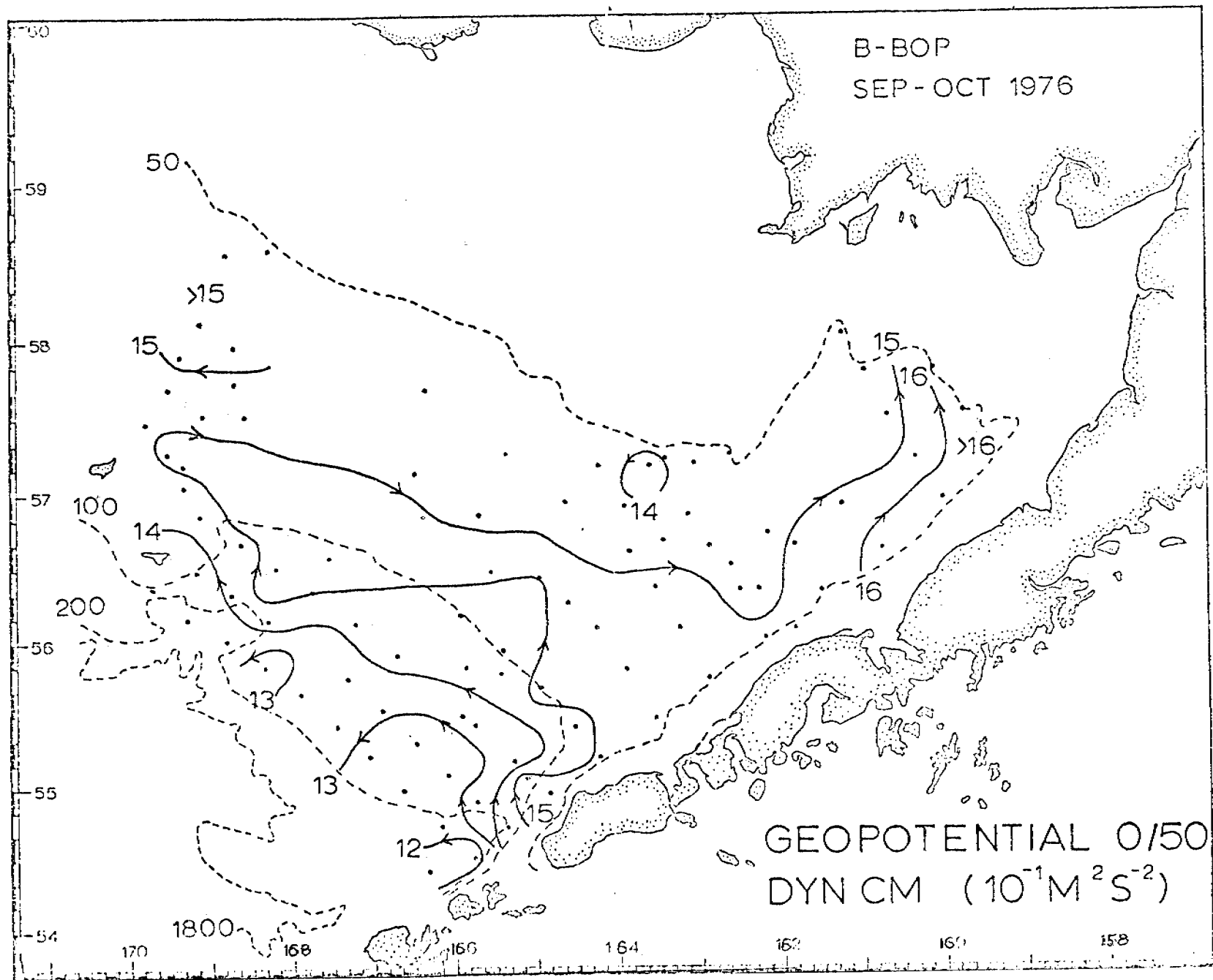


Figure 39. Geopotential, 0 over 50 decibars.

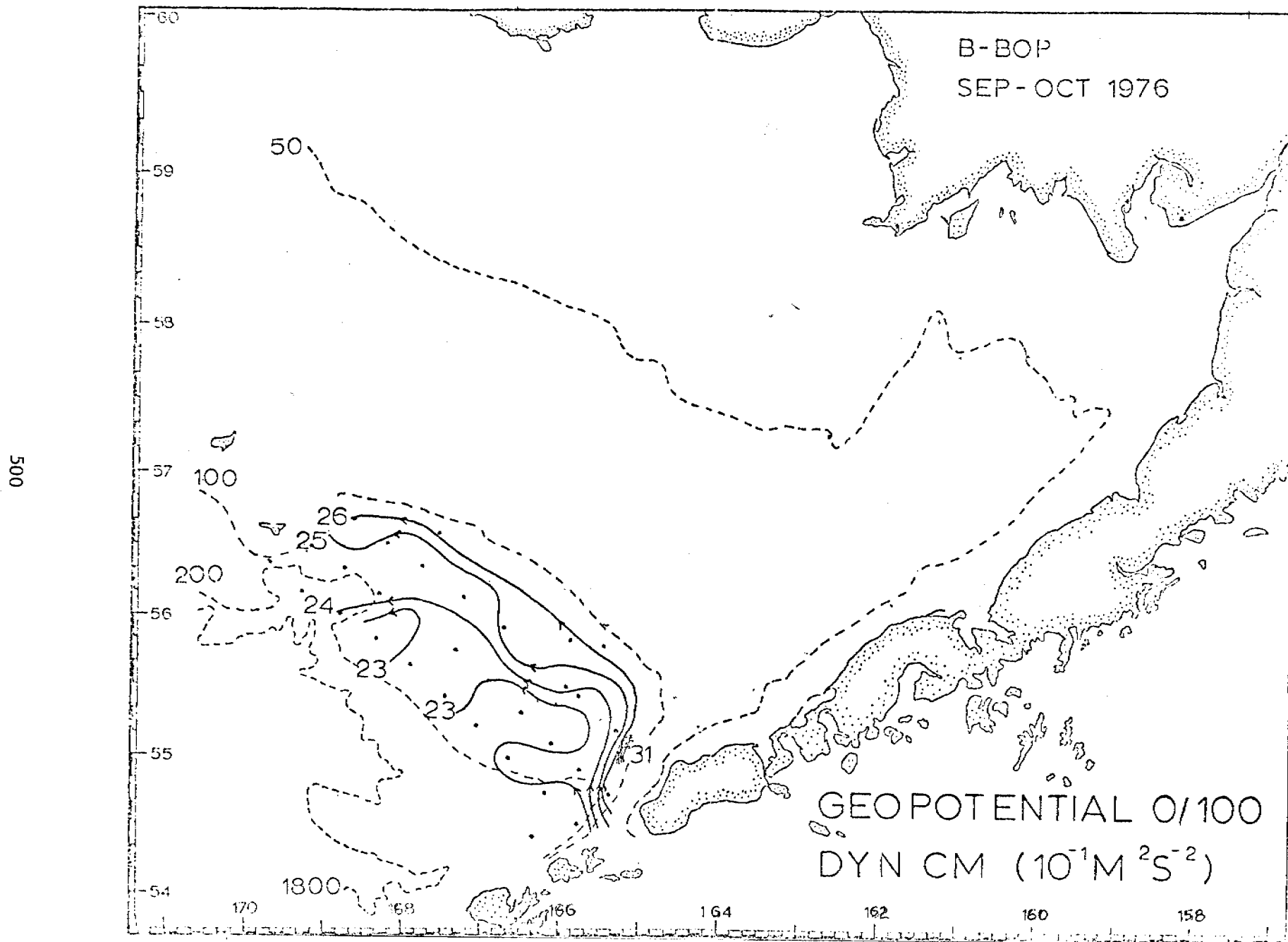


Figure 40. Geopotential, 0 over 100 decibars.

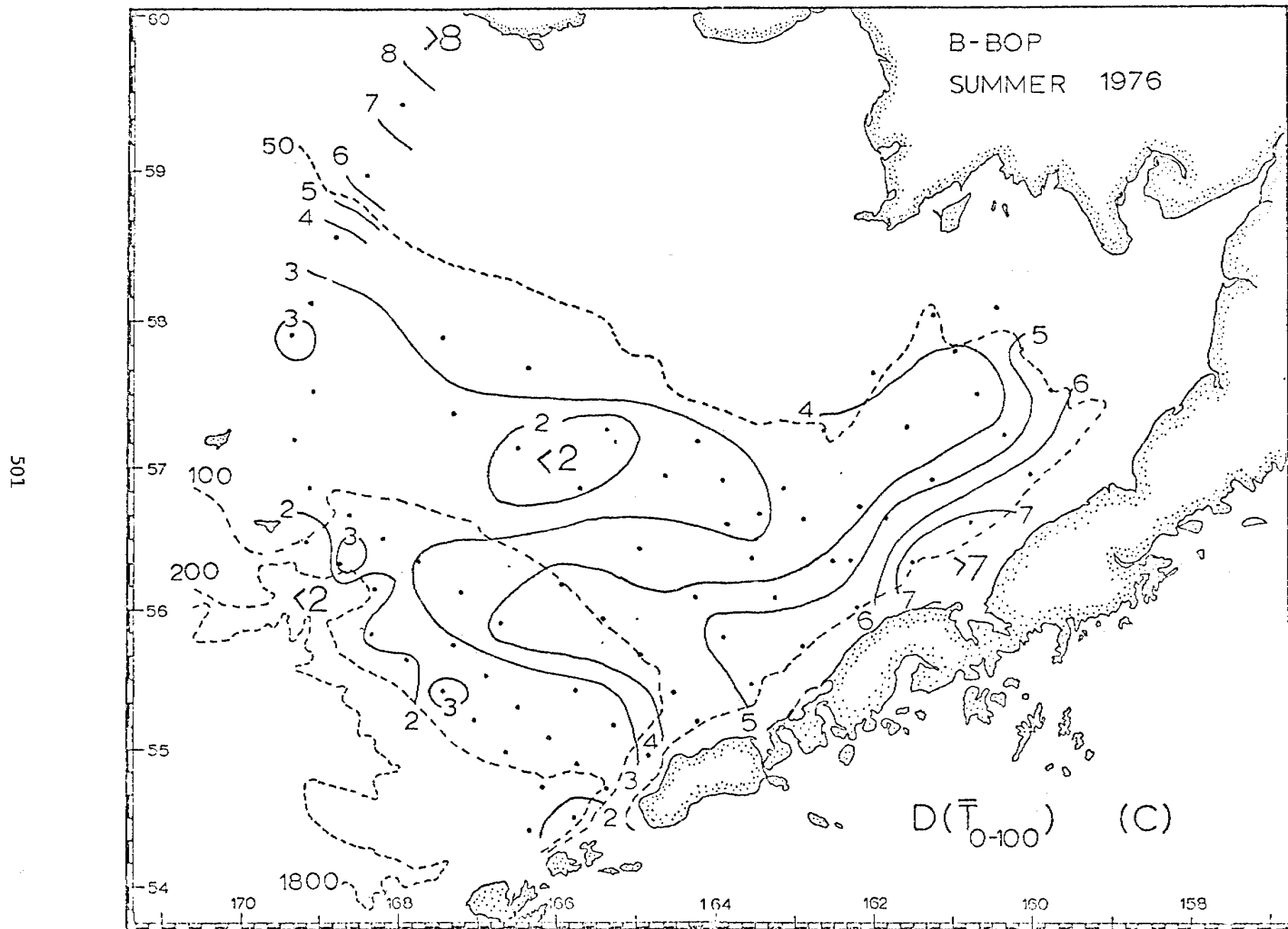


Figure 41. Change of vertical mean temperature, summer 1976.

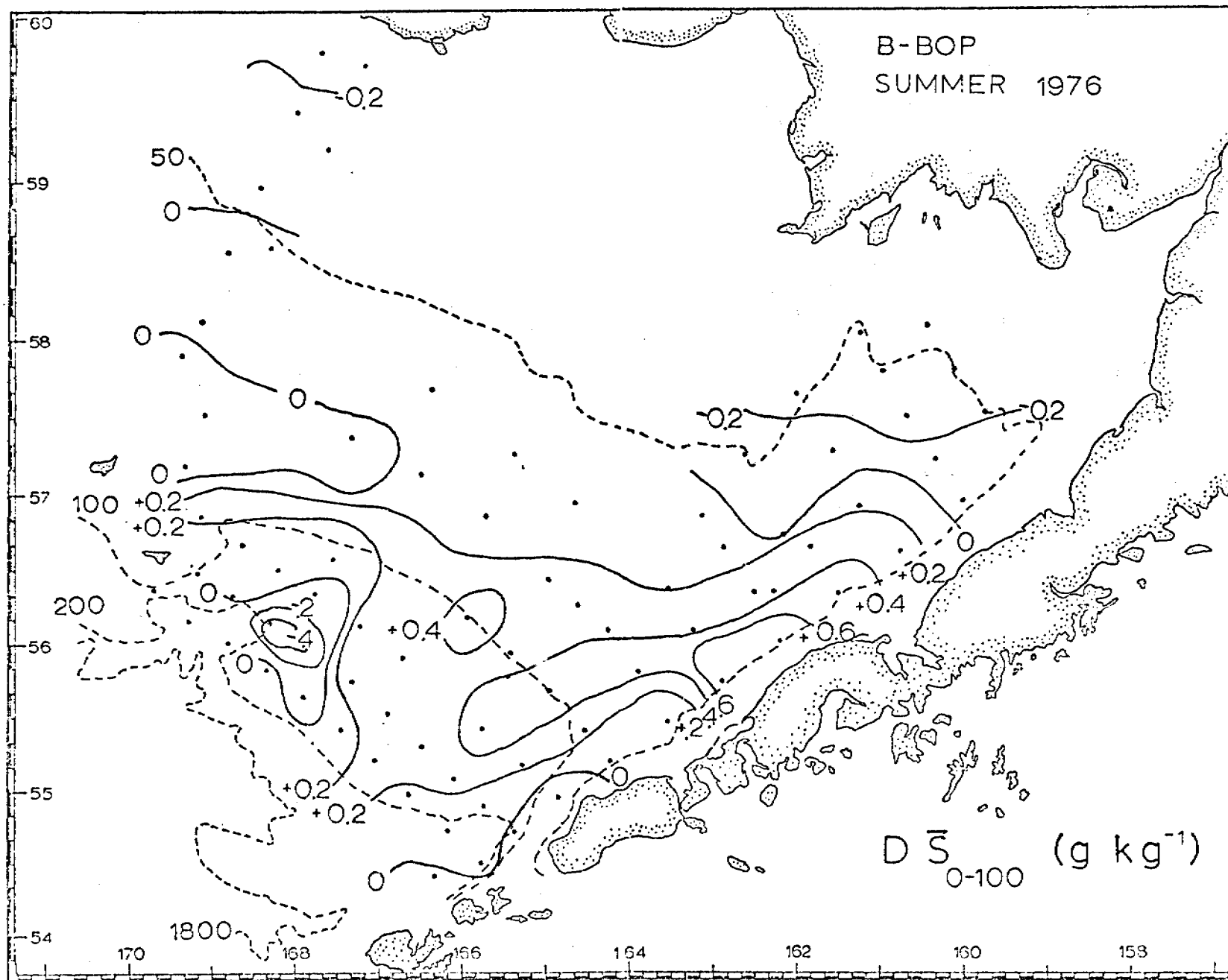


Figure 42. Change of vertical mean salinity, summer 1976.

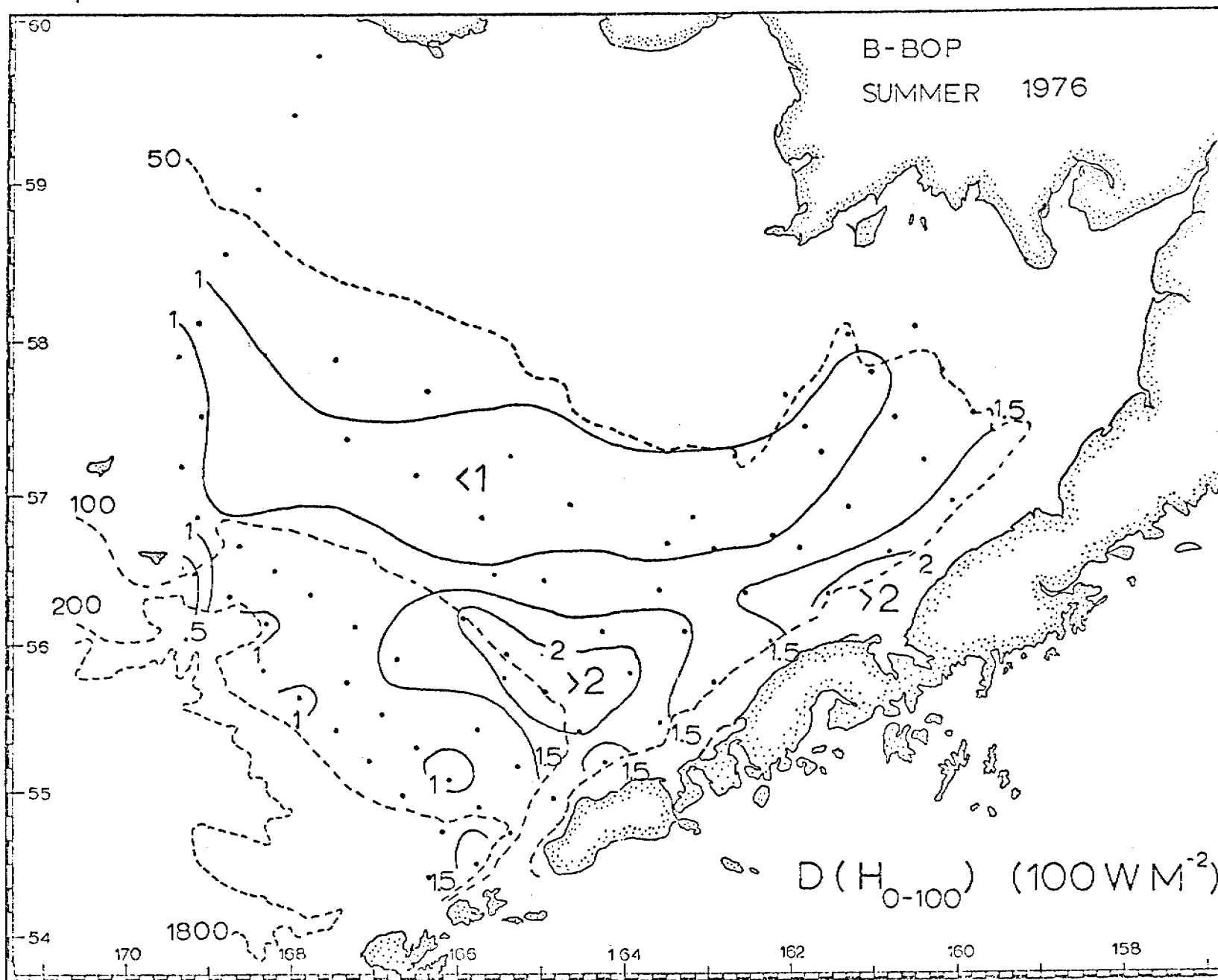


Figure 43. Change in heat per unit area (to 100 m or bottom), summer 1976.

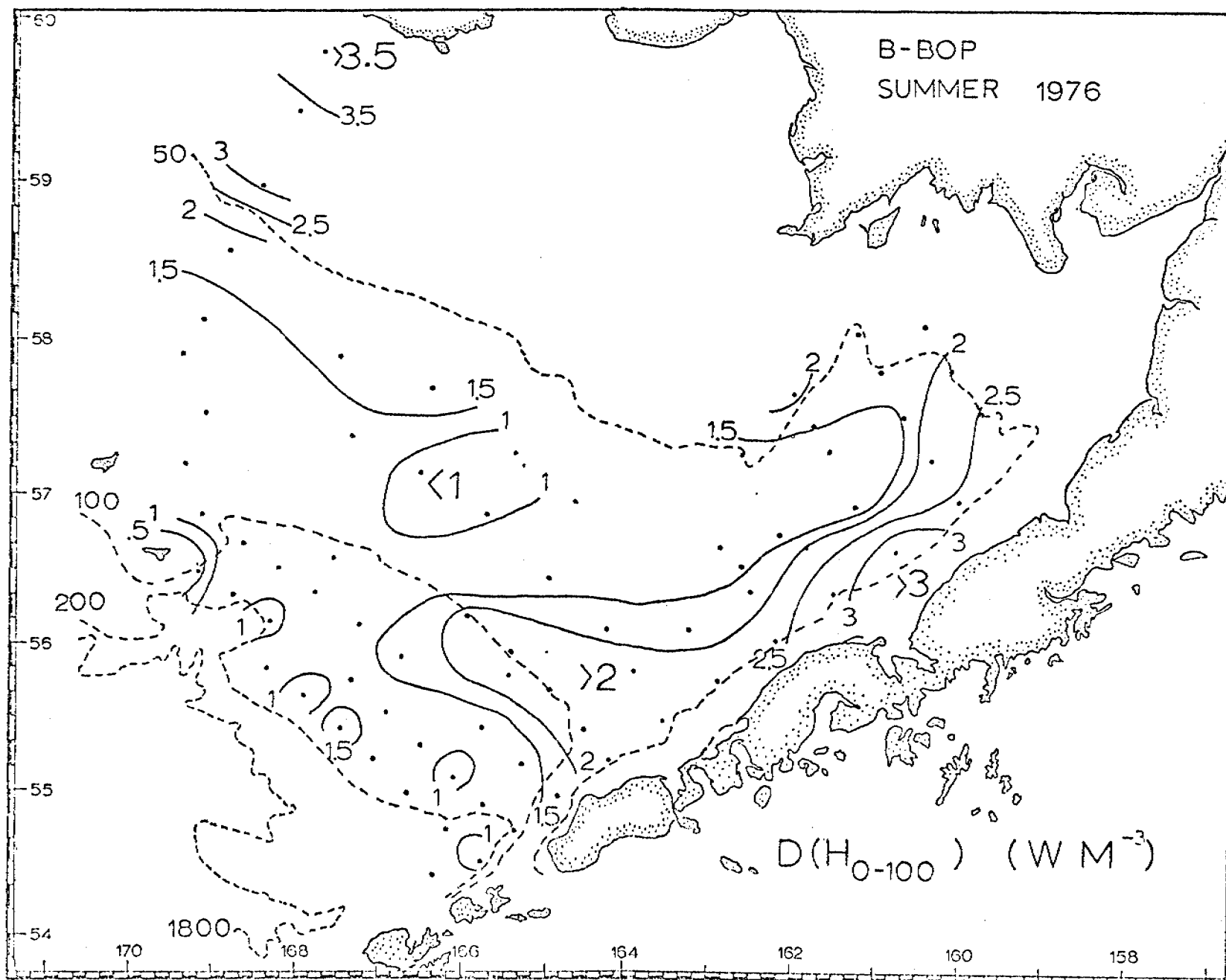


Figure 44. Change in heat per unit volume (to 100 m or bottom), summer 1976 (cf. Figure 41).

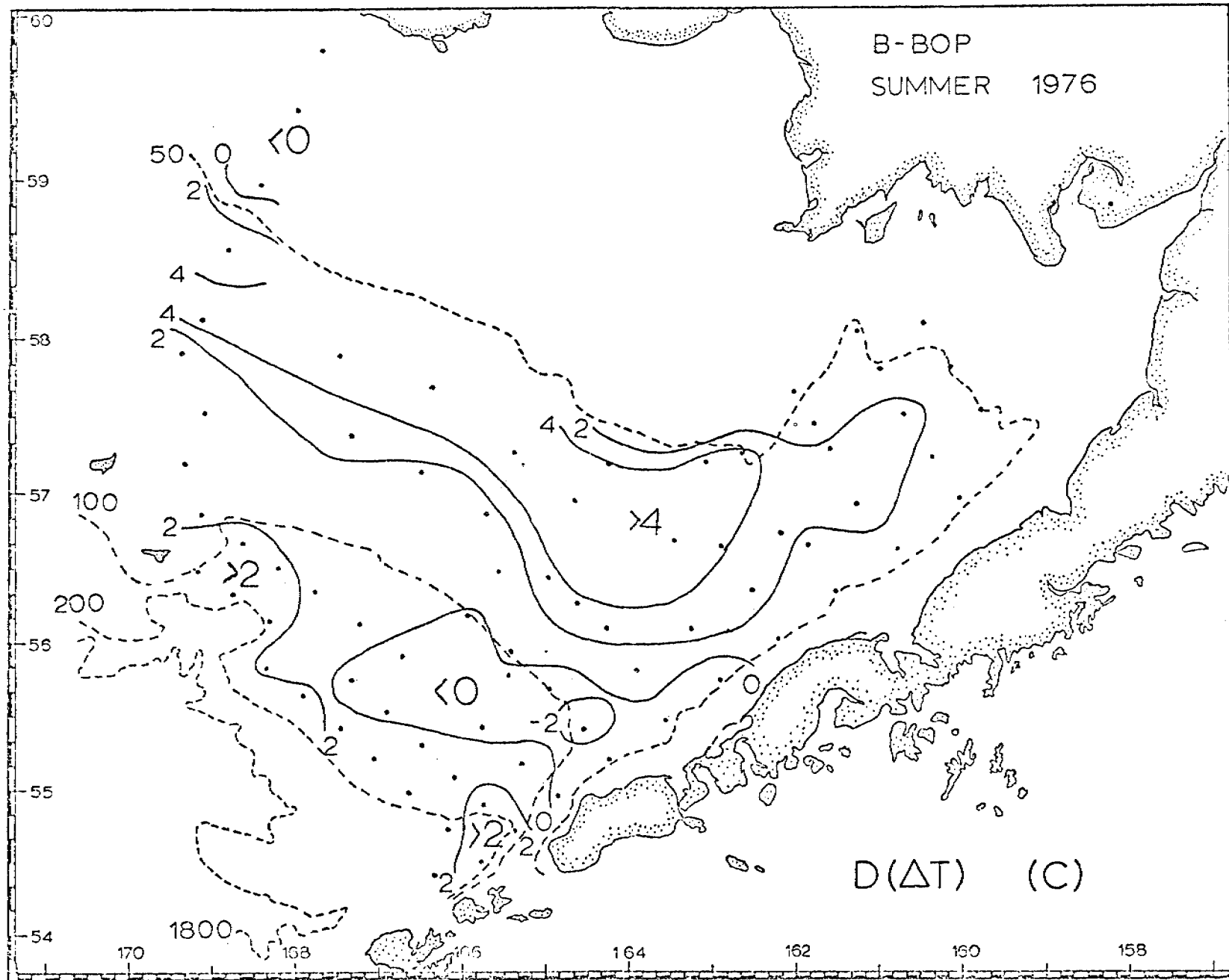


Figure 45. Change in vertical stratification (vertical temperature difference, summer 1976).

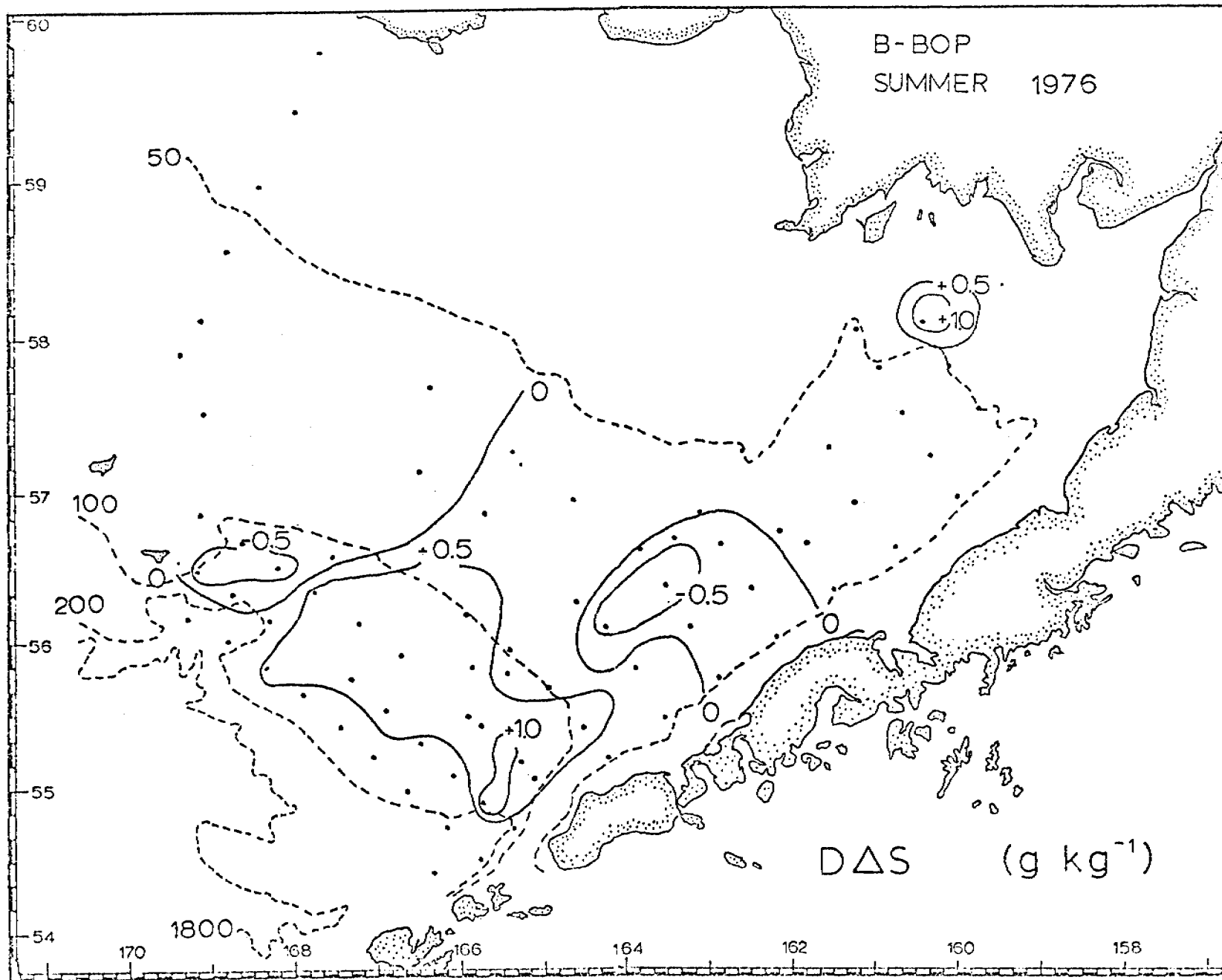


Figure 46. Change in haline stratification (vertical salinity difference), summer 1976.

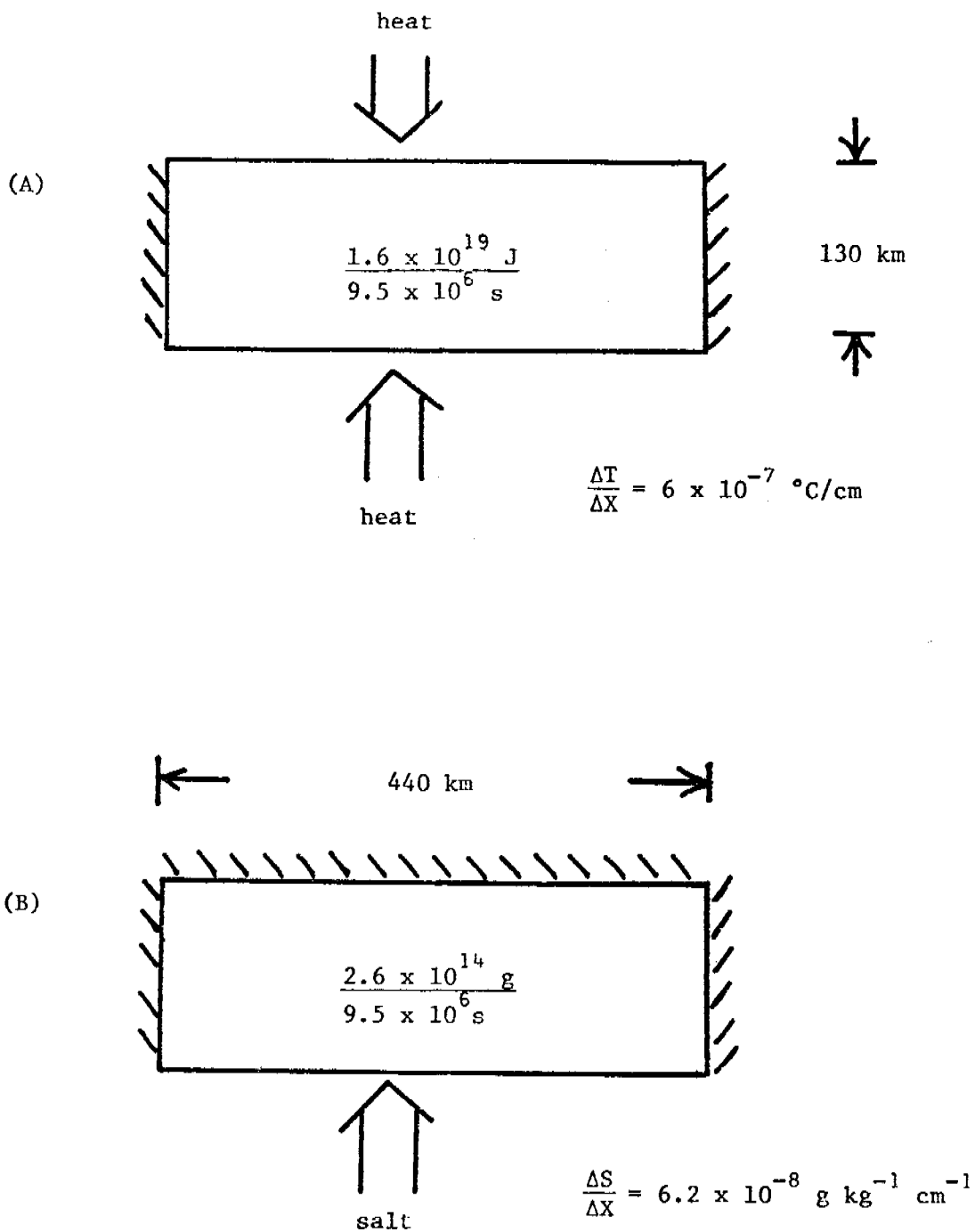


Figure 47. Schematic of box diffusion models. (A) heat. (B) salt.

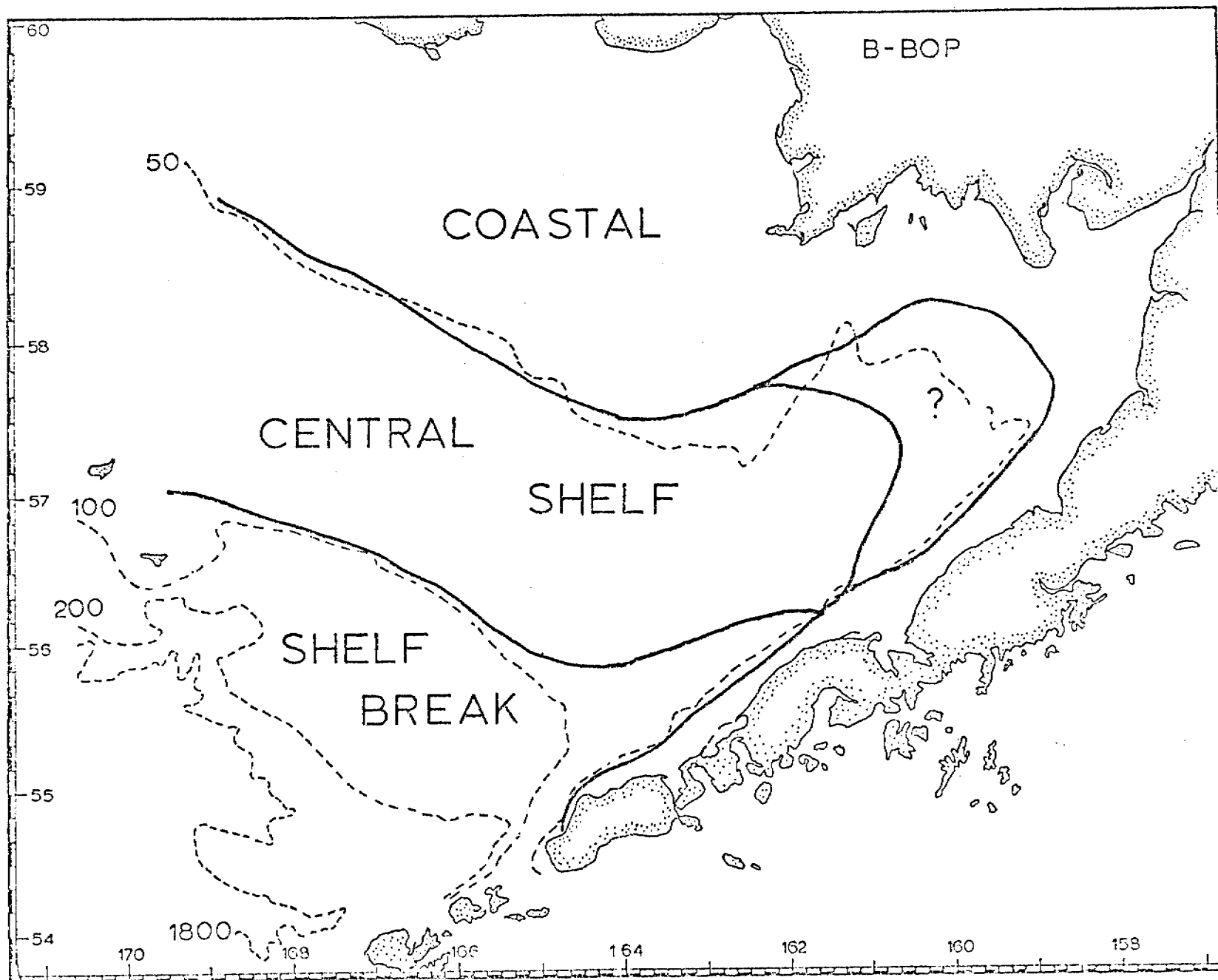


Figure 48. Approximate boundaries of water domains. The question mark in Bristol Bay indicates the authors' confusion (and honesty) over the boundaries there.

E. The Deep Eddy South of the Continental Shelf

After some of D. V. Hansen's drifters executed large cyclonic loops south of the continental shelf break (see his March 1978 Annual Report), we did 27 CTD stations in July 1977 to determine if these loops were reflected in the hydrography. We found close correspondence between the tracks of the drifter and the deep hydrographic distribution. Figure 1 shows the temperature at a depth of 500 m, and Figure 2 shows the geopotential at 100 db relative to 1500 db. In both cases a cellular feature, nearly coincident with the eddy delineated by the drifters, appears.

Using data collected by Felix Favorite, National Marine Fisheries, in the spring 1971, we attempted to determine if the eddy seen in 1977 is permanent. These earlier data do show a cyclonic tendency near the position occupied by the eddy in 1977, but gradients are smaller and the distributions appear more chaotic during 1971. The eddy also looks different than the cell observed in the outer reaches of Pribilof Canyon in 1974 (Kinder, T.H. and L.K. Coachman, 1977, *J. Phys. Oceanogr.* 7 (6): 946-952). The eddy is significantly larger, and there is no evidence for a cell near the canyon in the 1977 data. So historical data seem to support the permanence of the eddy only weakly, if at all.

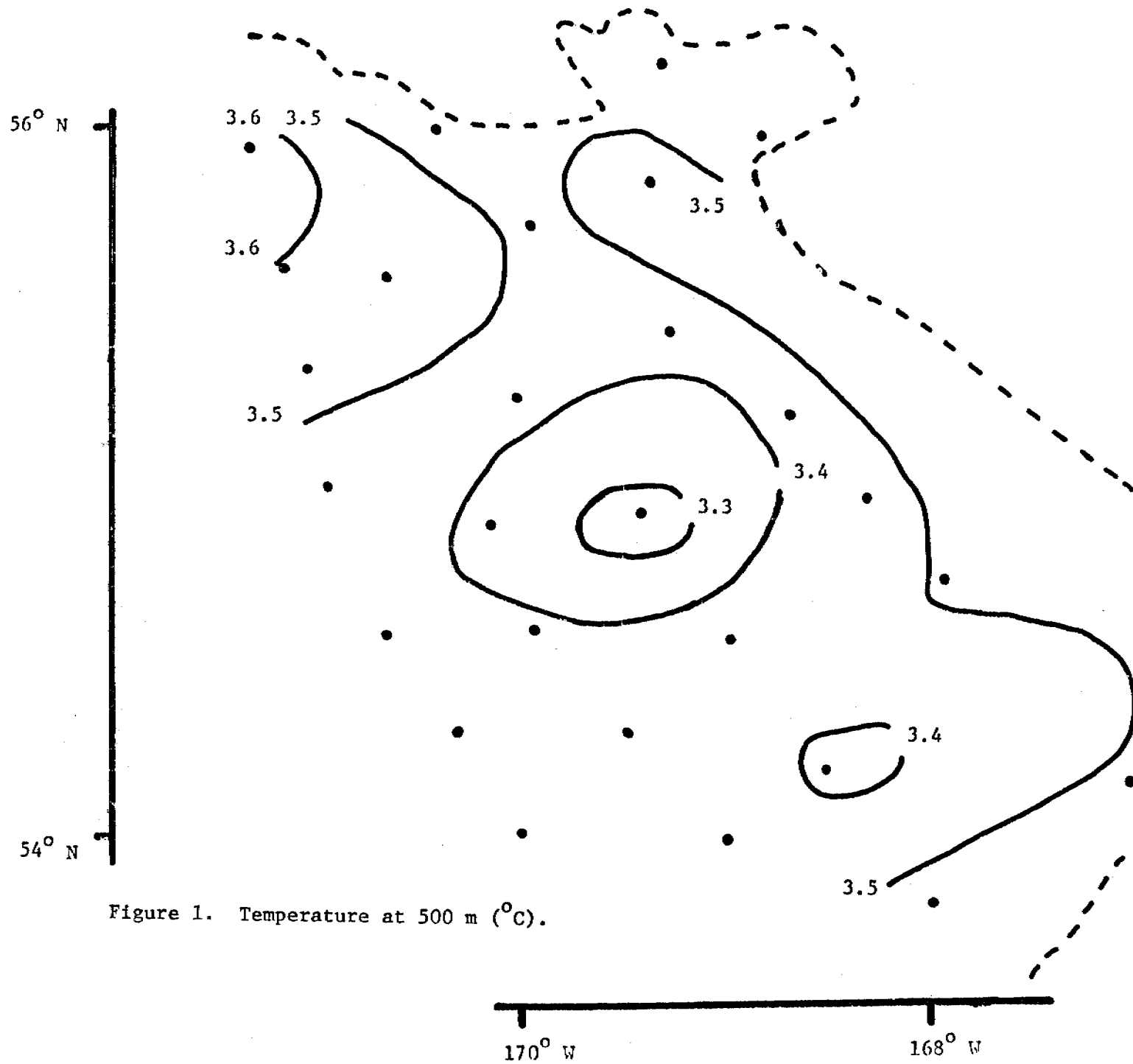
During February 1978 we also did nineteen CTD stations encompassing the July position of the eddy. A very preliminary perusal of the raw data indicates that if the eddy existed in February 1978, it was considerably weakened compared to July 1977 and had perhaps moved.

We plan to continue our analysis, and to relate the hydrographic structure to the drifter tracks, and to compare the July data to the February data, when the latter is processed. We should then be able to illuminate somewhat the circulation in the deep Bering Sea's southeastern corner, which is a boundary of the OCSEAP study region.

F. Tidal Analysis

We have completed a draft of a manuscript describing the tides of Bristol Bay. This description discusses the phenomena, in the central bay, which sees the marked reduction in tidal currents during summer months. The state of oceanographic theory at this stage is insufficient to explain the observations. These measurements raised a series of questions about the system which need to be answered before we can proceed with an appropriate explanation. With these questions in mind, a specialized field experiment was implemented during July 1977.

The objective of this field experiment was to examine the structure of current near the pycnocline and to measure short term vertical movement within the pycnocline. To do this we occupied time-series of current meter and CTD measurements at one location, for approximately 30 hours. CTD casts were made at hourly intervals interspersed with several series when the CTD fish was held at a fixed level within the pycnocline. At three-hourly intervals, current meter profiles were made using a deck read-out current meter held temporarily at between 5 and 10 discrete levels in the water



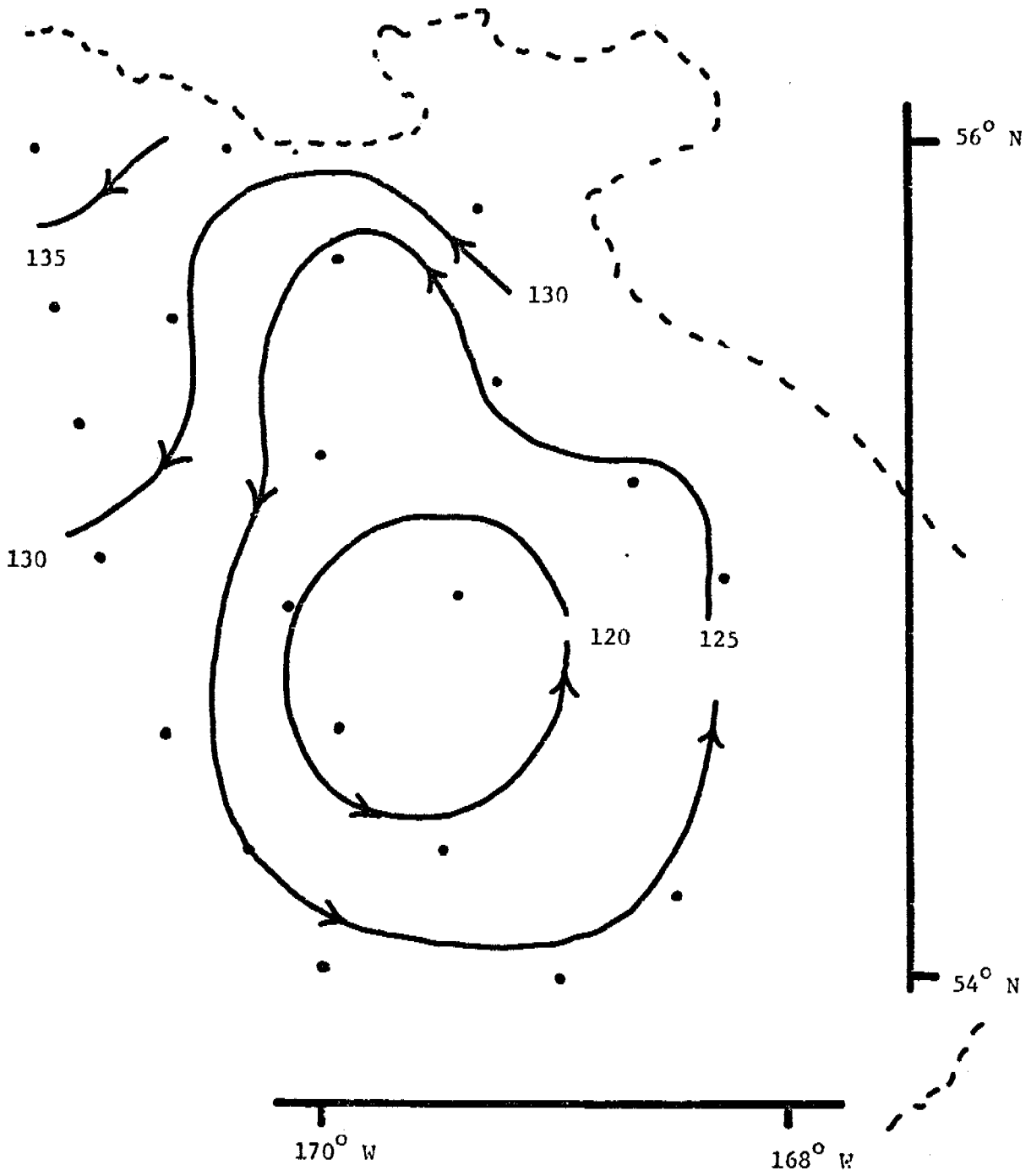


Figure 2. Geopotential, 100 over 1500 decibars (dynamic centimeters).

column. This observational series was made during exceptionally good weather (23-25 July, 1977) at standard station 91, approximately 30 km northwest of current meter station BC-14.

Data from this experiment, plus prior and subsequent observations, demonstrate the following set of features:

1). There is little vertical movement of the pycnocline during periods of reduced tidal currents. This suggests the phenomena does not result from destructive interference between an internal and external mode.

2). At any site, the currents are largely barotropic. There is a slight reduction in speed in the lower layer which appears amplified during periods of maximum current reduction. This reduction, however, may simply be due to the poorer signal to noise ratio.

3). This effect of reduced tidal currents is spatially coherent. The same features appear in the same manner at all central bay stations where diminution was observed.

4). The greatest reduction of tidal current appears when stratification is strongest (see Figure 1.). For BC-15, on the well-mixed side of the structural front, there is little variation in the harmonic constituents. At BC-2 and BC-14, where the stratification varies seasonally, the reduction occurs only during periods of strong stratification.

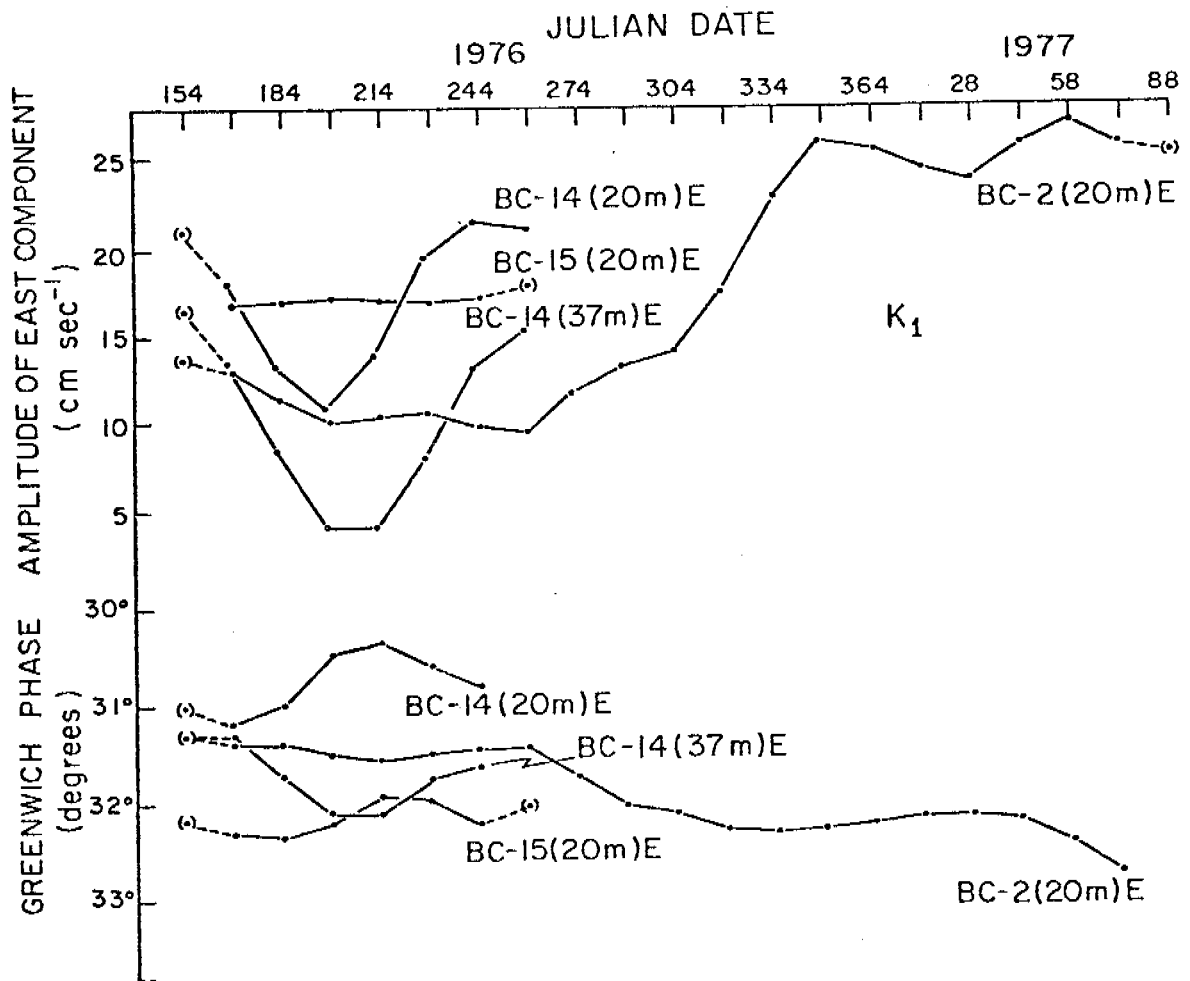
5). It appears, from examination of BC-2 current data over several years, that harmonic constituents vary throughout the year and do not always return to similar values each winter. These variations may result from variable weather patterns affecting ice cover and stratification.

6). While there are factor-of-6 changes in the magnitude of tidal currents, pressure observations suggest that the surface elevation range is altered by only a few percent.

The original Bristol Bay tidal report is being modified to include these new data. It is apparent that no unified theory can be developed at this time to explain the tidal current behavior in Bristol Bay. One of the more promising avenues of analysis is the joint activity with Jan Leendertse and Dave Liu at Rand Corporation. We have planned jointly several numerical experiments for the Bristol Bay model that should provide useful insight into the controlling mechanism for the observed tidal modification.

G. Sub-tidal Flow During Summer in Bristol Bay (current meters, drifters, meteorology)

Current records from BC-2C, 5A, 6A, and 14A collected over the summer of 1976 are being processed in a format compatible with Nimbus drifter (Hansen, AOML) and wind data (Bakun model). These data are being examined using various correlation techniques to describe low-frequency flow during summer, and to investigate the importance of wind forcing. Included in this study is a determination of the relative accuracy of the Bakun winds in comparison to observations from St. Paul Island, Cold Bay, and shipboard measurements. Preliminary examination of Bakun wind versus current records indicates that: 1) winds were generally light (≤ 5 m/s) and variable in direction, 2) there were several wind events with speed exceeding 10 m/s, and 3) during these events there were concomitant current events; the water response, however, does not appear consistent. Thus, we expect little correlation over the entire record, with much higher correlation during events. Lagrangian data will be decomposed into components and correlated to both wind and current time-series. These data will be used to investigate spatial coherence of the sub-tidal flow in Bristol Bay.



H. Winter Hydrography

During February 1978, we obtained hydrographic data in the vicinity of the seasonal ice cover (see cruise reports below). Preliminary analysis of the data suggests that melting ice over the central shelf establishes a hydrographic regime similar to that in summer. As illustrated in Figure 1, the ice, which freezes farther north, establishes a two-layer stratification over the central shelf, but apparently not in the shallower coastal domain (i.e., inshore of the 50 m isobath). Presumably, convective overturn and winter storms mix most of the shelf to vertical homogeneity, but the addition of melt water over the central shelf causes haline stratification during winter. Whether the stratification persists until spring probably depends on the weather, and likely varies for different locations as well.

The conceptual formation of the three water columns in Figure 1 is as follows: (1) 80 m During autumn and winter the water column has cooled and mixed, so that it is vertically uniform, but still warmer than the freezing point. (2) 60 m Here the water column, having once looked like (1), is stratified by melting ice. The upper layer is cooled and freshened by melting ice until reaching the freezing point. The formation of a two-layer system arrests (at least temporarily) further cooling of the lower layer. (3) 40 m Here, in the well-mixed coastal domain, cooling and freshening of the water column by melting ice proceeds until the freezing point is reached throughout.

We plan to test this concept against the data, when processed, and to examine the transition on both the shoreward and seaward sides of the two-layered domain. Our initial impression is that the concurrent helicopter and shipboard measurements are complimentary, and more valuable than two separate cruises.

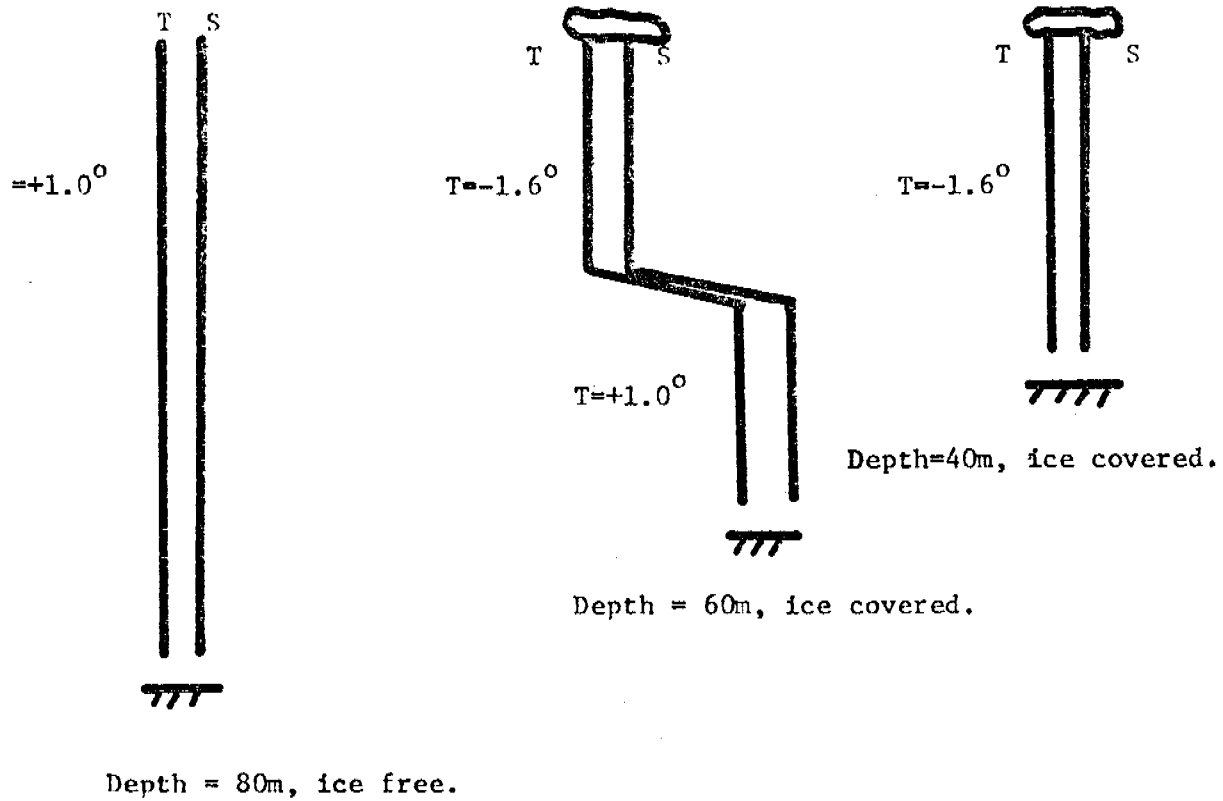


Figure 1. Schematic of winter temperature and salinity profiles near melting ice.



U.S. DEPARTMENT OF COMMERCE
National Oceanic and Atmospheric Administration
ENVIRONMENTAL RESEARCH LABORATORIES
Pacific Marine Environmental Laboratory
3711-15th Avenue N.E.
Seattle, WA 98105

DATE: March 8, 1978
TO: Herbert E. Bruce, OCSEAP Project Manager, Juneau
FROM: Jim Schumacher, Chief Scientist, PMEL JDS
SUBJECT: UH-1H Helicopter CTD/ICE Operations in Bristol Bay

Objectives

This operation was a continuation of field studies in support of PMEL's Bristol Bay Oceanographic Processes (RU141) research program. The general objective is to describe and understand circulation in order to characterize advective and diffusive processes and to examine their relation to waterborne substances resulting from petroleum development.

This mission represented a physical oceanographic survey to investigate: (1) the general hydrographic structure of the water column below the ice; (2) verify the existence of a structural front during winter months, similar to the one present in the summer; (3) verify the existence of a horizontal salinity gradient as supporting evidence of a salt transport mechanism to the nearshore regions of Kuskokwim Bay and Etolin Strait.

Accomplishments

CTD casts were conducted at 16 locations (see Table 1) with duplicate casts at stations 13, 23, and 11. A preliminary examination of the data, using the ODEC field tape reader, revealed the following: little or no stratification in waters less than 50 m depth and stratification in deeper waters, eg. at station 5 the observed temperature difference (surface minus bottom) was -0.8°C and the salinity difference was -0.35 kg/m^3 . Station 11 was conducted aboard the NOAA ship Surveyor. The ODEC system was suspended below the ship's 9040 CTD and two casts were made. Using the ship's computer and readout system, a comparison between uncalibrated (ie., from Niskin bottle samples and reversing thermometers) 9040 data and ODEC data indicated a temperature offset between the two instruments of 0.01°C and 0.05 kg/m^3 salinity offset. At this station the temperature difference (from the 9040 system) was -0.86°C with a salinity difference of -0.32 kg/m^3 . These values yield a sigma-t difference of -0.23 units. All data indicates that the front existed under the ice in the vicinity of the 50 m isobath. A sufficient number of stations were occupied to address the question of the existence and magnitude of a horizontal salinity gradient; however, this will require data processing in order to determine vertical mean values at each station.



Mammal species, abundance and location were recorded during transit between stations; however, due to poor visibility most of the time, lack of observations does not imply no animals. See Table 2 for details.

Comments

In addition to addressing the aforesaid objectives, this operation was the first extensive test of the ODEC CTD system. Every component of the system functioned perfectly. The system was tested after each transportation point was reached and after each field day. At no time was battery drain greater than 25%. Although a cassette was loaded after each cast (which will no longer be necessary after file gapping hardware is added), the procedure of opening the recorder package presented no problems. Loss of the wench baseplate and A-frame by Wein did complicate matters; however, on station time was still less than 30 mins.

The two factors which resulted in the success of the operation were, 1) the competence of the flight crew: Lt. Bill Harrigan and Bob Nield who also unselfishly aided in scientific operations and 2) the enthusiasm and expertise of Charles McLean who hounded the freight offices, tenderly cared for the ODEC CTD system, and dealt most effectively with the people of Mekoryuk.

Acknowledgements

I wish to thank Lt. Andy Snella, NOAA Liaison Officer in Anchorage for his assistance with logistics, and George Lapiene for ensuring that we were more than adequately outfitted for this operation and last but not least Myrtle.

OCSEAP-cached Jet Fuel Status

No fuel remains at Mekoryuk. The missing varrels of Jet-B fuel (about 6) are being used for the tie-downs at Bethel Airport.

All fuel at Mekoryuk airfield was used.

Scientific Personnel

J. Schumacher
C. McLean

cc: Adm. Taylor, PMC

TABLE 1
(See Figure 1)

<u>CTD Station</u>	<u>Date</u>	<u>Position</u>	
5 (01)	19 Feb 0150	58 59.6	169 09.2
13 (02)	20 Feb 0048	58 33.2	165 40.0
13 (03)	20 Feb 0100	58 33.2	165 40.0
14 (04)	20 Feb 0200	59 08.2	165 49.6
15(05)	20 Feb 0310	59 32.3	165 57.6
7 (06)	20 Feb 2245	58 33.4	168 24.3
8 (07)	20 Feb 2345	58 56.0	167 54.4
9 (08)	21 Feb 0130	59 19.0	167 30.0
4 (09)	21 Feb 2255	59 38.0	170 00.0
22 (10)	22 Feb 0020	59 42.0	169 32.0
5 (11)	22 Feb 2228	58 49.9	169 08.8
23 (12)	22 Feb 2310	59 12.7	168 30.9
23 (13)	22 Feb 2320	59 12.7	168 30.9
10 (14)	23 Feb 0100	59 37.4	167 03.1
11 (15)	24 Feb 0130	57 50.0	165 29.9
11 (16)	24 Feb 0230	57 50.0	165 29.9
16 (17)	25 Feb 0100	58 40.3	165 13.6
17 (18)	25 Feb 0200	59 07.0	164 51.4
19 (19)	25 Feb 0300	59 23.3	165 08.9

This completes operations from Mekoryuk. On 26 and 27 February, we were unable to operate due to lack of fuel and poor weather. We flew out of Bethel on 28 February in order to occupy stations 18, 20 and 21 but encountered no ice.

TABLE 2

Mammal Observations

The following marine mammals were identified by Lt. B. U. Harrigan:

Baluga whales	4	59 30	167 36
Bearded seal	1	58 53	165 39
Bearded seal	1	58 33	165 34
Walrus	~30	58 29	165 34

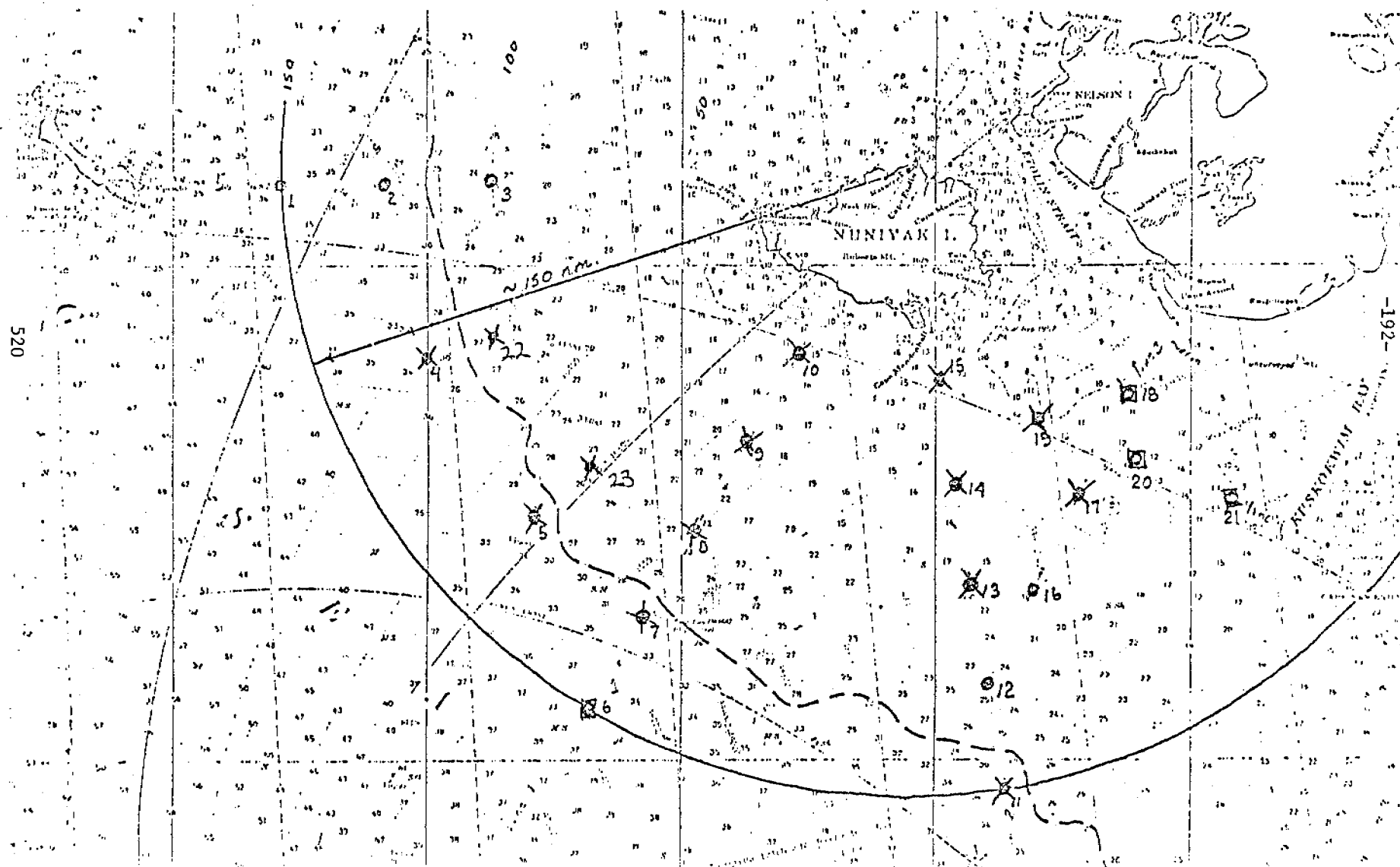
This group was located on the eastern side of a lead which extended 5 miles from the ice edge and was about 2 miles wide.

Helicopter Operations Under Ice Station Plot

FIGURE 1

Feb. 18, 1978 to 1 March 1978:

X indicates an occupied station
□ station with no ice



1. Introduction

This cruise is part of a cooperative study between the University of Washington and the Pacific Marine Environmental Laboratory (PMEL), Environmental Research Laboratories, National Oceanic and Atmospheric Administration (NOAA). This study, Bristol Bay Oceanographic Processes, is one component of the Outer Continental Shelf Environmental Assessment Program (OCSEAP), funded by the Bureau of Land Management and conducted by NOAA. The goal of our study is to elucidate the circulation and water masses of the southeastern Bering Sea in order to contribute to understanding the possible impact of petroleum development.

2. Objectives

The specific objectives of this cruise were: A) to make CTD casts over the slope and deep basin in the vicinity of the deep eddy found there during summer, 1977; B) to make CTD casts near the ice edge to examine the hydrographic structure there; C) to make soundings of the atmosphere using airsondes to examine the modifications that occur with distance from the ice edge during northerly winds, and D) to make observations of the structure of the ice, in part for comparison with LANDSAT satellite passes.

3. Narrative

Surveyor departed pier 91, Seattle, at 0900 13 February with the scientific party embarked. At 1700, after refueling at Manchester, Washington, Surveyor headed for the Bering Sea via the Strait of Juan de Fuca and the Gulf of Alaska.

While transiting the Gulf of Alaska, we tested, with limited success, a new atmospheric sounding device, the airsonde. Passing through Unimak Pass on 19 February, we began work (see Figures) in the Bering Sea.

The first nineteen CTD stations, taken over the continental slope and rise, were designed to determine if the deep eddy observed in July 1977 remained in place. The first station, B-BOP 9 (Bristol Bay Oceanographic Processes), was a calibration cast done in accordance with the Pacific Marine Center Oceanographic Manual, and was completed about 2100 (see Table; all times in the narrative are local). During the third station, B-BOP 3 on 20 February, one strand of the CTD cable parted with about 600 m of wire out. The cable was repaired with seizing wire, and since the messengers couldn't pass the repair, we took calibration samples at 500 m depth instead of at the greatest depth. On the eighteenth station, B-BOP 13 on 22 February, a second strand parted with about 1300 m of wire out. We only did sixteen stations deeper than 500 m, and had two strands break, even though the cable on the winch is new. With B-BOP 22 on 22 February, we finished the deep stations, and headed across the shelf for the ice edge.

We did stations from B-BOP 32 to B-BOP 85 to examine the hydrographic structure across the shelf. Following B-BOP 85 at 1045 23 February, we headed for B-BOP 96.1 to rendezvous with the NOAA helicopter which was flying from Nunivak Island. Dr. Jim Schumacher, chief scientist on the helicopter operations, was taking CTD stations through the ice to complement our stations. He requested the rendezvous to calibrate his portable CTD instrument against the ship's system.

At 1200, the ship encountered isolated blocks of ice, and by 1430 when the helicopter landed, we were in an ice concentration of 5 Oktas. This ice was in a band, a few km wide, with several leads. We used one of these leads to make two calibration casts with the portable CTD suspended beneath the ship's sensors. During the calibration casts, Jane Bauer, our ice observer, took a 20-minute ride in the helicopter to observe the ice from an altitude of 3000 feet.

After the helicopter departed at 1730, we left the ice pack reaching the edge of the closely-packed ice at 1830. We then did a line of closely-spaced stations normal to the local ice edge (B-BOP 96.2 to 96.5), and then steered parallel to the ice during the night (B-BOP 96.5 to 84). According to the reported ice position, we should have encountered ice again between B-BOP 84.2 and 94.1 on the morning of 24 February, but easterly winds apparently had blown the ice to the northwest. In fact, we found the ice edge again at station 106.1 close to our position on the 23rd. We spent that night close to the ice edge doing a closely-spaced series of CTD stations, B-BOP 106.1 to 106.7, and then entered closely-packed ice (3 to 4 Oktas caked in a matrix of slush) near B-BOP 996.1 at 0900 25 February. We spent all day in the ice, taking CTD stations B-BOP 996.1 to 996.5 in the ice, along the ice edge, and in the leads.

Upon emerging from the ice at 1700, the plan was to head east to about 163W, and then do a long line of stations across the shelf to Unimak Pass. By 2000, however, the wind rose to a steady 40 knots from the east so that leaving B-BOP 105 at 2200 25 February, we didn't arrive at B-BOP 104.1 until 1215 26 February. We then did a closely-spaced section across

the 50 m isobath (B-BOP 104.1 to 104.6), and headed for Unimak Pass. All remaining stations were canceled because of the time lost to weather, except for B-BOP 00 above the sill of Unimak Pass at 1000 27 February. Surveyor arrived in Kodiak at 1300 1 March, five hours late after bucking 15 to 25 knot headwinds continuously from Unimak Pass.

4. Methods

CTD casts were taken with a Plessey Environmental Profiling System, Model 9040. The sensors, serial 5914, had a range of -2 to 35 degrees C, 10 to 60 mmho/cm, and 0-1500 meters. Data were recorded on magnetic tape and returned to Seattle for processing by PMEL.

During this leg, the CTD was closely monitored by Art Cooper, electronics technician. He monitored output channels with an oscilloscope, examined all analog plots, and had the data tapes read daily by the ship's PDP-8 computer. Infrequent conductivity spikes were corrected by demagnetizing the conductivity head, and a failure of the temperature channel was repaired by replacing the digital data logger drawer.

Calibration temperature and salinity samples were obtained by Nansen bottle at about one-half the stations. Salinity samples were analyzed on board using a Bissett-Berman 6210 portable salinometer, calibrated by Northwest Regional Calibration Center (NRCC) in January 1978. Unfortunately, the thermometers supplied by NRCC were of non-uniform quality (several were scientifically unsuitable) and calibration data were incomplete.

Airsondes, new balloon-lifted radiosondes, were tested in anticipation of an air-mass modification experiment downwind from the ice edge. Our efforts quickly produced a workable launch procedure, but telemetry problems limited data return to less than 800 mb altitude on the best launches;

700 mb was desired. The correct winds never occurred, but the airsonde performance would probably have been disappointing if they had.

5. Personnel

Dr. T. H. Kinder	Chief Scientist	University of Washington
Tom Hiester	Meteorologist	PMEL
Jane Bauer	Ice Observer	University of Washington
Art Cooper	Electronics Technician	PMEL

6. Statistics

CTD Stations	64
Airsonde launchings	7
Ice Observations	
Ship	14 hours
Helicopter	20 minutes
Photographs	220

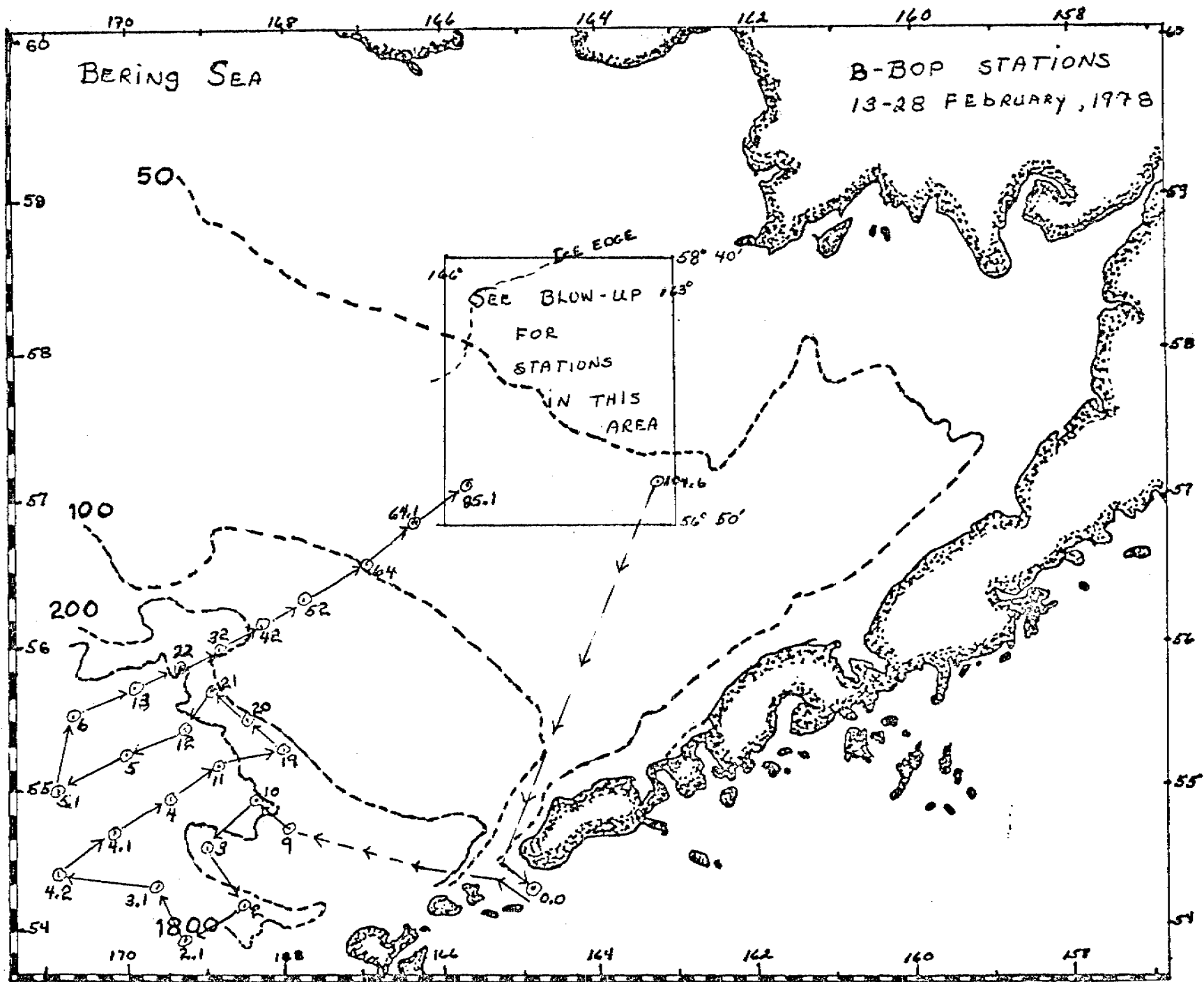
LIST OF CTD STATIONS
BERING SEA 1978

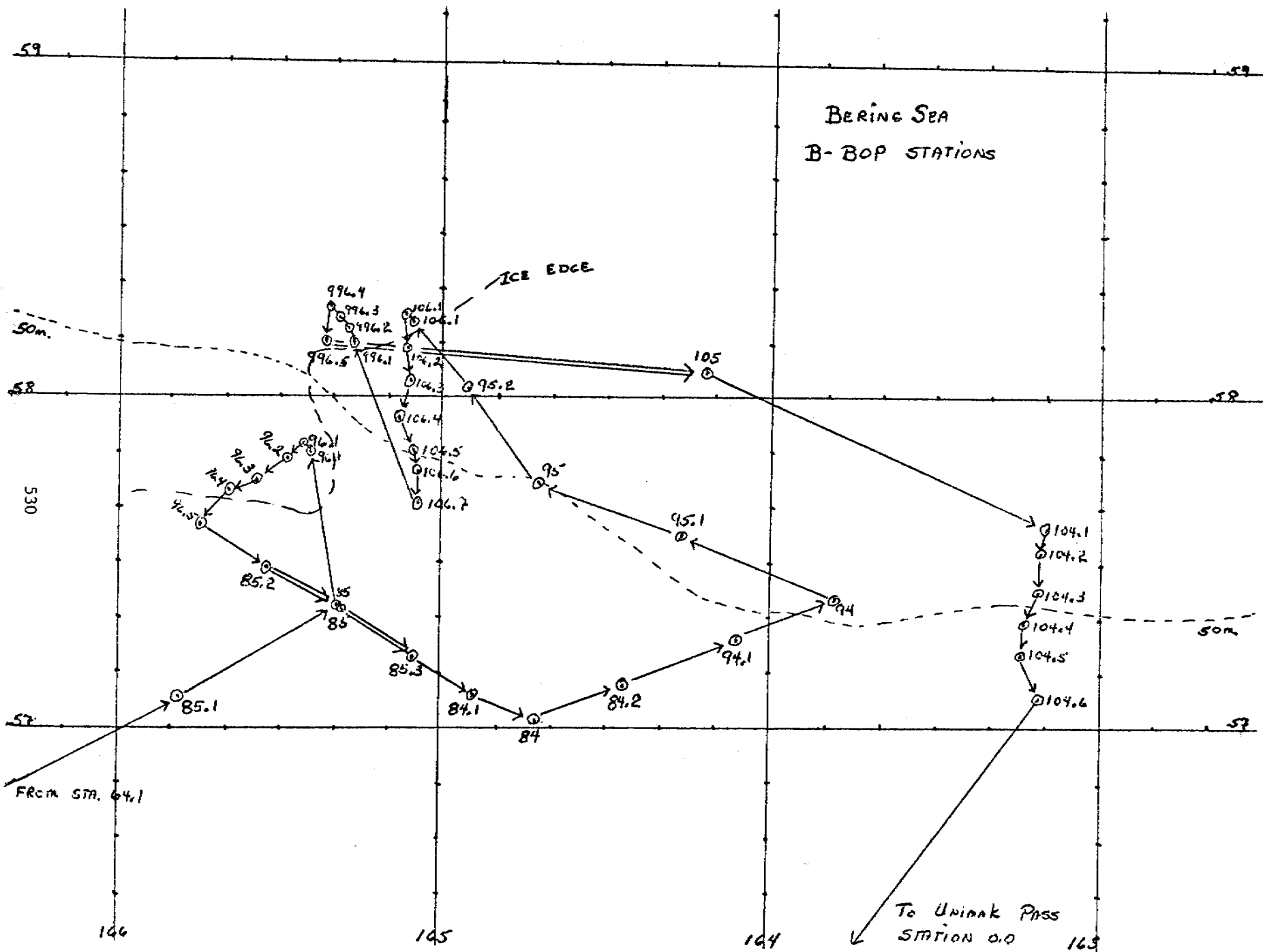
B-BOP GRID #	TIME (GMT)	DATE	LATITUDE (N)	LONGITUDE (W)	DEPTH (M)
1	9	0609	20 FEB 54 44.4	167 54.3	1500
2	10	0926	54 57.1	168 19.6	1730
3	3	1406	54 33.5	168 58.8	1500
4	2	1753	54 10.6	168 30.6	2500
5	2.1	2152	53 56.1	169 13.6	1760
6	3.1	0137	21 FEB 54 18.5	169 35.5	2080
7	4.2	0630	54 22.9	170 47.7	2100
8	4.1	1024	54 41.1	170 05.6	1820
9	4	1358	54 55.1	169 26.2	2820
10	11	1745	55 11.2	168 41.6	1995
11	19	2222	55 19.7	167 56.1	270
12	20	0030	22 FEB 55 30.9	168 23.1	282
13	21	0228	55 40.2	168 50.9	349
14	12	0505	55 26.6	169 15.8	2270
15	5	0847	55 15.8	170 00.6	2500
16	5.1	1230	55 02.2	170 48.0	3150
17	6	1655	55 33.5	170 40.2	3146
18	13	2228	55 43.7	169 57.2	2415
19	22	0302	23 FEB 55 50.0	169 20.3	1610
20	32	0609	55 58.1	168 48.1	585
21	42	0822	56 08.0	168 17.3	162
22	52	1102	56 20.1	167 44.1	128
23	64	1404	56 35.1	166 57.1	97
24	64.1	1628	56 50.6	166 22.4	76
25	85.1	1841	57 07.0	165 49.4	71
26	85	2050	57 21.5	165 20.3	68
27	96.1	0131	24 FEB 57 50.0	165 25.9	55
28	96.1	0228	57 51.7	165 27.3	55
29	96.2	0445	57 49.5	165 29.2	58
30	96.3	0559	57 46.4	165 35.2	60
31	96.4	0716	57 44.0	165 40.7	62
32	96.5	0838	57 37.5	165 45.2	64
33	85.2	1029	57 30.0	165 32.8	62
34	85	1205	57 21.9	165 19.6	64
35	85.3	1337	57 14.1	165 06.9	64
36	84.1	1453	57 07.5	164 55.5	68
37	84	1611	57 01.8	164 44.7	68
38	84.2	1736	57 08.5	164 28.3	67
39	94.1	1917	57 17.5	164 07.7	64
40	94	2040	57 24.4	163 49.3	57
41	95.1	2247	57 35.5	164 17.7	55
42	95	0035	25 FEB 57 44.6	164 43.2	51
43	95.2	0223	58 00.4	164 56.7	43
44	106.1	0356	58 13.0	165 06.5	42

B-BOP GRID #	TIME (GMT)	DATE	LATITUDE (N)	LONGITUDE (W)	DEPTH (M)
45	106.1	0528	25 FEB 58 14.8	165 07.4	43
46	106.2	0715	58 08.6	165 07.6	48
47	106.3	0814	58 02.7	165 07.2	49
48	106.4	0923	57 55.8	165 08.4	49
49	106.5	1025	57 49.8	165 06.0	51
50	106.6	1127	57 44.9	165 05.8	58
51	106.7	1227	57 39.0	165 05.0	59
52	996.1	1920	58 10.9	165 17.4	46
53	996.2	2001	58 12.2	165 17.5	46
54	996.3	2124	58 14.1	165 18.3	46
55	996.4	2310	58 17.2	165 21.4	46
56	996.5	0246	26 FEB 58 11.4	165 21.7	44
57	105	0756	58 07.7	164 13.6	47
58	104.1	2225	57 37.6	163 10.4	47
59	104.2	2322	57 31.1	163 12.2	45
60	104.3	0020	27 FEB 57 24.4	163 12.1	49
61	104.4	0114	57 19.2	163 14.0	53
62	104.5	0203	57 13.6	163 14.0	53
63	104.6	0317	57 06.6	163 11.3	60
64	000.0	2016	54 19.0	164 51.5	55

AIRSONDE FLIGHTS

	<u>Time (GMT)</u>	<u>Position (N, W)</u>	<u>Remarks</u>
1.	0000 17 February	Gulf of Alaska	Balloon underinflated, sonde hit water before ascending.
2.	0000 19 February	54-12.1, 157-22.8	Poor launch procedure; styrofoam flange, glued to body, parted dropping sonde.
3.	0100 19 February	54-11.9, 157-32.5	Poor telemetry, range ≈100 m.
4.	2000 20 February	54-02, 168-57	Good data to 1400 m, different antenna.
5.	0400 23 February	55-50.6, 169-20.1	Good data to 1000 m.
6.	0400 24 February	57-51.6, 165-27.2	Good data to 800 m, changed antenna lead.
7.	2000 25 February	58-13.4, 165 17.7	Good data to 800 m.





I. The Front Overlaying the Continental Slope
 in the Eastern Bering Sea

T. H. Kinder and L. K. Coachman

Department of Oceanography
University of Washington
Seattle, Washington 98195

Abstract

We use hydrographic data to delineate a diffuse, large (nearly 1000 km long), and persistent (years) haline front which overlies the continental slope in the eastern Bering Sea. The front marks a transition between the waters above the deep basin where the horizontal salinity gradient is almost zero and the flow is geostrophic, and the waters above the broad shelf where salinity gradients are large and the flow is tidally dominated. We suggest that the change in mixing, from the oceanic regime above the deep basin to the tidal regime over the shelf, is responsible for the front. Because our arguments do not depend upon features unique to the Bering Sea slope, similar fronts should be found where freshwater runoff can dominate the density gradient and where strong boundary currents are absent.

Introduction

Many of the deep oceanic basins are bordered by broad continental shelves which receive considerable freshwater runoff. Across large portions of these shelves, advection by the mean currents appears unimportant in the salt balance; the speeds of the mean currents are low, and both the mean streamlines and isohalines parallel the bathymetric contours. Instead, the salt balance seems to be governed by advection during shorter period events such as result from tides and storms. Thus, investigators often treat the salt balance as "diffusive" with respect to the longer term (*e.g.*, seasonal or annual) mean. Over the continental slope, the geological transition between the continental shelf and the oceanic basin, the mixing processes change from a shallow water regime dominated by tides and weather events to a typical oceanic regime. Within the water column, the signature of this transition frequently is a front such as that found south of New England (Voorhis *et al.*, 1976; Beardsley and Flagg, 1976). A diffuse haline front overlies the continental slope of the eastern Bering Sea, separating the waters of the tidally dominated regime above the broad continental shelf from those of the oceanic regime above the Aleutian Basin (Fig. 1).

Dodimead *et al.* (1963) recognized the presence of a front over this continental slope, but did not elaborate upon the frontal structure or upon the implications of its presence. Others have focused on the front (*e.g.*, Natarov, 1963; Kitano, 1970; and Ohtani, 1973), but they have emphasized the front's thermal character. We believe that the front results from the salt balance between the upper waters of the Aleutian Basin and the waters of the adjacent shelf, and further we note that in the generally cold subarctic waters of the Bering Sea the salinity controls the density. Thus the haline features are

fundamental, while the thermal properties of the front are incidental.

Using both our own and historical data, we describe the structure of this haline front. We also suggest the cause of its generation, and compare it to a similar front over the New England slope.

Setting

The continental slope of the eastern Bering Sea extends from near Unimak Pass, Alaska (eastern Fox Islands) to Cape Navarin, Siberia (Fig. 1), over 1000 km, and nearly bisects the sea into equal parts of shallow continental shelf and deep basin. Some of the world's largest submarine canyons incise this slope, including Pribilof and Zhemchug canyons, which head in shallow troughs on the continental shelf (depth <200 m) and debouch onto the floor of the Aleutian Basin at depths greater than 3000 m (Scholl *et al.*, 1970). Our data include the results of two closely spaced hydrographic surveys, one from near Pribilof Canyon and one from near Zhemchug Canyon.

Over the slope, the salinity distribution undergoes a marked change. Long-term salinity distributions computed using different data (Arsen'ev, 1967; Ohtani, 1973; Favorite *et al.*, 1976) show the same pattern: over the Aleutian Basin the horizontal salinity gradient is nearly zero, while over the slope a strong gradient appears, extending landward over the shelf (Fig. 2). Over the basin, surface salinities vary from 32.8 to 33.2 g/kg over distances of \approx 500 km, while over the slope a decrease from 32.8 g/kg to 32.0 g/kg occurs in about 100 km. The salinity decreases further to about 31.5 to 31.0 g/kg near the coast (away from rivers).

The current regime also undergoes a transition over the slope. Flow over the basin is geostrophic, and the inner band of the Bering Slope Current System flows to the northwest, paralleling the shelf break (Kinder *et al.*, 1975). In

contrast, recent current measurements (Schumacher and Coachman, 1977) show that tidal currents dominate the flow over the shelf. Over the slope, between these two regimes, the mean current apparently satisfies geostrophy, but the tidal components are more energetic than the mean flow (Kinder and Coachman, 1975). Thus measurements show that the velocity regime undergoes a transition over the slope, coincident with the diffuse haline front.

Frontal Structure

Even long-term average salinity distributions reveal the front (Fig. 2). The rapid transition over the slope is evident, from greater than 33.0 g/kg over the basin to less than 32.0 g/kg over the shelf, and salinity continues to decrease as the coast is approached inside the 100 m isobath, but less rapidly. Also evident in long-term mean and synoptic salinity distributions (*e.g.*, Ohtani, 1973; Arsen'ev, 1967) is the intrusion of higher salinity water onto the shelf at the ends of the front. We are discussing the front that overlies the central part of the slope; near Cape Navarin to the northwest and at the Fox Islands to the southeast (Fig. 1), we can find no clearly expressed front. It is at these ends of the front where the flow onto the shelf, necessary to supply the outflow at Bering Strait (about $1.5 \times 10^6 \text{ m}^3/\text{s}$, see Coachman *et al.*, 1975), probably occurs. We exclude these important endpoints from consideration, and concentrate on the large portion of the central slope where the front is present.

From historical data (Table 1), we constructed 13 sections normal to the slope, computed the mean 0-100 m (or 0 m to the bottom where the depth was less than 100 m) salinities, and plotted the results versus distance from the shelf break (Fig. 3). Averaging the salinities over the upper 100 m smooths many of the anomalies that appear when salinity is plotted on one level. These lines

Table 1. Sources of station data for Figure 3.

<u>Cruise</u>	<u>Stations</u>	<u>Source</u>
M/V <i>Attu</i> June 1958	14-19	Scripps Institution of Oceanography, 1958
M/V <i>Attu</i> June 1958	20-25	Scripps Institution of Oceanography, 1958
M/V <i>Tordenskjold</i> June 1959	31-40	Scripps Institution of Oceanography, 1959
M/V <i>Tordenskjold</i> June 1959	23-30	Scripps Institution of Oceanography, 1959
T/S <i>Oshoro Maru</i> 9 summer 1964	48,78,46,55-57	Hokkaido University, 1965
T/S <i>Oshoro Maru</i> 14 summer 1965	11-15,17,104	Hokkaido University, 1966
T/S <i>Oshoro Maru</i> 14 summer 1966	19-24,46,86	Hokkaido University, 1966
T/S <i>Oshoro Maru</i> 19 summer 1966	7,8,56-61	Hokkaido University, 1967
T/S <i>Oshoro Maru</i> 19 summer 1966	15-18,20,45,48	Hokkaido University, 1967
T/S <i>Oshoro Maru</i> 28 summer 1968	23-29	Hokkaido University, 1969
T/S <i>Oshoro Maru</i> 28 summer 1968	15-22	Hokkaido University, 1969
T/S <i>Oshoro Maru</i> 32 summer 1969	10-15	Hokkaido University, 1969
R/V <i>Thomas G. Thompson</i> 71 summer 1972	43-53	unpublished

crossed the shelf break between 168-00 W and 177-50 W, and the station spacing was typically 100 km. Figure 3 shows the uniformly high salinity (>33 g/kg) over the basin, and the lower salinities (<33 g/kg) and more variable distribution over the shelf. From a value of about 33.0 g/kg at the shelf break, salinity decreases toward the coast at a mean rate of $3.7 \times 10^{-3} \text{ g kg}^{-1} \text{ km}^{-1}$ to less than 31.5 g/kg. The transition between the salinity distribution of the shelf to that of the basin usually occurs 0 to 100 km seaward of the shelf break, although the resolution of Figure 3 is poor. On this scale, the front does not appear as a sharp transition in the salinity, but as a transition in the horizontal gradient of salinity.

Based on data from the summers of eight different years, Figure 3 also implies that the front is a permanent feature of the central slope during summer. All the sections that we have examined support the presence of the front every year, although the details of the frontal structure vary between sections. Winter data are very sparse, but sections based on data from this season presented by Natarov (1963) suggest that the front persists throughout the year.

When viewed in cross section, data from widely spaced (30 to 100 km) stations, similar to those used to construct Figure 3, reveal a consistent pattern (Fig. 4). In the upper 50 m, the isopycnals rise from their depth over the shelf to intersect the surface above the shelf break and upper slope; in many sections this occurs farther seaward of the shelf break than in Figure 4. Beneath this diffuse surface front, the deeper isopycnals bend downward toward the slope. These three features are common to cross sections constructed from widely spaced stations: (1) a diffuse surface front, (2) a frontal position 0 to 100 km seaward of the shelf break, and (3) beneath the surface front a downwarping of the deeper isopycnals toward the slope.

We have also obtained data from more closely spaced surveys, extending from the edge of the shelf to the basin. The maps of the salinity averaged from 0 to 100 m depth (Figs. 5 and 6) provide a better resolution of the mean salinity distribution (Fig. 3). Near Zhemchug Canyon in 1973 (Fig. 5) the isohalines were nearly parallel to the bathymetry, but they were more curved than in Figure 3. Farther to the east, near Pribilof Canyon in 1974, the distribution was even more contorted than it was at Zhemchug Canyon. The horizontal salinity gradient at Zhemchug Canyon was $5 \times 10^{-3} \text{ g kg}^{-1} \text{ km}^{-1}$ and at Pribilof Canyon it was $13 \times 10^{-3} \text{ g kg}^{-1} \text{ km}^{-1}$, or about 1.5 to 4 times greater than the long-term mean. Distributions at 10 m and 100 m depth at Pribilof Canyon (Fig. 7) show that there is an even greater curvature of the isohalines at a single depth, and that the horizontal gradients remain high: $8 \times 10^{-3} \text{ g kg}^{-1} \text{ km}^{-1}$ at 100 m depth, and $16 \times 10^{-3} \text{ g kg}^{-1} \text{ km}^{-1}$ at 10 m depth. Horizontal salinity gradients are compared in Table 2, and we see that the Bering Sea gradients are comparable to those of the broad oceanic transition zones, but are smaller than those of fronts associated with coastal upwelling or river plumes.

The salinity gradient also seems to be higher near the shelf break than it is farther on the shelf. For instance, if we compare the salinity gradient in the first 100 km shoreward from the basin to that farther inshore using the data in Figure 3, linear regressions yield $4.7 \times 10^{-3} \text{ g kg}^{-1} \text{ km}^{-1}$ for the seaward segment ($S = 4.7 \times 10^{-3} D + 32.75$, $n = 37$, $r = 0.82$), and $3.9 \times 10^{-3} \text{ g kg}^{-1} \text{ km}^{-1}$ for the shoreward segment ($S = 3.9 \times 10^{-3} D + 32.69$, $n = 22$, $r = 0.68$). Additionally, stations occupied over the upper slope and shelf east of Pribilof Canyon in June 1976 show a much higher salinity gradient within about 100 km of the shelf break than farther shoreward (Kinder, 1977). Finally, the data from

Table 2. Horizontal Salinity Gradients

(g kg⁻¹ km⁻¹)

Front	- Gradient -		
	<u>0 m</u>	<u>100 m</u>	<u>0-100 m</u>
mid-ocean ¹ (subarctic)	20 x 10 ⁻³	-	-
mid-ocean ¹ (subtropic)	8 x 10 ⁻³	-	-
mid-ocean ¹ (doldrum)	17 x 10 ⁻³	-	-
Bering Sea (Fig. 2)	-	-	3.7 x 10 ⁻³
Zhemchug Canyon	8 x 10 ⁻³	5 x 10 ⁻³	5 x 10 ⁻³
Pribilof Canyon	16 x 10 ⁻³	8 x 10 ⁻³	13 x 10 ⁻³
Upwelling ²	160 x 10 ⁻³	-	-
River Plume ³	6000 x 10 ⁻³	-	-

¹Roden (1975)

²Stevenson *et al.* (1974, Fig. 4)

³Garvine and Monk (1974, Fig. 4)

the surveys near the canyons show higher salinity gradients than the data from more widely spaced stations (Table 2). Individually, each of these pieces of evidence is weak: the slopes in Figure 3 do not differ much, the 1976 data are near the southern boundary of the frontal region, and the higher gradients in the canyon surveys may only be reflecting small-scale variability. We believe the cumulative weight of evidence, however, is that the salinity gradients are higher near the shelf break.

Density and temperature cross sections at Zhemchug and Pribilof canyons (Figs. 8 to 10) show, in more detail, the same features as the wider spaced section (Fig. 4): a shallow surface front about 0 to 100 km seaward of the shelf break underlain by downwarped isopycnals. Again, the shallow isotherms do not reveal the surface front. Somewhat deeper, near 50 m, isotherms are downwarped in some of the sections, and at 200 m all six sections have downwarped isotherms beneath the surface front.

During the survey at Pribilof Canyon, nutrient samples were also taken. Surface distribution of nitrate and phosphate (Figs. 11 and 12) outline the front more strongly than salinity (cf. Fig. 7), but the nutrients show a pattern congruent with the shallow salinity distribution. Decreasing from seaward to shoreward, the phosphate changes by a factor of 5 and the nitrate by a factor of 10. Phosphate and nitrate concentrations are not conservative properties because of their involvement in biological processes. Thus, the nutrient distributions suggest that the front strongly influences the biology, at least near Pribilof Canyon. Sparse nutrient data from the Zhemchug Canyon survey (Kinder, 1976) suggest a similar cross-slope nutrient distribution. Unlike salinity, however, there are no data to construct long-term mean distributions along the shelf analogous to those for salinity (*e.g.*, Fig. 2), so

that we cannot extrapolate these local results to the entire front.

Most of our data came from discrete sampling with Nansen bottles, rather than continuous profiling instruments, so that small-scale vertical features ($\lesssim 10$ m) were not resolved. An STD (salinity-temperature-depth) survey along the slope in 1972 (see Kinder *et al.*, 1975), however, showed multiple interleavings of shelf waters over the slope. Additionally, extensive CTD (conductivity-temperature-depth) surveys over the outer continental shelf and upper slope southeast of the Pribilof Islands (Fig. 1) during 1976 have revealed a rich finestructure in the vertical profiles of temperature and salinity (Coachman and Charnell, 1977; Kinder, 1977). While we have not done the careful tracking of interleaving boluses of water that Voorhis *et al.* (1976) did over the slope south of New England, the measurements so far suggest that similar processes of exchange occur in the vicinity of these two transitions.

Salt Balance and Frontal Generation

Noting that the front is basically haline, we investigate the salt balance over the shelf, seeking the reason for the front. Assuming the masses of salt and water remain constant above the shelf, we compute a salt and water balance (Table 3). We know that the mean outflow at Bering Strait is about 1.5×10^6 m³/s of water at a salinity of 32.4 g/kg (Aagaard and Grøisman, 1975), and that about 1.3×10^4 m³/s of freshwater runoff flows into the Bering Sea (Lisitsyn, 1966; Roden, 1967). Both the water and the salt balances can be satisfied by a flow onto the shelf of about 1.49×10^6 m³/s at a salinity of 32.68 g/kg: this implies an advective salt flux across the shelf break of 4.9×10^4 t/s (one ton = 1 t = 10^6 g). Based on the long-term mean salinity distribution (*e.g.*, Fig. 2), the salinity of the onflow from the basin cannot be much less

Table 3. Advective salt and water Mass Balances for Shelf

water:	inflow	+	runoff	=	outflow	(m ³ /s)
	1.49x10 ⁶		1.3x10 ⁴		1.5x10 ⁶	
salinity:	32.68		0		32.4	(g/kg)
salt flux:	4.9x10 ⁴		0	=	4.9x10 ⁴	(t/s)

The mass balances assume that the masses of salt and water over the shelf are constant, and that the runoff, the outflow, and the salinity of the outflow are given. If part of the salt flux is diffusive, then water flowing onto the shelf may have a lower salinity than 32.68 g/kg.

than 32.5 g/kg: even at this low salinity, advection accounts for 99% of the salt balance. It is the residual salt flux, however, that is interesting here.

Over the central part of the shelf, away from the Siberian coast (*e.g.*, the Gulf of Anadyr, where we suspect that the advective salt flux occurs), the mean flow as well as the isohalines appear to parallel the isobaths. This mean flow is small, about 1 cm/s, compared to the tides which are typically 20 cm/s (Schumacher and Coachman, 1977). Both long-term hydrographic distributions (*e.g.*, Favorite *et al.*, 1976) and detailed synoptic surveys (*e.g.*, Kinder, 1977) reinforce the assertion that salt advection by the mean flow is negligible over the central shelf. Nevertheless, salt must be added to the freshwater runoff at the coast to raise its salinity to about 31 g/kg (see Fig. 2). It is reasonable to attribute the salt balance over this portion of the shelf, as distinguished from the balance for the entire shelf, to "turbulent diffusion", here defined to include tidally-driven salt transport. We exclude wind-driven transport, as current records (Schumacher and Coachman, 1977) show that the tides account for over 90% of the energy variance. Similar arguments for turbulent diffusion have been presented in considerable detail by Csanady (1976).

To examine this diffusion more closely, we envision a rectangular portion of the shelf, with one side about 750 km long and centered above and parallel to the shelf break, and the two perpendicular sides paralleling the Alaska Peninsula and about 550 km long. The fourth side, 750 km long, closes the box adjacent to the coast.

Along the coastal boundary of the box rivers add about $1.5 \times 10^3 \text{ m}^3/\text{s}$ of freshwater; rivers discharging along the Siberian Coast (*e.g.*, Anadyr) or north of the central shelf (*e.g.*, the Yukon River, which empties into Norton Sound, east of St. Lawrence Island) do not add to the box. To raise the salinity on

the coastal boundary to 31.0 g/kg, in agreement with long-term mean salinity, about 50 t/s of salt must diffuse across the box: this residual flux is about 0.1% of the advective salt flux, and so the gross salt balance of the shelf is not affected.

Because of the difference in time scales and energies of the tidal and mean flows, it seems reasonable to model this vertically integrated diffusive flux as:

$$\dot{s} = \rho h K_s \frac{ds}{dx}$$

where \dot{s} = salt flux per unit length

ρ = density

h = depth

K_s = diffusivity coefficient, and

$\frac{ds}{dx}$ = cross-shelf salinity gradient (vertically integrated).

Across the coastal boundary, $\sim 0.6 \text{ g cm}^{-1} \text{ s}^{-1}$ of salt diffuses to raise the salinity of $20 \text{ cm}^2/\text{s}$ of freshwater to 31.0 g/kg. Taking $\rho = 1.02 \text{ g/cm}^3$, $h = 5 \times 10^3 \text{ cm}$, and estimating $\frac{ds}{dx} \sim \frac{33.0 - 31.0 \text{ g/kg}}{550 \text{ km}} \sim 3.6 \times 10^{-11} \text{ cm}^{-1}$: $K_s \sim 3 \times 10^6 \text{ cm}^2/\text{s}$. For comparison, Csanady (1976) similarly estimated $K_s \sim 2 \times 10^6 \text{ cm}^2/\text{s}$ for the mid-Atlantic bight.

The actual mechanism of the diffusion is hidden within K_s . For the salinity gradient to increase near the shelf break, as observed, K_s must decrease, *i.e.*, the diffusion mechanism must become less efficient. We hypothesize that this can be due to tidally induced lateral diffusion, as follows. The degree of horizontal mixing caused by tidal motions must be directly proportional to the tidal excursion. As depth increases, for a given tidal wave the excursion will be less and hence also the degree of horizontal mixing (diffusion). As the mixing

is parameterized in K_s , its value will also decrease. More formally, assume that the salt flux $= K_s \frac{ds}{dx} = C U_T S_T$, where U_T and S_T are the amplitudes of the velocity and salinity components near tidal frequencies, and C is the correlation coefficient between these components. To scale K_s , the tidal speed, U_T , and tidal excursion ℓ_T , are reasonable choices (analogous to a mixing length assumption): $K_s \propto U_T \ell_T$. But $\ell_T \propto U_T T$, where T = the tidal period, a constant. Thus $K_s \propto U_T^2$. For a given tidal wave conserving momentum over a shelf of varying depth (h), $U_T \propto h^{-1}$, or $K_s \propto h^{-2}$. Using the expression for salt flux, which we take as constant across the box, $\text{const.} = \dot{s} = \rho h K_s \frac{ds}{dx} \propto \rho h (h^{-2}) \frac{ds}{dx}$, or $\frac{ds}{dx} \propto h$. This model predicts that the salinity gradient should increase as the depth increases. In fact, there does appear to be about a threefold increase in the salinity gradient near the shelf break (mean depth ~ 170 m) compared to gradient near 50 m depth (Kinder, 1977; also cf. Figs. 3 and 4).

We have assumed that the salt balance across a large portion of the shelf, from the shelf break to coastal waters, is controlled by a "turbulent" diffusion dominantly due to the ubiquitous tidal currents (tidal diffusion?). At the shelf break, oceanic conditions maintain a high salinity reservoir at 33.0 g/kg, while freshwater additions near the coastal boundary require a salt flux of $0.6 \text{ g cm}^{-1} \text{ s}^{-1}$ to maintain the salinity at 31.0 g/kg. The diffusive flux across the shelf within the box is driven by the tidal currents, and this mixing mechanism is more efficient (relative to the salinity gradient) in shallower water, leading to higher gradients near the shelf break.

We have assumed that vertical variations in salinity and velocity are unimportant such that a vertically averaged approach makes sense. Figure 7, for example, clearly demonstrates significant haline stratification near the shelf break during summer, and over most the shelf the surface to bottom salinity

difference is about 0.5 g/kg (Kinder, 1977). The measured velocities are similar in both the upper and lower layers, however, so that there is no evidence for a significant quasi-estuarine flow (Heaps, 1972; Csanady, 1976) wherein long-term vertical salinity and velocity variations are important.

This idea that over a large part of the shelf the salt flux is caused by tidal advection is based on current and hydrographic measurements. Over the basin, the flow is nearly geostrophic (Kinder *et al.*, 1975), and the transition to the tidally dominated shelf regime occurs over the slope, coincident with the haline front. Our one-dimensional model of the cross-shelf salt flux highlights the critical role of the salt flux in frontal formation, but since it views the deep basin as an infinite salt source, details of the cross-frontal flux are ignored. Mixing processes and dynamical balances across the front are complicated.

For instance, there may be a surface convergence and resultant sinking at the front. While the downwarped isopycnals (Figs. 4, 8, and 9) could merely indicate a geostrophic adjustment, temperature-salinity, nutrient-nutrient, and nutrient-oxygen correlations suggest downward mixing of waters originating at shallower depths (Kinder, 1976). Together with the high gradients of the shallow nutrient distributions (Figs. 10 and 11), the evidence makes plausible a surface convergence and downward sinking, similar to observations of other fronts (*e.g.*, Voorhis, 1969; Wooster, 1969; Stevenson *et al.*, 1974; Garvine and Monk, 1974). We do not attempt a full explanation of the frontal processes, but argue that the salt flux and the transition between oceanic mixing processes and the tidally dominated mixing regime over the shelf must be given full consideration when developing the full explanation.

Discussion

No observed features of this front, nor our ideas to explain these features, are unique to the Bering Sea. The major requirements for the formation of similar fronts seem to be: a broad and shallow continental shelf separating the coast from the continental slope, significant runoff from rivers at the coast, a strong effect of salinity on density, a shelf current regime dominated by high frequencies (relative to seasonal currents), and the absence of a strong boundary current. The first four requirements permit a tidal-mixing regime over the shelf, transporting the buoyancy input at the coast towards the deeper water. The last requirement excludes an obvious case where a separate mechanism will dominate the dynamical regime over the continental slope. One obvious possibility for a similar front is the slope south of New England.

North of Cape Hatteras, along the continental margin of the United States, all the conditions for a front overlaying the slope are met. Hydrographic sections across the slope there in summer (*e.g.*, Steffanson *et al.*, 1971; Bumpus, 1973) are very similar to those across the Bering Sea slope. In winter there is no source of buoyancy as severe cooling makes the shelf water denser than the off-shelf water. Voorhis *et al.* (1976) and Beardsley and Flagg (1976) recently described this front in detail, and it apparently is very similar to that in the Bering Sea. The many small intrusions which Voorhis *et al.* mapped may be similar to interleaving suggested by the finestructure found in the Bering Sea (Coachman and Charnell, 1977; Kinder, 1977). The same essential processes probably form and maintain the transition zones over the slopes in the eastern Bering Sea and south of New England.

Two aspects of these fronts emphasize their importance. First, the fronts are boundaries between different current regimes: the tidally dominated shelf

regime, and the geostrophic deep water regime. As a boundary, the front permits treating each regime independently. Second, the front is a boundary for water properties, including nutrients (Figs. 10 and 11), plankton, and pollutants. Thus the front may control the mixing and exchange between coastal and offshore waters. Additionally, if a surface velocity convergence exists, as we think likely, then buoyant material (*e.g.*, plankton or light petroleum products) will be concentrated at the surface. Once these fronts are understood, the prediction and understanding of their effect upon mixing and the distribution of properties may be the most important result.

Acknowledgments

Primary support for this research was provided by the National Science Foundation under Grant GA 11147 A3, with some additional assistance from the Outer Continental Shelf Environmental Assessment Program which is administered by the National Oceanic and Atmospheric Administration for the Bureau of Land Management. T. H. Kinder received further assistance from the Graduate School Research Fund of the University of Washington. J. A. Galt and J. D. Smith critically read an earlier report of this work, and D. Hanzlick and J. Swift usefully commented on this draft. We also wish to thank the reviewers who made encouraging and insightful comments. We are recovering rapidly from the resulting schizophrenia. The results from cruise 71 of R/V *Thomas G. Thompson*, C. Clampitt commanding, and cruises 49 and 53 of T/S *Oshoro Maru*, Dr. T. Fujii commanding, contributed substantially to this study. Contribution Number xxxxx, Department of Oceanography, University of Washington.

References

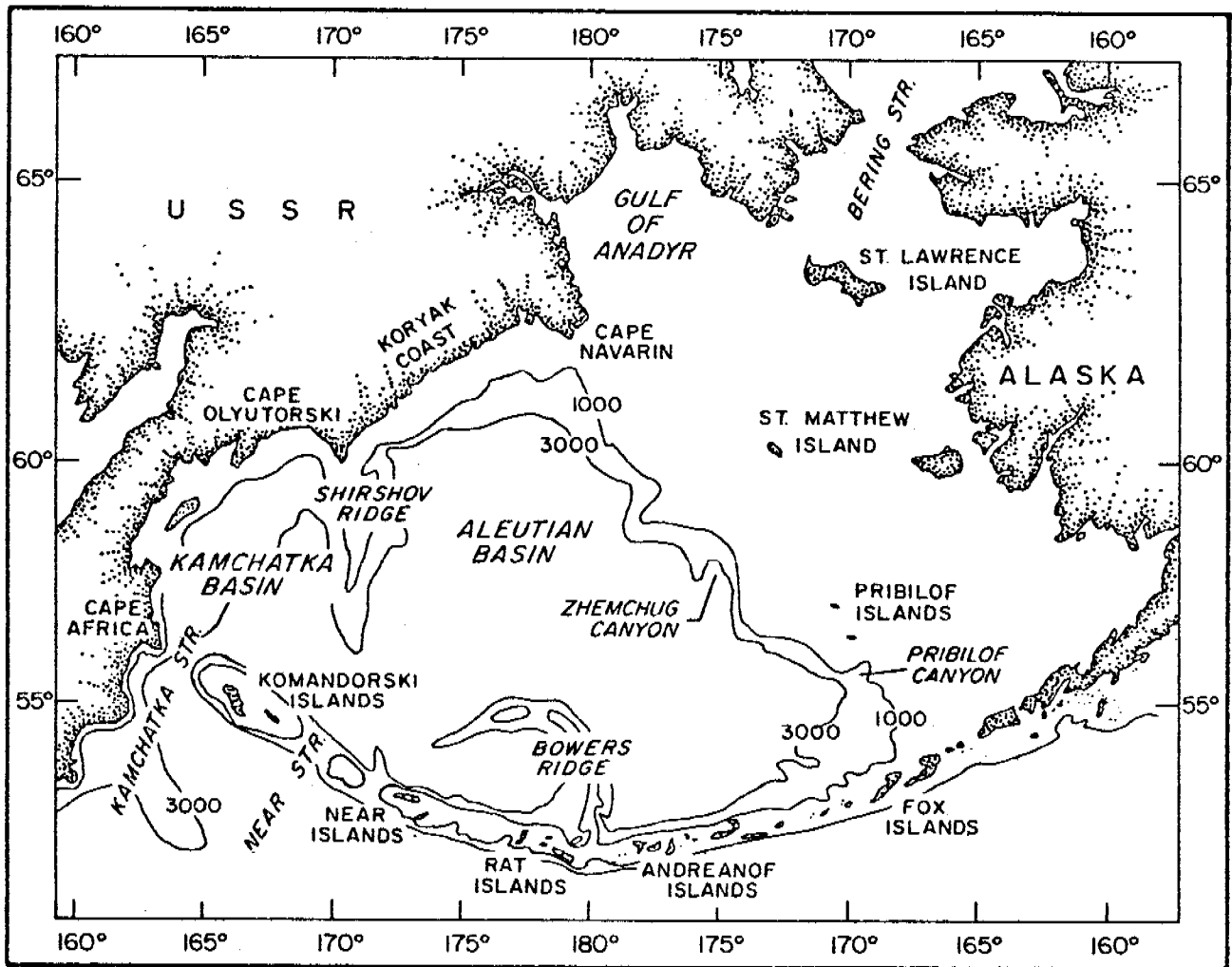
- Aagaard, K., and P. Greisman, Towards new mass and heat budgets for the Arctic Ocean, *J. Geophys. Res.*, 80, 3821-3827, 1975.
- Arsen'ev, F. S., *Currents and Water Masses of the Bering Sea*, Izd. Nauka, Moscow (in Russian) (transl. 1969, Nat. Mar. Fish. Serv. Biol. Lab., Seattle), 146 pp., 1967.
- Beardsley, R. C., and C. N. Flagg, The water structure, mean currents, and shelf-water/slope-water front on the New England continental shelf, *Mem. Soc. Roy. Sci. Liège, Ser. 6, 10*, 209-225, 1976.
- Bumpus, D. F., A description of the circulation on the continental shelf of the east Coast of the United States, *Progr. Oceanogr.*, 6, 111-156, 1973.
- Coachman, L. K., K. Aagaard, and R. B. Tripp, *Bering Strait: The Regional Physical Oceanography*, University of Washington Press, Seattle, 172 pp., 1975.
- Coachman, L. K., and R. L. Charnell, Finestructure in Outer Bristol Bay, Alaska, *Deep-Sea Res.*, 24 (10): 869-890, 1977.
- Csanady, G. T., Mean circulation in shallow seas, *J. Geophys. Res.*, 81, 5389-5399, 1976.
- Dodimead, A. J., F. Favorite, and T. Hirano, *Salmon of the North Pacific, Part II: Review of Oceanography of the Subarctic Pacific region*, Int. N. Pac. Fish. Comm., Bull. 13, Vancouver, 195 pp., 1963.
- Favorite, F., A. J. Dodimead, and K. Nasu, *Oceanography of the Subarctic Pacific Region, 1960-71*, Int. N. Pac. Fish. Comm., Bull. 33, Vancouver, 187 pp., 1976.
- Garvine, R. W., and J. D. Monk, Frontal structure of a river plume, *J. Geophys. Res.*, 79, 2251-2259, 1974.
- Heaps, N. S., Estimation of density currents in the Liverpool Bay area of the Irish Sea, *Geophys. J. R. Astr. Soc.*, 30, 415-432, 1972.

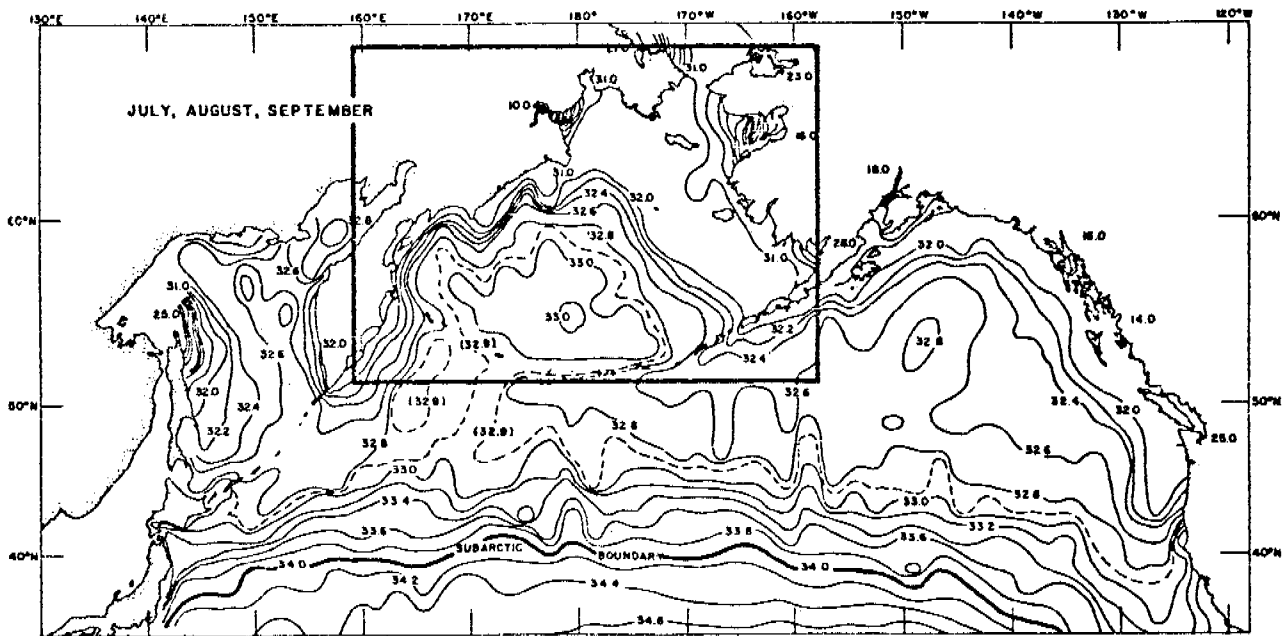
- Hokkaido University, Faculty of Fisheries, *Data Record of Oceanographic Observations and Exploratory Fishing*: No. 3, 296 pp., 1959; No. 6, 283 pp., 1962; No. 9, 343 pp., 1965; No. 10, 388 pp., 1966; No. 11, 383 pp., 1967, and No. 13, 406 pp., 1969.
- Kinder, T. H., The continental slope regime of the Eastern Bering Sea, Ph.D. dissertation, University of Washington, 272 pp., 1976.
- Kinder, T. H., and L. K. Coachman, *An Analysis of Current Meter Measurements from Pribilof Canyon*, University of Washington, Department of Oceanography, Technical Report, Ref: M75-121, 85 pp., 1975.
- Kinder, T. H., L. K. Coachman, and J. A. Galt, The Bering slope current system, *J. Phys. Oceanogr.*, 5, 231-244, 1975.
- Kitano, K., A note on the thermal structure of the Eastern Bering Sea, *J. Geophys. Res.*, 75, 1110-1115, 1970.
- Lisitsyn, A. P., *Recent Sedimentation in the Bering Sea*, Izd. Nauka, Moscow, translated by the Israel Program for Scientific Translations, Jerusalem, 1969 (available Clearinghouse for Federal and Scientific Information, Springfield, VA), 614 pp., 1966.
- Natarov, V. V., On the water masses and currents of the Bering Sea, *Tr. VNIRO*, 48; *Isv. TINRO*, 40 (Translation, 1968: Soviet Fisheries Investigations in the northeast Pacific, NTIS, Springfield, VA), 110-130, 1963.
- Ohtani, K., Oceanographic structure in the Bering Sea, *Mem. Fac. Fish. Hokkaido Univ.*, 21, 65-106, 1973.
- Roden, G. I., On river discharge into the northeastern Pacific Ocean and the Bering Sea, *J. Geophys. Res.*, 72, 5613-5629, 1967.
- Roden, G. I., On North Pacific temperature, salinity, sound velocity and density fronts and their relation to the wind and energy flux fields, *J. Phys. Oceanogr.*, 5, 557-571, 1975.

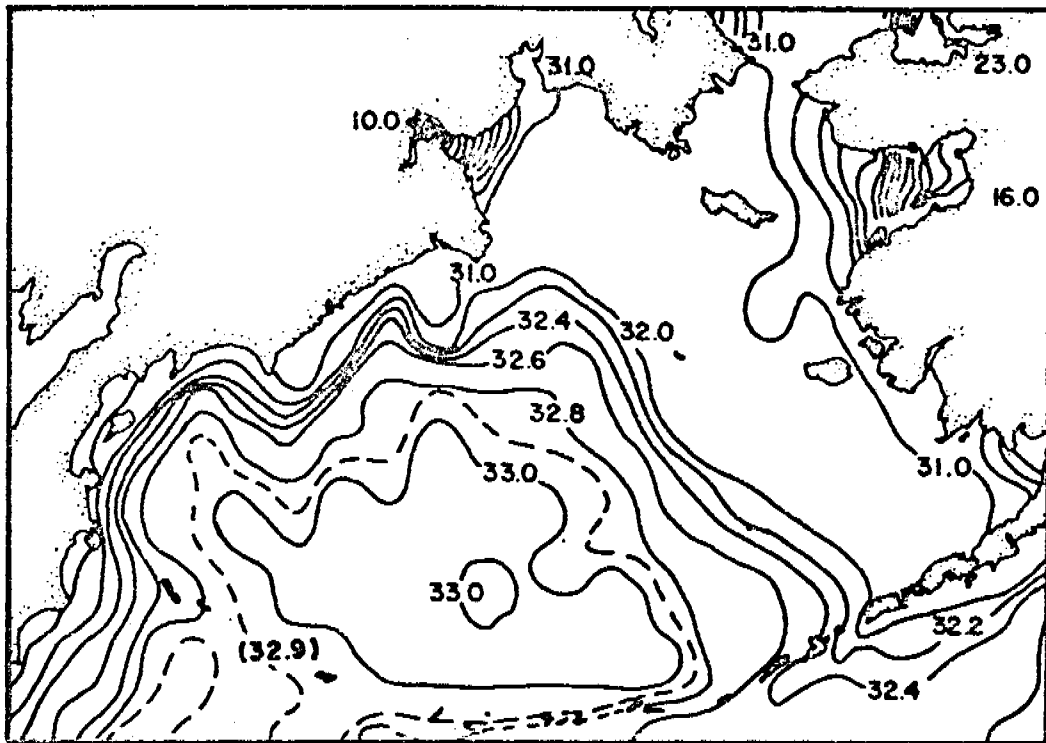
- Scholl, D. W., E. C. Buffington, D. M. Hopkins, and T. R. Alpha, The structure and origin of the large submarine canyons of the Bering Sea, *Mar. Geol.*, 8, 187-210, 1970.
- Schumacher, J. D., and L. K. Coachman, *Bristol Bay Oceanographic Processes (B-BOP)*, Second Annual Report, unpublished, 63 pp., 1977. Available from Kinder and Coachman.
- Scripps Institution of Oceanography of the University of California, *Oceanic Observations of the North Pacific*, University of California Press, Berkeley, 804 pp., 1958; 901 pp., 1959.
- Steffanson, U., L. P. Atkinson, and D. F. Bumpus, Hydrographic properties and circulation on the North Carolina shelf and slope waters, *Deep-Sea Res.*, 18, 383-420, 1971.
- Stevenson, M. R., R. W. Garvine, and B. Wyatt, Lagrangian measurements in a coastal upwelling zone off Oregon, *J. Phys. Oceanogr.*, 4, 321-336, 1974.
- Voorhis, A. D., The horizontal extent and persistence of thermal fronts in the Sargasso Sea, *Deep-Sea Res.*, 16, suppl., 331-337, 1969.
- Voorhis, A. D., D. C. Webb, and R. C. Millard, Current structure and mixing in the shelf/slope water front south of New England, *J. Geophys. Res.*, 81, 3695-3708, 1976.
- Wooster, W. S., Equatorial front between Peru and the Galapagos, *Deep-Sea Res.*, 16, suppl., 407-419, 1969.

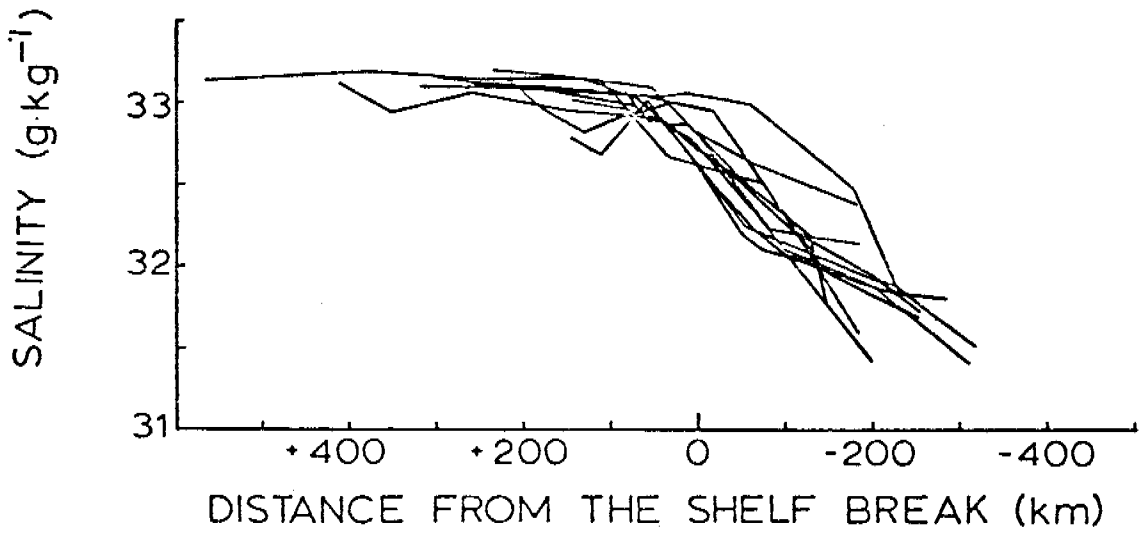
Figure Legends

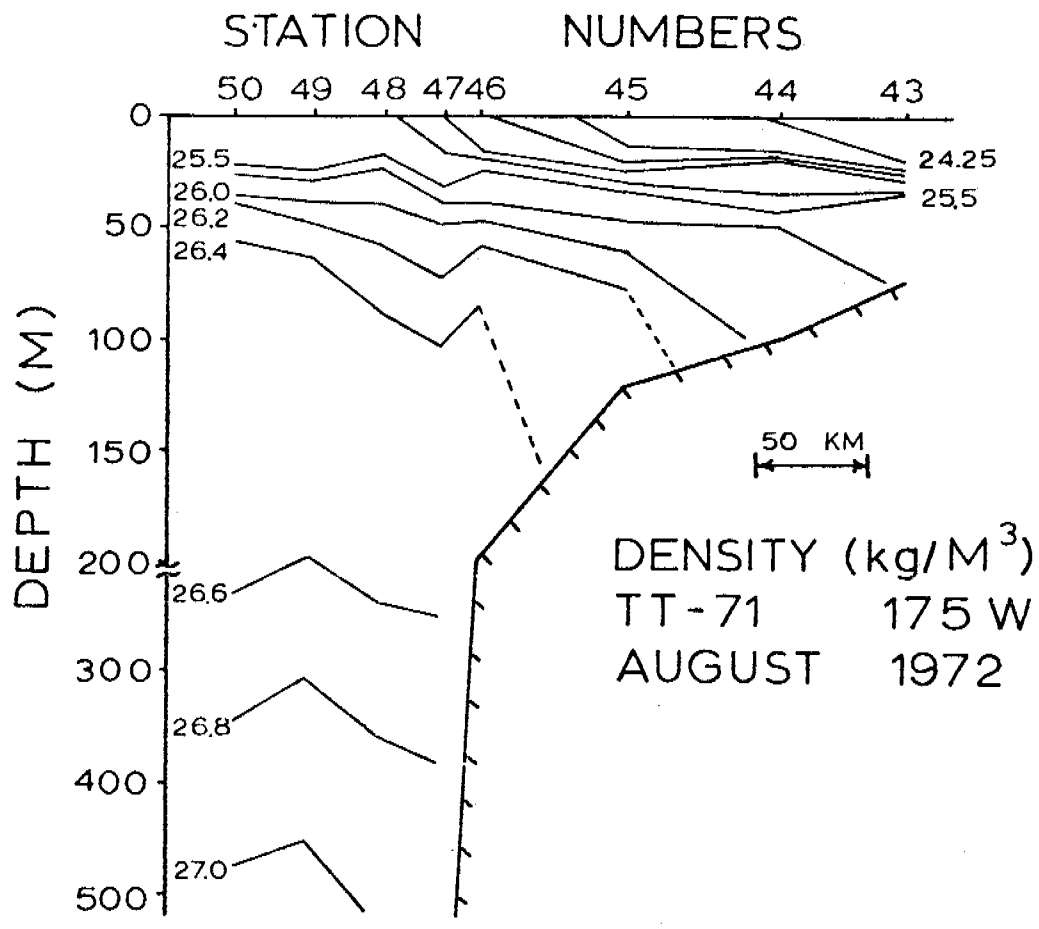
1. The Bering Sea. The 1000 m and 3000 m isobaths delimit the continental slope, which is incised by large submarine canyons such as Zhemchug and Pribilof. The shelf break, which occurs at about 170 m depth, lies 25 to 50 km northeast of the 1000 m isobath that runs from Cape Navarin to the Fox Islands.
2. The surface salinity distribution in summer. (A) The northern North Pacific and (B) the Bering Sea (from Favorite *et al.*, 1976, p. 135). (g/kg)
3. Mean 0 to 100 m salinity versus distance from the shelf break. An abrupt change in the salinity gradient occurs 20 to 80 km seaward of the shelf break (+: towards the basin). See Table 1 for sources of data.
4. Density cross section at 175°W in August 1972. The shallow surface front and underlying downwarped isopycnals seaward of the shelf break are evident. Data were acquired with an STD, sampling about once per 1.5 m. (kg/m^3)
5. Mean 0 to 100 m salinity, Zhemchug Canyon. (g/kg)
6. Mean 0 to 100 m salinity, Pribilof Canyon. (g/kg)
7. Salinity distribution, Pribilof Canyon. (A) 10 m (B) 100 m. (g/kg)
8. Density cross sections, Zhemchug Canyon. Note the surface front and downwarped isopycnals ($\sigma_t \approx 26.5$ and 26.6) beneath. Data are from Nansen bottle samples at 0, 10, 20, 30, 50, 75, 100, 125, 150, 200, and 250 m depth. (kg/m^3)
9. Density and temperature cross sections, Pribilof Canyon. The front is clearly defined in density but not temperature. Sampling as in Fig. 8. (kg/m^3 and °C)
10. Temperature cross sections, Zhemchug Canyon. Sampling as in Fig. 8. (°C)
11. Surface phosphate, Pribilof Canyon. ($\mu\text{g-at/l}$)
12. Surface nitrate, Pribilof Canyon. ($\mu\text{g-at/l}$)

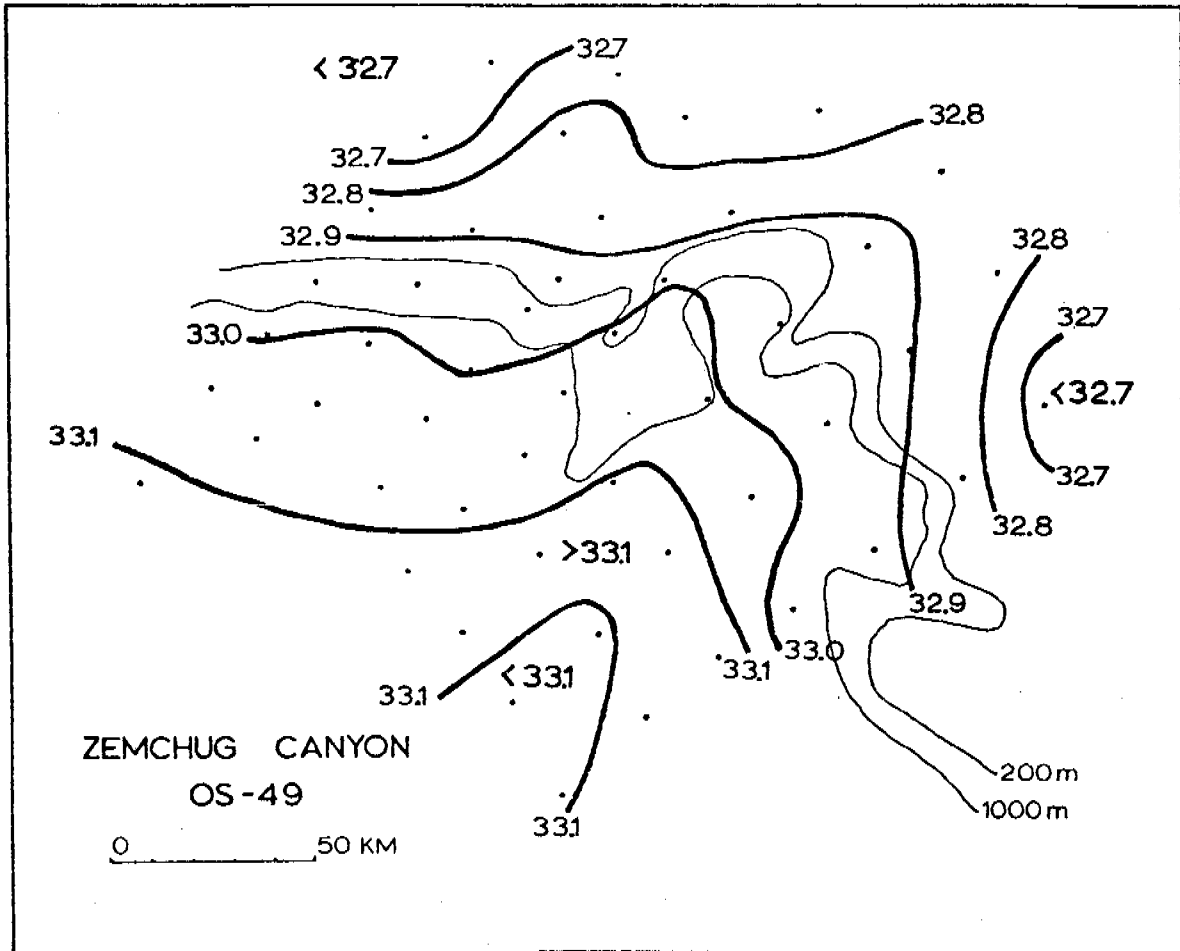


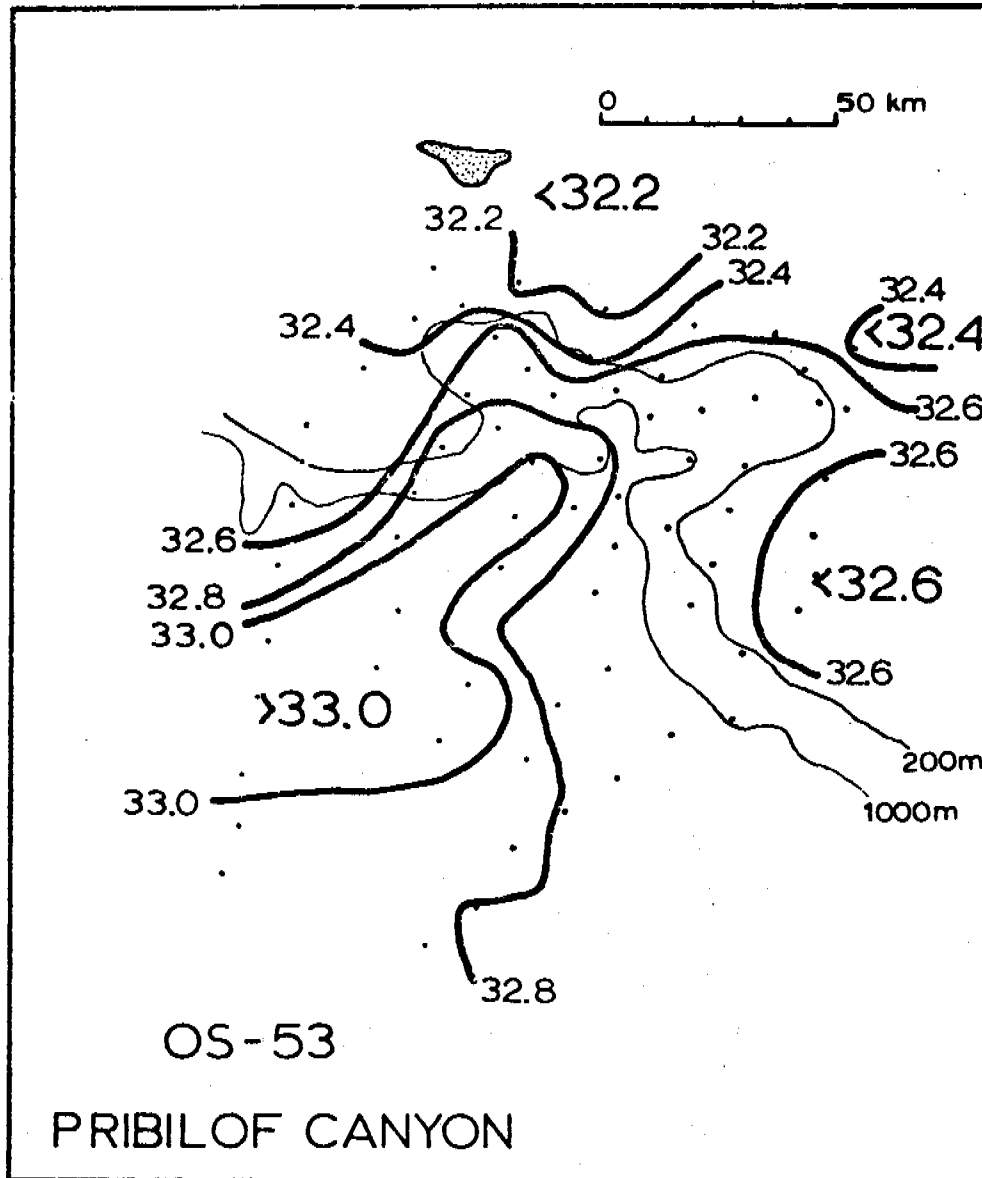


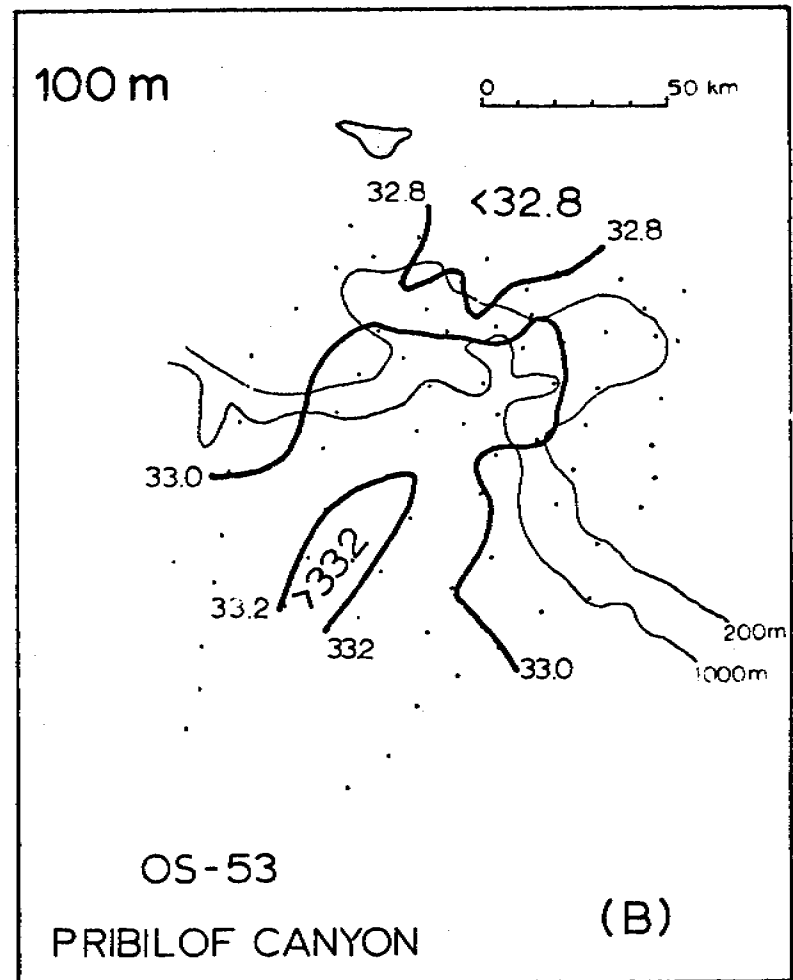
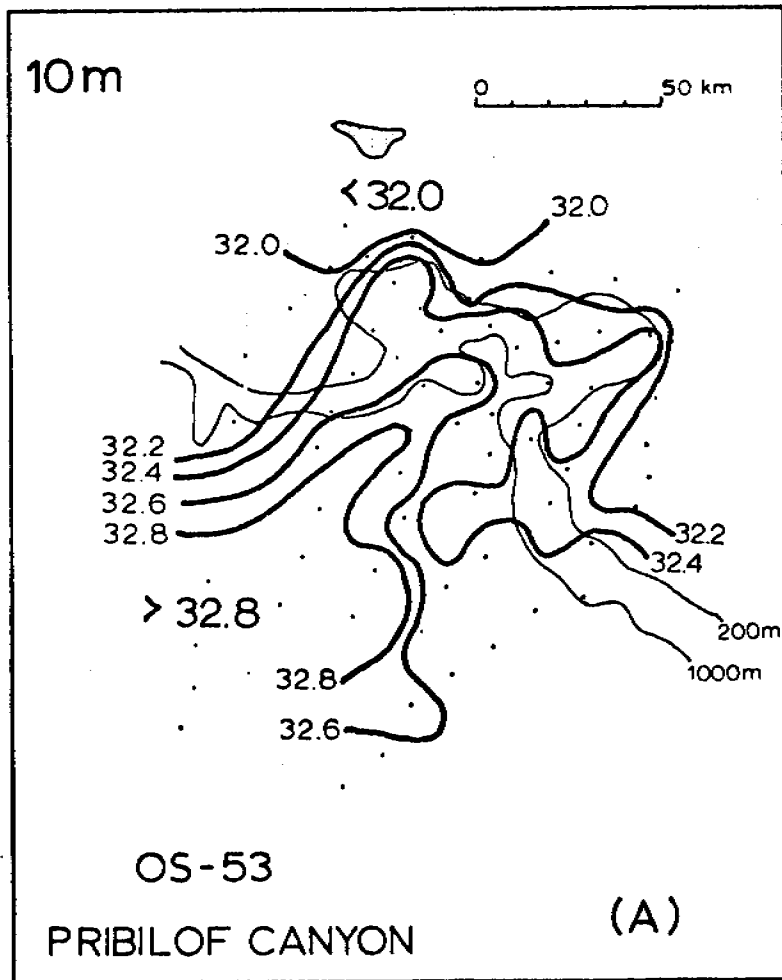


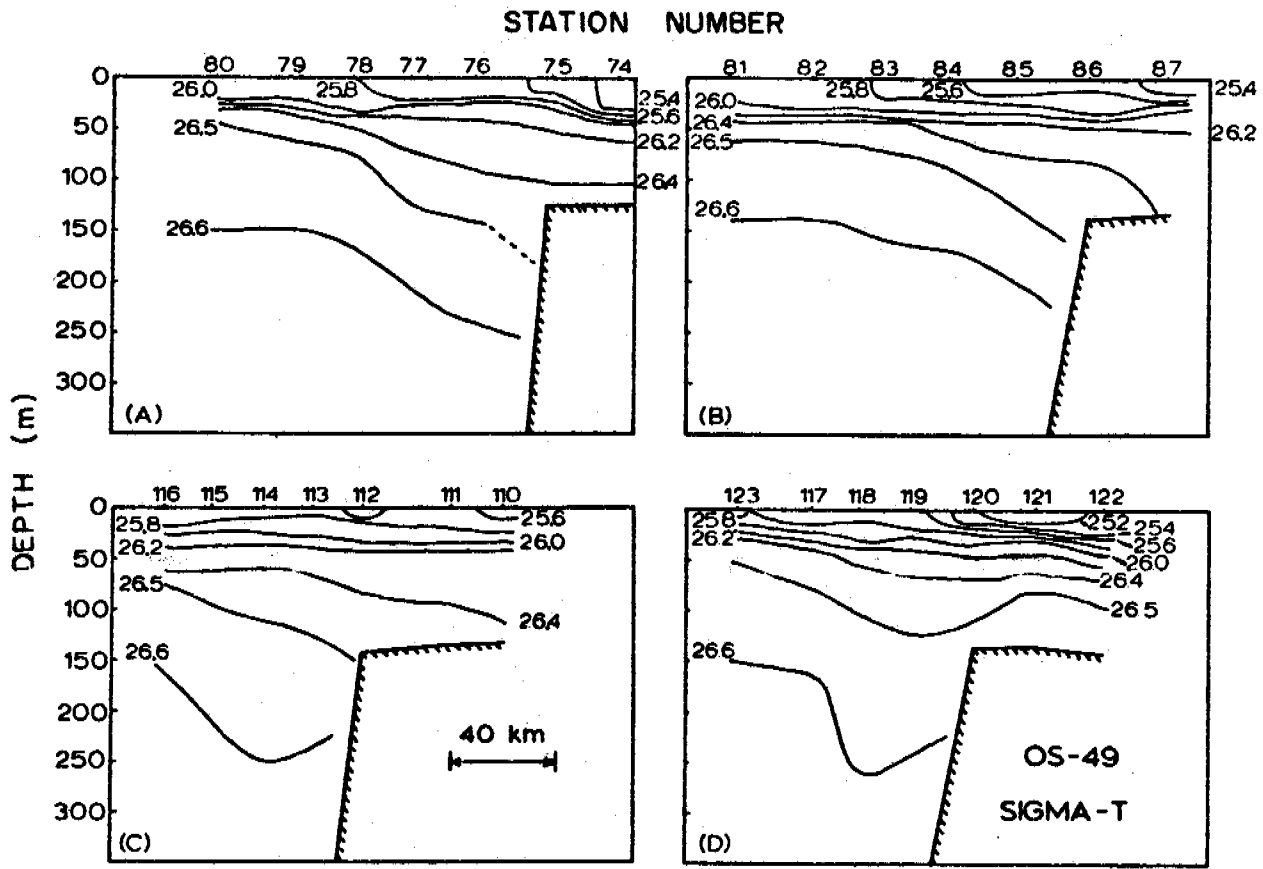


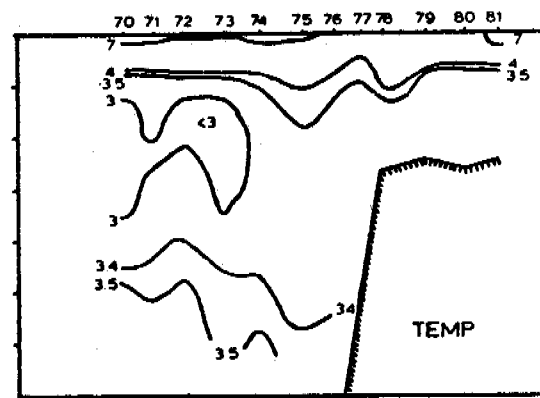
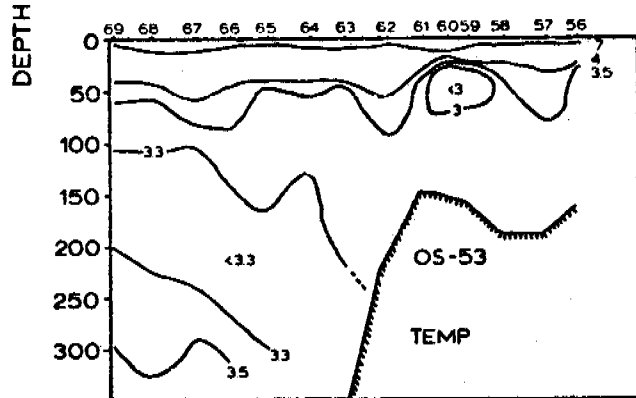
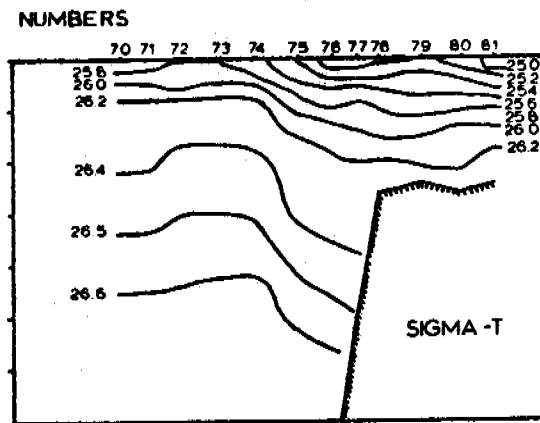
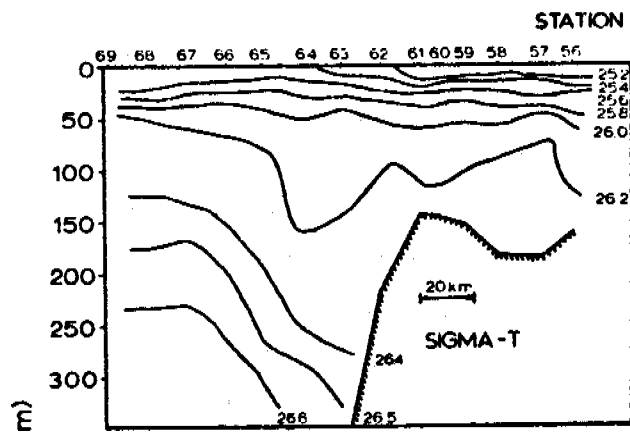


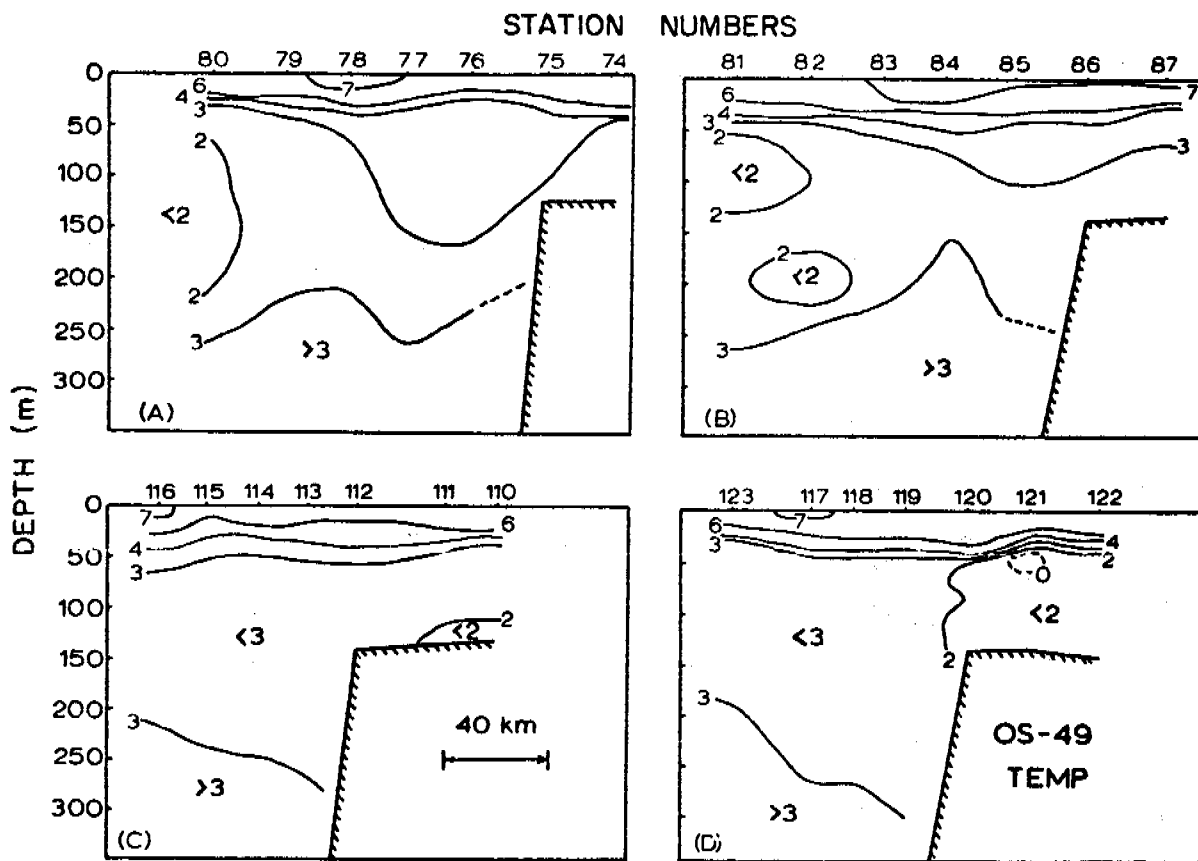


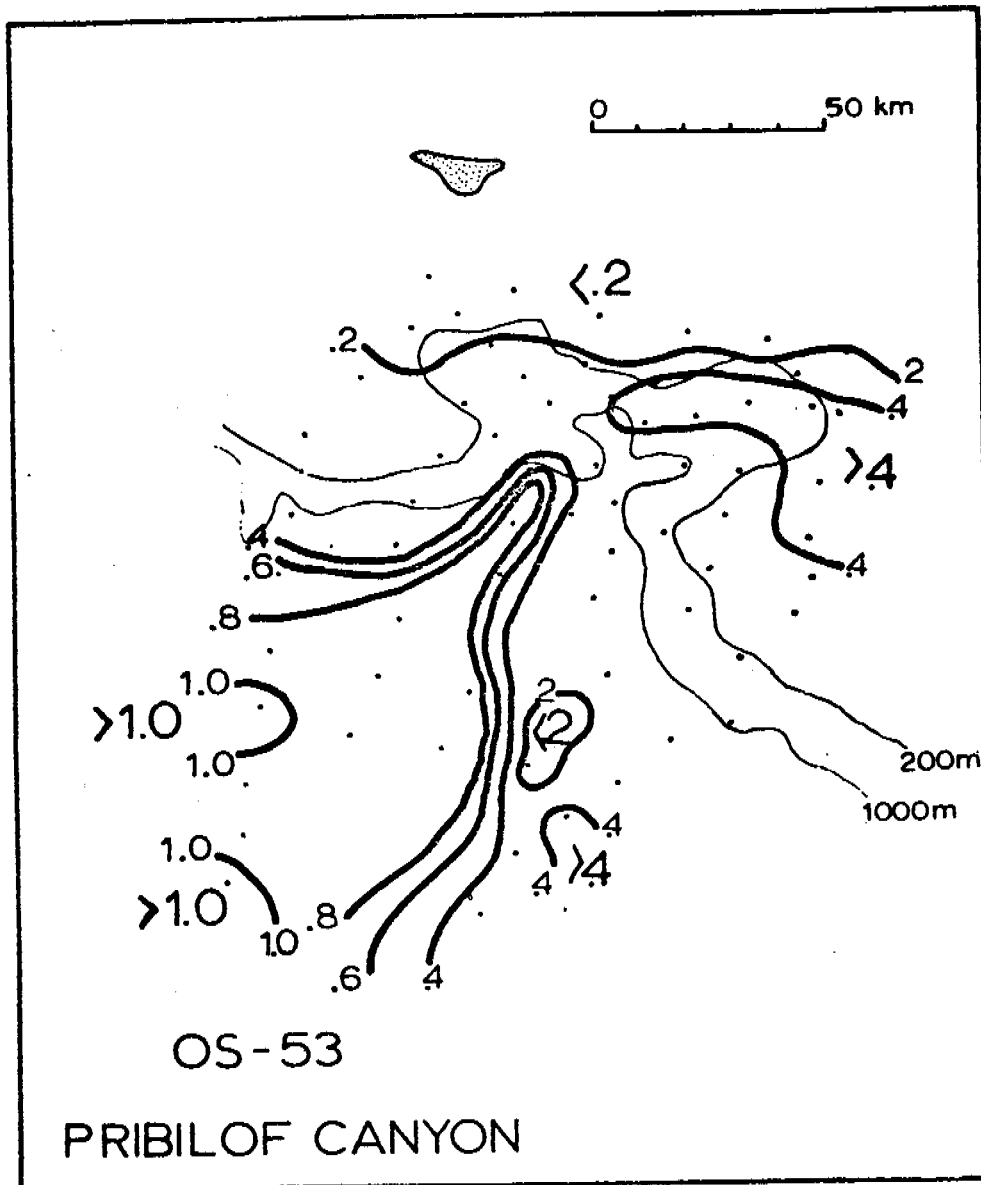


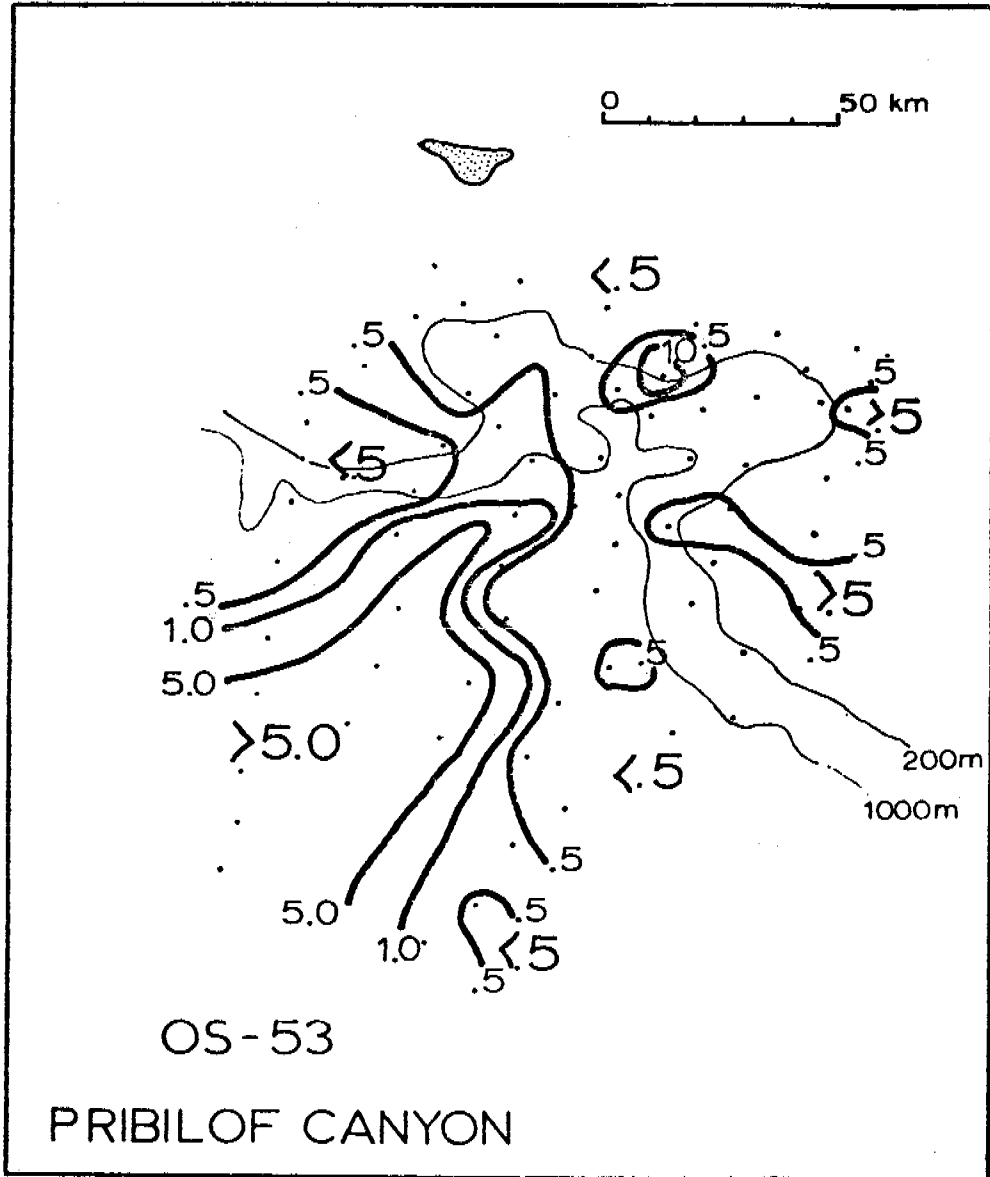












V. Cooperation

We are cooperating with several research units as follows:

289 (Royer) Satellite imagery usefully delineates the structural front and the seasonal ice cover.

435 (Leendertse) We provide hydrographic, current and pressure data. Together we attempt to understand the tidal regime.

217 (Hansen) We are trying to understand the deep eddy, initially revealed by drifters, and to compare current meter and drifter records where appropriate.

206 (Vallier and Gardner) We are exchanging thoughts and data on the St. George Basin regime.

83 (Hunt) We are attempting to relate the bird distributions to the structural front near the Pribilof Islands.

367 (Reynolds) We are exchanging ideas and data on the effects of local meteorology on the oceanography.

VI. Publications Resulting from Bristol Bay Work

1. Coachman, L.K. and R.L. Charnell, 1977. Finestructure in Outer Bristol Bay, Alaska. *Deep Sea Res.* 24 (10): 869-889.
2. Coachman, L.K. and R.L. Charnell, Lateral water mass interactions - a case study, Bristol Bay, Alaska, submitted to *J. Phys. Oceanogr.*
3. Kinder, T.H., 1977. The hydrographic structure over the continental shelf near Bristol Bay, Alaska, June, 1976. University of Washington, Department of Oceanography, Technical Report M77-3, 61 pp.
4. Kinder, T.H. and L.K. Coachman, 1978. The front overlaying the continental slope of the Eastern Bering Sea. *J. of Geophys. Res.*, in press.*

*This work was funded primarily by the National Science Foundation, and mostly reflects earlier work. This paper is included, however, because OCSEAP work was somewhat involved and because the paper is relevant to OCSEAP objectives.

5. Kinder, T.H., J.D. Schumacher, R.B. Tripp, and J.C. Haslett, 1978. The evolution of the hydrographic structure over the continental shelf near Bristol Bay, Alaska, during summer 1976. University of Washington, Department of Oceanography Technical Report.
6. Muench, R.D. and R.L. Charnell, 1977. Observations of medium scale features along the seasonal ice edge in the Bering Sea. *J Phys. Oceanogr.* 7 (4): 602-606.
7. Reed, R.K., 1978. Heat budget in the eastern Bering Sea. *J. Geophys. Res.*, in press.
8. Schumacher, J.D., T.H. Kinder, D.J. Pashinski, and R.L. Charnell. A structural front over the continental shelf of the Eastern Bering Sea. Submitted to: *J. Phys. Oceanogr.*

Additionally, several talks were given at the fall American Geophysical Union Meeting, and several are scheduled for the forthcoming spring meeting (see *EOS* 58 (12) and *EOS* 59 (4) for abstracts).

VII. Needs for Further Study

We believe that the continued study of Bristol Bay should emphasize analysis of data already obtained, with selected field work directed at specific questions. Some of the questions under study are:

- A. Fine structure. The nature and distribution of the rich fine structure in the shelf heat domain is well documented. What are the implications to mixing? Is there a fine structure in velocity? Is the microstructure (i.e., scales of less than one meter) as rich as present measurements suggest?
- B. Structural front: The gross description of the structural front is established. What is the velocity field close to the front? What is the dynamical balance of the front? What effect does the front have on mixing? On the biology?
- C. Tidal analysis. Tidal analysis, in cooperation with numerical modeling, has elucidated some features of the tides in Bristol Bay. What are the tidal currents in Bristol Bay? What is the character of the anomalous reduction in tidal currents, and what causes this reduction?
- D. Low frequency currents. Episodic and quasi-oscillatory currents appear in the data at frequencies below the diurnal. What is their nature? What causes them? How do drifters and current meters compare?
- E. Deep Eddy. A deep eddy was observed hydrographically and by drifters during 1977. How are the hydrographic and drifter data related? Is the eddy permanent? What causes the eddy?

These and similar questions are best addressed by a combination of studying data already obtained, numerical and analytical investigations, and carefully designed field experiments.

VIII. Conclusions

Field work in the Bristol Bay region has yielded better understanding of the physical oceanography. This understanding is reflected in Section IV of this report (present status), in previous reports, and in the publications listed in Section VI.

Major elements include:

- (1) the shelf exhibits low mean flow and the energy variance is tidally dominated;
- (2) the hydrographic structure in summer separates into three distinct domains: coastal, central shelf, and shelf break;
- (3) melting ice in winter may partially re-establish this structure;
- (4) strong finestructure is ubiquitous in the shelfbreak domain, and is evidence of lateral water mass interaction;
- (5) the central shelf and coastal domains are separated by a structural front which probably results from a varying balance between buoyancy input and tidal mixing;
- (6) a similar front exists near the Pribilof Islands and probably has biological implications;
- (7) tidal currents show anomalous diminution at some locations while tidal heights do not, in apparent association with stratification;
- (8) a deep eddy was seen in summer 1977;
- (9) the heat balance over the central shelf during summer primarily involves atmospheric exchange;
- (10) certain ice-edge features are associated with the wind; and,
- (11) low frequency (less than diurnal) flow is episodic or quasi-periodic.

Many of these elements receive amplification and discussion of their implication in papers, while others are the subject of preliminary reports. Thus far, many interesting features have been identified and these need to be more fully understood. Further analysis of data in hand, numerical and analytical investigation, and selected field work are required, with the emphasis on data analysis. Once these salient features are understood, a reasonable synthesis of the regional physical oceanography will be possible.

APPENDIX A.

Hydrographic Summary

In addition to the data reported in IV. H. above, four cruises collected hydrographic data as summarized in the Table and figures 1-4.

<u>Cruise</u>		<u>Dates</u>	<u>Casts</u>	<u>XBT</u>
<u>Discoverer</u>	RP-4-D1-77A Leg V	26 April- 16 May	239	-
<u>Miller Freeman</u>	RP-4-MF-77B Leg VI	23 May- 11 June	104	116
<u>Surveyor</u>	RP-4-SU-77B Leg III	20 July- 8 August	210	49
<u>Discoverer</u>	RP-4-D1-77C Leg I	6-29 September	186	-

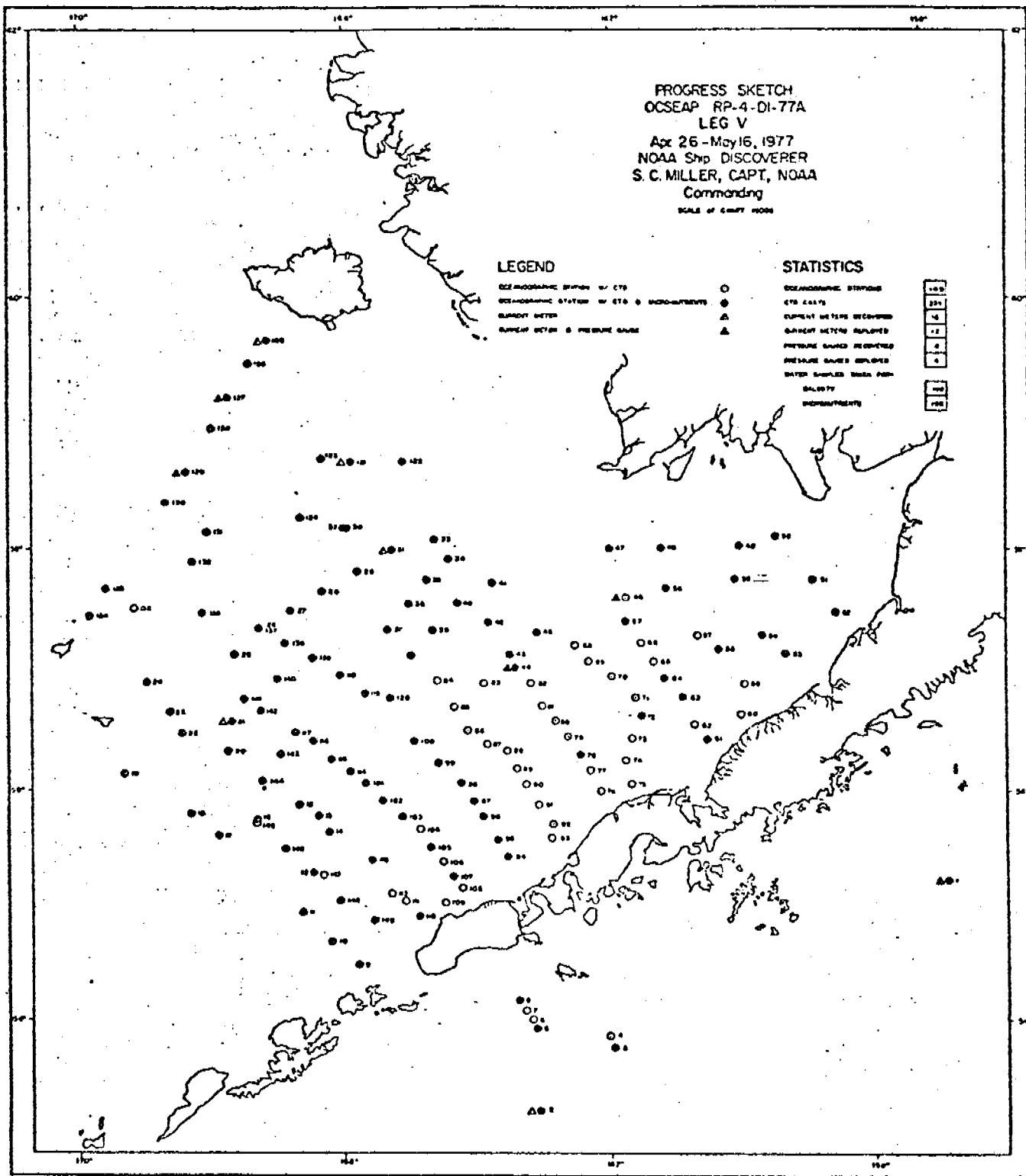


Figure 1

PROGRESS SKETCH

RP-4-MF-778

LEG VI

MAY 25 to JUNE 11

NOAA Ship MILLER FREEMAN

S. R. PETERSEN CDR NOAA

COMMANDING OFFICER

FROM CHART 10000

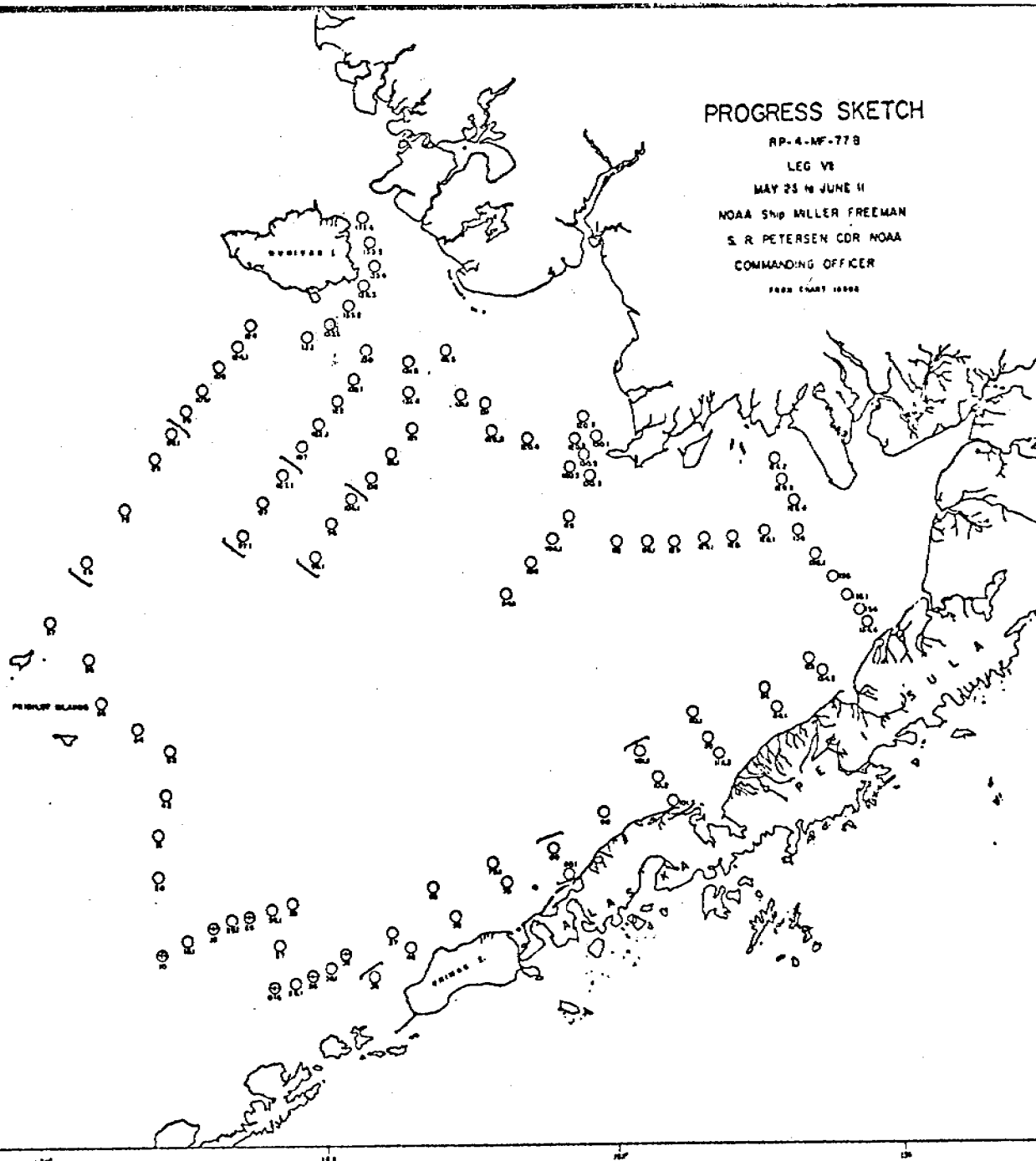
STATISTICS

CTD's 104
 MNRUS CTD's 8
 SURFACE SAL's 28
 XBT's 118

LEGEND

○ CTD STATION
 ⊕ DRIFTERS (MNRUS)
 — XBT - Under Icebergs

Figure 2



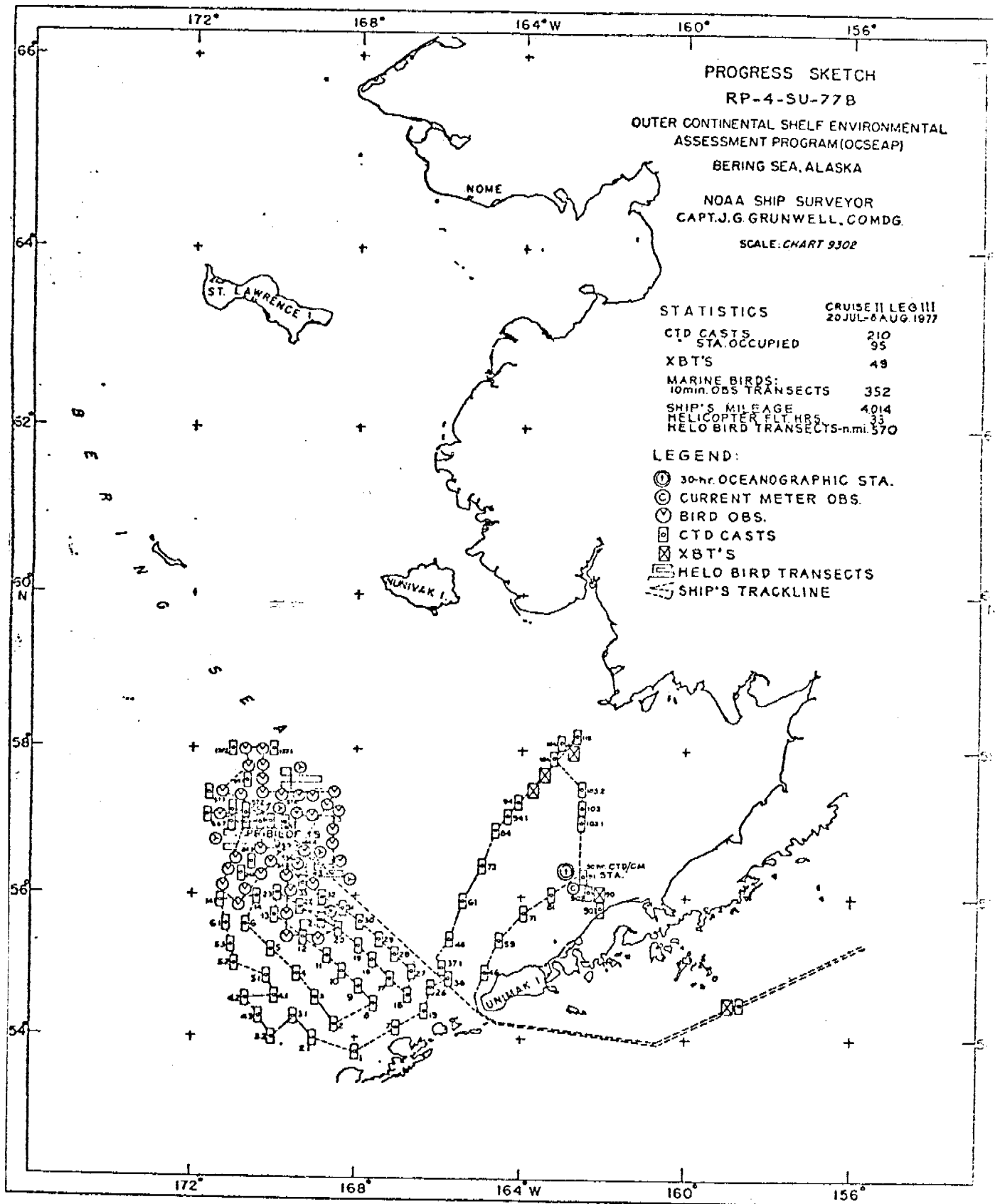


Figure 3 571

APPENDIX B.

Mooring Summary

- 1) Mooring BC-4E
Latitude: 58-366 N
Longitude: 168-21.7 W
 - (a) Current meter depth: 48 meters
Data period: 5/13/77 to 6/28/77
 - (b) Current meter depth: 20 meters
Data period: 5/13/77 to 7/15/77
 - (c) Pressure gauge depth: 54 meters
Data period: 5/13/77 to 9/12/77

- 2) Mooring BC-9C
Latitude: 59-12.0 N
Longitude: 167-43.2 W
 - (a) Current meter depth: 23.5 meters
Data period: 5/12/77 to 9/10/77
 - (b) Current meter depth: 33.5 meters
Data period: 5/12/77 to 8/30/77
 - (c) Pressure gauge depth: 39.5 meters
Data period: 5/12/77 to 7/27/77

- 3) Mooring BC-18A
Latitude: 59-40.1 N
Longitude: 167-07.5 W
 - (a) Current meter depth: 20.5 meters
Data period: 5/12/77 to 9/3/77

- 4) Mooring BC-19A
Latitude: 58-42.6 N
Longitude: 163-52.8 W
 - (a) Current meter depth: 22.5 meters
Data period: 5/12/77 to 5/23/77

NOTE: The University of Washington has been late in submitting the above data to the OCSEAP Project Office for the following reason. The Department of Oceanography changed computer systems last fall which has necessitated extensive reprogramming and debugging of the system. This delay has been beyond our control. However, we anticipate having all the data submitted by the end of April.

- 5) Mooring BC-2E
Latitude: 57-02.5 N
Longitude: 163-26.0 W
 - (a) Current meter depth: 20 meters
Data period: 5/4/77 to 9/10/77
 - (b) Current meter depth: 55 meters
Data period: 5/4/77 to 9/10/77
 - (c) Pressure gauge depth: 62 meters
Lost pressure gauge.

- 6) Mooring BC-16A
Latitude: 57-59.2 N
Longitude: 165-15.8 W
(a) Current meter depth: 20 meters
Data period: 5/3/77 to 9/11/77
(b) Current meter depth: 38 meters
Bad time base.
- 7) Mooring BC-15C
Latitude: 57-39.0 N
Longitude: 162-41.4 W
(a) Current meter depth: 20 meters
Data period: 5/4/77 to 9/10/77
(b) Current meter depth: 35 meters
Data period: 5/4/77 to 9/10/77
(c) Pressure gauge depth: 45 meters
Data period: 5/4/77 to 9/10/77
- 8) Mooring BC-13D
Both meters lost due to trawling.
- 9) Mooring BC-17B
Lost.

Annual Report

Contract No.: 03-5-022-67, T.O.1
Research Unit No.: 151
Reporting Period: 1 April 1977-31 March 1978
Number of Pages: 14

STD Measurements in Possible Dispersal Regions
of the Beaufort Sea

Knut Aagaard

Department of Oceanography
University of Washington
Seattle, Washington 98195

29 March 1978

I. Summary

New results since last year include:

- A. The direct influence of freezing extends far below the local pycnocline, due to the differential movement of waters from a variety of locations seeking their density level.
- B. There are considerable year-to-year differences in hydrography and anomalies can persist through several seasons.
- C. It seems likely that in the mean there is a net flow of saline water onto the shelf in the lower part of the water column.
- D. The temperature signal of the Bering Sea water is largely erased within a month or two after freeze-up.

The major implication of the STD work with respect to the transport and dispersal of pollutants is that at least the outer part of the shelf, e.g., that portion deeper than about 50 m, is an active area even after freeze-up. There is ample evidence both of large-scale motion along the shelf, and of cross-shelf flux and exchange with the Arctic Ocean to the north.

II. Introduction

The general objective of this research unit has been to provide seasonally distributed synoptic temperature-salinity mappings of the Beaufort Sea shelf and slope. In the first year of work, the sections were distributed along the entire Alaskan shelf, one each running normal to the shelf from Pitt Point, Narwhal Island, and Humphrey Bay. They were run in the fall (October-November), winter (February), and spring (May). The intent was to provide broad areal coverage. The second year the sections were concentrated in two locations, *viz.* off Lonely and Oliktok. In each region, two parallel lines of stations were run in order to more closely examine the along-shelf coherence of the hydrography. Because of the similarity in winter and spring conditions during the first year, we felt it sufficient the second year to sample only in the fall and winter.

The general thrust of this work is, of course, toward understanding the diffusive and advective processes which transport and disperse pollutants and substances of biological and geological importance.

III. Current State of Knowledge

Except for the brief ice-free period during summer, hydrographic stations had never been taken in this area prior to the present work. Knowledge was therefore restricted to summer conditions, which briefly appear to be as follows. There are large temperature and salinity ranges (and gradients) on the shelf,

with temperatures varying from near-freezing to more than 5°C, and salinities from brackish to greater than 33 ‰. In summer, an eastward intrusion of relatively warm water originating in the Bering Sea appears to be a regular feature of the circulation on the outer shelf, being typically located seaward of the 40 m isobath. This water has been identified at least as far east as 143°W. Summer observations have also indicated the likelihood of an intermittent upwelling regime on the eastern part of the shelf. The upwelled water is relatively cold, low in oxygen, and high in nutrients. It has been postulated that the upwelling is a response to locally strong easterly winds and that the upwelled water on the shelf moves westward.

The first year-and-a-half (Cruises W21, W22, W24, and W25) of work under Research Unit No. 151 added substantially to this picture. In particular, the normal seasonal hydrographic progression was determined. Shortly after freeze-up in the fall, the entire shelf is still markedly stratified in salinity (and therefore in density), with a strong gradient below 20-30 m. This is a remnant of summer conditions. Above the pycnocline, the salinity varies considerably, both in time and space, but at any given station the upper layer is nearly homogeneous in both temperature and salinity. The temperature in this layer is very close to the freezing point, reflecting the conditioning of the layer by the freezing process with its attendant thermohaline convection. In the fall, there is still a wide-spread temperature maximum below the mixed layer. This maximum can be associated with a variety of different salinities, but it frequently very clearly indicates the presence of Bering Sea water. That is, the temperature signal resulting from the Bering Sea intrusion is not erased until somewhat later in the year.

In the winter, the overall stratification on the shelf is markedly less than in the fall, and the upper mixed layer extends deeper, typically below 30 m. At the same time, the upper-layer salinity is also higher, generally being above at least 31 ‰ everywhere on the shelf. While both a reduced stratification and an increase in salinity are to be expected as winter progresses, due to the separation of salt by freezing, the salinity changes that occur from fall to winter are generally larger than can reasonably be explained by this process. For example, from early November to early March the mean salinity typically increases by 1-1.5 ‰, which would require about 250-350 cm of ice to be formed in the intervening months. This is an unreasonably large amount, probably by a factor of 2-3. The conclusion must therefore be that there is a net advective flux of salt onto the Beaufort Sea shelf. The source of the salt remains uncertain. Another normal feature of the winter salinity distribution is a seasonal decrease of the upper-layer salinity, typically by at least 0.5 ‰ across the shelf. Again, the source of the feature is uncertain, although it seems likely that a transverse circulation would be associated with it. Some possible circulation mechanisms were discussed in last year's annual report. The winter temperatures are typically about 0.1°C colder than in fall, and there is indication of a slight (a few hundredths of a degree) of supercooling, relative to the freezing point at surface pressure.

In spring, conditions appear very similar to those in winter. The salinity and density structure is about the same, but there are some slight differences

in the temperature of the upper layer: it is not quite as cold, but is instead beginning to show a slight spring warming. Specifically, there is not much evidence of supercooling (relative to surface pressure); rather the temperature near the surface varies from the freezing point to 0.1-0.2°C above. This slight warming is restricted to a thin layer (e.g., the upper 5 m) and is frequently accompanied by a salinity that is slightly lower than that of the underlying water.

Over the slope, it is common to find that the isopleths rise on approaching the shelf. The most remarkably developed case of this was during Cruise W25 in the fall of 1976. In each of the four sections of that cruise, Atlantic water (or water closely akin to it), which is normally found well below 200 m farther offshore in the Beaufort Sea, could be seen on the shelf. For example, in the Oliktok East section, water warmer than 0°C and more saline than 34.5 ‰ was observed at 91 m; and at the Lonely West section, the effect of relatively warm and saline water was apparent even at the innermost station, where the bottom 10 m were warmer than -1°C and more saline than 34 ‰. Conceivably, a deep onshore flow of such saline water could both serve as the salt source discussed earlier and drive the transverse circulation probably associated with the upper-layer salinity distribution. It is important to note, however, that the inclined isopleths observed during W25 are not readily explainable as the result of wind-driven coastal upwelling, such as has been proposed by summer investigators. This is because neither during nor within at least 10 days prior to the section occupation were there the necessary strong easterly winds.

In connection with the sloping isopycnals, which are common over the slope, it may be significant that there is often a notable change in the sign of the geostrophic shear at the outermost stations, typically between 50-80 m. The simplest interpretation is of a core of relatively dense westerly-moving water at mid-depth, i.e., 50-100 m, over the slope.

Finally, the first year-and-a-half of work has shown that not only are there large seasonal changes in the hydrography, but conditions are different from one year to the next. One therefore has to exercise caution in attempting to generalize from a relatively short time base.

IV. Study Area

The most general area of interest extends eastward from Point Barrow along the entire northern Alaskan coast, i.e., from about 156° 30' W to 141° W, a lateral distance of nearly 600 km. The shelf is narrow, with the shelf break typically 80-90 km offshore. The total runoff is relatively small, highly seasonal, and concentrated in a very few rivers of any consequence, the largest of which is the Colville. The area is covered by sea ice, both first- and multi-year, through all but 2-3 months. Even during the height of summer, ice is usually found well onto the shelf.

V. Data Collection

The rationale of data collection has been discussed in the two previous annual reports and in Section II of this report.

VI. Results

The last field work under this contract was Cruise W27, the preliminary report of which was submitted as an appendix to the last annual report. The data from W27 have been processed and submitted to the project data office, properly formatted on magnetic tape. Pictorial representations of the W27 sections are included in Section VII of this report.

VII. Discussion

Figures 1-2 show the sections from W27. They are typical for winter, with a nearly homogeneous upper layer extending to 30 m or more, within which the temperature is at or very slightly below the freezing point. It is important to note, however, that the depth to which a layer is mixed, in the sense that above this depth the density is nearly uniform, is considerably shallower than the depth to which the water is at the freezing point. Two examples are shown in Figure 3, portraying both a fall and a winter station. At both stations, a notable pycnocline (of about 0.05 in σ_t per meter) begins at about 20 m, while the water is at the freezing point to more than twice this depth. Thus, water that has clearly been conditioned by the freezing process, subsequently can be found within or below a pycnocline. The water has simply moved obliquely down to the depth locally appropriate to its density. An observed water column is thus not simply representative of a local and vertically extensive mixing process driven by freezing, but rather it represents a layering of waters that may have been influenced by freezing at a variety of locations and times. After being cooled, and probably also having their salinity altered, the various parcels of water then arrange themselves in a stably stratified layer through differential motion. In other words, T-S distributions, such as the two shown in Figure 3, suggest that the time history of a column of water involves considerable vertical shearing.

The presence of year-to-year variations was remarked on in Section III. A good example is afforded by comparison of the salinity distributions from the winter of 1976 (W22) with those from 1977 (W27). In both years, the upper nearly-homogeneous layer was about the same depth (32 m on the average), but the mean density of this layer was greater in 1977 by 1.0 in σ_t , corresponding to a salinity difference of 1.2 ‰. Figure 4 shows the Pitt Point section from 1976, which can be contrasted with Figure 1. In 1976, the surface salinity was typically 30.3-30.4 ‰, while in 1977 it was near 31.5 ‰. Similarly, the salinities on the shelf in the Narwhal Island section in 1976 (W22) were about 1 ‰ lower than in the Oliktok sections in 1977 (W27). If one likewise compares the preceding fall conditions, i.e., 1975 (W21) and 1976 (W25), one also finds considerably lower salinities in the former year, both off Pitt

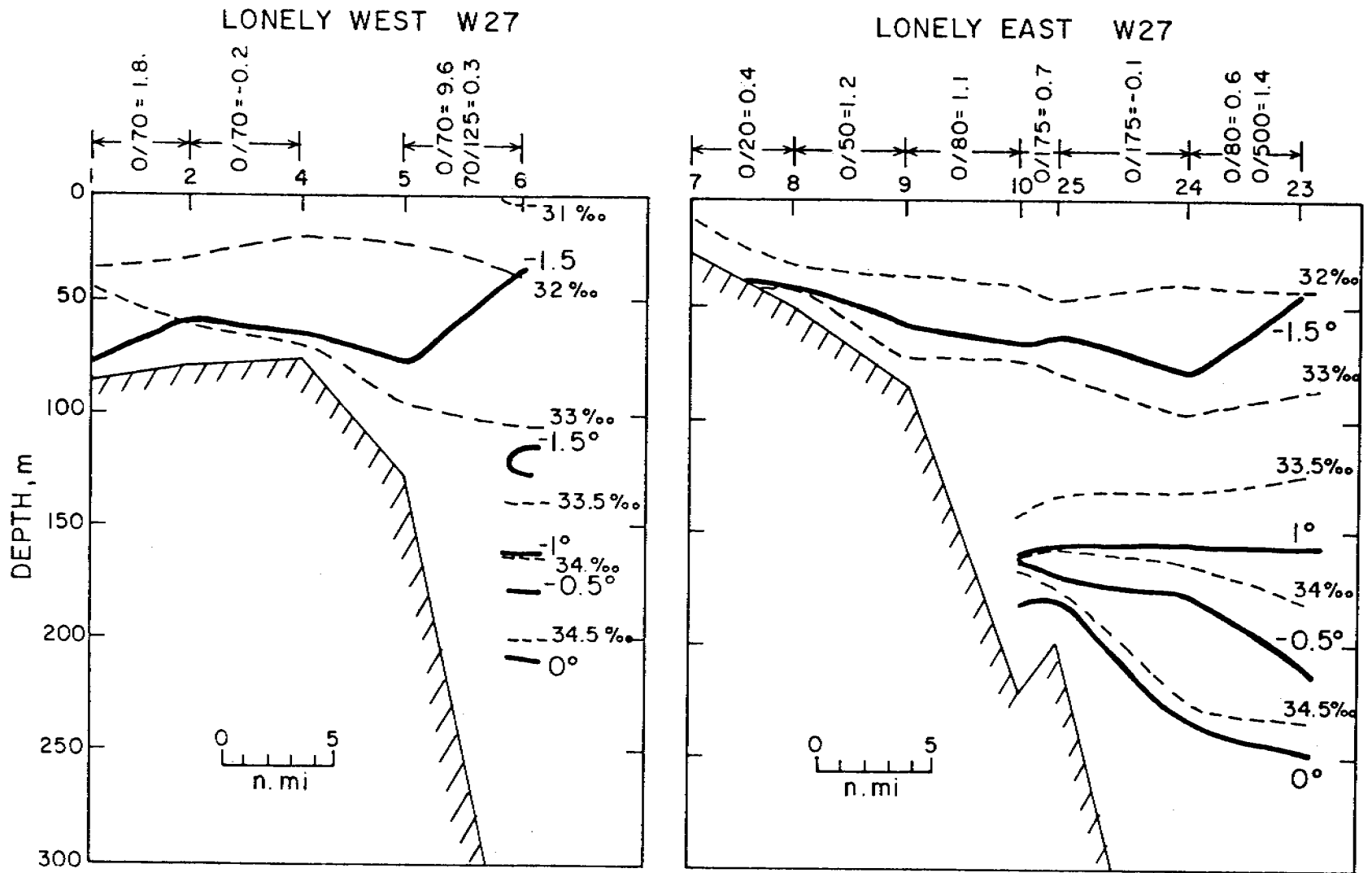


Figure 1

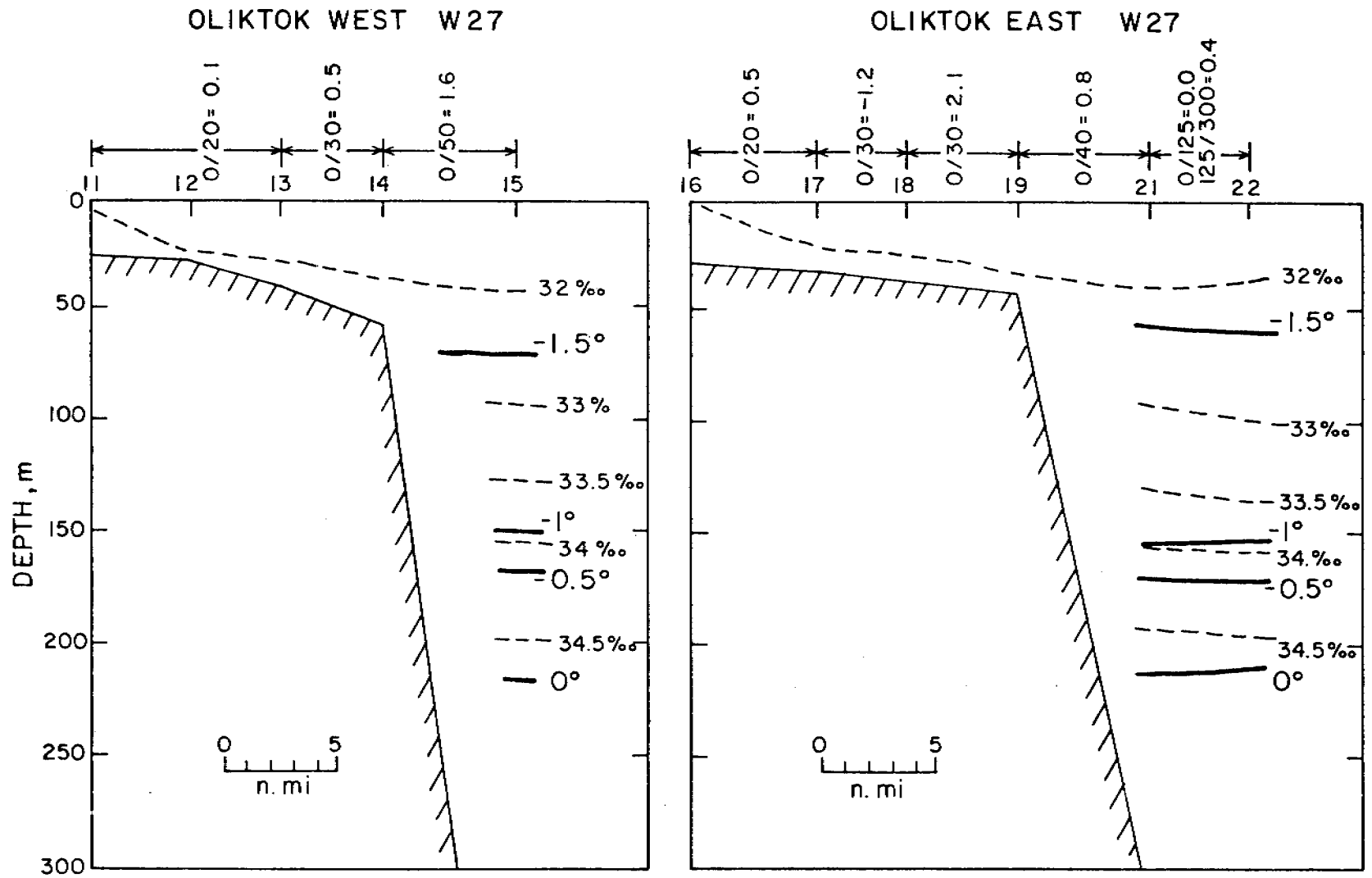


Figure 2

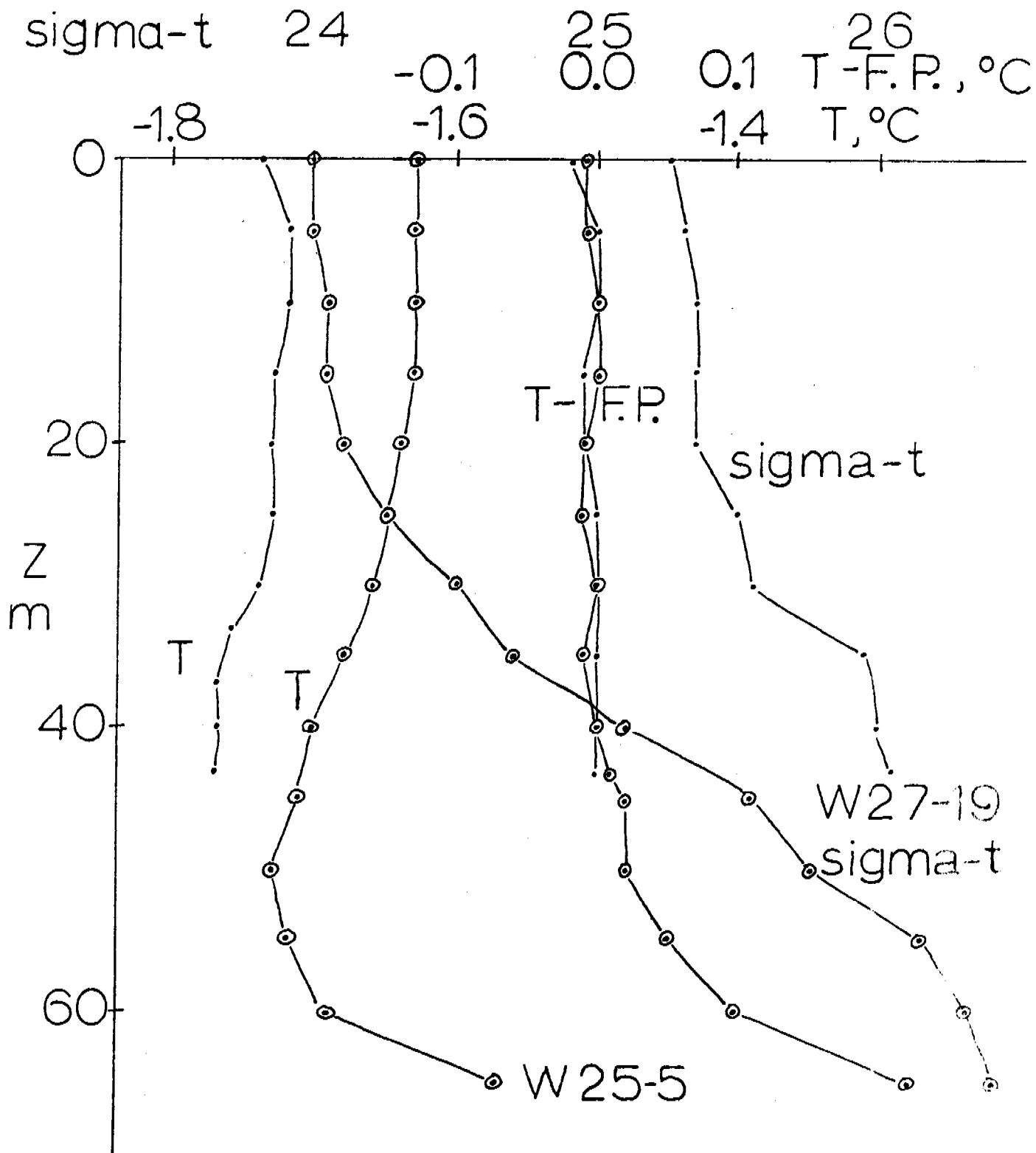


Figure 3

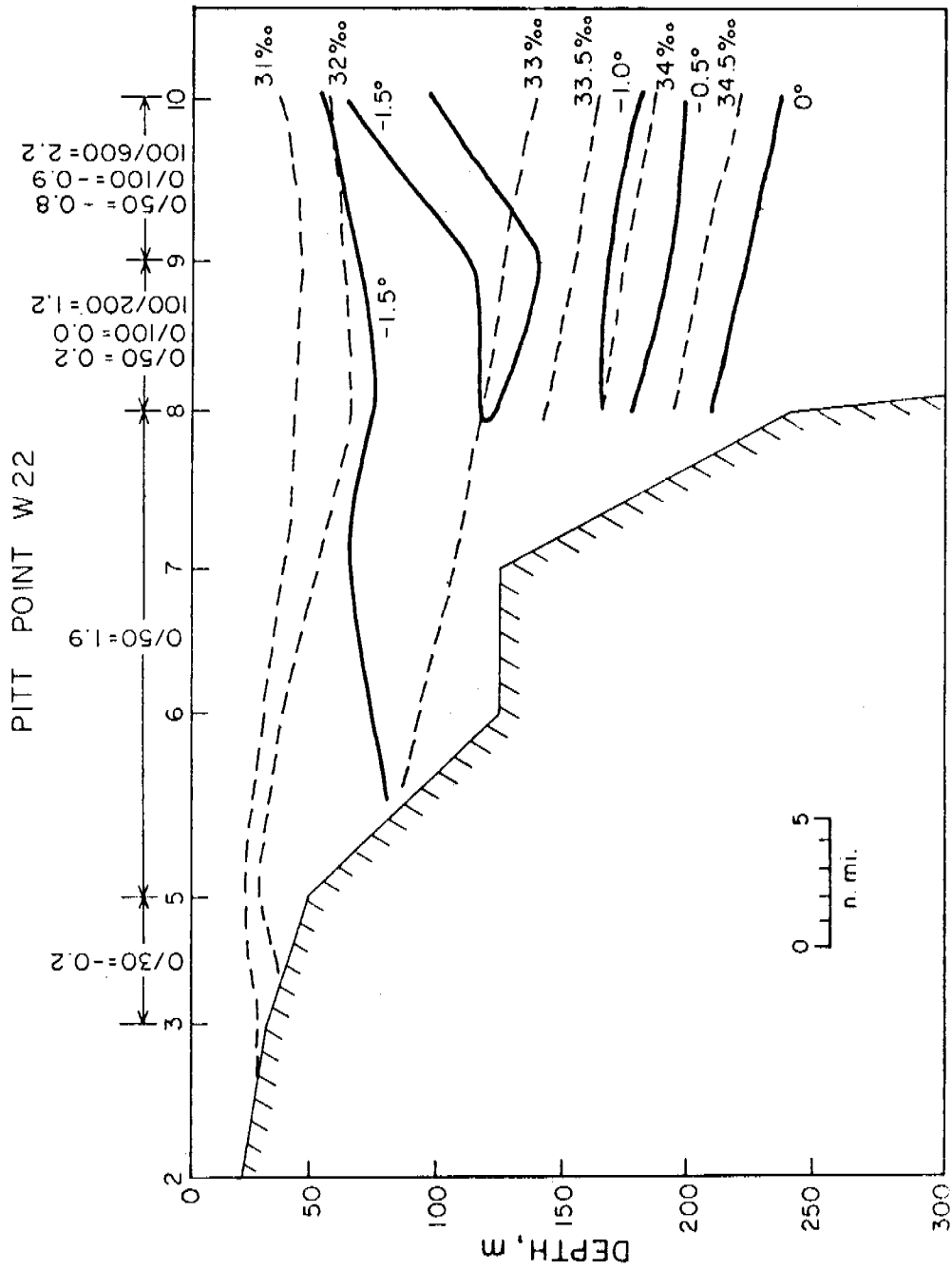


Figure 4

Point/Lonely and Narwhal Island/Oliktok. Therefore, not only can there be considerable salinity differences year-to-year, but such differences can persist through an entire seasonal progression.

As in 1976, the surface salinity in 1977 again decreased seaward across the shelf by 0.4-0.9 ‰ which, according to the earlier discussion, appears to be the norm. While the mechanism behind this distribution must still be considered uncertain, it appears increasingly likely that it is caused by an onshore flux of salt in the lower part of the water column over the shelf. There are several reasons for this tentative conclusion. First, the isohalines in general tend to slope upwards toward the coast at all depths above at least 100 m. Therefore, the seaward decrease of salinity at some level is not merely a near-surface phenomenon. Second, since the sloping of the isohalines is generally seen to extend down to and include at least the 33 ‰ isopleth (corresponding to a density in excess of 26.5 in σ_t), the slope cannot reasonably be attributed to the offshore flow of dense water originating on the shelf; there simply are no significant amounts of water this dense that are native to the shelf. For example, the relatively dense Bering Sea water so apparent on the shelf in summer and fall does not extend much beyond $\sigma_t = 26$. Third, there is observational evidence for a deep onshore flux of salt, particularly in the W25 sections, when saline Atlantic water was found on the shelf in the presence of a very strong geostrophic shear (cf., last year's annual report). Finally, an onshore flux of salt is an attractive hypothesis because it can satisfy the requirements of the salt budget, as discussed in Section III. All this is not to say that there is a simple, steady transverse circulation across the shelf. Rather, it is probable that, among other complications, a strong time dependence is involved. It may well be, for example, that the salt flux is in some sense a series of pulsations. Certain of these matters may sort themselves out as the current measurement analysis proceeds. Nonetheless, it now seems likely that in the mean there is a net flow of saline water onto the shelf in the lower part of the water column.

The dynamic height calculations for W27 are very much in keeping with those from the majority of earlier cruises. Generally, the geostrophic shear is that appropriate to a westward flow along the continental slope.

Finally, comparison of the W25 stations with those from W27 is instructive with regard to the temperature signal of the Bering Sea water. Figure 5 shows the T-S correlation in the depth range 30-52 m at station W25-19, the innermost station in the Lonely West fall section. The vertical distributions of temperature, salinity and density at this station are shown in Figure 6. The temperature maximum of about -0.9°C at 43 m occurs at $\sigma_t = 25.8$, which unquestionably represents Bering Sea water having rounded Point Barrow earlier in the year at a higher temperature. The underlying water, including the deeper temperature maximum with a salinity in excess of 34‰, represents water having moved onto the shelf from intermediate depths in the Arctic Ocean as discussed earlier. The temperature signal of the Bering Sea water was thus being eroded by heat diffusion into the water both above and below. By winter the temperature signal has effectively been erased on the shelf, as shown by the T-S

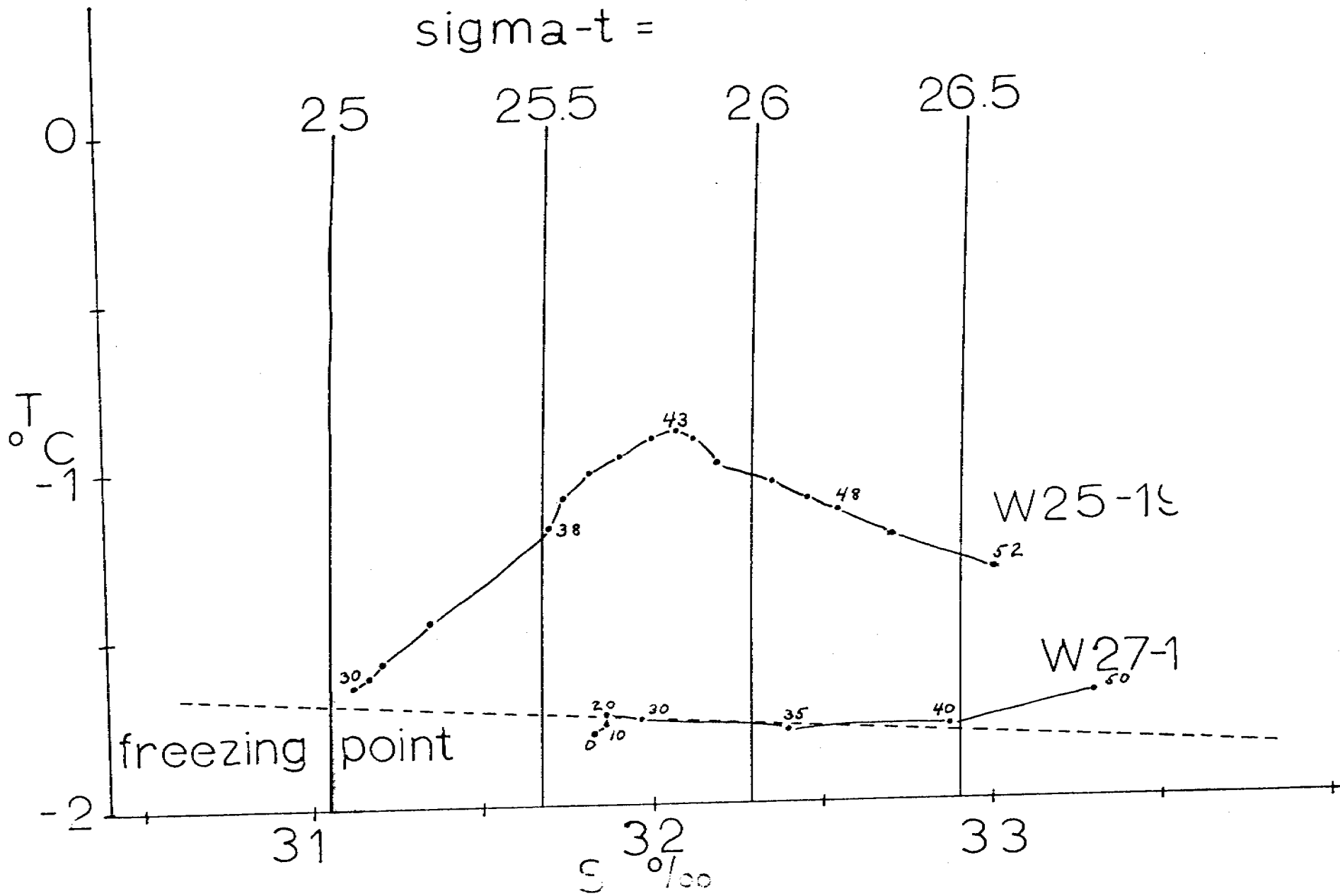


Figure 5

STD PLOT

W-25 19

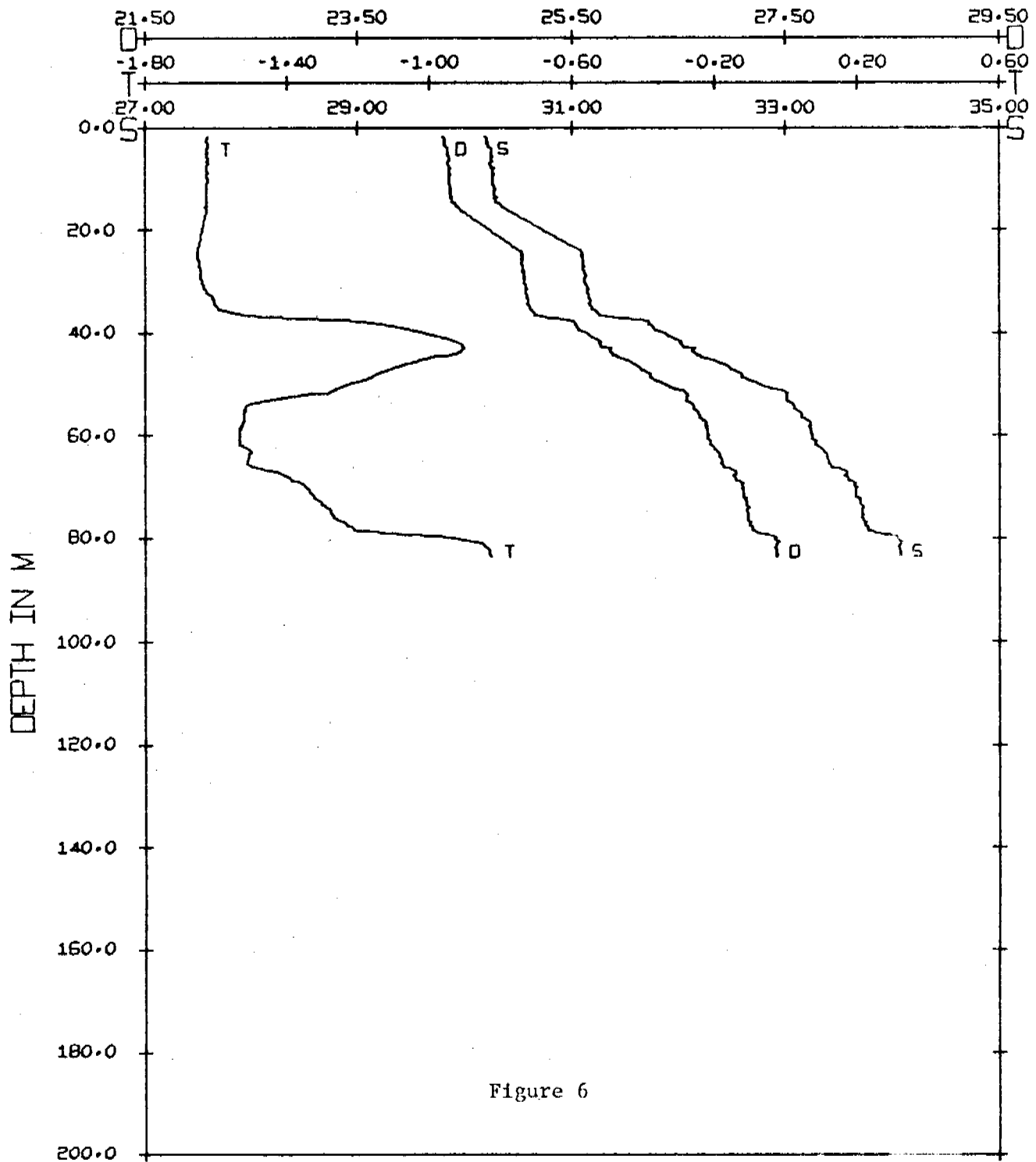


Figure 6

LATITUDE 71-21.8N LONGITUDE 152-58.1W	T = TEMPERATURE - C S = SALINITY - 0/00 D = SIGMA-T	DATE 4 NOV. 1976 BEGIN 2016
--	---	--------------------------------

correlation in the upper 50 m at station W27-1 (Figure 5), the innermost station in the Lonely West winter section. Down to about 40 m, where the density is 26.5 in σ_t , the temperature is effectively at the freezing point. These conditions, i.e., the direct influence of freezing (as evidenced by temperatures at the freezing point), extending into or past the density range of the core of Bering Sea water, are typical in winter on the shelf. [One can, in fact, find near-freezing temperatures extending through the density range of the Bering Sea water already in November, e.g., station W25-5 (Figure 7)]. Only at occasional stations is a Bering Sea influence still clearly visible. Principally these stations occur over the slope, an example being the outermost station in the Oliktok West section of W27-8 (Figure 8), where a small temperature spike can be seen just below 50 m. Both above and immediately below the spike, the water is near the freezing point. One can therefore in general not trace the Bering Sea water on the Beaufort shelf much past freeze-up in the fall.

VIII. Conclusions

- A. The direct influence of freezing extends far below the local pycnocline, due to the differential movement of waters from a variety of locations seeking their density level.
- B. There are considerable year-to-year differences in hydrography, and anomalies can persist through several seasons.
- C. It seems likely that in the mean there is a net flow of saline water onto the shelf in the lower part of the water column.
- D. The temperature signal of the Bering Sea water is largely erased within a month or two after freeze-up.

IX. Needs for Further Study

Were further STD work to be done in the Beaufort Sea, it should be process-oriented rather than of a surveying nature. Most likely, it would be done in conjunction with current measurements.

X. Summary of 4th Quarter Operations

A. Field Operations

None

B. Problems

None

C. Estimate of Funds Expended to 31 March 1978

All allocated funds are expected to be expended by 31 March, the end of the contract as extended.

STD PLOT
W-25 5

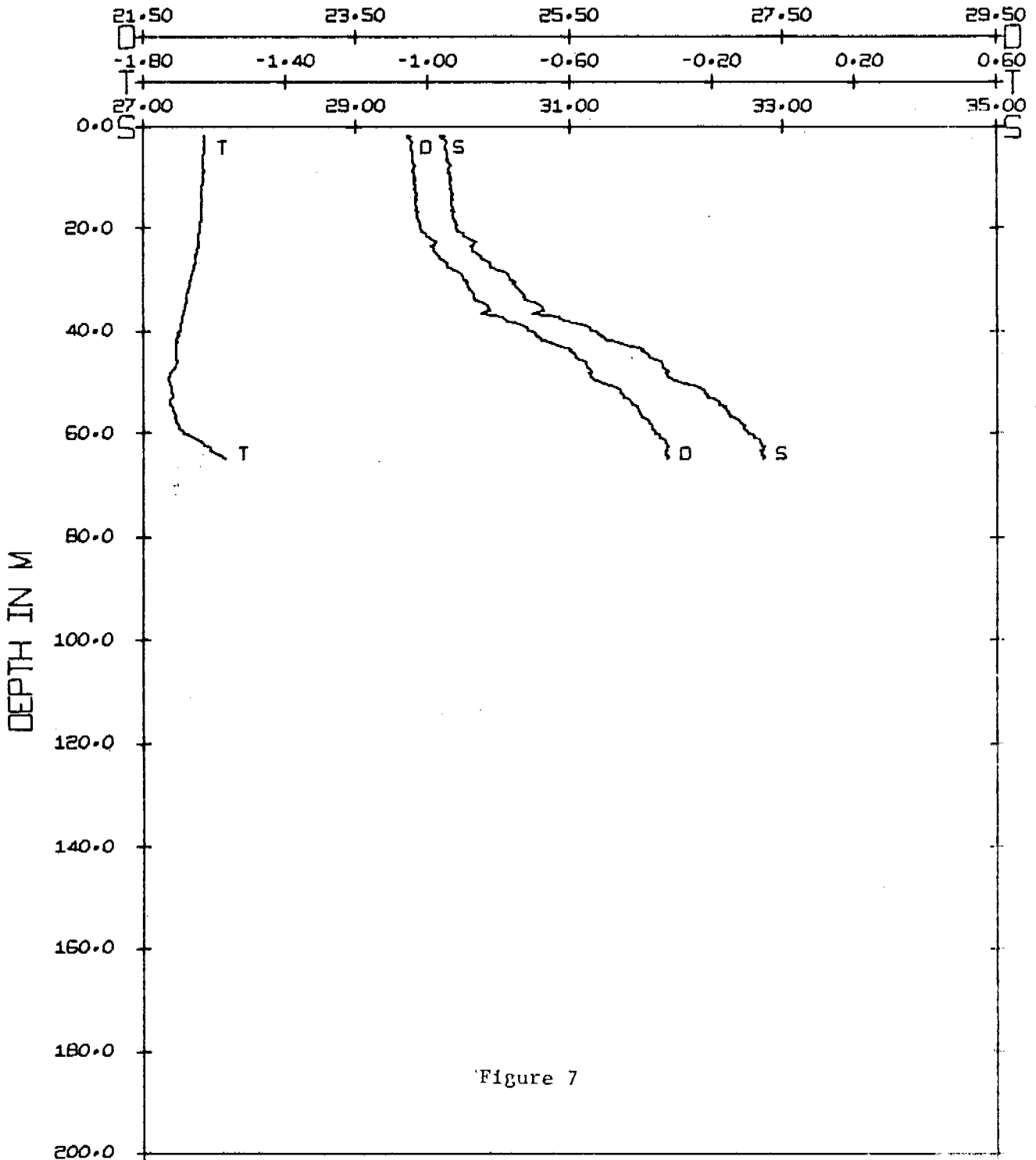


Figure 7

T = TEMPERATURE - C
S = SALINITY - 0/00
D = SIGMA-T

LATITUDE 71-14.1N
LONGITUDE 149-59.9W

FILE IMOOS

DATE 31 OCT 1976
BEGIN 2104

STD PLOT

W-27 15

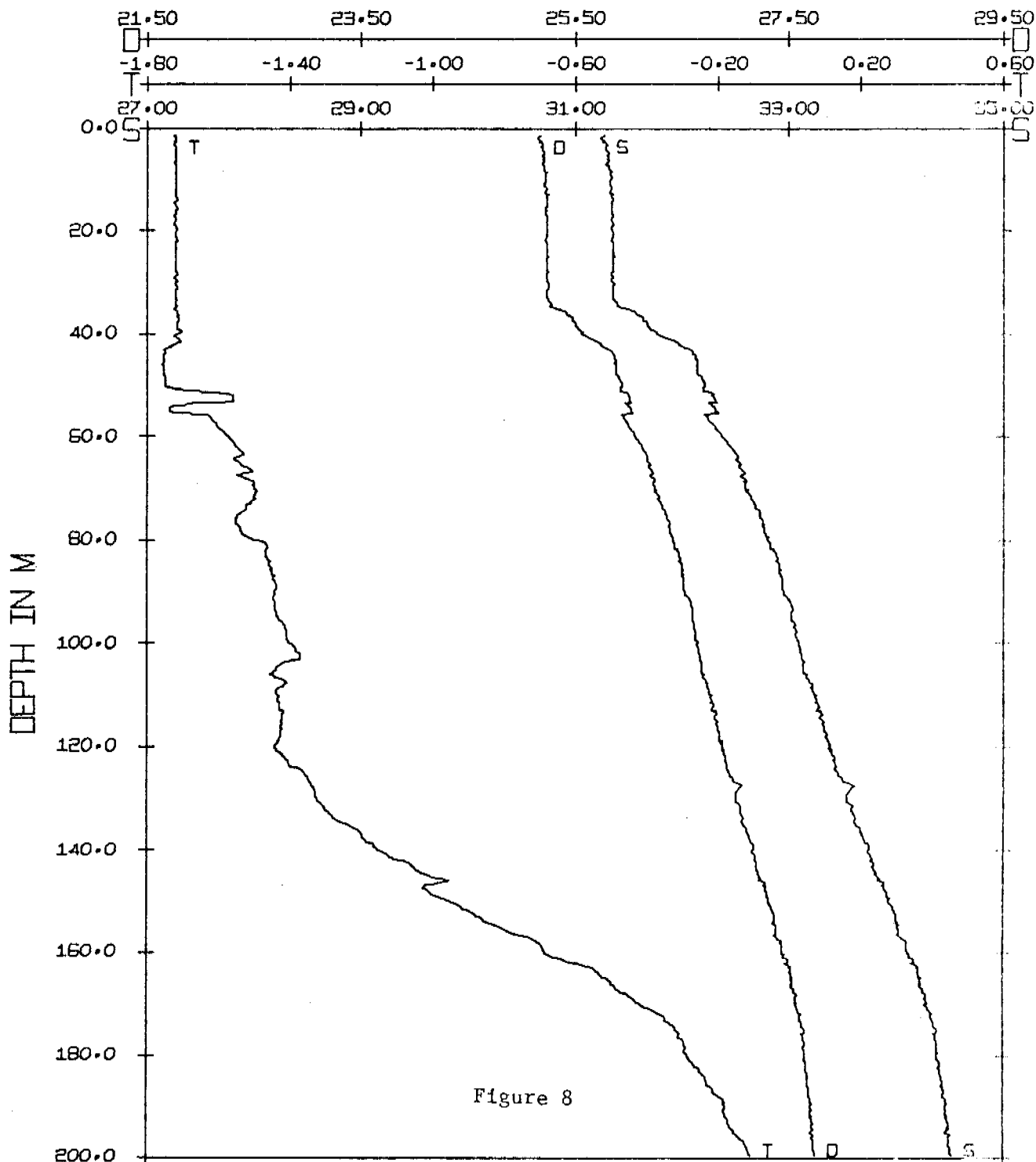


Figure 8

T = TEMPERATURE - C
 S = SALINITY - 0/00
 D = SIGMA-T

LATITUDE 71-14.4N
 LONGITUDE 149-59.3W

FILE IM015

DATE 3 OCT. 1977
 BEGIN 253

ANNUAL REPORT

Research Unit 217

LAGRANGIAN SURFACE CURRENT MEASUREMENTS
ON THE OUTER CONTINENTAL SHELF

Donald V. Hansen
NOAA/AOML
Miami, Florida

15 March 1978

ANNUAL REPORT - OCSEAP

I. Summary

The objectives of this work unit are to obtain Lagrangian current data for assessment of probable trajectories of oil spills in the Gulf of Alaska and the S.E. Bering Sea using drogued free drifting buoys located several times daily by a satellite positioning system. During the 1977 field season six (6) buoys were deployed S.E. of the Pribilof Islands in the S.E. Bering Sea. These deployments were as successful as those of 1976. The longest surviving buoy has recently terminated transmission after nearly 7½ months of successful operation since May 1977. An average buoy lifetime in excess of 135 days was achieved during this year. It is believed that most of the buoys failed after being caught in the ice at the end of the field year. One buoy grounded on St. George Island less than two months after deployment, and another grounded on St. Paul Island about six months after deployment. Overall, more than 820 days of surface current data were obtained in the region 54°- 59°N, 163°- 178°W. A principal early conclusion that can be drawn is that surface currents in the S.E. Bering Sea are characterized by extensive eddying with several day average current speeds on the order of 20 cm/sec or less. Sustained current speeds of greater than 30 cm/sec are rarely seen, at least during Summer and Fall. The net displacement of water from the region is even more sluggish. Typical long term displacements are on the order of 400 km in 100 days.

II. Introduction

The general objective of this work unit originally was to collect near surface Lagrangian current data for the NE Gulf of Alaska OCS region with particular interest in the region from Yakutat Bay to Prince William Sound. Extensive (probably adequate, at least for the

Spring and Summer seasons) data were collected in this region during 1976. Starting in 1976 and continuing more successfully in 1977, the area of interest was enlarged to include the S.E. Bering Sea. During 1978 the data collection effort will concentrate on the region around Kodiak Island and westward to the Aleutian Islands.

The methodology for collecting this information is use of expendable free drifting (drogued) buoys electronically located several times daily by means of the Random Access Measurement System (RAMS) aboard the NIMBUS-6 satellite. Two different buoy configurations have been used. A high endurance buoy with a drogue at 30 meters depth and carrying sea surface temperature, wind speed and drogue loss sensor has been used for the challenging Gulf of Alaska environment, and a smaller, more economical buoy carrying a drogue at 10 meters to lessen the risk of grounding in the extensive shoal areas has been very successfully used in the Bering Sea.

The principal objective originally was to obtain Lagrangian statistical data on the relatively large scale coastwise current in the northern Gulf of Alaska for input to advanced surface contaminant dispersion models. A secondary objective was to obtain sets of characteristic flow trajectories which have high visual impact, and are easily understood by lay and professional people alike, and are therefore of substantial value for scenario discussion and other forms of debate on issues of hydrocarbon resources development. In the conduct of the work, an unplanned benefit has been discovered in the way of increasing interpretability and credibility of other lines of physical oceanographic data. The original primary objective still seems to be valid in the Bering Sea, but the combination of very short transit times and the discovery of important site-specific characteristics, such as semi-permanent eddies and persistent flow into coastal inlets, has made the secondary and tertiary application the more valuable in the Gulf of Alaska.

III. Current State of Knowledge

During the last year new concepts have emerged of near surface currents in the Gulf of Alaska and Bering Sea as regards transport of surface materials. Lagrangian data collected by this project, by NORPAX investigators, and large scale Lagrangian model simulation by HIG indicate that the northern Gulf of Alaska may be an accumulation point for surface materials. Surface materials tend not to escape from this area, but rather to be swept into it from over an extensive area of the North Pacific Ocean, and to go ashore in the area. The evidence for these statements is presented mostly in graphical form in the annual report of April, 1977 and the quarterly report of October, 1977.

The concept of circulation that is emerging for the S.E. Bering Sea in Summer is of sluggish circulation, dominated by extensive eddying, but weak net displacement. The preliminary evidence for this statement is presented in this report.

IV. Study Area

The area of study is the entire northern Gulf of Alaska, from Yakutat Bay to the Aleutian Islands, and the S.E. Bering Sea. Data collection to the present time has been limited to the northern Gulf of Alaska east of Kodiak Island, and the S.E. Bering Sea. Activities during FY'78 include further interpretation of earlier data, and new data collection around and west from Kodiak Island.

V. Sources, Methods, and Rationale of Data Collection

The data collection effort for this research unit is entirely dependent upon use of the experimental Random Access Measurements System of the NIMBUS-6 satellite operated from Goddard Space Flight Center (NASA). Buoys at 60°N are in view of the satellite for about three (3) orbits twice a day. This usually provides three (3) to

five (5) positions per day. During 1977 and 1978, buoy sensors have been reduced to only a drogue loss sensor in order to maximize the amount of current information obtained within available resources. The buoy identification, time, and Doppler information are relayed from the satellite receiving station to GSFC where position and parameter data are determined for the system user. The user then converts these data into time series of position and derived parameter data for further analysis. It is expected that NASA will operate this system through 1978, but probably not much longer. A succeeding operational system will be offered for use by the French Space Agency, CNES, but at considerably greater cost to the user. Information of the data processing routines used for buoy data at AOML are on file in OCS Project Office-Juneau. In general, available information for the OCS area of interest is adequate to determine in advance the general direction of the large scale regional flows. Buoys are deployed at the perceived upstream side of the respective regions to collect information on the rate and structure of the flow.

VI. Results

The generally successful operation of 1976 was if anything improved upon in 1977. Six (6) buoys were deployed in two lines across the continental slope of the St. George Basin. All six (6) of these buoys functioned well, exhibiting a generally similar behavior, extensive eddy motion with only very weak net displacements. It would be extremely difficult, expensive, or impossible to delineate these currents by means of conventional current meter mooring or shipboard observations. The essence of these movements is shown in the figures included with this report. Of course, from these limited Lagrangian observations alone, nothing can be said of flow in other (Winter) seasons, or of year to year variation. Joint interpretation of these data with more conventional data should contribute to answering these questions however.

VII. Discussion

Sufficient Lagrangian surface data have now been collected in the Northeast Gulf of Alaska and Bering Sea regions to begin synthesis with other kinds of data. These activities have been initiated jointly with UA/IMS personnel in regard to the Gulf of Alaska, and with PMEL and UW personnel in regard to the Bering Sea. Contact has also been established with biological components of PROBES in which a mutual interest in physical and biological processes in the Bering Sea was discovered. It is expected that collaboration in this area will be of benefit to OCSEAP. Work will also be initiated directly on computation of Lagrangian correlation functions from the Bering Sea data set.

VIII. Conclusions

The principal new conclusion emerging from the past year's results are as stated in III above: the perception that surface materials deposited in the northern Gulf of Alaska, or possibly in a sizable part of the North Pacific Ocean tend to be trapped and ground on northern Gulf beaches, and that circulation in the S.E. Bering Sea is exceedingly variable, quite unlike the Gulf of Alaska. Preliminary results indicate that steady state circulation modelling may be of extremely limited utility in the S.E. Bering Sea.

IX. Needs for Further Study

Additional data collection is required in the Gulf of Alaska west of Prince William Sound, and more detailed interpretation is required with the data previously collected in the Gulf of Alaska and the Bering Sea. These topics are being addressed during the present year.

X. Summary of January-March Quarter

No new field deployments were made during this quarter. Residual data collection by buoys deployed in May 1977 was completed. Refurbishment and new buoy procurement activities for 1978 deployments have largely been completed, and are undergoing electronic testing. It is expected that probably 15 buoys will be deployed during 1978. The first five (5) deployments are planned for the May STD cruise.

XI. Auxiliary Material

A. Reference has been made in this report to the Quarterly Report of October, 1977, and the Annual Report of April, 1977. None of that material is included here. The interested reader is referred to those reports for details and supporting materials.

B. Joint papers are in preparation with Dr. Royer and Mr. Pashinski on shelf circulation in the Gulf of Alaska, and with Drs. Shumacker, Kinder, and Mr. Pashinski on circulation in the Bering Sea.

Illustrations

The following figures summarize the drift experience of buoys deployed in May 1977 in the S.E. Bering Sea. All of these buoys were attached to a subsurface drogue by a 10 meter long nylon line. The small circular points along the trajectories denote six hourly intervals in the smoothed and interpolated position data, and the numbers along the trajectory denote days elapsed following deployment in May.

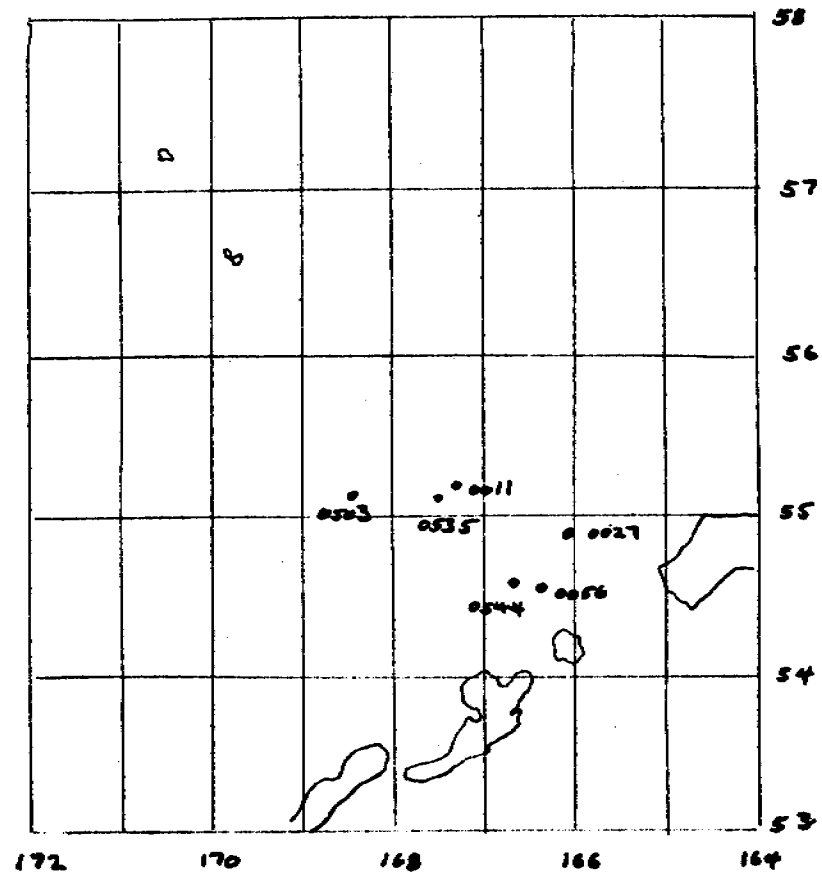


Figure 1. Buoy deployment pattern of May 1977.

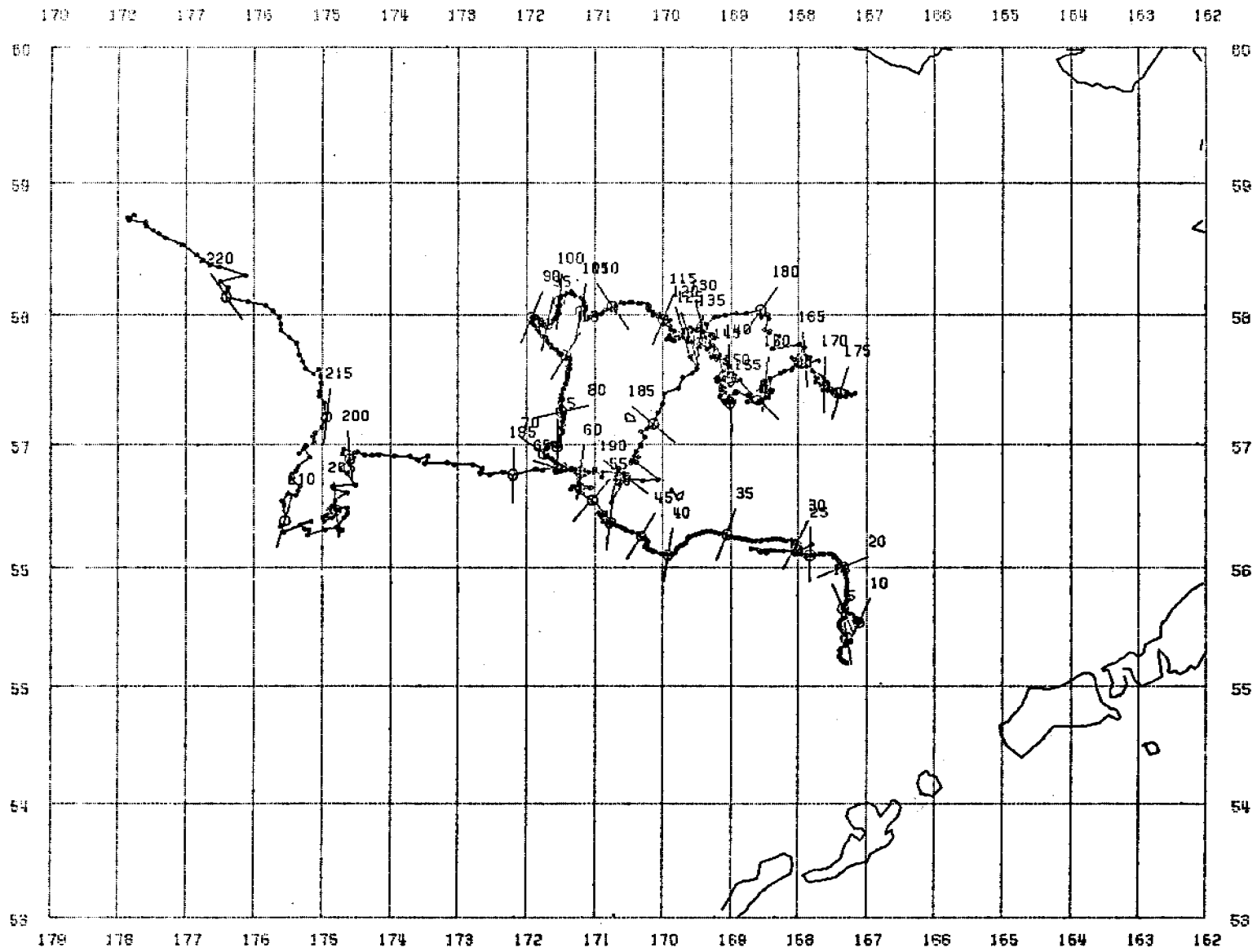


Figure 2. Buoy ID 0011 trajectory.

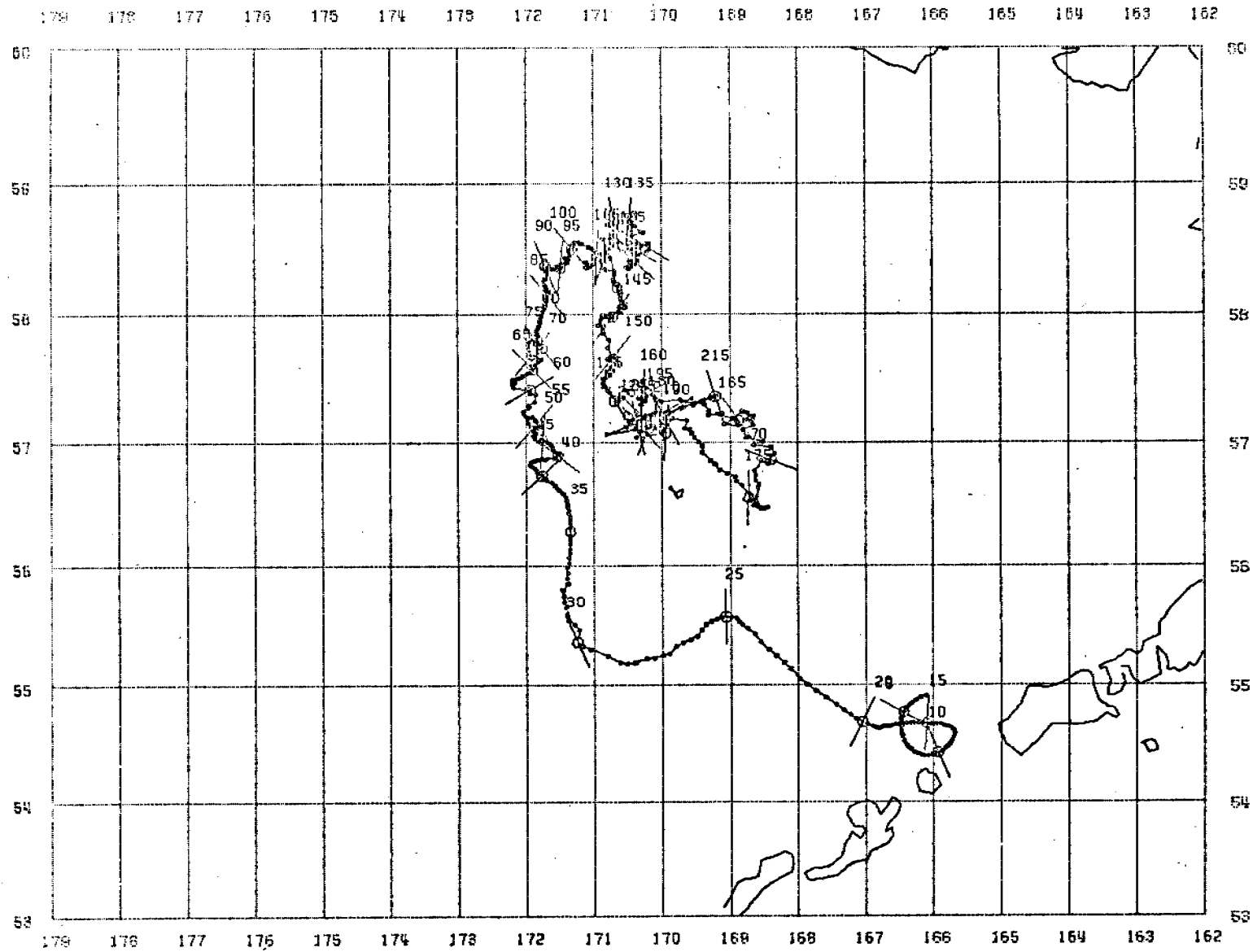


Figure 3. Buoy ID 0027 trajectory. This buoy appears to have grounded temporarily in shoal water near St. Paul Island around days 180 to 186, and again around days 193 to 208.

009

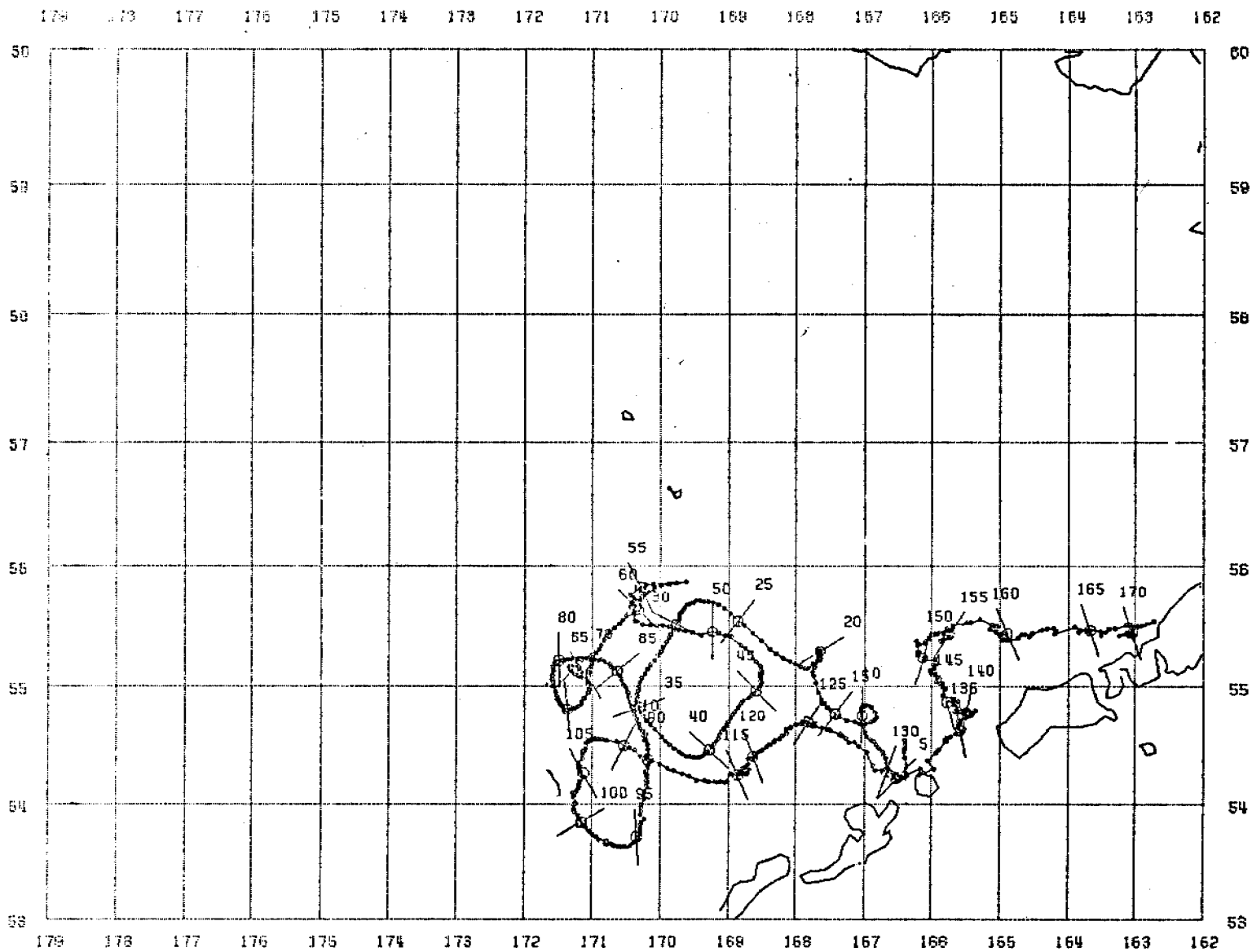


Figure 4. Buoy ID 0056 trajectory.

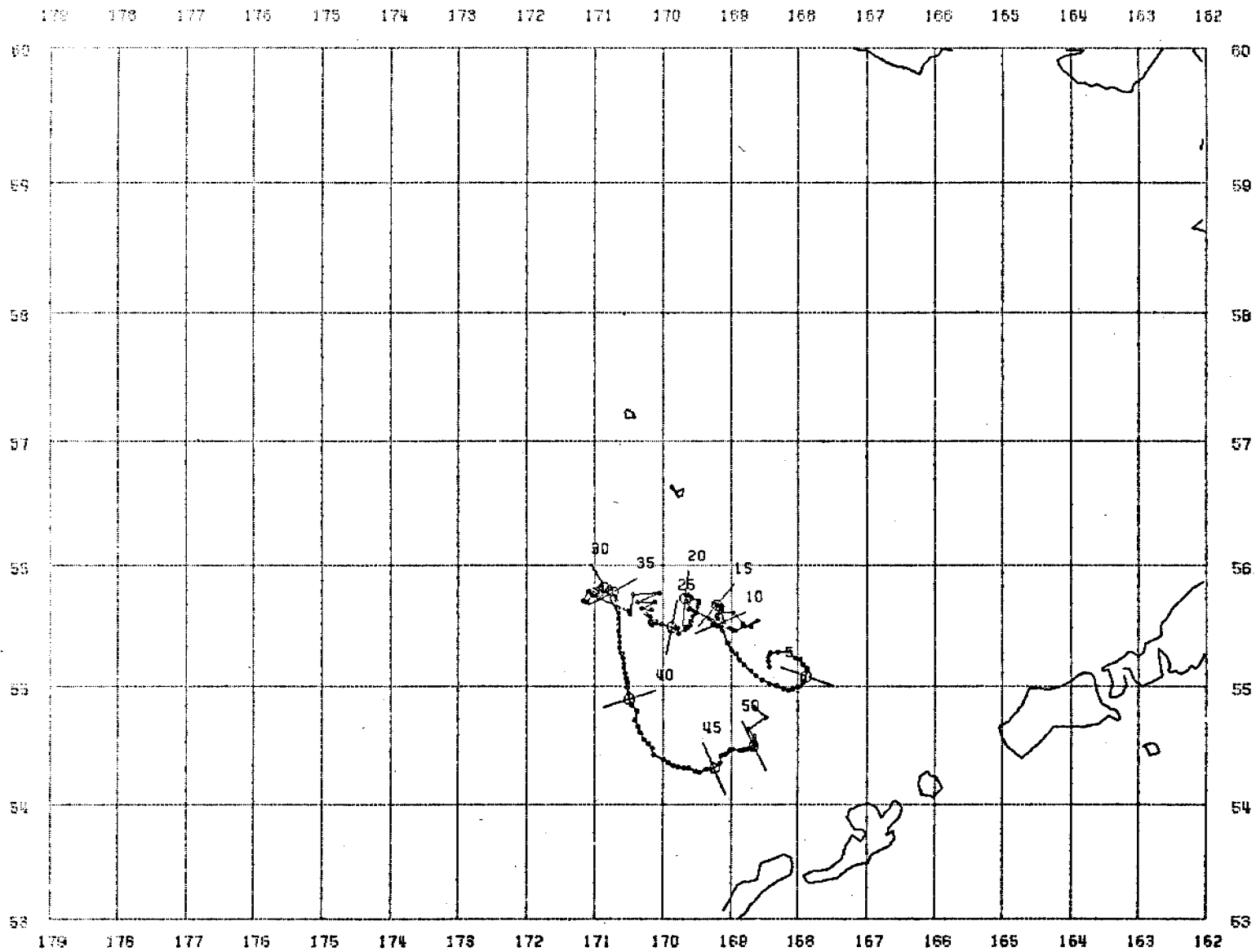


Figure 5. Buoy ID 0503 trajectory. This is the only buoy of the six deployed in 1977 to terminate transmission prior to planned duration of operations.

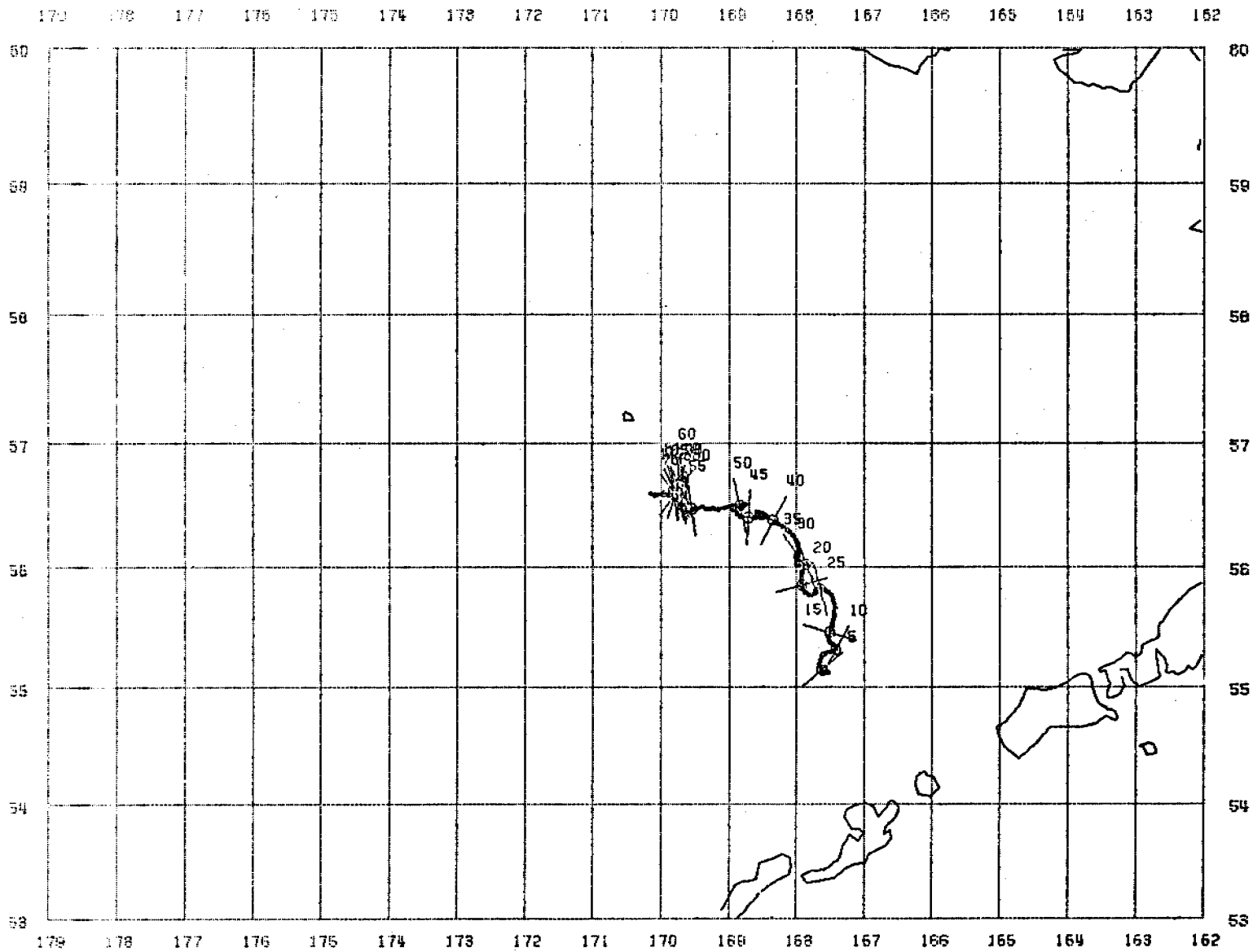


Figure 6. Buoy ID 0535 trajectory. This buoy grounded in shoal water near St. George Island about 55 days after deployment and continued transmission from its anchored position for another two months.

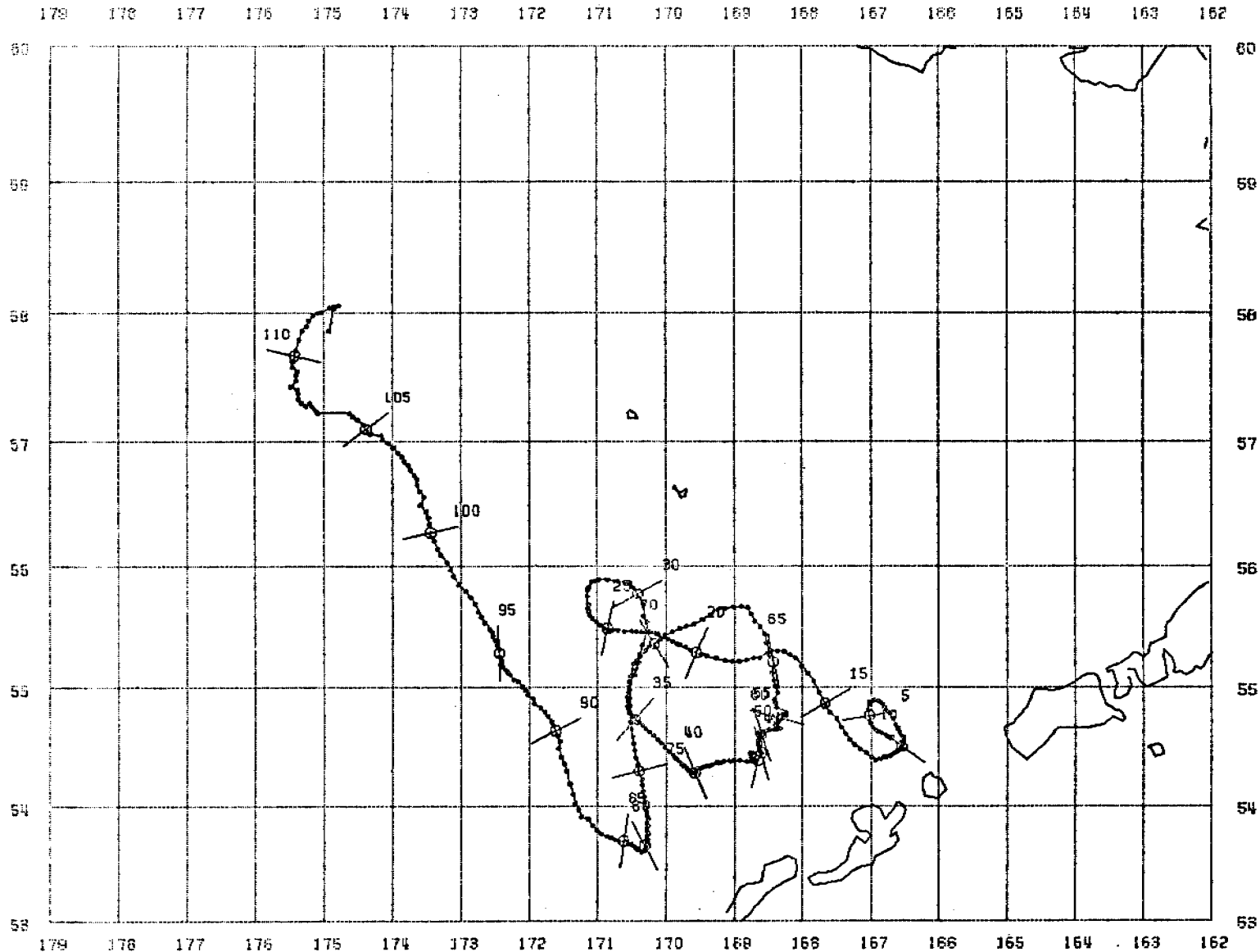


Figure 7. Buoy ID 0544 trajectory. This buoy, like 0011, provides some indication that the circulation westward from the St. George Basin may be stronger and more persistent. Note the remarkable divergence of this trajectory from the vicinity of 54°N, 171°W from that of buoy 0056 that transmitted the same region some two weeks later.

ANNUAL REPORT

Contract #03-5-022-91

Research Unit #244

Reporting period: 1 April 1977 -
31 March 1978

Number of Pages: 120

STUDY OF CLIMATIC EFFECTS ON FAST ICE EXTENT
AND ITS SEASONAL DECAY ALONG THE
BEAUFORT-CHUKCHI COASTS

Principal Investigator

R.G. Barry

Associate Director, Professor of Geography

Institute of Arctic and Alpine Research

University of Colorado 80309

31 March 1978

SUMMARY

The objectives of this project are (1) to delimit the extent of fast ice along the Beaufort and Chukchi coasts prior to and during the decay season; (2) to define and characterize the nature of the summer decay of fast-ice from remote sensing data; (3) to determine climatic processes and meteorological synoptic events contributing to the spatial and temporal characteristics of fast-ice break-up and to examine their amenability to predictive assessment.

The most significant hazard to petroleum development along the Beaufort Sea coast is posed by the occurrence of sea ice.

Major findings that can be identified as reasonably firm are as follows:

- 1) Light-ice summers are associated with southerly surface winds and a tendency for higher than normal pressure over the Arctic Basin centered about 80°N , 120°W , and lower than normal pressure over the East Siberian Sea, centered on 75°N , 170°E . The reverse is true for heavy-ice summers.
- 2) Air temperature, sea-level pressure distribution, and surface wind direction account for most of the year-to year variance in northward pack ice retreat and their correlation with ice retreat increases as the summer progresses.
- 3) The trends in sea-level pressure at 80°N , 120°W and 75°N , 170°E since 1939 and summertime TDD's since 1921 indicate a decline in favorable mean ice conditions. Since 1953, 13 of 24 summers have accumulated over 400 TDD's (required for a northward retreat of the pack ice) while 28 of 32 summers had done so before 1953. Heavy-ice conditions, such as those during 1955, 1975, and other recent summers, may not have occurred since before the mid-1920's.
- 4) Monthly temperatures at Barrow in summer show some persistence that can be applied to forecasting breakup conditions. Summers with a predominance of monthly mean temperatures below normal, even with some normal months, will become severe ice years. Temperature persistence increases in late summer-autumn, implying applicability also to the timing of freeze up.

II. INTRODUCTION

A. General Nature of the Study

Nearshore ice along Alaska's Beaufort Sea and Chukchi Sea coasts undergoes an annual cycle of formation, extension, modification, ablation, and breakup. Many of the processes which contribute to this cycle are poorly understood, although it is generally recognized that meteorological and climatological factors are important influences for ice formation, motion, deformation, ablation, and breakup. This study is attempting to interpret ice characteristics and their time variations from remote sensing data supplemented by aircraft and field observations. This derived information covering both the Beaufort and Chukchi coasts is then compared with concurrent coastal weather conditions and regional atmospheric pressure patterns. On this basis, a systematic set of weather-ice relationships is being derived which, apart from their descriptive aspects of typical anomalous conditions, also can provide a framework for predictive schemes.

B. Specific objectives

- (1) Complete the mapping of ice characteristics and behaviour during the decay season of 1976 from available remote sensing data.
- (2) Investigate surface weather data from the coastal stations and synoptic-scale atmospheric pressure patterns over the region to determine relationships between important ice-related weather "events" and the atmospheric circulation.
- (3) Examine the possibilities for predictive assessments of climatic factors influencing fast-ice decay and pack ice retreat.

C. Relevance to Problems of Petroleum Development

Offshore petroleum development may involve temporary operations on the winter fast-ice surface or in the open waters during summer. Alternately, large, ice-resistant structures may be used year-round. An accurate assessment of the best operational modes and of the seasonal distribution of ice hazards requires that the normal patterns and variabilities of fast-ice characteristics and breakup processes be specified. Also, the pathways of pollutants deriving from oil spills or blow-outs are dependent to some degree on the season, and, in summer, on the

relative progression of the breakup. It also seems significant that various faunal populations utilize the coastal environment, above and below the ice and in the open water areas. Seasonal and interannual variations in the weather and ice characteristics are important factors affecting the distribution and movements of these populations. These questions are elaborated in the report of the Beaufort Sea Synthesis Meeting (Feb. 1977).

The timing of major phases of the seasonal ice regime in the near-shore zone (i.e. melt in situ, first openings and movement, clearance along coast, etc.) and their interannual variability are of primary and most direct importance to offshore operations. The results summarized above address these questions. In particular, the basis for a long-range ice forecasting technique has been developed, using air temperature at Barrow. This technique can be used to determine (i) when shipping can be expected to begin; (ii) the approximate length of the shipping season; (iii) the relative severity of summertime ice conditions.

III. CURRENT STATE OF KNOWLEDGE

The general characteristics of fast ice have been known for some time (e.g. Zubov, 1943), while more recent review of conditions in the Beaufort Sea fast-ice zone are given by Kovacs and Mellor (1974) and Reimnitz et al. (1976). The regional-scale dynamics of the fast-ice zone could not be effectively studied in detail until the launch of LANDSAT (formerly ERTS) in 1972. A good deal of literature has emerged since that time treating the information content of LANDSAT imagery of sea ice, but the OCSEAP Project represents the first systematic applied study of the regional scale surface morphology, composition and dynamics of fast-ice along the Beaufort and Chukchi Sea coasts.

Weather and climate have been studied by a number of authors (see e.g., Watson, 1968; Selkregg, 1974; Holmgren and Weller, 1974) for the Alaska region, and the Arctic atmospheric circulation has likewise been treated (e.g. Keegan, 1958; Reed and Kunkel, 1960; Wilson, 1967; Hare, 1968; Weller and Bowling, 1974). However, the relationships between ice decay processes and weather variations has hitherto received little attention, especially on the detailed scale required for BIM planning.

IV. STUDY AREA

The fast ice zone along the Beaufort and Chukchi Sea coasts between Demarcation Point and the Bering Strait represents the study area for this project. The seaward extent is variable according to season and location.

V. DATA

A. Remote Sensing

Regional scale mapping of the ice characteristics and behaviour for 1973-76 has been carried out from LANDSAT imagery. Details of frames interpreted are given in the Quarterly Reports. Interpretation of categories of age, deformation, puddling of the ice, etc., is made with the aid of other remote sensing products (particularly aircraft SLAR and CIR) as well as reconnaissance observations and hand-held photography of the ice from aircraft.

B. Meteorological Data

The sources of data for the studies included here have been:

(1) National Weather Service station meteorological data for Kotzebue for 1953-76 and for Barrow and Barter Island for 1953-75 respectively. These data were published as local climatological data. Data used were temperature (sometimes converted into thawing degree days), wind speed and direction, barometric pressure, cloud cover.

(2) Sea-level pressure maps for the Beaufort Sea prepared by AIDJEX for summer 1975.

C. Climate-Ice Interaction Case Studies

These studies utilised the above data sources and also tabulations of the retreat of fast-ice and pack ice off Barrow on September 15 of each year since 1953 (Barnett, 1976). Each summer is ranked according to its ice severity.

The analytical methods used in the case studies involved the characterization of particular ice events identified on LANDSAT imagery in terms of preceding and concurrent meteorological conditions. Indices employed in the analysis included cumulative thawing degree-days (sums of positive departures of daily average temperature above 32°F).

VI. RESULTS

A. Remote Sensing Interpretation and Ice Mapping

1. Ice Maps

The mapping of shorefast ice extent and morphological characteristics, as inferred from available cloud-free LANDSAT imagery, has now been completed for the entire Beaufort Sea and Chukchi Sea coasts for the spring-summer seasons of 1973 through 1976.

For convenient reference a summary is given of the reports containing these ice maps:

	1973	1974	1975	1976
A. Beaufort Sea:				
Barrow Sector	QR Sep. 77	AR March 77	QR Sep. 77	QR Dec. 77
Prudhoe "	AR Mar 77	QR Sep 76	"	} This Report }
Barter Is. "	QR Sep. 77	—————>		
B. Chukchi Sea:				
Barrow Sector	} QR Dec. 76	Annual Report	}	QR Sep 77
Pt. Hope "		March 1977		"
Kotzebue "				"

The Prudhoe and Barter Is. sectors of the Beaufort Sea coast for 1976 are included here for the first time (Appendix 1).

2. Analysis of Near Shore Ice Conditions in the Barrow-Prudhoe Sectors

In previous reports we have presented interpreted LANDSAT imagery covering the Beaufort coast of Alaska during 1973-76. Here we have gathered imagery from the Barrow and Prudhoe sectors for the four years, in order to compare the ice conditions of most significance to shipping. Specifically, we checked for any noteworthy differences (or lack of them) in ice conditions during the summer of 1975 as compared with the other years for which we have LANDSAT imagery.

Barrow Sector

The interpreted imagery here covers two time periods. The first covers late July when, according to the timetable given in Table 1, breakup and removal of the fast ice should be well advanced in the near shore areas. The second group shows the area during the first week of July, at the end of the stable ice period. The interpreted maps are reproduced from earlier reports, or the appendices to this report, for convenient reference.

1. 21 July 1974, 23 July 1975, 18 July 1976

Figure 1 shows enough of the sector in 1974 to give us an idea of the extent of the first year ice (now no longer shore fast) and the location of the pack ice. Some bays and near shore areas are not yet wholly free of ice, but the ice in these areas is decayed and breaking up. The pack lies about 10-20 km offshore in the Beaufort and is immediately offshore along the Chukchi coast.

23 July 1975 is shown in figure 2. The pattern of decay is quite similar to that shown in 1974 except that in some areas the ice seems not to have broken up quite as much. The pack is situated 10-30 km offshore in the Beaufort and is not present along the Chukchi side.

Imagery for 1976, figure 3 exhibits the least advanced stages of decay in this group. There are fewer areas of open water and most of the first year ice does not appear to be in advanced stages of decay, especially that ice seaward of the barrier islands that are to the southeast of Barrow. The pack is now 20-40 km from the Beaufort coast and is also present along the Chukchi shore.

2. 07 July 1973, 06 July 1975

These two scenes shown in figures 4 and 5, respectively, exhibit a very similar melt pattern, except that in 1975 the pack ice seaward of the continuous ice is much less consolidated as compared with 1973. In 1973, the pack is about 20 km seaward of Dease Inlet and in 1975 the pack is about 30 km offshore in the same area. We should note that just prior to the July 1973 imagery, winds in the area were NNW and would tend to close leads and areas of open water in the pack ice near shore.

If we were to extrapolate these data from the Barrow sector we would reasonably conclude that the summer of 1976 should have been the worst of these four years for navigation along the Beaufort coast. In fact, however, 1976 was a rather average navigation year as were 1973 and 1974, whereas 1975 is recognized to have been a particularly bad year for shipping.

Late summer conditions in the Barrow sector cannot be evaluated, due to a lack of imagery. For this reason, the Prudhoe sector is examined for this stage of the breakup.

Late summer conditions in the Prudoe sector are examined with respect to the location of the edge of the pack ice, there being no first year ice of any consequence left at this time. Six analyzed LANDSAT images are presented: 23 August 1973, figure 6; 06 September 1974, figure 7; 04 August 1975, figure 8; 09 September 1975, figure 9; 17 August 1976, figure 10; and 05 September 1976, figure 11.

The imagery for late August 1973 shows that the pack was over 100 km offshore, whereas in 1974 close pack was only 60-70 km north of Prudoe Bay. In early August 1975 the edge of the pack was 5-25 km offshore but by September the pack was 25-50 km distant, showing less open water than in the previous years, but still more than adequate for navigation. Mid August 1976 saw the pack 5-25 km from shore in the Prudoe sector and by early September open water was greater in extent although in the immediate vicinity of Prudoe Bay the pack was still about 20 km offshore.

These data also suggest that in 1976 conditions would be worst for shipping, in line with the inferences that would be made from the early summer data for the Barrow sector. An important difference is that no ice that would impede shipping is visible in the Prudoe sector for all the years shown. This is particularly important since the ice never cleared completely off Point Barrow in 1975. If there was no first year ice present in the Prudoe sector by late summer 1975, and if we have correctly interpreted the LANDSAT imagery as to the progress of the melt in the Barrow sector in that year, then it seems likely that the first year ice in the Barrow sector would also have decayed by September 1975.

In conclusion, therefore, the LANDSAT imagery for the Barrow and Prudoe sectors of the Beaufort Sea coast for 1973-76 indicates that early summer melt patterns varied little over the four seasons. In contrast, the extent of open water in the late summer in the Prudoe sector varied substantially, but was never an obstacle to navigation. It is almost certain that the continuous (first year) ice was no longer present at Barrow during late August 1975 in sufficient quantity to prevent shipping, hence the pack ice must have moved southward during that summer to produce the worst navigation year along the Beaufort Sea in the last 20 years. Tracks of the AIDJEX data buoys and manned camps during summer 1975 show anomalous southeastward displacements (rather than

westward), in implying large-scale northwesterly flow, in accordance with this inference.

3. The Role of in situ Decay of the Fast Ice in Breakup

Three modes of fast ice decay are detectable on LANDSAT images. These are in situ melting at river mouths, ice sheet break-up in the polynyas created by the rivers, and cracking due to displacements of the pack ice. Table 1 lists average dates for the various stages of icebreak-up that we have previously identified.

An investigation of the fourth and fifth of these stages, the first flooding of near-shore ice by rivers and the effective break-up and disappearance of fast-ice has been carried out. The objective was to determine, if possible, whether estuary melting produced any spatial or temporal variability in the decay of near-shore ice. The available imagery shows that the deltas do have an important effect on the rate and location of melting, although other factors are also operative. The following summary indicates the variability which exists:

1973

2 July	Beechey Point	melting taking place at all visible river mouths. Cracks and leads further out seem unrelated to delta location
16 July	Barter Isle	entire shore open

1974

21 June	Barter and Barrow	melting at river mouths small
26 June	" "	melting at river mouths has expanded lots of cracks and leads in pack
29 June	Beechey Point	melting at river mouths expanding slowly
12 July	Barter	fast ice intact, extent of melting at river mouths indeterminable
14 July	Prudhoe	large open spaces around deltas, some large cracks in fast ice near Colville River
15 July	"	large open areas near all river outlets, ice that remains is dark
15 July	Harrison Bay Pitt Point	ice still close in to shore
20 July	Pt. Barrow	ice remains on both sides of barrier islands
2 August	Harrison Bay	clear of ice, (no view of Pt. Barrow)

1975

28 June	Prudhoe	slight melting at river mouths
6 July	Pt. Barrow	" " " " "
18 July	Harrison Bay	melting extending from river mouths all along coast; also open water between fast ice and pack.
20 July	Harrison Bay Pitt Point	ice still close to shore
22 July	Prudhoe	large areas of open water around mouth of Colville River
23 July	Pt. Barrow	Dease Inlet and Harrison Bay clear, but not Pt. Barrow

1976

29 June	Pt. Barrow	beginning stages of river mouth melting between Pt. Barrow and Harrison Bay
13 July	Harrison Bay	full of ice, open water around mouth of Colville
14 July	Prudhoe	large open area at Colville plus large cracks northwest of the delta; ice is close to shore on eastern and western side of Colville estuary.
18 July	Pt. Barrow	Dease Inlet half melted, ice is still intact on both sides of barrier islands
29 July	Prudhoe	shore clear of ice
31 July	Prudhoe	broken ice lies beyond open water, and more open water beyond the broken-up swath
2 August	Prudhoe	cracks and break-ups seem greatest near river mouths and less on closed coasts, broken ice and open water appear on the farther edge of the fast ice.

It is obvious on the imagery that an alternating pattern of open water/ice/open water/ice is produced by the alternation of estuaries and shoreline. In addition, large cracks on the shoreward edge of the fast ice appeared near the river mouths. There is definite geographic variability. The entire Pt. Barrow-Pitt Point vicinity seems to lag behind areas to the east by as much as a month. The ice inside the barrier islands at Pt. Barrow appears to be the slowest to melt, and Harrison Bay was also slow to clear.

The effect of melting at river mouths also varies with their size. The most obvious example of this is at the mouth of the Colville, which affects a larger area more rapidly than any of the other estuaries. There are other factors which could produce this difference also, however, such as wind exposure, pack ice movement and coastal configuration.

Uncertainties in the exact role of river melting are suggested by the fact that broken-up ice and open water are apparent on the seaward side of the fast ice

in addition to break-up and melting on the shoreward side. This seaward activity is probably not related to freshwater inflow from the estuaries, but rather to movement of the pack ice.

In summary, it can be stated that the rate and extent of fast ice melting is strongly affected by in situ decay near river mouths. However, based on the available imagery, it cannot be said that estuaries along control or determine fast ice decay along the coast. It seems clear that they operate in concert with other factors.

Table 1. Average Dates of Ice Decay Stages on the Beaufort Sea Coast

- 1) First in situ puddling - June 11
- 2) First openings inside fast ice - June 29
- 3) First darkening in river channels - April 22
- 4) First flooding of near-shore ice by rivers - approximately May 25
- 5) Fast ice effectively broken and gone - July 28
- 6) New ice forming - October 4

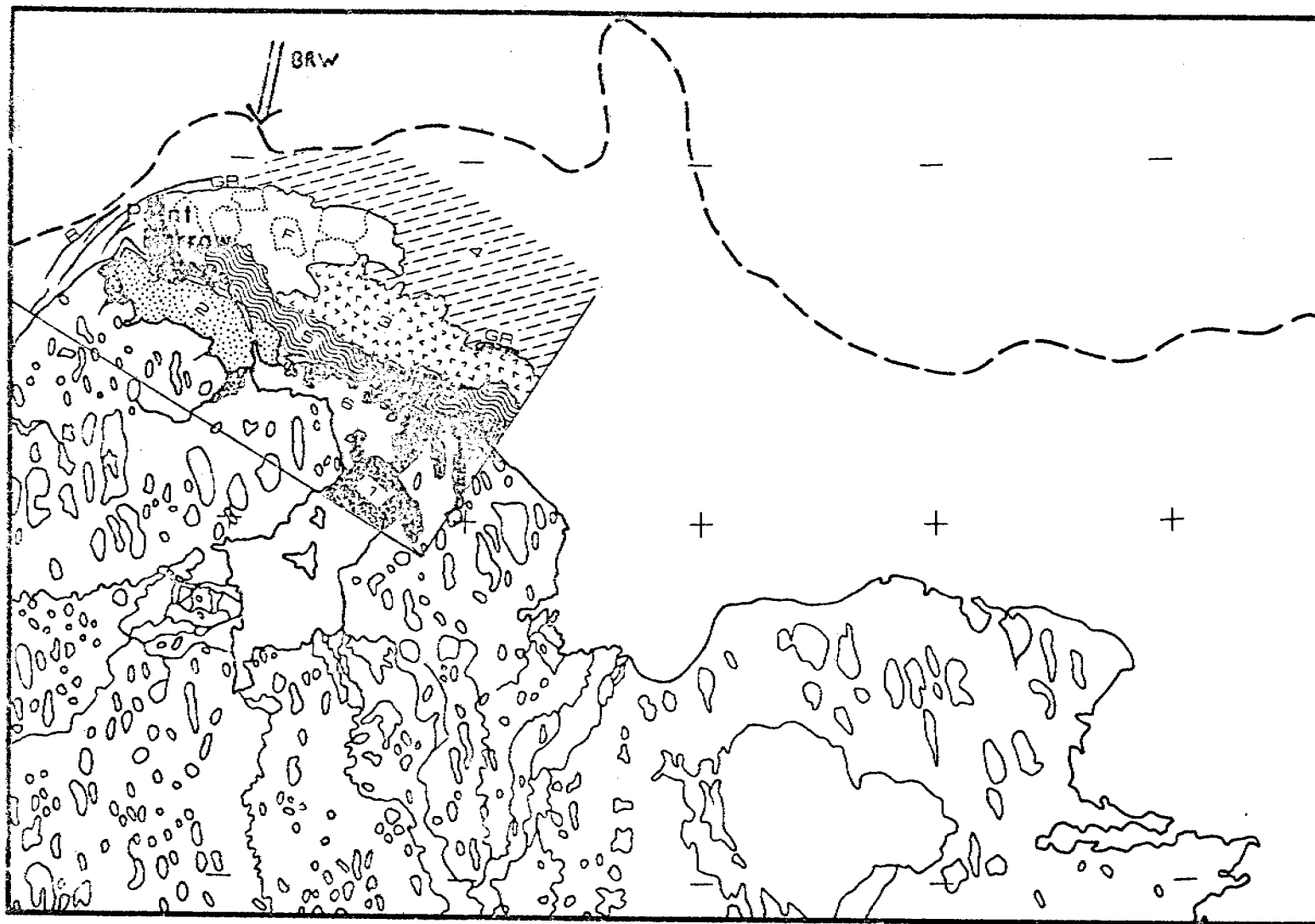
Note: The interannual variability in the dating of these events was considerably less than the uncertainty in the dating due to gaps in coverage of LANDSAT data.

FIGURE 1

21 July 1974: Scene 1728-21540

This scene shows ice conditions in the vicinity of Pt. Barrow. Some notable changes occurred in the time interval 20-21 July. On this scene, zone 2 represents partially-drained, 1st-year ice which has broken up into floe-like ice pieces since 20 July. Zone 1 is open water, and has undergone some areal enlargement near Dease Inlet. Zone 3 again represents light-toned floes in a matrix of open water and rotten ice, some of which floes are older than 1st-year, especially in the eastern part of Zone 3 on this map. Zone 4 is fairly-light ice representing compact pack ice on this date. Zone 5 comprises rotten, broken-up 1st-year ice which was formerly mainly level 1st-year ice. Zone 6 contains 1st-year pans and floes of 5/10 concentration in a matrix of open water. Both grounded ridge systems (GR) have remained in place since 20 July. The floes in the ice lagoon formed by the western grounded ridges have undergone displacements since 20 July, but these are not in agreement with the Barrow resultant wind vectors (double arrows). The displacement vectors for the ice floes are shown on the supplementary map.

617

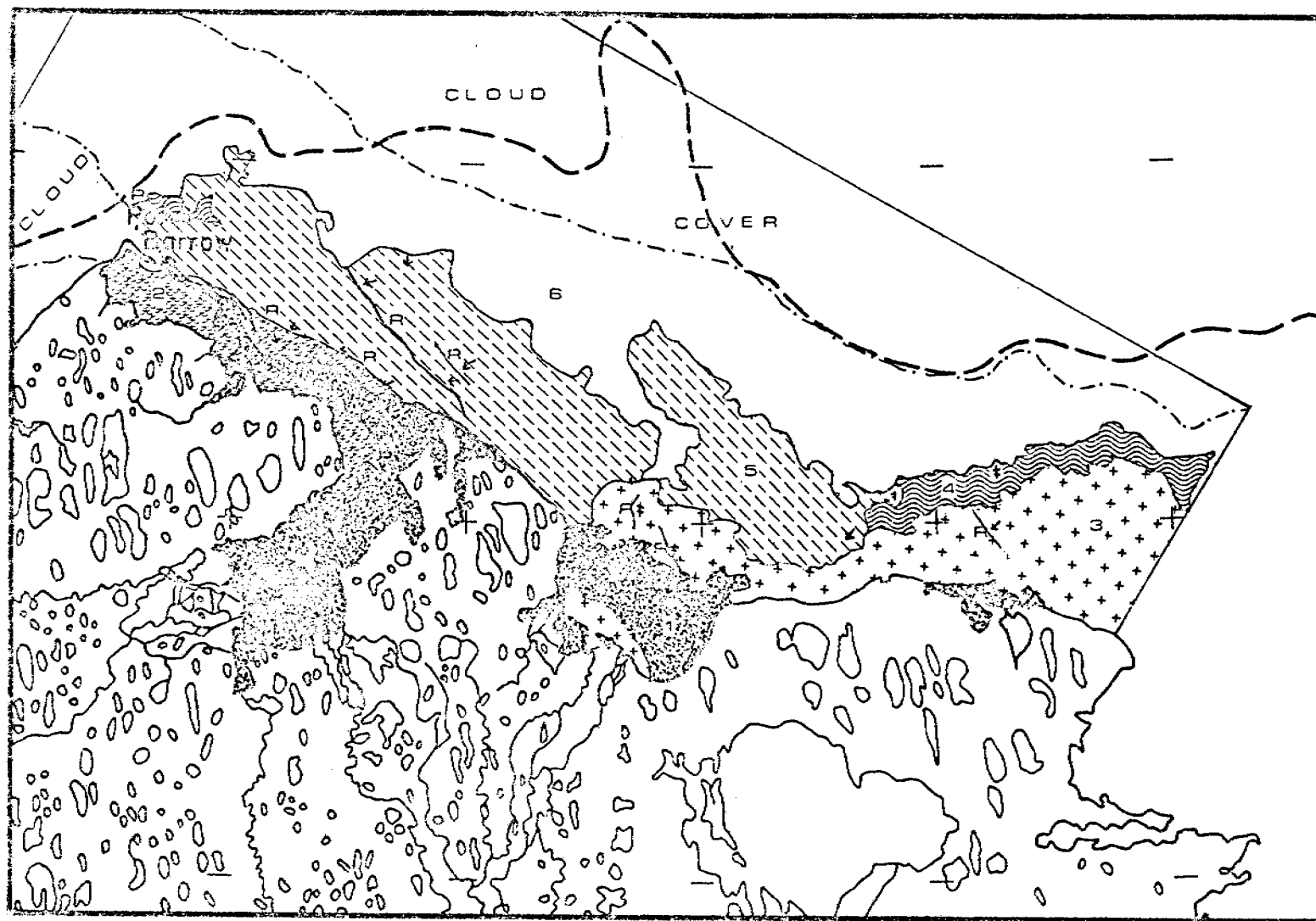


SHOREFAST SEA ICE
SURFACE MORPHOLOGICAL CHARACTERISTICS
BEAUFORT SEA COAST: BARROW SECTOR
21 JULY, 1974

Figure 2

23 July 1975: Scene E-2182-21394

This frame covers the area from Pt. Barrow eastward, nearly to Harrison Bay. Clouds cover the area northwest of Pt. Barrow and along the seaward part of the pack ice. There has not been a great deal of change from the previous frame. Movements have been mapped (arrows), and were generally 0.5 to 1 km in length, to the west and southwest. A † symbol indicates no movement. Zone 1 is mainly open water with small amounts of ice (less than 10%). Most of the ice is located in Smith Bay and the seaward half of Dease Inlet. Zone 2 consists of smooth-looking nearshore ice. The ice is fairly dark overall, but includes some large light toned (drained) areas. A ridge is located along the seaward edge of zone 2. It has moved shoreward less than or equal to 1 km since 18 June. Zone 3 is medium grey toned smooth-looking ice. There are some darker areas along the seaward boundary that appear ready to melt out or break up. There are also many small open water areas and several light toned lineations (possible ridges) within this zone. Zone 4 is open water with many big to vast sized floes (approximately 20% ice). Zone 5 is medium grey tone overall, but with much tonal variation. The ice appears similar to zone 3, but looks rougher. There are some small open water areas in this zone, and some darker areas indicating more water on the surface of the ice. There are a number of light lineations in this zone; some appear to be ridges (R). The ridge (R) on the zone 5/zone 6 boundary north of Pt. Barrow is in the same location as the fast ice edge on the 10 March frame. The shoreward boundary of the pack ice (6) is somewhat arbitrary due to gradual tonal changes of the ice. The boundary north and northwest of Pt. Barrow cannot be mapped due to cloud cover. The pack ice is fairly light toned. There are many small areas of open water, but otherwise the ice is continuous.



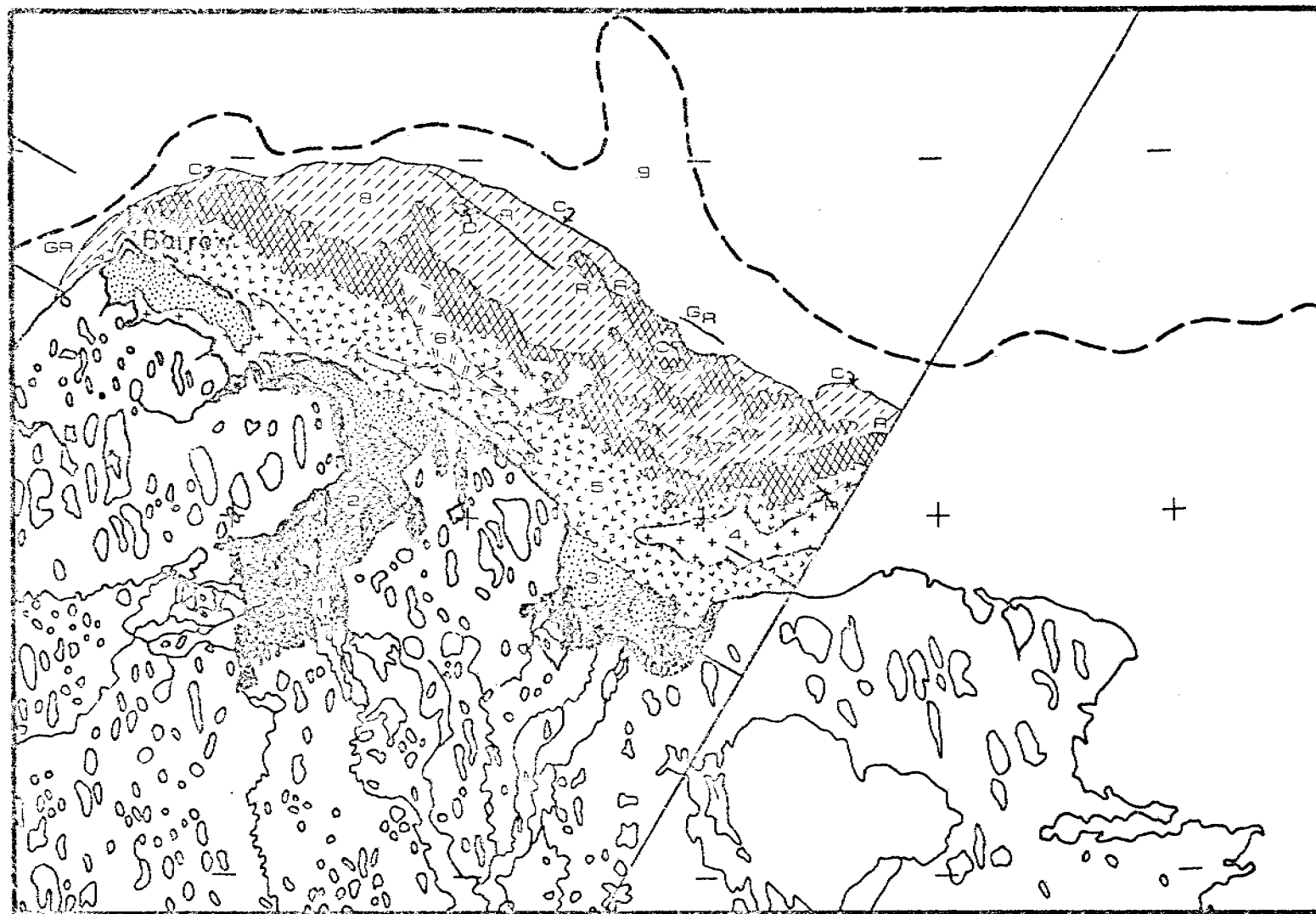
SHOREFAST SEA ICE
SURFACE MORPHOLOGICAL CHARACTERISTICS
BEAUFORT SEA COAST: BARROW SECTOR
23 JULY, 1975

FIGURE 3

18 July 1976: Scenes E-21543-21382 and E-2543-21380

Very few changes have occurred in the ice since the previous frame (16 July) in the area of overlapping coverage. No ice movements can be observed between the two frames, but the ice is less consolidated in Dease Inlet and Smith Bay on the 18th. The continuous ice edge (C) is distinct on this frame. The pack ice (9) remains consolidated with the exception of open water along the shoreward edges in the western part of the zone. The fast ice remains continuous with a wide variety of puddling characteristics (zone 2-8). Open water (1) is present along the coast, especially in Dease Inlet and Smith Bay. Zones 2 and 3 are composed of smooth, nearshore ice. Zone 2 consists of darker, more rotten-looking ice, while in zone 3 the ice appears to have drained. Zone 4 is mottled ice of a fairly dark tone overall, while zone 5 is mottled ice with an overall light tone. There are a number of small, distinct areas of darker tone within zone 5, presumably due to increased melt. Smooth-looking, medium gray toned ice makes up zone 6. Zone 7 is composed of dark toned ice with a number of light toned linear features and some lighter mottling. There are several cracks (CR) in the seaward part of the zone, and it appears that the ice surrounding them will soon be part of the pack. Overall, zone 8 is a medium gray tone, although there is much tonal variation within this zone. There are several ridges (R) within this zone. The ridge system northwest of Pt. Barrow (CR) on the continuous ice edge has remained stationary since the 25 February frame. Another ridge (GR), located just beyond the continuous ice edge north of Smith Bay, has also remained stationary since the 25 February frame. However, this ridge is not present on the next frame (2 August). The very dark toned areas (D) mentioned on the 16 July frame has remained in the same place, but now appears to be open water.

621



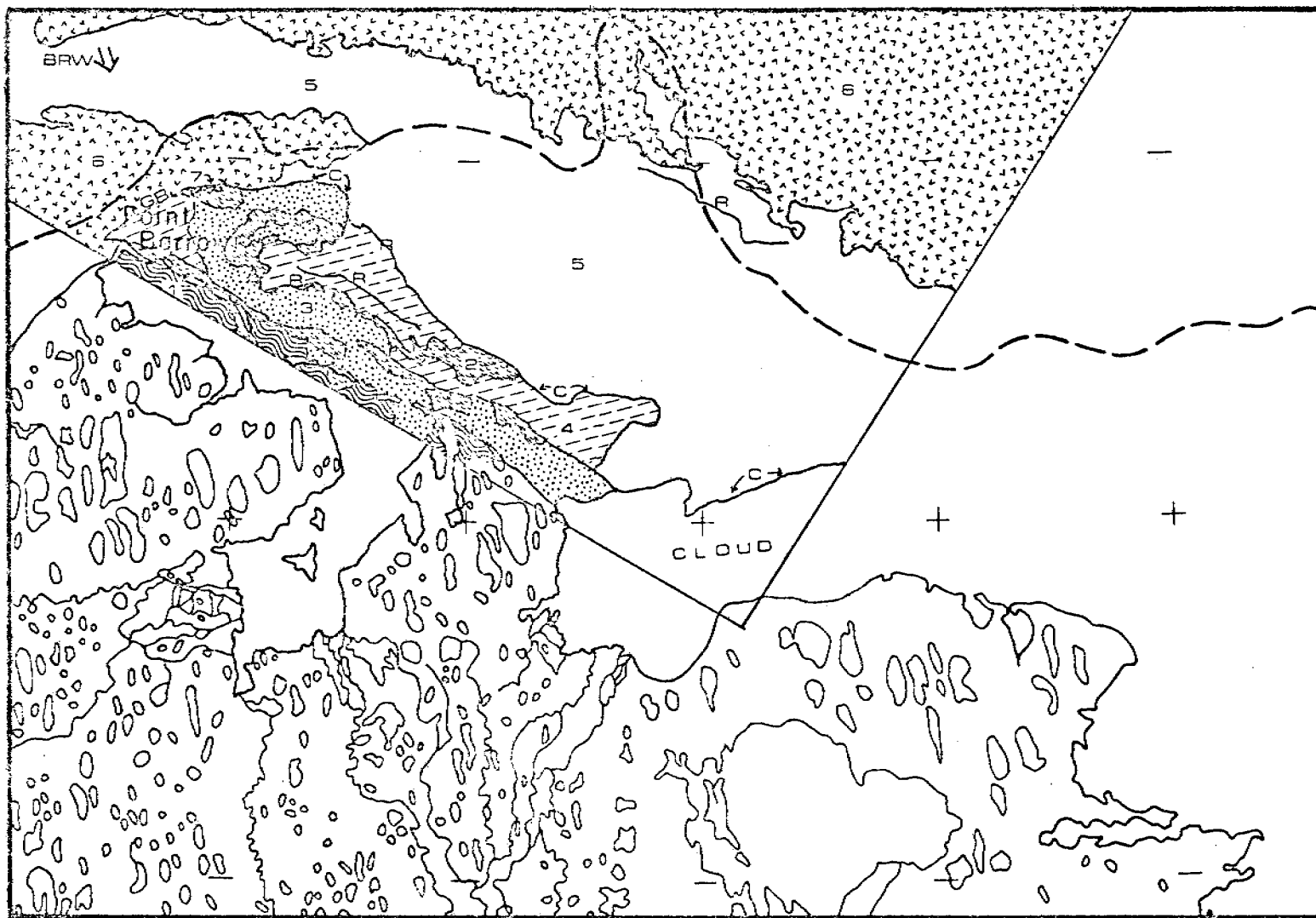
SHOREFAST SEA ICE
SURFACE MORPHOLOGICAL CHARACTERISTICS
BEAUFORT SEA COAST: BARROW SECTOR

18 July 1976

Figure 4

7 July 1973: Scene 1349-21564

In this summer scene, covering the area from Pt. Barrow to western Smith Bay, the ice is still quite continuous. There are some areas of open water (7) in the pack ice just outside the continuous ice edge (c). Winds for 6 July at Barrow (BRW) were 2.4 m/sec from the NNW. Pack ice movements on this frame cannot be measured, however, due to a lack of earlier summer coverage in this area. Two zones are present in the pack ice: zone 5 is the darker, apparently more puddled zone, while zone 6 is lighter in tone. There appears to be a ridge (R) present in zone 5 approximately 55 km seaward of Smith Bay. The area from the coastline to approximately 4 km shoreward of the barrier islands is not covered by this frame and clouds obstruct the view of the ice seaward of Smith Bay. Therefore, a limited amount of the continuous ice is shown. There appears to be heavy puddling or flooding in zone 1, but very little open water. Zone 2 is also quite puddled, appearing relatively dark in all bands. There are some light areas in this zone as well. The lightest toned ice (3) has probably drained by this date. Zone 4 is characterized by a mottled tone, but overall appears quite light. There are several ridge systems (R) in this zone. These ridges may be grounded, since they have been stationary since 17 June. Possibly some older ice is present in this zone, however this cannot be determined without using other types of imagery. Northwest of Pt. Barrow, along the northwest boundary of zone 4, is a larger ridge system (GR), possibly grounded. It appears to coincide with the 14 May and 23 March continuous ice edges.



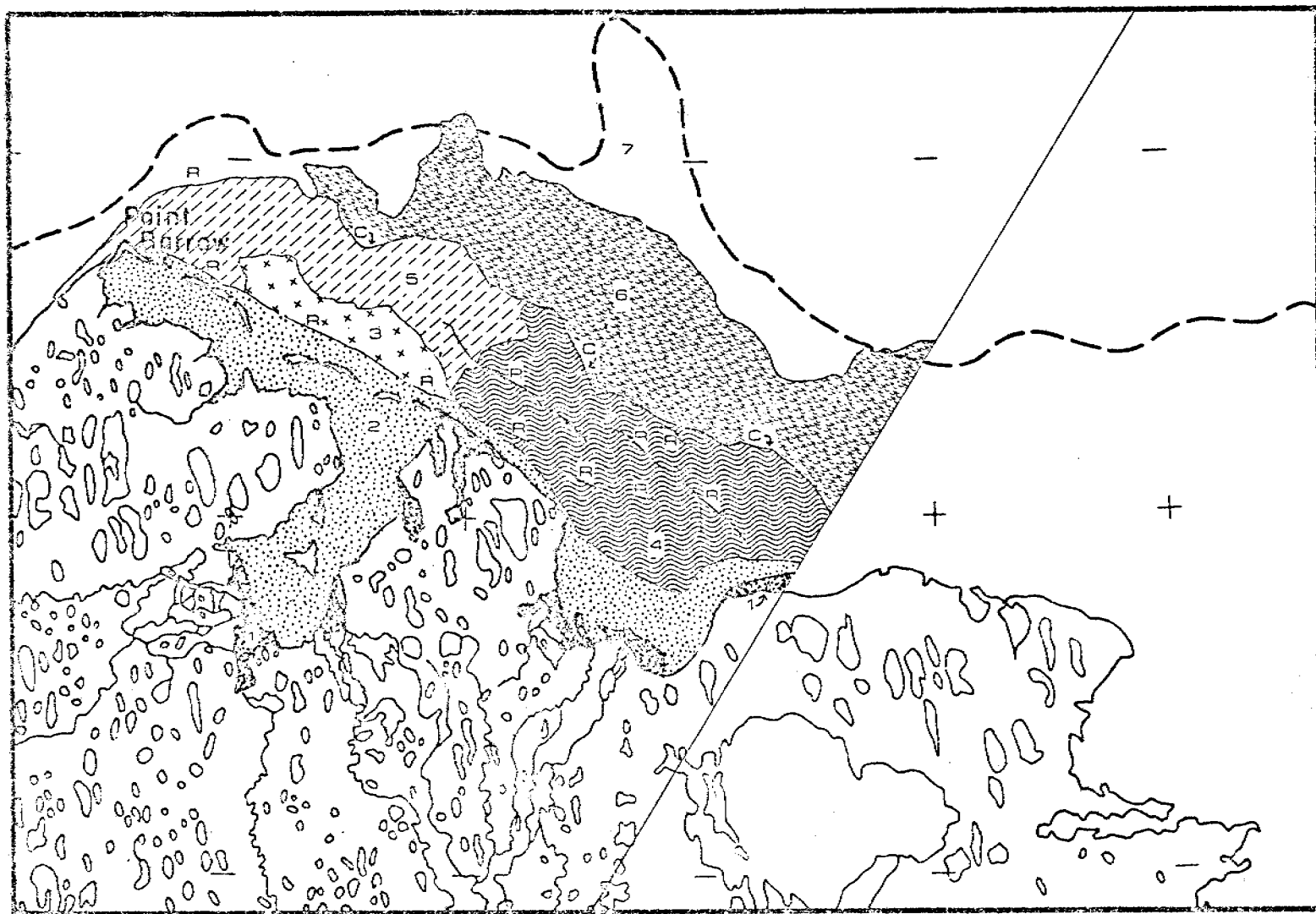
SHOREFAST SEA ICE
SURFACE MORPHOLOGICAL CHARACTERISTICS
BEAUFORT SEA COAST: BARROW SECTOR

7 JULY, 1973

Figure 5

6 July 1975: Scenes E-2165-21452 (top) and E-2165-21454 (bottom)

By the time of this early summer scene, the ice has darkened considerably. Part of the continuous ice edge of 18 June (northeast of Pt. Barrow, marked as a ridge, R) has remained, but appears to have moved approximately 3 km to the southeast. It is difficult to tell, however, due to cloud cover on 18 June. The remainder of the continuous ice edge (C) has changed. Two zones are present in the pack ice. Zone 6, which is partly former continuous ice, is composed of open water (less than 25%) and variously sized floes. There is much variation in the tone of the ice, from heavily puddled to very light toned, possibly drained ice. Five zones are present within the continuous ice. Open water (I) is present along the shore in a narrow band, especially in Dease Inlet and Smith Bay. Zone 2 is composed of very dark, fairly uniformly toned, smooth-looking ice. There are darker areas near Pt. Barrow and in Smith Bay and lighter areas in Dease Inlet. There is a ridge (R) along the seaward boundary of the zone, which has remained stationary since 18 June. Zone 3 consists of uniformly toned ice that is slightly lighter in tone than the other zones within the continuous ice. Zone 4 ice is similar to zone 2 ice, but zone 4 has more light lineations and is a lighter tone. Zone 4 also has less light lineations, is slightly darker, and appears slightly smoother than zone 5. There is some ridging (R) in this zone. Zone 5 appears quite rough with many light lineations. It is a fairly dark tone overall, but not a uniform tone. Some large, dark, smooth-looking areas resemble zone 4 more than the rest of zone 5, but since zone 5 contains such a variety of tones and textures, these areas have been included in zone 5.



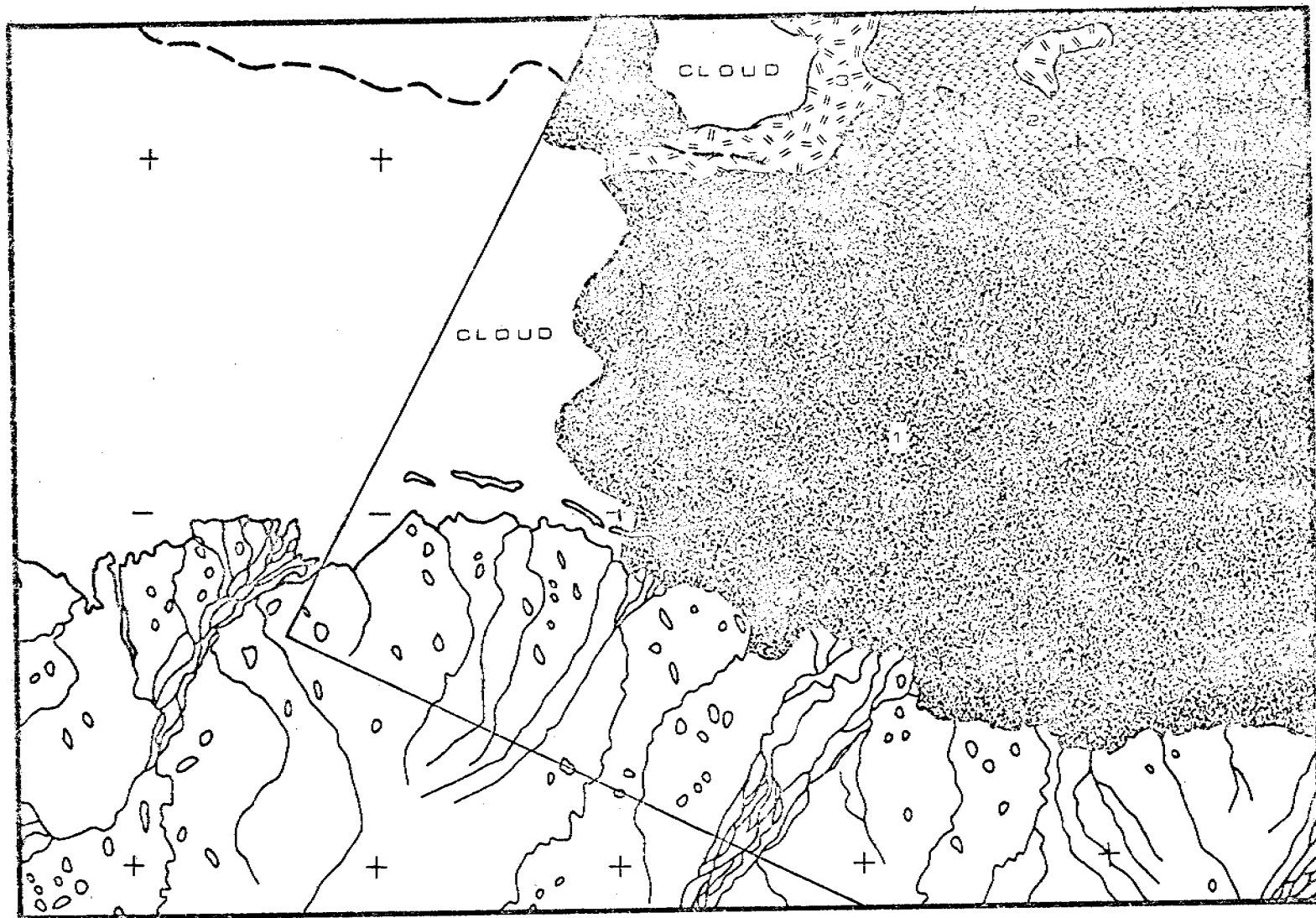
SHOREFAST SEA ICE
SURFACE MORPHOLOGICAL CHARACTERISTICS
BEAUFORT SEA COAST: BARROW SECTOR

6 JULY, 1975

FIGURE 6

23 August 1973: Scene E-1396-21162

In this late summer scene, the ice is nearly gone. There is some cloud cover obstructing the view of the ice and the sea in the western part of the frame. Virtually no ice is present in a zone approximately 60 to 90 km wide along the coast (zone 1). Floating ice in approximately 30% concentration is present in zone 2, and zone 3 contains ice in approximately 50 to 60% concentration.



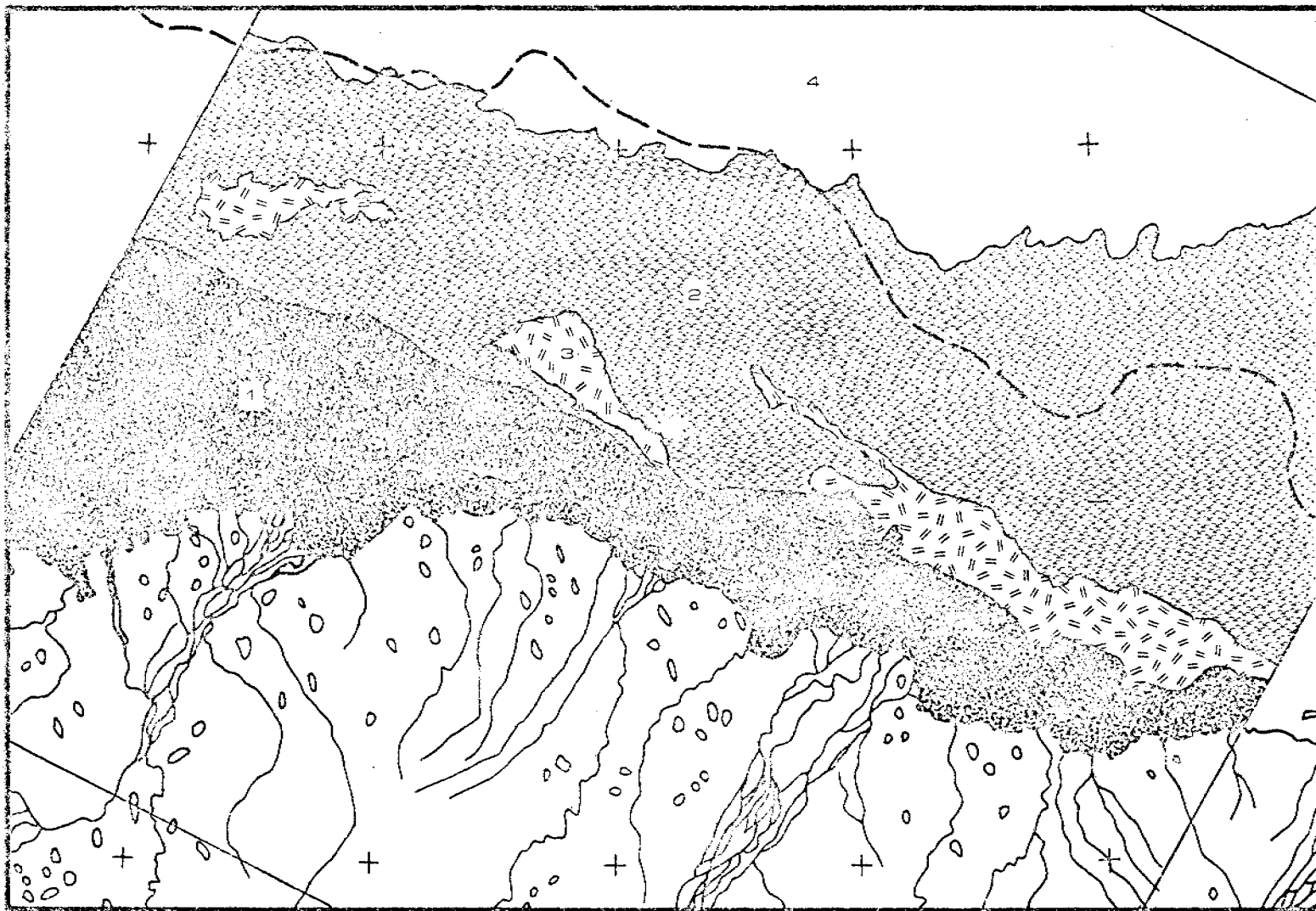
SHOREFAST SEA ICE
SURFACE MORPHOLOGICAL CHARACTERISTICS
BEAUFORT SEA COAST: PRUDHOE SECTOR

23 August 1973

FIGURE 7

6 September 1974: Scene E-1775-21124

This late summer scene covers nearly the entire sector. Ice is gone from a zone 10 to 35 km wide along the coast (zone 1). Zone 2 consists of scattered ice floes in approximately 30 to 40% concentration. Zone 3 consists of much larger floes of similarly toned and textured ice. This ice is quite consolidated, ranging from approximately 50 to 80% ice. Zone 4 ice is also well consolidated. This ice is fairly light toned overall.



SHOREFAST SEA ICE
SURFACE MORPHOLOGICAL CHARACTERISTICS
BEAUFORT SEA COAST: PRUDHOE SECTOR

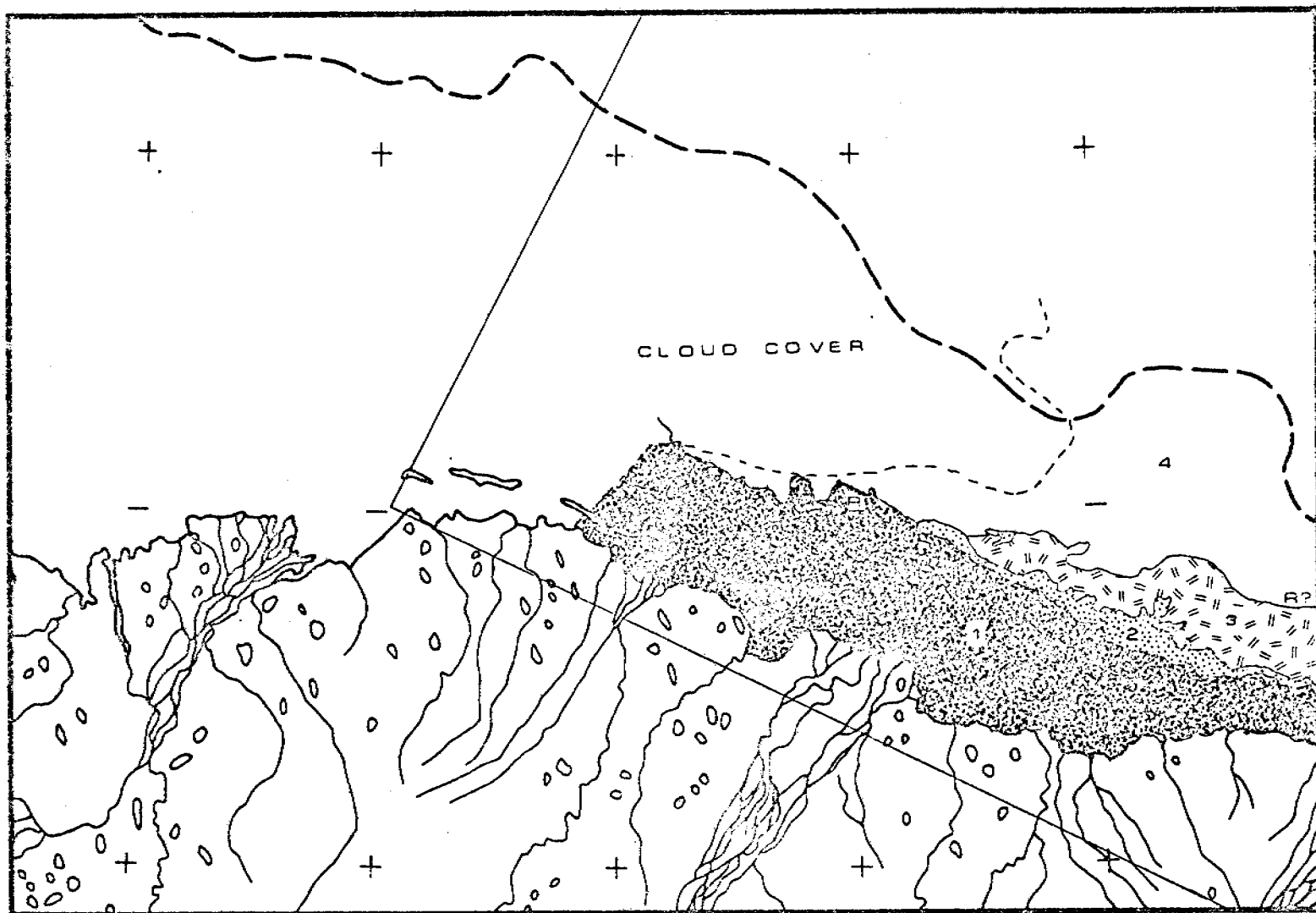
06 September 1974

Figure 8

4 August 1975: Scene E-2194-21050

In this late summer scene, clouds cover much of the western part of the frame and the pack ice. Open water (zone 1) extends along the coast in a band 5 to 25 km wide. This frame covers much of the same area as the 18 July frame, so comparisons can be made. The large body of "continuous" ice present in late July is completely gone. The pack ice edge is approximately the same on both frames (very close to the 10 fm contour). There appears to have been some tonal lightening in the pack ice since 18 July, however it is difficult to tell due to the cloud cover. The ridge 30 km northeast of Prudhoe Bay has not moved since 6 March. Several zones were distinguished in the ice based on tonal differences. Zone 2 is the darkest toned ice. It has quite a uniform tone, so it appears smooth. This ice looks ready to melt or break away and move into zone 1. Zone 3 is transitional between zones 2 and 4: it looks smoother and slightly darker in tone than zone 4 and more mottled and lighter toned than zone 2. Zone 4 is mainly cloud covered, however the ice appears well consolidated with some small areas of open water. There may be some ridging along the boundary with zone 3. Ice in zone 4 is a mottled tone and appears quite rough.

631



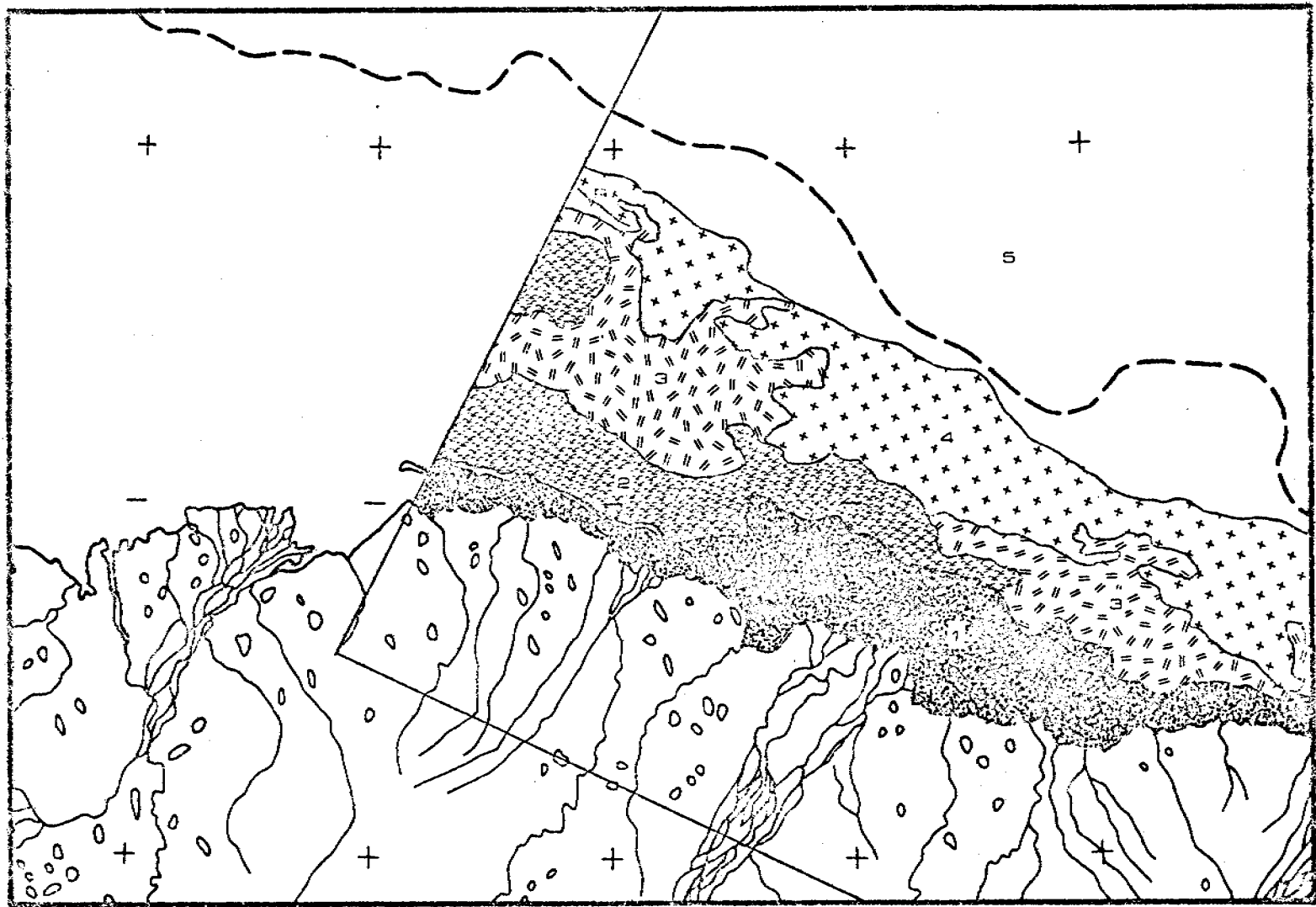
SHOREFAST SEA ICE
SURFACE MORPHOLOGICAL CHARACTERISTICS
BEAUFORT SEA COAST: PRUDHOE SECTOR

4 AUGUST, 1975

FIGURE 9

9 September 1975: Scene E-2230-21042

Ice is virtually gone in a zone approximately 5 to 20 km wide along the coast (zone 1). Seaward of this zone, scattered floes are present in approximately 20% concentration (zone 2). Larger floes and more concentrated ice (approximately 30 to 50%) comprise zone 3. Zone 4 consists of quite consolidated ice of a fairly light tone. A ridge (R) approximately 10 km in length is present in the seaward part of the zone. Zone 5 consists of the most consolidated ice, with only very limited areas of open water.

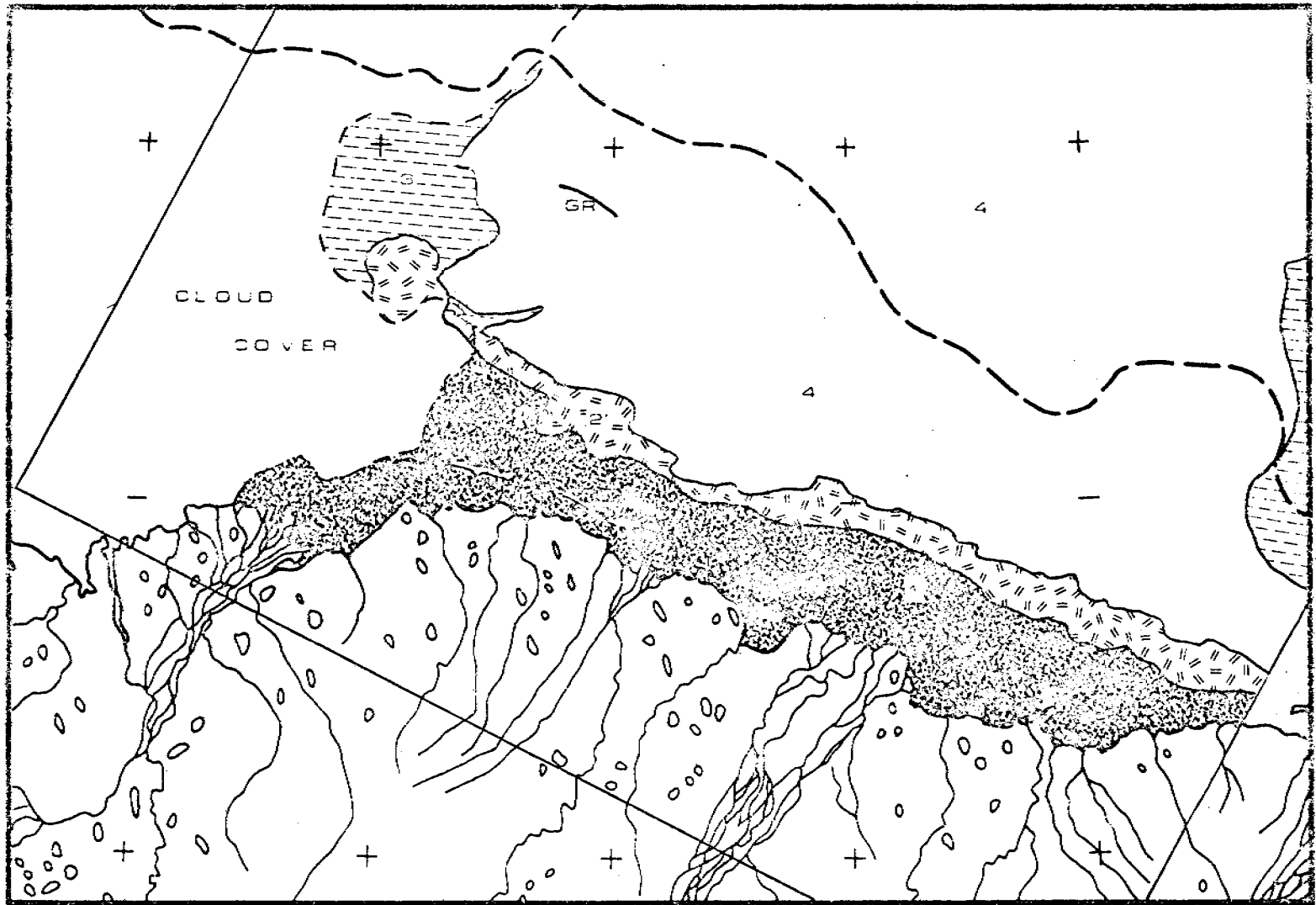


SHOREFAST SEA ICE
SURFACE MORPHOLOGICAL CHARACTERISTICS
BEAUFORT SEA COAST: PRUDHOE SECTOR

FIGURE 10

17 August 1976: Scene E-2573-21030

Clouds cover the ice in the western part of this frame. Open water (zone 1) is present in a band from 5 to 25 km wide along the coast. A narrow zone of open water with approximately 10% floating ice (zone 2) is located seaward of zone 1. Zone 3 consists of floating ice in approximately 70% concentration. Zone 4 consists of fairly consolidated ice, although the shoreward edges of this zone have less consolidated ice. The grounded ridge (GR) shown in zone 4 has been present since the February frames.



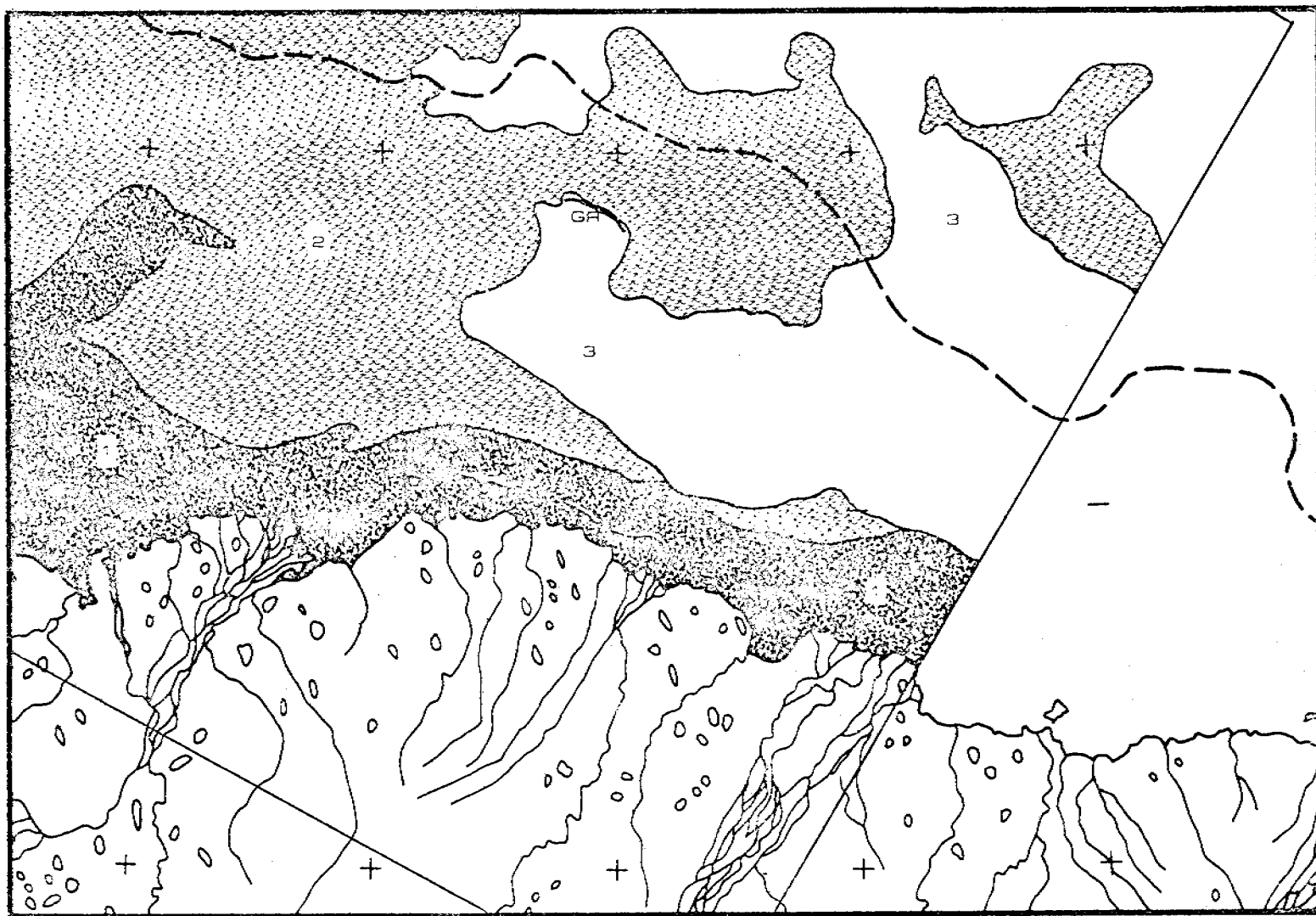
SHOREFAST SEA ICE
SURFACE MORPHOLOGICAL CHARACTERISTICS
BEAUFORT SEA COAST: PRUDHOE SECTOR

17 August 1976

FIGURE 11

5 September 1976: Scene E-2592-21082

Some thin clouds are present over much of the frame, however their effect is minimal. Zone 1 consists mainly of open water. Open water with some floating ice composes zone 2. The overall concentration of ice in this zone is generally less than 50%. Zone 3 consists of more consolidated ice. The overall concentration of ice in this zone is approximately 90%. A large ridge (CR), which has remained stationary since the February frames, is present on a boundary of this zone.



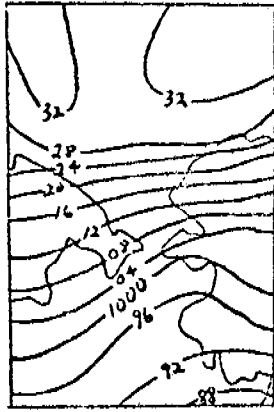
SHOREFAST SEA ICE
SURFACE MORPHOLOGICAL CHARACTERISTICS
BEAUFORT SEA COAST: PRUDHOE SECTOR
05 September 1976

B. Synoptic Climatological Analysis

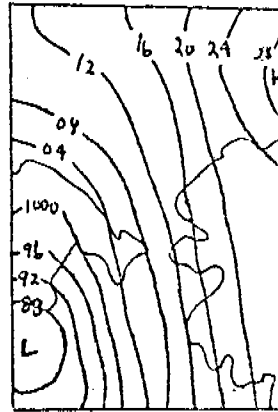
1. Synoptic Climatology of the Chukchi Sea Coast

A detailed analysis of the climatic characteristics associated with the MSL pressure pattern types for the Chukchi area at Kotzebue, Alaska was presented in the September 1977 Quarterly Report. A synopsis is given here. Statistical tests indicate that the 22 pressure types are associated with distinctive climatic conditions. Maps of the 22 types are shown in Figures 12-15. Their seasonal temperature and precipitation characteristics are summarized in Figures 16-17, and the annual regimes of temperature conditions occurring with cyclonic and anticyclonic types are given in Figures 18 and 19.

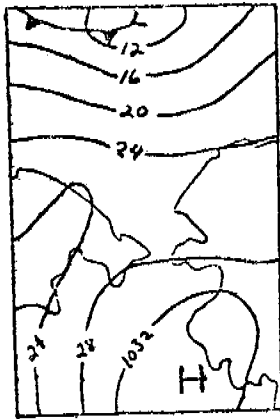
- (i) Winter - Type 1 (Arctic High Pressure with subpolar easterlies at Kotzebue) is dominant, bringing near normal weather characteristics. Interruptions by anticyclonic (the most common) systems bring cold, dry weather to Kotzebue because they are associated with cold, continental air masses with weak northerly winds and little cloud cover which tend to reinforce the Arctic inversion. Cyclonic interruptions (less common) bring warmer than average, moist weather to Kotzebue because they are associated with warm maritime airmasses with strong southerly to easterly winds that tend to break-up the Arctic inversion and large cloud amounts that influence the net radiation budget by absorbing and re-radiating (terrestrial) radiation.
- (ii) Summer - In summer there is a greater variety of types and the difference between cyclonic and anticyclonic types is not readily apparent. The main factor influencing temperature is geostrophic wind direction, with easterly winds causing continental outflow of warm air and westerly winds causing cool air advection from the Chukchi Sea. Because ice conditions are closely related to temperature conditions, warm types with easterly flow (1, 2, 13, 17) are probably important in helping force summer ice break-up. Cold westerly types (3, 10, 15) are probably important for delaying that breakup. Type 3 which is closest to the mean pressure pattern is the most common type in July.



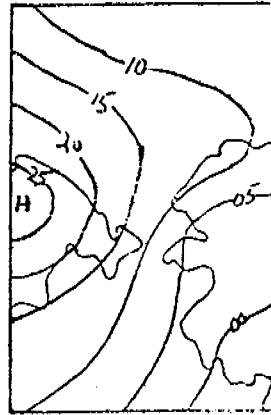
Type 1. 14 March 1970



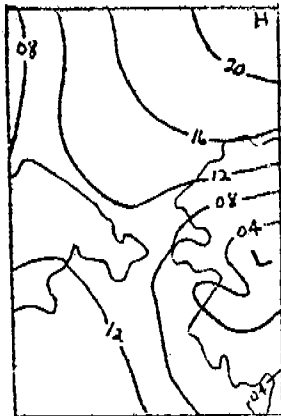
Type 2. 7 August 1968



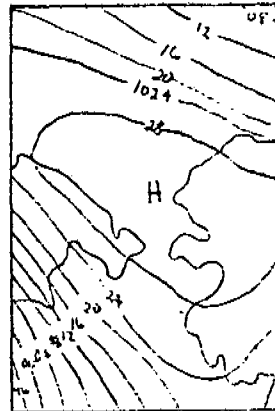
Type 3. 20 March 1967



Type 4. 2 February 1961

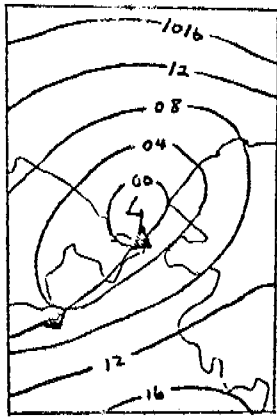


Type 5. 23 June 1969

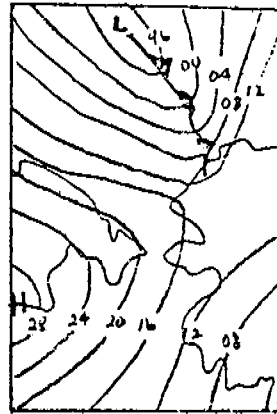


Type 6. 12 March 1955

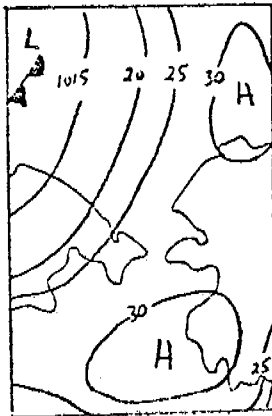
Figure 12. Chukchi Synoptic Types 1 - 6 (isobars in mb, omitting 1000 or 900)



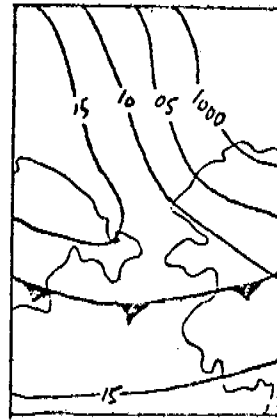
Type 7. 16 July 1966



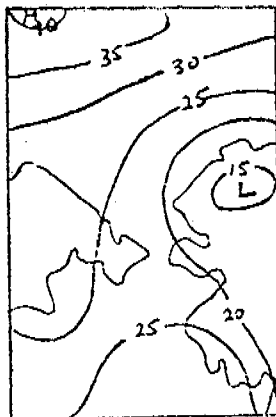
Type 8. 26 September 1957



Type 9. 17 April 1948



Type 10. 28 August 1948

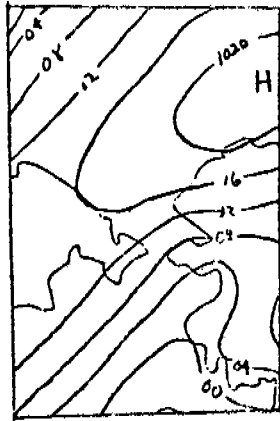


Type 11. 4 February 1955

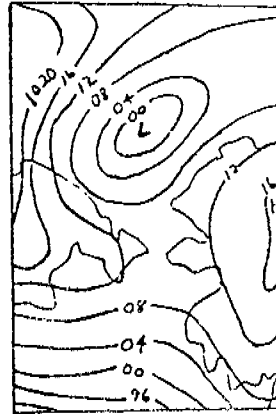


Type 12. 8 September 1946

Figure 13. Chukchi Synoptic Types 7 - 12 (isobars in mb, omitting 1000 or 900)



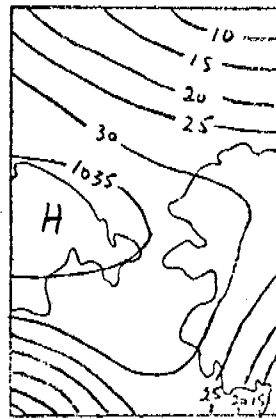
Type 13. 16 June 1969



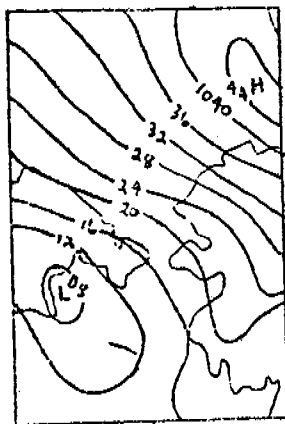
Type 14. 19 December 1966



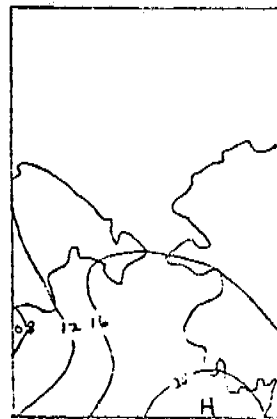
Type 15. 16 June 1960



Type 16. 4 March 1956

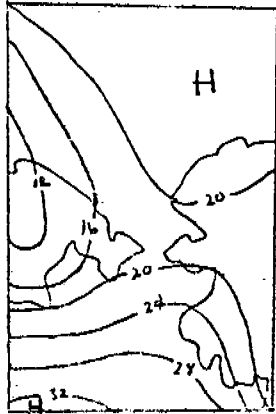


Type 17. 26 December 1968

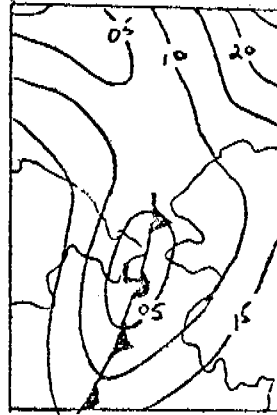


Type 18. 19 July 1963

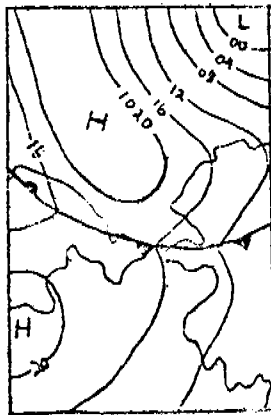
Figure 14. Chukchi Synoptic Types 13 - 18 (isobars in mb, omitting 1000 or 900)



Type 19. 17 October 1964



Type 20. 24 April 1959



Type 21. 7 June 1970



Type 22. 1 January 1956

Figure 15. Chukchi Synoptic Types 19 - 22 (isobars in mb, omitting 1000 or 900)

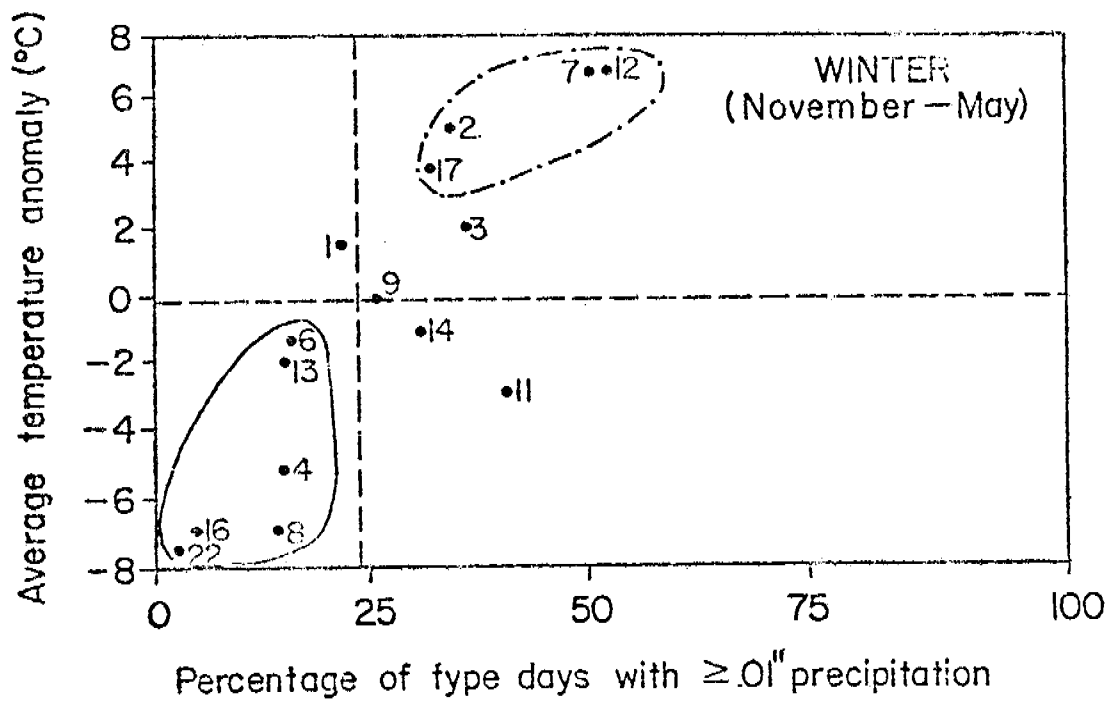


Figure 16 Temperature and precipitation characteristics of winter types.

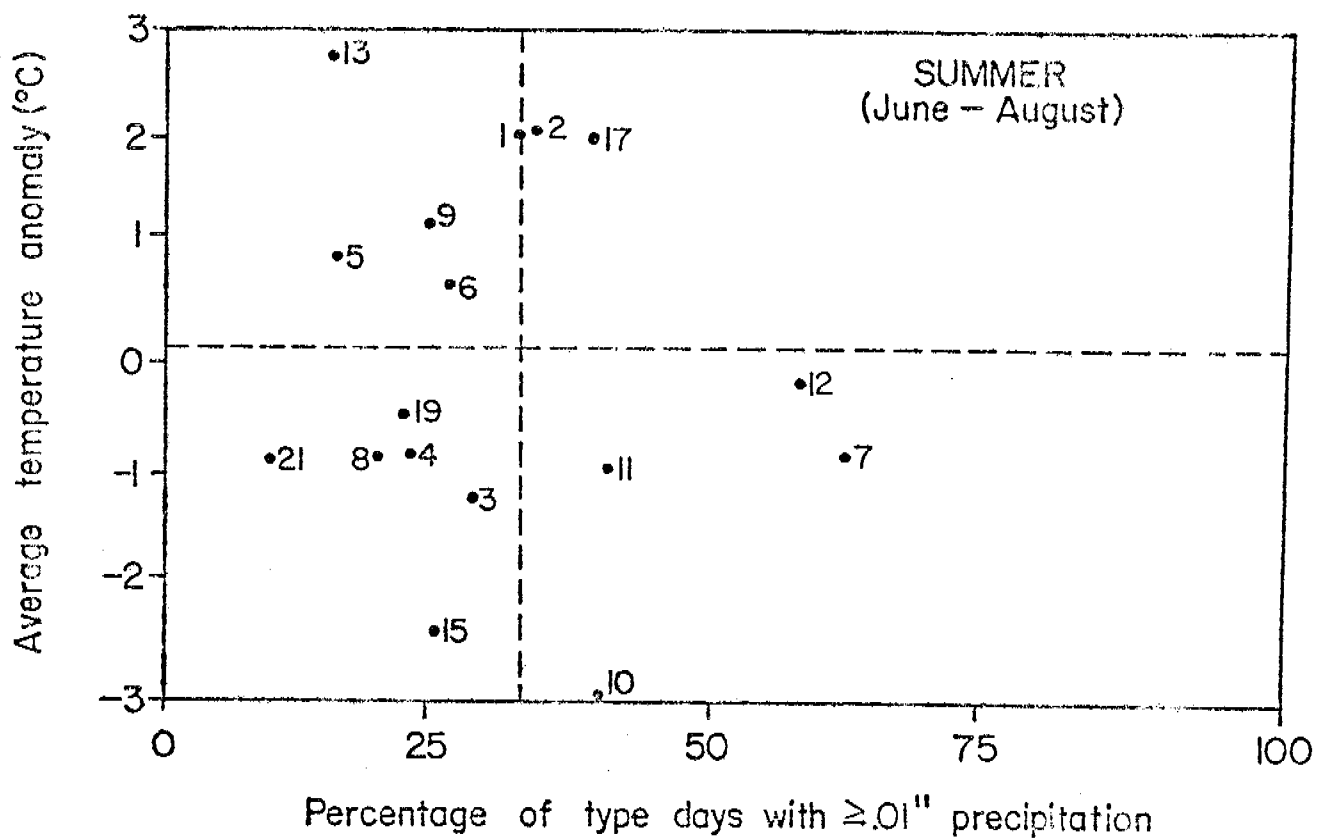


Figure 17. Temperature and precipitation characteristics of summer types.

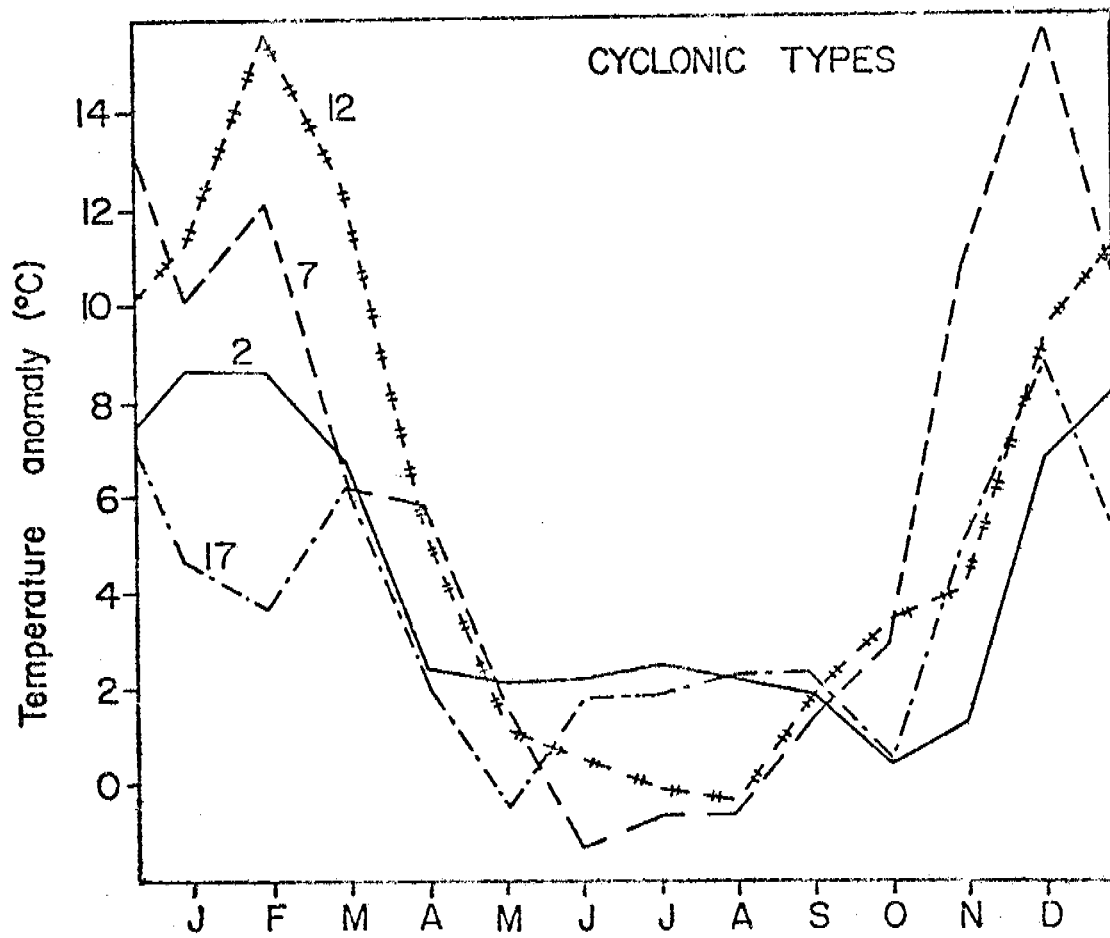


Figure 18 Temperature departure characteristics of the major cyclonic types, at Kotzebue, 1955-1974.

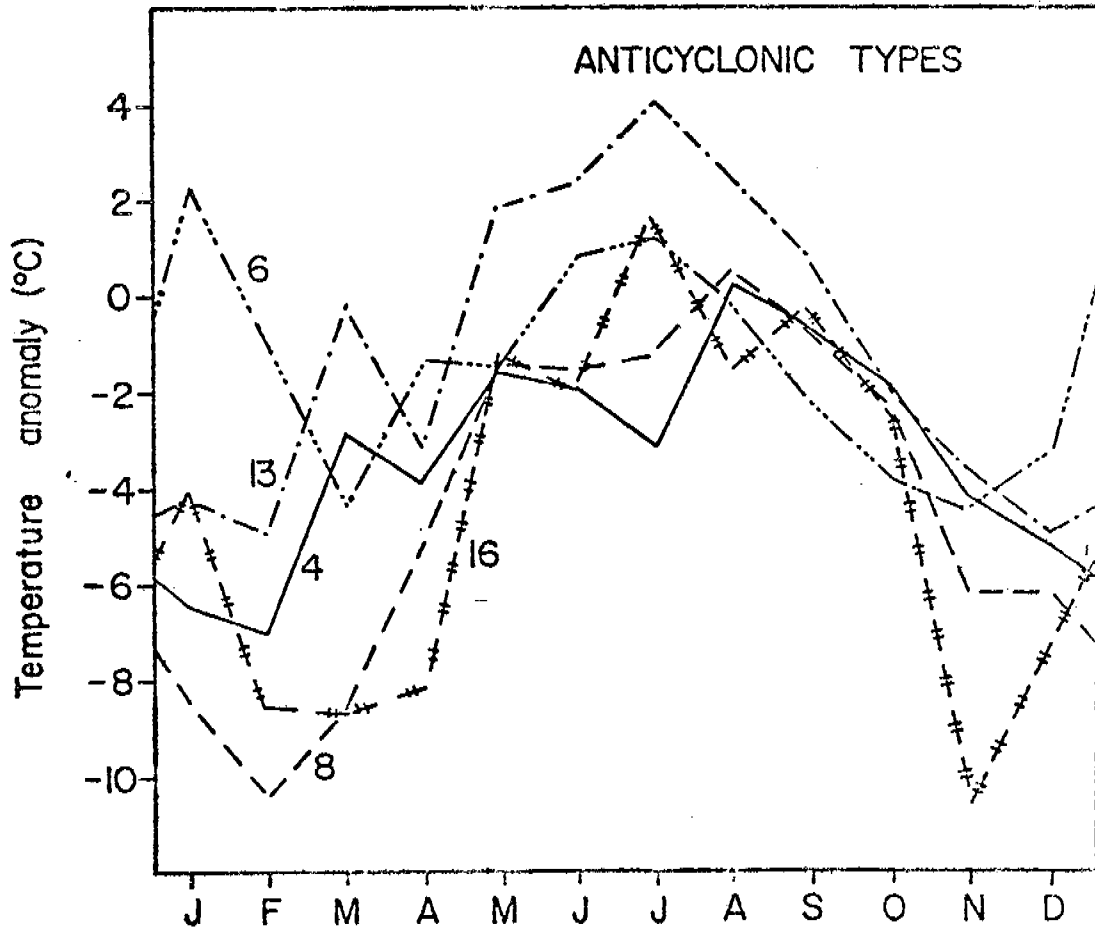


Figure 19 Temperature characteristics of the major anticyclonic types, at Kotzebue, 1955-1974.

During Summer, a mean storm track is established from south to north up the Bering Sea and through the Bering Strait, following the northwest coast of Alaska in the Chukchi Sea. Hence, summer is a time of heightened cyclonic activity, with cyclonic types 2,7,12,17 bringing considerable precipitation. It is likely that the role of open water in the Bering and Chukchi Seas is important in supplying latent heat and moisture to storms moving along this track, which are less frequent during the frozen winter period.

2. Wind temperature relationships in summer at Kotzebue

A relationship between the onset of "monsoon" westerly winds and accumulated thawing degree days (TDD's) in summer has been established (Figure 20). Probably because of the influence of interior high temperatures and resultant thermal low, westerlies tend to blow inland at Kotzebue during summer, unless interrupted by strong opposing pressure types. The earlier these winds set in, the lower the total TDD's at Kotzebue.

There is some relationship between these winds and ice conditions at Barrow: the five years of earliest westerly onset were also the years with most severe summer ice conditions at Barrow. The causal mechanism behind this association is not yet established, but the relationship has some predictive value. If the westerlies set in prior to May 4 at Kotzebue, it is likely to be a severe ice summer on the Beaufort Sea Coast.

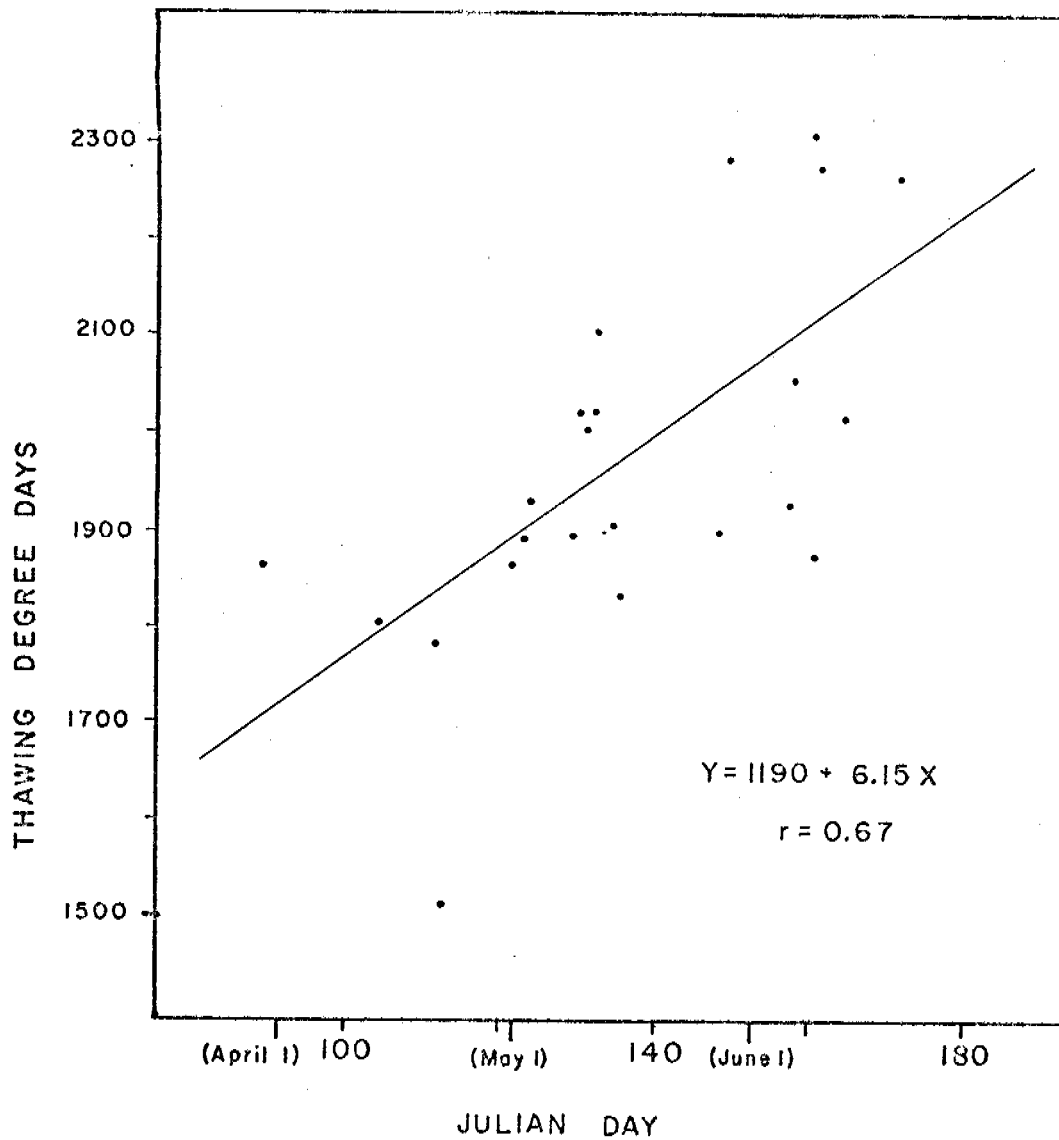


Figure 20 Date of westerly wind onset and accumulated thawing degree days at Kotzebue, 1953-1976 (except 1973). The outlier at approximately 1500 TDD represents the severe summer of 1975.

3. Evaluation of Synoptic Types for the Beaufort Sea Coast

Our synoptic typing scheme for the Beaufort Sea area, described in Barry (1976), is being tested for accuracy in a limited geographical sector covering the Beaufort coast of Alaska from Pt. Barrow to Barter Island and seaward of this coast (the Beaufort Sea proper). Accuracy is being determined for the summer of 1975 by comparing daily surface pressure distribution as given by the key day for each type with NMC grid point data and surface pressure maps prepared by AIDJEX. All pressure data are for 00 hours GMT and are verified by NWS Barrow, Ak., observations at 1400 AST of the preceding date.

Preliminary results indicate that NMC grid point data do not always accurately indicate the intensity of storms that track across the Beaufort Sea. This in turn means that the synoptic typing scheme will be inaccurate where the features of a particular pattern are primarily over the Beaufort Sea, since the typing program searches for intense surface pressure systems. Nevertheless, by grouping synoptic types according to their wind direction at Barrow some correspondence is observed between the occurrence of certain "wind direction groups" and the severity of the ice that summer (as determined by D. Barnett). This is being examined statistically at the present time.

There is also evidence of local sea breeze effects on the Beaufort Coast in summer. This component may give rise to further deviations between the inferred geostrophic wind from map data and that locally observed at coastal stations. An analysis of this effect is given in Appendix 2.

C. Ice Forecasting Techniques

The relationships between climatic parameters and stages of fast ice decay and northward retreat of the pack ice have now been firmly established (Annual Report, March 1977 and Rogers, Appendices 3,4). Air temperature is the parameter most highly correlated with summertime ice conditions, although air temperature anomalies depend upon sea level pressure distribution (see Appendix 3, Figure 2) and the resultant airflow. The relationship between ice conditions and surface wind direction is summarized in Table 2.

The technique developed for forecasting Beaufort Sea ice conditions employs three monthly mean temperature anomaly categories (above normal temperatures, normal, and below normal) at Barrow, defined in Appendix 4, Table 3. To use the technique one finds the temperature anomaly for any late spring month, usually May or June, and assumes that it will persist (i.e. recur) in the subsequent month or months

TABLE 2 Frequency of daily mean surface wind direction at Barrow, 1 July - 15 September, 1953-1975.

		350-	20-	50-	80-	110-	140-	170-	200-	230-	260-	290-	320-
		<u>10°</u>	<u>40°</u>	<u>70°</u>	<u>100°</u>	<u>130°</u>	<u>160°</u>	<u>190°</u>	<u>220°</u>	<u>250°</u>	<u>280°</u>	<u>310°</u>	<u>340°</u>
Heavy-ice	Mean	5.6	8.0	10.8	14.0	5.9	1.9	1.6	4.1	7.8	6.9	5.5	3.1
Summers	s.d.	3.5	2.4	5.3	5.1	5.0	1.9	1.5	3.3	4.5	3.2	2.4	2.1
Light-ice	Mean	3.2	4.2	9.2	17.2	9.1	4.6	4.4	3.6	7.2	5.6	4.6	3.0
Summers	s.d.	2.2	2.2	5.5	5.7	3.4	2.7	2.7	2.7	3.6	3.3	2.7	1.8

Under this assumption, for data back to 1921, the May anomaly has persisted to June, 54% of the summers; July to August, 48%; August to September, 50% (Appendix 4, Table 4). Persistence also occurs for 2 month lags, i.e., July to September, 50%, etc. (Appendix 4, Table 6).

While these percentages of persistence anomalies may seem low, it was found that light-ice summers (better conditions and longer shipping; few hazards for possible summertime drilling) are associated with both normal and above normal temperature anomalies (see Appendix 4, Tables 2 and 3) while heavy or severe-ice summers are strictly associated with below normal and an occasional normal month. With this fact in mind, the combined anomaly categories recur with a persistence upwards of 75% during the past summers. This indicates that the tendency for light or heavy ice summers is set by late spring/early summer, that it is indicated by the monthly air temperature anomalies and that it persists with a high degree of dependability.

In addition, the monthly or overall summer temperature anomaly are good indicators of anomalies in September-October (Appendix 4, Tables 4 and 6) and, hence, of the timing of the autumn freeze-up.

VII. CONCLUSIONS

The conclusions stated below are those which relate most directly to operations in the near-shore zone. All are considered to be reasonably firm.

- (i) Light-ice summers, characterized by early break-up and disappearance of fast ice and considerable northward retreat of pack (so that shipping is safe and easy) are associated with high pressure to the northeast of the Beaufort Sea. This results in more frequent southerly winds from 135° - 195° (360° = North). The opposite pressure distribution and airflow occur in heavy or severe ice summers, generally characterized by little or no pack ice retreat. These parameters determine the air temperature anomaly for the summer, a factor which is most highly correlated to ice conditions.
- (ii) Air temperature at Barrow accounts for much of the observed variance in ice conditions from year to year in the Beaufort Sea (see Appendix 3, Table 2).
- (iii) Trends in temperature since 1921, and in pressure since 1939, indicate an increasing frequency of unfavorable ice conditions (Appendix 3, figures 3 and 4).

Our results, and those of Hunt and Naske, suggest that the

summer climate, and the associated ice characteristics, have undergone several significant fluctuations. The Barrow temperature data and the whaling logs indicate that a period of mild summers from the 1920's to 1950's has been followed by more frequent occurrences of severe ice conditions, perhaps similar to those in the late nineteenth century. There is, therefore, the possibility that important changes in ice conditions could occur during the total period of offshore oil and gas development.

- (iv) The amount of open water in the Beaufort Sea by late September 15 (late summer) has an influence on subsequent ice conditions and air temperatures. Generally, the more open water there is, the later the date of freeze-up and autumnal re-advancement of pack ice (see Appendix 4, Tables 4 and 6). Thus, a mild summer is followed by a mild autumn and a delay in the time before a solid ice cover is established.
- (v) Long-range forecasts of summertime ice decay and break-up can be successfully developed by predicting the persistence of monthly temperature anomalies at Barrow at key times of spring and early summer (see Appendix 2, 4, and 6).

IX. SUMMARY OF 4TH QUARTER ACTIVITIES

A. Office Activities

2. Personnel

R.G. Barry, PI

J.C. Rogers, Graduate Research Assistant (25%)

R.E. Moritz " " " (through Aug. 1977)

G. Wohl " " "

B. Warmerdan " " " (from June 1977) (25%)

A. Jane Reynolds " " " (from Sep. 1977)

C. Wright-Locke Professional Research Assistant (25%)

5. Data Collected/Analyzed

(a) Historical Ice Data

Work is in progress using the extensive historical record of ships' logs compiled by W.R. Hunt and C-M Naske is being used for two purposes. From the comments about ice made in the logs, we are able to label summers as severe, mild, or normal. Although this is obviously not as accurate as the use of thawing degree

days, it provides a useful check of the ranking we have already compiled for summers 1921-52 at Pt. Barrow, Barter Island and Kotzebue, as well as extending our record back to 1872. The pre-1921 data will be examined to determine ice conditions in individual years and to make comparisons with the post-1921 observations.

(B) Synoptic Climatology (Kotzebue)

The role of the contribution of the Chukchi synoptic types to the temperature departure characteristics of the cold summers at Kotzebue has been investigated. The two factors involved are changes in frequencies of the types and within-type temperature changes during cold years. To investigate the relative importance of each of these factors, the temperature and frequency characteristics of the types during warm and cold Julys at Kotzebue were examined. The warm years are 1955, 1958, 1962, 1968, 1970, 1971, 1972; the mean temperature departure from average of the period 1955-1974 is + 1.73°C. The cold years are 1959, 1961, 1963, 1964, 1965, 1969, 1973; the mean temperature departures is -1.67°C.

The method of investigation described below is modified from that given by Barry and Perry (1973). The mean temperature departure, \bar{T}_w , of the warm Julys is

$$\bar{T}_w = \sum_{i=1}^k \frac{(F_i) (T_i)}{n} \quad \dots (1)$$

where F_i = the frequency of type i during warm Julys,

T_i = the mean temperature departure of type i during warm Julys,

n = the total number of days in the warm July set (217).

The mean temperature departure, \bar{T}_c , of the cold Julys is

$$\bar{T}_c = \sum_{i=1}^k \left\{ \frac{(F_i + \Delta F_i) (T_i + \Delta T_i)}{\bar{n}} \right\} \quad \dots (2)$$

where ΔF_i = the change in frequency of type i between warm Julys and cold Julys,

ΔT_i = the change in mean temperature departure of type i between warm Julys and cold Julys.

The difference in mean temperature departure, $\Delta \bar{T}$, between warm and cold Julys is

$$\Delta \bar{T} = \bar{T}_c - \bar{T}_w = \sum_{i=1}^k \left\{ \frac{(F_i + \Delta F_i) (T_i + \Delta T_i)}{n} - \frac{(F_i) (T_i)}{n} \right\} \quad \dots (3)$$

Equation (3) can be expanded to

$$\Delta \bar{T} = \sum_{i=1}^k \left\{ \frac{(F_i) (\Delta T_i)}{n} + \frac{(\Delta F_i) (T_i)}{n} + \frac{(\Delta F_i) (\Delta T_i)}{n} \right\} \quad \dots (4)$$

The three terms in (4) can be described as follows. The first term on the left is the component due to within-type temperature changes (i.e. it is the contribution of changing T_i and keeping the original frequency constant). The second term is the component due to changes in type frequency (i.e. it is the contribution of changing F_i and keeping the original temperature constant). The third term is an error correction term that may be positive or negative depending upon whether the effect of changing both the temperature and the frequency at the same time is reinforcing or self-cancelling. It is necessary to use departure from average temperature values for T_i because of the lack of real dimension to the parameter (i.e. the place of the zero-value in Kelvin, Celsius, and Fahrenheit systems is arbitrary). Hence, the temperature reading must be related to a meaningful value from which it can vary, otherwise the value of $(\Delta F_i)(T_i)/n$ will become inflated beyond its true importance.

By computing each term of (4) for each of the types the relative contribution of each type to $\Delta \bar{T}$, the importance of within-type temperature changes, and the importance of changes in type frequency both for each type and overall can be examined. The results of the computations are shown in Table 3.

The most important component of $\Delta \bar{T}$ overall is the within-type temperature change, which would have accounted for about 80% of $\Delta \bar{T}$ if the frequency of the types had remained constant; this factor actually accounted for about 67% of $\Delta \bar{T}$. Of the 24 types, 17 had lower mean temperatures during cold Julys than during warm Julys, with the greatest changes in types 1, 5, and 17. In most cases, the change in frequency counteracted the effect of the change in temperature (i.e. the type became colder but also less frequent, so $(\Delta F_i)(\Delta T_i)/n$ was positive); types 3 and 15 are exceptions.

The most important types contributing to $\Delta \bar{T}$ were, in order of importance, types 1, 2, 3, 10, 5, 9, and 12 which together accounted for about 70% of the change (Table 4). Of these, only type 10 contributed mainly through changes in frequency. Types 1 and 3 produce zonal flow at Kotzebue; type 1 is associated with easterly flow of warm interior air and experienced a major drop in both frequency and temperature during cold Julys. Type 3 is associated with westerly flow of cool maritime air and experienced lower temperatures and increased frequency during cold Julys. Types 2 and 12 are cyclonic types which were considerably cooler during cold Julys; type 2 also experienced the greatest drop in frequency of all types. Type 9 is a generally mixed anticyclonic-cyclonic type with highly variable characteristics that was also considerably cooler during cold Julys. Types 5 and 10 are marginally cyclonic types associated with advection of cool maritime air

by westerly and northwesterly flow. Type 10 is generally the coldest summer type; it underwent little temperature change but increased 460% in frequency during cold Julys. Its converse, type 13, which has high pressure northwest of Kotzebue and advects warm air from the interior, also experienced little temperature change but was very rare during cold Julys. It is clear that the pressure situation over the Beaufort Sea and Brooks Range is an important factor in summer temperatures at Kotzebue.

The reasons for within-type temperature changes are not known for certain and are likely quite complex. They could result from differences in mean airflow trajectories or days recognized as a single type (Barry and Perry, 1973). This would imply that the typing scheme is inconsistent and inadequately describes the synoptic situation, either as a result of poor design or from the inaccuracy of pressure data at high latitudes. This is probably not the case, since statistical tests have revealed that the types have distinct weather characteristics associated with them.

Another possibility is changes in sea-surface temperatures and associated air-mass modification of temperature and moisture conditions. This air-sea interaction is complex and merits further study. Local changes in such parameters as surface and cloudiness could depress temperatures rather independently of the synoptic situation. To examine this it is necessary to test the types against data from other northwest Alaskan stations. Finally, changes in type persistence rather than frequency may be of some importance (Perry, 1970).

In conclusion, it is worth noting that nearly every type associated with positive temperature departures from normal during warm Julys underwent a decrease in frequency during cold Julys, and that nearly every type with a negative temperature during warm Julys underwent an increase in frequency during cold Julys. Hence, frequency changes were a factor, but were overridden by the effect of within-type temperature changes.

Based on the analyzes for Kotzebue, a general model of a cold July on the Chukchi Sea coast can be outlined.

- 1). Major cyclonic types (2, 7, 12, 17) decrease in frequency, from 77 days in 7 warm Julys to 38 days in 7 cold Julys indicating that the normal storm track up the Bering Sea, Bering Strait, and eastern Chukchi Sea does not become well established
- 2). Marginally cyclonic types increase (types 5, 10, 11, 15) in frequency from 29 days in warm years to 57 days during cold years. This may indicate

a shift of the normal storm track to the east, over continental Alaska. This track tends to advect cool air from the Chukchi Sea to Kotzebue by reinforcing the prevailing NW and N winds.

- 3). A logical reason for such a shift would be the establishment of a mean upper trough over the Chukchi Sea tending to "steer" surface storms to the east of Kotzebue. Such a trough would also bring cold Arctic air over the Chukchi Sea, tending to delay ice breakup. It would be associated with upper divergence over the Beaufort Sea, which favors the development of lower pressure in this key area. Low pressure in the Beaufort Sea brings northwest surface flow at Kotzebue, again strengthening the prevailing westerlies.
- 4). Delayed ice breakup in the Chukchi Sea tends to bring about lower sea surface temperature and cooler conditions in general at Kotzebue, as indicated by the decrease in average temperature of most of the other types at Kotzebue.

In view of the importance of the upper-level circulation grid point data on 500 mb heights over Alaska (prepared by NMC) are being acquired in order to develop a 500mb typing scheme. This will delineate the large-scale geostrophic flow and enable us to assess the effect of upper-level "steering" on surface storm activity and storm tracks.

6. Milestone Chart and Data Submission Schedule

The ice mapping has now been completed and all maps included in submitted reports.

The remaining tasks - checking and testing associations between synoptic events and meteorological variables or ice conditions, and reviewing the historical ice data are expected to be completed within the time framework of the next two quarters when funding for this project terminates. Emphasis will be placed on synthesizing and evaluating results already produced. For example, we are examining the degree of variability of ice conditions along the Beaufort Sea coast that might occur in summer months when temperatures at Barter Isle differ considerably from those at Barrow. This will provide information on the spatial applicability of some of the climate - ice relationships obtained earlier.

B. PROBLEMS/RECOMMENDED CHANGES

None

TABLE 3
COMPONENTS OF TEMPERATURE DIFFERENCE BETWEEN WARM AND COLD
JULYS AT KOTZEBUE ACCORDING TO PRESSURE TYPE

Type	Fi	ΔFi	Ti	ΔTi	(ΔFi)(Ti)/n	(Fi)(ΔTi)/n	$\frac{(\Delta Fi)(\Delta Ti)}{n}$	Ci *
1	30	-19	+5.71	-8.48	-.50	-1.17	+.74	-.93
2	43	-30	+3.17	-3.72	-.44	-.74	+.51	-.67
3	16	+23	+0.87	-4.06	+.09	-.30	-.43	-.64
4	2	+2	-6.82	+0.75	-.06	+.01	+.01	-.04
5	14	-9	+6.04	-8.16	-.25	-.53	+.34	-.44
6	7	0	+1.68	-0.57	0	-.02	0	-.02
7	5	+2	-0.52	-0.94	0	-.02	-.01	-.03
8	9	-2	+0.12	-2.73	0	-.11	+.03	-.08
9	18	-6	+5.35	-5.25	-.15	-.44	+.15	-.44
10	5	+23	-5.32	-0.46	-.56	-.01	-.05	-.62
11	3	+7	-5.32	+1.20	-.17	+.02	+.04	-.11
12	17	-1	+2.21	-5.03	-.01	-.39	+.02	-.38
13	7	-6	+9.82	-1.14	-.27	-.04	+.03	-.28
14	2	0	-1.82	+1.50	0	+.01	0	+.01
15	7	+7	-1.46	-4.15	-.05	-.13	-.13	-.31
16	1	-1	+5.68	0	-.03	0	0	-.03
17	12	-10	+5.01	-8.83	-.23	-.49	+.41	-.31
18	2	0	-0.82	-2.00	0	-.02	0	-.02
19	0	+10	----	0	-.16**	0	0	-.16
20	1	+2	+5.68	-6.33	+.05	-.03	-.06	-.04
21	3	0	-3.32	-3.00	0	-.04	0	-.04
22	0	0	----	0	0	0	0	0
NT	13	+6	+0.91	-3.55	+.03	-.21	-.10	-.28
MD	0	+2	----	0	0	0	0	0
TOTAL	217	0	----	----	-2.71	-4.65	+1.50	-5.86

* Ci is the contribution of type i to $\Delta \bar{T}$ $\sum_{i=1}^k C_i = \Delta \bar{T}$

** This component was computed from $(\Delta Fi)(Ti + \Delta Ti)/n = (\Delta Fi)(Tci)/n$
where Tci = mean temperature departure of type i during cold Julys

TABLE 4

PERCENTAGE OF MEAN TEMPERATURE DIFFERENCE BETWEEN WARM AND COLD
JULYS AT KOTZEBUE ACCOUNTED FOR BY INDIVIDUAL PRESSURE TYPES

Type	%	Cumulative Percent	Major Component of Difference
1	15.9	15.9	Temp
2	11.4	27.3	Temp
3	10.9	38.2	Both
10	10.6	48.8	Freq
5	7.5	56.3	Temp
9	7.5	63.8	Temp
12	6.5	70.3	Temp
17	5.3	75.6	Temp
15	5.3	80.9	Both
13	4.8	85.7	Freq
NT	4.8	90.5	Temp
19	2.7	93.2	Freq
11	1.9	95.1	Freq
8	1.4	96.5	Temp
4	0.7	97.2	Freq
20	0.7	97.9	Both
21	0.7	98.6	Temp
7	0.5	99.1	Temp
16	0.5	99.6	Freq
6	0.3	99.9	Temp
18	0.3	100.2	Temp
22	0	100.2	----
MD	0	100.2	----
14	-0.2	100.0	Temp

REFERENCES

- Barnett, D.G., 1976. A Practical Method of Long Range Ice Forecasting for the North Coast of Alaska, Pt. 1. FLEWEFAC Tech. Rept. #1, Suitland, Md. 16 pp.
- Barry, R.G., 1976b. Study of climatic effects on fast ice extent and its seasonal decay along the Beaufort sea coast. In: Environmental Assessment of the Alaskan continental shelf. Vol. 14, Ice, pp. 58-116.
- Barry, R.G., 1977a. Study of climatic effects on fast ice extent and its seasonal decay along the Beaufort-Chukchi coasts. In: Environmental Assessment of the Alaskan continental shelf. Vol. 14, Transport, pp. 574-743. NOAA, Environmental Research Labs., Boulder.
- Barry, R.G. (ed.) 1977b. Sea Ice. Panel Report, Beaufort Sea Synthesis Meeting, (Barrow), OSCEAP Arctic Project Office, 14pp. Memo + 9 figures.
- Barry, R.G., and Perry, A.H., 1973. "Recent Temperature Changes Due to Changes in the Frequency and Average Temperature of Weather Types over the British Isles." Meteorological Magazine, 102: 73-82.
- Hare, F.K., 1968. The Arctic. Quart. J. R. Met. Soc., 94, 439-458.
- Holmgren, B., Benson, C., and Weller, G., 1975. A Study of Breakup on the Arctic Slope of Alaska by Ground, Air and Satellite Observations. In: Climate of the Arctic, 24th Alaska Science Conf. (G. Weller and S. Bowling, eds.) Geophysical Inst., Fairbanks, 358-366.
- Keegan, T.J., 1958. Arctic Synoptic Activity in Winter. J. Met., 15, 513-521.
- Kovacs, A. and Gow, A.J., 1976. Some Characteristics of Grounded Floebergs near Prudhoe Bay, Alaska. Appendix #1 to OCSEAP RU #88 report, March 31, 1976 (submitted to Arctic). 9 pp. + figures.
- Kovacs, A. and Mellor, M., 1974. Sea Ice Morphology and Ice as a Geologic Agent in the Southern Beaufort Sea. In: The Coast and Shelf of the Beaufort Sea (J.C. Reed and J. Sater, eds.) Arctic Institute of North America, Washington, D.C. 113-161.
- Perry, A.H., 1970. "Changes in Duration and Frequency of Synoptic Types over the British Isles." Weather, 25: 123-126.
- Reed, R.J. and Kunkel, B., 1960. The Arctic Circulation in summer. J. Met., 17, 489-506
- Selkregg, L., 1974. Alaska Regional Profiles: Arctic Region. University of Alaska AEIDC, Anchorage. 28 pp.
- Watson, C.E., 1974. The Climate of Alaska. In: Climates of the States, NOAA, Water Information Center, 481-501
- Weaver, D.F., 1970. Radiation regime over Arctic Tundra Lakes, 1966. Report, Dept. of Atmos. Sci., Univ. of Washington, Seattle, 112 pp.

Weller, G. and Bowling, S. (eds.), 1975. Climate of the Arctic, 24th Alaska Science Conference, Geophysical Inst., Fairbanks, 436 pp.

Wilson, C.V., 1967. Climatology. Introduction, Northern Hemisphere I. CRREL Report IA3, Cold Regions Research and Eng. Lab., Hanover, 141 pp.

Zubov, N.N., 1943. Arctic Ice. Translation by U.S. Navy Oceanographic Office and Amer. Met. Society. 491 pp.

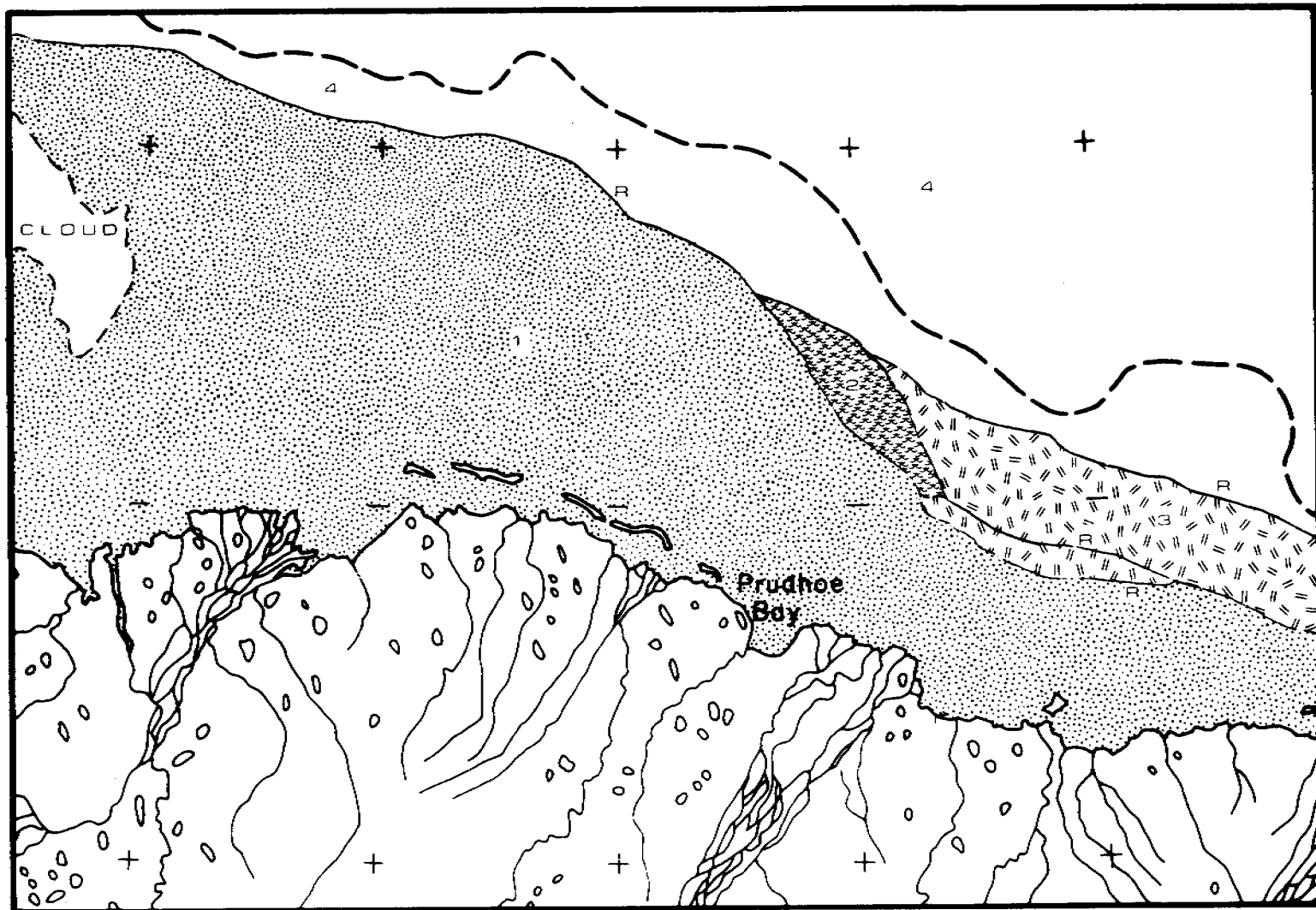
APPENDIX I

ICE MAPS FOR THE BEAUFORT SEA COAST, 1976

(Prudhoe and Barter Island Sectors)

18, 19, 20, 21 February 1976: Scenes E-2392-21023, E-2393-21081,
E-2394-21135, E-2395-21193

This series of winter frames covers the entire sector, with the exception of outer Harrison Bay, which is cloud covered. No ice movements or other significant changes could be determined between frames. Four zones were mapped, based on tonal characteristics and surface features. Light toned, smooth-looking ice (1) extends along the coast in a zone 17 to 70 km wide. No major deformational features were seen within this zone, however a major ridge system (R) is present along the seaward edges. Zone 2 consists of dark toned, smooth-looking ice which is probably newly formed. The pack ice was divided into two zones, 3 and 4. This ice is well consolidated in both zones, however the floe-like objects within zone 3 are of a smaller size and appear to have been broken apart to a greater extent than those within zone 4. Two ridged areas (R) are present within the pack ice.

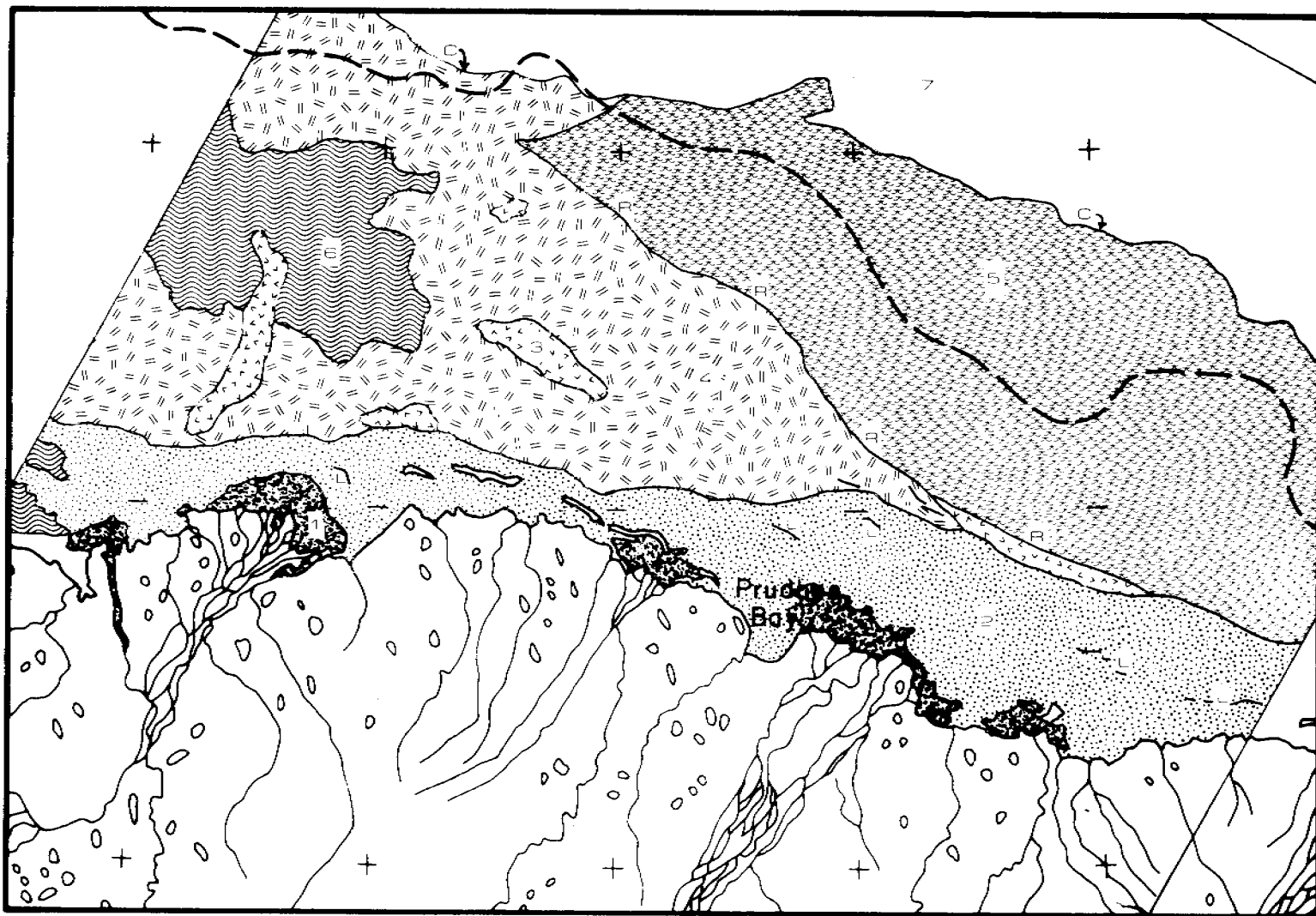


SHOREFAST SEA ICE
SURFACE MORPHOLOGICAL CHARACTERISTICS
BEAUFORT SEA COAST: PRUDHOE SECTOR

15, 19, 20 & 21 February 1975

6 June 1976: Scene E-2501-21051

By this date, large rivers and river mouths have melted out, forming fairly large areas of open water and flooded ice (1). The fast ice (zones 2-6) has also begun to darken. Light toned, smooth-looking ice composes zone 2. A number of small leads (L) are present within this zone. Zone 3 also consists of smooth-looking ice, however the ice is a darker tone than that of zone 2. Overall, zone 4 consists of fairly light toned ice with some degree of mottling. Several small areas of open water are also present within zone 4. A prominent ridge system (R) is located on the zone 4/zone 5 boundary. This system was also noted on the February frames. Zone 5 ice appears similar to that in zone 4 (having mottled tones and some small areas of open water), however zone 5 is a darker overall tone. Zone 6 consists of ice of varying tones from light to dark. This zone consists of the darkest toned ice overall on this frame. No open water was observed within this zone. The pack ice/fast ice boundary (C) is quite distinct on this date. The pack ice (7) is fairly well consolidated.

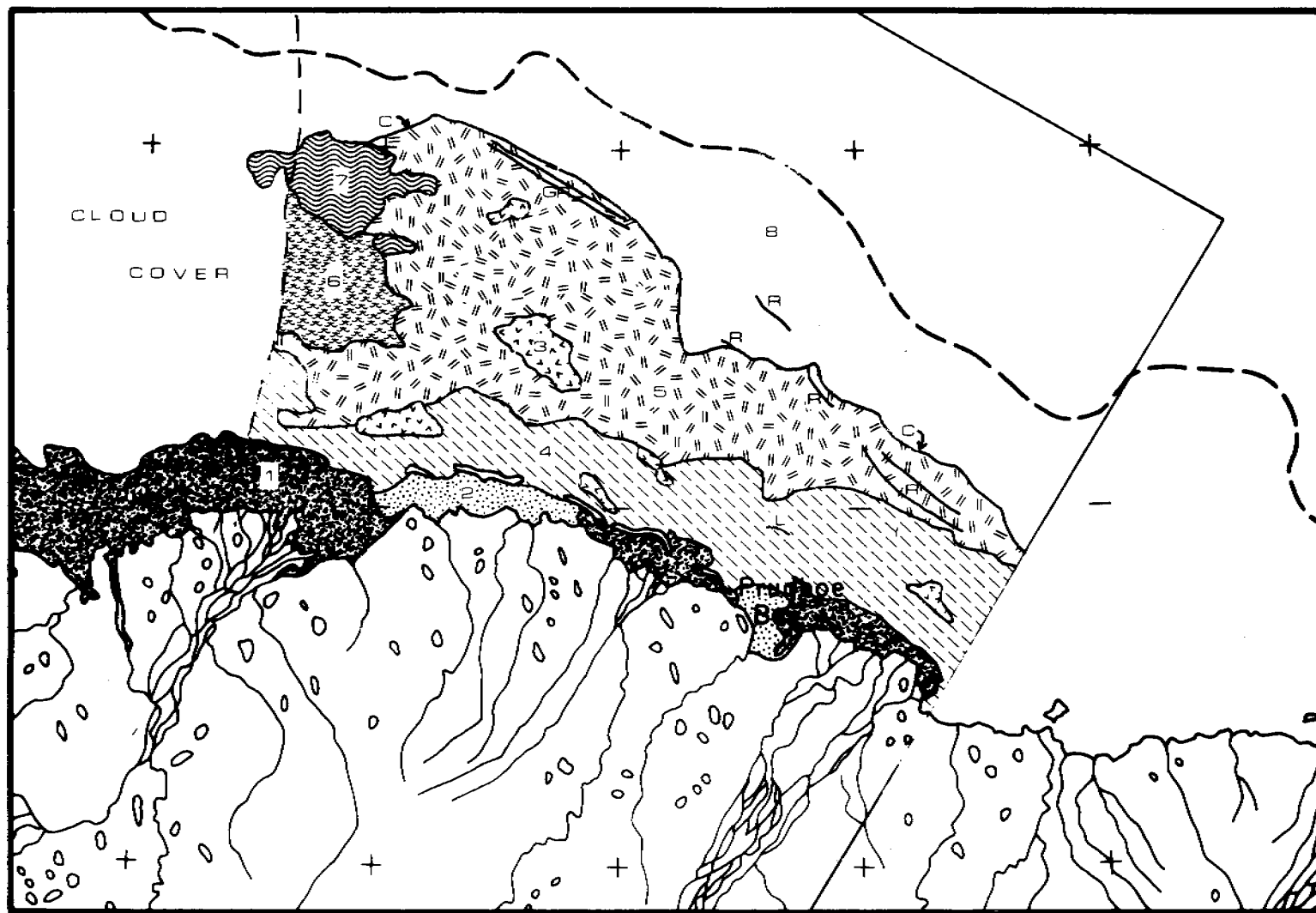


SHOREFAST SEA ICE
SURFACE MORPHOLOGICAL CHARACTERISTICS
BEAUFORT SEA COAST: PRUDHOE SECTOR

10 June 1978

13 July 1976: Scene E-2538-21095

Clouds cover the ice west of the Colville River on this frame. The shorefast ice is gone in a band 4 to 10 km wide (zone 1), except in the vicinity of Cliktok Point and Prudhoe Bay. In these two areas, the ice (zone 2) is light toned (probably drained) and appears smooth. In the Prudhoe Bay area, this ice has broken up into separate floes. Zone 3 consists of small areas of smooth-looking, fairly light toned ice. The three largest areas of zone 3 have not changed a great deal since the 6 June frame. Zone 4 consists of fairly dark toned ice, although there are some lighter toned areas within this zone. Several small leads (L) are also present. Medium toned mottled ice composes zone 5. There are some light lineations within this zone, which are possibly ridges. There is some major ridging (R) along the seaward boundary of zone 5, which has been present since the February frames. Overall, the ice within zone 6 is fairly dark toned. However, zone 7 consists of the darkest toned ice. Some small areas of lighter toned ice are also present. The pack ice/fast ice boundary (C) is quite distinct on this frame. The pack ice is well consolidated.

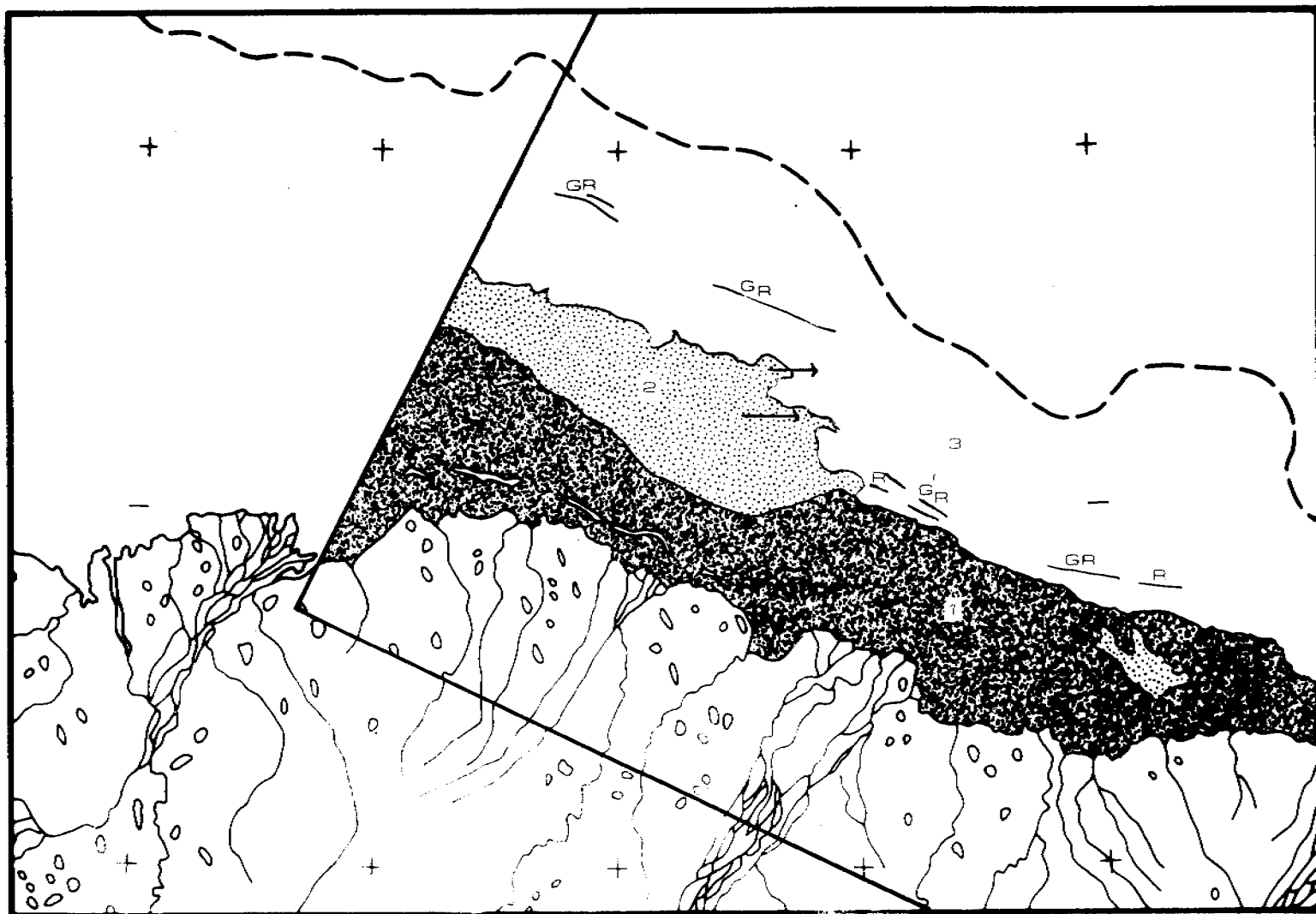


SHOREFAST SEA ICE
SURFACE MORPHOLOGICAL CHARACTERISTICS
BEAUFORT SEA COAST: PRUDHOE SECTOR

10 July 1971

29 July 1976: Scene E-2554-20575

The shorefast ice is gone by this date in a band 10 to 30 km wide along the coast. Zone 1 consists of open water with very small amounts of floating ice (less than 5%). Open water with a large amount of floating ice (greater than 80%) composes zone 2. Zone 3 consists of well-consolidated ice. There are a number of ridges (R) present in this zone, some having remained stationary (GR) since the February frames. The 30 July frame (scene E-2555-21034) was not separately mapped, however movements were determined from the 29 July frame to the 30 July frame. It was difficult to trace ice motions, but two floes were seen to have moved 9 km to the East (shown by arrows on the map).

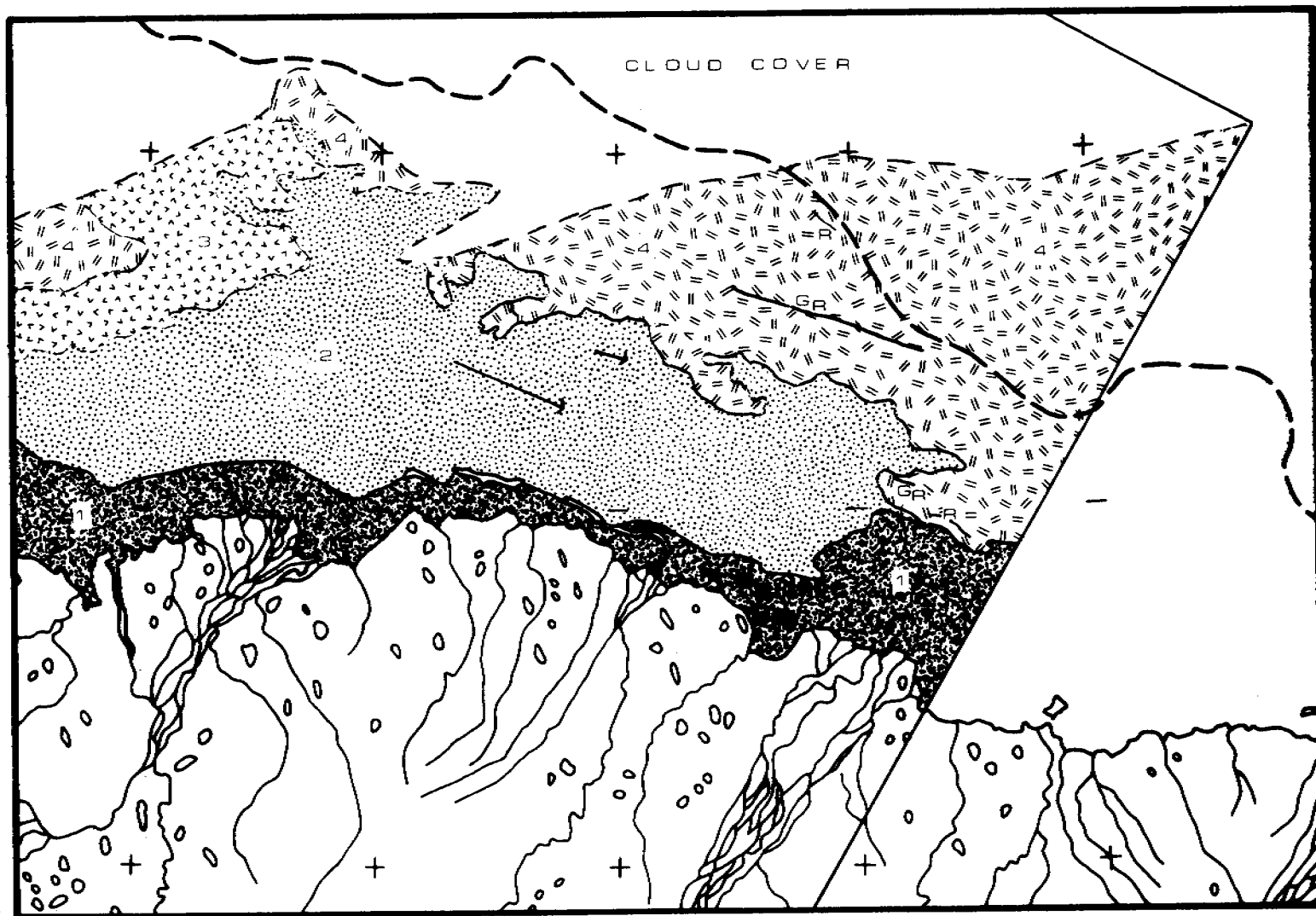


SHOREFAST SEA ICE
SURFACE MORPHOLOGICAL CHARACTERISTICS
BEAUFORT SEA COAST: PRUDHOE SECTOR

22 July 1971

31 July 1976: Scene E-2556-21092

Open water is present along the coast in a zone 5 to 20 km wide (zone 1). There is very little ice present within this zone. Zone 2 consists of a large area of floating ice (greater than 60% ice). Small to vast sized floes of variously toned and textured ice are present within this zone. Uniformly dark toned ice that is quite continuous makes up zone 3. Clouds cover the seaward part of the frame, so boundaries cannot be drawn for some parts of zones 3 and 4. Zone 4 consists of fairly continuous ice of various tones, overall fairly light in tone. There are some light lineations present and several ridges (GR) which have been stationary since the February frames. Movements were determined from the 30 July frame (E-2555-21034) to the 31 July frame. It was difficult to trace ice motions, but two floes were seen to have moved to the southeast; one moving 6 km and the other 20 km. This is shown by arrows on the map.

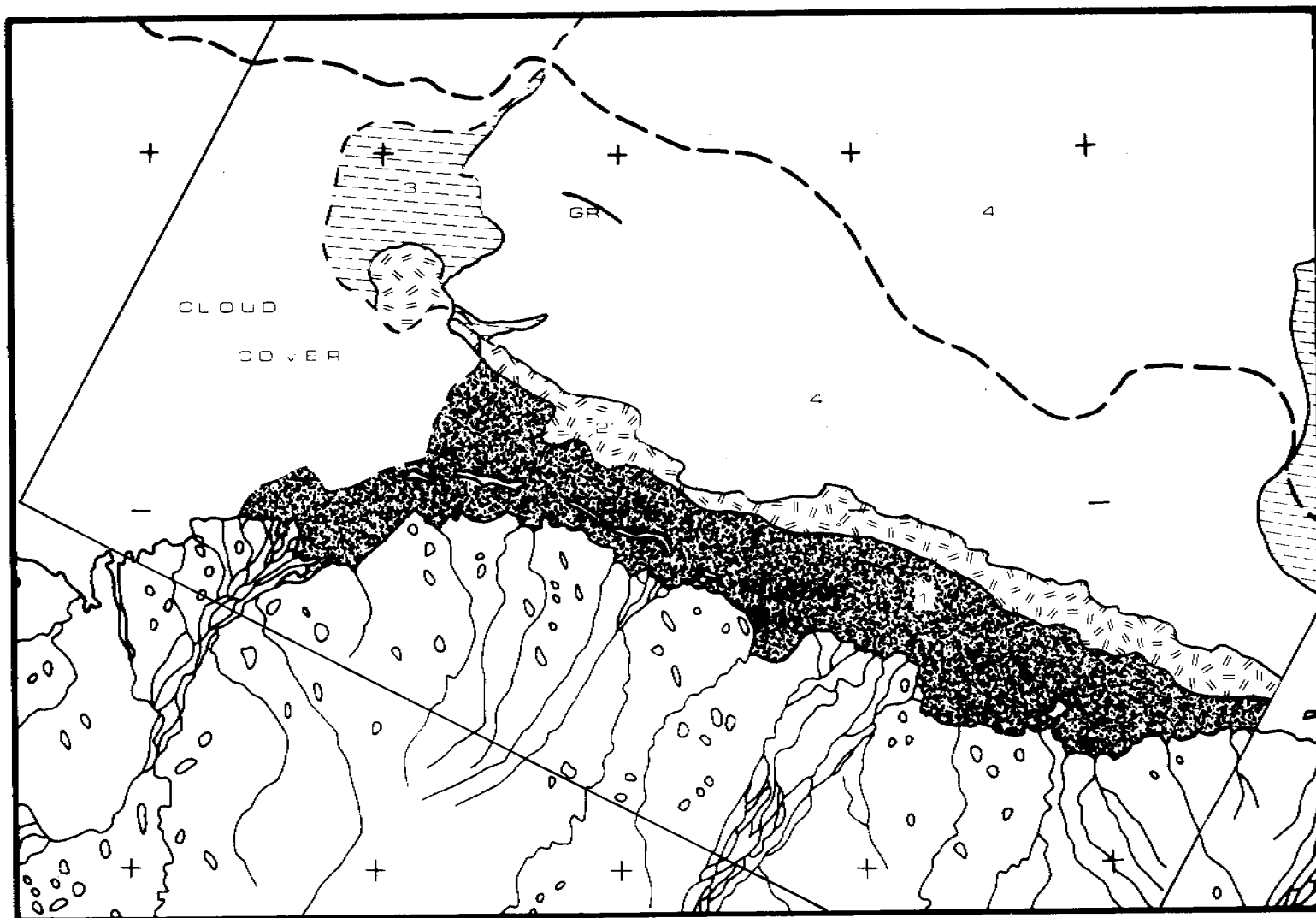


SHOREFAST SEA ICE
SURFACE MORPHOLOGICAL CHARACTERISTICS
BEAUFORT SEA COAST: PRUDHOE SECTOR

21 JULY 1977

17 August 1976: Scene E-2573-21030

Clouds cover the ice in the western part of this frame. Open water (zone 1) is present in a band from 5 to 25 km wide along the coast. A narrow zone of open water with approximately 10% floating ice (zone 2) is located seaward of zone 1. Zone 3 consists of floating ice in approximately 70% concentration. Zone 4 consists of fairly consolidated ice, although the shoreward edges of this zone have less consolidated ice. The grounded ridge (GR) shown in zone 4 has been present since the February frames.

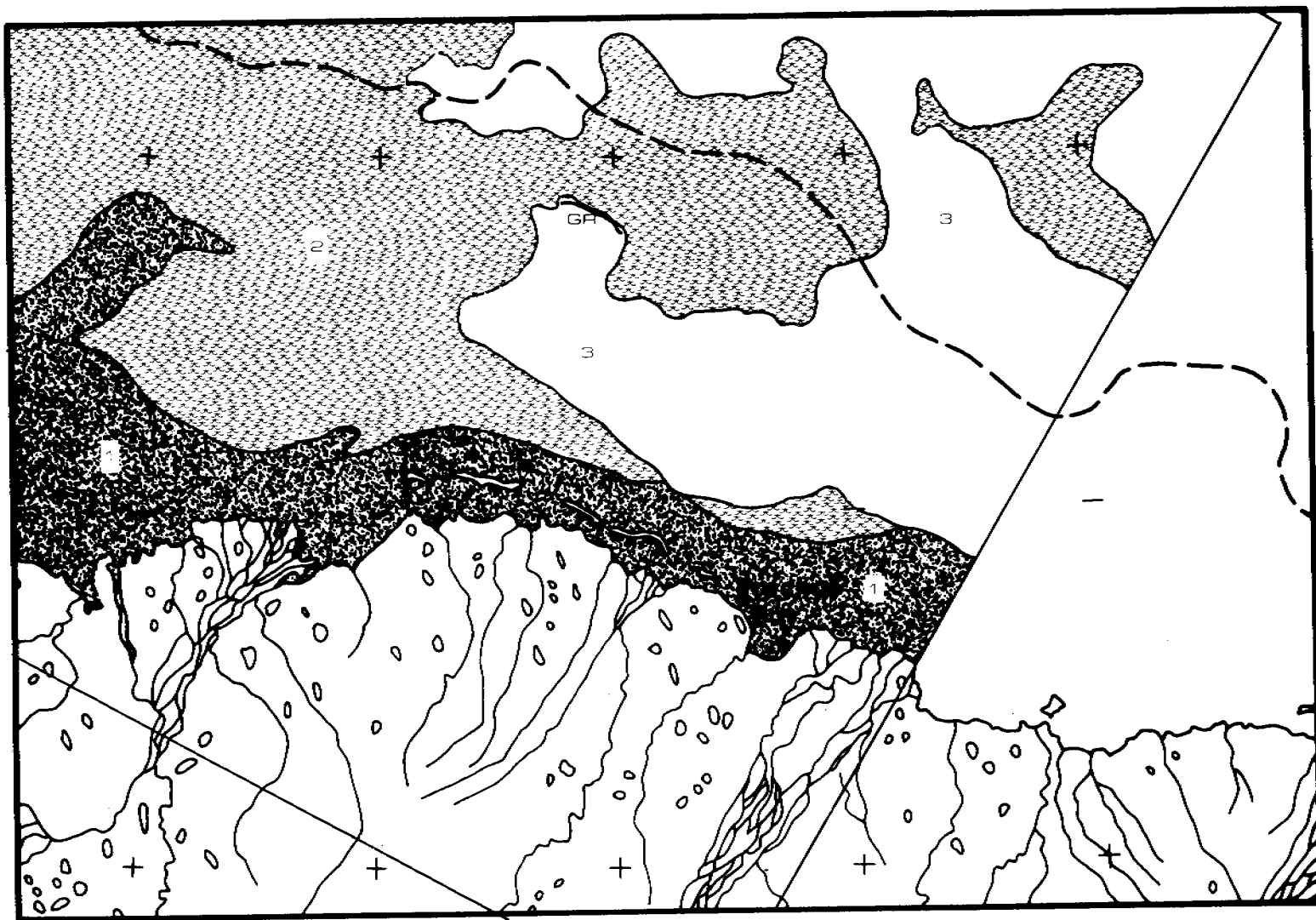


SHOREFAST SEA ICE
 SURFACE MORPHOLOGICAL CHARACTERISTICS
 BEAUFORT SEA COAST: PRUDHOE SECTOR

17 Dec 1971

5 September 1976: Scene E-2592-21082

Some thin clouds are present over much of the frame, however their effect is minimal. Zone 1 consists mainly of open water. Open water with some floating ice composes zone 2. The overall concentration of ice in this zone is generally less than 50%. Zone 3 consists of more consolidated ice. The overall concentration of ice in this zone is approximately 90%. A large ridge (GR), which has remained stationary since the February frames, is present on a boundary of this zone.



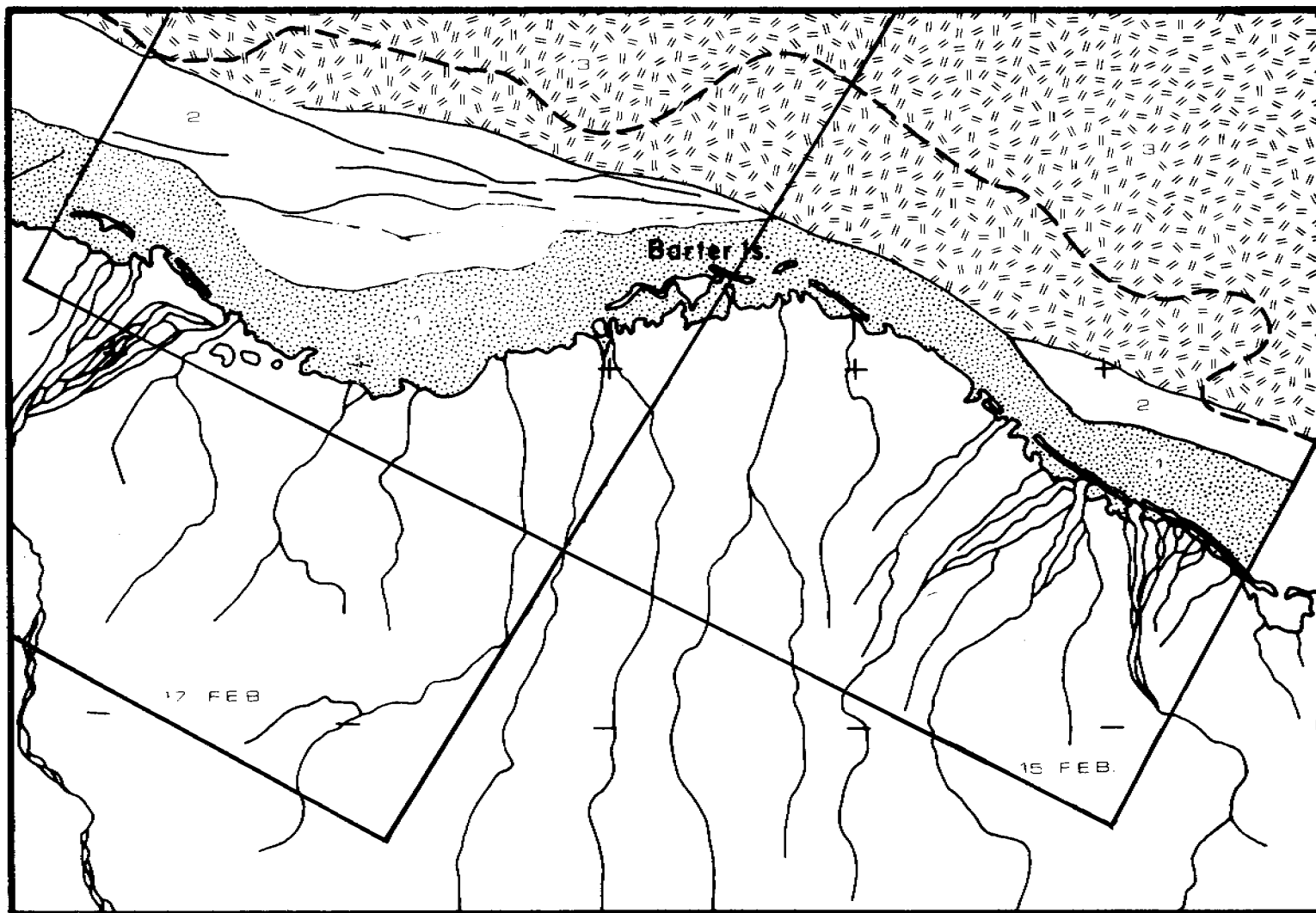
SHOREFAST SEA ICE
SURFACE MORPHOLOGICAL CHARACTERISTICS
BEAUFORT SEA COAST: PRUDHOE SECTOR

05 September 1970

15 and 17 February 1976: Scenes E-2389-20452 and E-2391-20564

These two winter scenes cover the entire sector, with the exception of Demarcation Bay. Smooth-looking, light toned fast ice (1) extends along the shore in a zone approximately 10 to 20 km wide. Seaward of this ice is an extensive area of deformational features (2). The ice appears very rough, with a large number of ridges (shown by lines) throughout the zone. Zone 3 consists of well consolidated pack ice.

677

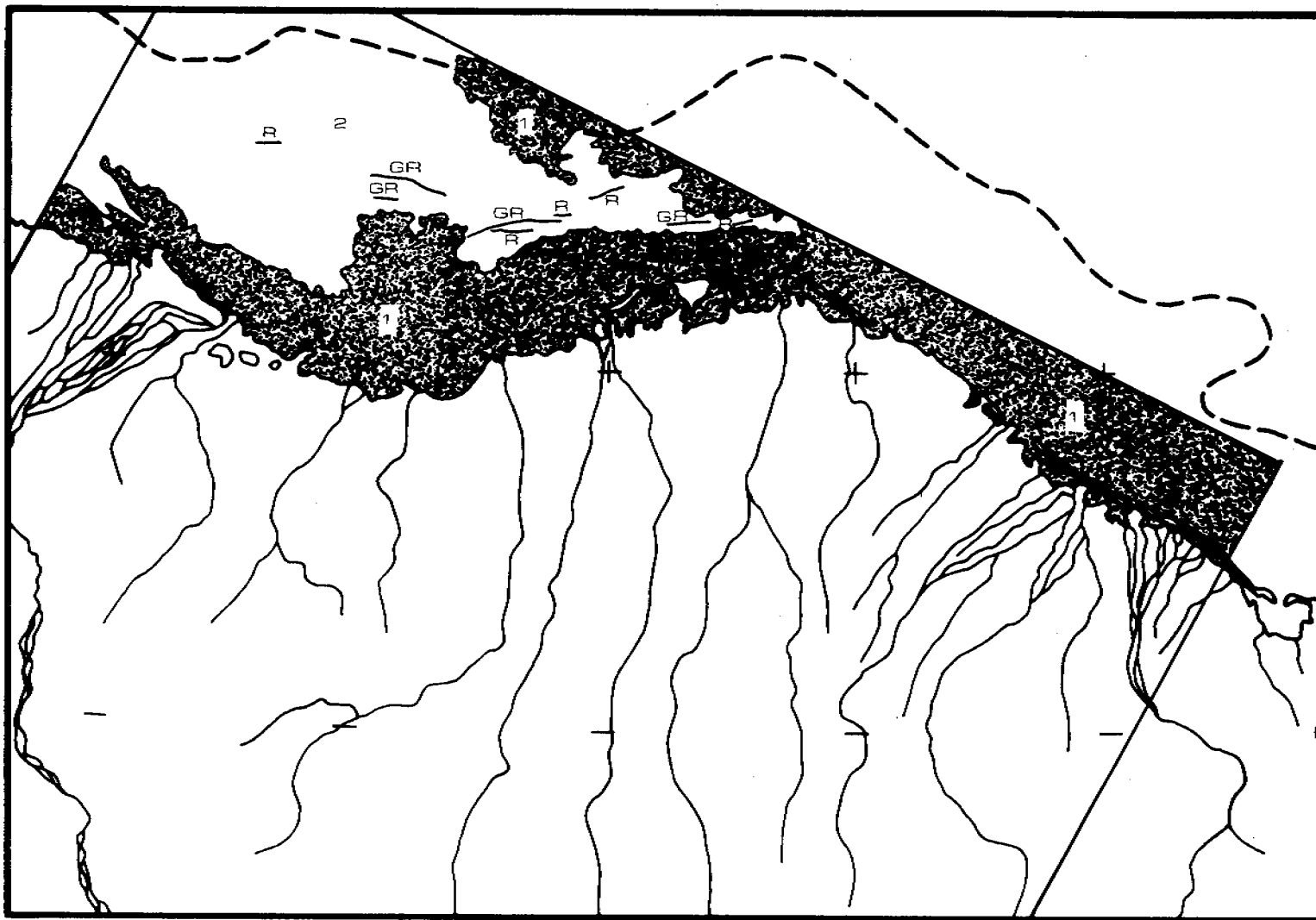


SHOREFAST SEA ICE
SURFACE MORPHOLOGICAL CHARACTERISTICS
BEAUFORT SEA COAST: BARTER IS. SECTOR

15 & 17 February 1977

13 August 1976: Scene E-2569-20404

By this date, the shorefast ice is gone. Zone 1 consists of open water with small amounts (less than 25%) of floating ice. Remnants of the extensive ridges (R) are still present in zone 2, and several appear to have remained in the same place since February (GR). The ice in zone 2 appears to be quite rotten, especially in the shoreward portion.



SHOREFAST SEA ICE
SURFACE MORPHOLOGICAL CHARACTERISTICS
BEAUFORT SEA COAST: BARTER IS. SECTOR

13 August 1976

APPENDIX 2

(See following reference)

Moritz, Richard E. (1977) On A Possible Sea Breeze Circulation Near Barrow, Alaska, Arctic and Alpine Research, Vol. 9, No. 4, pp 427-431.

APPENDIX 3

Meteorological Factors Affecting Interannual
Variability of Summertime Ice Extent in the Beaufort Sea

Jeffery C. Rogers

Institute of Arctic and Alpine Research
University of Colorado
Boulder, Colo. 80309

February, 1978

ABSTRACT

The relationship between meteorological factors, measured at Barrow, Ak., and summertime Beaufort Sea ice conditions along the shipping route between Pt. Barrow and Prudhoe Bay was investigated using data available from 1953 to 1975. Light-ice summers are associated with higher than normal sea level pressure (SLP) northeast of the Beaufort Sea (centered on $80^{\circ}\text{N } 120^{\circ}\text{W}$), lower than normal SLP over the east Siberian Sea, and with more frequent surface winds primarily from the directions 135° - 195° . A reversal in this pressure and wind direction pattern occurs during heavy-ice summers.

Air temperature, in the form of thawing degree days (TDD's), is the parameter most highly correlated with the summertime ice margin distance ($r = 0.815$) and it is highly correlated with SLP and wind direction. Correlation coefficients between these meteorological factors and ice margin distance increase during the summer suggesting their increasing importance to melt processes with time. The amount of open water by late summer and during autumn in the Beaufort Sea influences subsequent air temperatures, but has little or no influence upon subsequent local surface winds or the SLP distribution over the Northern Hemisphere. This interaction between ocean and overlying air, which encourages mild summers to be followed by mild autumns, accounts for the bimodal distribution in maximum accumulated TDD's noted at Barrow.

Analysis of Landsat images of sea ice conditions and concurrent TDD's between 1972 and 1976 showed that at least 400 TDD's are needed to assure favorable ice conditions. Trends in SLP and TDD's since 1939 and 1921, respectively, suggest increasingly severe ice conditions as

only 13 of 24 summers have accumulated 400 TDD's since 1953 while 28 of 32 had done so between 1921 and 1952. This was associated with a decline in Barrow mean summer temperature of 0.4°C from 1921-1952 to 1953-1975.

1. Introduction

The southern Beaufort Sea (Fig. 1) is normally ice free for only 3 months of the year, from late July to early October. Breakup begins in late May or in June with the melting and puddling of the landfast ice (Barry et al., 1976). Areas of open water soon appear in the southernmost parts of the sea and the landfast ice zone, extending approximately to the 18 m isobath (Stringer, 1974), is usually gone by late July. Subsequently, the adjacent Arctic pack ice begins melting and retreating northward. It can retreat up to about 400 km as occurred during the summers of 1958 and 1968 (Barnett, 1976), or it may not retreat at all as during the summer of 1975. The mean date of readvancement of the pack ice and freeze up in the landfast ice zone of the Beaufort Sea is in early October.

Despite the variability in ice conditions, shipping along the Beaufort Sea has increased due to the development of oil and gas resources. Not only has the need for supplies increased, but exploratory drilling in the ice-covered ocean is becoming a possibility. This has in turn emphasized the need for short-, extended-, and long-range forecasts of the expected ice conditions and movements in this area. Modelling studies by Maykut and Untersteiner (1971), Semtner (1976), and Washington et al. (1976) have shown how thermodynamics determine the mean ice extent and thickness distribution over the Arctic Ocean. However, these models have not as yet been tested to see if they can explain the large interannual variability in summertime ice extent on the polar seas, and the parameters used in the models to reproduce ice features are not directly applicable for prediction.

The dynamics of nearshore and Arctic pack ice have been examined by Pritchard et al. (1977), and by Hibler and Tucker (1977). These papers have shown how large scale ice motion and extent also responds to ice stresses, ocean currents, and other driving forces as well as responding in accordance with ice viscosity laws. The effect of winds upon the Beaufort Sea ice edge has been considered by Wendler (1973) and by Sater et al. (1974). Wendler showed that ice conditions depend upon resultant surface wind directions derived from 5-day mean sea level pressure (SLP) maps, while Sater et al. derived hypothetical ice drift vectors for the Beaufort Sea based upon the SLP distribution during summers from 1948-1967.

This paper represents an extension of these studies in that it considers wind direction and other factors such as the large scale circulation of the Northern Hemisphere, cloud cover, air temperature, and preceding winter severity upon the large scale summertime variability in Beaufort Sea ice. It also approaches the question of the direction of feedback mechanisms in the atmosphere-ice-ocean layer in the Arctic. The shipping route between Pt. Barrow and Prudhoe Bay was analyzed due to availability of both meteorological and sea ice data since 1953.

2. Data

Many factors are associated with variability of Beaufort Sea ice. Some important meteorological factors will not be considered here due to insufficient data. They include surface and ice albedo data, radiation budget elements, and sea temperature. The data used are those that are readily available from land-based stations.

a. Ice data

Ice data were taken from Barnett (1976) and from Landsat imagery

for the summers 1972-1976. Barnett tabulates the distance from Pt. Barrow northward to the boundary of 4/8 pack ice concentration on 10 August and 15 September during the summers 1953 through 1975. These distances are listed in order of increasing ice severity in Table 1. Barnett obtained the ice information from Naval Oceanographic Office annual ice reports from 1953-1970 and from ice charts prepared by Fleet Weather Facility between 1971 and 1975.

Summertime ice severity was ranked on the basis of such parameters as the distance northward to the ice edge, the initial date when the sea route to Prudhoe Bay had less than or equal to 4/8 concentration, the date when combined ice concentration and thickness dictated a prudent end to navigation, and the distance northward to 4/8 concentration (used in Table 1). The first 3 factors account for any discrepancies between the given distances and the actual ranking of the summer in Table 1. Barnett described the 4/8 concentration boundary as the "division between conditions easily navigable by unescorted vessels and those conditions posing a threat to safe passage". The 23 summers were divided into light and heavy-ice summers with the division between the 11th and 12th (1957 and 1967).

Landsat imagery, available from the EROS data center in Sioux Falls, was used to further analyze ice conditions and their relationship to meteorological parameters between 1972 and 1976. Imagery was obtained for the Beaufort Sea Coast to Prudhoe Bay from April through November during those years. Generally, either band MSS 4 or 7 was used. Comparison of satellite images in those bands is particularly useful in detecting areas of open water in ice covered seas and lakes. Barring days with

clouds, repetitive Landsat images of ice conditions can be obtained at least every 18th day. Due to convergence of satellite orbit ground tracks there is considerable overlap of images and an area of the Arctic could possibly be viewed for 3 or 4 consecutive days, increasing the chance of cloud-free images.

b. Meteorological data

Monthly SLP data from digitized grid point values of daily weather maps are available at the National Center for Atmospheric Research (Jenne, 1975). Data are given at 5° intervals between 20°N and 85°N and 0°E to 355°E . Arctic pressure data are generally unreliable before 1945 and therefore caution is employed in interpreting some of the results.

Air temperature, wind direction, speed, and cloud cover data were available from the U.S. Department of Commerce Local Climatological Data (1953-1976). Air temperature data were converted into thawing degree days (TDD's) or freezing degree days (FDD's). A TDD is the positive departure of mean daily temperature by 1°F from 32°F while a FDD is a similar negative departure from 32°F . The 32°F base was used here because of its use in the Local Climatological Data. Monthly air temperature data to 1921 from the World Weather Records were also used.

Daily geostrophic wind data were computed for points near Barrow on the Beaufort Sea coast from the NMC grid pressure data, made available by NCAR. Geostrophic wind speeds were separated into the U (alongshore, west-east) and V (offshore, south-north) components which, due to the nature of the NMC data, were measured at two separate points $71.5^{\circ}\text{N } 158.7^{\circ}\text{W}$ and $71.0^{\circ}\text{N } 153.5^{\circ}\text{W}$ while Pt. Barrow is located at $71.4^{\circ}\text{N } 156.5^{\circ}\text{W}$.

3. Results

a. Sea level pressure distribution during summers of heavy and light ice

The difference in SLP distribution between heavy and light-ice summers (defined in 2a) was investigated. Subtracting mean SLP distribution during light-ice summers from that of heavy-ice summers resulted in maximum differences of up to -3 mb centered primarily on $80^{\circ}\text{N } 120^{\circ}\text{W}$ (Fig. 2). The area of statistically significant SLP difference (95% level) between the 2 series of ice summers includes the Canadian Archipelago, Greenland north of 75°N , and an area south of the Taimyr Peninsula.

The SLP difference distribution of Fig. 2 resembles that of heavy-ice summers in that lower than normal pressure is centered on $80^{\circ}\text{N } 120^{\circ}\text{W}$ (-1.6 mb departure) and higher than normal pressure covers the western Beaufort and the East Siberian Sea. The overall resultant geostrophic flow from these anomalies would be northerly along the Beaufort Sea shipping route, helping to keep the pack ice near shore. During light-ice summers higher than normal pressure (+1.4 mb) characterizes the region centered on $80^{\circ}\text{N } 120^{\circ}\text{W}$. Simultaneously, the region to the west of the Beaufort Sea centered on $75^{\circ}\text{N } 170^{\circ}\text{E}$ (with an overall +1.4 mb difference in Fig. 2) has lower than normal pressure. The net effect is for more southerly and southeasterly (offshore) flow.

b. Surface and geostrophic wind direction

The frequencies of daily mean surface wind direction were tabulated for twelve 30° sectors ($346^{\circ}-015^{\circ}$, $016^{\circ}-045^{\circ}$, etc.) for the periods 1 July to 10 August and 1 July to 15 September, the latter dates in each period being when ice data are available. For both periods winds from 76° to 195° are more frequent during light-ice summers while the remaining

sectors tend to be more frequent during heavy-ice summers. The difference in mean frequency of the wind directions was statistically significant, using a two-tailed t-test, for 136° - 165° and 166° - 195° (99% confidence level), and for 16° - 45° (99.8%) during the latter period. Frequencies for sectors 346° - 15° and 106° - 135° were significantly different at the 90% level. From 1 July to 10 August winds from 346° - 45° have significantly different frequencies (98% level).

Frequencies of daily mean geostrophic wind directions were tabulated for eight 45° sectors (16° - 60° , etc.) for the same periods. Sectors between 151° and 285° are associated with light-ice summers while the remaining 5 sectors occur more frequently during heavy-ice summers. The difference in mean daily frequencies was only significant between 61° - 105° (95% level) for the period ending 15 September.

A similar analysis of mean cloud cover and surface and geostrophic wind speeds tabulated for the 2 periods showed no significant differences in their mean frequencies between heavy and light-ice summers.

c. Surface air temperature

The mean maximum accumulated TDD's at Barrow (which normally occurs by mid-September) is 647 during light-ice summers and 355 during heavy-ice summers. This difference was statistically significant at the 99.8% level as was the difference in TDD accumulations to 10 August.

The histogram distributions of maximum accumulated summertime TDD's for 1921-1975 and 1953-1975 are given in Fig. 3. The former distribution is bimodal while the latter, with only 23 cases when ice data were available, is irregular but can be broken into 2 major sections on either side of 526-600 TDD's. The use of a t-test is therefore questionable in analyzing

the TDD difference given above, but the apparent significance of those t-test results are borne out. The 8 summers to the right of the 525-600 TDD accumulation gap are all light-ice summers given in Table 1. All heavy-ice summers lie to the left of the 525-600 TDD gap as do 3 light-ice summers, 1959, 1961, and 1963 (441, 456, and 371 TDD's respectively). It is not apparent from the meteorological data why these 3 exceptions occurred. Nevertheless, in 20 of the 23 previous summers the individual light and heavy-ice summers are associated with distinctly mild and severe thermal conditions, respectively.

Winters preceding the light-ice summers have a mean total of 8652 FDD's whereas 9093 FDD's normally accumulate before heavy-ice summers. While this suggests that colder winters precede heavy-ice summers, large standard deviations were also associated with those accumulations (487 and 674 FDD's respectively), and the difference was not statistically significant using a two-tailed t-test.

d. Correlation analysis

A correlation matrix between the meteorological parameters and the distance to the pack ice on 15 September is shown in Table 2. This matrix is abbreviated, showing only the highest and most significant correlations from the original matrix which considered all parameters mentioned above (Section 3) and many combinations of surface and geostrophic wind directions.

The results show that the highest correlated parameter to the 15 September distance northward to the 4/8 concentration of ice is maximum accumulated TDD's ($r = 0.815$), followed by the number of days with northerly or southerly surface winds, the V component speed of the geostrophic wind, and the SLP at $80^{\circ}\text{N } 120^{\circ}\text{W}$. Correlation coefficients

do not exceed $r = 0.515$ (TDD's with ice distance) for a similar matrix (not shown) of the 1 July to 10 August data. The next highest correlations were found for surface wind direction frequencies from 75° - 135° ($r = 0.494$) and SLP at 80° N 120° W ($r = 0.468$). The results indicate that the correlation between meteorological parameters and ice retreat distance becomes higher as the summer progresses.

4. Climatic variations and associated ice conditions

The availability of temperature data to 1921, reliable SLP data since the 1940's and the high intercorrelations between those parameters and pack ice distance, permits an analysis of 20th century trends in both summertime climate and Beaufort Sea ice conditions. The summertime (JJA) trends in SLP at grid points 80° N 120° W and 75° N 170° E since 1939 are shown in Fig. 4. The latter trend line is statistically significant.

When the SLP at 75° N 170° E is above normal it is generally below normal at 80° N 120° W and vice versa. These 2 modes of SLP distribution near the Beaufort Sea change from summer to summer in a random pattern and the trends in Fig. 4 plus the results of Section 3a indicate a general decline in favorable ice conditions.

Fig. 5 shows the trend in summertime TDD's since 1921 (-2.26 TDD/year) and also suggests increasingly heavy-ice conditions. Over the last 56 years the mean Barrow temperature has decreased enough to affect ice conditions. In particular, since 1953 several summers have occurred with TDD accumulations of approximately equal to or greater than one standard deviation below the long term mean accumulation ($\bar{X} = 532$, st. dev. = 181).

Using Landsat imagery and summertime temperature data from 1972-1976, the relationship between TDD's and stages of landfast and pack ice

breakup and retreat was derived. The number of TDD's associated with various stages of breakup along the shipping route are given in Table 3. The turning point between favorable and unfavorable ice conditions for shipping lies between stages 3 and 4, and depends upon whether or not northward retreat of the pack ice occurs. The results of columns 3 and 4 of Table 3 indicate that 28 of 32 summers to 1952 had accumulations of more than 400 TDD's while only 13 of 24 summers since then have accumulated more than 400 TDD's. A chi-square test of the difference between the 2 periods after combining stages 1 to 3 and 4 and 5 showed that the shift toward colder and icier summers after 1952 was statistically significant (97.5%). The results indicate a decrease in the number of summers during which the pack ice retreats. The length of the shipping season is also reduced, sometimes to less than a week as in 1955 (Winchester and Bates, 1958) and 1975.

The bottom lines of Table 3 indicate that a mean decline of 65 TDD's has occurred since 1953 compared to the earlier period. Assuming 90 days per summer the increasingly unfavorable ice conditions are associated with only a 0.4°C (0.7°F) decline in mean summer temperature. A complete change in ice conditions from one category to another requires a maximum change of 150 TDD's or a 0.9°C change in mean summer temperature.

5. Discussion

The correlation coefficients of Table 2 show that SLP, surface wind direction, and air temperature (TDD's) are intercorrelated and are highly correlated with the distance to the pack ice margin by late summer (15 September). Using available data it is possible to analyze subsequent

interactions between the atmosphere-ice-ocean layer of the Beaufort Sea. Another series of correlation coefficients using Barrow autumn data are given below:

- 1) TDD's accumulated between 10 August and 15 September vs distance of pack ice retreat between those dates (subtract column 3 from 4 in Table 1) $r = 0.712$.
- 2) 10 August ice distance vs TDD's from 10 August to 15 September, $r = 0.465$.
- 3) 15 September ice distance vs September temperature, $r = 0.773$.
- 4) 15 September ice distance vs October temperature, $r = 0.608$.
- 5) 15 September ice distance vs November temperature, $r = 0.440$.

Correlation 1) indicates that TDD's and the meteorological factors which influence them are increasingly correlated to 15 September ice conditions. However, by late summer (sometime between mid-August and late September) the influence of ice conditions and presence of open water on air temperature increases dramatically as seen in correlations 2) and 3) above. The 15 September ice distance (amount of open water) continues to have a statistically significant correlation with subsequent air temperature through November [4) and 5)] above. This implies that the amount of open water in the Beaufort Sea will have some influence upon time of freeze up, another air temperature related phenomenon.

Other correlations (not presented) indicated little or no relationship between mid-September ice conditions and either subsequent autumnal wind direction frequencies or SLP anywhere in the Northern Hemisphere (including $80^{\circ}\text{N } 120^{\circ}\text{W}$). Concurrent wind direction frequencies also were not as

highly correlated to September, October, and November air temperatures as were 3), 4), and 5) above.

The pattern which emerges, using a mild summer example, is one in which the SLP distribution and more frequent southerly surface winds advect warm land-heated air over the ice, inducing rapid ice melt. The advected warm air and southerly winds continue to melt the ice and push it northward until late summer when the open water begins exerting a maritime influence, keeping the coast and sea warmer for a few weeks more than they would be during severe, icy, summers. This accounts for the bimodal distribution (Fig. 3) in Barrow TDD accumulations. Light-ice summers remain warm, and accumulate even more TDD's due to the oceanic influence while heavy-ice summers become cold by September when cold air outbreaks cannot be modified by open water and favorable overland winds.

The increase in correlation between air temperature and ice decay during the course of the Arctic summer (Section 3d) was also noted by Wittmann and MacDowell (1964). They noted an increase in correlation coefficients from 0.49 to 0.70 through the summer as the pack ice concentration decreased. Here the correlation to 10 August and 15 September improved from $r = 0.515$ to $r = 0.815$ with a coefficient of $r = 0.712$ for the intervening period. Since correlations of all meteorological parameters improved with time here, one can argue (as Wittmann and MacDowell did regarding air temperature) that the importance of meteorological factors to ice decay increase with time and that during early summer non-meteorological factors are of primary importance.

Some non-meteorological factors of considerable importance to early summer (late May and June) ice decay would be variations in oceanic heat flux to the underlying ice surface and in albedo of the ice cover

(Maykut and Untersteiner, 1971; Semtner, 1976; Washington et al., 1976). Another factor noted on Landsat images between 1972 and 1976 is the amount of warmer river runoff water on the ice coming from the mountains to the south of the Beaufort Sea (Barry et al., 1976).

Wendler (1973) initially noted the importance of surface wind direction on ice conditions in the Beaufort Sea, and Sater et al. (1974) noted the apparent lack of relationship between geostrophic wind direction and the distance to the ice margin. They attributed their results to low quality ice data gathered from 1948-1967. More likely explanations which now emerge are that either geostrophic wind direction is not the best parameter to use in determining the large scale end of summer ice position, or that geostrophic wind data are not reliable in the Arctic. None of the frequencies of geostrophic wind direction are significantly correlated with ice retreat or TDD's while surface wind directions are.

6. Conclusions

The meteorological factors associated with the variability of summertime ice breakup and northward retreat along the Beaufort Sea shipping route have been analyzed. The results indicate that the SLP distribution, resulting surface wind directions, and air temperature at Barrow are primary parameters to consider in forecasts of the varying sea ice conditions in this area. Except for very early in summer, meteorological factors are important in determining ice distribution at the end of summer and they become increasingly important as the summer progresses. The results also show that some parameters, previously thought to play an important role in ice breakup, such as geostrophic wind, preceding winter temperatures, and cloud cover, account for little of the variance in summertime ice conditions.

The major conclusions are as follows:

- 1) Light-ice summers are associated with a tendency for higher than normal pressure to develop northeast ($80^{\circ}\text{N } 120^{\circ}\text{W}$) of the Beaufort Sea and are associated with lower than normal pressure over the East Siberian Sea (centered on $75^{\circ}\text{N } 170^{\circ}\text{E}$). The reverse is true for heavy-ice summers. Light-ice summers are in turn associated with more southerly surface winds, primarily those from over-land directions 135° - 195° , which advect warmer air from the land and result in higher temperatures over water and ice.
- 2) Air temperature, SLP distribution, and surface wind direction account for most of the year-to-year variance in northward pack ice retreat and their correlation with ice retreat increases as the summer progresses.
- 3) During light-ice summers, when considerable open water appears, the ocean plays a major role in determining subsequent autumn air temperature anomalies. The amount of mid-September open water, or distance of ice retreat, does not substantially influence the subsequent SLP distribution or surface wind directions during autumn.
- 4) The trends in SLP at $80^{\circ}\text{N } 120^{\circ}\text{W}$ and $75^{\circ}\text{N } 170^{\circ}\text{E}$ since 1939 and summertime TDD's since 1921 (Figs. 4 and 5) indicate a decline in favorable mean ice conditions. Since 1953, 13 of 24 summers have accumulated over 400 TDD's while 28 of 32 summers had done so before 1953. Comparison of Landsat imagery with TDD data show that 400 TDD's are required during summer before the pack ice begins retreating northward. Heavy-ice conditions, such as those during 1955, 1975, and other recent summers, may not have occurred since before the mid-1920's.

The more frequent heavy-ice summers have been associated with only a 0.4°C decline in mean summer temperature since 1953. A mean summer temperature decline of 0.9°C is necessary before end of summer ice conditions change from one category (Table 3) to another.

Acknowledgments

The author wishes to thank R.G. Barry of INSTAAR, University of Colorado, and H. van Loon of NCAR for reading and commenting on the manuscript. Programming assistance was provided by W. Spangler of NCAR.

This study was supported by the Bureau of Land Management through interagency agreement with the National Oceanic and Atmospheric Administration, under which a multi-year program responding to needs of petroleum development of the Alaskan continental shelf is managed by the Outer Continental Shelf Environmental Assessment Program Office (contract #03-5-022-91, RU #244, R.G. Barry, principal investigator).

References

- Barnett, D. G., 1976: A practical method of long-range forecasting for the north coast of Alaska, Part 1. Tech. Rept. #1, Fleet Weather Facility, Suitland, Md., 16pp.
- Barry, R. G., R. E. Moritz, and J. C. Rogers, 1976: Studies of climate and fast ice interaction during the decay season along the Beaufort Sea Coast. Proc. of the 27th Alaskan Science Conf., Vol. II, Univ. of Alaska, Fairbanks, Ak., in press.
- Hibler, W. D. III, and W. B. Tucker III, 1977: An examination of the viscous wind-driven circulation of the Arctic ice cover over a two year period. Arctic Ice Dynamics Joint Experiment Bull. #37, AIDJEX, Univ. of Washington, Seattle, Wa., 95-133.
- Jenne, R. L., 1975: Data sets for meteorological research. NCAR Tech. Note NCAR-TN/1A-111, 194pp. Available from the NCAR publications office, Boulder, Co. 80307.
- Maykut, G. A., and N. Untersteiner, 1971: Some results from a time dependent thermodynamic model of sea ice. J. Geophys. Res., 76, 1550-1575.
- Pritchard, R. S., M. D. Coon, M. G. McPhee, and E. Leavitt, 1977: Winter ice dynamics in the nearshore Beaufort Sea. Arctic Ice Dynamics Joint Experiment Bull. #37, AIDJEX, Univ. of Washington, Seattle, Wa., 37-93.
- Sater, J. E., J. E. Walsh, and W. I. Wittmann, 1974: Impingement of sea ice on the north coast of Alaska. In The Coast and Shelf of the Beaufort Sea. J. C. Reed and J. E. Sater (eds.), Arlington, Va., Arctic Inst. of North America, 85-105.

- Semtner, A. J., 1976: A model for the thermodynamic growth of sea ice in numerical investigations of climate. J. Phys. Oceanogr., 6, 379-389.
- Stringer, W. J., 1974: Morphology of the Beaufort Sea shorefast ice. In The Coast and Shelf of the Beaufort Sea, J. C. Reed and J. E. Sater (eds.), Arlington, Va., Arctic Inst. of North America, 165-172.
- U.S. Dept. of Commerce, 1953-1976: Local Climatological Data, Barrow, Ak. U.S. Dept. of Commerce, Nat. Climatic Center, Asheville, N.C., monthly.
- Washington, W. M., A. J. Semtner, C. Parkinson, and L. Morrison, 1976: On the development of a seasonal sea ice change model. J. Phys. Oceanogr., 6, 679-685.
- Wendler, G., 1973: Sea ice observations by means of satellite. J. Geophys. Res., 78, 1427-1448.
- Winchester, J. W., and C. C. Bates, 1958: Meteorological conditions and the associated sea ice distribution in the Chukchi Sea during the summer of 1955. In Polar Atmosphere Symposium, Part I, R. C. Sutcliffe (ed.), London, Pergamon Press, 323-334.
- Wittmann, W. I., and G. P. MacDowell, 1964: Manual of short term sea ice forecasting. Spec. Pub. 82, Washington, D.C., U.S. Naval Oceanographic Office, 142pp.

TABLE 1 Beaufort Sea ice-severity ranking of summers 1953-75 (after Barnett, 1976) and associated distance from Pt. Barrow to the 4/8 concentration of pack ice on 10 August and 15 September.

Rank	Year	10 Aug.	15 Sept.
		Distance (km) to 4/8 Ice <u>Concentration</u>	Distance (km) to 4/8 Ice <u>Concentration</u>
<u>Mildest</u>			
1	1958	93	390
2	1968	56	370
3	1962	56	280
4	1961	28	250
5	1973	9	350
6	1963	9	240
7	1959	37	120
8	1972	56	167
9	1954	37	390
10	1974	19	185
11	1957	130	111
12	1967	56	93
13	1966	9	83
14	1965	0	130
15	1953	9	65
16	1971	0	56
17	1960	40	37
18	1964	0	9
19	1970	9	0
20	1956	0	74
21	1969	0	56
22	1955	9	28
23	1975	9	0

Table 2. Correlation coefficients between primary meteorological parameters associated with 15 September ice retreat distance since 1953. *Italicized and bold face coefficients are statistically significant at the 95% and 99% level respectively.*

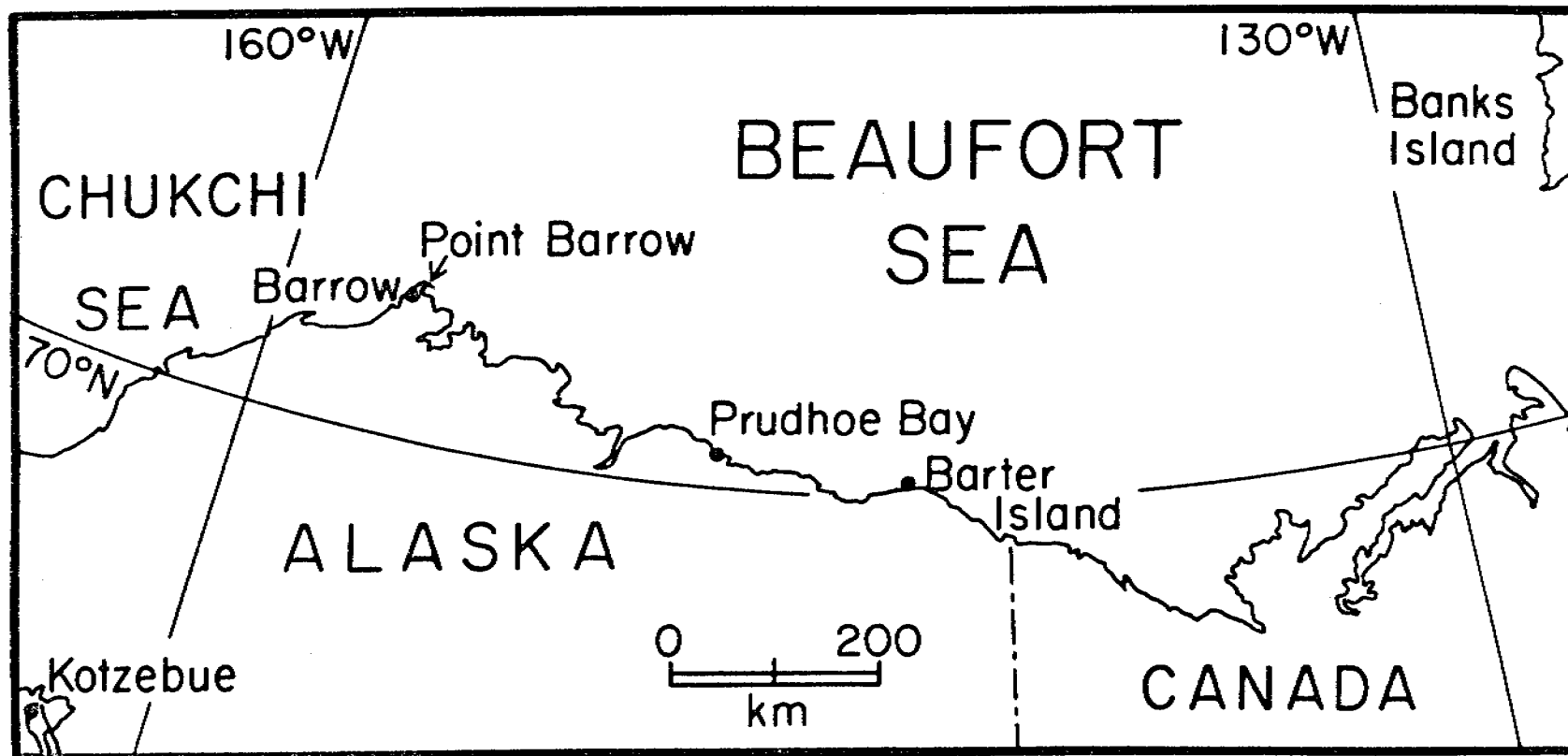
	9/15	SLP at		Geos.	Geos.	Geos.	Surf.	Surf.	
	Dist.	80°N	75°N	U	V	freq.	freq.	freq.	
	to ice	TDD's	120°W	170°E	Comp.	Comp.	61-105°	135-195°	345-45°
Distance	1.000	<u>.815</u>	<u>.598</u>	-.225	.271	<u>.614</u>	-.381	<u>.760</u>	<u>-.718</u>
TDD's		1.000	<u>.612</u>	<u>-.416</u>	.260	<u>.579</u>	-.357	<u>.606</u>	<u>-.623</u>
80°N			1.000	.195	-.344	-.015	.147	.326	<u>-.582</u>
75°N				1.000	<u>-.573</u>	<u>-.415</u>	<u>.473</u>	-.197	-.025
U Comp.					1.000	<u>.544</u>	<u>-.922</u>	<u>.502</u>	<u>.493</u>
V Comp.						1.000	<u>-.514</u>	<u>.687</u>	-.308
Geos. 61°-105°							1.000	<u>-.605</u>	.257
Surf. 135°-195°								1.000	<u>-.524</u>
Surf. 345°-45°									1.000

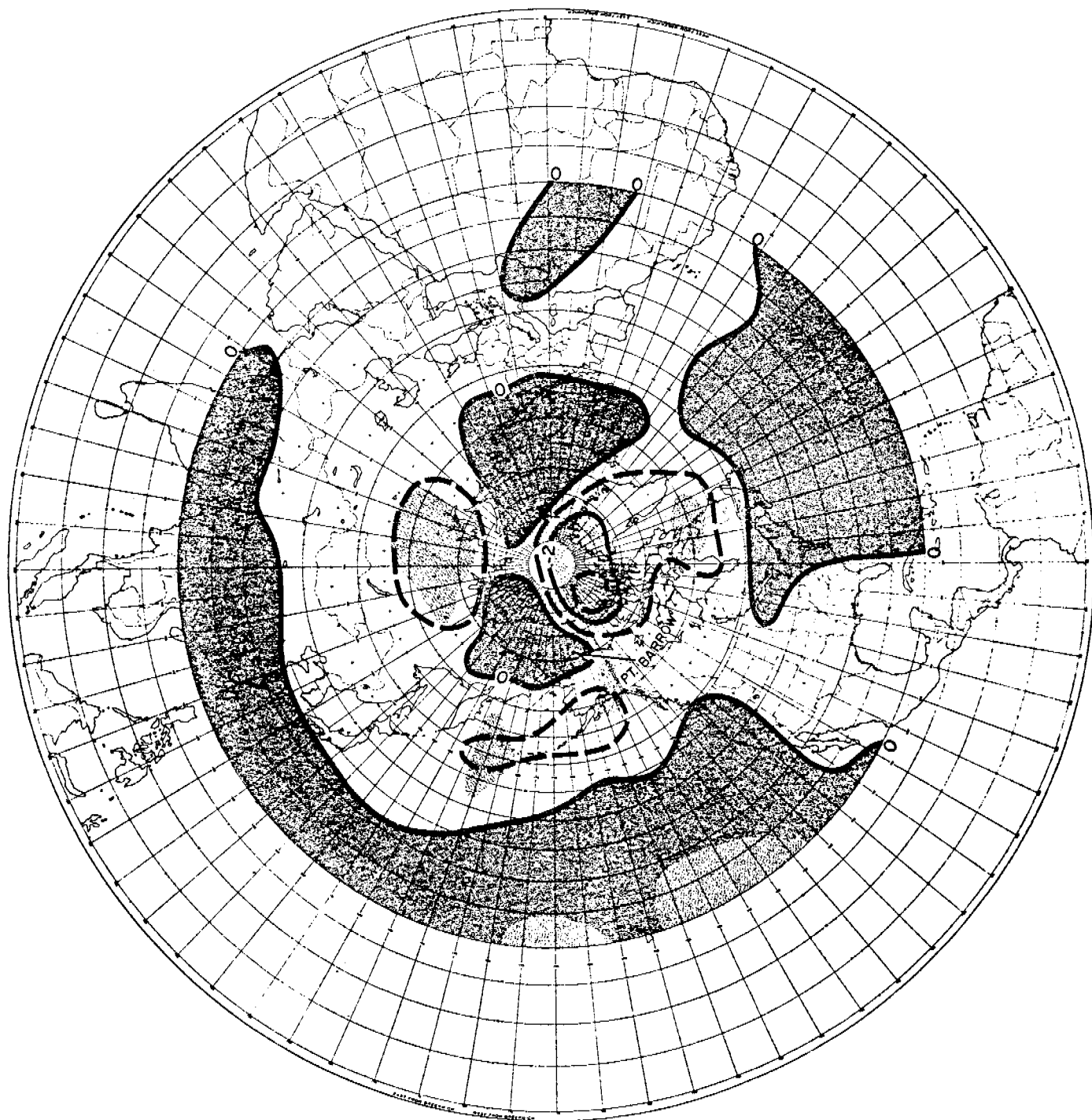
Table 3. Stages of ice breakup and frequency of occurrence of associated TDD accumulations (°F) during summers between 1921 and 1976 at Barrow.

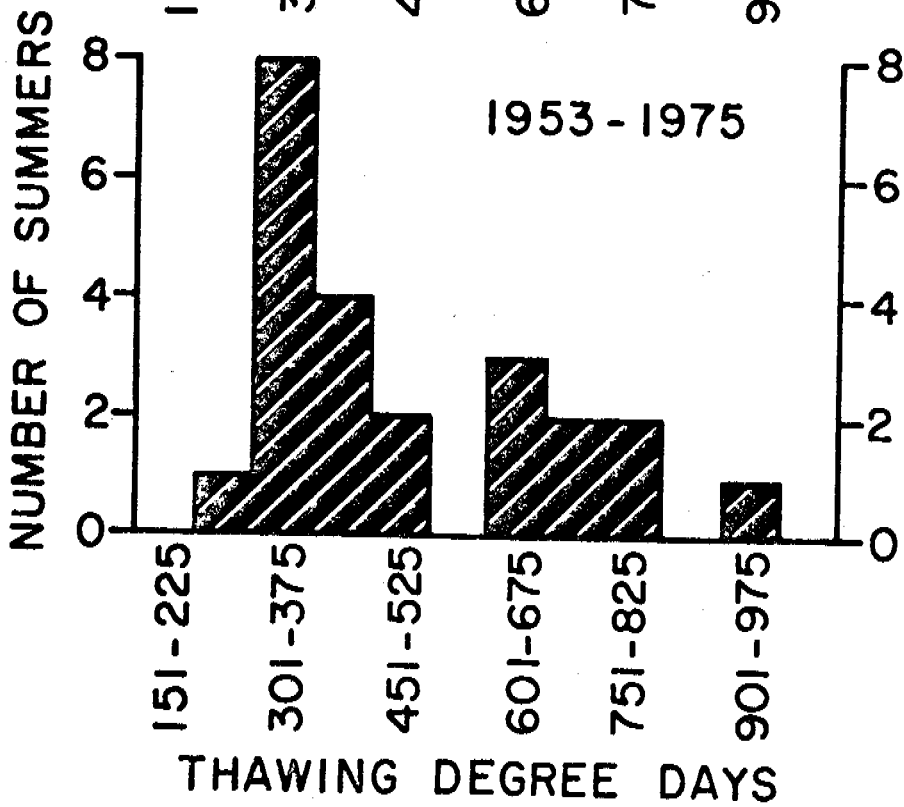
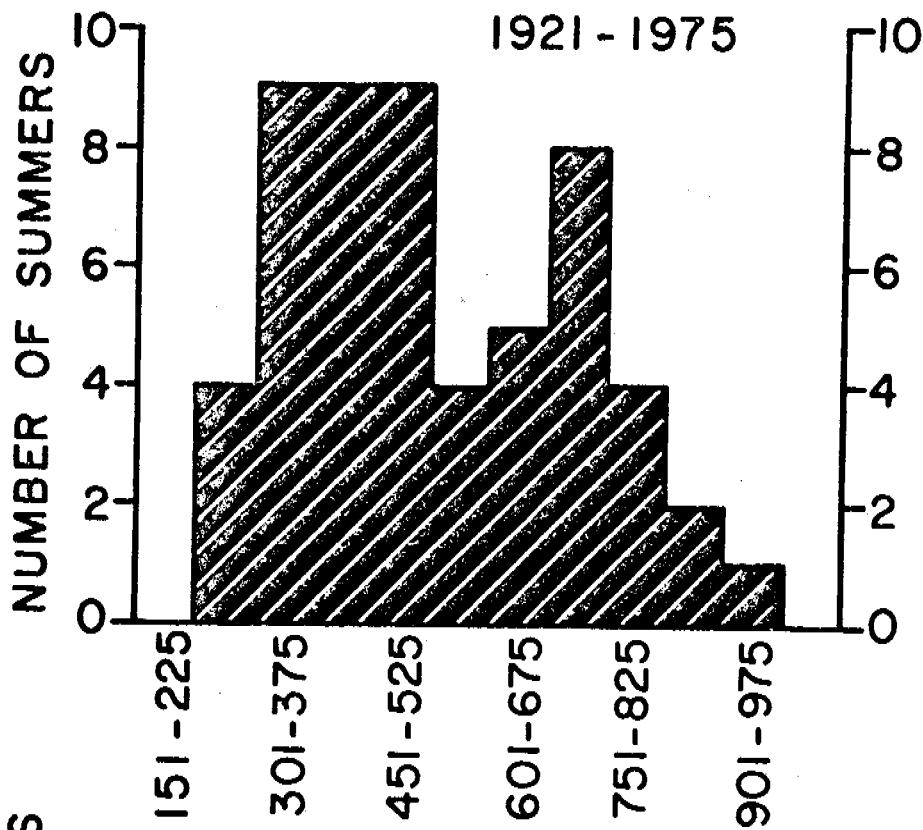
Stage of ice breakup and pack ice retreat	Associated TDD accumulation	Freq. of occurrence during summers from...	
		1921-52	1953-76
1) Initial thawing of fast ice.	<100	0	0
2) Fast ice breakup, open water appears.	100 to 250	1	1
3) Fast ice gone, pack ice starts melting.	250 to 400	3	10
4) Pack ice retreats up to 100 km.	400 to 550	12	5
5) Pack ice retreats over 100 km.	>550	16	8
Mean summer TDD accumulation		559	494
Standard deviation		173	187

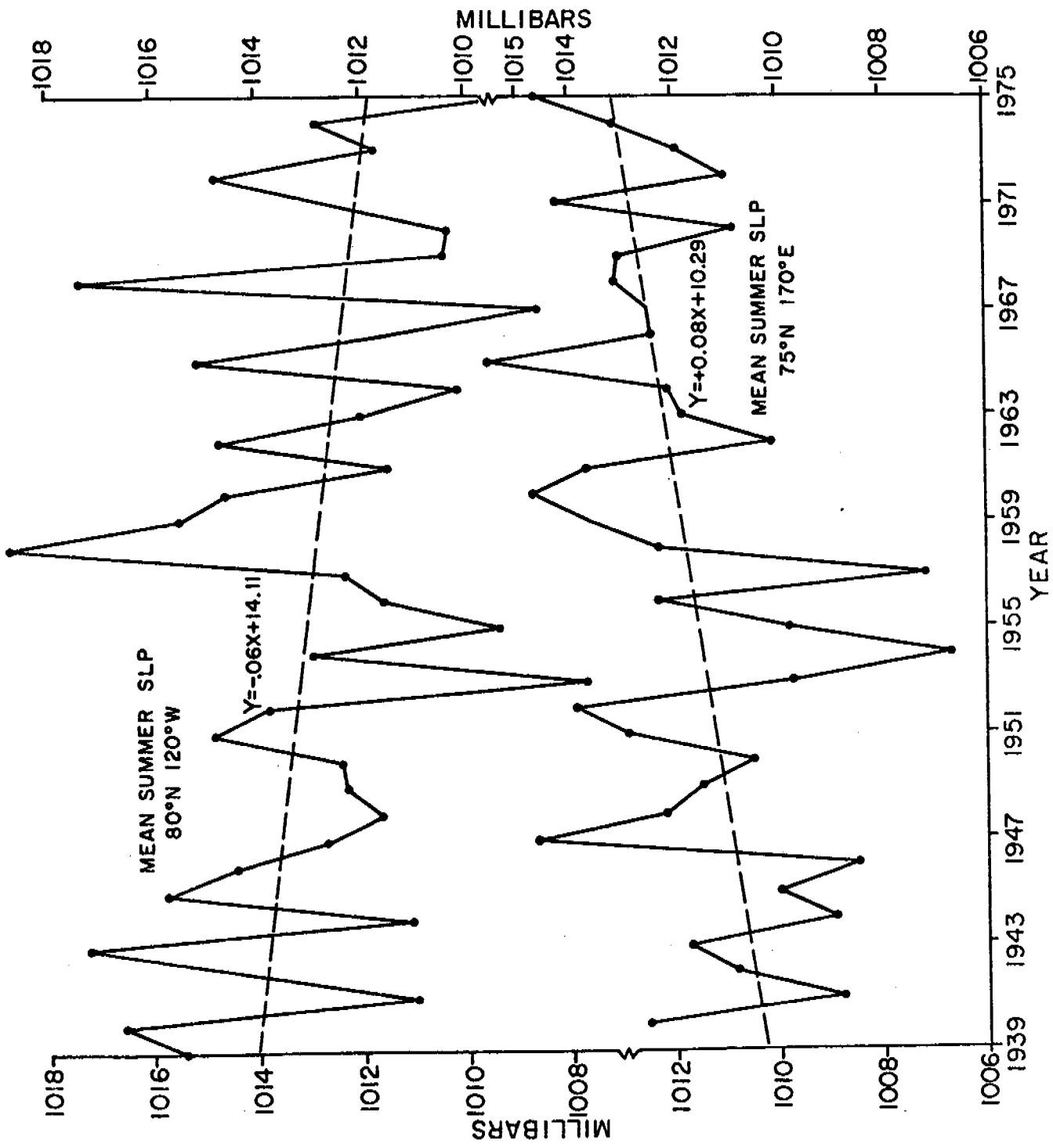
FIGURE LEGENDS

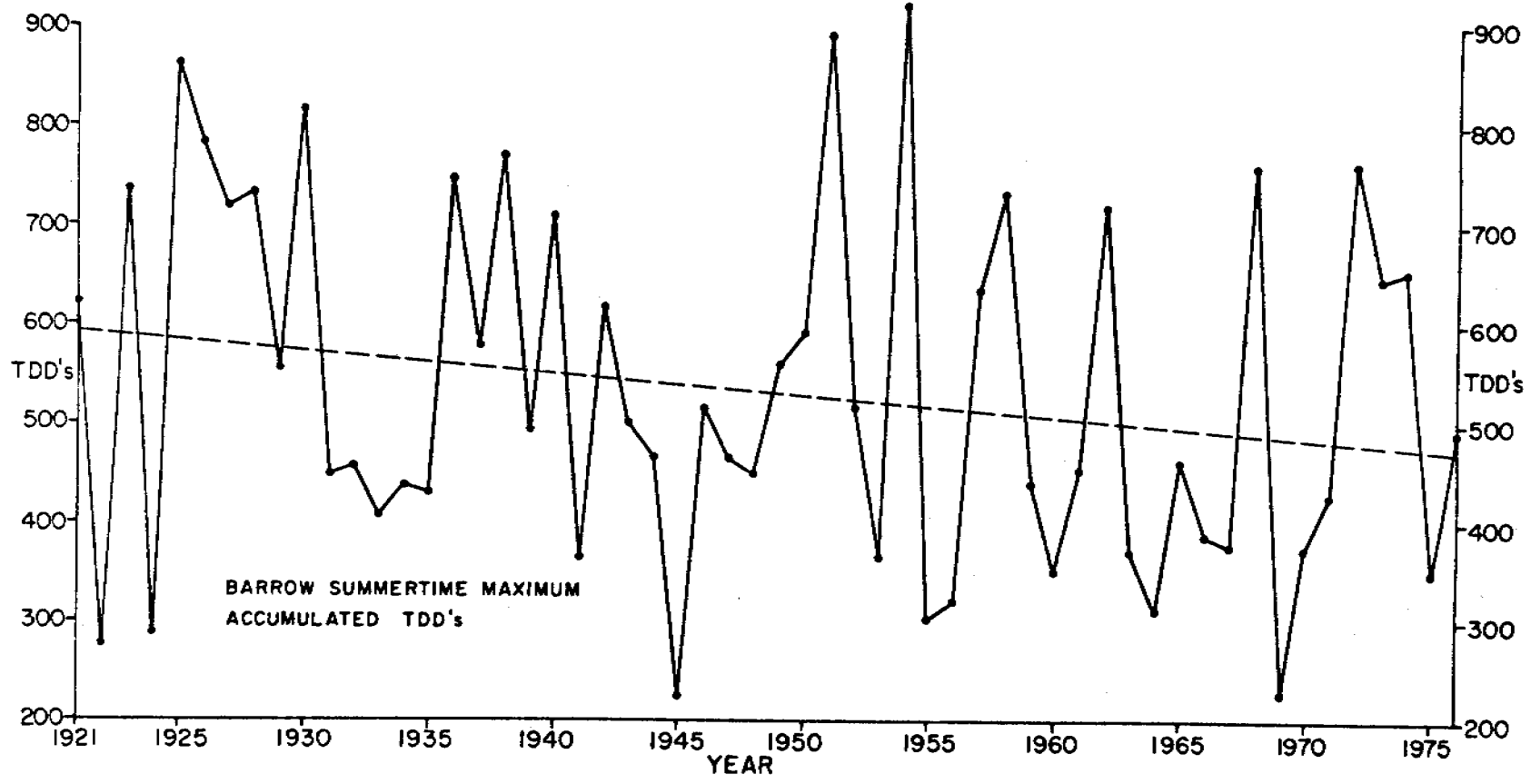
- Figure 1. The Beaufort Sea and its summertime ice variability are analyzed here primarily between Pt. Barrow and Prudhoe Bay.
- Figure 2. Mean SLP difference (mb) over the Northern Hemisphere obtained by subtracting SLP during light-ice summers from heavy-ice summers in the Beaufort Sea. Positive SLP differences are the darker shade and areas of statistically significant difference in SLP (95%) are more lightly shaded. Dashed lines are intermediate values (mb).
- Figure 3. Histogram of Barrow summertime maximum accumulated TDD's from 1921-1975 and 1953-1975.
- Figure 4. Mean summer (JJA) SLP (mb) at $80^{\circ}\text{N } 120^{\circ}\text{W}$ and $75^{\circ}\text{N } 170^{\circ}\text{E}$ since 1939. Dashed linear regression lines and their equations are indicated, and the constant values (14.11 and 10.29) are in mb above 1000 mb.
- Figure 5. Barrow summertime maximum accumulated TDD's since 1921. The dashed linear regression line through the data is $Y = -2.26X + 598.17$.











A METEOROLOGICAL BASIS FOR LONG-RANGE FORECASTING OF SUMMER AND EARLY
AUTUMN SEA ICE CONDITIONS IN THE BEAUFORT SEA

Jeffery C. Rogers
Institute of Arctic and Alpine Research, Univ. of Colorado
Boulder, Colo., 80309, U.S.A.

INTRODUCTION

The beginning of drilling operations and the movement of supplies and resources between Point Barrow and Prudhoe Bay, Alaska, has made an assessment of the Beaufort Sea ice regime imperative. Under the Offshore Continental Shelf Environment Assessment Program (OCSEAP) of NOAA/BLM one such appraisal is underway (Barry et.al., 1977). The Beaufort Sea is ice covered approximately nine months of the year. Only between late July and early October (in favorable ice summers) is it possible to safely ship supplies along the coast. In more severe ice summers such as those of 1955 (Winchester and Bates, 1958) and 1975 shipping can be delayed or halted. Using meteorological data as the predictor, the purpose of this paper is to develop possible long-range forecasting techniques of the expected summer-time ice severity along the Beaufort Sea Coast between Pt. Barrow and Prudhoe Bay.

There are two primary procedures used in developing a meteorologically based sea ice forecasting scheme. The first is to discover the important meteorological parameters which are associated with sea ice breakup and the second is to develop a suitable forecasting scheme which employs those parameters. Historically the most useful meteorological parameter in both breakup and freezeup forecasting has been air temperature from land based stations (Lee and Simpson, 1954; Wittmann, 1958; Bilello, 1961). Considerable variability occurs when one reviews the actual forecasting schemes developed by these authors. Lee and Simpson determined the ice potential of an area from heat budget analysis and then used air temperature as a final predictor of the time of freezeup. Wittmann converted air temperatures into accumulated thawing degree days (TDD's), which were in turn associated with different phases of breakup, and then predicted future TDD accumulations and ice conditions using conventional meteorological forecasts. A TDD is the negative departure of 1°C from 0°C . Bilello showed that regression equations, with air temperature as the independent variable, can be used to predict the growth and decay of sea ice. This paper will develop long-range forecasting schemes by using both persistence in monthly anomalies of air temperature and long term periodicities in summertime monthly air temperatures. Preceding that is a discussion of the interrelated meteorological parameters which affect sea ice conditions between Pt. Barrow and Prudhoe Bay.

DATA

The data used for this study consisted of:

1. Barrow, Alaska, monthly mean temperatures from January 1921 through December 1976, and daily mean temperatures (usually converted to accumulated TDD's during

summer months) since 1953.

2. The distance northward from Pt. Barrow to the southernmost limit of 4/8 concentration of pack ice on Sept. 15 between 1953 and 1975. These data were taken from Barnett (1976) who ranked each summer in order of its ice severity. Severe summers are those during which the ice is closest to Pt. Barrow and during which there are relatively few ice free days along the sea route to Prudhoe Bay. Ranked in Barnett's order of increasing severity these unfavorable summers are those of 1967, 1966, 1965, 1953, 1971, 1960, 1964, 1970, 1956, 1969, 1955, and 1975.

3. Surface prevailing and resultant (after 1964) wind directions for Barrow taken from the NOAA publication Local Climatological Data. Data were tabulated from July 1 through Sept. 15 from 1953 through 1975.

4. Monthly sea level pressure values (at each $5^{\circ} \times 5^{\circ}$ grid point interval) from May to October from 1939 to 1975 and made available by the National Center for Atmospheric Research at Boulder and originally derived from historic weather maps.

5. LANDSAT imagery of the Beaufort Sea Coast between 1972-76.

METEOROLOGICAL PARAMETERS ASSOCIATED WITH BEAUFORT SEA ICE BREAKUP

As discussed in the Introduction, the primary parameter used in long and extended-range forecasts of sea ice decay and breakup has been air temperature. Although these data are usually collected from a nearby (to the ice) land station, a high degree of relationship has been established (Wittmann, 1958) between such data and stages of breakup. In the Beaufort Sea the breakup process begins with thawing and ponding of landfast ice which approximately extends to the 20 m. isobath. The landfast ice then breaks and clears from that zone and thawing and thinning of the areal concentration of the adjacent polar pack ice begins. Although the southernmost boundary of the pack ice may vary with winds, the pack ice will normally retreat northward about 150 km. by mid-September (based on Barnett's data).

Recent studies (Barnett, 1976; Walsh, 1977) have suggested the importance of sea level pressure distribution as an important forecasting parameter. In addition, Wittmann (1958) noted that the Beaufort Sea near Pt. Barrow is geographically situated such that ice may become trapped in the area and offshore and onshore winds play very important roles in determining the characteristics of breakup.

In view of the importance of other meteorological parameters beside air temperature an attempt was made (Rogers, 1977) to determine the interrelationship between such parameters and Beaufort Sea breakup. The primary meteorological parameters which emerged from that analysis are shown in Table 1. Table 1 shows that summertime accumulated TDD's, the number of days with southerly and northerly winds, and the Sept. 15 distance to the pack ice are highly intercorrelated. These factors were affected by the sea level pressure distribution which was best represented by the grid point pressure values at $80^{\circ}N120^{\circ}W$ and $75^{\circ}N170^{\circ}E$. A mild ice summer was characterized by high pressure near $80^{\circ}N120^{\circ}W$, lower pressure northwest of Point Barrow ($75^{\circ}N170^{\circ}E$) and the resultant southerly (overland) winds and higher temperatures. The opposite pattern (northerly winds) occurred during severe ice summers.

Despite the interrelationship between these parameters it appears that air temperature remains the primary factor associated with breakup. The ease with which air temperature forecasts can be applied or obtained from other sources as compared to wind direction and pressure data has resulted in it being the primary parameter of interest here. Nonetheless forecasts based upon the pressure at the grid points given in Table 1 were also considered.

TABLE 1 - Correlation matrix of meteorological parameters associated with the distance to the pack ice margin on Sept. 15 since 1953 (after Rogers, 1977). Statistically significant coefficients are underlined (95%).

	Dist.	TDD	140	350	80N	75N
Sept. 15 dist. to ice margin	1.000					
TDD's	<u>0.815</u>	1.000				
# of days winds from 140-190°	<u>0.760</u>	<u>0.606</u>	1.000			
# of days winds from 350-040°	<u>-0.718</u>	<u>-0.623</u>	<u>-0.524</u>	1.000		
Pressure at 80°N120°W	<u>0.598</u>	<u>0.612</u>	0.326	<u>-0.582</u>	1.000	
Pressure at 75°N170°E	-0.225	<u>-0.416</u>	-0.197	-0.025	0.195	1.000

As a prediction guide the number of accumulated TDD's associated with the stages of Beaufort Sea breakup and pack ice retreat were tabulated. Based upon LANDSAT images of ice conditions along the Beaufort Sea Coast from 1972-76 the ranges of TDD accumulations associated with breakup stages are given in Table 2. Wittmann (1958) found that 170-180 TDD's (average) accumulate when the ice is removed near Pt. Barrow (stage 3 below).

TABLE 2 - Accumulated TDD's associated with stages of sea ice breakup and retreat in the Beaufort Sea.

	TDD (°C) accumulation
1. Initiation of ponding and thawing	0 to 55
2. Fast ice breakup, open water appears	56 to 140
3. Fast ice removed to 20 m. isobath, pack melting	141 to 225
4. Pack ice retreat, possibly up to 80 km.	226 to 305
5. Pack ice retreat greater than 80 km.	306 or more

PERSISTENCE OF MONTHLY AIR TEMPERATURE ANOMALIES AT BARROW

The monthly temperatures at Barrow for May through October from 1921 to 1976 were divided into three categories, above normal (AN), below normal (BN), and normal. A monthly mean temperature was characterized as normal if it was within ± 0.5 standard deviations of the 56 year (long term) monthly mean temperature. AN and BN months lay outside those limits of normal. This method of determining the monthly temperature anomaly categories resulted in approximately 40% of all months being normal and about 30% each being AN or BN during the 56 year period for any given month. Table 3 shows the 56 year mean and the range of normal monthly temperatures for May through October. Persistence between any two months occurs if they have the same temperature anomaly category, and it was assumed when developing the forecasting technique that persistence always occurs between any pair of months.

The first of the two months in a persistence (or non-persistence if the above assumption is incorrect) pair is the predictor month and the second is the predictand month. The predictor month must always occur earlier in the year than the predictand month, therefore May is always a predictor while October is always a predictand in the data set analyzed here.

A test of the persistence assumption was made to determine if persistence could be further considered as a forecasting technique. If persistence between any pair of months occurred in more than 33.3% to 40% of the past 56 years then it was assumed

TABLE 3 - Long term (56 year) mean temperature, range of normal temperatures, and range of mean monthly TDD accumulation for May through October.

MONTH	MEAN Temp. (°C)	Temperature range of normal category	Range of TDD accumulation during normal cat. months
May	-7.3	-8.1 to -6.6	0*
June	0.9	0.3 to 1.3	28 to 56
July	4.1	3.4 to 4.8	107 to 150
Aug.	3.3	2.4 to 4.3	74 to 135
Sept.	-0.9	-1.7 to 0.1	0 to 22
Oct.	-9.1	-10.6 to -7.6	0*

* TDD's do not accumulate during AN category months either.

that it occurred with a frequency greater than chance and that it could be used as an air temperature forecasting technique between those months. If persistence between any pair of months occurred in about 33.3% to 40% or fewer of the past 56 years then there is no persistence occurring other than what might be expected by chance. The 33.3% to 40% chance limit is a result of there being one chance in three that the anomaly category of the predictand month is the same as that which occurred in the predictor month, and as a result of there being a slightly better chance of a normal month occurring (about 40% of the months).

Starting with a one month lag between predictor and predictand months (May to June,... etc.... Sept. to Oct.) the number of month pairs with the same anomaly categories since 1921 were tabulated and are shown in Table 4. The percentage of these persistent month pairs is given in the lower right corner of each part of Table 4. The results show that all months except the June-July pair exhibit persistence to a greater degree than would be expected by chance. The persistence indicated in the one month lags of Table 4 is even better when considering that AN and BN category predictor months are very seldom followed by BN or AN (respectively) predictand months. For example, from Table 4C an AN July was followed by a BN August only once.

Whether or not persistence also existed for lags of two or more months was also tested. May-July, June-Aug., July-Sept., and Aug.-Oct. persistence existed in 36%, 39%, 50%, and 48% of the last 56 years. Generally only about one-half of the months intervening between the predictor and predictand months had the same anomaly category when persistence occurred between them. This frequent dissimilarity in the anomaly category of the intervening months implies that the useful degree of persistence in the July-Sept., and Aug.-Oct. pairs is more statistically sound than physically sound. The persistence at three months lag (May-Aug. = 32%; June-Sept. = 36%; and July-Oct. = 45%) occurred during even fewer years.

Table 5 further shows the degree of persistence (correlation) between the various predictor-predictand month pairs. In particular Table 5 shows that May and June are statistically significantly correlated with each other but not with any of the other months. This can be seen from Table 4 where May-June persistence occurs during 54% of the years, however when either May or June are predictors for other month pairs on any time lag scale there is little persistence. Table 5 also shows that there should be a good degree of persistence between most month pairs from July through November (which hasn't been considered in the analysis up to this point). This suggests that persistence may be successfully applied to freezeup forecasts as well as toward late summer breakup forecasts.

TABLE 4 -- One month lag persistence and non-persistence occurrences between temperature anomaly categories since 1921 for May through October. The percentage of persistent years for each pair of months appears on the lower right.

JUNE					JULY				
Cat.	AN	N	BN	Total	Cat.	AN	N	BN	Total
AN	7	7	2	16	AN	7	6	3	16
N	5	13	5	23	N	4	9	10	23
BN	4	3	10	17	BN	4	8	5	17
Total	16	23	17	54%	Total	15	23	18	38%

TABLE 4A. May vs. June

TABLE 4B. June vs. July

AUGUST					SEPTEMBER				
Cat.	AN	N	BN	Total	Cat.	AN	N	BN	Total
AN	8	6	1	15	AN	8	5	2	15
N	6	10	7	23	N	8	11	5	24
BN	1	8	9	18	BN	1	7	9	17
Total	15	24	17	48%	Total	17	23	16	50%

TABLE 4C. July vs. August

TABLE 4D. August vs. September

OCTOBER				
Cat.	AN	N	BN	Total
AN	11	5	1	17
N	9	9	7	25
BN	1	3	10	14
Total	21	17	18	54%

TABLE 4E. September vs. October

TABLE 5 - Correlations between mean monthly temperatures at Barrow, 1921-76. Underlined coefficients are significant at the 99% level.

MONTHS	MAY	JUNE	JULY	AUGUST	SEPTEMBER	OCTOBER	NOVEMBER
MAY	1.000						
JUNE	<u>0.347</u>	1.000					
JULY	0.132	0.307	1.000				
AUGUST	-0.086	0.138	<u>0.383</u>	1.000			
SEPTEMBER	0.159	0.180	0.251	<u>0.445</u>	1.000		
OCTOBER	0.146	0.292	<u>0.387</u>	<u>0.481</u>	<u>0.666</u>	1.000	
NOVEMBER	0.083	0.188	<u>0.386</u>	<u>0.434</u>	<u>0.384</u>	<u>0.501</u>	1.000

The remaining months, January through April, and December, were not significantly correlated to any of the months May through November or with each other. This would suggest that useful air temperature anomaly predictions using persistence could only be made between May and June and during combinations of months from July through November. The May-June discontinuity with the remainder of the warm season not only hinders the chance for reliable early long-range temperature anomaly forecasts, it is also difficult to explain physically. Perhaps the explanation depends upon surface feature changes such as in albedo when the land and sea ice snow cover decreases in May and June and/or in atmospheric circulation changes at this time of year such as those described by Barry et.al. (1977).

An analysis of possible seasonal persistence in temperature anomalies was done in the same manner as the monthly analysis and revealed that persistence greater than that which would be expected by chance does not exist between winter and spring (29%), or winter and summer (36%, see Table 6F), or between spring and summer (25%, see Table 6E). There is however, persistence between summer and September (54%, see Table 6C), and summer and October (55%, see Table 6D). This further suggests that air temperature anomaly forecasts might also be applied to freezeup forecasting in this area. Warmer summers are associated with warmer water and more ice free area in the Beaufort Sea, and this in turn takes longer to freeze in the autumn and modifies otherwise cold air masses in the area during those months. The persistence tables of Table 6 show that AN or BN summers are seldom followed by BN or AN (respectively) categories in either September or October.

The persistence of anomalies of sea level pressure at $80^{\circ}\text{N}120^{\circ}\text{W}$ and $75^{\circ}\text{N}170^{\circ}\text{E}$ was also tabulated using data since 1939. The results showed that the persistence between predictor and predictand month pairs is slightly greater than that which would be expected by chance at $80^{\circ}\text{N}120^{\circ}\text{W}$ but not at $75^{\circ}\text{N}170^{\circ}\text{E}$ for a one month lag. The May to June,...etc... September to October one month lags showed persistence in 43%, 46%, 30%, 43%, and 38% of the years since 1939 at $80^{\circ}\text{N}120^{\circ}\text{W}$ and in 31%, 31%, 32%, 41%, and 38% of the years since 1939 at $75^{\circ}\text{N}170^{\circ}\text{E}$. Lags of two or more months showed no persistence. Since these results are poorer than those obtained using air temperatures, sea level pressure was not considered further as a predictor of summertime pressure or ice conditions.

Table 6 includes additional air temperature persistence tables between two month lag pairs described above especially July-Sept., Aug.-Oct., May-July and June-Aug.

PERIODICITIES IN THE BARROW MONTHLY TEMPERATURE TIME SERIES

Predictability based upon periodicities in monthly air temperature was also considered. Spectrum analysis of monthly normalized Barrow temperatures from January 1948 through December 1974 (324 months) showed that a periodicity of about 50 to 66 months (frequencies between 0.015 and 0.020 cycles per month) occurred in the low frequency variance (Figure 1). The spectral estimates at these frequencies were the only ones to be statistically significant at the 99% confidence limit in the entire spectrum. Spectrum analysis of the 56 year time series for each month showed that several, primarily summer months, had spectral estimates which peaked above their white noise continuum at frequencies between 0.20 and 0.25 cycles per year which corresponds to a periodicity between four and five years. Further testing of these data showed that these spectral estimates were not statistically significant.

Cospectrum analysis of the 56 years of data for adjacent months also revealed a four to five year periodicity along with one of slightly more than two years. Cospectrum analysis is a statistical technique in which the relationship or

TABLE 6 - Two month lag persistence and non-persistence occurrences and seasonal persistence between temperature anomaly categories since 1921. The percentage of persistent years for each pair appears on the lower right.

Cat.	SEPTEMBER			Total
	AN	N	BN	
AN	7	6	2	15
N	7	12	4	23
BN	3	6	9	18
Total	17	24	15	50%

TABLE 6A- July vs. September

Cat.	OCTOBER			Total
	AN	N	BN	
AN	10	3	2	15
N	9	8	7	24
BN	2	6	9	17
Total	21	17	18	48%

TABLE 6B - August vs. October

Cat.	SEPTEMBER			Total
	AN	N	BN	
AN	8	5	3	16
N	9	11	2	22
BN	0	7	11	18
Total	17	23	16	54%

TABLE 6C - Summer vs. September

Cat.	OCTOBER			Total
	AN	N	BN	
AN	9	5	2	16
N	12	8	2	22
BN	0	4	14	18
Total	21	17	18	55%

TABLE 6D - Summer vs. October

Cat.	SUMMER			Total
	AN	N	BN	
AN	3	7	6	16
N	9	6	7	22
BN	4	9	5	18
Total	16	22	18	25%

TABLE 6E - Spring vs. Summer

Cat.	SUMMER			Total
	AN	N	BN	
AN	4	8	5	17
N	7	9	6	22
BN	5	5	7	17
Total	16	22	18	36%

Table 6F - Winter vs. Summer

Cat.	JULY			Total
	AN	N	BN	
AN	6	4	6	16
N	6	9	8	23
BN	3	10	4	17
Total	15	23	18	36%

TABLE 6G - May vs. July

Cat.	AUGUST			Total
	AN	N	BN	
AN	5	6	5	16
N	6	11	6	23
BN	4	7	6	17
Total	15	24	17	39%

TABLE 6H - June vs. August

correlation between two time series is separated into individual contributing frequencies or periodicities. Therefore taking the cospectrum between the August and September and September and October time series (which are correlated by $r=0.445$ and $r=0.666$ respectively from Table 5) as an example shows that the primary contribution to those correlations comes from periodicities in the four to five year range. Even some of the winter and early spring months had spectra with larger than expected estimates in this period range even though their correlations were low and insignificant. (In general however, many of the cospectrum between adjacent months did not have any statistically significant estimates despite the apparent peaks above the white noise continuum between four and five years period. The fact that this periodicity recurs in most months suggests that it should be investigated further.

Barnett (1976) found a five year periodicity in his Beaufort Sea ice data between 1953 and 1975. He cited the fact that severe ice summers had occurred in 1955, 1960, 1965, 1970, and 1975 as one piece of evidence for this. Severe ice summers also occurred in 1956, 1964, and 1969 and mild summers have occurred in 1954, 1958, 1962, 1968, and 1972 which suggests that there are elements of a four year periodicity also. A subjective analysis of Barrow mean summer temperatures indicated as expected from the above results (Table 1 and the spectrum analysis) that there is a four to five year gap between very mild summers and very cold summers. Analysis of the pre-1953 temperature record in a similar manner seemed to indicate that such a periodicity may have been less pronounced or even nonexistent before the late 1940's. This was the rationale for choosing the 1948 to 1974 time series for the spectrum analysis of Figure 1. Comparison of the low frequency portion of that spectrum to another of the equal length period 1921 to 1947 in Figure 2 shows that the 50 to 66 month periodicity does not exist. This earlier period time series is characterized by significant long term periodicities between 100 and 200 months and one at about 25 months (nonsignificant). In view of this additional fact that the nature of the spectrum of the Barrow temperature time series changes then the significance of any of the periodicities should be doubted. The existence of this periodicity is more a function of statistics than physics of the atmosphere.

CONCLUSIONS AND APPLICATION OF MONTHLY TEMPERATURE PERSISTENCE AND PERIODICITIES TO BEAUFORT SEA ICE FORECASTING

The results have shown a high correlation between air temperature (TDD's) at Barrow, Alaska, and the extent of ice breakup in the Beaufort Sea from Point Barrow to Prudhoe Bay (Tables 1 and 2). Analysis of the temperature time series at Barrow showed persistence between anomalies during about 50% of all month pairs for one month lags (Table 4). This represents 30% to 50% more cases of persistence than might be expected by chance. Two month lag forecasts would only be successful using July, August, or summer temperature anomalies as predictors of September and October anomalies (see Table 6). May is a good predictor of June anomalies but neither of these months could be used directly as predictors of the remaining warm season months (Table 5). In addition it was found that a four to five year periodicity which has been noted since about 1950 in the Beaufort Sea ice (Barnett, 1976) and temperature record is a statistical manifestation, indicating that it must be applied with caution in sea ice forecasting.

Despite the problems indicated above the desired long-range sea ice forecast is relatively simple; only a determination of whether the ice summer will be severe or mild is required. Table 3 shows that during a summer in which only normal months would occur, anywhere from 209 to 363 TDD's (computed by summing the ranges of monthly TDD accumulations in the fourth column of Table 3) can be expected.

These ranges of normal category month TDD accumulations were based upon actual accumulations since 1953. Comparing this range of net accumulated TDD's to the results of Table 2 shows that such a normal summer would generally favor shipping and mild ice conditions. Since only four severe ice summers (1971, 1967, 1966, and 1965) as defined in the data section had TDD accumulations of more than 209 TDD's (and none of them exceeded 256 TDD's) it can be assumed that summers predominated by BN months with some normal months will become severe ice summers. While it is possible that a summer with all normal months could become severe the monthly temperature anomaly data shows that the BN category always occurs during some or most of the severe ice summer months.

It is therefore necessary to discern only between summers which will have a combination of AN and normal months (which will result in mild ice summers) and those which will have a combination of BN and normal months (becoming severe ice summers). Based upon the results of one (Table 4) and two (Table 6) month lags starting in July there is a high degree of persistence when AN or BN months occur. If July is AN or BN one can be relatively assured that that anomaly category will recur, or at least that a normal month will follow.

Waiting until the end of July to make a relatively useful high persistence forecast may be too late to be of operational value to shippers and others. As a result two questions emerge:

1) How can one make a useful early sea ice forecast around the May-June discontinuity with the remainder of the summer and around the possibility that July may become a normal category month which would prolong the indecision of the forecast of the nature of the ice summer since AN or BN categories could follow with approximately equal probability?

2) How can a forecaster distinguish a severe ice summer which will seriously delay or halt shipping from one that will not greatly hamper shipping? As mentioned above the summers of 1955 and 1975 were in the former category.

The answer to the first question derives from information which persistence tables (Tables 4 and 6) indicate does not have a high probability of occurring. Since the primary concern is whether one or more of the months July, August, and September will be either AN or BN and we are confident from Table 4 that they will almost never mix, there are two possible approaches:

1) Generally there is approximately a 60% chance or more that the anomaly category for one of these three primary summer months will be normal or opposite (in terms of AN and BN) the category in May or June (see Tables 6G and 6H).

2) Similarly there is a good chance that the temperature anomaly category for the summer will be normal or opposite (in terms of AN and BN) the anomaly category of the preceding winter or spring (see Tables 6E and 6F for example).

The answer to the second question posed above is more difficult. Persistence of categories such as BN cannot separate extremely severe ice summers from those during which a modest amount of shipping can take place. Perhaps the best possible answer lies in applying the four to five year periodicity observed in the ice and temperature record despite the lack of a physically sound basis for it. Assuming that this periodicity will continue to exist in the near future it is possible to suggest that after the severe summer of 1975 three summers of gradually improving ice conditions will follow with 1978 being the most favorable. This in turn will be followed by a rapid decline in ice conditions with the summer of 1980 being the most likely to be very severe. During the summer of 1976 sufficient melting and retreat of the pack ice occurred to permit shipping although the ice margin was well south of its normal position. It appears from June 1977 field work

done by the author that melt and decay of the fast ice was about two weeks ahead of that which occurred in 1976.

The overall results suggest that persistence of monthly air temperature anomalies at Barrow in conjunction with cautious application of periodicities in those temperatures can be successfully used as predictors of the severity or mildness of summertime Beaufort Sea ice conditions. Depending upon user needs these meteorologically based prediction techniques could feasibly be used in other aspects of sea ice forecasting, particularly the time of freezeup.

ACKNOWLEDGMENTS

This work was supported by the NOAA/BLM Outer Continental Shelf Environment Assessment Program (OCSEAP) Office contract #03-5-022-91, RU#244, Dr. Roger G. Barry, principal investigator.

REFERENCES

- Barnett, D.G., "A Practical Method of Long Range Ice Forecasting for the North Coast of Alaska, Part 1", Tech. Rept. #1, Fleet Weather Facility, March, 1976, 16 pp.
- Barry, R.G., Moritz, R.E., and Rogers, J.C., "Studies of Climate and Fast Ice Interaction During the Decay Season along the Beaufort Sea Coast", in press as the Proceedings of the 27th Alaskan Science Conference held in August 1976, 1977.
- Bilello, M.A., "Formation, Growth, and Decay of Sea Ice in the Canadian Arctic Archipelago", Arctic, Vol. 14, #1, March, 1961, pp. 3-24.
- Lee, O.S., and Simpson, L.S., "A Practical Method of Predicting Sea Ice Formation and Growth", Tech. Rept. #4, U.S. Navy Hydrographic Office, Sept. 1954, 25pp.
- Rogers, J.C., "The Meteorological Factors Affecting Breakup and Retreat of Landfast and Pack Ice in the Beaufort Sea", in preparation, 1977, copies available from the author upon request.
- Wittmann, W.I., "Continuity aids in Short-Range Ice Forecasting", in Proceedings of the Conference on Arctic Sea Ice, NAS-NRC Pub. 598, 1958, pp.244-255.
- Winchester, J.W., and Bates, C.C., "Meteorological Conditions and the Associated Sea Ice Distribution in the Chukchi Sea During the Summer of 1955", in Polar Atmosphere Symposium, Part 1, Meteorology Section, R.C. Sutcliffe (ed.), 1958, pp.323-334.
- Walsh, J.E., personal communication, 1977. Dr. Walsh is currently investigating the use of empirical orthogonal functions of Alaskan temperature, pressure, and areal ice extent patterns to determine if such patterns have predictability value.

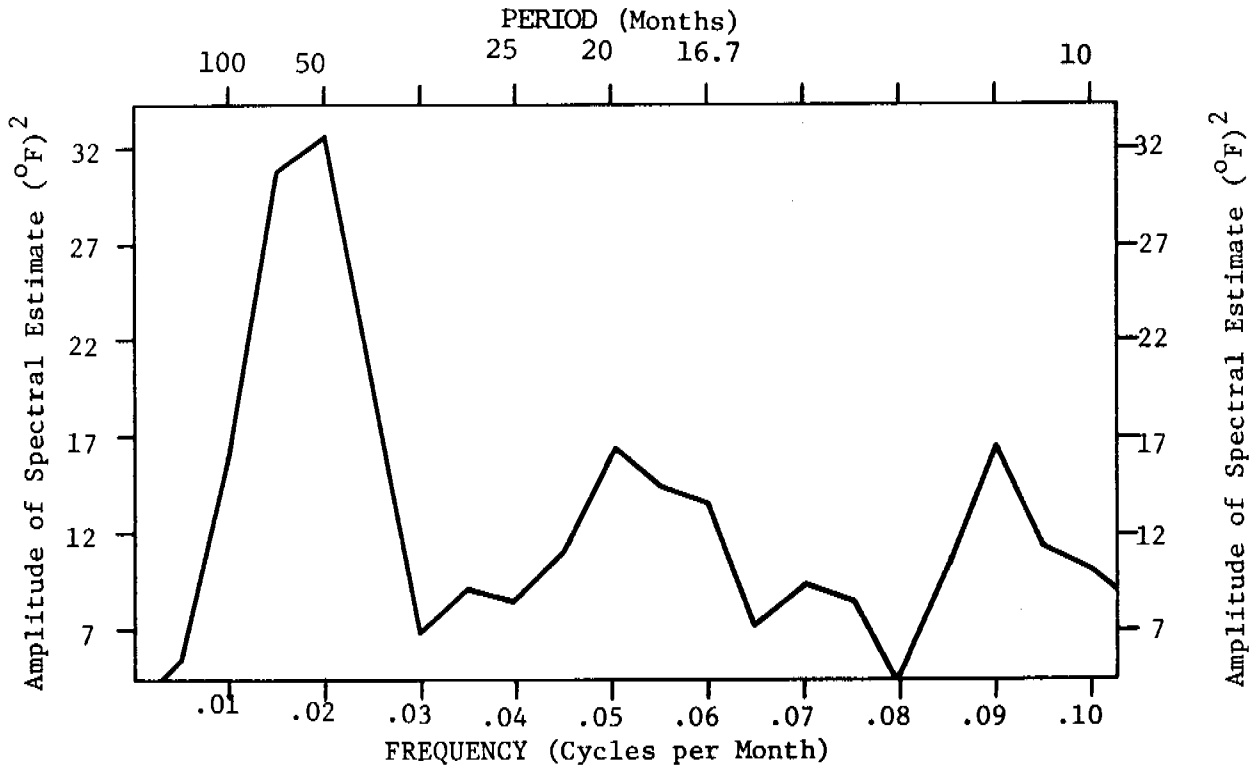


FIGURE 1 - The spectrum at low frequencies of monthly normalized air temperatures at Barrow, Alaska, from January 1948 through December 1974.

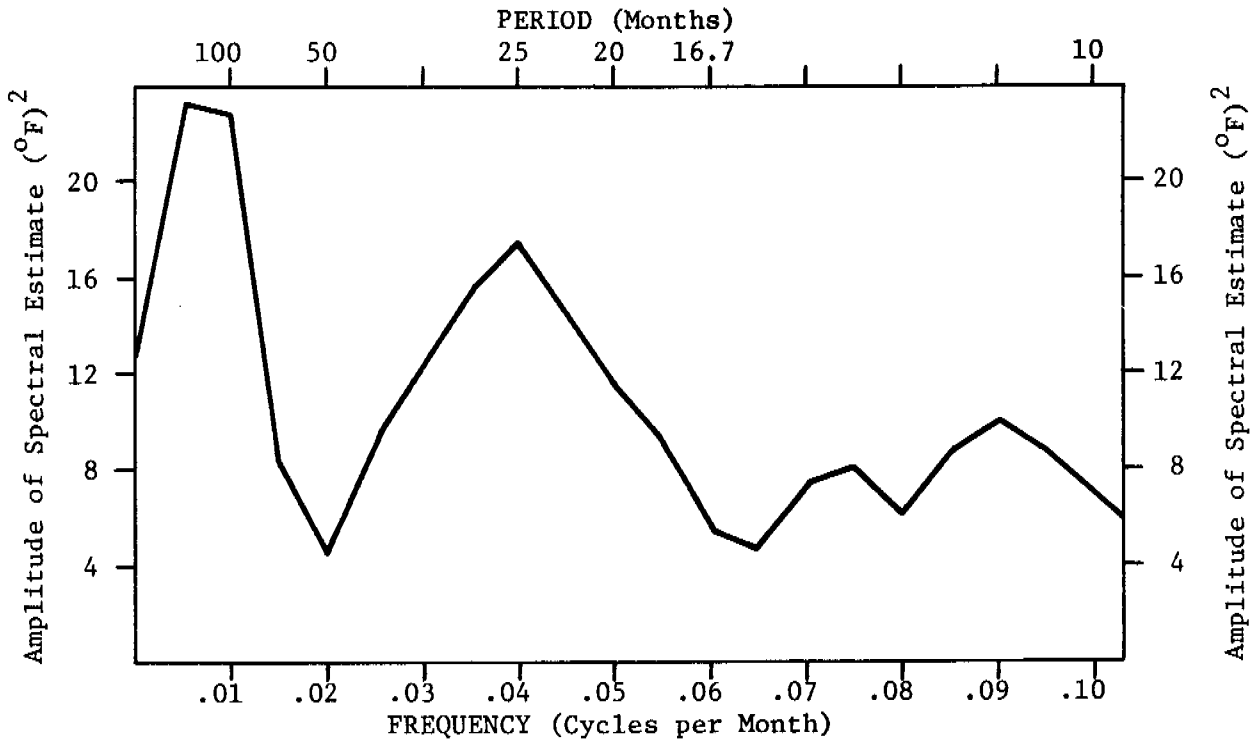


FIGURE 2 - The spectrum at low frequencies of monthly normalized air temperatures at Barrow, Alaska, from January 1921 through December 1947.

ANNUAL REPORT

Contract Number: 03-5-022-55

Research Unit Number: 250

Task Order Number: 11

Reporting Period: April 1, 1977 to March 31, 1978

Number of Pages:

MECHANICS OF ORIGIN OF PRESSURE RIDGES, SHEAR RIDGES
AND HUMMOCK FIELDS IN LANDFAST ICE

Lewis H. Shapiro
Howard F. Bates
William D. Harrison

Geophysical Institute
University of Alaska
Fairbanks, Alaska 99701

March 31, 1978

TABLE OF CONTENTS

Page

I.	SUMMARY OF OBJECTIVES, CONCLUSIONS AND IMPLICATIONS	
II.	INTRODUCTION	
	A. General Nature and Scope of Study	
	B. Specific Problems	
	C. Relevance to Problems of Petroleum Development	
III.	CURRENT STATE OF KNOWLEDGE	
IV.	STUDY AREA	
V.	SOURCES, METHODS AND RATIONALE OF DATA COLLECTION	
VI.	RESULTS	
VII.	DISCUSSION	
	SECTION 1	
	II. THE MODEL	
	III. SYMBOLS USED	
	IV. VIBRATION OF FLOATING ICE	
	V. DISCUSSION	
	SECTION 2	
	I. INTRODUCTION	
	II. FORMULATION OF THE SOLUTION	
	III. ILLUSTRATIVE EXAMPLES	
	IV. DISCUSSION	
	SECTION 3	
VIII.	CONCLUSIONS	
IX.	SUMMARY	
	REFERENCES	

I. SUMMARY OF OBJECTIVES, CONCLUSIONS AND IMPLICATIONS

The present stage of this project has two objectives. The first is to extend the study of overriding and ridging along the beach at Barrow during break-up. This work is important for OCS development because break-up is a time of extreme hazard from potential override of installations by the ice sheet. This results from the increased mobility of the ice sheet during this time of year, coupled with a general warming of the ice sheet which increases its ductility and therefore, its ability to flex and glide up inclined surfaces. The study is directed toward understanding the motions and failure mechanisms of the ice sheet during break-up, as well as determining the meteorological conditions and the magnitudes of the stress fields which drive the motion. During the past year, a set of measurements of the coefficients of static and kinetic friction between the ice and typical beach gravels were made. This permitted a set of calculations to be made regarding the stress required to drive the ice sheet up the beach; this calculation has been done using data acquired from the field study of the 1975 episode of override of the beach at Barrow as a model. Additional calculations of driving stresses for that same episode have also been made using a modified form of Parmerter and Coon's (1973) kinematic model of pressure ridging, which accounts for grounding of the ridge keel. The results are in good agreement, and indicate that the maximum distributed stress along the edge of the fast ice during the movements probably did not exceed 60 KPa (about 10 psi) and were possibly lower.

The second phase of the study is an investigation of the relationship between long-period vibration of the ice sheet and the occurrence of relatively high levels of compressive stress. As described in the last annual report, these have been observed on several occasions and thus provide the potential for developing an early warning system for the build up of high stresses in the ice. The study of this phenomenon involves three steps. The first is a theoretical study of the types of long period waves which can propagate in the ice-water system. This is done by considering the impulse response of a perfectly elastic plate floating on a fluid. The solution indicates that long period gravity waves can indeed propagate in the system. The second step involves the introduction of small energy losses by permitting the ice sheet to be imperfectly elastic. This provides information on the amplitudes of the waves, and indicates that the onset of long period waves may be associated with (relatively) large amplitudes of vibration. The studies leading to these conclusions are given below.

In the third stage, the study will be extended to the case of viscoelastic plates which will permit the association between high amplitudes and long period waves to be tested. This work will be done during the next reporting period.

II. INTRODUCTION

A. General Nature and Scope of Study

This project is concerned with the mechanisms and processes involved in the deformation of landfast ice, including ridging and hummocking and the forces associated with these. Further, interaction of the ice with the sea floor and the shoreline is also being considered.

The initial phase of the project was directed toward the study of ridges which formed in the field-of-view of the University of Alaska sea ice radar system at Barrow. However, in the two field seasons during which the project has been active, no suitable ridges developed for which the motion of the ice at the time of formation could be determined. Thus, this phase of the program has lagged. However, it has been possible to observe two episodes of overriding of the beach by the ice sheet during break-up, and the study of the process has been actively conducted. The importance of potential overriding of structures, barrier islands, and beaches by the ice sheet is recognized as a significant hazard to OCS development, and this study will contribute towards providing information with which to evaluate the associated hazards. Much of the future effort on the project will, therefore, be directed toward that problem.

During the course of other studies, observations were made of the occurrence of long-period vibrations of the ice sheet in association with rising levels of compressive stress. The background was described in the last annual report of the project. A theoretical analysis of the problem is currently in progress for the purpose of analysing the possible relationships between these vibrations and the occurrence of high stresses. Additional field measurements are planned, but ice conditions during the current field season do not appear to be suited to this purpose.

Finally, a cooperative project to study ice gouging in the Barrow area has been initiated with P. Barnes of the U.S.G.S. The purpose of the study is to gather data on the rate of formation of gouges in the sea floor through repeated side-scan sonar surveys. The University of Alaska sea ice radar system will be utilized to monitor ice movement in the study area to aid in interpretation of the sonar data.

B. Specific Objectives

The specific objectives of this project are:

1. To develop an understanding of the processes involved in deformation of the landfast ice sheet in general, and specifically, during the break-up period when the override hazard is most severe.
2. To investigate the relationship between the occurrence of long period vibrations in the ice sheet and high compressive stress levels, in order to determine whether such an association might be useful as an early warning system for potential ice movement.
3. To provide ice motion information for use in interpretation of data regarding the rate of formation of gouges in the sea floor.

C. Relevance to Problems of Petroleum Development

All three phases of this project are directly relevant to the design of offshore structures for OCS development and to the safe conduct of related operations. Potential override by the ice sheet is a recognized hazard in all phases of exploration and development in the offshore area of the Beaufort Sea coast, and the state of the ice during the break-up period makes this a particularly hazardous time. During break-up the ice sheet is relatively thick and mobile. In addition, when warm, the ice is ductile, in contrast to its brittle nature during the colder months, and this ductility gives the ice the ability to bend through relatively large angles without failing. Thus, an ice sheet which, in winter, would tend to fracture and ridge or pile after relatively short movement up a ramplike surface, may be driven for large distances up such an incline when it is ductile. It is therefore important to understand the nature of the motion which can be anticipated during break-up, and the likely results of the interaction of the ice in its ductile state, with structures, beaches, or barrier islands.

Attempts have been made by industry to develop sensors which can be used to provide early warning of impending ice motion in the vicinity of a structure. The study of ice vibrations in progress under this project may prove to be a relatively simple and inexpensive method for accomplishing this. In addition, the study may aid in understanding the mechanism of stress transmission through the ice sheet.

Finally, the hazard that gouging of the sea floor presents to offshore operations is well-known and additional studies of the rates of formation of gouges, such as are being done under this project, are required in that area.

III. CURRENT STATE OF KNOWLEDGE

The current state of knowledge regarding the problems above has been reviewed in previous annual reports of this project. Background regarding the vibration study is introduced as required in the following sections.

IV. STUDY AREA

The site of most of the field work is the Naval Arctic Research Laboratory at Barrow, where the University of Alaska sea ice radar system is located. Field studies are done in the field-of-view of the radar so that details of the ice motion related to the features being examined are known.

V. SOURCES, METHODS AND RATIONALE OF DATA COLLECTION

Data for this project comes from field study, from interpretation of the radar data, and from side-scan sonar surveys. Details are given in previous annual reports.

VI. RESULTS

During the past year, two studies related to the association of the long period vibrations with high compressive stresses have been completed, and these are presented in the following two sections. In addition, a series of measurements of the coefficients of both static and kinetic friction between ice and beach gravel were made, and these results have been used to calculate the stresses involved in driving the ice sheet up the beach at Barrow in July, 1975. The results of these calculations are comparable to the forces required to form the ridges along the beach which also developed at that time. The latter forces were calculated from a modified version of the kinematic model of pressure ridging presented by Parmerter and Coon (1973). These results are given in the third section below.

VII. DISCUSSION

SECTION I

The Propagation of Long Period Waves in Floating Sea Ice

by

Howard F. Bates and Lewis H. Shapiro

This study is based upon a series of observations of vibrations of landfast and drifting ice sheets which appear to be associated with rising stress levels in the ice. The phenomenon was first observed in July, 1975, when the landfast ice sheet was driven ashore at Barrow, overriding the beach and forming ridges along the shoreline. For several hours prior to the movement of the ice a bubbler tide gauge operating on the sea floor under the ice, recorded vibrations of the ice sheet with amplitudes of a few centimeters and an apparent period of about ten minutes. That the ice was indeed vibrating was independently verified by examination of 8 mm time-lapse motion pictures of the ice taken at the time. The tide gauge record indicates an increase in the amplitude of the vibration until the bubbler was destroyed by the movement of the ice.

Direct measurements of rising stress levels in the ice sheet, associated with vibrations with the above period were made at Barrow in April 1976. In that example, sinusoidally varying stresses superimposed on a rising stress curve were recorded by an array of stress transducers embedded in the ice approximately 100 meters from a tide gauge installation. At that time the tide gauge, (also a bubbler gauge, resting on the sea floor) was indicating vibrations in phase with those on the stress transducers emphasizing the correspondence between the two events.

An array of stress transducers installed north of the barrier islands in the Prudhoe Bay area during the spring of 1976 also recorded similar events (Nelson, et al, in press), although these are unsupported by tide gauge records.

Finally, numerous examples of vibration of drifting ice sheets as a precursor to movement have been recorded by the University of Alaska sea ice radar system at Barrow. Unfortunately, frequency information cannot be extracted from these data in a simple manner.

Based upon the above, it is reasonable to assume that at least some cases of vibrations of floating ice sheets with periods of the order of ten minutes are associated with rising stress levels in the ice. If verified and understood, observations of vibrations may prove to be a simple and efficient method of predicting high stress levels in the ice around off-shore structures. The present work is directed toward that end.

Our basic premise is then, that if long period waves do indeed accompany high compressive stress in the ice, then by monitoring wave motion under the ice sheet, one can provide advance warning of possible ice motion when the wave amplitude at some period passes some critical amplitude level. The goal of the theoretical study is to understand the physics of the situation well enough to determine whether the suggested technique provides a valid early warning for high stress levels in the Arctic ice.

There are a number of steps needed to study this problem. The first is to determine what waves are possible in the ice at the long periods of interest. This factor is explored in this section by examining the impulse response of a perfectly elastic plate floating on a perfectly compressible fluid. The solutions of that formulation provide the characteristic frequencies of those gravity waves that can possibly propagate. From that result it is concluded that long period waves are indeed possible, and that they can be identified as two types of gravity waves. That is about as far as the analysis of this solution can be carried, because amplitude information is not obtainable with the theory derived as above when losses are not considered.

The next step is to examine the problem that includes small energy losses due to an imperfectly elastic plate floating on perfectly compressible water. The first phase of this study has also been completed and is reported in the next section. It is found that for small amplitude waves, the flexural gravity mode (periods near 10 s) predominates. However, for large amplitude waves, it is found that the pure gravity mode (periods greater than 500s) may predominate. Thus, it is concluded that as the stress in the ice increases, thereby increasing the wave amplitude, the period of the predominant wave may change from about 10 s to about 500 s. If this occurs, such a switch in frequency of the dominant wave would provide an excellent means of experimentally determining when the stress level passes some predetermined level--in this case the threshold value for the mode-frequency switch.

For the study above small but undetermined losses were introduced into the system. The next step would be to use viscoelastic plate theory to derive the loss coefficients theoretically in terms of the physical parameters of the system; the assumption made here is that the losses in the system occur primarily in the ice. From these values, the mode-switching level would be derived. Another important feature to be derived from this third phase study is the non-linearity (variation with frequency or amplitude) of the loss terms,

because that variation might explain why the periods of the long period waves has been found to form strong, relatively narrow spectral lines in the 5 to 20 min range, as was noted in the last annual report. While one explanation of the observed line spectra is that they result from the boundary conditions on the sheet (analogous to the line spectrum resulting for example from a vibrating rod), the answer might also lie in some non-linearity of the loss coefficients that produces quasi-resonant peaks.

The final step of the study would be to compare theoretical and observed results so that the experimental validity of the technique could be proved. Part of the overall project will be to devise and carry out experimental measurements of the wave amplitudes and frequencies, and the accompanying stress levels.

II. THE MODEL

The problem to be examined here is that of an infinite elastic sheet of sea ice of constant thickness floating on sea water of constant depth. In this section the ice and water are considered to be lossless. It will be shown that the coupling between sea and ice is a buoyant or Hooke's Law force. Thus, the floating ice acts mathematically as though it were an elastic plate supported by an elastic foundation, thereby simplifying the visualization of the problem.

Instances of observed long-period waves in the ice-sea system in the University of Alaska study occurred when the ice was known to be under compressive stress accompanied by strong local winds. Hunkins (1962) noted that the wind generally exceeded 5 m/sec when he recorded long period waves. Thus, for the model a compressive stress due primarily to wind will be assumed. The coupling between wind and ice is assumed such that a wind of 5 m/sec acting over 100 km of 1.5 m thick ice produces a lateral pressure of about 3.5 kPa while a 10 m/sec wind acting over 250 km produces a pressure of 35 kPa.

The waves in the ice-sea system contain far more energy than could be coupled directly from wind to ice. Thus, we suggest that the energy is introduced into the system by the impulsive breaking of the ice during ridging accompanying compressive stress. Calculations show that the power flow necessary to supply the energy in waves of a few centimeters amplitude is a relatively small fraction of the total needed to build, for example, ten average pressure ridges spaced over 100 km for a wind with velocity 5 m/sec. The power flow in the waves is predominantly in the water rather than in the ice sheet.

The method of solving the problem of the vibrating ice sheet is to find the impulse response (Green's function) for the lossless vibrating plate, assumed to be loaded by a laterally compressive stress and by the water-ice coupling. The solution sought is that for a horizontally-travelling, transverse gravity wave whose surface of constant phase is a vertical plane. The flexural displacement of the plate is assumed to be sinusoidal vertically; hence, the plate-water interface is a sinusoidal cylinder, upon which Bernoulli's Law is evaluated to find the coupling between sea and floating ice.

The Laplace Transform is used to obtain the dispersion relation for the floating plate. The root-locus method from automatic control theory is used on the dispersion relation to determine the behavior of the impulse response. The impulse response is sought because, through the use of the superposition integral and any desired boundary and initial conditions, the impulse response (Green's function) provides the solution for any arbitrary driving function. Thus, the impulse response, or Green's function solution, presented here is sufficient to show the general behavior of plane waves propagating in a floating ice sheet; calculating the impulse response seems particularly appropriate because the excitation postulated to exist is a series of impulses in time and space due to ice breaking during the ridging process.

III. SYMBOLS USED

The symbols used in this paper are listed below. SI units are used.

ϕ	Velocity potential	c	Speed of sound in water
ω	Angular frequency	λ	Wave length
v	Phase velocity	f	Frequency
α	Attenuation constant	g	Acceleration of gravity
$s=\alpha+j\omega$	Laplace transform variable	d	Water depth
$k=\frac{\omega}{v}$	Propagation constant	D	Flexural rigidity of ice
ρ	Density	σ	Poisson's ratio
h	Ice thickness	n	Vertical displacement
S_x	Laterally compressive ice stress	E	Young's Modulus

IV. VIBRATION OF FLOATING ICE

The first step is a brief review of the classical derivation of small amplitude, irrotational gravity waves in the sea. The water is assumed to be compressible. The subscript w is used as needed to indicate quantities that pertain only to the water. Because the motion is irrotational, the motion can be derived from a potential function. Classically, the velocity potential ϕ has been used, such that (e.g. Lamb, 1945; Stoker, 1957)

$$\vec{\nabla}\phi = \dot{\vec{X}}_j \quad (1)$$

The starting point for the derivation of water waves is the wave equation [e.g. Eq. 1.35, p. 12, Meyer and Neumann, (1972)] for the velocity potential in a perfect (lossless) fluid.

$$\frac{1}{c^2} \frac{\partial^2 \phi}{\partial t^2} = \nabla^2 \phi \quad (2)$$

A substantial simplification is possible because we know the desired solution a priori. The solution sought is the dispersion relation for small amplitude sinusoidal travelling waves. The waves are assumed to be plane waves; that is, a surface of constant phase is a plane, taken in this case to be normal to the x_1 -axis. The original three-dimensional coordinate system (x_1 and x_3 horizontal, and x_2 vertical) therefore reduces to the two-dimensional system of x (horizontal) and y vertical.

Furthermore, because a sinusoidal travelling wave solution is sought for the plate displacement η , the time and horizontal coordinates are related and can be combined as follows:

$$\eta = \eta_0 \cos \omega \left(t - \frac{x}{v} \right) = \eta_0 \cos \omega z \quad (3)$$

The argument z is the same argument used for the retarded vector potential of electromagnetic field theory. The derivation using the retarded wave function greatly simplifies solving the problem, because it is reduced by one dimension.

When the above simplifications are made, (2) reduces to

$$\frac{\beta^2}{v^2} \frac{\partial^2 \phi}{\partial z^2} = \frac{\partial^2 \phi}{\partial y^2}, \quad \beta^2 = 1 - \frac{v^2}{c^2} \quad (4)$$

Because waves with a vertical plane of constant phase are sought, the independent variables in (4) are separable, such that,

$$\phi(z, y) = Z(z) Y(y) \quad (5)$$

Only forward propagating waves (i.e. positive z) are desired, so the function $Z(z)$ is assumed to be of the form

$$Z = \sin \omega z \quad (6)$$

Combining (4), (5) and (6) yields

$$\frac{d^2 Y}{dy^2} - \beta^2 k^2 Y = 0 \quad (7)$$

The solution to (7) for a vertical velocity of zero at the bottom of the sea of depth d and for a sea with sinusoidal surface displacement $\eta(z)$ is

$$\phi = \frac{\cosh k\beta(y+d)}{k\beta \sinh k\beta d} \frac{d\eta}{dz} \quad (8)$$

Bernoulli's Law must be satisfied as a boundary condition at the water surface S. If the non-linear velocity term is dropped, Bernoulli's Law is

$$\frac{p}{\rho_w} = - \frac{\partial \phi}{\partial t} - gy \quad \text{on } S \quad (9)$$

To obtain ordinary gravity waves in the free-surface sea, the surface pressure is taken to be constant. The classical technique is to evaluate the potential function on the half-space $y=0$. This leads to an apparent problem with the bouyancy term, so the technique used in the past has been to evaluate the time derivative of (9). Thus at $y=0$ for constant pressure,

$$0 = \left[\frac{\partial^2 \phi}{\partial t^2} + \frac{\partial}{\partial t} \left(\frac{p}{\rho} \right) + g \frac{dy}{dt} \right]_{y=0} = \left[-\omega^2 \phi + g \frac{\partial \phi}{\partial y} \right]_{y=0} \quad (10)$$

Both terms on the right of (10) can now be meaningfully evaluated at $y=0$. The result is the usual dispersion relation, modified slightly for the compressibility of the fluid, for the phase velocity of gravity waves in open water,

$$v_w^2 = \frac{g}{k} \tanh \beta kd \quad (11)$$

The phase velocity in (11) is a monotonically increasing function for increasing wavelength. This feature will be considered again in Part IV.

The necessary equations for sea waves are developed above. Next, those for the ice sheet are obtained. The subscript i is used where needed to denote quantities that refer only to the ice.

The ice sheet is assumed to be a thin elastic plate of infinite extent. The equation of motion for the vertical displacement of a lossless elastic plate is (Skudrzyk, 1968)

$$D \nabla^4 \eta + \rho_i h \frac{\partial^2 \eta}{\partial t^2} = p_j \quad (12)$$

For this problem the loading pressure p_j is assumed to be composed of two parts: (1) the waves propagating in the water couple a vertical pressure onto the plate, and (2) the ice sheet is under lateral compression. The coupling pressure between ice and water is given by the term in the left brackets in (10). Thus, from (10) the pressure of the water on the ice is

$$p_1(z) = \int (-\rho_w \omega^2 \phi + \rho_w g \frac{\partial \phi}{\partial y}) dz \quad (13)$$

The method to this point is essentially that used by Ewing and Crary (1934) to solve the problem of the propagation of elastic waves near the speed of sound in floating ice. As discussed in Section IV, however, it is not clear that the gravity wave theory developed by this technique is applicable to elastic waves near the speed of sound.

When (8) is combined with (13) and the two terms are evaluated on the half space at $y=0$,

$$p_1(z) = - \left(\rho_w g - \frac{\rho_w \omega^2}{k \beta \tanh k\beta d} \right) \int \frac{d\eta}{dz} dz . \quad (14)$$

The pressure is obtained by integrating (14), defining p_0 as indicated and using (11) to bring in the phase velocity for free-surface water waves as a parameter:

$$p_1(z) = - \rho_w g \left(1 - \frac{v^2}{v_w^2} \right) \eta = - p_0 \eta . \quad (15)$$

It is important to note here that the free-surface phase velocity v_w enters merely as a parameter and is not a physical quantity in the ice covered sea.

According to (15), there is no pressure between the ice and the water when the phase velocity of the wave in the ice exactly equals that for free-surface water at the same wave length. This conclusion is reasonable because, when the velocities are exactly equal, both the water and the ice are separately vibrating at exactly the same frequency and wavelength; in that event the system would be in lossless mechanical resonance, and the coupling pressure would indeed vanish (except for a constant buoyant force that does not affect wave propagation).

Before proceeding further, let us digress a bit. Let us consider that the wave in the ice has a slightly lower phase velocity than the gravity-wave phase velocity in free-surface water. When the difference Δv in phase velocities is small, the pressure due to the ice-sea coupling is approximately

$$p_1 = - \frac{2\rho_w g}{v_w} \eta \Delta v . \quad (16)$$

Such a pressure is proportional to the displacement, so that it is in effect a Hooke's Law force. The floating ice sheet can thereby be thought of as an elastic plate on an elastic foundation as an aid in visualizing the behavior of the system. In this model the elastic constant would vary as the difference between phase velocity of the ice and that for free surface water at the same frequency.

The second part of the driving force is the loading component normal to the sheet due to lateral compression. For a constant compressive force parallel to the x-axis, the component of pressure p_2 acting to produce vertical motion is [e.g. Eq. 6.7a, Jaeger (1964)].

$$p_2 = S_x \frac{\partial^2 \eta}{\partial x^2} . \quad (17)$$

The lossless floating-plate equation of motion for a unit impulsive driving force therefore becomes, for plane travelling waves propagating parallel to the x-axis:

$$\frac{\partial^4 \eta}{\partial x^4} + \frac{\rho_i h}{D} \frac{\partial^2 \eta}{\partial t^2} - \frac{S_x}{D} \frac{\partial^2 \eta}{\partial x^2} + \frac{p_0}{D} \eta = \frac{p_0}{D} \delta(t, x) . \quad (18)$$

The first step in our solution of (18) is to transform it into an ordinary differential equation representing a forward-travelling plane wave with vertical displacement. Making the variable change indicated in (3) accomplishes this task.

$$\frac{d^4 \eta}{dz^4} + \frac{\rho_i h v^4 - S_x v^2}{D} \frac{d^2 \eta}{dz^2} + \frac{p_0 v^4}{D} \eta = \frac{p_0 v^4}{D} \delta(z) . \quad (19)$$

A digression into the mathematics of the problem is in order at this point. Because (18) is a fourth order partial differential equation, the impulse response without boundary conditions has four infinite sets of wave functions as solutions; thus, the impulse response has four infinite sets of characteristic frequencies or eigenvalues associated with it. Equation (19), being an ordinary differential equation, has only four wave functions as a solution. However, these four wave functions depend upon the phase velocity of the wave, a parameter introduced to reduce (18) to (19). Because each set of possible phase velocities is an infinite set, each of the four wave functions of (19) has, in fact, an infinite set of characteristic frequencies. Thus, the wave-function solution of (19) is as general as is that of (18): in the absence of boundary conditions, the impulse response consists of four infinite sets of wave functions.

A simplification of (19) is possible. As noted above, the compressive stress S_x varies from approximately 3.5 kPa for a 5 m/sec wind acting over 100 km fetch, to 35 kPa for a 10 m/sec wind acting over a 250 km fetch. However, large though these numbers may be, considered relative to the inertial component in (19), the compressive stress term is small enough that it does not significantly modify the equation of motion of the sheet. Therefore the quantity γ is defined such that

$$\gamma^2 = 1 - \frac{S_x}{\rho_i h v^2} . \quad (20)$$

For reasonable values of the phase velocity and for the range of stress values cited above for 1.5 m thick ice,

$$0.90 < \gamma < 0.97 \quad .$$

For numerical evaluation in the remainder of this work the average value $\gamma = 0.94$ will be used and the velocity dependence of the term will be ignored.

Even though (19) is readily solved as it stands, Laplace Transform analysis will be used here because it allows the application of stability analysis from automatic control theory. The Laplace Transform of (19) is given below for the case of zero initial conditions; (the result is perfectly general because any initial conditions can be accounted for in the superposition integral.)

$$(s^4 + \frac{\gamma^2 v^4 \rho_i h}{D} s^2 + \frac{p_0 v^4}{D}) H(s) = \frac{p_0 v^4}{D} \quad , \quad (21)$$

where the wave function solution is the inverse Laplace transform of $H(s)$:

$$n(z) = L^{-1} [H(S)] = A_1 e^{s_1 z} + A_2 e^{s_1^* z} + A_3 e^{s_2 z} + A_4 e^{s_2^* z} \quad . \quad (22)$$

The last equation reflects the result that the inverse Laplace Transform is the sum of residues evaluated at the zeroes (eigenvalues) of (21), i.e. the poles of the impulse response $H(s)$. Also reflected in (22) is the result that two of the eigenvalues s_i^* are complex conjugates of the other two s_i .

For simplicity, the polynomial in s in (21) is defined as $N(s_i)$,

$$0 = N(s_i) = s_i^4 + \frac{\gamma^2 v^4 \rho_i h}{D} s_i^2 + \frac{p_0 v^4}{D} \quad . \quad (23)$$

The eigenvalues s_i can be readily found with the aid of the quadratic formula because (23) is a biquadratic. However, before doing that, it is enlightening to use stability criteria of automatic control theory to study the impulse response.

First, we note that the Hurwitz criterion [e.g. Ch. 6 Melsa and Schultz (1969)]--discussed further in Section IV--requires that p_0 be a positive quantity if the solution of (21) is to be stable, i.e. physically possible. Thus p_0 must be non-negative because the ice-covered sea is a passive system and unfounded wave solutions cannot exist. The implications of this point are discussed further in the last part of this section. Physical solutions exist only for those frequencies for which the phase velocity $v(\omega_i)$ in the ice-sea system is less than the corresponding phase velocity $v_w(\omega_i)$ for gravity waves in free-surface water at the same frequency ω_i . Physically, the case of a negative p_0 implies a negative bouyant or Hooke's Law force. Consider, for example, a mass suspended on a spring. A negative Hooke's Law force implies that if the mass is pulled downward, the spring responds with a downward force to move it further, instead of opposing the motion with an upward force as a real spring would do. The response of such a system clearly grows without bound, is thereby defined as unstable, and is not physically possible for passive linear systems.

For a floating ice sheet there are two real frequencies (for which the variable s is imaginary) at which the coupling pressure is zero--at zero frequency and at the non-zero resonant frequency. The hydrostatic buoyancy force is neglected here because it does not affect the impulse response of the system. This result, plus the behavior of the characteristic frequencies as the pressure varies, is shown directly using the root-locus method of automatic control theory [e.g. Ch. 7, Melsa and Schultz (1969)] described below.

The root locus of $N(s_i)$ is the locus plotted in the complex s -plane of all of the zeroes of $N(s_i)$. There is one branch of the plot for each possible root. In the case at hand there are four roots, so four branches exist; two are the mirror image about the real axis of the other two.

The function $M(s_i)$ is derived from $N(s_i)$ such that for some parameter K in $N(s_i)$,

$$N(s_i) = 0 \rightarrow M(s_i) + K = 0; \quad (24)$$

then for each eigenvalue s_i ,

$$M(s_i) = -K = \underline{K/180^\circ}, \quad (25)$$

where the usual phasor notation (modulus/argument) has been used. A root-locus plot of $N(s_i)$ is therefore the plot of all points in the s -plane where

$$\arg M(s_i) = 180^\circ. \quad (26)$$

Each branch of the root locus begins at a zero of $M(s_i)$ and ends at a pole of $N(s_i)$ (in this example at $s_i = \infty$). (The actual construction of a root-locus plot is easily accomplished using a digital computer and a number of rules that can be found in any modern text on control theory.) For the problem at hand (24) is manipulated to yield:

$$M(s_i) = \frac{D}{v^4} s_i^2 \left(s_i^2 + \frac{v^4 \gamma^2 \rho_i h}{D} \right) = p_0 \underline{/180^\circ}. \quad (27)$$

The starting point for each branch is a zero of (27), for which $p_0 = 0$. The two starting values in the upper half-plane are

$$s_i = j0, j\omega_r, \quad (28)$$

where the resonant frequency ω_r has been defined as

$$\omega_r = v_w^2 \gamma \sqrt{\frac{\rho_i h}{D}}. \quad (29)$$

The mirror image in the lower half of the s-plane is now ignored, and only the two branches of upper half-plane eigenvalues will be discussed. One branch starts at ω_r on the real frequency (imaginary) axis and extends downward [that this branch cannot extend upward is shown after (30) is derived], while the other starts at zero and extends upward along the real frequency axis. The two branches meet at the breakaway frequency ω_b , as shown in Figure 1 and then branch out into the complex s-plane. Each point s_i on a branch represents one possible eigenvalue of (22). Thus, the root locus plot in Figure 1 is a graphical representation of all of the possible characteristic frequencies of (19). As noted below, wave function solutions to (19) exist only for eigenvalues on the imaginary axis (real frequency) in Figure 1; where the root-locus plot does not extend, no wave function solutions can exist. Thus stability analysis presents a simple way of finding the frequencies of those wave solutions that exist, as well as the range of frequencies for which wave solutions do not exist. As noted in the next part of this section, this latter point has apparently not been considered by previous workers.

Each positive value of p_0 uniquely determines one point s_i on each branch. As p_0 increases, the two eigenvalues move toward each other, until at the breakaway frequency they coalesce. For values of p_0 greater than the breakaway value, one of the resulting eigenvalues lies in the right half plane, so that it has a positive real part. This causes one wave solution in (22) to grow exponentially without bound, thereby violating energy conservation. Thus, a maximum pressure p_0 exists, above which no waves are possible.

In summary, therefore, the only physically possible solutions are those for eigenvalues lying on the real frequency axis between the resonant frequency and the origin. Hence, the range of possible pressures has an upper limit, thereby establishing a limit on the possible range of phase velocities.

Figure 1 contains a root locus plot of $N(s_i)$ as a function of the coupling pressure for specific values of the system parameters. The plotting of Figure 1 required only that two quantities-- ω_b and ω_r --be calculated. The rest of the plot was obtained by using the general rules of the root locus method.

The easiest to obtain of these two quantities is the resonant frequency, at which the wave phase velocity equals the free-surface value. The frequency and the phase velocity are unknown, so the free-surface dispersion relation (11) and the defining relation between frequency, phase velocity and wave-lengths are solved simultaneously with (29) by an iterative process.

To produce illustrative results for this paper, the following values were used:

$$d = 50 \text{ m}, \quad h = 1.5 \text{ m}, \quad E = 4.0 \times 10^8 \text{ Nm}^{-2}, \quad \sigma = 0.30,$$

$$\text{and } D = \frac{Eh^3}{12(1-\sigma^2)} = 1.25 \times 10^8.$$

From these values the following quantities were computed for resonance between sea and ice (i.e. coupling pressure zero):

$$\omega_r = 0.659 \text{ rad s}^{-1}, \quad \lambda_r = 139 \text{ m}, \quad T_r = 9.54 \text{ s} \quad \text{and} \quad v_r = 14.6 \text{ m s}^{-1}.$$

Two methods are available to find the breakaway point. On the root locus plot, the breakaway point occurs where p_0 has its largest value along the

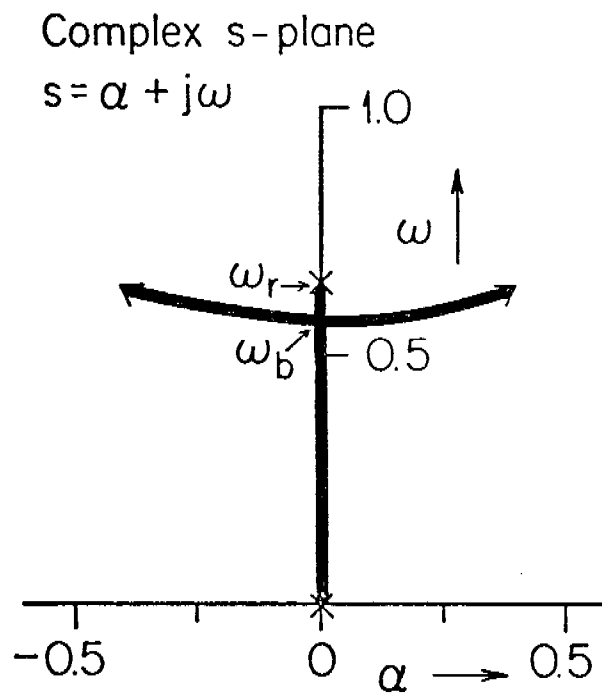


Fig. 1. Locus of characteristic frequencies of floating plate equation as the coupling pressure changes. Zero coupling is indicated by the x at one end of each branch. Physically possible wave functions exist only for those eigenvalues lying on the real frequency (imaginary) axis. The resonant and breakaway frequencies are shown. The upper branch is the flexural gravity wave branch; the lower is the pure gravity wave branch.

imaginary axis. However, because $N(s_i)$ in (23) is a biquadratic, the quadratic formula provides an easier solution. The positive (upper half-plane) eigenvalues s_i of $N(s_i)$ in (24) are:

$$s_i = j v^2 \gamma \sqrt{\frac{\rho_i h}{2D}} \sqrt{1 \pm \sqrt{1 - \frac{4 D p_0}{v^4 \rho_i^2 h^2 \gamma^4}}} \quad (30)$$

That physical characteristic frequencies above cannot exist above ω_r is shown by (30). Equation (11) shows that v_w decreases with increasing frequency, so that the maximum possible s_i in (30) is $j\omega_r$. Characteristic frequencies greater than ω_r are roots of (30) only for the case of $v > v_w$ [as Hunkins (1962) and Wadhams (1973) show]; however, such eigenvalues do not provide real solutions because physical wave functions exist only for the case $p_0 \geq 0$ so that $v_w \geq v$.

The breakaway frequency ω_b occurs where the inside radical in (30) vanishes. This condition provides two relations

$$\omega_b = v_b^2 \gamma \sqrt{\frac{\rho_i h}{2D}} \quad \text{and} \quad 4D p_0 = v_b^4 \rho_i^2 h^2 \gamma^4 \quad (31)$$

which along with (11) and the relation between wavelength, frequency and phase velocity are solved iteratively to obtain the following values:

$$\omega_b = 0.568 \text{ rad s}^{-1}, \quad \lambda_b = 178 \text{ m}, \quad T_b = 11.1 \text{ s}, \quad v_b = 16.08 \text{ ms}^{-1} \quad \text{and} \quad v_{wb} = 16.24 \text{ ms}^{-1}.$$

Because the phase velocity increases as an eigenvalue moves downward along the upper branch on the root locus plot for increasing p_0 , the possible range of values for the upper eigenvalue, subscripted u , is small compared to that of the lower eigenvalue, subscripted l . In terms of the period the ranges of the upper and lower branch eigenvalues for the values cited above are:

$$11.1 \text{ s} \leq T_l < \infty \text{ s} \quad \text{and} \quad 9.5 \text{ s} \leq T_u \leq 11.1 \text{ s}.$$

The periods above were computed for the values of the parameters noted above, and other values for the parameters might realistically have been used. However, considering the calculation just below we suggest that the values used are representative enough that choosing reasonably different values would not significantly change the results. As an example, substantial changes in the elastic modulus might be considered because the value used above is about one-tenth that which would be obtained from the measured speed of sound. [The low value was chosen to make allowance for plastic flow occurring in the ice as it flexes at the low observed frequencies.] It might be argued that during strong compressive stress, the breaking of the ice sheet during ridging may seriously decrease the elastic modulus even when averaged over a wavelength. Accordingly, Young's modulus was decreased two orders of magnitude, and the computations were made again with $h = 1.5 \text{ m}$, $\gamma = 0.94$ and $d = 50 \text{ m}$ as before. The resulting resonant parameters are

$$\omega_r = 1.443 \text{ rad s}^{-1}, \quad \lambda_r = 29.7 \text{ m}, \quad T_r = 4.36 \text{ s}, \quad \text{and} \quad v_r = 6.80 \text{ ms}^{-1}, \quad \text{and the parameters at the breakaway point are}$$

$$\omega_b = 1.242 \text{ rad s}^{-1}, \quad \lambda_b = 38.05 \text{ m}, \quad T_b = 5.06 \text{ s}, \quad v_b = 7.52 \text{ ms}^{-1}, \quad \text{and} \quad v_{wb} = 7.89 \text{ ms}^{-1}.$$

A decrease of two orders of magnitude in the elastic modulus roughly halved the possible periods T_u of the upper branch solution from $9.54 \text{ s} < T_u < 11.06 \text{ s}$ to $4.36 \text{ s} < T_u < 5.06 \text{ s}$. Thus, it is concluded that the upper branch wave solution is narrow in spectral width, and that the resonant frequency is nearly insensitive to expected changes in the elastic modulus of the ice, the ice thickness or the water depth.

V. DISCUSSION

Two infinite sets of positive characteristic frequencies were derived in Part III of this section for a stressed sheet of ice floating on sea water. One set of eigenvalues--the upper set--is confined to a small range of frequencies below the resonant frequencies, while the other--the lower set--extends from the upper set downward to zero frequency. It is instructive in identifying these two sets of eigenvalues to expand (30) in a series for small values of p_0 , take just the first two terms and use (16). The resulting two frequencies for small p_0 are

$$\omega_u = v_u^2 \gamma \sqrt{\frac{\rho_i h}{D}} \quad \text{and} \quad \omega_l = \frac{1}{\gamma} \sqrt{\frac{2\rho_w g \Delta v}{\rho_i h v_w}}$$

By making the above expansion, we are restricting the identification of the upper and lower branch wave functions to those characteristic values lying away from the breakaway point in Figure 1. These are the regions where the coupling pressure is small.

The upper branch frequencies ω_u contain the ratio of mass to flexural rigidity, the quantity that determines how an elastic plate freely vibrates. The lower branch frequencies ω_l contain no information about the elastic properties of the ice. Thus, considering only small pressures, for upper branch eigenvalues the ice sheet behaves almost as if it were a freely vibrating laterally compressed elastic plate, while for those on the lower branch the ice sheet acts as a membrane with mass but no elastic properties. The upper and lower branch wave functions for small coupling pressure therefore respectively represent flexural gravity and pure gravity waves. When the coupling pressure is appreciable, this separation is not possible and the resulting waves are a mixture of the two types.

The term 'flexural wave' used in this paper is used in the customary sense: as a wave crest passes a point, the top surface of the plate expands while the bottom surface contracts. Thus, a flexural wave is that wave for which any plane initially normal to the unflexed neutral surface in the plate will remain normal to that neutral surface as the plate flexes due to the wave. This behavior is contrasted with that of an elastic shear wave (i.e. seismic S_y wave), for which vertical planes in the unflexed material remain vertical as the wave passes.

A recent study (Wadhams, 1973) of sea waves propagating into pack ice provides experimental support for the gravity wave behavior deduced above. To show this, let us consider a semi-infinite elastic plate floating on the surface of an infinite fluid in which gravity waves propagate perpendicularly toward the plate. Waves with periods less than the resonant period cannot propagate in the ice covered sea (because p_0 is negative), so they are completely

reflected at the edge of the plate; however, due to the evanescent wave, motion at these periods extends a few wavelengths (hundreds of meters) into the plate-fluid system with a high attenuation rate. This situation is analogous to that occurring in electromagnetic wave guides at frequencies below cut-off, or outside the edge of a prism that is totally internally reflecting light.

Waves at the resonant period propagate through the free-surface--plate interface as though the plate did not exist because the same phase velocity exists on either side of the interface. Waves above the resonant period undergo a small amount of reflection that depends upon the difference in phase velocity across the interface. The usual optical transmission and reflection coefficients, based on the change in phase velocity at an interface, are directly applicable.

Thus, wave measurements made on the ice a few wavelengths behind the interface would show the following: the resonant wave would have the peak amplitude because all other waves suffer some loss of amplitude at the interface due to reflection. The evanescent waves (periods less than the resonant period) will be attenuated rapidly with distance from the interface, while those with greater periods will undergo only the small attenuation of the system (primarily bending losses in the ice).

The predictions above are satisfied by Wadhams (1973) results:

1. He reported a spectral peak near periods of 12 s.
2. For periods less than 10 s, the attenuation rate he deduced was far too great to be explained by his ice-creep model of bending losses in the ice.
3. The ice-creep model predicted the observed attenuation rate for periods greater than 10 s.

Thus, we conclude that Wadhams' results confirm the existence of a resonant period with a pass band above it and a stop-band below it with a value of 10 to 12 s as the resonant period. A value of 12 s is obtained from (29) by changing the ice thickness and/or Young's modulus a small amount from that used above--for example, $h=1.5$ m and $E = 1.2 \times 10^9 \text{ Nm}^{-2}$, or $h = 2.0$ m and $E = 6.0 \times 10^8 \text{ Nm}^{-2}$. The ice thickness used is comparable to that of Wadhams, while the elastic modulus is smaller by a factor of 5 to 10. The value $\gamma = 1.00$ was used for these computations because there would be no compression.

The root-locus plot in Figure 1 indicates that no gravity waves can exist in the ice-sea system at frequencies above the resonant frequency. The coefficient p_0 is positive only for frequencies below the resonant frequency ω_r because only there is the ice-sea system phase velocity at any given frequency less than that for free surface gravity waves at the same frequency. Thus, only below ω_r can physical solutions exist for gravity waves.

This result does not agree with those of Ewing and Crary (1934), Hunkins (1962), or Wadhams (1973) even though the techniques used are basically the same. The key to identifying the discrepancy lies in Figures 13 of Hunkins and 4 of Wadhams: each of these shows that the phase velocity in the ice covered sea exceeds that in the sea. As discussed above, that situation cannot exist physically because for such a system a finite driving force would cause an infinite displacement.

The difficulty arose because apparently the various workers just solved their quartic dispersion relations [comparable to (23)] for real roots only and discarded any accompanying complex roots without examining their effect. As feedback theory shows, unstable roots cannot be disposed of by discarding them. Rather, for a passive system such as the one discussed here, the range of unstable roots must be interpreted as the range over which real wave solutions do not exist, because physical wave solutions cannot exist for any parameter that leads to an unstable eigenvalue of the impulse response. That one of the eigenvalues is unstable for $p < 0$ is shown below. The eigenvalues of (23) are given by (30). For $p < 0$ two of the roots are imaginary (these are the two real-frequency roots found by the other workers) while the other two are real, one positive and the other negative. Thus, one of the roots lies on the real axis in the right-half of the s -plane, and the corresponding wave function is unstable. It is this root that Ewing and Crary (1934), Hunkins (1962) and Wadhams (1973) ignored when they discarded non-real roots.

The waves found above are denoted gravity waves because they are driven by gravity waves in the water, and they have the basic characteristics (i.e. phase velocity and wavelength) of free-surface water waves. Another type of flexural wave can exist in the ice--flexural elastic waves--and these waves have been examined by a number of authors in the past [e.g., Ch 6-3, Ewing, et al., (1957)]. A basic difference between these two types of flexural waves is the phase velocity (10 to 20 $m s^{-1}$ for the gravity wave and 1 to 2 $km s^{-1}$ for the elastic wave). It is these waves to which Ewing and Crary (1934) applied the gravity wave theory they derived. The applicability of the theory to elastic waves is questionable, because contrary to Hunkins' (1962) and Wadhams' (1973) results, the elastic and gravity wave branches do not connect as they indicate.

In summary, we have found two sets of travelling gravity-wave solutions for a lossless elastic plate that is laterally compressed and is floating on a perfectly compressible fluid. For small coupling pressures one set of waves represents pure gravity waves, and the other set represents flexural gravity waves. The flexural gravity waves exist over a narrow band of frequencies below the ice-sea resonant frequency, and these frequencies are relatively insensitive to changes in parameters. The lower branch gravity waves exist at all frequencies below the band of flexural waves. For small coupling pressures they are independent of the elastic properties of the ice; thus, for these waves the ice sheet acts as a non-elastic membrane with mass. No gravity waves can exist above the resonant frequency, indicating that for floating ice, the elastic and gravity wave branches are separate. This conclusion is supported by experimental results.

The lossless solutions provide considerable insight into the problem of how gravity waves propagate in the ice-covered sea. However, amplitude data--an important characteristic of the problem--cannot be obtained from the loss-

less formulation. Because the frequency response of the system is of interest, the next step is to include small losses in the equation of motion. This has been done and is reported in the next section. One interesting finding suggests that as the flexural losses in the ice increase non-linearly (as might be expected as the amplitude increases), the dominant wave may switch from the flexural gravity wave branch to the pure gravity wave branch.

SECTION 2

The Propagation of Long Period Gravity Waves in a Floating Ice Sheet

by

Howard F. Bates

I. INTRODUCTION

During times of high compressive stress in a floating ice sheet, long period waves have been observed (Hunkins, 1962). A theoretical study of the problem was discussed in the previous section, in which the ice was modelled as a perfectly elastic thin plate floating on a perfectly compressible fluid. That study provided two infinite sets of characteristic frequencies (eigenvalues) for the wave function solutions found, one of which was identified as a flexural gravity wave and the other as a pure gravity wave. However, amplitude information was not derivable because losses were neglected. The aim of the second phase of the study, reported here, is to include small losses in the problem in order that the amplitude response of the system can be investigated using stability analysis of automatic control theory.

II. FORMULATION OF THE SOLUTION

As in the lossless case, the ice sheet is assumed to be an elastic plate whose thickness is constant. The plate is assumed to be thin enough that wave propagation in one direction (i.e. a plane wave) is possible in the plate, and to contain small frictional losses of energy. The water is assumed to be of constant depth, compressible, and lossless.

The quantities derived for the fluid in the last section that are needed here are the velocity potential:

$$\phi = - \frac{v\eta_0 \text{Cosh } k\beta(y+d)}{\text{Sinh } k\beta d} \text{Sin } \omega z \quad (1)$$

the dispersion relation for the phase velocity of free-surface water waves;

$$v_w^2 = \frac{g\beta}{k} \tanh k\beta d; \quad (2)$$

and the pressure at the interface for a sinusoidal displacement;

$$p = -\rho_w g \left(1 - \frac{v^2}{v_w^2}\right) \eta_0 \cos \omega z \quad (3)$$

In the last section a purely sinusoidal wave was found to be an exact solution. Now that losses are to be included, the wave functions are no longer pure sinusoids, but rather exponentially damped sinusoids. The damping, however, is assumed to be so small that for evaluating the interface condition (3), the displacement can be represented by

$$\eta = \eta_0 \cos \omega z = \eta_0 \cos \omega \left(t - \frac{x}{v}\right) \quad (4)$$

The velocity potential can therefore be written as before,

$$\phi = \frac{\cosh k\beta(y+d)}{k \sinh k\beta d} \frac{d\eta}{dz} \quad (5)$$

so that the pressure at the interface is again written

$$p_1 = -\rho_w g \left(1 - \frac{v^2}{v_w^2}\right) \eta = -p_0 \eta \quad (6)$$

As in the lossless case the free-surface phase velocity v_w enters (6) as only a parameter; it is important to note that v_w is not linearly related to the length and the frequency of the wave that is propagating in the ice-sea system. However, even though v_w is not a physical quantity in the floating ice systems, its introduction proves useful. The manner in which the motion of the ice sheet modifies the water wave system is easily seen in (6): the wave in the ice sheet propagates at a slightly slower speed than does the free-surface wave at the same frequency.

For a lossless laterally compressed floating plate the equation of motion for vertical displacement η is for a unit impulse:

$$D\nabla^4 \eta + \rho_i h \frac{\partial^2 \eta}{\partial t^2} - S_x \frac{\partial^2 \eta}{\partial x^2} + p_0 \eta = p_0 \delta(t) \quad (7)$$

A one-dimensional (plane) transverse travelling wave solution is desired, so the transformation in (4) is applied to (7) to reduce the partial differential equation to an ordinary differential equation. The Laplace Transform of the resulting equation of motion for a unit impulse driving function is:

$$\left(s^4 + \frac{\gamma^2 \rho_i h v^4}{D} s^2 + \frac{p_0 v^4}{D} \right) H(s) = \frac{p_0 v^4}{D} \quad (8)$$

where γ is the compression term as defined in the previous section.

The Laplace variable $s = \alpha + j\omega$ is the complex frequency. The imaginary part of s is the real frequency of the wave solution, while the real part is the attenuation constant. The Laplace Transform is useful in sinusoidal wave problems because the inverse transform is automatically a wave solution to the problem. In the preceding section two wave solutions, each containing an infinite set of wave functions, were found for the impulse response (Green's function) in (8); one solution was identified as the pure gravity wave solution, while the other was termed the flexural gravity wave solution. Associated with each wave solution was an infinite set of characteristic frequencies (eigenvalues) that were real, so that the resulting wave solutions were pure sinusoids. Stability analysis was used to show that the characteristic frequencies have a maximum ω_r , above which a physically possible wave function can not exist. That maximum frequency was termed the resonant frequency of the system because at that frequency, if there were no losses in the system, the water and the ice sheet would vibrate exactly in phase with zero coupling force between them. The characteristic frequencies ω_f of the flexural gravity wave solution exceed those ω_g of the pure gravity wave solution, and the two sets of eigenvalues extend continuously below the resonant frequency to zero.

Much of the remainder of the development focuses on whether a wave solution is physically possible. To study this point, we use the stability theory devised for analyzing automatic control systems. In a control system there are sources of power (active elements) present. If positive feedback occurs in the system, the response to a finite impulse grows theoretically without bound. Such a response, termed an unstable response, is characterized by having one or more eigenvalues with positive real parts. In a real control system an unstable response is highly undesirable because it can lead to the destruction of the unit.

The floating ice is a conservative or passive system, in that once a wave is launched by an impulse, there are no active elements present to amplify the energy in the wave. In fact, the only physically possible wave functions are those that decrease as the wave propagates, because part of the wave energy is transformed into heat by friction in the ice. Such wave functions are termed 'absolutely stable' by the criteria of control theory. Unstable wave functions grow without bound and are therefore not physically possible.

Each value of phase velocity v is associated with four eigenvalues in the ice covered sea. If any one of these eigenvalues is in the right half of the s plane, then that value of phase velocity is forbidden and all four eigenvalues must be discarded. It is not permissible to discard just the unstable eigenvalue. The eigenvalues of physically possible wave functions must therefore all have negative real parts. Stability criteria from automatic control theory provide an easily applied technique for determining those eigenvalues whose real parts are negative.

The solutions to (8) are not absolutely stable. However, because they remain finite after infinite time, the solutions are conditionally stable. The Hurwitz criterion for absolute stability [e.g. Ch 6, Melsa and Schultz (1969)] that all powers of s below the highest must have positive coefficients is not satisfied by (8). Thus, terms including the first and third derivatives of the displacement must be present in (8) before absolutely stable solutions can exist. The true floating plate equation (after Laplace Transformation) must therefore be of the following form, for a unit impulse driving function and for positive a_1 and a_3 :

$$\left(s^4 + a_3 s^3 + \frac{\gamma^2 \rho_i h v^4}{D} s^2 + a_1 s + \frac{p_0 v^4}{D} \right) H(s) = \frac{p_0 v^4}{D} . \quad (9)$$

The Hurwitz criterion is a necessary condition for the system to be stable, but it is not sufficient. The Routh test [e.g. Ch 6, Melsa and Schultz (1969)] provides necessary and sufficient conditions on the coefficients of (9) for stability. For (9) to have absolutely stable solutions, the coefficients must be positive and satisfy the inequalities

$$\frac{\gamma^2 \rho_i h v^4}{D} > \frac{a_1}{a_3} \quad (10)$$

and

$$\frac{\gamma^2 \rho_i h v^4}{D} > \frac{a_1}{a_3} + \frac{p_0 v^4}{D} \frac{a_3}{a_1} . \quad (11)$$

Because (11) includes (10), (11) above is necessary and sufficient that stable solutions exist for (9).

To represent the long distance propagation of travelling waves in the ice-sea system, each wave function solution of (9) must have an eigenvalue s_j whose real part (attenuation constant) is very small compared with the angular frequency. Thus, the wanted eigenvalues of (9) lie in the left-half of the s -plane close to those of the lossless floating plate equation (8), which lie on the real frequency axis (Figure 1).

The coefficients a_1 and a_3 are unknown, and to find them requires solving the visco-elastic plate problem. That problem is to be examined as the third phase of the overall study. However, considerable insight into the physics of the situation can be obtained by using the root locus method to estimate the behavior of the eigenvalues of (9).

The root-locus method of automatic control theory provides a simple graphical way of finding the eigenvalues of a linear differential equation as a function of some parameter of the system. In the preceding section the locus of the eigenvalues was found as a function of the driving pressure between water and ice. In this section we shall examine the behavior of the eigenvalues as the loss coefficients a_1 and a_3 are varied. These results will be used to gain insight into the behavior of the existing non-linear system.

First, a digression is in order to consider the physics of the problem. The following is a simplistic explanation of the loss terms that were added to the equation of motion. In (9) the first-degree term in s corresponds to a force term that is proportional to the velocity; thus a_1 represents the coefficient of velocity dependent friction, or, as it is frequently termed for electromechanical devices with oiled bearings such as motors, viscous friction. The third derivative in the plate equation represents a measure of the deformation due to bending. Hence the third-degree term in s in (9) in a sense represents the energy transformed into heat due to the flexing of the plate. Because we require long distance propagation, the ratio of energy propagating as waves to that lost as heat must be small; hence the coefficients a_1 and a_3 must be small enough that the real part of the resulting eigenvalues is small compared to the imaginary part.

Returning to (9), the root-locus technique provides an easy way of finding the roots of the quartic equation in s represented by (9) without actually having to solve the quartic. If $N(s_i)$ is defined to be the quartic part in s in (9), the roots s_i of $N(s_i)$ are those values for which

$$N(s_i) = 0 \quad . \quad (12)$$

A polynomial function $M(s_i)$ is derivable from $N(s_i)$ such that for some non-negative parameter K in $N(s_i)$

$$\frac{1}{K} + M(s_i) = 0 \quad . \quad (13)$$

Thus, the roots s_i of $N(s_i)$ are those values for which

$$M(s_i) = -\frac{1}{K} = \frac{1}{K} \angle 180^\circ \quad , \quad (14)$$

where the usual phasor notation--modulus /argument--is used.

A root-locus plot is a plot of all of the points s_i in the s -plane such that the argument of $M(s_i)$ is 180° as the parameter K varies over all non-negative values. In general these eigenvalues are easy to find by the rules prescribed in any modern text on control theory and by digital computer.

In the problem at hand the periods for which we wish to examine the behavior of the eigenvalues for pure gravity waves are in the range of 300 to 1200 s. As noted in the preceding sections the periods of the flexural gravity waves are confined to roughly 5 to 15 s, so that the two frequencies differ by two orders of magnitude. The preceding section shows that for such a large separation between eigenvalues, the flexural gravity wave frequency ω_f lies very close to the resonant frequency ω_r . Thus, if ω_g is the pure gravity wave frequency and

$$\omega_g < 0.01 \omega_r \text{ then } \omega_f \approx \omega_r \quad , \quad (15)$$

so that if the loss rates (real part of s_i) are very small, then $N(s_i)$ can be written approximately as

$$N(s_i) = s_i^4 + a_3 s_i^3 + \omega_r^2 s_i^2 + a_1 s_i + \omega_r^2 \omega_g^2 = 0 \quad . \quad (16)$$

For the first root-locus plot the following $M(s_i)$ is derived from (16) to provide a root-locus plot as a_3 varies and the rest of the coefficients remain constant.

$$M(s_i) = \frac{s_i^3}{s_i^4 + \omega_r^2 s_i^2 + a_1 s_i + \omega_r^2 \omega_g^2} = \frac{1}{a_3} \angle 180^\circ \quad . \quad (17)$$

For small $\epsilon > 0$ (18) factors approximately as,

$$\frac{s_i^3}{[(s_i - \epsilon)^2 + \omega_r^2][(s_i + \epsilon)^2 + \omega_g^2]} = \frac{1}{a_3} \angle 180^\circ \quad (18)$$

The root-locus plot of (18) shows how the eigenvalues of (9) move in the complex s -plane as the coefficient a_3 --roughly representing heating due to flexing--varies over all possible values when a_1 --the coefficient representing roughly the heating due to velocity dependent friction--is constant.

Another way of viewing the situation is to vary a_3 while the ratio a_1/a_3 remains constant. The $M(s_i)$ for that case is

$$\frac{(s_i^2 + a_1/a_3)s_i}{s_i^4 + \omega_r^2 s_i^2 + \omega_r^2 \omega_g^2} = \frac{1}{a_3} \angle 180^\circ \quad (19)$$

When (15) holds true, (19) factors approximately to

$$\frac{s_i(s_i + \omega_1^2)}{(s_i^2 + \omega_r^2)(s_i^2 + \omega_g^2)} = \frac{1}{a_3} \angle 180^\circ \quad (20)$$

where ω_1 is defined by

$$\frac{a_1}{a_3} = \omega_1^2 \quad (21)$$

Using the Routh criterion in (11), we find that for long period waves, physically possible solutions result only when

$$\omega_r^2 > \omega_1^2 + \frac{\omega_g^2 \omega_r^2}{\omega_1^2} \quad (22)$$

III. ILLUSTRATIVE EXAMPLES

To illustrate the results of the previous section, the sample root-locus plots in Figures 2 and 3 were made for the following parameters, which are scaled such that the pure gravity wave frequency ω_g is unity.

$$\omega_r = 100, \omega_g = 1.00, \epsilon = 0.50, \omega_1 = 70 \text{ s}^{-1}.$$

The values of ϵ and ω_1 were chosen so that the figures would clearly exhibit the desired behavior. Thus, the values used are probably not realistic values for a floating ice sheet. For example, the value $\epsilon = 0.5$ violates the requirement that ϵ be small so that (17) can be factored as shown. However, the root-locus behaves so nearly the same for all $\epsilon < 0.5$ that using the high value to make a more easily understandable illustration does not invalidate the results.

The illustrations all show only the upper half of the s-plane, because the root locus in the lower half-plane is the mirror image of that in the upper half-plane. Absolutely stable solutions exist only for those eigenvalues lying in the left half of the s-plane.

There is one branch of a root-locus plot for each eigenvalue. Each branch of a root locus begins at a pole of $M(s_i)$ --denoted by an X in the figures, and ends at a zero--denoted by an O. (Some zeroes occur at infinity.) For each value of a_3 there is one eigenvalue on each branch. The technique for finding the eigenvalues corresponding to a particular value of a_3 once a root-locus plot has been obtained is to iteratively solve

$$a_3 |M(s_i)| = 1 \quad (24)$$

for each s_i on each branch. To illustrate this process, Figure 4 was plotted from (19) for $\omega_r = 100$, $\omega_g = 1.00$, $\epsilon = 0.01 \text{ s}^{-1}$. The values are plotted logarithmically in Figure 4 with the right and left half-planes joined at $\alpha = \pm 10^{-4}$. Particular values of a_3 are shown with their corresponding eigenvalue on each branch.

IV. DISCUSSION

Figure 2 shows that for fixed a_1 , real wave functions exist only over part of the range of a_3 . For a_3 near zero the upper branch is in the right half-plane, while above some larger value of a_3 , the lower branch is in the right half-plane. This behavior is illustrated for numerical values of a_3 in Figure 4 for $\epsilon = 0.01 \text{ s}^{-1}$, a value that satisfies the various size requirements. Figure 4 shows that for small a_3 , the attenuation of the flexural gravity wave is near zero, but that of the pure gravity wave is near its maximum. As a_3 increases, the attenuation of the flexural wave increases, while that of the gravity wave decreases. When a_3 is large enough that the gravity wave attenuation approaches zero, the attenuation of the flexural wave is so high that it can no longer propagate.

Figure 3 shows the effect of holding the ratio a_1/a_3 constant for $\omega_1 < \omega_r$ as a_3 is varied. In this case both gravity wave branches begin with zero attenuation, and the range of values of a_3 over which the wave functions are stable is infinite. Inequality (10) is satisfied only for values $\omega_1 < \omega_r$; the wave functions are unstable if $\omega_1 \geq \omega_r$.

Let us now consider that a_3 increases with increasing wave amplitude; that is, the heating due to bending is non-linear with amplitude. If the velocity dependent frictional losses remain linear (a_1 constant), Figures 2 and 4 describe the behavior of the gravity waves in the ice-sea system. For low amplitudes the flexural gravity wave predominates while the pure gravity wave is appreciably attenuated. As the amplitude increases, the attenuation of the flexural wave increases while that of the gravity wave decreases; thus, at some amplitude both waves propagate equally. Then, as the wave amplitude increases further, the flexural wave becomes highly attenuated while the gravity wave propagates with little attenuation.

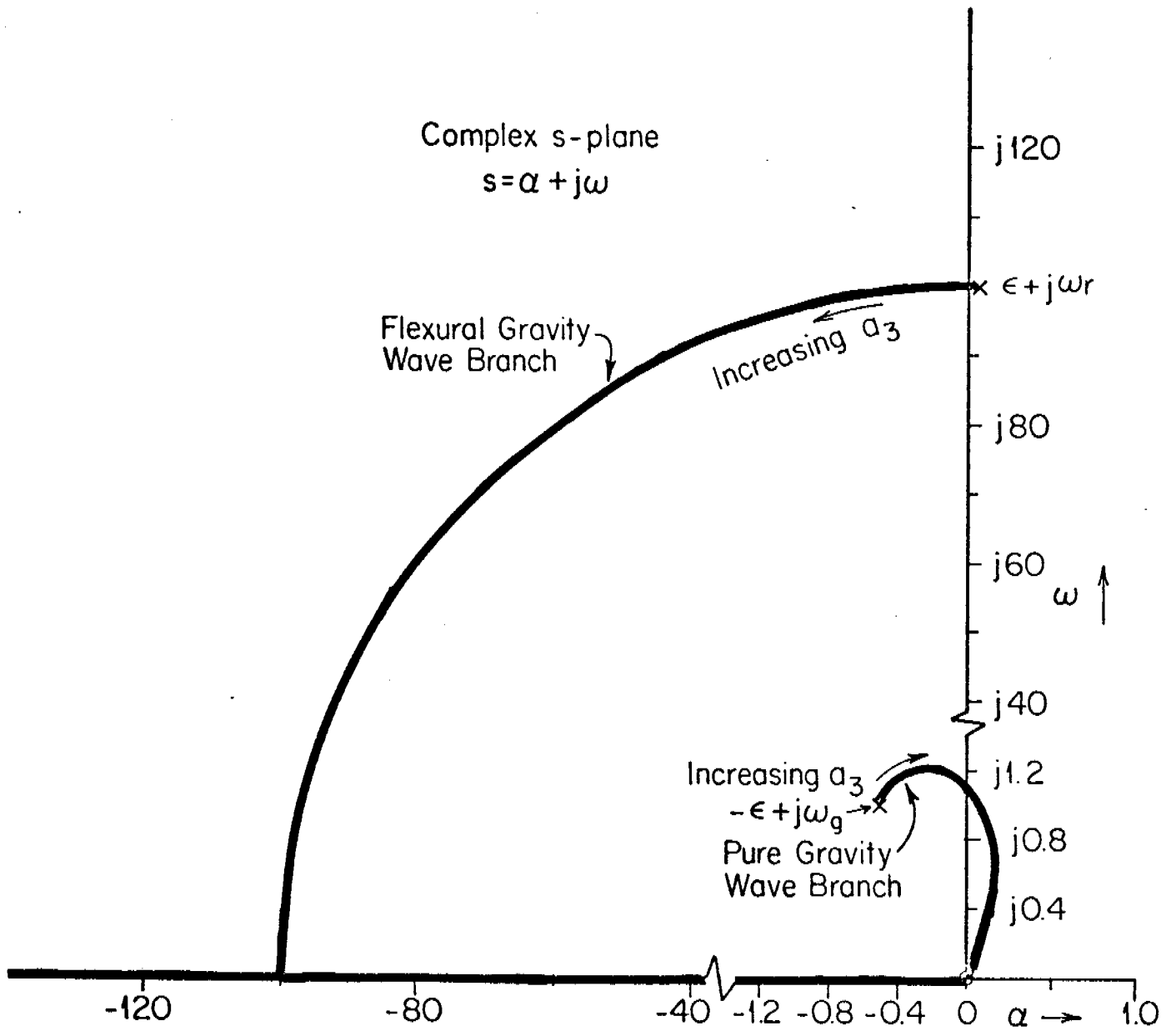


Fig. 2 Locus of characteristic frequencies of floating plate equation as the coefficient a_1 is held constant and a_3 varies over all positive values, increasing in the direction shown. Physically possible wave functions exist only for those characteristic frequencies in the left half of the s-plane.

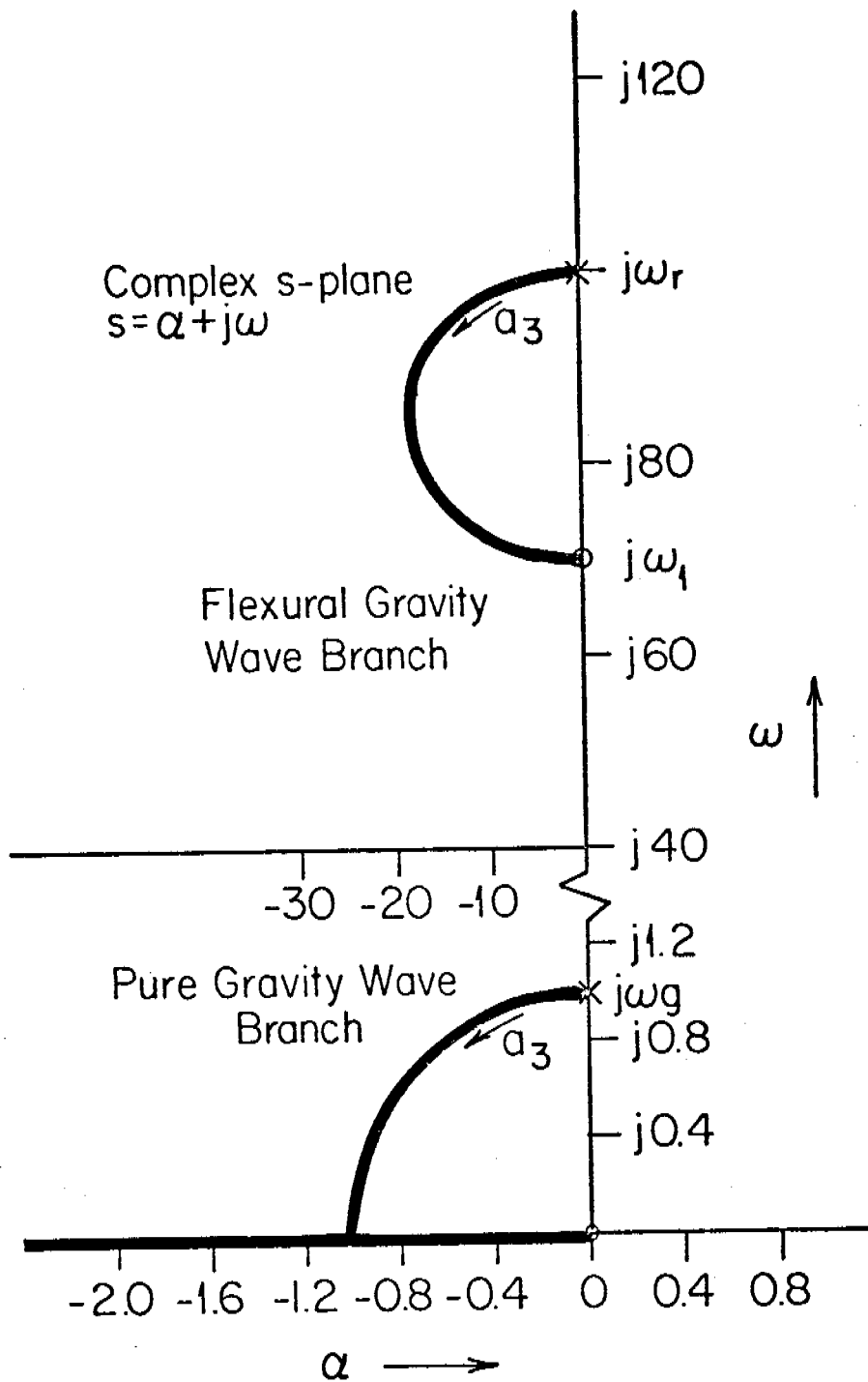


Fig 3. Locus of characteristic frequencies as the ratio a_1/a_3 is held constant and a_3 is allowed to vary over all positive values.

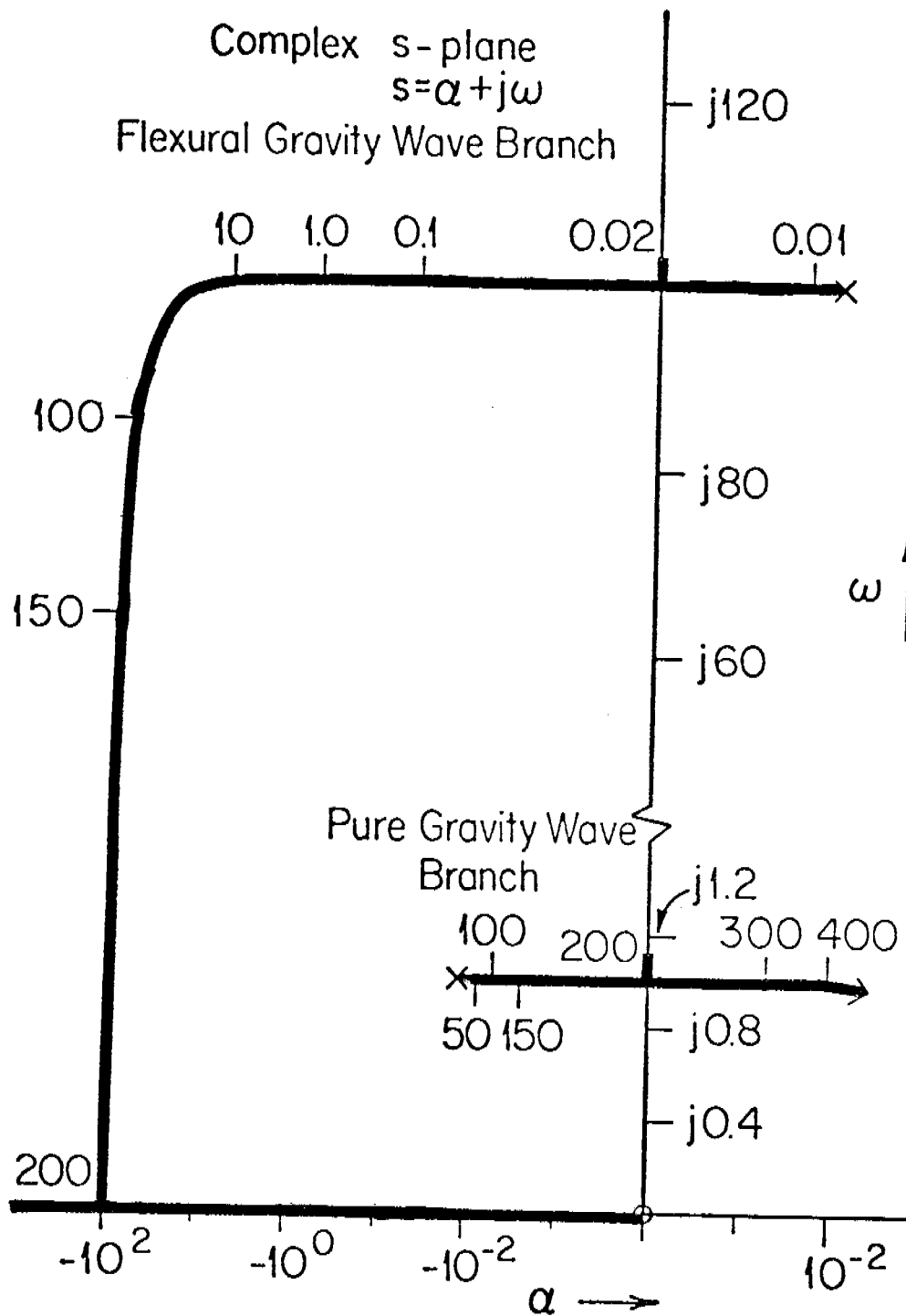


Fig. 4. Locus of characteristic frequencies for $a_1/a_3 = 1$, $\epsilon = 0.01$, and a_3 varying over all positive values. The numbers along each branch represent the values of a_3 at the indicated points. For the particular set of values chosen, physical wave functions are possible only $0.02 \leq a_3 \leq 200$. The real axis is composed of two logarithmic scales superimposed at $\alpha = \pm 0.0001$.

As a limiting case, the example above is instructive. However, it is probably not realistic to assume that one component of the heating is constant while the other increases with amplitude. Thus, another extreme would be to assume that the two increase linearly such that the ratio a_1/a_3 remains constant. (This assumption is equivalent to assuming that bending losses are more important than those from velocity dependent friction.) In this instance both branches begin with zero attenuation, but calculation shows that for $a_1/a_3 \approx \omega_1^2$, the attenuation for the gravity wave grows with increasing a_3 far more rapidly than does that for the flexural wave. Thus, for the case where the heating coefficients increase with amplitude at the same rate, the flexural wave will always dominate because its attenuation is less than that for the gravity wave.

In the real world, the truth probably lies between the above extremes. It seems likely that the loss coefficients a_1 and a_3 do indeed increase with amplitude, but that a_3 probably increases the fastest. Thus a_1/a_3 probably decreases as a_1 and a_3 both increase with wave amplitude. Calculations similar to those used for Figure 3 for other values of ω_1 show that if ω_1 decreases as a_1 and a_3 increase, the attenuation of the flexural wave grows at a higher rate than does that of the gravity wave. Thus, even though the attenuation of the flexural wave initially increases at a slower rate, as ω_1 decreases, the attenuation of the flexural wave eventually equals or exceeds that of the gravity wave. In conclusion therefore, if a_1 and a_3 increase and ω_1 decreases with amplitude, the flexural gravity wave predominates for small wave amplitudes, while for large wave amplitudes the pure gravity wave might predominate.

In summary, two gravity wave modes have been found for an infinite ice sheet floating on an infinite shallow sea. The flexural gravity wave mode is confined to an infinite set of frequencies very near but below that frequency for which the system is in mechanical resonance. Pure gravity waves propagate at frequencies below the range of the flexural gravity waves. The results presented in this paper suggest that at small wave amplitudes, flexural gravity waves predominate, while at large amplitudes pure gravity waves predominate.

Long period waves of the type identified here as pure gravity waves have been observed experimentally (Hunkins, 1962) and are described in the last section. Whether the modes switch from flexural to gravity waves as the amplitude increases beyond some critical value needs to be determined experimentally.

However, the experimental evidence, albeit limited, suggests that regardless of whether the wave modes switch in frequency, the observed increase in long period wave amplitudes with increasing stress indicates that as the stress increases, the attenuation decreases. This result is interpreted as experimental support for the theoretical conclusions presented above. If the waves in the ice sheet do indeed behave in this manner, sea-wave measurements would provide a simple means of determining when high stress levels (or levels above some critical value) exist in the Arctic sea ice. Wave measurements might be employed as an early warning of high stress against man-made structures in or near sea ice.

SECTION 3

Distributed Stresses in Landfast Ice

by

Lewis H. Shapiro

In the last annual report of this project, a description was given of two episodes in which the landfast ice sheet was driven toward the shore at Barrow during break-up, resulting in overriding of the beach and formation of pressure ridges along the shoreline. The first of these occurred in July, 1975, and the second in June, 1976. In both instances, the ice along about 5 km of the shore overrode the beach for various distances. Within this area, local examples of failure of the ice in compression and in buckling were noted, but over most of the beach, the movements caused only override and subsequent ridging or piling. A cross-section through a typical ridged area is shown in Figure 5.

The sites of failure of the ice in compression and in buckling occurred in areas where the magnitudes of the stresses in the ice sheet could reach relatively high values. It is obvious that these conditions are anomalous and result from some restriction in the free movement of the ice sheet. The limiting local stress values in such situations is simply the strength of the ice sheet in the relevant failure mode which, in turn, is a function of the geometry of the feature impeding the movement and of the interaction proper. Of interest also however, is the distributed force at a distance from the zone of interaction, which is responsible for the movement. This value provides the boundary conditions for calculation of stresses transmitted by the ice to features of known geometry, such as offshore structures.

The observations of the beach ridges noted above provide the basis for two independent calculations of the magnitude of the driving forces. These are described below and it is shown that the agreement is surprisingly good, and indicates that distributed stresses were in the range of 10 to 50 kPa (i.e. up to about 10 psi).

The simplest method of estimating the distributed force is based upon measurements of the distance that the leading edge of the ice sheet was driven up the beach prior to the initiation of ridging. The force required to accomplish this is simply

$$F = w(\sin s + f \cos s) \quad (1)$$

where w is the weight of the ice sheet which is entirely out of the water and on the beach, s is the slope of the beach, and f is the coefficient of friction between the ice and the beach. Note that the part of the ice sheet in contact with the beach, though still partially in the water, is not considered. In addition, the effect of buoyancy in reducing the effective weight of the lower end of the ice sheet on the beach (i.e., some of the load would be supported by the vertical shear stress between the floating and grounded ice) has also been neglected. These effects operate in opposite senses, and would therefore tend to cancel.

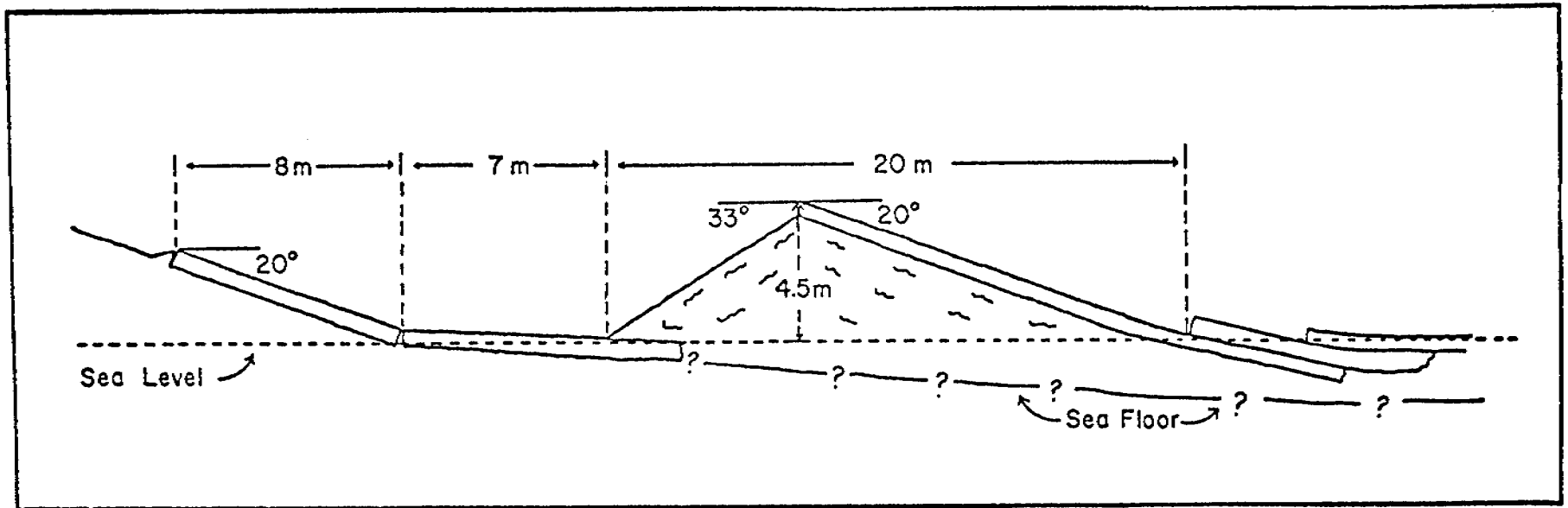


Figure 5

The parameters w and s are readily obtained for any particular case, but an appropriate value of f is less certain. Accordingly, a large-scale experiment was conducted at Barrow in June, 1977 in which two large slabs of ice were cut from the ice sheet along the shore, and dragged along the beach by a bulldozer. The dimensions of the blocks were measured and several density determinations were made so the weights could be calculated. These were 12,028 kg, and 10,597 kg. A dynamometer was placed in the cable between the bulldozer and the block being dragged, and the magnitudes of the forces required to move the block were recorded by an observer.

Both blocks were approximately rectangular in plan, with surface areas 2.7×4.3 m and 3.1×2.7 m, and a thickness of 1.2 m. The leading edge of the larger block was rounded, so that it tended to ride up over the beach gravel with minimal plowing. In contrast, the square front of the second block did tend to plow, but there is no apparent difference in the results for the two blocks. This is not unexpected, however, because of the low shear strength of the unconfined and unconsolidated beach gravels over which the ice was moved.

A total of 51 separate measurements were made on the two blocks. In each case, the force required to initiate movement was recorded, from which the coefficient of static friction was later calculated. Once moving, the block was dragged a distance of about 2 m, during which time the dial face of the dynamometer was continually observed. An average value of the force developed during this time was estimated based upon the range indicated on the dial, and used for calculation of the coefficient of kinetic friction. Note that during movement, the force ranged through about $\pm 20\%$ of the value recorded on any individual test.

On the first day of testing, both blocks were dragged up the 18° slope of the beach in 2 m increments. On the second day, one of the blocks was dragged parallel to the beach. In Figure 6, the results of the calculations of f for all tests are plotted against the sequential test number. These suggest a slight decrease in the value of f for tests on the second day, which is probably due to a combination of weight loss of the block through melting and smoothing of the bottom of the block during dragging. However, the differences do not appear to be significant.

Before applying equation (1), the question of whether f is to be taken as the kinetic or static friction must be considered. If the movement of the ice up the beach is considered to occur as a continuous glide, then kinetic friction could be used with the assumption that the movement ceases when the force resisting the displacement exactly balances the driving force. However, observations indicate that the movement of the ice up the beach occurs as a series of short pulses separated by intervals of no movement. Thus, resisting forces associated with static friction must be overcome for motion to occur, and the force required to cause motion from rest, at the farthest advance of the ice up the beach, represents an upper limit of applied forces during any one sequence of advances. It is this hypothetical force, which is not reached, which is calculated below. It is also of interest to consider that failure of the advancing ice sheet and subsequent ridging or piling along the beach, occurred at force levels which were too low to cause further advance of the ice sheet up the beach.

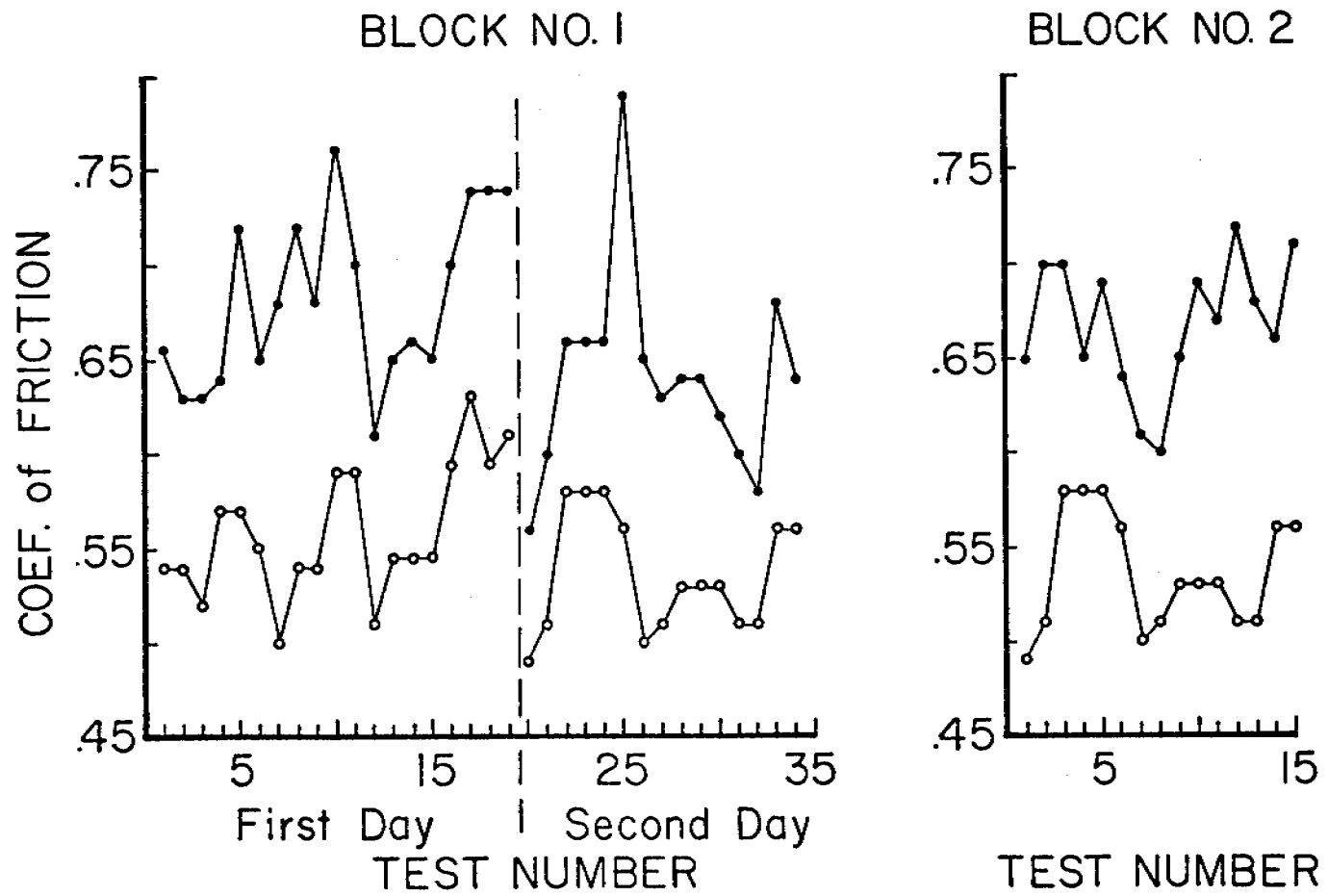


Figure 6

In areas along the beach where ridging occurred, the maximum advance of the ice sheet prior to failure was about 10 m at a location where the beach slope was 20°. The force required to cause additional motion up the beach can be calculated as 85.7 kPa (12.4 psi). The maximum advance noted was 12 m on a beach sloping at 6°. However, in that area, the ice sheet was in contact with the sea floor for a distance of 30 m from the water's edge. Considering the effect of buoyancy to be linear out to 30 m (i.e. 1 m depth 30 m from shore) equation (1) gives a stress of .17 MPa (24.6 psi) for the upper limit. This implies that failure leading to ridging may have resulted from bending stresses arising from the required flexing of the ice from the horizontal up the steeper beaches, because these stress values are well below the anticipated buckling strength of the ice.

It should be noted that the values calculated above apply to local areas along the beach and are not typical of the true distributed force when the term is taken to mean the average force transmitted through a large cross-section of the ice sheet. However, they may be representative of the force across segments of the beach up to about .5 km, a figure which is based upon the spacing between major fractures in the ice sheet normal to the shoreline. In this context, it is noteworthy that the segment of the ice sheet which was driven 12 m up the beach was adjacent to another large ice sheet which was not advanced far enough to reach the beach. As a general average, observations indicate that typical values of beach slope and ice advance are about 15° and 4 m respectively. This corresponds to a force of about 30 kPa (4.5 psi) which might be more representative of the distributed force along the seaward edge of the landfast ice sheet.

A second estimate of the forces active during this episode of ice advance can be obtained by consideration of the force levels required to do the work necessary to build the ridges. For this purpose, the geometric model of a floating pressure ridge developed by Parmerter and Coon (1973) can be modified to account for the case when a ridge is grounded instead of free-floating. The derivation closely follows the method in that work. The starting point is the model shown in Figure 7, with dimensions considered to be constant along the ridge. The volume of the ridge per unit length is given by

$$V = \frac{H_I^2}{\tan \theta} + \frac{D_I^2}{\tan \phi} \quad ,$$

and the length l is

$$l = \frac{D_I}{\tan \phi} - \frac{H_I}{\tan \theta} \quad .$$

Now, let the ridge be grounded in water of depth D_g and then continue to grow from that point with the assumptions that the symmetry is maintained and that the length l is constant. The cross-section then assumes the form shown in Figure 8. The volume in this case is given by

$$V_g = \frac{H_g^2}{\tan \theta} + \frac{2 D_g (H_g - H_I)}{\tan \theta} + \frac{D_g^2}{\tan \phi} \quad . \quad (2)$$

Then, if ρ_r is the mass density of the ridge and g the acceleration of gravity, the gravitational potential energy of the grounded ridge is

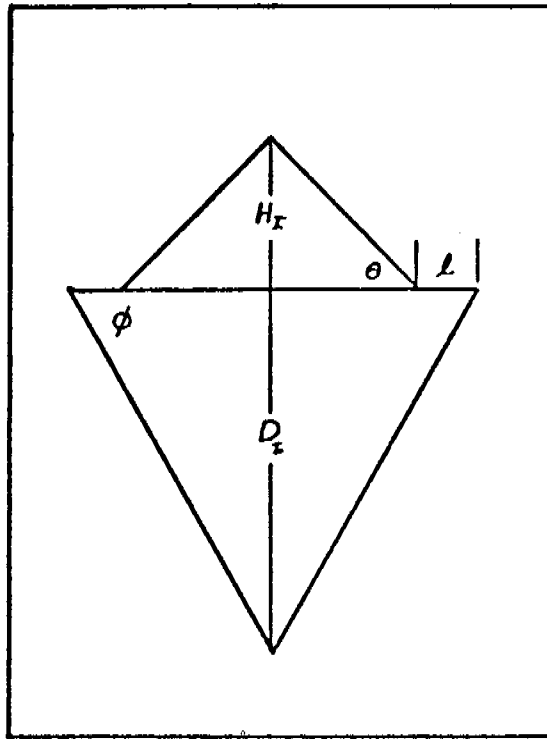


Figure 7

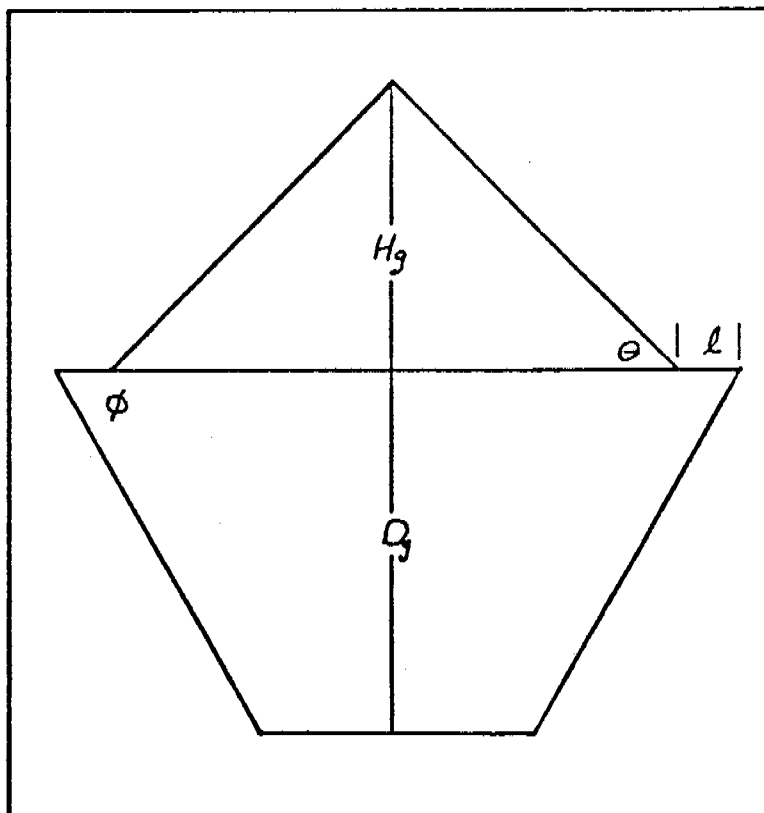


Figure 8

$$E = \frac{\rho_r g}{3 \tan \theta} H_g^3 + (\rho_w - \rho_i) \frac{\rho_r}{\rho_i} g \left[\frac{D_g^2}{2 \tan \theta} (H_g - H_I) + \frac{D_g^3}{3 \tan \theta} \right]. \quad (3)$$

The work required to produce this potential energy is FU , where F is the average force necessary to move the advancing ice sheet a distance U . U , in turn is determined by considering the distance through which an ice sheet of a given thickness must be moved in order to supply the ice needed to build a ridge of a given volume. Thus, for an increment of movement dU , the volume of the ridge is increased by $\frac{\rho_i}{\rho_r} t dU$. Equating this to the derivative of equation (2), noting that D_g is constant, and solving for dH_g then gives

$$dH_g = \frac{\rho_i t}{2\rho_r} \frac{\tan \theta}{(H + D_g)} dU \quad (4)$$

The increment in gravitational potential energy with ridge height is the derivative of equation (3) with respect to H_g . Performing this and substituting from equation (4) gives an expression for normal force per unit length of ridge as a function of ridge height, depth of grounding and ice thickness;

$$F = \frac{gt}{2(H + D)} [\rho_i H^2 + (\rho_w - \rho_i) D^2] \quad (5)$$

For the example considered here, a value of 3.5 m is probably representative of the average height of the ridges along that portion of the beach where ridging occurred. Then, using the values $\rho_i = 900 \text{ kg/m}^3$ and $\rho_w = 1.1 \times 10^3 \text{ kg/m}^3$, a 3.5 m ridge formed of ice 1 m thick required a stress^w of 15.4 kPa (2.2 psi) for grounding at the beach where $D = 0$. For $D = 1$ m the required stress drops to 12.1 kPa (1.75 psi) and for $D = 2$, the result is 10.2 kPa (1.48 psi). Finally, the stress required to build the highest pile in the area (4.5 m) gives, for $D = 0$, 19.9 kPa (2.9 psi).

The forces required to form the observed ridges, as calculated from the assumed ridge geometry, are thus found to be comparable to those calculated by Parmeter and Coon (1973) from the free-floating ridge model, and somewhat lower than those indicated from consideration of the force required to drive the ice sheet up the beach. This result is consistent with observations of the sequence of events during movement episodes described, in which no ridging or piling occurred until the movement of the ice up the beach was complete.

It is also of interest to note that numerous blocks of multi-year ice of various sizes, which were grounded throughout the landfast ice sheet were displaced along with the ice sheet, with no indication of differential movement. Further, this is also true of the first year ridges which formed the seaward boundary of the landfast ice. The latter, in fact, moved as a unit along a front several kilometers wide, so that it could obviously not withstand the distributed forces calculated above. The force against any particular grounded block which moved could be calculated if the geometry of the contact area between the block and the surrounding ice sheet were known, and this would provide an upper limit for the strength of the bond between these blocks and the sea floor. However, melting had advanced significantly before the movements occurred, and the blocks had floated higher, further reducing the strength at the boundary with the sea floor. Thus, the importance of such a calculation is questionable.

The results of the calculations above for the distributed stresses are consistent with the stresses which might be anticipated as resulting from moderate winds with fetches on the order of tens of kilometers. In addition, Nelson, et. al., (1978 in press) monitored the stress in landfast ice outside the barrier islands north of Prudhoe Bay during the spring of 1976, and, based upon these results, suggested an upper limit to the distributed stress along the pack ice-landfast ice boundary of about .21 MPa (30 psi). This compares well with the stresses calculated above.

VIII. CONCLUSIONS

(1) Two types of gravity waves, a flexural wave and a pure gravity wave, have been identified as traveling in the ice-water system. The first is confined to an infinite set of frequencies near, but below the frequency at which the system is in mechanical resonance. The second mode travels at frequencies below the range of the flexural gravity waves. Experimental results support the theory.

(2) The type of wave which propagates may depend upon the amplitude of vibration, with the flexural wave predominating at small amplitudes and pure gravity waves at large amplitudes. Further work utilizing viscoelastic theory, needed to complete the study, is planned as the next phase of the theoretical study. Experimental work is also needed.

(3) There is a possibility that the change in mode from one wave type to the other may occur at some critical value of the amplitude, which in turn is stress-dependent. If verified experimentally, this would provide a basis for an effective system of anticipating the development of high stresses in the ice sheet.

(4) The study of the distributed stresses in the landfast ice sheet at Barrow associated with movement during break-up gives results which are consistent with those of Nelson et. al., (1978, in press), these suggest that a value of about 0.2 MPa or 30 psi, represents a conservative upper limit for the magnitude of the distributed stress across the boundary between the landfast ice sheet and the adjacent pack ice.

IX. SUMMARY OF 4TH QUARTER ACTIVITIES

A. Results

The results of all 4th quarter activities are included in the studies described above.

B. Milestone Chart

Installation of tide gauge and stress transducer array scheduled for the 4th quarter was not accomplished because of problems in acquiring the instrumentation. However, it is still planned that the tide gauge will be installed in time to monitor break-up motions of the ice sheet.

Other items on the milestone chart of the original proposal are unchanged.

REFERENCES

- | | | |
|--|------|---|
| Ewing, M. and A. P. Crary | 1934 | <u>Physics</u> , <u>5</u> , 181. |
| Ewing, W. M., W. S. Jardetsky,
and F. Press | 1957 | <u>Elastic Waves in Layered Media</u> ,
McGraw-Hill, New York. |
| Hunkins, K. | 1962 | <u>J. Geophys. Res.</u> , <u>67</u> , 2477. |
| Jaeger, L. G. | 1964 | <u>Elementary Theory of Elastic Plates</u> ,
McMillan, New York. |
| Jaeger, L. G. | 1964 | <u>Elementary Theory of Elastic Plates</u> ,
MacMillan, New York. |
| Lamb | 1945 | <u>Hydrodynamics</u> , Dover, New York. |
| Melsa, J. L.
and D. G. Schultz | 1969 | <u>Linear Control Systems</u> , McGraw Hill,
New York. |
| Meyer, E. and E.-G. Neumann | 1972 | <u>Physical and Applied Acoustics</u> ,
Academic Press, New York. |
| Parmarter, R. and M. Coon | 1973 | Mechanical models of ridging in the
Arctic sea ice cover, AIDJEX Bull.,
19, 59-112. |
| Skudrzyk, E. | 1968 | <u>Simple and Complex Vibratory Systems</u> ,
Pennsylvania State University Press,
University Park. |
| Stoker | 1957 | <u>Water Waves</u> , Interscience, New York. |
| Wadhams, P. | 1973 | <u>J. Geophys. Res.</u> , <u>78</u> , 3552. |

ADF&G HABITAT LIBRARY



32345000066218